Universidad de GRANADA
Escuela de Doctorado de Ciencias, Tecnologías e Ingenierías
Programa de Doctorado en Física y Ciencias del Espacio

Electron Thermal Runaway in Atmospheric Electrified Gases

a microscopic approach

Anthony Schmalzried

Instituto de Astrofísica de Andalucía

Under the supervision of

Dr. Alejandro Luque Estepa
Dr. Nikolai G. Lehtinen

A dissertation submitted as a partial requisite to the fulfilment of the degree of

Philosophiæ Doctor (PhD)

August, 2023

Thesis supervisors

Dr. Alejandro Luque Estepa

Dr. Nikolai G. Lehtinen

Tribunal

Presidenta :

Dra. María Rosario González Ferez
Universidad de Granada

Secretaria :

Dra. Marta Anguiano Millán
Universidad de Granada

Reviewer :

Dr. Christoph Köhn
Danmarks Tekniske Universitet

Reviewer :

Dr. Sébastien Célestin
Université d'Orléans

Reviewer :

Dr. Vincenzo Laporta
Istituto per la Scienza e la Tecnologia dei Plasmi

Examination Date : 30$^{\text{th}}$ of October 2023

August, 2023

Contents

Summary

In recent years, electric discharges have been found to be prolific sources of high-energy radiation [2, 252, 267]. In particular, terrestrial gamma ray flashes are observed in correlation to lightning activity [725] and bursts of X-rays are measured in experiments with laboratory sparks [517]. The gamma/X-ray photons are produced from Bremsstrahlung (braking radiation) of fast electrons scattering from atomic nuclei present in the vicinity of the discharge. The fast electrons may themselves either be spawned by cosmic radiation or accelerated in very intense and localised electric fields in the discharge.

The latter mechanism (acceleration) is the one studied in this thesis and denominated as "thermal electron runaway". In the current state of knowledge, it poses many challenges to our understanding of discharges. For instance, the fluence of X-rays (number of photons traversing a unit area) surpasses the one predicted by current models of thermal runaway in discharges. Concretely, the probability of accelerating a thermal electron to high energies, where it radiates through bremsstrahlung, is found to be too low at typical electric fields encountered at the head of streamers (self-sustained ionisation waves). Conversely, the plausibility of very high electric fields which enable thermal runaway is uncertain.

From the modelling perspective, the abundance of thermal runaway electrons has been found to depend strongly on the model chosen to represent electron scattering with molecules [169, 218, 677]. In particular, in a comparative study [811], we showed that various models of elastic scattering give significantly different distributions of high-energy electrons.

Hence, we identify two necessities precluding a sound study of thermal runaway:

1. Find a physical environment, composed of the electric field and the state of air, that fosters the conditions which enable thermal runaway. Then, in this environment, be able to model events of extreme rarity, down to arbitrarily low probabilities.

2. Possess a highly reliable and accurate modelling of electron-molecule collisions, consistent throughout a broad energy range: from zero to several MeV.

The first necessity is answered by the first part of the thesis where we investigate the abundance of high-energy electrons obtained in Monte Carlo simulations under various conditions of the electric field, the air composition and temperature. In a second article [813], we adapted the Monte Carlo importance sampling methodology into a "compaction" algorithm which enhances the statistics of high-energy electrons to an arbitrarily low probability of occurrence, however, at the cost of deteriorating the resolution of low-energy electrons.

The second necessity is addressed in the second part of the thesis, where an almost complete set of electron-molecule cross sections has been assembled independently from the databases that are currently in use. The assembly combined an exhaustive gathering (up to 2022) of experimental cross sections, accurate quantum mechanical calculations and simple analytical representations. The modelling of elastic scattering is based on our third article [812] for calculating differential cross sections of electrons scattering elastically from diatomic molecules.

Furthermore, this thesis also contains a third part which supplements the first two parts with a thorough documentation of the process for constructing the new cross section database. It provides an overview of techniques for fitting experimental data and comparisons of various electron-molecule cross section databases currently in use.

So far, most of the literature has focussed on plausible mechanisms which lead to formation of intense electric fields in ionisation fronts. In this thesis, we turned toward a less frequented perspective by considering the change in chemical composition of air due to the discharge activity preceding thermal runaway. Contrary to the wont applied to dissertations in the sciences, this thesis is an original work which does not include text extracted from the publications written during the doctoral program. It is therefore not to be regarded as a reformulation of the content of these articles [811–813], but as the prime continuation thereof.

With the wherewithal that we developed – the compaction algorithm and the new set of cross sections – we have probed preliminarily the phenomenon of electron thermal runaway in hitherto understudied territories; low electric fields and varying gaseous compositions. As an open conclusion, we fancy that preconditioning of the gaseous medium by streamer coronas is relevant to unveil some of the mysteries shrouding our current understanding of thermal runaway.

Publications of the present author

811. Schmalzried, Luque, "Influence of Elastic Scattering on Electron Swarm Distribution in Electrified Gases", *J. Geophys. Res.: Atmos.* **125**, e2019JD031564 (2020) (vii–xii, 32, 117, 399, 534, 546, 557).

812. Schmalzried, Luque, Lehtinen, "Combined molecular and atomic potentials for elastic cross sections of electrons scattering off diatomic molecules at intermediate energies", *Phys. Rev. A* **106**, 032813 (2022) (vii–viii, x–xii, 322, 360, 370, 372, 400, 403, 412, 563).

813. Schmalzried, Luque, Lehtinen, "Enhancing higher-energy spectral resolution for electron particle simulations in air", *Comput Phys Commun* **277**, 108366 (2022) (vii–xii, 98–99, 101–102, 104, 150, 217).

Resumen

Desde hace poco se sabe que los rayos de tormentas en la Tierra son fuentes prolíficas de radiación de alta energía [2, 252, 267]. En particular, se han observado destellos terrestres de rayos gamma, con duración de poco más de 1 ms asociados a la actividad de rayos de tormenta [725]. Así mismo se han detectado estallidos de rayos-X emitidos por chispas en laboratorios [517]. Los fotones gamma o X de estos destellos están producidos por *Bremsstrahlung* (radiación de frenado) de electrones rápidos desviados por los núcleos de los atomos presentes cerca de las descargas. Esos electrones rápidos pueden ser engendrados como productos secundarios de ionización por rayos cósmicos o bien ser acelerados desde energías más bajas en campos eléctricos en las descargas muy intensos y localizados.

Este último mecanismo (la aceleración) se conoce cómo *runaway* térmico y su estudio es el tema principal de la presente tésis. Actualmente, desconocemos la relación precisa entre estre proceso y la física de las descargas. Por ejemplo, la fluencia medida de rayos-X (número de fotones atravesando una superficie unitaria) supera las predicciones de modelos teóricos del *runaway* térmico en descargas. La probabilidad de acelerar un electron térmico hasta energías altas en las cuales empieza a irradiar por *bremsstrahlung* es demasiado baja en los campos eléctricos cerca de las cabezas de los dardos (canales de ionización llamados *streamers* en inglés). Los campos eléctricos necesarios para el *runaway* térmico son aún más altos y por tanto poco plausibles.

En los modelos físicos, la abundancia de electrones térmicos en *runaway* depende mucho de cómo se describe la dispersión de electrones por moléculas [169, 218, 677]. En particular, en un estudio comparativo [811], hemos demostrado que varios modelos de dispersión elástica dan lugar a distribuciones significativamente diferentes de electrones de alta energía.

De ahí, hemos identificado dos necesidades para dar una base sólida al estudio del *runaway* térmico:

1. Hallar un entorno físico apropiado, incluyendo el campo eléctrico y el estado del aire. Es necesario tener la capacidad del modelizar eventos de rareza extrema en este ambiente, con probabilidades arbitrariamente bajas.

2. Poseer un modelo altamente fiable y preciso de la colisiones de electrones con moléculas que sea consistente en un rango amplio de energías: desde cero hasta varios MeV.

La primera parte de la tesis da respuesta a la primera necesidad; en ella investigamos la abundancia de electrones de alta energía obtenidos en simulaciones Monte Carlo bajo varias condiciones de campo eléctrico y de composición y temperature del aire. En nuestro segundo artículo [813], adaptamos la técnica del muestreo de importancia (*importance sampling*) en simulaciones de Montecarlo para implementar un algoritmo de compactación que mejora la estadística de electrones de alta energía a cambio de deteriorar la resolución sobre electrones de baja energía.

La segunda parte de la tesis abarca la segunda necesidad. En esta parte compilamos una colección casi completa de secciones eficaces de colisión entre electrones y moléculas independiente de bases de datos actualmente usadas. Empleamos una recopilación exhaustiva hasta 2022 de

secciones eficaces experimentales, cálculos precisos de mecánica cuántica junto a representaciones analíticas sencillas. El modelado de dispersión elástica está basado en nuestro tercer artículo [812], en el que calculamos seciones eficaces diferenciales de dispersión elástica de electrones por moléculas diatómicas.

Además, la tésis contiene también una tercera parte que suplementa las dos primeras y contiene una documentación minuciosa del proceso de construcción de la nueva base de datos de secciones eficaces. Provee una reseña de técnicas de ajuste de datos experimentales y comparaciones entre varias bases de datos de secciones eficaces de colisiones entre electrones y moléculas actualmente usadas.

Hasta ahora, la mayoría de la literatura se ha centrado en vías plausibles de formación de campos eléctrico intensos en frentes de ionización. En esta tesis hemos cambiado la perspectiva hacia el efecto que conlleva un cambio en la composición química del aire debido a la actividad de descarga que precede el *runaway* térmico. La tesis extiende y completa los trabajos publicados anteriormente [811–813].

Con los medios que hemos desarrollado –el algoritmo de compactación y la nueva base de datos de secciones eficaces– hemos explorado el fenómeno de *runaway* térmico de electrones en territorios hasta ahora poco estudiados: en campos eléctricos más bajos y en composiciones gaseosas variables. Planteamos la hipótesis de que el preacondicionamiento del medio gaseoso por coronas de dardos es relevante en el proceso de *runaway* térmico.

Resumo

En lastaj jaroj, elektraj disŝarĝoj estis trovitaj esti produktivaj fontoj de alt-energia radiado [2, 252, 267]. Aparte, surteraj gamaradiaj ekbriloj estas observitaj en korelacio al fulmagado; kaj ekestoj de Rentgenradioj estas mezuritaj en eksperimentoj kun laboratoriosparkoj [517]. La gama/Rentgen-fotonoj estas produktitaj el Bremsstrahlung (bremsa radiado) de rapidaj elektronoj dispersantaj de atomkernoj ĉeestantaj en la najbareco de la disŝarĝo. La rapidaj elektronoj povas esti generitaj aŭ per kosma radiado aŭ akcelitaj en tre intensaj kaj lokalizitaj elektraj kampoj en la disŝarĝo.

Ĉi-lasta mekanismo (akcelado) estas tiu studita en ĉi tiu tezo kaj nomita “termida elektrona fuĝo”. En la nuna stato de scio, ĝi prezentas multajn defiojn al nia kompreno de disŝarĝoj. Ekzemple, la flueco de Rentgenradioj (nombro de fotonoj transirantaj unuareon) superas tiun antaŭdiritan de nunaj modeloj de termida fuĝo en disŝarĝoj. Konkrete, la probableco de akceli termikan elektronon al altaj energioj, kie ĝi radias tra bremsstrahlung, estas trovita esti tro malalta ĉe tipaj elektraj kampoj renkontitaj ĉe la kapo de fluaĵoj (mem-subtenaj jonigaj ondoj). Inverse, la kredebleco de tre altaj elektraj kampoj, kiuj ebligas termidan fuĝon, estas necerta.

De la modeliga perspektivo, la abundo de termidaj fuĝaj elektronoj dependas forte de la modelo elektita por reprezenti elektrondisperson disde molekuloj [169, 218, 677]. Aparte, en kompara studo [811], ni montris ke diversaj modeloj de elasta disperso donas signife malsamajn distribuojn de alt-energiaj elektronoj.

Tial, ni identigas du necesaĵojn malhelpadas solidan studon de termida fuĝigo:

1. Trovi fizikan medion, kunmetitan de l’ elektra kampo kaj la stato de aero, kiu krei la kondiĉojn kiuj ebligas termidan fuĝigon. Tiam, en tiu medio, povi modeli okazaĵojn de ekstrema maloftaĵo, al arbitraj malaltaj probablecoj.

2. Posedi tre fidindan kaj precizan modelon de elektrono-molekulo kolizioj, kohera ĉie energioj: de nul ĝis pluraj MeV.

La unua neceso estas respondita per la unua parto de la tezo, kie ni esploras la abundon de alt-energiaj elektronoj akiritaj en Monte Carlo simuladoj sub diversaj kondiĉoj de la elektra kampo, la aera kunmetaĵo kaj temperaturo. En dua artikolo [813], ni adaptis la Monte Carlo gravecprovaĵmetodaron en "kompaktigan" algoritmon kiu plifortigas la statistikojn de alt-energiaj elektronoj al arbitre malalta probableco de okazo, aliflanke, je la kosto de plimalbonigado de la difino de malalt-energiaj elektronoj.

La dua neceso estas traktita en la dua parto de la tezo, kie preskaŭ kompleta aro de elektron-molekulaj laŭaj sekcioj estis kunvenita sendepende de la datumbazoj nuntempe uzataj. La asembleo kombinis ĝisfundan kunvenon (ĝis 2022) de eksperimentaj laŭaj sekcioj, precizaj kvantumaj mekanikaj kalkuloj kaj simplaj analitikaj reprezentadoj. La modeligado de elasta disperso baziĝas sur nia tria artikolo [812] por kalkuli diferencialajn sekciojn de elektronoj dispersantaj elaste el diatomaj molekuloj.

Cetere, ĉi tiu tezo ankaŭ enhavas trian parton, kiu kompletigas la unuajn dua partojn per ĝisfunda dokumentado de la procezo por konstrui la novan laŭan sekcian datumbazon. Ĝi disponigas superrigardon de teknikoj por konvenado de eksperimentaj datumoj kaj komparoj de diversaj elektron-molekulaj laŭaj sekciaj datumbazoj nuntempe uzataj.

Ĝis nun, la plej granda parto de la literaturo temis kredindajn mekanismojn, kiuj kondukas al formado de intensaj elektraj kampoj en jonigaj frontoj. En tiu tezo, ni turnis nin al malpli vizitata perspektivo konsiderante la ŝanĝon en la kemia kunmetaĵo de aero pro la disŝarĝa agado antaŭ termida fuĝo. Kontraŭe al la kutimo aplikita al disertacioj en la sciencoj, ĉi tiu tezo estas tute originala verko sendependa de la artikoloj publikigitaj ĝis nun dum la doktora programo. Tial ĝi ne devas esti rigardata kiel reformulado de la laboro realigita en tiuj artikoloj [811–813], sed kiel la ĉefa daŭrigo de ĝi.

Kun la rimedoj, kiujn ni ellaboris – la kompakta algoritmo kaj la nova aro de laŭaj sekcioj – ni sondis antaŭtempe la fenomenon de elektrona termida fuĝo en ĝis nun nesufiĉe studitaj teritorioj; malaltaj elektraj kampoj kaj ŝanĝadaj gasaj kunmetaĵoj. Aperta konklude, ni imagas, ke antaŭkondiĉigo de la gasa medio per fluaĵaj coronoj estas temrilata por malkaŝi iujn el la misteroj, kiuj kovras nian nunan komprenon pri termida fuĝado.

Preface: how to read this thesis?

The research conducted in this thesis was originally motivated by helping to understand the mechanism, known as electron thermal runaway, whereby high-energy electrons are being produced from the acceleration of free electrons in electric discharges in the atmosphere.

As often happens in scientific investigation, during the process of obtaining results, we realised that the data upon which our modelling relied were outdated and required thorough revision. After a careful consideration, we took the decision to undertake the revision ourselves despite the risks involved of not succeeding.

The creation of a new database entailed the extension of the thesis to its present length*. In exchange, this enabled us (i) to establish more steady foundations for the investigation of electron thermal runaway in discharges and (ii) to improve the applicability of simple models to the representation of electron-molecule collisions useful for modelling weakly ionised plasmas.

Structure of the thesis

The present thesis is structured into three parts each composed of six chapters.

- Part I investigates the main objective of the thesis about electron thermal runaway in atmospheric gases.
- Part II sets the foundations for revising the cross sections for collisions between electrons and molecules.
- Part III gathers and complements the research in part II in order to provide data required as input to part I.

The first two parts follow a parallel structure of 6 chapters.

i) Context. The first chapters are an introduction into the topic and motivation in relation to the thesis.

I. chapter 1 is a phenomenological introduction to electric discharges, including high-energy processes, occurring in the atmosphere.

II. chapter 7 introduces basic notions of electron scattering with molecules, how they are measured and calculated.

ii) Model. The second chapters introduce the theoretical background used to construct the physical model.

*For an efficient browsing through the hyperlinks embedded in the electronic version of the thesis, please check your `.pdf` reader's navigation shortcuts. For many readers, the shortcut is `Alt` + ←, → to quickly switch back and forth.

I. chapter 2 explains how electrons are modelled in weakly ionised plasmas, particularly in the framework of Monte Carlo simulations.

II. chapter 8 presents the modelling of electron scattering off molecules from the quantum mechanical perspective based on the optical potential approach.

iii) Numeric. The third chapters present the numerical methods required to implement the physical models.

I. chapter 3 regroups the methods used by Monte Carlo simulations of electron swarms.

II. chapter 9 explains how to calculate differential cross sections from an optical potential.

iv) Critique. The fourth chapters contain information about difficulties encountered in the construction and implementation of the models used.

I. chapter 4 is a collection of points that require attention when modelling electron swarms in gases from the Monte Carlo approach and how to assess the validity of the simulations.

II. chapter 10 is an extended discussion and comparison of approximations and semi-empirical models used to calculate electron-molecule cross sections in the optical potential approach.

v) Results. The fifth chapters present the results obtained from the application of the model and its numerical implementation after it has been examined in the preceding chapter.

I. chapter 5 presents Monte Carlo simulations of electrons in gases and a specific emphasis on the production of high-energy electrons through thermal runaway acceleration.

II. chapter 11 assembles the necessary information (theoretical, experimental) in order to produce concrete electron-molecule cross sections classified according to their reaction channel.

vi) Discussion. The sixth and last chapters provide an overview of the work done, highlight the main points found in the results chapters and propose perspectives for future investigation.

I. chapter 6 connects and comments the results obtained for electron thermal runaway in relation to the context described in the first chapter.

II. chapter 12 summarises the results obtained of electron-molecule cross sections for each atmospheric species: N_2, O_2, NO, Ar, O and N.

The structure of the third part is different.

Appendices. The first two chapters are appendices to the work done in chapter 11.

- chapter 13 is a detailed presentation of how we fitted analytical expressions to experimental data.
- chapter 14 is a collection of analytical formulae obtained in the first Born approximation for representing elastic scattering of electrons from molecules at high energies.

Database. The next two chapters present the newly constructed database of cross sections.

- chapter 15 explains how the database was created from the information in chapter 11 and how to use it.

- chapter 16 compares the new database to other existing databases hosted on LXCat and to experimental data.

Comments. The last two chapters are comments of the author about the thesis.

- chapter 17 is a comment on the importance of having an international language for science.
- chapter 18 is a personal comment about the challenges and issues encountered during the thesis, concluded by acknowledgements.

Readers that are interested in the new material can refer to the lists in the conclusion sections 6.3 and 12.2, or directly consult:

- the particle compaction methodology that we developed in section 3.3.2,
- the elastic differential cross sections which we obtained in section 11.1,
- the analytical impact excitation cross sections in section 11.4.2 and the ensuing sections,
- the binary-encounter-dipole model for impact ionisation which we improved in section 11.5.3,
- the revised database in chapter 15,
- and of course, the chapter about results of electron swarms and runaway electrons in chapter 5.

Finally, users of the new database can directly skip to section 15.2, where the table 15.1 presents an overview of how the database was constructed.

Before plunging into the reading, in the following sections, the readers can acquaint themselves with the notation and abbreviations that we use throughout the thesis. An overview specific to the atomic system of units is given at the end of chapter 7.

The electronic version with hyperlinks for equations, sections, tables, figures and citations with embedded DOI links in the bibliography may be downloaded in the link:

`https://doi.org/10.5281/zenodo.8370074`

also reachable by scanning the QR code to the right.

Notation

The mathematical symbols typewritten in this thesis try to follow the guidelines of the revised standard ISO 80000-2 [432]. In particular the usage of *italic* versus roman font is reminded below:

Italic font is reserved for:

- ✓ physical variables or constants (e.g. x, y, z for space coordinates or c, $\hbar$, e for speed of light in vacuum, Planck's reduced constant or the elementary charge)
- ✓ subscripts which relate either to a continuous or discrete variable/quantity. Thus the molecular polarisability may be written as α_R signifying its parametric dependence on the interatomic distance R of molecular hydrogen H_2. The spatial components of a vector p_x, p_y, p_z to denote the projections in each of the $\vec{x}, \vec{y}, \vec{z}$ directions. All indexes i, n, m that count objects in a sum or that designate elements (A_{ij}) in a tensor/matrix shall be written in italic as well.

Roman upright font is used for a wide range of cases:

- ✓ International units: meters m, nano-seconds ns, kelvins K, Rydbergs Ryd, etc.
- ✓ Abbreviations of chemical elements and excited states
- ✓ Mathematical constants: notably Euler's constant – e – root of the natural logarithm, and the imaginary number – i.
- ✓ Mathematical operators, in particular the differential $\mathrm{d}x$ instead of carelessly dx; and named functions : 'sin' for sine, 'ln' for natural logarithm and '$\mathrm{J}_n(r)$' for Bessel's function of the first kind and of degree n.
- ✓ subscripts of variables or a quantities that refer to an abbreviation, to a concept or a notion. As an example, the energy in the *relative* frame is typewritten ε_{r} not $\not{\varepsilon}_r$, or the *ionisation* cross section is σ_{i} not $\not{\sigma}_i$.

This prescription was transgressed in the particular case of the velocity – v. I chose to preserve a consistent typewriting between the velocity as a vector, its norm and components. Thus, if $\mathbf{v}$ represents the velocity (vector) of a particle:

$$\|\mathbf{v}\| = \mathrm{v} \quad \text{but not :} \not{\mathrm{v}},$$
$$\mathbf{v} \cdot \boldsymbol{E} = \mathrm{v}_E \quad \text{but not :} \not{\mathrm{v}_E}.$$

This is because the 'italic' font for v looks too much like an 'upsilon' υ. I decided to reserve $v = 0, 1..$ only for the vibrational excitation quantum of diatomic molecules.

Next, I reserve some special meaning to accents:

$\hat{\mathbf{q}}$: a unit vector → $\|\hat{\mathbf{q}}\| = 1$

$\hat{a}$: a unit complex number → $|\hat{a}| = 1$

$\acute{s}(x)$: a cumulative integral (can be normalised) → $\acute{s}(x) = \dfrac{\int_{x_0}^{x} \frac{\mathrm{d}\sigma}{\mathrm{d}x}\,\mathrm{d}x}{\left(\int_{x_0}^{x_1} \frac{\mathrm{d}\sigma}{\mathrm{d}x}\,\mathrm{d}x\right)}$ with $x \in [x_0, x_1]$

$\bar{s}$: an average or a magnitude factor[#] → $\bar{s}(x) = \dfrac{\int_{y_0}^{y_1} s(x,y) f(y)\,\mathrm{d}y}{\int_{y_0}^{y_1} f(y)\,\mathrm{d}y}$

$\langle s \rangle$: an average over a discrete set or continuous space → $\langle s \rangle = \dfrac{1}{N}\sum_{i=1}^{N} s_i$

$\dot{s}(x)$: a reference, an accurate estimation of a quantity

$\tilde{s}(x)$: an approximation, correction, perturbation, fluctuation e.g. : $\tilde{s}(x)$ could be $\dot{s}(x) - \bar{s}$

Abbreviations

Part I

Acronyms

* EEDF : electron energy distribution function
* MC : Monte Carlo
  - PIC : particle-in-cell
* RREA : relativistic runaway electron avalanche
* TEB : terrestrial electron beam
* TGF : terrestrial gamma-ray flash
* VLF : very low frequency

Indexes

□ 'a' or 'att' : attachment

□ 'b' : binary

□ 'c' : critical

□ '*c*' : collision (index)

□ 'd' : drift

□ 'e' : electron

Part II

Acronyms

* a.u. : atomic units
* BED : binary encounter dipole (model)
* CS : cross section
  - DCS : differential cross section
  - SDCS : singly differential CS
  - DDCS : doubly differential CS
  - TDCS : triply differential CS
  - ICS : integral cross section
  - MTCS : momentum-transfer CS
* DFT : density functional theory
  - KDF : kinetic density formulation
* EELS : electron energy loss spectrum
* FCF : Franck-Condon factor
* FEG : free electron gas
* HF : Hartree-Fock (variational method)
* MERT : modified effective range theory

[#]This could either be a constant or a function if the average is performed on a sub-dimensional space of a multi-variable function

- □ 'exc' : excitation
  - 'diss' : dissociation
  - 'el' or 'e' : elastic
  - 'in' : inelastic
  - 'elt' : electronic
  - 'rot' : rotational
  - 'vib' : vibrational
- □ 'g' : gas
- □ 'i' or 'ion' : ionisation
- □ 'k' : breakdown
- □ 'm' : momentum transfer or measurement
- □ 'r' : runaway
- □ 's' : super-electron (or streamer)
- □ 'th' : threshold
- □ 'tot' : total
- □ ′ (prime) : centre-of-mass frame
- □ '+' : posterior to a collision
- □ '-' : prior to a collision
- □ '0' : initial (also before a collision)
- □ '1' : primary (in impact ionisation)
- □ '2' : secondary (in impact ionisation)
- □ '*' : target (compaction)
- □ '∞' : nominal/stationary (compaction)

* MPSA : molecular phase shift analysis
* OS : oscillator strength
  - OOS : optical oscillator strength
  - DOS : dipole oscillator strength
  - GOS : generalised oscillator strength
* O_2 spectrum :
  - HPC : Herzberg pseudo-continuum
  - SR : Schumann-Runge (continuum)
  - LB : longest band
  - 2B : second band
* PCI : post-collision interaction (after ionisation)
* PWBA : plane-wave (or first) Born approximation
  - IAM : independent atom model
  - SR : screened Rutherford (differential cross section)
* RBEB[a] : relativistic binary encounter Bethe
* SC : semi-classical
  - SCF : semi-classical Fermi (free electron gas)

Indexes

- 'd' : dipole
- 'r' : relative (centre of mass)
- 're' : residual elastic
- 'rm' : residual momentum transfer
- 'rd' : residual dissociation

[a] also RBEQ = RBEB with a Q parameter

Glossary

Part I

Einstein coefficient (A^{nm}) ◁
electric acceleration (eE/m_e)

angle between electric and magnetic fields
Townsend's first ionisation coeff. : α_i ◁
("magnetic field") magnetic flux density
impact parameter
magneto-electrostatic drift velocity : β_d ◁
speed of light ≡ 299 792 458 m/s
$\parallel \mathbf{E} : D_\parallel$, $\perp \mathbf{E} : D_\perp$ } swarm diffusion coeff.

duration Δt or distance Δr ▷
small timestep (δt), energy interval ($\delta\varepsilon$) ▷
electric field
elementary charge
Euler's number
excitation energy
electron kinetic energy
average friction force
energy distr. func. : f_ε, velocity distr. : f_v, phase space : $f(\mathbf{r},\mathbf{v},t)$ } distribution
azimuthal angle in the plane $\perp \mathbf{E}$
...
azimuthal angle
index for a gas species □
Lorentz relativistic factor

predissociation ratio : η_pd ◁
angle between velocity and electric field
...
...
scaling energy in the first Born approx.
Boltzmann's constant : k_B ◁

distance travelled by an electron

electron mean free path : $\bar{\lambda}$ ◁
Coulomb logarithm : Λ_c ◁
electron's mass
electron's mass
mass of a molecule/atom

Part II

A scattering length
a atomic radius in $\exp(-r/a)$
▷ a_0 : atomic Bohr radius
α ≈ 0.007 297 35 : fine structure constant
▷ α_d : molecular dipole polarisability
B binding energy in an atomic orbital (B_o)
b ...
β e^- velocity in relativistic units $\beta = \mathrm{v}/c$
c $= 1/\alpha$ a.u. ≈ 137.036 a.u.
D static dipole moment
d forbiddance degree in $\sigma \propto 1/\varepsilon^d$
Δ ◁ energy difference $\Delta\mathcal{E}$
δ □ δ_ℓ : phase shift bound to the ℓ wave
E ...
e ≡ $1.602\,176\,634 \times 10^{-19}$ C = 1 a.u.
e ≈ 2.718 282
$\mathcal{E}$ energy of a system, a state
ε ...
F generalised oscillator strength
f optical oscillator strength
scattering amplitude
ϕ atomic orbital wavefunction
▷ ϕ_B : Coulomb interference term
φ rotating the scattering plane
g degeneracy degree of a state
γ $= 1/\sqrt{1-(\mathrm{v}/c)^2}$
Γ resonance width (energy)
H Hamiltonian operator
η screening parameter $\eta = 1/(2ka)^2$
χ polar angle from the internuclear axis
I ionisation potential
J quantum number for rotational excitation
K reactance matrix
k electron wave number
L ▷ $\mathbf{L}$: orbital angular momentum operator
$\mathcal{L}$ e^--molecule total angular momentum
l harmonic degree of a molecular potential
ℓ e^- angular momentum quantum number
λ decay rate in Yukawa/Slater potentials
Λ projection of $\mathbf{L}$ on the internuclear axis
m angular momentum projection on the z-axis
▷ $m_\mathrm{e} \approx 9.109\,38 \times 10^{-31}$ kg
M projection of rotational angular momentum

	$\mathcal{M}$	z-projection of total angular momentum
cosine of scattering angle $\cos\theta$	μ	e$^-$ reduced mass $\mu = m_e M/(M+m_e)$
electron mobility : μ_e ◁		
number of electrons in a swarm : N_e ◁	N	number of electrons in a molecule/orbital
electron : n_e / gas : n_{gas} } density	n	principal quantum number in an orbital □ index for degree or order
total collision : ν_{tot} / electron avalanche : ν_e / runaway production : ν_r } rate	ν	
electron kinetic momentum	p	...
kinetic momentum of a molecule (or ion)	P	Legendre polynomial
probability	$\mathcal{P}$	...
heating rate	Q	static quadrupole moment
	q	momentum transfer in a collision
	R	internuclear separation
electron position	r	radial position
	ρ	electronic density in atoms
source term in kinetic equation	S	scattering matrix
	$\mathcal{S}$	e$^-$molecule spin
(unbiased) standard deviation	s	electron spin projection on the z-axis
cross section	σ	...
temperature	T	transition matrix
time	t	...
relaxation : τ / mean free : $\bar{\tau}$ / average runaway : τ_r } time	τ	resonance lifetime
electron scattering angle	θ	...
e$^-$ kinetic energy in a bound orbital	U	... reduced potential : $U(x) = 2V(x/k)/k^2$ / evolution operator (unitary)
	u	radial function (partial wave)
electron velocity	v	$\equiv k$ in atomic units
...	v	vibrational quantum number
molecule velocity	V	atomic/molecular potential
super-electron statistical weight	w	a weight factor $w < 1$
instance from a random uniform variable	x	position-spin coordinate $x = (\mathbf{r}, s)$
a ratio	ξ	a variable in a series
...	Z	atomic charge number
ionisation degree : ζ_i ◁	ζ	dimensionless variable used in integrals
	Ψ	total electron-molecule wavefunction
	ψ	electron scattering wavefunction
...	ω	vibrational/rotational angular frequency
...	Ω	solid angle of scattering

Part I

Electron swarms in electrified gases

Prologue

Like most scientific research conducted nowadays, it is hard, at first glance, to figure out the purpose behind a study such as "electron swarms in electrified gases". Although we are fortunate to live in a technologically developed environment to start unfurling words to defend our cause — such as laser, discharge lamps/tubes, plasma air purifiers, chemical reaction catalysers; plasma needles, bullets, beams for biomedical treatments, microelectronic ashing and etching, arc discharge prevention in electronic/electrical equipments; and then, of course, the delight of measuring gas properties derived from swarm experiments that give cross-sections, excitation, ionisation and transport coefficients; — still, in almost any application, the connection with the present study is far from obvious, even for specialists. This leaves us with the last, oldest and unrelenting purpose of science: to study natural phenomena, such as lightning. Therefore, it should not be surprising that despite all the possible industrial applications aforementioned, this thesis has been fundamentally motivated with the aim to help understanding some of the numerous mysteries about the sensational characteristics of lightning.

There are many ways in which an investigation about phenomena related to lightning could be made. With the bountiful means of the present time, we would typically combine observations with many different instruments positioned at various viewpoints: through electric field mills or antennas positioned on the ground surface just below or hundreds to thousands of kilometers from the thunderstorm activity; with local balloon and in-situ probe measurements, planes flying nearby, above or venturing inside thunderclouds; or even from very distant places such as satellites or monitors located on the ISS comfortably watching the spectacular scene from space.

Next, we would conduct experiments from small sparks in glass tubes, electrodes in laboratories to outdoor majestic discharges with massive power-voltage generators, or going as far as bridging the gap with the natural scale of lightning through rocket-triggered strikes that take advantage of the great potential difference present in thunderstorms. Then, launch numerous simulations each more sophisticated than previous ones, starting from individual electron swarms (of which this thesis covers a small part), fluid models of streamers, adding leaders, then deriving electromagnetic emission activity from electric currents, black-body radiation of heated air, molecular de-excitation, electron bremsstrahlung emission, sometimes just focussing on high-energy particles, othertimes on thermal ones, looking how this radiation provokes transient luminous events elsewhere in the atmosphere, etc. In other words, much has already been done, and much more is yet to be done, as always; not least in assembling the research into a comprehensive (and hopefully comprehensible) scientific field.

Faced with this impressive, indeed staggering amount of investigation, I would nonetheless like first to turn towards somewhere we typically look less frequently for cognitive insight about lightning : namely cultures [265]. In a world where we have access to unrivalled, accurate and reliable information from measurements and simulations, looking at how humans regard lightning through their cultural background seems naive. As it turns out, this is actually a very good start; for naiveness in science is often well rewarded.

It is needless to remind what tight link lightning and thunder has to religions and deities. Both were personified as the deeds of a supernatural being. While lightning strikes were almost invariably thought of a fiery projectile: slingshot, stone, axe, bolt; hurled to the ground or into the air, the rumbling and clashing of thunder had diverse interpretations. In northern Europe and Indian, thunder could be the rolling of a heavenly chariot ridden by the god of lightning. In Asia, it rather was the beating of drums, while in some American and African cultures it was the flapping of the wings of a giant Thunderbird whose eyes blinked to launch strokes.

The overwhelming power of thunderstorms compelled many cultures to regard gods of lightning also as sovereigns over all atmospheric phenomena including rain and wind. They ranked

among the highest positions in the vast majority of pantheons and sometimes, as in Greco-Roman mythology, the god of lightning (Zeus/Jupiter fig. 0.1) was considered the supreme leader that dispensed justice upon the world. The belief that storms, rains and strikes were wilful divine feats, inevitably led to attempts of attracting the god's favour. Rituals, offerings and often sacrifices were conducted to attract good rains in regions where harvests were at the mercy of droughts, such as in Mayan and Inca cultures. Sometimes, lightning was associated also with fertility, as in Shintoism and native American religions. The Incas even characterised intra-cloud as male lightning and cloud to ground as female, thinking the latter could somehow affect pregnancy.

The destructive capabilities of lightning strikes inspired fear and awe toward gods. As the only natural force that can be channelled into singular destinations (rocks, trees, buildings, tall pointy objects, and also people), it shouldn't come as a surprise that lightning was long believed to emerge from divine will of punishment or as ominous signs to mortals.

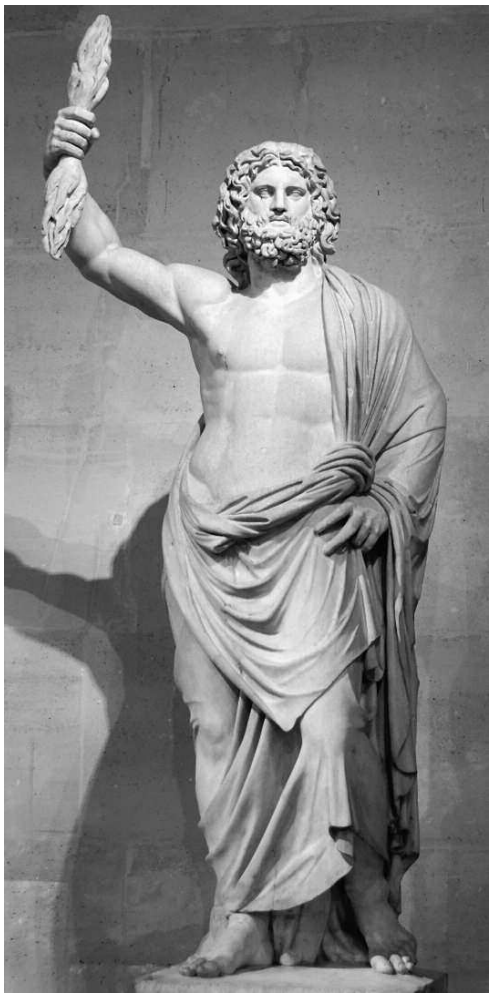

Figure 0.1: Statue of Jupiter holding a thunderbolt at the Musée du Louvre in Paris. [265, p.20]

Places struck by lightning were invariably thought as chosen or targeted by the gods. The implications of a strike were diverse. Etruscans would interpret animals and humans struck as sanctified and they would bury them on the spot. Occasionally, shrines would be erected on spots stuck by lightning. The physical damage after a strike was almost universally imputed to divine projectiles whose remains – "thunderbolts" or "thunderstones" – possessed magical protective powers. As a consequence, many fossils, crystals and prehistorically carved stone tools were misidentified as thunderbolts and carried as amulets, mounted on rooftops or door lintels, or used in rituals to ward off lightning strikes; believing that the gods had no apparent reason to strike the same spot twice.

The dilemma of recognising both the destructive and beneficial power of lightning was deformed by Christian religious crisis into a witchcraft paranoia that, notwithstanding our technologically advanced society, still persists today in some rural regions of the globe. From the fifteenth to the early eighteenth centuries, damage by lightning or storms was almost systematically imputed to some dark plotting of mortals along with the devil to take abuse of divine powers.

In modern times, although our interpretations of lightning changed drastically, our nature remains unchanged and our beliefs recycled. It is thus not unusual to be tempted by the zeitgeist thinking that lightning could or should be harvested in some way to help us overcome the foretold energy crisis. In connection with lightning hazards, fortunately no one will be accused of wizardry, tortured and burned; though damage to buildings and electrical equipment can be imputed to inadequate engineering design. More than ever, lightning (or simply electric discharges) is pictured as a spark of fertility through experimental evidence of laboratory-triggered snow [471], rain provoked from clouds, and speculations that lightning activity might have played a role in

life formation [647]. Belief in superpowers is not necessarily shaken either, simply restated. A person witnessing and surviving a lightning strike hitting in the vicinity of a few meters where no other pointy or conductive object could have scientifically justified its landing, will be strongly tempted to ascribe such fortune to a sort of divine intervention, or simply luck. There is always room for new beliefs or postulates to emerge and the puzzling phenomenon of ball lightning is, in this respect, one of the most fertile fields. An extensive discussion of the folklore and myths inspired by lightning and thunder can be found in Sibley [850], a somewhat shorter introduction to its cultural aspect is given in Elsom [265].

Regardless of its hundreds of actual and potential technological applications, it should be pointless to justify the use in studying lightning from a natural point of view. Whereas technological achievements magnify the illusion of our omnipotence and can at times promote distrust by pushing afar the boundaries of fatality, a natural perspective to science restores the primal interest we have about lightning : why there, why then, how thus ?

It is unfortunately not the aim nor even the capacity of this thesis to answer these questions. However, despite not giving clear answers, we strive to provide new or updated tools to help in elucidating one of the numerous mysteries about lightning : namely its relationship to high-energy radiation.

Chapter 1

Context

An extremely insightful experience a scientist can make without equipment, budget and preliminary research is to ask a random person on the street: how do electrons relate with lightning?

Depending on whether we feel too complacent about the wealthy and rigorous vocabulary we are wont to employ, we would either see the person as utterly untaught or on the contrary, realise how often knowledge can be overridden by our intuition and way of expressing ourselves.

In reality, such a benign question might equally stun one speechless, as if being asked what role does water play in life. For that reason, without falling to the temptation of wielding equations to glue our reasoning, we will first slowly descend in conceptualisation, from thunderstorms to lightning, through discharges, to swarms and individual electrons. Hoping on the way, that we can grasp the great scales of magnitude over which electrical phenomena unfold in the atmosphere. This chapter should prepare us to frame better the research of this thesis centred on electron swarms.

1.1 Lightning in nature

From a global perspective, lightning is now recognised as part of an immense power generator to the global electric circuit in which the Earth can be seen as a conductive sphere coated by an insulating positively-charged layer of atmosphere that steadily recovers its conductivity above 60 km of altitude at the base of the lower-ionosphere. At such heights, the conductivity is mostly due to the presence of free electrons seeded (directly or through ionisation) by perpetual cosmic and solar radiation. For this reason, this conductive layer is referred to as the "electrosphere", sustaining a positive potential difference to the ground of 300 kV.

This fact uncovers a new fictional futuristic scenario for an electrified world with appliance cords hanging here and there from the sky. Nonetheless, in our modest realistic scenario, it instructs us to continue learning about atmospheric electricity.

Naturally, this potential difference causes electrons to leak continuously from Earth into the atmosphere. Thunderstorms complete the cycle by replenishing electrons to the ground. We start describing the basic meteorological mechanisms driving thunderstorms.

1.1.1 Thunderstorms

Clouds form as the ground, heated by the sun, supplies and warms moist parcels of air, rising into the atmosphere as their thermal expansion lowers their local air density. In normal weather conditions, the moisture in parcels condensates as the temperature drops at higher altitudes and forms suspended water droplets that compose cumuli, i.e. regular clouds. Depending on the

temperature profile of the atmosphere and the humidity of the air, the updraft can be stronger and further lift the air parcel several kilometers above the cloud base altitude usually between 700 to 1 km above sea level. This leads to the creation of cumulonimbi or thunderclouds which can tower up to 18 km in height. At some point in altitude, known as the tropopause, the atmospheric temperature goes through a minimum before rising again. This stops the mechanism (buoyancy) by which warm parcels ascend and they spread horizontally instead, giving to thunderclouds their typical anvil shape. An example of a temperature profile with a tropopause at 16 km is displayed in figure 1.1.

Along the ascent, as the local temperature cools below the freezing point depending on pressure, the water contained in the air can adopt a great variety of forms. Some droplets can crystallise while others remain liquid: they become known as supercooled water droplets. Tiny ice crystals can grow in size as supercooled droplets and other ice crystals aggregate to create heavier particles known as graupel. The various water particles populating clouds are generically named hydrometeors. Through the competitive force of gravity and updraft, a velocity differential is created among particles varying in size which then collide. Whereas smaller ice crystals are carried by the updraft and soar, heavier graupel fall slowly or at best remain in suspension where the updraft is still strong enough. Their collisions result in a charge exchange reaction whose effectiveness and sign is conditioned by the ambient temperature.

The overall charge structure of a thundercloud is therefore layered according to its temperature profile (which depends on the latitude, season, orography, climate, etc.). It is most often modelled as a tripole with a main upper positive charge region between 6 to 14 km and -20 to -40°C, a main negative charge in the middle between 2 to 7 km around -10°C and a lower positive layer at the cloud base and above 0°C. As a response to the electric field, layers of screening charges form in the more conductive regions of the surrounding environment. Thus, the cloud boundaries can be shrouded with a screening layer, essentially negative at the top. Additionally, the ground below the thunderstorm reflects the tripolar structure by accumulating negative, positive and again negative charges in roughly concentric regions right below to far from the thundercloud base. The right of figure 1.1 illustrates the basic electric structure of a thunderstorm in relation to the altitude and temperature.

The charge accumulated in the main regions can range from a few tens to over a hundred Coulombs (~10–100 C). Their separation up to several kilometers leads to potential differences typically around 10–100 MV and once reported up to a GV [386]. From ground to cloud top, the electric field profile varies and changes in direction each time a layer of opposite charge is crossed [631].

At ground level, an accumulation of charges in tall structures (trees, buildings, etc.) enhances the local electric field. This enhancement, if intense enough, may lead to the formation of a special kind of discharge called ‘corona’, the physics of which are introduced later in section 1.2.2. The current generated by the corona redistributes charges in the vicinity of the field-enhancing object until this field becomes screened. The charges filling this volume form a corona ‘space charge’. They are represented around the miniature tree and house on the bottom right of figure 1.1. Finally, the effect of this corona is to screen the field measured at ground to a range of 1–10 kV/m [866]. In absence of corona charges (such as on plane surfaces like desert plains or lakes), the electric field can reach up to a hundred kV/m [933].

Maximum fields inside clouds are between 100–300 kV/m [764, p.83:table 3.2]. Further elevation of this field can occur in areas of higher charge concentration and especially through the enhancement at the tip of ice crystals. Initiation of electric discharges is likely to emerge and attach at those tips when the local field enhancement is close to the electric breakdown threshold of air. One can see how this threshold varies with altitude on the scaled axis in the middle of figure 1.1.

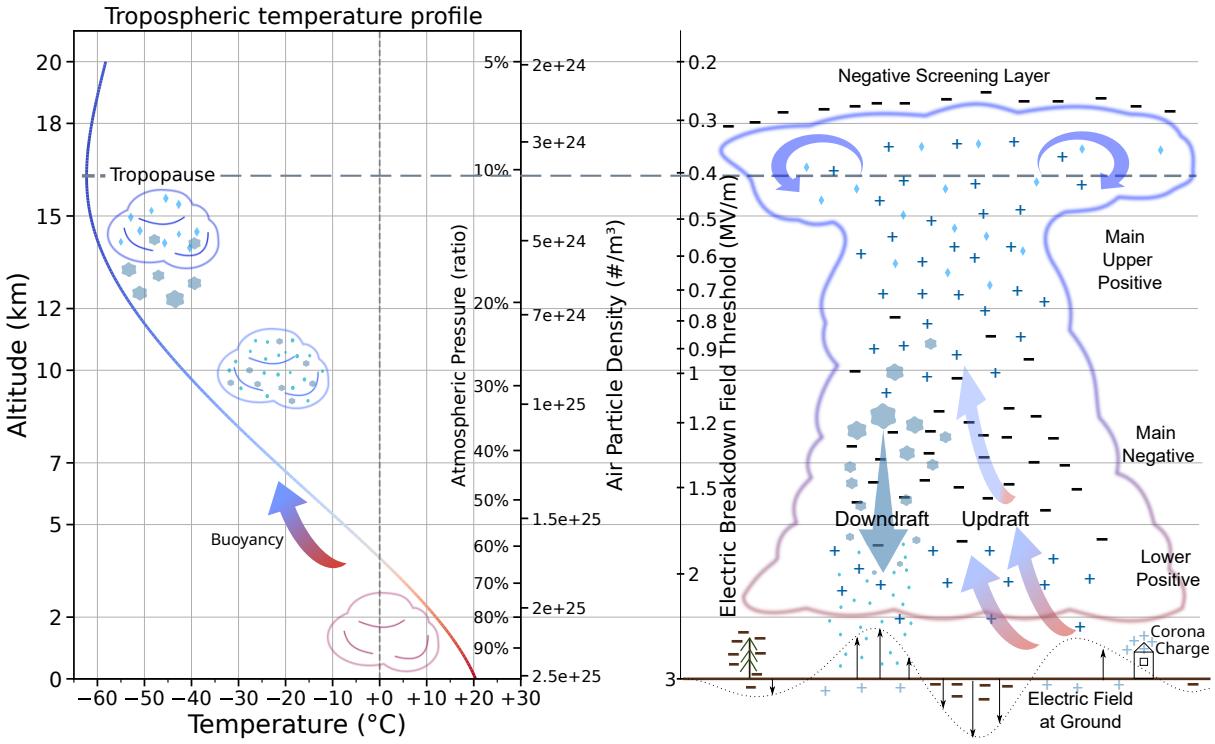

Figure 1.1: Formation and structure of thunderclouds according to the temperature profile of the troposphere calculated with the NRMLSISE-00 atmosphere model. The tropopause corresponds to the first minimum in the temperature profile. Convection stalls at the tropopause, but there may be a slight overshoot marking the top of the thundercloud.

Thunderstorms develop through various phases. The formation phase is characterised by a strong updraft carrying moist parcels of air and benefiting great birds such as hawks and eagles gliding, soaring and most probably being thuswise at the origin of the Thunderbird myth [265, Chapter 1 §The Americas]. As the cloud swells, graupel is generated and the charge separation mechanism takes place, giving way to occasional breakdowns laying out a soft rumbling of thunder. At some point the supply of warm air depletes, the updraft weakens and heavier particles start to engender a downdraft which permeates the core of the cumulonimbus, stifle the remainder of the updraft and provoke the outburst of downpour. More turbulence agitates the cloud's core and fosters electrical activity. In case of a simple unicellular storm, there is no adjacent cell or region that can resupply the cloud with water droplets and crystals. After a few hours, the thundercloud subsides, dissipates and clears the sky.

Although the mechanism described so far is generic to many thunderstorms, these can adopt very complex structures and present many variants. The convection can be either induced by orography (i.e. by mountains, hills), or by cold air fronts. A storm can comprise multiple cells or supercells with coexisting regions of intense updrafts and downdrafts, it can also be linked to cyclones. Broader information about the physics and variety of thunderclouds can be found in Cotton *et al.* [195]. Nevertheless, we suggest Cooray [189] for its insightful explanation of thunderstorm structures. Quantitative information and detailed referencing has been gathered in Rakov and Uman [764, Chapter 3, p.67-93]. Of course, lightning is not exclusive to hydroclouds and occurs in volcanic or nuclear plumes, sandstorms and other planetary atmospheres with different chemical compositions. We now turn ourselves to the observed characteristics of discharges in thunderstorms in the next section.

1.1.2 Lightning Discharge

So far, we have depicted thunderstorms as a sort of gigantic machines that separate and unevenly distribute charges over vast volumes in the troposphere and over the ground. The overall result is that the space is permeated by an increased electric field. Generally, any mechanism which restores fully or partially the charge balance between regions of opposite polarities can be called a "discharge". Therefore, this applies to any electric current, insofar as it depletes a charge imbalance, weak as it may be. We have already seen above that the corona is a kind of discharge whose effect is to slowly dissipate the regions of accumulated charges in objects on the ground.

However, we most often associate the term "discharge" with a more spectacular phenomenon such as lightning. In this case, the discharge is accompanied by *breakdown*. This term might seem obscure and ambiguous as it could point toward various aspects which "break down":

1. Breakdown of resistivity: air transformed into a (weakly ionised) plasma channel ceases to be an electric isolator.

2. Breakdown of the medium*: air blazes, molecules dissociate, atoms ionise.

3. Breakdown of the electric field: the charges are transported in a fraction of a second and rapidly screen the field much faster than the charging of clouds.

In this section, we present the basic mechanism by which this "triple breakdown" occurs.

Electron avalanche. The initiation of breakdown is a stochastic process that triggers under certain conditions: when the electric field is above a certain threshold over a certain volume for a certain period and with a source of free electrons. Apart from local build-ups of free charges created by background (natural and cosmic) radiation [795], those conditions are best met at the tip of hydrometeors [745] where charges accumulate both through migration and polarisation of the material [741]. At standard ground atmospheric conditions†, the conventional breakdown threshold of dry air is at 3 MV/m. As the air becomes rarer at higher altitudes, this threshold decreases as shown on figure 1.1-right by numbers scaled on a vertical axis. Free electrons in the vicinity of threshold fields start ionising the surrounding air whereby they multiply and create local avalanches converging toward the hydrometeor tip [777]. The availability of electrons in air is strongly hampered by the ability of oxygen molecules to detain them and form negative ions. This process is known as electron *attachment*. Thus, an electron may not travel long distances in air while staying free and the inception of an avalanche is subject to the *local* production of electrons within the enhanced field region of the hydrometeor.

Avalanche to streamer. Under more specific conditions, which are actually still subject to active research, the initial avalanches can expand by carrying an accumulation of charges which sweeps forward, leaving behind a channel of weakly ionised air known as a *streamer* [606, 704, Chapter II]. This corresponds to the first stage of breakdown: the resistivity of air drops several orders of magnitude from ~10^{14}–$10^{10}\,\Omega$m down to 10^{3}–$10\,\Omega$m [762, p.343] due to the presence of free electrons inside the channel which carry the electric current as they drift in the field. A streamer's growth is conditioned by the external electric field [299] and the composition of air which may eventually be preionised or preconditioned to have metastable species. Together, the

*This is not considered as being encompassed by the traditional terminology of breakdown. Nonetheless, we propose it here as a useful additional classification to refer to different stages of a lightning discharge.

†There are many "standards" (and they changed throughout history). Ours adopts 15 °C and 1013.25 hPa, see later section 2.1.1.

electric field and gas composition affect the production and depletion balance of free electrons in the streamer channel [356]. In virgin air, free electrons may be produced from ionisation in a number of different ways: from high-energy radiation to radioactive decay. Nonetheless, streamers, once formed, do not depend on external sources of free electrons. They are self-sustainable discharges that ionise air ahead and may propagate until they slow down to a halt after then enter regions where the electric field is below a certain critical threshold [733].

Streamer to leader. During the evolution of a streamer, the air in the weakly ionisation channel is gradually heated by the electric current. Initially, the channel's conductivity, although much higher than virgin air, is still relatively mild, and therefore Ohmic heating is fostered until the second stage of breakdown occurs at higher temperatures: the breakdown of air. At this state, the molecules in air are mostly (oxygen) or partly (nitrogen) dissociated into atoms and a small but non-negligible fraction ($>10^{-3}$) of ions is present [762, p.344]. Whereas streamers' conductivity at ambient temperatures is hindered by collisions with diatomic molecules* and attachment to oxygen, the present sharp rise in conductivity beyond several thousand kelvins ($\gtrsim$1500–2000 K[11, 311, p.1343, §3.3]) is due to an increase of availability of free electrons and maybe even their mobility [376, fig.3]. The resistivity of this plasma could be between 10^{-2}–$10^{-4}\,\Omega$m. This evolution stage is known as a *leader*: it leads a corona of streamers (or *streamer zone*) attached at its tip, to ionise the air ahead and allow for further propagation.

By now, the initial hydrometeor should have vaporised through the intense heating induced by the electric current of ~ 100 A. Core temperatures attain 6000 K or higher [11, 311, §4, fig. 13]. At the other end of the leader, the channel propagates in the opposite direction feeding new charges into it. The leader becomes bidirectional, curiously like the thunderbolts held by Zeus, Jupiter or Sumerian gods of lightning as in figure 0.1. Both ends are of opposite polarity and assimilate pools of opposite charges as they propagate. Furthermore, the structure of leaders can become complex as new branches can emerge, and old branches can die or revive again, depending on the competitive demand in electric current necessary to maintain a channel alive. Initially a submetric stem, leaders can extend over several kilometres in total length. An image of a leader during a lightning strike can be seen on the upper-right side of figure 1.2.

The polarity of a leader/streamer's tip determines the direction of the electric field ahead (outward or inward). Positive (negative) tips attract (repel) electrons, creating avalanches inward (outward) through impact ionisation of air molecules. In both cases, the channel propagates faster than the electrons drift and, in a metaphor of snowploughing, accumulates a dense region of charges at the front [733]. Typical velocities of streamers are around ~ 10^6 m/s [517, §3.1] and depend on their size [109, fig. 7b], on the gas density and on the external field [578]. In order to propagate further, streamers require that the external electric field be above a certain threshold [299]. This is known as the stability field† [109, §3.3] which is about 5 kV/cm for positive [733, §1] and 10–12 kV/cm for negative streamers [704, §3.5] in air at atmospheric pressure.

Leader propagation can be notably different from streamers. Negative leaders can proceed through rapid (< µs) expansions called steps, repeatedly interrupted over 5–80 µs. Steps can span gaps as wide as ~ 0.5–100 meters. A similar phenomenon was also observed for positive leaders in laboratory sparks [341, 536] as discontinuous current pulses, when the air absolute humidity is high (~ 10 g/m^3) [582] or during the initial development phase for slowly rising voltages at the electrode ($\lesssim$ 5 kV/µs) [340].

*The actual picture is more complex. What distinguishes a leader from a streamer is a much larger density (over 1000×) of free electron in the channel. In air, this is marked even more by the occurrence of attachment which significantly depletes free electrons in the wake of a streamer.

†This concept is nonetheless hard to define since the electric field is rarely homogeneous and it is not straightforward to differentiate what is the "unperturbed" field if the streamer were not present.

Figure 1.2: Photograph of a lightning strike in Waterloo (Belgium). The luminosity and structure of a return stroke on the left may be compared to a branched leader emerging from the cloud base on the right.

Most of the time however, positive leaders propagate continuously and the nature of their pulsed propagation is thought to be radically different from the stepping observed in negative leaders, which is reflected in a different terminology for those pulses, namely: restrikes [536, 582], pulsewise propagation [341].

The average propagation speed of leaders is an order of magnitude slower $\sim 10^5$ m/s than streamers, with a somewhat faster (slower [70]) tendency for negative (positive) types [536]. Nevertheless, external conditions and the development stage of leaders can greatly affect their progression rate which can be slow to $\sim 10^4$ m/s [536, p.5:§4] or peak around 10^6 m/s [341].

Leader touchdown. Ultimately, the conductive channel of the leader clears out a route for the charges to flow between two separate regions of different electric potential. When this potential difference is evened, the third stage of breakdown has been accomplished: the breakdown of the electric field.

The path traced by a leader can go, for instance, from the main negative layer to the main positive layer of the same cloud (intra-cloud), between layers of different neighbouring clouds (inter-cloud); it could stop outside the cloud in a patch of air (cloud-to-air) as on the right side of fig. 1.2, or make its way completely to the ground (cloud-to-ground) as seen on the left side of figure 1.2.

In this latter case, the leader connects to the ground at one or several attachment points. The *attachment* process is complex because the ground reacts to the nearing presence of a highly enhanced field carried at the tip of the leader. Very often, streamers emerge from the ground at local points of higher charge density. If a tall conductive pointy object stands erect nearby, an upward leader springs from its tip and rushes to the encounter of the descending leader [796]. When the connection between the counter-propagating leaders establishes through their streamer zones, a surge of current known as the *return stroke*, runs through the channel upward at about $\sim 10^8$ m/s, a significant fraction of the speed of light. This peak of current at some tens of kA, ignites the channel blazing at 30 000 K [500, 722, fig. 6d], and produces the flash visible to the eye. The same channel can flare up several times by subsequent surges of current. Each subsequent stroke is preceded by the retracing of the channel by dart leaders

that rush steadily at higher speeds $\sim 10^7$ m/s, unless they are stepped, in which case they pace slower $\sim 10^6$ m/s. Between consecutive strokes, the channel can be kept active by a continuous, eventually fluctuating, current of a few ~ 100 A for a typical interval of 1—100 ms. When no more charges can be fed into the channel, it finally dissipates.

1.1.3 Repercussions

The traces left behind by a flash are many and profound. Most obvious to us is the acoustic shockwave from the sudden expansion of the superheated channel which produces thunder in a concerto of rumbling, roaring and booming notes. Next, the currents in the channels emit radio-waves that can be measured at far distances from the storm. Some special frequencies are selected through resonance in the gap formed between the surface of the Earth and the ionosphere. They constitute Schumann resonances that perennially permeate the globe. Furthermore, the excitation, dissociation and ionisation of air prepare the molecules for various chemical reactions to take place. New species are created, notably traces of CO, NO, NO_2, ozone O_3 and their ions can be detected after a flash occurred.

In case of cloud-to-ground strokes, severe physical damage can result from intense electric heating at the attachment point. Notably, the humidity contained within a material can instantly vaporise and produce a spectacular explosion of tree trunks and parts of a wall or roof. Dry burnable materials can be set ablaze whereas dry sandy grounds are fused together and produce tubular structures known as fulgurites, literally "lightning-rocks". Those should probably be the scientific equivalent of the mythical thunderbolt.

After the flash is over, a massive amount of charge, several tens of Coulombs, has been displaced over a large hecto- or kilo-metric distance in just a fraction of a second. The total effect is measured as a *charge moment change* of most often several hundreds [447] but sometimes reaching up to some thousands of C × km [59]. This sudden change in electric configuration induces a response from charges contained in the upper parts of thunderclouds. A whole range of events were identified in connection with large charge moment changes ($\gtrsim 1000$ C×km) [409, figs. 4&6] such as sprites, jets and halos; each with their own phenomenology and typology. Additionally, the electromagnetic pulses produced by current surges induce an expanding glowing ring in the ionosphere known as an ELVE. All those phenomena are regrouped under the terminology of *transient luminous events*.

Finally, the implications of lightning extend also to the range of high-energy physics. Recently, it was found that:

1. leader steps are accompanied by X-ray bursts [252];

2. strong beams of gamma rays known as terrestrial gamma-ray flashes (TGF) were detected from space [291], onboard planes [857] and on ground [239] in connection to intense lightning activity;

3. the gamma rays produce photo-nuclear reactions in the atmosphere leading to emissions of fast neutrons from nitrogen nuclei [267].

The common root to those high-energy events is the production of gamma photons through bremsstrahlung radiation of very fast electrons deviated by atomic nuclei. The acceleration mechanism capable of turning slow ambient electrons into high-energy ones is called thermal runaway. Its conditions of occurrence are not well understood and constitute the main drive for this thesis.

1.2 Discharges in laboratories

Electric discharges produced experimentally differ mainly from natural lightning both in scale and through their initial charge distribution fixing the electric field. Instead of spreading over large areas as in thunderclouds, charges in laboratory experiments are densely accumulated on conductive surfaces called electrodes. They are shaped as a spike, a sphere or a plane; and eventually some combination, like an array of spikes on a conductive plate. The negatively (positively) charged electrode, releasing (capturing) electrons is called the cathode (anode). The nomenclature is due to Faraday in 1834 [271], on the suggestion of W. Whewell in analogy to hydraulic flow: the higher (*άνοδος*) and lower (*κάθοδος*) paths from and to which the electric current (going opposite of the electrons) flows in the medium between electrodes. Just as near the tip of hydrometeors, the electric field is greatly enhanced around sharp contours of the electrodes' surface. A historical introduction to the realm of laboratory discharges can be found in the first chapter of Hirsh and Oskam [404].

1.2.1 Discharge typology

A rich variety of distinct discharge types is revealed through different configurations of the experimental conditions. One can change: the electrode shape, its material type, the gas filling the chamber (composition, pressure, temperature), the gap length between the electrodes, the resistance of the external circuit, the voltage applied and its rise temporal steepness and eventually frequency.

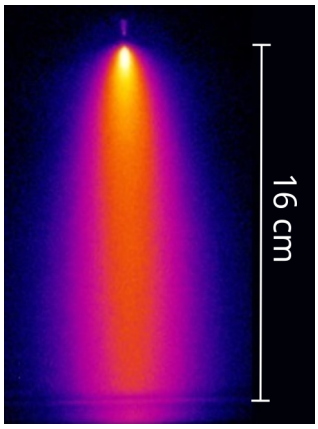

Figure 1.3: A diffuse glow discharge in air at 25 hPa from a positively charged electrode at the top given a pulse of 14.6 kV with 15 ns rise time and 10 µs decay time. The photograph extracted from Nijdam *et al.* [703, fig. 5], was exposed for about 2 µs.

If the voltage is low (not much more than a few hundred volts) and electrodes are relatively flat, the gap would only hold a very weak current of *slowly drifting* ions and electrons sparsely produced by natural radioactive decay and cosmic ray ionisation. As the voltage rises and by stimulating the cathode to emit electrons, a (dark) *Townsend discharge* unravels by an acute increase of current. At low pressures (a few hPa=mbar) and sufficiently large gaps, the discharge starts *glowing* diffusely and more or less uniformly in the gap as in photograph 1.3. This is used in low pressure gas discharge lamps for street and office lighting. Raising the pressure and shortening the gap gives way to small and bright *arc discharges* flushing a peak of current (about 1 A) in an instant (some tens of ms). At high pressures, high voltages and large gaps, a *corona* of dim filaments (fig. 1.4b) may form in high-electric field regions from convex electrode contours. The occurrence of corona streamers is due to a high concentration of charges at the electrode. This effect can be enhanced by taking pointy instead of plate or spherical electrodes. The corona produces free electrons and ions that sustain a current between the distanced electrodes as can be fancied from photographs 1.4b&c. At this point, only a slight increase of voltage or reduction of the gap length may trigger a *spark* from the sustained corona discharge (fig. 1.4d). Here, we excluded the very broad domain of pulsed and oscillating-field discharges. We redirect the reader toward Raizer [762] for a seminal description of discharge typology.

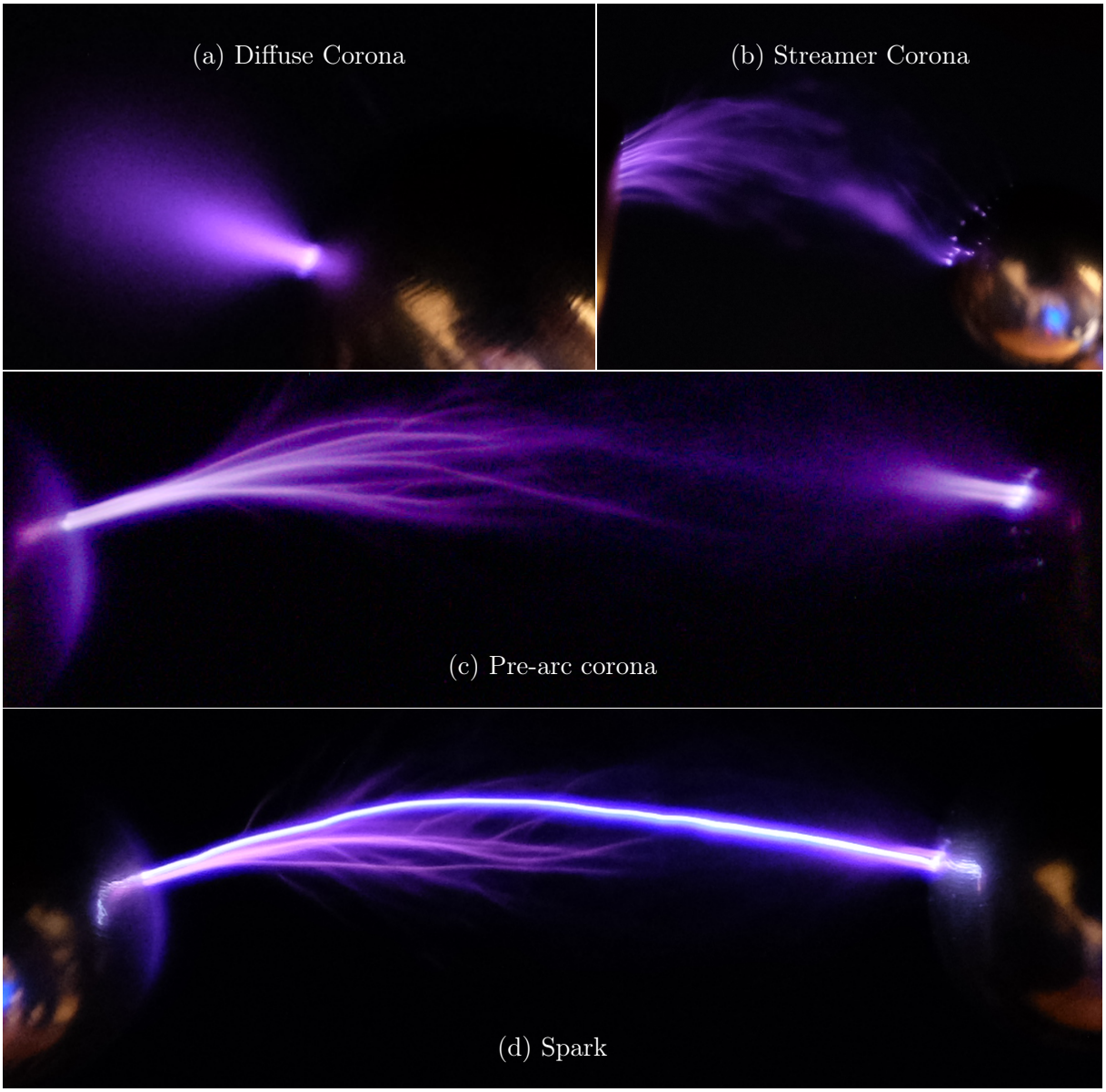

Figure 1.4: Photographs of 1 ms exposure of corona and spark discharges between spherical electrodes (and a plate electrode on the left of fig. b) separated by a gap of 4 cm in a laboratory experiment at the Instituto de Astrofísica de Andalucía in Granada. Courtesy: Oscar Van del Velde (2019) from Kieu [501, p.6:fig.1.5]

1.2.2 Sparks and coronas

Of all the types of discharges introduced, it is the latter two: spark and corona discharges, that present most likeness to natural lightning. Powerful long sparks produced in laboratory or outdoors display identical leader structures ended by a streamer zone (or streamer corona), progressing through steps or continuously according to their polarity. Also, it is not improbable that coronas form at the tip of hydrometeors [745] when the electric field reaches its maximum value before lightning initiation occurs. Therefore, considerable insight about the mechanism behind lightning initiation can be gained from studying laboratory sparks [652].

Coronas may be of two types: diffuse and filamentary as seen by comparing figure 1.4a and b. A diffuse corona is a volume discharge in which the electrons converge to (positive) or diverge from (negative) the electrode. If filamentary, the corona is composed of many streamers that emerge from the connection point near the electrode and expand further until they vanish or merge into a leader. Of important note, one must mind the integration time used in photographs of coronas. Longer exposure times blur together light emissions at different times. Therefore, it is not certain whether the diffuse image of corona in figure 1.4a, unlike the glow discharge at 25 hPa in figure 1.3, was (or not) composed of many streamers which emitted light at different moments and positions so as to give a uniform glow over 1 ms.

We have seen previously in section 1.1.1, that one effect of the electric current generated in corona discharges is to disperse an initially high concentrated region of charges over a greater volume and thereby to reduce the potential drop at the electrode (or charged object) to which the locally enhanced electric field is related. The repeated exposure to corona discharges can cause the gas to reach temperatures of about ~1000 K [311, 404, p.248, §3.2]. More insightful information about coronas can be found in the reference book Goldman and Goldman [339].

Experiments [109, 341, 582] show that coronas emerge under lower electric fields at the anode (+) than at the cathode (−). Physically, this is explained [575] by electrons converging toward higher electric fields near the tip; whereas electrons around cathodes diverge (move away) from the high-field region. From this reasoning, we may infer that the electrodes on the left (right) of figures 1.4 are anodes (cathodes). Similarly, one may suppose that in thunderclouds, positive streamers emerge before negative ones. This would imply that for downward negative cloud-to-ground lightning, it is actually the positive end that forms first; pointing upwards (downwards) at the base (top) of the main negative charge layer.

The inception time of coronas and sparks depends on the availability of free electrons to start the initial avalanches near the electrode and on the formation time of the streamer (usually much shorter). Free electrons may either be ejected from ionisation by cosmic rays or be detached from negative oxygen ions. The presence of electronegative species to which electrons may attach greatly affects the time lag, formation and properties of streamers. The implications of attachment and subsequent formation of negative oxygen ions in air are far-reaching. As will be introduced in the forthcoming sections, it is suspected [621] that leader stepping and therefore X-ray bursts are some consequences of attachment to oxygen.

A general introduction to spark discharges and the streamer initiation mechanism subjected to a stochastic inception time can be found in Loeb and Meek [606]. An excellent recent review of streamer physics is given by Nijdam *et al.* [704].

1.2.3 Stepping

A major insight on negative leader stepping was gained from high-resolution images of sparks in laboratories. Each step is characterised by a sudden extension of the radiant leader channel followed by burst of streamer corona at the newly formed tip, as nicely photographed in 1.6b. As seen in the previous section, the corona is a complex system of streamers through which electric current flows and a global space charge is deposited in the volume ahead of the leader tip. Each individual streamer propagates until it reaches a region where the electric field emanating from the leader head is screened by the corona space charge to the point where it is below the threshold to sustain further streamer propagation. Even though streamers eventually subside, in their passage they leave behind charge carriers that precondition the air [39] for fostering subsequent breakdown.

In particular, small glowing patches spontaneously appear in the wake of negative streamers. Their origin is still under debate. In photographs of laboratory discharges [518, fig. 10], they are observed as small isolated round weakly shining dots left behind bright negative streamer heads circled in blue on the right of figure 1.5. Theoretically, their emergence was proposed [621] as resulting from a disruption of the conductivity in the streamer channel reinforced by instability of electron attachment to oxygen, conducing to a region of enhanced electric field and glow through molecular de-excitation. Those small dots are sometimes named '*beads*' [520, §6] but are possibly another manifestation of the structures that are sometimes called *space stems* [69, 311, 583, 621]. Formation of beads is not exclusive to negative streamers, similar glowing structures have been observed in sprites after the passage of positive streamers. The connection remains, however, quite mysterious as the ambient air density is much lower at sprite altitudes (~50–80 km and starting at ~ 70 km [737, fig. 4]).

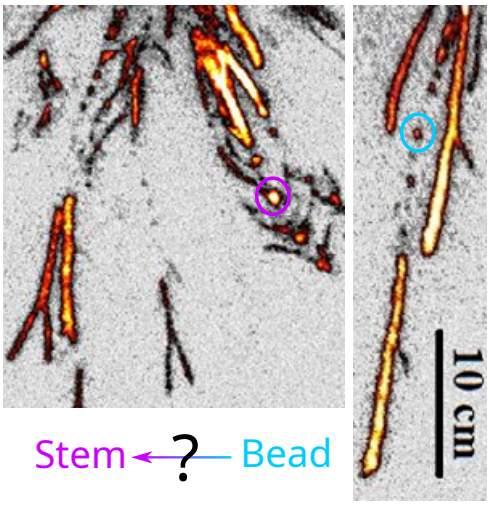

Figure 1.5: Photographic 50 ns exposure image of beads (blue circle) 'sowed' by negative streamers and evolving later into space stems (violet circle) from which positive streamers emerge. Extracted from Kochkin *et al.* [518, fig. 10:(a)–right and (b)–left].

Local and regularly spaced disruptions in conductivity are suspected to form a succession of beads left by the passage of a streamer head. This suggests that the ideal model of a negative streamer as a uniformly-stretched weakly conductive channel of electrons is too simple and does not take into account the limitations imposed by electron attachment to oxygen molecules. Instead, a quick degradation of the conductivity in the channel takes place as electrons deplete [520, §5.1].

What distinguishes a bead from a space stem is uncertain [45, §1]; the same dilemma might be given to a botanist about when to call a germ 'a sprout', or when to call a sprout 'a stem' (to keep the analogy) and whether the sprout and the germ are words of distinct etymologies for the same concept. Intuitively, we may designate by 'bead' the round shiny balls that the name suggest. When a bead 'grows' (if it grows and does not vanish) it may be called a space stem as described in the next paragraph.

The evolution of a space stem is a mysterious and presently actively discussed phenomenon. On photographs, space stems seem to give birth to a series of small interrupted streamer corona expansions of both polarities and follow the trail of the negative corona [340]. A glimpse was caught in figure 1.6c where the negative (positive) streamers point downward (upward). Those bipolar systems of counter-propagating coronas are called *pilot* (systems) [311, 520].

The growth pattern of pilots is rather atypical in the realm of discharges. In a first stage, positive streamers emerge almost perpendicularly from the sides of the glowing stem and then curb toward the positive electrode along the electric field lines, avoiding the path previously traced by the passed negative streamer. This 'Ψ' shape can be noticed on the left photograph of figure 1.5 where lateral positive streamers emerge from space stems of which one is circled in violet [520]. After a while, it seems, from the structure on photograph 1.6c., that a central corona of positive streamers forms connected to the space stem and propagates toward the electrode while new negative streamers emerge from the opposite end of the space stem. The system may now be called a pilot composed of two coronas of opposite polarities and direction of propagation. The relationship, if any, between the first generation of (lateral) 'Ψ' positive streamers (1.5-left) and the central positive streamer corona (1.6c) is undetermined and poses another intrigue.

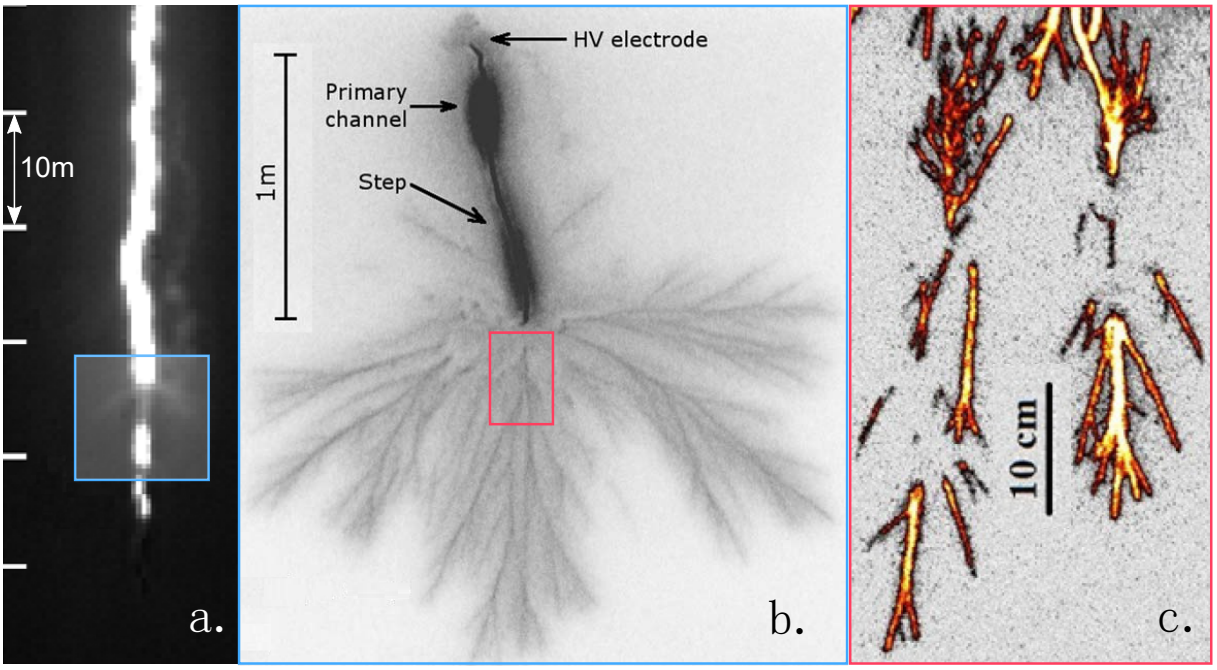

Figure 1.6: Different scales involved in negative leader stepping. (a) : Photograph from Biagi *et al.* [69] of space leader glowing bead ahead of a natural lightning leader channel. (b) Photograph from Kostinskiy *et al.* [536] of a streamer corona burst after a step in a negative lab discharge. (c) : Photograph from Kochkin *et al.* [518] of pilot systems emerging from local space stems in the wake of a negative streamer corona burst.

As it grows and stretches, the channel between the positive and negative coronas is disrupted (or so it looks on the photographs) and the system eventually wanes out. Nevertheless, a new space stem emerges from the previous point where the negative corona subsided and the process may thuswise repeat several times [311, §3.6.1]. It would not be inadequate, that being said, to adopt the Phenix as the totemic animal of negative leaders in lightning.

There may be several space stems launching new pilot systems in the area swept by a negative streamer corona. The current generated by the pilots flows into the space stem and gradually heats the region subtended between the coronas to about a thousand kelvins [581]. The critical temperature for the streamer to leader transition is situated between 1000–2000 K when the release of attached electron to oxygen anions induces a surge of current [311, §3.3]. If this current is maintained long enough to support the continuation toward leader formation, maybe through the connection of several aligned pilot systems, the heated space stem may eventually reach temperatures comparable to leader cores; it is then called a *space leader* [583]. Those latter were observed in fast-camera pictures of triggered downward negative lightning leaders [69]. As opposed to space stems which look like faintly glowing dots that follow the trail of negative streamer coronas [340], space leaders grow bidirectionally into elongated streaks and glare with the same brightness as the main channel in figure 1.6a. Gradually, the interstitial region between the main and space leader channels shrinks. The systems of opposite streamers emanating from the main and space leader tips interpenetrate and are sometimes observed [518] or thought to collide into each other [190]. Their embrace is concluded by a sudden elongation of the leader accompanied by a bright burst of corona streamers [68, p.8161-2].
In brief: another *step* has been taken.

In summary we present the following cycle in negative leader progression:

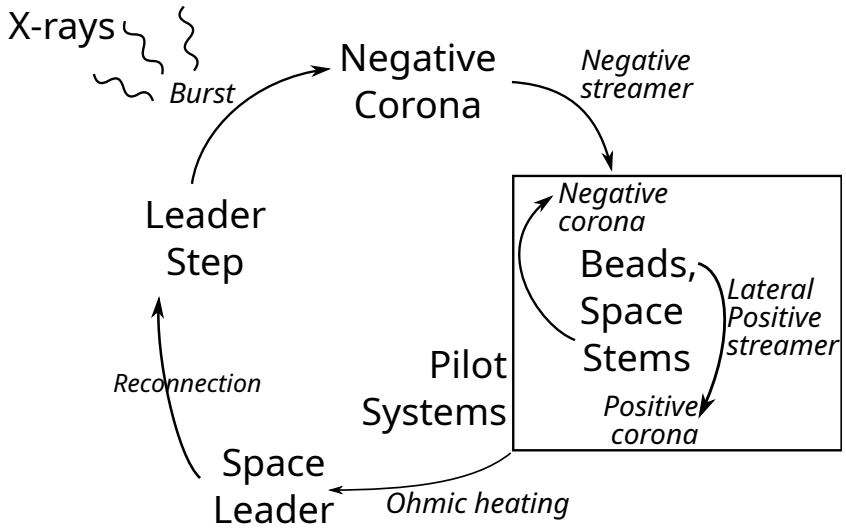

Most interestingly, X-rays were observed in correlation to the corona burst concluding the step in long spark, just as in natural lightning. Furthermore, even beams of fast neutrons were reported in laboratory experiments [6]. In the next section, we explore this intriguing high-energy facet of discharges.

1.3 High-energy radiations

The energy of elementarily-charged particles in electric fields is most commonly described in electron-volts (eV) which is simply the energy that an elementary charge $e = 1.602 \times 10^{-19}$ C gains from a potential difference of one volt. The domain of "high energies" is always relative to the phenomenon studied. When mentioning X-rays and gamma-ray photons in relation to lightning activity, we will consider the range between 10 keV and 100 MeV as the high-energy domain of lightning radiation. For practical purposes, the traditional terminology qualifies "soft" for less and "hard" for more energetic photons in the domain defined previously.

Although high-energy photons can be produced in various ways, their primary origin in discharges is acknowledged as *bremsstrahlung* (braking radiation) from fast electrons scattering off atomic nuclei or (to a lesser extent*) electrons [528]. Actually, any charged particle deviated by an electromagnetic field induces an electromagnetic perturbation that can propagate as a real photon†. However, "bremsstrahlung" in the rest of this thesis will exclusively refer to the electron-nucleus context. How many "fast" electrons can be obtained in a given electric field will be briefly introduced in the next section before turning into the primary concern of this thesis.

It must be noted that the historical classification of X- and gamma rays is not based on energy but on their mechanism of emission. While X-rays are associated with electron processes such as bremsstrahlung and de-excitation of higher energy states to core orbitals in heavy atoms; gamma rays were the third type (after alpha and beta) of radiation from radioactive decay (i.e. atomic nuclei). Although it is certainly true within this context, that gamma rays tend to be

*This is because radiations from binary electron collisions arise from the quadrupole moment as opposed to the dipole moment in electron-nucleus collisions

†When it comes to observers in different frames which are not bound by a Lorentz transformation, radiation is subject to the reference frame considered. This was a long-lived stimulating paradox [783] and still perplexing nowadays.

more energetic than X-rays from atomic deexcitations; a "bremsstrahlung-ray", which should pertain to the definition of an X-ray, can perfectly span over gamma energy ranges. In lightning research, there is not (yet) a consensus for strict terminology, and many authors tacitly adopt the conventional boundary of 50 keV. Nevertheless, there is a growing trend [250, §2.4] to separate gamma rays - as photons that emanate inside the thundercloud, from X-rays - as linked to stepping of long-sparks and lightning leaders reaching ground levels.

In the rest of this section, we will follow this tentative line of distinction between gamma-ray (thundercloud) and X-ray (leader) emissions in connection to lightning activity. Below, we present some of their characteristics and mention other forms of high-energy radiation in a third subsection. At last, we will end this section by covering the hypothesised production of fast electrons that prefigure gamma-ray emissions.

1.3.1 Gamma-rays

Once emitted by bremsstrahlung, gamma rays interact with molecules as they propagate through air in the following four ways:

- Coherent *Rayleigh* scattering : deviation without loss of energy;
- Incoherent *Compton* scattering : with the ejection of an electron formerly bound to an atom/molecule, whereupon another photon is re-emitted with a different wavelength;
- Photo-absorption* : upon ionising or (super)exciting a molecule, the photon is fully absorbed;
- Pair production : production of an electron-positron pair† under the influence of the electric field of a nucleus.

We redirect the reader to Hertel and Schulz [400] for an introduction to these interactions. The combination of those processes implies that the original gamma rays get strongly attenuated as they propagate through thick layers of the atmosphere; they deviate from their original trajectory and thus can occasionally be detected at larger angles (from their supposed location source); and most importantly, they leave behind traces of their interaction with matter: production of more electrons, positrons and other species. The graphs in figure 1.7 give an idea of the relative importance of each interaction according to its cross section with nitrogen atoms‡ along photon energy. As we will clarify below, a careful consideration [724] of those effects is instrumental in interpreting measurements of gamma rays emanating from thunderstorms.

To-date, there are two classes of events identifying gamma-ray emissions from thunderstorms. The first (historically [735]) is the gamma-ray glow which lasts long from seconds [521] to several minutes [179, 935], whereas the second is the terrestrial gamma-ray flash (TGF) which usually lasts less than a millisecond. Those two classes are also very well distinguished by clear evidence showing glows often appearing as terminated by lightning [255, 521, 636, 949] whereas TGFs relate simultaneously to discharges taking place in thunderclouds.

*Abbreviation to the full term: "photo-electric absorption". Sometimes it would seem that the term "photo-ionisation" is used as a synonym of "photo-absorption". We deprecate this usage for two reasons: (1) A high-energy photon can be fully absorbed but only lead to an excitation (inner core electrons of heavy elements) and (2) Compton scattering also ionises (but a photon is remitted).

†Muon pairs could be produced too if the photon energy were high enough ($\gtrsim$200 MeV), usually only the case for cosmic rays.

‡At energies >keV, one can assume that the photon cross section with a molecule is simply the sum of the cross-sections with each atom in the molecule. More will be disclosed in the second part of this thesis.

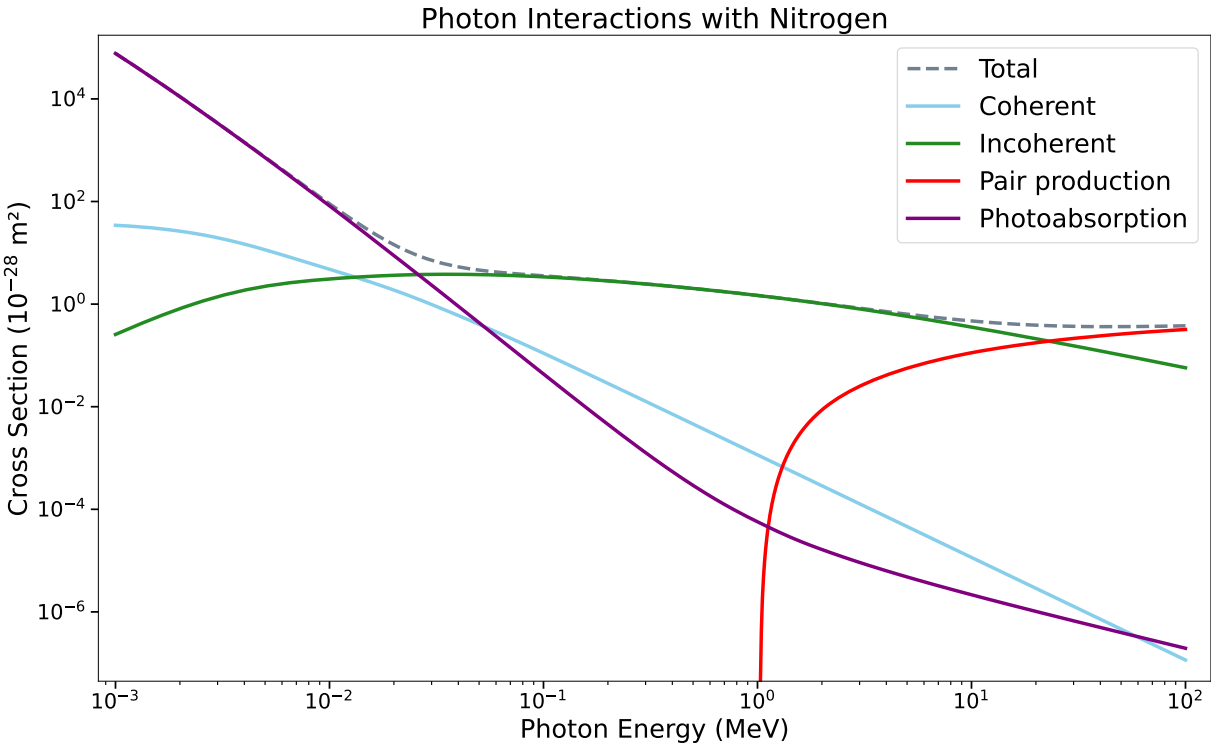

Figure 1.7: Gamma-ray interaction with nitrogen atoms‡ : cross-sections for Rayleigh, Compton scattering, Photo-electric absorption and pair production from the EPDL [744].

Gamma-ray Glows. The conditions for gamma-ray glowing are thought to be quite straightforward [256, 637]: electric fields high enough and over sufficiently long distances (several hundred of meters) [934, 935] to permit self-sustained avalanches [47] of fast electrons seeded by cosmic rays [369]. However, if the field is close to the breakdown threshold, a discharge can set off; and thereby abate the ambient electric field through screening by the space charge effectively displaced [255]. Prior to the abatement, the electric field is locally boosted by the charge accumulated at the leader tip. As a result, depending on the geometry of the glowing region with respect to the leader propagation, glows can intensify both in particle flux [636] (number of counts per second) and in hardness [947] (larger fraction of higher-energy counts) before an abrupt stop. In one case, a glow was seen to give way to a TGF before a lightning flash quelled the electric field [971]. Furthermore, it appears that the amount of charges displaced inside the cloud by the electric current of a glow is non-negligible compared to that of lightning [484], suggesting that glows and lightning flashes are rivalling mechanisms of electric discharge.

Terrestrial Gamma-ray Flashes. On the other hand, the mechanism(s) by which Terrestrial Gamma-ray Flashes are produced, constitute a fervently discussed field of research. Known in short as TGF, they are reputed to be the latest discovery, only thirty years ago [291], of high-energy phenomena in connection to lightning. They are observed from space [78, 639, 695, 858, 919], on airborne detectors [99, 857] and from ground [1, 246, 385] as very intense but short spurts of gamma rays beamed in a relatively narrow cone. Their characteristics described below are illustrated in figure 1.8. In this hypothetical scenario, the TGF resulting from a relativistic runaway electron avalanche (RREA sec. 1.4.4) was seeded from a cosmic ray at 12 km of altitude in the high electric field region of a thundercloud.

Time

The duration of a single TGF is typically [725] < 1 ms: mostly between a few tens to about 500 µs [628, figure 5]. However, a burst can sometimes be composed of multiple pulses with a separation time of a few milliseconds [292, 628, figure 8, table 2]. Photon detection requires a certain reading time during which the detector cannot process new information. This lapse of insensitivity is referred to as *deadtime*. In some cases, short <500 µs double-pulsed TGF can emerge as an artifact from the detector's deadtime causing paralysis [335, figure 5].

Multi-pulsed TGF are more frequently observed from ground as shorter pulses [2] < 10 µs separated by a few hundred µs, or even < 2 µs over a total of 16 µs [943]. It is probable that actual TGF durations are shorter than observed on average due to significant delaying by scattering in the atmosphere [162]. Sometimes, pulses emitted from the same thunderstorm region separated by several seconds ($\gtrsim$ 10 s) would rather be considered as two separate consecutive TGF [874, table 1]. They suggest that TGFs are capable of significantly discharging a cloud region which needs some time to recharge. Other temporal characteristics can be retrieved from their lightcurve displaying the photon counts along their time of arrival. A majority (about 2/3) of pulses have asymmetrical [297] time profiles. Their rise time can be very short $\lesssim$ 50 µs [292, 630] while fall times are usually longer. Also, harder photons tend to arrive before softer ones [692]. Asymmetry is compatible with the Compton scattering [162]; both softening and delaying photons as they make their way out of the atmosphere [354].

Spectrum

One of the most distinctive feature of TGFs is their spectral hardness [627, figure 2]. It presents an inverse power-law in energy [859, figure 2-right] in accordance with photon distribution from bremsstrahlung [515, Table I] and a steeper decrease beyond 10 MeV explained by the exponential cut-off energy about 7 MeV for relativistic runaway spectra [245, §8] which will be described below. Deviations from power-law spectrum can be explained with photo-absorption effects below 50 keV and softening of harder photons by Compton scattering above 1 MeV [245, sec.3].

The maximal gamma-ray energy observed kept breaking records for a decade [627, 859, 918]. For a while, it had been thought that TGFs reach up to 100 MeV [918]. It was later shown [629, figure 5] that this had been an instrumental artifact known as *pile-up*, where two (or more) photons enter and deposit their energy into the detector within the same "reading time" and so are confusedly counted as one harder photon. Nevertheless, the upper energy limit [627] could possibly lie around 40 MeV. This is a quite challenging energy since, under an electrostatic assumption, a free electron would need to traverse from the main negative layer to cloud top in a massively charged thundercloud to reach such an energy. On top of that, it should remain unscathed by the dangers of losing energy through collisions with molecules. A mechanism known as relativistic feedback presented later 1.4.4 could explain this energy by seeding high-energy electrons at the foot of the high electric field region.

Fluence

At spacecraft altitudes, on average each cm^2 will be traversed by 1 gamma-ray during a TGF event [110, 630, §2.3] (the definition of fluence). The flux density, expressing the count rate per second per unit surface, estimated to peak [110] at several thousand photons/(s.cm^2) leaves not enough time for the detectors to recover (deadtime) and thus is often difficult to derive. Fluences on ground are highly dependent on the relative detector location to the TGF beam [2] and can be as high as almost a million photons [970] passing in a cm^2 !

In total, a TGF can produce around 10^{15} [630] to 10^{18} [970] photons in the brightest cases. However, this number is more meaningful when a lower energy threshold is fixed and depends on how losses by absorption and pair production are taken into account. The detection efficiency also plays a significant role in the fluence estimation. The detector's deadtime is responsible for a loss of photon counts [354] when their flux is too high. Correction of this effect implies that there could exist fainter TGFs comprising 10^{14} or even 10^{12} photons, suggesting a higher occurrence of 35 TGFs/min [723].

Geometry

Temporal, spectral and flux properties of TGFs are obviously affected by the geometry between the source origin, its orientation and the point of observation. As a result of more absorption and scattering, TGFs observed at larger angles from their source present a softer spectrum [724], fainter, flatter and longer light-curves [391]. Combining the source geolocation and spectra of observed TGFs, the average beaming half-angle of a TGF was estimated to lie between 30°and 40°, with 20°being the maximal deviation of the electric field from the vertical [334].

Production Altitude

Localising the origin of TGF in altitude accurately is a complicated process which requires Monte Carlo modelling of gamma-ray propagation in the atmosphere or timing analysis with concurrent radio-waves detected on ground.

Initially it was thought that TGFs must emerge from high altitudes [291] because of strong atmospheric gamma-ray absorption rate below 30 km or so [692, 859], and thereby related to sprites [423]. This presumed that after an intra-cloud discharge neutralises the main charge layers, the electric field above the cloud becomes strongly enhanced and pointing downward due to the negative screening layer over cloud tops. As a result, a breakdown occurs launching the sprite discharge [54]. At the same time, the electric field above cloud tops (~20–25 km) may exceed the runaway breakdown threshold and avalanches of fast electrons would be the final kick for a TGF to spring upward [576, 787, fig.7, fig.8.c].

Later, Monte Carlo simulations of gamma-ray generated by runaway electron avalanches and their propagation through the atmosphere [152, 245] situated the initial guess to lower altitudes of 15-21 km. Depending on the height of the tropopause at a given region, this would correspond to the upper part of, or some kilometres above thunderclouds.

In the recent past years, it became gradually more and more surmised that TGF may well be produced at even lower altitudes [2], say, within the large inter-charge region of maximal electric fields [970]; and that the TGFs seen from space may constitute just a minor portion of a whole. The controversy about initial guesses could partly be imputed to deadtime corrections of the detector [335] and also to underestimation of TGF intensities.

Observations from ground revealed that the upward TGF had a twin: the downward TGF. At first, the ground detection of gamma rays from lightning activity did not venture to mention any link with TGF [118], or this link was very timidly [239, §13] laid. Nonetheless, it was clear that those events comprised much harder spectra than "x-ray" bursts observed in correlation to lightning leaders [252]. With time, similarities in temporal characteristics, spectral hardness and concurrence with radio-emissions led to recognise that gamma-ray burst from ground and TGFs from space were part of the same family. A decade later, TGFs had conquered unpresumed regions in the inner depths of thunderclouds [1] below the main negative charge layer [970], to be accepted as part of their cradle.

Radio Signature

As a powerful discharge resulting from acceleration and multiplication of relativistic electrons, a TGF fills the space with many free charges whose migration in the ambient field generate strong electric currents. As mentioned before, any non-uniformly moving charge stirs electromagnetic radiation. Thus, any discharge process; breakdown initiation, leader activity, return strokes and a large portion of TGF, are all found in simultaneity with radio-waves [188, 615] known as *sferics*, a contraction for "atmospheric waves". Those are **v**ery **l**ow **f**requency (VLF) electromagnetic pulses between 3–30 kHz (100–10 km-long wavelengths) that can last about one millisecond [202, §1.]. They can reach very far distances as they propagate in the waveguide delimited by the conductive layers: ground and ionosphere. Shorter TGF pulses should in principle produce higher current peaks [248], and so present a greater association rate with sferics. The time analysis of TGF and sferics led to a significant progress in understanding their connection to lightning discharges [619]. A VLF signal of the magnetic field in relation to high-energy photon counts • (from [336, fig. 4]) is represented by the black fuzzy curve on the bottom of figure 1.8.

Relation to lightning

Finally, one of the greatest enigmas of TGF is their connection with lightning. After TGFs had been known to develop in high electric field regions *inside* [829] thunderclouds, it was natural to ask what role would they play in relation to discharges: as an auxiliary [610] or as an antagonist [484], or simply as a witness?

Due to limitations imposed by timing accuracy, a causality relationship between discharges and TGF is a difficult to ascertain observationally. Initially, some sferics were found to emanate from intra-cloud discharges that were delayed from lightning a few milliseconds *after* the TGF [875, table 2,]; whereas in other cases, positive cloud-to-ground discharges seem to appear within 1 ms *before* [202]. Later, with improved timing analysis and calibration, it was found that sferics and TGF are simultaneous events to within ~1 ms [336] without any systematic delay of one over the other [626, figure 3].

Notwithstanding, on longer timescales, there is a resurgence of lightning activity observed about half a second after the occurrence of a TGF [592, §4.2]. Much evidence points also toward a link between TGF and early [610, 829, 854] or late [20, 754] leader development. In the former case, the TGF seems to occur simultaneously with leader steps [56, 610] implying a possible connection to the streamer-to-leader transition (see figure 1.9). In the latter case the TGF is observed at the outset of a significant leader step detected by the radio-pulse of its current surge. In rocket-triggered lightning events, TGF were observed when the leader unleashed itself just after vaporising the trailing wire [239, figure 4]. When it comes to the return stroke, observations are again ambiguous, with TGF clearly starting some hundreds of microseconds *before* [592, 754] and *after* [943, figure 3] the stroke onset.

On the one hand, the concept that the avalanche generated by TGF could actually foment breakdown due to an intense region of ionisation is not ill-founded [369]. On the other hand, the evidence that TGF are related to leader stepping is overwhelming [1, 56, 696] and supported by possible scenarios [246].

Moreover, the possibility that some TGFs be not related with lightning discharges remains open, both theoretically [248] and observationally [860, §3.4-(figure 9)]. The timing analysis of TGF with sferics is a delicate process that relies on the clock and geolocation accuracy of all instruments involved; the correct deconvolution of signals originating from the same source dispersed and delayed over an array of detectors; and the synchronicity constraints imposed by the user. Any time or spatial imprecision will smear the clues about the order in which the events

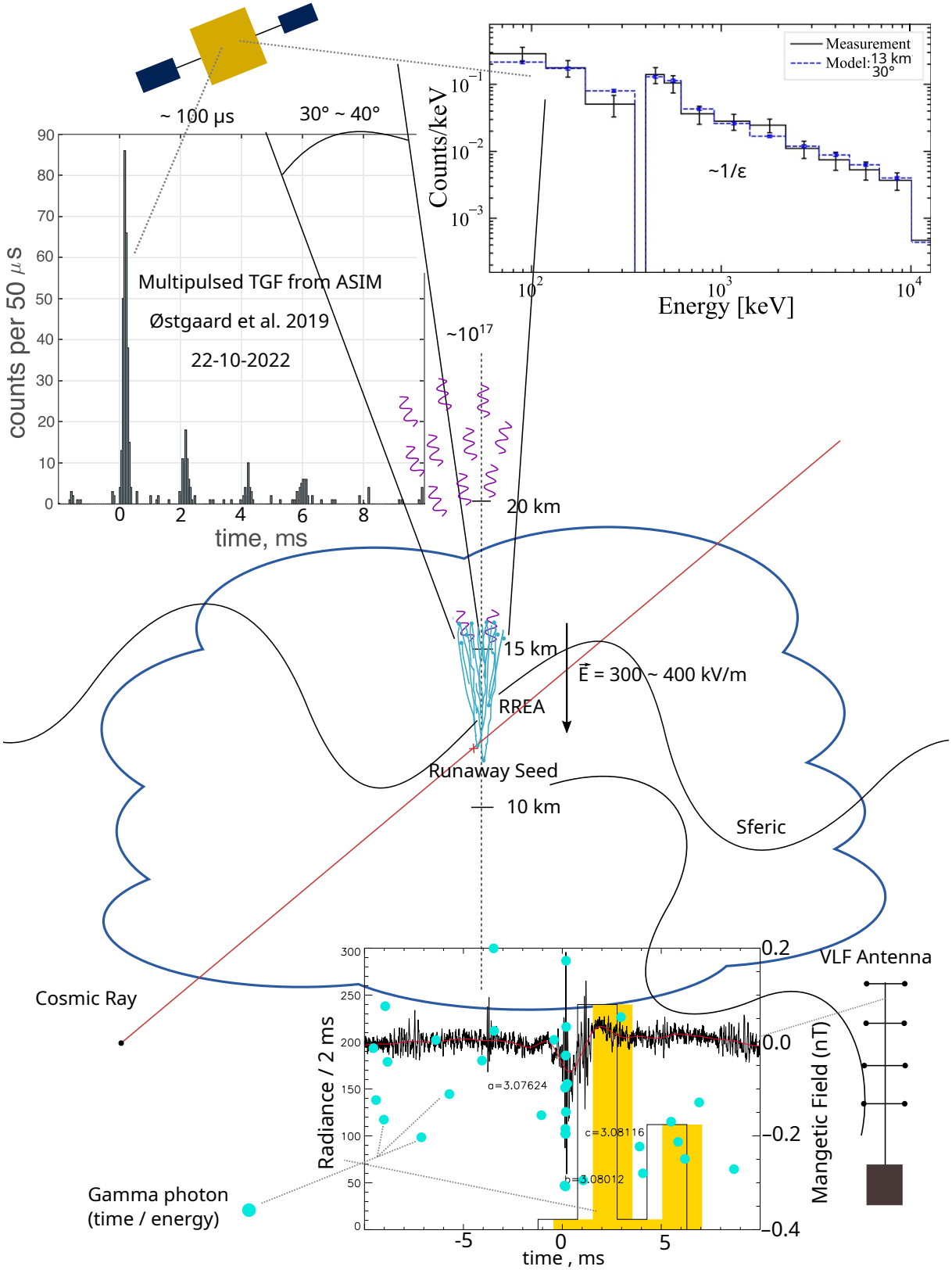

Figure 1.8: Sketch of a TGF beam from relativistic runaway avalanches and its characteristics observed from space.

occurred. As a result, despite the high association rates seen in some studies [619, 829], it is not always possible to find a match in sferics [628, §5.6.1] or light flash for every TGF detected. In principle, a TGF is a glow with considerably more runaway avalanching and terminated by a sharp screening of the electric field by the discharge. Why does a thundercloud region yield glows instead of a series of pulsed TGFs is a still a difficult subject.

For now, we may reasonably suppose that TGFs can at least emerge from two regions of intense electric fields: between the main negative and upper (lower) positive layers for upward (downward) types. Additionally, since the atmosphere is opaque to gamma rays [239], and that TGF beam in a relatively narrow cone, there is a high chance that only the brightest TGFs are actually detected from space [619], which would imply that the phenomenon is commoner [112, 723] than observations lead to think [859]. We may also speculate that TGF have a special relationship with leaders that lift the electric field above the runaway threshold and also that could sooner or later yield seed electrons provoking a relativistic avalanche, if the ambient field is high and long-lasting and spatially extended enough. The pulsed characteristic of TGF is an indication that their playground is repeatedly confiscated through an efficient screening of the electric field by the charges displaced in the process of the discharge [246].

A recent monitor specifically aimed at observing TGF and transient luminous events in relation to lightning named the **A**tmosphe-**S**pace **I**nteractions **M**onitor [695] improved considerably the TGF statistics [592] through finer temporal and spatial resolutions of its detector, a higher detection efficiency and most importantly: a synchronous observation in the UV and visible domain [696]. If all of the possible TGF-lightning scenarios come to be correct, then many new members are expected to enliven the typology of TGF in the next years [619].

To sum up, it is difficult to determine a clear relationship (causal or concurrent) between a discharge and a terrestrial gamma ray flash. If thunderstorms were a theatre play, TGF would be susceptible to literally pop up at any act, provoking a frenzy among spectators and infuriating the playwrights. To spark further the atmosphere, in the next subsection we shortly expose some additional effects of gamma-ray and X-rays in discharges that attest to the great amount of energy released in bursts.

1.3.2 Collateral radiation

On a causality scale, runaway electrons may be viewed as the first high-energy particles yielded by discharges and their bremsstrahlung photons are secondary products. In this subsection, we consider the third effect of a runaway discharge which is radiation induced by those photons. There are essentially three tertiary radiation types that are generated in the torrentuous wake of gamma rays in a TGF:

- Electrons ejected in almost any gamma-ray interaction with molecules : Compton scattering and photo-absorbing ionisation and pair production.
- Positrons produced exclusively by pair-production, most of which will annihilate back to release two 511 keV photons.
- Neutrons through photo-nuclear reactions* with nitrogen [308] nuclei which are accompanied by a beta-electron.

Electrons produced by gamma rays may potentially have a significantly different impact than ordinary bulk runaways. At elevated altitudes, the air molecules rarefy so that the motion of

*Protons predicted by another open channel of this reaction were not observed in natural or laboratory discharges

charged particles is gradually less dominated by collisions and become governed more under the influence of electric and geomagnetic fields. If a gamma-ray escapes the cloud and sows an energetic electron/positron in the upper atmosphere, the latter can evade toward satellite altitudes. Such electrons (possibly including positrons [111]) form terrestrial electron beams (TEB) which follow geomagnetic lines [249] and eventually become trapped in the magnetosphere bouncing back and forth by mirroring near the poles [806]. This reflective signal made them considerably easier to distinguish from TGF by satellite detectors [111].

During two flight campaigns inside thunderclouds [251, 516], important numbers of positrons were detected from their annihilation peak at 511 keV. They appeared in connection with electric discharges triggered by the aircraft body [516, figure 8]. Only photons above 2×511 keV ≈ 1 MeV can produce electron-positron pairs (fig. 1.7). Additionally, the production efficiency is higher for heavier nuclei [392, §20.1 p.195(7)]. Thus, one could imagine that the positrons were produced by gamma-ray beams impinging on the aircraft shell, generated themselves from runaway electrons produced by the attached discharges. Although positronic emissions were observed in natural lightning [267] supposedly from downward-directed positron beams [951], the absence of similar reported results in laboratory sparks makes the phenomenon intriguing.

Another fascinating discovery was the observation of neutron beams in relation to lightning [174] and even, reportedly, in laboratory sparks [6]! At first, it was mistakenly thought that neutrons came out as products of deuterium fission in the hot plasma channel of a return stroke [825]. It was shown [33] however, that the neutron yield would be much more likely [49] related to runaway electrons through photo-absorption of their bremsstrahlung gamma rays by nitrogen nuclei [267], in which case they are baptised *photoneutrons*. Detection of neutron enhancements at ground is of phenomenal significance. First, most photoneutrons thermalise through multiple collisions with air molecules and are captured by nuclei whereupon a nuclear reaction triggers [267, Extended-data figure 4]. Thus, detecting just a few tens of neutrons in a short period can indicate a very consequential number [153], some 10^{12} of neutrons at the production source of thundercloud altitudes [48]. Second, the threshold for this photonuclear reaction is about 10 MeV, and its cross-section represents a minor ~ 5% of the total gamma-ray interactions. Generation of neutrons requires therefore a high flux of energetic photons. Third, various works report detection of fast neutrons (>10 MeV) [876], intense neutron fluxes [362] and neutron pulses before the formation of a leader in laboratory discharges [5]. This spurred a debate about the plausibility of photonuclear reactions as a unique source of neutrons [174, footnote 4] and raised many doubts [37] about the credibility [34] of the neutron detection instruments. Neutron beams related to discharges currently feature as the most puzzling topic in this domain.

An extensive review of high-energy radiations in electric discharges was conducted in Babich [32], where more details of observations, experiments and models are available. Before we zoom onto mechanisms of electron runaway in gases, we propose to turn toward the subject of X-rays bursts which may have a relationship to neutron production in lightning.

1.3.3 X-rays

As opposed to TGF, X-ray bursts are unambiguously identified to correlate both temporally and spatially with negative leader steps [241] or dart-leader tips [244]. On a few occasions, X-rays were detected from positive natural leaders [994, Flash B] and positive laboratory sparks [243].

The typical scales of X-ray burst in natural and triggered lightning are reduced compared to TGFs. They are briefer $\lesssim$ µs [240], and less energetic $\lesssim 1$ MeV [659].

In laboratory sparks, the duration of a burst can be as short as a few nanoseconds [518, 519, fig. 3-right-bottom]. The voltage of the setup is typically [242, 517] above 1 MV. Prompter voltage rise times and higher peaks promote the occurrence of bursts [625]. Surprisingly, X-rays

were also detected for lower voltages [203] of 100 kV and shorter gaps [242] ~10 cm. In lab sparks, an individual X-ray burst comprises about ~ 10^4 photons [519, 698] emitted in roughly all directions although recent experiments with rings of detector arrays reveal a more structured multi-beamed pattern [7, figs 7–9], pointing toward a link with runaways from streamers. Though hard, the spectrum of X-ray bursts seems softer than TGF, with an exponential decrease at a characteristic energy of roughly 200 keV [518, 519] as opposed to an inverse power law.

As expected, leaders of triggered and natural lightning can present more intense and energetic bursts than lab sparks [244]. Their emission pattern seems to vary between diffuse (roughly isotropic) and compact (beamed) modes [808].

The most favourable conditions to X-ray bursting are primarily sought at the encounter of negative and positive streamers [191] just at the culmination of a leader step. Indeed those two tips of opposite polarities can be regarded as mobile electrodes closing into each other, strongly enhancing the field in the middle gap. The electrons ahead of the negative streamer are subject to intensifying fields and as the threshold for thermal runaway is crossed, they rush out spurting bremsstrahlung X-rays after they reach high-energies around 1 MeV. Two doubts press against this scenario: is the threshold crossed? If it is, does it last long enough to allow enough electrons to accelerate toward beyond the runaway energy threshold of the ambient field domain*? So far, simulations have been mostly sceptical [44, 170, 422, 531, 579].

Meanwhile, observations have been providing more evidence that thermal runaway not only occurs in sparks but also in a rich diversity of laboratory experiments not associated [203, 827] with streamer collisions and stepping. X-rays in various energy ranges were routinely observed in helium chambers [301, 707], streamer corona [826] and diffuse corona [828] discharges from pulsed voltages [827]. Also, since the efficiency of bremsstrahlung increases proportionally to the square of the material atomic number (Z^2) [515, Table I], it must be kept in mind that the anode or any metal plate in general are bountiful sources of X-ray emissions [203].

Notwithstanding, regardless of whether the X-ray origin lies in the gap or at the anode, their presence attests that electron thermal runaway is much more ubiquitous than one could initially imagine. Perhaps most perplexing is the fact that the energy gain of runaway electrons in gases can exceed the total potential difference [913] (see also [548, p.215]). This observation was not due to pile-up effects in detectors corresponding to the addition of simultaneous X-ray deposited energies within the detector time resolution. This implies that space charge effects in avalanches [913, 990], streamer tips [171, 243, §34] and ionisation fronts [612, 957] play a role in the runaway mechanism. Understanding in each case (diffuse corona, streamer tip, pilot encounters) what conditions permit this phenomenal electron acceleration in spite of the overall friction force by the gas is a challenging issue [170]. An overview of mechanisms able to generate runaway electrons in gas discharges is available in Lagarkov and Rutkevich [548], which stresses the importance of forming an ionisation wave where the electric field peaks at its highest point due to high concentration of space charges at the ionisation front. The hypothesised production of runaways in discharges is represented on figure 1.9. We may summarise them into three categories:

(a) SAEB: supershort avalanche electron beams in very brief and steep voltage pulses (~ 2 ns with a 0.5 ns rise time of an amplitude of a few hundred kV) on cathodes lead presumably to a local enhancement of the electric field beyond the thermal runaway threshold [913]. The runaway electrons generated would not only produce X-rays in the gap and at the anode, but also preionise the surrounding air which explain the formation of a diffuse discharge [826]. To our knowledge, this scenario has never been tested theoretically.

*The minimum of the electron average friction curve in air 1.10 is slightly above 1 MeV. In principle, runaways seeded at lower energies could thus reach the MeV domain provided that the ambient field is above the absolute runaway threshold field.

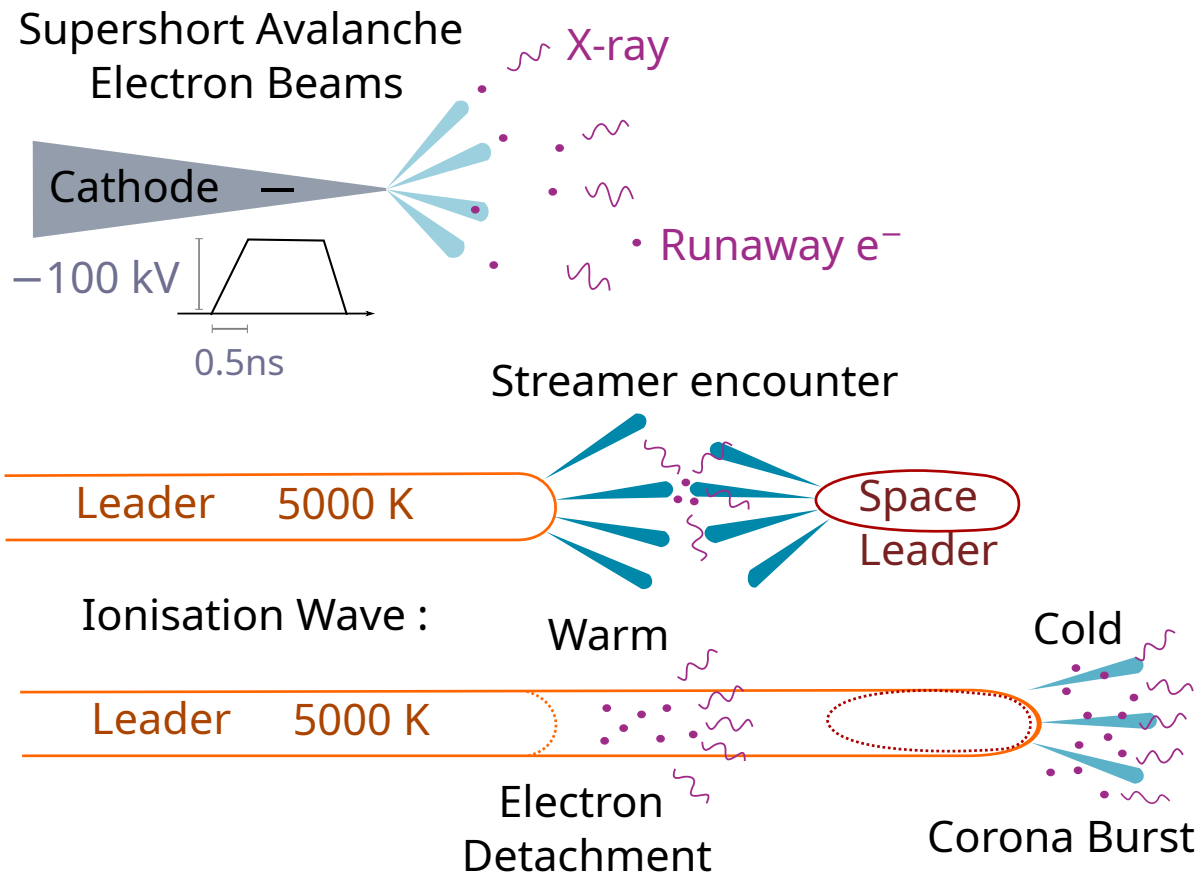

Figure 1.9: Hypothetical X-ray emissions from runaway electrons for various stages of a spark discharge: (a) supershort avalanche beams near short-pulsed electrode [828, 912] (b) pilot (counter-streamer) encounter [190] (c) warm and cold ionisation wave surfing from a sudden expansion of the leader channel [36, 39].

(b) Streamer encounters: the electric field in the gap between oppositely charged streamers is locally enhanced beyond the thermal runaway threshold. This hypothesis modelled by numerous independent researchers has not given convincing results [44, 531, 579].

(c) Ionisation waves: an ionisation wave propagates much faster ($\gtrsim 2\times10^7$ m/s) than a streamer front. It is self-sustained by preionisation of the air by very fast runaway electron ahead of the wave and by a high concentration of electrons in the head which leads to an enhancement of the electric beyond the thermal runaway threshold. This might be called "surfing" in the image that fast electrons keep up with or ahead of the ionisation wave, as opposed to streamer heads which propagate faster than the electrons in the head because it hosts no runaways. This scenario was proposed in Babich *et al.* [36] and Luque [612] and seems theoretically plausible [38, 39], but requires further investigation.

We will come back to the potential role of ionisation waves in the next section. We now finally move to the electron runaway mechanisms at the root of high-energy radiation, operating ubiquitously behind the scenes.

1.4 Fast Electrons

Ordinary electrons roving freely in gases have low sub-eV energies much below excitation and ionisation thresholds of molecules. In case a moderate electric field is applied, some electrons may gain more energy reaching at best a few eVs. Even under fields above conventional breakdown at 3 MV/m in standard conditions, most electrons barely accumulate several tens of eV before they lose it by impact ionisation of molecules. Their fate glooms far below the bewildering domain of MeV fast runaway electrons producing bremsstrahlung photons discussed above.

It is thus not unreasonable to categorise electrons according to the effects they may induce in their medium. We distinguish at least three "classes" of electrons:

- Bulk (~ eV) : those electrons form the vast majority of the total electron population present in a gas with a mean energy situated in the eV range that increases with the electric field (cf. fig. 4.13-bottom).
- Runaway ($\gtrsim 100\,\mathrm{keV}$): those energetic electrons above hundreds of keV, may gain energy from acceleration in the electric field which exceeds the average energy loss rate from collisions with the gas particles.
- Intermediate (~10 eV–10 keV): there is a very large range of energies over which electrons are neither part of the bulk, nor can they run away. Nonetheless, this region is populated with electrons that actively ionise the gas and foster avalanche multiplication.

A useful illustration of this separation is represented in the next chapter's figure 2.1 at the beginning of section 2.2.1, showing also the corresponding electron velocities. The boundaries between these categories are loose and are affected by the intensity of the electric field. Physically, the dual separation (bulk vs. runaway) from which an "intermediate" class emerges, can be best grasped looking at figure 1.10 showing the average friction force acting upon an electron propagating in a gas [786, figure 1]. This force, strongly dependent on the kinetic energy, represents the average energy loss rate through inelastic collisions per unit of trajectory length. It only slightly differs from the stopping power that expresses the loss rate in terms of penetration depth in a medium; disregarding the tortuous deviations an electron can take as it collides with atoms and molecules. Obviously, a denser gas offers proportionally more resistance to electron motion. For this reason, to compare electric to friction forces scalable in density, it is customary to divide the external electric field E by the gas particle number density n to give a *reduced* electric field : E/n traditionally measured in *Townsends* (Td=$10^{-21}\,\mathrm{V\,m^2}$).

From a mechanically deterministic perspective, an electron in a field surpassing (scanting) its average friction ought to gain (lose) energy. The shape of the friction curve in air presents a global maximum around 150 eV mainly due to losses through impact ionisation and a secondary peak below at 2–4 eV due to vibrational excitation of nitrogen molecules. The broad bump between 15 eV–10 keV can be considered as delineating the intermediary region between ordinary (bulk) and energetic (runaway) electrons. All electrons to the right, whose friction is below the horizontal bar of the given electric field are deterministically bound to accelerate up to higher energies beyond MeV to become runaways and start radiating bremsstrahlung photons. For the rest, the friction prevents electric acceleration and hampers electron motion in the gas. Three special field values have been set out in figure 1.10. Starting from the lowest:

- Runaway Threshold : 200✠ kV/m equiv. 7.8 Td
  Corresponds to the minimum field capable of sustaining a runaway electron (close to 1 MeV) in air [250, §2.2.1 eq-2.1]. Below that threshold, no runaway can occur, all electrons would thermalise after several collisions.

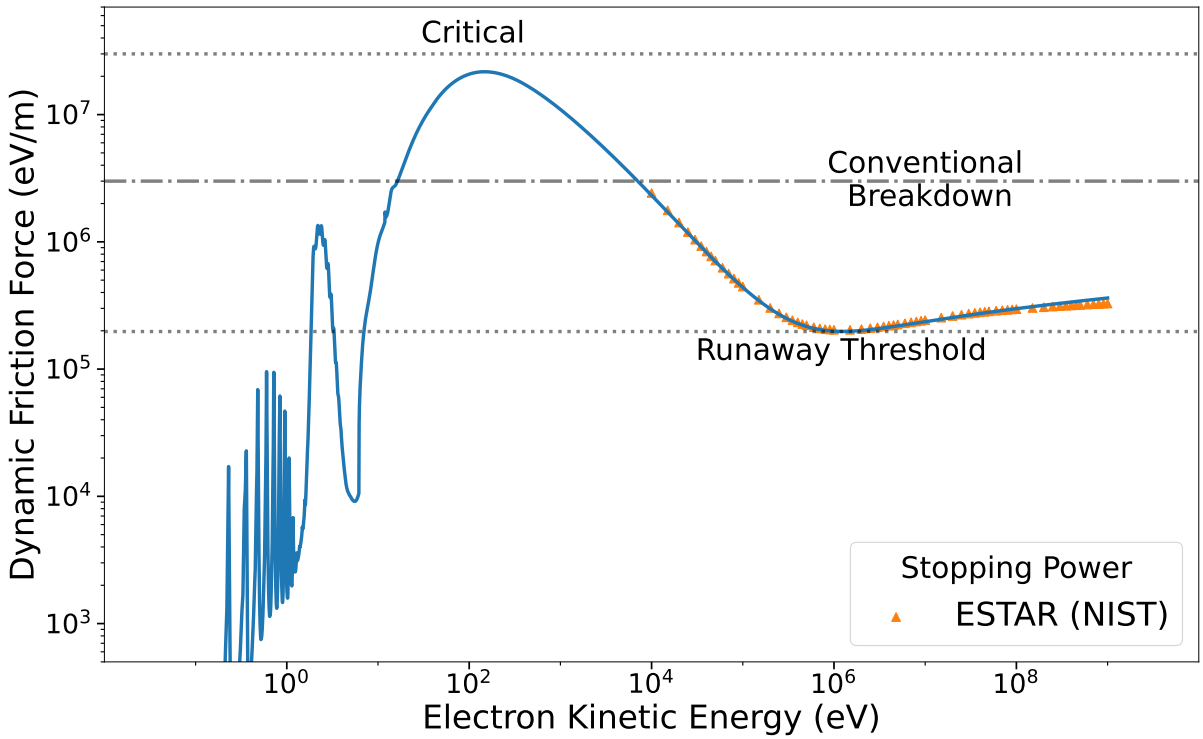

Figure 1.10: Average friction force acting upon electrons depending on their kinetic energy, due to their inelastic collisions with air molecules. Computed with the database created in this thesis (see part II) in standard dry air atmospheric conditions (see next chapter 2.1).

- Conventional Breakdown : 3✠ MV/m equiv. 118 Td
  At this special value, free electrons in air are capable of acquiring enough energy to ionise molecules just so to compensate for their loss through attachment to oxygen [761]. It is not a coincidence that this value happen to be just above the secondary peak between 2–4 eV, enabling thus a few electrons to accelerate into the middle dale at some tens of eV beyond the ionisation energy threshold around ~ 1Ryd ≃ 13.606 eV.

- Critical Threshold* : 30✠ MV/m equiv. 1180 Td
  This field, if attained, would rapidly flush all free electrons into the runaway regime. This process would also generate an exponential avalanche of new electrons from ionisation and an intense beam of bremsstrahlung X-rays. Such a high field would not be able to sustain itself for long as it would be quickly screened by the massive charge displacement instigated.

Interestingly, those three thresholds form a trio; each separated by an order of magnitude which makes them easy to memorise: ~(0.3,3,30) MV/m in standard air or ~(10,100,1000) Td. Their exact value is not fixed. For instance, the minimum of the present dynamic friction curve✠ is actually at 0.2 MV/m, but because of the dispersion effect of scattering from electron-molecule collisions, the true runaway threshold is estimated at ~282 kV/m [40, 236, 579, p.3, p.613("δ = 1.3"), appendix C.], hence the 0.3 MV/m value in the trio.

*Of interest, this field is known as the Dreicer field when applied to *fully* ionised gases [230, eq.(20)]. We ought not to adopt the same name in the present situation where the gas is *weakly* ionised where the premises for the theory [231] do not hold.

✠At standard atmospheric conditions temperature 15 °C and pressure of 1013.25 hPa.

Conventional breakdown might be determined experimentally from laboratory experiments [762, §7.2.5], though it inevitably presents a certain sensitivity range to the electrode shape and gap length. Formally, it can be defined as the field in which the net ionisation by electron impact is exactly zero. Some electrons ionise molecules whereas other attach to oxygen, keeping the overall balance of free electrons constant.

A more precise value, for each of the thresholds defined, can be estimated by simulations. The runaway threshold is the minimal field at which a high energy electron can sustain itself. At conventional breakdown, the swarm's growth annihilates because ionisation compensates attachment. Interestingly, the conventional breakdown intersects the friction force at about 16 eV, close to the ionisation threshold of nitrogen molecules (15.6 eV). The critical runaway threshold is perhaps the hardest to determine due to the stochastic nature of electron acceleration in electrified gases. In principle, there is always a non-zero probability that after a finite (although indefinitely long) period of time, an electron might flip into the runaway regime. Thus, one must constrain better the concept of thermal runaway: impose time limits and probability thresholds. This issue will be explored later in chapter 5.3. In any case, the influence of elastic scattering raises the actual value of the thresholds due to additional energy lost by dispersion of electrons [169, 811]. Furthermore, the thresholds conjectured from simulations using different cross-sections databases also present some differences that could be used to estimate the uncertainty of these thresholds.

Without further delay, we describe below the four basic mechanisms capable of supplying fast electrons as a requisite for intense bursts of bremsstrahlung radiation.

1.4.1 Thermal Runaway

When no source of energetic electrons is at disposal, thermal runaway [368, 371] is the only possibility to obtain so-called "seed" electrons to start a runaway multiplication. One could define that a *seed* corresponds to an electron at an energy beyond the runaway threshold determined by the "ambient" electric field. We could attempt to categorise studies upholding this thermal seeding mechanism in the four following strategies.

Near-critical electric fields are sought at leader heads [163, 677], streamer tips [161, 170, 171, 587], inter-streamer gaps [44, 422, 531, 579], ionisation fronts [39, 192], and even supershort avalanches [913]. Their existence in a small region for a sufficient period of time would permit to accelerate electrons beyond the runaway threshold.

Stochastic acceleration holds that if the field be high enough [43, table 3], though not critical, the chances that some electrons can reach the runaway regime are greater [218] if: the field be long-lasting (≫ns), and/or the available electrons be plentiful ($\gg 10^9$).

Pre-conditioning of the surrounding air includes many effects that each make a modest contribution to facilitate thermal runaway. Since the corona is composed of thousands of streamers repeatedly waning and re-flaring at the leader/electrode tip, it is not unreasonable to suppose that the air swept by the corona have its conditions altered by: a neutral plasma of free ion and electron charges [421], a non-equilibrium excitation temperature [852] or even a lower density due to thermal expansion [530]. The pre-ionised channel would enable an enhancement of the electric field [36] while the thermally excited and expanded gas would decrease the average friction force.

Inter-electron Coulomb collisions[379] could occur in very localised dense regions of electrons such as at in ionisation fronts. In this case, electrons would be able to transfer energy amongst themselves which would affect their spectral (energy) distribution [376] and thus the probability that an electron become* runaway.

*Readers disturbed by the missing 's' may consult chapter 17.1 about the almost extinct use of subjunctive in English.

The compartmentalisation defined above results from an observation of strategies adopted in studies devoted to thermal runaway. Their importance decreases in order of presentation and the hypothesis that Coulomb collisions could bring a contribution to runaway generation has been suggested [579, p.6499&Appendix B] but, to our knowledge, has not been tested yet in Monte Carlo simulations of discharges in air. Nonetheless, in the light that experimental observations show a manifold of discharge types capable of producing runaway electrons [244, 520, 826, 828, 913], it is not improbable that the recipe for runaway in each situation lies in a carefully chosen conjunction of the effects presented.

Presently, thermal runaway is the only viable mechanism explaining X-ray bursts from leader stepping [164] and hard corona streamer emissions. Furthermore, due to its ubiquitous manifestation in discharges, it also qualifies as a promising candidate for TGFs related to leader activity [161], especially those with the hardest spectra [163]. The other mechanisms of runaway avalanche presented below require very extended regions (some hundreds of meters) with an electric field sustained above the runaway threshold in order to yield a significant amount of runaway electrons.

1.4.2 Runaway Avalanche

The three main sources of free electrons in the atmosphere are radioactive decay of Radon (Rn^{222}) [660], cosmic background comprising both solar and extrasolar ionisation [952], and so-called extensive air showers [795] of secondary electrons and other particles provoked by singular extremely energetic $> 10^{15}$ eV cosmic rays. The supply of fast ~ MeV electrons depends strongly on the altitude and can present accentuated variations due cosmic weather conditions and geographical location. At ground level, radon decay [290] releases 5–7 (0.1 at 10 km) fast 0.1–1 MeV electrons/(m^3.s) [660, figure 3]. Cosmic background [952, figure 1] produces in total $\sim 2 \times 10^6$ (40×10^6 at 10 km) electrons/(m^3.s) of which only a tiny fraction (~ 3 in a million) is in the MeV range or above. In contrast, the electron densities induced by air showers are highly inhomogeneous spatially and temporally [795], and can peak to 10^9 /m^3 in the shower core at thundercloud altitudes. Notwithstanding, only a minor fraction of those electrons exceed the runaway threshold set by the field inside a thundercloud.

The first suggestion that fast electrons* might accelerate in high electric fields of thunderclouds and produce X-ray radiation and secondary electrons, was made by Wilson [986]. Deeper implications arise if some of the secondaries have energies beyond the runaway threshold. In this case, the electrons produced by impact ionisation are divided into two sub-populations: runaways that feed the avalanche and bulk that quickly thermalise as they cause more ionisation [646, figure 5]. The separation line between both populations corresponds to the *runaway threshold* which lies close to 1 MeV and decreases for higher fields according to the braking force (fig. 1.10). The currents carried by the bulk thermal charges emit radio-waves and lead to a gradual screening of the field [364]. This form of discharge is known as runaway breakdown (RB) [365]. Its peculiarity is distinguished by the dependence of the thermal bulk on the runaway few. The field does not enable non-runaway electrons to multiply, they can only be seeded by runaways. In the long-term, the space charge of the bulk attenuates the ambient field below the runaway threshold and the avalanche subsides on its own. Long-lasting gamma-ray glows in thunderclouds [369] could be attributed to an equilibrium between runaway breakdown and cloud electrification [236, §10].

*They were usually referred to as β particles but without specific relation to a radioactive decay.

1.4.3 Relativistic Runaway Avalanche

In principle, there is no unanimous distinction between Runaway Breakdown (RB) and its re-baptised name of Relativistic Runaway Electron Avalanche (RREA) discussed in the present subsection. The former (RB), was proposed by Gurevich *et al.* [365] as a responsible mechanism for inducing a lightning discharge and thus a breakdown of the electric field [369, 370]. The model of RB was mostly supported by kinetic theory based on the Boltzmann equation [789] (see sec. 2.3.2).

Later, Monte Carlo (MC) simulations of the relativistic runaway avalanche process were implemented [42], in which the individual erratic motions of runaway electrons could be tracked. Such a stochastic description of RREA brought a considerable improvement over kinetic models [41, 576] and insight into the relationship between runaways and bulk electrons [247]. We discuss those characteristics below.

The spectral distribution of runaway electron energies in an avalanche is almost independent of the electric field [250, figures 3-4] and fits well with an exponential distribution of characteristic (and average) energy at 7.3 MeV [786, table 9]. It can be interpreted as the average energy gained by a runaway per avalanche length traversed. The shape of the spectrum changes abruptly below the runaway energy threshold where it roughly follows a power-law [247, figure 3] due to the gradual energy degradation of sub-runaway electrons from the dynamic friction force.

At any given time, the total length of an avalanche is the distance Δl from its source (starting point) to the front line* (leading edge) beyond which virtually no ionisation has yet occurred. Its measure in terms of the characteristic e-folding (Euler's exponential constant) length λ yields the amplification factor used to approximate the number of electrons $\exp(\Delta l/\lambda)$ at the front. Together with the temporal exponential growth scale τ, the avalanche propagation speed $v_{av} = \lambda/\tau$ is determined to be loosely constant at 90% of the speed of light [184, figure 1-bottom]. Indeed, the avalanche length λ and characteristic time τ are found to decrease correspondingly at higher fields and air densities [40].

To this day, there is an ongoing discussion about the relationship of relativistic avalanches with lightning activity. There are two conflicting views whether the avalanche may lead to breakdown of the electric field or not. We present two opposite scenarios.

1. **Inception of Breakdown** : As the avalanche extends, more electrons accumulate at its front; to the point where space charge effects start to dominate over the ambient electric field. Beyond a certain electron density threshold, charge displacement by conductivity dominates over the attachment to oxygen and the electrons can form a cold patch of plasma. As a response to the ambient electric field, the patch polarises and raises the field at its boundary [369]. When it reaches the breakdown threshold, the patch may foster the formation of a streamer [864]. This mechanism would suggest runaway avalanches as precursors to lightning breakdown [646]. Whether the electron bulk produced by the relativistic avalanches may introduce a significant breakdown of conductivity and spur the formation of a streamer in a region of locally enhanced electric field, poses an intriguing question [35, 795].

2. **No Breakdown** : Monte Carlo simulations do not endorse the assumption that the displacement of the bulk space charges produced, lead to a breakdown (significant screening) of the electric field. To the contrary of previous claims [364], the bulk electrons produced in RREA, seeded and sustained by cosmic-ray background or even an extensive air shower, would not be sufficient for causing a breakdown of the high-field region [247, §52-56]. The

*Actually a surface over a solid angle in 3D

terminology of "runaway breakdown" was thus argued as being inappropriate [245, 247]. Furthermore, the lateral spreading of an avalanche [237, §4] would not allow the densities at the leading edge to reach the critical value for streamer formation [247, §51]. Observations of TGFs actually point toward an opposite relationship, where gamma-ray bursts from avalanches emerge after lightning breakdown has been initiated [610, 829].

In search of conciliation, due to the polyvalence implied by the word "breakdown" (see previous section 1.1.2), we could conceptually distinguish relativistic runaway electron avalanches (RREA) from "ordinary" runaway avalanches (RA) in the previous subsection (1.4.2) when space charge densities at the leading edge of the avalanche are high enough to cause a significant change in conductivity (breakdown of conductivity).

After all, depending on the spatial extension and intensity of the electric field, one could perhaps differentiate micro runaway avalanches that employ thunderclouds as an X-ray converter and amplifier of fast electrons seeded by cosmic rays or radioactive decay; and more intense RREA that could potentially provide enough free charges for the formation of a streamer if the electric field were enhanced enough.

Independently of lightning initiation, the original idea of runaway breakdown was that the space charges produced would be sufficient to cause screening and therefore breakdown of the electric field. Monte Carlo simulations showed that the amplification through avalanching is not intense enough to reach this situation [245]. This mechanism requires a further ingredient which is disclosed in the next section.

1.4.4 Relativistic Runaway Avalanche with feedback

The major problem of an electron avalanche is that it always flows opposite to the electric field but cannot flow backward where the potential (for avalanching) is highest. This means that it can only build up as far as the high-field regions extend. This limitation changes radically with the introduction of a feedback mechanism [236] capable of injecting seeds back at the starting point of the high-field region.

Such seeding may be executed by gamma rays or positrons [363] that can retrograde along the electric field to the avalanche top and produce energetic ionisation. An essential requirement for feedback is that the high electric field region have a wide lateral extent to be able to capture the gamma-ray or positron as it scatters whilst retrograding [236].

The role of feedback may be understood as to enhance the multiplication rate of a RREA within the same avalanche length. Thus, feedback allows RREA to produce stronger fluxes of runaways over a given region of high electric fields. In a certain sense, the effect of feedback is to "fold" an extended avalanche over a smaller region. To this picture, one must however consider also that feedback widens the lateral spreading of the avalanche and produces a significant amount of space charges that screen the electric field.

With this supplementary feedback, the idea of runaway avalanches fostering conventional breakdown can be restated. The accumulation of space charges at the bottom of an avalanche does not lead to formation of a plasma seed any more. Instead, the electric field may be enhanced beyond the conventional breakdown and conduce to a large scale discharge [237]. This scenario operating over milli-seconds [237, §14] could correspond to the build-up of gamma-ray glows [947] before lightning occurs [237, §18], but not to TGFs.

The TGF time scale of a few tens of micro-seconds is best reproduced when combining the RREA with feedback in the presence of leader channels [246]. The high potential difference between the charge layers is gradually spatially compacted as the leader progresses. When the electric field breaches runaway threshold, a RREA with feedback triggers and instigates a

discharge lowering the field ahead of the leader. The number of electron runaways produced thus can reach $\sim 10^{17}$ [238, §V.A], about the right amount to reproduce the fluence of a bright TGF [245]. This process can repeat several times and produce multipulsed TGF if the leader traverses a long distance within the cloud [246, §6.2 figure 9].

Because the feedback empowers runaway avalanches to accomplish breakdown of the electric field, it was proposed [238] to be named more compactly "relativistic breakdown".

Altogether

The four mechanisms described above (thermal, avalanche, relativistic runaway, feedback avalanche) reflect but a conceptual compartmentalisation of discharge mechanisms involving fast electrons. They emerge from the understandable necessity to grasp the physical phenomena at play. With time, much progress was put forth in recent years to incorporate each of those mechanisms into a coherent orchestration.

Nevertheless, still today, the causality of runaway to discharges is blurry. In small sparks, runaway definitely depends on the field enhancement from streamer tips. Additionally, it is thought that they aid streamer propagation [828, §VI]. In thunderclouds, it seems that runaway processes emerge spontaneously without assistance from a lightning discharge, yet their posterior occurrence to leader formation is well established observationally based on correlation with TGFs which are thought to be generated by RREA with feedback.

Comprehensively, it is not excluded that TGF and X-ray bursts reflect two extreme situations [860] of the relationship between the leader potential and the ambient electric field [164]. Lower and limited fields would only permit X-rays, leaving full-fledged TGFs for higher and vaster fields. Nonetheless, the war between theories of runaway is not over: does avalanching remain restricted to the vicinity of the streamer zone [162, 164] or does it flush ahead in the vast high field regions of the thundercloud [246, 248]? In other words, would X-rays be the signal related to seed runaways, whereas TGF would correspond to those seeds amplified with considerable multiplication with (brighter) or without (fainter) feedback? Furthermore, the contrast between a multi-pulsed TGF on a "silent" background versus a minute-long sustained high-energy radiation of gamma-ray, electrons, positrons and neutrons [174, 948, 951] poses a challenge. Why would runaway maintain a steady relation to its nurturing electric field in glows without provoking a brutal discharge, meanwhile it stammers as intense interrupted bursts when correlated with lightning? Finally, the possibility that TGFs present a harder high-energy tail than yielded by the 7.3 MeV exponential spectra of RREA, remains an open question [629]. Acceleration of electrons coupled with the leader advancement constitutes a tempting place for investigation.

1.5 Motivation

One can realise how relatively recent the discovery of gamma rays produced in thunderclouds is, by comparing the state of the art of discharge typologies and their technological applications against the hazy relationships between runaway mechanisms and discharges. Moreover, one can acknowledge the poor understanding we have of gamma ray flashes when we are unable to agree how to relay a beautiful story of their emergence. On an even greater scope, studying the connection between high-energy radiations and discharges is a great piece to the puzzle of the phenomenon of Lightning [367].

By now, we hope that the motivation of elucidating the fundamental mechanisms behind high-energy radiation from discharges is self-justified. If not, we ought mention that radiation doses to aircraft passengers near thunderstorms can be a topic to worry about [730].

Throughout this chapter we showed how high-energy processes in lightning are enrooted in electron runaway bremsstrahlung radiation. Similarly, breakdown initiation stems from free thermal electrons. Thus, we have two families of electron avalanching mechanisms, one at high energies (runaway) and another at low energies (thermal) which play a fundamental role in electric discharges in nature. Yet, the relationship between both is poorly understood.

In order to draw a coherent picture, we take the challenge to model the stochastic behaviour of electrons in atmospheric gases regardless of their energy. Therefore, electrons will be the main protagonists of this thesis.

We would like to point out that the branch of runaway electrons in electrified gases has been studied *extensively* :

- Thermal Runaway (TR) : for leaders [162, 368, 677], for streamers [44, 161, 170, 171, 587] for ionisation fronts [39, 192]
- Runaway Avalanche (RA) : [365, 369, 370, 787]
- Relativistic Runaway Electron Avalanche (RREA) : [42, 184, 576, 786]
- Relativistic Runaway Avalanche with feedback (RREA+) : [46, 236, 238, 246]

Because relativistic runaway avalanches have a longer history than thermal runaway, their parameters and characteristics have been studied in detail at different altitudes and configurations of the electric and magnetic fields [40, 184, 236, 576]. So far, the support for thermal runaway does not tally to the advanced models of RREA.

Therefore, it might seem hard at first to find new paths for further research, except by building in complexity over previous models like those of Köhn [529] and Li [585]. Such was not the trajectory opted in this thesis, however. Instead, it was deemed reasonable to undertake an *intensive* approach to thermal runaway modelling.

A Monte Carlo approach represents a very efficient and appropriate methodology capable of tackling the stochastic nature of thermal runaway. Previous models [368, 677] had almost taken for granted that the pathway from thermal to relativistic energies was well paved with electric fields over the critical threshold. Nevertheless, as we shall see, there are many holes in a complete characterisation of electron processes in gases at intermediate energies situated between the thermal bulk and the runaway regime.

Very recently (toward the end of this thesis), some studies [43, 86, 482] showed more diligence toward correctly simulating the stochastic process of electrons in electrified gases. This bespeaks how timely a renewed study of runaway by Monte Carlo method is today.

Together with these recent works, this thesis will aim to improve our understanding and capabilities of reproducing the thermal electron runaway process based on the stochastic method of Monte Carlo particle simulations.

As an important side note, we must emphasise that electron (or even ion) runaway is of high concern in fusion plasmas such as in tokamaks [104]. As a result, this issue is studied intensively by the fusion plasma community. Unfortunately, results taken from that field of research are inapplicable in the present situation of electron runaway in discharges within atmospheric gases. The reason for this is that *fully* ionised plasmas in fusion reactors are fundamentally different from *weakly* ionised plasmas in discharges in air because of the absence (or insignificant presence) of Coulombic electron-ion collisions in the latter case. Actually, even in weakly ionised plasmas, it is not certain that the streamer–leader hierarchy, stepping and runaway mechanisms observed in nitrogen-oxygen mixture discharges are concepts applicable to discharges in pure monatomic gases where the mechanisms of ionisation are different and no attachment occurs.

This makes the study of electron runaway in natural discharges a highly desirable field of investigation. It might help understanding furthermore the emergence of runaway mechanisms in the intermediate range of *partially* ionised plasmas.

1.5.1 Questions and Goals

Asking simple questions may help us set off in our research journey. As was hinted in the introduction, it seems that thermal runaway occurs under specific conditions: elevated electric fields, sustained long enough, extending far enough and supplied with many free electrons.

Then, questions spring up spontaneously: what is quantitatively "elevated", "long" (time), "far" (space) and "many"? Or together: after how long, how many initially thermal electrons will eventually become runaways and what distance will they have traversed if the electric field is thus high?

The Monte Carlo study of runaway electrons in discharges opened wide an impressive agora for discussions about the role they play in lightning, streamer propagation, leader stepping, TGF, X-ray bursts, etc. The phenomenal trait of runaway production and avalanching is its singular dependence upon a particle. If the conditions are right, only one electron (or any adequately energetic ionising particle) might suffice to "trigger the spark" (or formally, provoke an avalanche potentially leading to breakdown).

For a century, a "*radius ex machina*"* had to be summoned each time to start the show. This cosmic romanticism, however, could not survive to the foreboding neutron beams allegedly observed to gush out in laboratory sparks. The purpose of this thesis is to elaborate a fertile model to seek out the *electron in situ* through thermal runaway.

1.5.2 Structure of part I

In the next chapter (2) we will lay out the fundamentals of electron motion in electric fields frequently interrupted by collisions with molecules. From tracking individual electrons we will gradually move to a more macroscopic description of swarms. Mainly focused on Monte Carlo representations, we will introduce a methodology for noise reduction in the electron energy spectrum that will be vital for an accurate tracking of thermal runaway. We will also give a few notions in kinetic and fluid descriptions, often used in swarm dynamics.

After laying down the theory, the details of numerical implementation will be covered in chapter 3, structured according to our code's architecture. Considered an essential part of scientific success, a whole chapter (4) will be devoted to analyse contagious mistakes occurring in the field, as well as avowing those perpetrated throughout the thesis.

After this safety check, results of our simulations will fill chapter 5 which will be divided into analysing the bulk properties of swarms in electrified gases (sec. 5.2), then the statistics of runaway (or high-energy) electrons (sec. 5.3) and finally explore particular situations which may related to thermal runaway (sec. 5.4). The results will be then overviewed in the last chapter 6, which will also include the conclusions and perspectives for future work of this first part.

*The latin expression *Deus ex machina* dates back to theatre plays when the protagonist encountered him or herself in such utter hopelessness, that the "hand of God" was invoked to intervene to save the tragedy. The term *ex machina* means 'coming out a crane' (the machine hoisting decor elements on the stage). In this analogy, we satirise the role of cosmic rays ('*radius*' in latin) as if they were sent by the hand of God from the universe-machine so that we could have a terrestrial gamma ray flash on Earth. The point here in this thesis is that we do not necessarily need any cosmic intervention to have high-energy radiation from thunderstorms. With the mechanism of thermal runaway, 'indigenous' electrons (*in situ*) may be converted to high-energy ones through acceleration in the intense electric fields from discharges on Earth.

Chapter 2

Physical Models

In the previous introductory chapter, we described the meteorological context in which lightning strikes. Among the many mysteries related to lightning, we brought to the reader's attention the mechanism whereby X-rays and gamma rays are emitted in correlation to leader activity as bremsstrahlung radiation from energetic electrons. Though the electrons may be initially seeded by cosmic rays, we would like to explore the possibility of thermal runaway: that is the acceleration of low energy electrons up to relativistic energies in the MeV region from intense electric fields due to local enhancements in streamer channels.

This chapter presents the physical background used to model thermal electron runaway in a uniform gas under an electric field. We adopt a microscopic approach over short timescales, of a few nanoseconds at most, and study the prompt response of electrons to the local conditions of the environment.

Of major importance, will be to understand how the microscopic scales of electrons, as studied presently, fit into the macroscopic world of discharges as presented in the previous chapter. The structure of this chapter consists of three sections:

2.1 : a brief characterisation of the model of the gaseous medium

2.2 : dynamics of an individual electron in an electro-magnetic field [2.2.1], when colliding with a gas molecule [2.2.2] and its average motion in gases [2.2.3].

2.3 : the behaviour of electrons when considered as a swarm (ensemble) from a discrete [2.3.1], kinetic [2.3.2] and fluid [2.3.3] perspective.

Before plunging into the equations, the reader might wish to get familiar with our nomenclature and notation convention on page xvi. In particular, unit vectors are noted with a "hat" : $\|\hat{\mathbf{v}}\| = 1$.

2.1 Gases

From the long introduction presented in the former chapter, we remember that the conditions of the gas medium vary significantly at different stages of a discharge. Initially at ambient pressure and temperature, the air in a leader channel heats beyond 5000 K which entails an expansion shockwave from the sudden increase in pressure, as well as a change in composition from chemical reactions.

It is therefore interesting to consider how may electron thermal runaway be affected under different conditions of the gas in a discharge channel. Some studies already explored the effects of density fluctuations from heating [530] and preionisation of air [38, 39, tab. 1, §3] from former streamers. Presently, we wish to understand how does the temperature and chemical composition of the gas at a given electric field affect the behaviour of an electron swarm.

As we will see later, the electric fields required required to accelerate electrons in gases to relativistic energies are very high ($> 10\,\mathrm{MV/m}$). Since such fields may not sustain themselves for long periods of time, we may reasonably suppose that thermal runaway in discharges is a fast (shorter than a few tens of microseconds) transient phenomenon that unfolds only when certain conditions are met. Therefore, as a fundamental working hypothesis, we will assume that during a thermal runaway event, the state of the surrounding gas is not changed by the electron discharge. This does not prevent the gas to have spatial inhomogeneities such as a temperature gradient or variations in composition. However, those inhomogeneities are not expected to change with time throughout the acceleration process leading to runaway. As a consequence, we start describing the stationary model of the ambient gas that will form the basis of our studies.

2.1.1 Macroscopic state

By default, the simulation space is supposed to be uniformly filled by the gas at a number density n_{gas} and temperature T_{gas} obeying the law of perfect gases giving the pressure p through Boltzmann's constant k_{B}:

$$p = n_{\mathrm{gas}} k_{\mathrm{B}} T_{\mathrm{gas}} \tag{2.1}$$

Ambient conditions of air at ground are determined by the *U. S. Standard Atmosphere* [950]:

Air composition:

N_2 :	78.08 %
O_2 :	20.95 %
Ar :	0.97 %

Thermodynamic state:

$$p_0 \equiv 1\,\mathrm{atm} = 101\,325\,\mathrm{Pa}\,, \tag{2.2}$$

$$T_0 \equiv 15\,^{\circ}\mathrm{C} = 288.15\,\mathrm{K}\,, \tag{2.3}$$

$$n_0 \cong 2.547 \times 10^{25}\,\mathrm{m}^{-3}\,. \tag{2.4}$$

The air density profile n_{air} along the altitude h decays exponentially on a scale of about 7 km:

$$n_{\mathrm{air}}(h) = n_0 \mathrm{e}^{-h/7\,\mathrm{km}}\,. \tag{2.5}$$

The chemical composition changes drastically at elevated temperatures such as those encountered in hot ionised channels. Assuming thermal equilibrium and a constant particle density, we reproduce in table 2.1 the ratios of the most frequent species created from nitrogen and oxygen. The data were reported in Hilsenrath and Klein's tables [402]; the first two rows at 1500&2000 K come from Lemmon *et al.* [580, table 11].

It is absolutely not clear how to characterise the state of a very quickly (in tens of microseconds) heated strip of gas in an electric discharge. We took the liberty to assume that dilution from the thermal expansion is somewhat compensated by the duplication of gas particles through dissociation so that the gas particle density n_{gas} remains constant during the heating process. This guess comes from the fact that the timescales of thermal expansion ($\gtrsim$ µs) [776, fig.2] are somewhat similar to the time during which the air is heated in discharges $\lesssim$ µs. This assumption is a prerequisite to the characterisation of the chemical composition compiled in table 2.1.

Nevertheless, assuming a constant particle density might not be a good approximation [530] and could require adjustment when modelling gas expansion in (space-)leader cores [532]. The streamer-to-leader transition study of da Silva and Pasko [204, figure 10] predicts an abrupt drop of the gas density by roughly one order of magnitude coincident with a steep increase in the temperature in about 0.2 µs from ambient initial conditions in a streamer traversed by a

Table 2.1: Chemical species in hot air extracted from Hilsenrath and Klein [402] in function of temperature T at constant particle (atom or molecule) density $n_0 \approx 2.687\,\mathrm{m}^{-3}$ (Loschmidt's number). The first two rows at 1500&2000 K come from Lemmon *et al.* [580, table 11]. The ratios do not sum exactly to 1 due to residual species (mostly CO, CO_2 and NO_2) and round-off errors. A 0.000 value implies that the unshown next digit would be between 1 and 5.

T (K)	N_2	O_2	Ar	NO	N	O	N^+	O^+
1500	0.780	0.209	0.009	0.002				
2000	0.777	0.206	0.009	0.008				
2500	0.768	0.196	0.009	0.024		0.002		
3000	0.752	0.178	0.009	0.046		0.014		
3500	0.727	0.145	0.009	0.067		0.051		
4000	0.695	0.098	0.009	0.079	0.000	0.117		
4500	0.666	0.055	0.008	0.078	0.002	0.191		
5000	0.646	0.026	0.008	0.068	0.006	0.246		
5500	0.631	0.012	0.008	0.055	0.016	0.278		
6000	0.612	0.006	0.008	0.044	0.036	0.294		
6500	0.582	0.003	0.008	0.035	0.072	0.299		
7000	0.538	0.002	0.007	0.030	0.126	0.298		
7500	0.477	0.001	0.007	0.023	0.165	0.291		
8000	0.404	0.001	0.007	0.018	0.288	0.280		
8500	0.327	0.000	0.006	0.013	0.384	0.267	0.000	0.000
9000	0.251	0.000	0.006	0.011	0.475	0.260	0.000	0.000
9500	0.184	0.000	0.006	0.008	0.556	0.241	0.001	0.000
10000	0.130	0.000	0.005	0.006	0.620	0.231	0.002	0.000
10500	0.090	0.000	0.005	0.005	0.667	0.223	0.004	0.001
11000	0.061		0.005	0.004	0.698	0.218	0.005	0.001
11500	0.041		0.005	0.003	0.717	0.213	0.008	0.001
12000	0.028		0.005	0.002	0.727	0.210	0.012	0.002
12500	0.019		0.005	0.002	0.729	0.206	0.016	0.003
13000	0.013		0.005	0.001	0.726	0.203	0.021	0.003
13500	0.010		0.005	0.001	0.719	0.200	0.028	0.004
14000	0.007		0.004	0.001	0.708	0.197	0.035	0.006
14500	0.005		0.004	0.001	0.694	0.193	0.044	0.007
15000	0.004		0.004	0.000	0.677	0.189	0.054	0.009

constant electric current at 1 A. This is accompanied by a screening of the electric field when the streamer becomes part of the leader core.

Since thermal runaway is most prone to occur just before the electric field drops, the gas density may be assumed not to have changed significantly while the gas heating already breaches a few thousand Kelvins. Thermal runaway might dwell at the ideal crossing point where the gas is hot and slightly diluted, while the electric field remains still unscreened. If one is, however, interested in studying thermal runaway in a preheated channel, then the air composition needs to be checked in equilibrium at a density n_{hot} of a factor of 10 lower than the ambient n_0.

In any case, considering a change in chemical composition at all, represents a first step to differentiate electron acceleration in hot air from ambient conditions.

2.1.2 Microscopic state

At the molecular level, the distribution of energies in equilibrium conditions follows the Maxwell-Boltzmann statistics reviewed in appendix B. At a given gas temperature T_{gas}, the probability $f_\varepsilon(\varepsilon_k)\,\mathrm{d}\varepsilon_k$ that a molecule or atom finds itself at a kinetic energy between ε_k and $\varepsilon_k + \mathrm{d}\varepsilon_k$ is given by:

$$f_\varepsilon(\varepsilon_k) = \frac{2/\sqrt{\pi}}{(k_{\text{B}}T_{\text{gas}})^{3/2}}\sqrt{\varepsilon_k}\mathrm{e}^{-\dfrac{\varepsilon_k}{k_{\text{B}}T_{\text{gas}}}} . \tag{2.6}$$

This can also be expressed in terms of the speed V of a molecule of mass M :

$$f_{\text{v}}(V) = \left(\frac{M}{2\pi k_{\text{B}}T_{\text{gas}}}\right)^{3/2} 4\pi V^2 \mathrm{e}^{-\dfrac{MV^2}{2k_{\text{B}}T_{\text{gas}}}} . \tag{2.7}$$

f_{v} and f_ε are known as the Maxwell distributions of speeds and kinetic energies.

Diatomic molecules such as molecular nitrogen and oxygen have also rotational and vibrational degrees of freedom. As opposed to kinetic distributions which are continuous, the energy levels ε_i of excited states in the framework of quantum mechanics follow discrete distributions f_{exc} described by the Boltzmann statistics succinctly recalled in appendix B.2.

$$fexc(\varepsilon_i) = \frac{g_{\text{exc}}(\varepsilon_i)\mathrm{e}^{-\varepsilon_i/k_{\text{B}}T_{\text{exc}}}}{\sum_{i=0}^{\infty} g_{\text{exc}}(\varepsilon_i)\mathrm{e}^{-\varepsilon_i/k_{\text{B}}T_{\text{exc}}}} . \tag{2.8}$$

The subscript 'exc' stands for the mode of excitation considered ('rot' or 'vib') and g_{exc} is the degeneracy of the discrete level indexed by i. Energy distributions such as f_ε or f_{rot} and f_{vib} are commonly referred to as *spectra*, in relation to the electromagnetic radiation emitted by such distributions. The temperature of a spectrum determines the brightness of the emitted radiation.

Energy transfers between molecules occur during collisions. From a general perspective, the average energy transferred through a collision from vibrational, rotational and translational (kinetic) degrees of freedom is not equal [150, Chapters 1-3]. The transfer of energy between two vibrational modes is typically larger than between a vibrational and a rotational mode or a translational energy [150, §3.1]. Therefore, the time (or number of collisions) needed to thermalise (converge to the Maxwell-Boltzmann distribution) an isolated system of vibrational excitations is shorter than the full thermalisation of a vibrational system with a rotational or translational system which is about ~ms for diatomic molecules. Since the timescale of electron thermal runaway may be much shorter (depending on the electric field) than the thermalisation time of the gas, it is not inconceivable that, within this short time interval, different temperatures T_{exc} be associated to populations of vibrational T_{vib} and rotational T_{rot} modes of excitations.

Rotational levels of excitation are indexed by $i \equiv J$ and are most commonly approximated by the *rigid rotator* model. Their energies ε_J at a temperature $T_{\text{exc}} \equiv T_{\text{rot}}$ are populated as (2.8) with [399, §3.3.2-3] :

$$\varepsilon_J = B_{\text{rot}}(J+1)J , \tag{2.9}$$

$$g_{\text{rot}}(\varepsilon_J) = g_{\text{s}}[(-)^J](2J+1) , \tag{2.10}$$

where $(-)^J$ determines the parity (− odd ; + even) of the level J. Rotational constants B_{rot} for typical diatomic molecules are given in table 2.2. The degree of degeneracy g_{rot} comes from

Table 2.2: Diatomic molecular constants for interatomic separation R rotational B_{rot}, vibrational $\hbar\omega_{\text{vib}}$ excitations, electronic excitation threshold $\mathcal{E}_{\text{th}}$, dissociation $\mathcal{E}_{\text{diss}}$ and ionisation $\mathcal{E}_{\text{ion}}$ energies [499]. The nuclear spin degeneracy (g_{s}) for rotational states is shown on the bottom row.

	N_2	O_2	H_2	NO
R (nm)	0.11	0.12	0.074	0.115
B_{rot} (meV)	0.2477	0.1783	7.544	0.2073
$\hbar\omega_{\text{vib}}$ (eV)	0.2924	0.1959	0.5457	0.2361
$\mathcal{E}_{\text{th}}$ (eV)	6.17	0.977	6.9	4.747
$\mathcal{E}_{\text{diss}}$ (eV)	9.76	5.116	4.48	6.534
$\mathcal{E}_{\text{ion}}$ (eV)	15.58	12.07	15.43	9.26
$g_{\text{s}}(J$ even : odd)	6 : 3	0 : 1	1 : 3	1 : 1

quantum theory of angular momenta and expresses the $2J+1$ different projections that a linear rotator can take on a given axis. More information about rotational excitations is to be found in chapter 11.2.

When applied to concrete molecules, additional considerations must be taken into account depending on the molecular wave-function parity. Skipping the details of such discussion, the degeneracy for odd and even J is given for each diatomic molecule on table 2.2 and also found in [305, read § between eq.8-9 on p. 1624]. For all heteronuclear molecules $g_{\text{s}}(J) \equiv 1$ because no indistinguishability criterion is imposed between the nuclei.

Vibrational levels of excitation are indexed by $i \equiv v$ and for low $v \lessapprox 10$, are approximated by the *harmonic oscillator* model. Their energies ε_v at a temperature of $T_{\text{exc}} \equiv T_{\text{vib}}$ are populated as (2.8) with [399, §3.3.5] :

$$\varepsilon_v = \hbar\omega_{\text{vib}}(v + 1/2) \,, \tag{2.11}$$

$$g_{\text{vib}}(\varepsilon_v) = 1 \,. \tag{2.12}$$

For diatomic molecules, vibrational modes are non-degenerate; their degeneracy is independent of v in combined rotational+vibrational (="rovibrational") spectra. The vibrational frequency ω_{vib} is obtained from the harmonic oscillator model.

The geometric series in the Boltzmann distribution (2.8) for the harmonic oscillator model (2.11) can be summed to give a straightforward expression :

$$f_{\text{vib}}(\varepsilon_v) \approxeq \exp(-v\hbar\omega_{\text{vib}}/k_{\text{B}}T_{\text{vib}})(1 - \exp(-\hbar\omega_{\text{vib}}/k_{\text{B}}T_{\text{vib}})) \,. \tag{2.13}$$

Electronic levels of excitation could in principle also be attributed a Boltzmann distribution at a certain temperature. Nevertheless, electronic excitation thresholds $\mathcal{E}_{\text{th}}$ often lie considerably higher than rovibrational levels as can be seen on table 2.2. Only from very high temperatures $\gtrsim 30\,000$ K, would those states be thermally populated if the molecules were not all dissociated long before then as seen in the previous section (table 2.1). The situation is different for atoms, for which vibration, rotation and dissociation do not exist. There, some states may be metastable with a long lifetime (e.g. close to a minute for Argon [283, §1]) and therefore, the gas can retain memory of having incurred intense discharges in the recent past. In atmospheres dominated by atoms (He, Ar, etc.), taking into account subspecies of excited metastable states could make sense even beyond the notion of thermal equilibrium.

An overview of the more involved nomenclature of electronically excited states is available in the appendix C at the end of the second part.

Super-excited states corresponds to any – electronic, vibrational (rarely rotational) – modes of excitation whose energies lie above the dissociation or ionisation threshold of the molecule. They are important to take into account because they might decay into a dissociation or ionisation event (or both!) and thereby contribute to those channels when analysing electron-molecule collisions [834, p.284]. Their decay time affects the chemical evolution of the heated gas in non-equilibrium.

2.1.3 Thermal Equilibrium

Of fundamental importance to the Boltzmann statistics (2.8) is the assumption of *thermal equilibrium*. As a general thermodynamic rule, all energy exchange processes, considered as a whole, contribute toward bringing the medium into equilibrium. The pertinent question is to know how long does it take to bring a disturbed population back into equilibrium, and whether it takes longer than the perturbation to emerge.

The time necessary for a pack of molecules in disequilibrium to reach the temperature of an ambient gas is know as the *relaxation time* τ, widely covered in Capitelli *et al.* [150]. Translational and rotational relaxation time from to inter-molecule collisions in air is within the sub-nanosecond to a few nanoseconds range at ambient temperatures [155] and atmospheric pressure. It is thus safe to assume that those populations are in thermal equilibrium.

However, vibrational and some electronic states may take several tens of microseconds to relax in atmospheric conditions [76, 296], so that equilibrium might be a more questionable issue depending on the circumstances.

One can consider that within a certain time-lapse in the first few micro-seconds of a discharge [203, fig. 10], vibrational excitations form an internal energy reservoir at a temperature $T_{\text{vib}} \neq T_{\text{gas}}$, separate from translational and rotational excitations. Beyond non-stationary aspects, such differences can also arise as spatial inhomogeneities [57, fig. 4].

At the microscopic level, not all collisions are equally effective at transferring energy between various channels. While collisions between an atom and a molecule can only exchange vibrational for translational energy (V-T process), molecules between themselves can also exchange a vibrational quantum (V-V process). Furthermore, collisions with highly excited vibrating molecules can induce chemical reactions.

Thus, Boltzmann statistics, which are based on weak interaction between particles, can also inadequately describe non-equilibrium vibrational distribution functions which are subject to selective efficient energy exchange processes [609, fig. 2&5].

Of concrete interest, some chemical processes in the atmosphere can create durable departure from the Boltzmann distribution. For example, the stratosphere can typically withhold vibrationally excited oxygen populations as high as $v = 20$ due to photolysis of ozone [738, fig. 4]. Moreover, though fundamentally different than high-pressure discharges, radio-frequency modulated and continuous discharges in low-pressure plasma simulations [485, figure 2&5] show that non-Maxwellian vibrational temperatures can surpass 10 000 K while the gas ambient temperature remains fairly low $\sim$ 500 K.

It is thus not inconceivable to have locally disturbed oxygen vibrational distributions in the early stages of an electron avalanche.

When it comes to conversion of energy from electronically excited molecules, the situation is even more complex. It depends also on their vibrational sublevel of excitation and the nature of the inter-molecular interaction. Due to a higher potential energy available in the collision process, some excited states present higher probabilities in provoking an exchange of electronic energy, deexcitation or a chemical reaction depending on the collision partner. In general, depopulation of an excited species through collision is known as *quenching* and is described in kinetic models through reaction rates.

State-specific dynamics Rate coefficients k_r for electronic deexcitation through collisions between various molecules can be found in Capitelli *et al.* [150, Chapter 9.2]. They are expressed in cm^3/s for binary collisions. To obtain the quenching rate Q of a certain species, e.g. $\mathrm{N}_2(\mathrm{B}\,^3\Pi_g)$ through collisions with O_2(X - ground state):

$$\mathrm{N}_2(\mathrm{B}) + \mathrm{O}_2(\mathrm{X}) \rightarrow \mathrm{N}_2(\mathrm{X}) + 2\mathrm{O}$$

we simply multiply by the density of oxygen $n_{\mathrm{O}_2} \simeq 0.21 n_0$:

$$Q(\mathrm{N}_2(B)) = k_r n_{\mathrm{O}_2}\,.$$

This gives the *fractional number* of deexcited nitrogen molecules per second in air. The decrease rate $1/Q$ of excited species is thus exponential and this gives an estimate of the heating rate of the gas from quenching (for that particular case).

The full description of a gas' composition involves coupled equations of species densities with source and sink terms. The evolution of the gas composition (distinguishing also excited species) depends on the balance between mechanisms which populate and depopulate a particular species m through reaction rate coefficients k^g_{im} and k^g_{mj} with another species g:

$$\frac{\mathrm{d}n_m}{\mathrm{d}t} = \sum_g n_g \left(\sum_i k^g_{im} n_i - \sum_j k^g_{mj} n_m \right) - A^m n_m + \dots\,. \tag{2.14}$$

The interpretation of this balance equation (2.14) is to consider all possible sources terms coming from "cascading" deexcitations $i \rightarrow m$ mediated by collisions with any species g and compare against all sink terms which bring $m \rightarrow j$ to a lower state. We also include the decay from spontaneous emission $A^m n_m$ seen in the next paragraph. Eventually, one could also consider higher order effects such as three-body collisions*. The number of terms involved can sometimes be quite large depending on the richness of the discharge medium. When temperatures rise, many new species are created and can participate in the chemical bloom.

An example of such evolution is given in Flitti and Pancheshnyi [296, figures 2&3] in N_2-O_2 with a sustained electric field and in Šimek and Bonaventura [852, figures 4-5, 9–10] for a pulsed 1.3 ms train discharge.

The maximal order of deexcitation rate coefficients [150, p.159-160:tables 9.3-4] of N_2 and O_2 is around $\sim 10^{-10}\,\mathrm{cm}^3/\mathrm{s}$. Under standard atmospheric conditions, this would give a (minimal) order for the relaxation time of electronic species of $\tau = 1/(\sum_{g,j} k^g_{mj} n_g) \sim 0.4\,\mathrm{ns}$. In practice, the heating rate from deexcitation of electronic states has a steady value around 28% shortly after the onset of the discharge [759]. It then increases sharply after ~10 µs to over 50% [296, fig. 7]. Nevertheless, a non-negligible part of that energy can also go into vibrational channels of the diatomic ground states instead of directly heating the gas. Those are thus overestimates [204, fig. 9].

*Involving a formation of a 'dimer' see p. 432

Additionally, some metastable excited states (e.g. N_2 $A\,^3\Sigma_u^+$, $a\,^1\Pi_g$) can maintain themselves for longer periods [852, fig. 4-5 right] due to feeding from higher deexcitations.

Radiative relaxation Relaxation is most of the time systematically assimilated to collisional processes. Radiative deexcitation plays nonetheless a very important role [150, §9.1], particularly in atmospheric glows [466, 620]. Excited states m may decay to lower states n by spontaneous emission given by the Einstein rate coefficient $A^{mn}_{v'v''}$, which also depends on the vibrational levels v' and v''. Some high lying, typically optically allowed Rydberg states in nitrogen, have high emission rates $\gtrsim 10^8\,\mathrm{s}^{-1}$ which give lifetimes of a few nanoseconds, much faster than collisional quenching.

Overall, radiative transfers would also tend to thermalise if the medium could be considered as a black body. In discharges, this is hardly the case; the plasma channels are usually thin (optically) and radiation either escapes or sows free electrons outside the channel. This mechanism is of special importance in front of streamers and particularly positive ones.

Chemical Composition Another fundamental aspect to take into account is the air chemical composition dependence on the temperature. Oxygen molecules beyond $\gtrsim 2000\,\mathrm{K}$ will start dissociating through inter-molecular collisions (either with N_2 or O_2) and become fully dissociated [52, §2.1.1] around 5000 K, whereas nitrogen will persist mainly in molecular [52, §2.3] form up to 8000 K and vanish beyond 12 000 K. The relaxation time for dissociation of N_2 at 10 000 K and 20 000 K at ground density is about 150 and 2 ns [954]; whereas oxygen would dissociate in $\sim 300, 30$ and 3 ns at 5000,7000 and 9000 K respectively [417, figure 1]. We may thus reasonably expect that the chemical composition of air in a hot ionised channel $> 4000\,\mathrm{K}$ lies close to the one given by thermal equilibrium conditions, especially since there is additionally a direct contribution to the dissociation rate from electron-molecule collisions.

In conjunction with temperature effects, quenching rates rise neatly in presence of reactive species such as O and O_3. Their appearance at intermediate temperatures bring a swift change in the chemical evolution of the streamer during its maturing development stage.

Non-equilibrium All of the present discussion strongly undermines the assumption of thermal equilibrium of excited (vibrational and electronic) species in the description of Boltzmann statistics. To derive the distribution of states at a certain time during a discharge, a kinetic model comprising both electron and gas processes would be necessary [203, 609, 852]. Generally speaking, the channel in the early stage of a leader at temperatures below 5000 K is far away from a local thermal equilibrium condition, but this disequilibrium is gradually smeared as chemical processes operate at faster rates at higher temperatures [311, §3.5.4].

What can be retained from here, is that the state of the gas in discharges may be very distinct from the ambient conditions. Also, if one wants to model a time segment over which the gaseous medium could be considered in a thermodynamically steady state (whether in equilibrium or not), the duration must be inferior to the microsecond. Up to several tens of nanoseconds, we may assume that the state of the gas is dominated by electron impact processes and fast radiative emissions.

Whether within this time-frame the heating caused by an electron avalanche is capable of provoking meaningful local departures from equilibrium in the gas is an open question to be discussed along the way in this thesis. The critical quantity in this aspect is the peak reached by the exponentially-growing electron density.

2.2 Electron Dynamics

2.2.1 Acceleration in Electric Fields

The motion of an electron of elementary charge $-e \approxeq -1.602 \times 10^{-19}\,\mathrm{C}$, in uniform and static electromagnetic $(\mathbf{E}, \mathbf{B})$ vacuum is given by its relativistic momentum $\mathbf{p}$ change [446, §12.3]:

$$\frac{\mathrm{d}\mathbf{p}}{\mathrm{d}t} = -e(\mathbf{E} + \mathbf{v} \times \mathbf{B})\,. \tag{2.15}$$

The momentum is relativistically bound to the electron mass $m \approxeq 9.11 \times 10^{-31}\mathrm{kg}$ and velocity $\mathbf{v}$ as: $\mathbf{p} = m\mathbf{v}\gamma$, through the relativistic (Lorentz) factor γ. Together with the *kinetic* energy ε, the relativistic linkage [available in 398, §1.2.1] between the quantities' norms is weaved in the universal metric set by the speed of light c :

$$\gamma = 1 + \frac{\varepsilon}{mc^2} \quad = \sqrt{1 + (p/mc)^2} \quad = \frac{1}{\sqrt{1 - \mathrm{v}^2/c^2}} \quad = \frac{\mathring{\varepsilon}}{mc^2}\,, \tag{2.16a}$$

$$\varepsilon \quad = mc^2(\gamma - 1) \quad = \mathring{\varepsilon} - mc^2\,, \tag{2.16b}$$

$$p = m\mathrm{v}\gamma \quad = mc\sqrt{\gamma^2 - 1} \quad = \frac{1}{c}\sqrt{\varepsilon^2 + 2mc^2\varepsilon} \quad = \sqrt{(\mathring{\varepsilon}/c)^2 - (mc)^2}\,, \tag{2.16c}$$

$$\mathrm{v}/c \equiv \beta \quad = \sqrt{1 - \frac{1}{\gamma^2}} \quad = \frac{cp}{mc^2 + \varepsilon} \quad = \frac{cp}{\mathring{\varepsilon}}\,. \tag{2.16d}$$

The rest mass of the electron $mc^2 \approxeq 511\mathrm{keV}$ outlines the separation between the relativistic and classical regimes. Added to the kinetic energy, the *total* energy is written as $\mathring{\varepsilon} = mc^2 + \varepsilon$.

A scaled chart is given in figure 2.1 to help navigate in electron kinetics. We can see that even when travelling at one tenth of the speed of light around 2.5 keV, relativistic effects are moderate. Additionally, we anticipate the categorisation of electrons in electrified gases (p. 218).

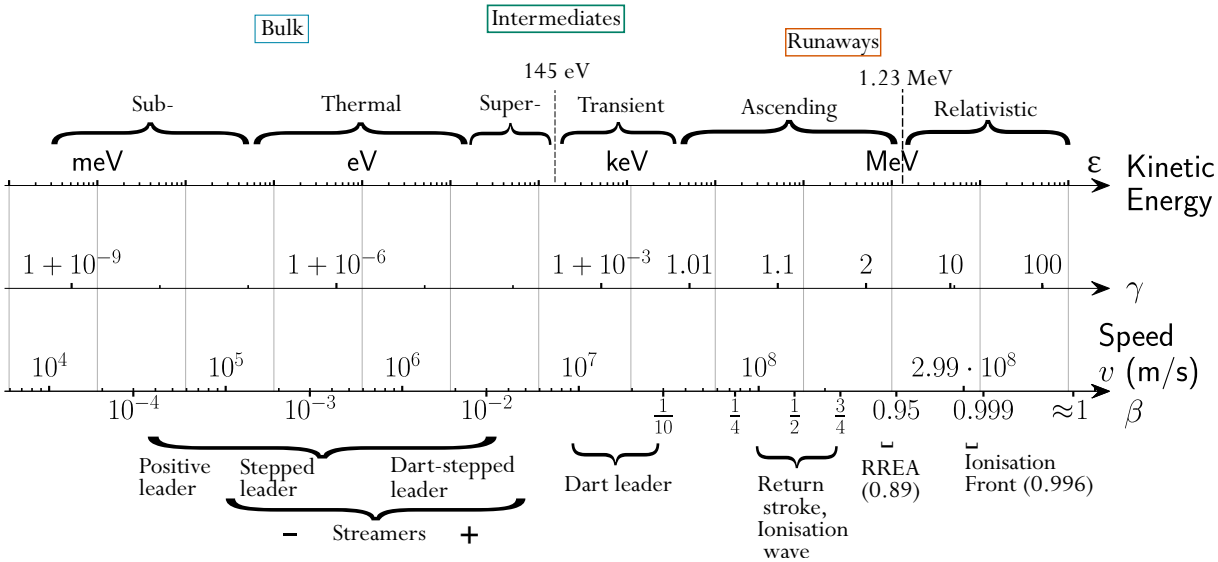

Figure 2.1: Electron kinetics scales. On the upper part we display the qualitative classification of electrons used in this first part of the thesis, reflected on figure 6.6. On the lower part, we give the order of magnitude of the propagation speed of various ionisation waves in air.

The propagation velocities of various plasmic front waves cannot be directly compared with electrons moving in gases, nonetheless, they give an idea of the energy order of magnitude required for an electron to travel with the wave.

The fundamental equation for conservation of energy is obtained by projecting (2.15) on the momentum $\mathbf{p}$ and switching to γ with (2.16c).

$$\mathbf{p} \cdot \frac{\mathrm{d}\mathbf{p}}{\mathrm{d}t} = \frac{1}{2}\frac{\mathrm{d}(\mathbf{p}\cdot\mathbf{p})}{\mathrm{d}t} = \frac{(mc)^2}{2}\frac{\mathrm{d}\gamma^2}{\mathrm{d}t} = (mc)^2\gamma\frac{\mathrm{d}\gamma}{\mathrm{d}t} \,. \tag{2.17}$$

Together with the right side of (2.15) and replacing $\mathbf{p} = m\gamma\mathbf{v}$, the energy progression rate reads:

$$mc^2\frac{\mathrm{d}\gamma}{\mathrm{d}t} = -e\mathbf{E}\cdot\mathbf{v} \,. \tag{2.18}$$

Taking α as the angle between the electric and magnetic fields (see frames on 2.2&2.3), the motion of the electron is critically determined by the ratio of the perpendicular electric field to the magnetic field:

$$\boldsymbol{\beta}_\mathrm{d} = \frac{\mathbf{E}\times\mathbf{B}}{cB^2} = \frac{E}{cB}\sin\alpha\hat{\boldsymbol{\beta}}_\mathrm{d} \,, \tag{2.19}$$

which defines a dimensionless **d**rift velocity $\beta_\mathrm{d} = \mathrm{v}_\mathrm{d}/c$ with respect to the speed of light.

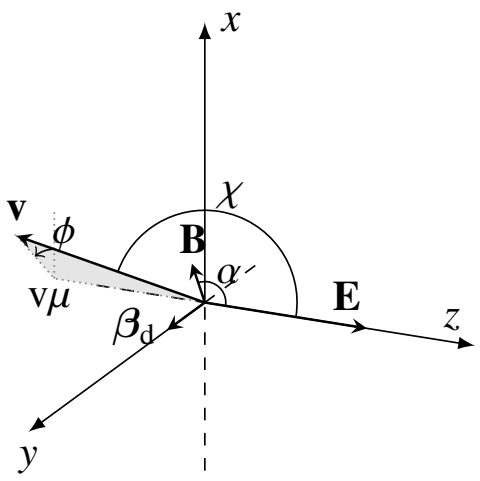

Figure 2.2: Reference frame chosen to describe the motion of an electron in a uniform electromagnetic field $(\mathbf{E}, \mathbf{B})$ when B is absent or weak ($cB \ll E$). The electric field $\mathbf{E} \parallel \hat{\mathbf{z}}$ and the drift velocity $\boldsymbol{\beta}_\mathrm{d} \parallel \hat{\mathbf{y}}$ (2.19). Thus, the residual magnetic field perpendicular to $\mathbf{E}$ is oriented along $\mathbf{B}_\perp \parallel \hat{\mathbf{x}}$.

If the magnetic field is weak so that $\beta_\mathrm{d} \geq 1$, the electron is merely deviated but not trapped. Then, the motion can be described in spherical coordinates as represented in figure 2.2. The z-axis is aligned with the electric field $\mathbf{E} = E\hat{\mathbf{z}}$, the y-axis $\hat{\mathbf{y}} \parallel \mathbf{E}\times\mathbf{B}$ is perpendicular to both electric and magnetic fields, so that the x-axis collects the residual magnetic component $\mathbf{B} = B(\cos\alpha\hat{\mathbf{z}} + \sin\alpha\hat{\mathbf{x}})$. Then, the electron is fully located with $\mu = \cos\chi$ from the polar angle χ and the azimuthal angle ϕ in the (x, y) plane. The vectorial equation (2.15) translates into [40, eq. (5)]:

$$\begin{cases} \dfrac{dp}{\mathrm{d}t} = -eE\mu \quad , & \text{(2.20a)} \\[2ex] \dfrac{d\mu}{\mathrm{d}t} = -eE(1-\mu^2)/p - e\mathbf{B}\cdot(\hat{\mathbf{z}}\times\mathbf{v})/p & \text{(2.20b)} \\[2ex] \qquad = -eE(1-\mu^2)/p + \dfrac{eB}{m\gamma}\sin\alpha\sqrt{1-\mu^2}\sin\phi & \\[2ex] \dfrac{d\phi}{\mathrm{d}t} = \dfrac{e\mathbf{B}}{p\sqrt{1-\mu^2}}((\hat{\mathbf{x}}\times\mathbf{v})\sin\phi - (\hat{\mathbf{y}}\times\mathbf{v})\cos\phi) & \\[2ex] \qquad = \dfrac{eB}{m\gamma}(\cos\alpha - \sin\alpha\dfrac{\mu}{\sqrt{1-\mu^2}}\cos\phi) \quad ; & \text{(2.20c)} \end{cases}$$

after having projected along the electron's direction (2.20a), along the electric field (2.20b) and at last (2.20c): perpendicularly to both $(-\sin\phi\hat{\mathbf{x}} + \cos\phi\hat{\mathbf{y}})$. The differential equation in μ has two singularity points $\mu = \pm 1$ when $\mathbf{v} \parallel \hat{\mathbf{z}}$. The first derivative becomes zero but not the second. This only results from the behaviour of the cosine projection. Those singularities disappear in the fully angular description of the motion.

As expected, one can better see that:

- The momentum gained by the electron depends exclusively on its direction μ with respect to the electric field.
- The magnetic field, when not parallel to the electric field, plays a distracting role, deviating the electron from its otherwise uniform electric acceleration.

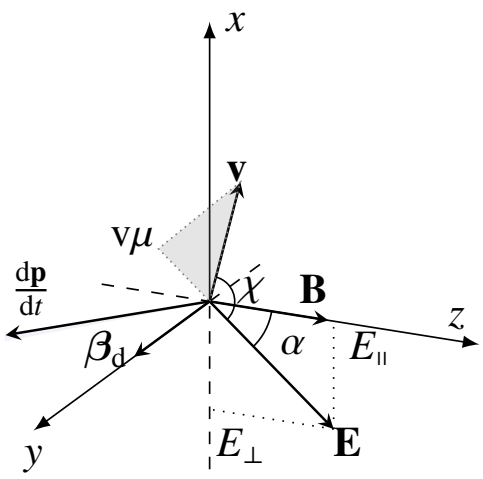

Figure 2.3: Reference frame in a uniform electromagnetic field $(\mathbf{E}, \mathbf{B})$ when B is strong ($cB > E$). The magnetic field $\mathbf{B} \parallel \hat{\mathbf{z}}$ and the drift velocity $\boldsymbol{\beta}_\mathrm{d} \parallel \hat{\mathbf{y}}$ (2.19). Thus, the residual electric pulling force on an electron perpendicular to $\mathbf{B}$ is oriented along $-e\mathbf{E}_\perp \parallel \hat{\mathbf{x}}$.

The trajectory of the electron is qualitatively different when $\beta_\mathrm{d} < 1$; it traces cycloids at the (Larmor) gyration frequency $\Omega = -eB/m$. In this regime, the most suitable reference frame would adopt cartesian coordinates as represented in figure 2.3 with $\mathbf{B} \parallel \hat{\mathbf{z}}$ and $\beta_\mathrm{d} \parallel \hat{\mathbf{y}}$, which conveniently aligns the perpendicular electric force $-e\mathbf{E}_\perp \parallel \hat{\mathbf{x}}$ for the negatively charged electrons.

$$\begin{cases} \dfrac{\mathrm{d}\mathrm{v}_x\gamma}{\mathrm{d}t} &= eE_\perp/m + \Omega \mathrm{v}_y \quad , & (2.21a) \\ \dfrac{\mathrm{d}\mathrm{v}_y\gamma}{\mathrm{d}t} &= -\Omega \mathrm{v}_x \ , & (2.21b) \\ \dfrac{\mathrm{d}\mathrm{v}_z\gamma}{\mathrm{d}t} &= -eE_\parallel \ . & (2.21c) \end{cases}$$

The sign of the gyration frequency Ω orientates the rotation as (counter-)clockwise for (negative) positive charges in the xy plane. The physical meaning borne by $\mathrm{v}_\mathrm{d} = c\beta_\mathrm{d}$, is a drift velocity along $\hat{\mathbf{y}}$, which can be noticed after having replaced $\mathrm{v}_y(t) = \tilde{\mathrm{v}}_y(t) + \mathrm{v}_\mathrm{d}$ in (2.21a). In the non-relativistic case as treated for instance in Bittencourt [73, §5.1 eq.-5.14], the motion can be analytically solved and comprises a uniform acceleration $-e\mathbf{E}\cdot\mathbf{B}/B$ to which a cycloid is superposed.

For relativistic particles, no analytical solution has been given yet for arbitrary field orientations. Nonetheless, some useful relations as given in Parks [736, eq. 2.50] can be obtained between the velocities, Lorentz factor and the particle displacement $\Delta\mathbf{r}$ by integrating (2.21a) and (2.18).

$$\begin{cases} \mathrm{v}_x\gamma &= \dfrac{eE_\perp}{m}\Delta t + \Omega\Delta y + v_{x0}\gamma_0 \ , & (2.22a) \\ \mathrm{v}_y\gamma &= -\Omega\Delta x + v_{y0}\gamma_0 \ , & (2.22b) \\ \mathrm{v}_z\gamma &= \dfrac{-eE_\parallel}{m}\Delta t \ , & (2.22c) \\ \gamma &= \dfrac{-e\mathbf{E}\cdot\Delta\mathbf{r}}{mc^2} + \gamma_0 = \dfrac{-e}{mc^2}(E_\perp\Delta x + E_\parallel\Delta z) + \gamma_0 \ . & (2.22d) \end{cases}$$

Those four equations can be combined to give a constraint on the trajectory :

$$(eE_\perp\Delta x + eE_\parallel\Delta z)^2 - 1 = \left(\frac{eE_\perp}{m}\Delta t + \Omega\Delta y + v_{x0}\gamma_0\right)^2 + \left(-\Omega\Delta x + v_{y0}\gamma_0\right)^2\left(\frac{-eE_\parallel}{m}\Delta t\right)^2 \ . \qquad (2.23)$$

For $\mathbf{E} \parallel \mathbf{B}$, the acceleration is uniform and reaches asymptotically the speed of light while the effective gyration frequency Ω/γ in the horizontal plane decreases. The Larmor radius $r_c = v_\perp \gamma/\Omega$ is a constant of motion due to the conservation of the perpendicular momentum [213, eq. 16].

In the other $\mathbf{E} \perp \mathbf{B}$ special case, the cycloid motion breaks down into a slow arc [909, eq. 23] at $\beta_\mathrm{d} = 1$ or a straight line [909, eq. 21] for $\beta_\mathrm{d} > 1$ given by $\Delta y = \Delta x/\sqrt{\beta_\mathrm{d}^2 - 1}$.

In the general case, the motion can be computed numerically and an analytical determination of the asymptotic velocity was obtained recently [688]. As the particle accelerates in the parallel direction, the cycloid motion slows and shrinks gradually. The drift now comprises also a component along $\hat{\mathbf{x}} \parallel -e\mathbf{E}_\perp$ even when $\beta_\mathrm{d} < 1$ [688, §A].

In relation to our interest in runaway electrons, except when $\mathbf{E} \perp \mathbf{B}$ with $E < cB$, all configurations are capable in principle of thermal runaway acceleration. This poses a great challenge on plasma magnetic confinement [93] in fusion reactors [94]. Thermal runaway in that context constitutes a threat to the equipment and must be mitigated with an adequate non-uniform configuration of the magnetic field [92].

For the sake of simplicity, we presented results in uniformly static fields. The trajectory in non-uniform and variable fields can be obtained by joining together segments on smaller scales where local homogeneity and stability is assumed. To illustrate the relation between temporal and energy scales, we simulated how much time would be required to accelerate an electron of negligible energy up to 1 MeV for different magnetic inclinations as a function of the electric field. The magnetic field was set to 1 mT, corresponding approximately to the field generated by a current of 1 kA at 5 cm from an infinite straight wire. Such order of magnitude should be easily produced from currents in electric discharges.

Under low electric fields where $\mathrm{v_d} < c$, the acceleration time needed to reach an energy ε is nothing more than the time for a uniform acceleration of the electric field $\mathbf{E}_\parallel$ along $\mathbf{B}$:

$$\Delta t(0 \to \varepsilon) \approx \frac{1}{ceE_\parallel}\sqrt{\varepsilon^2 + 2\varepsilon mc^2}\,. \tag{2.24}$$

For static initial conditions, the periodic kinetic energy gain variation due to the cycloid motion in the xy plane can be derived from the Larmor radius at the cycloid apex when $\mathrm{v}_y = 2\mathrm{v_d}$. Using the effective gyration frequency one has :

$$r_c\Omega/\gamma = 2\mathrm{v_d} \Leftrightarrow r_c = \frac{2E_\perp m\gamma}{eB^2} = \frac{2E\sin\alpha\, m\gamma}{eB^2}\,. \tag{2.25}$$

This implies a kinetic energy variation of $r_c\, eE_\perp = 2m\mathrm{v_d^2}\gamma$. Since at the apex:

$$\gamma = 1/\sqrt{1 - (\mathrm{v_d^2} + \mathrm{v}_z^2)/c^2}\,,$$

we can infer that as $\mathrm{v_d}$ approaches c, this variation is non-negligible compared to the gain from $E_\parallel$ and increases with $\sin^2\alpha$. The contribution to the acceleration in the xy plane is observed in figure 2.4 as wobbles that intensify with $E_\perp = E\sin\alpha$.

As predicted, a change of behaviour takes place at $E\sin\alpha = cB$ where the motion of the electron is virtually unaffected by the presence and orientation of the magnetic field. Differences in time lapses that could span an order of magnitude before, are rapidly erased at higher electric fields.

For our application of thermal runaway in gases, the effect of magnetic deviation is mitigated by the frequent electron collisions with molecules. Additionally, the electric field necessary for thermal runaway must greatly surpass the breakdown threshold at 3 MV/m in standard air, which at any rate is far beyond the region where typical magnetic fields possess influence.

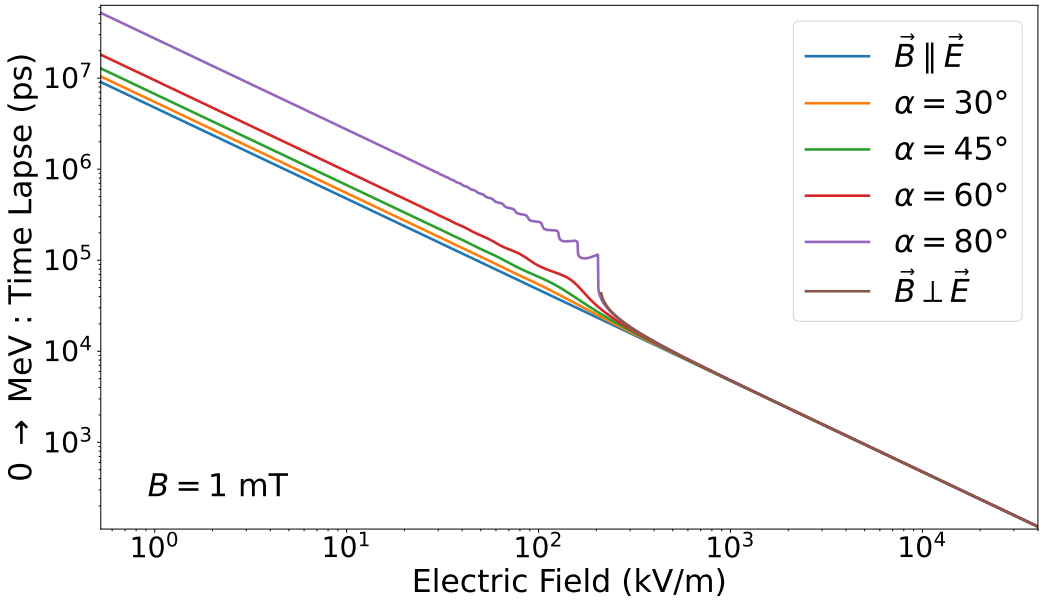

Figure 2.4: Time lapses required for an electron to be accelerated up to 1 MeV in uniform and static electromagnetic fields oriented relatively by an angle α.

Nevertheless, this threshold decreases exponentially with altitude at a characteristic height of 7 km. In the thesis by Lehtinen [577], it is shown that electron runaway beams at high altitudes above about 35 km start following geomagnetic lines instead of proceeding along the electric field [576, §4.2]. Runaway avalanching can be impeded above 40 km in the magnetic equator regions [366, 576] where the geomagnetic field is nearly perpendicular to the vertical electric fields above thunderclouds. Similarly, if one considers the possibility of thermal runaway at higher altitudes in relation to sprites for instance, the magnetic field could potentially interfere [366].

In the next section, we will see how the very simplistic trajectory of electrons in uniform fields in vacuum changes completely in the presence of a filling gas.

2.2.2 Collisions with Gas Molecules

In the presence of a gas, the electron's flight described above is repeatedly interrupted by collisions with the constituent molecules. For neutral molecules, the interaction potential is localised in a few Bohr atomic radii and the spatio-temporal scales of flight and collisions are well separated. An electron around 1 meV flies at 18 km/s which makes a collision in a potential of nanometric range last for only 1 nm / 18 km/s ≈ 0.05 ps, a negligible amount compared to the corresponding 200 ps of mean flight time in standard air.

Collisions in a neutral gas of uniform density N_{gas} can thus be modelled as independent instantaneous stochastic processes following a Poisson distribution at the collision frequency ν :

$$\nu(\varepsilon') = N_{\text{gas}} \mathrm{v}' \sigma(\varepsilon') \,. \tag{2.26}$$

The cross-section σ reflects the probability that a particle randomly located over a unit area interact with a target of area σ. It has a strong dependence on the kinetic energy ε' of the collision. Rigorously, the velocity v' should be taken as the *relative* speed between the colliding

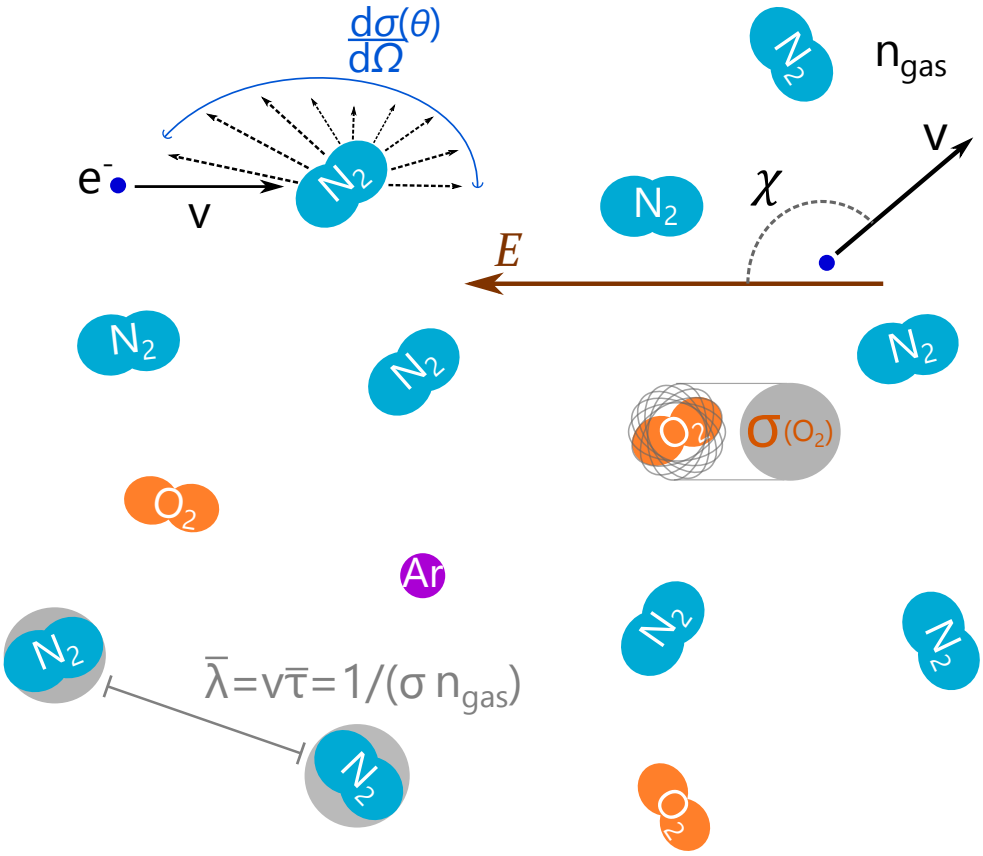

Figure 2.5: A fanciful representation of an electron's collisional peripeteia in air. The grey shaded circular area represent the collision cross section with atoms and molecules which are statistically averaged over the molecular orientation (or more rigorously over their rotational state). The cross section σ is obtained from the integral of the differential cross section $\mathrm{d}\sigma/\mathrm{d}\Omega$ which stochastically characterises the scattering distribution of the electron by the gas. Together, the gas density n_{gas} and cross section σ help to define the mean free path $\bar{\lambda}$ of the electron, or equivalently its mean flight time $\bar{\tau}$ according to its velocity v. The polar angle χ is defined between the electric field $\mathbf{E}$ and the electron velocity $\mathbf{v}$.

particles (which is why we include the prime). Nevertheless, the mass ratio and the thermal disequilibrium of electrons impinging on molecules allow us to neglect the speed of the gas so that one can take $\varepsilon' = \varepsilon$ and $\mathrm{v}' = \mathrm{v}$. A quantitative justification is given further below.

The mean time between collisions $\bar{\tau}$, or mean flight time, is defined as the inverse of the collision frequency : $\bar{\tau}(\varepsilon) \equiv 1/\nu(\varepsilon)$. A representation of an electron colliding on molecules in standard air is illustrated in 2.5

The number K of collisions incurred by an electron during an interval Δt is a Poisson variable of mean value $\nu\Delta t$, following a probability distribution :

$$\mathcal{P}(K = k, \Delta t) = \frac{(\nu\Delta t)^k}{k!} \mathrm{e}^{-\nu\Delta t} \,. \tag{2.27}$$

The distribution of time intervals between successive collisions is the time for which no collision occurred ($K = 0$), and follows a negative exponential :

$$\mathcal{P}(\Delta t) \equiv \mathcal{P}(K = 0, \Delta t) = \mathrm{e}^{-\nu \Delta t} \ . \tag{2.28}$$

In the presence of an electric field, the collision frequency changes as the electrons are accelerated. Then, the average number of collisions $\nu\Delta t$ in (2.27-2.28) should be replaced by the integral $\int_0^{\Delta t} N_{\mathrm{gas}} \mathrm{v}'(t) \sigma(\varepsilon'(t))\, \mathrm{d}t$.

The total collision cross-section σ in a gas of g constituents with abundance ratios x_g is the weighted sum of all individual collision types :

$$\sigma = \sum_g \sum_c x_g \sigma_{g,c} \qquad \text{with} \quad \sum_g x_g = 1 \ . \tag{2.29}$$

An electron in/elastically colliding with a molecule or an atom will alter/preserve its initial internal state. Collision types c are classified according to the final state of target molecule:

- Elastic (σ_{e})
  - –Non-radiative(σ_{el})
  - –Bremsstrahlung(σ_{br})
- Inelastic (σ_{i})
  - –Impact Excitation (σ_{exc})
    - Rotational(σ_{rot})
    - Vibrational(σ_{vib})
    - Electronic(σ_{elt})
  - –Superelastic (σ_{sup})
  - –Impact Ionisation (σ_{ion})
  - –Attachment (σ_{att})

Elastic collisions conserve the total kinetic energy of the colliding (and outgoing) particles. It may seem unusual to classify Bremsstrahlung as elastic. There are three good reasons for this choice. First, as a massless particle, a photon's energy is only kinetic. Second, from a purely conceptual point of view, all elastic collisions should actually be viewed as Bremsstrahlung because any deviation suffered by a charged particle must be accompanied by the emission of an electromagnetic wave [822]. Notwithstanding, the latter's wavelength might be so large that the energy lost through radiation is negligible compared to the electron kinetic energy. In this case, the collision is considered as *non-radiative*. Third, the cross-section of radiative processes is much lower than that of non-radiative ones, so including them both under elastic collisions will not significantly affect the total elastic cross-section. For this reason, in the rest of this thesis, "elastic collisions" will implicitly refer to the non-radiative type.

Inelastic collisions imply a change on the target state before and after the event. This change may either result in a (de-)excitation (from) to a higher target energy-state, or in the creation/annihilation of an ion. Excitations of atoms can only involve electronic orbitals, whereas molecules additionally possess rotational and vibrational levels, and any combination of all three kinds. Impact de-excitations transfer energy from an initially excited state to the free electron. From this perspective, they are known as *superelastic* collisions.

Ionisations are accompanied by the release of a secondary electron from the target's electronic shell. Conversely, the attachment implies that the originally free electron settles around a neutral target with an elevated electronic affinity such as oxygen. The inverse process of impact ionisation, whereby an electron neutralises of a positive ion upon encounter, is known as recombination and will not be considered here.

Electron Scattering

At the outcome of any collision except attachment, the electron veers suddenly. This deviation is commonly referred to as *scattering*, underlining the dispersion particles experience as they traverse a medium of *unstructured* matter such as gases. The outgoing direction follows a stochastic distribution given by the (angular) *differential* cross section $\mathrm{d}\sigma/\,\mathrm{d}\Omega(\theta,\varphi)$ into the element of solid angle $\mathrm{d}\Omega$ around the orientation determined by polar (θ) and azimuthal (φ) angles. An illustration is given in the upper left corner of 2.5.

For collisions involving emission of a secondary particle such as an electron or a photon, the differential cross section can comprise additional degrees of freedom on the energy ε_2 of the secondary particle and its direction of emission Ω_2. This leads to the notion of doubly and triply differential cross sections. The cross section σ used to determine the collision frequency (2.26) is obtained from the differential cross section through the integral:

$$\sigma \equiv \int_0^{\varepsilon/2}\int_0^{2\pi}\int_0^{\pi} \frac{\mathrm{d}\sigma}{\mathrm{d}\Omega_2\,\mathrm{d}\varepsilon_2} \underbrace{\sin\theta\,\mathrm{d}\theta\,\mathrm{d}\varphi}_{\equiv\mathrm{d}\Omega_2}\mathrm{d}\varepsilon_2\ . \tag{2.30}$$

Electron scattering constitutes a whole topic on its own and will be covered in the second part of this thesis starting from page 239. In the rest of this chapter we shall assume that the outcome for all degrees of freedom in a collision are given. Practical sampling techniques are exposed in the next chapter, section 3.2.3. Below, we characterise for each collision type how incoming and outgoing electron velocities relate to initial and final target states.

Elastic Collisions

The momenta of an electron $\mathbf{p}$ and a *non-relativistic* molecule $\mathbf{P}$ before $(\mathbf{p}_-,\mathbf{P}_-)$ and after $(\mathbf{p}_+,\mathbf{P}_+)$ an *idealised non-radiative elastic* collision are bound by the conservation laws of total energy $\mathring{\mathcal{E}}$ and momentum $\mathbf{\Pi}$. For a schematic representation, please refer to figure A.1 in appendix A on page 227.

$$\mathbf{\Pi} = \mathbf{p} + \mathbf{P} = m\gamma\mathbf{v} + M\mathbf{V}\ , \tag{2.31}$$

$$\mathring{\mathcal{E}} = mc^2\sqrt{1+(p/mc)^2} + Mc^2\sqrt{1+(P/Mc)^2}\ . \tag{2.32}$$

We introduced the mass M and velocity V of the molecule. Collision kinematics are reviewed in the appendix A and are conveniently treated in the relative frame of the centre of mass* drifting at a speed $\boldsymbol{\mathcal{V}} = c^2\mathbf{\Pi}/\mathring{\mathcal{E}}$.

In a properly elastic collision, the electron's kinetic energy ε' in the centre-of-mass frame is conserved : $\varepsilon'_- = \varepsilon'_+$. Lorentz transformations between the fixed and relative frames forth and back help to establish the electron momentum $\mathbf{p}_+$ and kinetic energy ε_+ *after* the collision :

$$\varepsilon_+ = \frac{e'}{1-(\frac{\mathcal{V}}{c}\cos\theta_+)^2}\left(1+\cos\theta_+\frac{\mathcal{V}}{c}\sqrt{1-(1-(\frac{\mathcal{V}}{c}\cos\theta_+)^2)\frac{(mc^2)^2}{(e')^2}}\right) - mc^2\ , \tag{2.33}$$

$$p_+ = \frac{e'/c}{1-(\frac{\mathcal{V}}{c}\cos\theta_+)^2}\left(\cos\theta_+\frac{\mathcal{V}}{c}+\sqrt{1-(1-(\frac{\mathcal{V}}{c}\cos\theta_+)^2)\frac{(mc^2)^2}{(e')^2}}\right)\ . \tag{2.34}$$

*In this chapter, all quantities noted with a prime ′ are defined in the relative (centre of mass) frame

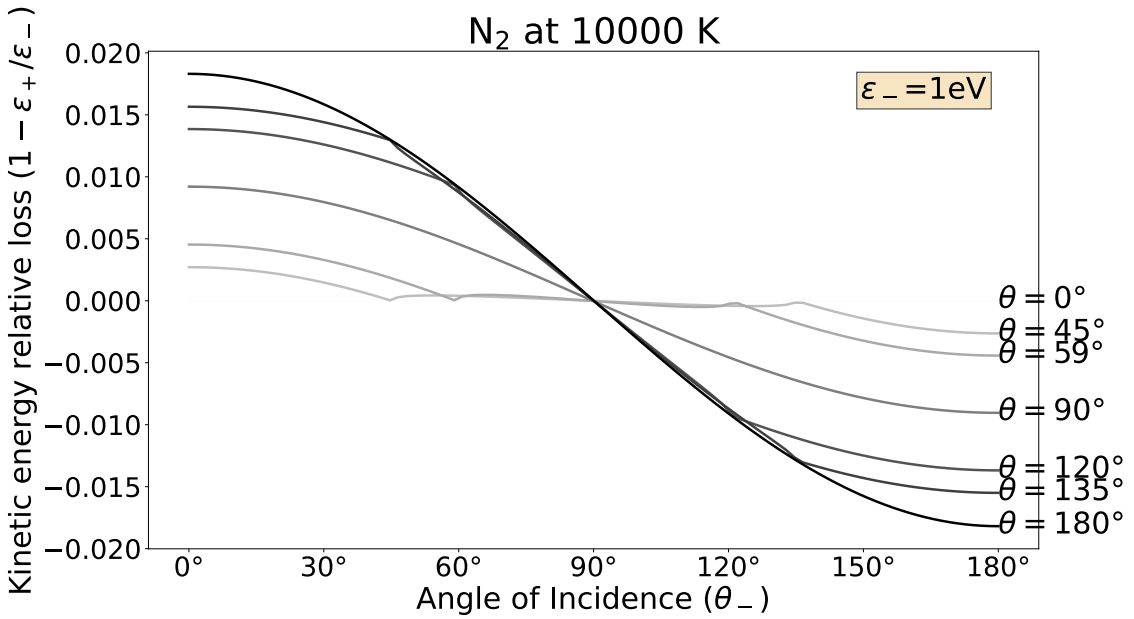

Figure 2.6: Relative energy loss for an electron initially at $\varepsilon_- = 1$ eV colliding elastically in a hot N_2 gas at 10 000 K. The curves were obtained by first integrating over the Maxwellian distribution of molecular velocity norms. Then the loss must also be averaged over the cone for which θ is fixed (cf. appendix A fig. A.2).

The quantity e' is equal to the relative total energy $\varepsilon' + mc^2$ obtained with a forward Lorentz transform from the fixed frame :

$$e' = \varepsilon_- + mc^2 - \boldsymbol{\mathcal{V}} \cdot \mathbf{p}_- \,, \tag{2.35}$$

$$= \varepsilon_- + mc^2 - \cos\theta_- \frac{\mathcal{V}}{c} \sqrt{\varepsilon_-^2 + 2mc^2\varepsilon_-} \,. \tag{2.36}$$

The angles $\theta_\pm$ are formed by the electron momenta after and before the collision with respect to the total momentum Π : $\cos\theta_\pm = \hat{\mathbf{p}}_\pm \cdot \hat{\mathbf{\Pi}}$. Due to the axial symmetry of the scattering problem, for each pair θ_+, θ_-, there is a continuum of deflection angles θ seen on figure A.3 presented in the appendix A.

In a gas at equilibrium, the molecules' velocities V follow an isotropic distribution given by the Maxwell statistics reviewed in appendix B.1. As a result, we shall be interested in the average outcome of an elastic collision in a gas at a given temperature T. When the gas temperatures are low and the electron energies are high, the majority of the momentum is carried by the electron which implies that $\theta_- \approxeq 0 \Rightarrow \theta \approxeq \theta_+$. We show in figure 2.6 the relative energy loss $1 - \varepsilon_+/\varepsilon_-$ as a function of θ_- for an electron scattering off nitrogen at a temperature of 10 000 K. Different values of θ_- are obtained by varying the relative orientation of the molecule's velocity with respect to the electron's initial direction.

As expected, the maximum exchange of momentum occurs at opposite scattering $\theta = 180°$. Then, trends change at $\theta = 90°$. In forward scattering $\theta < 90°$, the zone $\sin\theta_- > \sin\theta$ (flat zone) is characterised by a lessened average loss of energy because $\cos\theta_+$ spreads both over negative and positive values (beyond and beneath $\pi/2$). To the contrary, in backscattering mode $\theta > 90°$, losses of energy are reduced in the $\sin\theta_- < \sin\theta$ zone. This is because θ_+ avoids the region around $\theta^+ = 180°$ where momentum exchange is heavier.

When the usual approximations are applied ($V \cong 0$, $\gamma \cong 1$ and $m \ll M$), noting that $\mathcal{V} \cong mv/M$, the equation (2.33) reduces to the simpler forms :

$$\left.\begin{array}{l} V \cong 0 \\ \gamma \cong 1 \end{array}\right\} \Rightarrow \qquad \varepsilon_+ \cong \varepsilon_- \left(1 - 2\frac{mM}{(m+M)^2}(1 - \cos\theta_+ \sqrt{1 - (\frac{m}{M}\sin\theta_+)^2} - \frac{m}{M}\sin^2\theta_+)\right) , \tag{2.37}$$

$$m \ll M \Rightarrow \qquad \approx \varepsilon_- \left(1 - 2\frac{m}{M}(1 - \cos\theta_+)\right) . \tag{2.38}$$

The first equation (2.37) is equivalent to a non-relativistic treatment of a collision with a stationary target as given for instance in [589, eq. 3.2.18]. The second equation (2.38) is obtained when $m \ll M$ is additionally assumed. This latter form (2.38) corresponds actually to the previous form (2.37) when the angle θ_+ is replaced by θ'_+ in the relative centre of mass frame. Nonetheless, as seen from (A.9), $m \ll M \Rightarrow \mathcal{V}\mathring{\varepsilon}'/c^2 p' \approx m/M$ which makes the difference $\theta - \theta'$ imperceptible from (A.13). This is why (2.38) is the most widespread formula for electron energy losses due to elastic collisions [88, 677, 953, p.2174, eq.12, §44:eq.43,].

The role of gas temperature can be understood by comparing figures 2.7a and 2.7b. It increases the quantity of kinetic energy possibly exchanged in elastic collisions. Also, it reinforces the symmetry of energy losses and gains which depend on the electron initial energy. For nitrogen molecules the mass ratio $m/M \lessapprox 2 \times 10^{-5}$. In thermal equilibrium at 300 K, the speed of bulk electrons would be ~ 225 times the one of molecules and the maximal energy loss in frontal or parallel collisions wouldn't exceed 0.5% as seen on figure 2.7a.

A comparison of the exact and approximate treatments of elastic collisions can be made when averaging losses over the velocity distribution in the gas. This would correspond to averaging over θ_- in figures 2.6 or 2.7a. The result is given in figure 2.8a for a deck of gas temperatures attainable in spark discharges. One can see that the most limitative approximation is to assume $V = 0$ in (2.37) since even at ambient temperatures a deformation is observed compared to the basic formula (2.38) corresponding to the curve at 0 K. The overall temperature effect is to reduce (increase) energy losses below (beyond) 90°of scattering. For low-energy electrons, elastic energy losses in hotter gases is gradually reduced until energy can be gained from forward scattering when the average gas energy is higher than the electron energy.

On the other hand, temperature effects become increasingly negligible for higher-energy electrons, as expected. There, the least applicable approximation is the non-relativistic assumption. Figure 2.8b shows that recoil losses from fast electrons become very important and can even surpass inelastic losses in a single impact excitation. For instance, a MeV electron scattered beyond 60° can transfer 100 eV to a molecule. Nonetheless, such an event is highly improbable and would most likely be accompanied by bremsstrahlung emission of an energetic photon for which scattering is more important. [716, §IV]

Radiative losses In the *radiative* case, the total momentum after the interaction is shared between three bodies: the electron, the emitted photon and an atomic nucleus via the reception of a so-called *virtual* photon. This latter photon acts as an intermediary for momentum exchange between the electron and the nucleus. Its "virtual" character denotes the fact that it cannot be spotted but operates behind the scenes.

As a massless particle, a photon's energy ε_γ and momentum ε_γ are directly proportional :

$$\varepsilon_\gamma \equiv \hbar\omega = c\hbar k \equiv c p_\gamma , \tag{2.39}$$

and linked respectively to the angular frequency ω and the wave-number k. After replacing those values into the equation (A.30) for ternary collisions, the kinetic energy of an electron

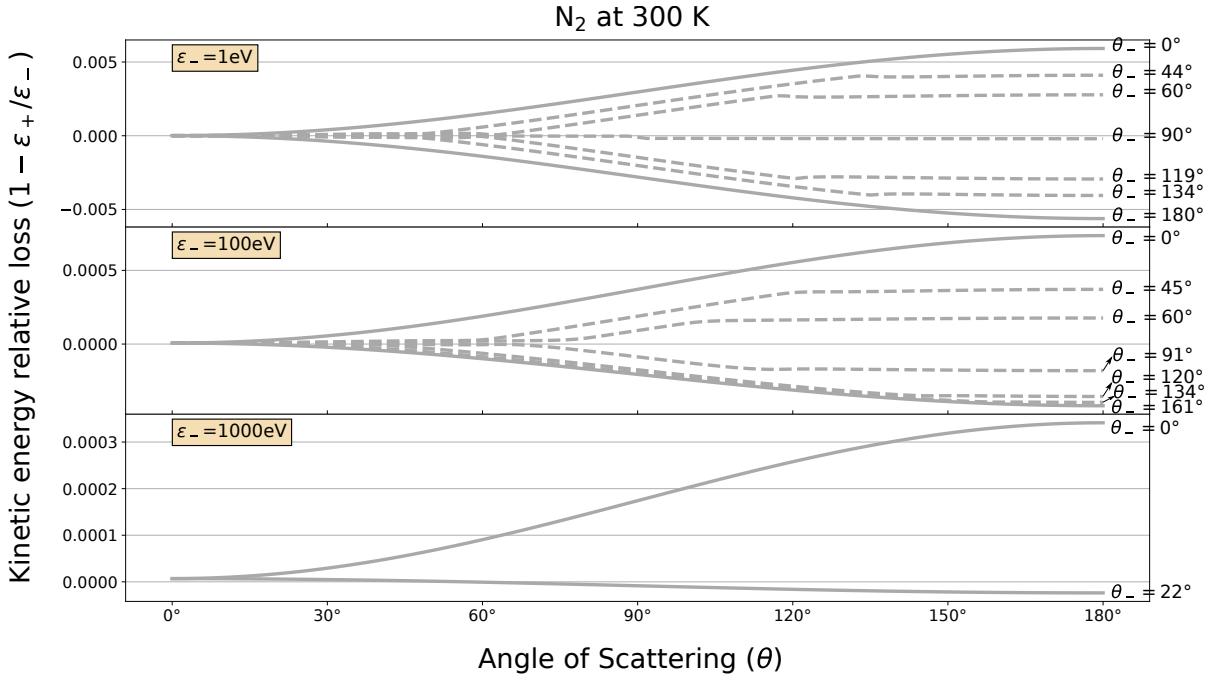

(a) Relative energy loss for an electron initially at $\varepsilon_- = 1$, 100 and 1000 eV colliding elastically in N_2 gas at 300 K and as a function of the scattering angle θ at various incident angles θ_-.

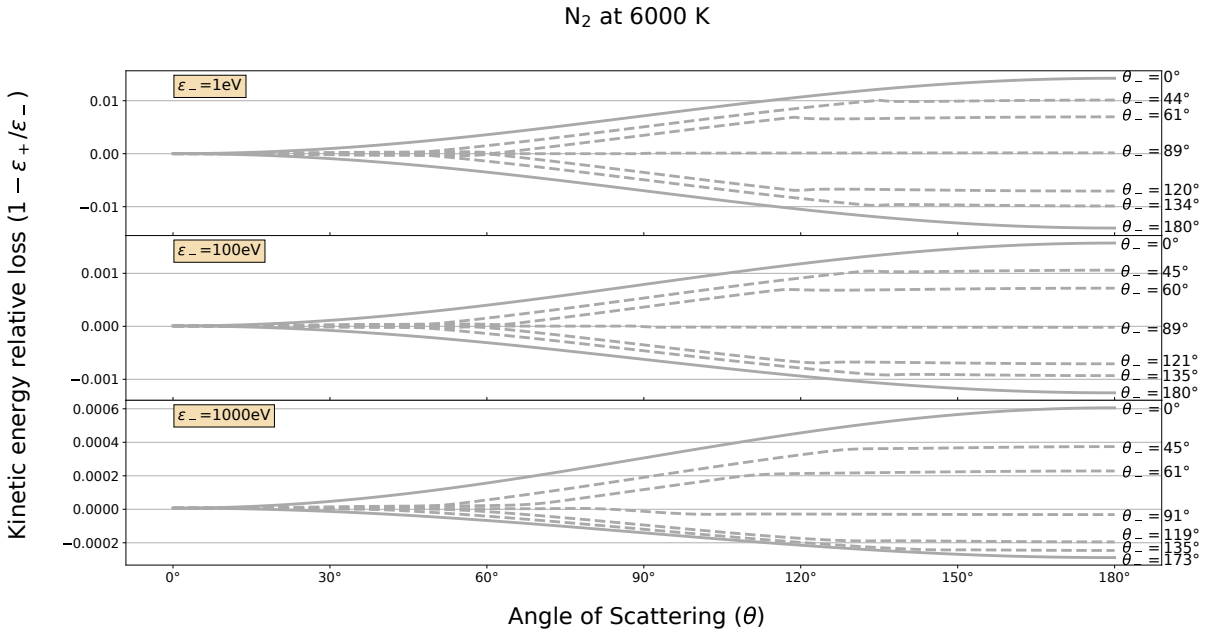

(b) Relative energy loss for an electron initially at $\varepsilon_- = 1$, 100 and 1000 eV colliding elastically in N_2 gas at 6000 K and as a function of the scattering angle θ at various incident angles θ_-.

Figure 2.7: The effect of higher temperatures is to broaden and symmetrise the gains in frontal ($\theta_- = 180°$) collisions to the losses in rear ($\theta_- = 0$ deg) collisions. The curves were obtained by first integrating over the Maxwellian distribution of molecular velocity norms. Then the loss must also be averaged over the cone for which θ is fixed at a determined θ_- (cf. appendix A fig. A.2).

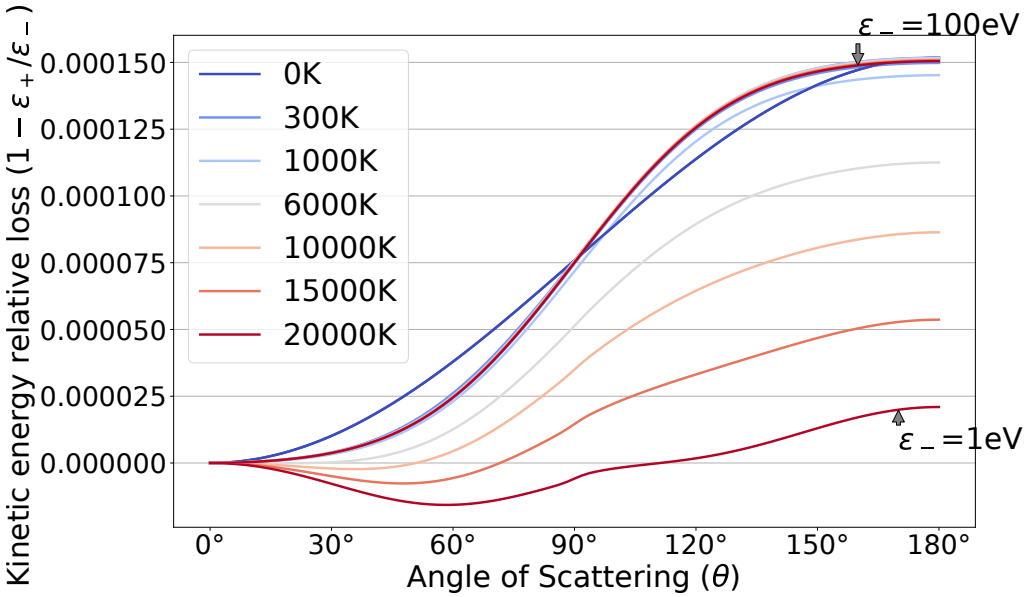

(a) Relative energy loss for an electron initially at ε_- = 1 and 100 eV colliding elastically in N_2 gas. Electrons can get a slight boost at low energies and forward scattering angles when the temperatures are high enough. There is virtually no difference at 0 and 300 K between 1 and 100 eV curves. The set of curves packed on top of each other are all related to 100 eV.

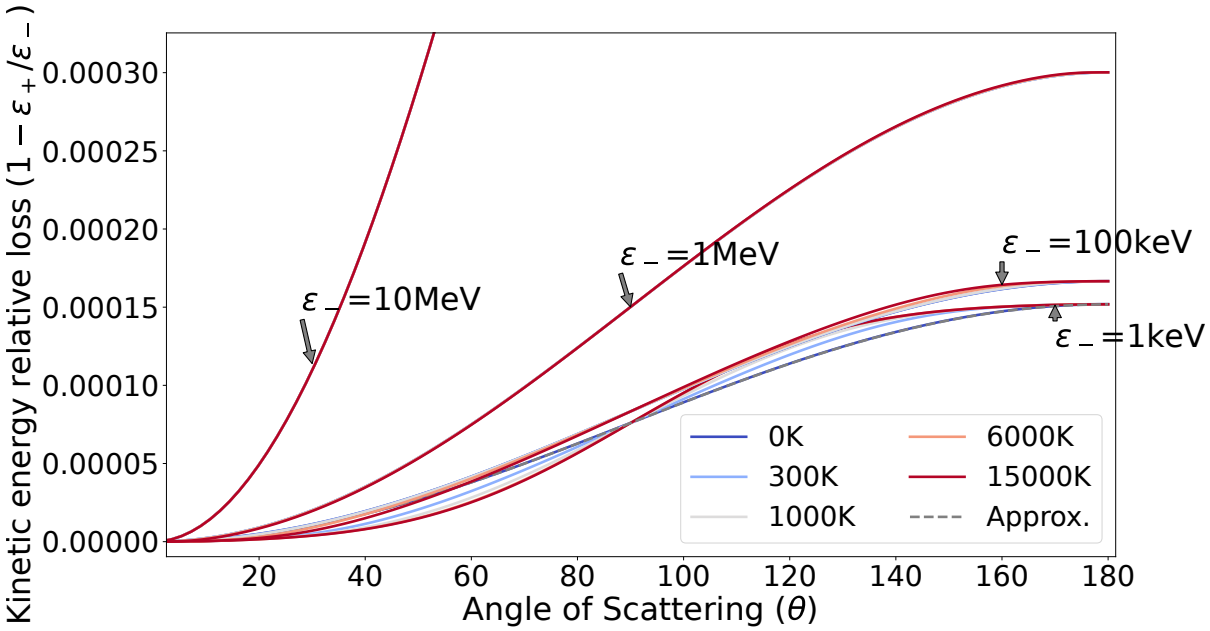

(b) Relative energy loss for a set of electron energies from ε_- =100 keV to 10 MeV. Relativistic effects start to be meaningful above 100 keV, at the same threshold where temperature effects are negligible. Below 10 keV, the approximation (2.38) is indistinguishable from the accurate formula (2.33) at 0 K.

Figure 2.8: Relative kinetic energy losses in elastic scattering averaged over any molecular orientation and speed distribution set by the temperature. Temperature effects dominate at low energies, they are gradually compacted until only relativistic effects become appreciable. The virtual zero K temperature is however somewhat different in shape than all other temperatures.

after radiating a bremsstrahlung photon is given by (2.33) with e' this time interpreted as:

$$e' = \sqrt{(mc^2)^2 + (cp'_+)^2}\sqrt{1 - \mathcal{V}^2/c^2}\,, \tag{2.40}$$

The relative electron momentum in the centre of mass reference frame is given by:

$$p'_+ = \frac{\tilde{\mathcal{E}}'_0\sqrt{(2\hbar\omega' mc^2\cos\theta')^2 + ((\tilde{\mathcal{E}}'_0)^2 - (\tilde{M}+m)^2c^4)((\tilde{\mathcal{E}}'_0)^2 - (\tilde{M}-m)^2c^4)} - \hbar\omega'\cos\theta'((\tilde{\mathcal{E}}'_0)^2 - (\tilde{M}^2 - m^2)c^4)}{2c((\tilde{\mathcal{E}}'_0)^2 - (\hbar\omega'\cos\theta')^2)} \tag{2.41}$$

The tilde notation affects quantities that are modified by the photon :

$$\tilde{M} \equiv \sqrt{(Mc^2)^2 + (\hbar\omega)^2}\,, \tag{2.42}$$

$$\tilde{\mathcal{E}}'_0 \equiv \mathcal{E}'_0 - \hbar\omega = \sqrt{\mathring{\mathcal{E}}^2 - (c\Pi)^2} - \hbar\omega\,, \tag{2.43}$$

$$\tilde{\theta}' \measuredangle (\mathbf{p}'_+, \hbar\mathbf{k})\,. \tag{2.44}$$

We recall that $\mathcal{E}'_0$ corresponds to the rest energy of the electron-molecule system. In practice, the energy losses due to recoil in Bremsstrahlung are negligible compared to the energy of the emitted photon. Only super-relativistic electrons > 50 MeV with deflections above 60° can present an additional loss over 1% of the photon energy [716]. This picture might be very different for electron-electron bremsstrahlung which however is of minor importance.

Overall, effective radiation events apply only to relativistic electrons > MeV, are rare, when they occur, photons of smaller energies are most often emitted, preferentially in the forward direction; so that one can ignore the deflection suffered by the electron let alone its energy lost by recoil. Thus, the energy of the electron after a radiative collision is simply:

$$\varepsilon_+ \simeq \varepsilon_- - \hbar\omega\,. \tag{2.45}$$

Excitation

A collision with (de-)excitation of the target molecule involves a loss (gain) of energy $\Delta\mathcal{E}$ on account of the electron. The kinetic energy after such collision is given rigorously by taking:

$$e' = \frac{(\mathcal{E}'_0)^2 + (mc^2)^2 - (Mc^2 + \Delta\mathcal{E})^2}{2\mathcal{E}} = \varepsilon_- + mc^2 - \boldsymbol{\mathcal{V}}\cdot\mathbf{p}_- - \Delta\mathcal{E}\frac{Mc^2}{\mathcal{E}}(1 + \frac{\Delta\mathcal{E}}{2Mc^2})\,, \tag{2.46}$$

and inserting it in (2.33). However in practice, the energy losses due to scattering in inelastic collisions is indisputably negligible compared to excitation thresholds except for lowest rotational levels which lie around 0.2 meV for most diatomic molecules. One can thus set :

$$\varepsilon_+ \simeq \varepsilon_- - \Delta\mathcal{E}\,. \tag{2.47}$$

The residual loss of energy $\varepsilon_- - (\varepsilon_+ + \Delta\mathcal{E})$ that we qualify as "inelastic scattering" is non-zero at $\theta = 0°$ due to the necessity of momentum conservation. For this reason, even if marginal, it is nonetheless overall greater than elastic losses. This can be seen on figure 2.9 which compares the energy losses due to inelastic scattering relative to elastic ones: Inelastic$(\varepsilon_- - \varepsilon_+ - \Delta\mathcal{E})$/Elastic$(\varepsilon_- - \varepsilon_+)$, for an illustrative excitation of 5 eV at ambient temperature.

Of greater interest is the effect of temperature on inelastic collisions. Usually, at low temperatures, the excited states of the gas described earlier in section 2.1.2 are scarcely populated compared to the ground state. One can then assume that electron energy losses predominate. However, when the temperatures rise, the contribution of superelastic collisions from excited states for low-energy electrons are expected not to be negligible and ought to be taken into account. As a consequence, the average energy loss in collisions should decrease for electrons whose energies are close to the average energy of the gas.

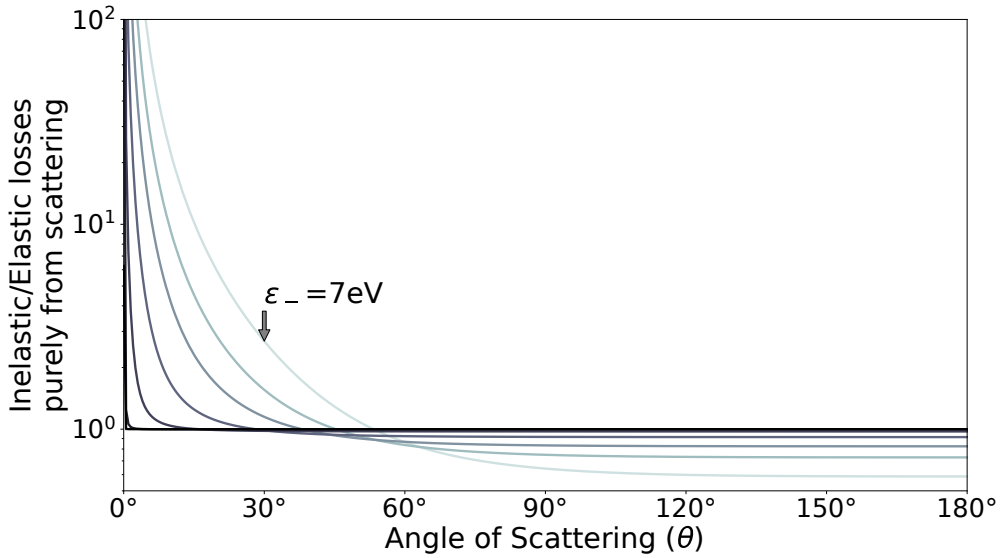

Figure 2.9: Relative inelastic over elastic scattering energy loss : Inelastic($\varepsilon_- - \varepsilon_+ - \Delta\mathcal{E}$)/Elastic($\varepsilon_- - \varepsilon_+$), for $\Delta\mathcal{E}$ = 5 eV at 300 K. The curves gradually increase in initial energy ε_- = 7, 10, 15, 30, 100, 1000, 10000 eV.

Rotational Excitations We test this hypothesis on the rotational excitation levels of N_2 defined earlier by (2.9). During a collision at an energy ε and deflected by an angle θ, if we know the excitation probability $\mathcal{P}(J_i \to J_f; \varepsilon, \theta)$ from an initial state $J = J_i$ to a final state at $J = J_f$, we may determine the average energy lost $\Delta\mathcal{E}_{\text{rot}}(\varepsilon, \theta)$ in rotational excitations:

$$\Delta\mathcal{E}_{\text{rot}}(\varepsilon,\theta) = \sum_{J_i,J_f}^{\infty} B(J_f(J_f+1) - J_i(J_i+1))\mathcal{P}(J_i \to J_f;\varepsilon,\theta)\frac{(2J_i+1)\exp(-BJ_i(J_i+1)/k_{\text{B}}T_{\text{rot}})}{\mathcal{Z}(T_{\text{rot}})}, \tag{2.48}$$

The fraction on the right hand side of (2.48) represents the population ratio of rotationally excited molecules at $J = J_i$ at a temperature of T_{rot}. The partition function $\mathcal{Z}(T_{\text{rot}})$ is a normalising constant defined in appendix B.2. It is equal to the denominator in (2.8). As explained at the beginning of this chapter in section 2.1.2, the rotational constant B gives the energy associated with the state J: $BJ(J+1)$.

The details of how to obtain all the transition probabilities $\mathcal{P}(J_i \to J_f)$ are presented in the second part section 11.2. For simplicity and elegance, we use the *spectator model* presented in the second part section 11.2.3 on page 415. Unfortunately, this model is not valid at low energies around ~ eV as well observed on figure 11.15. Conversely, the first Born approximation applied to a linear rigid rotor as defined in section 11.2.1 gives transitions $\Delta J = \pm 2$ which are valid only at sub-eV energies. In order to preserve a consistent way of representing rotational losses, we normalised the set of transition probabilities in (2.48) with more accurately computed cross sections $\sigma_{0\to J}$ [digitised from 546, figure 7a], and used the angular distribution of the spectator model, notwithstanding its inaccuracy. The combination is expressed by (11.35).

The resulting average loss in N_2 can be observed in figure 2.10 for 0.5 eV to 2 eV electrons at various gas (rotational) temperatures. Contrary to elastic scattering, the average energy exchanged in rotational excitations is either a loss or a gain over all angles of scattering. The transition between both regimes can be easily determined from the principle of equipartition of energy [547, §9.2, p.241]. An electron will be considered *rotationally* subthermal if its energy $\varepsilon < 2\frac{k_{\text{B}}T_{\text{rot}}}{2}$ is less than the energy stored in the rotational degrees of freedom (~ 2) of the gas.

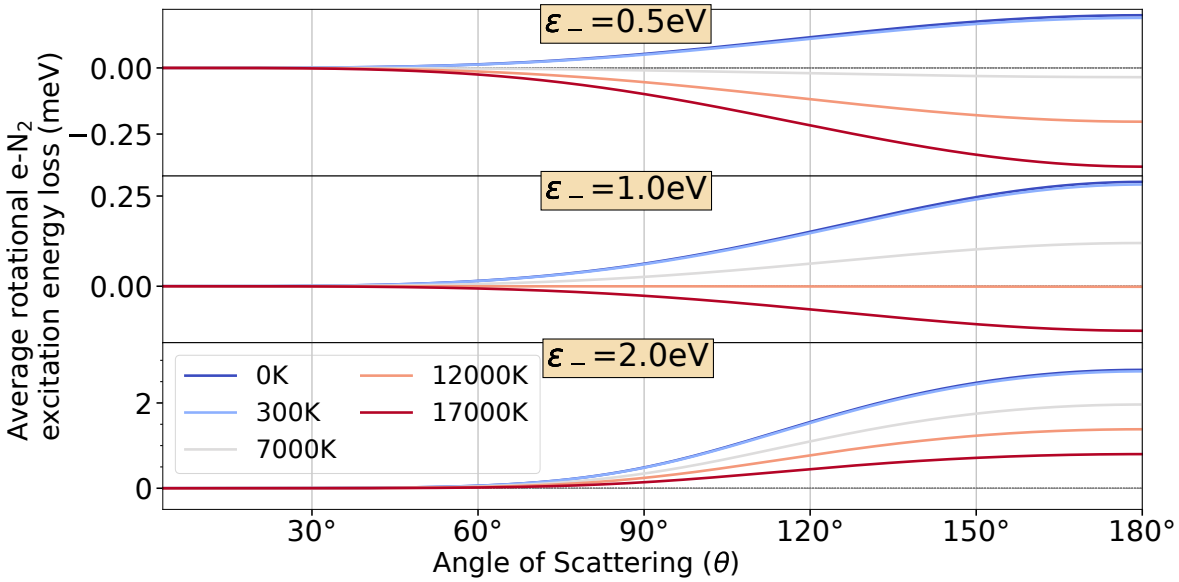

Figure 2.10: Average kinetic energy loss $\Delta\mathcal{E}_{\text{rot}}$ in a low-energy electron-N_2 vibrationally elastic collision at various gas temperatures, calculated with (2.48) in the spectator model (11.35). The average includes rotationally elastic $J_i = J_f$ collisions.

For an electron of $\varepsilon = 1\,\text{eV}$, this transition happens at $T_{\text{rot}} \simeq 12\,000\,\text{K}$, as can be seen by the straight line on the middle graph of figure 2.10. As expected from the magnitude of the rotational constant B, the absolute average losses per collision lie in the ~ meV range.

At higher energies, an interesting phenomenon known as a "rotational rainbow" [535] unlocks larger transitions $\Delta J \gtrsim 6$ during a backscattering event. The 3D projection on figure 2.11 shows the average energy loss for each transition ΔJ incurred by electrons of higher energies according to the angle they scattered off molecular nitrogen. One can see that the peak loss moves toward larger ΔJ as a result of a higher probability as the energy and angle increase. Note that the effect of temperature enables a larger energy exchange for a fixed ΔJ as can be seen from $(J+\Delta J)(J+\Delta J+1) - J(J+1) = \Delta J(2(J+\Delta J)+1)$ when higher J states are populated.

Overall, elastic losses approximated by (2.38) which scale relative to the initial energy ε_-, can be compared to purely rotational losses from (2.48), which vary less in magnitude, as a function of ε_- and θ as shown on figure 2.12. The graph can be decomposed into zones where electrons gain or lose energy on average in collisions. The crest at low-energies coincides with the $^2\Pi_g$ resonance [820, §III.A.5, p.548] in electron-nitrogen rotational excitation located around 2.4 eV [105]. Rotational gain/losses dominate at low energies and become gradually negligible compared to pure scattering losses at higher energies. Also, although both (elastic and rotational) losses are null at $\theta = 0°$, their slopes can be quite different. In the spectator model (11.30), the probability of rotational excitations in forward scattering is much smaller than elastic scattering.

In homonuclear diatomic molecules (or molecules without a permanent dipole), rotational excitations take place as a result of quadrupole interaction. Ridenti *et al.* [774] showed that very good agreement with experimental swarm parameters at low electric fields can be obtained with isotropic quadrupole DCS calculated in the first Born approximation (see section 11.2.1 eq. 11.21b). The situation is radically different when the molecule is polar, (i.e. has a permanent dipole) as NO, CO, water, etc. In this case, the rotational cross sections are much larger in magnitude and present a prominent shape in the forward direction. The effect of anisotropic scattering from dipole-induced rotational excitations in CO was shown by Vialetto *et al.* [961] to be important at low electric fields.

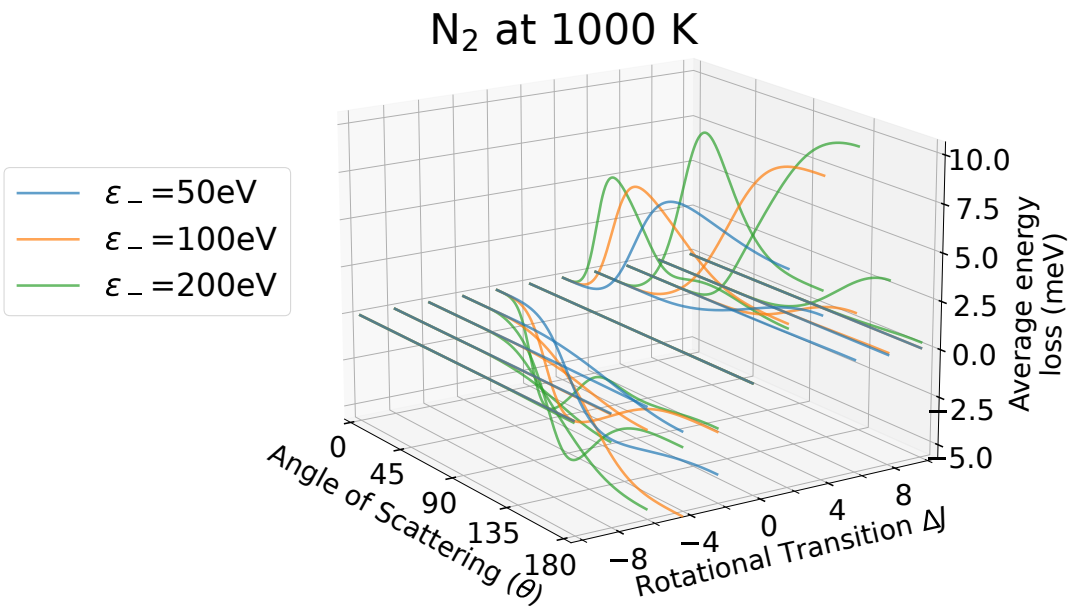

Figure 2.11: Rotational rainbows from the spectator model (11.35) in intermediate energy electron-N_2 collisions for various ΔJ transitions at a gas temperature of 1000 K. Large scattering angles and higher energies promote greater exchanges of energy in a single collision.

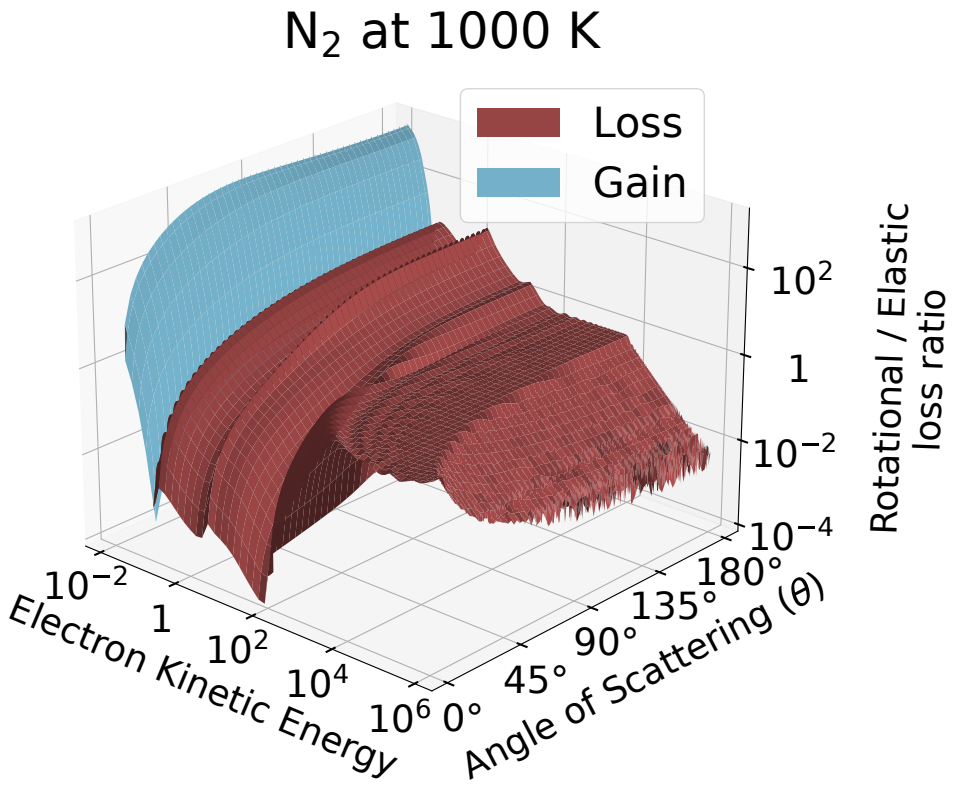

Figure 2.12: Ratio of average rotational losses $\Delta\mathcal{E}_{\text{rot}}$ (2.48), over approximate losses (2.38) in elastic scattering. Rotational excitations dominate at low-energies $< 10\,\text{eV}$ and large angles $> 90°$. The backscattering peak at 2.4 eV is reminiscent of the rotational resonance for N_2.

Vibrational Excitations The vibrational threshold for nitrogen lies close to ~ 0.29 eV but is about two-thirds lower for oxygen at ~ 0.195 eV. The dominant mode of excitation is through $^2\Pi_g$ resonance scattering in the region between 1—4 eV for N_2 and 0.2—1 eV for O_2. If we adapt the energy loss in (2.48) to a vibrationally populated gas at T_{vib} we get:

$$\Delta\mathcal{E}_{\text{vib}}(\varepsilon,\theta) = \sum_{v_i,v_f}^{\infty} \Delta\mathcal{E}_v \mathcal{P}(v_i \to v_f;\theta,\varepsilon)\frac{\exp(-\mathcal{E}_i/k_{\text{B}}T_{\text{vib}})}{\mathcal{Z}(T_{\text{vib}})} \,. \tag{2.49}$$

We use the shorthand notation $\Delta\mathcal{E}_v \equiv \hbar\omega_{\text{vib}}(v_f - v_i)$ and $\mathcal{E}_i \equiv \hbar\omega_{\text{vib}}(v + \frac{1}{2})$. The advantage when handling a set of vibrational excitations is that, when v_i is not too high (< 10), the energy loss among excitations for a fixed Δv differs only by a few percent. This means that instead of having to specify collisions as $v_i \to v_f$, we can regroup the energy losses due to collisions corresponding to a certain Δv.

Nonetheless, unlike for rotational transitions, there exists not any straightforward way to compute $\mathcal{P}(v_i \to v_f)$. Instead, one can use a fundamental relation in scattering known as *detailed balancing* (7.6) to associate a transition $v_i \to v_j$ to its reciprocal $v_i \leftarrow v_f$. In case of vibrational excitations, it is given by:

$$\sigma_{v_i \leftarrow v_f}(\varepsilon) = \frac{\varepsilon + \Delta\mathcal{E}_v}{\varepsilon}\sigma_{v_i \to v_f}(\varepsilon + \Delta\mathcal{E}_v) \tag{2.50}$$

Then, the balance between losses and gains in vibrational excitations reads:

$$\begin{aligned}\Delta\mathcal{E}_{\text{vib}}(\varepsilon,\theta) = \sum_{v_i<v_f}^{\infty} \Delta\mathcal{E}_v \mathcal{P}(v_i \to v_f,\theta,\varepsilon)\frac{\exp(-\mathcal{E}_i/k_{\text{B}}T_{\text{vib}})}{\mathcal{Z}(T_{\text{vib}})} \\ \times\left(1 - \frac{\varepsilon + \Delta\mathcal{E}_v}{\varepsilon}\frac{\sigma_{ij}(\varepsilon + \Delta\mathcal{E}_v)}{\sigma_{ij}(\varepsilon)}\exp\left(-\frac{\Delta\mathcal{E}_v}{k_{\text{B}}T_{\text{vib}}}\right)\right) \,.\end{aligned} \tag{2.51}$$

Gain from superelastic vibrational collisions is promoted when $\varepsilon < k_{\text{B}}T_{\text{vib}}$ and $k_{\text{B}}T_{\text{vib}} \gg \Delta\mathcal{E}_v$ but also if $\sigma_{ij}(\varepsilon + \Delta\mathcal{E}_v) > \sigma_{ij}(\varepsilon)$. This latter case occurs at the foot of a resonance region distanced by $\Delta\mathcal{E}_v$ from the first peak. When the temperatures are high enough to populate the first vibrational level ($T_{\text{vib}} \gtrsim 3400$ K in N_2 ; 2300 K in O_2), one can expect under-resonant electrons to get an overall energy boost from superelastic collisions.

The peculiarity about resonant scattering is that its angular distribution shape is fairly independent of the energy and the vibrational transition, and adopts the symmetry set by the decaying negative-ion temporarily formed (see fig. 11.23). This is why we can assume as a first approximation that the pattern of the energy transferred in resonant collisions is independent of the scattering angle, so that the vibrational loss analysis is only displayed as a function of energy unlike in rotational and elastic scattering.

We use the set of vibrational cross sections computed by Laporta *et al.* [552, 554] to test this hypothesis. They are the most recent available set in good agreement with experimental data. Using formula (2.51) in the range 0—15 eV at various temperatures, the average losses are displayed on figure (2.13) for N_2 and O_2.

The resonant nature of vibrational scattering is very prominent through the spikes in the energy losses between 0 and 4 eV. The electronic structure of a diatomic molecule can lead to significant differences as seen between O_2 and N_2. The strong electron-O_2 affinity intuitively explains the sharp spikes at low energies. Increasing the vibrational temperature activates superelastic collisions from vibrationally excited states. As a result, the resonant structure is attenuated because resonant peaks in cross sections with vibrationally excited states are shifted to different positions, and therefore they compensate each other when averaged.

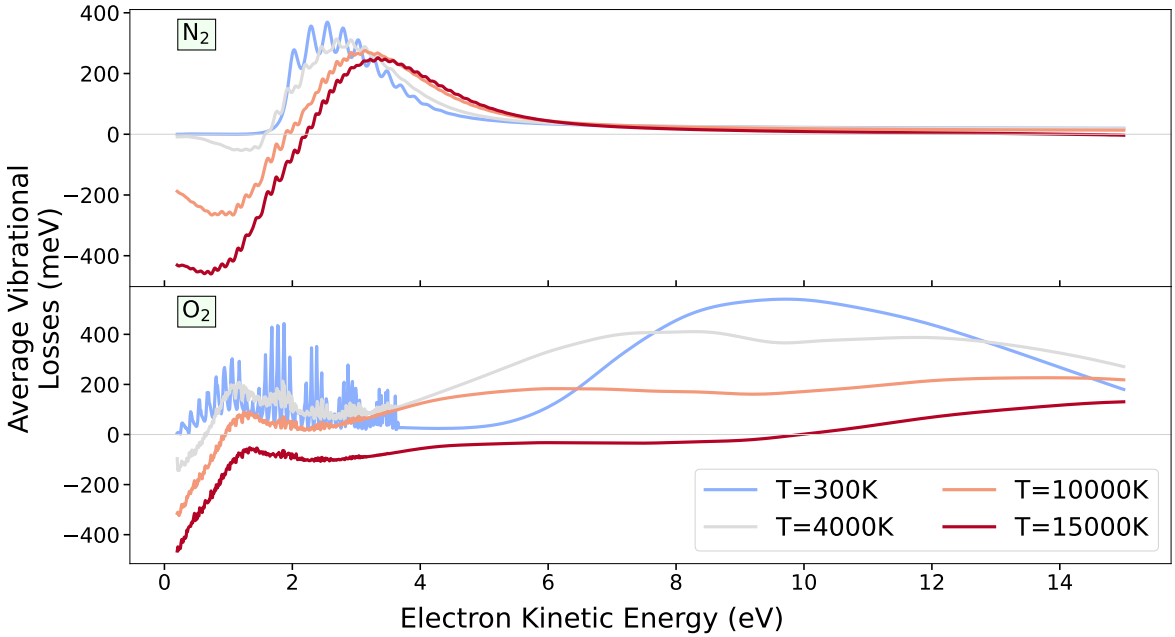

Figure 2.13: Vibrational losses of electrons in N_2 and O_2 at various temperatures.

Furthermore, increasing the vibrational temperature of N_2 enhances the contrast between regions of average gain and losses which are shifted toward higher energies. The trend is more complex in O_2. The difference around 10 eV in O_2 (which has a broad bump) and N_2 (which is flat) is due to the omission of core-excited resonances in the cross section set of N_2 [554]. For more information about resonant scattering, readers may consult section 11.3 of part II.

Electronic Excitations: Compared to the relative coherence of rotational and vibrational excitations, the realm of collisions with electronic excitations is unruly. We convey this in the tabbing below:

Excitations	Rotational	Vibrational	Electronic
Coherent law for transition probabilities	✓ (eq. 11.24)	×	×
Coherent law for excitation thresholds	✓ (eq. 2.9)	✓ (eq. 2.11)	×(tab. 11.6–11.11)

Thus, there is no straightforward way to compute a set of electronic excitation energy levels nor to derive the transition probabilities from states $A \to B$ from the ground excitations $X \to A$ and $X \to B$. The electronic excitation energy thresholds for diatomic molecules and atoms are gathered in separate tables 11.6,11.7,11.8,11.9,11.10,11.11 in chapter 11 of part II.

In any case, as explained at the beginning of this subsection, electronic states would require unrealistic temperatures to present decent populations of excited levels. Nonetheless, how temperatures may significantly affect the energy loss rate is through the change in the gas' chemical composition. Molecule dissociation can occur through various processes: direct dissociation, dissociative attachment, and predissociation from various super-excited vibrational or electronic states [834, p.4&67]. The dependence of the average energy loss on the temperature through chemical composition of a gas is shown in a later chapter 5 in figure 5.11.

Ionisation

The characteristics of an ionising collision present their own complexity due to the many subprocesses involved. Most often, the term "ionisation" is implicitly associated to the simplest case of non-dissociative, non-exciting, single ionisation event where part of the impacting electron's energy is yielded to knock away one shell electron from the molecule with an ionisation threshold at $\Delta\mathcal{E}_{\text{ion}}$. In reality, ionisations regroup a class of large energy loss events that can also leave the ionised molecule in a dissociated and/or excited state. In the extreme but not inexistent situation where two shell electrons are ejected, known as a double ionisation, the energy redistribution among the scattered particles is difficult to describe theoretically and experimental data is absent.

Notwithstanding, if the ejection angles of the fragments are known, just as in the elastic radiative collision, one can derive rigorously the outgoing electron's energy and momentum with (A.30). From the ternary collisions covered in the appendix A.1, we label the secondary electron's energy-momentum in the centre of mass frame as $(\varepsilon'_2, \mathbf{p}'_2)$:

$$p'^{+} = \Big[\check{\mathcal{E}}'_0\sqrt{(2cp'_2mc^2\cos\check{\theta}')^2 + ((\check{\mathcal{E}}'_0)^2 - (\check{M}+m)^2c^4)((\check{\mathcal{E}}'_0)^2 - (\check{M}-m)^2c^4)}$$
$$- cp'_2\cos\check{\theta}'((\check{\mathcal{E}}'_0)^2 - (\check{M}^2-m^2)c^4)\Big]\frac{1/2c}{(\check{\mathcal{E}}'_0)^2 - (cp'_2\cos\check{\theta}')^2} .$$

The cusp notation relates quantities affected by the secondary ejected electron :

$$\check{\mathcal{E}}'_0 \equiv \mathcal{E}'_0 - (mc^2 + \varepsilon'_2) , \tag{2.52}$$
$$\check{M} \equiv \sqrt{(Mc^2 + \Delta\mathcal{E}_{\text{ion}})^2 + (cp'_2)^2} , \tag{2.53}$$
$$\check{\theta}' \measuredangle (\mathbf{p}'_+, \mathbf{p}'_2) . \tag{2.54}$$

Again, like for bremsstrahlung, the recoil losses for non ultra-relativistic electrons are negligible and one can be content with merely subtracting the kinetic energy of the secondary ε_2 and the ionisation threshold $\Delta\mathcal{E}_{\text{ion}}$:

$$\varepsilon_+ \simeq \varepsilon_- - \varepsilon_2 - \Delta\mathcal{E}_{\text{ion}} . \tag{2.55}$$

The threshold $\Delta\mathcal{E}_{\text{ion}}$ and secondary energies ε_2 may be sampled from partial and differential ionisation cross sections given by the RBEQ* model (11.119–11.120) presented in section 11.5.4. Sampling techniques in Monte Carlo simulations are explained in sections 3.2.2 and 3.2.3.

Rarely, the angular scattering distributions θ_1, θ_2 of the ejected electrons is known. Although measurements of doubly differential cross sections are gradually more resolved and accurate, there is still a vacuum in the literature about accurate and comprehensive databases of those angular distributions. Some information is disclosed in the second part on page 492.

Presently, Monte Carlo simulations recur to rudimentary approximations that lead to a deterministic scattering in ionisation events from the binary encounter model (see 11.5.2). In this model, it is assumed that the electron collides only with a bound electron and thus no recoil is communicated to the molecule. Although energy losses due to recoil are indeed negligible, it is physically rather crude to account for the ionisation threshold $\Delta\mathcal{E}_{\text{ion}}$ without taking into consideration the recoil *momentum* $\mathbf{P}_{\text{i}}$ of the ion. In other words, the momentum after an ionisation event must be shared between both electrons and the ion in order to amount to the total momentum $\mathbf{\Pi}$:

$$\mathbf{\Pi} \equiv \mathbf{p}_+ + \mathbf{p}_2 + \mathbf{P}_{\text{i}} \Rightarrow \begin{cases} 0 = p_+\sin\theta_+ + p_2\sin\theta_2 + P_{\text{i}}\sin\theta_{\text{i}} , \\ \Pi = p_+\cos\theta_+ + p_2\cos\theta_2 + P_{\text{i}}\cos\theta_{\text{i}} . \end{cases} \tag{2.56}$$

The secondary electron is then ejected at an angle θ_2 determined by :

$$\cos\theta_2 = \frac{(\Pi - P_\mathrm{i}\cos\theta_\mathrm{i})^2 - p_+^2 + p_2^2 - P_\mathrm{i}\sin\theta_\mathrm{i}(P_\mathrm{i}\sin\theta_\mathrm{i} + 2p_+\sin\theta_+)}{2(\Pi - P_\mathrm{i}\cos\theta_\mathrm{i})p_2} \,. \tag{2.57}$$

From this point, we can derive four levels of approximations:

a) We may assume that the ion suffers little deviation from the direction $\hat{\mathbf{\Pi}}$ of the total momentum, implying that $\cos\theta_\mathrm{i} = 1$.

$$\cos\theta_2 = \frac{(\Pi - P_\mathrm{i})^2 - p_+^2 + p_2^2}{2(\Pi - P_\mathrm{i})p_2} \,. \tag{2.58}$$

The value of P_i can be fixed from the most stringent requirement that when $p_2 = 0$ the momentum conservation relies only on $\mathbf{P}_\mathrm{i}$ and $\mathbf{p}_+$ which are both aligned along $\mathbf{\Pi}$:

$$P_\mathrm{i} = \Pi - p_+ \Leftrightarrow (\Pi - P_\mathrm{i}) = \sqrt{(\mathcal{E} - \Delta\mathcal{E}_\mathrm{ion})^2 + 2mc^2(\mathcal{E} - \Delta\mathcal{E}_\mathrm{ion})} \,. \tag{2.59}$$

The energy $\mathcal{E}$ is the total energy of the collision which, in addition to ε_-, may include the kinetic energies of the initially bound electron U and of the molecule.

b) If we assume that the bound electron is initially at rest in its orbital $U \simeq 0$, then the total momentum and energy are only carried by the incident electron before the collision: $\Pi = p_-$ and $\mathcal{E} = \varepsilon_-$. Using the energy conservation (2.55) and replacing in (2.59) and (2.58) we obtain the relativistic $\varepsilon_- \gtrsim mc^2$ and near threshold $\varepsilon_- \simeq \Delta\mathcal{E}_\mathrm{ion}$ expressions:

$$\cos\theta_+ = \sqrt{\frac{\varepsilon_+((\varepsilon_- - \Delta\mathcal{E}_\mathrm{ion}) + 2mc^2)}{(\varepsilon_- - \Delta\mathcal{E}_\mathrm{ion})(\varepsilon_+ + 2mc^2)}} \tag{2.60}$$

$$\cos\theta_2 = \sqrt{\frac{\varepsilon_2((\varepsilon_- - \Delta\mathcal{E}_\mathrm{ion}) + 2mc^2)}{(\varepsilon_- - \Delta\mathcal{E}_\mathrm{ion})(\varepsilon_2 + 2mc^2)}} \tag{2.61}$$

c) At high incident energies $\varepsilon_- \gg \Delta\mathcal{E}_\mathrm{ion}$ we may neglect the energy loss of the primary due to the ionisation threshold. Actually, this also tacitly implies $\varepsilon_2 \gg \Delta\mathcal{E}_\mathrm{ion}$ which of course is not necessarily verified. Nonetheless, we obtain the following simple pair of equations [160, 576, eq(19a), eq(3-4)] :

$$\cos\theta_+ = \sqrt{\frac{\varepsilon_+(\varepsilon_- + 2mc^2)}{\varepsilon_-(\varepsilon_+ + 2mc^2)}} \,, \tag{2.62}$$

$$\cos\theta_2 = \sqrt{\frac{\varepsilon_2(\varepsilon_- + 2mc2)}{\varepsilon_-(\varepsilon_2 + 2mc2)}} \,. \tag{2.63}$$

d) Furtherless*, in the non-relativistic limit, the electrons are ejected perpendicularly giving $p_-^2 = p_+^2 + p_2^2 = (p_+ \cos\theta_+ + p_2 \cos\theta_2)^2$ as implemented in Boeuf and Marode [88, eq(22), with the square root omission presently corrected], and thus :

$$\cos\theta_+ = \sqrt{\frac{\varepsilon_+}{\varepsilon_+ + \varepsilon_2}}\,, \tag{2.64}$$

$$\cos\theta_2 = \sqrt{\frac{\varepsilon_2}{\varepsilon_+ + \varepsilon_2}}\,. \tag{2.65}$$

The assumption that little momentum is transferred to the parent molecule is experimentally verified in triply differential cross sections (TDCS) at high incident energies $\varepsilon_- \ggg \Delta\mathcal{E}_{\text{ion}}$, small primary scattering angles $\theta_+ < 10°$ and not low secondary energies $\varepsilon_2 > \Delta\mathcal{E}_{\text{ion}}$ [810]. A lobe is observed more or less perpendicularly or at least obliquely tilted to the scattered direction of the primary electron (see fig. 11.49 p. 495). Theoretically, this assumption is supported by the so-called "Bethe-ridge" of the differential dipole oscillator strength density when the secondary electron energy ε_2 is not too low. More information can be found in the second part of the thesis in section 11.5.3.

In practice, none of those approximations apply as $\varepsilon_- \simeq \Delta\mathcal{E}_{\text{ion}}$ because there, the whole impulse approximation fails. Also, whenever ε_2 is small, the angular distribution of secondary electrons is virtually isotropic (see fig. 11.47) and cannot be assumed to be preferential in one particular direction θ_2.

In the computations of this thesis, we decided to model the emission of secondary electrons stochastically according to a hybrid model between the deterministic binary encounter (2.58) and an isotropic distribution at low ε_2:

$$\cos\theta_2 = \frac{\varepsilon_2}{\varepsilon_2 + \Delta\mathcal{E}_{\text{ion}}}\sqrt{\frac{\varepsilon_2((\varepsilon_- - \Delta\mathcal{E}_{\text{ion}}) + 2mc^2)}{(\varepsilon_- - \Delta\mathcal{E}_{\text{ion}})(\varepsilon_2 + 2mc^2)}} + \frac{\Delta\mathcal{E}_{\text{ion}}}{\varepsilon_2 + \Delta\mathcal{E}_{\text{ion}}}(1 - 2x)\,. \tag{2.66}$$

where $x \in [0,1]$ is a sample from a uniformly distributed random variable (see also eq.11.132 on page 494).

In principle, instead of appealing to the weighted formula (2.66), one could stochastically sample the initial momentum $\mathbf{p}_o$ of the bound electron in the orbital o from an isotropic distribution with a radius $p_o = 2mU/\hbar^2$ where U is the average kinetic energy on the orbital o (given in part II 11.5.4 table 11.12 on page 490). This would determine the total momentum $\mathbf{\Pi} = \mathbf{p}_- + \mathbf{p}_o$ with $p_- - p_o \leq \Pi \leq p_- + p_o$, to be used in (2.58). We did not opt for this alternative because the binary model is invalid at low ε_2 and an isotropic distribution as seen experimentally cannot be explained by the inclusion of initial momentum from the bound orbitals. One would need to understand better how interaction between both electrons and the ion core perturbs the ideal situation of a binary encounter.

For more information, the interested reader may want to consult section 11.5.4 of part II, and figures 11.47–11.49 where experimental data show a significant contribution of large angle scattering compared to the punctual angle corresponding to a simple binary electron collision. Whether a proper modelling of the angular distribution of secondary electron from ionisation has a statistically observable impact on transport parameters and thermal runaway, is unknown and could be tested in the future.

*We are regressing toward a cruder approximation, we are thus not going further~~more~~ but rather 'furtherless' in accuracy.

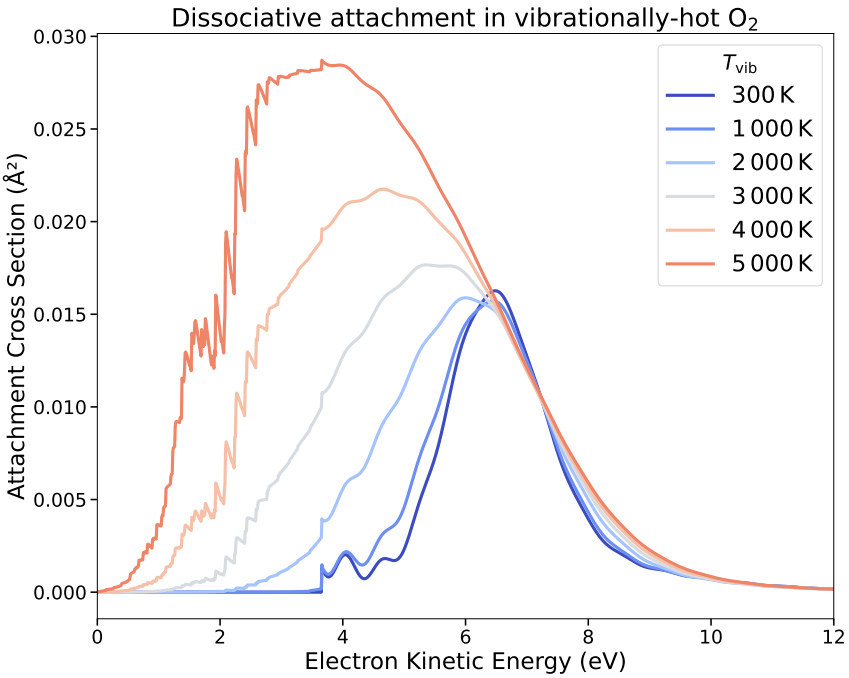

Figure 2.14: Dissociative attachment in oxygen is sensitive to the (vibrational) temperature. The cross sections predicted by Laporta *et al.* [558] of an electron attaching to a vibrationally excited $O_2(v')$ have a lower threshold and a higher peak as the average vibrational level v' increases along with the temperature.

Attachment

At last, we finish this preliminary tour of electron-molecule collisions with the electron attachment on oxygen which has a positive electron affinity. This constitutes another example of resonant processes. At first, it may be thought that attachment offers the delight of not having to bother discussing any electron scattering outcome. In reality, the post-traumatic consequences ensuing the withdrawal of an electron's liberty are not to be taken lightly.

Due to the restrictions imposed by energy-momentum conservation laws, "pure" attachment cannot take place; it is rather the consequence of a resonant collision process that leads to stable attachment to oxygen. As the e-O_2 compound is created, it vibrates at a certain level for which two different scenarios lead to long-term attachment :

Dissociative Attachment happens when the electron energy is high enough $\gtrsim 4\,\text{eV}$ to excite an elevated vibrational level beyond the dissociation limit of the $O_2^-(^2\Pi_u)$ anion. In that case, the compound encounters itself in a repulsive bond state and dissociates with one of the two oxygen atoms keeping the electron attached [820, p.472, §VI.B]. This enables the initial momentum to be carried by the fragments scattered apart.

Three-body attachment consists in a formation of a metastable electron-molecule compound which then becomes a stable anion after colliding with a third body. It occurs at lower energies when the electron excites long-living $O_2^-(^2\Pi_g)$ vibrational states that, when colliding with another molecule, deexcite to a lower stable level [820, p.472, §VI.A.5]. Stable means that it cannot spontaneously autodetach because its energy is below the neutral oxygen ground state as represented in figure 11.18 of section 11.3.4.

Note that those two processes correspond to two distinct energy regions and resonances : lowest-energies – $^2\Pi_g$ for three-body; and $\gtrsim 4\,\text{eV}$ – $^2\Pi_u$ for dissociation. Since attachment and resonant vibrational excitations are so tightly linked, dissociative attachment is facilitated with increasing temperatures [393]. This is seen on the set of cross sections displayed in figure 2.14 from [558]. We provide additional information on attachment in section 11.3.4 of part II.

2.2.3 Average Motion

The motion of electrons in gases, as sketched in 2.5, may be very chaotic at low energies because of the frequent collisions that interrupt the electromagnetic acceleration and drastically change the electron's momentum. Nevertheless, the individual effect of each collision decreases at higher electron energies above the keV domain. It is therefore very useful to describe somehow the overall combined effect of many collisions on the electron's trajectory through the average friction (or braking) force as described in Raizer [762, §2.1.1:p.8–11].

We remind the basic notions related to the average motion of an electron in a gas:

- $\bar{\lambda}$: the "mean free path", an average distance that an electron traverses between two collision events;
$$\bar{\lambda} \equiv 1/(\sigma n_{\text{gas}}) \,. \tag{2.67}$$
- $\bar{\tau}$: the "mean free time", the average timespan between two collisions;
$$\bar{\tau} \equiv \bar{\lambda}/\mathrm{v} \,. \tag{2.68}$$
- ν : the "collision frequency", or inverse of the mean free time: $\nu \equiv 1/\bar{\tau}$;
$$\nu \equiv n_{\text{gas}} \sigma \mathrm{v} \,. \tag{2.69}$$
- $\langle \cos\theta \rangle$: the "mean scattering cosine", the average cosine of the electron's outgoing velocity after a scattering event defined as:
$$\langle \cos\theta \rangle \equiv \frac{2\pi}{\sigma} \int_0^\pi \frac{\mathrm{d}\sigma}{\mathrm{d}\Omega} \cos\theta \, \sin\theta \, \mathrm{d}\theta \,. \tag{2.70}$$

As we will see below (2.81&2.84), the presence of anisotropy, such as an external electric field, slightly distorts the definition of the collisional parameters. This is because (i) the velocity v of the electron changes during its flight time but also (ii) the cross section $\sigma(\varepsilon)$, who may sharply depend on the electron's kinetic energy ε.

Average Friction Force

In high-energy particle physics, the energy lost per unit length $-\mathrm{d}\varepsilon/\mathrm{d}l$ due to collisions by a fast particle traversing a medium of atomic density n_{at}, is known as the *stopping power* : S_{col}, [see for instance 60, p.4, eq(2.1)]. Roughly speaking, for fast electrons, this energy is lost by knocking atomic electrons off their shells.

$$S_{\text{col}} \equiv \int_0^{\varepsilon/2} W n_{\text{at}} Z \frac{\mathrm{d}\sigma_{\not e}}{\mathrm{d}W} \mathrm{d}W \tag{2.71}$$

The product $n_{\text{at}}Z$ represents the density of atomic electrons of the medium and $\mathrm{d}\sigma_{\not e}/\mathrm{d}W$ is the cross section corresponding to a loss of kinetic energy W. The integration goes up to half of the initial kinetic energy due to the indistinguishability of the two electrons emerging from a collision. The convention is to identify the electron possessing the higher kinetic energy as the original one. The equation (2.71) can be conveniently separated into large and small energy losses. When the energy lost by the fast electron is appreciably higher than the shell electron's atomic binding energy, as in light atoms and non-core orbitals, the collision can be described by Møller scattering between two free electrons (see part II section 8.5.5 eq. 8.148).

Smaller losses on the other hand are incorporated via the Bethe theory [67] (reminded in 11.5.1) which introduces a mean excitation energy [427, p.333, eq(4.62)] I_0 (11.96) given in table 2.3. Then, the stopping power adopts its well-known formula in the high-energy approximation [66, p.254]:

$$S_{\text{col}} = Z N_{\text{at}} \frac{2\pi r_e^2 mc^2}{\beta^2} \left[\ln\left(\frac{\varepsilon^2(\gamma+1)}{I_0^2} \right) + \frac{1}{\gamma^2}\left(1 + \frac{(\gamma-1)^2}{8} \right) - \left(1 - \frac{1}{\gamma^2} - \frac{2}{\gamma} \right) \ln 2 - \delta \right] \tag{2.72}$$

The classical electron radius is defined as $r_e \equiv e^2/4\pi\epsilon_0 mc^2$. The additional correction δ is called density effect [60, p.5] due to the medium polarisation and is actually negligible in gases for electrons up to 40 MeV, as can be seen in tables 12.3 and 12.4 in Berger *et al.* [60].

Gas	N_2	O_2	Air
I_0 (eV)	82	95	85.7

Table 2.3: Mean ionisation energy loss I_0 in the stopping power (2.72) for different gases.

For less fast (but not slow) electrons, the energy loss rate can be calculated in more detail by distinguishing each inelastic collision involved in a gas of n_{gas} number density. During a period Δt longer than the inter-collision mean time $\bar{\tau} = 1/n_{\text{gas}}\sigma \mathrm{v}$, the overall energy lost in inelastic processes with cross sections σ_i and thresholds $\Delta\varepsilon_i$ can be idealised as a uniform loss rate:

$$\frac{\langle \Delta\varepsilon \rangle}{\Delta t} = \sum_i \frac{\Delta\varepsilon_i}{\bar{\tau}_i} = \mathbf{F}_{\text{D}} \cdot \mathbf{v} \tag{2.73}$$

$\Delta t/\bar{\tau}_i$ gives the average number of collisions of type i during Δt. We introduced the notion of *dynamic friction force* $\mathbf{F}_{\text{D}}$ for which a vast terminology of equivalent terms exists: "drag", "slowing-down", "dynamic friction", "braking" force were used in different studies for the same concept. If one assumes that the friction F_{D} is antiparallel to the speed v, then its norm is:

$$F_{\text{D}} = \sum_i \frac{\Delta\varepsilon_i}{\bar{\tau}_i \mathrm{v}} = \sum_i \Delta\varepsilon_i \sigma_i \ . \tag{2.74}$$

Alternatively, the concept of an average drag force could also be defined according to the rate of momentum change $\Delta\mathbf{p} = \mathbf{p}_+ - \mathbf{p}_-$:

$$\mathbf{F}_{\text{B}} \equiv \frac{\langle \Delta\mathbf{p} \rangle}{\Delta t} = -\sum_i (1 - \left\langle \frac{p_+}{p_-} \cos\theta \right\rangle_i) \frac{\mathbf{p}_-}{\bar{\tau}_i} \tag{2.75}$$

Here, the averaging $\langle \mathbf{p} \rangle$ over the momentum change must be understood as fixing $\mathbf{p}_-$, while varying $\mathbf{p}_+$ according to the scattering distribution $\mathrm{d}\sigma_i/\mathrm{d}\Omega$ of the collision process i. Assuming azimuthal symmetry, this implies averaging over the quantity $-(p_- - p_+\cos\theta)$: i.e. the parallel momentum loss. Away from excitation thresholds, one may neglect variation of p_+ with θ and thus perform averaging only on the cosine. Furthermore, under the high electron energy approximation $\varepsilon_- \gg \Delta\varepsilon_i$, one can additionally write:

$$\langle \cos\theta \rangle \frac{p_+}{p_-} = \langle \cos\theta \rangle \frac{\sqrt{\varepsilon_+^2 + 2mc^2\varepsilon_+}}{cp_-} \simeq \langle \cos\theta \rangle \left(1 - \frac{\Delta\varepsilon_i}{(\mathrm{v}p)_-} \right) . \tag{2.76}$$

Replacing back into (2.75), the average braking force would be :

$$\mathbf{F}_{\text{B}} \simeq -\sum_i n_{\text{gas}} \sigma_i (\mathrm{v}\mathbf{p})_- \left(1 - \langle \cos\theta \rangle_i \sqrt{1 - \frac{2\Delta\varepsilon_i}{(\mathrm{v}p)_-}} \right) \approxeq -\hat{\mathbf{v}} \sum_i n_{\text{gas}} \sigma_i \big((1 - \langle \cos\theta \rangle_i)(\mathrm{v}p)_- + \langle \cos\theta \rangle_i \Delta\varepsilon_i \big) \tag{2.77}$$

We now understand that the concept of dynamic friction is ill-defined unless the average deviation cosine $\langle\cos\theta\rangle_i \simeq 1$. Only then, do the definitions (2.77) and (2.73) coincide. Otherwise, in addition to the stopping power, the idealised friction force should also include the "scattering power" $(1-\langle\cos\theta\rangle)p/\bar{\tau}$. If the average deviation is null (isotropic) or negative (backscattering), the "scattering force" from (2.77) would be superior to the loss of the entire kinetic energy ε_- over the mean free path $\bar{\lambda}$. This expresses the fact that low-energy collisions can dominate electron kinematic conditions.

Furthermore, the incorporation of attachment collisions to the friction force poses another difficulty. An electron having attached, not only loses all of its kinetic energy but also becomes inactive. Nonetheless, in anticipation of swarm dynamics introduced in the next section, if we considered an electronic gas carrying a total momentum, the attachment collisions would remove, one at a time, momenta carried by individual electrons at the attachment frequency ν_{att}. If we know that an electron of initial kinetic energy ε will, on average, attach after having propagated a certain time $\bar{\tau}_{\text{att}}$, then we may conceive that it is braked by an "attachment force" at a rate of $\varepsilon/\bar{\tau}_{\text{att}}(\varepsilon)$.

The concept of force as an additive vector that represents a change of momentum per unit time is undeniably very hard to reconcile with the stochastic occurrence of collisions. Nevertheless, when collisions are modelled as an average friction or braking force, they enable a dialectical debate on which of the electric or frictional force takes over on average. This was used to determine a criteria for electron runaway: electrons which, on average, are more accelerated by the electric field than braked through collisions.

A. For **relativistic** runaway, scattering in the high-energy domain is characterised by small relative energy losses and small angular diffusion. This enables a sound comparison between the stopping power and electric force as represented for instance in Gurevich *et al.* [365, figure 1] or Lehtinen *et al.* [576, figure 1] and used in subsequent works [40, 236].

Recently, Lehtinen and Østgaard [579, p.6950:§C1] introduced a new notion of "effective friction force" F_{eff} which does not operate on the average level of a single electron, but on the average angular equilibrium distribution of an electron swarm. This effective friction balances an imaginary mono-energetic electron swarm distribution maintained in equilibrium at a certain momentum p by a fixed electric field E_{eq} [579, Appendix C]:

$$F_{\text{eff}} \equiv eE_{\text{eq}} \quad : \quad \frac{\mathrm{d}p}{\mathrm{d}t} = 0 = eE_{\text{eq}}M(p,E) - |F_{\text{D}}|\,, \tag{2.78}$$

$$\text{where } M(p,E) = \frac{1}{\tanh(\xi)} - \frac{1}{\xi} \quad \text{with } \xi = \frac{2eE}{\nu_{\text{m}}p}\,. \tag{2.79}$$

$M(p,E)$ is the average cosine deviation of the electron swarm with respect to the opposite direction of the electric field and $\nu_{\text{m}} = \sigma_{\text{m}}\text{v}n_{\text{gas}}$ is the momentum-transfer collision frequency. The quantity $\nu_{\text{m}}p$ is called the parallel momentum loss rate from elastic collisions.

B. When interested in **thermal** runaway, the collisional term in kinetic equations at high-energies [788, p.6-eq(7)] qualified as a drag force, was extended to much lower energies and used for illustrative purposes in Bakhov *et al.* [50] and Dwyer *et al.* [250, figure 1] to represent the barrier imposed by collisions to electron acceleration. Later, Moss *et al.* [677, eq(1)-figure 2] plotted the dynamic friction in the full energy range down to below 1 eV. Nevertheless, it was pointed out in Diniz *et al.* [218], that thermal runaway cannot be properly viewed in this picture due to several issues, notably the scattering power which plays a major role below several tens of eV, and the highly stochastic process of collisions.

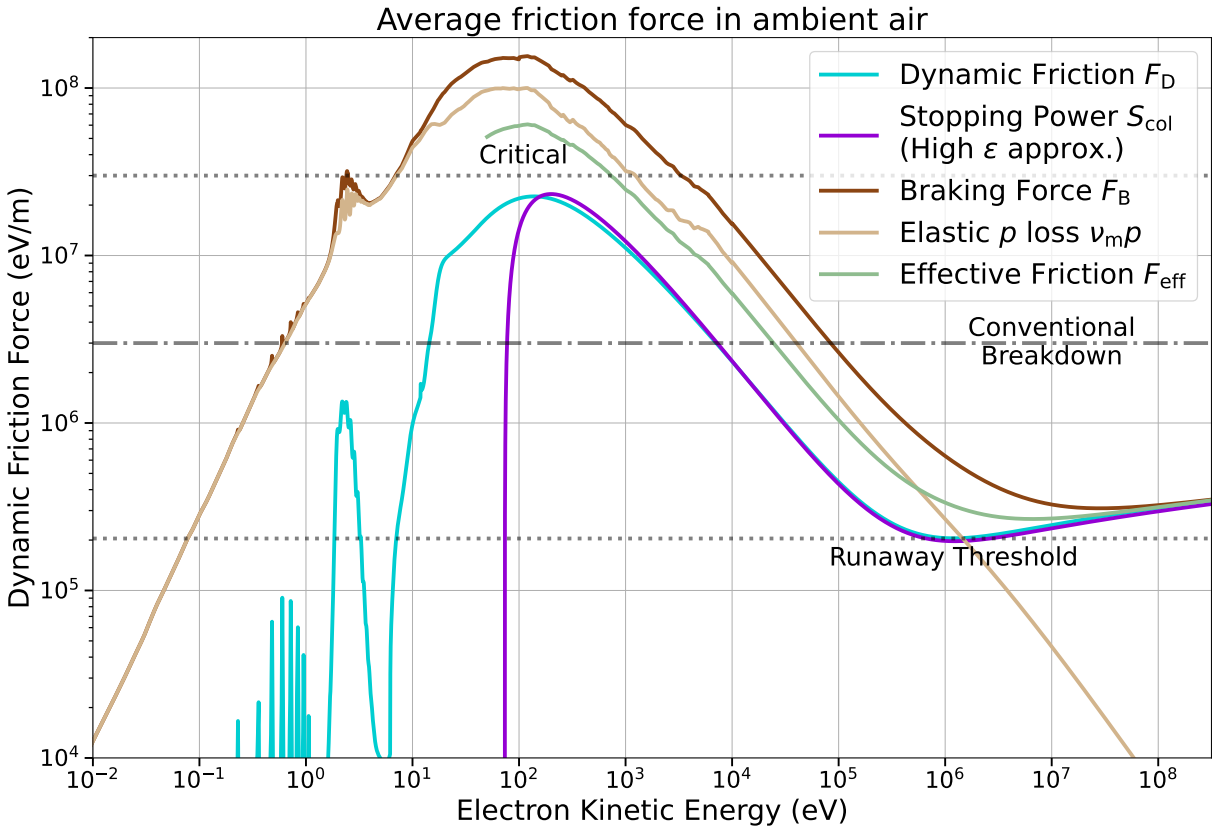

Figure 2.15: Different concepts underlying the same idea of representing the effect of electron-molecule collisions through a "force".

Putting things together, we take the liberty of distinguishing five "collisional force" concepts, which we represent in figure 2.15 for electrons in standard air (see page 40):

* F_D : "dynamic friction" force from its definition (2.73) which coincides with (2.77) when $\langle\cos\theta\rangle \simeq 1$;
* S_{col} : "stopping power" in the high-energy approximation (2.72) of F_D;
* $\nu_m p$: "elastic (parallel) momentum loss" is the amount of momentum lost in elastic collisions from the average deviation incurred in a scattering event through $\langle\cos\theta\rangle$;
* F_{eff} : "effective friction" from Lehtinen and Østgaard [579, p.6950:§C1] (2.78). It represents the effective friction which balances an electron swarm distribution in (angular dispersion) equilibrium at a certain energy and a fixed electric field.
* F_B : "braking force" or occasionally called "scattering force" from (2.75–2.76). It approximately amounts to the dynamic friction plus the elastic momentum loss: $F_B \cong F_D + p\nu_m$. It is nonetheless slightly higher as it includes attachment losses $\varepsilon_-/\bar{\tau}_{att}$ and accounts for additional momentum loss in inelastic collisions from the deviation through the average cosine $\langle\cos\theta\rangle$. At non-relativistic energies, this force is significantly "stronger" than the dynamic friction, following the semantic intuition that "braking" is more drastic than "friction";

These concepts will be useful when we try (later in sec. 5.3) to determine the runaway energy threshold of fast electrons according to the electric field.

For more information about average frictions and scattering at high energies, an overview of fast electron and photon interactions with gas atoms and molecules for Monte Carlo codes can be found in Salvat and Fernández-Varea [802]. In the next subsection, we study furthermore the balance of electron energy between two collisions.

Average energy loss

Another way to preserve the idea of comparing electric acceleration to the average effect of collision on electron propagation is to abandon the perspective of forces and shift toward the more tangible concept of energy gains between collisions contrasted with energy losses in a single collision event. Not only does this approach place us in the continuity of the whole material covered in the last section, but it also enables a more pertinent comparison in the regimes where a collision is threateningly capable of erasing the entire efforts of electric pull during electron free flight.

Electron trajectories in uniform fields between collisions can be seen as mean free path $\bar{\lambda}$-long parabola segments. The energy gain $\Delta^+\varepsilon$ between two collisions of an electron with an arbitrary initial velocity $\mathbf{v}_0$, accelerated in a uniform field $\mathbf{E}$ is (less than $+eE\bar{\lambda}$ and greater than $-eE\bar{\lambda}$):

$$\Delta^+\varepsilon = \int_0^{\bar{\lambda}} -e\mathbf{E}\cdot\mathrm{d}\mathbf{x} \lessgtr \pm eE\bar{\lambda}\,, \tag{2.80a}$$

$$= \int_0^{\bar{\tau}} -e\mathbf{E}\cdot\mathbf{v}\,\mathrm{d}t = \left(-e\mathbf{E}\cdot\mathbf{v}_0\bar{\tau} + \frac{(eE)^2}{m}\frac{\bar{\tau}^2}{2}\right). \tag{2.80b}$$

The infinitesimal segment $\mathrm{d}\mathbf{x} = \mathbf{v}\,\mathrm{d}t$ follows the electron's displacement. The mean distance $\bar{\lambda}$ or equivalently the mean duration $\bar{\tau}$ between collisions are bound by the curvilinear integral of the electron's free motion:

$$\bar{\lambda} \equiv \int_0^{\bar{\tau}} \|\mathbf{v}\|\,\mathrm{d}t \tag{2.81}$$

$$\begin{aligned}
\bar{\lambda} &= \int_0^{\bar{\tau}} \Big\|\mathbf{v}_0 - \overbrace{\frac{e\mathbf{E}}{m}}^{\equiv\mathbf{a}} t\Big\|\,\mathrm{d}t = \int_0^{\bar{\tau}} \sqrt{\mathrm{v}_0^2 - 2\cos\chi\frac{eE}{m}\mathrm{v}_0 t + \left(\frac{eEt}{m}\right)^2}\,\mathrm{d}t\,, \\
\bar{\lambda} &= \frac{1}{2a}\left[(a\bar{\tau} - \mathrm{v}_0\cos\chi)\|\mathbf{v}_0 + \mathbf{a}\bar{\tau}\| + \mathrm{v}_0^2\cos\chi + \mathrm{v}_0^2\sin^2\chi\ln\left(\frac{(a\bar{\tau} - \mathrm{v}_0\cos\chi) + \|\mathbf{v}_0 + \mathbf{a}\bar{\tau}\|}{\mathrm{v}_0(1-\cos\chi)}\right)\right].
\end{aligned} \tag{2.81a}$$

where we defined the electron acceleration from the electric pull $\mathbf{a} = -e\mathbf{E}/m$ and the angle $\cos\chi = \hat{\mathbf{v}}_0\cdot\hat{\mathbf{E}}$. When the electron's initial velocity is (anti-)aligned with the electric field $(-)\mathbf{v}_0 \parallel \mathbf{E}$, replacing $\cos\chi = \mp 1$ in (2.81a), we get an equivalence with (2.80).

The mean distance and times between collisions are formally defined as the path length or time for which on average one collision should occur throughout the integral of the trajectory:

$$\int_0^{\bar{\tau}} n_{\mathrm{air}}\sigma_{\mathrm{tot}}(\varepsilon(t))\mathrm{v}\,\mathrm{d}t = 1\,. \tag{2.82}$$

The *total* collisional cross section σ_{tot} depends on the energy ε which varies along the path. In absence of an electric field, the velocity v is a constant of motion, in which case we would obtain the trivial relations:

$$\bar{\tau}n_{\mathrm{air}}\sigma_{\mathrm{tot}}\mathrm{v} = \bar{\tau}\nu_{\mathrm{tot}} = \bar{\tau}\mathrm{v}\bar{\lambda} = 1\,, \tag{2.83}$$

which are those of the mean free path and time introduced earlier (2.67–2.68).

Due to the anisotropicity introduced by the presence of the electric fields, it follows that $\bar{\lambda}$ (and $\bar{\tau}$) actually depend on the initial condition $\mathbf{v}_0$ of the electron and thus differ from the mean free path and time. Nevertheless, for a dense enough gas, the electron's energy should not vary much during a mean free flight.

To measure this effect, we refer to the very useful notion of *reduced* electric field : $\mathbf{E}/n_{\text{air}}$. Indeed (2.80) implies that the average gain $\Delta^+\varepsilon \propto E\bar{\lambda}$ while (2.82) expects that $\bar{\lambda} \propto 1/n_{\text{air}}$ so that $\mathbf{E}/n_{\text{air}}$ becomes a scalable measure of the average acceleration of electrons in gases. The unit of the reduced electric field is the Townsend $\text{Td} \equiv 10^{-21}\ \text{Vm}^2$.

When E/n_{air} becomes high, the mean distance $\bar{\lambda}$ might either be slightly extended or shortened depending on the behaviour of $\sigma_{\text{tot}}(\varepsilon)$ as a function of the electron energy ε. We can analyse this effect by taking the first order linear dependence defining σ'_{tot} as the slope: $\sigma_{\text{tot}}(\varepsilon_0 + \Delta\varepsilon) = \sigma_{\text{tot}}(\varepsilon_0) + \sigma'_{\text{tot}}(\varepsilon_0)\Delta\varepsilon + o(\Delta\varepsilon)$. Replacing this cross section and the instant velocity $\text{v} = \|\mathbf{v}_0 - e\mathbf{E}t/m\|$ in the equation (2.82) for the mean duration between collisions, we obtain a typical integral encountered in multidimensional motion paths :

$$\int_0^{\bar{\tau}} n_{\text{air}} \overbrace{\left[\sigma_{\text{tot}} + \sigma'_{\text{tot}}\left(-e\mathbf{E}\cdot\mathbf{v}_0 t + \frac{(eEt)^2}{2m}\right)\right]}^{\simeq\sigma_{\text{tot}}(\varepsilon)} \overbrace{\sqrt{\text{v}_0^2 - 2\frac{e\mathbf{E}}{m}\cdot\mathbf{v}_0 t + \left(\frac{eEt}{m}\right)^2}}^{=\text{v}} \,\text{d}t = 1\,. \tag{2.84}$$

$$\begin{aligned}
\Leftrightarrow 1 &= n_{\text{gas}}\sigma_{\text{tot}}\bar{\lambda} + n_{\text{gas}}\frac{\sigma'_{\text{tot}}\varepsilon_0}{8a}\left[\|\mathbf{v}_0 + \mathbf{a}\bar{\tau}\|(a\bar{\tau} - \text{v}_0\cos\chi)\left(1 - 3\cos^2\chi + 2\frac{a\bar{\tau}}{\text{v}_0}\left(\frac{a\bar{\tau}}{\text{v}_0} + 2\cos\chi\right)\right)\right.\\
&\qquad \left. + \text{v}_0^2\cos\chi(1 - 3\cos^2\chi) + \text{v}_0^2\sin^2\chi\frac{(1 + 3\cos^2\chi)}{2}\ln\left(\frac{\|\mathbf{v}_0 + \mathbf{a}\bar{\tau}\| + \text{v}_0\cos\chi - a\bar{\tau}}{\|\mathbf{v}_0 + \mathbf{a}\bar{\tau}\| - \text{v}_0\cos\chi + a\bar{\tau}}\tan^2\frac{\chi}{2}\right)\right]\\
&= n_{\text{gas}}\left(\sigma_{\text{tot}} - \frac{(1 + 3\cos^2\chi)}{8}\sigma'_{\text{tot}}\varepsilon_0\right)\bar{\lambda}\\
&\qquad + n_{\text{gas}}\frac{\sigma'_{\text{tot}}\varepsilon_0}{8a}\left[\|\mathbf{v}_0 + \mathbf{a}\bar{\tau}\|(a\bar{\tau} - \text{v}_0\cos\chi)\left(\frac{3}{2}\sin^2\chi + 2\frac{a\bar{\tau}}{\text{v}_0}\left(\frac{a\bar{\tau}}{\text{v}_0} + 2\cos\chi\right)\right)\right.\\
&\qquad\qquad \left. + \text{v}_0^2\cos\chi\frac{3}{2}\sin^2\chi + \text{v}_0^2\sin^2\chi\frac{(1 + 3\cos^2\chi)}{2}\ln\left(\frac{\|\mathbf{v}_0 + \mathbf{a}\bar{\tau}\| + \text{v}_0\cos\chi - a\bar{\tau}}{\text{v}_0(1 + \cos\chi)}\right)\right]\,.
\end{aligned} \tag{2.85}$$

This last equation represents the implicit definition of the mean duration $\bar{\tau}$ and distance $\bar{\lambda}$. If the cross section may be assumed locally constant around ε_0: i.e. $\sigma'_{\text{tot}} \simeq 0$, then the mean distance between collisions equals the mean free path $\bar{\lambda} = 1/(n_{\text{air}}\sigma_{\text{tot}})$. The mean duration $\bar{\tau}$, however, still depends slightly on the electron's parabolic trajectory through the implicit equation (2.81a). The dependence of the cross section on the electron's energy, further complicates the determination of the mean inter-collision parameters. Although one could try to solve (2.85) to determine $\bar{\tau}$, this dreadful task can be circumvented in practice with a stochastic sampling of the collision event known as the "null collision method" [538] presented in chapter 3 about numerical algorithms.

Putting aside the issue of representing the average motion of a single electron, we now switch to the task of representing the average motion of a great ensemble of electrons where statistical averaging enables us to ascribe collective characteristics.

2.3 Swarm Dynamics

When considering a large ensemble of electrons, the motion of each individual electron becomes less relevant than the collective behaviour of the swarm as a whole. This section describes three different perspectives for modelling an electron swarm which are ordered in increasing abstraction coarseness of the properties pertaining to individual electrons.

2.3.1 Super-particles

The number of physical electrons in a patch of plasma exceeds by far the storage capabilities in a simulation. A one-to-one correspondence between a physical and a simulated electron is unrealisable. Therefore, one needs to devise some kind of agglomerating scheme for the representation of a very large number of particles. The philosophy of a Monte Carlo code is not to represent each single physical particle but a sample of their population which would accurately reflect their statistical properties.

For instance, to sample a real swarm of 10^{12} electrons, one can simply select and simulate 100 000 and attribute to each of them a statistical weight of $w = 10^7$. Each simulated electron represents a number w of actual electrons. To distinguish between both, one calls an electron in the simulation a "super-electron".

We define therefrom the following quantities:

- N_e : the actual number of physically represented electrons, or "real" electrons,
- N_s : the number of sampled electrons or "super"-electrons featuring in the swarm simulation,
- w_n : the statistical weight of the n^{th} super-electron.

They are bound by a conservation law:

$$N_\mathrm{e} \equiv \sum_{n=1}^{N_\mathrm{s}} w_n \ . \tag{2.86}$$

We can furthermore keep track of some average quantities of the swarm such as:

Average kinetic energy
$$\bar{\varepsilon} \equiv \frac{1}{N_\mathrm{e}} \sum_{n=1}^{N_\mathrm{s}} w_n \varepsilon_n \ , \tag{2.87}$$

Centre of mass
$$\bar{\mathbf{r}} \equiv \frac{1}{N_\mathrm{e}} \sum_{n=1}^{N_\mathrm{s}} w_n \mathbf{r}_n \ , \tag{2.88}$$

Spatial spread variance
$$\overline{\mathbf{r}^{②}} - (\bar{\mathbf{r}})^{②} = \frac{1}{N_\mathrm{e}} \sum_{n=1}^{N_\mathrm{s}} w_n (\mathbf{r}_n - \bar{\mathbf{r}})^{②} \tag{2.89}$$

Flux velocity
$$\bar{\mathbf{v}} \equiv \frac{1}{N_\mathrm{e}} \sum_{n=1}^{N_\mathrm{s}} w_n \mathbf{v}_n \ . \tag{2.90}$$

Position-velocity correlation
$$\overline{\mathbf{r} \otimes \mathbf{v}} \equiv \frac{1}{N_\mathrm{e}} \sum_{n=1}^{N_\mathrm{s}} w_n \mathbf{r}_n \otimes \mathbf{v}_n \ . \tag{2.91}$$

The dyadic (or outer) product between two vectors $\mathbf{u} = (u_x, u_y, u_z)$ and $\mathbf{q} = (q_x, q_y, q_z)$ produces a (3×3) matrix:

$$\mathbf{u} \otimes \mathbf{q} = \begin{pmatrix} u_x q_x & u_x q_y & u_x q_z \\ u_y q_x & u_y q_y & u_y q_z \\ u_z q_x & u_z q_y & u_z q_z \end{pmatrix} . \tag{2.92}$$

From there, we took the liberty in (2.89) of inaugurating the shorthand notation $\mathbf{u}^{⊗2} \equiv \mathbf{u} \otimes \mathbf{u}$, which is probably the most understandably natural way to abridge that expression.

As we will see later in section 3.3.3:

- from the linear variables $\bar{\mathbf{r}}$ (2.88) and $\bar{\mathbf{v}}$ (2.90), one can estimate the bulk and flux drift velocity (and mobility) of the swarm;
- from quadratic variables $\overline{\mathbf{r}^{⊗2}}$ (2.89) and $\overline{\mathbf{r} \otimes \mathbf{v}}$ (2.91), one can estimate bulk and flux diffusion tensors respectively.

Then, from the collision rates $\nu_c(\varepsilon_n)$ of each electron n, one can estimate the average reaction rate $\bar{\nu}_c$ of the swarm on a specific process c whose cross section is σ_c:

$$\bar{\nu}_c = \frac{1}{N_\mathrm{e}} \sum_{n=1}^{N_\mathrm{s}} w_n \overbrace{n_\mathrm{gas} \sigma_c(\varepsilon_n) \mathrm{v}_n}^{\equiv \nu_c(\varepsilon_n)} . \tag{2.93}$$

The growth, avalanche or net multiplication rate $\bar{\nu}_\mathrm{e}$ of the swarm is given by the balance between the ionisation ν_i and attachment ν_a rates:

$$\bar{\nu}_\mathrm{e} \equiv \bar{\nu}_\mathrm{i} - \bar{\nu}_\mathrm{a} = \frac{n_\mathrm{gas}}{N_\mathrm{e}} \sum_{n=1}^{N_\mathrm{s}} w_n \mathrm{v}_n (\sigma_\mathrm{i}(\varepsilon_n) - \sigma_\mathrm{a}(\varepsilon_n)) . \tag{2.94}$$

At a time $t = 0$ with a total real number $N_{\mathrm{e},0}$, one can therefore expect the swarm to grow instantaneously as:

$$N_\mathrm{e}(t) \simeq N_{\mathrm{e},0} \mathrm{e}^{\bar{\nu}_\mathrm{e} t} , \tag{2.95}$$

not to be confused with the growth rate of the super-electrons, of rather numerical interest:

$$\bar{\nu}_\mathrm{s} = \frac{n_\mathrm{gas}}{N_\mathrm{s}} \sum_{n=1}^{N_\mathrm{s}} \cancel{w_n} \mathrm{v}_n (\sigma_\mathrm{i}(\varepsilon_n) - \sigma_\mathrm{a}(\varepsilon_n)) , \tag{2.96}$$

where we highlighted the difference with (2.94) which consists in disregarding the super-electron weight w_n. When unconstrained, the number of super-electrons electrons is similarly expected to grow as $N_\mathrm{s}(t) \simeq N_{\mathrm{s},0} \exp(t\bar{\nu}_\mathrm{s})$, an issue to be kept in mind and which we will tackle in the next chapter 3.

In addition to the instantaneous average position moments $\bar{\mathbf{r}}$ and $\overline{\mathbf{r}^{⊗2}}$, one can also calculate their time derivatives from (2.88) and (2.89). One must however be extra cautious of the fact that the total $N_\mathrm{e}(t)$ also increases (2.94) and the complication posed by the statistical weights $w_n(t)$ and super-electron $N_\mathrm{s}(t)$ number which also vary with time. The overall effect is:

$$\frac{\mathrm{d}\bar{\mathbf{r}}}{\mathrm{d}t} = \frac{1}{N_\mathrm{e}} \sum_{n=1}^{N_\mathrm{s}} \overbrace{\frac{\mathrm{d}\mathbf{r}_n}{\mathrm{d}t}}^{\mathbf{v}_n} w_n + \frac{\mathrm{d}N_\mathrm{s}}{\mathrm{d}t} \sum_{i>N_\mathrm{s}} \frac{\mathbf{r}_i t w_i}{N_\mathrm{e}} + \frac{1}{N_\mathrm{e}} \sum_{n=1}^{N_\mathrm{s}} \mathbf{r}_n \overbrace{\frac{\mathrm{d}w_n}{\mathrm{d}t}}^{?} - \overbrace{\frac{\mathrm{d}\ln N_\mathrm{e}}{\mathrm{d}t}}^{\bar{\nu}_\mathrm{e}} \frac{1}{N_\mathrm{e}} \sum_{n=1}^{N_\mathrm{s}} \mathbf{r}_n w_n = \bar{\mathbf{v}} + \overline{\nu_\mathrm{e} \mathbf{r}} - \bar{\nu}_\mathrm{e} \bar{\mathbf{r}} . \tag{2.97}$$

One must somehow include both $\mathrm{d}w_n/\mathrm{d}t$ and the contribution of $\mathrm{d}N_\mathrm{s}/\mathrm{d}t$ to the sum. Separately, they cannot be known until one decides how to manage the number of super-electrons N_s which is the theme of subsection 3.3.2. Nevertheless, together, they must equal the combined production-rate-and-position overall correlation ($\overline{\nu_\mathrm{e} \mathbf{r}}$) of the newly generated electrons.

In particular if we decide to maintain N_s constant (we are free to do so), then $\mathrm{d}N_\mathrm{s}/\,\mathrm{d}t = 0$ and we may calculate the derivative of w_n in the following way:

$$\frac{\mathrm{d}w_n(t)}{\mathrm{d}t} = \nu_\mathrm{e}(\varepsilon_n)w_n \,. \tag{2.98}$$

In physical terms, we are considering a number of w_n (real) electrons all at the same energy ε_n and same position $\mathbf{r}_n$. We wish to calculate how many new electrons (of any energy) emerge at the position $\mathbf{r}_n$. This is given by the growth rate of one (super-)electron $\nu_\mathrm{e}(\varepsilon_n) = \nu_\mathrm{i}(\varepsilon_n) - \nu_\mathrm{a}(\varepsilon_n)$ multiplied by w_n (because there are w_n real electrons that have collided and spawned new electrons). As a result, we obtain that the derivative of the centre of mass with time – the bulk drift – is not exactly the flux velocity $\bar{\mathbf{v}}$ because of the variable number N_e of electrons in the swarm. This is anticipates the discussion in subsection 2.3.3 about bulk and flux coefficients, whose numerical calculation is assigned to section 3.3.3.

As rendered evident here, the methodology of super-particles is very handy and requires no special effort for estimating a swarm's properties. Nevertheless, its accuracy is limited by the allocated number N_s of super-electrons and their representativeness w_n. The average quantities introduced here must not be understood as the exact properties of the electron swarm, but as estimates thereof. In statistical terms, $\bar{a}$ is a sample from a random variable whose real average $\dot{a}$ is unknown. However, if we can assume that the samples $\bar{a}_k$ are *independent* from each other, then their distribution obeys the central limit theorem. Therefrom, we may constrain $\dot{a}$ into a confidence interval through an average value $\langle a \rangle$ over many N_m ("m" for "measurement") such samples $\bar{a}_k$:

$$\langle a \rangle = \frac{1}{N_\mathrm{m}} \sum_{k=1}^{N_\mathrm{m}} \bar{a}_k \,. \tag{2.99}$$

The precision of $\langle a \rangle$ is deteriorated by three aspects:

▷ Quality : First, if the sampling of the *super-electrons* in $\bar{a}$ is very uneven, meaning that there is a large disparity in the statistical weights w_n, the accuracy of the average swarm properties is reduced since there is a smaller number of super-electrons (in a sample $\bar{a}_k$) whose weight w_n is significant. There are two ways to improve the quality of a sample $\bar{a}_k$:

  i. set all weights $w_n = N_\mathrm{e}/N_\mathrm{s}$ equal: but this disables the possibility of enhancing electron statistics in specific regions of the spectrum;

  ii. increase the number of super-electrons N_s featuring in a sample (i.e. in the swarm); and thus we shall do.

◁ Quantity : Second, the *size* N_m of the sample limits the precision one can attain for $\langle a \rangle$. The *standard error* $\tilde{a}$ on $\langle a \rangle$ scales as:

$$\tilde{a} \simeq \frac{s_a}{\sqrt{N_\mathrm{m}}} \,, \tag{2.100}$$

which depends on the standard deviation s_a of the variable a, itself estimated as:

$$s_a^2 = \mathrm{var}[a] \simeq \frac{1}{N_\mathrm{m} - 1} \sum_{k=1}^{N_\mathrm{m}} (\bar{a}_k - \langle a \rangle)^2 \,. \tag{2.101}$$

The notation $\mathrm{var}[a]$ signifies the variance of the quantity a. For the readers curiously peeping at the $(N_\mathrm{m} - 1)$ denominator, the answer to why "$\ldots/N$ is a biased whereas $\ldots/(N-1)$ is an unbiased estimator of the variance $\mathrm{var}[a]$" lies in Kendall [486, chapter 17].

▽ Correlation : Third, if the samples $\bar{a}_k$ are taken from the same simulation and that their *time interval* is too small, they cannot be rightfully considered as independent measurements. Having correlated samples does not only deteriorate the precision but it also blurs the estimate of the uncertainty because it obliterates* the assumptions of the central limit theorem.

In order to reduce the contamination from correlation, the sampling should be significantly less frequent than the "memory retention" time of the system, which depends on the reduced electric field $\mathbf{E}/n_{\text{gas}}$ in the gas. 1000 samples within 1 ps are not worth 1000 samples over 1 ns. One can strive against correlation either by:

(a) Performing multiple independent simulations,

(b) Sampling measurements of a same simulation at random times with a minimal time separation to be determined.

Taking the precautions mentioned above, if we admit that $\bar{a}$ is a sample from a distribution obeying a normal (Gaussian) of mean value $\dot{a}$ and variance $\dot{s}_a$, then we know from inference statistics [486, chapter 20] that:

$$\text{the random variable } \frac{\langle a\rangle - \dot{a}}{s_a/\sqrt{N_{\text{m}}}} \text{ follows Student's } t \text{ distribution of } N_{\text{m}}-1 \text{ degrees of freedom.}$$

This enables us to establish a confidence interval over the value of $\dot{a}$:

$$\dot{a} \in [\langle a\rangle - \tilde{a}p_{N_{\text{m}}-1}; \langle a\rangle + \tilde{a}p_{N_{\text{m}}-1}] \text{ with } 95\,\% \text{ of probability.}$$

The value $p_{N_{\text{m}}-1}$ represents the 97.5 % percentile† of Student's t distribution with $N_{\text{m}}-1$ degrees of freedom (N_{m} samples). The exact value of $p_{N_{\text{m}}-1}$ depends on N_{m} of course but its dependence weakens very fast as N_{m} increases. As an example:

$$\text{For } N_{\text{m}} \in [100; 1000000] : p_{N_{\text{m}}-1} \in [1.984; 1.96] \simeq 2\ .$$

Therefore, our confidence intervals will be based on the timeless "2σ" rule for normal distributions.

Dealing with super-particles is an easy task. However, if one craves a "clean" statistical characterisation of a swarm, lots of such super-particles are needed to sample the swarm distribution. When "lots" means "too many", one might change perspective and try to characterise the statistical distribution governing the swarm population directly instead of conjecturing it from samples thereof. Ironically, we might say that if one does not wish to mingle with statistical inference (as we have to with particle-based swarms), then one should 'embed' the statistics directly into the physical model from the start. This leads us to the next subsection.

*"oblitterare" – "erase the letters" in Latin. Its current use in English is, unfortunately, a forlorn euphemism.

†The correspondence between the confidence of 95 % and the 97.5 % percentile of the t distribution is a classic examination question in an undergraduate statistical course. It is because the interval is double-sided so that one combines the certainties that $\dot{a} \leq$ upper boundary and $\dot{a} \geq$ lower boundary, thus having to leave out 2.5 % on both sides.

2.3.2 Kinetic Equations

When the number N_e of physical electrons is very high, say $>10^6$, one could attempt to characterise the electron swarm as a continuous distribution in configuration $\mathbf{r}$ and velocity $\mathbf{v}$ space. Such description is known as the kinetic theory. Since our electrons are indistinguishable, we may define an:

$$\text{Electron distribution function in position-velocity space}: f(\mathbf{r},\mathbf{v};t)\,,$$

representing the number of electrons per unit volume in this 6-dimensional position-velocity space at a time t. Thus, $f(\mathbf{r},\mathbf{v};t)\,\mathrm{d}^3\mathbf{r}\,\mathrm{d}^3\mathbf{v}$ gives the overall number of electrons located within the infinitesimal volume $\mathrm{d}^3\mathbf{r}\,\mathrm{d}^3\mathbf{v}$.

In the most general case, the kinetic description of a plasma involves all the species (electrons, neutral molecules, ions) composing the plasma. Then, one ought to define also distributions f_α for the other species α (molecules and ions) present in the plasma. Nevertheless, we rewind to our assumptions exposed in section 2.1: namely, that the gas is static and homogeneous; i.e. the molecules do not budge and their population does not change. This model is a classic in plasma physics and is known as the *Lorentz gas* [816, chapter 6:p.134] in which:

I. $m \ll m_\alpha$: electron mass negligible compared to molecules and ions

II. $n_\mathrm{e} \ll n_\mathrm{gas}$: electron density much smaller than gas molecules density

In this idealisation, one needs to track the evolution of the electron distribution $f(\mathbf{r},\mathbf{v};t)$ in time which obeys a conservation law from the displacement of the electrons, due to their velocity and acceleration imposed by the electric field $\mathbf{E}$, and from their collisions with the molecules [378a, eq.(1)]:

$$\frac{\partial f}{\partial t} + \mathbf{v}\cdot(\nabla f) - \frac{e\mathbf{E}}{m}\cdot(\nabla_\mathbf{v} f) = C[f] \tag{2.102}$$

This equation is known as the *Boltzmann equation* (for a Lorentz electron gas) and constitutes the central part of the kinetic theory of plasmas. The crux of the Boltzmann equation lies in the collisional term $C[f]$ which regroups all the alterations incurred by the distribution f due to electron-molecule collisions. Depending on the assumptions and approximations taken on $C[f]$, the Boltzmann equation may take a variety of different names.

A. For instance, if one discards collisions altogether ($C[f] = 0$), (2.102) becomes the Vlasov equation [55, p.32:eq.(2.3)] which describes collision-less plasmas, afar from the situation in which our electrons in air lie.

B. Alternatively, one can include the effect of *binary collisions* between electrons and individual atoms and molecules. This is what we have been doing hitherto in section 2.2.2, where we distinguished various processes c (elastic, inelastic), each characterised by their differential cross section $\mathrm{d}\sigma_c/\mathrm{d}\Omega$. Remaining faithful to our previous assumptions, we neglect the relative motion of the gas molecules compared to electrons. The binary collision term C_b for electrons with still (motionless) molecules is [73, §21.2:p.593:eq.(2.12)]:

$$C_\mathrm{b}[f] = n_\mathrm{gas}\sum_c \left[\int \underbrace{\mathrm{v}'\frac{\mathrm{d}\sigma_c'}{\mathrm{d}\Omega}(\mathbf{v}'\to\mathbf{v})f(\mathbf{r},\mathbf{v}')}_{\text{entrance flux}}\,\mathrm{d}^3\mathbf{v}' - \int \underbrace{\mathrm{v}\frac{\mathrm{d}\sigma_c}{\mathrm{d}\Omega}(\mathbf{v}\to\mathbf{v}'')f(\mathbf{r},\mathbf{v})}_{\text{exit flux}}\,\mathrm{d}^3\mathbf{v}'' \right].$$

It is a balance of fluxes between the incoming electrons originating from various $\mathbf{v}'$ velocities and ending up in $\mathbf{v}$ through a collision, and the outgoing electrons which are exiting the $\mathbf{v}$ cell after colliding.

The binary collision term may be developed further for elastic scattering by assuming that electron velocity distributions are not correlated with the scattering distributions. Exploiting symmetry properties from the detailed balancing between direct and reverse scattering we have [73, §21.4:p.609:eq.(4.8)]:

$$C_{\mathrm{b,e}}[f] = n_{\mathrm{gas}} \int [f(\mathrm{r}, \mathbf{v}'; t) - f(\mathrm{r}, \mathbf{v}; t)] \mathrm{v} \frac{\mathrm{d}\sigma_{\mathrm{e}}}{\mathrm{d}\Omega} \, \mathrm{d}\Omega \, . \tag{2.103}$$

The same symmetry argument applied to inelastic scattering would involve the distribution of excited states j of molecules n_j so as to include direct $i \to j$ collisions but also reverse superelastic collisions from a state j to i (i.e. $[f(\mathbf{v}_j) n_j \, \mathrm{v}_i / \mathrm{v}_j - f(\mathbf{v}_i) n_i] \mathrm{v}_i \sigma_i$).

C. In weakly or partially ionised plasma, one should complement binary collisions with long-range Coulomb collisions of electrons among themselves or with ions.

First, one must define the Debye shielding λ_{D} as the limiting distance for Coulomb interactions between charged particles in a quasi-neutral plasma. That is, a charged particle only interacts with other (charged) particles that lie within a sphere of λ_{D} [73, p.8:eq.(2.3)]:

$$\lambda_{\mathrm{D}} = \sqrt{\frac{\epsilon_0 k_{\mathrm{B}} T}{n_{\mathrm{e}} e^2}} \, , \tag{2.104}$$

where ϵ_0 is the vacuum electric permittivity, k_{B} Boltzmann's constant, T_{e} the temperature of the plasma* (electrons in this case but not of the neutral gas $T_{\mathrm{e}} \neq T_{\mathrm{gas}}$) and n_{e} the electron density.

From the Debye length, one can retrieve the renowned Coulomb logarithm $\ln \Lambda_{\mathrm{c}}$ as [55, 816, chapter 1:p.12–4:eqs.(1.12–20), eq.(6.3.26)]:

$$\Lambda_{\mathrm{c}} \equiv \frac{\lambda_{\mathrm{D}}}{b_{\frac{\pi}{2}}} = \frac{4\pi\mu \langle \overleftrightarrow{\mathrm{v}}^2 \rangle \sqrt{\epsilon_0^3 k_{\mathrm{B}} T_{\mathrm{e}}}}{\sqrt{n_{\mathrm{e}}} e^3 z} \tag{2.105}$$

This term corresponds to the ratio between the Debye length λ_{D} and the impact parameter of Coulombic collisions whose deviation corresponds to an angle of 90° [55, 816, eq.(1.13), eq.(6.3.17)]. Its value depends on the properties of the colliding charged particles, through the reduced mass μ, the (square average of the) relative collision velocity $\langle \overleftrightarrow{\mathrm{v}}^2 \rangle$ and the charge number z. Therefore [73, p.585:eq.(8.14)]:

*For a non-Maxwellian electron distribution, which is always our case, one should interpret $k_{\mathrm{B}} T_{\mathrm{e}}$ as equalling two-thirds of the electrons' average kinetic energy as an *ad hoc* adjustment.

$$\text{For e-ion collisions } : \begin{cases} \mu \approx m \\ \langle \overleftrightarrow{\mathrm{v}} \rangle \approx \langle \mathrm{v} \rangle = \sqrt{\dfrac{8k_\mathrm{B}T_\mathrm{e}}{\pi m}} & \text{(ions are ~immobile)} \\ z = Z_\mathrm{i} & \text{(usually just 1)} \end{cases}$$

$$\text{For e-e- collisions } : \begin{cases} \mu = \dfrac{m}{2} \\ \langle \overleftrightarrow{\mathrm{v}} \rangle \approx \dfrac{3k_\mathrm{B}T_\mathrm{e}}{m/2} \\ z = 1 \end{cases}$$

for a Maxwellian electron distribution at a temperature of T_e. Most likely, the average ionisation degree Z_i of the ions (for weakly ionised plasma) is only $Z_\mathrm{i} \simeq 1$.

With the assumptions above, the momentum-transfer cross section between electrons and ions is defined with the Coulomb logarithm as [73, 590, §20.8:p.585:eq.(8.10–3), p.683:eq.(18.1.20)]:

$$\sigma_{\mathrm{m,i}} = 4\pi \left(\frac{Z_\mathrm{i} e^2}{4\pi\epsilon_0 m \mathrm{v}^2} \right)^2 \ln \Lambda_\mathrm{c} \,. \tag{2.106}$$

Consideration of long-range Coulomb collisions restricted to the Debye sphere leads to the Fokker-Planck collision term [55, 533, p.304:eq.(4), chapter 13.2:p.385:eq.(13.20)]:

$$C_\mathrm{c}[f] = -n_\mathrm{ion} \nabla_\mathbf{v} \cdot \left(f(\mathbf{r}, \mathbf{v}; t) \boldsymbol{\mathcal{V}} + \frac{n_\mathrm{ion}}{2} \nabla_\mathbf{v} (f(\mathbf{r}, \mathbf{v}; t) \underline{\boldsymbol{\mathcal{D}}}) \right) \,. \tag{2.107}$$

The vector $\boldsymbol{\mathcal{V}}$ represents an average velocity change per unit time from Coulomb collisions while the tensor $\underline{\boldsymbol{\mathcal{D}}}$ is a diffusion tensor (velocity rate change correlation per unit time). For electrons, both depend on the Coulomb logarithm $\ln \Lambda_\mathrm{c}$ (2.105) and the relative collision velocity $\overleftrightarrow{\mathbf{v}}$ as [73, p.615:eq.(5.15)]:

$$\boldsymbol{\mathcal{V}} = \frac{Z^2 e^4}{4\pi\epsilon_0} \frac{\ln \Lambda_\mathrm{c}}{m\mu \overleftrightarrow{\mathrm{v}}} \hat{\overleftrightarrow{\mathbf{v}}} \tag{2.108}$$

$$\underline{\boldsymbol{\mathcal{D}}} = \frac{Z^2 e^4}{4\pi\epsilon_0} \frac{1}{m^2 \overleftrightarrow{\mathrm{v}}} (\ln \Lambda_\mathrm{c} \delta_{ij} - (\ln(\Lambda_\mathrm{c}) - 1) \delta_{iz} \delta_{jz}) \tag{2.109}$$

The velocity change rate $\boldsymbol{\mathcal{V}}$ is aligned with the direction of the relative inter-particle collision velocity $\overleftrightarrow{\mathbf{v}}$. The diffusion tensor is expressed in the reference frame where the z axis is aligned with $\overleftrightarrow{\mathbf{v}}$.

Those approximations depend on an accurate knowledge of the electron distribution function f which ... is at the heart of our preoccupations. In other words, if no further approximations are made, Boltzmann's equation (2.102) is deterringly integro-differential.

Two-term approximation

The treatment of the Boltzmann equation (2.102) can be considerably simplified if one makes reasonable assumptions on the electron distribution $f(\mathbf{r}, \mathbf{v})$. Without any external electric field, the solution of the Boltzmann equation is well known to converge to a Maxwellian distribution in velocity space (see section B.1) and a gradually flattening distribution in configuration space

whose exact shape depends on the initial conditions [73, chapter 7]. In presence of an electric field, the Maxwell distribution should be deformed to reflect the anisotropy.

For a relatively "weak" electric field $\mathbf{E}$, the distribution can be approximated by a truncation of a Legendre expansion in the angle χ between the electron's velocity $\mathbf{v}$ and $\mathbf{E}$ (as sketched in 2.3)[73, 414, p.45:eq.(2.5), §21.4.1:eq.(4.1)]:

$$f(\mathbf{r},\mathbf{v};t) = \underbrace{P_0(\cos\chi)f_0(\mathbf{r},\mathrm{v};t) + P_1(\cos\chi)f_1(\mathbf{r},\mathrm{v};t)}_{\text{Two term approx.}} + P_2(\cos\chi)f_2(\mathbf{r},\mathrm{v};t) + \dots \tag{2.110}$$

Due to symmetry, the dependence in the azimuthal angle ϕ disappears. The restriction to the two first terms is known as the two-term approximation comprising:

- f_0 : the isotropic distribution component ($P_0 = 1$)
- $\cos\chi\, f_1$: the anisotropic perturbation ($P_1 = \cos\chi$)

Under this approximation, the various binary electron-neutral and Coulomb collision terms may be calculated by integrating over χ with the postulated simple angular distribution in velocities. Putting the terms together, we get two coupled equations governing the evolution of f_0 and f_1 after projecting (2.102) on P_0 and P_1 respectively and integrating over $\cos\chi$ and ϕ [590, p.682:eqs.(18.1.14&11)]:

$$\frac{\partial f_0}{\partial t} + \frac{\mathrm{v}}{3}\frac{\partial f_1}{\partial z} - \frac{eE}{m}\frac{1}{3\mathrm{v}^2}\frac{\partial(\mathrm{v}^2 f_1)}{\partial \mathrm{v}} = C_0^{\mathrm{en}} + C_0^{\mathrm{ei}} + C_0^{\mathrm{ee}} \tag{2.111a}$$

$$\frac{\partial f_1}{\partial t} + \mathrm{v}\frac{\partial f_0}{\partial z} - \frac{eE}{m}\frac{\partial f_0}{\partial \mathrm{v}} = C_1^{\mathrm{en}} + C_1^{\mathrm{ei}} + C_1^{\mathrm{ee}} \tag{2.111b}$$

The collision terms are now separated into electron collisions with neutral molecules (C^{en}), with ions (C^{ei}) and with other electrons (C^{ee}) [590, p.682–3:eqs.(18.1.11–23)]:

$$\text{Isotropic}: \begin{cases} \text{e-neutrals: } C_0^{\mathrm{en}} \\ \text{e-ions: } \quad C_0^{\mathrm{ei}} \end{cases} = \underbrace{\frac{m}{M_g}\frac{1}{\mathrm{v}^2}\frac{\partial}{\partial \mathrm{v}}\left[\mathrm{v}^3\nu_{\mathrm{m},g}\left(f_0 + \frac{eT_g}{m\mathrm{v}}\frac{\partial f_0}{\partial \mathrm{v}}\right)\right]}_{\text{Scattering}} - \underbrace{\sum_{c\in g}\left(\nu_c f_0 - \nu_c' f_0'\right)}_{\text{Inelastic collisions}} \tag{2.112a}$$

$$\text{inter-e}^-\text{: } \quad C_0^{\mathrm{ee}} = \sigma_{\mathrm{ee}}\mathrm{v}^2\frac{\partial}{\partial \mathrm{v}}\left[H(\mathrm{v})f_0 + \frac{\mathrm{v}}{3}G(\mathrm{v})\frac{\partial f_0}{\partial \mathrm{v}}\right] \tag{2.112b}$$

$$\text{Anisotropic}: \begin{cases} \text{e-neutrals}: C_1^{\mathrm{en}} \\ \text{e-ions}: \quad C_1^{\mathrm{ei}} \end{cases} = -\nu_{\mathrm{m},g} f_1 \quad \text{see comment in Huxley [414, p.47]} \tag{2.113a}$$

$$\text{inter-e}^-: \quad C_1^{\mathrm{ee}} = \dots \quad \text{see Hagelaar [376, eq.(19)]} \tag{2.113b}$$

In (2.112a), we use the shorthand $f_0' \equiv f_0(\mathbf{r},\mathrm{v}';t)$ at the velocity v' corresponding to the energy $\varepsilon' = \varepsilon + \Delta\mathcal{E}_c$ from the inelastic collision c with excitation threshold $\mathcal{E}_c$. The collision frequency ν_c' of superelastic collisions may be related to the inelastic process: $\nu c' = n_c \mathrm{v}'\sigma'_c(\mathrm{v}') = \nu_c\, n_c/n_g\, \mathrm{v}/\mathrm{v}'$, but requires the knowledge of the density of excited states n_c at the energy $\mathcal{E}_c$.

The electron collision terms with neutral molecules and ions have the same structure: the first term corresponds to the effect of scattering in elastic (and inelastic) collisions whereas the second term regroups the outgoing and incoming flux from inelastic collisions. If excited species were present, one would additionally have superelastic terms which would resemble (2.51).

The distinction between ions (g='i') and neutral (g='n') is conveyed in the parameters: mass M_g, momentum transfer rate $\nu_{\mathrm{m},g}$ and temperature T_g. The most important difference lies in the momentum transfer rate $\nu_{\mathrm{m},g}$ which is obtained from the density n_g of the particles (neutral or ion) and the momentum-transfer cross section:

$$\nu_{\mathrm{m},g} = n_g \mathrm{v} \sigma_{\mathrm{m},g} \tag{2.114}$$

The momentum transfer cross section between electrons and ions $\sigma_{\mathrm{m},i}$ has been given above in (2.106), whereas the one with neutrals is obtained from measurements or quantum calculations as treated in the second part chapter 11.1.

The electron-neutral/ion collision term for the anisotropic part $C_1^{\mathrm{en/i}}$ (2.113a) has a simpler form which depends on the momentum transfer rate ν_{m}. In principle, this should include also the momentum transferred due to inelastic collisions through the formally correct cross section (7.7). In practice, as commented by Huxley [414, p.(47)], momentum losses are predominantly due to elastic collisions so one usually calculates ν_{m} only from these.

Electron-electron interactions depend on the inter-electron momentum-transfer cross section σ_{ee} obtained also from (2.106) with the appropriate value for the Coulomb logarithm (2.105). The terms in the bracket of (2.112b) are known as the Rosenbluth *et al.* potentials given by [590, eqs.(18.1.22–3)]:

$$H(\mathrm{v}) = 4\pi \int_0^{\mathrm{v}} f_0(\mathbf{r}, \mathrm{v}'; t) \mathrm{v}'^2 \, \mathrm{d}\mathrm{v}' \,, \tag{2.115}$$

$$G(\mathrm{v}) = 4\pi \left(\frac{1}{\mathrm{v}^2} \int_0^{\mathrm{v}} f_0(\mathbf{r}, \mathrm{v}'; t) \mathrm{v}'^4 \, \mathrm{d}\mathrm{v}' + \mathrm{v} \int_{\mathrm{v}}^{\infty} f_0(\mathbf{r}, \mathrm{v}'; t) \mathrm{v}' \, \mathrm{d}\mathrm{v}' \right) , \tag{2.116}$$

which result from a more elaborate treatment [785] of the Fokker-Planck collision term given above in (2.107).

The inter-electron collision term C_1^{ee} for the anisotropic distribution part is a more cumbersome expression which is given in Hagelaar [376, eq.(19)] and references therein.

The relative importance of the isotropic and anisotropic collision terms in (2.112–2.113) depend on the densities of the colliding particles. Thus, one defines the degree of ionisation as the ratio between the densities of ions n_{ion} and the gas molecules n_{gas} (neutrals and ions alike) [816, p.394:eq.(12.6.4)]:

$$\zeta_{\mathrm{i}} \equiv \frac{n_{\mathrm{ion}}}{n_{\mathrm{gas}}} \,. \tag{2.117}$$

One can equivalently define a 'degree of ionisation' from the electron density n_{e}. However, because strong charge separations entail intense electric fields which tend to be quickly screened by the free electrons, the densities of ions n_{ion} and of electrons n_{e} are comparable in magnitude. Therefore, one often assumes the quasi-neutral approximation $n_{\mathrm{e}} \cong n_{\mathrm{ion}}$. This is why, the term 'degree of ionisation' is often used ambivalently to denote either $n_{\mathrm{e}}/n_{\mathrm{gas}}$ [e.g. 816, p.149:eq.(6.2.3)] or $n_{\mathrm{ion}}/n_{\mathrm{gas}}$ [816, p.394:eq.(12.6.4)].

Gases are considered to be *weakly* ionised when the degrees of ionisation are lower than $\zeta_{\mathrm{i}} < 10^{-6}$ [376, fig.3]. Still, in monatomic gases (noble gases in particular), Coulomb collisions are important at low electric fields because there are essentially no inelastic losses of electrons at low energies with neutral atoms (no rotational or vibrational excitations). Therefore, some authors consider that the limit $\zeta_{\mathrm{i}} < 10^{-8}$ defines *very weakly* ionised gases, where Coulomb collision bear no importance irrespective of the electric field [816, §6.2:eq.(6.2.7)].

Stationary Electron Energy Spectrum

Boltzmann's equation (2.102) expresses the evolution of a swarm in space and velocity distribution. As we know, electrons react very swiftly to changes in the electric field E and one might take a further step in simplification by separating the spatial and kinetic dependence of the distribution, that is [378a, eq.(8)]:

$$f_{0,1}(\mathbf{r},\mathrm{v};t) = \frac{1}{4\pi} f_{\mathrm{v}}^{0,1}(\mathrm{v};E/n_{\mathrm{gas}}) n_{\mathrm{e}}(\mathbf{r},t) \; . \tag{2.118}$$

The variation of the kinetic distribution f_{v} in space and time is implicit through the electric field $E(\mathbf{r},t)$. This implies that one disregards the relaxation of the kinetic distribution to a stationary shape f_{v} which depends only on the local reduced electric field E/n_{gas}. One only considers the non-stationary evolution of the swarm through its density n_{e} varying in space (drift and diffusion) and time (exponential growth).

The kinetic distribution is normalised so as to verify [378a, eq.(4)]:

$$\int_0^\infty f_0(\mathbf{r},\mathrm{v},t) 4\pi \mathrm{v}^2 \,\mathrm{d}\mathrm{v} = n_{\mathrm{e}}(\mathbf{r},t) \qquad \Rightarrow \int f_{\mathrm{v}}^0(\mathrm{v}) \mathrm{v}^2 \,\mathrm{d}\mathrm{v} = 1 \; . \tag{2.119}$$

Most of the time, instead of considering the kinetic distribution (in v), one prefers to work with the electron kinetic energy ε:

$$f_{\mathrm{v}}(\mathrm{v})\mathrm{v}^2 \,\mathrm{d}\mathrm{v} = f_{\mathrm{v}}(\mathrm{v}(\varepsilon))\varepsilon \frac{2}{m}\frac{\mathrm{d}\mathrm{v}}{\mathrm{d}\varepsilon}\,\mathrm{d}\varepsilon = \underbrace{f_{\mathrm{v}}(\mathrm{v}(\varepsilon))\frac{1}{2}\left(\frac{2}{m}\right)^{\frac{3}{2}}}_{\text{EEDF : } \equiv f_\varepsilon(\varepsilon)} \sqrt{\varepsilon}\,\mathrm{d}\varepsilon \; . \tag{2.120}$$

From there, one defines the electron energy distribution function (EEDF) $f_\varepsilon^0 \equiv f_\varepsilon$ which only refers to the isotropic part, so that the index '0' will be implicit in the notation. The ratio f_1/f_0 is known as the anisotropy. According to (2.119), the EEDF verifies the following normalisation:

$$\int f_{\mathrm{v}}^0(\mathrm{v})\mathrm{v}^2 \,\mathrm{d}\mathrm{v} = \int f_\varepsilon^0(\varepsilon)\sqrt{\varepsilon}\,\mathrm{d}\varepsilon = 1 \; . \tag{2.121}$$

Hence, the combined isotropic distribution function $f_0(\mathbf{r},\varepsilon,t)$ can be written as [378a, eq.(8)]:

$$f_0(\mathbf{r},\varepsilon,t) = \frac{2}{4\pi}\left(\frac{m}{2}\right)^{\frac{3}{2}} n_{\mathrm{e}}(\mathbf{r},t) f_\varepsilon^0(\varepsilon) \; . \tag{2.122}$$

In absence of electric fields, the stationary energy distribution of electrons in a gas or plasma at a temperature T_{gas} is the well-known Maxwellian which is reminded in appendix B.1 (B.13).

In presence of an electric field, the stationary distribution depends on the relative importance of electron-molecule and electron-electron collisions through the parameter [548, p.42:eq.(2.1.28)]:

$$\bar{\zeta} \equiv \int_0^\infty \frac{\overline{\Delta\mathcal{E}}}{\varepsilon}\frac{\sigma_{\mathrm{tot}}(\varepsilon)}{\sigma_{\mathrm{ee}}(\varepsilon)} f_\varepsilon(\varepsilon)\sqrt{\varepsilon}\,\mathrm{d}\varepsilon \; , \tag{2.123}$$

which compares the average energy loss $\overline{\Delta\mathcal{E}}$ in an electron-neutral collision of cross section σ_{tot} to the effect of electron-electron collisions through σ_{ee}. An EEDF f_ε must be assumed to estimate this parameter and can be taken roughly as a Maxwellian at the mean energy $\bar{\varepsilon}$ of the swarm.

There are essentially two analytical approximations to the EEDF in a weakly ionised plasma dominated by electron-neutral collisions:

Davydov. At moderate but not high electric fields $1\,\mathrm{Td} < E < 100\,\mathrm{Td}$, the electron-neutral collisions dominate and the distribution is in non-equilibrium. This is because the temperature of the gas T_{gas} is much lower than the average energy of electrons* and also because electrons practically do not exchange energy among themselves. In these conditions, the isotropic term f_0 is given by the Davydov distribution [548, p.44:eq.(2.1.35)]:

$$\tilde{f}_0(\varepsilon) = C \exp\left(- \int_0^{\varepsilon} \frac{\mathrm{d}\varepsilon'}{k_{\mathrm{B}} T_{\mathrm{gas}} + (2e^2/3\delta_\varepsilon m)(E^2/\nu_{\mathrm{tot}}(\varepsilon'))} \right) , \tag{2.124}$$

where C is just a normalising coefficient. The parameter δ_ε represents the average relative energy loss of an electron in a collision and depends on the gas composition. When the gas is monatomic, one can assume that most energy losses come from elastic collisions and thus that $\delta_\varepsilon = 2m/M$ from the relative energy loss in an elastic collision of isotropic scattering with M being the mass of a gas molecule (see eq.2.38 on p. 56 when $\langle \cos\theta \rangle = 0$).

Druyvesteyn. Most often, the temperature of the gas T_{gas} is negligible compared to the energy gained by electrons from the electric field between two collisions. Thus, one can neglect the $k_{\mathrm{B}} T_{\mathrm{gas}}$ term in (2.124). Additionally, if one takes the (horribly rough) approximation that the total cross section is constant $\sigma_{\mathrm{tot}}(\varepsilon) = \mathrm{cst.}$; then, the collision frequency is simply proportional to the velocity: $\nu_{\mathrm{tot}} \propto \sqrt{\varepsilon}$. Then, the integral in (2.124) can be calculated and one obtains the Druyvesteyn distribution [762, p.97:eq.(5.39)]:

$$\tilde{f}_0(\varepsilon) = C \exp\left(-3\delta_\varepsilon \frac{\varepsilon^2}{(eE\bar{\lambda})^2} \right) , \tag{2.125}$$

where $\bar{\lambda} = 1/n_{\mathrm{gas}}\sigma_{\mathrm{tot}}$ is the mean free path, so that $eE\bar{\lambda}$ is traditionally interpreted as the mean energy gained by electrons between two collisions (as discussed on p. 73). What is important to remember is that the tail of the Druyvesteyn distribution decreases faster $\sim \exp(-\varepsilon^2)$ than a typical Maxwellian $\sim \exp(-\varepsilon)$. This implies that there are relatively less high-energy electrons in non-equilibrium weakly ionised plasmas at moderate electric fields (than if they were thermalised at the temperature $T_{\mathrm{e}} = 2\bar{\varepsilon}/(3k_{\mathrm{B}})$ corresponding to their average kinetic energy).

In general, EEDF may not be expressed analytically, and must be either calculated from the two-term kinetic approximation or through Monte Carlo simulations as done presently. In section 3.3.1, we explain how we calculate the EEDF of our simulated electron swarms. The EEDF is the connection point between our simulations and the kinetic approach. From the EEDF and the set of collision cross sections of electrons with the gas molecules, one can, under the two-term approximation, calculate all other relevant transport coefficients (mobility, diffusion, growth rate) which are given in the next subsection 2.3.3. Thus, an agreement in EEDF between the kinetic and the super-particle approach is key to the validation of our model which we undertake in section 4.3.3.

The two term approximation (2.110) enables us to integrate Boltzmann's equation in velocity angular space and obtain (2.111). With the stationary spectrum (2.118), the velocity distribution of the swarm is known and "frozen". So one might leave it aside altogether and integrate the distribution over the velocity space and only treat the electron density in configuration space and track its evolution in time. This leads us to the next subsection.

*If that were not the case, then there would be a conflict with the assumption that the plasma is weakly ionised from the Boltzmann-Saha equation.

2.3.3 Fluid Equations

The kinetic approach to an electron swarm strives to describe the evolution of gas distribution both in configuration space and velocity. The fluid approach is obtained from Boltzmann's equation through the integration of the distribution in velocity space [234, §2.2] leaving the continuity equation for the density $n_\mathrm{e}(\mathbf{r},t)$ [587, eqs.(1–2)]:

$$\frac{\partial n_\mathrm{e}}{\partial t} - \nabla\cdot\left(n_\mathrm{e} \underbrace{\dot{\mu}_\mathrm{e}\mathbf{E}}_{\equiv-\dot{\mathbf{v}}} + \underline{\dot{D}}_\mathrm{e}\cdot\nabla n_\mathrm{e}\right) = S\ , \tag{2.126}$$

evolving according to a source term S and transport parameters: the electron mobility $\dot{\mu}_\mathrm{e}$ and diffusion tensor $\underline{\dot{D}}_\mathrm{e}$. The product of the mobility and the electric field defines an average flux velocity of the electron swarm:

$$\dot{\mathbf{v}} \equiv -\dot{\mu}_\mathrm{e}\mathbf{E}\ , \tag{2.127}$$

oriented opposite to the electric field in virtue of electrons' negative charge. One should note that this velocity is <u>not</u> the average drift velocity $\mathrm{v_d}$ at which the swarm progresses in the gas. This is because new electrons may emerge (or electrons may disappear) from the source (or sink) term S which is calculated from the balance between the production and destruction rate of electrons from ionisation and attachment respectively:

$$S = \iiint n_\mathrm{gas}\mathrm{v}(\sigma_\mathrm{ion}(\mathrm{v}) - \sigma_\mathrm{att}(\mathrm{v}))f(\mathbf{r},\mathbf{v},t)\,\mathrm{d}^3\mathbf{v} \equiv \nu_\mathrm{e} n_\mathrm{e}\ , \tag{2.128}$$

where in the last term, we express the source S simply as an exponential growth rate ν_e of the electron swarm of local density n_e.

Due to the non-conservative total number of electrons, one should distinguish between *flux* and *bulk* transport coefficients:

- ◦ Flux coefficients – noted with a dot "$\dot{a}$" : emerge from the immediate transport properties determined by the swarm's velocity distribution $f(\mathbf{r},\mathbf{v},t)$ at a position $\mathbf{r}$ and time t;
- • Bulk coefficients : represent the average transport properties of the swarm when taken as a whole and accounting for non-conservative collisions: ionisation and attachment.

This dual distinction is a well-known classic in the plasma community and more information can be found in Petrović *et al.*'s review [747, §4.1–4.5]. In particular, Li *et al.* [588, §2.2.1:eq.(25)] recommends not to use bulk coefficients in fluid equation (2.126) to approximate non-local effects due to the source term. A discussion of the extension of fluid models to include non-local effects is given in Li [585, §4.2:p.57–69].

In a steady-state configuration such as a Townsend discharge, the local density $n_\mathrm{e}(\mathbf{r})$ depends only on the space coordinate. Then, one can define Townsend's (first) ionisation coefficient α_i [606, 640, p.52–66, p.2–7], expressing the spatial growth of the swarm due to ionisation, as [378a, eq.(16)]:

$$\alpha_\mathrm{i} \equiv -\frac{1}{n_\mathrm{e}}\hat{\mathbf{E}}\cdot(\nabla n_\mathrm{e})\ . \tag{2.129}$$

Simple expressions may be derived to calculate flux coefficients with the following assumptions:

- • Low anisotropy: at low to moderate electric fields (below conventional breakdown), the velocity distribution can be approximated by the two-term expansion (2.118) with a small anisotropy $f_1/f_0 \ll 1$.

- Local equilibrium: $f_\mathrm{v}(\mathbf{v},t)$ relaxes faster than the swarm density $n_\mathrm{e}(\mathbf{r},t)$ drifts and diffuses over spatial scales of inhomogeneities in the medium (electric field, gas density, temperature, composition).

- Steady-state: the swarm drifts and diffuses but the density $n_\mathrm{e}(\mathbf{r})$ remains stationary from the steady production of electrons through ionisation.

Then, the mobility μ_0, the (isotropic or lateral) diffusion D_0, source S_0 and ionisation α_i coefficients are obtained from the isotropic velocity distribution f_0 [590, p.685:eq.(18.1.28–9)]:

$$\mu_0 = -\frac{4\pi e}{3mn_\mathrm{e}n_\mathrm{gas}}\int_0^\infty \frac{1}{\sigma_\mathrm{m}}\frac{\partial f_0(\mathrm{v})}{\partial \mathrm{v}}\mathrm{v}^2\,\mathrm{d}\mathrm{v} \tag{2.130}$$

$$D_0 = \frac{4\pi}{3n_\mathrm{e}n_\mathrm{gas}}\int_0^\infty \frac{\mathrm{v}}{\sigma_\mathrm{m}} f_0\mathrm{v}^2\,\mathrm{d}\mathrm{v} \tag{2.131}$$

$$S_0 = 4\pi n_\mathrm{e}n_\mathrm{gas}\int_0^\infty \mathrm{v}(\sigma_\mathrm{ion}(\mathrm{v}) - \sigma_\mathrm{att}(\mathrm{v}))f_0\mathrm{v}^2\,\mathrm{d}\mathrm{v} = n_\mathrm{e}\nu_0 \tag{2.132}$$

$$\alpha_\mathrm{i} = \frac{\mu_0 E}{2D_0}\left(1 - \sqrt{1 - \frac{4D_0\bar{\nu}_\mathrm{e}}{(\mu_0 E)^2}}\right) \approx \frac{\nu_0}{\mu_0 E} = \frac{\nu_0}{\mathrm{v}_0} \tag{2.133}$$

For non steady-state regimes, such as the temporal exponential growth of swarms, one may add a correction term to the momentum transfer cross section σ_m which accounts for the creation of new electrons as proposed by Hagelaar and Pitchford [378a, eqs.(11–2)]. When the (isotropic) diffusion D_0 and multiplication rates ν_0 are much smaller than the drift velocity v_0, the Townsend's ionisation coefficient α_i may be very simply estimated as the ratio between ν_0 and v_0.

For the expression giving the longitudinal $D_\parallel$ diffusion coefficient (along the direction of the electric field $\mathbf{E}$), one can consult Huxley [414, eq.(50b)].

In general, one does not need to rely on the two-term approximation nor the stationary spectrum assumption to obtain transport parameters of mobility and diffusion. Those, as used in (2.126), can be estimated in regimes beyond the validity of those approximations from Monte Carlo simulations such as described in Li *et al.* [588, §2.1.3]. The underlying assumption, nonetheless, is the local equilibrium with the electric field $\mathbf{E}(t,\mathbf{r})$ (and gas characteristics) at a given time and position $(t,\mathbf{r})$.

For instance, electrons in a gas at reduced electric fields near conventional breakdown ($\sim$ 100 Td) reach a stable velocity distribution in a matter of $\lesssim$ 10 ps (see our relaxation time chart 5.6). One can generally assume in a discharge that the electron kinetic distribution at any instant and position $(t,\mathbf{r})$ conforms to the local electric field. From there, the transport parameters $\mu_\mathrm{e}(E), \underline{D}_\mathrm{e}(E)$ are made functions of the electric field.

This enables a very computationally efficient coupling of Monte Carlo particle codes with fluid simulations as the former yield the transport parameters as input to the fluid equation (2.126), which are then used to derive the field $\mathbf{E}$ from Poisson's equation of the electronic n_e and ionic n_i densities* [588, eq.(23)]:

$$\nabla\cdot\mathbf{E} = \frac{-en_\mathrm{e} + en_\mathrm{i}}{\epsilon_0}\,. \tag{2.134}$$

*Note that in this case, the ionic density comprises the ionisation degree of each ion, so for instance doubly charged ions would be counted twice in n_i.

Notwithstanding, the place where large inhomogeneities are concentrated on small spatial scales is at the streamer head or ionisation fronts. There, non-local effects may be important [686]. This occurs when electrons of higher energies, generated in a region of high electric field, escape the region and penetrate neighbouring zones where the electric field is screened. In these zones, the electron distribution in velocity is not in equilibrium with the local electric field and one needs to include corrections due to such non-local displacement [586]. For greater accuracy, it is rather necessary to describe the full kinetic electron distribution and recur to Monte Carlo simulation of high-energy electrons to unveil the physics at play [281, 587]. The latter requirement, namely modelling the high-energy tail of electron swarms, is at the core preoccupation of the first part of this thesis. Further discussion of modelling low-temperature plasmas in the fluid approach can be found in Robson *et al.* [781].

In the next chapter 3, we explain how our particle code is implemented numerically and how to retrieve EEDF and swarm parameters from the simulation results.

Chapter 3

Numerical Modelling

After having presented several aspects of the physical model used to describe electron swarms in electrified gases, the present chapter regroups the various methodologies used to implement this model numerically.

The structure of the code is as follows. We store the electron swarm information into a structured array of N_s rows with the following entries:

- Initial conditions
  - t_0 : initial time of creation
  - $\mathbf{r}_0$: initial location of creation (useful to locate positive ions)
  - ε_0 : initial kinetic energy (useful to runaway statistics)
- Current conditions
  - t : current time
  - δt_f : free flight time (till next null/collision event)
  - $\mathbf{r}$: current position
  - $\hat{\mathbf{v}}$: velocity direction (unit vector)
  - Kinetic variables
    - ε : current energy
    - v : velocity (norm)
    - p : momentum (norm)
    - γ : Lorentz factor (2.16a)
  - w : super-electron statistical weight
  - A boolean value indicating whether the electron is destroyed or alive

The array is passed to routines who perform operations such as propagation in an electric field (3.1), collisions (3.2) and scattering (3.2.3), or calculation of collective swarm properties (3.3). These tasks are explained in the ensuing sections.

The swarm simulation is orchestrated by a minimal time-step δt which we recommend to take as the inverse of the maximal collision frequency:

$$\delta t \equiv \frac{1}{\nu_\mathrm{max}} \quad \text{where} \quad \nu_\mathrm{max} \equiv \max_\varepsilon \left(\sigma_\mathrm{tot}(\varepsilon)\mathrm{v}n_\mathrm{gas}\right) \ . \tag{3.1}$$

3.1 Electron Motion

The free motion of an electron in an electromagnetic field has been exposed in section 2.2. In the context of thermal runaway, we only focused on the acceleration in an electric field $\mathbf{E} \parallel \hat{\mathbf{z}}$ aligned with the z axis in gases at atmospheric pressure.

We consider an electron whose initial position is $\mathbf{r}_0$ and momentum $\mathbf{p}_0$ forms an angle $\cos\chi_0 = \mathbf{p}_0 \cdot \mathbf{E}/(p_0 E)$ with the direction of the electric field. After a time interval Δt, the electron state is described by:

$$\mathbf{p} = -e\mathbf{E}\Delta t + \mathbf{p}_0 \,, \tag{3.2a}$$

$$\mathbf{r} = \mathbf{r}_0 + \frac{-\hat{\mathbf{E}}}{eE} mc^2(\gamma - \gamma_0) + \frac{\hat{\mathbf{p}}_\perp c}{eE} \ln\left(\frac{-p_0\cos\chi_0 + eE\Delta t + \sqrt{(mc\gamma_0)^2 + (eE\Delta t)^2 - 2p_0 eE\Delta t\cos\chi_0}}{mc\gamma_0 - p_0\cos\chi_0} \right) . \tag{3.2b}$$

The vector $\mathbf{p}_\perp$ is the component of $\mathbf{p}_0$ which is perpendicular to $\mathbf{E}$: i.e. $\mathbf{p}_\perp = (\mathbf{p}_0 - p_0\hat{\mathbf{E}}\cos\chi_0)$.

In practice, the time interval Δt is sampled from the mean collision time from the null collision method as described in the next section 3.2.1 (3.3).

3.2 Sampling of Collisions

The collisions are modelled as stochastic processes regardless of the electron energy. That is, we do not approximate high-energy scattering and collisions through a continuous friction force (2.72).

Every collision is described by a discrete set (or continuous distribution) of possible outcomes to which a probability (or probability density) is associated. Every time we need to sample the outcome of a collision event from a certain probability density distribution $p(\zeta)$ of a quantity ζ, we sample the value of a random variable X, uniformly distributed between 0 and 1. Instances of X will be denoted by x with $0 \le x \le 1$.

3.2.1 Null collision

From the discussion in section 2.2.3 page 73, we realise that one cannot simply use the total collision frequency $\nu_{\text{tot}}(\varepsilon) = \sigma_{\text{tot}}(\varepsilon) n_{\text{gas}} \text{v}$, to sample the next collision occurrence of an electron whose current energy is ε. This is because (i) the electron velocity v varies during the flight time due to acceleration by the electric field and (ii) the cross section $\sigma_{\text{tot}}(\varepsilon)$ varies with energy (and may promptly vary near resonances).

Nevertheless, one can perform a stochastically equivalent method to the sampling of an electron's collision with the so-called "null-collision" technique proposed by Lin and Bardsley [591] and further developed by Koura [537] and Koura [538]. Since the total cross section σ_{tot} of electron interaction with the gas molecules is known, one can find the maximal total collision frequency $\nu_{\max}$ of that electron within the gas in (3.1). Thus, one knows the maximal rate at which an electron may collide on average with a molecule. This maximal rate gives a baseline for sampling randomly collisions of any smaller rate.

The null collision technique proceeds as follows:

1. Sample (with x) a mean free flight δt_f from a Poisson process at a ν_max probability rate per unit time:

$$\delta t_\mathrm{f} = -\frac{\ln(1-x)}{\nu_\mathrm{max}} \,. \tag{3.3}$$

2. Let the electron propagate by this free time δt_f in the equation of motion (3.2). The electron is now at a new energy ε'.

3. Sample (with another x') whether a physical collision ought to take place at the energy ε' from the total cross section:

$$x_\mathrm{coll} \equiv \frac{\sigma_\mathrm{tot}(\varepsilon')\mathrm{v}'}{\nu_\mathrm{max}} \begin{cases} x_\mathrm{coll} \leq x' & \text{A physical collision is sampled} \rightarrow \text{proceed to step 4} \\ x_\mathrm{coll} > x' & \text{A “null collision” event} \rightarrow \text{return to step 1} \end{cases} \tag{3.4}$$

4. In the case $x' < x_\mathrm{coll} = \sigma_\mathrm{tot}(\varepsilon')\mathrm{v}'/\nu_\mathrm{max}$, then recycle the randomly sampled x' through:

$$x'' \equiv \frac{x'}{x_\mathrm{coll}} \,, \tag{3.5}$$

and use x'' to select which collision has occurred with algorithm 3.2.2.

These steps are repeated as many times as necessary until the mean free time δt_f sampled from (3.3) exceeds the minimal timestep δt from (3.1) at the current time of the simulation as: $t + \delta t_\mathrm{f} > N_t \delta t$ where t is the current time of the electron and N_t the current clock (counted in minimal timesteps δt) of the simulation. Therefore, the particular choice of δt has no physical influence on the simulation.

The null collision technique fills the space of collision processes with an imaginary “null collision” whose presence accounts for the variation of the true collision frequency $\nu_\mathrm{tot}(\varepsilon)$ of an electron at any energy ε. For a clearer introduction, there are numerous useful graphical explanations of this methodology available in the literature [588, 677, fig. 6, fig. 1].

From the x'' value of step 4, we now proceed to the selection of the collision type which is explained in the next subsection.

3.2.2 Discrete

We consider a discrete set of processes s_i with $i = 1..N_\mathrm{c}$. Each process s_i has an occurrence probability $p_i(\varepsilon)$ which depends on the electron energy.

We define the cumulative sum $\acute{C}_i$ of probabilities:

$$\acute{C}_i(\varepsilon) \equiv \sum_{k=1}^{i} p_k(\varepsilon) \quad \text{and} \quad \acute{C}_0 \equiv 0 \,. \tag{3.6}$$

From a randomly sampled instance x'', the process s_i that shall be selected verifies:

$$i \,:\, \acute{C}_{i-1} < x'' \leq \acute{C}_i \tag{3.7}$$

Since, most of the time, the processes are not uniformly distributed $p_i(\varepsilon) \neq p_j(\varepsilon)$ for $i \neq j$, there is no straightforward way to select the process s_i than through an iteration loop over i.

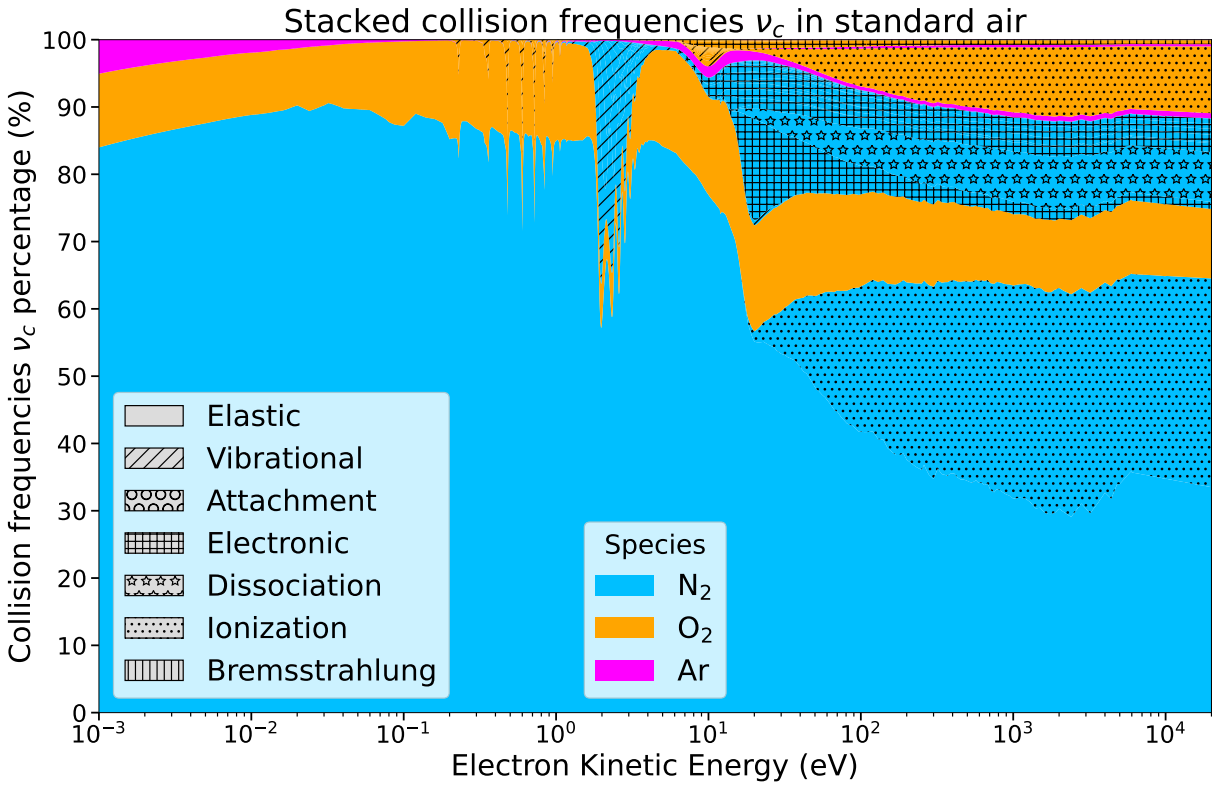

Figure 3.1: Relative proportion all of electron-molecule collision cross sections in ambient air according to importance of collision type and abundance of species.

This iteration is applied concretely to select which collision event c occurs when an electron is bound to collide after having successfully undergone the test (3.4) step 3 of the null collision method. The probabilities are the ratios $p_c(\varepsilon) = \sigma_c(\varepsilon)/\sigma_{\text{tot}}(\varepsilon)$ for the collision c.

In order to be efficient, the collisions with most important cross sections and most abundant species are ordered first in the iteration list. The relative importance of cross sections can be visualised on figure 3.1 where the coloured areas represent the proportion of each collision process to the total cross section in ambient air. From bottom to top, the cross sections types have been ordered so as to have the most important ones at the bottom (first in the list).

Our ordering algorithm sets the priority in the following way:

$E < E_{\text{k}}$

1. Elastic
2. Ionisation
3. Attachment
4. Vibrational ($v = 0 \to 1, 2, \dots$)
5. Electronic including Dissociation ($\mathcal{E}_{\text{th}}$ ascending)
6. Bremsstrahlung

Evidently, at low electric fields E below the conventional breakdown $E_{\text{k}} \simeq 3\,\text{MV/m}$, there is no or little ionisation since the average electron kinetic energy is in the eV range. Then, it makes

no sense to put the ionisation cross section second in place. In this case ($E < E_k$), the ionisation events are moved to the penultimate place of the list (before Bremsstrahlung).

Another application of the discrete sampling (3.6–3.7) is when selecting different levels of partial ionisation due to a particular subshell (of binding energy B_i) of an atom/molecule; or when selecting a vibronic transition $0 \to v'$ from the same electronic level.

For ionisation, we compute the cross sections σ_i for each subshell i according to (11.120) from the model developed in the second part section 11.5.

For excitations, we use Franck-Condon (or transition probability*) factors which are assumed independent of the electron energy (see appendix D.2 and references throughout 11.4).

3.2.3 Continuous

The generalisation of the previous situation to a continuous distribution of processes is not difficult. The probability distribution of the processes labelled by a continuous variable ζ constrained to the interval $[\zeta_0, \zeta_1]$, is noted as $(\zeta; \varepsilon)$, which depends usually on the electron energy.

We define the (normalised) cumulative integral $\acute{C}(\zeta; \varepsilon)$ by :

$$\acute{C}(\zeta; \varepsilon) \equiv \int_{\zeta_0}^{\zeta} p(\zeta; \varepsilon)\, \mathrm{d}\zeta \quad \text{for } \zeta \in [\zeta_0, \zeta_1] \quad \text{with} \quad \acute{C}(\zeta_1; \varepsilon) = 1 \tag{3.8}$$

The selection of ζ in a random event sampled at x consists in reversing the integral equation:

$$x = \acute{C}(\zeta; \varepsilon) = \int_{\zeta_0}^{\zeta} p(\zeta; \varepsilon)\, \mathrm{d}\zeta \tag{3.9}$$

Naively, this would require each time to find the root of $\acute{C}(\zeta) - x = 0$. Fortunately, this costly method can be avoided by resorting to either of three more practical solutions to revert (3.9).

A) A simple, yet accurate analytical expression can be found for $\acute{C}(\zeta; \varepsilon)$ and then reversed to express $R(x; \varepsilon) = \zeta$.

B) The function $R(x; \varepsilon)$ can be approximated by an analytical expression, typically a polynomial.

C) The last resort is to store $R(x; (\varepsilon))$ on a uniformly sampled grid (with a scaling transformation $\mathcal{T}(\varepsilon)$ on the energy ε if need be). Then, a linear interpolation on a uniform grid can be as fast (or faster) than an analytical expression. The main drawback is memory consumption though it did not pose any problem for our purposes.

Thus, we concretely used the solution C) for three different applications:

I. Scattering: when sampling the angle θ (standing for ζ) of a differential cross section $\mathrm{d}\sigma/\mathrm{d}\Omega$:

$$x = \frac{\displaystyle\int_0^{\theta} \frac{\mathrm{d}\sigma}{\mathrm{d}\Omega}(\theta; \varepsilon) \sin\theta\, \mathrm{d}\theta}{\displaystyle\int_0^{\pi} \frac{\mathrm{d}\sigma}{\mathrm{d}\Omega}(\theta; \varepsilon) \sin\theta\, \mathrm{d}\theta} \tag{3.10}$$

Due to the axial symmetry in scattering events, the azimuthal angle φ is sampled uniformly as $\varphi = 2\pi x$.

*Careful that a Franck-Condon factor is given through the approximation underlying (D.5), whereas a transition probability $\mathcal{P}_{Xa'}(0 \to v')$ can be estimated experimentally. Thus their values are not necessarily equal.

At energies above 10 keV, we indulged in using the analytical reverse formula of a screened Rutherford expression (11.4) whose shape we fitted in order to reproduce the average scattering cosine $\langle\cos\theta\rangle$ of our computed DCS in the high energy Born approximation from section 11.1.4. Thus:

$$\cos\theta(\varepsilon > 10\,\text{keV}) = 1 - x\frac{2\bar{\eta}}{1 - x + \bar{\eta}} \quad \text{with} \quad \bar{\eta} = \frac{1}{(2k\bar{a})^2}\,, \tag{3.11}$$

where $\bar{a}$ is to be picked from the first row of table 11.4, but not without reading section 11.1.4 so as to understand the implications and premises.

II. Excitation continuum: sometimes, the energy $\mathcal{E}$ lost by an electron in an excitation is distributed continuously over a segment $[\mathcal{E}_0, \mathcal{E}_1]$, ($\mathcal{E}$ stands for ζ). This is the case of the Schumann-Runge continuum and Herzberg pseudo-continuum of molecular oxygen.

The cumulative integral of the generic probability distribution given in (11.66) is:

$$\begin{aligned}\acute{C}_\text{M}(\mathcal{E}) &= \int_{\mathcal{E}_0}^{\mathcal{E}} (\zeta - \mathcal{E}_0)^s (\zeta - \mathcal{E}_1)^2\,\mathrm{d}\zeta\,, \\ &= (\mathcal{E} - \mathcal{E}_0)^{s+1}\left(\frac{(\mathcal{E} - \mathcal{E}_0)}{s+3}(\mathcal{E} - 2\mathcal{E}_1) - 2\frac{(\mathcal{E}_1 - \mathcal{E}_0)}{s+2} + \frac{(\mathcal{E}_1 - \mathcal{E}_0)^2}{s+1}\right)\cdot\frac{(s+3)(s+2)(s+1)}{2(\mathcal{E}_1 - \mathcal{E}_0)^{s+3}}\,.\end{aligned} \tag{3.12}$$

The difficulty in reversing this equation forced us to use a uniform sampling in the cumulative space.

Note that when the electron's kinetic energy lies below the maximal excitation energy loss $\varepsilon < \mathcal{E}$, one has to restrict the integral to $\zeta < \varepsilon$. Then, the uniformly sampled variable X must be rescaled down to $\acute{C}(\varepsilon)$. This is explained again in the next chapter section 4.1.1

III. Ionisation: requires sampling on the secondary electron's kinetic energy ε_2. This time, the technical difficulty is that one must sample in a region of two-dimensional space $\varepsilon_0 \times \varepsilon_2$ of the incident and ejected kinetic energies, which is not a rectangle product since $\varepsilon_2 \leq (\varepsilon_0 - B)/2$. We circumvented this problem by defining the ratio of the secondary energy to its maximal value:

$$\xi_\varepsilon \equiv \frac{2\varepsilon_2}{\varepsilon_0 - B}\,. \tag{3.13}$$

Thence, we generated a 5000×1000 matrix $\mathcal{M}_{\varepsilon_0,\xi_\varepsilon}$ of $[\varepsilon_0, \xi_\varepsilon]$ values for the initial energy of the electron prior to ionisation $\varepsilon_0 \in [I, \varepsilon_\text{max}]$ and normalised secondary energies $\xi_\varepsilon \in [0, 1]$. The values in ε_0 were logarithmically spaced whereas a transformation $\xi_\varepsilon = (10^x - 1)/9$ was used from a uniformly distributed variable $x \in [0, 1]$ so as to have an enhanced resolution at small ξ_ε which are more probable at higher energies.

Given the matrix $\mathcal{M}_{\varepsilon_0,\xi_\varepsilon}$, we computed the cumulative integral $\acute{C}_{\mathrm{RBEQ*}}$ of the RBEQ* model which is:

$$\acute{C}_{\mathrm{RBEQ*}}(\varepsilon_0,\xi_\varepsilon) \equiv \int_0^{\varepsilon_2} \frac{\mathrm{d}\sigma_{\mathrm{RBEQ*}}}{\mathrm{d}\varepsilon'}\,\mathrm{d}\varepsilon' \,, \quad \text{where} \quad \varepsilon_2 = \xi_\varepsilon \frac{(\varepsilon_0 - B)}{2} \,; \tag{3.14}$$

$$= \frac{4\pi a_0^2 \alpha^2 N}{\tilde{\beta}^2}\left[\frac{Q}{2}\left(\ln(\frac{mc^2\beta_0^2\gamma_0^2}{2B}) - \beta_0^2 + C_\mathrm{d}\right)\left(1 - \frac{B^2}{(\varepsilon_2+B)^2} + \frac{B^2}{(\varepsilon_0-\varepsilon_2)^2} - \frac{B^2}{\varepsilon_0^2}\right)\right.$$
$$\left. +(2-Q)\left(1 - \frac{B}{\varepsilon_2+B} + \frac{1}{(\varepsilon_0-\varepsilon_2)} - \frac{B}{\varepsilon_0} + \varepsilon_2\left(\frac{B}{mc^2\tilde{\gamma}}\right)^2 - \frac{(2\tilde{\gamma}-1)B}{\tilde{\gamma}^2(\varepsilon_0+B)}\ln\left(\frac{(\varepsilon_2+B)\varepsilon_0}{(\varepsilon_0-\varepsilon_2)B}\right)\right)\right] .$$

Whenever we need to sample ε_2 for a given ε_0, we inverse the interpolated $\acute{C}_{\mathrm{RBEQ*}}[\mathcal{M}_{\varepsilon_0,\xi_\varepsilon}]$ matrix and retrieve ε_2 from (3.14).

For the secondary electron's scattering angle cosine $\cos\theta_2$, as remarked in section 11.5.4 on pages 492–494, we use equation (2.66). The cosine of the primary electron $\cos\theta_1 = \cos\theta_+$, on the other hand, is simply obtained from the conservation of momentum (2.62).

This concludes all the necessary algorithms used for the electron interactions with molecules. In the next section, we present methods to calculate average collective properties of the electron swarm and handle the swarm as a whole.

3.3 Swarm

3.3.1 EEDF

There are plenty of ways one can compute numerically the electron energy distribution function (EEDF) from (2.120) of a given swarm. One could compute the histogram in velocity norm space or in energy space and then convert it to the EEDF. After trying various methods we chose the most efficient one that we use throughout the thesis.

Given the set of kinetic energies ε_n and weights w_n of our N_s super-electrons, we first calculate the density in energy space $h(\varepsilon)$ through a histogram.

The histogram bins' edge positions $b_{\varepsilon,i}$ are determined either:

a) according to Knuth's binning rule [514, eq.(32)], with a fixed bin width $\delta b_\varepsilon = b_{\varepsilon,i+1} - b_{\varepsilon,i}$;

b) or through the Bayesian method [807] for a more robust representation [756, figs. (1–2)], with a variable bin width.

For spectra that extend over several orders of magnitude in energy, we use a constant bin width on a logarithmic scale in electron energy ($\delta(\ln\varepsilon)$) instead of in the linear scale.

To obtain the EEDF, we use the differential correspondence:

$$f_\varepsilon(\varepsilon)\sqrt{\varepsilon}\,\mathrm{d}\varepsilon = g(\varepsilon)\,\mathrm{d}\varepsilon \Leftrightarrow f_\varepsilon(\varepsilon)\frac{\mathrm{d}(\varepsilon^{3/2})}{3/2} = g(\varepsilon)\,\mathrm{d}\varepsilon\,, \tag{3.15}$$

which becomes, in the numerical world where $\mathrm{d}\varepsilon$ becomes a $\delta b_\varepsilon = (b_{\varepsilon,i+1} - b_{\varepsilon,i})$, i.e. the interval between the consecutive bin edges $b_{\varepsilon,i}$ and $b_{\varepsilon,i+1}$:

$$f_\varepsilon(\varepsilon) = g(\varepsilon)\frac{\delta b_\varepsilon}{\delta(b_\varepsilon^{3/2})}\frac{3}{2} = g(\varepsilon)\frac{3}{2}\frac{b_{\varepsilon,i+1} - b_{\varepsilon,i}}{(b_{\varepsilon,i+1}^{3/2} - b_{\varepsilon,i}^{3/2})} \quad \text{where} \quad b_{\varepsilon,i} \le \varepsilon \le b_{\varepsilon,i+1}\,. \tag{3.16}$$

If, on the other hand, we used a kernel density estimator, we would have simply divided the kernel density $k(\varepsilon)$ by $\sqrt{\epsilon}$: i.e. $f_\varepsilon(\varepsilon) = k(\varepsilon)/\sqrt{\varepsilon}$. A major drawback from kernel and Bayesian blocks, is that their computational time becomes immoderate at the typical number $N_\mathrm{s} \sim 5\times10^5$ of super-electrons that we simulate.

In general, we preferred using the fixed-width Knuth histogram (in linear or most often in logarithmic scale) because it also enabled us to easily estimate the variance of each bin's height $h_\mathrm{Knuth}(\varepsilon)$ through [514, p.5:eq.(47)]:

$$\mathrm{var}[h_\mathrm{Knuth}(\varepsilon)] = \left(\frac{M_\mathrm{b}}{A_\varepsilon(N_\mathrm{s} + \frac{M_\mathrm{b}}{2})}\right)^2 \frac{(h_\mathrm{Knuth}(\varepsilon) + \frac{1}{2})(N_\mathrm{s} - h_\mathrm{Knuth}(\varepsilon) + \frac{(M_\mathrm{b}-1)}{2})}{N_\mathrm{s} + \frac{M_\mathrm{b}}{2} + 1}\,, \tag{3.17}$$

from which one can attribute an uncertainty ($\sqrt{\mathrm{var}[h]}$) to the EEDF obtained.

We illustrate the looks of EEDFs of an electron swarm from various numerical methods in figure 3.2. The kernel density estimator is the most computationally costly.

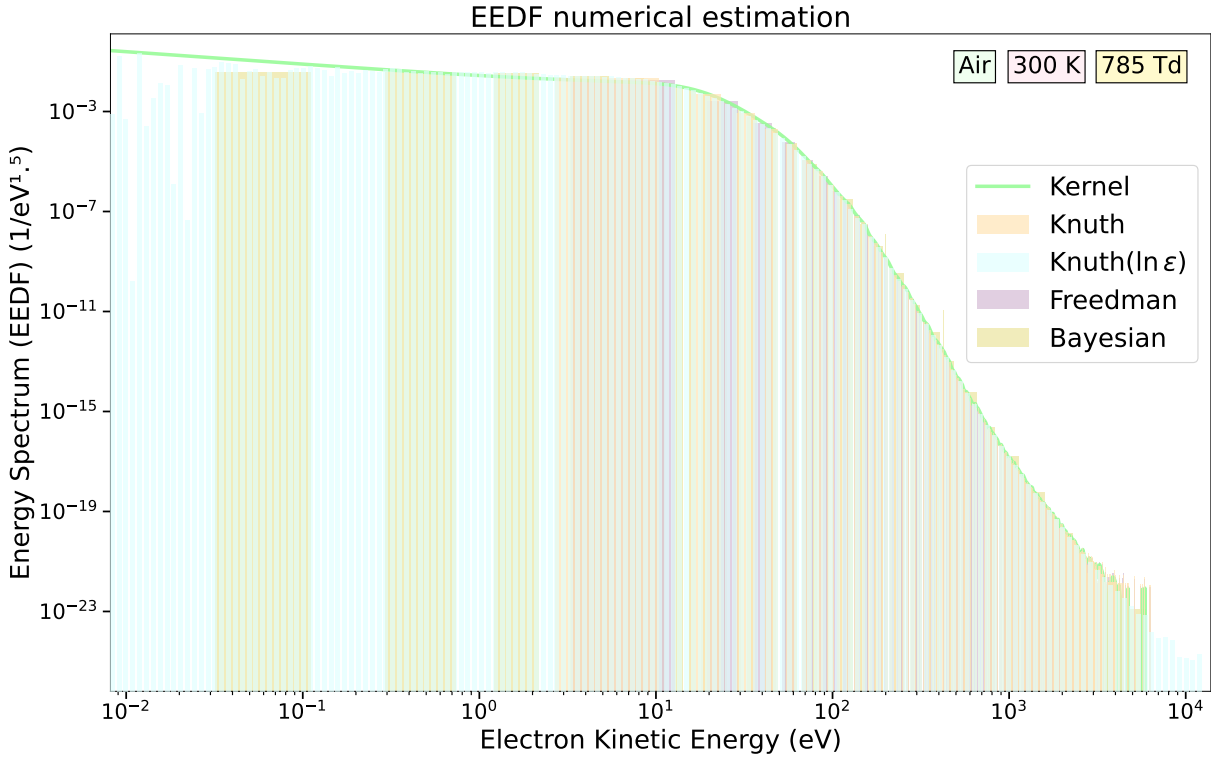

Figure 3.2: Calculation of the electron energy spectrum (EEDF) of a swarm ($N_s = 5 \times 10^4$) from various density estimators. We compare fixed bin width histograms from Knuth's rule [514] and Freedman and Diaconis's rule [303] to Bayesian blocks of variable bin widths [807]. Also shown is the kernel density estimation with an Epanechnikov kernel. When the spectrum extends over multiple orders of magnitude, it is significantly better to use fixed bins on a logarithmic scale i.e. $\ln \varepsilon$ as seen on the bar plot "Knuth($\ln \varepsilon$)" which unveils the high-energy tail up to 10 keV. All densities were calculated from the `astropy.stats` module on Python.

From an efficiency-accuracy perspective, the logarithmic Knuth binning histogram (light blue on figure 3.2) is the most suitable. It is fast and spans the widest range of energies without deteriorating its accuracy.
Worthy of note, the statistics `numpy` module used for generating histograms uses a cumulative sum to calculate the number of particles per bin. It is not optimised for the great disparity of super-particle weights w as present in our spectra. To circumvent the issue of losing accuracy at the tail of the spectrum sheerly due to numerical round-off error from the cumulative sum, we:

1. invert the order of binning (starting from the end),
2. use negative energies and bin edges (so as to preserve monotonically increasing bins),

before calling the `histogram` module routine.

A reliable yet fast calculation of the EEDF is an essential ingredient to the good functioning of the super-electron spectral enhancement algorithm described in the next section. This algorithm is itself key to our investigation of thermal runaway.

3.3.2 Compaction

The reason why we use a Monte Carlo particle code to simulate electron swarms is primarily because we want to investigate the stochastic process linked to thermal runaway as accurately as possible. However, there are two issues that we must address:

i. First, above conventional breakdown the number of particles $N_s(t)$ (super-electrons) grows exponentially;

ii. Second, the fraction of super-electrons pertinent to the phenomenon of thermal runaway, i.e. at energies above the ionisation peak in the friction force at $\sim 120\,\mathrm{eV}$ (fig. 1.10), may be below our maximal resolution capability (e.g. only 1 electron out of 10^{-9}).

Therefore, we devised a particle management algorithm which we described in detail in Schmalzried *et al.* [813]. In this section, we will outline how the algorithm works and what recent improvements we have brought ("Old"§ versus "New"§).

The "compaction" algorithm has a double-sided goal:

1. Curtailment: discard surplus super-electrons spawned by ionisation from the simulation and maintain their number $N_s(t)$ close to a desired value $N_s^*(t)$ and progressively conduce them to a nominal value N_s^∞ (see fig. 3.4):
$$\lim_{t\to\infty} N_s^*(t) = N_s^\infty \quad ;$$

2. Spectral enhancement: increase the resolution $g_s(\varepsilon)$ (number of super-electrons per energy interval) at higher energies by adhering to a target super-electron density $g_s^*(\varepsilon,t)$ in energy space which gradually converges to a nominal distribution g_s^∞ (see fig. 3.5):
$$\lim_{t\to\infty} g_s^*(\varepsilon,t) = g_s^\infty(\varepsilon) \quad ,$$
so as to highlight the study of thermal runaway from a stochastic perspective.

To maintain physical consistency, the weights w of the super-electrons are adapted according to the real spectral electron density $g_e(\varepsilon)$ [813, eq.(3)]:

$$g_s(\varepsilon,t)\left[\sum w(\varepsilon,t)\right] = g_e(\varepsilon,t) = g_s^*(\varepsilon,t)w^*(\varepsilon,t)\,, \tag{3.18}$$

where the sum extends over all super-electrons present in an energy bin of width $\delta\varepsilon$.

Concisely, we may distinguish three quantities which are all subject to vary with time t:

- **Physical** quantities relate to the represented electrons in swarm (see sec. 2.3.1) and which should be left intact by the compaction process.
  - $N_e(t)$: the physical number of electrons (2.86);
  - $g_e(\varepsilon,t)$: the electron density in energy space* (blue histogram on fig. 3.3-bottom), related to the EEDF by $g_e(\varepsilon) = f_\varepsilon(\varepsilon)\sqrt{\varepsilon}$ (3.15).

*Number of electrons per infinitesimal energy interval.

△ **Numerical** quantities related to the super-electrons present in the simulation as a sample of the physical electrons.

- $N_s(t)$: actual number of super-electrons;
- $g_s(\varepsilon, t)$: the density of super-electrons in energy space (purple histogram on fig. 3.3-bottom);
- $w(t)$: the statistical weight borne by each super-electron (may vary for each electron even at the same energy ε, see blue dots ∴ on fig. 3.3-top).

*** Target** quantities govern how the super-electrons ought to be managed according to the user specifications. There are two types:

Instantaneous ($*$ short-term)

- $N_s^*(t)$: instantaneous target number of super-electrons at the time t;
- $g_s^*(\varepsilon, t)$: instantaneous target density (red — curve on fig. 3.3-bottom). There is no direct definition of $g_s^*(\varepsilon, t)$, it is obtained from $w^*(\varepsilon, t)$ through the second equation in (3.18).
- $w^*(\varepsilon, t)$: the statistical weight that every super-electron of energy ε should adopt (red — curve on fig. 3.3-top) in order to reproduce the target density $g_s^*(\varepsilon, t)$. It is obtained from w^∞ in the relaxation equation (3.29).

Nominal (∞ long-term)

- N_s^∞ : nominal number of super-electrons to be hosted in the simulation when the steady-state regime is reached;
- $g_s^\infty(\varepsilon, t)$: nominal target density which has an enhanced high-energy tail as specified in (3.23) (dashed red - - - on fig. 3.5);
- $w^\infty(\varepsilon, t)$: distribution of nominal target weights w^∞ which depends on the physical density g_e and g_s^∞ through (3.18).

The name "compaction" stands for two operations:

(1.) Curtailment: reduction of the overall swarm information to a smaller portion of the super-electron population,

(2.) Enhancement: the allocation of more memory space to super-electrons of higher energies and, therefore, higher scarcity.

Below, we consecutively describe those two objectives. At the end, we explain how they are treated together uniformly in (3.) the compaction step.

1. Curtailment: $N_s(t) \to N_s^\infty$

Old. In our original method [813], we tried different ways of restricting the number $N_s(t)$ of electrons, where we would suddenly reduce it to the nominal value N_s^∞ every once in a while. We determined that the algorithm was optimal when the change from $N_s(t)$ to N_s^∞ was minimal, and thus that the algorithm ought to be applied continuously (at every elementary timestep δt 3.1). Nonetheless, there arises a problem at the initiation of the simulation. What if there is a very large disparity between the initial number of electrons $N_s(t = 0)$ and N_s^∞?

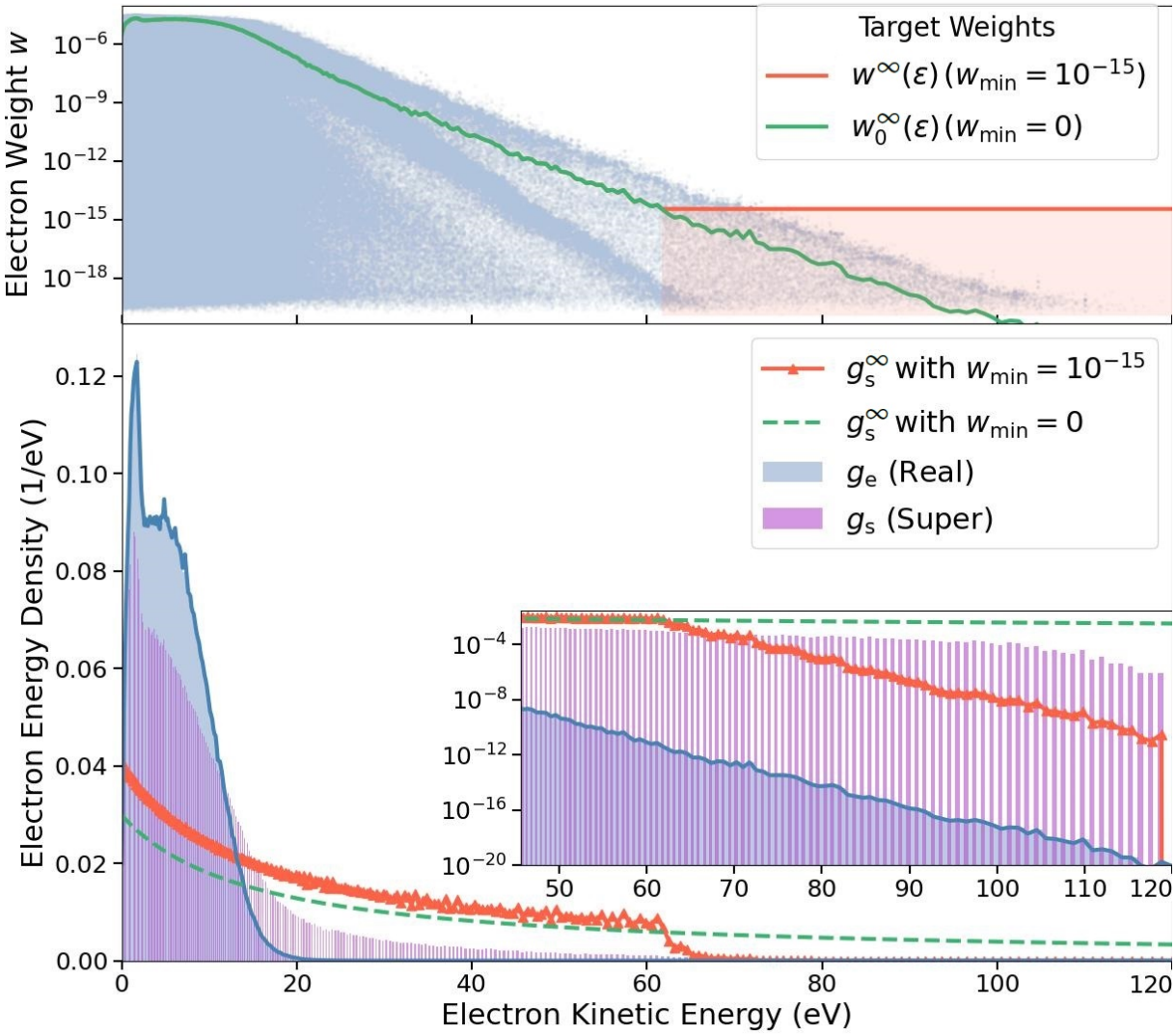

Figure 3.3: Nominal target weights w^∞ determined by the nominal density g_s^∞ (3.23) set by the user. All super-electrons whose actual weights $w > w^\infty(\varepsilon)$ will be split into two, three or more electrons. All other electrons with $w < w^\infty(\varepsilon)$ will undergo a selection procedure ("Russian roulette") based on a probability test which, if successful, will promote their weights w to the desired value w^∞.
The effect of the minimal weight ratio $w_{\min}$ is shown: it puts a minimal threshold to the allowed nominal weight w^∞ which otherwise (if $w_{\min} = 0$) would generate an indefinitely widening magnitude gap between the commonest and scarcest super-electrons (low and high ends of the energy spectrum).
The swarm presented is a composite of two snapshots from a simulation in argon (2.8 MV/m–inner ridge) and molecular nitrogen (5 MV/m–outer ridge) which is why the weights distribution appears with two ridges which corresponded to their respective target spectra in their separate simulations.

New. Presently, the novelty we bring is to let the target number of super-electrons be a dynamical quantity: $N_\mathrm{s}^\star(t)$. In this way, the algorithm will smoothly compact $N_\mathrm{s}(t)$ toward N_s^∞ over several iterations as represented in figure 3.4. This goes in line with our main conclusions [813, fig.6–7] that abrupt changes are detrimental to the quality of the super-electron statistics; i.e. they foment high peaks of fluctuation in the average $\bar{a}$ quantities presented in section 2.3.1 and used in the next section 3.3.3.

Conformably, we devised a proportional-integral retroaction loop, based on control theory [302, §4.3.4], acting on the super-electron target number $N_\mathrm{s}^\star(t)$ which, in consequence, follows:

$$\frac{\mathrm{d}N_\mathrm{s}^\star(t)}{\mathrm{d}t} = \overbrace{\bar{\nu}_\mathrm{s}N_\mathrm{s}^\star(t)}^{\text{Free System}} \overbrace{-\bar{\nu}_\mathrm{s}N_\mathrm{s}^\star(t)\left(1+\underbrace{2\kappa_\mathrm{r}S(N_\mathrm{s}^\star(t),N_\mathrm{s}^\infty)}_{\text{proportional}}+\underbrace{\kappa_\mathrm{r}^2\int_{t-t_\mathrm{m}}^{t}S\left(N_\mathrm{s}^\star(t'),N_\mathrm{s}^\infty\right)\mathrm{d}t'}_{\text{integral}}\right)}^{\text{Imposed Control Correction}}, \tag{3.19}$$

$$\text{with } S(N_\mathrm{s}(t),N_\mathrm{s}^\infty)=\log\left(\frac{N_\mathrm{s}(t)}{N_\mathrm{s}^\infty}\right) \quad : \quad \text{the deviation term,} \tag{3.20}$$

$$\text{and } t_\mathrm{m}=\frac{1}{2\bar{\nu}_\mathrm{s}\kappa_\mathrm{r}} \quad : \quad \text{the memory retention time.} \tag{3.21}$$

$$\left(\text{by default } \kappa_\mathrm{r}=3 \quad : \quad \text{the compaction reactivity.}\right) \tag{3.22}$$

In this way, we emulate the evolution of a system (our ensemble of $N_\mathrm{s}(t)$ super-electrons) which normally grows at a steady exponential rate given by ν_s (2.96). This system is controlled retroactively by a proportional term and converged by the integral term. It is inspired from the retroactive loops used in automation engineering [302, §4.3] in order to stabilise a property of a system ($N_\mathrm{s}(t)$ in our case). If the system (our simulation) incurs a perturbation, its response in the immediate moment is to initiate an exponential decay that counters this perturbation.

Conceptually, our application of control is atypical. In control theory, the equation (3.19) determines the response function of the system to a prompt perturbation (Heaviside function). Here, our system's response is virtually immediate because at any time, we can decide to curtail as many super-electrons as we wish. To prevent such an abrupt behaviour, we compute a desired theoretical response function $N_\mathrm{s}^\star(t)$ which serves to determine the evolution of $N_\mathrm{s}(t)$, which in turn at the next timestep will predict yet another path for $N_\mathrm{s}^\star(t)$ and so on...

Also, our retroaction in the second term on the right-hand side of (3.19) is heavily non-linear:

- the deviation function $S(N_\mathrm{s}(t),N_\mathrm{s}^\infty)$ (3.20), instead of a linear difference $N_\mathrm{s}(t)-N_\mathrm{s}^\infty$,
- the memory retention time t_m (3.21), which in a linear system would be infinite (going as far as the initial conditions of the system).

The coefficients of the non-linear system have been determined by trial and error so as to yield a subjectively swift yet gradual convergence to N_s^∞. We left only one parameter κ_r freely determinable by the user which we call the "compaction **r**eactivity" and is set to 3 by default.

The promptness of the response function depends on the instant super-electron multiplication rate $\bar{\nu}_\mathrm{s}(t)$ (2.96) at the time t; not to be confused with the physical exponential growth rate $\bar{\nu}_\mathrm{e}$ of the swarm. The system is vulnerable to fluctuations on $\bar{\nu}_\mathrm{s}(t)$. For instance, the response function calculated by our algorithm would be more abrupt if we instantly added 10 000 super-electrons of MeV, because they would induce an important multiplication of super-electrons. Nonetheless, the response of the system to initial conditions in disequilibrium ($N_\mathrm{s}(t=0)\neq N_\mathrm{s}^\infty$) is relatively smooth. An example of a run with initial conditions $N_\mathrm{s}(t=0)=4/3N_\mathrm{s}^\infty$ is shown in figure 3.4.

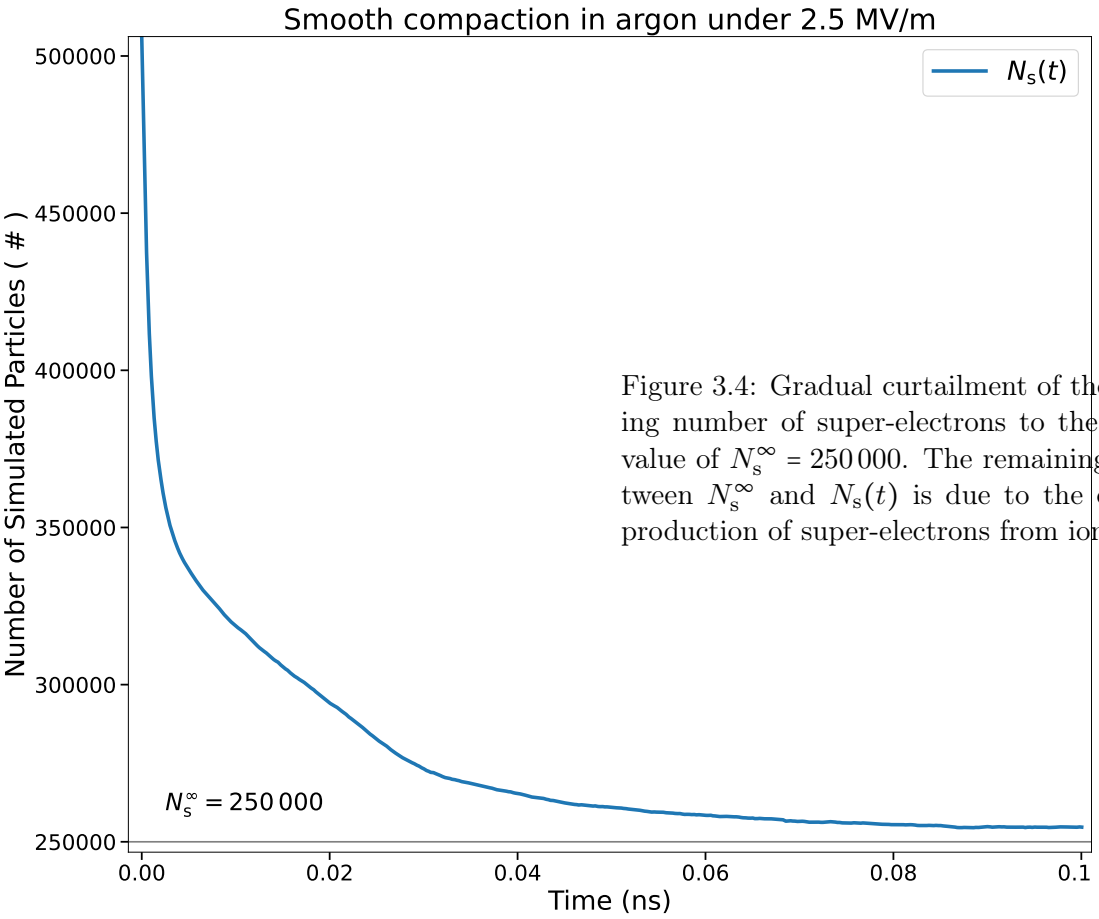

Figure 3.4: Gradual curtailment of the exceeding number of super-electrons to the nominal value of $N_s^\infty = 250\,000$. The remaining gap between N_s^∞ and $N_s(t)$ is due to the continual production of super-electrons from ionisation.

2. Enhancement : $g_s(\varepsilon, t) \to g_s^\infty(\varepsilon)$

The EEDF of a typical swarm in an electrified gas will decay at an exponential rate steeper than a Maxwellian (B.13) but not as steep as a Druyvesteyn distribution (2.125). In numerical simulations, this would mean that if we wanted to increase the maximally observed energy ε_{max} of an electron in the swarm by a factor ξ, we would have to increase our number of super-electrons by an exponential factor $\exp(\xi)$.

Ideally, we would like to have a totally different dependence, for instance that increasing ε_{max} by a factor ξ only requires to increase N_s by a factor $\ln \xi$. This is what motivated us to propose the following (nominal) target spectrum in [813, eq.(18)]:

$$g_s^\infty(\varepsilon) = \frac{N_s^\infty}{\varepsilon_c \ln(1 + \varepsilon_q/\varepsilon_c)} \frac{1}{1 + \varepsilon/\varepsilon_c} , \tag{3.23}$$

$$\text{where :} \begin{cases} \text{Cutoff energy :} & \varepsilon_c = 15\,\text{eV} , \\ \text{Upper energy } \varepsilon_q : & \sum_{n=1}^{N_s} (\varepsilon_n < \varepsilon_q) = q N_s , \quad \text{with } \ 0.92 < q \leq 1 . \end{cases}$$

It is a logarithmic distribution with a cutoff energy $\varepsilon_c = 15\,\text{eV}$ around the ionisation thresholds of constituent molecules and atoms in air. This spectrum (3.18) emerges naturally from the desire of having an equal number of super-electrons per logarithmic energy interval from its cumulative distribution:

$$\acute{g}_s^\infty(\varepsilon) = \frac{\ln(1 + \varepsilon/\varepsilon_c)}{\ln(1 + \varepsilon_q/\varepsilon_c)} , \tag{3.24}$$

which obviously has to be curbed at lower energies by ε_c and restricted to an upper boundary ε_q

in order to be normalisable. This upper boundary ε_q is not a fixed quantity but adapts to the swarm. It is the q quantile of the super-electron distribution in energy.

In specific cases, it may be interesting to have $q < 1$ which is robust against spectra with large unoccupied gaps in the energy spectrum. This is useful for the study of concurrent runaway MeV electrons in coexistence with a bulk thermal population at low electric fields below conventional breakdown (as in fig. 5.27). Having $q < 1$ does not imply more freedom on the statistical weights of the last $1-q$ fraction of high-energy super-electrons but less strain* on the target weights w^∞ of high-energy super-electrons, who would otherwise be significantly lower. Visually, the strain exerted on the weights w corresponds to vertical distance between points lying above the green curve on the top graph of figure 3.3.

The target weights w^∞ are related to the real electron conservation equation by (3.18):

$$w^\infty(\varepsilon,t) = \min\left(\frac{g_e(\varepsilon,t)}{g_s^\infty(\varepsilon)}, w^*_{\min}(t)\right), \quad \text{where } w^*_{\min}(t) \equiv N_e(t) w_{\min} \tag{3.25}$$

What critically restricts the strain is the *absolute* minimal weight $w^*_{\min}(t)$. It expresses the fact that a super-electron may not represent a smaller number of real electrons than $w^*_{\min}(t)$. This minimal weight depends on the total number of real electrons $N_e(t)$ and the minimal *relative* weight $w_{\min}$. The effect of this minimal weight is conspicuous on figure 3.3 both on the target weight w^∞ (top) as on the spectrum g_s^∞ (bottom) from the green (—) and orangered (—) curves. While the user is free to fix the (relative) minimal weight $w_{\min}$ at will, this value should be physically meaningful. For mere illustration, we show in the next chapter section 4.2 what happens in case one lets $w_{\min} = 0$.

The minimal threshold $w_{\min}$ affects the target spectrum $g_s^\infty(\varepsilon,t)$ through (3.18) and (3.25). Although it is impossible to predict with exactitude, $g_s^\infty(\varepsilon,t)$ will nonetheless decay exponentially at the same rate as the high-energy tail of the physical spectrum $g_e(\varepsilon,t)$ of the swarm. This is because once the statistical weight reaches the constant threshold $w^*_{\min}$, the super-electrons directly reflect the physical spectrum. This exponential tail is visible on the right side of figure 3.5 and thus explains the orangered broken tail of the target spectrum g_s^∞ on figure 3.3-bottom.

3. Compaction

As we said earlier, curtailment and enhancement performed together constitute a compaction step. Curtailment consists in removing super-electrons stochastically and raising the weights of those that permain†. Enhancement is performed by increasing the number of super-electrons at a certain energy and dividing their weights.

From a given distribution of nominal target weights $w^\infty(\varepsilon,t)$ (3.25), we may estimate:

$$\text{the desired change in the number of super-electrons } = \frac{w(\varepsilon,t)}{w^\infty(\varepsilon,t)}, \tag{3.26}$$

For each super-electron of weight w, energy ε and at a time t, there are two possibilities:

1) Curtailment: when $w < w^\infty$, this means that these super-electrons are too numerous and will have to be discarded according to:

$$\text{the probability of vanishing : } \mathcal{P}^\infty(\varepsilon) = 1 - \frac{w(\varepsilon,t)}{w^\infty(\varepsilon,t)}. \tag{3.27}$$

*If a super-electron is under "strain", it will be split into fragments of smaller weights. The stronger the strain, the more fragments will be produced.

†"Permanere" in Latin: "to continue to be". Although still present in most Latin languages, English contented itself with its closest sibling "to remain". Nevertheless, "to permain" evokes the ability to pass through, endure; which I thought corresponds astutely to the meaning ascribed here.

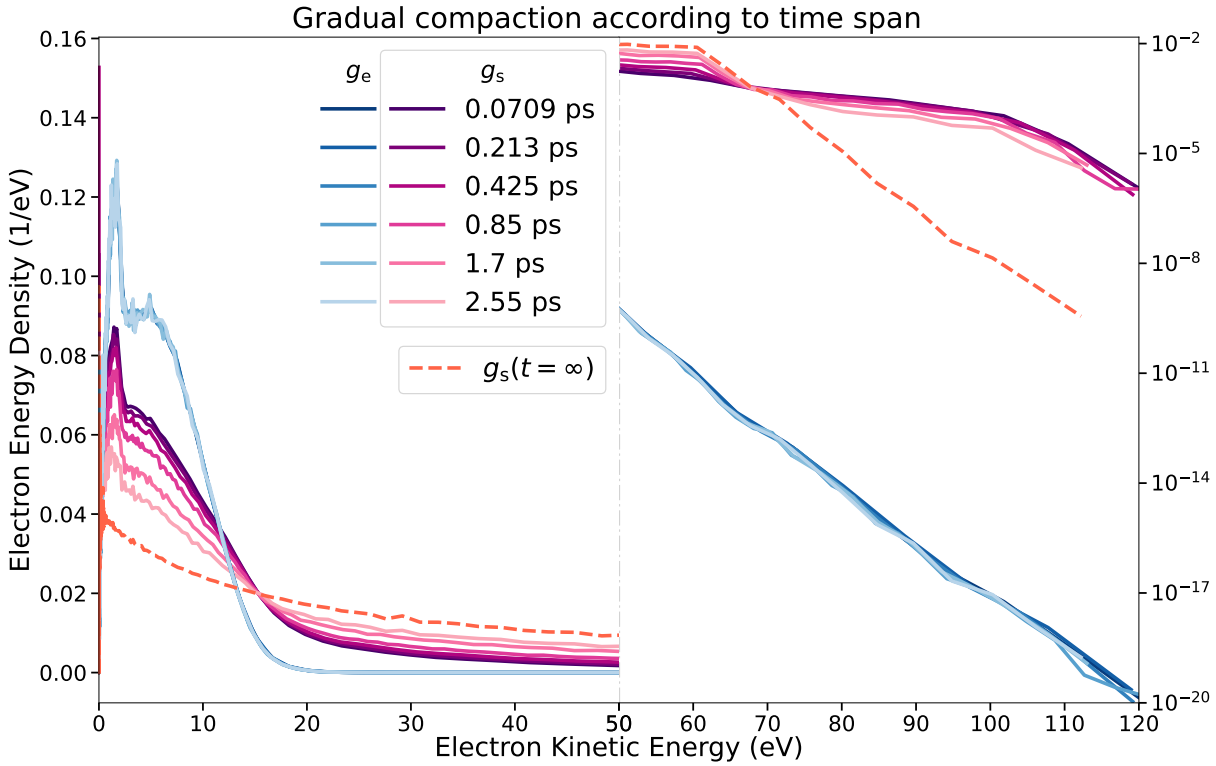

Figure 3.5: The intensity of the compaction depends on the time span given δt. After an infinite time the super-electron energy density, in tones of violet $g_s(t) \xrightarrow{t\to\infty} g_s^\infty$, converges to the desired spectrum and at the same time $N_s(t) \xrightarrow{t\to\infty} N_s^\infty$. Meanwhile, the physical spectrum, $g_e(t)$ in tones of blue, is preserved *on average* as it should. The midline separation enables to see, on a logarithmic scale, the enhancement of the spectrum at higher energies by comparing the magnitudes of the violet g_s (super-electron) to the blue g_e (physical electron) curves.

2) Enhancement: when $w > w^\infty$, this means that there is scarcity of super-electrons and an average ratio of $(w(\varepsilon,t)/w^\infty(\varepsilon,t))$ more, will have to be added by splitting existing super-electrons into two or more and distribute their weights evenly.

Old. In our original method [813, eq.(7)] the target weights $w^\infty(\varepsilon)$ were obtained according to (3.25) from the *nominal* spectrum g_s^∞. The algorithm, written in Python, that instantly compacts a spectrum g_s to g_s^∞ is accessible on `https://osf.io/c6wyh`. Again, this means that if the current distribution in super-electrons g_s is very different from the nominal g_s^∞, the compaction will be very strong: a lot of super-electrons will have to be discarded to make space for those that are to be added.

New. Just as in the curtailment paragraph on p. 99, $N_s(t)$ gradually converges to N_s^∞ on figure 3.4, so should the compaction bring the spectrum $g_s(\varepsilon,t)$ smoothly to $g_s^\infty(\varepsilon)$ as illustrated in figure 3.5. Instead of adopting the perspective of a target spectrum $g_s^\star(\varepsilon,t)$ it is easier to think at the level of individual super-electrons.

At a given time t, each super-electron at an energy ε, is expected to adopt the nominal weight $w^\infty(\varepsilon,t)$ determined by equation (3.25). This weight w^∞ depends on the physical spectrum $g_e(\varepsilon,t)$ which can fluctuate. Nonetheless, we can expect that g_e will relax very quickly to a more

or less stable distribution increasing exponentially but uniformly. Under these conditions (steady or slowly varying g_e), we may imagine that the super-electron will follow an instantaneous target weight $w^*(\varepsilon, t+\delta t)$ bounded by two conditions on the interval of time considered δt:

$$\begin{cases} \lim\limits_{\delta t \to 0} w^*(\varepsilon, t+\delta t) = w(\varepsilon, t) \ , & \text{(3.28a)} \\ \lim\limits_{\delta t \to \infty} w^*(\varepsilon, t+\delta t) = w^\infty(\varepsilon, t) \ . & \text{(3.28b)} \end{cases}$$

Still, we need to decide how fast should $w^*(\varepsilon, t)$ converge to $w^\infty(\varepsilon)$. We do this by ascribing a relaxation time τ_s to the target weight $w^*(\varepsilon, t)$. Taking into account the boundary limits (3.28), the expected number of super-electrons relaxes as follows:

$$\frac{w^\infty(\varepsilon)}{w^*(\varepsilon, t+\delta t)} = 1 - \mathrm{e}^{-\delta t/\tau_s}\left(1 - \frac{w^\infty(\varepsilon)}{w(\varepsilon, t)}\right) \ . \tag{3.29}$$

The relaxation time may be chosen as one wishes. It may, but needs not, be equal to the relaxation time of $N_s(t)$ as in (3.19). Presently, we set it as:

$$\tau_s = \frac{1}{\bar{\nu}_s \kappa_r} \ , \tag{3.30}$$

where we remind that the compaction reactivity $\kappa_r = 3$, but can be adjusted to one's preference.

From w^*, irrespectively of whether $w \lessgtr w^*$, we define a generalised 'probability' $\mathcal{P}^*(\varepsilon, \delta t)$ both for curtailment and enhancement by replacing w^∞ in (3.27) with w^*. The resulting probability now depends on the regular time interval δt chosen for performing the compaction (we recommend using 3.1). The compaction algorithm works in the following way.

A compaction step on a time interval δt involves a test based on the vanishing 'probability':

$$\mathcal{P}^*(\varepsilon, \delta t) = \left(1 - \frac{w(\varepsilon, t)}{w^\infty(\varepsilon)}\right)\left(1 - \mathrm{e}^{-\frac{t}{\tau_s}}\right) \tag{3.31}$$

For every super-electron n roll a uniformly distributed random variable $x_n \in [0\,;1]$ and consider the individual generalised probability $\mathcal{P}^*_n \equiv \mathcal{P}^*(\varepsilon_n)$ of vanishing.

- ▸ Curtailment $1 > \mathcal{P}^*_n(\delta t) > 0$:

$$\begin{cases} x_n \le \mathcal{P}^*_n & \text{the super-electron is discarded :} \quad w_n(t+\delta t) \to 0 \\ x_n > \mathcal{P}^*_n & \text{the super-electron permains (survives) :} \quad w_n(t+\delta t) \to w^*(\varepsilon_n, t+\delta t) \end{cases}$$

- ▷ Enhancement (splitting) $\mathcal{P}^*_n(\delta t) < 0$, the super-electron is split into :

$$\begin{cases} x_n \le |\mathcal{P}^*_n| \% 1 & \lceil |\mathcal{P}^*_n| \rceil \text{ fragments} : w_n(t+\delta t) \to \dfrac{w_n(t)}{\lceil |\mathcal{P}^*_n| \rceil} \\ x_n > |\mathcal{P}^*_n| \% 1 & \lfloor |\mathcal{P}^*_n| \rfloor \text{ fragments} : w_n(t+\delta t) \to \dfrac{w_n(t)}{\lfloor |\mathcal{P}^*_n| \rfloor} \end{cases}$$

In the last equations of the frame, '$a\%1$' represents the fractional part of the real number a, '$\lfloor a \rfloor$' the floor and '$\lceil a \rceil$' the ceiling.

With this probability $\mathcal{P}$ dependent on the time interval δt (chosen as 3.1), we show in figure 3.5 how the enhanced super-electron spectrum g_s gradually converges to g_s^∞ (orangered - - -). The convergence rate is determined by the super-electron relaxation time τ_s.

3.3.3 Transport Coefficients

Transport coefficients obtained from swarm Monte Carlo simulations may be used in the fluid model (2.126) to emulate self-consistency through (2.134). Such codes combining fluid and particle simulation are called hybrid code, of which the work by Li [585] is a prominent example.

Although we did not undertake this route of investigation, we nonetheless calculate transport coefficients in order to compare our results with kinetic solvers (sec. 4.3.2) and experimental data (sec. 4.3.3). The third use of calculating transport parameters is to compare how swarms behave under different gas conditions (sec. 5.2).

Reflecting what we highlighted on page 86, we distinguish the flux and bulk transport coefficients as derived from our swarm statistics [588, p.1026:eqs.(11–7)]:

Flux coefficients : averages

$$-\dot{\mu}_\mathrm{e}\mathbf{E} = \dot{\mathbf{v}} \simeq \langle \mathbf{v} \rangle \pm \tilde{\mathbf{v}} \tag{3.32a}$$

$$\dot{\underline{D}}_\mathrm{e} \simeq \langle \underline{D}_\mathrm{e} \rangle \pm \tilde{\underline{D}}_\mathrm{e} \tag{3.32b}$$

Flux coefficients : samples

$$-\bar{\mu}_\mathrm{e}\mathbf{E} = \bar{\mathbf{v}} = \frac{1}{N_\mathrm{e}} \sum_{n=1}^{N_\mathrm{s}} \mathbf{v}_n w_n \tag{3.33a}$$

$$\bar{\underline{D}}_\mathrm{e} = \overline{\mathbf{r} \otimes \mathbf{v}} - \bar{\mathbf{r}} \otimes \bar{\mathbf{v}} \tag{3.33b}$$

$$= \frac{1}{N_\mathrm{e}} \sum_{n=1}^{N_\mathrm{s}} (\mathbf{r}_n - \bar{\mathbf{r}}) \otimes (\mathbf{v}_n - \bar{\mathbf{v}}) \tag{3.33c}$$

Bulk coefficients : averages

$$-\mu_\mathrm{e}\mathbf{E} = \mathbf{v}_\mathrm{d} \simeq \langle \frac{\mathrm{d}\bar{\mathbf{r}}}{\mathrm{d}t} \rangle = \langle \mathbf{v} \rangle + \langle \overline{\nu_\mathrm{e}\mathbf{r}} - \bar{\nu}_\mathrm{e}\bar{\mathbf{r}} \rangle \tag{3.34a}$$

$$\underline{D}_\mathrm{e} \simeq \frac{1}{2} \Big\langle \frac{\mathrm{d}\langle \mathbf{r} - \bar{\mathbf{r}} \rangle^{②}}{\mathrm{d}t} \Big\rangle = \frac{1}{2} \Big\langle \frac{\mathrm{d}\overline{\mathbf{r}^{②}}}{\mathrm{d}t} \Big\rangle - \frac{1}{2} \Big\langle \frac{\mathrm{d}\bar{\mathbf{r}}^{②}}{\mathrm{d}t} \Big\rangle \tag{3.34b}$$

Bulk coefficients : samples

$$\bar{\mathbf{v}}_\mathrm{d} = \bar{\mathbf{v}} + \overline{\nu_\mathrm{e}\mathbf{r}} - \bar{\nu}_\mathrm{e}\bar{\mathbf{r}} \tag{3.35a}$$

$$\bar{\underline{D}}_\mathrm{b} = \overline{\mathbf{r} \otimes \mathbf{v}} - \bar{\mathbf{r}} \otimes \bar{\mathbf{v}} + \overline{\nu_\mathrm{e}\mathbf{r}^{②}} - \bar{\nu}_\mathrm{e}\overline{\mathbf{r}^{②}} \tag{3.35b}$$

Bulk coefficients : coarse

$$\mathbf{v}_\mathrm{d} \simeq \frac{\Delta \bar{r}}{\Delta t} \tag{3.36a}$$

$$\underline{D}_\mathrm{e} \simeq \frac{\Delta \left(\overline{\mathbf{r}^{②}} - \bar{\mathbf{r}}^{②} \right)}{2\,\Delta t} \tag{3.36b}$$

The hazy notation requires some clarification. As a preliminary, one can view a graphical representation of the various concepts on figure 3.6 for a concrete simulation data in ambient pure N_2 above conventional breakdown.

Then, we remind the following conventions:

- $\bar{\mathbf{v}}$: the average *instantaneous* velocity of the swarm from all super-electrons (2.90). Therefrom, any overlined property e.g. $\overline{\nu_\mathrm{e}\mathbf{r}^{②}}$ is given by the average:

$$\overline{\nu_\mathrm{e}\mathbf{r}^{②}} \equiv \frac{1}{N_\mathrm{e}} \sum_{n=1}^{N_\mathrm{s}} \nu_\mathrm{e}(\varepsilon_n)\mathbf{r}_n^{②} w_n$$

- $\langle \mathbf{v} \rangle \pm \tilde{\mathbf{v}}$: the mean and standard error over the N_m samples of the average instantaneous velocity $\bar{\mathbf{v}}$.

- $\dot{\mathbf{v}}$: the ideal statistical *flux* velocity of the swarm, corresponds to the mean $\langle \mathbf{v} \rangle$ over an infinite set of samples from swarm experiments (under identical conditions).

- $\mathbf{v}_\mathrm{d}$: the *bulk* drift velocity of the swarm given by the overall displacement of the swarm's centre of mass $\bar{\mathbf{r}}$.

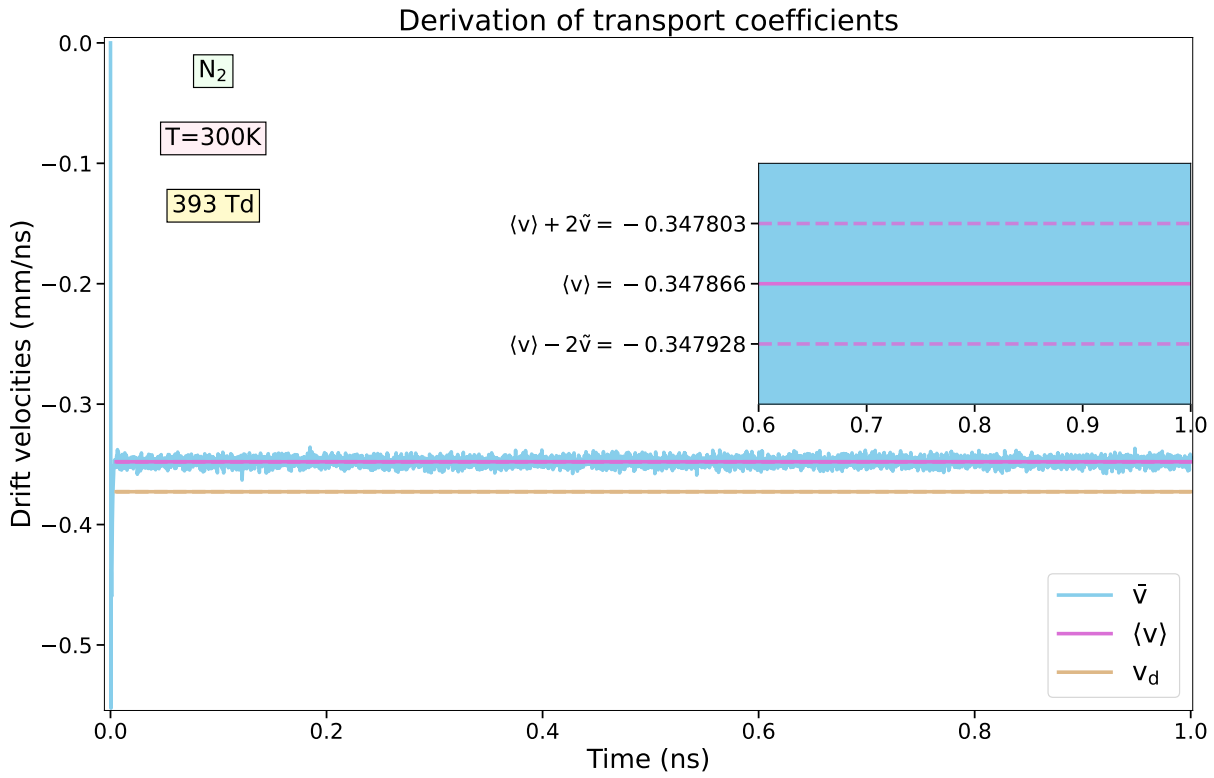

Figure 3.6: Derivation of flux $\langle \mathrm{v} \rangle \pm \tilde{\mathrm{v}}$ velocities from the 9948 samples of the average instantaneous swarm velocities $\bar{\mathrm{v}}$ for a swarm of $N_\mathrm{s} \sim 500000$ super-electrons in molecular nitrogen. The bulk velocity $\mathrm{v_d}$ differs from the flux velocity due to the growth of the swarm.

We have already described the difference between $\bar{\mathbf{v}}$, $\langle \mathbf{v} \rangle$ and $\dot{\mathbf{v}}$ in the previous chapter 2 section 2.3.1. We remind that the 95 % confidence interval of $\dot{\mathbf{v}}$ lies within $\sim \pm 2\tilde{\mathbf{v}}$: i.e. two standard errors about the mean $\langle \mathbf{v} \rangle$.

To suppress possible correlation between measurements $\bar{\mathbf{v}}_k$, they are sampled at a minimal time interval of $t_\mathrm{min} = 4\,\mathrm{ps}$. This time was determined by:

$$t_\mathrm{min} = 5/\nu_\mathrm{min} \,, \qquad \text{where} \qquad \nu_\mathrm{min} = \min_{\varepsilon > \varepsilon_\mathrm{min}} \left(n_\mathrm{air} \sigma_\mathrm{tot}(\varepsilon) \mathrm{v} \right) \,,$$

is an estimation of the minimal collision frequency of an average electron in the gas. The energy ε_min ensures that this frequency is not zero (at $\varepsilon = 0$). For simplicity, we set $\varepsilon_\mathrm{min} = k_\mathrm{B} T_\mathrm{air} 3/2$, although this energy could be a monotonically increasing function of the electric field. The minimal time t_min is a loose estimate of the swarm's memory retention time of its microstate at a previous time t_min ago, when the swarm is assumed in a steady state.

The estimation of diffusion tensors relies on the dyadic product (2.92). We see that with this definition of the dyad, the diffusion tensor is not symmetric.

In the present case, with our reference frame where $\mathbf{E} \parallel \hat{\mathbf{z}}$, symmetry implies that only diagonal elements of the diffusion tensor are expected to be non-zero; giving only two independent coefficients: the transversal $D_\perp$ (in any direction $\perp \mathbf{E}$) and longitudinal $D_\parallel$ (in both directions $\parallel \mathbf{E}$). Thus, we may write:

$$\underline{D}_\mathrm{e} = \begin{pmatrix} D_\perp & 0 & 0 \\ 0 & D_\perp & 0 \\ 0 & 0 & D_\parallel \end{pmatrix} . \tag{3.37}$$

In presence of a magnetic field, the situation is quite different. One can consult Bittencourt [73, p.645–7] where the diffusion tensor has diagonal and antisymmetrical elements in virtue of the rotation induced by the magnetic field. In the general case of arbitrarily oriented magnetic and electric fields, all elements are expected to be non-null.

Flux coefficients are derived as statistical averages (2.99) using (3.32–3.33) over the N_m samples extracted from our simulation in *steady-state* regime.

The detection of the regime is quite straightforward as seen on figure 3.6. We detect the "flat" region's onset where:

$$|\bar{\varepsilon} - \mathrm{median}[\bar{\varepsilon}]| < \mathrm{iqr}[\bar{\varepsilon}]\ . \tag{3.38}$$

The "iqr" is the interquartile range. This cheap requirement would not be robust on every data in general, but was found to fulfil satisfactorily our purpose in all our simulations. It mainly works thanks to the fact that the mean kinetic energy $\bar{\varepsilon}$ fluctuates little around its mean (see figure 3.7 on the side) as can the drift velocity in figure 3.6 for instance.

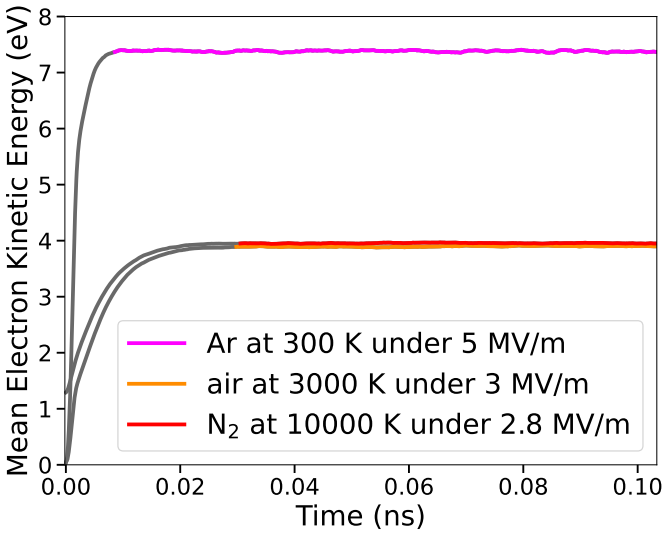

Figure 3.7: Steady-state regime (coloured region) detection based on the mean kinetic energy in (3.38), illustrated for simulations under diverse conditions. The grey zone is classified as a rapid transient relaxation lapse.

Bulk coefficients on the right side of (3.35) are seen to be related to the flux samples (3.33) on the left, but with the additional contribution from the relative growth rate of the swarm $\bar{\nu}_\mathrm{e}$ (2.94).

In principle, the derivation of *bulk* diffusion coefficients from a simulation could stem from equations (3.34) and (3.35); and performing the averaging over samples $\langle \ldots \rangle$ as in (2.99) just as we do for flux coefficients. This was however not the method we chose. To begin with, the fluctuations of $\bar{\nu}_\mathrm{e}$ are more important at lower electric fields because ionisation comes from electrons of higher energies, whereas bulk properties of diffusion and drift are attributable to all electrons regardless of their energies. Statistically, this means that our estimation of $\bar{\nu}_\mathrm{e}$ is deteriorated in quality (see p. 77). With the algorithm of particle weights described in the previous section 3.3.2, the resolution of the electron high-energy tail is enhanced.

Notwithstanding, the fluctuations over $\bar{\nu}_\mathrm{e}$, howsoever attenuated, are amplified anyway when multiplied by the centre of mass' displacement $\bar{\mathbf{r}}$ as in (3.35). The bulk coefficients would then be obtained from the subtraction of two quantities $\overline{\nu_\mathrm{e}\mathbf{r}} - \bar{\nu}_\mathrm{e}\bar{\mathbf{r}}$ whose fluctuations are amplified as time flows. This is why using (3.34) and (3.35) to derive bulk coefficients is *deprecated*.

Instead, we use the 'coarse' method (3.36) based on the average displacement $\Delta\bar{\mathbf{r}}$ and spread $\Delta(\overline{\mathbf{r}^{②}} - \bar{\mathbf{r}}^2)$ of the swarm over a lapse of time Δt. This actually corresponds more closely to the overall effect of transport parameters which is measured experimentally. Further information can be found in a dedicated subsection 7.3.1 to swarm experiments in the second part, together with the references therein.

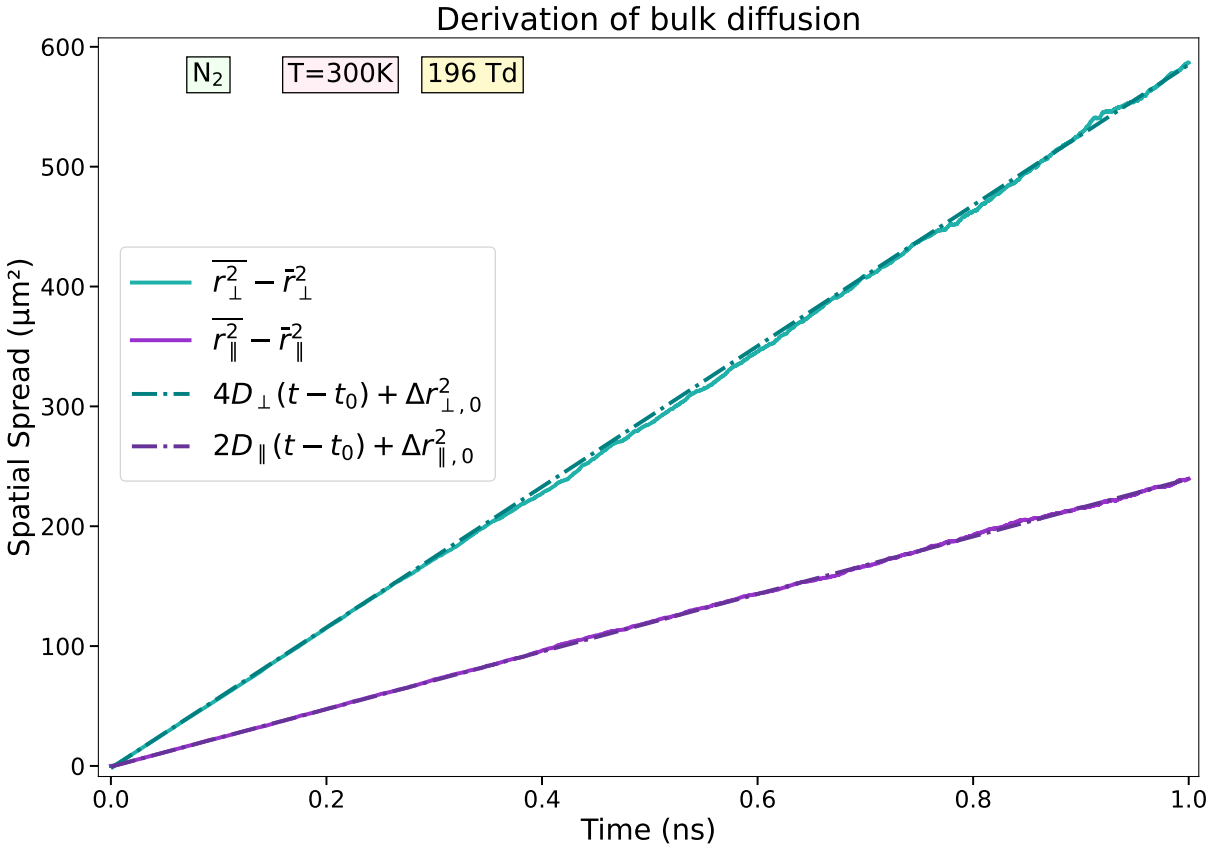

Figure 3.8: Linear regression over the steady-state region in a simulation in order to derive the bulk transversal $D_\perp$ and longitudinal $D_\parallel$ diffusion coefficients with (3.36), but with (many) more sample points ($N_\mathrm{m} = 9868$). The notation $\Delta r_{\perp,0}^2$ is a shorthand for $\overline{r_\perp^2(t_0)} - \bar{r}_\perp^2(t_0)$.

To make our estimations less "coarse", instead of using two points only, we make a linear regression on the steady state region determined through (3.38). The present method, illustrated in figure 3.8, is an improvement over Li *et al.* [588, eqs.(11–16)], which allegedly relies only on two points and thus informs not about the uncertainty. This improvement is of fundamental importance since because of our spectrum tail enhancement algorithm (compaction), our bulk data is contaminated with more noise (see discussion in previous subsection 3.3.2).

The same method is used for estimating the swarm exponential growth rate $\bar{\nu}_\mathrm{e}$; a linear regression on the logarithm of the number of electron $\ln N_\mathrm{e}$:

$$\nu_\mathrm{e} \simeq \frac{\Delta \ln N_\mathrm{e}}{\Delta t}\,, \tag{3.39}$$

which is exemplified on figure 3.9 for various electric fields in pure argon.

We note that higher order transport coefficients may also be calculated as done in Kawaguchi *et al.* [482, p.10–11:§3.3] which is useful for comparison with leading-edge experimental results from the same research team [483].

The extraction of transport coefficients concludes the numerical algorithms and methods used in our simulations. Before moving to the results chapter 5, we dedicate the next chapter 4 to tackling some issues and important remarks relative to the implementation of our simulations.

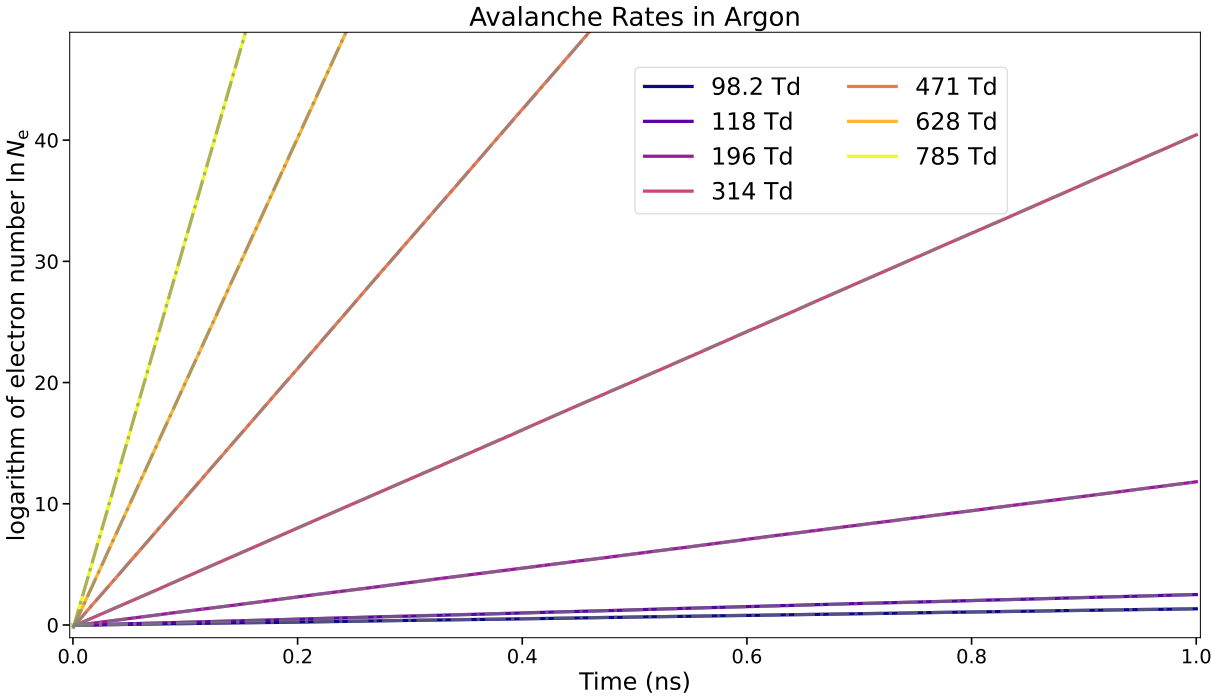

Figure 3.9: The derivation of the electron multiplication rate ν_e from the exponential growth of the swarm is very accurate due to the attenuated fluctuations of $\ln N_e$ from the logarithm. The grey dash-dotted curves (–·–) show the linear regression from which the multiplication (or 'avalanche') rate ν_e is derived.

Chapter 4

Scrutiny and Examination

In the process of implementing our model of electron swarms in electrified gases, there are many hurdles to overcome and issues to handle. Some may be related to the intricacies of the numerical model whereas others stem from more fundamental questions. Before we present results, we must be very vigilant of how they were obtained, what assumptions do they rely on and what could put their relevance under question.

In this chapter, we discuss and regroup specific issues related to modelling and how we handle them concretely. It is divided into three parts:

- 4.1 : the representation of cross sections and collisions,
- 4.2 : the handling of super-electrons,
- 4.3 : assessment of our model: code together with cross sections.

Here, we first focus on some fundamental physical aspects such as cross section coherence, collision rate consistency, energy conservation, axial symmetry, etc. Then, we compare transport swarm parameters with a kinetic solver named BOLSIG+ and with experimental data of swarm experiments under ideally uniform conditions. In the next chapter 5 dealing with results, we will expound further the underlying hypothesis of the model in relation to plasmas in electric discharges.

4.1 Cross sections

The cross sections (CS) we use are stored in files each specific to a species. Those files are freely available and will be uploaded to the LXCat server in the near future. We use two formats and their combination:

- Numerical: two columns, [electron energy $\varepsilon[i]$; cross section $\sigma[i]$].
- Analytical: one row of parameters to be used in either of (11.61–11.64, 11.120) for electronic excitations or impact ionisation.
- Hybrid: numerical table at low energies to be extrapolated by an analytical formula at high energies (typically elastic and total cross sections).

Whenever possible, we recommend using a log-log interpolation scheme*:

$$\sigma(\varepsilon) = \sigma[i] \exp\left(\log(\varepsilon/\varepsilon[i]) \frac{\log(\sigma[i+1]/\sigma[i])}{\log(\varepsilon[i+1]/\varepsilon[i])} \right) \quad \text{for } \varepsilon[i] \leq \varepsilon < \varepsilon[i+1] ,$$

except at threshold of course, when $\sigma[i] = 0$, where a linear interpolation is needed.

In the following subsections we discuss the proper handling of cross sections near threshold, the consistency of a set of cross sections and a few words on the scattering (differential) CS.

4.1.1 Near threshold

The most important rule to verify for a cross section near threshold is that it annihilates at the very least at its excitation threshold $\mathcal{E}_{\text{th}}$. Failure to comply with this rule will cause some electrons to exit a collision process with a negative energy and completely ruin the simulation's statistics. Although this rule seems very simple and obvious, it can be put in danger as the description of a process becomes more involved.

In the most rudimentary description, a collision process is simply a double-column table with the incident electron energy $\varepsilon[i]$ mapped to the corresponding cross section $\sigma[i]$. In this case, one just needs to include a sanity check in the code to ensure that:

$$\sigma[i \leq i_0] = 0 \quad \text{where} \quad \varepsilon[i] \leq \mathcal{E}_{\text{th}} \ \forall i \leq i_0 \tag{4.1}$$

If the cross section is defined by an analytical fit f_σ, the problem amounts to verifying the identity $f_\sigma(\varepsilon < \mathcal{E}_{\text{th}}) = 0$.

As the modelling became more sophisticated, there were three situations in which this rule had to be enforced by other means: partial excitations from a vibronic band or from ionisation, rotational excitations and deexcitations.

Partial excitations

To make the code more efficient, some excitations are grouped together under a common cross section. This is the case of vibronic bands. Some databases on LXCat (`Phelps`, `Biagi`) divide the bands into subgroups with a common threshold as for instance $N_2(A\ ^3\Sigma_u^+ : v = 0 \to 4;\ v = 5{-}9;\ v = 10 - \dots)$. Then, the problem poses not itself. In our case, we subsampled the vibronic threshold in a band from probability ratios (either Franck-Condon-based or experimentally-based). There, the threshold had to be manually adjusted after sampling in order to lie always below the incident energy.

The most critical case was the Schumann-Runge continuum (and also the Herzberg pseudocontinuum) for O_2, whose excitation probability density we represented with an asymmetric shape (11.66). The energy loss $\mathcal{E}$ is distributed continuously between $\mathcal{E}_0 = 6.12\,\text{eV}$ and $\mathcal{E}_1 = 9.7\,\text{eV}$. If an electron has an energy ε such that $\mathcal{E}_0 < \varepsilon < \mathcal{E}_1$, the energy loss $\mathcal{E}$ must be sampled only up to ε.

Since the whole cumulative integral (3.12) is normalised on the full $[\mathcal{E}_0\,;\mathcal{E}_1]$ range, one must rescale the instance x sampled from a uniform random variable X. This rescaling is done by defining a new x':

$$x' = x/\acute{C}_{\text{M}}(\varepsilon) , \tag{4.2}$$

with $\acute{C}_{\text{M}}$ defined in the previous chapter (3.12). Note that the scaling for energies higher than the maximal loss $\mathcal{E}_1 < \varepsilon$, is equal to 1. This new x' should be used to find from (3.9) the corresponding loss $\mathcal{E}_0 < \mathcal{E} < \varepsilon$.

*Unlike some databases on LXCat that were interpolated linearly as can be seen on the "stone skipping" pattern in figures 16.3,16.7 of chapter 16.

A similar issue is present with partial ionisation from different subshells. We use the relativistic binary-encounter dipole model presented in the second part section 11.5. Normally, it is guaranteed that every partial process annihilates at its B_o binding energy:

$$\sigma_o(\varepsilon) = 0 \ \forall \varepsilon \leq B_o \tag{4.3}$$

To ensure that this remains true for all $\varepsilon < B_o$ a mask must be explicitly set to zero for all energies below B_o. Then, the sampling of each subshell can be performed according to the cumulative sum (3.6).

Rotational excitations

If rotational excitations are treated as other excitations with a well defined threshold marking the onset of their cross section, then there is nothing to worry about.

If, nonetheless, we treat rotational excitations as an inseparable component of elastic, and inelastic scattering (then forming rovibrational or rovibronic bands), then some additional care must be taken. We proposed to use the spectator model in order to emulate average energy losses due to rotational excitations in a scattering event. In this case, the probability of excitation to a certain rotational level varies according to the angle of scattering θ.

At a fixed (rotational) temperature, one can calculate the average energy loss $\Delta\mathcal{E}_{\text{rot}}(\varepsilon, \theta)$ (2.48) at a given angle θ and incident energy ε of the scattered electron. This energy loss should preferably be expressed as a fractional loss of ε instead of an absolute value. This is because, if this loss is accidentally subtracted on an electron who suffered an inelastic loss very close to the excitation threshold, its energy could become negative after subtracting the contribution from rotational and elastic scattering.

We define thus the general rule when one includes subsequent miniature energy losses:

> Losses due to elastic scattering and rotational excitations should be expressed as a fraction < 1 and be multiplied to the electron's energy ε_+ after the inelastic (vibrational, electronic) threshold was subtracted.

Failure to do so will provoke the occurrence of very rare events whereupon a negative or zero kinetic energy is attributed to an electron after an inelastic collision very near threshold. In practice, those energy losses are so minute compared to the rest that it does not matter much to include them in the simulation. However, for whatever reason, for example if one is interested in keeping track of the overall energy lost in different channels and decides to include such losses, then this precaution should be taken.

Deexcitations

Modelling deexcitations is very convenient thanks to the detailed balance formula, wherefrom the cross section for the deexcitation between states $b > a$ is given by (see chapter 7 eq.7.6):

$$\mathrm{d}\sigma_{a\leftarrow b}(\varepsilon - (\varepsilon_b - \varepsilon_a), \theta) = \frac{g_a}{g_b}\,\mathrm{d}\sigma_{a\to b}(\varepsilon, \theta)\frac{\varepsilon}{(\varepsilon - (\varepsilon_b - \varepsilon_a))}\,. \tag{4.4}$$

This equation represents the equilibrium of electron density currents that flow after an event that changes a molecule from state a to b and vice-versa. The statistical abundance of states a and b is represented by the factors g_a and g_b. It expresses the fact that cross sections $\mathrm{d}\sigma_{a\to b}$ are typically averaged over the initial g_a degenerate states but summed over the g_b final states. Electrons that excited a molecule will leave with a slower speed and this is expressed by the shift $\varepsilon - (\varepsilon_b - \varepsilon_a)$ in the denominator.

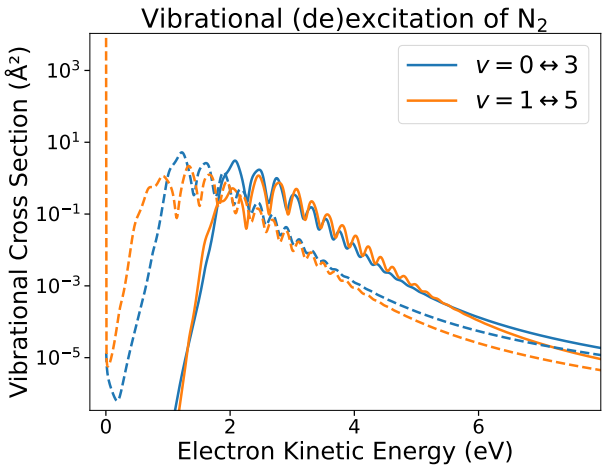

Figure 4.1: Undetected zero-division errors contaminating deexcitation cross sections (- - -) derived through (4.4)

In a numerical implementation, we can immediately spot the danger coming from sampled values $\varepsilon[i] \simeq (\varepsilon_b - \varepsilon_a) \equiv \varepsilon_{\text{th}}$. If somehow numerical errors contaminate $\varepsilon[i]$ and ε_{th} separately so that they do not match exactly, then an unphysically high value will contaminate the deexcitation cross section at $\varepsilon = 0$. This is illustrated in figure 4.1, where solid lines (—) are excitations from which deexcitations (dashed - - -) are deduced. Only one (out of 50) vibrational deexcitation ($v = 1 \leftarrow 5$) derived through (4.4) got a misrounded threshold value and therefrom an abnormally high value at the origin.

We recommend to check the narrowest interval $\delta\varepsilon$ in the sampled energies and after subtraction $\varepsilon[i] - \varepsilon_{\text{th}}$: discard all values situated closer to zero than half this interval.

4.1.2 Consistency

A set of assembled cross sections must obey at least two principles of consistency:

I. The sum of all cross sections must be equal to the "grand total" scattering cross section : $\sum_c \sigma_c \stackrel{?}{=} \sigma_{\text{tot}}$.

II. The elastic integral and momentum transfer cross sections are bound by the first moment of the elastic DCS : $\sigma_{\text{m}} = \int_\Omega \frac{\mathrm{d}\sigma_{\text{e}}}{\mathrm{d}\Omega}(1 - \cos(\theta))\,\mathrm{d}\Omega = \sigma_{\text{e}}(1 - \langle\cos\theta\rangle)$.

Summed/Total

The first principle corresponds to the first validation standard announced in Itikawa [435]. Nevertheless, Itikawa acknowledges that it can be hard to verify this relation for two reasons:

- At low energies, rapidly changing cross sections from resonant scattering can invalidate the consistency of the summed/total CS, because of uncertainties in the energy position of the peaks or simply because of a low resolution of datapoints.
- At high energies, the high uncertainty (~20–30%) over elastic integral cross sections can cause a systematic mismatch with the total CS.

To those two difficulties we add a third one:

- Some measured cross sections may have overlapping contributions, that is, the underlying processes are related. We found two major examples of such overlap:

  a) For species with attachment processes (O_2 and NO in our case), the *three-body attachment* cross sections form a proportion of the *resonant* vibrational excitations. It

is difficult to determine the "branching ratio" (proportion) which goes into the attachment channel. The attachment cross section $\sigma_{\text{3b-att}}$ should depend on the gas density n_{gas}, temperature (albeit slightly) and an efficiency ratio ξ_{att} of attachment per intermolecule collision. See part II section 11.3.4 and (11.43) for further information. Presently, we reckon that:

> Under identical temperature conditions although variable pressure, the sum of three-body attachment $\sigma_{\text{3b-att}}$ and vibrational excitation cross sections $\sigma_{\text{vib}}(0 \to v')$ of an electron with an electronegative molecule in a gas should remain constant:
>
> $$\sum_{v'=0}^{v_{\max}} \sigma_{\text{vib}}(0 \to v') + \sigma_{\text{3b-att}} \quad \text{ought to be constant}$$
>
> Ideally, resonant vibrational excitations and three-body attachment should be modelled as one process with a probability rate of decaying based on the lifetime of the electron-molecule compound and the branching ratio to attachment.

The study of Dujko *et al.* [235] showed that three-body attachment has a large impact on swarm transport parameters.

b) For collisions with molecules, one must discount predissociation from the dissociation cross section. Many high-lying electronic excited states may, after a while, decay into a repulsive state which subsequently dissociates. This process, known as predissociation, takes place after the collision and is not considered as a direct dissociation. Nonetheless, predissociation is accounted both in those high-lying electronic excitations and in the total dissociation cross section into neutral fragments (atoms in our case).

> To avoid counting predissociation events twice in the set of collisions, one has to subtract the predissociation branching ratio η_c times the corresponding electronic excitation cross sections σ_c from the total dissociation cross section σ_{diss}:
>
> $$\text{Discount predissociation :} \quad \sigma_{\text{diss}} - \eta_c \sigma_c \,.$$

Such precaution, although advised by Itikawa [439] and Kawaguchi *et al.* [482, p.51, p.5], is not necessarily followed in all studies [779, 964, p.1434]. The appendix D in part II discusses predissociation. Branching ratios η_{pd} for predissociation of N_2 and O_2 can be found in tables 11.6–11.7.

Notwithstanding these issues, given the facts that (i) electronic excitations have a minor contribution to total scattering, (ii) ionisation cross section are usually determined with a certainty comparable or superior to the total cross section, (iii) vibrational cross sections are negligible outside of the resonance region, and (iv) rotational cross sections are mostly mixed with pure elastic scattering; we can assume that discrepancies are mostly imputable to the definition of the (vibrationally) elastic cross sections. As a consequence, we recommend to perform the consistency check the other way around as:

$$\sigma_{\text{tot}} - \sum_{c \in \{\text{e}\} \setminus \{\text{rot}\}} \sigma_c \stackrel{?}{=} \sigma_{\text{e}} + \sigma_{\text{rot}} \,; \tag{4.5}$$

by subtracting all inelastic ($\{\text{e}\}$) except rotational (rot) processes from the total CS σ_{tot}, and comparing to the elastic CS σ_{e} in the database. This seemingly innocuous change of perspective can

actually reveal itself very useful in practice. Indeed, measurements of total scattering are often the most abundant and best resolved experimental data there are about a target molecule/atom. It would be a pity not to benefit from this advantage. Compared to this, elastic CS data from integrated beam measurements are sparse and not well determined due to extrapolation difficulties at large and especially at low angles. Moreover, elastic and rotational scattering in particular are equally important in the resonance region where they are actually very hard to measure accurately due to a rapidly changing DCS both in energy and angle. Finally, there has been recently a considerable improvement in matching theoretically calculated vibrational resonant cross sections to experimental high-resolution measurements (see section 11.3 next part).

Combined together, those reasons advocate for the benefit of deriving elastic cross sections as the subtracted product of inelastic processes from total scattering. These (vibrationally) elastic cross section from (4.5) are qualified as *residual*. They are introduced in the second part, chapter 11.1.5 in the equation (11.10), and compared in figures 11.14 with various cross-beamed measurements reported in the literature. A comparison with other databases is given in the figures of chapter 16. One very important note is that:

> *Residual* elastic cross sections are obtained for N_2, O_2, NO and Ar from their total cross section through (11.10) at 300 K. This residual cross section is assumed *independent* of the temperature (i.e. independent of the initial excited state)!

This assumption is equivalent to saying that all vibrationally elastic cross sections for a given species $v \rightarrow v$ are equal, something that is hardly supported by theory as seen in 4.2. A naive workaround would have been to set the residual elastic cross section only equal to the ground $v = 0 \rightarrow 0$ process and then add all other $v > 0 \rightarrow v > 0$ processes from theoretical calculations. We dared not use this workaround because the theoretical cross sections we use from Laporta *et al.*'s database on LXCat include only the resonant contribution. One can visit chapter 11.3 in particular graph 11.19 showing that one may not replace vibrationally elastic CS by their resonant contribution even in the resonance region!

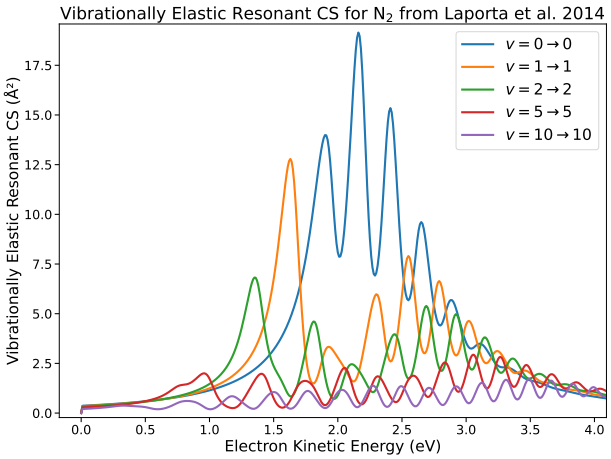

Figure 4.2: Vibrationally elastic cross sections from Laporta *et al.* [554] are very different depending on the vibrational excitation level v of the molecule.

Momentum/Elastic

Several times already, has it been noted in the literature [752, p.12:left column] that the integrated elastic cross section used in Monte Carlo simulations should correspond to the momentum transfer cross section used in Boltzmann solvers, according to the differential cross section used to represent scattering. Thus, if one tries different schemes for the implementation of the elastic differential cross section, the momentum transfer cross section should be kept as a constant while the elastic cross section should be adapted as:

$$\sigma_e = \frac{\sigma_m}{1 - \langle \cos\theta \rangle} \quad \text{with} \quad \langle \cos\theta \rangle \equiv \frac{\int_0^\pi \frac{d\sigma_e}{d\Omega} \cos\theta \sin\theta \, d\theta}{\int_0^\pi \frac{d\sigma_e}{d\Omega} \sin\theta \, d\theta} \,. \tag{4.6}$$

It might seem that this second requirement(4.6) clashes with the previous one (4.5) for the total cross section. Actually, this is not the case, because this time, the requirement acts upon the average deviation cosine $\langle \cos\theta \rangle$ which must be adjusted so as to respect (4.6). This might be a very useful guidance in checking extrapolated differential cross sections.

However, if one wishes to impose the shape of the DCS, then $\langle \cos\theta \rangle$ is defined as well. In this other case, the total cross section is not required to match the summed cross section and one must ensure that the momentum cross section σ_m is kept untouched [588, eqs.(7-10)]. This was noted by Kunhardt and Tzeng [542] when comparing the effect of the DCS shape on the electron energy distribution in electrified gases. Various analytical expressions of DCS in the first Born approximation are gathered in chapter 14 of part III.

The importance of preserving the momentum transfer CS (rather than the integral elastic CS) becomes greater at higher energies where the scattering is mostly forward peaked. Thus, even an apparently innocuous change in the DCS shape can severely affect the result and utterly undermine the comparisons made and even the conclusions drawn therefrom. Unfortunately, this precaution, although self-evident from a Boltzmann approach, is not necessarily taken in Monte Carlo simulations [677]. I, the author, must sadly repent myself for having fallen to this trap as well in Schmalzried and Luque [811].

The momentum transfer cross section is usually given only at lower energies; below either 100 eV (`Itikawa`) or 1 keV (`Phelps`). This means that, anyhow, the investigator must 'invent' first how to extrapolate $\sigma_m(\varepsilon > 100 \text{ eV})$, and then proceed to a standardised comparison. At higher energies (>keV), the screened Rutherford expression (11.4) is the predominant DCS shape used to model elastic scattering. Nevertheless, although a myriad of screening fits were used in the literature [445, 677, 683, 713, 896], no consensus was made so as to establish a common momentum transfer cross section. Each time, elastic scattering was invariably defined directly from the integration of the DCS. This means that great attention should be paid to which elastic DCS was used when comparing results from Monte Carlo simulations of thermal (or relativistic) runaway.

In summary there are two options:

A) If one wishes to be as precise as possible, the summed/total and elastic/momentum requirements can help to constrain the shape of the elastic DCS.

   1. Construct the total cross section from a solid base of experimental data (see part II chapter 11.6);
   2. Subtract all cross sections from inelastic processes (except rotational) to derive the vibrationally elastic cross section (11.10);

   This is the route we opted for.

B) On the other hand, if a shape is assumed for the DCS from the start (see the different existing DCS in chapter 14), then, one can only stick to the elastic/momentum requirement.

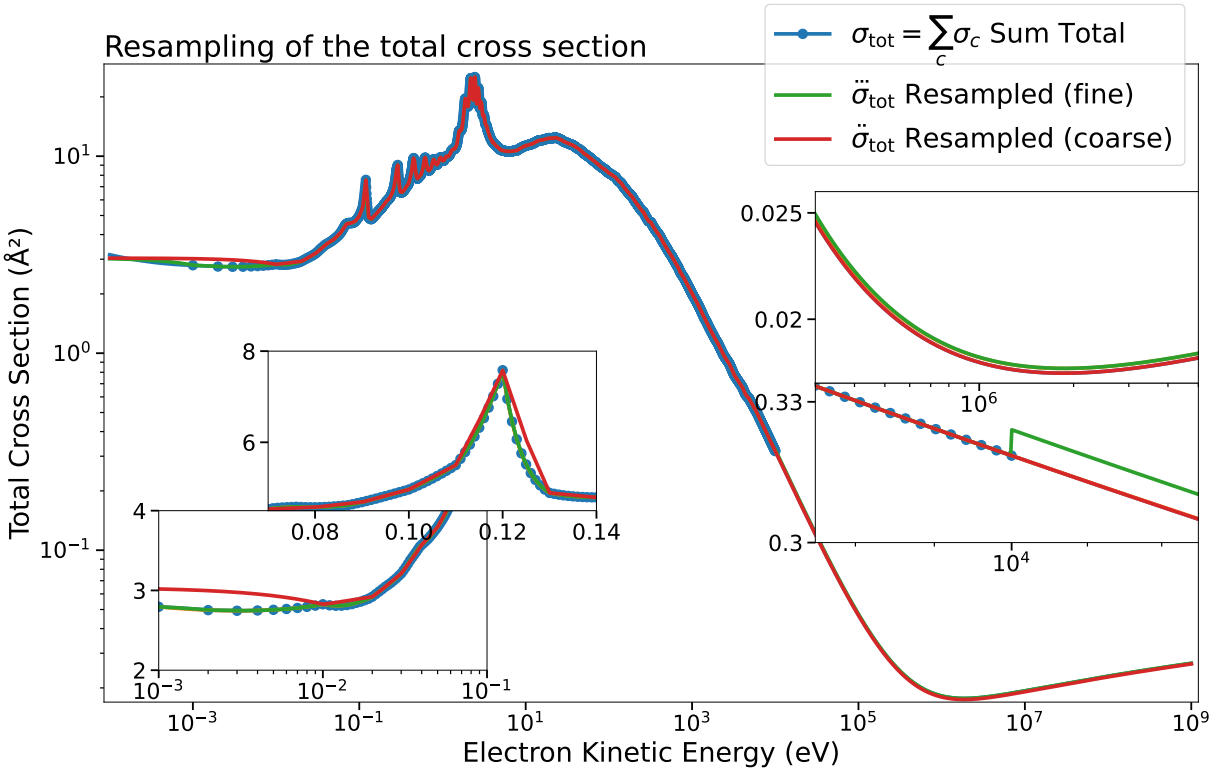

Figure 4.3: Resampling of the sum total cross section in a gas causes some very localised mismatches with the true sum of the cross section set. One must choose a good compromise between computational efficiency and exactitude. At high energies, the green curve is superposed with the blue (exact sum total).

Resampling

When we construct the total cross section for the whole gas, we have to add individual cross sections from each species and their excited states populated according to Boltzmann statistics for the given temperature T. The resulting cross section is thus called the "sum total" or "grand total" cross section σ_{tot}. It is of fundamental importance because it is used to calculate the collision frequency rate ν_{tot} at any electron energy ε as used in the null collision method (see previous chapter section 3.2.1).

In our simulations, this cross section must be called at every time step for an array of many electron energies. From a time efficiency perspective, it is important to make the computation of this cross sections as fast as possible so as not to drastically slow down our simulations.

For that matter, we use a *resampling* algorithm that regenerates an array of regularly-spaced energies so as to speed-up interpolation methods. The resampled energy space is divided into three regions delimited by a lower ($\varepsilon_<$) and upper ($\varepsilon_>$) boundaries:

- $\varepsilon < \varepsilon_<$: linear grid with $\delta\varepsilon_<$ interval,

$$\begin{cases} \text{if atomic nitrogen is present :} & \varepsilon_< = 0.5\,\text{eV and } \delta\varepsilon_< = 1\,\text{meV}, \\ \text{if molecular oxygen is present :} & \varepsilon_< = 1\,\text{eV and } \delta\varepsilon_< = 2.5\,\text{meV}, \\ \text{else :} & \varepsilon_< = 4\,\text{eV and } \delta\varepsilon_< = 5\,\text{meV}; \end{cases}$$

- $\varepsilon_< < \varepsilon < \varepsilon_>$: logarithmic grid of 2500 points;

- $\varepsilon_> < \varepsilon$: analytical Born-Bethe formula (11.139).

Above the threshold $\varepsilon_>$ set at 10 keV, we use the analytical Born-Bethe coefficients for the total cross section summarised in table 11.13. To have regularly spaced energies over multiple orders of magnitude is very challenging because the resolution required may vary a lot depending on local resonances (as seen in figure 4.3). Thus, we used a fine linear spacing at low energies followed by a logarithmic spacing up to 10 keV. The interpolation routine then first checks in which of the three (linear,logarithmic,analytical) regions we are situated and then interpolates (or calculates) the cross section.

For computational efficiency, the resampled total cross section $\ddot{\sigma}_{\text{tot}}(\varepsilon)$ is the one we truly use to perform the null-collision test in eq. (3.4) (p. 91). By resampling the total cross section, one must protect the collision selection algorithm (3.7) so as to treat cases when the cumulative sum does not amount exactly to 100 % of the resampled CS.

Due to sharp resonances and the fact that some cross sections are expressed fully analytically, the resampled cross section may not exactly amount to the true total from the sum of all individual collisions as shown in zoomed areas of figure 4.3:

$$\ddot{\sigma}_{\text{tot}} \neq \sigma_{\text{tot}} = \sum_c \sigma_c \,.$$

This difference is of course too small to affect the average swarm quantities but it does pose a danger on the handling of collisions. There are two cases to beware. Locally, the resampled cross section might either exceed or fall short of the sum as can be seen by the ratio of $\ddot{\sigma}_{\text{tot}}/\sigma_{\text{tot}}$ in the grey line on top of figure 4.4.

△ $\ddot{\sigma}_{\text{tot}} > \sigma_{\text{tot}}$: This means that we summon the routine for selecting the collision (step 4 on page 91) more frequently than the electron truly collides. This can be very simply amended. In the selection algorithm (3.6–3.7), if the total sum C_i falls short of the sampled value of x, then we simply ignore the collision. It is completely equivalent to the null-collision technique but with occasionally a loss of computational time in the rare case when $x > \sigma_{\text{tot}}/\ddot{\sigma}_{\text{tot}}$. Thus, the only damage is that every percent of difference represents on average some computation time lost by calculating cross sections for no avail.

▽ $\ddot{\sigma}_{\text{tot}} < \sigma_{\text{tot}}$: This is the situation that, if not minimised, may introduce some bias in the results. Fortunately, since the probabilities $p_c(\varepsilon) = \sigma_c(\varepsilon)/\ddot{\sigma}_{\text{tot}}$ in the cumulative sum (3.6) are scaled to $\ddot{\sigma}_{\text{tot}}$, all collisions whose cumulative sum $C_i(\varepsilon) < \ddot{\sigma}_{\text{tot}}(\varepsilon)/\sigma_{\text{tot}}(\varepsilon)$, are sampled without bias. The remaining collisions (above the grey line in fig. 4.4) are sheerly lost. One should then ensure that the effect of those collisions is benign at the energy ε considered. In particular, all ionisation collisions should always be positioned below this line. Otherwise, at high energies, where the analytical (11.139) expression $\tilde{\sigma}_{\text{tot}}$ might slightly differ from the actual sum σ_{tot}, the ionisation losses might be underestimated and this could affect the statistics of runaway electrons!

As seen from the discrepancies in figures 4.3 and 4.4, there is only one way to avert the risk of biasing collisions at high energies, it is to move the high-energy threshold $\varepsilon_>$, where the analytical expression $\tilde{\sigma}_{\text{tot}}$ is used, to even higher energies (100 keV or a few MeV). This is because at 10 keV, the Bethe approximation to the total inelastic cross section might be accurate to only a few percent (see discontinuity jump on right middle inset panel of fig. 4.3).

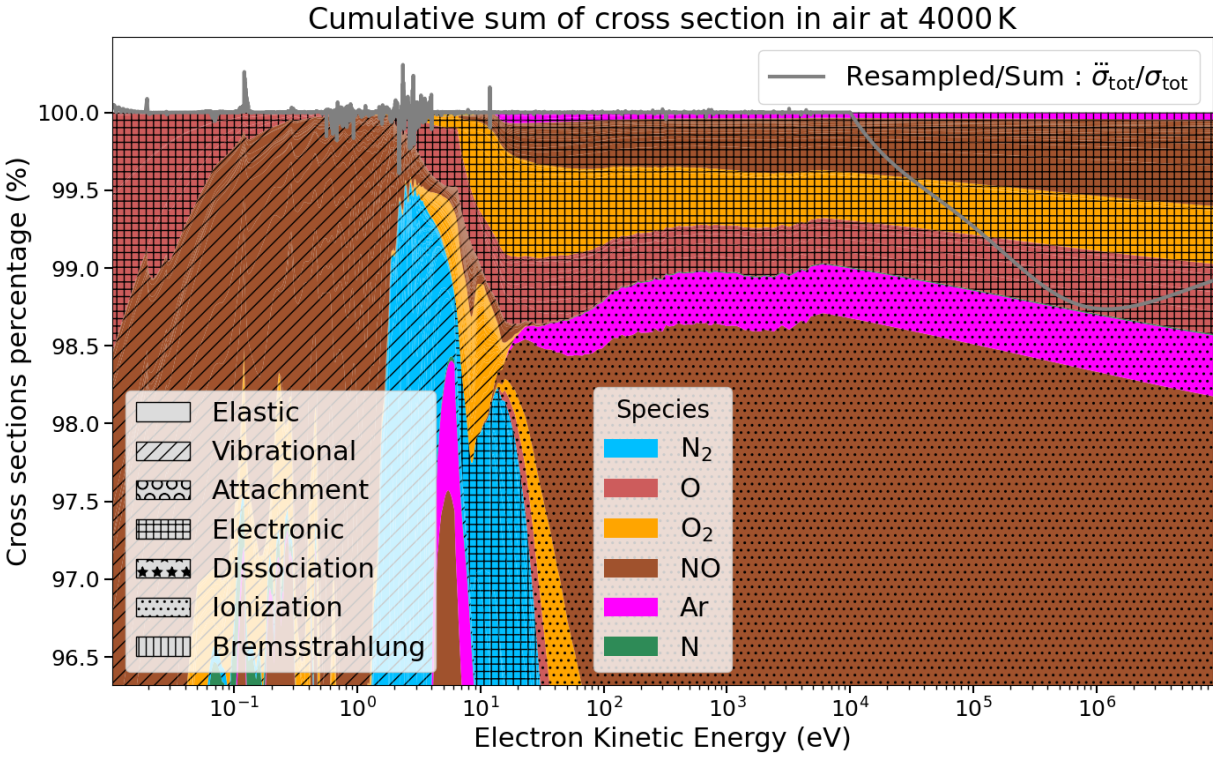

Figure 4.4: A 2D representation of the cumulative sum $\acute{C}_i(\varepsilon)$ of the set of cross sections for all collision processes according to the electron energy ε. The grey line on top of the graph display the ratio of the resampled – used for fast computation – to the exact sum total cross section : $\ddot{\sigma}_{tot}/\sigma_{tot}$

4.1.3 Scattering

Our code stochastically models the scattering of electrons throughout the whole energy spectrum. At high energies, the DCS becomes very forward peaked as seen on figure 4.5. Above 10 keV, the sampling of the scattering angle is done with (3.11). This expression does not account for the relativistic correction to the DCS where large angle scattering is significantly attenuated.

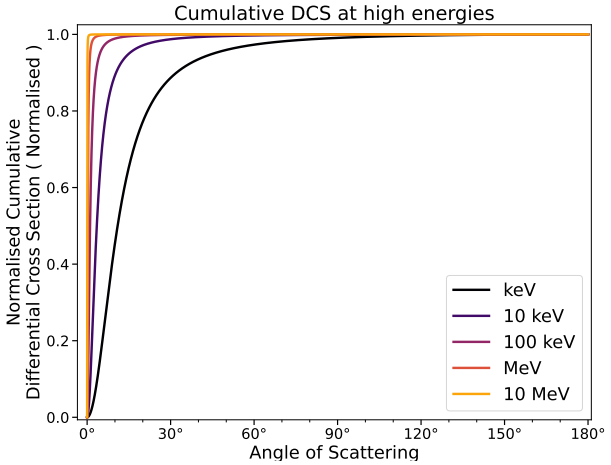

Figure 4.5: Illustration of increasingly forward-peaked scattering at very high electron energies scattering elastically from nitrogen molecules.

Although the difference between the relativistic expression (which includes the $1 - \beta^2 \sin^2\theta/2$ factor) and the non-relativistic DCS appears very small, we did not check whether the effect is negligible on the propagation of high energy electrons. At high energies, the elastic collision rate is high whereas the scattering probability distribution is very peaked at forward angles. Therefore, it is difficult to realise how a minor difference in the forward scattering could lead to a larger overall scattering after being repeated many times after many collisions.

To give an example, the probability that a MeV electron be deviated beyond 60° in a single elastic scattering event is 1.5×10^{-5} in the non-relativistic screened Rutherford approximation whereas it is 1.1×10^{-5} from a more accurate model. This difference persists even at lower energies. On average, there are 1.36 more high-energy electrons that are scattered beyond 60° at energies above 10 keV.

We did not check whether this makes a significant difference in the number of runaway electrons that can sustain themselves in air under a high-enough electric field. Nonetheless, we must advise the user against potential systematic biases dispersed in our code!

4.2 Super-Electrons

The clock of our simulation advances at a regular interval δt. Let us suppose that it has ticked N_t times and thus, that the simulation time is currently at $N_\mathrm{t}\delta t$. Here, we remind the elementary steps of our code comprised within one loop of the time interval δt:

1. First, we assign the null collision time δt_f (3.3) to every super-electron in our swarm.
2. a. We propagate super-electrons in their free motion (3.2) by δt_f
   b. We collide (or not) super-electrons with the (null-)collision scheme steps 3&4.

   Second, we alternate steps a. and b. as many times as they fit within one elementary time step δt until $(N_\mathrm{t}+1)\,\delta t < t + \delta t_\mathrm{f}$.
3. Third, we perform measurements of quantities used to derive average properties of the swarm (see section 3.3.3).
4. Fourth, we compact our electron swarm according to the spectral enhancement $g_\mathrm{s}^*(\varepsilon)$ that we chose (see section 3.3.2)

At the end of the loop, the clock of the code, previously at a time $N_\mathrm{t}\,\delta t$, has 'ticked' (advanced) of δt and is now at $(N_\mathrm{t}+1)\delta t$.

Of the many points that one must worry about when modelling electron swarms with super-electrons, we will highlight here the three that, in our opinion, are most important regarding their effect on the statistics of the swarm.

I. $w_\mathbf{min} > 0$ We recall that the compaction algorithm, presented earlier in section 3.3.2, enables the user to probe the high energy regions of the swarm's spectrum at the cost of increasing the statistical noise due to a reduction of super-electrons at lower energies. The unique parameter that fixes the maximal resolution desired is the minimal weight ratio w_min which can be as small as one wishes but should never be put to zero if one wishes to preserve the decency of the results at the end of a simulation. What we mean by "decency" is illustrated in figure 4.6, whose sole purpose is to show what happens if one allows $w_\mathrm{min} = 0$.

II. Splitting The compaction algorithm is composed of two parts: curtailing and splitting. When we split a super-electron into two or more fragments there is an extremely important point to heed:

> All N super-electrons that are created after splitting one super-electron, should preserve the collisional free time δt_f that had been assigned to that original super-electron.

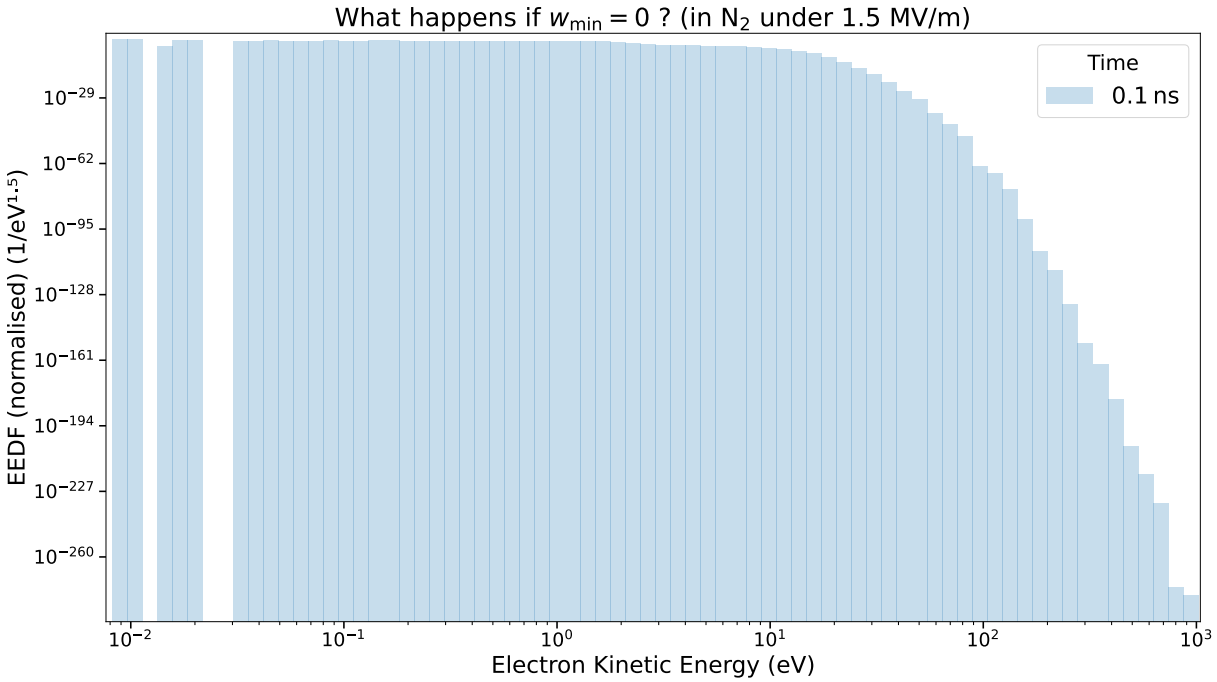

Figure 4.6: Demonstration of the power of our compaction algorithm when the minimal weight ratio $w_{\min}$ is set to zero; a deprecated use case. This causes the spectrum resolution to plunge down to the machine numerical precision limited to 10^{-323}. The results are going to be unpredictable because the resolution (number of super-electrons) at lower energies will not be properly constrained, and this will considerably amplify the stochastic fluctuations of average quantities.

This seems quite obvious but when one delves into the code, the structure of routines and calls may cause him or her to forget about the physical meaning of this precaution. In our case, when we added a super-electron in the simulation, we wonted using the same routine for (1) adding split super-electrons and (2) spawning secondary electrons from ionisation. The only change was to adapt the statistical weights w/N in the former case (1).

This fundamental mistake caused us to alter the physical collision rates of the swarm just because we would resample the random collision time δt_{f} on the split-electrons after it had already been assigned! At the end of step 2, all super-electrons have an assigned mean free time δt_{f} that would propagate them ahead of the current simulation time t. If at the end of the compaction step 4, we reassign a new δt_{f}, we are forcing some electrons to collide one (or twice, thrice, etc.) more within the interval δt than they should.

As a result, our average kinetic energy of the swarm got affected (lowered) because we were physically forcing collisions to occur with a higher probability. Such mistake is very far from obvious and actually very interesting, because it stems from the very implementation of compaction and collisional dynamics. This mistake was subsequently corrected and is not present neither in the results of our publications nor in this thesis.

III. Measuring For data analysis, we need to measure average quantities (energy, velocity, position, etc.) on a regular basis from which we derive transport coefficients (see section 3.3.3). This is done at step 3. At this instant, our super-electrons are *asynchronous*, their times t_n are all different according to the stochastic amount of time (successive δt_{f}) they have propagated within a time step δt. In order to eliminate bias:

> Before performing a measurement, the super-electrons must all be propagated to the time of the measurement t by the amount $t - t_n$ where t_n is the current time of the n^{th} super-electron.

Failure to do so will under-estimate the average kinetic energy, displacement and velocity of the swarm. This is because under the influence of an electric field, the velocity distribution of the electrons is anisotropic so that electrons tend to be more oriented opposite to the electric field. This means that if we omit to propagate them, their average quantity will always be slightly lower than it should really be at the time t of the measurement. This bias worsens as the reduced electric field E/n_{gas} is stronger.

These three mistakes, we committed them, of course. Fortunately, the essential checks that we describe in the next section 4.3.1 helped us uncover those mistakes and amend them.

4.3 Assessment

The code, whose underlying model we presented in chapter 2 and numerical implementation in 3, will be named ΘeRMIAA in order to enable unequivocal comparison with other sources. A more proper introduction will be given in the next chapter 5.

Before presenting results, we need to ensure that our model works coherently and as expected. By "model", we mean (1) the Monte Carlo code that we developed throughout (the present) part I and (2) the cross sections that we assembled in (the next) part II. In particular, we need to verify whether the augmentation of the Monte Carlo simulation with the compaction algorithm presented in section 3.3.2 does not physically affect the simulation results. We divided this section into three parts which are aimed at assessing different aspects of the model.

A. Physical: these are simple tests that enable to verify whether the code does not violate some general physical laws such as symmetry, energy conservation, collision rates and the convergence to thermal equilibrium.

B. Numerical: this test ensures that our results coincide with calculations from a different methodology (the kinetic approach) under identical input conditions and cross sections.

C. Experimental: finally, by comparing transport parameters with experimental measurements we will be able to assess the relevance of the cross sections that we assembled.

This structuring helped us identify severe discrepancies and subsequently enabled us to amend duly the issues encountered.

4.3.1 Checking physical consistency

Once a working implementation of the code is established, various useful checks can be made to help uncover possible fundamental inconsistencies. Those checks are only based on general principles and, as opposed to the *validation* step presented in the next chapter, they do not require any reference data to be compared with. We selected here four sanity checks as a preliminary verification of our code based on : isotropicity, energy conservation, collision rates and thermal equilibrium. Those tests might seem trivial, however, as we implemented a super-particle management scheme on top of an ordinary Monte Carlo implementation of electrons, we also have to ensure that this does not introduce artifacts.

Isotropicity

In absence of electromagnetic fields and in a homogeneous and isotropic medium, the velocity distribution of electrons ought to be isotropic. This successful check on figure 4.7a is to ensure that our implementation of scattering is not biased in a certain direction of space due to our choice of coordinates.

In presence of an electric field $\mathbf{E} \parallel \hat{\mathbf{z}}$, the velocity distribution should be axially symmetric about $\hat{\mathbf{z}}$. This is checked in figure 4.7b.

Energy conservation

The electron swarm does not conserve the energy it gets from the electric field because it loses a large part of it in inelastic collisions with the gas molecules. What is meant by "energy conservation" is that the kinetic energy of the swarm, the potential energy gained from the field and all the energy lost in collisions should amount to the initial kinetic energy of the swarm:

$$\mathcal{E}_{\text{kin}}(t) + \mathcal{E}_{\text{pot}}(t) + \mathcal{E}_{\text{coll}}(t) = \mathcal{E}_{\text{kin}}(0) \ . \tag{4.7}$$

By default, the initial potential energy is null. We have:

$$\mathcal{E}_{\text{kin}} = \sum_{n=1}^{N_{\text{s}}} w_n \varepsilon_n \ , \tag{4.8}$$

$$\mathcal{E}_{\text{pot}} = \sum_{n=1}^{N_{\text{s}}} w_n e\mathbf{E} \cdot (\mathbf{r}_n - \mathbf{r}_{n,0}) \ , \tag{4.9}$$

$$\mathcal{E}_{\text{coll}} = \sum_{n=1}^{N_{\text{s}}} w_n \left(\sum_i \Delta\mathcal{E}_{i,n} \right) \ , \tag{4.10}$$

where $\Delta\mathcal{E}_{i,n}$ represents the energy lost in the i^{th} collision of the n^{th} electron. To account for the energy lost in attachment, one must include the potential lost $e\mathbf{E} \cdot (\mathbf{r}_n - \mathbf{r}_{n,0})$ and the kinetic energy lost ε_n at the time of the attachment event.

Without our compaction algorithm (sec. 3.3.2), this total energy is conserved almost to the numerical precision of the computing machine ($\sim 10^{-16}$) as seen by the straight line on figure 4.8a. Much more interesting is to ensure that the compaction algorithm satisfies the energy conservation. This, seems to be verified on average from the 8 different runs that we performed for identical initial conditions in N_2 at 5 MV/m. Nevertheless, we also see very clearly that the "memory" of the initial energy deteriorates very fast with time. The ensemble deviation of the three reservoirs of energy dominates over the initial kinetic energy. This is because each of the three energy reservoirs in (4.7) increases with time as seen on figure 4.8b. Thus their sum loses precision ($\mathcal{E}_{\text{pot}}$ is negative, thus the difference between fluctuating big numbers becomes very imprecise).

What mostly increases the fluctuations in energy conserved is probably the fact that do not consider the spatial proximity of super-electrons. We place on equal footing all super-electrons that are at the same energy irrespective of their location in space. Suppose that two super-electrons share the same energy ε but one has travelled much farther opposite to the field than the other. If we remove the one which has travelled farther, the effect on the total potential energy $\Delta\mathcal{E}_{\text{pot}}$ will be stronger than if we removed the other one. One possible improvement of the compaction method, could be to include spatial binning as well as the present spectral binning.

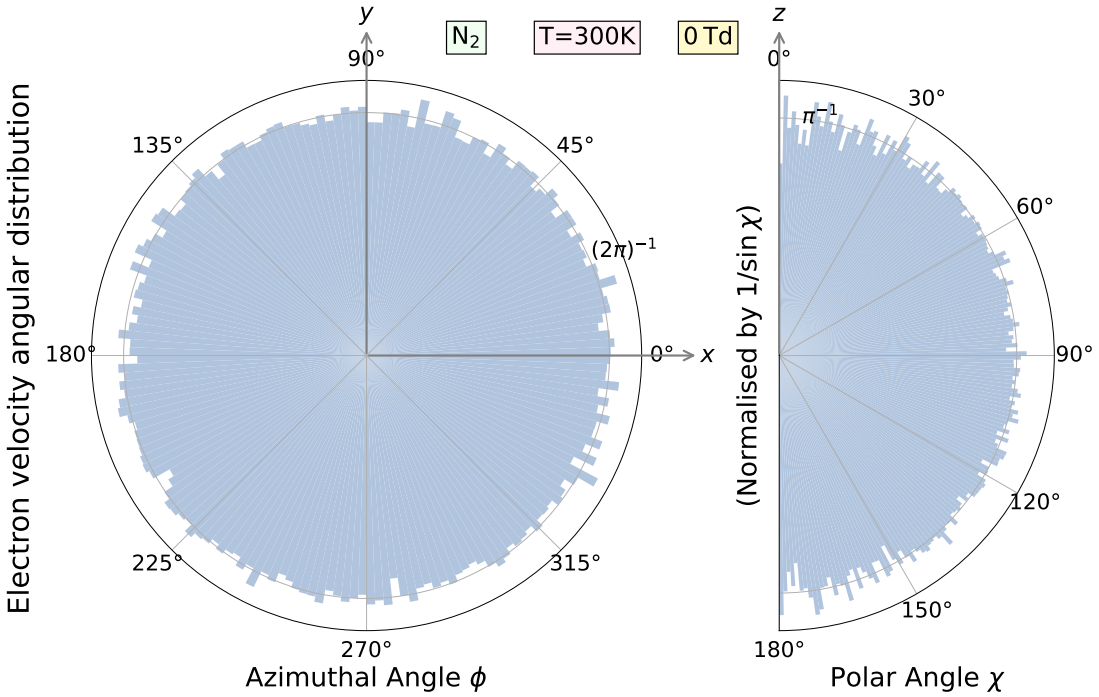

(a) In absence of any force, the electron velocity distribution is isotropic.

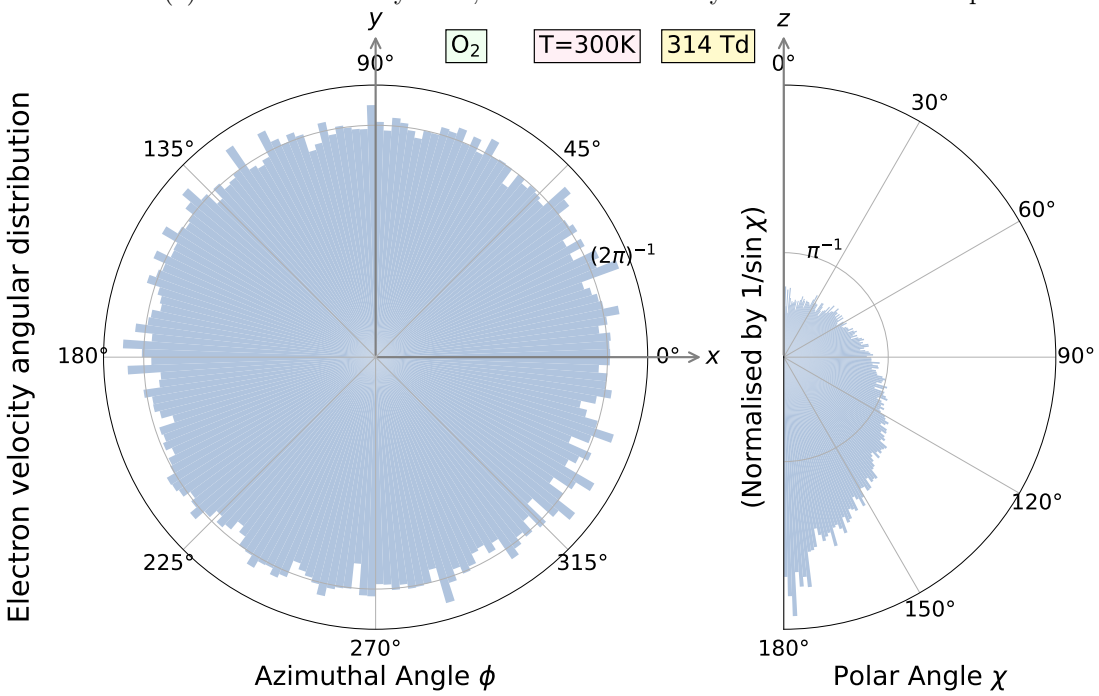

(b) In presence of an electric field $\mathbf{E} \parallel \hat{\mathbf{z}}$, the electron velocity distribution is axially symmetric about $\hat{\mathbf{z}}$.

Figure 4.7: Verification of axial and isotropic symmetries of the electron swarm. The distribution in the polar angle χ (between the velocity and z axis) is corrected by the $\sin\chi$ factor in spherical coordinates.

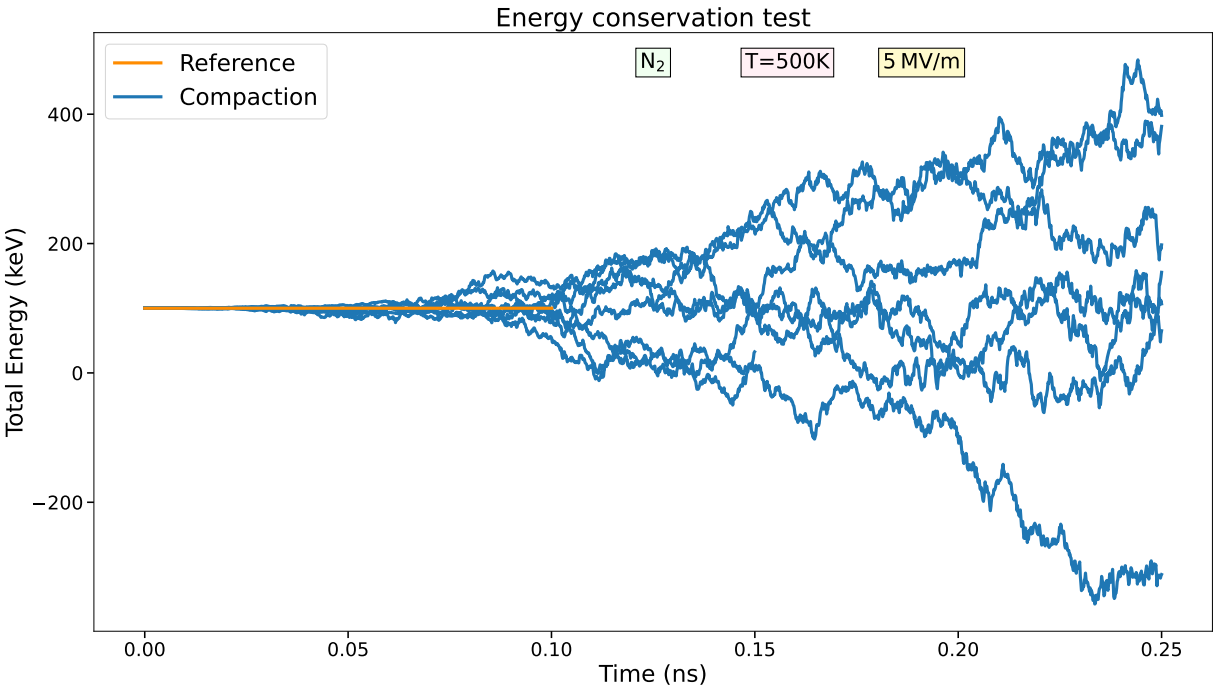

(a) Record of total energy from 8 batches of simulations at exactly the same initial conditions with the compaction algorithm (sec. 3.3.2) activated (blue —). The orange reference line (—) is a simulation without applying compaction.

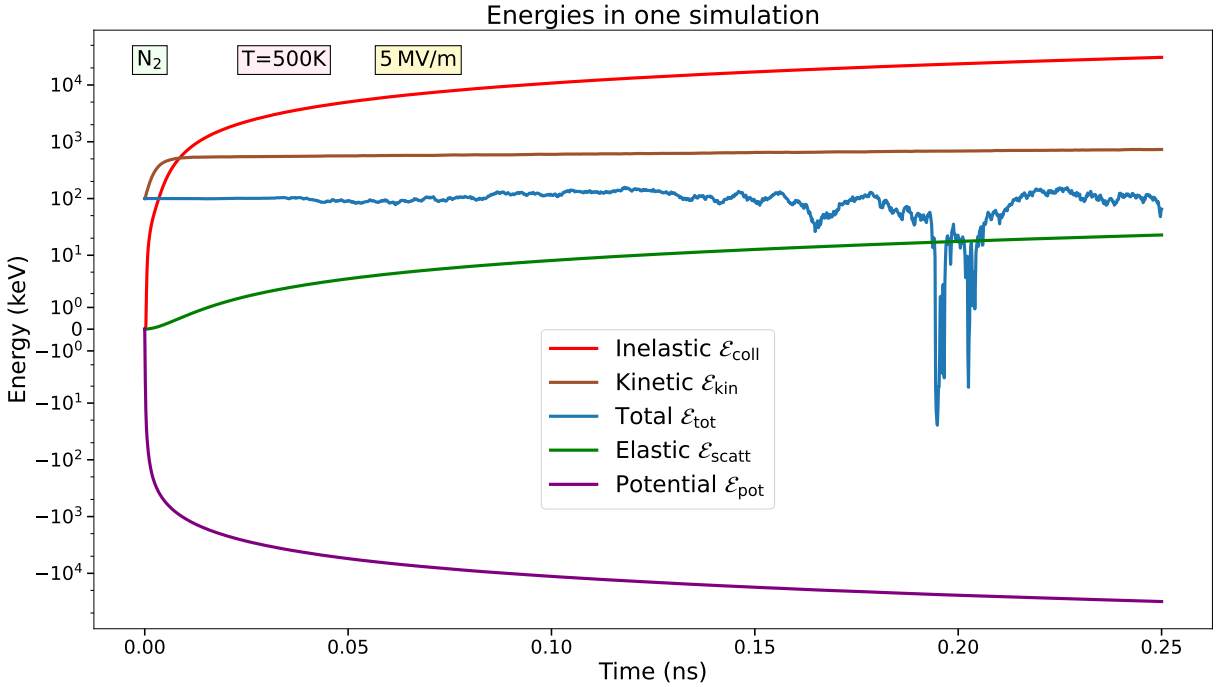

(b) Records of the energy reservoirs from one of the simulations shown in the upper figure. The ordinate scale is in asinh (arc of the hyperbolic sine). In addition to the total kinetic $\mathcal{E}_{kin}$, inelastic collision $\mathcal{E}_{coll} > 0$ and potential energies $\mathcal{E}_{pot} < 0$, we also show the very small losses from scattering (mainly elastic) $\mathcal{E}_{scatt}$. The large increase in time of the (negative) potential energy $\mathcal{E}_{pot}$ counterweighted by (positive) inelastic losses $\mathcal{E}_{coll}$ explains why the total energy, $\mathcal{E}_{tot}$ constructed from their sum, is contaminated with fluctuations that swell with time.

Figure 4.8: Energy conservation test applied on our compaction algorithm.

Nevertheless, although the fluctuations rise severely, we still affirm that:

> Our compaction algorithm presented in section 3.3.2 conserves on average the total energy in the simulation and thus does not introduce a bias in the transport parameters and spectra retrieved from the simulation.

Collision Rate

Isotropicity and energy conservation are very general requirements that do not depend on the electron collision frequency with the gas. They just show that there is no detectable systemic bias neither in the orientation nor in the energy of the electron swarm.

Presently, we must show that the electrons collide as it is expected from them; i.e. that the previsions about collision frequencies match the effective recorded number of collisions per unit time. This is verified on figure 4.9 for various examples in air, O_2, Ar and different collision types.

We recall that at any instant t, one may predict the average collision frequency $\bar{\nu}_c$ (per physical electron in the swarm) of a process labelled by c:

$$\bar{\nu}_c = \frac{1}{N_\mathrm{e}} \sum_{n=1}^{N_\mathrm{s}} w_n \mathrm{v}_n \sigma_c(\varepsilon_n) n_\mathrm{gas} \,. \tag{4.11}$$

One the other hand, we record the number of collisions δN_c of each process c during an elementary time step δt. This number is obviously weighted by the statistical weight w_n of the super-electrons that are selected to collide. We may then compare whether:

$$\delta N_c(\delta t) = N_c(t+\delta t) - N_c(t) \overset{?}{\simeq} \int_t^{t+\delta t} N_\mathrm{e}(t') \bar{\nu}_c(t') \,\mathrm{d}t' \,. \tag{4.12}$$

Numerically, this should be verified by defining an effective collision rate ν_c (per physical electron) over a time interval Δt:

$$\nu_c \equiv \frac{\int_{\Delta t} \bar{\nu}_c(t') N_\mathrm{e}(t') \,\mathrm{d}t'}{\int_{\Delta t} N_\mathrm{e}(t') \,\mathrm{d}t'} \simeq \frac{\int_{\Delta t} \bar{\nu}_c(t') N_\mathrm{e}(t') \,\mathrm{d}t'}{\left(N_\mathrm{e}(t+\Delta t) - N_\mathrm{e}(t)\right)/\nu_\mathrm{e}} \,, \tag{4.13}$$

which leads to the following relation:

$$\Delta N_c = N_c(t_j) - N_c(t_i) = \frac{\nu_c}{\nu_\mathrm{e}} \left(N_\mathrm{e}(t_j) - N_\mathrm{e}(t_i)\right) \simeq \langle \bar{\nu}_c \rangle (t_j - t_i) \frac{\left(N_\mathrm{e}(t_j) - N_\mathrm{e}(t_i)\right)}{\ln\left(N_\mathrm{e}(t_j)/N_\mathrm{e}(t_i)\right)} \,, \tag{4.14}$$

between two (not necessarily consecutive) samples $i < j$ of the simulation separated by a total interval $\Delta t \equiv t_j - t_i$. Here, we used the estimator of the electron multiplication rate $\nu_\mathrm{e} \simeq \Delta \ln N_\mathrm{e}/\Delta t$ (3.39) which we saw at the end of the previous chapter.

The windowing over a larger time interval $\Delta t > \delta t$ enables to reduce the noise (fluctuation) observed on the collision frequency when the time step δt is too short: i.e. when $\nu_c < 1/\delta t$. Of course, when there is no growth of the swarm $\nu_\mathrm{e} \sim 0$ then one should use the limit:

$$\lim_{\nu_\mathrm{e} \to 0} \frac{\nu_\mathrm{e}}{N_\mathrm{e}(t+\Delta t) - N_\mathrm{e}(t)} = \lim_{\nu_\mathrm{e} \to 0} \frac{\nu_\mathrm{e}}{N_\mathrm{e}(t)(1 + \nu_\mathrm{e}\Delta t - 1)} = \frac{1}{N_\mathrm{e}(t)\Delta t} \,. \tag{4.15}$$

Reversing (4.14), we may estimate the effective collision rate $\langle \bar{\nu}_c \rangle$ over a time interval Δt:

$$\nu_c = \frac{\left(N_c(t_j) - N_c(t_i)\right)}{\Delta t} \frac{\ln\left(N_\mathrm{e}(t_j)/N_\mathrm{e}(t_i)\right)}{\left(N_\mathrm{e}(t_j) - N_\mathrm{e}(t_i)\right)} \tag{4.16}$$

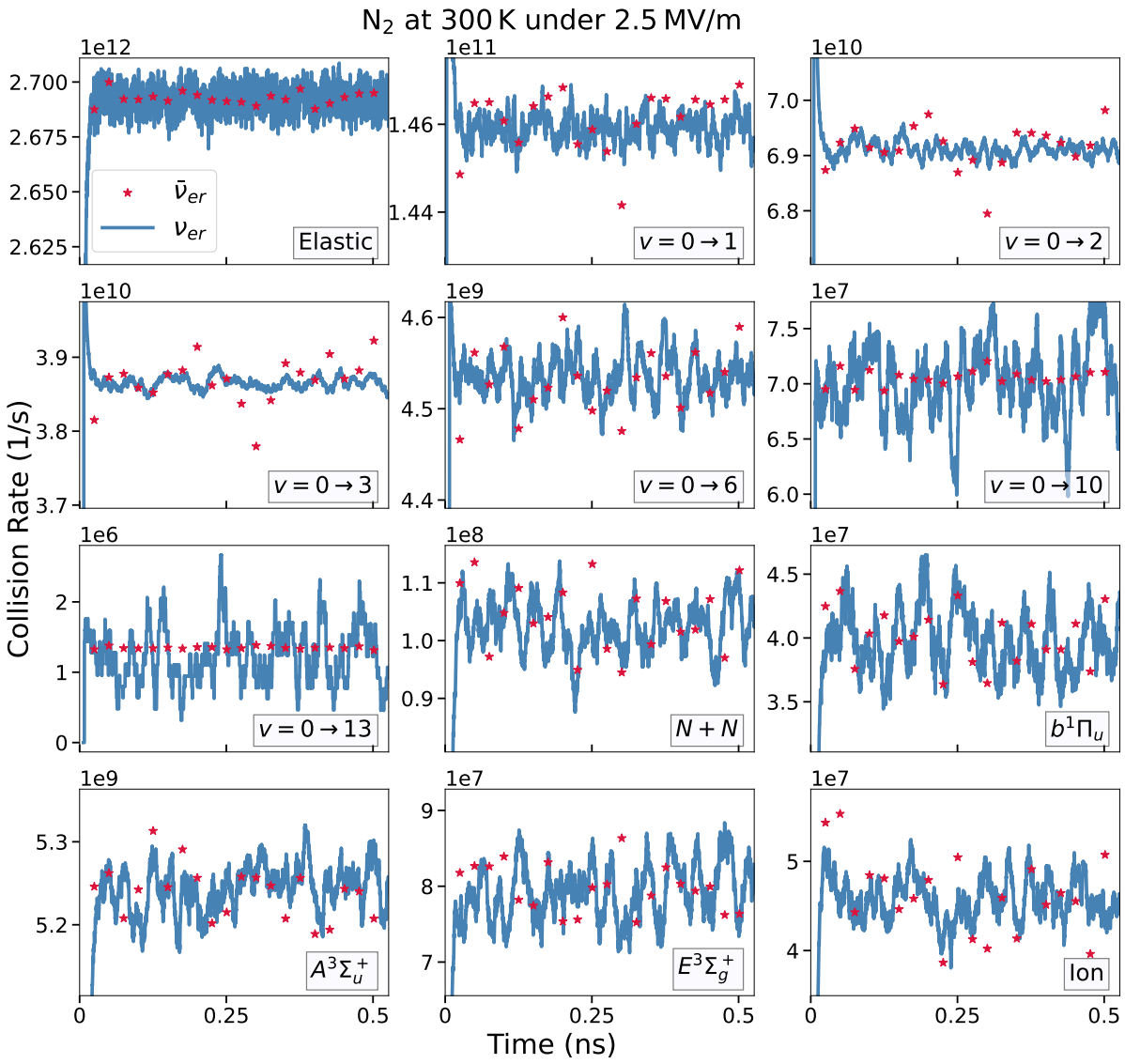

Figure 4.9: Recorded (blue) and predicted ($\star$) collision rates sampled from a simulation in pure molecular nitrogen under 98 Td. We may say that they match statistically which confirms the consistency of our handling of collisions.

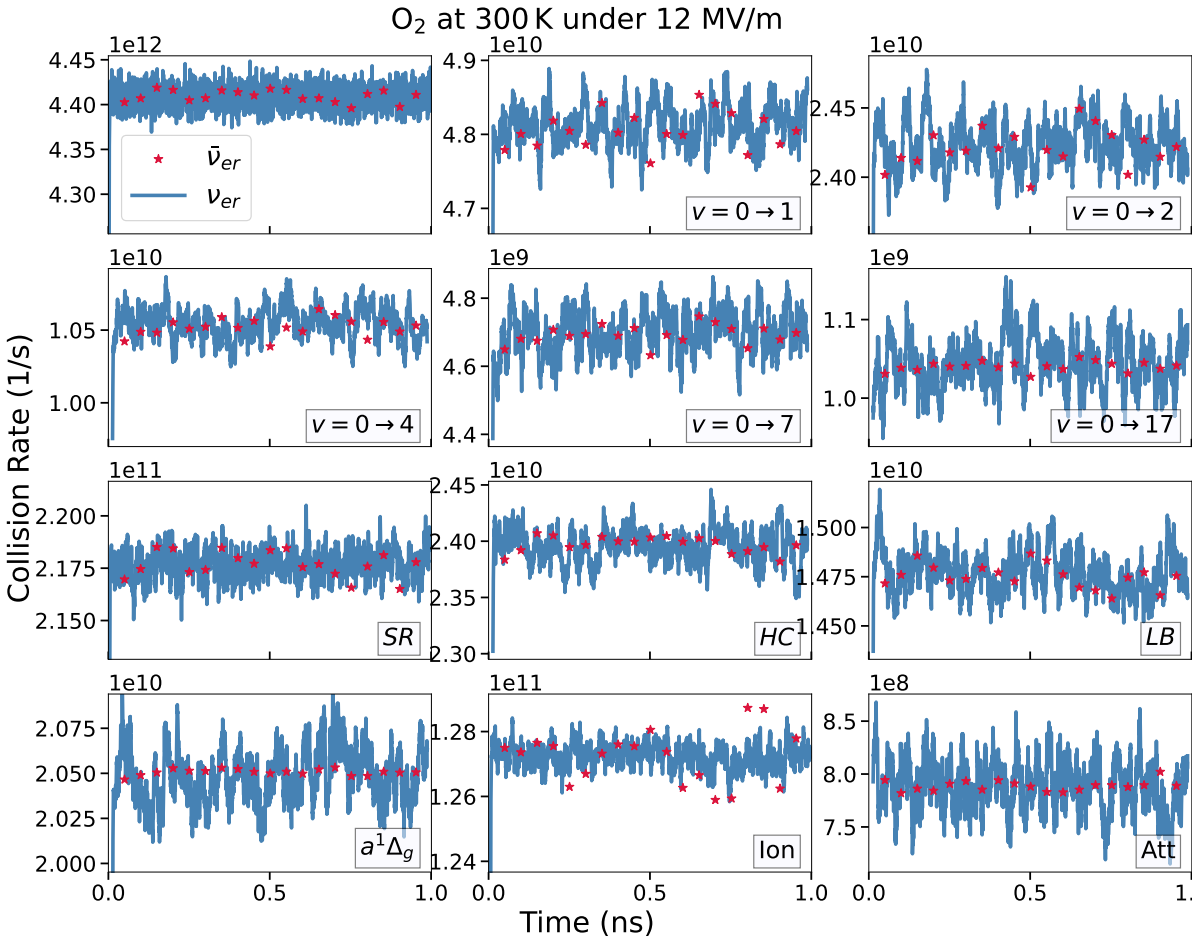

Figure 4.10: Recorded (blue) and predicted (⋆) collision rates sampled from a simulation in pure molecular oxygen under 471 Td. We may say that they match statistically which confirms that our compaction algorithm does not alter the consistency of the collision frequencies.

The question in (4.12) reduces to $\nu_c \stackrel{?}{\simeq} \bar{\nu}_c$. To be sure that we understand the difference, $\bar{\nu}_c$ is calculated from the instantaneous collision rates *predicted* by the swarm velocity distribution (4.11), whereas ν_c (4.13) is the effective collision rate from the recorded collisions that *really* occurred within the time interval $[t_i; t_j]$. Obviously, if our code works as it should, those two quantities should be equal *on average* $\bar{\nu}_c \stackrel{?}{\simeq} \nu_c$. This we check in two figures for a number of different collisions:

i. fig. 4.9 : at an electric field with slow multiplication without the use of our compaction algorithm,

ii. fig. 4.10 : at a high electric field and our compaction algorithm activated.

The stars in red ⋆ represent $\bar{\nu}_c$ whereas ν_c is the noisy line in blue —. The first figure 4.9 demonstrates that our simple code handles collisions consistently with the predicted frequencies whereas the second figure 4.10 shows that compaction does not affect the collision statistics.

Thermalisation

At last, we perform the least relevant test for thermal runaway but the most interesting one from a physical perspective: whether in the absence of an electromagnetic field, the electron energy distribution function (EEDF) converges to the Maxwellian distribution. In equilibrium in a gas at a uniform temperature T_{gas} the thermalised electron energy distribution should follow the Maxwell-Boltzmann distribution (B.13) with an average kinetic energy given by:

$$\bar{\varepsilon} = \frac{3}{2} k_{\text{B}} T_{\text{e}} \quad \text{with} \quad T_{\text{e}} = T_{\text{gas}} \,. \tag{4.17}$$

Here, we must emphasise what temperature T_{gas} is it that we should consider. At very low electron energies, the major losses are due to elastic scattering and rotational excitations. Although, we dedicated some time in chapter 2 to the study of elastic losses, we did not implement those since their relevance lies quite far from our purpose of studying thermal electron runaway.

On the other hand, we implemented in (2.48 p. 60) the scheme of average rotational losses $\Delta\mathcal{E}_{\text{rot}}(\varepsilon, \theta)$ sampled from a rectangle grid $\varepsilon \times \theta$ of the incident electron energy ε and scattering angle θ. That is, we model an ensemble of rotational transitions $J_0 \to J$ as a single process with an average energy loss without straggling.

Since, in absence of electric fields, the electrons may only change energy during a collision, this average energy loss modelling of rotational excitations is not suitable. Indeed, the electron swarm will actually converge to a monoenergetic isotropic distribution (a pure sphere in the velocity space) about the energy at which the energy loss annihilates $\mathcal{E}_{\text{rot}}(\varepsilon, \theta) = 0$. This gradual shrinkage of the electron energy spectrum is what we obtained in figure 4.11.

As a result, presently, we may neither model thermalisation from elastic nor from rotational excitations. The only remaining process whereby our electrons may thermalise with molecules is through their *vibrational* (de)excitations. We consider a pure N_2 gas at a (vibrational) temperature of $T_{N_2} = 5000\,\text{K}$ which corresponds to an average energy of $\simeq 0.31\,\text{eV}$ from Boltzmann's statistics (sec. B.2). At this temperature, the expected average energy of electrons should be from (4.17) around $\sim 0.646\,\text{eV}$ though the spectrum seen on figure 4.12 has an average energy of $\bar{\varepsilon} = 0.584\,\text{eV}$. The shape of the spectrum beyond 0.5 eV seems to follow the theoretical Maxwellian at 5000 K but deviates significantly from this law at lower energy. We surmise, just as in the previous case at 300 K (fig. 4.11), that this must be mainly due to a too crude handling of rotational excitations through (2.48).

Of the four check tests: isotropicity, energy conservation, collision rate consistency and thermalisation; our code only fails the latter. Does it subvert its applicability to the study of thermal runaway? No, fortunately.

This is because the electric fields required to provoke thermal runaway are very high ($\gtrsim 10\,\text{MV/m}$) which is far beyond the region where the electron energy spectrum is dominated by rotational and elastic collisions which we model vaguely (from the energy loss perspective). This shortcoming only limits the applicability of our code for the derivation of transport parameters at low electric fields. We nonetheless presented this study in order to (1) forewarn the user against a potential misuse and (2) highlight future improvements on the usefulness of our code.

From this perspective, the Monte Carlo approach beautifully complements the kinetic modelling based on the two-term velocity distribution in the Boltzmann equation (see p. 81). As the electric field becomes lower, one may approximate elastic scattering as isotropic and account for thermal effects through the collision terms in (2.112a). Rotational excitations may be accounted for by an adequate balance between inelastic and superelastic cross sections weighted by the proportion of populated rotational states following a Boltzmann distribution [774, eqs.(3–6)]. Then, the kinetic approach offers a considerably faster and more accurate solution to the velocity distribution of an electron swarm at low electric fields.

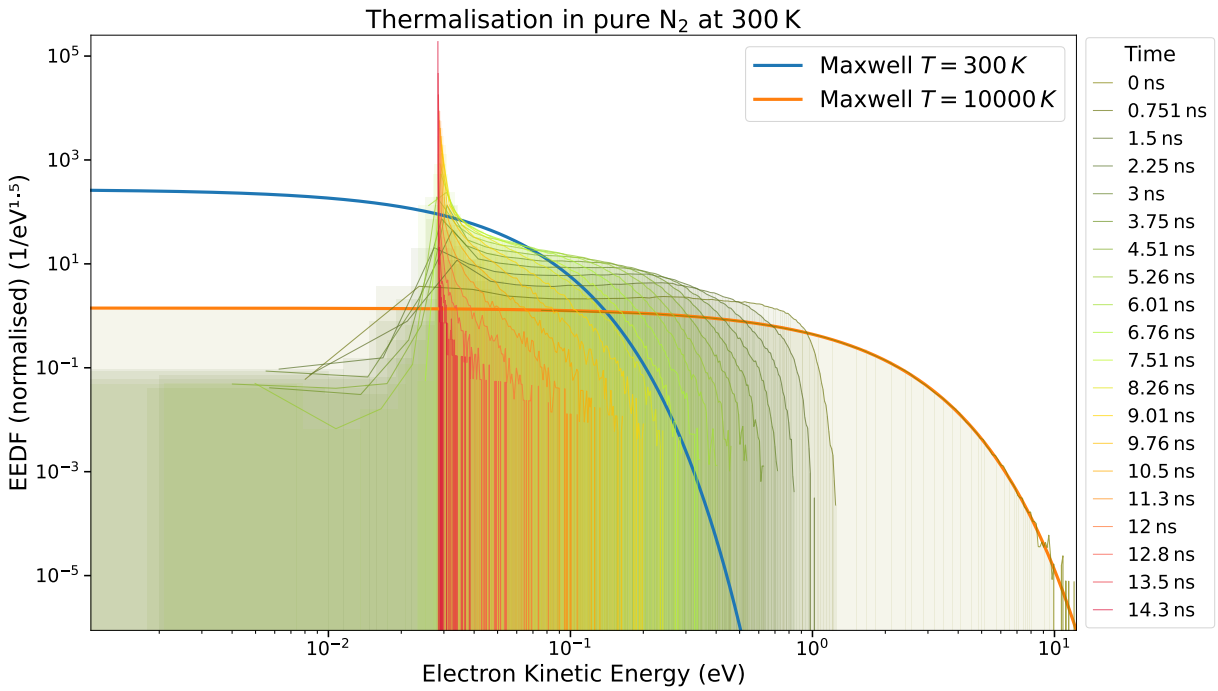

Figure 4.11: Evolution of the EEDF in pure N_2 at 300 K in absence of electric field. It shrinks to a nearly monochromatic isotropic (see fig. 4.7a) sphere due to the crude representation of rotational excitations as average deterministic energy losses (from eq. 2.48).

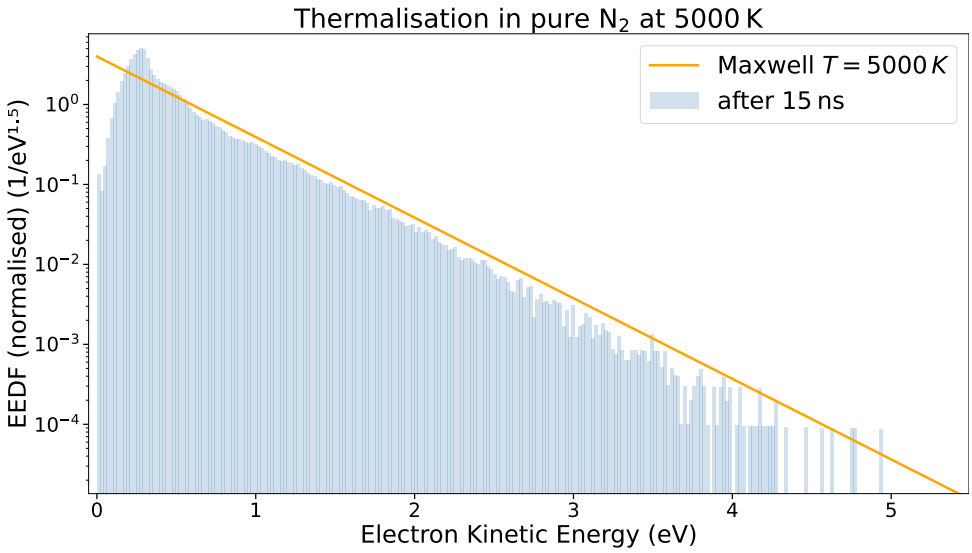

Figure 4.12: Incomplete thermalisation of the electrons in N_2 without applied electric field. Beyond 1 eV the tail of the spectrum seems to follow more or less the exponential tail of a Gaussian (Maxwellian) distribution at 5000 K. Below that, the spectrum is very different. This is because we only model vibrational (de)excitations with greater accuracy whereas rotational excitations are modelled very crudely through a deterministic average. Also, thermal effects on elastic scattering are not taken into account, which is why the low energy spectrum differs strongly from the expected Maxwellian distribution.

How low can the electric field be before our results break? We shall see below (fig. 4.3.2–4.17).

4.3.2 Verification from BOLSIG+

In the previous section, we performed four checks to assess the sanity of our code. This was based on purely physical arguments restricted to the ideal of theory. Here, we confront ourselves with the assessment of our transport parameters, whose calculation is explained in section 3.3.3. They are compared against BOLSIG+ [378]: an independent program based on a two-term kinetic solvers of the Boltzmann equation (see p. 81) developed by Hagelaar and Pitchford [378a] and available to download from the LAPLACE laboratory server in Toulouse. This will serve to validate our code. Comparison with experimental results in the next subsection 4.3.3, on the other hand, will serve to assess our cross sections.

As we have seen in 2.3.2, the two-term approximation (2.111) in the Boltzmann equation is valid when the anisotropy of the velocity distribution is small; thus at reduced electric fields $< 100\,\mathrm{Td}$, below the conventional breakdown. In this electric field region, a pertinent comparison with transport parameters from BOLSIG+ requires to understand the differences between the kinetic and the present code ΘERMIAA relying on a Monte Carlo approach.

A. Elastic scattering in BOLSIG+ is incorporated by the momentum transfer cross section σ_m. We thus have two choices:

   (1) Either use the momentum transfer cross section σ_m with isotropic scattering, implying that the average cosine is null $\langle\cos\theta\rangle = 0$. Thus, that the integral elastic equals the momentum-transfer cross section $\sigma_\mathrm{el} = \sigma_\mathrm{m}$.
   This is done for all simulations using `Phelps` database (see fig. 4.13).

   (2) Or use the integral elastic cross section $\sigma_\mathrm{el} \neq \sigma_\mathrm{m}$ given in the database and use an anisotropic scattering distribution with an average deviation cosine given by

$$\langle\cos\theta\rangle = 1 - \frac{\sigma_\mathrm{m}}{\sigma_\mathrm{el}}\,.$$

   This is the case of all simulations using the present database (see fig. 4.14) and ensuring that the correct σ_m is given as input to BOLSIG+. Information about how we construct our elastic (integral and momentum-transfer) cross sections can be found in part II section 11.1.5.

B. The effect of the gas temperature on the energy loss in elastic collisions (discussed in chapter 2 p. 54–56 and conspicuous on fig. 2.7–2.8) has not been implemented in our code. For a true comparison at very low electric fields ($< 0.01\,\mathrm{Td}$), the temperature of the gas must be set to $T_\mathrm{gas} = 0\,\mathrm{K}$ in the input parameters. This effect is very small, however.

C. Rotational excitations in ΘERMIAA are treated as part of elastic scattering whereas in BOLSIG+, they feature as separate excitations. For comparison, we made two sets of runs:

   - when using the `Phelps` database, we treated rotational excitations as a separate excitation in the single level approximation for N_2 at 20 meV as described in the appendix of Hake and Phelps [381]. Also, in this particular case, we did not include superelastic collisions from rotational excitations, so that one needs to set the excitation temperature in BOLSIG+ to zero: ($T_\mathrm{rot} = 0\,\mathrm{K}$ in figure 4.13).
   - when using our own database ("present"), we included simulations without rotational excitations (labelled "pure elastic" in the figure 4.14 below)

D. As mentioned previously, we do not model inter-electron interactions, so that this option must be turned off in BOLSIG+ to enable validation from comparison.

With these details in mind, we compare below results from two sets of simulations obtained with two different cross section databases.

Phelps database

In order to get rid of any possible artefact due to the use of our cross sections, we first perform a test taking as input the widely used cross sections from the `Phelps` database on LXCat which were collected by Phelps and Pitchford [749, 750]. A succinct comparison of the various databases hosted on LXCat is included in chapter 16 of the third part.

From the comparison in figure 4.13, the effect of the excitation temperature starts to build up below 2 Td. This is where the superelastic collisions from the single level at 20 meV become important. As for the effect of the translational temperature (velocity of the gas molecules), it is negligible even down to 0.01 Td. One can see in the study of Pitchford *et al.* [752, figs. 5&6] conducted on Argon, that electron swarm transport parameters are indeed affected by translational temperature of gases below about 0.01 Td.

The agreement of our calculations with BOLSIG+ is very good for the (bulk) drift velocity v_d and the average kinetic energy $\langle\varepsilon\rangle$. The (transversal) diffusion coefficient $D_\perp$ (or D_T) agrees well below 10 Td but is somewhat lower at higher electric fields. The first point corresponds to a very low field 100 V/m (~ 0.04 Td) and has a large uncertainty because the simulation has not fully converged to steady-state (requires more than 15 ns).

Present (IAA) database

Next, we show in figure 4.14 calculations made with own set of cross sections (baptised "IAA", presented in chapter 15, detailed in chapter 11 and compared in 16). The agreement is good, except again for the diffusion coefficient at very low and high electric fields. Notably, due to our compaction algorithm we start seeing important fluctuations of the diffusion beyond 200 Td. An example of such fluctuations in shown in figure 4.16 in argon.

At the low end of electric fields, the effect of our treatment of rotational losses can be seen. The blue curve — (on the bottom graph of figure 4.14) saturates around 0.283 eV, which is the energy ε at which the average loss $\Delta\mathcal{E}_{\text{rot}}(\varepsilon,\theta)$ annihilates. The large uncertainty of the first data point at 0.004 Td is again due to a non-fully converged simulation. The convergence is indeed very slow when the only energy losses are due to elastic collisions.

At last, we offer in figure 4.15 a comparison of the electron energy distribution function (EEDF) normalised to unity*. The overall agreement is good. Differences start arising above the conventional breakdown. At 314 Td, the high-energy tail of the Monte Carlo simulation (enhanced by our compaction algorithm to a minimal resolution of $w_{\min} = 10^{-20}$) is more prominent than predicted by BOLSIG+. This is mainly due to anisotropic scattering†.

There exist other sources with which our calculations could be compared, such as the time-dependent Boltzmann solver ELENDIF [661]. We did not attempt to conduct an exhaustive comparison. Instead, in the next subsection, the results with BOLSIG+ are also be compared to experimental transport coefficients.

*This is by definition of the EEDF in (2.121)

†We remind that in order to make a meaningful comparison, one should use identical *momentum-transfer* elastic cross sections σ_m in both simulations and not integral elastic cross sections σ_{el}. See the discussion in section 4.1 for more information.

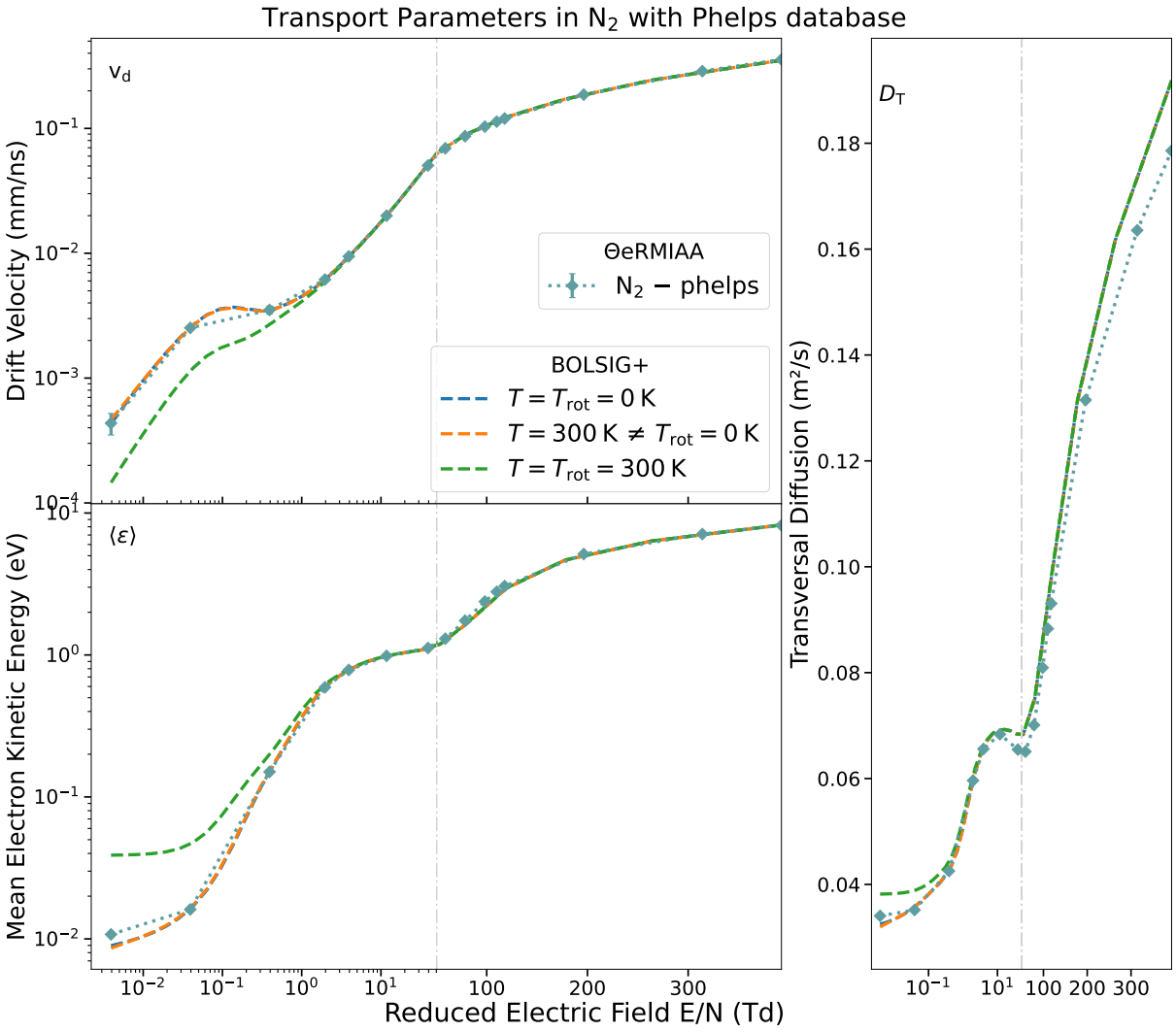

Figure 4.13: Comparison of the bulk drift velocity v_d (top), mean energy $\langle\varepsilon\rangle$ (bottom) and bulk transversal diffusion D_T (right) of electrons in molecular nitrogen at various electric fields below conventional breakdown, derived from BOLSIG+ and our calculations ("ΘeRMIAA") using the same input cross sections from the `Phelps` database and isotropic scattering. The dashed curves show calculations from BOLSIG+ with various inputs of the gas temperature (T) and excitation temperature (T_{rot} which mainly affects rotational excitations modelled at a unique excitation energy of 20 meV).

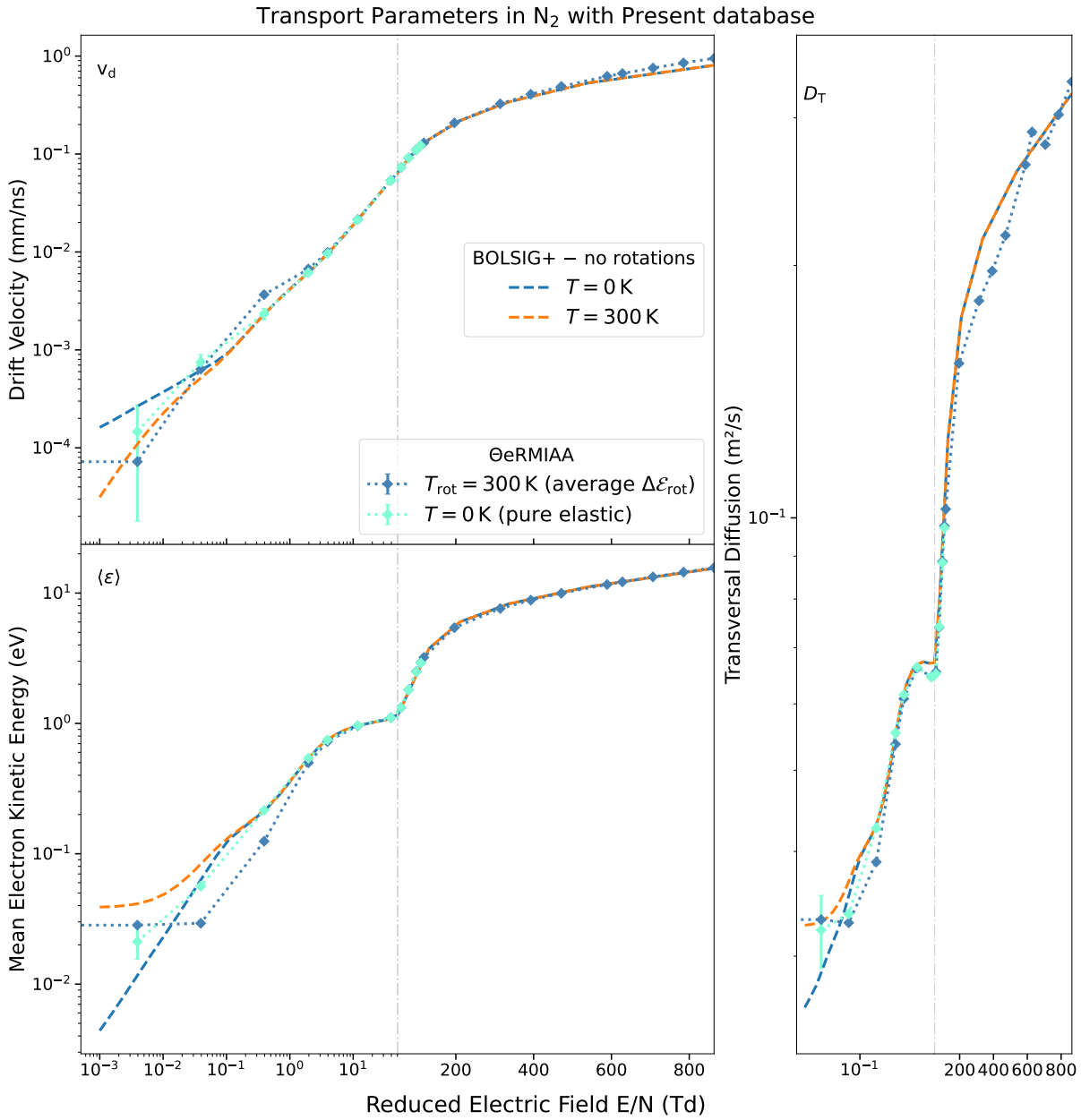

Figure 4.14: Comparison of the bulk drift velocity v_d (top), mean energy $\langle\varepsilon\rangle$ (bottom) and bulk transversal diffusion D_T (right) of electrons in molecular nitrogen at various electric fields below conventional breakdown, derived from BOLSIG+ and our calculations ("ΘeRMIAA") using the same input cross sections from the present database (constructed in part II) and anisotropic scattering. This set does not include rotational excitations explicitly but as part of elastic scattering and through an average rotational loss $\Delta\mathcal{E}_{rot}(\varepsilon, \theta)$ (see eq. 2.48). Thus, one should expect the turquoise curve (— without rotational losses) to match with the calculations of BOLSIG+ at 0 K (blue dashed - - -).

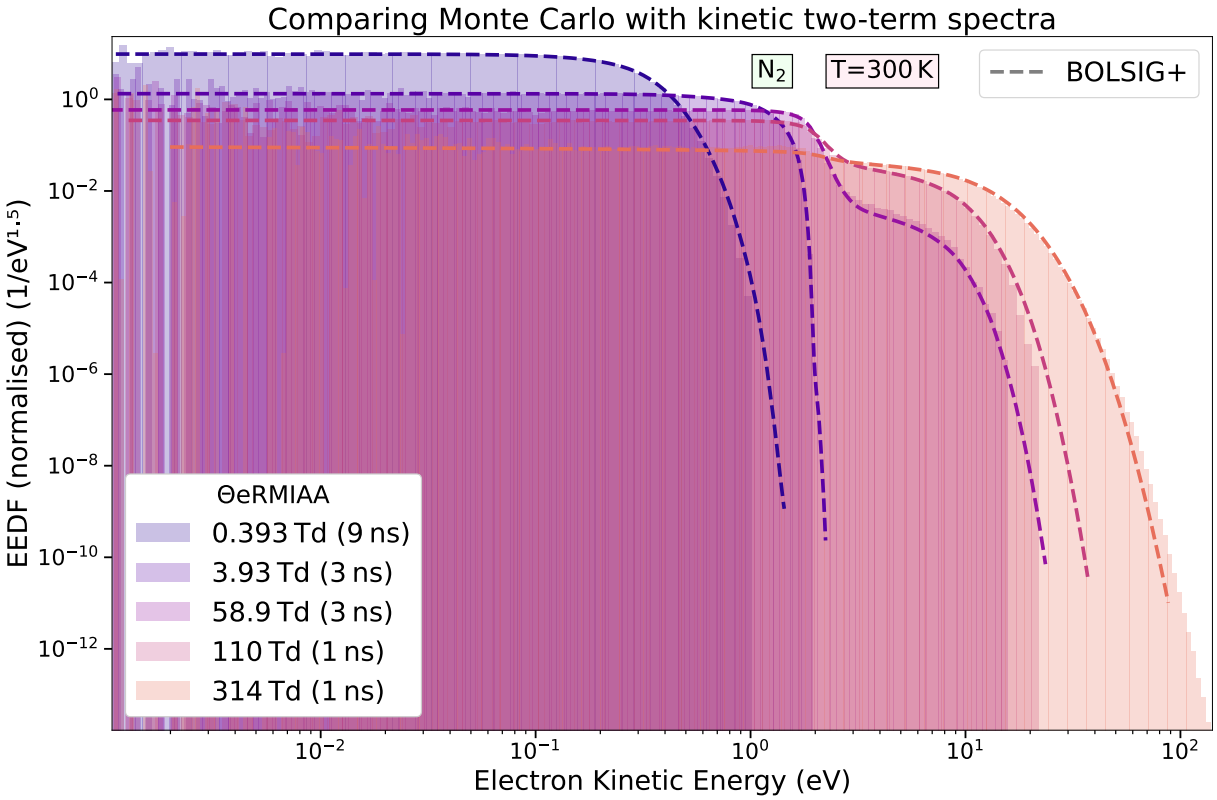

Figure 4.15: electron energy distribution functions (i.e. normalised to unity) of calculations of BOLSIG+ and our Monte Carlo simulations using our set of cross sections for various electric fields. Anisotropic scattering in our simulations seems to have a noticeable effect only from high electric fields above conventional breakdown $\gtrsim 100\,\mathrm{Td}$ when comparing the high-energy tail of the spectrum.

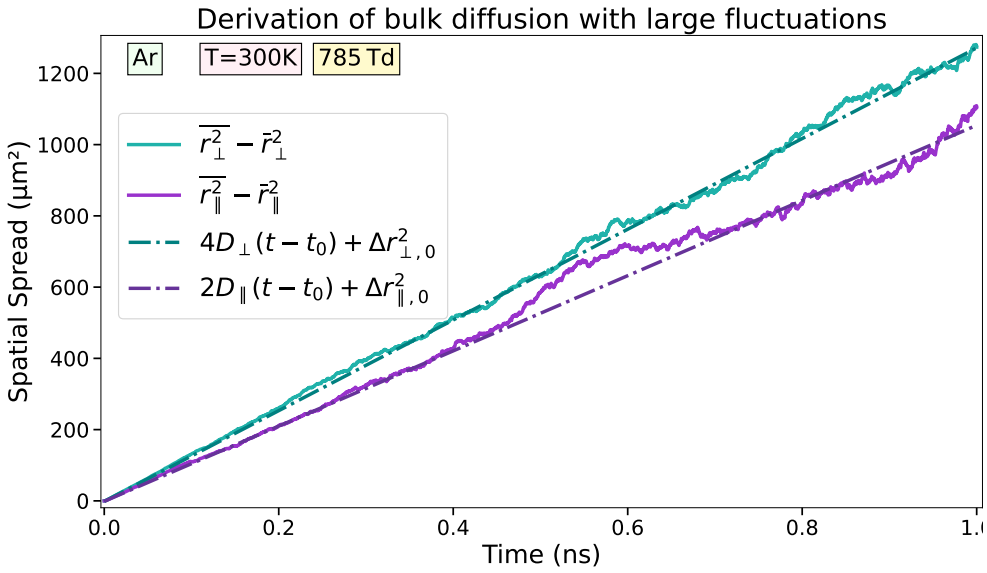

Figure 4.16: Fluctuations from the inevitably intense compaction at very high electric fields deteriorate the accuracy over the derivation of diffusion coefficients.

4.3.3 Validation from Experiments

The purpose of the following comparison is to unveil the validity range of our model and also of our cross section database whose assembly is amply discussed in part II. It is of fundamental importance to understand whether the discrepancies are due to (A) the method or (B) the input data. A proper validation will enlighten the path toward future improvements.

From the previous subsection, we conclude that our simulations agree with the kinetic approach to Boltzmann's equation in the range of electric fields between 0.01 Td and 200 Td. This validates our method but not our set of cross sections. By comparing transport with experimental measurements collected and centralised on the LXCat server, we can assess the validity of the present database of cross sections.

We offer in figures 4.17a,4.17b and 4.17c, a comparison of four main swarm transport parameters obtained from our simulations with our database against various experimental data available in numerical format from the databases (of electron swarm parameters) on the LXCat server.

The parameters are:

1. Mobility : $\mu_e \mathbf{E} = v_d$. It is obtained as the ratio between the *bulk* drift velocity v_d and the electric field. We remind that v_d is obtained in our simulation with (3.36a).

2. Diffusion : it is a tensor with two independent components which express the *bulk* spatial spread rate of electrons :

   ∥ Longitudinal : $D_L \equiv D_\parallel$ in the direction of the electric field. Depending on the target, the scatter between experimental data of the longitudinal diffusion does not enable a sound validation of a set of cross sections (for instance N_2 in figure 4.17a-bottom graph).

   ⊥ Transversal : $D_T \equiv D_\perp$ in the plane perpendicular to the electric field. In the LXCat server, the transversal diffusion is not given explicitly but may be obtained through Einstein's relation (see (7.8)) of a characteristic swarm energy $\langle\varepsilon\rangle$:

   $$\frac{D_\perp}{\mu_e} = C\langle\varepsilon\rangle \,, \tag{4.18}$$

   with a proportionality coefficient C that depends on the EEDF.

   Both components are obtained from a linear regression in (3.36b) of the quadratic moment tensor in space $\overline{\mathbf{r}\times\mathbf{r}}$.

3. Townsend's first ionisation coefficient : $\alpha_i = \nu_e/v_d$. It is the ratio of the avalanche rate to the bulk drift velocity and expresses the spatial growth rate of the electron swarm under the assumption of a steady-state Townsend discharge.

In each graph, our Monte Carlo results are represented by lozenges (blue ♦ for N_2 golden-brown ♦ for O_2 and magenta ♦ for Ar) connected by a dotted line (···). Then we include a multitude of experimental results as scattered points. At last, we include the output (bulk) parameters of BOLSIG+ when given as input the `Phelps` and two versions of our database:

○ Complete : as described in the subsections labelled 'Completion' to each corresponding species in chapter 16 in part III.

◐ Incomplete : raw taken as is from chapter 11 of part II.

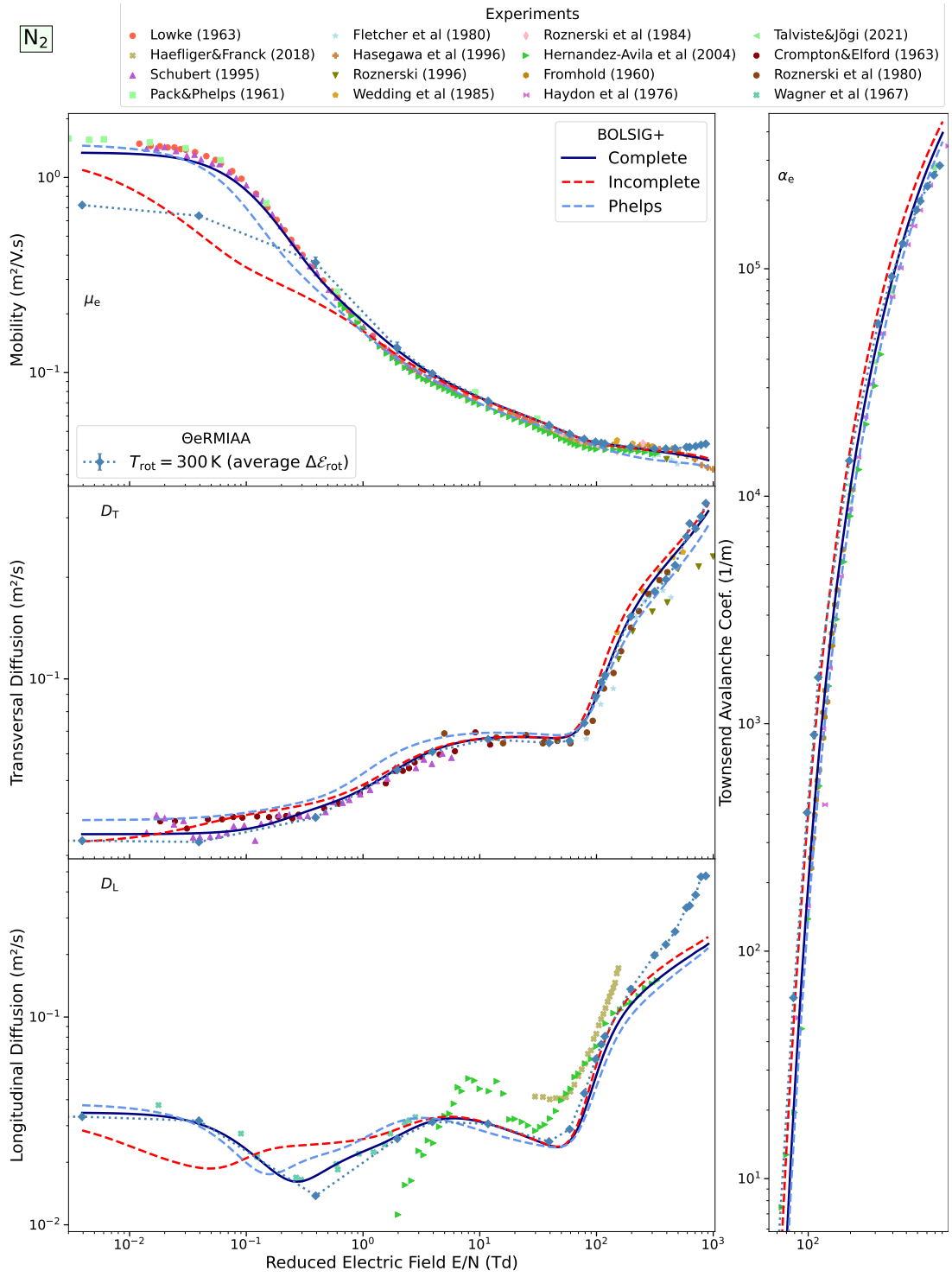

(a) Transport parameters in ambient pure molecular nitrogen.

Figure 4.17: Comparisons of transport coefficients calculated with kinetic solvers (dashed and solid lines) and our Monte Carlo simulations with ΘeRMIAA (Lozenges connected by dots) against experimental data. The input cross sections for the Monte Carlo simulations are the same as for the red dashed line (- - -) of the "Incomplete" database. The present "Complete" database (—) is compared against the `Phelps` database (- - -) of LXCat.

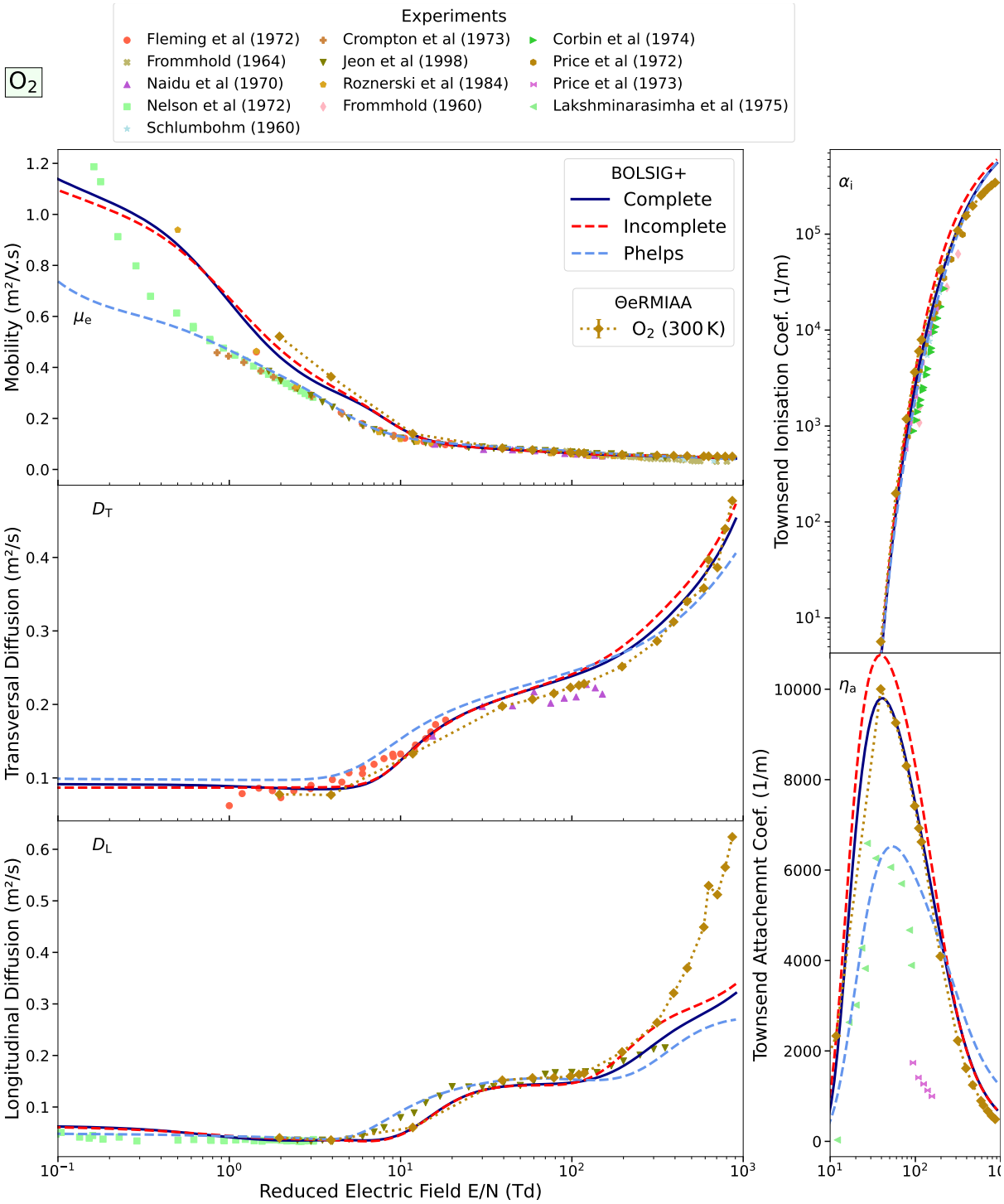

(b) (continued from fig. 4.17) Transport parameters in ambient pure molecular oxygen.

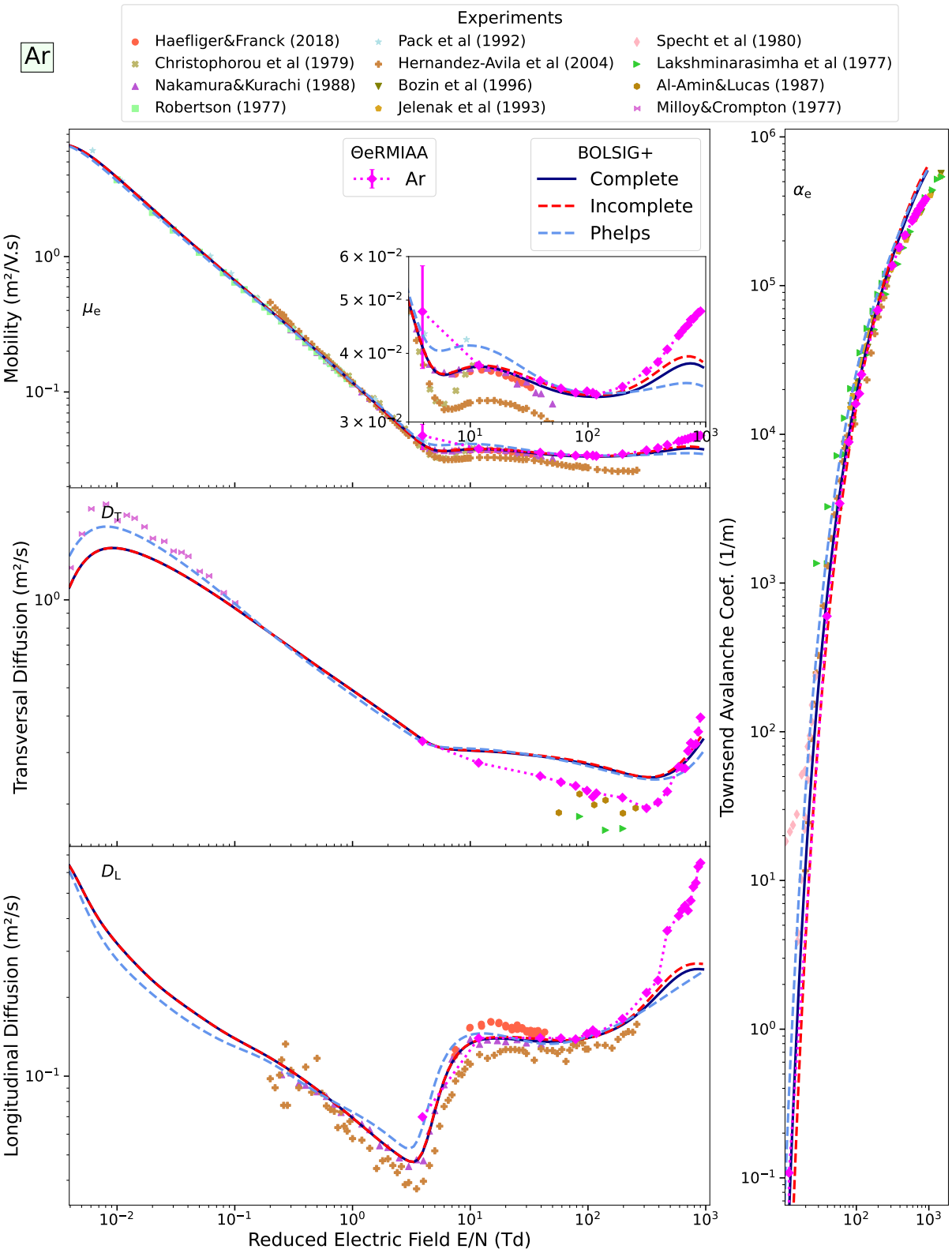

(c) (continued from fig. 4.17) Transport parameters in ambient pure argon.

¿What does ‘completion’ mean, why is it necessary and how did it spring up?

In the process of assessing our cross sections, we came upon realisation that, alone, our assembled database did not match satisfactorily experimental transport coefficients. We immediately sought after explanation and quick remedy. We conducted a thorough process-to-process comparison of the databases available on LXCat and ours. Some of this comparison is illustrated the figures of chapter 16. There, we realised that, despite of our profound survey of the literature, significant differences distinguished our database from others. In particular, for all species, our total inelastic cross section for electronic excitations was almost systematically lower than any other of the databases used for computing transport parameters.

A ‘complete’ database comprises a complementary cross section $\sigma_{\text{▷}}$ whose sole purpose is to patch the inelastic losses of electrons from high excitations near the ionisation threshold which are unaccounted in any of the identified excitations. Also, for diatomic molecules, it includes state-to-state rotational transitions modelled separately from elastic collisions.

We then realised the relevance and importance of accounting for complementary inelastic losses from electronic excitations (at high electric fields) and rotational excitations (at low electric fields). For more information to feed our perplexity, we invite our readers to jump to page 573 where we explain how exactly did we proceed to completion and why we think it is justified.

Because of our late realisation and time restrictions, all our Monte Carlo simulations were performed using the incomplete cross section set. Differences between the results of ΘeRMIAA and the dashed red curves on figures 4.17 reflect the accuracy brought by Monte Carlo simulations compared to the kinetic approach.

Overall, the agreement with experimental data is good for all three gases in the electric field range where our Monte Carlo code is relevant to the study of thermal runaway. The important improvements of the completed sets are:

+ N_2

1. Below 5 Td : the rotational set of cross sections obtained from Kutz and Meyer [546] with the sudden-impulse approximation 11.2.2 improves considerably the agreement with the experimentally measured mobility and diffusion.
2. One can note that the effect of the average rotational losses $\Delta\mathcal{E}_{\text{rot}}$ in Monte Carlo simulations (···◆···) is strong at low electric fields and approximately follows the more accurate solution given by the complete set (— dark blue line). This is particularly seen on the longitudinal diffusion D_{L}.
3. Above 50 Td : the incomplete set systematically overestimates the ionisation rate by a factor between 2 and 4. This overestimation is reduced to less than 10 % when including complementary inelastic losses from electronic excitations.

+ O_2

1. Below 1 Td : the quadrupole and anisotropic Born approximation used to calculate rotational losses is inaccurate. The cross sections are too low and do not reflect resonant scattering that probably characterises electron-oxygen rotational excitations.

2. From 1 Td to 20 Td : both our sets of cross sections overestimate the mobility μ_e and underestimate the longitudinal diffusion D_L. This is mainly due to the first $v = 0 \rightarrow 1$ vibrational excitation, too strong in our database compared to `Phelps`.
3. Above 30 Td : the Monte Carlo simulations differ slightly from the kinetic approach as follows. The mobility μ_e is about 5 % higher, the lateral diffusion D_T 7 % lower and longitudinal diffusion D_L 8 % higher in the Monte Carlo simulations. The differences highlighted tend to improve the agreement to the experimental results of Jeon and Nakamura [457] and Naidu and Prasad [687]
4. η_a : the Townsend reduced attachment coefficient ($\eta_a = \nu_a/v_d$) is overestimated more than what can be corrected by the completion of the set.
5. α_i : the ionisation coefficient is overestimated by a factor of 2 in the incomplete set, and still by 25 % in the complete set. These last 25 % can be eliminated if one uses a more accurate Monte Carlo approach. This is because the inelastic losses in the Herzberg and Schumann-Runge continua might not be well represented in the Boltzmann equation.

+ Ar

1. The agreement with experimental data is very good throughout the whole range of electric fields.
2. Below 0.1 Td : The transversal diffusion D_T measured by Milloy and Crompton [649] is better fitted with the `Phelps` data.
3. From 10 Td to 300 Td : Monte Carlo results differ markedly from kinetic results and tend toward the experimental results of Al-Amin and Lucas [25] for the transversal diffusion.
4. μ_e and D_L : all our results for the mobility and longitudinal diffusion in the 1 100Td range agree better with experimental data [375, 689] than the `Phelps` database.
5. α_i : calculations with the complete set for the Townsend ionisation coefficient are accurate within the experimental uncertainty.

Regarding molecular oxygen, the assessment becomes very delicate at intermediate electric fields below 10 Td. This is due to the fact that the transport parameters become significantly sensitive to the three-body attachment process. The only experiment conducted at the lowest electric fields is from Nelson and Davis [691] at a pressure of 4 torr (~5 mbar) so as to minimise the three-body attachment rate. As a result, we adapted the three-body attachement cross sections present the `Phelps` database to that pressure.

At last, our calculations for argon are reasonably well in agreement with all experimental data and databases, where instead of `Itikawa`, we used the `BSR` database from purely theoretical calculations of Zatsarinny [1000]. At low electric fields, we are mostly limited by the very slow relaxation of electrons in argon. This is because the first excitation in argon is at 11.55 eV. Thus, all energy losses below that threshold are purely from elastic scattering. Hence, our not fully converged solution at 4 Td has a large uncertainty bar.

Above 400 Td, we start having large fluctuations on the diffusion coefficients. This is because when we use our compaction algorithm to track high-energy electrons, we also increase the fluctuations of the bulk thermal electrons. This is inevitable since, in order to keep the number of super-electrons constant, we have to discard a significant fraction of them per time step.

We show one such instance of the increased fluctuations on the diffusion tensor in figure 4.16. At this electric field (~800 Td) the *super*-electron multiplication rate $\nu_s = 9 \times 10^{17}\,\mathrm{s}^{-1}$, meaning that, on average within 1 ps, we need to discard almost one million super-electrons, which is twice the number of super-electrons hosted in the simulations (500 000). We may say that the population of electrons is fully renewed every half picosecond! Thus, it is unsafe to study spatial correlation effects at very high electric fields with the present methodology. One should either increase the number of super-electrons in the simulation, or reduce the compaction reactivity κ_r (see eq. 3.22–3.30).

To wrap up this last subsection, we deem that our cross section sets, when completed, are valid for the study of thermal runaway which takes place at high electric fields. In some regions of the electric field, they yield less accurate transport parameters than obtained with other databases. Nevertheless, since they are virtually the only cross sections which have not been adjusted to fit electron transport coefficients in gases, we regard them as an invaluable tool for future scientific investigation beyond their use in practical plasma calculations. For a more detailed survey of the most accurate cross section databases currently in use, please refer to chapter 16 in part III.

Chapter 5

Results

After having explained our physical model in chapter 2, detailed its numerical implementation in chapter 3 and emphasised some thorny aspects of the code in the previous chapter 4, we are now ready to issue some results of our simulations.

The underlying motivation of the present research is to confirm or infirm* whether thermal effects of the gas in the plasma channel, formed during the evolution of a discharge in atmospheric gases, have an impact on electron thermal runaway production by those discharges. Drastic changes in the temperature of the gas entail thermal expansion and changes in chemical composition such as dissociation into atoms and presence of metastable excited states.

The objectives of this chapter are:

- Study the effect of the gas temperature and composition on the transport parameters and population of high-energy electrons
- Make a probabilistic characterisation of the electron thermal runaway phenomenon.
- Explore how spatio-temporal scales affect the production of thermal runaway electrons.

In this chapter, after stressing once again the restrictions of our physical model and its underlying hypothesis in section 5.1, we present some results of swarm energy distributions (sec. 5.2.1), transport parameters (sec. 5.2.2) and reaction rates (sec. 5.2.3) under various conditions of electric field, temperature and gas composition.

Then, we explore thermal runaway statistics (sec. 5.3) such as the eventual energy threshold for runaway and the runaway rate.

At the end, in section 5.4 we explore two (alternative) scenarios of heated gas conditions (sec. 5.4.1–5.4.2), a scenario of how swarms evolve when runaway electrons are present initially (sec. 5.4.3) and runaway electrons ahead of a planar ionisation front (5.4.4).

5.1 Working Hypothesis

In the previous chapter sections, we made two types of comparisons, (1) results based on our calculations and BOLSIG+ using the same input cross sections (CS) (sec. 4.3.2) and (2) calculations based on our set of cross sections and experimental data (sec. 4.3.3).

*Loaned from French "infirmer" (and Latin "infirmāre") as the natural antonym of "to confirm", I prefer it to "reject" because we are never sure...

1. From the computational perspective, we assessed that our code – ΘeRMIAA – matched the results of the kinetic approach at fields larger than at least 1 Td. In particular, the compaction algorithm, exposed in section 3.3.2 and tested in 4.3 figure 4.10, preserves the physical properties of the swarm. Since the investigation on thermal runaway is pertinent only above 100 Td, our code is therefore apt for that purpose.

2. We identified two major shortcomings of our cross section database when comparing with experimental transport coefficients.

   - At low electric fields (<1 Td), our deterministic approach to rotational cross sections from the average rotational loss $\Delta\mathcal{E}(\varepsilon,\theta)$ described by equation (2.48), which only depends on the energy ε and angle of scattering θ, becomes inaccurate. When the average gain of energy from the electric field between two collisions becomes comparable to the average loss $\Delta\mathcal{E}_{\text{rot}}$, we ought to model random fluctuations about the average loss as a noise term. However, this does have any effect on the investigation of thermal runaway at high electric fields.
   - At high electric fields (>100 Td), and only for molecular nitrogen, we realised that simulations with our cross sections systematically overestimate the first Townsend ionisation coefficient by a non-overlookable factor ranging from 2 to 4 in the worst case. This was due to an underestimation of inelastic losses from impact excitations.

As a consequence of these shortcomings stemming from our set of cross sections, we sought to amend them.

First, we would like to emphasise that our set of cross sections has been assembled, in part II, independently from any other database present in LXCat. It is thus very instructive to check in which respects do the present cross sections differ with others and how these differences transpear* in the transport coefficients calculated by two-term Boltzmann kinetic solver BOLSIG+ [378]. Such comparison between different databases is conducted in chapter 16 alongside experimental results.

Second, it should be promulgated that all cross-sections sets assembled from theoretical and experimental studies require some *ad hoc* adjustment in order to yield accurate transport coefficients. The importance of plainly disclosing these *ad hoc* adjustments has been depreciated over time. It is indeed rare to find a publication whose methodology is as properly documented as the section exposing the results. To restore focus, we deemed relevant to gather all the adjustments we performed in a dedicated chapter 15. We designated these adjustments with the terminology of "completion" because we realised that the full description of the energy losses of electrons in a gaseous medium might be incomplete even when one has conducted an exhaustive examination of inelastic collisions experimentally and theoretically hitherto documented.

Concretely, completion consists in the following changes to the "incomplete" cross section set:

1. "Rotation" : In order to make our cross sections relevant to the two-term Boltzmann equation, we need to include all state-to-state ($J_0 \to J$) rotational cross sections as separate excitations in the set used by BOLSIG+. These are calculated with the sudden-impulse approximation presented in the second part in section 11.2.2.

*"Transparaître": verbalised in French in the 16$^{\text{th}}$ century from the adjective "transparent", from Latin 'trans' : through + 'parens' : to appear. In this context, we mean to say how do differences in the cross sections "appear through" the transport coefficients.

2. "Complementary electronic" : Electrons passing through gases at a certain speed have a probability to lose a certain amount of energy in inelastic collisions. The distribution of energy losses is called the electron energy loss spectrum (e.g. fig. 11.32). A set of cross sections is a representation of this spectrum but may not be a complete representation. The purpose of the "complementary" inelastic cross section is to patch the energy loss spectrum so as to account for energy losses from high-lying electronic states close to (or beyond) the ionisation potential, which are not included in the identified set of cross sections.

3. "Effective" : Since the complete database comprises cross sections for rotational excitations, the purely (rotationally) elastic cross section must be deduced from the vibrationally elastic cross section by subtracting all rotational processes following the Boltzmann distribution at the given temperature T_{gas} of the gas. Thus, we provide a so-called "effective" momentum-transfer cross sections, used by BOLSIG+, which is the sum of the *vibrationally* elastic *momentum-transfer* cross section σ_{rm} at 300 K obtained from the residual integral elastic cross section σ_{re} (which we defined in section 11.1.5 (11.10)):

$$\sigma_{\text{rm}} = \sigma_{\text{re}}(1 - \langle \cos\theta \rangle) \ ,$$

and cross sections from all (non-rotational) inelastic processes.

In our Monte Carlo code, we rather use the "Total" cross section σ_{tot} for collisions with electrons and molecules which is the sum of σ_{re} (which includes rotational excitations) and inelastic (non-rotational) CS.

For a more detailed introduction to completion, please refer to page 569 in chapter 15.

The realisation of the necessity to complete our cross sections came at a very late stage in the thesis. In order not to delay furthermore the fulfilment of the thesis, we did not have time to rerun our Monte Carlo simulations with our complete database. Thus, once again, we warn the readers that:

All our results presented in this chapter were performed with ΘERMIAA Monte Carlo simulations using the incomplete set of cross sections of the present database.
Therefore, the conclusions drawn from these results must be taken with care. We will privilege qualitative observations and, at best, use the results to estimate the order of magnitude of the quantities measured.

In conjunction to what has already been exposed in chapter 2, our model consists of a fixed medium in which a swarm of uninteracting electrons evolves on a nanosecond timescale.

The medium is characterised by an electric field $\mathbf{E}$ pointing in the z direction and a gas (pure or mixture).

a) $\mathbf{E}(\mathbf{x}, t) = E\hat{\mathbf{z}}$: uniform electric field (except in sec. 5.4.4);

b) $\mathbf{B} = 0$: no magnetic field;

c) T_{gas}: homogeneous temperature of the gas (except in sec. 5.4.1 with $T_{\text{vib}} \gg T_{\text{gas}}$);

d) $n_{\text{gas}} = 2.547 \times 10^{25}\,\text{m}^{-3}$: homogeneous particle (molecule or atom) number density; obtained from $p_0 = n_{\text{gas}} k_{\text{B}} T_0$ at standard atmospheric pressure (see sec.2.1.1; p_0 = 1013.25 hPa and T_0 = 15 °C)

Table 5.1: Compositions in percent of air at temperatures selected to mimic different stages of a discharge. They were extracted from table 2.1 by disregarding ions and normalising the sum to 100% (neglecting all other minor gas species). The coloured cells highlight the severity of disregarding ions (and in parenthesis the predicted ion composition percentage at thermal equilibrium).

Mimicked Environment	Temperature (K)	N_2	O_2	Ar	NO	O (+) (%)	N (+)
		Percentages					
Ambient	300	78.07	20.95	0.98			
Space Stem	3000	75.28	17.80	0.93	4.57	1.42	
(Space) Leader	5000	64.61	2.65	0.82	6.75	24.58	0.58
	10000	13.09	0.01	0.53	0.61	23.29 (0.05)	62.46 (0.16)
Return Stroke	15000	0.40		0.47	0.05	21.08 (1)	78.01 (6)

We performed our simulations on several values of the electric field, ranging between 300 kV/m (runaway breakeven threshold [579, p.6951]) and 24 MV/m, and a few values of the air temperature which could reflect very localised regions encountered at different stages of laboratory discharges at ground atmospheric pressure. The variation of the air composition reported in chapter 2.1 is used. Since we have presently no means to model efficiently electron-ion interactions, all atomic ions at high temperatures >8000 K had to be replaced by neutral atoms. The compositions used* are given explicitly in table 5.1. Note that even neglection of only 0.01 % of an ionic component can have a great consequence on electron swarm properties [376, figs.(6–9)] due to the large cross sections from Coulomb interactions with ions (2.106).

In this homogeneous medium, the initial conditions of the electron swarm are:

At $t = 0$ the simulation is initiated as:

- ◊ $T_e(t = 0) = T_{gas}$: Maxwellian distribution (isotropic) in thermal equilibrium with the gas;
- ◊ $N_e(t = 0) = 1$: one seed electron is deposited at $\mathbf{r}_0 = 0$;
- ◊ $N_s(t = 0) = 250\,000$: but this seed is stochastically represented by 250 000 super-electrons. This is an arbitrary choice for scaling purposes.

In some simulations, these conditions may vary, for instance, when studying runaway thresholds and seeding directly runaway electrons in section 5.3, we use a logarithmic distribution of energies between ε_{min} and ε_{max}. Every time our swarm is initiated with such special conditions, we shall mention it explicitly. For all fields above conventional breakdown (which depends on the gas' temperature), the statistics of high-energy super-electrons are enhanced by our compaction algorithm in section 3.3.2.

Physically, our simulations rely on many assumptions which are scattered through chapter 2. Objections and concerns are addressed duly in the forthcoming chapter 6. Here, they are plainly stated for convenience.

* Actually, some batch of simulations at high temperatures were conducted at a slightly smaller gas number density n_{air} and therefore at a different reduced electric field E/n_{air}.

I) Isopykl[♪]: simulations at any temperature are conducted assuming that the number of particles (molecules or atoms) per unit volume is constant. This would mean that the thermal expansion of the gas compensates the dissociation rate of molecules. Assuming the perfect gas law is obeyed, this corresponds to a conservation of the pressure to temperature ratio : $p_{\text{air}}/k_{\text{B}}T_{\text{air}} = n_{\text{air}} = \text{cst}$.

II) Local thermodynamic equilibrium: all species populations (vibrational, electronic) are based on a Boltzmann distribution at the same temperature as the gas.

III) Air composition: conformably to the two previous points, the variation of the chemical composition of air with temperature assumes (I) an equal number of gas molecules or atoms per unit volume and (II) chemical reaction equilibrium (dissociation versus recombination).

IV) Constant gas: despite the reactions induced by the electron swarm on the gas, there is no variation of the gas temperature, density nor composition (nor excited specie population) with time.

V) No ions: the model does not account for the coulombic electron-ion interaction.

VI) No inter-electron repulsion: the electrons do not interact between each other, their diffusion is governed by the external electric field and the collisions with the gas.

VII) Limited superelastic: for vibrational excitations we do include any super/in-elastic transition from $v \to v'$. For electronic excitations, only the transitions between fine-structure states of atomic oxygen are fully accounted for. For all other electronic inelastic processes, we only account for de-excitations to the ground state but not to another excited state.

VIII) Invariable elastic: the elastic cross section with any excited state of the target (molecule or atom) is assumed to be equal to the elastic cross section with the ground state. Thus, the elastic cross section is not affected by temperature.

IX) Instant collisions: no delay in resonant collisions is included.

X) No three-body attachment: only the *dissociative* attachment to molecular oxygen and nitric oxide is accounted for. The three-body processes, which are not modelled, should represent a proportion of the resonant vibrational excitations.

XI) Average rotational excitations: average energy loss $\Delta\mathcal{E}_{\text{rot}}$ through (2.48) as part of (vibrationally) elastic collisions. Included only at energies below 20 eV and electric fields below 100 Td where their effect is most relevant.

On the last point, we remind that the elastic cross section (normally) includes all processes that preserve the initial state of the target molecule or atom. In principle, this should exclude rotational and very low-lying fine-structure degenerate states. In practice, distinguishing purely elastic from weakly inelastic collisions is unfeasible and it is better to find an alternative. For more information, please refer again to pages 114–116 of section 4.1.

[♪] "ισο" + "πυκλος": "equally dense" in ancient Greek. This terminology naturally extends the trilogy of 'isotherm', 'isobar' and 'isochore' curves that respectively preserve the temperature, the pressure and the volume in thermodynamic processes of gases.

Our model assumptions being now clearly refreshed in the minds of our readers, we may now proceed to the results of our swarm simulations.

5.2 Swarm Studies

Our main goal is to understand how does electron thermal runaway occur, under which conditions and what factors may influence it. Electrons that become runaways represent an extremely small portion of the entire electron swarm. Therefore, as a preamble to the study of runaway electrons, it may be of interest to describe how does an electron swarm behave in a uniform electric field under various:

i. gas compositions (at identical temperatures).

ii. (reduced) electric fields $E(/n_{\mathrm{gas}})$,

iii. temperatures of air (which also affect its composition as in table 2.1),

In particular, we would like to characterise how fast does the swarm grow, the overall spatial extension rate (drift and diffusion) and the heating (or reaction) rate. These quantities depend on the electron energy spectrum (and the angular velocity distribution). Thus, we first show how this spectrum is affected in the next subsection. Then, we present transport parameters and reaction rates.

5.2.1 Spectrum

What we call "spectrum", is the electron energy distribution function (EEDF) obtained from the velocity distribution but in energy space. We calculate EEDF from the method presented in section 3.3.1 based on a histogram using the Knuth fixed-width rule in logarithmic space ($\ln\varepsilon$) of the electron energy ε.

Above 3 MV/m, our EEDF is enhanced with the compaction algorithm that we first published in Schmalzried *et al.* [813] and which we further improved in sec. 3.3.2. Spectral enhancement may be appreciated on figure 5.3a by comparing the short and noisy tail of the EEDF at 2.8 MV/m compared to the protracted tail at 5 MV/m, whose maximal resolution was limited with the $w_{\min}$ parameter (see eq. 3.25) down to a ratio of 10^{-20} high-energy electrons over the total number of electrons in the swarm. This enhancement enables us to see what happens with the distribution of high-energy electrons as the temperature, gas composition or electric field changes.

i. Gas. We first show in figure 5.1 the EEDF at 300 K and 12 MV/m (~ 470 Td) in pure nitrogen (dark blue), pure oxygen (light orange), pure argon (magenta) and in standard air (p. 40).

Ar The spectrum in argon has the highest electron density around 10 eV due to its first inelastic excitation at 11.55 eV.

N_2 A salient characteristic in nitrogen is the first drop of the EEDF right at 2 eV corresponding to the onset of the $N_2^-\ ^2\Pi_g$ resonant collisions for vibrational excitations (see, for instance, fig. 11.25–top). Inelastic losses in N_2 are important, and the spectrum at high energies is the lowest.

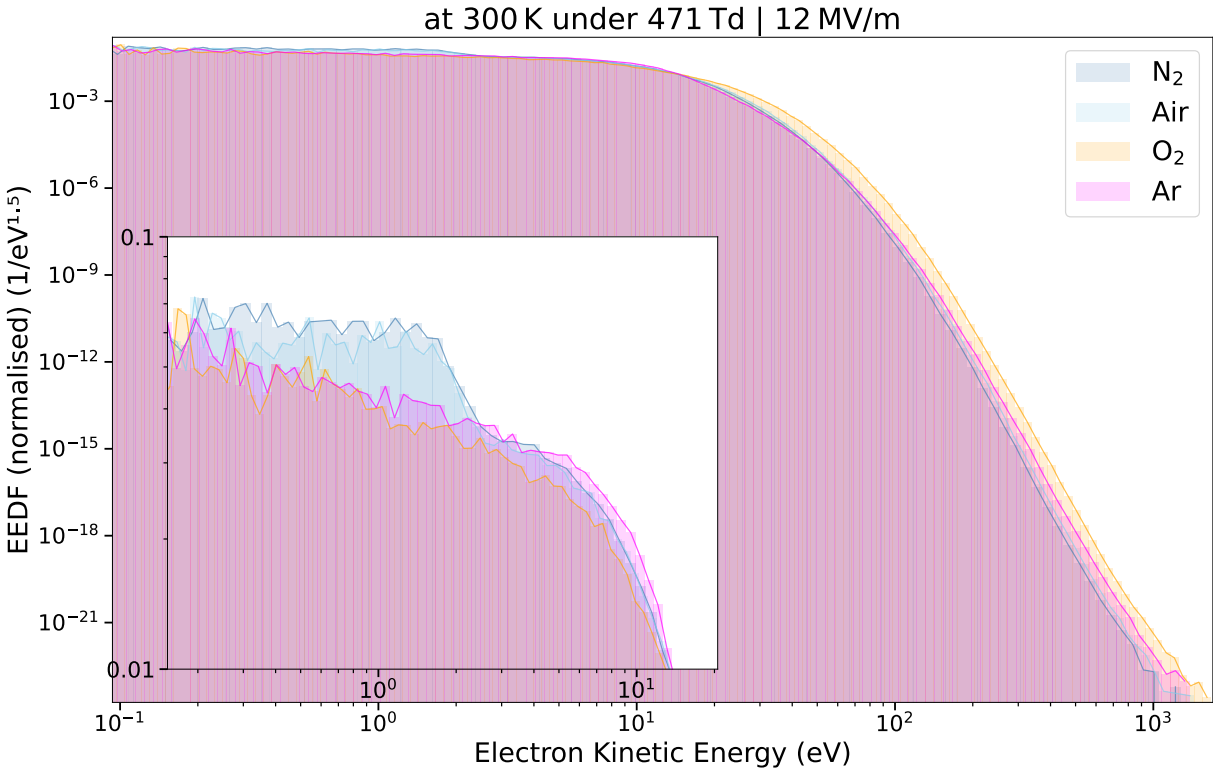

Figure 5.1: Steady-state electron energy distribution functions in different atmospheric gases at ambient temperature and at a high electric field of 12 MV/m. The inset shows a zoom of the upper part in the same energy range.

O_2 Vibrational CS in oxygen are very different from nitrogen. They have much sharper, well-separated peaks located at energies below 1 eV. As a result, the drop in the spectrum at low electric fields is characterised by a series of undulations as seen in figure 5.2 from 0.1 to 1 eV, each associated to one vibrational resonant peak. In figure 5.1, this drop is not observed because the electric field is too high, and also because of the noise. On the other hand, we observe a depletion of electrons in the 5–10 eV segment compared to EEDF in other gases, due to the dissociative attachment (to be seen on fig. 11.29). In contrast, there are comparatively more electrons at energies > 15 eV in O_2.

Air Qualitatively, the electron spectrum in air looks very much like a weighted averaged between the spectra in N_2 ($\times 4/5$) and O_2 ($\times 1/5$).

A notable characteristic of swarm spectra in molecular gases compared to monatomic gases is the presence of a tall plateau followed by a sharp drop at energies around the electron-Volt. This is due to strong resonant vibrational cross sections which act as a barrier to low-energy electrons being accelerated in the field. This barrier is overcome either by increasing the electric field (fig. 5.3-inset) or by increasing the (vibrational) temperature of the gas which populates excited states and enables superelastic collisions from vibrationally excited molecules (illustrated in section 5.4.1, inset of figure 5.24).

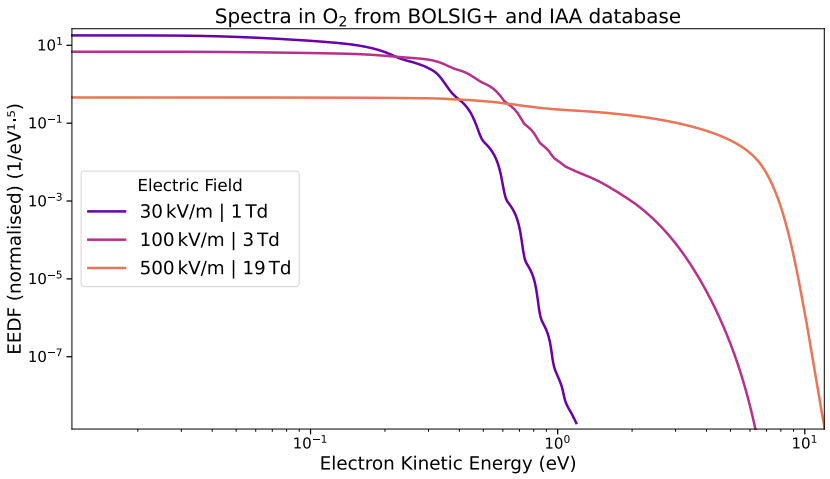

Figure 5.2: Steady-state electron energy distribution function in molecular oxygen at three different uniform electric fields calculated by BOLSIG+ with our complete set of cross sections. We illustrate the transpearence of oxygen's sharp vibrational resonances peaks as undulations on the declining edge of the EEDF between 0.2–1 eV.

ii. Electric field. Second, we see in figure 5.3 how increasing the electric field pushes more electrons toward higher energies. The "vibrational plateau" shown in the insets becomes less tall and less steep. Another interesting feature is the apparition of a tail to the electron energy spectrum. It is noticeable from the kink* in the spectrum observed between 1–2 keV.

The observation of this tail supports the distinction of two electron populations which we introduced long before in section 1.4 and illustrated in figure 2.1: (A) the bulk consisting of thermal electrons and (B) the runaways which accelerate in the field. Raising the electric field swells the tail and reduces the kink. This implies a weaker separation between bulk and runaways because of the electric pulling force's capacity to overcome electron energy losses in collisions. A runaway tail of the spectrum appears at lower electric fields in air at higher temperatures (and constant density) because of the dissociation of molecules into atoms. This diminishes the average friction force as can be appreciated in figure 5.11.

iii. Air temperature. On figure 5.4, we stacked three graphs where we compare simulations at different temperatures for three fixed values of the electric field. While at 200 Td, the effect of temperature is rather small, we see that at 400 Td (10 MV/m), a tail of high-energy electrons in air can be present only in heated air above about 8000 K. This emergence of this tail extends to all temperatures when the field is above 500 Td. The graph at 400 Td which is not far from the range of peak fields calculated on streamer heads [575, fig. 5d], suggests that the emergence of high energy electrons could also be promoted by an ionisation wave propagation in a strongly dissociated channel without necessarily needing to raise the electric field by a significant factor.

5.2.2 Transport

An overview of transport parameters in air at different temperatures as a function of the reduced electric field is displayed in figure 5.5. For an explanation of transport parameters, consult section 2.3. As expected, electron swarms in hotter air and at stronger electric fields are more expansive: they move, diffuse and multiply faster, their average energy $\langle\varepsilon\rangle$ is higher.

We draw our attention to the attachment rate coefficient (ν_a) in the lower-right panel of figure 5.5. There seems to be an optimal temperature (~3000 K) and electric field (~200 Td) at which the attachment rate is maximal in air. Under these conditions, the electrons in the 5–10 eV energy range attach massively to oxygen molecules through resonant dissociative attachment as observed in figure 11.29 (p. 434) in the second part of the thesis.

*From Collins: "A kink is a curve or twist in something which is otherwise or normally straight."

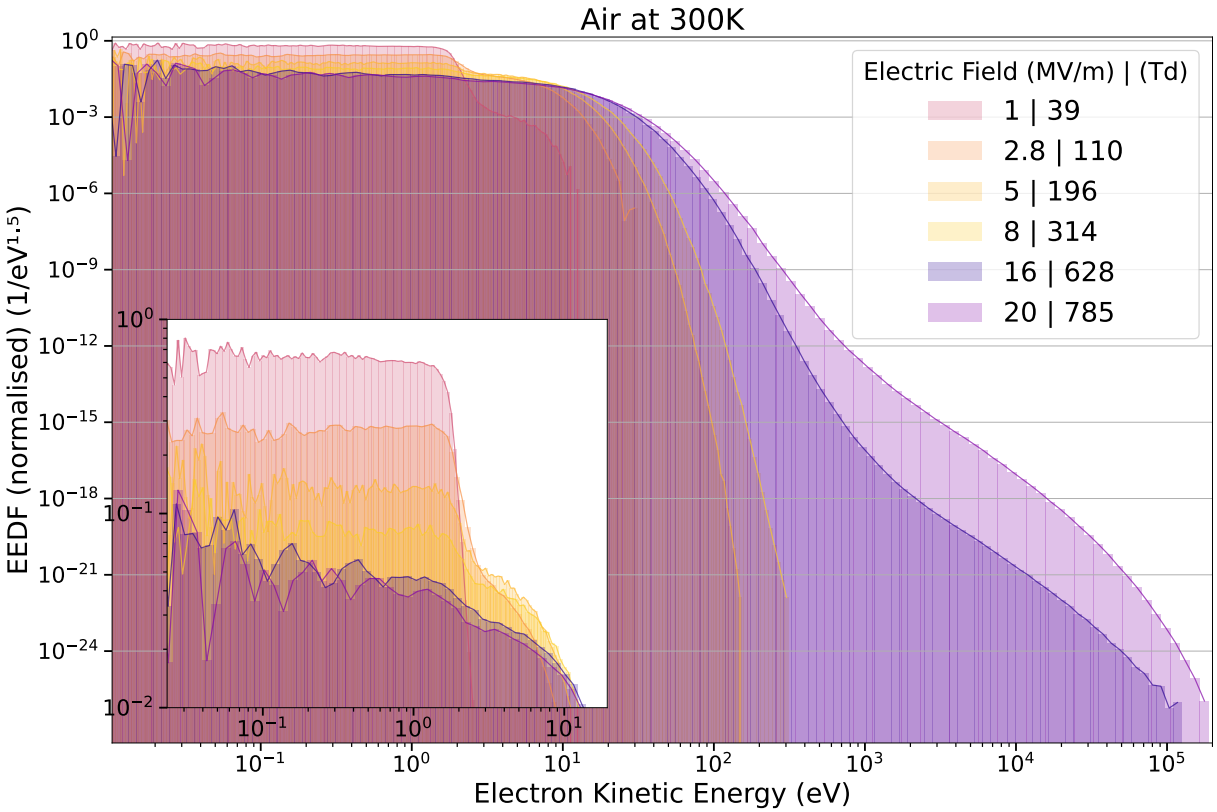

(a) In ambient air, raising the electric field enables electrons to overcome the barrier from resonant vibrational excitations starting at 2 eV. The spectral enhancement algorithm in sec. 3.3.2 is activated at fields above 3 MV/m. It unveils the high-energy tail of the spectrum but deteriorates the signal-to-noise ratio at lower energies <0.1 eV.

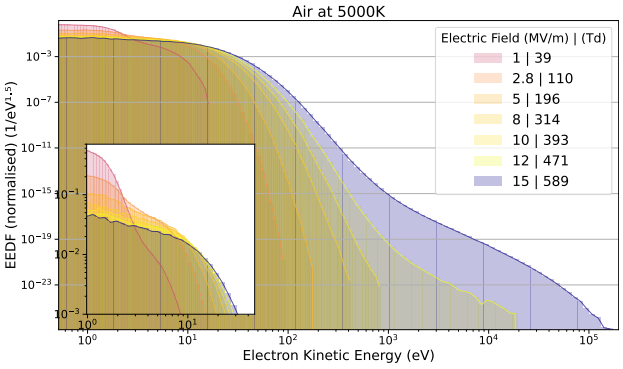

(b) At 5000 K molecular oxygen is almost completely dissociated and the vibrational barrier of nitrogen is lessened by 10 % of dissociation and vibrationally excited states.

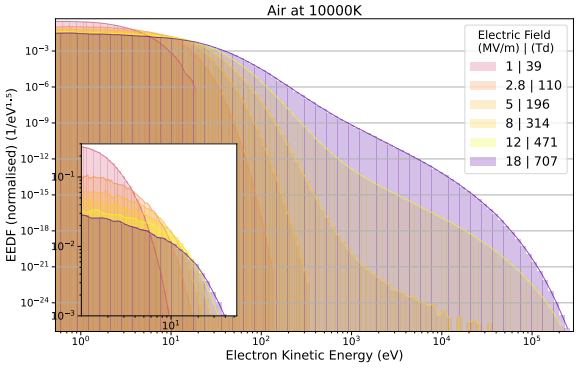

(c) At 10 000 K molecular nitrogen is mostly dissociated and thus the barrier of vibrational excitations disappears.

Figure 5.3: Electron energy distribution functions calculated with (3.16) in air at three temperatures and composition as in tab. 5.1, with increasing electric fields.

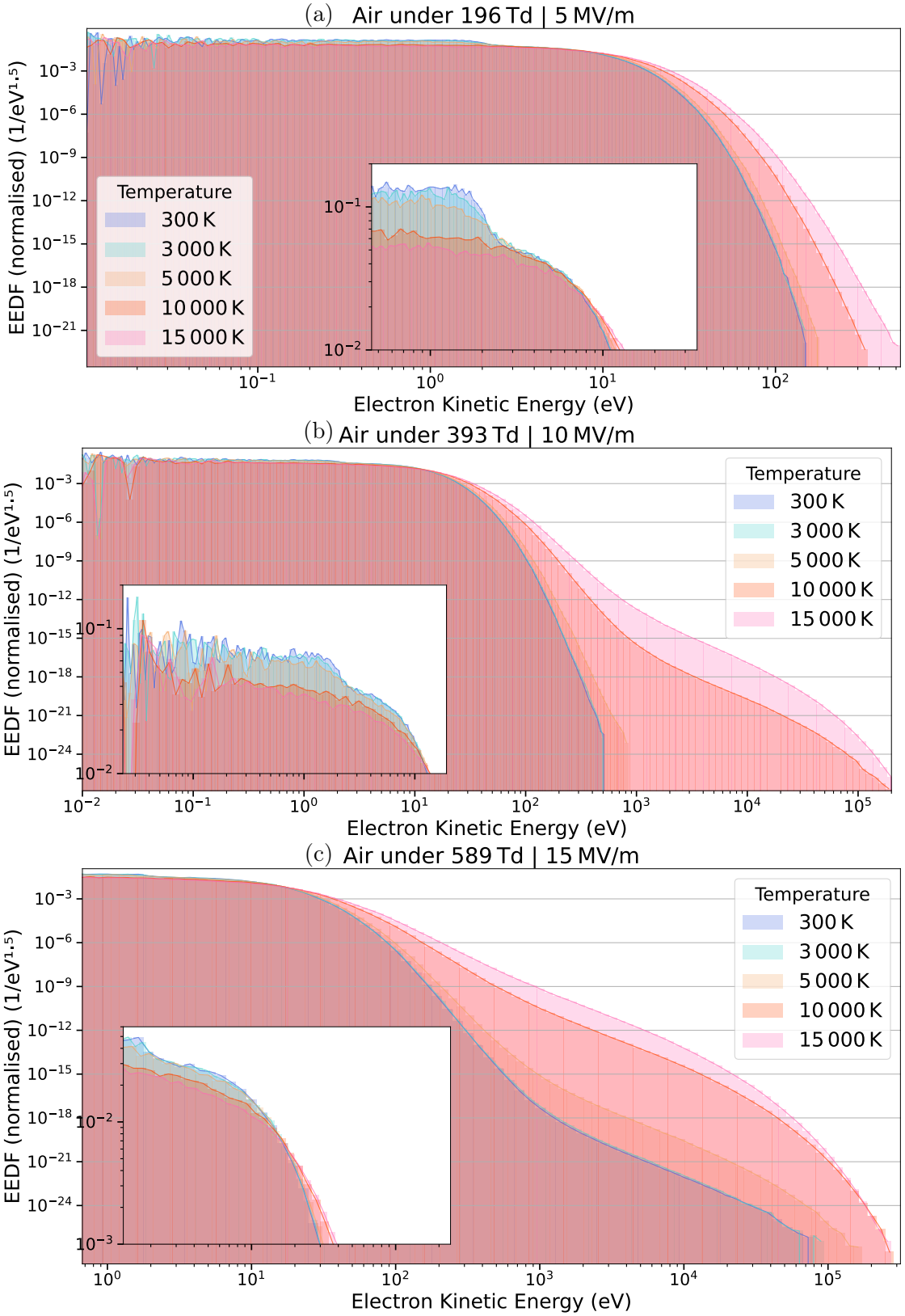

Figure 5.4: Influence of air temperature (and composition) on the electron energy distribution functions at three different electric fields.

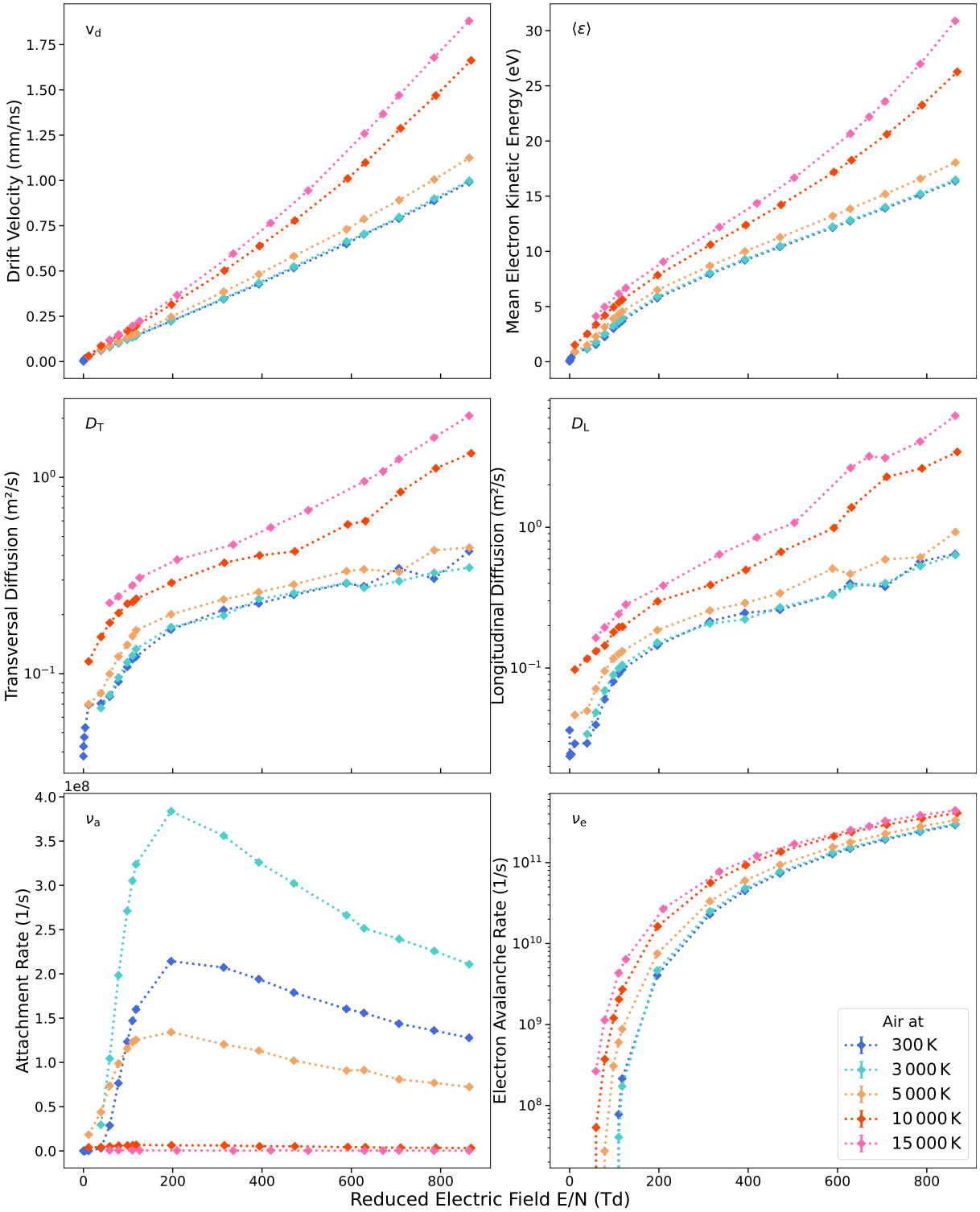

Figure 5.5: Transport parameters in air at various temperatures which determines its composition as in table 5.1 and according to the electric field at atmospheric density. Electron swarms are more expansive at higher air temperatures and electric fields.

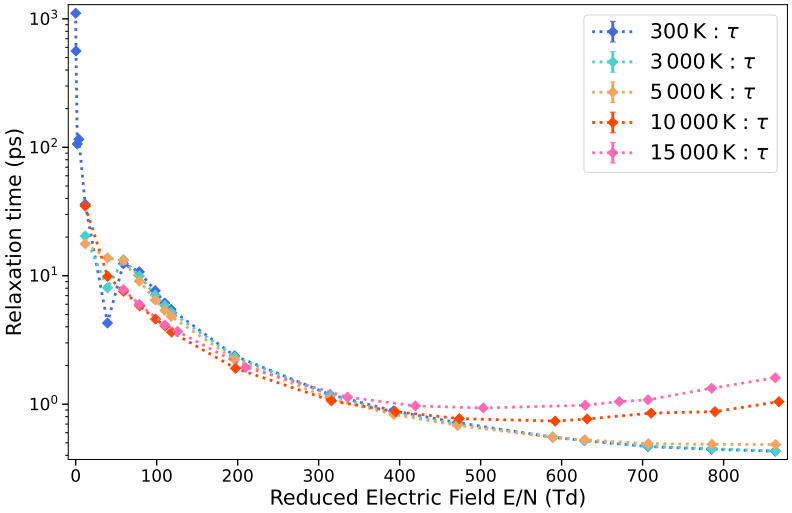

Figure 5.6: Relaxation times are fitted to exponential-like relaxation curves of the average kinetic energy $\bar{\varepsilon}(t)$ according to time. These are the grey coloured portions seen on fig. 3.7. We may remember that above 50 Td at atmospheric density, swarms relax in about 10 ps or less.

- Under 200 Td, the relative proportion of electrons in the 5–10 eV is maximal as seen on the light-orange curve in the inset of figure 5.3a.
- At 3000 K, oxygen is still present to 85 % in molecular form. The electron spectrum is virtually unaffected by the gas temperature (fig. 5.3) but the electrons attach more easily to vibrationally excited oxygen molecules (cf. fig. 2.14 p. 68). It is the vibrational temperature of oxygen that plays a role in this case.

Nevertheless, at high temperatures, there is evidence showing that electron detachment (not taken into account here) becomes important above 1000 K [11, §3.3]. Since attachment is enhanced by vibrational temperatures T_{vib} whereas detachment by kinetic temperature T_{gas}, vibrational relaxation is essential for understanding the evolution of conductivity in a heated strip of air. Benilov and Naidis [57, p.1834:§2] argue that oxygen molecules relax fast vibrationally and can be assumed to be thermalised ($T_{\text{vib}} \approx T_{\text{gas}}$). Still, Laporta *et al.* [559] found that a significant departure from the Maxwell-Boltzmann distribution (B.22) persists during the vibrational relaxation of a pure gas of oxygen molecules excited by a swarm of non-thermal electrons. One should remember thus, that it could be possible that a *vibrationally* super-heated (but not thermalised) plasma channel would reinforce the attachment instability which may form in the wake of a streamer and give birth to space stems [621].

Transport parameters describe the average motion of the electron swarm after it has relaxed within ~ 10 ps for electric fields above 50 Td in a homogeneous medium as seen on figure 5.6. This relaxation time is much longer at low electric fields below breakdown and can last a nanosecond or more. However, the estimation of relaxation times is subject to large uncertainties.

At electric fields above breakdown, the exponential growth of electrons defies the applicability of our results to the physical modelling of swarms. There are two main aspects that need to be checked when the number of electrons becomes very high:

× When the density of electrons n_{e} becomes a significant proportion of the gas density n_{gas}, inter-electronic (and ionic) forces dominate over electron-neutral collisions.

× When the electric field E_{SC} generated between the swarm and the space-charges (electrons in the swarm and ions left behind) becomes of the order of the external electric field E_0, the electron avalanche transforms into a streamer front [548, p.3].
This condition ($E_{\text{SC}} = E_0$) is also known as the Meek criterion [641].

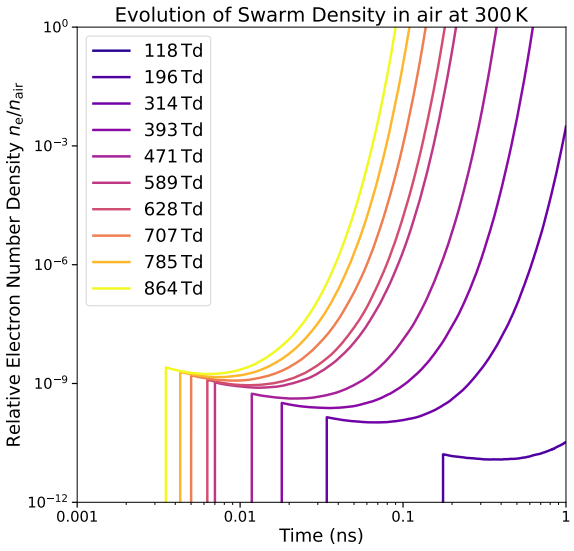

(a) Coarse estimation of the core swarm density n_e at high electric fields. The first value appears when there are at least two physical electrons $N_e = 2$ in the simulation. Then, the swarm first diffuses in space before the exponential growth takes over. This behaviour is not necessarily physical, see text for explanation.

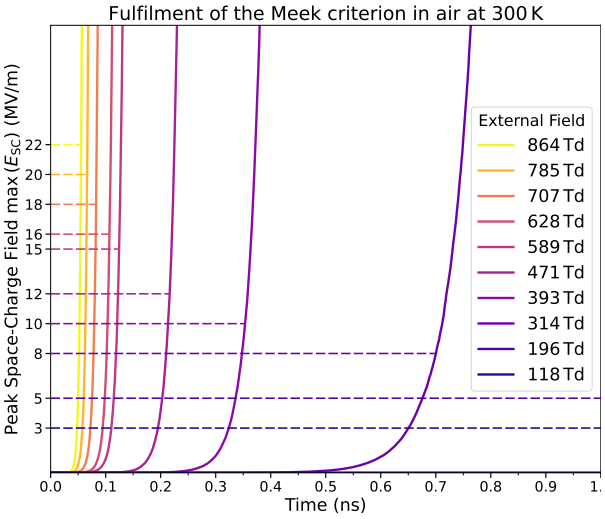

(b) Coarse estimation of space charge field E_{SC} at the midpoint between two spherical Gaussian distributions of charges: one for the static ions and one for the electron swarm. The dashed lines intersect the space charge field when it equals the external field E. At this intersection, the Meek criterion [641] is met.

Figure 5.7: Physical limits of our free swarm simulations in homogeneous conditions.

These two conditions are related. They are juxtaposed on figure 5.7, where we see an exponential increase for both. At any time of the simulation, we estimate the swarm density by assuming it is distributed in a Gaussian ellipsoid with two different spreads: the transversal $s_\perp^2$ and longitudinal $s_\parallel^2$ variances which are calculated as:

$$2s_\perp^2 = \frac{1}{N_e}\sum_{n=1}^{N_s} w_n\left[(x_n-\bar{x})^2+(y_n-\bar{y})^2\right] \tag{5.1}$$

$$s_\parallel^2 = \frac{1}{N_e}\sum_{n=1}^{N_s} w_n(z_n-\bar{z})^2 \tag{5.2}$$

Since the actual distribution is not perfectly Gaussian, we decided to estimate the average inner density of the swarm as the number of expected electrons in a cylindrical volume determined by $\pi s_\perp^2 \times s_\parallel$. This gives:

$$\tilde{n}_e = N_e\frac{\mathrm{erf}(1/\sqrt{2})(1-\mathrm{e}^{-0.5})}{s_\parallel\,\pi s_\perp^2} \approx 0.0855\frac{N_e}{s_\parallel s_\perp^2}\,, \tag{5.3}$$

where we replaced in the last equation, the numerical value calculated by the error function (erf) (integral of the axial 1D Gaussian) and the exponential (integral of the radial 2D Gaussian).

What is peculiar in our case, is that because of our use of super-electrons, we may arbitrarily calculate a swarm density for any number N_e of physical electrons, even when they are too few to make reasonable statistics. Our simulations start with 1 physical electron represented by $N_s = 250\,000$ super-electrons all located at the origin. It is thus logical to see our densities decrease first on figure 5.7a because of diffusion of our super-electrons before they rise again

from exponential growth. The aspect of the graph may reflect how real electrons would diffuse in a gas depending on the initial conditions, but the magnitude is incorrect. One would need to adapt the scale by a factor of 250 000, in which case each super-electron would represent a real electron, and adjust the spatial scale if necessary, for instance by spreading the real electrons over a larger volume.

The estimation of the space-charge field can be even more tedious. To preserve a simple analytical approximation, we model the charge distributions of the fixed positive ions and the drifting swarm as two Gaussian spheres separated by a distance between the two centroids. We keep track of the position of positive ions created at each ionisation event and assume that they are immobile. The centroid of the swarm is the mean of the actual electron positions ($\mathbf{r}(t)$) from equation (2.88). Denoting by d the distance between ionic and electronic centroids, the peak space-charge field* is calculated at the midpoint $d/2$:

$$\max_{\mathbf{r}} E_{\mathrm{SC}}(\mathbf{r}) = 2\frac{eN_{\mathrm{e}}\left[\mathrm{erf}(x) - \mathrm{e}^{-x^2}2x/\sqrt{\pi}\right]}{4\pi\epsilon_0(d/2)^2} \quad \text{with} \quad x = \frac{d/2}{\sqrt{2(s_{\parallel}^2 + 2s_{\perp}^2)/3}}\,. \tag{5.4}$$

This field corresponds to the addition of fields of two decentred oppositely-charged Gaussian spheres at their midpoint $d/2$. The value $(s_{\parallel}^2 + 2s_{\perp}^2)/3$ represents the average variance of the Gaussian over all three dimensions, we neglect its ellipsoidal shape. The expression in squared brackets is the proportion of particles contained in a 3D Gaussian spherical distribution.

We use very rough estimations just to understand the limits of our modelling of swarms. When either the electron density becomes a non-negligible fraction of the gas density $n_{\mathrm{e}} \simeq 10^{-4} n_{\mathrm{gas}}$ or when the space-charge field approaches the external field $E_{\mathrm{SC}} \simeq E$, we know that we have reached the limits of validity of our model. The avalanche-to-streamer transition was studied more thoroughly in Monte Carlo models by Kunhardt and Tzeng [543].

5.2.3 Reaction Rates

Swarm simulations enable us to retrieve reaction rates useful as input to more sophisticated codes to model for instance the emissions from excited molecular nitrogen bands and from atomic oxygen observed especially in the 777 nm peak. Some examples of reaction rates are shown on the side in figure 5.8. However, these rates may not be directly used to correlate the emission intensities in a discharge with the temperature because many other processes intervene before radiation is emitted.

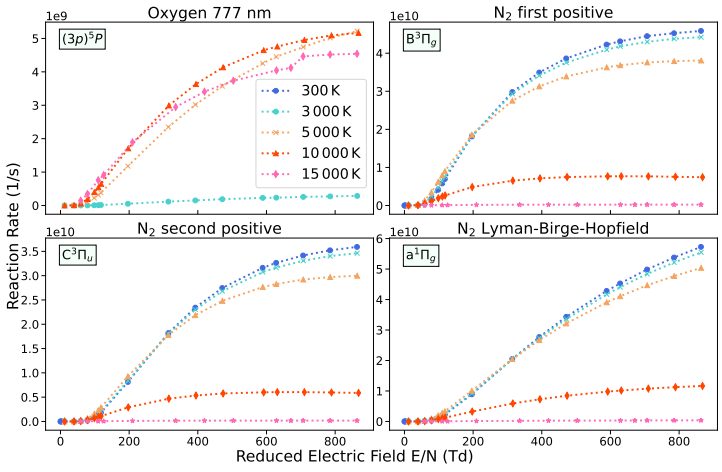

Figure 5.8: Reaction rates in air at various temperatures which affect the abundance of the species considered.

*Actually, the position of the maximum of the electric field generated by two opposite Gaussian charge distributions is more complex. In each sphere, the field peaks at the radial distance $r \approx 0.9678\sqrt{2}s$ for a variance s^2. When the spheres are close together, the maximal field is in the midpoint, but at a critical distance, the maximum splits into two peak images. However, we may assume that the electrons are never separated farther from the ions than the variance of their Gaussian distribution.

One has to account for chemical reactions in the gas, cascades, quenching and maybe even superelastic collisions before the radiation by spontaneous emission can estimated from the concerned excited species. The graph given here is only for illustration.

What we are interested to know, is whether electron swarms may significantly affect the temperature and chemical composition of the gas on very short timescales.

Heating

Since temperature is of concern to us, we explore in figure 5.9 the heating rates of the vibrational modes in diatomic molecules and the fast heating [759] through electronic excitations of all species comprised together. We remind that during the development stage of discharges, the energy lost by electrons to excitations is stored in separate reservoirs from where thermalisation takes place on different timescales. Rotational and translational energies are thermalised within a nanosecond, whereas vibrational energy stays apart over the order of a millisecond.

The energy in electronic states is harder to track. The conversion of the energy from excited electronic states into translational heat operates on different timescales depending on the state and the electric field [296, §2.4–5]. For some states, a great part of the energy may be lost by radiation. Other states, on the other hand, may be metastable over long durations. We did not perform any such distinction and we simply lump all inelastic losses to electronic excitations together in the last graph on the lower right corner of 5.9. More information and references on this issue were given in section 2.1.3.

What is important to notice is that the rate of energy transfer from the electron swarm to vibrational and electronic/ionic excited states are complementary in two ways:

- ▷ Transfer to electronically excited states is always a monotonically increasing function of the electric field and of the temperature of the gas*
- ▷ Transfer to vibrationally excited states decreases with the temperature of the gas and there is an optimal electric field at which it goes through a maximum. In a very short range of electric fields below breakdown, raising the temperature may also raise energy transfer to vibrational states by increasing the average kinetic energy of the electrons.

If we wish to convert the rate of energy loss into a heating rate, we must change the perspective from the electron swarm to the gas medium. If we consider all gas species g and all collisions c forming a common reservoir R of processes:

Swarm, dissipated power per electron:
$$\bar{h}_R = \sum_{g,c\in R} \underbrace{\frac{1}{N_\mathrm{e}} \sum_{n=1}^{N_\mathrm{s}} w_n n_g \sigma_{g,c}(\varepsilon_n) \mathrm{v}_n}_{\text{Reaction rate}} \Delta\mathcal{E}_{g,c} \,, \tag{5.5}$$

Gas, dissipated power to a molecule:
$$Q_R = n_\mathrm{e} \bar{h}_R / (\sum_{g\in R} n_\mathrm{g}) \,. \tag{5.6}$$

Obviously, the dissipated power Q_R depends on the electron density n_e which grows exponentially (cf. fig. 5.7a), and on the swarm dynamics, since we assume that the gas is fixed whereas the swarm drifts in the electric field. To obtain an average temperature rise rate, we may divide the average energy level in a reservoir by the dissipated power.

*Until perhaps unearthly temperatures would be reached where superelastic collisions take over.

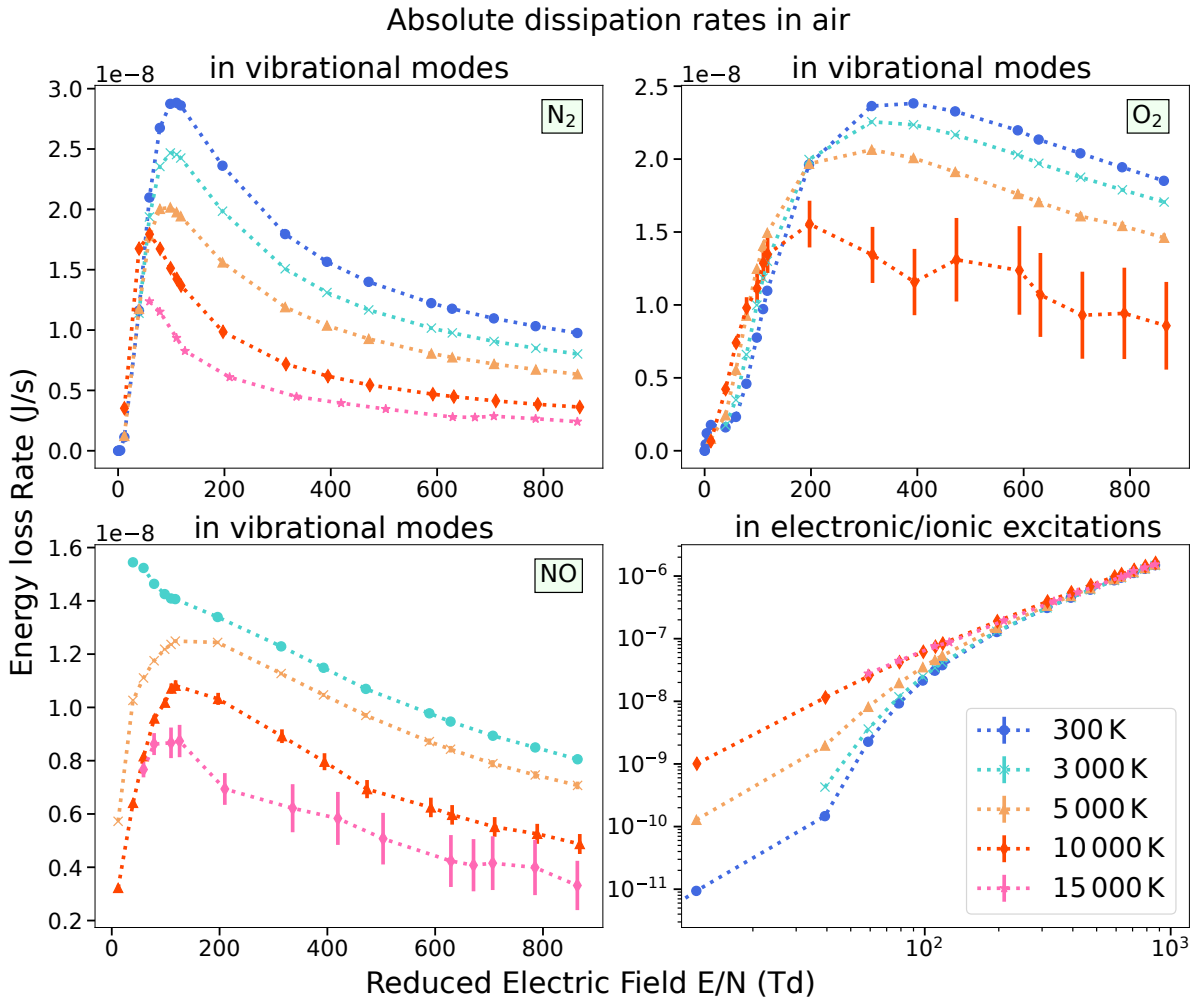

Figure 5.9: Dissipated power (energy loss rate) per electrons to different excitation modes in air at different temperatures and electric fields. The energy loss rates in each species are divided by the abundance ratio of that species. These are thus to be understood as the average energy transmitted from one electron to a given species. Physical heating rates are obtained by multiplying by the electron density n_e and dividing by the density of the gas: $n_{gas} = 2.547 \times 10^{25}\,\mathrm{m}^{-3}$.

From figure 5.9, we obtain that an overall magnitude of 2×10^{-8} J/s power is conceded to the vibrational modes of N_2 or O_2. If we let a swarm of relative density $n_e/n_{gas} = 10^{-6}$ pass over a patch of air for 1 ns, we would obtain an increase of roughly $\Delta T_{vib} = 1.5\,\mathrm{K}$ only. Therefore, we may remember that heating a gas in a plasma channel requires several µs to reach temperatures that would transform it into a hot leader core.

Dissociation

Next, we may wish to know what is the dissociation rate of molecules in a discharge channel and understand whether the swarm can induce a significant change in the chemistry in a short duration of time.

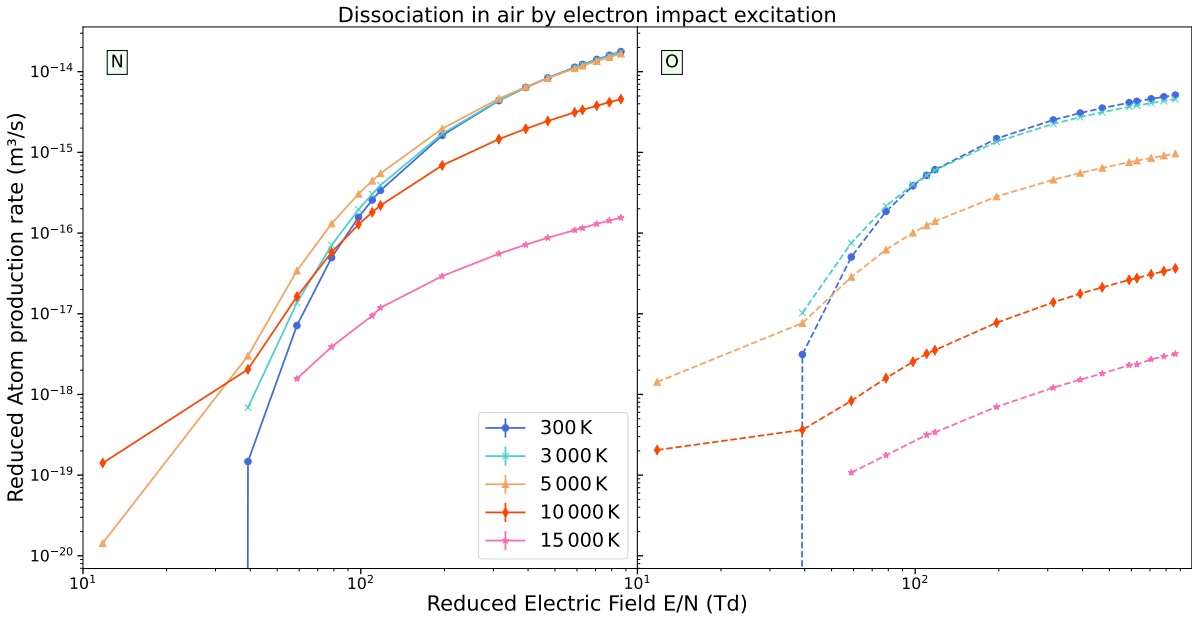

Figure 5.10: Reduced production rates of atomic nitrogen and oxygen by electron swarms in various temperature and electric field conditions. To obtain the characteristic time for dissociation of a molecular species, one has to divide the electron density n_e by half the production rate of atoms (because most come from diatomic homonuclear molecules).

On figure 5.10, we give directly the production rates of nitrogen and oxygen atoms from all dissociative processes (direct dissociation, predissociation, attachment but not dissociative ionisation). This is a lower boundary for the production of atoms. At different temperatures, the chemical composition changes and the species can rarefy. Because nitric oxide is easier to break than N_2, there is a small effect induced by the presence of NO when the electric field is weaker and the temperature around ~ 4000 K. A similar calculation to the one for heating reveals that gases in the wake of active streamer channels would dissociate over a characteristic time of a few µs also.

This concludes our study of electron swarms in homogeneous gases and electric fields. We see that electrons quickly relax to steady-state conditions in which the transport and reaction coefficients are constant. If one wishes to study the effect of electron swarms dynamically, as in the case of discharges, then, those coefficients may be "plugged" into more complex fluid simulations ([172, 531, 588, 621, 926] to name a few examples).

In the next section, we move toward a less studied aspect of electron swarms focussing now not on the bulk population but on the higher end of the energy spectrum: the intermediate and runaway electrons.

5.3 Runaway Electron Studies

⊛ ¿ What is a runaway electron ?

We may start from the definition given by:

Kunhardt *et al.* [544, p.444]

> “An electron is a runaway if it does not circulate through all the energy states available to it at a given E/n_{gas}, but on average moves towards high-energy states.”

Conversely, a thermal electron accelerates, bounces, decelerates so that, on average, its energy fluctuates around the mean kinetic energy of the swarm in the given conditions.

What supposedly separates both electron populations – runaways from thermals – is the runaway energy threshold $\varepsilon_{\text{r}}(E/n_{\text{gas}})$ which is the energy beyond which, at a given reduced electric field E/n_{gas}, all electrons are runaways; i.e. they keep accelerating to higher energies until they eventually escape the region of high-electric fields and therefore truly “run away”.

The difference in behaviour of thermal electrons from runaway electrons may be clearly seen by the aspect of the electron energy distribution function at low and high energies respectively. Such distributions were displayed in section 5.2.1. Nevertheless, there is no clear-cut separation between both regimes, but rather a continuous distribution of electrons ranging from a few eV to several MeV.

This separation is blurred by the stochastic nature of the collisions incurred by electrons. For instance, an electron at 10 keV might lose considerable amounts of energy in a series of quickly consecutive ionisation events and wind up in the thermal region, whereas another electron starting only at 1 keV might elude ionisation losses and accelerate up to 100 keV.

Defining a threshold ε_{r} that parts the population into two categories is not an easy task. One must compare how probable those two events are, and decide when they can be considered negligible. This probabilistic approach is to be addressed in the first subsection 5.3.1.

Admitting that such a threshold ε_{r} exists and may be determined from a salient characteristic, we may then ask:

⊛ ¿ How long does it take for an electron to become runaway ?

Suppose we unleash an initial swarm of 1000 electrons and set a stopwatch till we observe the first electron that reaches ε_{r}. This time corresponds stochastically to the minimal time measured amongst a set of 1000 experiments with a single electron. It is precisely not an average. Thus, should we repeat the experiment with a massive swarm of 10^9 electrons, this delay ought to be smaller. There is obviously a physical limit to the delay (see figure 2.4), and one would need an unruly number of electrons to summon such an improbable event. Nevertheless, what we are interested in, is to know whether there exists an average time delay after which, in a given electric field, we can expect an initially thermal electron to become a runaway. This is to be investigated in section 5.3.2.

If this delay can be defined, so we may wish to know:

⊛ ¿ How many runaways can be produced per unit time ?

Again, this question requires to examine the scaling of the problem. It does not make sense to adopt a single-electron approach since after an electron becomes runaway, the story ends. Here, instead, we ought to consider the whole electron swarm and count how many electrons per unit time cross the runaway energy threshold.

This defines a thermal runaway rate ν_r. The problem is that secondary electrons from ionisation are produced continuously, and furthermore, if the runaway threshold is estimated to be at 10 keV for instance, how should one discriminate electrons who toiled all the way from thermal energies to the runaway threshold from secondary electrons that were produced very near the threshold or even beyond the threshold. In other words, how should we (or should we at all) distinguish electrons that *became* runaway from those that were *born* runaway (from previous runaways)? That is the topic of section 5.3.3.

5.3.1 Thresholds

The state toward which an electron evolves is governed by the balance of the continuous electric pull and the regular but stochastic losses endured in collisions. As we know, at high energies, most collisions are frequent but "anodyne" in the sense that only small deviations and comparably small energy losses occur. Altogether, they may be modelled as a pseudo-continuous friction force or "stopping power" (2.71) whose various declinations we discussed on page 2.2.3. On figure 5.11, we represent dynamic friction forces calculated in air at four different temperatures. At a given electric field $\mathbf{E}$ the intersection of the friction force with the electric pull $|e\mathbf{E}|$ would give a definition of the runaway energy threshold.

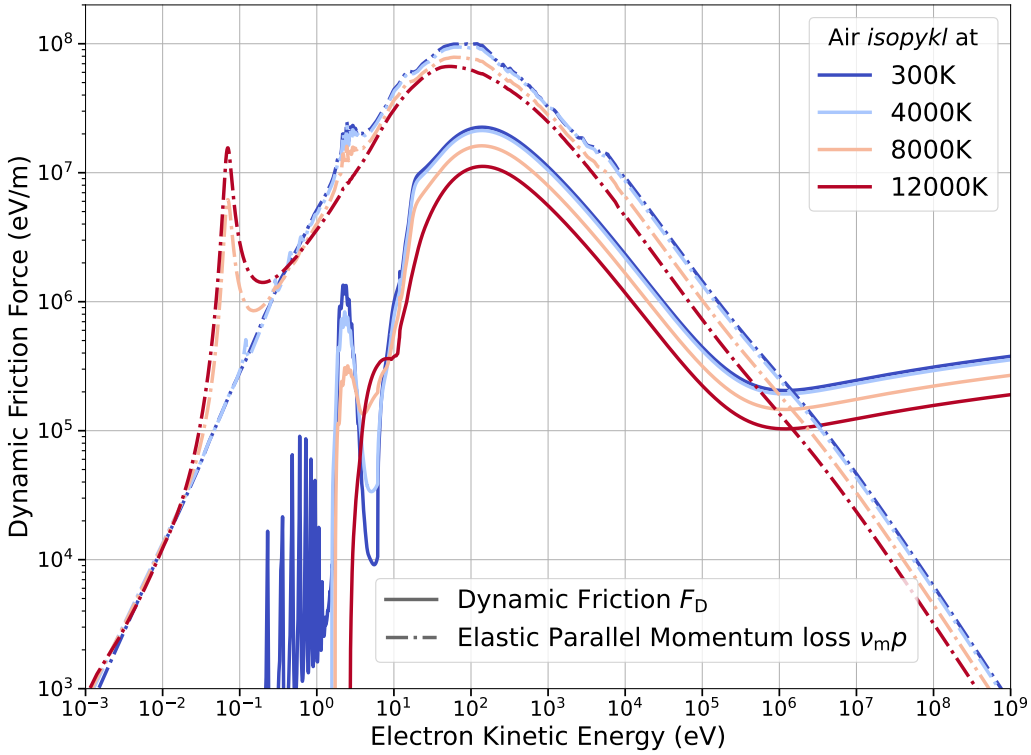

Figure 5.11: Dynamic friction forces and parallel momentum loss from elastic collisions in air at different temperatures changing its composition as reported in table 2.1. "Isopykl" means that the gas particle density is maintained constant (and equal to $2.547 \times 10^{25}\,\mathrm{m}^{-3}$). The friction and momentum losses are lowered at higher temperature because (1) the particle density is conserved and (2) the cross section (elastic or inelastic) of an atom is smaller than that of a diatomic molecule of that atom.

This ideal separation is blurred in reality because of the stochastic nature of electron propagation in gases examined in section 2.2.3 and discussed many times in the literature [218, 579].

There always persists a probability, albeit small, of a major energy loss or strong angular deviation that would demote an electron from the runaway regime. That event could be a high-energy bremsstrahlung or impact ionisation emission, but also a backscattering event (after which the electron starts decelerating). Moreover, even if we could exclude events of very low probability, the balance of forces from collisions and electric pull depends also on the orientation of the electron with respect to the electric field. Thus, the runaway threshold, if is exists, would not be a point at a given electric field and electron energy, but actually a dividing line on a 2D graph displaying the cosine $\cos\chi$ with respect to $\mathbf{E}$ and the velocity of the electron.

On figure 5.12, we display the average cosine $\langle\cos\chi\rangle$ of the direction of electrons and the electric field $\mathbf{E}$. The coloured zones show one standard deviation of the distribution of cosines according to the electron's energy ε. We see clearly that there is a correlation between the energy and the direction implying that fast electrons that are not anti-aligned with the electric field quickly decelerate toward lower energies.

A probabilistic study of runaway threshold at a fixed electric field and gas composition should therefore explore two variables: the initial electron energy ε_0 and the initial electron cosine $\cos\chi_0\hat{\mathbf{v}}_0\cdot\hat{\mathbf{E}}$ with respect to the electric field.
We thus performed several batches of simulations changing the initial conditions of the electrons.

Conditions of the medium:

- A fixed electric field $\mathbf{E}\parallel\hat{\mathbf{z}}$ varying between 0.3–22 MV/m
- Homogeneous air at four different temperatures 300 K, 4000 K, 8000 K and 12 000 K and constant particle density of $2.547\times10^{25}\,\mathrm{m}^{-3}$.

Initial conditions of the electrons:

- 500 000 fast electrons
- starting with energies ε_0 regularly spaced on a logarithmic scale between 100 eV and 2 MeV
- initially anti-aligned or aligned with the electric field or distributed isotropically.

We then tracked the energy ε of each electron every 5 ps for a total period between 400 ps and 700 ps. The electrons of lowest energy from impact ionisation events are automatically discarded from the simulation, only 'primary' electrons are kept.

Then, in relation to runaway, at any time t, we determine two different probabilities for an electron as a function of its starting energy ε_0.

▷ Acceleration probability $\mathcal{P}_{\varepsilon>\varepsilon_0}(t;\varepsilon_0)$: that an electron be accelerated to an energy ε higher than ε_0 (its initial energy).

▷ Run-to-MeV probability $\mathcal{P}_{\to\mathrm{MeV}}(t;\varepsilon_0)$: that an electron be above 1 MeV if it started at ε_0.

Those probabilities are determined through a windowing technique on the ensemble of 500 000 electrons. Over a window of width N_w, we calculated the ratio $\mathcal{P}_\mathrm{w}(\varepsilon_0) = N[\varepsilon > \varepsilon_0]/N_\mathrm{w}$ for N_w electrons spread around ε_0 by an equal factor (e.g. 1.1, 1.01). In words, this ratio is the number of electrons whose energy is higher than their respective starting energy divided by all the electrons considered. For the "run-to-MeV" probability, the criterion is not $\varepsilon > \varepsilon_0$ but $\varepsilon >$ MeV, but the subsequent analysis is the same.

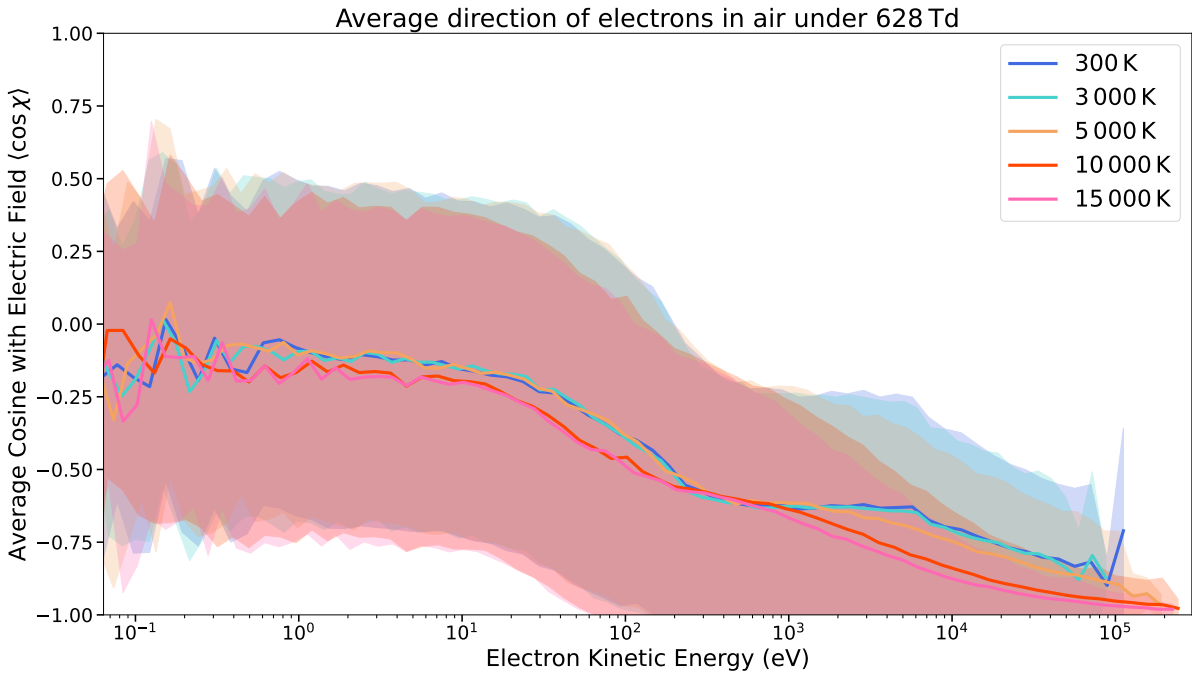

Figure 5.12: Distributions of the average cosine $\cos\chi$ of the electron orientation with the electric field $\mathbf{E}$ at 16 MV/m. The coloured zone shows one standard deviation away from the average value of the cosine. The N_s = 500 000 super-electrons were binned into 100 logarithmically spaced intervals of energy from the lowest to the highest value.

This windowing was made with 25 different windows with N_w varying between 20 and 1000 electrons. Then, we averaged the values obtained for the 25 windows. This last average is the probability that we show and discuss in all the figures of this section. Probabilities calculated near the lower and upper boundaries of the energy range probed are strongly deteriorated with noise because of the restricted number of electrons available in the window. One can see this by zooming very closely for instance on the midline of figure 5.13b.

We start by showing how the probabilities evolve with time on figures 5.13. Then, we fix the time close to the end of our simulations and show how the probabilities evolve according to the electric field in figures 5.15. The curves plotted have characteristic points marked with arrows which are reported on figures 5.14 (along time) and figures 5.16 (along the electric field).

Acceleration probability : $\mathcal{P}_{\varepsilon>\varepsilon_0}(\varepsilon_0, t)$. The curve of the probability that an electron have an energy higher than its initial energy is characterised by a bump which shrinks with time (fig. 5.13–left column). Evidently, when the electrons are initially propagation opposite to the electric field, they at first gain energy in the immediate time before they incur their first collision in the gas. Therefore, if we had included a snapshot at $\lesssim$0.1 ps after the start, we would see an almost perfectly straight line at 1, meaning that all electrons are obviously accelerated initially. At 5 ps after the start of the simulation, we already see that the portion of electrons at lower energies have already collided enough to lose a significant portion of their initial energy. As time progresses, the portion of inaccelerated electrons grows as they collide more times.

Below, we characterise the curves, their characteristic points and their evolution with respect to time, the electric field and the air temperature.

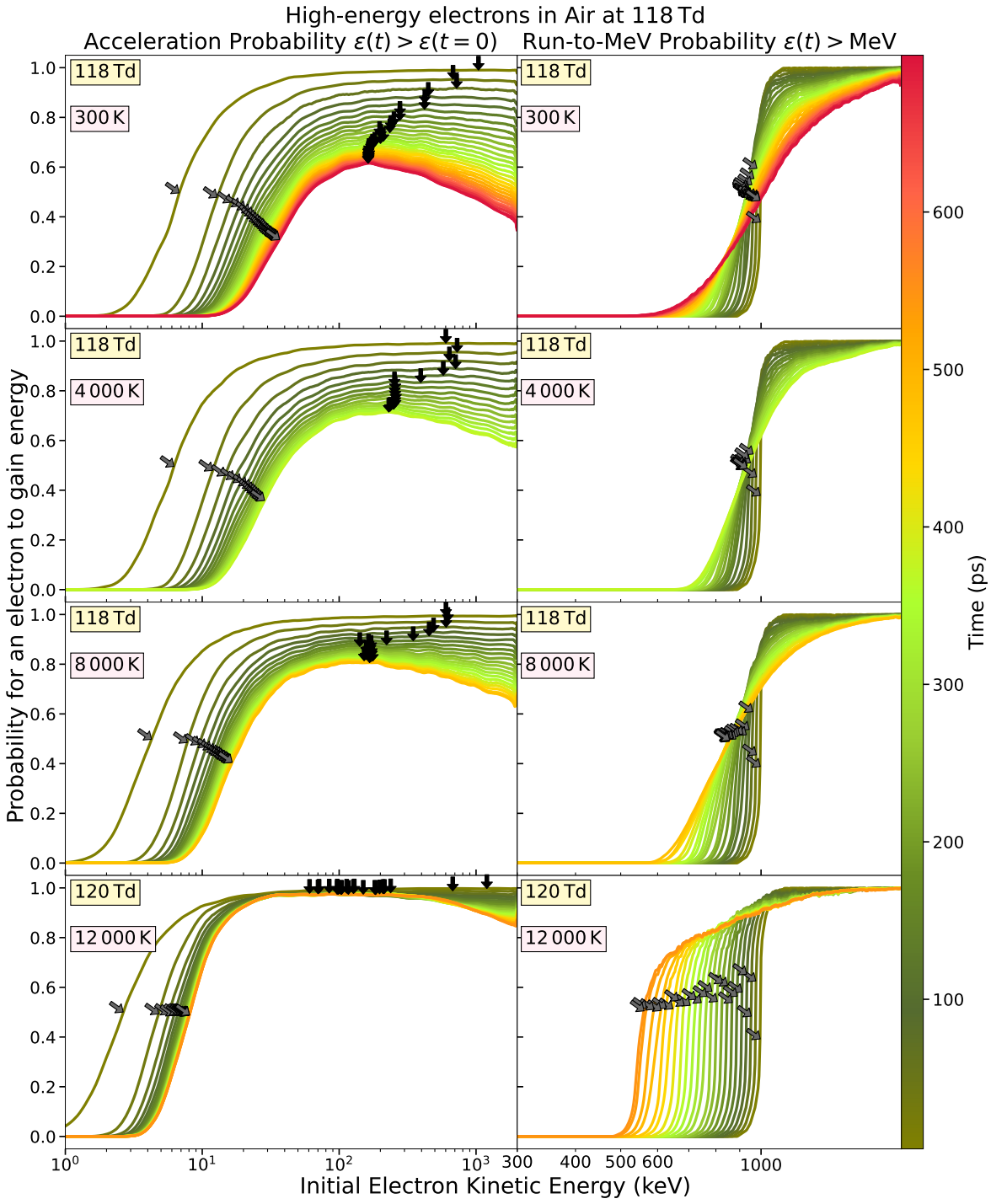

(a) Varying air temperature (and thereby composition through table 2.1). Electrons start anti-aligned against the electric field.

Figure 5.13: Starting with 500 000 electrons with energies ε_0 logarithmically spaced between 0.1—2000 keV, we compute the probability that these electrons have an energy higher than ε_0 (left column) or higher than 1 MeV (right column). The arrows show the detection of characteristic energies: the peak (maximal) probability and the (first) intersection with half of this probability.

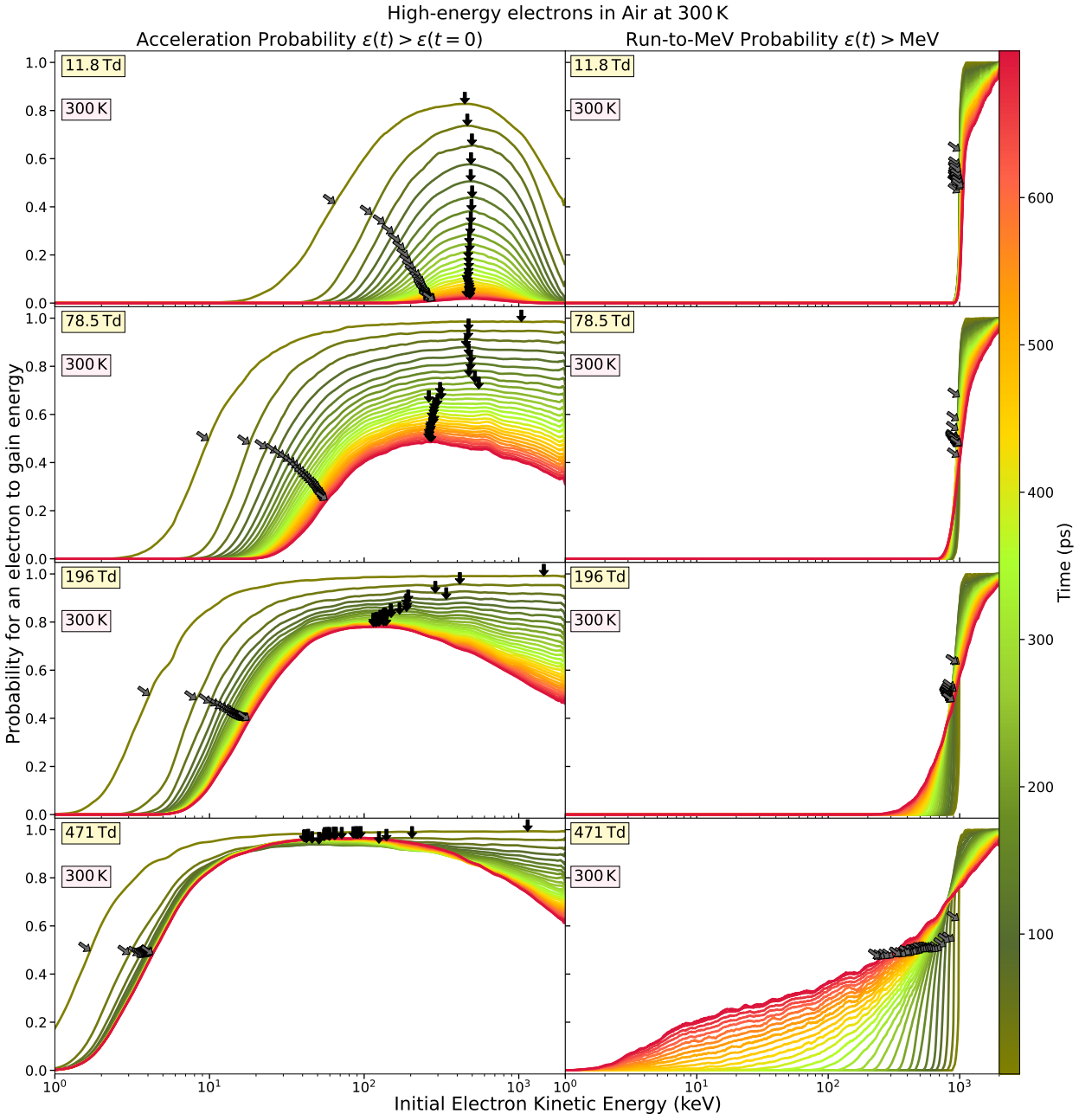

(b) (continued fig. 5.13) Varying the external electric field. Electrons start anti-aligned against the electric field.

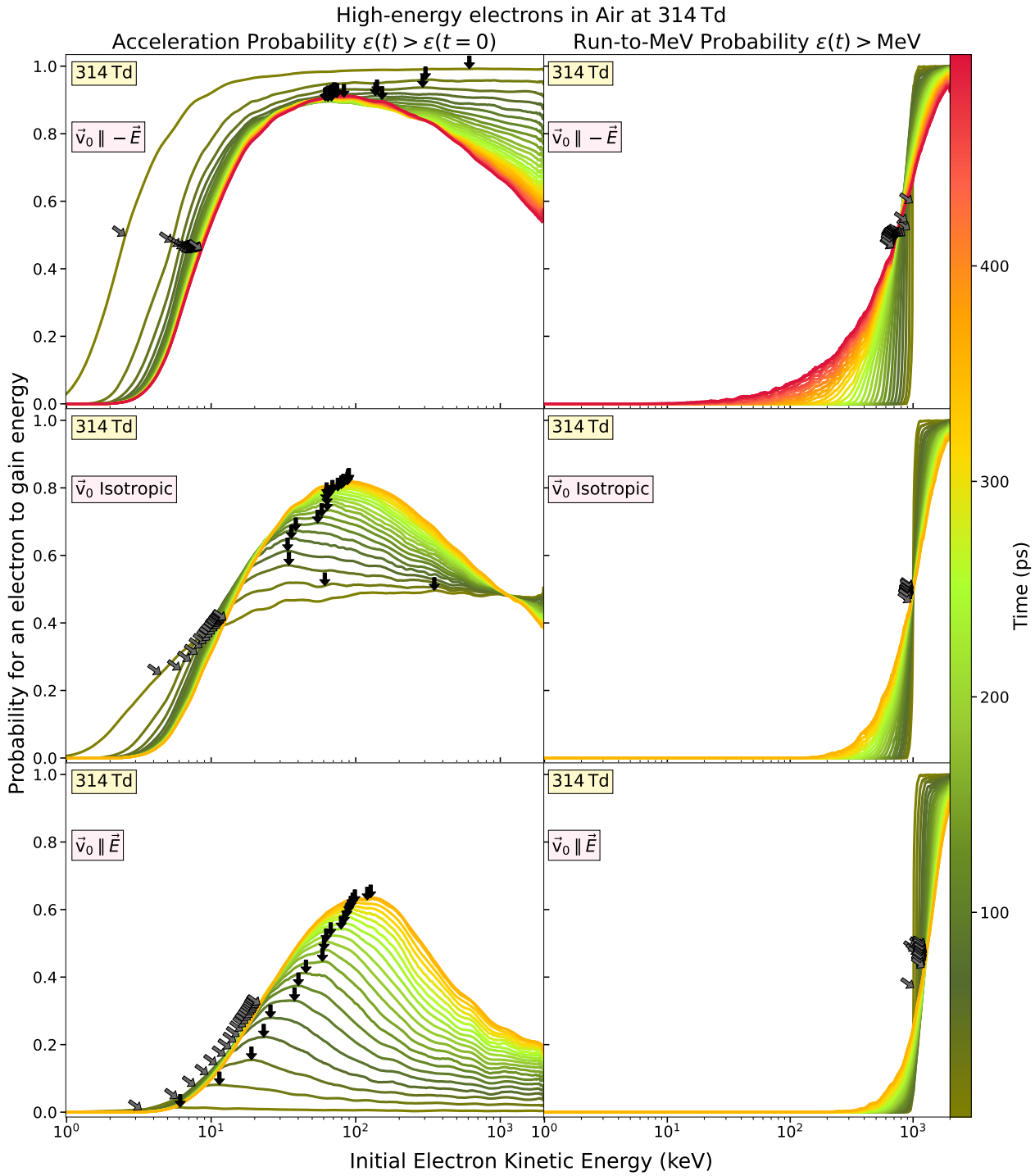

(c) (continued fig. 5.13) Varying the initial direction of the electrons.

Peak ($\varepsilon_\triangle$) : After a certain time, the bump is characterised by a maximum. The energy of this maximum is named "peak probability threshold" and noted $\varepsilon_\triangle$ (triangle for the peak). The presence of the maximum is due to the fact that the condition verified is more stringent when the energy of the electron is higher. At lower energies, the condition is less stringent but the probability to lose energy in collisions becomes higher. The position of the maximum is hard to distinguish sometimes because of the stochastic fluctuations in the simulation. As a result, it is not a good indicator for comparison as displayed on the bottom rows of figures 5.14–5.16 because of the significant noise, uncertainty on its position.

Half-Peak ($\varepsilon_{\triangle/2}$) : The (lower) energy at which the probability equals to half of the peak probability at a given time is defined as the "half-peak probability threshold" and noted $\varepsilon_{\triangle/2}$. Contrary to the peak threshold $\varepsilon_\triangle$, the half-peak threshold increases with time. After several hundreds of ps, if the electric field is strong enough on the left column of figure 5.15a, the half-peak probability stagnates both in energy threshold and at a value nearing 0.5 which goes well with its name.

Electric Field : When the field increases (fig. 5.15), the position of the peak raises and shifts to lower energies. When the electric field is high enough, there is even a bounce to the peak; it first lowers and rises back again at later time. This is because initially, electrons may lose energy stochastically and be decelerated on the short term. However, on the longer term, some electrons may be accelerated to much higher energies and the probability that they be decelerated again is much lower. Thus these electrons can be truly considered as runaways. The corresponding plot on the right column bottom row of figure 5.13b attests this reasoning: many of the electrons that had started with few tens of keV have successfully reached the MeV at a later stage.

Temperature : We see on figure 5.13a that the position of the peak probability is also affected by air temperature but to a lesser degree. The position $\varepsilon_\triangle$ of the peak is not important but the height and position of the half-peak probability are strongly affected by temperature. The threshold $\varepsilon_{\triangle/2}$ decreases with temperature. Overall, the bump becomes wider and taller in hotter air.

Time : Under some conditions, the distribution of high-energy electrons seems to stagnate and converge toward a stable configuration as seen for instance on the densely stacked bumps of figure 5.13. However, one may not always define a clear runaway boundary when the high-energy electrons slowly deplete as visible on the mid-graph of figure 5.14a. There is no upper asymptote to the blue curve at 300 K. One has to fix a time limit to the runaway process.

Critical Field : On the bottom-left graph of figure 5.15a, the upper range of electric fields are above the critical thermal runaway threshold in air at 12 000 K. The probability to runaway is non-zero at the boundary 100 eV which is below the maximum of the friction curve in fig. 5.11. In that case, no threshold can be determined for runaway, it is just a question of time that all electrons become runaway. The transition to critical thermal runaway can be seen by the collapse of the pink curve on the mid-panel of figure 5.16a.

Initial direction : The evolution and shape of the peak is most affected by the initial direction of the electron. When electrons are generated isotropically or along the electric field on figure 5.13c, the bump swells and takes a much rounder and less steep shape. The probabilities shown on the bottom graph are not merely related to acceleration but to

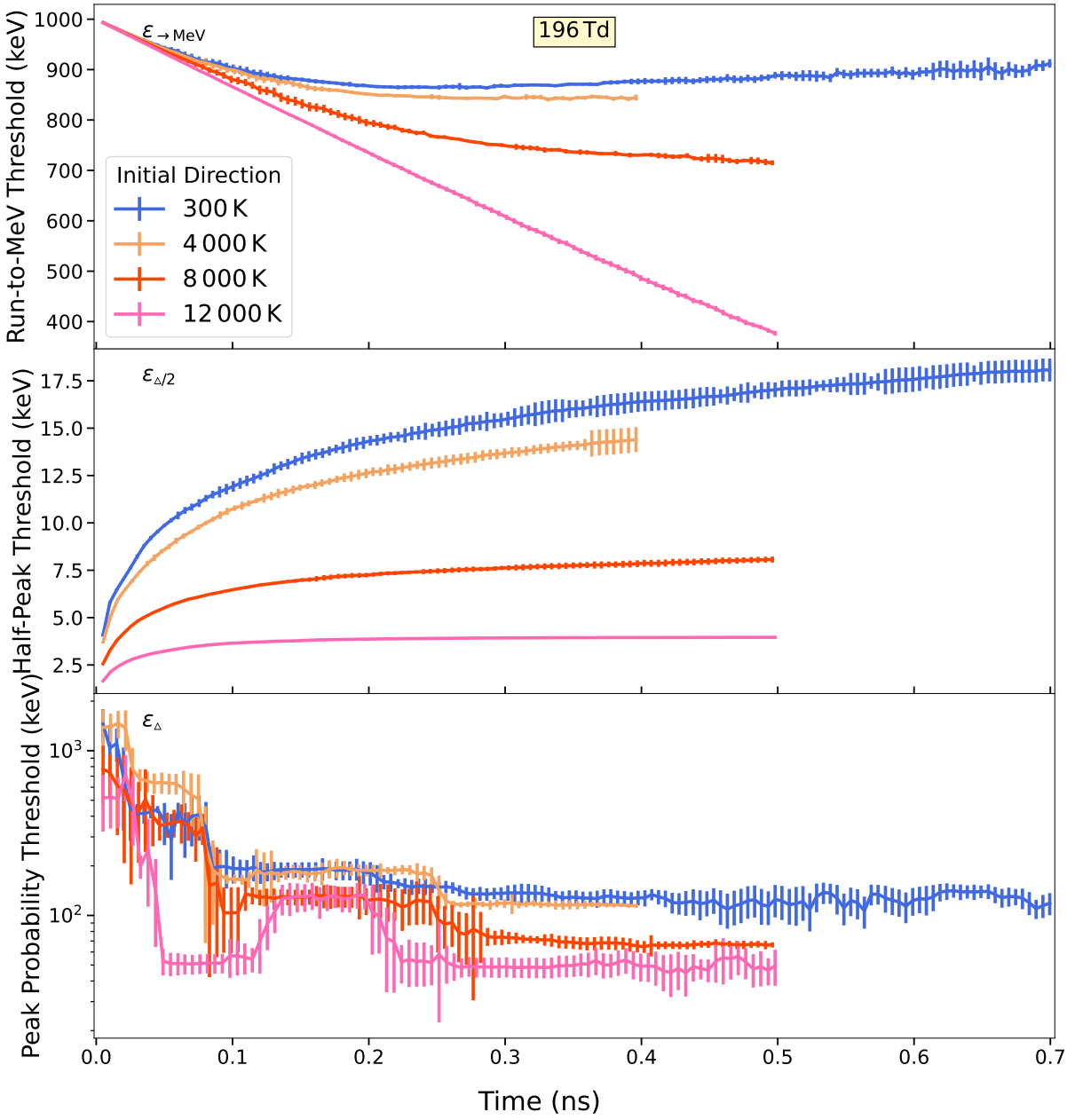

(a) Varying air temperature (and thereby composition through table 2.1. Electrons start anti-aligned against the electric field.)

Figure 5.14: The three characteristic energy thresholds identified by arrows on figures 5.13a and 5.13c are plotted along time. Top: run-to-MeV probability (arrows on the right column of fig. 5.13a). Middle: half-peak probability threshold (arrows on the slopes of the curves on the left column of fig. 5.13a). Bottom: peak probability threshold (arrows on the maxima of the curves on the left column of fig. 5.13a).

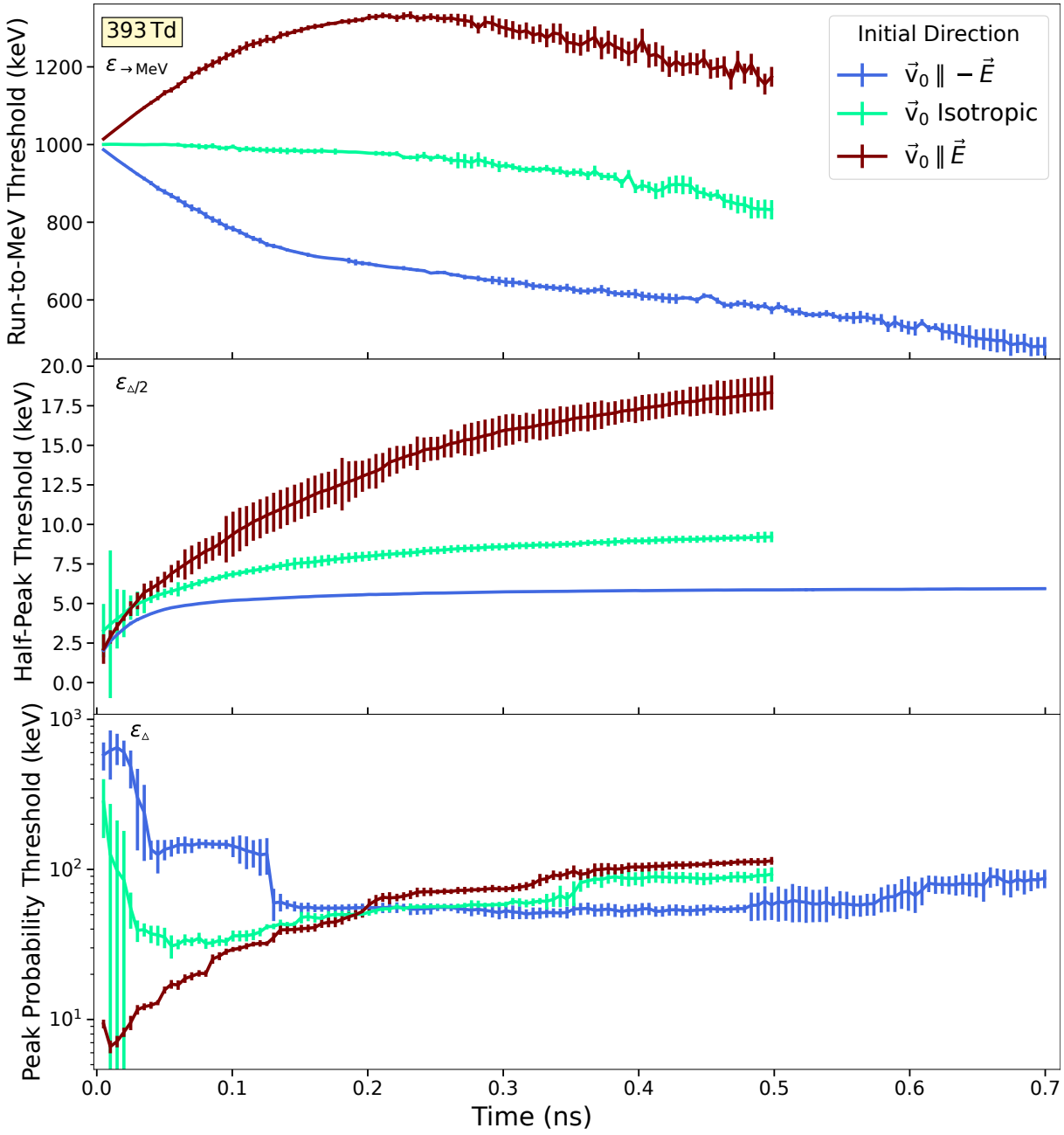

(b) (continued fig. 5.14) Varying the initial direction of the electrons. From the arrows identified on fig. 5.13c.

the probability that electrons turn 180° toward the opposite direction of the electric field. This probability is remarkable since more than half of 100 keV are capable of realigning themselves with the electric field after 400 ps.

Also, on figure 5.15b, the top of the curves are flatter and the decreasing slope at high energies is less steep when the electrons are initiated anti-parallel to the electric field. For isotropically oriented electrons, the curves are steeper. For electrons initiated along the electric field, the hills are skewed and the slopes at high energies are steepest because the probability for a 180° turn is much lower for a MeV electron than for an electron of a few 100 keV.

The fact that runaway threshold depends also on the initial direction of the electron and not only on its initial velocity can be best grasped on the middle graph of figure 5.16a where the half-peak threshold is clearly pushed to higher energies for electron not initially anti-aligned with the electric field.

Run-to-MeV probability. The curve showing the probability that an electron reach a MeV looks very much like the diffusion of an initially perfect square wall. The analogy is ill however, because the "transfer" is in the opposite direction: the probability rises if the electron has migrated and passed the border toward the right. The aspect of this curve may be significantly affected by the electric field and air temperature.

Run-to-MeV $\varepsilon_{\rightarrow \mathbf{MeV}}$: On the right columns of figures 5.13 and 5.15, we identify only one characteristic point to the curve which is merely the intersection of half of the maximal probability (usually but not necessarily 1, compare graphs on the right column of 5.15b). It is clear that when electrons are initiated in the direction opposite to the electric field, they all accelerate before they collide. However, as they collide with the molecules, some may be significantly delayed before they are able to reach 1 MeV. This is why at low electric fields, the curves rise very slowly, indicating that many electrons may require a significantly longer time to reach 1 MeV than when accelerated uniformly. More on this will be said in the next subsection 5.3.2.

Electric Field : At higher electric fields, the probability to accelerate to the MeV regime swells as seen on all graphs on the right column of figure 5.15. Most interesting is the transition in the shape of the curve observed along the rows of figure 5.13b. At low electric fields, the initially vertical wall at 1 MeV only slants in a mechanism that we compare to diffusion. This is a purely stochastic phenomenon: we introduce an artificial sharp boundary that is smeared with time, a universal phenomenon in nature. Then suddenly, after a while and at a high enough electric field, appears an inversion of curvature of the slope (right-bottom reddish curves of figure 5.15a). There is not merely diffusion in the energy space of electrons, but there is truly a runaway acceleration mechanism: electrons are being pumped away toward higher energies.

Time : Nonetheless, it is not possible to determine a precise value of the electric field that "activates" runaway. Rather, the occurrence of runaways is also subject to the question of time. Some of the curves on figure 5.13a are not fully converged and could change of shape at a later time. A 500 keV electron aligned opposite to a 2 MV/m electric field requires about 1 ns to reach 1 MeV in free flight. This time drops to hundreds of ps at fields above the conventional breakdown. This is why we see such a great difference in the curves on the right column of figure 5.15a, especially at 12 000 K.

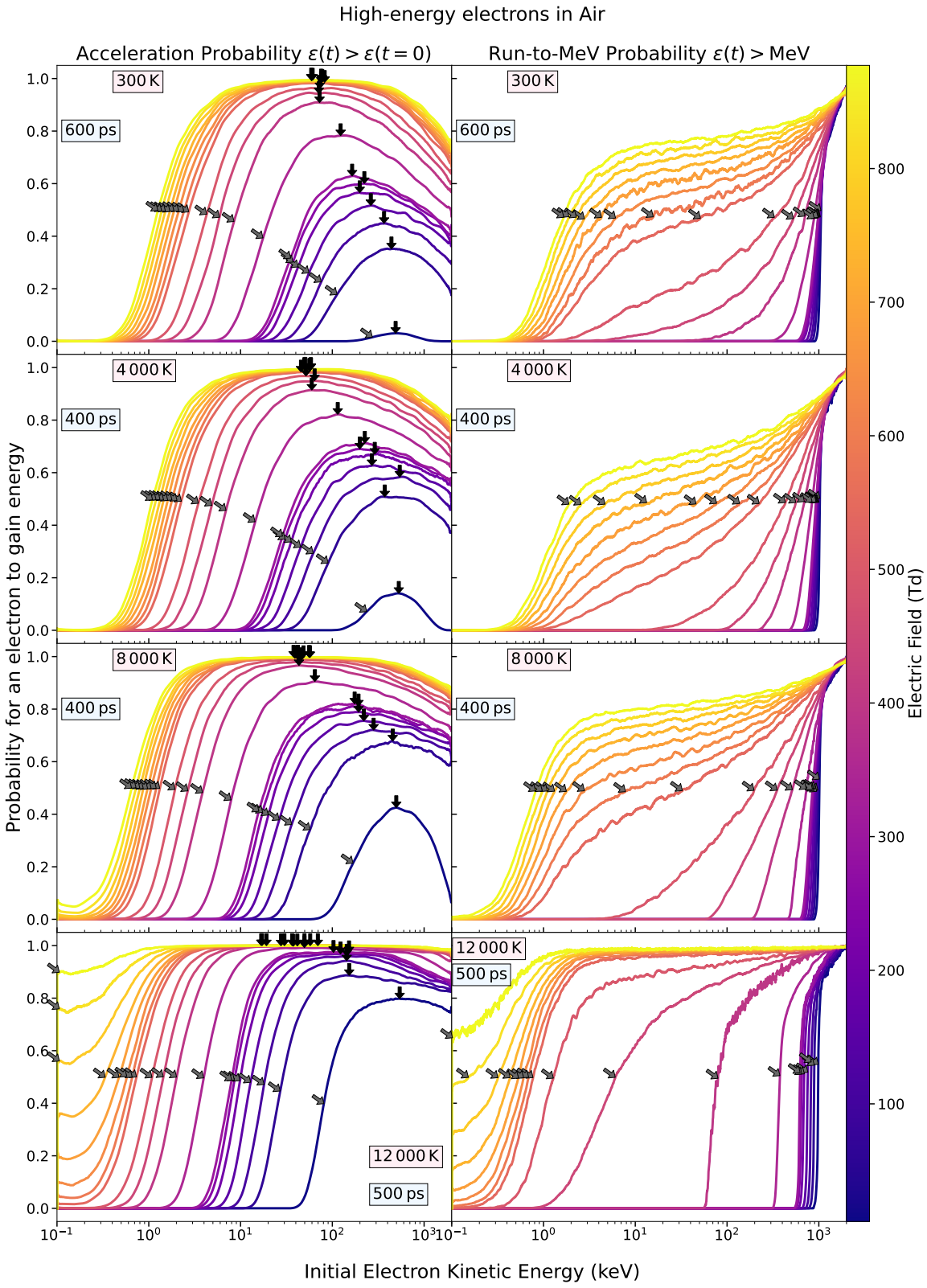

(a) (preceding fig. 5.15) Varying air temperature (and thereby composition through table 2.1. Electrons start anti-aligned against the electric field.)

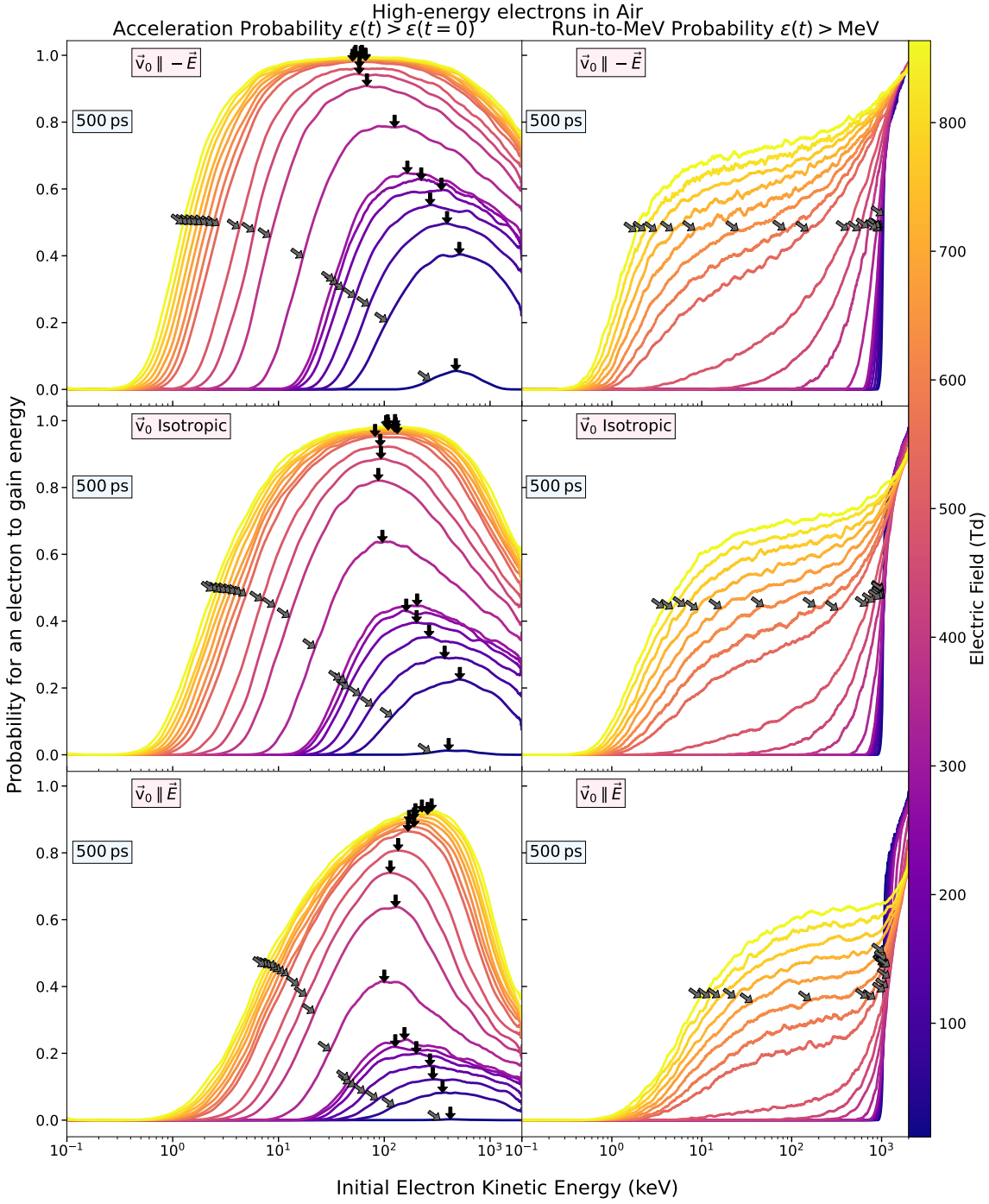

(b) Varying the initial direction of the electrons.

Figure 5.15: Starting with 500 000 electrons with energies ε_0 logarithmically spaced between 0.1—2000 keV, we compute the probability that these electrons have an energy superior to ε_0 (left column) or superior to one MeV (right column). The arrows show the detection of characteristic energies: the peak (maximal) probability and the (first) intersection with half of this probability.

Temperature : One can best appreciate what role does temperature play on the bottom right graph of figure 5.13a, where we see that runaway propagates as a wave of electrons massively accelerated almost uniformly starting at lower energies. That truly corresponds to a highly probable runaway mechanism since a large part of the population does indeed accelerate to the MeV regime. At lower temperatures, the probability to accelerate to the MeV is significantly lower and the initially straight slope of the curve slants to the side and downwards. The difference in runaway can also be observed on the graph showing the threshold along time on top of figure 5.14a. The threshold at temperatures below 10 000 K stagnates and even recedes at 300 K, whereas at 12 000 K it would propagate to lower energies if we had allowed the simulation to continue.

Initial Direction : From figure 5.15b, we may say that the effect of the initial direction is to reduce the number of electrons which may accelerate to relativistic energies at a given electric field. It also pushes the threshold to higher energies as seen on figure 5.16b. Initiating the electron in a direction different from the opposite of the field requires some time to readapt to the correct direction. This may be seen on the top graph of figure 5.14b where the curves first diverge but then recede with similar slopes.

Looking at various graphs of the runaway probability, one could perhaps identify three regimes of electron acceleration:

- Fast Runaway: flushes electrons to relativistic energies like a wave as seen in fig. 5.13a–bottom-right.

- Slow Runaway: electrons of high-energy gradually increase over a duration significantly larger than the delay required in free flight as seen on fig. 5.13b–bottom-right.

- Vanishing Runaway: very few electrons may accelerate to relativistic energies but their retention time at high energies is long enough to allow them to travel on spatial scales where the electric field may vary significantly. This could either be the graphs on the right panels at 200 Td and 300 K (fig. 5.13b) or at 120 Td and 4000 K (fig. 5.13a). However, those electrons are not proper runaways according to the original definition on p. 162.

To sum up, the runaway regime is affected by the electric field of course, but also the air temperature. The state of runaway should be characterised not only according to the starting energy of the electrons but also their starting direction and the time duration considered. With time, the initial conditions of the electron is blurred and one remains with a population of high-energy electrons which is characterised by the given electric field and air temperature.

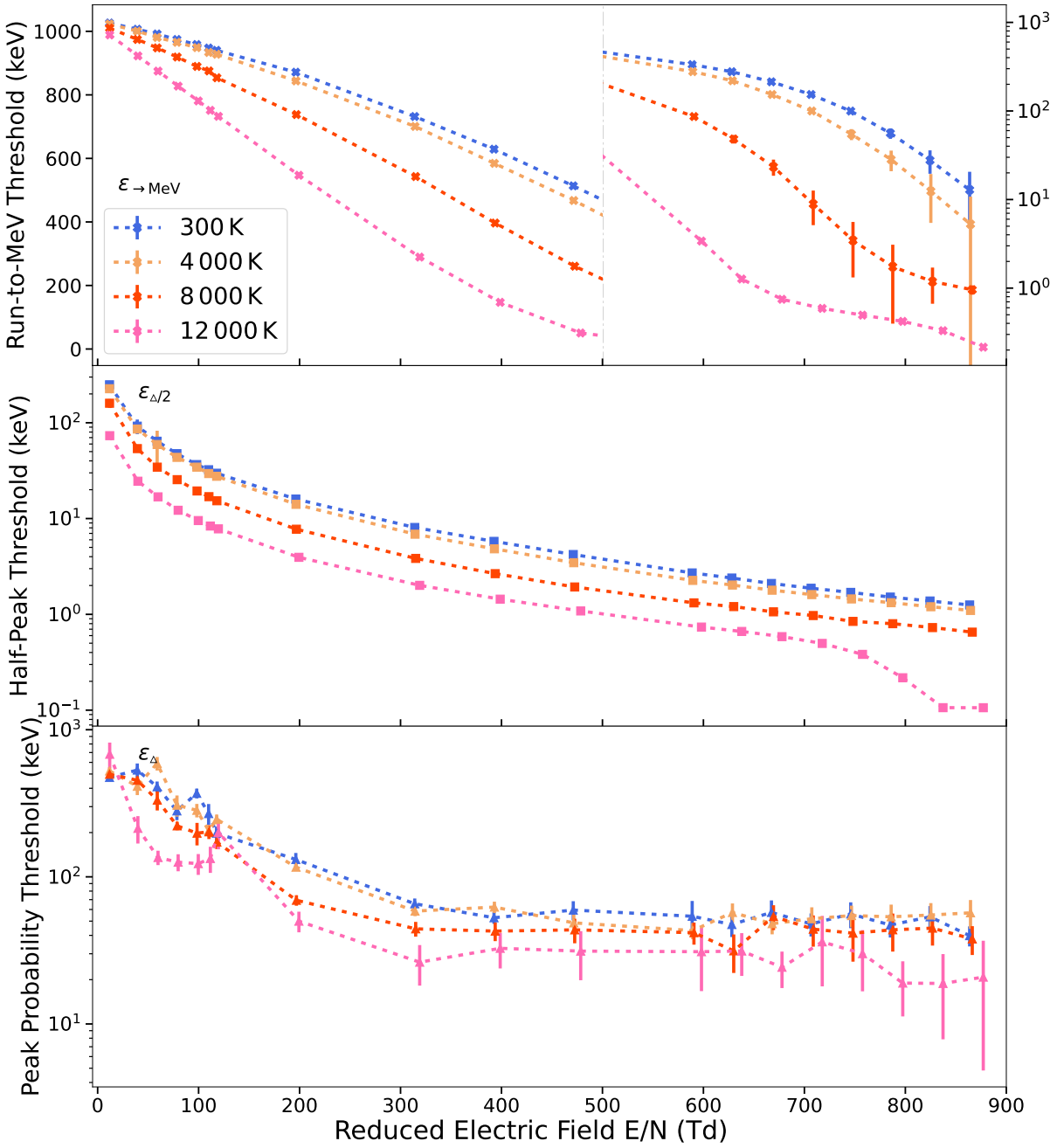

(a) Varying air temperature (and thereby composition through table 2.1. Electrons start anti-aligned against the electric field.)

Figure 5.16: The three characteristic energy thresholds identified by arrows on figures 5.15a and 5.15b are plotted along the intensity of the electric field $|\mathbf{E}|$. Top: run-to-MeV probability (arrows on the right column of fig. 5.15a). Middle: half-peak probability threshold (arrows on the slopes of the curves on the left column of fig. 5.15a). Bottom: peak probability threshold (arrows on the maxima of the curves on the left column of fig. 5.15a).

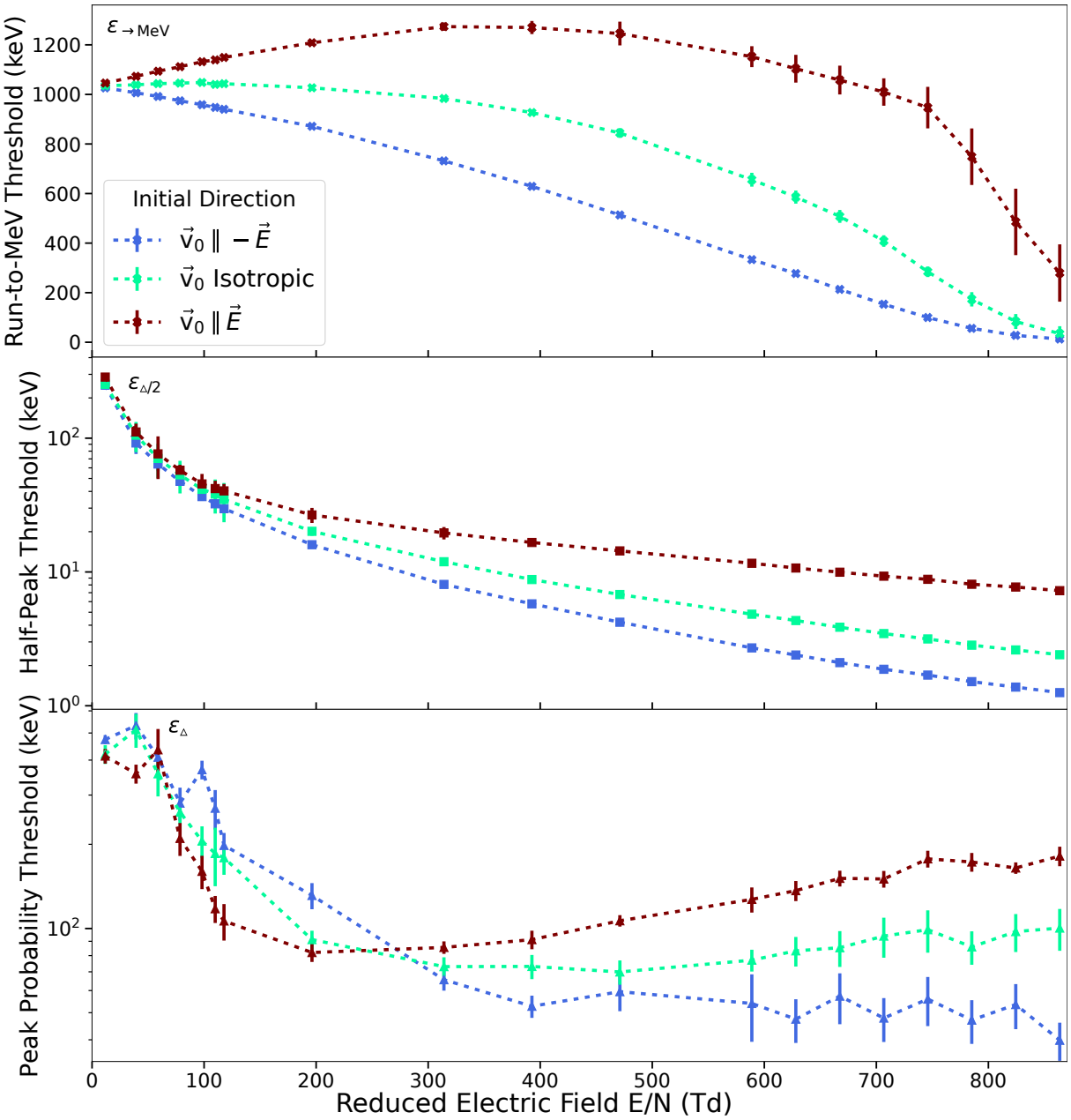

(b) (continued fig. 5.15a) Varying the initial direction of the electrons.

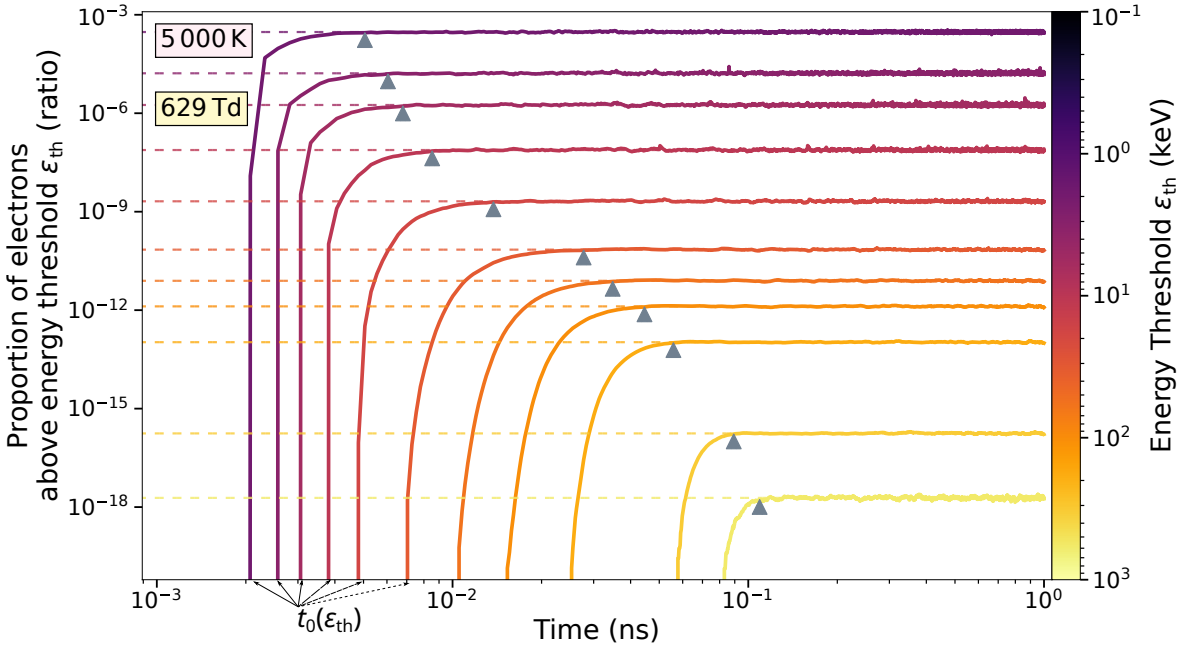

Figure 5.17: Proportion of physical electrons above a certain energy threshold ε_{th} as a function of time in a swarm initiated at a Maxwellian distribution of 5000 K equal to the temperature of air and under a homogeneous field of 16 MV/m. The dashed curves show the average value of the converged proportion and the triangles underline the time $\Delta\bar{t}$ at which the curve is detected to have converged. The criterion of convergence based on the deviation from the median was the same as in eq. (3.38), fig. 3.7 on p. 108. The first non-zero value of the ratio appears at the onset time t_0.

5.3.2 Delays

In the previous section, we were concerned with identifying an energy boundary to the runaway regime. We saw that we may indeed identify some very characteristic energy thresholds ($\varepsilon_{\triangle/2}$ and $\varepsilon_{\to\text{MeV}}$ among possibly many others). Under fixed external conditions, those thresholds depend sensitively on the initial direction given to the electrons and the time of observation. After a while, the thresholds may converge or on the contrary they vanish, in which case we consider that runaway is a vanishing process that cannot replete itself.

Here, we may wish to know, starting with thermal electrons, how long should we wait, allow the swarm to evolve before we observe runaway electrons. We commence by looking at figure 5.17 which shows the proportion of electrons which are above a certain energy threshold. We immediately see that these curves stabilise at a time noted $\Delta\bar{t}$ after a steep rise from the first non-zero value at a time that we note t_0. These times depend on the energy threshold ε_{th}, electric field E and are slightly affected by the air temperature T_{air}.

We represent these times $\Delta\bar{t}$ and t_0 on figure 5.19a as a function of the electric field at two different temperatures. Overall, the delay time for emergence of high-energy electrons decreases with the electric field and increases with the energy threshold considered (ε_{th}). The decrease of the delay with air temperature is very small.

Free acceleration ($t_\varnothing$) : The time $t_\varnothing$ required for an electron in vacuum initially at rest to accelerate in a field E up to an energy ε_{th} was given in equation (2.24). This delay is represented in figure 5.19a by dashed lines neatly stratified according to ε_{th}. The average delay when air is present, can be a factor of 2 to 3 higher.

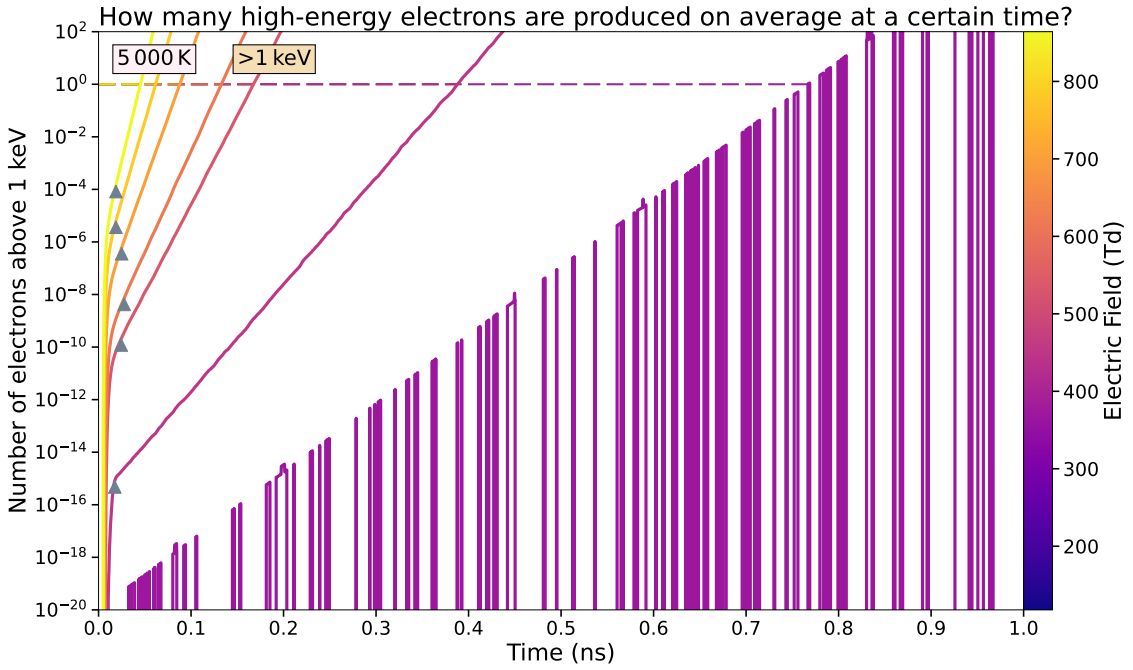

Figure 5.18: When multiplying by the exponentially growing number of electrons in the swarm, the flat curves on fig. 5.17 become also steep exponentials with different slopes depending on the electric field and time offsets depending on the electron energy threshold considered. The intersection of the horizontal line at $N_{>1\mathrm{keV}} = 1$ with the curves corresponds to the average time delay after which a swarm of initially 1 electron produced 1 energetic electron of at least 1 keV.

Onset (t_0) : Since our electron swarm is initiated as a Maxwellian at the temperature of the gas, the onset is generally greater than the free time $t_\varnothing$ ($t_0 > t_\varnothing$). This is the case when the acceleration time from 0 eV to the average initial energy $\bar{\varepsilon}_0$ of the swarm is negligible compared to the total acceleration time $t_\varnothing$.

If the electric field is high enough > 12 MV/m, we have checked that, under physically identical conditions, t_0 is independent (within the numerical time step resolution) of the number N_s of super-electrons allowed in the simulation. This is because of our compaction algorithm. At each collision time step, multiple copies of super-electrons at the highest energy are generated. Among those copies, the super-electron which has the highest probability to accelerate further is that which scatters forward and which does not lose a large portion of its energy. If the number N_s of super-electrons is not too low, there should always be enough copies of high-energy electrons so that at least one electron accelerates to an energy higher than prior to its last collision. Therefore, we think that t_0 could represent the average delay of an accelerating electron in air which never collides at an energy smaller than when it last collided.

Stabilisation delay ($\Delta\bar{t}$) : Physically, it is hard to ascribe a meaning to the "stabilisation delay" $\Delta\bar{t}$. We interpret it as the delay necessary to stabilise the proportion of electrons above a threshold ε_th after being initially released at 0 eV and allowed to multiply in a gas at a certain electric field. It is not the smallest delay nor an average of individual delays. The detection algorithm of the stabilisation time $\Delta\bar{t}$ is very sensitive to stochastic fluctuations of the simulations and so the statistics on figure 5.19a about $\Delta\bar{t}$ are poor.

1-in 1-out delay (Δt_{11}) : We could now take a different perspective and ask how long should one wait on average to obtain 1 high-energy electron, if the simulation started with 1 thermal electron. This, we call the 1-in 1-out delay (Δt_{11}) and is obtained at the intersection points on figure 5.18 of the horizontal line at $N = 1$ and the number of electrons above 1 keV (or any other threshold) which grows exponentially. We remind that, since we use super-electrons, we are able to represent an arbitrary fraction of real electron, even a 10^{-20}th of an electron. This number would have to be understood as the physical state that a real electron, at a given moment, would occupy at a probability of 10^{-20}. Thanks to this probabilistic scaling, we may indeed calculate an average 1-in 1-out delay for any energy threshold. This delay is considerably longer than the stabilisation delay as seen by comparing figure 5.19b with 5.19a.

Most important to realise is that, physically, the highest yellow dashed lines on any of the figures 5.19 is the delay required for a thermal electron to accelerate up to 1 MeV in vacuum. At any temperature and electric field, this run-to-MeV time is too long no matter the probability that the electron appears physically; this time exceeds the time by which the Meek criterion is satisfied; i.e. the time by which the electric field collapses due to screening by the space charges created by the swarm.

This is already a first argument against thermal runaway in static configuration: the time required to accelerate a thermal electron to runaway energies is too long compared to the overwhelming growth of the electron swarm at any given electric field. This is the reason why studies could not confirm emergence of thermal runaway in the enhanced field at the encounter place of counter-propagating streamers [422, 531, 579]. This is not due to any flaw of a not enough enhanced electric field, it is because thermal runaway most likely occurs on ionisation waves where space is traded for time and thence faster electrons may travel along with the region of intense electric fields whereas slower electrons remain behind the wave.

We continue our presentation of thermal runaway in the next section where we consider the production of high-energy electrons which we have already mentioned here.

5.3.3 Production

Characterisation of the production of high-energy electrons in a swarm at a fixed electric field is a task more difficult than it seems. In the literature, the thermal runaway production is characterised by a runaway rate ν_r which gives a flux (number of electrons per unit time) of electrons becoming runaways. This rate does not include electron avalanching.

Sterile Runaway

There are (at least) two definitions of thermal runaway rates without avalanche that one should be aware of.

Analytical. We believe the first determination of a runaway rate in a collisional plasma is attributable to Gurevich [371, eqs.(11–12)]. There, the "runaway rate" is interpreted as the flux of electrons, whose velocity component v_z anti-parallel to the electric field is increased on average accounting both for electrostatic acceleration and collisions with neutrals, ions and other electrons. This rate is computed up to the critical velocity v_c beyond which all electrons are assumed to accelerate uniformly in the electric field. Because the effect of electron scattering was not considered in the model, the calculated runaway rates were overestimated by about a factor of ~10.

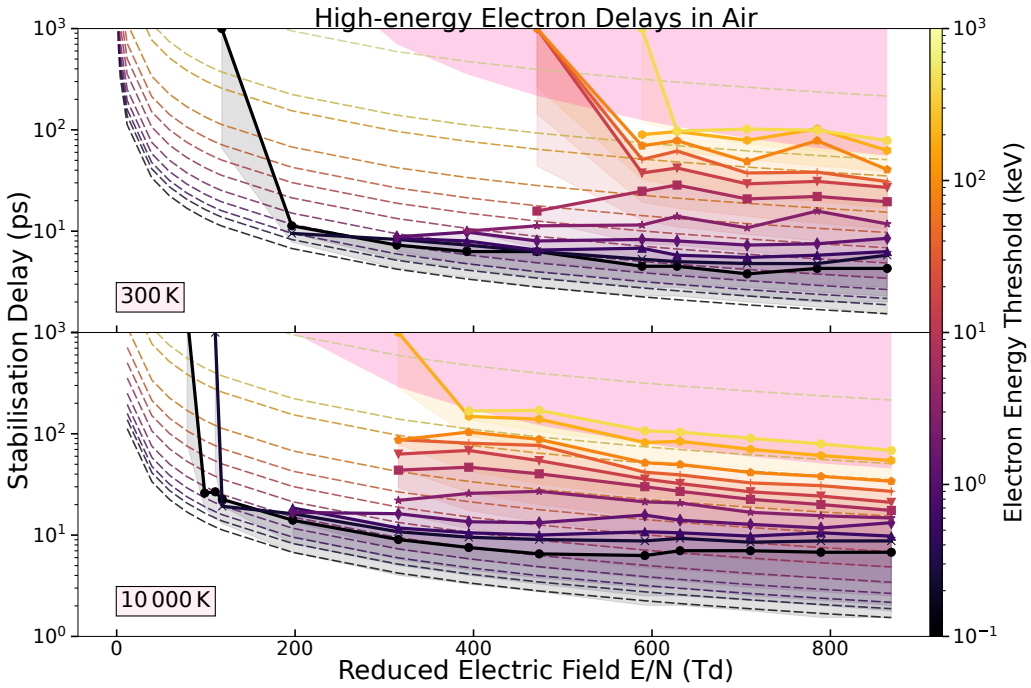

(a) Markers connected by solid lines represent the delay time $\Delta\bar{t}$ to stabilisation identified as triangles on fig. 5.17. At each energy threshold the coloured zone spans from $\Delta\bar{t}$ to the time of first non-zero value t_0 observed on yon figure.

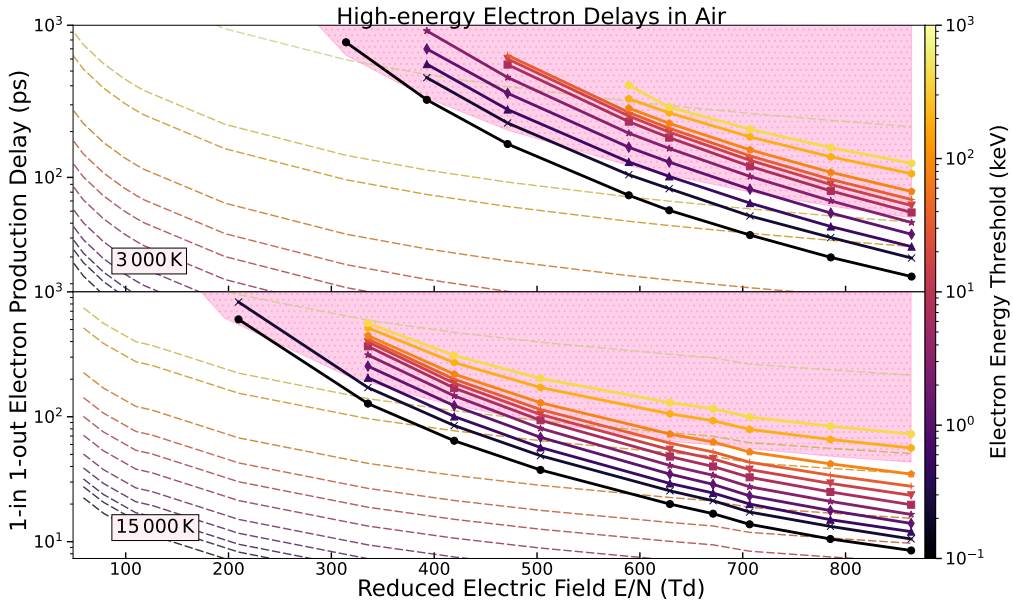

(b) Markers connected by solid lines represent the average delay time Δt_{11} after which a swarm initially composed on 1 electron produces 1 high-energy electron above a given energy threshold. This time is determined from the intersection point of the exponentially rising curves of the electron population with the horizontal line at $y = 1$ on figure 5.18.

Figure 5.19: Delays to obtain high-energy electrons in homogeneous swarm simulations starting at thermal conditions in equilibrium with the gas temperature. The dashed lines correspond to the delay $t_\varnothing$ of a free electron, initially at rest, accelerating uniformly in the electric field. The pink zone covers all times in which the swarm has reached Meek's criterion on figure 5.7b when the electric field of the space-charges equals the external electric field.

Stochastic. Later, an attempt to characterise the thermal runaway rate stochastically was conducted by Bakhov *et al.* [50] based on the definition of Sizykh [853] in which the runaway rate is defined as the number of electrons per unit time which reach the runaway energy threshold ε_{th} (corresponding to 'v_c' of [371]). This definition was used in subsequent studies of thermal runaway [43, 218]. The stochastic nature of thermal runaway was first explored by Bakhov *et al.* [50] who considered that even beyond ε_{th}, there might be a loss of runaways due to angular scattering (not accounted by the dynamic friction force which determines ε_{th}). Thus, they mapped the rate at which electrons reach an energy threshold situated between 150–8000 eV [50, fig.4]. Then, they determined, in the electric field range explored 24–40 MV/m in N_2, that beyond 4 keV, the runaway rate did very weakly vary with the energy threshold. This means that there is almost no loss of energetic electrons due to stochastic collisions once they reach 4 keV (for fields above 24 MV/m).

In the two definitions above, it is assumed that runaway is a leaking mechanism of thermal electrons contained in a reservoir of an initial number N_0 of electrons which decreases exponentially, at the rate by which runaway electrons $N_\text{r}(t)$ are produced [50, eqs.(9–10)]:

$$\frac{\text{d}N_\text{r}}{\text{d}t} = -\frac{\text{d}N_\text{e}}{\text{d}t} = \nu_\text{r} N_\text{e} \quad \text{and} \quad N_\text{e}(0) = N_0 \tag{5.7}$$

$$N_\text{r}(t) = N_0 \left(1 - \text{e}^{-\nu_\text{r}(t-t_0)}\right) \quad (\forall\ t \geq t_0)\,. \tag{5.8}$$

This way of counting runaways is statistically equivalent to the sum of N_0 *independent* Poisson random variables each of a constant probability rate (of having run away) per unit time noted by ν_r. This process requires an "activation" time t_0 which is related to the physical time needed for an electron to accelerate to the runaway threshold and which we determined in the previous section. We remind that $1-\exp(-\nu(t-t_0))$ for a Poisson variable of probability rate ν represents the overall probability that, after a time $(t-t_0)$, the (runaway) event have occurred. Thus, if this experiment is repeated N_0 times (the number of electrons), we ought to obtain the equation (5.8) mentioned above.

The production of secondary electrons from ionisation is completely omitted in this picture. As a result, for future reference, we suggest that this type of runaway rate be qualified as "sterile" runaway in relation to the fact that there are no offspring runaway electrons taken into consideration.

Although there already exist several studies that investigated sterile runaway rates in air [43, 50, 218, 677], we were unfortunately unable to reproduce those results. The runaway rates we obtained were greatly (3 orders of magnitude) below previously calculated ones. One can compare our estimates on figure 5.20 with [43, 50, fig. 7, fig. 5]. Those estimates were calculated, however, with a different approach explained in the following subsection.

Fertile Runaway

Presently, we offer an alternative characterisation of the production of runaway electrons which differs from the previous ones in two aspects. First, it includes all secondary electrons produced by ionisation. Second, it is conducted at electric fields below 24 MV/m which were previously investigated only by Diniz *et al.* [218]. We stress that the study of thermal runaway at subcritical electric fields is possibilitated by our very strong compaction algorithm of section 3.3.2 which enables the swarm to hold a super-electron resolution spanning arbitrarily many orders of magnitude.

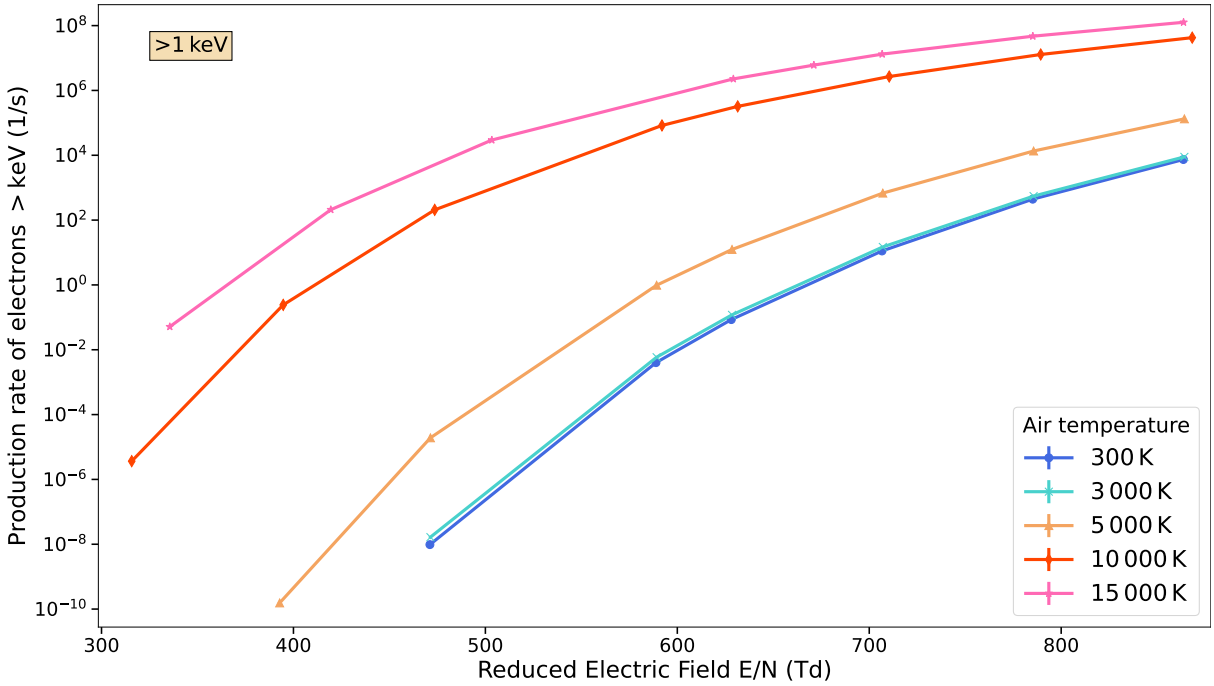

Figure 5.20: Production rate of electrons accelerated above 1 keV at different air temperatures. The rate ν_r is derived in the fertile runaway model (5.9) from the ratio ν_r/ν_e represented by dashed lines in figure 5.17.

If we superpose to the previous sterile runaway model above, the exponential growth of the swarm as a whole, we obtain the "fertile" runaway model composed of two electrons reservoirs:

$$\text{Bulk}: \begin{cases} \dfrac{\mathrm{d}N_e(t)}{\mathrm{d}t} = \nu_e N_e(t) \\ N_e(0) = N_0 \end{cases} \quad \Rightarrow \quad N_e(t) = N_0 e^{\nu_e t} \tag{5.9a}$$

$$\text{Runaways}: \begin{cases} \dfrac{\mathrm{d}N_r(t)}{\mathrm{d}t} = \nu_r N_e(t) \\ N_r(t) = 0 \quad \forall\ t \le t_0 \end{cases} \quad \Rightarrow \quad N_r(t) = \begin{cases} \dfrac{\nu_r}{\nu_e} N_0 \left(e^{\nu_e (t-t_0)} - 1\right) & \forall\ t \ge t_0 \\ 0 \quad \forall\ t < t_0 \end{cases} \tag{5.9b}$$

In accordance to what we determined in sec. 5.3.2 and displayed on figure 5.17, after an onset delay t_0, there is a very fast transient uprise $(1 - \exp(-\nu_e t))$ of the relative number N_r/N_e. There, we see that in the "fertile" model, it is the exponential growth rate ν_e of the swarm which governs the runaway production rate (this would be the 'fertile' runaway rate). On the other hand, the sterile runaway rate ν_r determines the *proportion* of runaways compared to the bulk.

Thus, we provide an alternative way to calculate sterile runaway rates through the ratio ν_r/ν_e which may be seen by the dashed lines represented on figure 5.17. The derived values of ν_r for electrons above 1 keV is represented on figure 5.20 at different temperatures of air. There, we see that the runaway production rate can be raised by several orders of magnitude in hot air > 5000 K and that the electric field threshold for production is lowered.

The fertile model is, however, an idealisation of a swarm evolving in a uniform field without taking into account the space-charge field produced by the exponentially growing swarm. In the next section, we discuss the limitations imposed on the production of high-energy electrons by the screening of the external field.

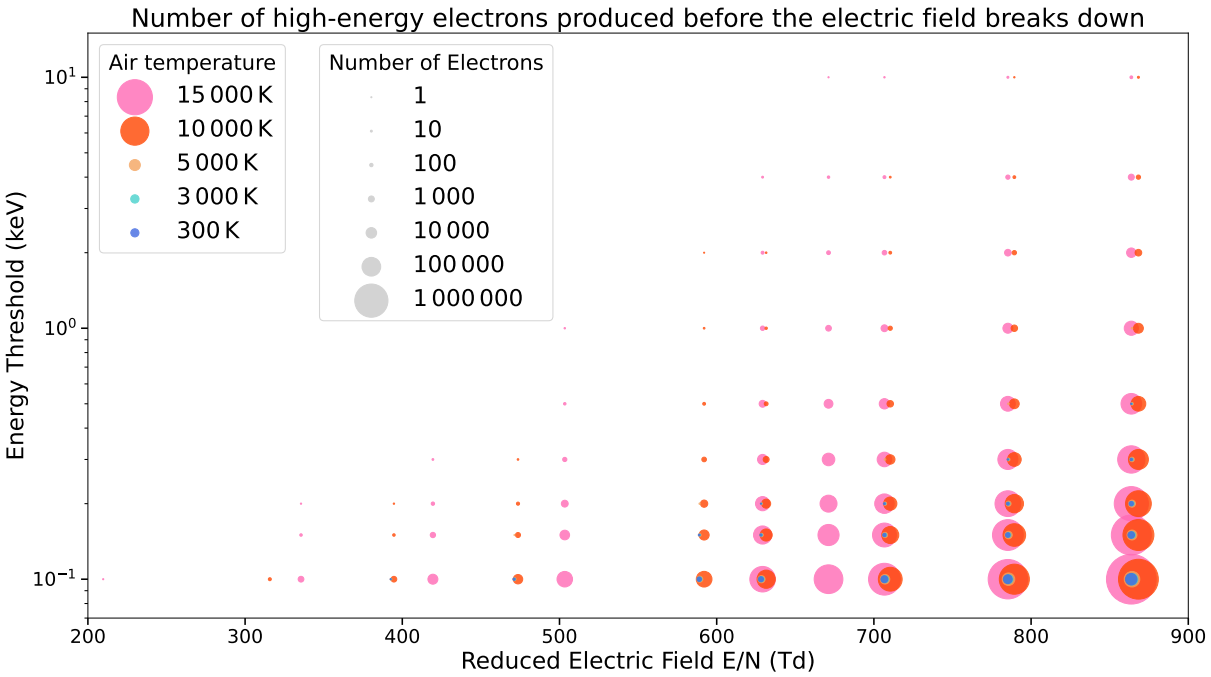

Figure 5.21: Estimation of the number of electrons produced above a certain energy threshold in uniform electric fields at different temperatures of air within the time before which the external field is screened by the peak field generated by the swarm as seen on figure 5.7b.

Constrained Runaway

From the previous sections 5.3.2 about runaway delays, we know already that the production of high-energy electrons in uniform fields is subject to many objections. We name three.

1. The first is that acceleration of an electron in gases is a stochastic phenomenon and thus the time required to produce a certain number of electrons may fluctuate depending on the particular circumstances. We may only describe an average time $t_0 + \tau_r$, after which a certain number of electrons is expected to emerge (see fig. 5.19a).

2. The second is that, by the time $> t_0$ that an electron reaches an energy considered high, the electric conditions will surely have evolved significantly as a result of the swarm's exponential growth and drift-diffusion (see fig. 5.19b).

3. The third, is that the very presence of high-energy electrons could introduce a change to the behaviour of the swarm because of the avalanche of lower energy electrons it leaves in its wake. Thus, after a swarm has "acquired" a high-energy population, it keeps growing exponentially at rate ν_e maintaining its spectral proportions fairly constant (see figure 5.17).

As the swarm grows, the electric field E_{SC}, generated between the ionic and electronic space charges, screens the external field E. To illustrate the restriction due to this screening, we calculate the number of high energy electrons produced above an energy ε_{th} within the time by which Meek's criterion ($E_{SC} = E$) [641] is reached on figure 5.7b.

We plot this estimate on figure 5.21 with coloured circles representing the imposed air temperature (colour) and amount (size) of the electrons produced above a certain energy threshold (ordinate) at a given uniform electric field (abscissa). The prospects of thermal runaway at uniform fields below 20 MV/m are very low. Not a single electron of 1 keV would be produced in

ambient air. At 5000 K (oxygen is almost fully dissociated), only 5 make it to 1 keV at 22 MV/m. At higher temperatures, a few hundred electrons are accelerated to more than 10 keV but not up to 50 keV.

As a result, to the three objections above, we add a fourth stating

4. Thermal runaway occurs in conditions of strongly inhomogeneous electric fields with constrained spatio-temporal dimensions. Those conditions correspond best to the ones found ahead of ionisation fronts.

The notions of sterile and fertile thermal runaway rates may be interpreted as two extremes of a phenomenon that probably lies somewhere in between.

— In a sterile setup, the region of enhanced electric field can be imagined to be so localised around each individual electron that the offspring electrons have no influence on the outcome. They merely attach back after they emerge.

— A fertile setup is the complete opposite, where a swarm has an infinite amount of space to grow and produce fast electrons along with its exponential growth.

In an intermediate scenario, we may suppose that the spatial inhomogeneities of the electric field restrict the exponential growth of electrons and thus that the runaway electrons are produced at an intermediate rate between the sterile (ν_r) and the fertile (ν_e) rates. What is certain, is that one needs to know more about the spatial scales over which thermal runaway comes about, in order to be able to compare with spatial scales of ionisation fronts.

Spatial Scales

In preparation of understanding how the spatial extent and temporal evolution of the electric field ahead of a front affects the generation of runaway electrons, we may try to characterise how does the spatial evolution of high energy electrons differ from bulk electrons. For electrons generated at the origin, we consider two spatial extents:

- $-r_\parallel(\varepsilon) = \mathbf{r}\cdot\hat{\mathbf{E}}$: the longitudinal distance of an electron of energy ε opposite to the z axis aligned with the electric field.
- $r_\perp(\varepsilon) = \|\mathbf{r} + \hat{\mathbf{E}} r_\parallel\|$: the transversal distance of an electron from the z axis.

From there, we define averages based on all electrons whose energy is higher than ε_th:

$$\bar{r}_\parallel(\varepsilon_\mathrm{th}) = \frac{1}{N_{>\varepsilon_\mathrm{th}}} \sum_{n:\varepsilon_n>\varepsilon_\mathrm{th}}^{N_\mathrm{s}} w_n r_\parallel(\varepsilon_n)\ , \tag{5.10a}$$

$$\bar{r}_\perp(\varepsilon_\mathrm{th}) = \frac{1}{N_{>\varepsilon_\mathrm{th}}} \sum_{n:\varepsilon_n>\varepsilon_\mathrm{th}}^{N_\mathrm{s}} w_n r_\perp(\varepsilon_n)\ ; \tag{5.10b}$$

with $N_{>\varepsilon_\mathrm{th}}$ representing the number of electrons above the energy threshold ε_th.

These total distances are plotted on figure 5.22a. The curves look like straight lines and we may associate therefore a longitudinal and a transversal drift to high-energy electrons. This is analogous to the bulk drift velocity $\mathrm{v_d}$ for bulk electrons. The coloured zones show the span in one standard deviation of from the average. We see that for higher electric fields, the electrons travel faster in the longitudinal distance (the curves are steeper), whereas the radial drift remains significantly smaller than the axial drift and the radial expansion shrinks at higher electric fields.

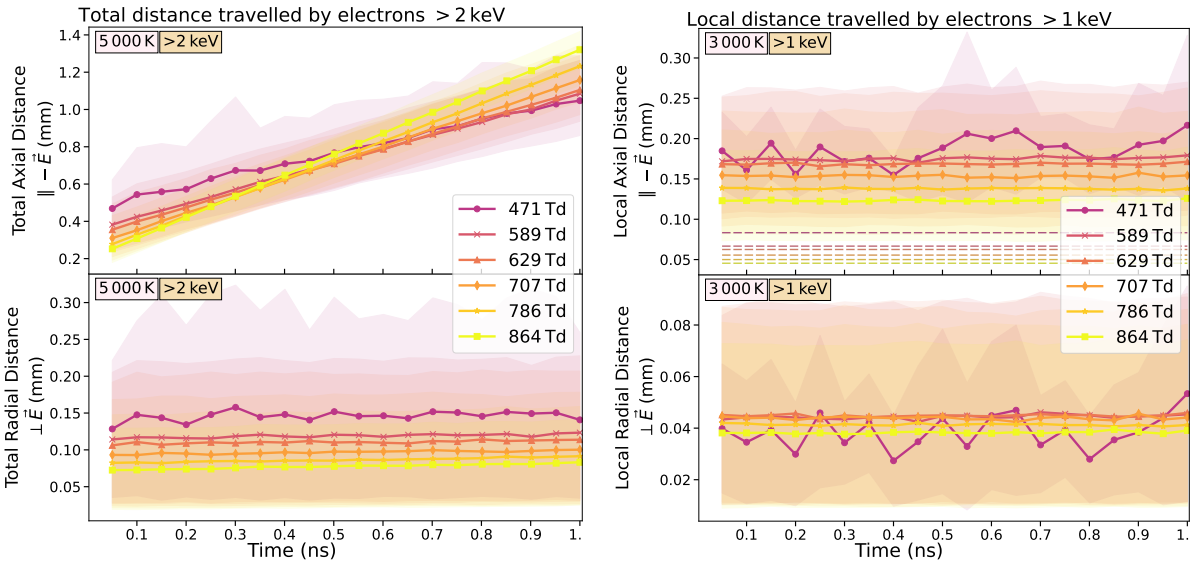

(a) Total average distances reached by all electrons with an energy higher than 2 keV since the initiation of the swarm at $\mathbf{r} = 0$.

(b) Local distances crossed by all electrons with an energy higher than 2 keV since their individual position of initiation at $\mathbf{r}_0$. Dashed lines show the distance required to accelerate an electron from 0 eV to 1 keV in vacuum at the corresponding absolute electric field.

Figure 5.22: Comparison of total and local distances travelled by high energy electrons. Top graphs : in the longitudinal (axial) direction opposite to the electric field. Bottom graphs : in the transversal (radial) direction perpendicular to the field (bottom graph).

Since the electrons in the swarm are continuously renewed as the avalanche progresses, we may also characterise the average distance that a high-energy electron travelled from its spawning place. We note this by $\Delta\mathbf{r} \equiv \mathbf{r} - \mathbf{r}_0$ and again, take the average values of the longitudinal (axial $\parallel$) and transversal (radial $\perp$) components. This time we see on figure 5.22b that the local distances take constant average values. These represent the average (axial and radial) distance that an energetic electron traverses in the swarm since its creation. It may be interpreted as the distance needed in air to accelerate to a given energy threshold ε_{th}. For comparison, we plotted by long dashed lines, the distance crossed by an electron accelerated from 0 eV to $\varepsilon_{\text{th}} = 2$ keV in vacuum at each given electric field. There is about a factor of three of difference. This factor is reduced when the energy threshold considered is higher and when the electric field is increased. Contrary to the drift velocities, $\Delta\mathbf{r}$ is relatively unaffected by air temperature.

Finally, in preparation of studying electron swarms in a dynamic setup instead of a static one, we represent the drift velocity (the slope of the axial curve on top of figure 5.22a) of electrons above 1 keV on figure 5.23. We see that those electrons drift faster than the bulk and thus that they may stay ahead of ionisation fronts in a fashion that is analogue to "surfing" on a wave.

In brief, we may conclude that spatial inhomogeneities, in the electric field or in air, are factors that have a high influence on thermal runaway. The electric field mostly affects the spatial scales, whereas air temperature may significantly lower the threshold to runaway and enhance the high-energy spectrum. The effect of the ionisation degree and electron-electron interaction may also play a role, though we have no means to assess its importance. We also surmise that the only viable region for fostering thermal runaway is located ahead of ionisation fronts, such as streamers, and we will try to explore this mechanism in the very last subsection 5.4.4.

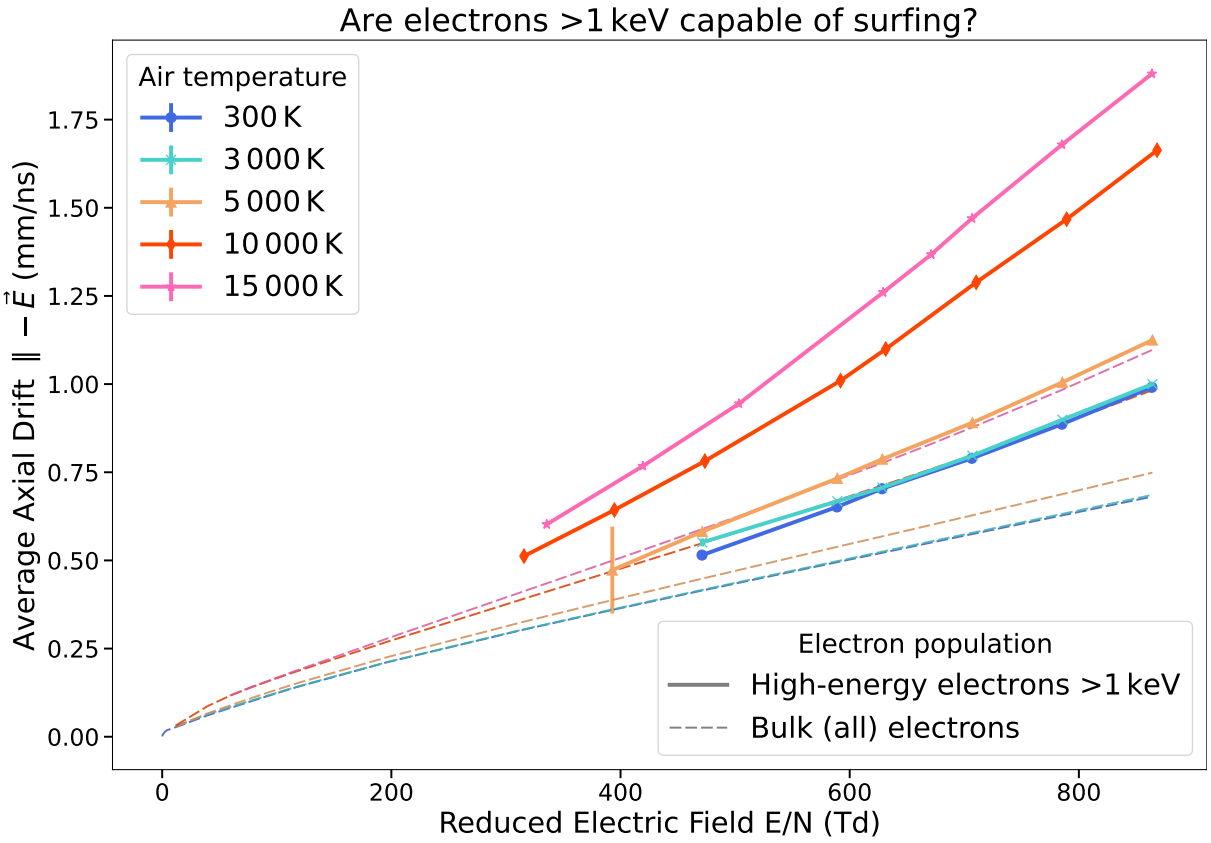

Figure 5.23: Average axial drifts (slopes obtained from figure 5.22a but at $\varepsilon_{\text{th}} = 1\,\text{keV}$) according to the electric field and air temperature. Dashed lines represent the drift velocities of the swarm bulk. Energetic electrons may propagate about twice faster ahead of the bulk.

5.4 Cases studies

In this last section, we explore deviations from the premises given at the beginning in section 5.1.

5.4.1 Vibrationally Superhot gas

In section 5.2.3, we saw that temporal scales of the dissipated power into vibrational excitations in discharge channels are separated by more or less 3 orders of magnitude from the temporal scales of thermalisation of the vibrational modes of excitation. This implies that the early stage of a discharge may be characterised by an overall cold strip of air that has nonetheless been super-heated vibrationally.

Hitherto, we have studied the effect of air temperature on the whole, taking into account its change in composition due to dissociation of molecules. Here, we may be interested in knowing what role does the vibrational temperature T_{vib} play by itself in the physics of the swarm. In figure 5.24 we plot the electron energy spectrum at two different electric fields for three vibrational temperatures.

On the upper graph, in the inset in particular, we see that electrons in a vibrationally-hot air can overcome the vibrational barrier of N_2 situated between 2–4 eV at relatively low electric fields near breakdown. This creates an enhancement of electrons at energies up to 10 eV but has very little effect on the high-energy part of the spectrum.

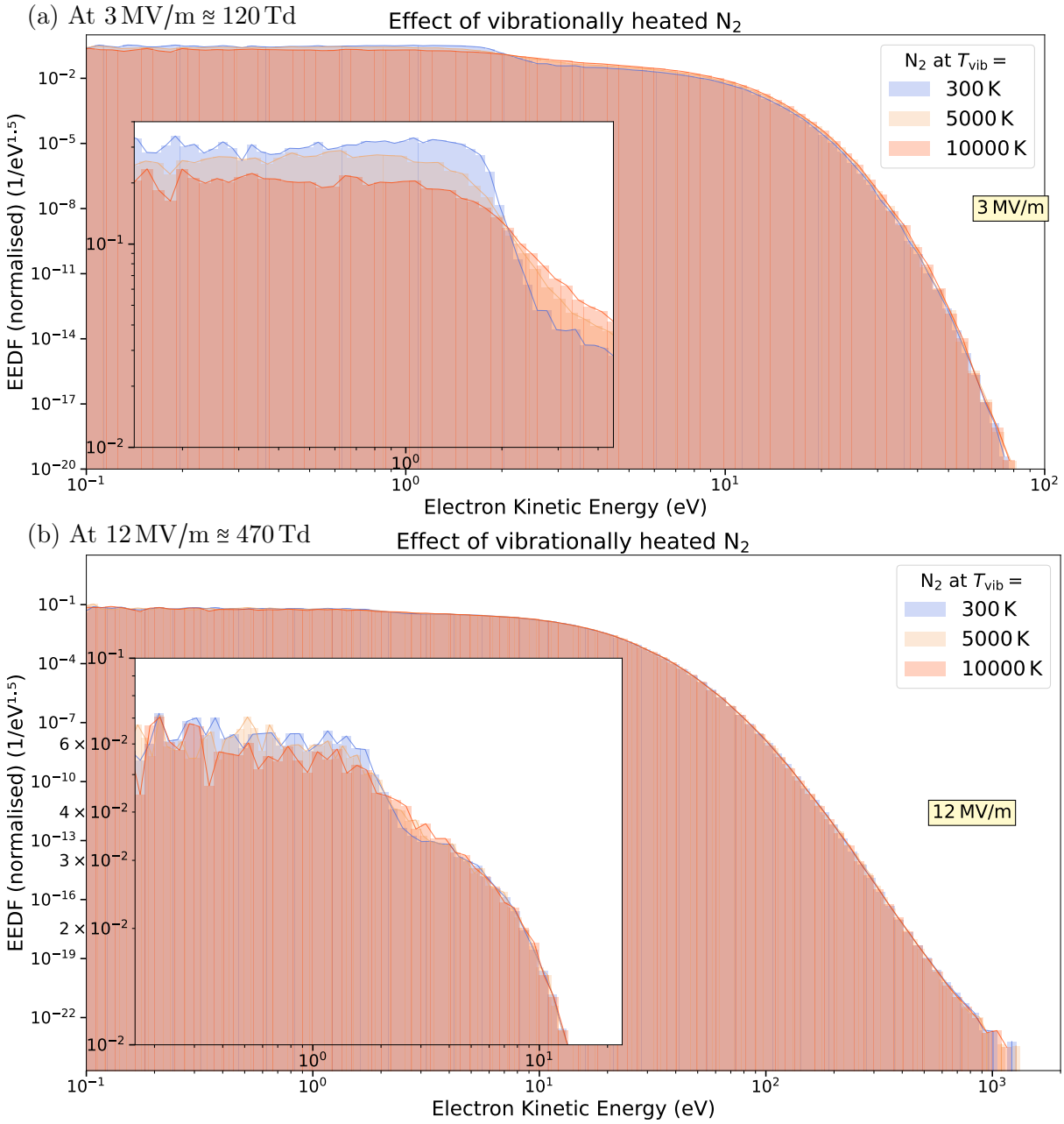

Figure 5.24: Two instances of vibrationally heated pure N_2 gas at three different temperatures maintaining the temperature at 300 K and changing T_{vib} only.

However, at high electric fields about 3 to 4 times the conventional breakdown field, the effect of vibrational temperature is practically irrelevant. There, the electron spectral distribution mostly results from the strong electric field rather than the vibrational temperature of the gas.

As a result, we conclude that if vibrational temperature has an effect on the development of discharges: its effect plays a role at low electric fields, thus in the wake of streamers but not in ionisation fronts and it promotes the energisation of thermal electrons into the 5–10 eV zone which is where attachment to oxygen molecules takes place. So that vibrationally super-heated N_2 molecules in air, in addition to O_2 molecules, can further endorse the attachment instability which was proposed as the mechanism behind the formation of the space stem [613].

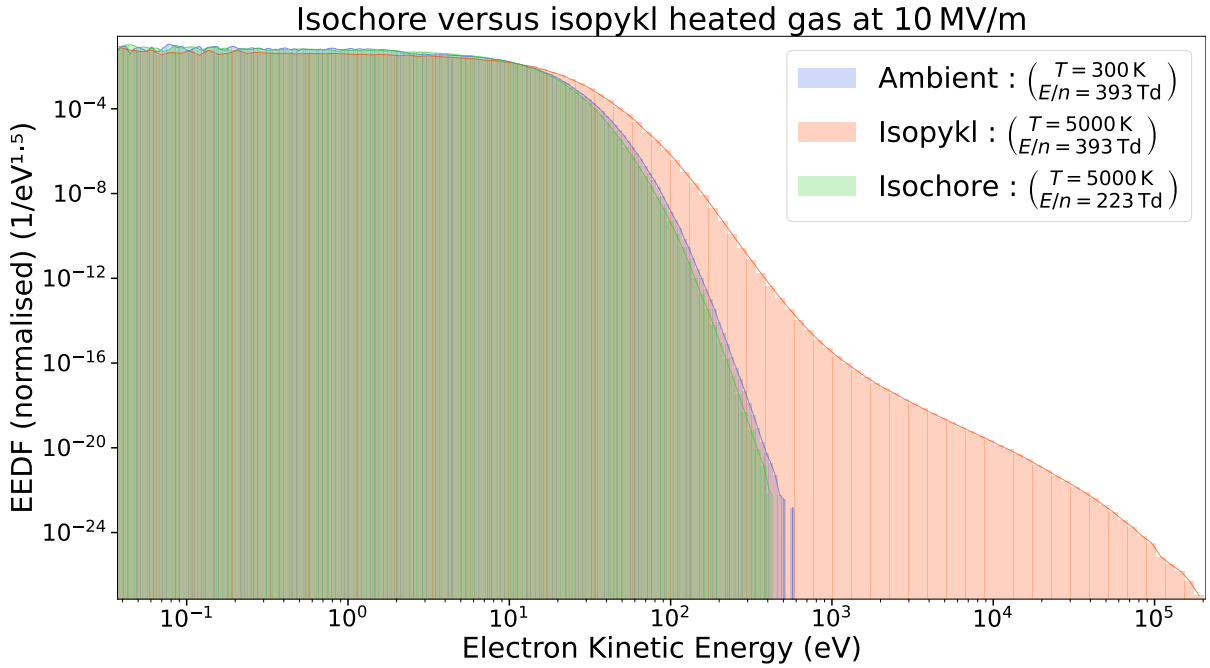

Figure 5.25: Comparison of the electron energy distribution functions obtained in air under 10 MV/m assuming different scenarios of the thermal expansion due to heating of air. Isopykl maintains the particles density to $n_{\text{air}} = 2.547 \times 10^{25}\,\text{m}^{-3}$ whereas isochore heating to 5000 K would cram atoms from dissociated molecules into a density of $n_{\text{air}} = 2.914\,\text{m}^{-3}$ thus lowering significantly the value of the corresponding reduced electric field.

5.4.2 Isochore Heated Air

In all the results presented so far, we assumed that the change in gas composition due to temperature was accompanied by a small amount of thermal expansion so that on average, the total number of gas particles per unit volume (n_{gas}) was kept constant. This we called the 'isopykl' expansion which means "same density" in Ancient Greek.

We may wish to model the extreme case where the gas has been super-heated intensely without allowing for thermal expansion to take place. This heating is known as 'isochore' implying that the volume occupied by a cell of the gas remains constant but the number of atoms inside this fixed volume increases due to dissociation. In figure 5.25, we observe that thermal expansion is key to reducing the average friction force in air and permitting thus the emergence of a runaway tail (red bar plot). Dissociation of atoms alone does not promote thermal runaway. On the contrary, it would inhibit it because the cross section of a molecule is generally (outside of resonances) inferior to the sum of cross sections of its constituent atoms. As a result, high-energy electrons would be rarer in an isochore heated gas (green bar plot on figure 5.25) compared to the ambient gas (blue bar plot).

Obviously, this situation is completely incoherent physically because the air composition taken in table 2.1 assumes (1) thermal equilibrium in the gas, and (2) that the air density is kept equal to the ambient air. This is one of the primary reasons why we postulated the "isopykl" hypothesis, in order to be able to make calculations and have an idea about thermal effects on electron swarms. It is evident that if one wishes to study rigorously the thermal effects of gases in discharges, then an *ab initio* model of gas heating would be needed, something totally beyond our current means.

We may conclude that thermal expansion brought about by heating of the gas is the main "thermal" effect on electron swarms. Change in chemical composition when the reduced electric field is maintained constant plays also a very large role on the shape of the EEDF, in particular the abatement of the vibrational barrier and the emergence of a high-energy tail due to reduced friction force. However, those effects should not be regarded as independent. When combined together, the total effect on electron swarms has far-reaching consequences even for generation of high-energy electrons.

Here, we completely omitted the presence of ionic species which appear in non-negligible proportions at high-energies. From the current observations, we surmise that their presence also has a strong impact on electron swarms.

5.4.3 Runaway–Thermal coexistence

We saw in the previous section, that generation of high-energy electrons from thermal runaway is in principle possible even at sub-critical electric field, but is mostly overwhelmed by the bulk of the swarm which grows at an exponential rate and whose presence would quickly alter the distribution of the electric field nearby.

In the spectra of section 5.2.1, we observed a change of shape in the high-energy part of the spectrum, which may be influenced either by air temperature (and composition) (fig. 5.4) or the intensity of the electric field (fig. 5.3). The change is characterised by the apparition of an inflexion point in the exponentially decaying portion of the spectrum at high energies. This attaches a high-energy 'tail' to the spectrum which decays again exponentially at its extreme. We identified this behaviour with a different kind of electron population: runaways which transit over large distances in the energy spectrum, as opposed to the bulk of the spectrum composed of electrons nearing the thermal energy (determined by the magnitude of the electric field).

In this section, we wish to explore what determines the emergence of the high-energy tail.

⊛ ¿ why do some swarms at given conditions have a tail of runaways and others not ?

To answer this question, we reverse our approach: instead of starting with thermal electrons, we initiate our simulations with a patch of relativistic electrons distributed evenly on a logarithmic scale between 0.5–2 MeV and we let the swarm evolve (keeping active however our compaction algorithm of section 3.3.2 which filters super-electrons according to their energy).

The situation is illustrated on figure 5.26a with snapshots of the spectrum taken at different times. We observe that the distribution of electrons slowly stagnates toward a solution which is different from a swarm initiated with thermal electrons in the same electric and gaseous conditions. The difference is the presence/absence of the high-energy tail. This is another argument to the fact that electrons in gases may be classified (at least) into two different populations.

The convergence is not absolute as attests the slowly decaying proportion of high-energy electrons on figure 5.26b. Nevertheless, the high-energy electrons persist on long enough times (several nanoseconds) to consider that the solution is different from the one starting with thermal electrons. The persistence of relativistic electrons comes from the fact that the electric field is above the runaway avalanche threshold which is around 300 kV/m≃ 12 Td [40, p.613("δ = 1.3")]. Nevertheless, runaway avalanche characteristic times are much longer than those of the bulk. At 60 Td the runaway avalanche characteristic time is about 50 ns [42, tab. 3 at δ = 5], which is significantly larger than the growth time of the bulk produced in impact ionisation by the runaway electrons.

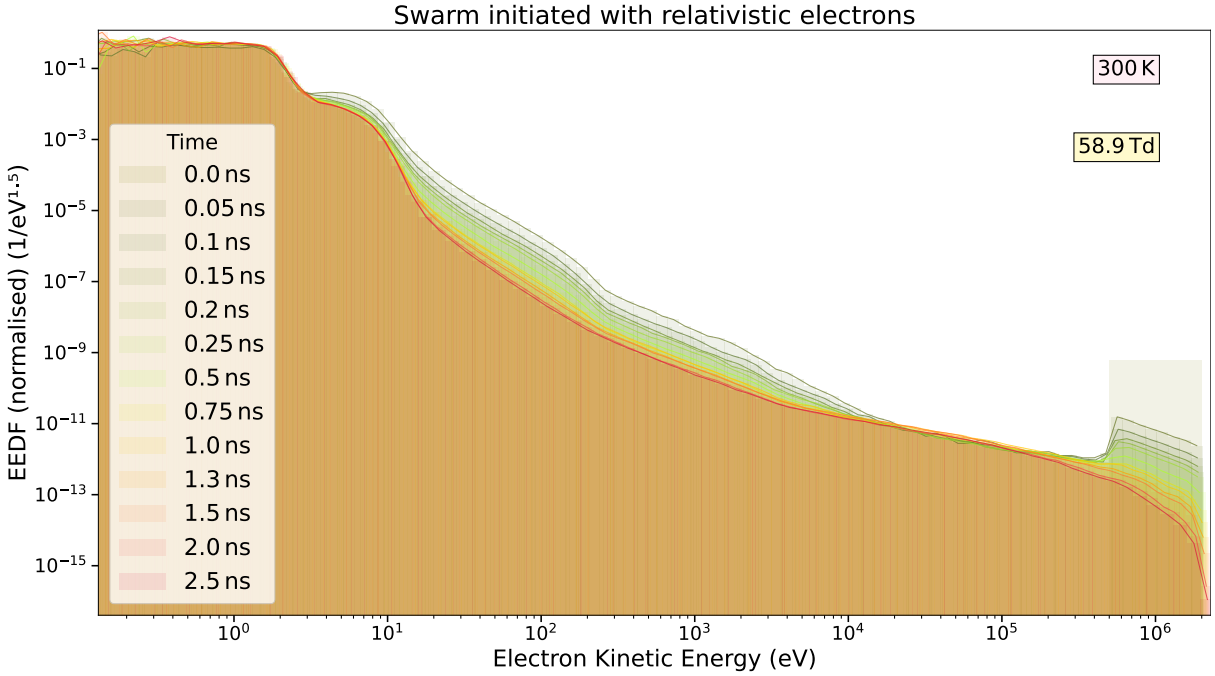

(a) Evolution of an electron swarm which has been initiated at $t = 0$ with a 300 000 electrons distributed between 0.5–2 MeV exactly as represented by the green towering square in the right bottom corner.

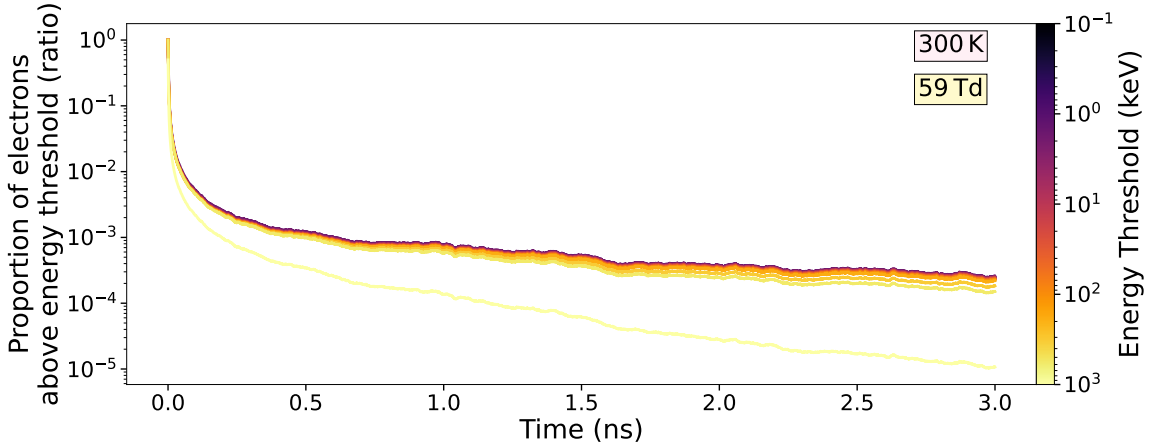

(b) Evolution of the proportion of high-energy electrons with time. This would be the proportion of the integral of the area on the right side of an energy threshold from spectra on figure 5.26a.

Figure 5.26: Evolution of a swarm which started with relativistic electrons.

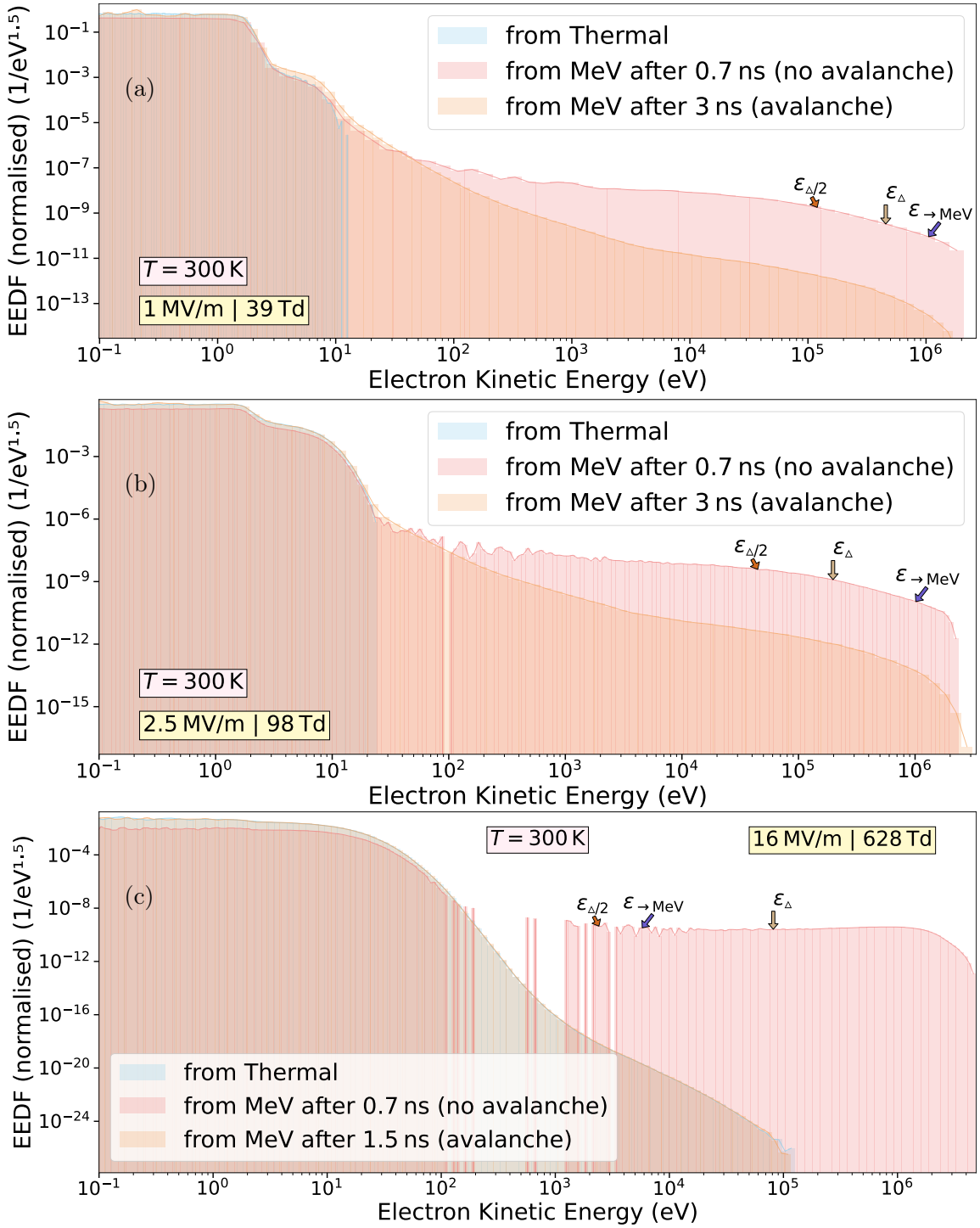

Figure 5.27: Spectra from three different simulations under identical electric and air temperature conditions. Blue swarms are initiated as Maxwellian distributions at 300 K, orange swarms are initiated with electrons between 0.5–2 MeV whereas red swarms between 0.1–2000 keV. In the red swarms, secondary electrons from ionisation are discarded (no avalanche) whereas they are added to the simulation in the orange swarms (avalanche). The arrows show characteristic points in the distribution of high-energy electrons as identified on the top row of fig. 5.15a at the corresponding electric field, also reported by the blue curve in fig. 5.16a.

On figure 5.27, spectra from three simulations are shown at different electric fields. When comparing the EEDF, one should remember that it is the aspect that matters (the proportions), not the absolute value (since the EEDF are normalised so that their integral equals 1).

Bulk electrons. At electric fields below conventional breakdown around 3 MV/m≃120 Td, the bulk of the swarm may not reproduce self-sufficiently. Its growth relies on the tail of high-energy electrons which seed electrons at lower energies. The comparison of the orange with the red spectra on figure 5.27a enables to assess the effect of secondary electrons from ionisation. We see that the part of the spectrum below 30 eV is practically identical in shape for all three simulations. Thus, this region of the graph is dominated by fast electron "thermalisation" in the electric and gaseous conditions imposed by the medium. Those are bulk electrons.

Transient electrons. Then, the region of the spectrum between 50–4000 eV, on the two first figures 5.27, is where simulations differ most in aspect. This region is absent in the blue simulations which started with electrons at 300 K. Partially, the fault is imputable to the fact that we do not use our enhancement algorithm. But even if it were activated, the shape of the EEDF would still differ significantly in this region. When electrons from secondary ionisation are included (orange), a "bridge" of high-energy electrons forms. These slowly degrade in energy before falling into the bulk. We call these the "transient" electrons because they cannot maintain themselves at their energy. Few of these electrons eventually accelerate and become runaways, but most of them decelerate faster and faster until they become thermal electrons.

The transience of these electrons is attested by the noisiness of the red simulation visible on figure 5.27b at these energies between 100 eV and 1 keV. These simulations come from those described in sec. 5.3.1; all super-electrons have equals statistical weights and the particle filtering is only the selection of the highest-energy electron at the outcome of each ionisation event. Thus, having noise in that portion (0.1–1 keV) of the graph is not imputable to a low super-electron number but to an impermanence of electrons. We interpret that the fluctuations come from a quicker rearrangement of electrons in the 0.1–1 keV energy space.

Another good indicator are the arrows pointing at the half-peak $\varepsilon_{\triangle/2}$ and peak $\varepsilon_{\triangle/2}$ thresholds that we defined in section 5.3.1 and indicated clearly on all figures 5.13–5.15. These two thresholds delineate the proportion of electrons which may sustain themselves at an energy higher than at their initiation. It is supposed to represent the state of runaway defined earlier in section 5.3. At low electric fields, those thresholds are relatively high; between 10–100 keV. Electrons below these thresholds may not maintain their state, and transit toward the bulk.

Runaway electrons. At higher electric fields, the dividing line between energetic electrons and the bulk is even more prominent since there are holes (absence of electrons) in the spectrum of the red simulation (as in fig. 5.27b–5.27c) which does not include electron production from ionisation. Therefore, we know that transient electrons in this region are mostly produced by secondary ionisation and that they must vanish soon because their fate is disputed between the collisional energy loss and the electric pull.

Starting from about 4–6 keV the spectra of the orange simulation with avalanche is similar in shape to the red simulation without avalanche. This means that the dominant mechanism determining the electron distribution at high energies between 5–2000 keV is not avalanching but acceleration. These electrons truly represent runaways. These are attested by the half-peak threshold $\varepsilon_{\triangle/2}$ which denotes electrons that are capable of accelerating toward higher energies.

The state of runaway is clearly affected by the strength of the electric field. Most conspicuous is the tearing of the spectrum into two halves at 630 Td between the bulk and the runaway in the

red swarm on figure 5.27c. There, the edge of the high-energy part of the spectrum practically coincides with the half-peak threshold $\varepsilon_{\triangle/2}$. Also, we see that the run-to-MeV threshold $\varepsilon_{\to\mathrm{MeV}}$ (probability that electrons accelerate to 1 MeV) has inverted its place with the peak probability threshold $\varepsilon_{\triangle}$.

Thermal runaway. The separation between runaways and bulk electrons might be clear on figure 5.27c on the red swarm but not so on the blue and orange which have actually merged to a common solution. At such a high electric field, the number of electrons produced in secondary ionisation is overwhelming and thus the shape of the spectrum changes significantly. The tail is shorter and more connected to the bulk compared to the spectra at lower electric field (figs. 5.27a–5.27b). The connectedness between the bulk and the runaway tail bespeaks the presence of thermal runaway: now the transient electrons transit in both directions in the spectrum, some ascend toward higher energies whereas others descend into the bulk. These transfers are balanced altogether with the production of secondary electrons from avalanche (ν_e). The argument in favour of thermal runaway is that, if there were not a significant runaway rate (ν_r) by which electrons are transferred from the bulk to the tail of the spectrum, then the EEDF would merely look like the abysmally decaying shape seen on figure 5.28 at advanced times (red hill).

This latter graph actually illustrates perfectly the issue of thermal runaway: it is a strife between two timescales:

- $\triangledown$ The growth (multiplication or avalanche) rate $\nu_\mathrm{e} \equiv 1/\tau_\mathrm{e}$ of the swarm bulk
- $\triangle$ The runaway rate $\nu_\mathrm{r} \equiv 1/\tau_\mathrm{r}$ of thermal electrons toward higher energies

When $\tau_\mathrm{e} \lll \tau_\mathrm{r}$ (a vanishing ratio $< 10^{12}$) there is virtually no thermal runaway, it is not probable enough and the presence of energetic electrons is merely a stochastic consequence: the greater the number of electrons, the higher the chances to have a few high-energy electrons.

When $\tau_\mathrm{e} \ll \tau_\mathrm{r}$ (a ratio $> 10^{12}$) then, the EEDF does not take a typical "stochastic" shape. On the one hand, some electrons – bulk – "spend" their time equally in all states that are energetically available to them. On the other hand, there start to appear other electrons – runaways – which "spend" their time only in some regions of the EEDF, namely in the high-energy tail. Therefore, the two phenomena somehow reach a balance: runaway electrons are small in number but they remain runaways and do not fall into the bulk. Their growth is governed by the transfer of bulk electrons into runaways; i.e. the thermal runaway rate ν_r. Bulk electrons, however, grow exponentially at the rate ν_e, but the more they are, the more convert to runaway proportionally. In the end, the balance obtained, represented by the fertile model (5.9) on p. 183, leads to the converged simulations on figure 5.27c from two opposite initial conditions.

In "usual" conditions, the avalanche time is always much smaller in magnitude than the characteristic runaway time: $\tau_\mathrm{e} \ll \tau_\mathrm{r}$. But these scales may be brought nearer equality in extreme conditions: at very high reduced electric fields. Then, the electrons accelerate systematically to high energies while ionising the gas in their wake. Therefore, the definition of the critical runaway field $E_\mathrm{cr}/n_\mathrm{gas}$ should be when $\tau_\mathrm{e} = \tau_\mathrm{r}$.

Drowned runaway. At *low* electric fields, we may say that our swarm is *bistable*.

A. It may sustain a bulk maintained by a population of high-energy runaway electrons.

B. But if the high-energy electrons disappear altogether, the bulk swarm adopts a stable configuration with no energetic electrons.

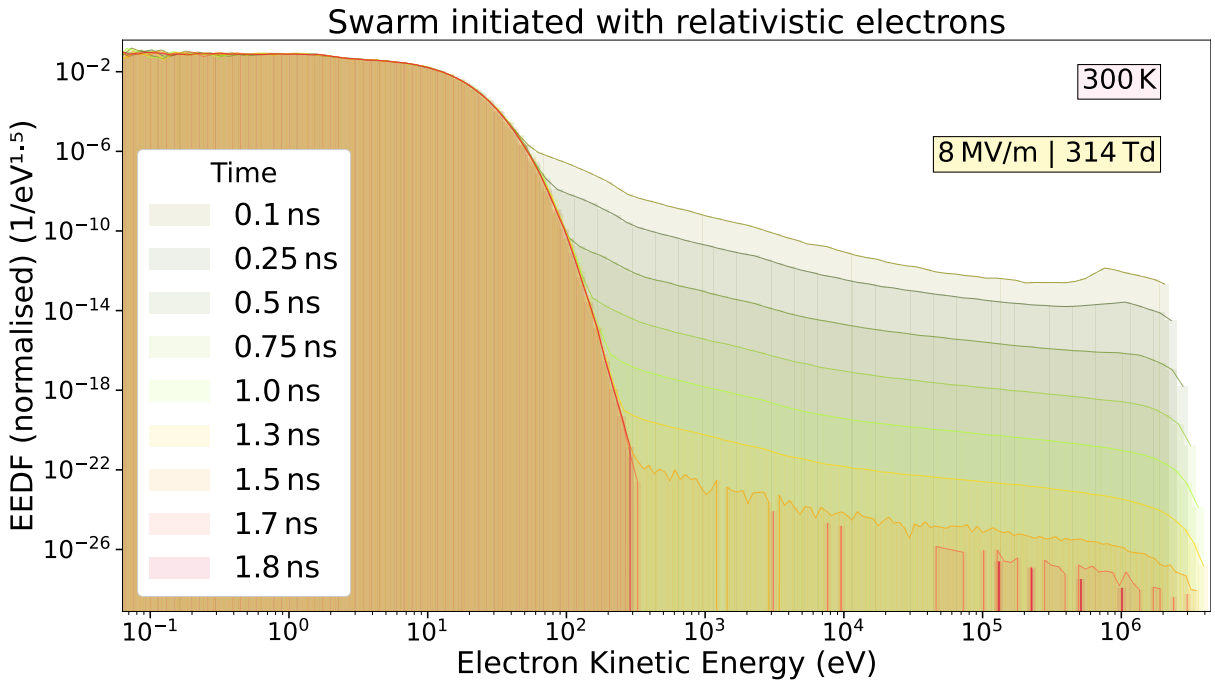

Figure 5.28: Above conventional breakdown, the exponential growth of the swarm bulk outnumbers the high-energy electrons present at the beginning of the simulation. Due to the maximal super-electron resolution limit $w_{\min}$ set by our compaction algorithm, when the high-energy super-electrons reach statistical weights $w < w_{\min}$ below the limit, they have to be discarded from the simulation until they vanish altogether.

Conversely, at *high* electric fields, the solution – in homogeneous conditions – is *unique* and independent of the initial conditions.

We may therefore wonder, '? at what fields do both solutions converge?

The answer is not simple. As the electric field strengthens, the avalanche rate of the bulk increases significantly whereas the runaway avalanche rate (the rate at which high-energy electrons multiply themselves) varies much less and the thermal runaway rate stays vanishingly small ($\nu_r \lll \nu_e$). The challenge in our simulation is that the spectral enhancement algorithm that we use cannot withstand an abysmally growing difference in the magnitude of the number of bulk electrons compared to the slowly growing runaway electrons. The latter are very quickly outnumbered by the former and the algorithm ends up having to discard energetic electrons. This is exactly what happens in figure 5.28. The high-energy electrons could perfectly maintain themselves in the field, but since we strive to model the swarm as a whole, their statistical weights become vanishingly small compared to the bulk electrons and this part of the spectrum sinks indefinitely. It is not until thermal runaway takes over, at even stronger electric fields $\gtrsim 12\,\mathrm{MV/m}$, that a tail of high-energy electrons may reappear in the spectrum as observed at the very beginning, in figure 5.3. The exact definition of the threshold would have to be determined.

Thus, once again, we may restate what we already deduced in the previous runaway section: thermal runaway and the subsequent production of high-energy electrons must be studied in relation to spatio-temporal restrictions on the regions of high electric fields such as those encountered ahead of ionisation fronts [548, chapter 3]. This we do so in the next last section.

5.4.4 Planar Front Surfing

The modelling of ionisation fronts is a complex topic. An introduction to the theory of ionisation waves may be found in Lagarkov and Rutkevich [chapter 3 of 548]. In the past, thermal runaway had already been successfully applied to realistic models of streamers [39, 161, 171] and streamer coronas emerging from a hot leader tip [36, 532]. All simulations showed very prospective results and it is openly known that thermal runaway is possible to trigger ahead of streamer ionisation fronts. What is however less known, is that one has to set up the stage with great heed in order to produce such results. There are too many parameters that have to be changed and set, and the Monte Carlo modelling of electrons is separate from the fluid part in such a way that it is hard to track energetic electrons while keeping all other bulk electrons in the simulation. Finally, the modelling of electron collision cross sections from low to high energies needs revision.

Here we use our Monte Carlo code ΘeRMIAA on a simplified version of the analytical model of a streamer as parameterised by Lehtinen [575]. The model consists of a cylindrical streamer of length L_s with a hemispherical front of radius a_s. At a given external electric field E_0 and streamer length L_s, the analytical model predicts that the radius a_s and instant velocity of propagation V_s are determined by the optimal configuration in which the velocity of propagation is maximal [575, fig. 4]. As the streamer grows in length, its velocity and radius increase accordingly [575, fig. 5]. For facility, the model we implemented is considerably simplified:

- The electric field is one-dimensional pointing toward and varying along the z-axis.
- We selected two values of the external electric field $E_0 = 2.5\,\mathrm{MV/m}$ and $5\,\mathrm{MV/m}$.
- The propagation velocity opposite to z is constant and calculated for a 12 cm-long streamer. At $2.5\,\mathrm{MV/m}$ $V_s \approx 18.5\,\mathrm{m/\mu s}$ while at $5\,\mathrm{MV/m}$: $V_s \approx 90\,\mathrm{m/\mu s}$

The model simulates a swarm swept by a planar (infinitely transversal) wave.

In brief, we consider that transversal dimensions of the streamer are infinite and we only model the electron swarm in relation to the axial and temporal variation of the electric field. With this model, we want to test two hypothesis each reflected by particular initial conditions of the swarm:

1. Thermal runaway : can an ionisation front generate thermal runaway electrons which subsequently accelerate in the field?

   ▷ In this first case, we initiate an electron swarm of 200 000 super-electrons at $\mathbf{r} = 0$, and set the time clock 1 ns before the arrival of the wave front. The variation of the electric field at $z = 0$ over time is represented by the red curve on figure 5.29.

2. Runaway surfing : how fast must electrons be in order to surf ahead of the ionisation front?

   ▷ In this second case, we initiate 200 000 super-electrons distributed logarithmically between 100 eV–2 MeV

No thermal runaway. A first simulation at $2.5\,\mathrm{MV/m}$ is represented on figure 5.29. There, we see that electrons were passed by the wave and receded behind. The velocity units of the front are directly comparable to the ones displayed in figure 5.23. We note that even electrons of 1 keV are not able to keep up with the ionisation wave.

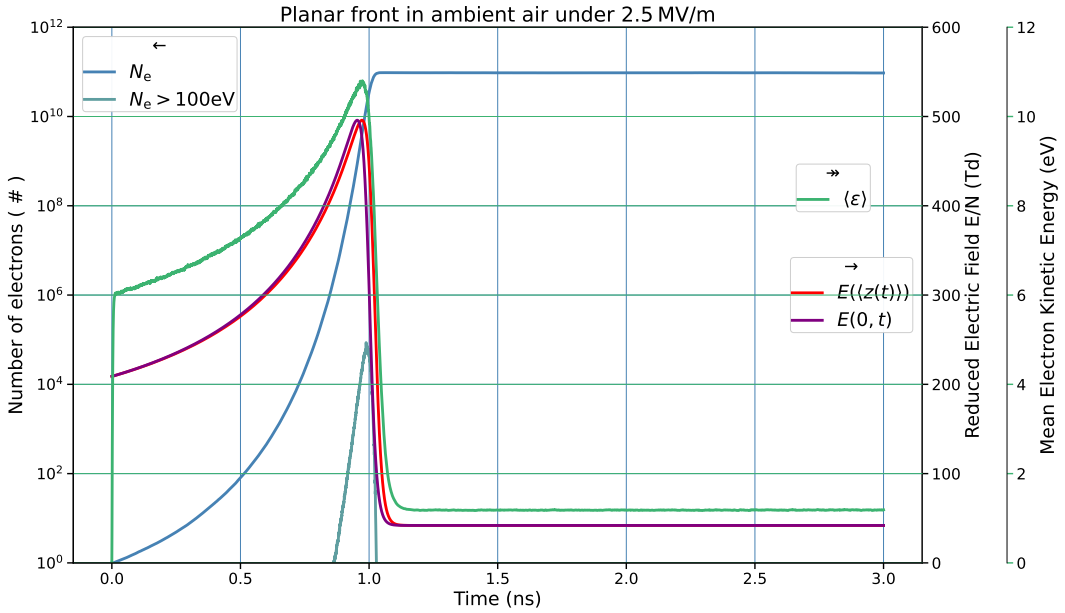

Figure 5.29: Evolution of a swarm initiated 1 ns before the arrival of a planar wave front in an external electric field of 2.5 MV/m. The red curve shows the evolution of the electric field at a fixed position at $z = 0$. Since the front advances at a speed $V_s \approx 18.5$ mm/ns opposite to the z direction, the time profile is the reverse of the field spatial variation in the z dimension. The purple curve shows the evolution of the field at the centroid of the swarm which shifts opposite to z but not fast enough compared to the velocity of the front. When the peak of the front reaches the average position of the swarm, the mean kinetic energy $\langle\varepsilon\rangle$ in green reaches is maximal value and the electron growth saturates (blue curve). In the wake of the front after about 1 ns, the electric field is significantly screened below the value of the external field and the swarm's high-energy electron population subsides (teal blue curve representing electrons above 100 eV).

This, we confirm on the bottom graph of figure 5.30a. The small proportion of electrons of energy higher than 1 keV is quickly overpassed by the ionisation front and vanishes altogether with all electrons above 100 eV about 50 ps after the arrival of the front. On the top graph (fig. 5.30a), looking at the field value at the average position of electrons higher than a certain energy threshold, we see that the high-energy electrons travelled for a while, staying in the high-field region immediately ahead of the front but could not maintain themselves.

Thermal runaway. Directly next to this figure on 5.30b, we show that for intenser fronts, if the field at the peak is high enough, MeV electrons may be generated. These are fast enough to keep up with the propagation of the front and stay ahead. Their presence seeds electrons ahead of the front which occasionally may induce local avalanche surges. These are observed as sudden peaks popping up in the black curve showing the number of electrons above 100 eV on the bottom of figure 5.30b.

This surfing mechanism is fragile however as shown by the on the top graph of figure 5.30b showing the electric field at the centroid position of electrons above a certain energy threshold. Electrons of 10 keV were first generated as the front arrived. A few of them luckily accelerated to over 100 keV. Nevertheless, even the 100 keV were caught up by the front, only those that would make it to the MeV maintain themselves at a stable distance at about 5 cm ahead of the front. This, we derived from the stability of the average electric field seen by electrons above

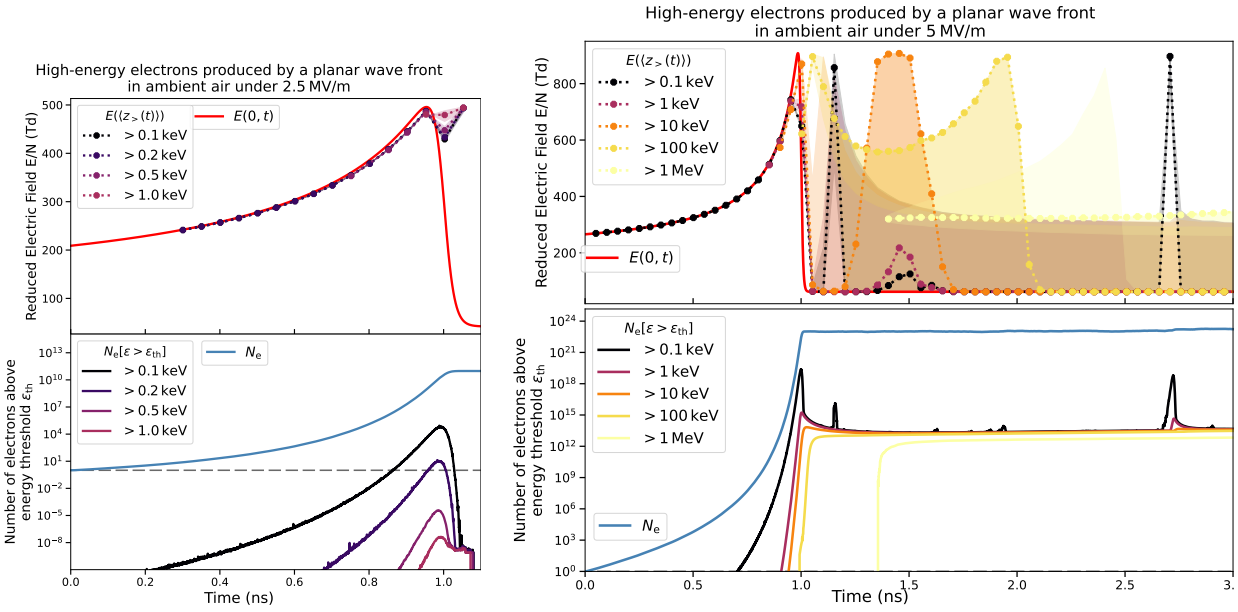

(a) Front wave in an external field of 2.5 MV/m, electrons in the swarm do not engage with the front.

(b) Front wave in an external field of 5 MV/m, MeV electrons are produced and surf ahead of the front.

Figure 5.30: Evolution in time of two swarms passed by a planar front in two different external electric field. Top graphs: Average electric field $E(\langle z_> \rangle, t)$ seen by electrons above an energy threshold ε_{th}. Bottom graphs: number of electrons $N_e[\varepsilon > \varepsilon_{\text{th}}]$ above an energy threshold ε_{th}.

1 MeV. The coloured zones show more or less the axial spread of electrons of a certain energy group. We thus see that some of the MeV electrons were also delayed and caught behind the ionisation front from the coloured triangular zone in pale yellow on top of figure 5.30b.

The production of >MeV does not stabilise as implied in figure 5.30b. This is a simulation artifact due to the compaction algorithm constantly discarding low-energy electrons. This algorithm is unaware of the position of electrons with respect to the ionisation front. This is why, after the simulation has been initiated, there are not enough super-electrons represented at the head of the front to continue the modelling of thermal runaway. Physically, the front must be bulging in electrons, so that there is no reason that MeV electrons be produced at one specific time and not somewhen else.

Runaway surfing. In the previous section, we studied the possibility of electron swarms below conventional breakdown maintained by the avalanche provoked by runaway electrons. The same is applicable here. In figure 5.31 we let MeV electrons ahead of the front under 2.5 MV/m (already simulated in figure 5.30a). We see that if MeV electrons were present ahead of the front they could subsequently sustain themselves in the high-field region ahead of the front and provoke avalanches of lower energy electrons which perpetually feed into the front. The situation stabilises at a certain distance ahead of the front, between 5–12 cm where the average propagation speed of electrons above 1 MeV is equal to that of the front.

The stratification of coloured zones in the centre of the top graph of figure 5.31 reveals the spatial structure of the runaway avalanche. The fastest (furthest ahead) electrons are > MeV.

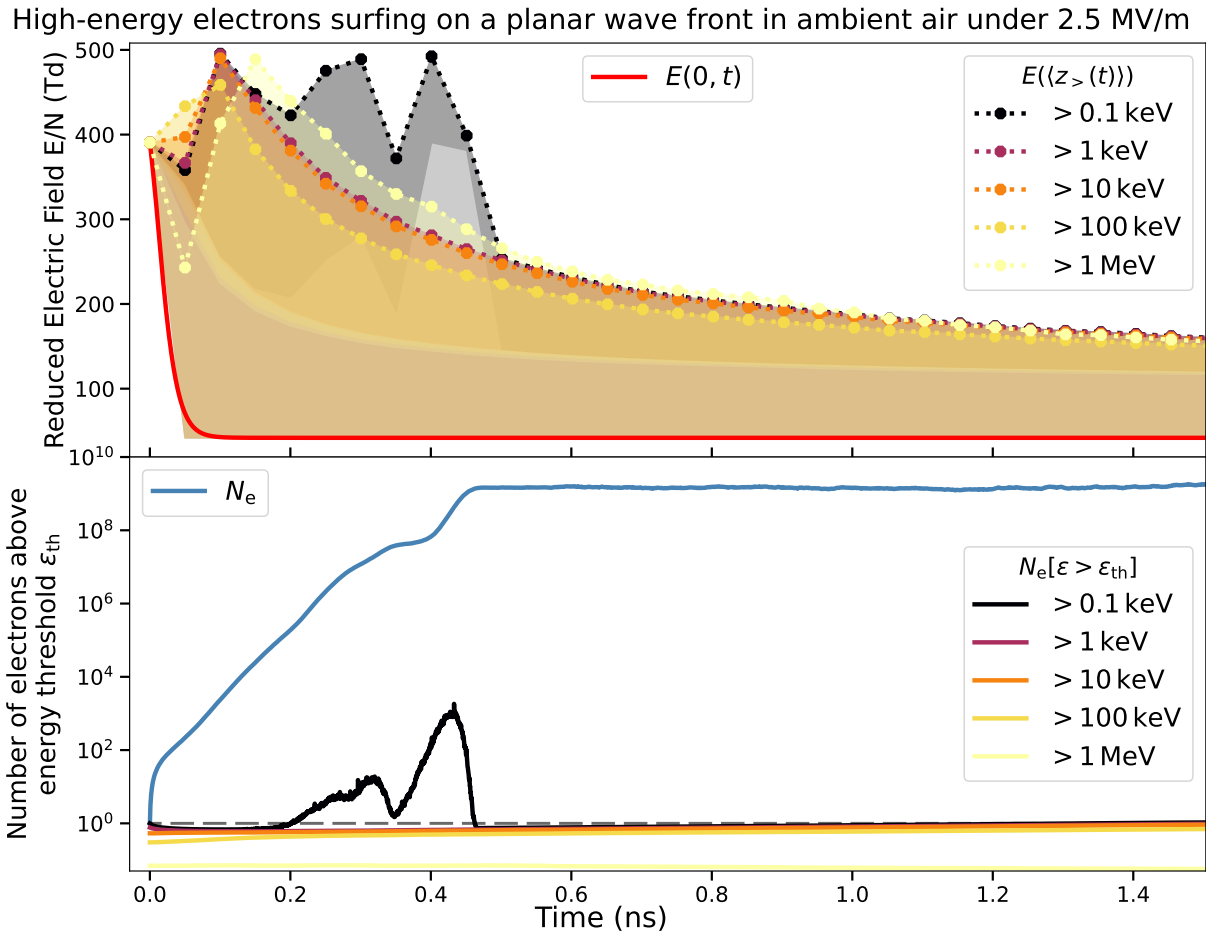

Figure 5.31: Population of high energy electrons surfing on a planar ionisation front in an external field of 2.5 MV/m. Circles joined by dots show the electric field at the average position of an energy-group (all electrons higher than an energy ε_{th}). Coloured zone spans the electric fields at the positions of the electrons, one standard deviation ahead of the mean position in their respective energy-groups (midline stratification). MeV electrons are present in the simulation from the start as opposed to figure 5.30a where only thermal electrons are present initially.

The present results are preliminary and more would have to be said when:

- the external electric field varies according to the one given by a leader tip and its corona;
- the variation of the electric field in the transversal plane is considered;
- the variation of the front propagation speed with its length is included;
- the state of the gas ahead of the channel is preionised or preheated.

Nevertheless, we believe that very simple studies as we endeavoured presently, enable us to understand some basic mechanisms that may be applied universally to situations more realistically found in natural discharges. This last section concludes our *microscopic* study of thermal runaway in atmospheric gases. In the next chapter, we will summarise the main points and present our perspectives on future investigation.

Chapter 6

Discussion

The present chapter gathers coherently the information scattered throughout the first part of the thesis related to the emergence of high-energy electrons from swarms in electrified gases.

6.1 Recapitulation

The context framing the research

At the very beginning of the thesis, we stressed the importance of studying natural phenomena. In the prologue (p. 3), we reminded that lightning is deeply embedded in all cultures as an archetype of might, wherefore it is almost impossible to ward off the common presumption that any scientific study related to lightning must be for harvesting the energy wielded in thunderstorms. Undeniably, the phenomena related to lightning, which we put into context in chapter 1, are many and fascinating. The lightning discharge is characterised by the formation of a conductive plasma channel called the "leader" whose propagation at the head is promoted by a corona of filamentary weakly-ionised plasma channels known as "streamers". Streamer heads consist in an ionisation wave front in which electrons either propagate toward the front (positive streamer) or with but most of them slower than the front (negative streamer). A negative leader head is composed of a corona of negative streamers (and oppositely).

A feature of negative leaders distinctive from positive ones, is that their propagation is intermittent with stops followed by sudden elongations of the leader channel called "steps". The accomplishment of a step is characterised by a bright burst of a streamer corona at the end of the newly formed tip and accompanied by a burst of X-rays lasting little less than a µs. This burst is not to be confused with a terrestrial gamma-ray flash, also related to negative leader activity but much harder and intenser, which is mostly observed from satellites orbiting Earth and lasting up to a ms.

Both X-rays and gamma-ray flashes are bremsstrahlung signatures of relativistic electrons maintained in regions of electric fields above 0.5 MV/m encountered in the vicinity of leader tips. While gamma ray flashes are most likely due to relativistic avalanches fed back over vast regions extending hundreds of meters ahead of leader tips [246], X-ray bursts must come from free electrons that have accelerated from thermal energies of a few eVs to very high energies above 100 keV. This acceleration mechanism is named "electron thermal runaway" but its intricate relation to the streamer corona of leaders is presently unknown, despite being actively studied [36, 164, 532].

Understanding which electric and gaseous conditions foster the emergence of thermal runaway electrons, has been our primary objective. As implied by the subtitle of this thesis, we decided to abstract away the very complex multi-scale structure of lightning discharges and focus on the emergence of thermal runaway from a microscopic point of view: electrons accelerated by an electric field while being intermittently braked through collisions with air molecules.

Construction of a model

When the molecules are neutral, the spatial and temporal scales of electron propagation and deviation through collisions are very well separated (by at least three orders of magnitude) so that one can model angular deviations and losses of kinetic energy through differential cross sections. This separation reflects the structure of the thesis into three parts:

I. The present first part dealt with electron propagation and acceleration in electrified gases.

II. The second part is only concerned by the determination of (differential) cross sections.

III. The third part complements the second part and links it to the first by analysing the relationship between a set of electron-molecule cross sections and electron swarm transport coefficients in a gas.

Another separation of temporal scales occurs between the evolution of the electron swarm (subnanosecond scale) and changes in the state of the gaseous medium (on the microsecond scale). This motivated the research of electron swarm properties in different conditions determined by the temperature of air which affects both its chemical composition and density.

A visual partition of the temporal scales of different processes involved in electric discharges is gaseous media is represented in figure 6.1. We can see that all electronic processes are very fast lasting typically $< 1\,\mathrm{ns}$. Gaseous processes on the other hand are not as fast, unfolding on the $> \mu\mathrm{s}$ scale, except for rotational and translation relaxation which is of the order of the mean free time between inter-molecule collisions $\sim$ ns. Between these two timescales lies the time required for thermal electrons to runaway between $\gtrsim 10\,\mathrm{ns}$ up to a few $\sim 100\,\mathrm{ns}$.

We took advantage of this timescale separation in chapter 2, where we distinguished the modelling of the gaseous medium (sec. 2.1) from the propagation of individual electrons (sec. 2.2) and the dynamics of the electron swarm as a whole (sec. 2.3).

In chapter 3, we presented how to implement this model numerically into a Monte Carlo code which follows the trace of each electron individually and which samples the outcome of collisions from (differential) cross sections (sec. 3.2).

The average motion of electrons in a gas, described in sec. 2.2.3, depends strongly on the electron energy.

- At low energies $< 10\,\mathrm{eV}$, it is erratic because of the many collisions with molecules that scatter electrons almost isotropically. Because the energy of an electron varies between two collisions, so does its collision frequency. Numerically, the stochastic modelling of collisions can be handled by the null collision sampling (sec. 3.2.1).

- At high energies $> 1\,\mathrm{keV}$, the motion is slowed and deviated by a series of many consecutive discrete collisions characterised with small relative energy losses and small angular deviations. These may be approximately modelled by an average friction force (p. 69), though we did not take this route in the thesis to preserve coherence.

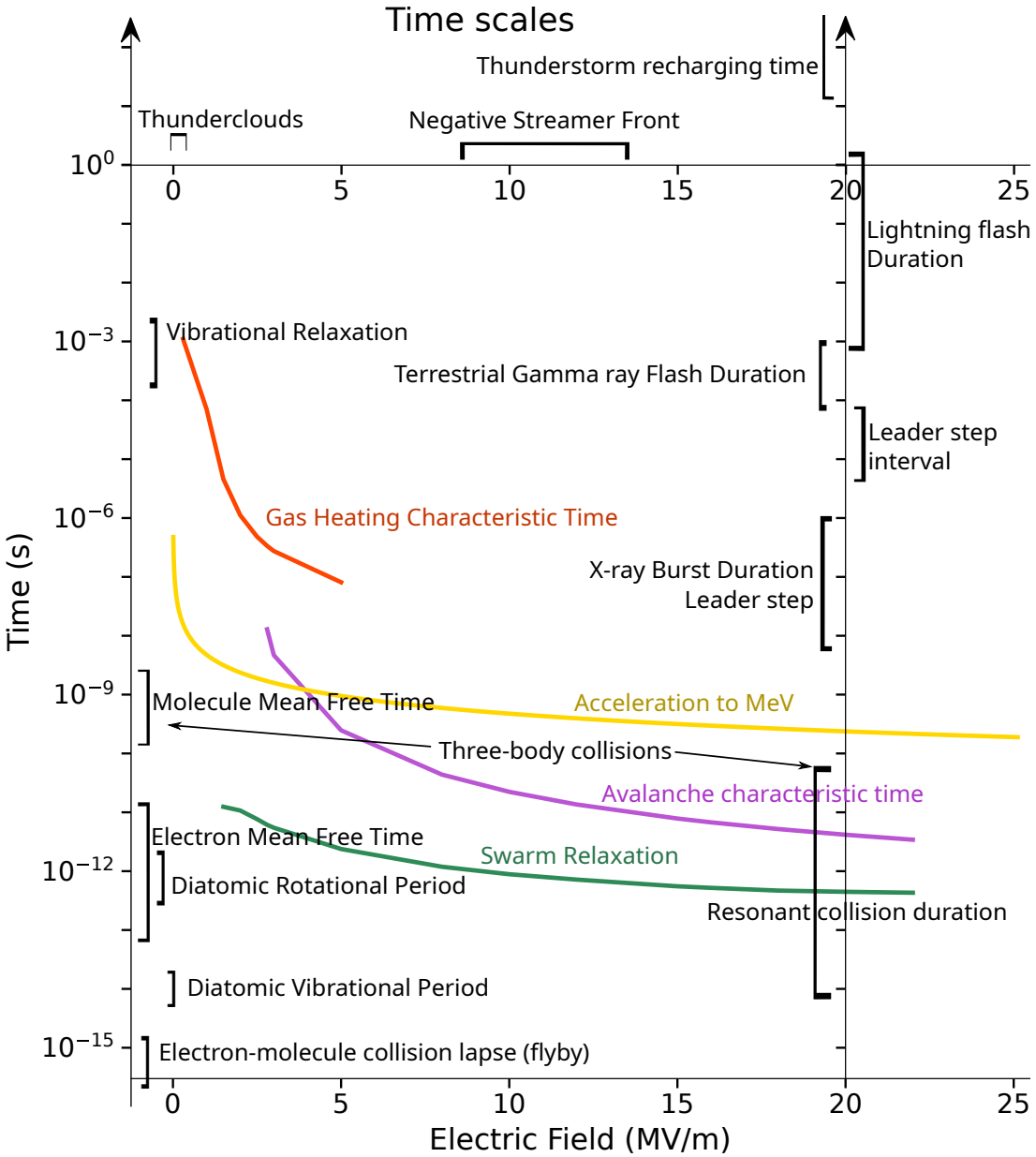

Figure 6.1: Different physical times scales of phenomena related to lightning discharges (to the right) and kinetics of electrons and molecules (to the left). The characteristic times for gas heating, avalanche growth and swarm relaxation all depend on the gas density which equals $n_{\mathrm{air}} = 2.547 \times 10^{25}\,\mathrm{m}^{-3}$. Gas heating scales also to the *relative* electron density which was assumed to be $\zeta_{\mathrm{i}} = 10^{-6}$ as typically encountered in streamer channels. The acceleration time is calculated in free flight. When taking into account delay from collisions, it is about a factor two longer, but is dispersed over large duration intervals. The probability that an electron accelerate to one MeV under 12 MV/m is completely negligible.

In both cases, high or low energies, the balance between electric acceleration and stochastic collisions of electrons with the gas molecules may be embodied in the ratio of the electric field E to the number density of molecules per unit volume n_{air}, which scales the collision frequency at a determined electron energy. This ratio is known as the reduced electric field E/n_{air} and measured in Td units (Townsends).

Electron swarms in electrified gases relax very quickly (fig. 6.1), in less than 10 ps for fields stronger than 1 MV/m at atmospheric density. This is why, information relevant to the macroscopic modelling of discharges may be encompassed in transport/reaction coefficients (sec. 3.3.3) [150, §8.2] and more generally in the electron energy distribution function (sec. 3.3.1) and angular distribution; all of which are functions of the local reduced electric field $E(\mathbf{r},t)/n_{\text{air}}$ at a certain position in space $\mathbf{r}$ and time t.

A scaling law may be established between reduced electron swarm properties and the reduced electric field. Maintaining E/n_{air} constant:

- $\propto n_{\text{air}},\ E$: all reaction rates (ν_{c}), avalanche rates (ν_{e}) scale *proportionally* to the gas density and electric field.

- $\propto 1/n_{\text{air}},\ 1/E$: all characteristic times τ (inverse rates, acceleration, relaxation – all coloured curves on fig. 6.1) and transport parameters (mobility and diffusion) scale *inversely* to the gas density and electric field.

At electric fields above the conventional breakdown, because of the exponential growth of the swarm, electrons of higher energies are always outnumbered by lower-energy electrons. To be able to represent many electrons on greatly differing abundance magnitudes, we use super-electrons with statistical weights. These weights are managed by a "compaction" algorithm presented in section 3.3.2 which liberates memory space occupied by low-energy electrons, by increasing their statistical weights. This allows the simulation to foster high-energy super-electrons of very low weights. Sometimes the weights may be below unity; in which case they represent a probability of being present in a situation with a physical electron density correspondingly scaled upward.

Caveats of the numerical implementation of cross sections (sec. 4.1) and super-electrons (sec. 4.2) were presented in chapter 4 before the whole code – baptised ΘeRMIAA – was assessed (sec. 4.3) through tests aiming at:

- ✓ the physical consistency (sec. 4.3.1);

- ✓ comparison with results from a 2-term Boltzmann kinetic solver (p. 81) known as BOLSIG+ (sec. 4.3.2);

- ✓ validation of calculated transport coefficients with swarm experiments (sec. 4.3.3).

A great hurdle to the validation of the modelling of electron-molecule collisions is that cross sections may be adjusted to yield macroscopically coherent transport coefficients, yet misrepresent electron-molecule collisions at the microscopic level. This is known as the non-uniqueness problem and addressed in swarm experiments designed to derive cross sections [690, 748]. We tackled this problem the other way around. We did not adjust any of the cross sections measured experimentally based on transport parameters but completed the set with inelastic processes as explained in the third part chapter 15 p. 569, thus not mixing known with unknown data.

Results obtained from the model

In the penultimate chapter 5 of this part, we analysed the behaviour of electron swarms in gases under various homogeneous electric fields and in air at five different temperatures. The motivation was to understand, on a microscopic level, how would free electrons respond to local conditions possibly encountered at different stages of a spark or lightning discharge. The research was structured in the following way:

Hypothesis 5.1 In a preliminary section, the conditions of the simulations and the hypothesis underlying the research were exposed in a framed list on p. 149. We highlight:

- Most simulations are conducted in homogeneous and static electric and gas conditions.
- Local thermal equilibrium determines the chemical composition of air from table 2.1 and distribution of metastable excited species (from Maxwell-Boltzmann statistics in sec. 2.1.2).
- The presence of ions and inter-electron interactions are completely disregarded.

The results were subsequently analysed in light of the limitations imposed by these hypothesis. What mostly restricts the application of thermal runaway in homogeneous external electric fields is that the electric conditions of the medium are rapidly overwhelmed by the exponential growth of swarms.

Bulk 5.2 First, we analysed swarms from their bulk properties:

5.2.1 The influence on the electron energy distribution function of the electric field, gas species, and temperature of air was analysed. As expected, a larger proportion of high-energy electrons is promoted by stronger electric fields, higher temperatures and monatomic gases with high excitation thresholds.

5.2.2 Transport parameters in air at various temperatures as a function of the reduced electric field reveal that increasing both the electric field and temperature enhances electron transport: they drift faster, diffuse more and multiply quicker.

5.2.3 The dissipated power and dissociation rates were compared as a function of the electric field and at different temperatures. Because vibrational excitations are mostly resonant processes, there exists an electric field at which the dissipated power is maximal. For other excitations, the dissipated power is a monotonically increasing function of the electric field.

Runaway 5.3 Second, we focussed on the small population of electrons at energies higher than the bulk.

5.3.1 We undertook a probabilistic approach to the determination of the runaway energy threshold as a function of the reduced electric field and at different air temperatures. We found that the probability that high-energy electrons permain* at a given electric field have very characteristic curves depending on the initial kinetic energy given to the electron and its orientation relative to the electric field.

5.3.2 Then, we estimated the average delays before an energetic electron emerges from a swarm which initially was at thermal equilibrium with the ambient gas. We identified two different delays:

*"permanere" see footnote on p. 103

1. t_0: the minimal delay time related to the time necessary for a low-energy electron to accelerate to an energy ε_{th} while being delayed in collisions.
2. Δt_{11}: the average time necessary for a swarm initially composed of 1 physical electron to yield 1 energetic electron, taking into account the exponential growth of the swarm.

5.3.3 Finally, we discussed a bit how to define the production rate of thermal runaway electrons. There, we proposed to distinguish two extreme 'modes' of production:

a) Sterile runaway (p. 180): that is the 'classical' definition of thermal runaway rate used in the literature. It assumes that thermal runaway is a draining mechanism of electrons initially at thermal energies and without production of secondary electrons (thus sterile). The runaway process is described by a Poisson variable characterised by a probability rate ν_{r} and a delay t_0 (the same as identified above). Two possibilities are overlooked by this view: high-energy electrons can (1) backscatter (2) be produced as secondary electrons from ionisation.

b) Fertile runaway (p. 182): this is the other extreme view modelled in this thesis whereby electrons have an infinitely free space to grow. High-energy electrons represent a stable proportion of the whole population due to the exponential growth of the swarm. Therefore, the production rate in fertile runaway is identical to the avalanche rate ν_{e} of the whole swarm.

c) Spatial restrictions (p. 185): sterile and fertile runaway production are two imaginary extremes of a more realistic situation where regions of high electric fields enabling thermal runaway are limited spatially and temporally. Then, the production of high-energy electrons should depend on the space available to accelerate, on the propagation speed of the high-field region and on the nearby presence of high-energy electrons capable of seeding electrons also at intermediate to high energies. There, we explored how electrons at high energies drift at different speeds and that electrons above a certain kinetic energy may be characterised by the average distance they travelled in the direction of the electric field (from their initial position). This enables us to frame the space needed to produce electrons above a certain energy threshold according to the conditions of air and the electric field as represented in figure 6.5.

Specific Cases 5.4 The study of thermal runaway under homogeneous electric and gaseous conditions are severely challenged by the evolution of electron swarms under electric fields high enough to enable thermal runaway. Therefore, we explored the effect of deviations from homogeneous and equilibrium conditions.

5.4.1 From fig. 6.1, vibrational relaxation is slower (~ms) than gas heating rates by electrons in discharges (~µs). Therefore, we studied electron swarms in a vibrationally super-hot gas composed of molecular nitrogen. At low electric fields < 120 Td the principal effect of vibrational temperature is to shift electrons trapped below 2 eV, at the foot of the vibrational N_2^- $^2\Pi_g$ shape resonance barrier, toward higher energies between 4–12 eV. This effect is smeared at electric fields > 250 Td which enable electrons to overcome the vibrational barrier regardless of the vibrational temperature. In any case, raising the vibrational temperature bears no consequence on high energy electrons.

5.4.2 The expansion of the gas due to pressure change is somewhat slower than its dissociation rate. It should expand on scales larger than a µs [776, fig.2]. The extreme case where the gas is assumed to have been heated and dissociated without having had

time to expand is known as "isochore" heating. We checked that thermal runaway is actually inhibited in isochore heated air, so that thermodynamic expansion of the discharge channel is instrumental in promoting thermal runaway influenced by air's thermo-chemical state.

5.4.3 Electrons at very high energies may in principle sustain themselves and create runaway avalanches at fields above the break-even threshold ~0.3 MV/m. On the other hand, the production of high energy electrons through thermal runaway becomes possible only above ~12 MV/m. Therefore, we observe a transition between electron swarms where high-energy electrons seed low-energy electrons below 4 MV/m and where the exponential growth of bulk electrons and their acceleration to higher energies overwhelm the distribution of high-energy electrons above 12 MV/m.

5.4.4 In discharges, high electric fields are encountered at the head of ionisation waves propagating at speeds between 10^6–10^7 m/s. We performed two very simple tests on analytical models of planar (1D) fronts:

1. Runaway Surfing: in principle, relativistic > MeV electrons are capable of sustaining themselves ahead of diverse ionisation fronts in a fashion analogical to surfing on a wave.
2. Thermal Runaway: should the peak electric field on the wavefront be high enough, the ionisation front can produce and emit high-energy electrons continuously as it propagates.

Hitherto, we have recounted the main structure of the results and our observations. In the next section, we offer concrete questions about electron swarms to which we provide an answer from our results.

6.2 Questions

6.2.1 About the swarm

Relaxation

Electrons in an electrified gas converge very quickly to a nonequilibrium but stationary distribution which has a tail decaying steeper than a Maxwellian. If the deviation (Δ) from their equilibrium distribution is important, the reaction of electrons is non-linear (with respect to Δ). After a short interval, the response follows a typical exponential relaxation (fig. 3.7) of a characteristic (relaxation) time τ roughly inversely proportional to the electric field (fig. 5.6). In ambient air electrons relax in about:

- Below < 100 kV/m: $\tau \gtrsim$ ns
- Between 0.1–1 MV/m: $\tau <$ 100 ps
- Above 3 MV/m : $\tau <$ 10 ps

Relaxation depends also on the gas composition. In monatomic gases, relaxation at electric fields < 1 MV/m can be five times slower than in molecular gases. This is because electron-atom collisions at low energies < 1 eV are practically entirely elastic, except when there is a fine structure splitting of the ground state. For molecules, vibrational and particularly rotational cross sections constitute significant losses at low energies.

Except near the head of ionisation waves [586, 686], electron transport and reaction rates can be modelled through the local equilibrium approximation to the reduced electric field E/n_{air}.

Multiplication

When the reduced electric field is above a threshold known as the conventional breakdown field E_k, electrons multiply at an exponential rate ν_e with a characteristic time $\tau_e = 1/\nu_e$. The importance of attachment to electronegative molecules compared to ionisation determines the breakdown threshold.

In absence of attachment, the number of electrons can only increase with time. In this case, the avalanche rate depends on a (reduced) characteristic field E_c such that, at low fields: $\nu_e \sim E_c n_{gas} \exp(-E_c n_{gas}/E)$ [762, §4.1.5:p.56]. In atomic gases, the characteristic avalanche field is lower due to absence of rotational and vibrational excitations.

Characteristic E_c	Breakdown E_k
Ar : $E_c \simeq 150\,\mathrm{Td}$,	O_2 : $E_k \simeq 125\,\mathrm{Td}$,
N_2 : $E_c \simeq 770\,\mathrm{Td}$,	Air : $E_k \simeq 110\,\mathrm{Td}$.

In air, when the temperature increases, the breakdown threshold first rises slightly and then suddenly decreases sharply. This is because dissociative attachment to oxygen molecules is enhanced but at the same time, the energy lost in vibrational excitations decreases principally due to dissociation of molecules and partly due to superelastic collisions. If we do not consider detachment, at 3000 K $E_k \simeq 120\,\mathrm{Td}$, but at 5000 K, $E_k \simeq 60\,\mathrm{Td}$. In reality, detachment is very important at high temperatures, so these values hold only at low densities of air (detachment is due to collisions of O^- with other atoms/molecules)

In absence of attachment, the avalanche rate is a monotonically increasing function of the electric field. In presence of dissociative attachment, there is a range of electric fields in which the attachment is more important than ionisation. This is because dissociative attachment is a resonant process which happens near the dissociation threshold of the anion which is always inferior to the ionisation potential of the molecule. This means that the *avalanche* rate passes through a negative minimum at a value E_a of the electric field:

O_2 : $E_a \sim 70\,\mathrm{Td}$,	Air : $E_a \sim 80\,\mathrm{Td}$.

The presence of this minimum implies the existence of an attachment instability which is currently the most plausible mechanism at the origin of the creation of a space stem in the wake of streamers. The attachment instability is actually a doubly non-linear mechanism:

i. as the local electric field inside the space stem rises between 10 Td to 80 Td, because of the accumulation of space charges, so does the attachment increase and the growth rate decrease.

ii. as the vibrational temperature of oxygen molecules increase through many electron excitations, the attachment cross section becomes even more important.

This instability vanishes quickly, however, when the electric field surpasses 120 Td or when the temperature of air exceeds 1000 K because of detachment [11, §3.3].

Above conventional breakdown, the electron swarms in air multiply at very fast rates. Combined with the displacement and diffusion of the swarm, we may infer the time lapse t_{as} for the creation of a **s**treamer front from an electron **a**valanche in a local electric field.

At 200 Td :	$\tau_e \simeq 300\,\mathrm{ps}$	$t_{as} > 5\,\mathrm{ns}$,
At 300 Td :	$\tau_e \simeq 60\,\mathrm{ps}$	$t_{as} \sim 0.8\,\mathrm{ns}$,
At 400 Td :	$\tau_e \simeq 25\,\mathrm{ps}$	$t_{as} \simeq 0.4\,\mathrm{ns}$,
At 500 Td :	$\tau_e \simeq 12\,\mathrm{ps}$	$t_{as} \simeq 0.2\,\mathrm{ns}$.

Thus, discharges in air should display two very distinct behaviours:

- If the applied external electric field rises steeply and above 120 Td, a cold streamer wave front should be formed, upon which it would propagate.
- If the applied external electric field varies smoothly and is maintained below ~120 Td, free electrons heat and deplete oxygen molecules present in the channel.

Heating and dissociation are discussed below.

Heating

When electrons collide with molecules, they deposit an energy which is stored in a particular mode of excitation. Some modes decay instantaneously and their energy is converted into other forms. Other modes are generated faster than they decay and this creates an accumulation of energy into reservoirs that are gradually levelled as time progresses [852, fig.4]. The subsistence* of excited states is set by the balance of flows between generation (inflow) and destruction (outflow). A large population of excited states is explained either by important generation or slow decay/quenching.

An ensemble of subsisting excited states does not imply that they are thermalised (following a Maxwellian distribution at a determined temperature) unless there is a preferential redistribution of stored energy to some states over others. This is the case of vibrational modes of excitation of N_2 which relax faster internally (transfer between different vibrational level v, v') than through conversion to translational or rotational modes [150, §7] which takes place in roughly ~ms [57]. In case of O_2, energy transfers from vibrational to translational modes are more efficient so that the separation of temperatures is less certain [685, p.2650].

On the other hand, electronically excited molecular and atomic states are more chemically reactive (the activation energy is reduced because the bonding is smaller). Also, if they are not metastable, they may quickly decay through spontaneous emission. Thus, energy in electronic excitations converts quickly ($<$ µs) into other forms [150, §9.2].

As a consequence, we made a crude distinction between dissipated power into vibrational excitations and all other forms of energy transfer which we consider to be 'fast' ($<$ µs). Dissipated power of electron swarms, represented in figure 5.9, is very dependent on the electric field. Since vibrational excitations by electrons are mainly resonant, they are important only around specific electron energies. Average vibrational dissipated power (per electron) is thus optimal at a definite electric field E_{vib}. In ambient air, the optimum is at:

$$N_2 \ : \ E_{\text{vib}} \simeq 100\,\text{Td},$$

$$O_2 \ : \ E_{\text{vib}} \simeq 400\,\text{Td}.$$

The difference is explained by the large resonance bump in O_2 around 10 eV mainly from the $O_2^-\ {}^4\Sigma_u^-$ resonance [552, p.7] whereas most of N_2 vibrational excitation takes place in the $N_2^-\ {}^2\Pi_g$ 2–4 eV resonance†.

*Originally a Latin loan-translation from Ancient Greek 'hypostasis' (*ὑπόστασις*) which is the underlying foundation supporting the being. Here, I mean the capability of persisting over a prolonged duration.

†There is also another resonant structure seen at 20 eV but it is modelled only for the $v = 0 \to 1$ transition. We think this would not significantly change the statistics about dissipated power to vibrational excitation of N_2.

Note that the dissipated power to vibrational excitations here is *immediate* (< ns). On longer timescales (~ µs), it becomes influenced by gas kinetics [149]. For illustration, we can estimate the total energy dissipated into vibrational excitations after the passage of an ionisation front. Assuming a $d_s = 1\,\text{mm}$ thick wave at 400 Td, of relative electron density $n_e/n_{air} = 10^{-5}$ and propagating at $V_s = 10^6\,\text{m/s}$, the average vibrational energy $\overline{\Delta\mathcal{E}_{vib}}$ received by a molecule would be (this is an estimate for the upper boundary):

N_2 : $\overline{\Delta\mathcal{E}_{vib}} \sim 0.85\,\text{meV} \ll 290\,\text{meV} \approx \mathcal{E}_{v=1}$,

O_2 : $\overline{\Delta\mathcal{E}_{vib}} \sim 0.33\,\text{meV} \ll 200\,\text{meV} \approx \mathcal{E}_{v=1}$.

So streamer fronts are indeed ineffective to the heating of air because the 'exposure time' to heating is about $d_s/V_s \simeq 1\,\text{ns}$

On the other hand, the non-vibrational dissipation (everything other than direct vibrational excitations) rises by two orders of magnitude between 40–100 Td. In the wake of a streamer, the relative electron density may stay around $n_e/n_{air} \simeq 10^{-7}$–$10^{-6}$ [621, fig.1]. Assuming that the formation of a space stem implies an electric field about ~80 Td, the heating would be around ~ 30–300 K/µs. We assumed the simple thermodynamic relationship for isochore heating $\bar{\mathcal{E}}_{air} = 5/2 k_B T_{gas}$ between the average energy and the temperature of a diatomic gas.

This heating rate is somewhat too low to explain the quick transition from space stem to space leader [68, 311]. The same was concluded by Malagón-Romero and Luque [621] who suggest that subsequent streamers propagating in preionised channels and pilot systems (counter-propagating streamers) may play a significant role in stem heating.

Dissociation

Electrons dissociate molecules in collisions at energies above the dissociation threshold which is around 9.76 eV for N_2 and 5.116 eV for O_2. Dissociation may be direct or indirect involving a transition probability of an excited state to a repulsive bond state. The latter is known as predissociation and has a branching ratio depending on its transition probability rate. Also, ionisation from core orbitals very often leads to dissociation of the molecule.

In ambient air, the threshold field for dissociation E_{diss} is around:

N_2 : $E_{diss} \simeq 25\,\text{Td}$,

O_2 : $E_{diss} \simeq 15\,\text{Td}$.

Similarly to heating, we may estimate the (upper boundary to) dissociation induced by the passage of a streamer front ($d_s = 1\,\text{mm}$, $V_s = 10^6\,\text{m/s}$, $E_{peak}/n_{air} = 400\,\text{Td}$, $n_e/n_{air} = 10^{-5}$):

- ~ 0.1 % N_2 molecules dissociated and
- ~ 0.18 % O_2 molecules dissociated.

In a space stem in the wake of a streamer ($E/n_{air} = 80\,\text{Td}$, $n_e/n_{air} = 10^{-7}$) we may calculate the characteristic time $\tau_{diss} = 1/\nu_{diss}$ of dissociation by electron excitations:

- For N_2 : $\tau_{diss} = 12\,\text{ms}$,
- For O_2 : $\tau_{diss} = 0.85\,\text{ms}$.

Thus, molecular dissociation of N_2 is mostly dominated by raising the temperature of the gas while for O_2 there should be a small contribution due to collisions with electrons depending on the density of electrons in the space stem.

6.2.2 About thermal runaway

In the previous section, we estimated the changes of the gas' state induced by electron swarms on streamer fronts and in space stems. Here, we focus on the generation of high-energy electrons from thermal runaway acceleration in intense electric fields.

Runaway threshold

At high energies > 1 keV, electron-molecule interactions are characterised mostly by small relative energy losses and small angular deviations. In a single collision:

- Ionisation: at 1 keV in N_2 the probability of an energy loss > 100 eV is of 6 %.
- Scattering: at 1 keV in N_2 the probability of a deviation > 30° is of 10 %.

Therefore, energy losses and scattering can be roughly represented by an average braking force F_B acting on the electron. The dynamic friction force, due to inelastic losses only, is noted F_D.

a) In a deterministic perspective, the runaway energy threshold ε_r at a certain electric field is given by the energy at which the friction force is equal in magnitude to the electric force: $F_B(\varepsilon_r) = eE$ on figure 2.15.

b) In a stochastic approach, the runaway threshold is rather defined as a characteristic energy $\varepsilon_{\triangle/2}$ (on figures 5.15) at which the probability that an electron remain at an energy higher than its initial energy ε_0, varies most steeply with respect to ε_0. We called it the "half-peak (probability) threshold" (middle panel of figure 5.16a and 5.14a).

This characteristic energy $\varepsilon_{\triangle/2}(t)$ varies with time but transits to a slow stabilisation between 12–40 Td which would correspond to the probabilistic electric field threshold of runaway acceleration.

The stabilised value of the half-peak threshold $\varepsilon_{\triangle/2}(t > 300\,\text{ps})$ is shown in figure 6.2 according to the reduced electric field and at four different temperatures of air.

These threshold values of $\varepsilon_{\triangle/2}$ are situated between those predicted by the braking F_B and dynamic friction F_D forces. They agree quite well with the predictions from the 'effective friction' F_{eff} defined by Lehtinen and Østgaard [579, eq.(C1)].

In ambient air, the characteristic half-peak threshold is located at:

- $\varepsilon_{\triangle/2} \simeq 125\,\text{keV}$ at 40 Td (1 MV/m),
- $\varepsilon_{\triangle/2} \simeq 80\,\text{keV}$ at 60 Td (1.5 MV/m),
- $\varepsilon_{\triangle/2} \simeq 45\,\text{keV}$ at 100 Td (2.5 MV/m),
- $\varepsilon_{\triangle/2} \simeq 17\,\text{keV}$ at 200 Td (5 MV/m),
- $\varepsilon_{\triangle/2} \simeq 9\,\text{keV}$ at 300 Td (7.5 MV/m).

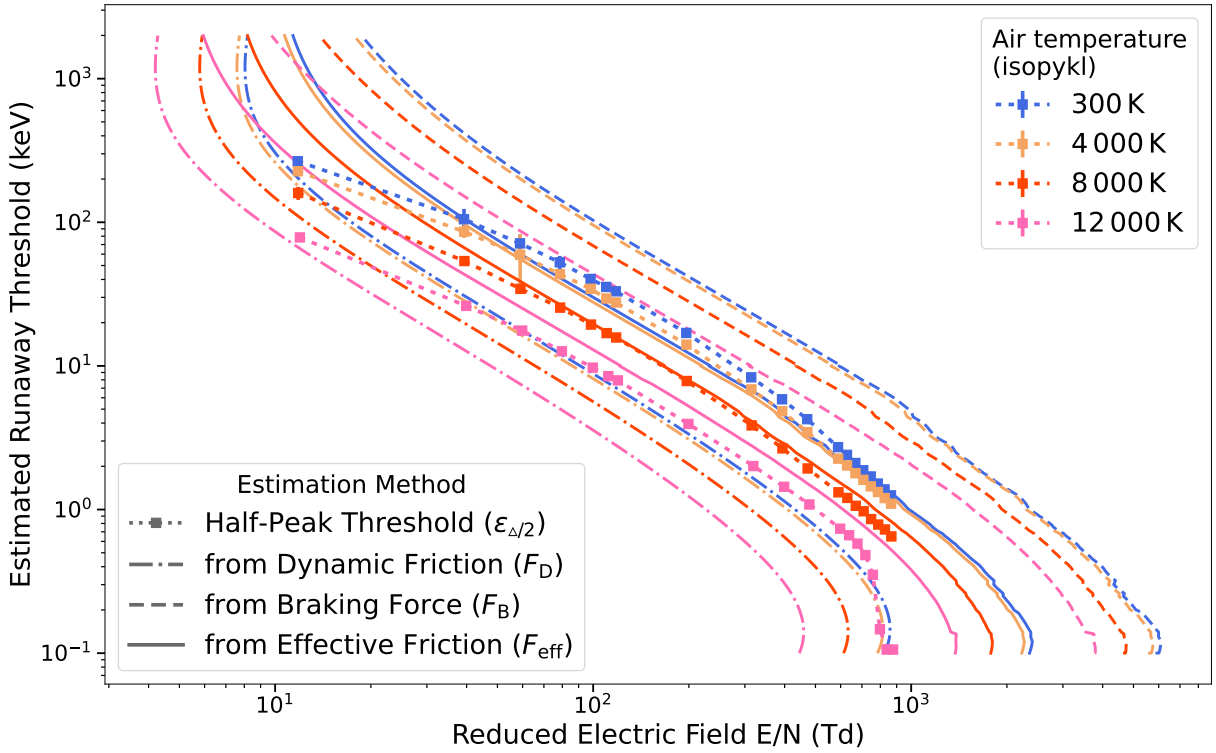

Figure 6.2: Probabilistic estimation of the runaway threshold from Monte Carlo simulations (··· ■ ··· filled squares linked by dotted lines) and from deterministic calculations based on the average dynamic friction forces from inelastic and scattering. These are defined on p. 72. The values are the average of characteristic energies $\varepsilon_{\triangle/2}(t)$ between 300—700 ps. The values at 12 Td (the break even field) were not converged.

Delays : how long?

The delay time before the production of a runaway electron may be characterised by an *onset* t_0 and a *characteristic time* τ_r which is the inverse of the (sterile) runaway rate ν_r.

The onset t_0 is physically bounded by the infimum $t_\varnothing$ for the acceleration of a thermal electron in vacuum (without collisions). While the probability that an electron scatter only elastically at forward angles during its acceleration in a gas is vanishingly small, we think that a value for $t_0 \neq t_\varnothing$ can be defined based on the very definition of a runaway electron (sec. 5.3): i.e. that on average it keeps accelerating.

Starting with a swarm at 0 eV, we let electrons accelerate and collide. After each collision, we retain only those super-electrons whose energy is larger than at their previous collision. The super-electrons are duplicated and their statistical weights divided. We repeat this process until all electrons have breached a given energy ε_{th} threshold. The average of the times at which each electron breached the threshold (weighted by the statistical weights when breaching) is the definition we propose for the minimal onset t_0.

We would have had to make special simulations to estimate t_0 with precision. Nonetheless, we represent the ratio $t_0/t_\varnothing$ in figure 6.3 from the values of t_0 determined as in fig. 5.17. Despite the noise due to stochastic fluctuations in the acceleration process (and initial energy $\neq$ 0 eV), the ratio $t_0/t_\varnothing$ appears as a decreasing function of the electric field and an increasing function of the energy threshold ε_{th} when $\varepsilon_{th} > 1$ keV.

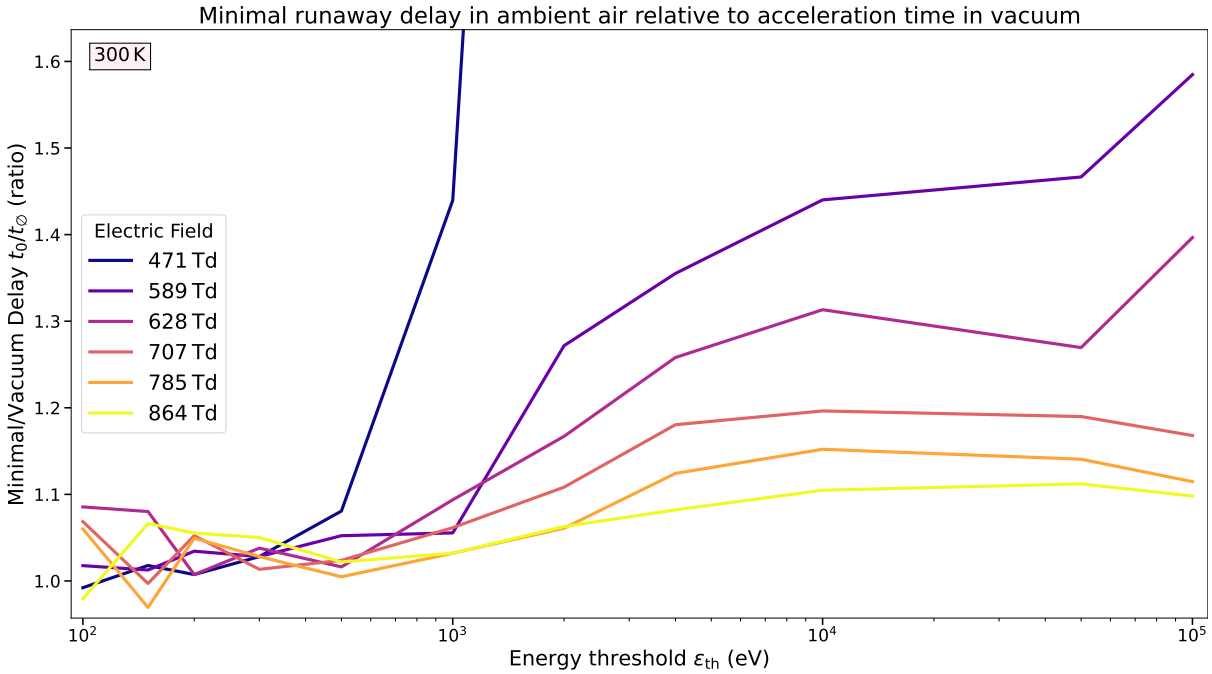

Figure 6.3: Ratio of the minimal onset time t_0 for a thermal electron to accelerate up to a given energy (x-axis) in ambient air, compared to the acceleration time in vacuum starting from 0 eV. At low thresholds ~ 100 eV, the noise comes partly from the non-zero initial electrons energy following a Maxwellian distribution at 300 K. This is also why the ratio is below 1 at high electric fields (the acceleration time from 0 eV to the highest initial kinetic energy is non-negligible on the timescale of the full acceleration to the energy threshold).

The minimal delay t_0 can, in principle, be defined at any electric field, even when the probability associated to thermal runaway is vanishingly small. Still, looking at the dark blue curve at 471 Td on figure 6.3, we can tentatively define a threshold electric field for thermal runaway as the field at which $t_0 = 2t_\varnothing$. This field depends on the energy threshold ε_{th} we are considering, but one can take $\varepsilon_{th} = \varepsilon_{\triangle/2}$ for a more rigorous definition. Currently, we estimate that the threshold field for *thermal* runaway in ambient air is above 12 MV/m or 470 Td.

In addition to t_0, we defined a 1-in 1-out delay Δt_{11} which corresponds to the average time that one high-energy electron be produced from one thermal seed electron in a high electric field. In fig. 5.19b, we compared this time Δt_{11} to the time for the formation of a streamer front in a spatially-unlimited uniform electric field. At low electric fields, Δt_{11} exceeds the streamer formation time, but for any threshold ε_{th} there exists a reduced field high enough at which Δt_{11} is shorter than the streamer formation time.

Distances : how far?

Under an electric field E in vacuum, the distance $l_\varnothing$ travelled by an electron accelerated uniformly from 0 eV to ε_{th} is directly given by $l_\varnothing = \varepsilon_{th}/eE$.

In a gas, the electron loses a certain energy on its way due to inelastic collisions and its energy ε at a certain position $\mathbf{r}$ cannot be deduced from a conservation law. We consider the distance $-\Delta r_\parallel = (\mathbf{r}(t) - \mathbf{r}_0) \cdot \hat{\mathbf{E}}$ that an electron (initially at position $\mathbf{r}_0$ and energy ε_0) travels opposite to the electric field to a posterior time t at a position $\mathbf{r}(t)$ and energy $\varepsilon(t)$.

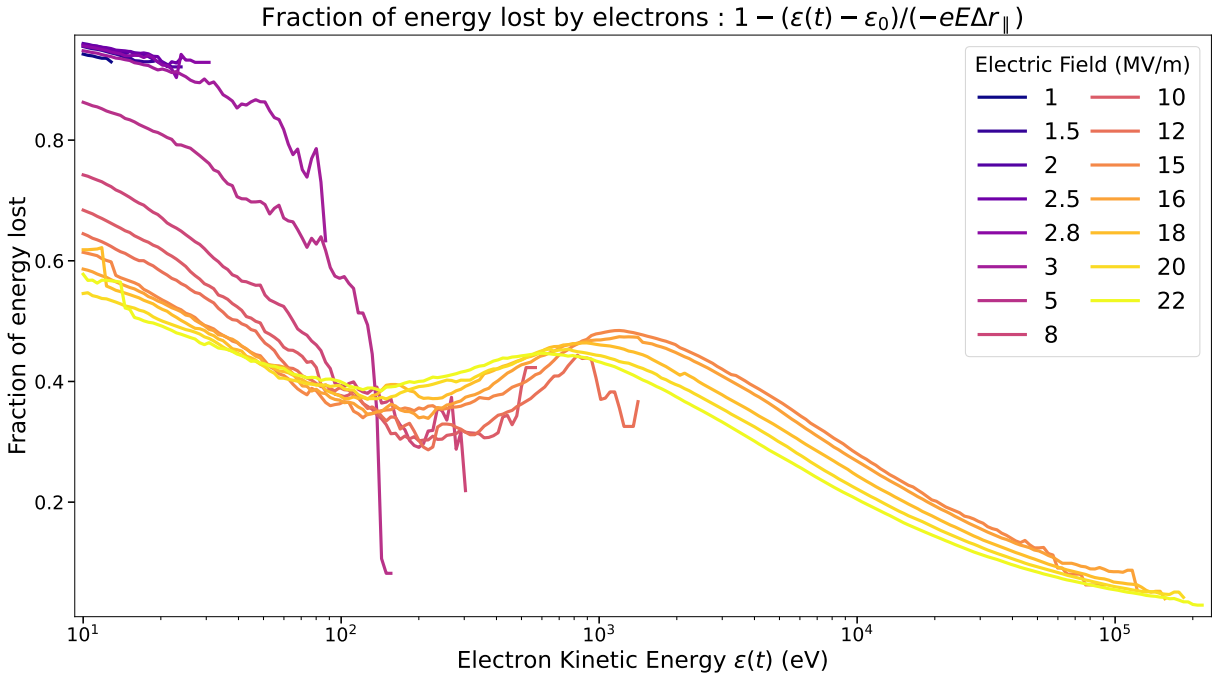

Figure 6.4: Fraction of energy lost by electrons to the gas compared to the total energy they received from their displacement in the electric field. The strange undulation is due to the presence of electrons generated at supra-thermal initial energies ε_0, which subsequently lose this starting energy and never recover $\varepsilon(t) < \varepsilon_0$. At higher energies, most electrons have accelerated from low energies which is why their loss fraction is comparatively lower.

Then, the fraction ξ_ε of energy lost by the electron in inelastic collisions can be deduced from:

$$\xi_\varepsilon \equiv 1 - \frac{\varepsilon(t) - \varepsilon_0}{-eE\Delta r_\parallel} \,. \tag{6.1}$$

This loss ratio, shown in figure 6.4, does not seem to be a straightforward monotonic function neither of the electric field nor of the actual energy $\varepsilon(t)$. This can be explained as follows: at higher electric fields, some electrons may be generated from impact ionisation at high initial energies $\varepsilon_0 > 20\,\mathrm{eV}$. These electrons can subsequently drift in the electric field but lose energy in inelastic collisions such that their current energy $\varepsilon(t) < \varepsilon_0$. This will cause the "loss fraction" $1-(\varepsilon(t)-\varepsilon_0)/(-eE\Delta r_\parallel)$ to be larger than 1. This means that electrons produced by secondary ionisation at supra-thermal energies lose more energy than they started with.

The fact that electrons become more and more accelerated as the electric field increases can be observed as a significant decrease in the proportion of energy lost by electrons between 10–100 eV. The presence of a maximum in the curves around ~ 1 keV, which shifts toward lower energies as the electric field increases, is another manifestation of the presence of thermal runaway. This maximum appears at fields above 12 MV/m.

Conversely, from the average energy loss ratio ξ_ε, one can reverse (6.1) to derive $\Delta r_\parallel \propto 1/E$. From figure 6.5, one can see that this relation is more or less applicable, with a certain scatter determined by the spread in ε_0.

We may thus remember, as a general rule, that if we want to produce $\gtrsim$ keV electrons in air from thermal runaway, we will need approximately twice the length if these electrons were to be produced in vacuum. That is:

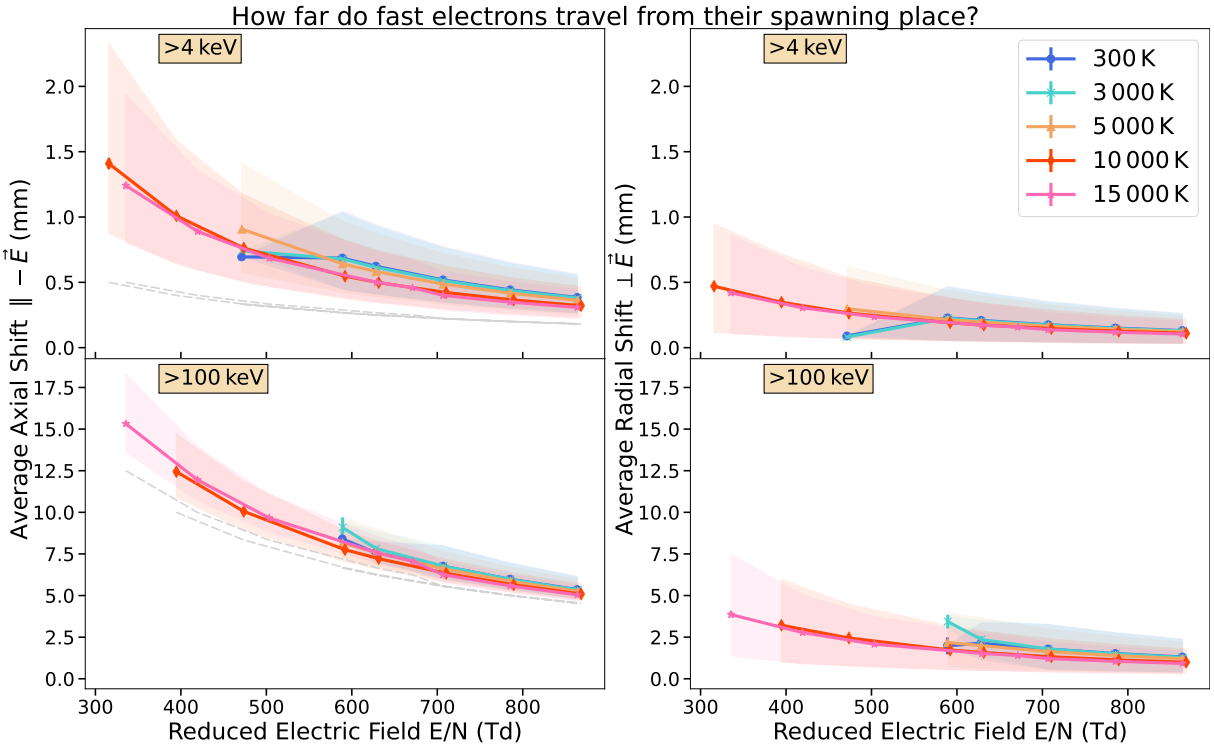

Figure 6.5: Average distance travelled by high-energy electrons anti-parallel (left) and perpendicular (right) to a homogeneous electric field in air at various temperatures. The coloured zones represent the dispersion in distances (minimal to maximal). The dashed grey lines show the distance that would be travelled by an electron accelerated in vacuum starting from 0 eV. The influence of the air temperature is almost insignificant compared to the electric field.

- At 12 MV/m : acceleration over a length of > 0.16 mm,
- At 15 MV/m : acceleration over a length of > 0.13 mm,
- At 20 MV/m : acceleration over a length of > 0.1 mm,
- and so on...

Production : how many?

The answer to the question of how many high-energy electrons may be produced in a discharge is the hardest. There have been many attempts to estimate the thermal runaway flux [39, 161, 532]; all with a sophisticated model of a leader channel and one streamer or a corona. Delay times and distances may be estimated because they constrain the spatio-temporal scales of runaway production by comparison to acceleration in vacuum. However, the runaway production itself relies heavily on the modelling of the electric field on an ionisation wave.

The models of sterile and fertile runaway provide two simple but extreme estimations to the actual production rate on an ionisation wave which depends on:

▷ The seeding of electrons ahead of the wavefront.

▷ The avalanche rate in the inhomogeneous and propagating electric field.

▷ The capability of accelerating while keeping up with the propagation of the wave.

▷ The transversal loss of high-energy electrons who scattered away from the wave.

We think therefore, that the actual runaway production rate from an ionisation wave cannot be simply plugged in from known rates in uniform fields without accounting for spatial-temporal dependence. Rates would have to be calculated from known wave profiles.

In light of the characteristics of electron acceleration in gases under uniform electric fields, we may estimate what requirements must a wave front satisfy to produce and maintain runaway electrons above a threshold $\varepsilon_{\mathrm{th}}$:

- The peak field should reach above 500 Td.
- The condition on the peak field can be significantly relaxed if one considers waves in a preheated channel above 5000 K.
- The average velocity of the thermal runaway acceleration V_{r} may be estimated as follows:
  - $\tau_{\mathrm{r}} = 1/\nu_{\mathrm{r}}$ is the characteristic time for runaway production.
  - $t_0 + \tau_{\mathrm{r}}$ is the average delay for runaway production.
  - $\xi\varepsilon_{\mathrm{th}}/eE$ is a multiple ($\xi > 1$) of the distance travelled by an electron accelerated from 0 eV to $\varepsilon_{\mathrm{th}}$ in vacuum. Over a wide range of energies, the value may be approximated by $\xi \approx 2$ as an estimation of the average axial length $\Delta r_{\parallel}$ required accelerate an electron up to $\varepsilon_{\mathrm{th}}$.
  - $V_{\mathrm{r}}(\varepsilon_{\mathrm{th}}) = \dfrac{\xi\varepsilon_{\mathrm{th}}}{eE(t_0 + \tau_r)}$ is the average propagation speed of the accelerated electrons.
- On the nanosecond timescale of thermal runaway, the propagation speed V_{s} of the ionisation wave can be considered to be steady.
- During the acceleration, the electron is first caught up by the front $V_{\mathrm{r}} < V_{\mathrm{s}}$.
- At a certain energy $\varepsilon_{\mathrm{tr}}$ there should be an equivalence : $V_{\mathrm{r}}(\varepsilon_{\mathrm{tr}}) = V_{\mathrm{s}}$.
- The necessary thickness l_{s} of the region of high electric field above > 500 Td can be estimated from:
$$l_{\mathrm{s}} > \int_0^{t_{\mathrm{tr}}} (V_{\mathrm{s}} - V_{\mathrm{r}}(t))\,\mathrm{d}t\ .$$
- The dependence of V_{r} on $t = t_0 + \tau_{\mathrm{r}}$ is determined by:
$$V_{\mathrm{r}}(t) = \frac{\xi\varepsilon_{\mathrm{th}}}{eEt}\ ,$$
where
  - $\xi(\varepsilon_{\mathrm{th}})$ is a function of $\varepsilon_{\mathrm{th}}$.
  - $\varepsilon_{\mathrm{th}}(t)$ has to be tabulated by reversing the correspondence of $t(\varepsilon_{\mathrm{th}}) = t_0(\varepsilon_{\mathrm{th}}) + \tau_{\mathrm{r}}(\varepsilon_{\mathrm{th}})$.
- Electrons that reach an energy $\varepsilon_{\mathrm{th}}$ such that $V_{\mathrm{r}}(\varepsilon_{\mathrm{th}}) > V_{\mathrm{s}}$ may be considered as thermal runaways which are subsequently capable of surfing on the streamer front.

These estimates could be used as handy guidelines for determining the prior likelihood of generating thermal runaway electrons on a wavefront. They rely on very general parameters (t_0, τ_{r}, ξ) that describe the average bulk acceleration of electrons in uniform fields. These parameters could be tabulated for electric fields down to 500 Td.

We leave this endeavour for the upcoming section of perspectives and move to conclusions.

6.3 Conclusions

In the history of mankind, the study of discharges brought a radical change. It opened a door to high-energy physics through the discovery, in 1895, of X-rays emitted as the bremsstrahlung of electrons accelerated in a vacuum tube under an applied electric field. To radiate X-rays, electrons must be accelerated to very high energies of several hundreds of keV before they eventually collide with atomic nuclei. The possibility of accelerating a very low-energy electron initially at ambient temperature to the relativistic domain, despite the energy lost sporadically in collisions with gas molecules, is known as electron thermal runaway.

When the gas is denser, the collisions are more frequent and therefore the losses as well. The relative importance of the electric force over the collisions with the gas is measured by the reduced electric field E/n_{gas}. Below a critical threshold of E/n_{gas}, electrons lose the ability to accelerate from low to relativistic energies. Nonetheless, since the average energy loss in collisions decreases for electrons at high non-relativistic energies, there is still a possibility to accelerate electrons initially at high energies > keV toward relativistic energies. This is known, by contrast, as relativistic runaway and was proposed in 1925 by Wilson [986] as an acceleration mechanism in intense electric fields extended over large distances inside thunderclouds.

Today, we know that electron thermal runaway does not only occur in laboratory experiments, but exists also on Earth as a natural phenomenon associated to lightning discharges. Lightning propagates by forming bright hot conductive plasma channels known as leaders. Negative leaders are capable of producing bursts of X-rays and intense gamma-ray flashes observed from space.

Emergence of thermal runaway electrons during the leader propagation implies the presence of intense electric fields above the critical runaway threshold. The most plausible occurrence of these fields is at the head of self-sustained ionisation front waves known as streamers. Although the plausibility of thermal runaway at such critical fields has been supported in many sophisticated models of streamers [39, 161, 532], the link between the origin of these streamers and the production of thermal runaway electrons producing bright bursts of X-rays is poorly understood. In particular, the relation, if any, between thermal runaway and the transition of a streamer initially at ambient temperature to a leader core at thousands of Kelvins is unknown.

In order to grasp better the constraints on thermal runaway, we decided to conduct a study at the microscopic level of electron swarms in uniform and homogeneous gases. This enabled us to reduce the number of parameters and broaden our understanding.

At the heart of our research, we developed a code for the study of electron thermal runaway in atmospheric gases named ΘeRMIAA as an acronym for THermal Electron Runaway Monte carlo code from the Instituto de Astrofísica de Andalucía. ΘeRMIAA relies on two indispensable tools:

1. An algorithm enabling to enhance the statistics of high-energy electrons published in [813] and improved in section 3.3.2.

2. A complete and updated set of electron-molecule cross sections from 0 eV to > 100 MeV presented in chapter 15

We summarise below the main points of our findings.

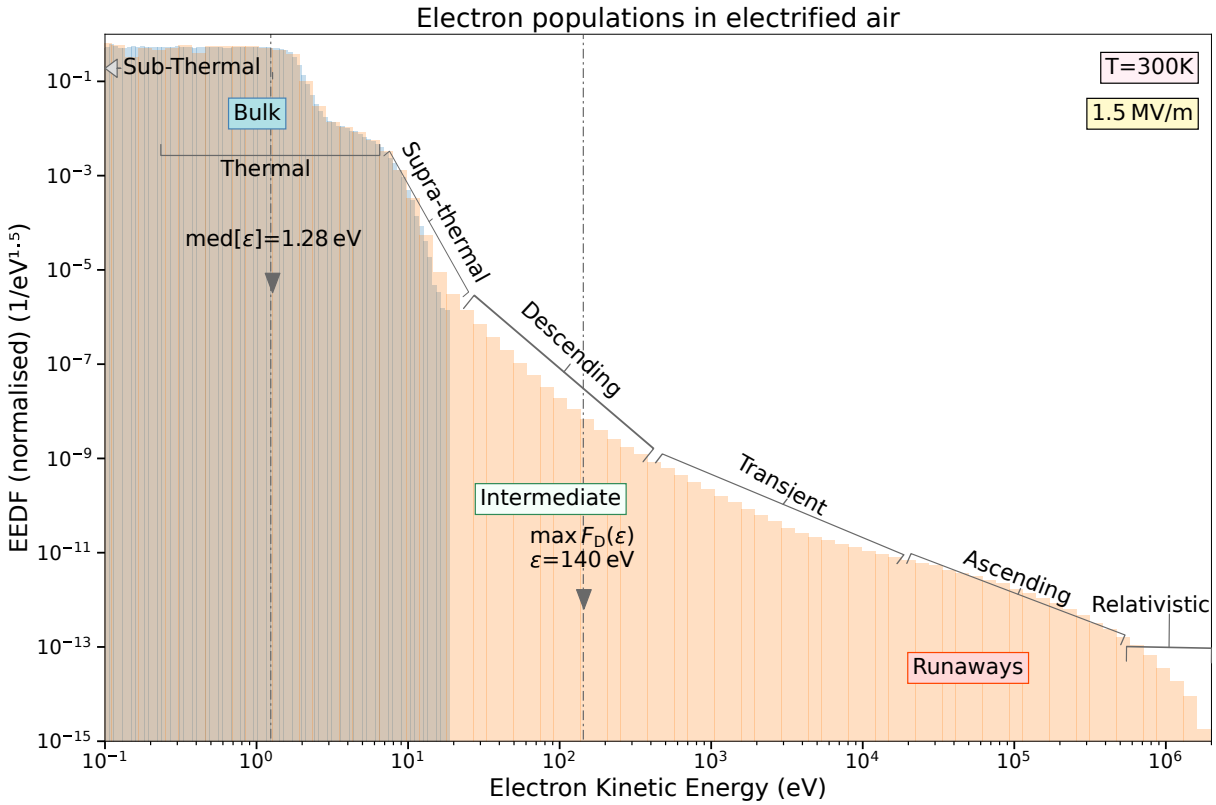

Figure 6.6: Separation of electron populations based on characteristics of the electron energy distribution function, the maximal point of the dynamic friction force $\max F_D(\varepsilon)$ and the electric field.

- Electrons in electrified gases may be categorised into three populations illustrated on figure 6.6:

  A. Bulk : low-energy electrons at a mean energy $\langle\varepsilon\rangle$ which constitute the vast majority $> 99.9\,\%$ of the swarm and determine the transport parameters and reaction rates. Part of the bulk are:

     – sub-thermal electrons which are two standard deviations below the $\langle\varepsilon\rangle$.
     – thermal electrons within two standard deviations of $\langle\varepsilon\rangle$.
     – supra-thermal electrons which govern the avalanche rate and are in the steeply decaying portion of the energy spectrum.

  B. Intermediate : high-energy electrons which cannot subsist in their state and form two subgroups:

     – Descending electrons decay fast toward the bulk because they straddle the maximal energy loss rates in collisions with molecules. They are either seeded by impact ionisation from runaway electrons or decelerated electrons from higher energies.
     – Transient electrons decay slower toward the bulk. A small portion can maintain themselves sufficiently long to be able to accelerate to higher energies and become runaways.

C. Runaways : electrons at high enough energies, above a threshold $\varepsilon_{\triangle/2}$, able to accelerate to the relativistic domain with a significant probability. We distinguish:
   - Ascending electrons are the counter part of descending electrons, they move away toward relativistic energies but cannot surf on ionisation waves.
   - Relativistic electrons are the main producers of runaway avalanches, Bremsstrahlung radiation and are capable of surfing on ionisation waves.

   The definition of the runaway threshold $\varepsilon_{\triangle/2}$ is based on a brisk change in the probability of an electron to accelerate to higher energies.

- What mainly keeps electrons at low-energies ($< 2\,\mathrm{eV}$) in air, is the barrier created by prominent resonant scattering between 2–4 eV with N_2 molecules. This barrier can be (i) overcome by raising the electric field above 300 Td or (ii) lowered by raising the temperature of air (in particular the vibrational temperature of nitrogen).

- Beyond the vibrational barrier of N_2 lies the resonant dissociative attachment to O_2 between 5–9 eV. This creates a depression in the multiplication rate of electrons in fields between 30–100 Td. The mechanism whereby increasing the electric field decreases the growth rate of the swarm is known as the attachment instability. This instability is greatly reinforced by increasing the vibrational temperature of oxygen molecules in air.

- Above 10 eV, the energy spectrum of the swarm has a typical shape for many different gas compositions of a decaying exponential-like slope steeper than a Maxwellian but much milder than the Druyvesteyn distribution ($\propto \exp(-\varepsilon^2)$), with a characteristic energy above the ionisation potential of the gas.

Specific to the production of high-energy electrons through thermal runaway in uniform fields, we found that:

- Thermal runaway to an energy threshold $\varepsilon_{\mathrm{th}}$ can be characterised by three parameters:

  a) The onset delay t_0 is the minimal time required by a thermal electron to accelerate up to $\varepsilon_{\mathrm{th}}$.

  b) The runaway rate $\nu_{\mathrm{r}} = 1/\tau_{\mathrm{r}}$ is the probability per unit time of generating an electron above $\varepsilon_{\mathrm{th}}$ modelled as Poisson process.

  c) The avalanche growth rate ν_{e}.

- In ambient air between fields 120–470 Td, the swarm grows exponentially but the field is not strong enough to produce thermal runaway electrons. This corresponds to the situation when $t_0 \to \infty$ or $t_0\nu_{\mathrm{e}} \ll 1$.

- Around 500 Td (13 MV/m at atmospheric pressure), a transition happens in the high-energy part of the spectrum: an inflexion point appears and a high-energy tail forms with a slope much less steeper than the decaying slope of supra-thermal electrons. We interpret this as the emergence of thermal runaway due to a gradual acceleration of electrons toward higher energies. We propose to call this field E_{tr}, the *threshold* field for thermal runaway. This corresponds to the situation when $t_0 \lesssim 2t_{\varnothing}$ where $t_{\varnothing}$ is the acceleration time in vacuum.

- As the field increases, the ratio $\nu_{\mathrm{r}}/\nu_{\mathrm{e}}$ increases and so does the production of thermal runaway electrons. There must exist a critical field at which $\nu_{\mathrm{r}}/\nu_{\mathrm{e}} = 1$ which we propose to be the formal definition of the *critical* field for thermal runaway E_{cr}.

- The air temperature which includes: (1) the change in gas composition, (2) the population of excited states and (3) thermal expansion; altogether has a significant influence on the production of thermal runaway at temperatures above 5000 K in a model assuming thermal equilibrium. The most significant effects come from (i) the dissociation of molecules into atoms and (ii) the expansion of the gas density which significantly lowers the average friction force of electrons at a constant reduced electric field.

Ionisation fronts. On the one hand, in discharges at atmospheric pressure, thermal runaway always competes with the exponential growth of the swarm. At electric fields where thermal runaway can take place, the screening of the field by the space charge generated by the swarm is always faster than the average production rate of runaway electrons. A steady production of runaway electrons therefore requires a mechanism filtering high energy electrons from the bulk. Such mechanism most probably occurs on ionisation fronts which naturally select electrons at higher energies capable of keeping up with the propagation speed of the front and abandon low-energy electrons behind where the external electric field is screened by the space charge of the front.

On the other hand, since the field in the vicinity ahead of the ionisation front in air is always superior to the break-even field of relativistic runaway, an ionisation front is, in principle, capable of nurturing and maintaining a relativistic runaway avalanche pacing ahead at the same average speed. Additionally, some ionisation fronts are capable of accelerating low-energy electrons seeded ahead of the avalanche and thereby produce a steady output rate of thermal runaway.

Overall, the preliminary study of thermal runaway in uniform electric fields might seem irrelevant, especially since numerical modelling of streamer fronts is well developed nowadays. In this thesis, we strived to demonstrate that, to the contrary, general considerations can be deduced and applied to understand better under which conditions does thermal runaway emerge.

6.4 Perspectives

Our research has led us to construct a good overview, not only of what is known, but also to what we should look for. From the theoretical perspective, there are three paths of investigation specific to Monte Carlo simulations that we propose to follow to help us enlighten further our understanding about electron swarms and runaway in discharges.

1. Swarms

Three-body attachment : Categorisation of electron-molecule interactions into separate processes may mislead us into treating three-body attachment and resonant vibrational excitations to molecular oxygen as if they were unrelated. To the contrary, these are very interrelated and the sum of their cross sections (including resonant elastic collisions) should amount to the vibrational excitation in the limit of zero molecular density. Attachment considerably increases the duration over which an electron is captured by an oxygen molecule. Nevertheless, the lifetime of $O_2^-\ ^2\Pi_g$ (and $NO^-\ ^3\Sigma^-$) compounds are very significant compared to the mean free time of thermal electrons in gases. Since, three-body attachment dominates transport in O_2 at low electric fields [235, §3.3], we expect that the effect of low-energy resonant collisions on electron transport should be significant (fig. 16.10).

Implementing a delay due to the lifetime τ_- of resonant compounds in Monte Carlo simulations should be an easy task and therefore is our first suggestion.

Transport and reaction : Fluid models for macroscopic discharges rely on tabulated or empirically fitted transport and reaction coefficients of electron swarms in determined conditions of the reduced electric field and gas composition.

With the newly presented set of cross section, it would be desirable to release an updated set of transport and reaction coefficients to improve the accuracy of fluid models, in particular in regions of intense electric fields. Most interesting would be to characterise transport for a large variety of gas compositions and temperatures which are in demand in the community investigating discharges in weakly ionised plasmas.

Coulomb interaction : the particle-in-cell (PIC) method enables to model self-consistently the electrostatic influence of space charges on electrons in Monte Carlo simulations. Similarly, one could attempt to model the electron interaction with ions and other electrons at the microscopic level by making use of the Coulomb logarithm 2.105 for momentum-transfer cross sections.

Long-range collisions affect especially electron transport at high energies and thus are important for the modelling of thermal runaway.

Excited states : the interaction of electrons with excited molecular states is very different from the ground state. When a large proportion of excited vibrational states exist, the barrier in the $N_2^-\ ^2\Pi_g$ is lowered and electron transport is significantly affected. Similarly, metastable states of electronic excitations may accumulate in discharges. The interaction with metastable states does not only enable superelastic collisions but also lowers significantly the ionisation potential of the molecule. Electron transport in gases with metastable excited states is poorly known and needs to be investigated.

2. Super-electron management

Bulk-Runaway separation : The compaction algorithm we devised to enhance high-energy electron statistics is useful to study thermal runaway but is not infallible. When the thermal runaway rate ν_r is nil or vanishingly small compared to the swarm bulk avalanche rate ν_e, the statistical weights of high-energy electrons drop below the resolution limit w_min, upon which they are discarded from the simulation (fig. 5.28).

If one wishes to preserve the representation of runaways independently of the bulk's growth, then there should be a separation between the treatment of bulk and runaway super-electrons with a facilitated transfer between both groups.

Spatial dependence : Our compaction algorithm is currently not suited for thermal runaway on ionisation fronts because it filters super-electrons only based on their energy and not on their position $\mathbf{r}$. The idea of filtering super-electrons was to enhance the statistics of super-electrons which are most likely to become thermal runaways. In homogeneous electric fields, there is no need to consider spatial dependence. On ionisation fronts, however, electrons ahead of the front have a much greater likelihood of becoming runaways than those behind.

Successful investigation of thermal runaway in inhomogeneous electric fields will require to filter electrons based on an abstract quantity $\mathcal{P}_\mathrm{r}$ which measures an electron's thermal runaway likelihood relying on criteria such as:

- The energy ε of the electron,
- The direction $\cos\chi$ with respect to the electric field,
- The value of the electric field $E(\mathbf{r})$ at the electron's position,

- The temporal derivative of the electric field $\mathrm{d}E/\mathrm{d}t$ at the electron's position (negative derivative means the electron is already behind the front).
- The state of the gas (temperature, composition, density) at the electron's position if gaseous inhomogeneities are modelled.

Failure to properly model super-electrons where they are relevant for thermal runaway can severely belie runaway statistics in inhomogeneous conditions (fig. 5.30b).

3. Thermal runaway

Longer timescales : There exist nowadays very accurate models of non-equilibrium plasma kinetics in discharges [148, 852]. These may efficiently track the evolution of chemical and excited species on longer durations > µs, where the state of the gas may evolve considerably. It would be desirable to model gas heating by the discharges and track the evolution of excited species, especially vibrational thermalisation. From there, it would be very interesting to plug-in Monte Carlo codes on top of these kinetic models and observe how the high-energy tail becomes affected as the discharge develops and the state of the gas changes.

Statistics on fronts : this thesis performed statistical studies on high-energy and accelerated electrons in uniform electric fields. By now, many accurate fluid models of streamers exist [38, 161, 171, 531, 579, 621]. To start determining what characteristics of the streamer front (radius, velocity, peak field, thickness) promote generation of high-energy electrons, it would be desirable to determine:

- Surfing thresholds: which electrons can surf ahead of the wave and what determines this threshold?
- Thermal runaway thresholds: which streamer profiles produce thermal runaway electrons?
- Runaway rates: how different are the runaway rates on a front from sterile runaway in homogeneous fields?
- Stratification: how does the average energy spectrum evolve according to the position ahead of the front ?
- Self-consistency: (how) do high-energy electrons surfing ahead of streamer fronts affect their propagation?

Continuous runaway Dart leaders propagating in the former channel heated up by a return stroke are known to be continuous sources of X-rays. Using the information we know about the air temperature and composition in hot channels of return strokes, we could also study the continuous production of thermal runaway electrons in hot air.

There are endless scenarios that one could set up to study the phenomenon of thermal runaway, from upward negative leaders to supershort avalanches in ns-pulsed laboratory discharges. The objective is not to list them all, but to have the necessary tools ready for use when a new idea sparks up.

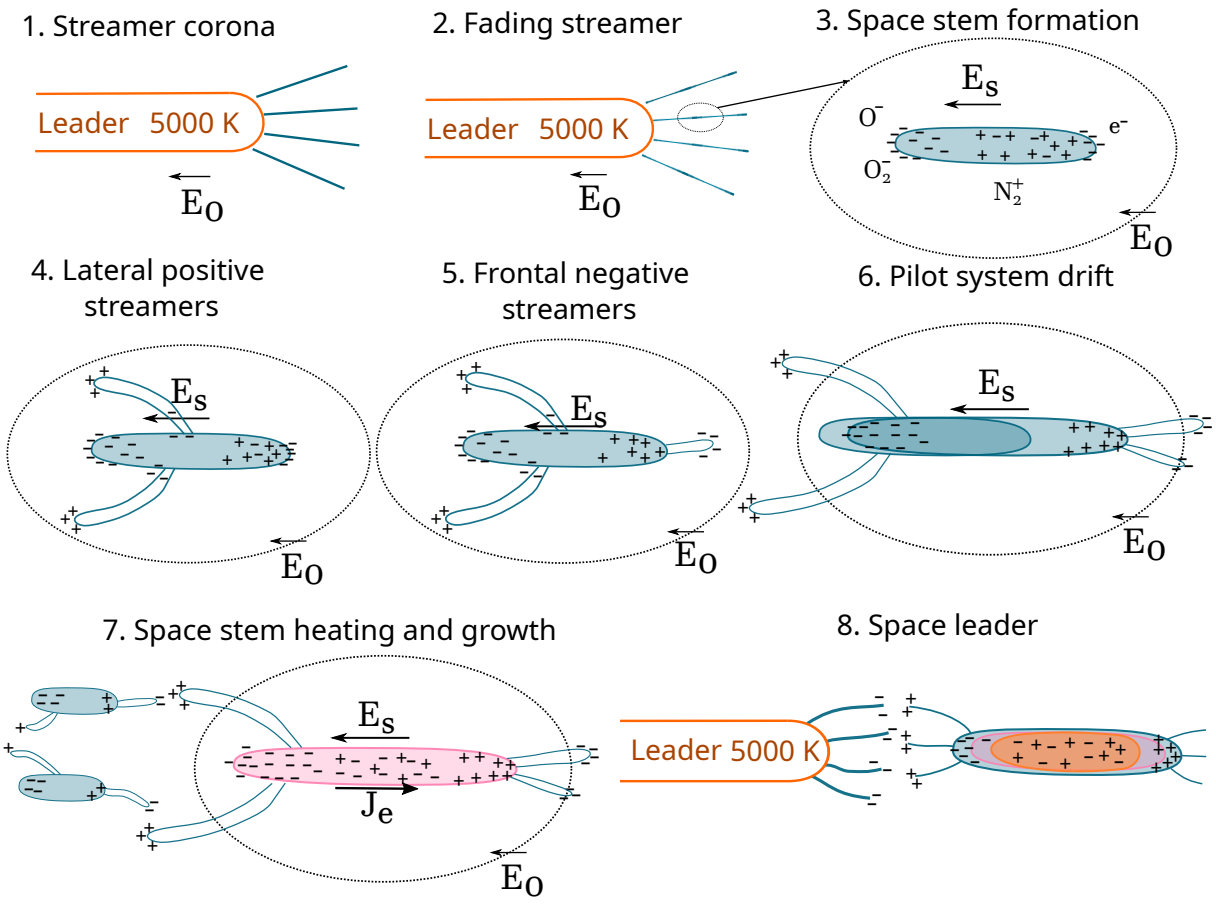

Figure 6.7: Hypothetical scenario of the development of a negative leader step through the emergence of a space leader in the corona streamer zone. The subsequent production of thermal runaway electrons after formation of the space leader is hypothesised under three different scenarios.

6.4.1 A hypothetical scenario

In this last subsection, from the knowledge we gleaned so far and the intuition we slowly nourished, we propose a new hypothetical scenario that would explain the X-ray bursts correlated to leader stepping in lightning and laboratory sparks.

We rewind to page 19 where we summarised the cycle of the stepping mechanism of a negative leader. From there, and experimental results on the study of leader steps, we reconstruct a plausible scenario behind the emergence of the space leader in the following steps schematised on figure 6.7:

1. Streamer corona: The streamers in the corona of a leader propagate outward in the enhanced electric field region at the tip of the leader.

2. Fading streamer: The electric field in the wake of a streamer wanes below conventional breakdown and the propagation of electrons in the streamer channel is hampered. Zones of lower conductivity are formed and the space charge distributes unevenly in the old channel.

3. Space stem: At the boundaries of the regions of lower conductivity the current decreases and a space charge starts to accumulate.

- (−) Closest to the leader tip (inner edge), an anionic space charge is formed due to important attachment to oxygen molecules.
- (+) Farther from the leader tip (outer edge), the electron density depletes slowly as they drift, leaving behind a space charge of positive ions.

In the region of lower conductivity between the two anionic and cationic space charges, the background electric field is enhanced $E_0 < E_s$. This enhancement provokes a rise in the attachment rate due to the attachment instability in air between 40–80 Td. This region of separated space charges, reinforced by instability, is what constitutes the space stem [621] which is thought to correspond to the glowing spots in laboratory experiments in the wake of negative streamers [520].

4. Lateral positive streamers: from the lateral sides at the positive outer edge of the space stem, avoiding the negative space charge on the inner edge, positive streamers emerge from the enhancement of the background electric field.

5. Frontal negative streamers: the lateral positive streamers transported away part of the positive space charge that was on the outer edge of the stem. This imbalance raises the electric field at the concentration of electrons that had left the space stem and liberated a positive space charge. On that side opposite to the leader tip, a negative streamer starts and continues in the preionised channel left behind by the original streamer (which had emerged from the leader).

6. Pilot system: the ensemble of space stem, lateral positive streamers and straight negative streamers form a pilot system of counter-propagating streamers. The region of enhanced field delineating the space stem is displaced due to the transportation of space charge carried by streamers. This causes the pilot system to slowly drift away from the main leader channel [340] (and maybe to lengthen).

7. Heating: multiple pilot systems connect into each other and feed current into their space stems which subsequently heat up. The rise of the temperature facilitates furthermore the deposition of both negative and positive ions due to the lowered threshold to dissociative attachment of O_2. The instability grows because the process retroacts on itself.

8. Space leader: when the space stem reaches a critical temperature, electrons trapped on oxygen atoms on the inner edge of the space stem are released and further accelerate the detachment process. This sudden release of electrons boost the conductivity of the space stem which has become a space leader. The polarity at the boundaries of the space leader reverses [36, fig. 1] because the increase of conductivity screens the formerly enhanced electric field in the space stem. There are now two regions of enhanced electric field beyond the boundaries of the space leader where the temperature and electron density decrease abruptly and so the conductivity.

There is a missing spot for the sudden emergence of thermal runaway and the resulting X-ray burst. We support the idea that thermal runaway occurs as a surfing mechanism on an ionisation wave. However, we do not know where the ionisation wave originates and toward where it propagates. We may imagine three different scenarios:

A. Preionisation: when the streamer coronas of the main and space leader connect, a surge of current arises as the potential of the main leader is transferred toward the tip of the space leader. When the current surge reaches the (outer) tip of the space leader, it flushes

into preionised channels of higher conductivity left by the negative space-leader corona. As proposed by Babich *et al.* [39], ionisation waves which subsequently propagate in the preionised channel of a previous streamer have a more concentrated electron density at the tip and therefore a high peak field. These ionisation waves may steadily produce thermal runaway electrons.

B. Warm runaway: the ionisation wave emerges where the electric field is maximal, at the place of encounter of oppositely charged streamer coronas. The electrons of the negative corona propagate into preionised channels of the positive corona. When the ionisation wave reaches toward the space leader, there is sudden surge of current due to the important detachment of the oxygen anions located at the cold edge just outside the space leader. The electric field peaks and some electrons are accelerated into the runaway regime due to the decreased friction force of the gas in the hot channel.

C. Surge and accumulation: the ionisation waves, wherever they emerge, if they emerge do not have the conditions fostering thermal runaway. The intense current communicating between the main and the space leaders heat the gap in the middle extremely fast $< \mu s$. The charge accumulated in the main leader and the streamer zone is transferred to the space leader, as so the potential. At the outer edge of the space leader, there is a sudden drop of conductivity. Due to the surge of current coming from the main leader and its streamer zone, there is a sudden accumulation of negative space charge at the edge of the space leader. The accumulation is intense enough so that the critical field for thermal runaway is breached. A significant number of electrons make it in the runaway regime and keep accelerating in the field of the leader which is not yet screened by a streamer corona. Finally, a new bright streamer corona burst coincides with an X-ray burst from thermal runaway electrons.

There are and have been many propositions to the origin of thermal runaway related to leader stepping. From our study, we think that thermal runaway is closely related to the formation of a space leader and the significant inhomogeneities of the gas temperature and plasma conductivity. However, our current understanding of ionisation waves and their relation to the space leader is too poor to support a particular mechanism of generation of thermal runaway electrons.

The beauty of it all is that it is not until the plasma community is able to join forces and the efforts of many research teams into the construction of a comprehensive model, that the intricacy behind leader stepping, streamer coronas, heating of space stems, development of space leaders, ionisation waves in hot air and thermal electron runaway; that this intricacy will be unveiled.

And hopefully,

that the credits

to these joint efforts

will bear the name

of a collaboration...

Appendix A

Collision Kinematics

In a fixed reference frame, two particles of masses m_1 and m_2 collide with velocities $\mathbf{v}_1$ and $\mathbf{v}_2$ as schematised on the top panel of figure A.1. General kinematic relations can be found in any textbook treating with particle scattering such as Berestetskii *et al.* [58, §66]. Here we are specifically interested in binding the outgoing $(\mathcal{E}_i^+,\mathbf{p}_i^+)$ to the incoming $(\mathcal{E}_i^-,\mathbf{p}_i^-)$ energy-momentum vectors of the particles $i = 1, 2$, as it was done by Blaton [84].

The collision system obeys the conservation laws of the total momentum $\mathbf{\Pi}$ and energy $\mathcal{E}$:

$$\mathbf{\Pi} = \mathbf{p}_1^{\pm} + \mathbf{p}_2^{\pm} = (m_1\gamma_1\mathbf{v}_1)^{\pm} + (m_2\gamma_2\mathbf{v}_2)^{\pm} \tag{A.1}$$

$$\mathcal{E} = \mathcal{E}_1^{\pm} + \mathcal{E}_2^{\pm} = (m_1c^2\gamma_1)^{\pm} + (m_2c^2\gamma_2)^{\pm} \tag{A.2}$$

$$= (m_1c^2\sqrt{1 + (p_1/m_1c)^2})^{\pm} + (m_2c^2\sqrt{1 + (p_2/m_2c)^2})^{\pm} \tag{A.3}$$

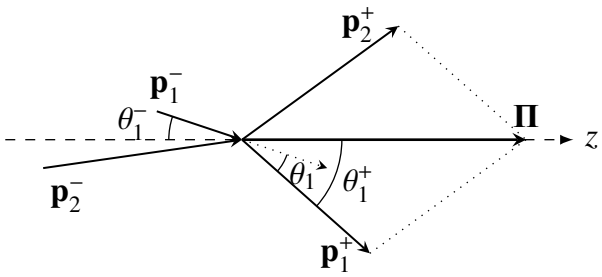

(a) Fixed reference frame

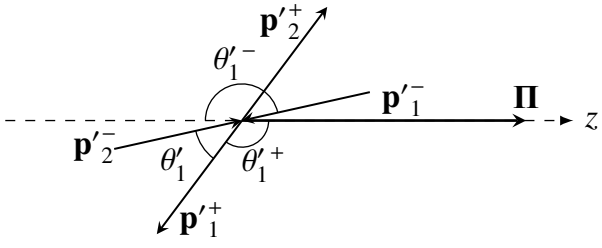

(b) Center of mass relative frame

Figure A.1: Binary collision kinematics

Elastic collisions conserve the particle rest masses $m_i^+ = m_i^-$, whereas in inelastic collisions, the internal excitation energy $\Delta\mathcal{E}_i$ of (one or both) of the particles can be assimilated to a change of its rest mass:

$$m_i^+c^2 - m_i^-c^2 = \Delta\mathcal{E}_i \,.$$

The problem of relating $\mathbf{p}_i^+$ to $\mathbf{p}_i^-$ through their angles of scattering $\theta_i^{\pm}$, is most easily solved in the system's centre of mass frame where both particles are observed to collide frontally with equally opposite relative momenta $\mathbf{p'}_1 = -\mathbf{p'}_2$ as seen on the bottom panel of figure A.1.

In the fixed frame, the centre of mass cruises at a steady velocity $\boldsymbol{\mathcal{V}}$ determined by the total energy and momentum [84, eq. 1.6]:

$$\boldsymbol{\mathcal{V}} = \frac{c^2\mathbf{\Pi}}{\mathcal{E}} \tag{A.4}$$

$$\Gamma = 1/\sqrt{1 - (\mathcal{V}/c)^2} \tag{A.5}$$

A Lorentz transformation from the fixed frame to the one cruising at $\boldsymbol{\mathcal{V}}$ gives the relative energies $\mathcal{E}'_i$ and momenta $\mathbf{p}'_i$:

$$\mathcal{E}'_i = \Gamma(\boldsymbol{\mathcal{E}}_i - \mathbf{p}_i \cdot \boldsymbol{\mathcal{V}}) \tag{A.6}$$

$$\mathbf{p}'_i = \mathbf{p}_i + (\Gamma - 1)\frac{\boldsymbol{\mathcal{V}} \cdot \mathbf{p}_i}{\mathcal{V}^2}\boldsymbol{\mathcal{V}} - \Gamma\frac{\boldsymbol{\mathcal{V}}}{c^2}\mathcal{E}_i \tag{A.7}$$

The rest energy of the cruising system can be defined as $\mathcal{E}'_0 = \sqrt{\mathcal{E}^2 - (c\Pi)^2}$. With this energy, the norm of the relative momentum p' can be calculated as the sum of total energies in the centre of mass frame:

$$\mathcal{E}'_0 = \mathcal{E}'^{\pm}_1 + \mathcal{E}'^{\pm}_2 = \sqrt{(m_1^{\pm}c^2)^2 + (cp'^{\pm})^2} + \sqrt{(m_2^{\pm}c^2)^2 + (cp'^{\pm})^2} \tag{A.8}$$

$$\Leftrightarrow p'^{\pm} = \frac{\sqrt{((\mathcal{E}'_0/c)^2 - (m_1^{\pm} + m_2^{\pm})^2c^2)((\mathcal{E}'_0/c)^2 - (m_1^{\pm} - m_2^{\pm})^2c^2)}}{2\mathcal{E}'_0/c} \tag{A.9}$$

Differential scattering cross sections are usually measured in the laboratory frame whereas theoretical calculations often take the centre of mass frame and then convert to the fixed frame. With the inverse Lorentz transformation, one can establish geometrical relations by projecting $\mathbf{p}$ and $\mathbf{p}'$ on $\boldsymbol{\mathcal{V}}$, introducing the angles $\theta_i^{\pm}$ and $\theta_i'^{\pm}$ as seen on figure A.1 :

$$\mathcal{E}_i^{\pm} = \Gamma(\boldsymbol{\mathcal{E}}'^{\pm}_i + \boldsymbol{\mathcal{V}} \cdot \mathbf{p}'^{\pm}_i) \tag{A.10}$$

$$(p\cos\theta)_i^{\pm} = \Gamma(p'^{\pm}\cos\theta_i'^{\pm} + \mathcal{E}'^{\pm}_i\frac{\mathcal{V}}{c^2}) \tag{A.11}$$

$$p_i^{\pm}\sin\theta_i^{\pm} = p'^{\pm}\sin\theta_i'^{\pm} \tag{A.12}$$

Combining (A.11) and (A.12), one finds angular relations between both frames:

$$\tan\theta_i^{\pm} = \frac{1}{\Gamma}\frac{\sin\theta_i'^{\pm}}{\cos\theta_i'^{\pm} + \mathcal{V}\mathcal{E}'^{\pm}_i/c^2p_i'^{\pm}} \tag{A.13}$$

$$\cos\theta_i'^{\pm} = \frac{(\mathcal{E}'^{\pm}_i/cp'^{\pm})}{1 - (\frac{\mathcal{V}}{c}\cos\theta_i^{\pm})^2}\left(\frac{-\mathcal{V}}{c}\sin^2\theta_i^{\pm} \pm \frac{\cos\theta_i^{\pm}}{\Gamma^2}\sqrt{1 - (1 - (\frac{\mathcal{V}}{c}\cos\theta_i^{\pm})^2)\frac{(m_i^{\pm}c^2\Gamma)^2}{(\mathcal{E}'^{\pm}_i)^2}}\right) \tag{A.14}$$

The outgoing energy-momenta can be determined [84, eq. 2.5] by combining the angular relations with (A.11):

$$\mathcal{E}_i^{+} = \frac{\mathcal{E}'^{+}_i/\Gamma}{1 - (\frac{\mathcal{V}}{c}\cos\theta_i^{+})^2}\left(1 + \frac{\mathcal{V}}{c}\cos\theta_i^{+}\sqrt{1 - (1 - (\frac{\mathcal{V}}{c}\cos\theta_i^{+})^2)\frac{(m_i^{+}c^2\Gamma)^2}{(\mathcal{E}'^{+}_i)^2}}\right) \tag{A.15}$$

$$p_i^{+} = \frac{\mathcal{E}'^{+}_i/\Gamma c}{1 - (\frac{\mathcal{V}}{c}\cos\theta_i^{+})^2}\left(\frac{\mathcal{V}}{c}\cos\theta_i^{+} + \sqrt{1 - (1 - (\frac{\mathcal{V}}{c}\cos\theta_i^{+})^2)\frac{(m_i^{+}c^2\Gamma)^2}{(\mathcal{E}'^{+}_i)^2}}\right) \tag{A.16}$$

The energy in the relative frame $\mathcal{E}'^{+}_i$ can be determined by:

$$\text{Elastic} \rightarrow \boldsymbol{\mathcal{E}}'^{+}_i = \boldsymbol{\mathcal{E}}'^{-}_i = \Gamma(\boldsymbol{\mathcal{E}}_i^{-} - \boldsymbol{\mathcal{V}} \cdot \mathbf{p}_-) \tag{A.17}$$

$$\text{Inelastic} \rightarrow \mathcal{E}'^{+}_i = \sqrt{(m_i^{+}c^2)^2 + (cp'^{+}_i)^2} \neq \mathcal{E}'^{-}_i \tag{A.18}$$

The relative momentum after the inelastic collision must be calculated with (A.9) where the rest masses $m_i^{+}c^2$ accordingly comprise the excitation energies $\Delta\mathcal{E}_i$ of the inelastic process.

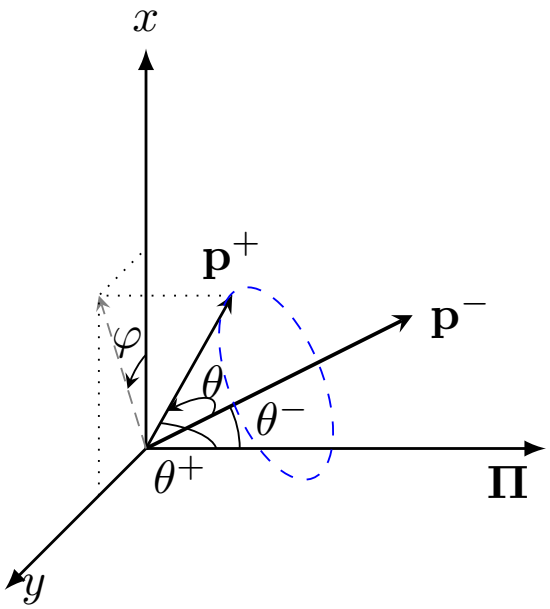

Figure A.2: Azimuthal angle φ determining the rotation of the scattering plane ($\mathbf{p}^+$, $\mathbf{\Pi}$) from the original plane ($\mathbf{p}^-$, $\mathbf{\Pi}$) around the total momentum $\mathbf{\Pi}$. The possible values of the scattering angle θ forms a cone (blue dashes - - -) of different directions $\mathbf{p}^+$ around the initial momentum $\mathbf{p}^-$.

Finally, the angle that we are most interested in is the angle of deviation between the original and scattered directions $\cos\theta_i = \hat{\mathbf{p}}_i^- \cdot \hat{\mathbf{p}}_i^+$. Considering the axial symmetry of the collisional system around $\mathbf{\Pi}$, θ_i can be defined with the help of the uniformly distributed azimuthal angle φ which determines the rotation of the scattering plane ($\mathbf{p}^+$, $\mathbf{\Pi}$) with respect to the original plane ($\mathbf{p}^-$, $\mathbf{\Pi}$) as represented on figure A.2:

$$\cos\theta_i = \cos\theta_i^+ \cos\theta_i^- + \sin\theta_i^+ \sin\theta_i^- \cos\varphi \tag{A.19}$$

$$\cos\theta_i^+ = \frac{\cos\theta_i^- \cos\theta_i \pm \sin\theta_i^- \sin\varphi \sqrt{\sin^2\theta_i - \sin^2\theta_i^- \sin^2\varphi}}{\cos^2\theta_i^- + \sin^2\theta_i^- \cos^2\varphi} \tag{A.20}$$

The volume spanned by the three angles θ, θ^+ and θ^- as φ varies can be seen on fig. A.3. This angular correspondence has two distinct and one special cases :

- When $\sin\theta_i < \sin\theta_i^-$, two independent solutions exist for each φ. They correspond to the wider and narrower angles θ_i^+ seen on figure A.2. In that case, φ must be restricted to :

$$\sin\varphi < \frac{\sin\theta_i}{\sin\theta_i^-} < 1 \tag{A.21}$$

- If $\sin\theta_i > \sin\theta_i^-$, φ covers the whole perimeter and since $\cos\varphi = \cos -\varphi$, the two branches ($\varphi \gtrless 0$) actually mirror each other so that for $\varphi \in [0, \pi]$, only one branch (whichever) can be retained. Taking the negative branch ($\theta < 0$) will systematically match the wider angle at $\varphi = 0$.

- The special case of $\sin\theta_i^- = \sin\theta_i$ gives way to :

$$\cos\theta_i^+ = \frac{\cos\theta_i \cos\theta_i^- \pm \sin^2\theta_i \cos^2\varphi}{\cos^2\theta_i + \sin^2\theta_i \cos^2\varphi} \tag{A.22}$$

where one branch degenerates into a single value at ± 1 for $\theta_i = \theta_i^-$ and $\theta_i = \pi - \theta_i^-$ respectively.

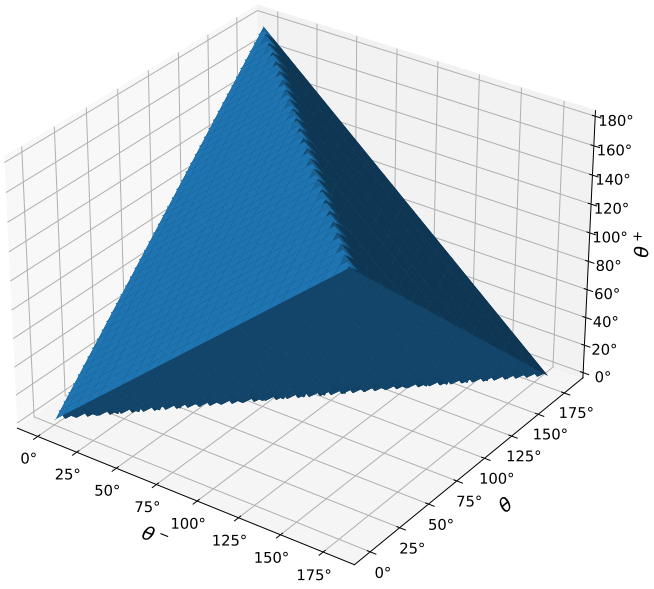

Figure A.3: Correspondence between angles θ^-, θ^+ and θ

As a closure note, binary collisions are a generic framework for collisions involving an arbitrary number of particles. One can always formally group the energy-momentum vectors of several particles together to form a system with a particular rest mass $\mathcal{M}_0$ obeying:

$$\mathcal{M}_0 c^2 = \sqrt{(\sum_i \mathcal{E}_i)^2 - c^2(\sum_i \mathbf{p}_i)^2} \tag{A.23}$$

If one particle can be isolated and have its outgoing direction fixed, then the recoil energy given to the system can be determined as well.

A.1 Ternary Outcome

In the particular case of interest when a binary collision results in the emission of three particles such as electron-nuclei bremsstrahlung or impact ionisation, one can adapt the results above to a ternary outcome. The conservation laws of energy and momentum now include the third body $(\mathcal{E}_3^+, \mathbf{p}_3^+)$ which is supposed to be known beforehand. Since this body 3 was part of body 2 before the collision, the quantity $\mathbf{p}_2^-$ embodies the momentum carried when they formed a whole.

$$\mathcal{E} = \mathcal{E}_1^- + \mathcal{E}_2^- = \mathcal{E}_1^+ + \mathcal{E}_2^+ + \mathcal{E}_3^+ \tag{A.24}$$

$$\mathbf{\Pi} = \mathbf{p}_1^- + \mathbf{p}_2^- = \mathbf{p}_1^+ + \mathbf{p}_2^+ + \mathbf{p}_3^+ \tag{A.25}$$

The kinematic connection before and after the collision is again made through the energy-momentum expressed in the centre of mass rest frame $\mathcal{E}_0'$:

$$\mathcal{E}_0' = \mathcal{E}_1'^- + \mathcal{E}_2'^- = \mathcal{E}_1'^+ + \mathcal{E}_2'^+ + \mathcal{E}_3'^+ \tag{A.26}$$

$$\mathbf{p}_1'^- + \mathbf{p}_2'^- = 0 = \mathbf{p}_1'^+ + \mathbf{p}_2'^+ + \mathbf{p}_3'^+ \tag{A.27}$$

Just as in (A.8), the 4-vector invariant of the second particle can be used to replace the expression for $p_2^{'+}$ in (A.26) by introducing the angle $\theta'_{13} \equiv \measuredangle(\mathbf{p}_1^{'+}, \mathbf{p}_3^{'+})$ formed between particle 1 and 3 directions in the centre of mass frame.

$$(p_2'^+)^2 = (p_1'^+)^2 + (p_3'^+)^2 + 2\cos\theta'_{13} p_1'^+ p_3'^+ \tag{A.28}$$

To temporarily alleviate the heavy notation, all quantities are expressed in the relativistic unit system $c \equiv 1$ and the $^+$ exponent is implicit. We denote the energy shared between particles 1 and 2 as $\mathcal{E}'_{12} \equiv \mathcal{E}'_0 - \mathcal{E}'_3$. Then we obtain a second degree equation in $p_1^{'+}$:

$$\begin{aligned}
&\Rightarrow \mathcal{E}'_{12} \equiv (\mathcal{E}'_0 - \mathcal{E}'_3) = \sqrt{m_1^2 + p_1^2} + \sqrt{m_2^2 + p_2^2} \\
&\Leftrightarrow \left[(\mathcal{E}'_{12})^2 - (m_1^2 + p_1'^2 + m_2^2 + p_2'^2)\right]^2 = 4(m_1^2 + p_1'^2)(m_2^2 + p_2^2) \\
&\Leftrightarrow (\mathcal{E}'_{12})^2\left[(\mathcal{E}'_{12})^2 - 2(m_1^2 + p_1'^2 + m_2^2 + p_2'^2)\right] + (m_2^2 - m_1^2 + \underbrace{p_2'^2 - p_1'^2}_{=p_3'^2 + 2\cos\theta'_{13} p'_1 p'_3})^2 = 0 \\
&\Leftrightarrow \frac{1}{2}(\mathcal{E}'_{12})^2\left[(\mathcal{E}'_{12})^2 - 2(m_1^2 + p_1'^2 + m_2^2 + p_2'^2)\right] + (m_2^2 - m_1^2 + p_3'^2)^2 \\
&\quad - 2p'_1 p'_3 \cos\theta'_{13}\left[(\mathcal{E}'_{12})^2 - (m_2^2 - m_1^2 + p_3'^2)^2\right] + 2p_1'^2(p_3'^2\cos^2\theta'_{13} - (\mathcal{E}'_{12})^2) = 0
\end{aligned}$$

We can regroup m_2 and p'_3 into an effective mass $m_{23} \equiv \sqrt{m_2^2 + p_3'^2}$. Finally, we can extract the relative momentum of the first particle $p_1^{'+}$ after collision :

$$\begin{aligned}
p_1^{'+} = \Big[&\mathcal{E}'_{12}\sqrt{(2p'_3 m_1\cos\theta'_{13})^2 + ((\mathcal{E}'_{12})^2 - (m_{23} + m_1)^2)((\mathcal{E}'_{12})^2 - (m_{23} - m_1)^2)} \\
&- p'_3\cos\theta'_{13}((\mathcal{E}'_{12})^2 - (m_{23}^2 - m_1^2))\Big]\frac{1/2}{(\mathcal{E}'_{12})^2 - (p'_3\cos\theta'_{13})^2}
\end{aligned} \tag{A.29}$$

or with the full notation restored :

$$\begin{aligned}
p_1^{'+} = \Bigg\{&(\mathcal{E}'_0 - \mathcal{E}_3^{'+})\Big[(2p_3^{'+} m_1^+\cos\theta'_{13})^2 \\
&+ \left((\mathcal{E}'_0 - \mathcal{E}_3^{'+})^2 - (\sqrt{(m_2^+)^2 + (p_3^{'+})^2} + m_1^+)^2\right)\left((\mathcal{E}'_0 - \mathcal{E}_3^{'+})^2 - (\sqrt{(m_2^+)^2 + (p_3^{'+})^2} - m_1^+)^2\right)\Big]^{1/2} \\
&- p_3^{'+}\cos\theta'_{13}\left((\mathcal{E}'_0 - \mathcal{E}_3^{'+})^2 - ((m_2^+)^2 + (p_3^{'+})^2 - (m_1^+)^2)\right)\Bigg\}\frac{1/2}{(\mathcal{E}'_0 - \mathcal{E}_3^{'+})^2 - (p_3^{'+}\cos\theta'_{13})^2}
\end{aligned} \tag{A.30}$$

With this, the formulae (A.15-A.16) can be used to determine the energy-momentum of particle 1 after the collision with the relative energy $\mathcal{E}_1^{'+} = \sqrt{(m_1^+ c^2)^2 + (cp_1^{'+})^2}$. We remark that setting $p'_3 \equiv 0 \equiv \mathcal{E}'_3$ in (A.29) reduces back to (A.7) in the simpler case of binary collision.

Appendix B

Maxwell-Boltzmann Statistics

We consider a system comprised of many individual particles, those could be electrons or molecules alike. Those particles can populate a set of energy levels. Under conditions where the state of the whole system is stable, the population distribution over those levels is fixed through equilibrium and corresponds statistically to the most probable configuration. It is known as the Maxwell-Boltzmann distribution in a classical description of weakly interacting particles. Below we give separate treatments for the continuum space of kinetic energies corresponding to the Maxwell distribution and the discrete space of energy levels leading to the Boltzmann distribution.

B.1 Continuous : Maxwell distribution

Let a system of N particles in a stationary state be determined by its total energy $\mathcal{E}$. Each particle i may occupy an individual state s corresponding to an energy $\varepsilon(s_i)$ with an associated probability $p(s_i)$. Since the energy of the system determines its state, we may assume that those probabilities depend on s_i only through the individual state energy $\varepsilon(s_i)$. Our objective is to determine a general formula for $p(\varepsilon_i(s_i))$, which reflects the principle of maximum entropy.

As a starting point, we may suppose that the system is momentarily in the configuration determined by the states s_i Its total energy $\mathcal{E}$ is simply the sum of energies of all occupied states:

$$\mathcal{E} = \sum_{i=1}^{N} \varepsilon(s_i) \tag{B.1}$$

The probability that the system takes this specific configuration is given by :

$$\mathcal{P} = \prod_{i=1}^{N} p(\varepsilon(s_i)) \tag{B.2}$$

If this configuration corresponds to a state of maximal entropy, then its probability must be stationary (and maximal). An adjacent configuration after a tiny perturbation that preserve the system's state is applied, should have the same probability $\mathcal{P}$ of occurrence. The energy shifts $\delta\varepsilon_i$ endured by each particle during the perturbation should preserve the total energy (B.1) :

$$\delta\mathcal{E} \equiv 0 = \sum_{i=1}^{N} \delta\varepsilon_i \tag{B.3}$$

The crux in the derivation of $p(\varepsilon(s_i))$ lies in considering the logarithm of the combined probability $\mathcal{P}$, to enable the separation of the individual perturbations $\delta\varepsilon_i$ applied. Since the

logarithm is a monotonically increasing function, if $f(x)$ has a maximum at x_m, so must $\ln(f(x))$ have. Thus, the logarithmic shift in probability is expressed as :

$$\delta(\log \mathcal{P}) \equiv \log\left(\prod_{i=1}^{N} p(\varepsilon(s_i) + \delta\varepsilon_i)\right) - \log\left(\prod_{i=1}^{N} p(\varepsilon(s_i))\right) \tag{B.4}$$

$$= \sum_{i=0}^{N} \frac{\mathrm{dlog}(p(\varepsilon(s_i))}{\mathrm{d}\varepsilon(s_i)} \delta\varepsilon_i + o(\delta\varepsilon_i) \tag{B.5}$$

Replacing the perturbations (B.3) in (B.5) and imposing that $\delta\mathcal{P} \equiv 0$ in a stationary configuration :

$$\delta(\log \mathcal{P}) \equiv 0 = \sum_{i=2}^{N} \left(\frac{\mathrm{dlog}(p(\varepsilon(s_i)))}{\mathrm{d}\varepsilon(s_i)} - \frac{\mathrm{dlog}(p(\varepsilon(s_1)))}{\mathrm{d}\varepsilon_1} \right) \delta\varepsilon_i + o(\delta\varepsilon_i) \tag{B.6}$$

There is only one straightforward solution valid for any arbitrary $\delta\varepsilon_i$ perturbation conserving $\mathcal{E}$ which consists in :

$$\frac{\mathrm{dlog}(p(\varepsilon(s_i)))}{\mathrm{d}\varepsilon(s_i)} = -K \Rightarrow p(\varepsilon(s_i)) = C \exp(-K\varepsilon(s_i)) \tag{B.7}$$

The constant K is related to the temperature of the system $K = k_\mathrm{B}T$ through Boltzmann's constant $k_\mathrm{B} \approx 1.380\,648 \times 10^{-23}$ J/K. The normalisation factor C is determined by the integral over all available states S : $1 = \int_S p(\varepsilon(s))ds$. If we regroup all states that relate energies in the range $\varepsilon \to \varepsilon + \mathrm{d}\varepsilon$ into the density $g(\varepsilon)$, we can integrate as follows :

$$1 = \int p(\varepsilon) g(\varepsilon)\, \mathrm{d}\varepsilon \tag{B.8}$$

Concretely, in the simplest classical case where particle states $s = (\mathbf{x}, \mathbf{v})$, are represented by their spatial $\mathbf{x}$ and velocity $\mathbf{v}$ coordinates, if the only relevant energy is kinetic: $\varepsilon = m\mathrm{v}^2/2$ for particles of mass m, then:

$$p(\varepsilon(s)) = C \exp\left(\frac{m\mathrm{v}^2}{2k_\mathrm{B}T}\right) \tag{B.9}$$

$$g(\varepsilon)\, \mathrm{d}\varepsilon = \int_{\varepsilon}^{\varepsilon+\mathrm{d}\varepsilon} \mathrm{d}\mathbf{v} = 4\pi\mathrm{v}^2\, \mathrm{dv} \tag{B.10}$$

$$g(\varepsilon) = 4\pi \frac{2}{m} \varepsilon \frac{\mathrm{d}\sqrt{2\varepsilon/m}}{\mathrm{d}\varepsilon} = \frac{4\sqrt{2}\pi}{m^{\frac{3}{2}}} \sqrt{\varepsilon} \tag{B.11}$$

The normalisation requirement reads :

$$1 = \int_0^\infty C \frac{8\pi}{m^{\frac{3}{2}}} \sqrt{\varepsilon} \exp(-\varepsilon/k_\mathrm{B}T)\, \mathrm{d}\varepsilon = C \frac{4\sqrt{2}\pi}{m^{\frac{3}{2}}} \frac{\sqrt{\pi}}{2} (k_\mathrm{B}T)^{\frac{3}{2}}$$

$$\Rightarrow\ C = \left(\frac{m}{2\pi k_\mathrm{B}T}\right)^{3/2} \tag{B.12}$$

Ultimately, we find the Maxwell distribution of velocities $f(\varepsilon)\, \mathrm{dv} = p(\varepsilon) g(\varepsilon)\, \mathrm{d}\varepsilon$:

$$p(\varepsilon(\mathrm{v})) g(\varepsilon) = \frac{2/\sqrt{\pi}}{(k_\mathrm{B}T)^{3/2}} \sqrt{\varepsilon} \exp\left(-\frac{\varepsilon}{k_\mathrm{B}T}\right) \tag{B.13}$$

$$f(v) = \left(\frac{m}{2\pi k_\mathrm{B}T}\right)^{3/2} 4\pi\mathrm{v}^2 \exp\left(-\frac{m\mathrm{v}^2}{2k_\mathrm{B}T}\right) \tag{B.14}$$

This distribution can be derived in more rigorous terms taking into account the phase-space described by the system, with eventually the use of generalised coordinates. Such derivations can be found in Jeans [the Chapter X of 455, especially §210-212]. The basic ingredients needed for this distribution are :

1. Conservation of a property (energy) – eq. (B.1)

2. Transformation of a product probability into a sum (logarithm) – eq. (B.5)

3. Principle of equipartition : the energy is equally shared between different degrees of freedom, or equivalently, the occurrence probability p is identical for all states s that correspond to the same energy ε, thus – $p(s) = p(\varepsilon(s))$

We recommend also to look into Bittencourt [the chapter 7 of 73, sections 1.3-1.4] which takes a totally different perspective, yet involves the three ingredients mentioned above. The important aspect is that no particle interaction that can structure the system was taken into account when deriving the Maxwell distribution.

B.1.1 General Maxwell distribution

In the more generalised case where the field of velocities present a first degree anisotropy given by the drift velocity $\mathbf{v}_0$, and in the presence of a potential $V(\mathbf{x})$, the energy ε' of a particle in the relative frame drifting at $\mathbf{v}_0$, takes the form:

$$\varepsilon' = \frac{m(\mathbf{v}-\mathbf{v}_0)^2}{2} + V(\mathbf{x}) \tag{B.15}$$

The generalised Maxwell distribution becomes:

$$f(\mathbf{v},\mathbf{x}) = C_x \left(\frac{m}{2\pi k_\mathrm{B} T}\right)^{\frac{3}{2}} \exp\left(-\frac{m(\mathbf{v}-\mathbf{v}_0)^2/2 + V(\mathbf{x})}{k_\mathrm{B} T}\right) \tag{B.16}$$

The potential V can be defined to an arbitrary constant level which simply multiplies the distribution by a constant factor. Its effect is swept away through the normalisation coefficient C_x when integrating over the volume Ω occupied by the system in configuration space:

$$\frac{1}{C_x} = \int_\Omega \mathrm{e}^{\frac{-V(\mathbf{x})}{k_\mathrm{B} T}}\, \mathrm{d}^3\mathbf{x} \tag{B.17}$$

For a potential defined by a homogeneous field of force $V \equiv -\mathbf{F}\cdot\mathbf{x}$, considering the subspace perpendicular to the field uniform, if the parallel coordinate stretches from $\mathbf{x}_0$ to $\mathbf{x}_1$:

$$C_x = \frac{F}{k_\mathrm{B} T} \frac{1}{\mathrm{e}^{Fx_1/k_\mathrm{B} T} - \mathrm{e}^{Fx_0/k_\mathrm{B} T}} \tag{B.18}$$

B.1.2 Properties of the Maxwell distribution

Three characteristic values for the distribution of speeds (B.14) are reminded here, they can be found in [73, §7.4].

$$\text{The most probable speed : } \mathrm{v_p} = \sqrt{\frac{2k_\mathrm{B}T}{m}} \tag{B.19}$$

$$\text{The mean speed : } \bar{\mathrm{v}} = \sqrt{\frac{8k_\mathrm{B}T}{\pi m}} \tag{B.20}$$

$$\text{The mean kinetic energy : } \bar{\varepsilon} = \frac{3k_\mathrm{B}T}{2} \tag{B.21}$$

B.2 Discrete : Boltzmann distribution

When the energy levels accessible to the particles in the system are distributed discretely, the demonstration takes on a slightly different path, paved with sums instead of integrals and countable degrees of energy degeneracy instead of density of states. In the end, the result is similar; the probability $p(\varepsilon_i)$ that a particle occupies any of the g_i degenerate states of energy ε_i is given by :

$$p(\varepsilon_i) = \frac{g_i \mathrm{e}^{-\varepsilon_i/k_\mathrm{B}T}}{\sum_{i=0}^{\infty} g_i \mathrm{e}^{-\varepsilon_i/k_\mathrm{B}T}} \,. \tag{B.22}$$

The denominator $\mathcal{Z} \equiv \sum_{i=0}^{\infty} g_i \mathrm{e}^{-\varepsilon_i/k_\mathrm{B}T}$ is known as the *partition function*. Many useful thermodynamic quantities can be derived from it. In this thesis, our primary use of the Boltzmann statistics will aim at molecular rotational and vibrational excitation populations.

Part II

Electron scattering by molecules

Perilogue

Let us imagine that this afternoon is a bright sunny day. A beam of light gushes-in through the windows and we are immediately tempted to go outside, just to wander a bit, both our body as our thoughts along. As soon as we step out of our main office building and go right into the park that every decent scientific complex should possess in its vicinity, our attention gets dispersed.

We see various objects around us, maybe some birds are chirping, perched up on high branches in the surrounding trees. Others are cheerfully splattering in the large fountain where some children toss small coins while others fling puffs of bread crumbs to feed the birds. Some cats are sunbathing on a quiet spot on the rim of a limestone wall bordering a kiosk. Occasionally, a generous soul comes in timidly to steal a few strokes. A blossoming magnolia tree protected by a circle of low freshly trimmed hedges coronates a small hilly lawn.

In such conditions, freedom is an abstraction of the mind that finds no practical realisation of itself. We might persist to keep strolling about, until soon we surrender to the delightful empty and clean bench from where one can pause for a while, let time flow on a different pace and contemplate.

The scenery that unfolds before us is of no strangeness to our eyes. We may be bemused by the peculiar feeling of familiarity that emerges from resting in the park; a place that we might have visited for the very first time, yet whose alleys and structure we recognise. We can expect where to find a pond, a bridge, a fountain, a paddock of flowers and the space well enclosed by trees which procure a universal feeling of protection and security.

We may start wondering: what would have this park looked like before, when it still belonged to untrodden wilderness? Probably a dangerous but surely bewildering jungle. Swampy grounds, covered cliffs and precipices, open cracks with springs rushing out into streams and merging into rivers, rotting tree trunks overgrown by lavish vegetation. In such a place, every little detail would look new to us. We could probably run in circles without noticing we are looking at the same tree, or conversely we could think we passed here before and be unable to see the differences.

We might spend our entire lifetime trying to get our way through this wilderness, or we might decide to make it more passable, akin to our cognition and perception. One typical place to start is to clear off the space, take away some samples and bring them to our world. At home, we may cast a closer inspection onto what we found. Undistracted by the fuzzy wild environment, we have better control and certainty over what we are observing.

This routine is so embedded in our scientific approach that it sounds ridiculously obvious to mention it. Nevertheless, we are constantly reminded to question it. In the first part of this thesis, we discovered how much of what makes the reality of lightning was discarded in order to focus on the details of thermal electron runaway under perfect and uniform conditions of the gaseous medium and the electric field. This second part will be no exception to this reductive practice. Armed with the approximation machete, we will have to trim down much of the lush vegetation growing in the realm of quantum mechanical approach to electron-molecule collisions. At the outcome of this second expedition, we are expected to have chopped enough logs to feed into the fire that sustains the first part of this thesis: namely, we need a complete set of cross sections.

Notwithstanding, the role of science is not to isolate us from immaculate reality, but to develop tools and idioms to apprehend it. In order not to disregard this deontological aspect of science, we shall also make an additional effort on our way. We will try to learn the names of the plants we see and discern more than a jungle of leaves and wood in this allegory to the realm of quantum physics. Though there are numerous textbooks on this matter, I believe it wrong to be exempted from the task of assembling the material used into a coherent ensemble.

It is in this sense that we may slowly recover from our raving thoughts and slide back into our self sitting there on the bench, somewhere in the park on a nice afternoon. The park is by no means a replacement to the wilder reality into which we project our scientific endeavour. Rather, it should be perceived as the meeting place between our ignorance and our knowledge. Where, from the place we sit or stand, we can observe them with a critical point of view; always bearing in mind that what we see, has been made to be observable, and keeping our imagination open to what might be out there that has not yet found its place in our park...

Chapter 7

Context

As we saw in the first part of this thesis, all interactions of electrons with the constituent molecules of air may be modelled with effective cross sections for collisions of several types. Those cross sections are related to the probability of interaction. Because the temporal and spatial scales of electron-molecule collisions are usually very small compared to the scales involved in the propagation of electrons in gases between collisions, it is very convenient to separate the electron motion into two very distinct modes:

I. Propagation in an electromagnetic field

II. Local interaction with a molecule

While the propagation involves a finite displacement in space $\Delta\mathbf{r}$ and time Δt, the local interaction is supposed to happen at a definite position $\mathbf{r}$ and a particular instant t. This sharp distinction justifies the structure chosen for this thesis into part I dealing with electron transport and part II only concerned with localised collisions isolated from all other external influences.

In this chapter, we introduce the concept of cross sections for electrons scattering from molecules; how they are defined, measured and calculated.

Of course, this dual view – electron propagation interrupted by localised collisions – has its own limitations and one of the challenges in plasma physics is to overcome them when treating long-term and long-range interactions such as resonances and collisions with ions. In the latter case, one needs to include interactions with multiple charged bodies (ions or electrons) present within the sphere defined by the Debye radius (2.104).

Let us imagine an electron roving at 1 eV near a molecule of nitrogen in gas at a density of 2.5×10^{25} molecules per cubic metre, with a fairly high background external field of 5 MV/m as could be attained in a discharge streamer channel at atmospheric pressure. The radius r_{int} delimiting the (spherical) region of interaction must be much smaller than either the (i) half the mean free path of the electron in the gas, (ii) the distance at which the external electric field is higher that the electrostatic field generated by the molecule. Those conditions delimit the range at which the electron is affected by (i) another molecule and (ii) the collective field generated by or imposed to the medium. Taking the total interaction cross section to be $10^{-19}\,\text{m}^2$ at 1 eV, and approximating the molecular field (attractive) as created by an induced dipole $E_{\text{mol}} = \dfrac{e}{4\pi\epsilon_0}\dfrac{4\alpha_{\text{d}}}{2r^5}$ with a polarisability of $\alpha_{\text{d}} \simeq 2 \times 10^{-30}\,\text{m}^3$ (see section 8.2.3), a numerical examination of both conditions give:

i. $r_{\text{int}} \lll \frac{1}{2}\frac{1}{2.5\times10^{25}\,\text{m}^3\times10^{-19}\,\text{m}^2} = 200\,\text{nm}$

ii. $E_{\text{mol}} \gg 5\,\text{MV/m} \;\Rightarrow\; r_{\text{int}} \ll \sqrt[5]{\frac{4\times2\times10^{-30}\,\text{m}^3\times5.3\times10^{-11}\,\text{m}\times13.6\,\text{eV}/e}{5\times10^{6}\,\text{V/m}}} \approx 1\,\text{nm}$

The numerical values introduced in the second condition come from the atomic Bohr radius and the Rydberg energy (in electron-Volts). The unit system and the details about the electrostatic potentials will be introduced later in sections 7.5 and 8.2.3.

We see that density effects in gases can be utterly neglected, as the molecules are very far apart. Thus the collisions may be considered as separated and unrelated events. Only at high relativistic energies ($\gtrsim 100\,\text{MeV}$) does the density effect [279] play a role due to simultaneous long-range interaction of the electron with the polarised molecules/atoms of the gas. This is because scattering at very high energies is mainly affected by long-range forces.

On the other hand, the effect of an applied uniform external electric field is stronger on low energy electrons especially in the high field regions present at the front of electron ionisation waves in discharges where the density of ions and electrons may be significant. The presence of an external electric field slightly modifies the outgoing flux distribution of the scattered electron and thereby the differential cross section. This mainly affects the scattering at forward angles ($< 10°$), which may be enhanced or inhibited depending on the orientation of the electric field with respect to the direction of the incident electron. Supposing an ionisation fraction of one thousandth, a rough estimation shows that this enhancement/inhibition is small $\lesssim 5\,\%$, but grows slightly with the incident energy.

More problematic is the situation in which an electron collides with ions in a non-weakly ionised plasma (ionisation fraction $> 10^{-3}$). There, the separation between propagation and collision is smeared. One needs to define an effective finite radius within which the collision takes place and treat the rest of the motion through the Coulomb interaction with multiple ions. In the kinetic treatment of plasmas, this leads to the Landau collision integral which accounts for collisions of weak but unscreened Coulomb interactions [816, §6.3.2]. This limiting case was touched upon already in part I on several occasions (p. 80). It is widely known that properly modelling Coulomb collisions in partially or fully ionised plasmas poses a challenge which lies just at the edge of the scope of this thesis aimed at electrons propagating in weakly ionised gases.

Looking now at the temporal scale, our electron at 1 eV should traverse an overall length of ~2 nm, representing the region of interaction with the molecule, in about $2\times10^{-15}\,\text{s}$; a very short time interval. Nevertheless, it may happen that this electron be delayed further because of trapping mechanisms in the attractive potential of the molecule. This is known as a resonance and occurs at particular values of the incident energy which typically lie in the range of a few eV or less. Resonances can introduce delays about 10 times longer than the value of an 'ordinary' collision time. However, very narrow resonances, particularly with oxygen molecules might trap the electron for 0.1 ns! Longer delays become affected by collisions between molecules in the gas, after which the electron may become attached to the molecule for even longer periods. This will be discussed in section 11.3.

Recognising that the microscopic spatial and temporal scales of collisions can present some overlap over larger scales, we shall nonetheless adopt the traditional approach in which collisions are considered isolated from external factors. In all practical situations, time delays can be simply added to the flight time of the collision and the effect of long-range external interactions can be incorporated as a corrective parameter affecting scattering at small angles.

7.1 Motivation

In the previous part, we realised how important it is to possess a reliable and consistent set of cross sections for representing electron-molecule interactions when modelling thermal runaway: a phenomenon that traces the acceleration of electrons from sub-eV energies to beyond hundreds of keVs. So far, this requirement is not met in the available databases hosted on LXCat, an online server with a wealth of data on electron and ion interactions with gaseous molecules. This is because most applications of weakly ionised plasmas are interested in the bulk behaviour of the electron swarms: its transport parameters and reaction coefficients to be plugged in a simulation over a greater scale involving, for instance, chemical reactions.

Undeniably, thermal runaway is also of concern to the plasma fusion community. Nonetheless, the context is still very different for at least three reasons: (i) fusion plasma are fully (or almost) ionised so that neutral ground species are virtually vacant; (ii) the gases involved are mainly hydrogen (its isotopes) and helium, so the focus is different than with atmospheric gases; and (iii) the perspective is totally different since the purpose there is to reduce risks of thermal runaway with appropriate use of magnetic confinement and reduction of electric fields in the fusion chamber. Although better acquaintance with the fusion community would surely enrich the knowledge in our community of atmospheric electricity, it cannot be denied that our focuses and the state of plasmatic matter are entirely different.

It became thus a secondary objective of this thesis to bring about an updated set of electron-molecule cross sections for the use in Monte Carlo simulations of electron swarms in electrified gases. Gradually, this 'secondary' objective grew in importance to the point that it may have curbed the original objective of this thesis about understanding thermal runaway in atmospheric discharges.

7.1.1 Questions and Goals

There are many questions that arise when one delves into the world of microscopic electron-molecule scattering. Notably, the progress of our current understanding of electron-molecule interactions from the second half of the past century to this day has been so intense, that there is a great barrier of knowledge, language (scientific jargon) and culture between the world of quantum mechanics computations and the weakly-ionised plasma physics community. By 'culture', we mean that it is utterly not uncommon to find a model considered 'inaccurate' by the quantum community, but used nonetheless in simulations of electron swarms.

- The degree of precision one requires is arbitrary and even the accuracy of a model is subjective. The plane wave Born approximation considered invalid still at 5 keV by a quantum physicist does not discourage an electron swarm physicist to adjust a formula based on the crudest atomic model and use it from 500 eV, 100 eV or even 15 eV.

- Differing perspectives emerge and give rise to a different use of language and terminology. R-matrix, S-matrix, T-matrix, adiabatic nuclei body-fixed-frame, lab-fixed-frame, angular-momentum coupling, close coupling, resonant scattering, $d\pi$-wave, Fano profile, binary-encounter, Franck-Condon factors, generalised dipole oscillator strength, etc. Those terms may be totally abstruse for a part-I physicist while being susceptible of popping out any time in a casual conversation between part-II physicists.

- The tools used for analysis and decomposition of cross sections are also different. A semi-empirical fit to experimental data might be constructed partly with off-diagonal T-matrix elements (in the body-fixed frame angular-momentum coupling) calculated in the first

Born approximation while leaving the first few diagonal elements as free parameters and completing all high order diagonal elements from their value given by the mean effective range theory. A data scientist would probably prefer to use a simple least square fit from Legendre polynomials and find a tricky way (cost functions or reduce/constrain the parameter space) to get around extrapolation problems.

To refer to those differences, we think it is appropriate to speak of 'scientific culture' beyond a simple difference in perspectives.

The questions addressed in this part concern the significance of microscopic phenomena on the macroscopic world. We should ask ourselves such things as: when should we pay attention to resonances? Can narrow resonances, for example, be disregarded? When can we use simple approximations such as the handy analytical first Born approximation?

In general, the question that best summarises this part is:

> What level of inaccuracy can we afford ourselves when modelling electron-molecule interaction on a broad scale? How far can we push this accuracy before we fall out of scope?

This question is unfortunately unanswerable if there is no prior consensus of what fraction (percentage) can be considered negligible, and what lies beyond the scope of this thesis.

For the first instance, we decided that 5 % would be an acceptable level of uncertainty on the differential and integral cross sections produced. This decision is not completely arbitrary because it reflects the overall precision with which cross sections are known experimentally (see next section 7.3).

For the second instance, we imposed a hard limit of not dealing with target wavefunctions*. This immediately set us apart from the Hartree-Fock description of the target wavefunction, variational methods, close-coupling, and many more top-edge methodologies that require a superior amount of time to be mastered – let alone be improved – than was available for this thesis.

Without any surprises, those two restrictions that we set upon ourselves lie on conflictual grounds. It was obviously not possible – in all instances – to get a 5 % level of accuracy yet discarding such a consequential part of the active field of research in the realm of quantum computations for electron scattering. Nonetheless, our goal was still met:

> The goal behind this second part is double sided:
>
> 1. Create and assemble an updated set of electron-molecule cross sections to be used in swarm simulations.
>
> 2. Make less vertiginous the growing abyss of knowledge between the makers and the users of cross sections.

7.1.2 Structure of Part II

Following a similar arrangement as the one chosen for the first part, we separated the second part in six chapters (7 to 12) and three appendices. The first chapter is a general introduction in the physics of electron scattering.

In the second chapter 8, we present the theoretical methodology used for computing cross section. The domain is too vast and we exploit only a minor part for our purposes. From general

*That could be considered heresy in the community of quantum physics computations.

considerations, we gradually zoom onto the approach that we adopted: modelling the scattering through an approximate local interaction potential.

The algorithms used to implement and solve the equations exposed in chapter 8, are described in the following chapter 9.

Chapter 10 is an attempt to tackle the difficulties encountered when trying to model a phenomenon whose complexity is beyond the reckoning of one's scientific background (or culture)*.

Notwithstanding the many doubts that will be cast in chapter 10, we will apply in chapter 11 simple yet reasonably accurate models for calculating cross sections of elastic and inelastic electron collisions with molecules. Differential cross sections are only obtained for (vibrationally) elastic scattering. Due to the simplicity of the approach taken, we had to recur to several semi-empirical adjustments or fits to obtain the level of agreement desired. In the case of vibrational cross sections, we believe there is no straightforward way to calculate cross sections due to their predominantly resonant nature. When data from more sophisticated models were available, we blended the published results of other works with our own fits or calculations in the vacant energy regions. The outcome of our investigation has been put together on files stored on a freely accessible repository.

Finally, in the last chapter 12, we summarise our efforts and propose various ways in which our work could be further improved.

In the rest of this chapter, we introduce how scattering of electrons by molecules is treated, measured and estimated in classical mechanics. A preamble to the adequate treatment in the framework of quantum mechanics is given at the end of the chapter in preparation of the following chapter on theoretical calculations.

7.2 Basics of Scattering

If a beam of electrons passes through a dilute gas, in addition to a transmitted current in the forward direction, electrons will spread diffusely over all directions. The distribution most often presents some non-uniformities. More electrons might be observed at certain angles of deviation and they will come out around certain energies. One may of course not predict deterministically the outcome of each individual collision. However, when treated as an ensemble, the electrons that collided obey a certain statistical distribution in their angle of deviation and energy lost.

The idea underlying scattering is to determine the probability with which an electron initially beamed in a forward direction at a determined velocity, will be deviated into a certain solid angle Ω and at a certain energy ε.

Let us suppose, as depicted in sketch 7.1, that an initially collimated beam of electrons carrying a current of I_{in} over a surface S, passes through a dilute gas at a density of n_{gas}. If we place an electron collector at a certain angle, covering a solid angle of $\delta\Omega$, the current I_{out} of electrons detected may be related to I_{in} through the proportionality :

$$I_{\text{out}} = I_{\text{in}} n_{\text{gas}} V_{\text{coll}}\, \delta\Omega \,. \tag{7.1}$$

The coefficient V_{coll} represents the effective volume of interaction between the electron beam and the gas per solid angle, so that the product $n_{\text{gas}} V_{\text{coll}}\, \delta\Omega$ represents an effective fraction of collisions with molecules that would send the electrons into the solid angle $\delta\Omega$. The effective volume V_{coll} may be alternatively seen as a fraction of the physical volume $V = S \cdot l$, where l corresponds to the length that the beam traverses in the gas. Technically, this effective volume

*Probably the mishap of every scientist.

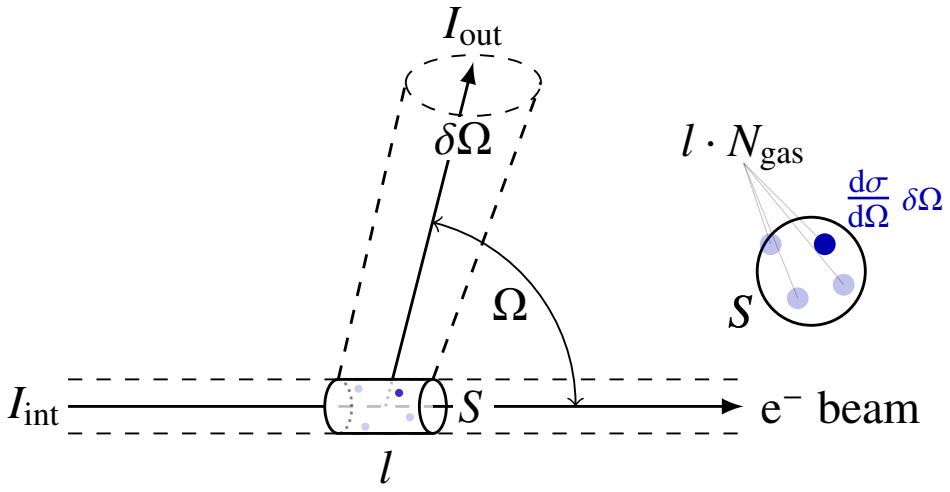

Figure 7.1: Conceptual definition of the scattering cross section for collisions between electrons and molecules.

could also be affected by the velocity of the molecules. However, in practice, molecules at ambient temperature are much slower (at least 30 times) than even meV electrons.

We may define an effective cross section $\delta\sigma = S\,V_{\text{coll}}\,\delta\Omega/V$ which defines the overall fractional area over the full beam section S (see close-up circle on the centre right of 7.1). We may write [147, §1.3:p.8]:

$$I_{\text{out}} = \frac{I_{\text{in}}}{S} S \cdot l\; n_{\text{gas}} \cdot \frac{\delta\sigma}{\delta\Omega}\,\delta\Omega\,. \tag{7.2}$$

The ratio I_{in}/S represents the density current of electrons and its multiplication by $\delta\sigma$ gives the number of collisions per unit time between the electrons impinging on one molecule placed in their path. Then, if one considers $n_{\text{gas}}\,S \cdot l$ molecules and counts the electrons over the solid angle $\delta\Omega$, one gets the total current I_{out} collected into $\delta\Omega$. For an infinitesimal solid angle, one may define the limit:

$$\text{Differential Scattering Cross Section}: \frac{\mathrm{d}\sigma}{\mathrm{d}\Omega}(\Omega) = \lim_{\delta\Omega\to 0} \frac{\delta\sigma}{\delta\Omega}(\varepsilon,\Omega)\,, \tag{7.3}$$

which gives the effective collision cross section for all events that scatter electrons at an energy ε into the direction defined by $\Omega = (\theta,\varphi)$. The polar angle $\theta = \measuredangle(\vec{I}_{\text{in}},\vec{I}_{\text{out}})$ is the angle formed between the incident $\vec{I}_{\text{in}}$ and deviated $\vec{I}_{\text{out}}$ stream of electrons. The azimuthal angle φ describes a rotation of the scattering plane where $\vec{I}_{\text{in}}$ and $\vec{I}_{\text{out}}$ both lie, with respect to a reference plane. In an anisotropic medium, a preferential direction of molecular alignment would introduce a dependence of the differential cross section on the azimuthal angle φ. In the present situation, we assume that the orientations of gas molecules are isotropic and thus there is no dependence on φ. This assumption could be disrupted, for instance, in a highly polar gas (water molecules) under a high electric field.

If we are interested in calculating the total flux of electrons that endured a collision with a molecule in the gas, we may integrate the differential cross section over the entire unit sphere of infinitesimal solid angle element $\mathrm{d}\Omega = \sin\theta\,\mathrm{d}\theta\,\mathrm{d}\varphi$, giving then the:

$$\text{Integral Cross Section}: \sigma \equiv \int_0^{2\pi}\int_0^{\pi} \frac{\mathrm{d}\sigma}{\mathrm{d}\Omega}(\theta,\varphi)\sin\theta\,\mathrm{d}\theta\,\mathrm{d}\varphi = 2\pi\int_0^{\pi}\frac{\mathrm{d}\sigma}{\mathrm{d}\Omega}(\theta)\sin\theta\,\mathrm{d}\theta\,. \tag{7.4}$$

There are four fundamental assumptions that must be verified in order to validate the definition of a cross section $\mathrm{d}\sigma_c/\,\mathrm{d}\Omega$ associated to a collision c through (7.2):

1. The electrons from the beam do not interact among themselves.
2. Each electron interacts at most with one molecule and is unaffected by any other molecule or external force.
3. The dimensions of the interaction volume V are tiny compared to the distance at which the electrons are collected.
4. The states of the molecules and of the electrons (kinetic energy) are perfectly defined.

Under these conditions, a close correspondence may be established between the idealised (differential) scattering cross section in (7.3) and the one derived from experiments based on (7.2). Some conditions may be relaxed, as will be seen in the next section 7.3; at the cost of requiring additional corrections to the measurements performed.

As we know already, an electron may also change the state (from i to f) of the molecule through a transfer of its kinetic energy during the collision. At the most basic level we may distinguish:

- Elastic collisions : in which the state of the molecule does not change ($i = f$) and thus, the total kinetic energy in the collision is conserved.
- Inelastic collisions : in which the initial and final states of the molecule differ ($i \neq f$) and a conversion of kinetic energy from or into other forms has taken place.

After an inelastic collision, the molecule may come out excited, dissociated or as an ion through ionisation (positive) or attachment (negative). The outcome of a collision is known as *channel*. A channel is open if the energy of the electron ε is sufficient to enable the reaction (excitation, dissociation, ionisation), otherwise it is closed.

To each channel $c = i \to f$, we may therefore associate a cross section $\sigma_c(i \to f, \varepsilon_i \to \varepsilon_f)$ that relates the kinetic energy loss of the electron $\varepsilon_f - \varepsilon_i$ with the transition of the initial i to the final state f of the molecule.

In many cases, the molecules in a gas are distributed over a continuum $[i', i'']$ or a discrete set of initial states $\{i_0..i_n\}$ spaced in energy. Also, they may be excited into a continuum $[f', f'']$ or a discrete set of final states $\{f_0..f_m\}$. Those might be the different rovibrational bands (discrete) of an electronic excitation, or the kinetic energy distribution after dissociation (continuum). In those cases, a cross section of a certain kind of collision might actually be the average over many initial states k and a summation over many final states j:

$$\sigma_c = \frac{1}{N_i} \sum_{k=0}^{n} \sum_{j=0}^{m} \int_{i'}^{i''} \int_{f'}^{f''} g_{k,i}(x_i) \frac{\mathrm{d}^2\sigma(i_k \to f_j)}{\mathrm{d}x_i\,\mathrm{d}x_f}\,\mathrm{d}x_i\,\mathrm{d}x_f\,. \tag{7.5}$$

The cross section for a continuum of transitions from initial to final states is expressed as a differential over the continuous variables x_i and x_f. The averaging over initial states comes through the normalisation to $N_i = \sum_k \int g_{k,i}(x_i)\,\mathrm{d}x_i$, where $g_{k,i}(x_i)$ describes the overall frequency of occurrence of the state k, x_i.

As an example, "elastic collisions" should in principle include only the process whereby an electron loses a very small amount of kinetic energy only due kinematic relations of binary collisions without altering the internal energy state of the molecule (see previous appendix A

for more information). However in practice, we should remember that 'elastic' cross sections comprise also all open channels for rotational excitations and possibly transitions between almost degenerate states in the fine structure of an atom/molecule. This is because the excitation thresholds to those processes are often much smaller than the energy resolution in the experiment so that pure elastic scattering may not be discriminated against those weakly inelastic collisions.

Cross sections for a specific collision resulting in transition between states i and f involve the output/input flux ratio. In virtue of flux conservation, one may therefore relate the cross sections between a direct $i \to f$ and its reverse $i \leftarrow f$ process through a relation known as *detailed balance* [834, p.11:eq.(15)]:

$$\varepsilon_i g_i \frac{\mathrm{d}\sigma_{i\to f}}{\mathrm{d}\Omega}(\varepsilon_i) = \varepsilon_f g_f \frac{\mathrm{d}\sigma_{i\leftarrow f}}{\mathrm{d}\Omega}(\varepsilon_f)\,. \tag{7.6}$$

The factors g_i and g_f represent the degeneracy of the states i and f respectively: i.e. how many definite channels are comprehended under the labels "i" and "f". As mentioned above, those can be different spin or rotational projections of the target. The presence of the energies associated to the initial ε_i and final ε_f states of the collision stems actually from a quadratic dependence of the outgoing v_f and incoming v_i electron velocities. This is because both the flux and the frequency of the collision are proportional to the velocities of the colliding particles. Instead of invoking the frequency, a more formal and correct way to interpret this proportionality, is to think in terms of density ratios in the continuum space of collision energies of the electron-molecule system. This is better demystified in Rodberg *et al.* [782, p.276:eq.(2.46)].

Knowing the total flux of electrons that is deviated does not necessarily inform us about the degree of deviation incurred. For this, one considers the average momentum loss of electrons in a collision.

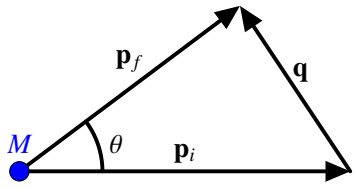

Figure 7.2: Momentum transfer $\mathbf{q}$ from an electron to a molecule M in a collision.

For a given process c, let us suppose that electrons colliding with an initial kinetic momentum $\mathbf{p}_i$, emerge with a final momentum $\mathbf{p}_f(\theta)$ which, by law of momentum conservation, depends on the angle of scattering. The momentum transferred* in the collision is defined as $\mathbf{q} = \mathbf{p}_i - \mathbf{p}_f$, forming a triangle as represented in 7.2. By azimuthal symmetry of the differential cross section (see eq. 7.4 and § above), the average momentum transferred to the gas after many collisions will be parallel to the incident beam direction $\hat{\mathbf{p}}_i$. The rate of (parallel) momentum transfer from the electron beam to the gas is conveyed by [834, Chapter 1:p.6:eq.(10)]:

Momentum Transfer Cross Section :

$$\sigma_\mathrm{m} = \int \frac{\mathrm{d}\sigma}{\mathrm{d}\Omega}(\Omega)\frac{\mathbf{q}\cdot\hat{\mathbf{p}}_i}{p_i}\,\mathrm{d}\Omega = 2\pi\int_0^\pi \frac{\mathrm{d}\sigma}{\mathrm{d}\Omega}(\theta)\left(1-\frac{p_f}{p_i}\cos\theta\right)\sin\theta\,\mathrm{d}\theta\,. \tag{7.7}$$

The rate of momentum transfer per time and thickness traversed in a gas of density n_gas by an electron flux I_in each carrying a momentum p_i, is $I_\mathrm{in}\, n_\mathrm{gas}\, l\sigma_\mathrm{m}\, p_i$. As before, one can define

*As often encountered in dual concepts, the formal definition of the momentum transfer q varies with the author. Whereas Canto and Hussein [147] and Taylor [922, p.147:fig. 9.1, p.159] choose "$\mathbf{q} = \mathbf{p}_f - \mathbf{p}_i$", Inokuti [427, p.298:§2.1] defines "$\hbar\mathbf{K} = \mathbf{p}_i - \mathbf{p}_f$" in his notation. Since literally "the momentum transferred from the electron to the molecule" is by conservation, the momentum "lost" by the electron, we shall always follow the latter definition: the momentum transferred is given by the initial minus final momentum. We will make repetitive emphasis on this convention throughout this thesis to avoid confusions.

a momentum transfer rate from a specific process (usually elastic scattering) or from various inelastic collisions. When modelling electron swarms, one should distinguish the elastic from the effective momentum transfer cross section which includes momentum loss from all open channels. It is common to find the factor p_f/p_i replaced by 1, for electrons colliding with molecules when the inelastic losses are negligible. We keep the distinction here in order to preserve the original meaning of momentum transfer [198, eq.(32)] instead of an average deviation.

For a further introduction of scattering and electron-molecule collisions, we recommend the first chapters of Shimamura and Takayanagi [834] and Canto and Hussein [147]. In order to grasp a better understanding of how to relate the conceptual notion of a cross section to its tangible value in reality, we describe in the next section how cross sections are derived from experiments.

7.3 Experimental Methods

The objective of the present section is to acquaint ourselves with the many diverse ways by which cross sections are measured experimentally. Although not a review, it is important to understand the limitations that apply to different techniques of measurement. Since the phenomenon of thermal runaway spans a wide range of electron energies from sub-eV to some hundreds of keVs, it is only natural that the data gathered must come from different experimental setups for which the uncertainties may differ significantly. In this regard, we will try to emphasise the assumptions underlying each type of experiment, which delimit their region of validity. We will see how different techniques beautifully complement each other and may be assembled together to produce a coherent overview of electron-molecule interactions over a broad range of energies.

A classification of experimental methods aiming to estimating electron-molecule cross section is uneasy. Although the experimental determination of a cross section requires basically that electrons impinge on target molecules and interact, there are many ways in which this can be performed. One could divide the types of experiments as:

A. Swarm experiments,

B. Optical measurements,

C. Static gas,

D. Cross-beam.

Nevertheless, this classification of experimental methods is somewhat ambiguous because optical measurements can also be conducted under static gas or crossed-beamed configurations. Perhaps a more representative classification should be displayed in a table rather than a list:

Gas \ Detection	Photons	Gas	Electrons	Swarm
Static	Optical (static)	Ion collection	Attenuation	Swarm
Beamed	Optical (beamed)	Beam analysis	Cross-beamed	×

This maps how the gas is introduced in the collision chamber versus what kind of signal is measured. Another classification could take the more pragmatic perspective of what quantity is derived: total, momentum, integral or differential cross section. Also, one could specify if a timing analysis is performed on the detection (e.g. time-of-flight or coincidence) and if there is spectrometry involved in the particles detected (e.g. for energy loss spectra).

Admitting the diversity of experiments that can be performed to probe electron interaction with molecules, for practical purposes we divide the present section into the four categories introduced above.

7.3.1 Swarm Experiments

This type of experiment bears a very special meaning in this thesis as it binds together the themes represented by the two first parts of this thesis: electron swarms in electrified gases together with electron scattering by molecules. It is the oldest of the experimental techniques unveiling electron interactions with molecules. By measuring some macroscopic transport parameters of electrons in given conditions of reduced electric field E/N_{gas} and gas temperature T_{gas}, one can roughly probe the overall effect of electron-molecule collisions in equilibrium conditions. A very good and well referenced overview of the experimental approach to electron swarms is given by Crompton [199], of which we highlight the most basic aspects here.

In the realm of scattering experiments, swarm experiments are an outlier because they operate under completely opposite experimental conditions compared to other techniques. An electric (or also magnetic) field is imposed and must fill the chamber as uniformly as possible. The velocity distribution of the electron swarm must reach a steady state as it propagates through the gas which implies that many collisions have taken place instead of only one as described in the schematics 7.1 of the previous section. The electrons are not produced at a definite energy like by electron guns, but they must be 'gated' appropriately when performing timing analyses.

There are mainly four transport parameters that are measured experimentally:

1. The drift velocity $\mathrm{v_d} = \mu_{\mathrm{e}} E$ [m/s], to which the electron mobility μ_{e} is related;
2. The lateral (transversal) diffusion coefficient D_{T} or $D_{\perp}$ [$\mathrm{m^2/s}$] which describes the electron diffusion in the direction perpendicular to the electric field;
3. The longitudinal diffusion coefficient D_{L} or $D_{\parallel}$ [$\mathrm{m^2/s}$] in the direction of the electric field;
4. The Townsend first ionisation coefficient α_{i} [1/m] = $(\nu_{\mathrm{i}} - \nu_{\mathrm{a}})/\mathrm{v_d}$ which expresses the multiplication rate of electrons per unit length traversed in the direction of the electric field through impact ionisation. It is related to drift velocity and the net multiplication rate $(\nu_{\mathrm{i}} - \nu_{\mathrm{a}})$ (per time) balancing ionisation ν_{i} against attachment ν_{a}.

The two first transport coefficients are most used for deriving cross sections whereas the Townsend coefficient serves to test the validity of a given set of cross sections. Drift velocities are measured in drift tubes where the duration between release and capture of a batch of electrons is measured after it propagates in the tube uniformly filled with gas. Lateral diffusion on the other hand may be measured in steady state conditions from the current collected at a certain radial distance from the positive electrode. The experimental accuracy for measurements of longitudinal diffusion is not as good as for drift and lateral diffusion. By varying the electric field, the spread and average energy of the electrons change and affect the transport parameters so that a weak dependence of the coefficients with the "overall" electron energy may be established.

An important relation ("Einstein relation") to the average electron energy $\langle\varepsilon\rangle$ in the swarm is given by the ratio of the lateral diffusion on the mobility [199, p.108:eq.(16)]:

$$\frac{D_{\mathrm{T}} e}{\mu_{\mathrm{e}}} = \frac{D_{\mathrm{T}} E e}{\mathrm{v_d}} = C\langle\varepsilon\rangle \,. \tag{7.8}$$

The proportionality coefficient C depends only on the shape of the electron energy (or velocity) distribution. For instance, a Maxwellian distribution yields $C\langle\varepsilon\rangle = k_{\mathrm{B}} T$ [748, p.129], thus $C = 2/3$. Division by the elementary charge e gives the value $D_{\mathrm{T}}/\mathrm{v_d}$ in electron-Volts. This relation is useful to estimate the average energy of an electron in the swarm and therefore to understand which energy region of the cross sections is probed in the experiment.

The derivation of cross sections from transport parameters measured at various electric fields is far from straightforward. It is an iterative process that relies on an initial guess of the cross sections to use as an input in Boltzmann's equation for electrons in a gas under an electric field. The solution to this equation yields the electron distribution in velocity space from which transport coefficients can be derived and then compared to the experimental data. This procedure requires a very good understanding of the effect of the microscopic cross sections on macroscopic transport properties of the electron swarm in order to guide the adjustment of estimated cross sections and yield a trustful value.

Reliable theoretical estimation of cross section is a keystone in analysing swarm experiments. The assistance of the mean effective range theory for parametrising the elastic cross section at low energies is a perfect example of how cross sections may be very accurately derived from swarm experiments (<2 %) when their energy dependence is well constrained. This is much better than measurements based on integration of the differential scattering cross sections. The advent of advanced data analysis and optimisation techniques such as with machine learning algorithms can potentially bring much improvement in the connection between cross sections and swarm measurements.

There are two major factors that restrict the range of applicability of deriving cross sections from swarm experiments:

1. There must be no or very few open inelastic channels at the energies probed by the distribution of electrons in the gas;

2. The cross sections must vary little in the energy range mainly covered by the swarm distribution in energy space.

Under theses assumptions, the dependence of the drift velocity and lateral diffusion on the momentum-transfer cross section can be found to approximately scale as* [199, p.115]:

lowest E/N	not low E/N
$\mathrm{v_d} \propto 1/\sigma_\mathrm{m}$	$\mathrm{v_d} \propto 1/\sqrt{\sigma_\mathrm{m}}$
$D_\mathrm{T}/\mu_\mathrm{e} \perp\!\!\!\perp \sigma_\mathrm{m}$	$D_\mathrm{T}/\mu_\mathrm{e} \propto 1/\sigma_\mathrm{m}$

The definition of what electric field is "low" and "not low" depends on the departure of the average kinetic energy $\langle\varepsilon\rangle$ of the swarm compared to the thermal energy of the gas $3k_\mathrm{B}T_\mathrm{gas}/2$ as described by Maxwellian statistics (see appendix B of part I).

The most suitable region for estimating cross sections from swarm experiments is thus at low energies far from pronounced resonances and below the threshold for inelastic scattering. The most successful application was to the lightest noble gases: helium and neon. Their first excitation level lies around ~ 20 eV and 17 eV respectively. This enables to probe the effect of elastic scattering alone throughout the whole 10 meV–12 eV energy range. The lower bound comes from the restriction upon the electric field to avoid contamination of the swarm by boundary effects around the electrodes. At lower electric fields (<0.1 Td), contact potential drops and surface charge layers spoil the uniformity and accuracy requirement of the electric field [199, p.132]. At higher electric fields (> 10 Td), the derivation of swarm parameters is less accurate. For heavier noble gases, the elastic cross section goes through a Ramsauer-Townsend minimum† [634, p.113–8:§2.31–2] (see section 8.4.1 and 10.1.5 eq.10.17a) and rises rapidly thereafter, which complicates the estimation of the cross section in that region.

*The symbol '⫫' is used statistics to denote that two random variables are independent. Here, I borrowed it to mean that a parameter is independent from another (analytically, not probabilistically).

†Caused by annihilation of the phase shift from the s-wave at a non-zero low electron energy.

For molecules, the necessity to include rotational excitations significantly complicates the derivation of cross sections. The least problematic case is given by hydrogen due to the higher energies of rotational excitation. The presence of open inelastic channels blurs the uniqueness between a given set of cross sections and measured transport parameters. A non-negligible adjustment of cross sections can result in an overall change of calculated transport parameters that stays within the experimental uncertainty. Then, additional criteria are needed in order to determine whether a cross section is truthful or not. Notwithstanding those difficulties, cross sections for momentum transfer and rotational excitations of H_2 and N_2 were derived from numerous swarm experiments [266, 305], which served as a basis for constructing cross section databases at lower energies. Additionally, swarm analyses may also enable a derivation of attachment rates and reaction rates that help to derive inelastic cross sections related to those processes. A review of cross sections derived from swarm and beam experiments is given by Buckman and Brunger [131] and reveals a good overall agreement for a variety of noble gases and light diatomic molecules.

The merit of swarm experiments extends farther beyond the possibility to derive cross sections: they represent a starting point for the assessment of constructed sets of cross sections [23, 24, 435]. Townsend's first ionisation coefficient α_i exposed above is not used for deriving cross sections* but is an important indicator for testing whether a set of inelastic cross sections, ionisation in particular are consistent with the exponential multiplication of electrons in gases under high electric fields.

A more detailed review of swarm experiments and measurements of swarm transport parameters is available in Hunter and Christophorou [411] and a succinct review is given by Phelps [748] for the subsequent derivation of cross sections. We now move to measurements of optical emissions in relation to electronic excitations of molecules.

7.3.2 Optical Emissions

A competing way to determine electron collision cross sections for electronic excitations is through optical emissions. If a beam of electrons is passed through a gas, the molecules that have been excited will de-excite either through spontaneous emission or inelastic collision with other particles. As explained in Trajmar and Nickel [940, p.84-6], if we measure the rate of photons that match a certain transition in the spectrum of the molecule, we may infer the deexcitation rate of molecules corresponding to that transition, and thereby their *line* excitation cross section through electron impact.

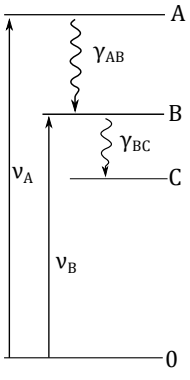

Because of photon emission/absorption, the mechanism populating an excited level of a molecule is not exclusive to electron impact excitations. Indeed, as represented in the scheme beside, a state B could also be reached from a radiative deexcitation producing a photon γ_{AB} from a higher-lying state A that was also produced by electron impact excitation at a rate ν_A, or itself coming from a deexcitation of an even higher state. The populating mechanisms $A \to B + \gamma_{AB}$ are called *cascade* contributions. Similarly, the state B may deexcitate radiatively to any optically reachable state C below, so that all the photons corresponding to these possible transitions are indicators or the presence of B. In order to trace the original presence of the species B from electron impact excitations, one must include all $B \to C$ branches and remove all $A \to B$ cascades [319, p.457:§II.A.4].

*A two-term approximation to Boltzmann's equation ceases to be accurate at the high electric fields ($\gtrsim 100\,\mathrm{Td}$) required to enable electron impact ionisation. A more accurate method is needed to calculate the electron velocity distribution under such anisotropic conditions.

Concretely, the electron beam of density flux J_e "pumps" up molecules at an initial state i in a gas of density n_i, to a multitude of excited states. Among the multiple deexcitations (due to spontaneous emission) that occur in the gas from those excited molecules, one can define a *line* excitation cross section Q_{BC} for the deexcitation process $B \to C$. This cross section Q_{BC} is in direct relation [940, p.86] with the measured photon flux Φ_{BC} through:

$$Q_{BC} = \eta \frac{\Phi_{BC}}{J_e n_i V} \tag{7.9}$$

The volume interaction between electrons and molecules in state i is idealised as V. The correction factor η accounts for the detection efficiency of photons and the geometry of the problem [284, §II.D], since photons are measured only in a solid-angular element $\Delta\Omega$. If the emission of photons is polarised, (i.e. anisotropic), then the correction for the photon flux is more elaborate [942, p.436]. Thus Q_{jl} is the ratio of an emitted flux of photons Φ_{BC} (per unit time) to $J_e n_i V$: the flux density of excitations of the $n_i V$ gas molecules, induced by an electron beam of flux density J_e (per unit time per unit area).

We quote the very astute physical interpretation of Q_{BC}:

Filippelli *et al.* [284, p.6:§C]

> Physically, Q_{BC} is the number of $B \to C$ photons/second emitted per unit beam length, per unit electron flux, and per unit target gas density.

The *direct* excitation cross section Q_B^{d} of the state B can be derived when all relevant deexcitations Q_{BC} and Q_{AB} cross sections are known [319, eqs.(30-31)]:

$$Q_B^{\mathrm{d}} = \underbrace{\sum_{C<B} Q_{BC}}_{\text{apparent}} - \underbrace{\sum_{A>B} Q_{AB}}_{\text{cascade}} , \tag{7.10}$$

where the first term on the right without the cascade (second term) is called the *apparent* excitation cross section to state B. In practice, one does fortunately not need to measure all $B \to C$ photon fluxes if the branching ratio ζ_{BC} for one of the lower C states is known through the Einstein coefficients for spontaneous emission [940, eq.(3)].

There are a few additional phenomena that may distort the presently idealised derivation of cross sections from optical measurements. They may be summarised as [284, 942, §II.A, §3.2:p.437]:

1. Collisional quenching*: if the inter-molecule collision rate is high (dense or hot gases), a non-negligible portion of an an excited specie B may be removed through inelastic non-radiative collisions which leave no visible trace a thus induce a systematic underestimation [178, p.373–4].

2. Slow decay: if the lifetime τ_{ij} of the emission monitored $i \to j$ is too long, even in sparse gases, the molecules might travel away from the interaction region and complexify the geometry linked to the detection of optical fluxes.

3. Radiation trapping: this bridges the gap between slow decay and collisional quenching. If the density of the gas is high and if the transition to the ground state is intense, then

*In addition to quenching through collisions, if the excited state is above the dissociation or ionisation threshold, the target may predissociate or autoionise without emitting radiation.

the absorption rate of the emitted photons might be non-negligible. Photons that are reabsorbed then re-emitted (up to several times) might lose their way to the detector for three reasons, the first two are from collisional quenching (increased risk) and displacement from the interaction region (problem equivalent to slow decay). The third comes from the fact that every time the photon is absorbed, the excited molecule might decide to deexcite through a different transition. All those three issues reduce the detection rate of the photons monitored.

4. Subsequent electron excitations: this is the sibling of collisional quenching but through electrons. It is always the least problematic point, since the probability that other electrons interact with previously excited species in the target is low when the gas density and electron beam fluxes are low.

5. Unsteady gas state: if the renewal of the gas in the collision chamber is slow, the measurements should not be performed for a period long enough to permit an accumulation of metastable states in the gas. For this, it is usually better to use a gas beam instead of static gas chamber.

Overall, the derivation of cross sections from photon detection yields results with larger uncertainties than direct measurement of electron or produced species. A comprehensive review of the optical methods for measuring cross sections is given by Filippelli *et al.* [284].

We now move to direct detection methods of electrons or ion products.

7.3.3 Static Gas

When the collision chamber in an experiment is filled uniformly with a gas, the electron beam interacts throughout the whole path it traverses before entering the detector. The derivation of cross sections requires a careful characterisation of the interaction volume idealised as the product of the area of the beam S and the path length l. There are essentially three types of beam experiments in a static gas chamber:

- Beam transmission
- Absolute cross sections
- Ion collection

Beam transmission

Historically, the earliest beam experiments consisted of measuring the transmitted flux of electrons that straightly traversed the chamber [28, 765]. The scattering probability per unit length of an electron traversing an infinitesimally thick $\mathrm{d}l$ patch of gas is given by the product $n_{\mathrm{gas}}\sigma_{\mathrm{tot}}\,\mathrm{d}l$, with the total scattering cross section σ_{tot}. Thence, the attenuation of an electron beam of current I_{in} over a total length l is straightforwardly given by the Beer-Lambert law [942, eq.(13)]:

$$I_{\mathrm{out}} = I_{\mathrm{in}} \exp(-n_{\mathrm{gas}}\sigma_{\mathrm{tot}} l) \,, \tag{7.11}$$

which can be interpreted also as the probability that no (scattering) event occur for a Poisson process with a parameter $\lambda = n_{\mathrm{gas}}\sigma_{\mathrm{tot}} l$.

The simplicity of this picture is, like in any experiment, torn by imperfections in the conditions [942, p.431:eq.(9)].

- Angular resolution: The detector is not a point, its distance from the end of the interaction volume and angular acceptance $\delta\Omega$ imposes a limit on the discrimination between slightly scattered and unscattered electrons. A finite angular resolution implies that the attenuation in (7.11) is measured for an *effective* cross section $\sigma_{\text{eff}} < \sigma_{\text{tot}}$ which is always slightly inferior to the total cross section.

- Detector response: the detection efficiency may vary significantly with the electron energy and the energy resolution (of the detector).

- Multiple-scattering: If the gas is dense, an electron might have a chance to scatter multiple times in the interaction volume. This is not necessarily a problem unless a scattered electron scatters back again into the direction of the beam. Its interaction with the medium will be concealed unless the energy resolution of the experiment allows to discriminate electrons that lost energy.

- Background signal: beyond multiple scattering, stray electrons reflected from the walls and guided by residual electric/magnetic fields might contaminate the detector with a background noise.

- The electron beam is not mono-energetic, its spectral width reduces the resolution of resonant peaks as, for instance, in the experiments of Kennerly [488] and Szmytkowski *et al.* [900].

- The initial divergence in the electron beam transforms the cylindrical interaction volume into a cone. An electron scattered withinside the cone will thus still be detected.

- Any spatial inhomogeneity in the gas and temporal fluctuations in the electron beam will induce uncertainty in the measurement.

These imperfections can be addressed by transforming the simple formula (7.11) into a line integral along the path described by the position x of the electron in the volume interaction as [942, p.431:eq.(9)]:

$$I_{\text{out}} = \int \frac{\mathrm{d}J_{\text{in}}}{\mathrm{d}\varepsilon_0}(\varepsilon_0) \exp\left(- \iint\limits_{\Omega_{\text{out}}(x)} n_{\text{gas}} S(x,\varepsilon_0) \frac{\mathrm{d}\sigma_{\text{tot}}}{\mathrm{d}\Omega}(\varepsilon_0)\, \mathrm{d}^3x\, \mathrm{d}\Omega \right) \mathrm{d}\varepsilon_0 \,, \tag{7.12}$$

when the beam is characterised by an energy distribution $\mathrm{d}J_{\text{in}}/\mathrm{d}\varepsilon_0$ and a geometrical distribution $S(x,\varepsilon_0)$, and the angular volume $\Omega_{\text{out}}(x)$ corresponds to all the directions that the electron may take from point x that will not lead into the detector.

Those issues can be circumvented with the time-of-flight technique which correlates the time distribution and energy of electrons emitted and detected one at a time [942, p.433-4:§3.1.3]. Measurements of total cross sections based on the timing technique give the highest accuracy.

Absolute Scattering

The beam attenuation method in a static gas chamber can also be used for measuring scattering into a certain solid angle. In that case, the detector is placed not directly opposite facing the incident beam but moved at a certain angle θ. A double slit system enables to delimit the overlap volume $S \times l$ whence electrons that are scattered can enter into the detector as schematised in figure 7.3.

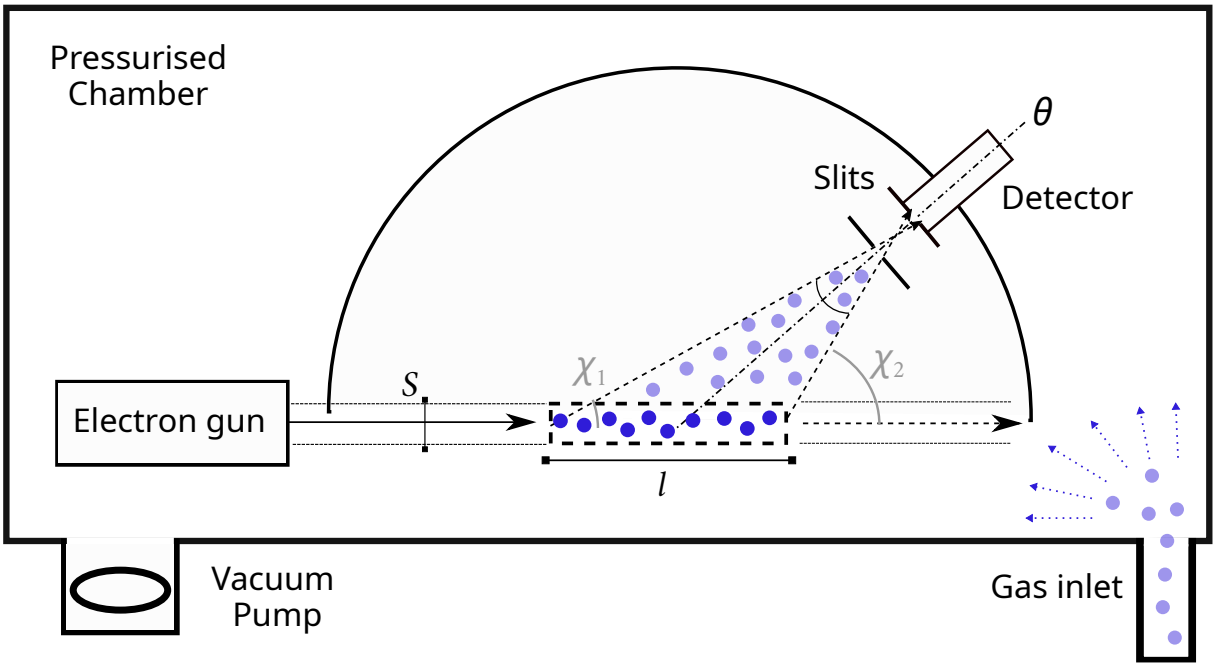

Figure 7.3: Experimental setup for absolute electron elastic scattering in gases based on Bromberg [113, fig. 1].

The flow of electrons entering the detector is given by an integral over the whole overlap volume $S \times l$ and over a certain solid angle volume $\delta\chi(x,s)$ around θ of the DCS which depends on the position (x,s) of the electron in the overlap volume [113, 942, p.3914–5:eq.(4), p.458:§4.2:eq.(31)]:

$$I_{\text{out}} = \iint_{l,S} \int_{\delta\chi(x,s)} J_{\text{in}}(s) \mathrm{e}^{-x\sigma_{\text{tot}}n_{\text{gas}}} \frac{\mathrm{d}\sigma}{\mathrm{d}\Omega}(\chi) n_{\text{gas}} \mathrm{e}^{-b\sigma_{\text{tot}}n_{\text{gas}}} \,\mathrm{d}\chi \,\mathrm{d}x \,\mathrm{d}s \tag{7.13}$$

The coordinate s is two dimensional and should be chosen suitably according to the geometry of the beam's transverse section S. The first exponential represents the attenuation of the electron beam from the source to the longitudinal coordinate x at which it is scattered. The second is the attenuation on the way into the detector of path length $b(x,s)$ which can be found from a geometrical relationship to the coordinates in the volume. At last, the integral over $\delta\chi(x,s)$ represents all the directions that lead straight into the detector when scattered from a position at (x,s). To be more precise, one should also account (i) for the possibility of multiple collisions that fortuitously scatter into the detector and (ii) for the energy distribution in the beam as given by (7.12) above.

The uncertainties on the measurements stem basically from the limitations already exposed for the beam transmission above. The advantage of this technique is that a stable and uniform distribution of the gas is attainable in the chamber. Beam attenuation can be measured by varying the pressure inside the chamber and extrapolating a semi-logarithmic curve [113, fig. 8]. Working under lower pressures reduces the probability of contamination by multiple scattering. Additionally, a spectral filter can be used to reduce the signal of stray electrons and those who endured collisions of a different energy loss that on the process monitored. Signals are less contaminated by background noise when operating at higher energies ($> 100\,\text{eV}$) where electrons are less vulnerable to larger scattering rates and deviation from electromagnetic fields. Direct normalisation of the cross section can then be performed directly by considering the geometry

of the problem as input to (7.13) and the instrumental characteristics (beam width and density distribution, detector response and acceptance angle).

Under well-determined experimental conditions, this method enables to measure absolute differential cross sections at high electron energies (> 200 eV) [113] with great accuracy $\lesssim 4\,\%$ [114]. The absolute measurements of Bromberg [113–116] served as a normalisation reference for many posterior works [206, 397, 453]. Those latter experiments did not need to measure the absolute value of the cross section, just the relative variation with angle. Normalisation enables one to use gas beams instead of static gas chamber which are better suited for electron scattering at low and intermediate energies from 1—100 eV. This will be described after the next subsection, which treats measuring accurate ionisation cross sections.

Ion collection

When measuring cross sections for total ionisation, the chamber is equipped with parallel plate electrodes around the interaction volume that collect the ions produced by electron impact. As opposed to transmission beam experiments, the measurement of ionisation is conducted under extremely low pressures. To give an idea, total scattering experiments operate with pressures around a few mTorr [489, 708, 900], whereas total ionisation experiments maintain the pressure below 1 mTorr [814] between 50—100 µTorr [768] or as low as 3 µTorr [888]. Under these conditions, the ionisation cross section may be found by the following ratio between the electron I_e and the ion I_i currents [319, eq.(27)]:

$$\sigma_\mathrm{ion} = \frac{I_\mathrm{i}}{I_\mathrm{e}} \frac{1}{n_\mathrm{gas} l} \,. \tag{7.14}$$

This relies on the assumptions that:

- All ions from the interaction volume are effectively collected, and only these ions,
- Secondary electrons produced by ionisation do not provoke more ionisation (at least inside the interaction volume whence the ions will be collected),
- A steady pressure and reliable estimation in the chamber (more difficult at lower pressures)

With a mass spectrometer, the experiment may further discriminate ions with a different charge-to-mass ratio thanks the acceleration of the ions and a time-of-flight analysis [888]. This allows to estimate partial ionisation cross sections of singly ionised molecules AB^+, singly ionised atoms A^+ and B^+ and multiply ionised products. When multiple ionisation is non-negligible, one may additionally be interested in distinguishing [596, p.2] the (i) *counting* cross section which simply counts the number of ions regardless of their charge, and the (ii) *gross* total $\sum i \cdot \sigma_i$ which weighs each partial cross section σ_i by the charge i of the ions produced.

Owing to the relative simplicity of experimental conditions, ionisation cross sections are among the best known measurements in scattering experiments with uncertainties as low as 3–5 %.

7.3.4 Crossed Beams

Not all gases are well behaved as inert ones. The static gas chamber cannot be used for corrosive, ionic, free radical and metastable excited targets. Furthermore, electrons at lower energies scatter more and become stray electrons which contaminate the signal measured by the detector. Instead, the gas can be injected (and prepared) through a nozzle to form a beam crossing electrons at right angles as sketched in 7.4.

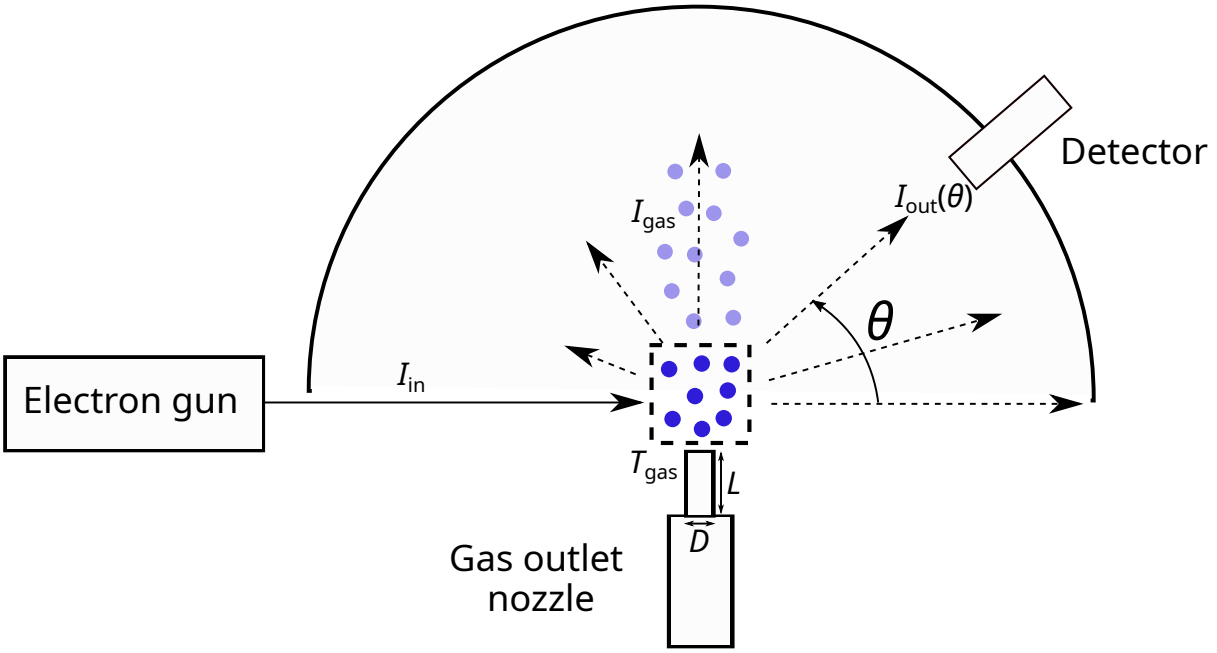

Figure 7.4: Experimental setup for cross-beam measurements of DCS relative to a reference.

Due to the necessity to properly control the characteristics of the target beam formed, this technique is more recent. It elegantly bridges the gap between very low-energy swarm experiments and high-energy static gas beam measurements. The normalisation procedure of the cross-beam configuration is further complicated by the non-uniform density distribution and geometry of the target beam. This is why most of cross-beam experiments measure *relative* differential cross sections that are scaled to an absolute reference with the relative flow technique of Srivastava *et al.* [872].

Using the same experimental apparatus and maintaining the conditions identical, one first measures DCS with a reference gas whose absolute DCS value is known accurately (typically helium [771]). Then, one performs the measurements just by replacing the reference by the target gas in the beam. The ratio of an unknown DCS to a reference DCS* can then be related to the ratios of measured electron and gas flow intensities [834, p.467:eq.(44)]:

$$\frac{\mathrm{DCS}(\varepsilon,\theta)}{\mathrm{DCS}^*(\varepsilon,\theta)} = \frac{I_{\mathrm{out}}(\varepsilon,\theta)}{I^*_{\mathrm{out}}(\varepsilon,\theta)} \frac{I^*_{\mathrm{gas}}\sqrt{M^*}}{I_{\mathrm{gas}}\sqrt{M}} \,. \tag{7.15}$$

It is a proportionality based on the flow rate of the target I_{gas} and reference I^*_{gas} gases and their respective molecular masses M and M^*. Qualitatively, the molecular masses scale the average velocities ($\bar{v}_{\mathrm{gas}} = \sqrt{3k_{\mathrm{B}}T_{\mathrm{gas}}/M}$) at a fixed temperature T_{gas}. Then, the target density in the beam scales inversely to the factor $I_{\mathrm{gas}}\sqrt{M}$.

There are several assumptions underlying the relative flow relationship (7.15) [700, §2]:

- Electron beam: the electron beam current is identical and unaffected by changing the gas.
- Background: the noise from stray electrons is identical for both gases.
- Detection efficiency: the detector's response function, angular and energy resolution may all depend strongly on the energy of the electron to be detected. Thus one needs to ensure that the energy characteristics of the scattered electron beam are kept constant.

- Gas stream: the flow regime of both gases based on the Knudsen number (mean free path divided by nozzle length L or diameter D) must be similar so that the molecules' density distribution in the beam may be scaled with the simple law in (7.15).

- Path correction: the angular dependence of the DCS for the reference and target gases may differ locally, which entails that the DCS ratio in (7.15) actually varies slightly over the acceptance solid angle $\delta\Omega$. This is, however, a very minor effect except near resonances [942, p.466].

The sensitivity of the detector's efficiency with electron energy implies that normalisation of cross sections from inelastic processes must be conducted in two steps. The first is the analysis of electron energy loss spectra and therefrom, calculation of ratios of excitation peaks on the elastic peak which is located at virtually zero energy. The second, is the normalisation of the elastic cross section from the relative flow technique. On a few occasions [460], a shortcut (bypassing the determination of elastic scattering) was used to normalise inelastic DCS directly to inelastic DCS with close energy thresholds of other atoms (He, Ne).

Measurements are limited to a certain angular range, usually from a few degrees up to no more than 160°. At smaller angles, the unaffected beam interferes with forward scattering; whereas backscattering measurement is hindered by the incident beam. It is worthwhile mentioning the recently developed magnetic angle changing technique by Zubek *et al.* [1014], which enables to separate the electrons backscattered from the incident beam and thus probe the full range of large angles up to 180° [644, 1015]. Two pairs of solenoids generate a localised magnetic field in the interaction region which curb the trajectory of the electrons passing through [see figure 3 of 19]. For more information, one can consult King [510].

The instrumental accuracy of cross-beamed experiments was greatly improved over time, notably through the work of Allan [17, 18] who largely focussed on the instrumentation.

Energy resolution is typically around ~ 50 meV [488, 841] at intermediate to low energies, but can be significantly worse (higher energy spread) at high and sub-eV energies. A resolution of 10 meV in the most accurate experiments [13, 344, 473] enabled to discriminate rotational excitations in N_2 in addition to H_2 [594, 873]. Experiments with higher resolutions (below 10 meV) at low energies (<eV) are underway [406]. At high energies, the resolution is relative to the incident electron energy [e.g. 0.3 % at 1 keV 396, p.65].

Angular resolutions are usually in the range 1–4° [731, table 1] at intermediate energies, but are significantly better at higher energies to be able to resolve scattering at forward angles [232, 453]. A good resolution is important when considering DCS with very sharp features such as critical minima in noble gases [651, fig. 3]. Apart from instrumental limitations, angular resolution is also limited by the necessity of maintaining a good signal-to-noise ratio. At high electron energies above 1 keV, the DCS is difficult to probe beyond 60° due to the very low signal of the scattered beam [e.g. 453]. Also, in doubly differential cross sections (from ionisation events) the angular acceptance can be as large as 10° [721], deteriorating significantly the precision of the data reported.

Because of these numerous aforementioned complications (and many not mentioned), experimental data from cross-beamed configurations have typically the worst uncertainties which roam around ~ $12 \mp 5\%$ [684, 838, 894, p.1231, p.2, p.926]. Sometimes they go up to 20–30 % [700, 871, 981, p.2160, p.1877, p.336] near minima and are often more optimistic than the disagreement between experimental values [check 288, figs. 1–2 and p.4403]. Due to the further necessity to rely on spectral deconvolution of peaks and ratios to elastic scattering, inelastic DCS from

crossed-beam are usually uncertain to 25–30 % [158, 351, 492, 898, p.1022, p.1387:table I, p.3797, p.11] and rarely better known than 20 % [897, p.2].

Normalisation is of course not restricted to the cross-beamed experiments. In the next two sections, we try to summarise the overall guidelines for calibrating the DCS measurements from a reference: (i) normalisation to an absolute scale, (ii) calibration of the energy of the electron beam, and the angle of scattering.

7.3.5 Normalisation

The measured signals in scattering experiments are count rates per unit time in a detector located at a certain angular position and covering a certain area equivalent to a solid angle. Ideally, the ratio of the deflected electron flux and the incident density flux is supposed to yield the absolute DCS as seen from the seminal equation (7.2) of scattering defined as a stochastic phenomenon. Notwithstanding, there are many issues that deform the ideal picture of scattering such as:

- Estimation of the beam fluxes
- Overlap interaction volume
- Background noise
- Limited resolution (angular, energetic)
- Detector response
- Gas state (pressure, temperature, beam shape)
- For data that need post-processing: spectral fitting and deconvolution introduce more uncertainty
- Other errors (human, operational, statistical, etc.)

It is not always feasible to properly characterise those sources of experimental discrepancy or uncertainty. To spare some strain on the experimentalists whose job is toilsome enough, an alleviating procedure is to conduct all measurements based on a well-known reference such as scattering by helium [693, 771]. Prior knowledge about this reference and an assured linear scalability of the operational conditions enables one to recur to normalisation (discussed already in the previous section eq.7.15).

Before accurate reference values were available from other gases, an alternative to normalisation was to derive absolute value for elastic scattering from accurate measurements of total CS [593, 938, 972]. This presented the disadvantage of having to rely on accurate determination of the proportion of all other inelastic processes at a given energy.

With time, more accurate and resolved elastic DCS became available, so that some older datasets were renormalised in subsequent reviews [see for instance 941, p.239:table 4-bottom and p.267:table 26].

In cross sections for excitation processes, most experiments measure inelastic-to-elastic ratios from integrals of peaks observed in an energy-loss spectrum as given for illustration in figure 11.32a. The proper identification of all processes contributing to an excitation in molecular gases is further complicated by the presence of multiple vibronic levels (see appendix D) forming a series of peaks that may drown under the noise level or may be superposed with bands pertaining to other transitions. To each vibronic excitation $a, v \to a', v'$ corresponds a peak centred on the average energy $\varepsilon_{a'v'} - \varepsilon_{av}$ and broadened by temperature, rotational sublevels and the

energy-time uncertainty of the level. Some very close lying transitions have overlapping peaks, in which case a decomposition must be done to identify the contribution proper to each process. A good example is the $X(v = 0 \to 5)$ vibrational excitation of O_2 with $X \to a\ ^1\Delta_g$ between 0.9–1 eV [599, p.397:fig. 1].

When comparing inelastic DCS from molecules, it is fundamental to examine how many bands could be identified and included in different works [for instance see 1012, table 1 and §3.3–4]. Furthermore, some works [492, 624, table II, table I] can use predicted Franck-Condon factors to account for all higher vibronic levels drowned in the background noise. Once the absolute value of the elastic cross section is determined, the inelastic DCS is put to absolute value from the ratio to the elastic peak. This entails that uncertainties of measuring inelastic DCS are usually a few percent (~5 %) larger than elastic ones.

Normalisation can be applied at 3 different levels, the asterisk $*$ represents a reference point (fixed). One measures the scattering signal $S(\varepsilon,\theta)$ of the unknown gas and compares it to the signal $S^*(\varepsilon,\theta)$ measured with the reference gas.

1. $\dfrac{\mathrm{d}\sigma}{\mathrm{d}\Omega}(\varepsilon,\theta) = \dfrac{\mathrm{d}\sigma^*}{\mathrm{d}\Omega}(\varepsilon,\theta) R_{\mathrm{d}\sigma}(\varepsilon,\theta) \qquad \text{where} \quad R_{\mathrm{d}\sigma} \equiv \dfrac{S(\varepsilon,\theta)}{S^*(\varepsilon,\theta)}$, The most meticulous one is to normalise each DCS measurement performed at a certain angle θ to the corresponding value at the same angle θ (and same energy ε) of a reference $\mathrm{d}\sigma^*/\mathrm{d}\Omega$. This is common for inelastic DCS from electronic excitation in crossed-beam experiments based on energy loss spectra as, for instance, in Brunger and Teubner [122], Cartwright *et al.* [158], and Khakoo *et al.* [491] etc. For clarity, some references may thus report tables of ratios $R_{\mathrm{d}\sigma}(\varepsilon,\theta)$ of differential cross sections [870, 872, tables I, II] (most often to helium or molecular nitrogen).

2. $\dfrac{\mathrm{d}\sigma}{\mathrm{d}\Omega}(\varepsilon,\theta) = \begin{cases} \dfrac{\mathrm{d}\sigma^*}{\mathrm{d}\Omega}(\varepsilon,\theta^*) R_{\mathrm{d}\sigma}(\varepsilon,\theta^*) S(\varepsilon,\theta) & \text{where} \quad R_{\mathrm{d}\sigma} \equiv \dfrac{S(\varepsilon,\theta^*)}{S^*(\varepsilon,\theta^*)} \\ \sigma^*(\varepsilon) R_\sigma(\varepsilon) S(\varepsilon,\theta) & \text{where} \quad R_\sigma \equiv \dfrac{\int S(\varepsilon,\theta)\,\mathrm{d}\Omega}{\int S^*(\varepsilon,\theta)\,\mathrm{d}\Omega} \end{cases}$

At a higher level, one can keep DCS shapes $S(\varepsilon,\theta)$ intact and normalise them at each energy ε. A connection point must be chosen for normalisation. This could be a value at a specific angle θ^* which can be at smaller ~30° when the scattering is forward peaked at higher energies or more traditionally at 90°, which is a trusted range with minimal signal contamination. This procedure is more common when measuring relative elastic DCS such as in Daimon *et al.* [206], Kambara and Kuchitsu [475], and Wakiya [972]. Then the calibration depends on the ratio $R_{\mathrm{d}\sigma}(\varepsilon,\theta^*)$ of the signals from the unknown S and reference gas S^* at θ^*.

Another possibility, in order to avoid depending on the uncertainty of one point θ^* only, is to normalise to the integrated DCS $\sigma^*(\varepsilon)$ at the energy ε.

3. $\dfrac{\mathrm{d}\sigma}{\mathrm{d}\Omega}(\varepsilon,\theta) = \sigma^*(\varepsilon^*) R_\sigma(\varepsilon^*) S(\varepsilon,\theta) \qquad \text{where} \quad R_\sigma \equiv \dfrac{\int S(\varepsilon^*,\theta)\,\mathrm{d}\Omega}{\int S^*(\varepsilon^*,\theta)\,\mathrm{d}\Omega}$

At the coarsest level, all measurements can be carried systematically in the same experimental conditions, varying only the energy of the electron beam and the angle of the detector. Then, a reference is chosen at a specific energy ε^* for normalising all measured values. This would never be done for DCS but only for techniques measuring ICS as in optical emissions or detection of excited species like in Mason and Newell [633] and Zubek [1012, table 1, figure 3]. If the measurements are consistent throughout the whole energy range, these uniquely normalised sets are most easy to handle in updating reviews.

Normalisation for unstable atomic targets such as oxygen and nitrogen presents additional difficulties. Atoms are generated through dissociation of molecules most of the time by microwave discharges. One needs to characterise the relative ratios of species produced by the discharge. In addition to the dissociation fraction of atoms/molecules, it is also important to keep notice to the presence of metastable states of atoms and molecules, and eventual ions. The dissociation fraction η_{D} may be estimated by comparing the scattering signal from a known molecular excitation $*$ when the discharge is on (I^*_{on}) and off (I^*_{off}), respectively [476, p.2653:eq.(3)]:

$$I^*_{\mathrm{on}} = (1-\eta_{\mathrm{D}})I^*_{\mathrm{off}} \Leftrightarrow \eta_{\mathrm{D}} = 1 - \frac{I^*_{\mathrm{on}}}{I^*_{\mathrm{off}}} \tag{7.16}$$

This fraction does not give directly the density ratio of atoms A to parent (homonuclear diatomic) molecules A_2 because it depends also on the velocity distribution which, assuming thermal equilibrium, gives [476, p.2664:appendix eq.(A.8)]:

$$\frac{n_A}{n_{A_2}} = \frac{\sqrt{2}\eta_{\mathrm{D}}}{(1-\eta_{\mathrm{D}})}\,, \tag{7.17}$$

There are other ways to measure the atom/molecule ratio [939, p.77–9], such as mass-spectrometry of the target beam [984], or energy-loss spectra at forward angle scattering and high electron energies with the help of known optical oscillator strengths [226].

Once this ratio n_A/n_{A_2} is known, then the DCS measurements of a well distinguished inelastic process from an atom may be normalised to the DCS of a well resolved inelastic process from a molecule. More information about dissociated mixed atomic-molecular beams can be found in the review of Johnson *et al.* [462, p.594–7] and references therein. Elastic DCS contain the superposition of both atomic and molecular collisions. To derive atomic DCS, one must subtract the contribution from molecular DCS [984].

7.3.6 Calibration

It is beyond the scope of this chapter to discuss the lengthy procedures involved in calibrating an instrument. Here, we simply ought to mention how DCS are calibrated on the two variables: electron energy ε and scattering angle θ.

Angular calibration is usually the least problematic. The most common procedure is to record the signal measured over a small angular range in the forward direction. This should give, for unpolarised beams, a symmetric profile whose centre determines the position of 0°. Typically, systematic uncertainties in angular position are around ~ 1—2° [644, p.3]. This should be also taken into account, in addition to the value of DCS, when comparing experimental data.

The most widespread method of calibrating the emitted energy in the electron beam is by means of very narrow, conspicuous and peculiar features in the transmission flux. One can for example use widely known resonances of noble gases such as $\mathrm{Ar}^-\,(^2P_{3/2})$. Instead of having to rely on a reference gas, a more straightforward way is to directly use features present in the molecule studied [512, §3.2], such as the $\mathrm{N}_2^-\,(R\,^2\Sigma_g^+)$ resonance at 11.497 eV [407].

Some discrepancies may also be solved by revisiting the calibration on the incident energy instead of indicting the cross section's normalisation. Nevertheless, when no prominent feature is seen, it is more difficult to determine the systematic shift in energy position.

Regrettably, we may not consecrate more time to the experimental world of determination of cross sections in order to focus our attention on their calculation from quantum theory. Our objective was to catch a glimpse of the reality behind the rows and columns of numbers that we will use as guidelines to assess our efforts in computing our own cross sections. The rest of this chapter will be a preparation to the theoretical framework for computing DCS.

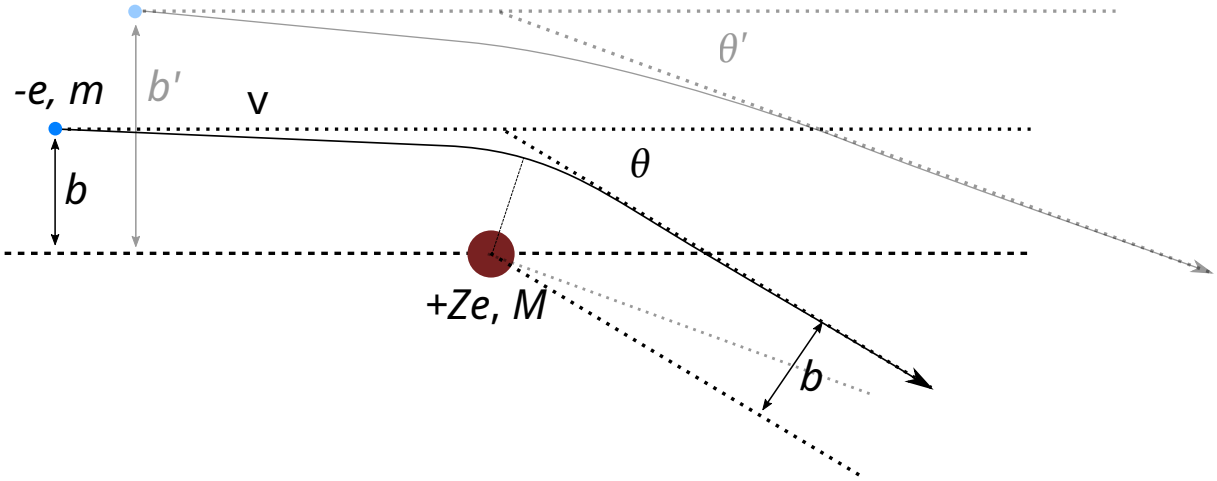

Figure 7.5: Classical Rutherford elastic scattering at θ of an electron by an atomic nucleus at an impact parameter b.

7.4 Classical and Quantum Approaches

In the first part of this thesis chapter 2.2, we considered electrons classically: as point-like elementary charges that are swayed by electromagnetic fields and instantly bouncing off molecules. While motion is deterministic, the outcome of collisions is stochastic so one might wonder where does this stochasticity emerge from.

> In this section we expose the connection point between classical and quantum mechanics in scattering processes through the impact parameter b.

We exemplify this with the most widespread case of Coulomb or Rutherford scattering: a collision between an electron and a point-like atomic nucleus.

7.4.1 Classical Rutherford Scattering

An electron (of charge $-e$ and mass m_e) coming at an initial speed of v from an infinite distance passes near an atomic nucleus of charge $+Ze$ and mass M_n. The shortest distance between the straight asymptotic trajectory of the incident electron and the nucleus is known as the *impact parameter* and designated as b. The situation is sketched in 7.5.

The full motion of the electron in a Coulomb field may be resolved analytically*. It is a hyperbolic curve with an exiting asymptote at a deflection angle of $\theta \in [0, \pi]$. The full symmetry of the trajectory is due to the spherical symmetry of the potential. For time-independent potentials, the asymptotic symmetry is a consequence of the conservation of the angular momentum $\mathbf{L}$ [147, p.15:eq.(1.34)]:

$$\mathbf{L} = \mathbf{b} \times m_e \mathbf{v} \, . \tag{7.18}$$

The correspondence between b and θ is univocally determined through [697, p.126:eq.(5.15)]:

$$\tan(\theta/2) = -\frac{Ze^2}{4\pi\epsilon_0 m_e \mathrm{v}^2 b} \tag{7.19}$$

*Technically, it should be described in the relative centre of mass frame with a reduced mass $\mu_e \approx m_e$. We omit it here since we neglect the of lightness of the electron compared to the heaviness of atomic nuclei.

The negative sign comes from the attractiveness of the Coulomb potential which deflects electron 'inward' instead of 'outward' for repulsive potentials. Relation (7.19) enables us to further establish a differential relationship between $\mathrm{d}b$ and $\mathrm{d}\theta$. This binds all electrons inciding* into an infinitesimally thick annulus between b and $\mathrm{d}b$, to a zonal stripe between θ and $\theta + \mathrm{d}\theta$.

$$\frac{\mathrm{d}b}{\mathrm{d}\theta} = -\frac{Ze^2}{4\pi\epsilon_0 m_\mathrm{e}\mathrm{v}^2}\frac{-1}{2\sin^2(\theta/2)} \,. \tag{7.20}$$

From there, we can express the differential cross section as the ratio between the area of the annulus and the solid angle covered by the zonal stripe [147, p.17:eqs.(1.45–6)]:

$$\frac{\mathrm{d}\sigma_\mathrm{Rutherford}}{\mathrm{d}\Omega} \equiv \frac{b\,\mathrm{d}b2\pi}{\sin\theta\,\mathrm{d}\theta 2\pi} = \left(\frac{Ze^2}{4\pi\epsilon_0 m_\mathrm{e}\mathrm{v}^2}\right)^2 \frac{1}{4\sin^4\frac{\theta}{2}} \tag{7.21}$$

We recognise the fundamental (non-relativistic) Rutherford differential cross section [697, p.126:§5.3] which scales inversely to the fourth power of momentum transfer $q = 2p\sin\theta/2$, where $p = m_\mathrm{e}\mathrm{v}$ is the kinetic momentum of the incident electron.

The infinite range of the Coulomb potential implies that there is no maximal finite value for the impact parameter for which the deflection angle is at 0°. Thus, the momentum-transfer cross section is theoretically infinite, which is unwieldy for representing the interaction of electrons with ions. In reality, there is always a spatial scale over which the Coulomb field is screened by the presence of other charges. For ions in a plasma, it would correspond to the Debye length. This upper bound for the impact parameter b_max is equivalent to a lower bound on the angle of scattering θ_min and gives rise to the well-known Coulomb logarithm in plasma physics (p. 80).

The foundational importance of this long-range Coulomb scattering brings us again at the crossroads between the first and second parts of this thesis, but also at the meeting point of classical against quantum mechanics. It is indeed a remarkable property of the Coulomb potential that the cross section in classical mechanics is the same as in the exact quantum approach and also under the first Born approximation [474]. We all have heard nonetheless of the limitations of classical mechanics, notably the failure to encompass the Heisenberg principle of uncertainty: an electron cannot be both known to dash at a velocity $\mathbf{v}$ and at a perpendicular distance b.

For more insight and examples about the classical scattering of a particle in a potential, the reader may find a wealth of information in practically any textbook about scattering, notably Canto and Hussein [147, p.14–22] or Newton [697, p.127–132]. In the following section, we briefly expose the framework that describes scattering in the quantum mechanical approach.

7.4.2 Quantum Plane Wave Scattering

In the formalism of quantum mechanics, the state of an electron is described not by a set of values for each parameter (position, velocity), but by a vector state $|\psi\rangle$ from which those parameters (and their probabilities) can be extracted with operators. A decent introduction to this formalism can be found in dedicated textbooks such as [797, chapter 1] for a standard introduction or [823] for a more philosophical insight.

Here, the objective is to highlight the basic concepts that underlie the quantum description of scattering and relate the differential cross sections as defined in an idealised experiment (7.3 and 7.2), to a mathematical object (7.28) exposed below in this subsection.

*'Incĭděre' in Latin : 'to fall into', it existed in older English but meant 'to cut into' or 'incise' because of the palatalisation of 'd' to 's'. In spoken English, it interferes with the homophonic 'inside', but we could resurrect its use in written English; 'impinge' is fine on a few occasions, but sounds too funny in general.

1. Uncertainty. Elementary notions of quantum mechanics reveal to us that particles – electrons in our case – are wave packets propagating at a group velocity $\mathbf{v}_g$ corresponding to the classical velocity but with a certain spread both in position and momentum spaces. The most rigorous way to model scattering microscopically is to take the conceptually elegant but mathematically hefty approach of time-dependent wave-packet propagation. Nonetheless, in the end, since we yearn to obtain a statistical description of electron-molecule scattering, instead of treating individual particles flowing one at a time, we may consider the mathematical limit at which the wave packet becomes so extended in space that it represents a continuous monochromatic beam of electrons of infinite (spatial) width that diffuses in the field generated by one molecule.

> The presently adopted quantum mechanical approach consists in a time-independent scattering of a plane wave (the electron beam) in an interaction potential (a molecule).

The notation for a plane wave of wavector $\mathbf{k}$ is $|\mathbf{k}\rangle$, representing a pseudo-state vector* in a Hilbert space. Mathematically, in $\mathbf{r}$ coordinate space, it is represented as an imaginary exponential:

$$\langle \mathbf{r}|\mathbf{k}\rangle = \frac{1}{(2\pi)^{3/2}} \exp(-\mathrm{i}\mathbf{k}\cdot\mathbf{r}) \,. \tag{7.22}$$

The wavelength λ of a plane wave is simply related to k by $\lambda = 2\pi/k$. The normalisation factor $1/(2\pi)^{3/2}$ comes from the requirement of orthonormality [922, §1-b:p.9]:

$$\langle \mathbf{k}'|\mathbf{k}\rangle = \frac{1}{(2\pi)^3} \int \exp(\mathrm{i}(\mathbf{k}'-\mathbf{k})\cdot\mathbf{r})\, \mathrm{d}^3\mathbf{r} = \delta_3(\mathbf{k}'-\mathbf{k}) \,, \tag{7.23}$$

where $\delta_3(x)$ is the Dirac peak in 3D space which is the product of $\delta(x_1)\delta(x_2)\delta(x_3)$ in a canonical coordinate space of the three-dimensional variable x.

The representation of a beam of electrons by a plane wave is evidently a mathematical idealisation that provides a convenient basis (plane-waves) from which an actual physical state is constructed. For a light introduction into this question, please consult Canto and Hussein [147, §1.6]. For a more comprehensive explanation, one can read Newton [chapters 6&7 of 697]. The most mathematically rigorous justification is elaborated in Taylor [922, chapter 3-e].

2. Discreteness. Another fundamental aspect of quantum physics is the one behind its etymology: the quantification of states. Formally, an electron's property (e.g. momentum or position) may not take any value distributed over a continuum, but may only take determined values (there can be a countable infinity). In the approach we shall take, the foremost one is the quantification applied to the *angular momentum* (7.18). The set of accessible values to the square of the angular momentum L^2 of a particle is composed of multiples of Plank's reduced constant $\hbar$ [956, §5.1.2:p.130]:

$$\text{Eigenvalues of}: \; L^2 \text{ are } \hbar^2\ell(\ell+1) \text{ with } \ell \in \mathbb{N}_0$$

$$L^2 Y_{\ell m} = \hbar^2 \ell(\ell+1) Y_{\ell m} \tag{7.24}$$

$$L_z Y_{\ell m} = \hbar m Y_{\ell m} \tag{7.25}$$

The eigenfunctions in the space representation of the operator L^2 are the well-known spherical harmonics $Y_{\ell m}$ with m being the projection quantum of the angular momentum on the z axis of a specified coordinate frame.

*It is not normalisable, but relates to the Dirac peak (7.23) instead.

Naively, this quantification would also imply that an electron, modelled as an infinitely wide plane wave, may only incide on a molecule at determined values of the classical impact parameter with the correspondence: $b = \sqrt{\ell(\ell+1)}\hbar/m_e v$. We see that very slow electrons $v \to 0$ impact the molecule either frontally $\ell = 0$ implying $b = 0$; or very far away $\ell > 0 \Rightarrow b \to \infty$. On the contrary, the available set of classical impact parameters densifies in space for faster electrons. Fast electrons may pass near molecules at many different distances, a situation which closely resembles the classical picture; whereas slow electrons may only be seen to pass at few distances. This can be related to the fact that electrons, as wave packets, spread over vaster regions of space when they are slower (longer wavelengths λ) than faster*.

One must however beware of simple analogies, since the impact parameter is not an observable quantity, while the angular momentum is [427, p.335:§ below eq.(4.74)]. They can aid our intuition but are unhelpful for drawing conclusions. In the next chapter, we will see how a plane wave elegantly decomposes into a sum of spherical waves, each with a determined angular momentum.

3. Indistinguishability. Unlike in classical mechanics where one could in principle identify the tracks of identically-looking particles and thereby distinguish them, in quantum mechanics, the observer is blind to the intricacy of what exactly occurs in a microscopic interaction between identical particles. In electron scattering, one can never be sure whether the electron that is scattered is the 'original' one that had incided on the molecule, or whether it has been ejected from an orbital and replaced. This leads to one of the most bemusing phenomena related to quantum physics: the Pauli principle [739] for electrons states that electrons in a system cannot occupy the same state. A consequence of this principle is that the total wavefunction of the electronic system must be antisymmetrical when two electrons are swapped in their respective states [398, §3.1.2].

In electron scattering, this means for example that the Mott cross section for the scattering of two electrons (presented in section 8.141) is markedly different from the classical Rutherford scattering between two charges seen previously in (7.21); which leads us to the next point.

4. Interference. The spectacular undulatory nature of matter was revealed in many experiments of which Davisson and Germer [212] is a prominent example of electron diffraction patterns in a crystal. If examined to the root, interferences in electron scattering arise from the principle of uncertainty in momentum and configuration space and from Pauli's exclusion principle. When we observe an electron, whichever, in a faraway direction at a determined position, we attempt, though unpurposefully, to simultaneously characterise its momentum and position which cannot be pinpointed together. Interferences emerge whenever:

i. A system is in a state A composed of various contributions identified as separate,†

ii. This system is observed in another state B which is not perpendicular to A (whose projection is non zero),

*Taylor [922, §3-d] offers a more rigorous analogy of the impact parameters between classical and quantum perspectives. A wave packet, which originally is centred at $b = 0$, can be offset to *any* distance $b \neq 0$, provided that the spatial spread of the packet is much larger that the size of the target. Then, the cross section in the quantum perspective is also an average over incident packets situated on a continuum of impact parameters $0 \leq b < \infty$. In our naive picture, it is rather better to say that the scattering at higher energies involves the partial waves of more angular quanta ℓ than at low energies. In inelastic collisions, the impact parameter b is connected to the inverse of the perpendicular momentum transfer in the collision [427].

†From a conceptual effort of our perception of reality, such as: "a diatomic molecule is a mixture of contributions coming from atom 1 and from atom 2"

iii. The phases and amplitudes of the separate contributions to A when projected on B are not anticorrelated so as to annihilate when summed together,

under those conditions, the probability given by the squared modulus of the amplitude has mixed terms which we identify as "interferences".

As an example, when scattering, our electron beam is in an obscure state given by $|\psi\rangle$ which can be expressed as a superposition of the incident plane wave $|\mathbf{k}\rangle$ with a scattered beam $|\psi_s\rangle$. The latter itself can be considered a superposition of different waves, such as radial waves, each associated with a spherical harmonic of a particular angular quantum ℓ and projection m on a determined axis: $|\psi_s\rangle = \sum_{\ell m} c_{\ell m}|\psi_{\ell m}\rangle$ (partial wave 8.4). Alternatively, it could be the superposition of waves scattered from different positions of the atoms in a molecule $|\psi_s\rangle = \sum_A \mathrm{e}^{\mathrm{i}\mathbf{k}_0\cdot\mathbf{R}_A}|\psi_A\rangle$ (independent atom approximation 8.5.3).

Suppose that we now have a detector able to measure electrons at a certain position $\mathbf{r}$ in the direction determined by the outgoing momentum $\hat{\mathbf{k}}' = \Omega$ of energy $\hbar^2 k'^2/2m_e$. We remember that the probability density of detecting an electron from the scattered wave at $\mathbf{r}$ is given by the square modulus of the projection:

$$\begin{aligned}|\langle\mathbf{r}|\psi_s\rangle|^2 &= \left(\sum_{\ell' m'} c^*_{\ell' m'}\langle\psi_{\ell' m'}|\mathbf{r}\rangle\right)\left(\sum_{\ell m} c_{\ell m}\langle\mathbf{r}|\psi_{\ell m}\rangle\right)\\ &= \sum_{\ell m}\underbrace{|c_{\ell m}|^2|\langle\mathbf{r}|\psi_{\ell m}\rangle|^2}_{\text{Pure Waves}} + \sum_{(\ell m)\neq(\ell' m')}\sum \underbrace{c^*_{\ell' m'}c_{\ell m}\langle\psi_{\ell' m'}|\mathbf{r}\rangle\langle\mathbf{r}|\psi_{\ell,\Lambda}\rangle}_{\text{Interferences}}\ .\end{aligned} \tag{7.26}$$

In addition to the sum of amplitude probabilities of 'pure' spherical waves, there are cross terms which do not necessarily annihilate and that can make a positive (constructive) or negative (destructive) contribution to the total probability of observing an electron at a given position $\mathbf{r}$. In classical mechanics, the probability of collecting an outcome from two independent phenomena would be the sum of individual probabilities. In quantum mechanics, the way electrons scatter (in different spherical harmonic patterns for the present purpose of illustration) cannot be considered independently. This is what is commonly meant as "interference".

There are however some very interesting cases where only a few or just a single spherical wave participates in the scattering of electrons. This is the case for example of resonant scattering of electrons with nitrogen molecules. Much is to be said about resonances. We defer this task to a later chapter's section 11.3. For the time being, we could profanely say that resonances act as a "filter" that scatter electrons at a determined state (energy, angular momentum and projection); while ignoring other electrons. As a result, we can find a surprisingly almost perfectly symmetrical distribution of electrons at 2 eV that excited N_2 vibrationally (see figure 11.23-top), which matches very closely the spherical distribution of an electron wave with $\ell = 2$ and $m = 1$ (in the reference frame where the z axis is aligned with the interatomic axis).

Interferences hide in every corner of the differential cross section observed. Nevertheless, they are most conspicuous when observed one at a time. A splendid example of interference between two waves (identified as separate) can be seen at high-energy scattering (> 500 eV) of diatomic molecules. At those energies, the electron's wavelength is just about (or below) half the interatomic separation. This implies, from the undulatory perspective, that one can roughly apply the coherent superposition of the waves scattered individually from each atom. This is the independent atom approximation presented in 8.5.3. As a result (with the isotropic averaging over the molecule's orientation), a nice cardinal sinusoidal (sinc) pattern appears, for instance, on the differential cross sections of N_2 at 800 eV and O_2 at 500 eV, as shown on the graphs 11.12.

Differential Cross Section

The question at the centre of our preoccupations is how to extract a quantity corresponding to the idea behind a differential cross section as in (7.2) and in the limit (7.3) considering the ratios of incident and scattered fluxes into the Ω direction. This information is obtained from the scattered wave $|\psi_s\rangle$ (whatever its decomposition) when observed at very long distances from the scattering region ($r \to \infty$), the spherically expanding wavefunction takes a generic form [147, p.23:eq.(1.60)]:

$$\lim_{r\to\infty} \langle r|\psi_s\rangle = \frac{e^{ik'r}}{r} f_{\mathbf{k}\to\mathbf{k}'}(\Omega) \,, \tag{7.27}$$

where $f_{\mathbf{k}\to\mathbf{k}'}(\Omega)$ is known as the *scattering amplitude*, and conveys all the dependence of the electron's state on the angle of observation Ω between the incident $\mathbf{k}$ and outgoing $\mathbf{k}'$ vectors of electron kinetic momenta.

In the most popular formalism of scattering from a quantum perspective, the wavefunctions $|\psi\rangle = |\mathbf{k}\rangle + |\psi_s\rangle$ all represent stationary states: a continuous flow of an electron beam which is partly transmitted and partly scattered. If one calculates the flow rates (current probability densities) of the incident and scattered waves [147, §1.5:p.23–4:eq.(1.67–8)], using (7.27), one obtains the fundamental formula for the differential cross section [551, p.32:eq.(6)]:

$$\frac{d\sigma}{d\Omega}(\mathbf{k}\to\mathbf{k}') = \frac{k'}{k}|f_{\mathbf{k}\to\mathbf{k}'}(\Omega)|^2 \,. \tag{7.28}$$

The ratio k'/k comes from the eventual differences of outgoing and incoming flux when the collision is inelastic.

This relation may also be obtained in the wave packet time-dependent formalism [147, §1.6.2]. The incident and emerging waves are described as a continuous distribution $\phi(\mathbf{k}'') = \langle \mathbf{k}''|\phi\rangle$ in the momentum space of plane waves $|\mathbf{k}''\rangle$. In this framework, the impact parameter b plays a role of dephasing of the plane waves in the direction perpendicular to the incident $\mathbf{k}$. The integration over the two-dimensional subspace of possible impact parameters leads to the definition of the cross section. For a proper introduction to the formalism of scattering in quantum mechanical perspective we recommend consulting Taylor [922, chapters 3, 10].

Cross Section

Once the differential cross section is obtained, one can in principle perform the integral (7.4) in order to derive the cross section. Nevertheless, there is an important direct relationship between the cross section σ and the imaginary part ('$\Im$') of the scattering amplitude $f_{\mathbf{k}\to\mathbf{k}'}$ which is known as the *optical theorem* [147, p.119–120:§4.2.1]:

$$\sigma = -\frac{4\pi}{k}\Im\{f_{\mathbf{k}\to\mathbf{k}}(\theta = 0^\circ)\} \,. \tag{7.29}$$

This is a useful relationship to save computational time when the treatment is known to be exact, or to check the consistency between the scattering amplitude and the cross section if the treatment is approximative.

In the next chapter, we will see how can the scattering amplitude $f_{\mathbf{k}\to\mathbf{k}'}$ be obtained from a decomposition of the scattered wave into partial spherical harmonic waves. Before so, in the next section, we present the atomic unit system which will be used throughout this part.

7.5 Atomic Units

In the microscopic world of quantum physics, a proper choice of units can significantly help by clearing away prepended magnitude factors of electric charge, mass, momentum, energy, etc., that are present in habitual formulae.

As an example, the electric potential V of a nucleus of Ze charge is expressed in the Système International (SI) units by:

$$V(r) = \frac{Ze}{4\pi\epsilon_0 r} \tag{7.30}$$

The elementary e charge together with the vacuum electric permittivity ϵ_0, are constant factors that could be properly set as a reference value from which all subsequent quantities scale accordingly.

The traditional units of atomic physics (atomic units: 'a.u.') are based on four pillar quantities:

$$\begin{aligned}
\text{elementary charge :} \quad & e = 1.602\,176\,634 \times 10^{-19}\,\text{C} && = 1\,\text{a.u.} \\
\text{vacuum permittivity}^* \text{ :} \quad & \epsilon_0 = 8.854\,187\,812\,8(13) \times 10^{-12}\,\text{F/m} && = \frac{1}{4\pi}\,\text{a.u.} \\
\text{Planck's constant :} \quad & h = 2\pi\hbar = 6.626\,070\,15 \times 10^{-34}\,\text{J s} && = 2\pi\,\text{a.u.} \\
\text{electron mass :} \quad & m_\text{e} = 9.109\,383\,701\,5(28) \times 10^{-31}\,\text{kg} && = 1\,\text{a.u.}
\end{aligned}$$

Due to the choice of standards, some quantities are known to a certain degree of precision expressed in parenthesis in units of the last digit. However, since 2019, the SI fixed some fundamental constants to an exact numerical value from which all other units can be derived. This is the case, among others, of the elementary charge e, Planck's constant h and the speed of light c below.

From thereon, one may define other units based on the atomic system used.

Units of length :

$$\text{Bohr's atomic radius :}\ a_0 \equiv \frac{4\pi\epsilon_0\hbar^2}{e^2 m_\text{e}} \approxeq 52.917\,721\,\text{pm} = 1\,\text{a.u.} \tag{7.31}$$

$$\text{Electron's classical radius :}\ r_\text{e} \equiv \frac{e^2}{4\pi\epsilon_0 m_\text{e} c^2} \approxeq 5.3251 \times 10^{-5}\,\text{a.u.} \tag{7.32}$$

$$\text{Electron's Compton wavelength :}\ \lambda_\text{e} \equiv \frac{h}{m_\text{e} c} \approxeq 2.426\,31\,\text{pm} \approxeq 0.045\,85\,\text{a.u.} \tag{7.33}$$

Energy units :

$$\text{Hartree :}\ E_h \equiv \frac{\hbar^2}{m_\text{e} a_0^2} = 2\text{Ryd} \approx 27.2114\,\text{eV} = 1\,\text{a.u.} \tag{7.34}$$

$$\text{Rydberg :}\ \text{Ryd} \equiv \left(\frac{e^2}{4\pi\epsilon_0}\right)^2 \frac{m_\text{e}}{2\hbar^2} \approx 13.6057\,\text{eV} = \frac{1}{2}\,\text{a.u.} \tag{7.35}$$

$$\text{electron-Volt :}\ \text{eV} \approx 0.036\,75\,\text{a.u.} \approx 1.602\,18 \times 10^{-19}\,\text{J} \tag{7.36}$$

*The kinetic energy of electrons will be noted ε everywhere, sometimes with a subscript ε_0 as well. The risk of confusion with the vacuum permittivity ϵ_0 is low, because the latter will (almost) always be accompanied by its 4π factor.

Velocity :

$$\text{Speed of light : } c = \frac{e^2}{4\pi\epsilon_0\,\hbar\alpha} = \frac{1}{\alpha}\text{a.u.} \approxeq 137.036\,\text{a.u.} \tag{7.37}$$

Thus the connection point between formulae expressed in relativistic units (where $c = 1\,\text{r.u.}$ and thus $e^2 = \alpha\,\text{r.u.}$) is made through the fine-structure constant α:

$$\alpha = \frac{e^2}{4\pi\epsilon_0\,\hbar c} = \frac{r_\text{e}}{\lambda_\text{e}/2\pi} \approx \frac{1}{137.036}\,, \tag{7.38}$$

which also binds the electron's classical radius to its Compton wavelength.

We remark that quantities of electron momentum p, wavenumber k and velocity v have equal numerical values in the atomic system of units for non-relativistic energies (the Lorentz factor $\gamma \approxeq 1$):

$$p = \hbar k = m_\text{e}\text{v}\gamma\,. \tag{7.39}$$

We will not consider finer effects such as the interaction between an electron's spin and the magnetic field of an atomic or molecular target. We nonetheless remind the value of Bohr's magneton μ_B:

$$\mu_\text{B} = \frac{e\hbar}{2m_\text{e}} = \frac{1}{2}\text{a.u.} \approx 5.7884 \times 10^{-5}\,\text{eV/T}\,. \tag{7.40}$$

An overview of constants and units in atomic and nuclear physics is available in every textbook, e.g. Berestetskii *et al.* [58, p.xiv–xv].

Chapter 8

Theory of Scattering and Models

In the previous chapter, we introduced the basic concepts about the scattering of electrons from molecules in a gas, how the differential cross section is defined, what assumptions it relies upon, the ways it is measured experimentally and also how it can be connected to theory. In this chapter, we present the necessary tools and introduce our own fits to the Hartree-Fock solution of atomic electron densities to compute differential cross sections of elastically scattered electrons in the quantum approach.

The differential cross sections for elastic scattering in this thesis are calculated from a one-electron optical potential with angular-momentum coupling in the adiabatic nuclei approximation of diatomic molecules. We present here the arsenal of equations, culminating in (8.106,8.129 and 8.137), underlying this approach.

8.1 General approach

In the most general albeit non-relativistic and non-magnetic coupling case, the scattering of a steady one-electron beam about a molecule of N electrons is represented by a state-vector $|\Psi\rangle$ of the whole system of total energy $\mathcal{E}$ which satisfies Schrödinger's stationary (and timeless) equation $\overline{H|\Psi\rangle = \mathcal{E}|\Psi\rangle}$, explicitly in configuration space as [325, p.357:§3:eq.(1)]:

$$\left[\sum_A \frac{-\hbar^2}{2M_\mathrm{A}} \triangle_A + \sum_{A\neq A'} \frac{e^2 Z_A Z_{A'}}{4\pi\epsilon_0 |\mathbf{R}_A - \mathbf{R}_{A'}|} + \sum_{i=0}^{N} \frac{-\hbar^2}{2m_\mathrm{e}} \triangle_i + \sum_A \sum_{i=0}^{N} \frac{-e^2 Z_A}{4\pi\epsilon_0 |\mathbf{r}_i - \mathbf{r}_A|^2} + \sum_{i\neq j} \frac{e^2}{4\pi\epsilon_0 |\mathbf{r}_i - \mathbf{r}_j|}\right] \times$$
$$\Psi(x_0, \ldots, x_N; \mathbf{R}_A \ldots) = \mathcal{E}\Psi(x_0, \ldots, x_N; \mathbf{R}_A \ldots) \tag{8.1}$$

The first two terms on the left are the kinetic energy and Coulomb repulsion operators of the atomic nuclei A, A', the next term is the electron-nuclei attraction, and the last two terms are the electron kinetic energy and inter-electron repulsion operators. The total energy of the electron-molecule system is $\mathcal{E}$. The spatial coordinate of electron j is $\mathbf{r}_j$ and of nucleus A of atomic number Z_A is $\mathbf{R}_A$. The notation x_j is a shorthand for the pair $(\mathbf{r}_j, s_j)$ comprising the space coordinate and the spin coordinate s_j. Formally, those coordinates emerge from the projection of an electron's state on the punctual pseudo-state $|\mathbf{r}\rangle$ and on the spin alignment state $|s\rangle$ along the z axis.

In what follows, we reserve the index '0' for the scattering electron and adopt a concise notation for the coordinates of all bound electrons $x_m = (x_1 \ldots x_j \ldots x_N)$. Since we are presently only interested in representing monatomic or diatomic molecules, we define the internuclear

separation vector $\mathbf{R} \equiv \mathbf{R}_A - \mathbf{R}_{A'}$. Writing the restructured equation (8.1) now in atomic units (see sec. 7.5), we can identify three terms [as in 156, p.14:eq.(2.12)]:

$$\left[\underbrace{\frac{-\triangle_0}{2}}_{\text{Free electron}} + \underbrace{\sum_{j=1}^{N} \frac{-Z_A}{|\mathbf{r}_0 - \mathbf{R}_A|} + \frac{-Z_{A'}}{|\mathbf{r}_0 - \mathbf{R}_{A'}|} + \sum_{j=1}^{N} \frac{1}{|\mathbf{r}_0 - \mathbf{r}_j|}}_{\text{electron-molecule Interaction}} + \underbrace{H_\mathrm{m}}_{\text{Molecule}} \right] \Psi(x_0, x_m, \mathbf{R}) = \mathcal{E}\Psi(x_0, x_m, \mathbf{R}) \,, \tag{8.2}$$

which correspond to the free kinetic energy operator of the scattering electron, the electron-molecule interaction potential energy and the internal Hamiltonian of the molecule H_m comprising Coulombic forces and kinetic operators of the bound electrons and the nuclei.

At the outset, the scattering of an electron does not look very different from the state function of a negative ion. The difference lies in the asymptotic initial and final conditions of the system that we must impose when the electron is far away from the target as $r_0 \to \infty$. The total wavefunction is therefore asymptotically the superposition of the (unique) initial i and (various) final f states of the scattering electron and the molecule [100, 551, eq.(3–4), eq.(2.9)]:

$$\lim_{r_0 \to \infty} \Psi(\mathbf{r}_0, s_0, x_m, \mathbf{R}) = \exp(\mathrm{i}\mathbf{k}_0 \cdot \mathbf{r}_0)\Phi_i(s_0, x_m, \mathbf{R}) + \sum_f \frac{\exp(\mathrm{i}k_f r_0)}{r_0} f_{f \leftarrow i}(\Omega)\Phi_f(s_0, x_m, \mathbf{R}) \,. \tag{8.3}$$

The electron's incident pseudo-state $\exp(\mathrm{i}\mathbf{k}_0 \cdot \mathbf{r}_0)$ is a plane wave (7.22), noted $|\mathbf{k}_0\rangle$ in the vectorial pseudo-basis, whereas its final scattering function leaving the molecule in a state $|\Phi_f\rangle$, is a radially expanding $\exp(\mathrm{i}k_f r_0)/r_0$ spherical wave, except if it attaches into a bound state. In the latter case, the wavenumber k_f would be positive imaginary, giving an exponentially vanishing wave.

The incident $\mathbf{k}_0$ and outgoing $\mathbf{k}_f$ kinetic momenta of the free electron are bound by the energy conservation law:

$$\frac{\hbar^2 k_0^2}{2m_\mathrm{e}} + \mathcal{E}_i = \frac{\hbar^2 k_f^2}{2m_\mathrm{e}} + \mathcal{E}_f \,. \tag{8.4}$$

The solid angle $\Omega = (\theta, \varphi)$ is formed by $\mathbf{k}_0$ and $\mathbf{k}_f$ in the centre of mass reference frame with a fixed axis parallel to $\mathbf{k}_0$. The angular dependence of the spherical wave is encompassed by the scattering amplitude $f_{f \leftarrow i}(\Omega)$ from which the differential cross sections to each process $i \to f$ can be calculated [551, eq.(6)]:

$$\frac{\mathrm{d}\sigma_{f \leftarrow i}}{\mathrm{d}\Omega}(\Omega) = \frac{k_f}{k_0} |f_{f \leftarrow i}(\Omega)|^2 \,. \tag{8.5}$$

We have to remember that the labels i and f apply to the state of the whole system. The medium could be composed of molecules in different initial states $|\Phi_i\rangle$, such as nearly degenerate fine-structure states as for atomic oxygen or different rotational states J_0, M_0 of molecules. In that case, since the free electron prior to scattering is uncoupled to the state of the molecule, one can always separate the problem into different systems i and later perform an averaging of the differential cross section (DCS) over the i initial states. This is useful for rotational magnetic sublevels of projection M or spin projections M_s.

On the other hand, after the interaction has taken place, the electron's outgoing wave is coupled to the final state of the molecule $|\Phi_f\rangle$. Each state $|\Phi_f\rangle$ is built from eigenstates of the isolated molecule's Hamiltonian H_m (8.6a) but includes coupling with the scattering electron's spin s_0 [as in 325, p.378:eq.(64–5)]. This is made in order to define states of determined *total*

spin $\mathcal{S}$ of the electron-molecule system which is conserved during the collision. The ensemble of final states f include all states energetically accessible to the system of energy $\mathcal{E}$, i.e. those for which the outgoing wavenumber k_f from (8.4) is real and positive. They form the set of channels *open* to the collision. If one cannot discriminate between different eventual outcomes f, then the differential cross section must be summed over the states f. We will return to this in (8.101).

Due to the asymptotic structure of this system (8.3), we may suppose* that the total electron-molecule state $|\Psi\rangle$ can be decomposed into a sum of one-electron scattering states† $|\psi_\alpha\rangle$, each coupled to a particular eigenstate α of the target $|\Phi_\alpha\rangle$ [551, eq.(10)]:

$$|\Psi\rangle = \mathcal{A}\sum\nolimits_\alpha |\psi_\alpha\rangle|\Phi_\alpha\rangle \; ; \tag{8.6}$$

$$\text{where } H_\mathrm{m}|\Phi_\alpha\rangle = \mathcal{E}_\alpha|\Phi_\alpha\rangle \; , \tag{8.6a}$$

$$\text{with the usual orthonormality } \langle\Phi_\alpha|\Phi_{\alpha'}\rangle = \iint \Phi^*_\alpha(x_m,\mathbf{R})\Phi_{\alpha'}(x_m,\mathbf{R})\,\mathrm{d}x_m\,\mathrm{d}\mathbf{R} = \delta_{\alpha\alpha'} \; . \tag{8.6b}$$

The eigenstates $|\Phi_\alpha\rangle$ form an orthonormal set (8.6b), whereas the scattering states $|\psi_\alpha\rangle$ are normalised according to the outgoing flux in the channel f [147, p.396:eq.(9.62–3)].

According to the Pauli principle, the total wavector $|\Psi\rangle$ must be antisymmetrical with respect to exchange of any pair of electrons (and nuclei if they are identical fermions). This is ensured by the antisymmetrisation operator $\mathcal{A}$. Assuming that the molecular wavectors $|\Phi_\alpha\rangle$ are already antisymmetrised between the bound electrons, the effect of the operator $\mathcal{A}$ is to antisymmetrise the total wavector by taking all possible permutations of the indexes 0 and j on the scattering and bound electronic coordinates and forming a total state:

$$\mathcal{A}|\psi(x_0)\rangle|\Phi_\alpha(x_m)\rangle = \frac{1}{\sqrt{N+1}}\left(|\psi(x_0)\rangle|\Phi_\alpha(x_m)\rangle - \sum_j^N |\psi(x_j)\rangle|\Phi_\alpha(x_{m_{0\leftarrow j}})\rangle\right) . \tag{8.7}$$

The antisymmetrised total wavefunction is normalised through the denominator $\sqrt{N+1}$. A concrete example of what $\Phi(x_m)$ looks like, is given by the Slater determinant in (8.16). In the notation above, we specify in parenthesis the electron to which each wavefunction is associated. The letter m is a shorthand for internal (molecular) coordinates. The operation $m_{0\leftarrow j}$ corresponds to the replacement of the coordinates $x_j = (\mathbf{r}_j, s_j)$ of the bound electron j by those of the scattering electron $x_0 = (\mathbf{r}_0, s_0)$ labelled by 0:

$$x_{m_{0\leftarrow j}} \equiv (x_1, x_2 \ldots \underset{\searrow 0}{x_j} \ldots x_N) \; . \tag{8.8}$$

If we inject (8.6) back into (8.2) and take individual projections on the molecular states $\langle\Phi_\alpha|$, we obtain a coupled set of integrodifferential equations (one for each α) [551, p.33:eq.(11)]:

$$\begin{aligned} -\frac{1}{2}\,\triangle\psi_\alpha(x_0) + \underbrace{V_{\alpha\alpha}(x_0)\psi_\alpha(x_0)}_{\text{Direct Static}} + \underbrace{\not\int\!\!\!\int W_{\alpha\alpha}(x_0,x')\psi_\alpha(x')\,\mathrm{d}^3x'}_{\text{Exchange Static}} \\ + \underbrace{\sum_{\alpha'\neq\alpha} V_{\alpha\alpha'}(x_0)\psi_{\alpha'}(x_0)}_{\text{Direct Coupled}} + \underbrace{\sum_{\alpha'\neq\alpha} \not\int\!\!\!\int W_{\alpha\alpha'}(x_0,x')\psi_{\alpha'}(x')\,\mathrm{d}^3x'}_{\text{Exchange Coupled}} = \underbrace{(\mathcal{E}-\mathcal{E}_\alpha)}_{\equiv k_\alpha^2/2}\psi_\alpha(x_0) \end{aligned} \tag{8.9}$$

*The assumption underlying (8.6) overlooks the more general case comprising a global correlation between the scattering electron's position and all other bound electrons [325, p.377:§4.2:eq.(63)].

†We follow the nomenclature of Lane [551, p.33:§A] who names $\psi_\alpha(x_0)$ a "scattering function" because it only describes an outgoing scattering wave as opposed to a wavefunction which ought to describe an electron's state. This semantic distinction is not always stressed in other references.

The meaning of the integrals $\oint \dots \mathrm{d}x'$ on the generalised coordinate $x' = (\mathbf{r}', s')$ of a bound electron[♠] is an integration over the continuous variable $\mathbf{r}'$ together with a sum on the discrete binary $s' = \pm 1/2$ coordinate. Technically, the orientation of an electron's spin is a vector in a 2D Hilbert space. In practice, when we consider an ensemble of electrons, what we need to know is how the spins of all electrons couple together or with their respective orbital angular momenta. Thus, we can just consider the binary discrete variable s', associated to either $\pm 1/2$ of a bound electron's spin projection on the z axis of the given reference frame. To fully account for the different possibilities of spin combinations with spatial occupied orbitals, one appeals to linear combinations of Slater determinants and thus the 'integral' involving spin should be understood as the sum over the configurations which compose the state α in the obscure wavefunction $\Phi_\alpha(x_m)$. For more insight, we redirect the reader to Hertel and Schulz [section 7.3 of 398].

1. $V_{\alpha\alpha}$**:** In the equation (8.9), we may identify the first term to the diagonal component $\alpha = \alpha'$ of the *direct* potential perceived by the scattering electron in the channel α:

$$V_{\alpha\alpha'}(x_0) = -\int \left[\frac{Z_A}{|\mathbf{r}_0 - \mathbf{R}_A|} + \frac{Z_{A'}}{|\mathbf{r}_0 - \mathbf{R}_{A'}|}\right] \nu_{\alpha\alpha'}(\mathbf{R})\, \mathrm{d}^3\mathbf{R} + \int \frac{\rho_{\alpha\alpha'}(\mathbf{r}')}{|\mathbf{r}_0 - \mathbf{r}'|}\, \mathrm{d}^3\mathbf{r}' \tag{8.10}$$

With the reference frame staying fixed at the centre of mass, the position $\mathbf{R}_A$ of each nucleus can be unambiguously determined from the internuclear separation $\mathbf{R}$. The average nuclear $\nu_{\alpha\alpha'}$ and electronic $\rho_{\alpha\alpha'}$ cross probability densities between states α and α' are defined as:

$$\nu_{\alpha\alpha'}(\mathbf{R}) = \int \Phi^*_\alpha(x_m, \mathbf{R}) \Phi_{\alpha'}(x_m, \mathbf{R})\, \mathrm{d}x_m \,, \tag{8.11}$$

$$\rho_{\alpha\alpha'}(\mathbf{r}') = \int \Phi^*_\alpha(x_m, \mathbf{R}) \Phi_{\alpha'}(x_m, \mathbf{R})\, \mathrm{d}x_{m\setminus\{j\}}\, \mathrm{d}^3\mathbf{R} \,. \tag{8.12}$$

Their diagonal elements $\alpha = \alpha'$ intervene in the direct terms whereas cross-densities between $\alpha \neq \alpha'$ enable coupling. The notation $x_{m\setminus\{j\}}$ signifies all internal molecular generalised coordinates except those of the electron j [♠].

2. $W_{\alpha\alpha}$**:** The second term in (8.9) is known as the exchange static potential of the state α and is *nonlocal* meaning that it possesses non-diagonal matrix elements in configuration space $\langle x|W_{\alpha\alpha}|x'\rangle$ which are not null. The exchange kernel $W_{\alpha\alpha'}$ is defined as [100, eq.(2.8)]:

$$W_{\alpha\alpha'}(x_0, x') = -\frac{\int \Phi^*_\alpha(x_m) \Phi_{\alpha'}(x_{m_{0\leftarrow j}})\, \mathrm{d}x_{m\setminus\{j\}}}{|\mathbf{r}_0 - \mathbf{r}'|} \,, \tag{8.13}$$

Most often, a Hartree-Fock description of the target state $|\Phi_\alpha\rangle$ is adopted (i.e. linear combination of Slater determinants (8.16) of singly occupied orbitals $\phi_{\alpha,j}$ for the state α). In that case, the integral in the numerator of (8.13) would decompose into a sum of products of single-electron orbitals[♭]: $\sum_j \phi^*_{\alpha',j}(x')\phi_{\alpha,j}(x_0)$ [551, p.47:eq.(110)].

[♠] Note that since the molecular states Φ_α are antisymmetrised (8.16), it matters not which electron's coordinates (1,2,.. j or N) are left out in the integral of (8.12). An easy way to see this is to remember that both Φ^*_α and $\Phi_{\alpha'}$ are antisymmetrical with respect to the permutation of two electrons' coordinates. This is why we abandoned the j subscript and write a primed $x'_{\setminus j}$. The same situation applies to the ground state density (8.15) of the next section 8.2 used in density functional theory.

[♭] When $\alpha' \neq \alpha$, we would also have to restrict the sum to only those orbitals $\phi_{\alpha',j}$ which differ from $\phi_{\alpha,j}$. Otherwise the integral over the other bound electrons would be nil in virtue of the orthonormality of bound orbitals.

3. $V_{\alpha\alpha'}$ **and** $W_{\alpha\alpha'}$**:** The third and fourth terms represent couplings to other molecular states and can be rightfully considered as a crux in scattering theory. They represent the reaction of the molecule due to the perturbation caused by the intruding electron.

Under the Born-Oppenheimer approximation in which the electronic states are separated and independent from the nuclear motion, the orthogonality of the electronic parts of $\Phi_{\alpha'}$ and Φ_α implies that $\nu_{\alpha\alpha'}$ is zero [551, §II.B]:

$$\text{Born-Oppenheimer approx.} : \quad \nu_{\alpha\alpha'}(\mathbf{R}) \simeq 0 \ \text{ for } \alpha \neq \alpha' \,. \tag{8.14}$$

It is thus not unusual that coupling in (8.10) is only made with electronic states through the cross probability density $\rho_{\alpha\alpha'}$ (8.12)

Those terms $V_{\alpha\alpha'}$ and $W_{\alpha\alpha'}$ enable transitions $i \to f$ between different initial i and final f states. The probability of a particular transition is directly related to the importance of the coupled terms for $\alpha = i$ and $\alpha' = f$.

This is readily exploited in the Born approximation (sec. 8.5.1) for inelastic scattering (11.44) leading to the generalised oscillator strength that will be presented in a later section 11.4.1 of chapter 11. Similarly, the transition between different vibronic bands in the triple combo of Born-Oppenheimer, Born and impulse approximations is represented by Franck-Condon factors (see appendix D.2 eq.(D.4)).

When the incident energy $k_0^2/2$ of the electron is insufficient (i.e. $k_0^2/2 < \mathcal{E}_b - \mathcal{E}_i$) to permit a transition $i \to b$, the channel is *closed* but the couplings still exist! These excited states b are called "virtual excitations". They arise during the process of scattering but cannot be observed at the outcome. Nonetheless, their existence is very noticeable in Feshbach resonant scattering, presented in section 11.3.1. Mathematically, the scattering functions $\psi_{b,i}(\mathbf{r}_0)$ associated to the energetically disallowed transitions $b \nleftarrow i$ vanish asymptotically (faster than $1/r_0$) at large distances $\mathbf{r}_0 \to \infty$ (due to $k_b \in \mathrm{i}\mathbb{R}^+$ in eq. 8.3).

Open or not, the presence of $\alpha' \neq i \wedge \alpha' \neq f$ states can significantly affect the scattering cross section of an electron. Coupling terms to electronically excited states can overall be represented by correlation-polarisation potentials presented in section 8.2.3 and reviewed in 10.3.3.

4. Finally, the remaining terms reduce to simple real numbers: $\mathcal{E}_\alpha = \langle\Phi_\alpha|H_\mathrm{m}|\Phi_\alpha\rangle$ is the energy of the state α. The attentive reader will have noticed that the exchange terms in (8.9):

$$\langle\Phi_{\alpha'}| \ \ldots\ |\psi_\alpha(x_j)\Phi_\alpha(x_{m_{0\leftarrow j}})\rangle \quad \text{from } \triangle_0/2,\ \mathcal{E} \text{ and } H_\mathrm{m} \text{ vanish.}$$

This stems from the orthogonality of the scattering state $|\psi_\alpha(x_0)\rangle$ to any bound one-electron orbital $|\phi_j(x_0)\rangle$ (if it were hypothetically occupied by the scattering electron). This may be justified in two different ways. Lane [551, p.47:§ above eq.(113)] reminds us that the total wavefunction $|\Psi\rangle$ remains unmodified if $|\phi_j(x_0)\rangle$ is added to $|\psi_\alpha(x_0)\rangle$. Because this means that two columns in the Slater determinant (8.7) would be identical and thus this additional term would annihilate anyway. This argument applies, however, only to occupied orbitals of the α state. A more general argument can be borrowed from the orthogonality theorem of Taylor [922, chapter 2:p.32] which reasons in the following way: if the scattering function $\psi_\alpha(x_0)$ is asymptotically unbound to the target, this means that after a sufficiently long time $t \to \infty$, the evolution operator $U(t) \equiv \mathrm{e}^{-\mathrm{i}Ht}$ will separate all bound orbitals from the (physical) scattering orbital (which is a wavepacket); implying thereby that their overlap integral is zero. Since, by unitarity of $U(t)$, if this overlap converges to zero for $t \to \infty$, then it must be zero at all times t.

While it remains true that the space to which $|\psi_\alpha\rangle$ belongs is perpendicular to the space of bound states, this does not, however, mean that the scattering electron could not settle into a bound orbital $|\phi_{\alpha',j}\rangle$ coupled to an excited state $|\Phi_{\alpha'}\rangle$ of the target! This possibility leads to the realm of resonant scattering which, from a physical perspective, is in total opposition of the "usual" direct scattering in which it is assumed that the interaction of the collision is very short and a number of useful adiabatic approximations can be applied. Resonances are ubiquitous in electron scattering with molecules, but we reserve only a small space to them in section 11.3 of chapter 11. Much insight can be gained from Shimamura and Takayanagi [834, chapter 3] and some applications in Čarský and Čurík [156].

Returning now back to the general Schrödinger equation (8.9) for the scattering electron, we formally have an infinite system of coupled equations: one for each target state α. The truncation to N_α equations corresponds to what is known as the *close coupling* approximation [147, chapter 9.1]. As a differential system of second order, it admits $2N_\alpha$ linearly independent solutions $\{\psi_{\alpha n}(r)\}_{N_\alpha}$, $n = 1..2N_\alpha$. They can be adequately used to construct the unique solution to the boundary condition of the scattering system. The regularity of the scattering function at the origin $\psi_\alpha(r = 0) = 0$, disqualifies the N_α solutions irregular at the origin [551, p.42]. The second boundary condition corresponds to the asymptotic limit (8.3) already introduced above, when the scattering electron is observed at a position $r_0 \to \infty$ which is much greater than the molecule's region of influence [100, 551, eq.(3–4), eq.(2.9)].

The apparent simplicity of the association between final scattering states $\psi_{f,i}(\mathbf{r})$ and target states $\Phi_f(s_0, x_m, \mathbf{R})$ conceals an underlying complexity of coupled states. While it seems obvious that the solution to the boundary condition (8.3) is actually the vector of N_α scattering functions $\{\psi_{f,i}\}_{N_\alpha}$ associated to the N_α possible final states f and starting from the initial state i, we have to remember that the idea behind a "final" or "initial" state applies to the whole electron-molecule system $|\Psi\rangle$. In particular, the free electron's spin (projection) s and angular momentum ℓ couples with the targets' (S,L) to form a total spin $\mathcal{S}$ [e.g. 551, eq.(25)] and angular momentum $\mathcal{L}$ [e.g. 442, eq.(8–9)]. As a result, each final scattering state $\psi_{f,i}(\mathbf{r})$ corresponds actually to a superposition of spherical harmonic waves of determined angular momenta, each coupled to various target wave function of determined momentum but different projections*. The decomposition of incoming and outgoing free electron plane waves into spherical harmonic waves is known as the *partial wave* decomposition [147, §9.3] which will be described in a forthcoming section 8.4.

The objective of this introduction, was to show how, by starting from the Schrödinger equation of the total electron-molecule system (8.1), one can tackle the problem through a one-electron system of equations (8.9) with an interaction potential operator $V_{\alpha\alpha'} + W_{\alpha\alpha'}$ that couples various components of the electron wave-vector (comprising many individual scalar scattering functions $\psi_\alpha(x_0)$). This does not, however, make the problem any less formidable. A very good and widely accessible introduction and overview of the complexity involved in electron-molecule scattering computations was written by Morrison [667].

As was forewarned in the introduction (perilogue) to this part, here is where we have to depart from the elegant formalism of Schrödinger's equation describing the electron-molecule interaction as a whole, and start building our way for the practical purpose of this part. A first step will consist in reducing the terms of the interaction potential with the molecule (8.9) into a manipulable and local scalar function whose gradient classically represents a force acting on our scattering electron. That is the purpose of the next section.

*This angular and spin coupling causes Clebsch-Gordan coefficients to run all over the formulae in electron-molecule scattering.

8.2 Potential Scattering

One of the great hurdles in electron-molecule scattering is the proper description of the interaction. In particular, in addition to the electrostatic potential of the molecule from the positions $(\mathbf{r}_m, \mathbf{R})$ of its constituent electrons and nuclei, one must also account for (i) the indistinguishability of the free and bound electrons and (ii) the distortion of the electronic cloud in the field of the scattering electron.

(i) The former (exchange) leads to an integro-differential equation (as 8.9) where we require the knowledge of the whole scattering wavefunction $\psi(\mathbf{r}', s)$ in order to evaluate the effect of electron exchange at one point $\mathbf{r}$ and for an electrons whose spin's projection is s.

(ii) The latter (distortion) couples one scattering wavefunction ψ_α to many other wavefunctions $\psi_{\alpha' \neq \alpha}$ associated to different excitation states α' of the molecule.

Considerable simplification can be obtained by seeking an approximate local exchange potential and an average perturbation potential that mimic the effect of the formally exact interaction. This is done through a so-called *optical* potential. The effect of exchange and distortion is to add an attractive correction to the whole potential. This correction can be interpreted as a lessened Coulombic repulsion caused by a reduced overlap between the wavefunctions of the scattering electron and the bound electrons. In addition to this, distortion also comprises an imaginary negative potential which emulates the loss of electron flux into different (inelastic) reaction channels when they are open (above the energy threshold of excitation). An introduction and overview of the construction of such optical potential* is given in [100, p.232-241].

A benchmark program for calculating differential cross sections (DCS) from isolated atoms and their arrangement in molecules or solids is ELSEPA [803]. This program also models electron scattering with an optical potential and we used it to check and compare our results. In the rest of this thesis, we will often display results obtained from ELSEPA as a way to illustrate the sensitivity of the DCS on the model chosen and eventually highlight the improvement that we bring forth.

> In this section, we only describe the potential model as we use it to calculate elastic cross sections given in chapter 11.1. For an overview of existing semi-empirical optical potential models, refer to section 10.3.

From now on, we drop the '0' subscript for the position $\mathbf{r}_{\not 0}$ and the spin projection $s_{\not 0}$ of the scattering electron, and reserve the '0' only for asymptotic initial quantities such as the incident energy ε_0, wavector $\mathbf{k}_0$ and velocity v_0, or also the ground state $|\Phi_0\rangle$ of the molecule. We remind the convenient notation of the generalised space–spin coordinate $x \equiv (\mathbf{r}, s)$.

The construction of the optical potential relies mostly on the description of the target through the average electron density $\rho(\mathbf{r}')$. According to the density functional theory [408], all static properties of the target (charge moments, multipoles, ...) may be derived from this density $\rho(\mathbf{r}')$ if it corresponds to the density derived from the "true" ground state $|\Phi_0\rangle$ of the target [416, p.594:eq.(6.1)]:

$$\rho(\mathbf{r}') \equiv \sum_{s'=\pm\frac{1}{2}} \int \Phi_0^*(x', x_2, \dots x_N)\Phi_0(x', x_2, \dots x_N)\,\mathrm{d}x_2 \dots \mathrm{d}x_N \,. \tag{8.15}$$

*The optical potential originated in nuclear physics [see footnote 5 of 922, p.385], in this thesis, we only cite references particular to electron-molecule scattering.

This is independent from the index of the coordinate x' left out of the integration since real states must be antisymmetrised according to Pauli's principle (see eq. 8.16 below). Potentials that are exclusively based on this average density $\rho(\mathbf{r}')$ are called density functionals.

Still, the problem is not bypassed because one requires the knowledge of $|\Phi_0\rangle$. One then relies on an approximation of this wavefunction of which the most fundamental is the Hartree-Fock-Slater model made from an antisymmetrised product – *Slater determinant* – of individual one-electron orbitals $|\phi_j\rangle$ and their spin-state $|\chi_j\rangle$ in a system of N electrons [398, p.504:eq.(10.28)]:

$$\langle x_1 \cdots x_N | \Phi_0 \rangle \simeq \frac{1}{\sqrt{N!}} \begin{vmatrix} \phi_1(\mathbf{r}_1)\chi_1(s_1) & \phi_2(\mathbf{r}_1)\chi_2(s_1) & \cdots & \phi_N(\mathbf{r}_1)\chi_N(s_1) \\ \phi_1(\mathbf{r}_2)\chi_1(s_2) & \phi_2(\mathbf{r}_2)\chi_2(s_2) & \cdots & \phi_N(\mathbf{r}_2)\chi_N(s_2) \\ \vdots & \vdots & \ddots & \vdots \\ \phi_1(\mathbf{r}_N)\chi_1(s_N) & \phi_2(\mathbf{r}_N)\chi_2(s_N) & \cdots & \phi_N(\mathbf{r}_N)\chi_N(s_N) \end{vmatrix} \tag{8.16}$$

The spin functions $\chi_j(s_j)$ of the electron j are either in one of $|\uparrow\rangle$ or $|\downarrow\rangle$ spin projection states. The various possible combinations of orbitals and spin-states imply that there exist different Slater determinants (8.16) in open-shell systems, i.e. when one or more spatial orbitals $\phi_j(\mathbf{r})$ are only occupied by one electron. A linear combination of Slater determinants is called a *configuration interaction* model [398, §10.2.3].

The obtention of an atom's or molecule's wavefunction through the Hartree-Fock variational approach (or more advanced approaches) lies completely outside the scope of this thesis. Atomic densities have been described, improved and updated over several decades. They are made available through analytical representations [196, 443, 522, 726, 800] best fitting numerical results [183] from freely distributed programs. The representation of diatomic densities is more complicated due to the breakdown of spherical symmetry of electrons about more than one nucleus. Although there exist tabulations and 2D analytical representations of molecules [e.g. 293, eq.(1)], we could not find both well-established and "easy-to-implement"* standards as in the case of atoms. Thus, we decided to restrict our modelling of molecules to the sheer overlapping of atomic densities without correlation effects. The closest amelioration within our reach for N_2 and O_2 would have been the correction to the independent atom densities given by Fink and Bonham [285, p.111–116:eq.(31–9) and p.119:table 1], which time restrictions did unfortunately not allow us to explore.

Overall, we have decided to privilege analytical representations over numerical tabulations, as they greatly facilitate and expedite the calculation of potentials, plane wave Born amplitudes and transformation in space. In practice, use of analytical expressions liberate us from annoying issues of numerical nature at boundary conditions and singularity points. Thus we modelled both atomic and molecular densities from a presently re-fitted expression of Slater-type 1s-orbital terms as in Pacios [726, eq.(1)]:

$$\rho_{1s}(r) = \frac{Z}{4\pi} \sum_{i=1}^{n_\rho} \gamma_i \frac{\lambda_i^3}{2} \exp(-\lambda_i r) \tag{8.17}$$

The normalisation of the density and weighting coefficients γ_i is chosen so that they verify:

$$\int_0^\infty \rho_{1s}(r) 4\pi r^2 \, \mathrm{d}r = Z \qquad \Rightarrow \qquad \sum_{i=1}^{n_\rho} \gamma_i = 1 \,, \tag{8.18}$$

from the total volume integral of the electron charge.

The parameters γ_i and λ_i are found in table 8.1 of the next subsection for the static potential. There, we describe more in detail the fitting procedure and the resulting analytical expression

*Here, we stumble onto an anthropological problem in scientific investigation: the investment in time.

of the static potential. For nitrogen and oxygen, we distinguish the density to be used when in molecular form and when in isolated atomic form which is taken from Pacios [726]. In the following subsections, we succinctly present the static, exchange, correlation-polarisation and absorption models used to construct our optical potential.

8.2.1 Static

The static potential V_s perceived by an electron from a distribution of charges ϱ_s is obtained through Poisson's equation (in atomic units) [755, p.8:eq.(2)–but with a change of sign due to the negative elementary charge of the electron]:

$$\triangle V_\mathrm{s}(\mathbf{r}) = -(-e)\frac{\varrho_\mathrm{s}(\mathbf{r})}{\epsilon_0} = 4\pi\varrho_\mathrm{s}(\mathbf{r})\,\mathrm{a.u.}\,, \tag{8.19}$$

which transforms into the integral equation [726, eq.(4)]:

$$V_\mathrm{s}(\mathbf{r}) = -\int \frac{\varrho_\mathrm{s}(\mathbf{r}')}{|\mathbf{r}-\mathbf{r}'|}\,\mathrm{d}^3\mathbf{r}'\,. \tag{8.20}$$

For a central distribution of charges $\varrho_\mathrm{s}(r)$, all but the isotropic terms from the Legendre expansion of $1/|\mathbf{r}-\mathbf{r}'|$ annihilate when integrated over the angular variables, leaving only the radial integral [799, eq.(1)]:

$$V_\mathrm{s}(r) = -\frac{1}{r}\int_0^r \varrho_\mathrm{s}(r')4\pi r'^2\,\mathrm{d}r' - \int_r^\infty \frac{1}{r'}\varrho_\mathrm{s}(r')4\pi r'^2\,\mathrm{d}r'\,. \tag{8.21}$$

Atoms

In the case of an atomic target, the charge distribution ϱ_s, assumed to be central, is simply the punctual nuclear charge $+Ze$ surrounded by the electronic density ρ described above: $\varrho_\mathrm{s}(r) = +Ze\delta_\mathrm{r}(r) - e\rho(r)$. The "**r**adial" Dirac δ_r peak is defined so as to properly amount to 1 when integrated over a spherical volume.

We distinguish three special cases of electronic distributions: the Yukawa, the exponential (or Slater $1s$) and the general Slater ns [927, eq.(21.1&2)]. Injection into (8.21) gives the generic static potentials:

$$\textbf{Y}\text{ukawa}: \qquad \rho_\mathrm{Y} = C_\mathrm{Y}\frac{\mathrm{e}^{-\lambda r}}{r} \qquad \Rightarrow \qquad V_\mathrm{Y}(r) = -Z\frac{\mathrm{e}^{-\lambda r}}{r} \equiv V_{n=0s}(r) \tag{8.22a}$$

$$\text{E}\textbf{x}\text{ponential}: \qquad \rho_\mathrm{X} = C_\mathrm{X}\mathrm{e}^{-\lambda r} \qquad \Rightarrow \qquad V_\mathrm{X}(r) = -Z\left(1+\frac{\lambda r}{2}\right)\frac{\mathrm{e}^{-\lambda r}}{r} \equiv V_{n=1s}(r) \tag{8.22b}$$

$$\text{Slater } ns: \qquad \rho_{ns} = C_n r^n\frac{\mathrm{e}^{-\lambda r}}{r} \qquad \Rightarrow \qquad V_{ns}(r) = -Z\left(\sum_{i=0}^{n}(\lambda r)^i\frac{n+1-i}{(n+1)i!}\right)\frac{\mathrm{e}^{-\lambda r}}{r} \tag{8.22c}$$

The coefficients $C_\mathrm{Y} \equiv C_0$, $C_\mathrm{X} \equiv C_1$ and $C_n = Z(n+1)!/(4\pi\lambda^{n+2})$ are normalisation factors so that the volume integral of the densities is unity.

Ideally, the general Slater distribution ρ_n and static potential V_n give the most accurate average description of atoms. On the downside, it is mathematically more cumbersome when expanding into spherical harmonics of diatomic potentials. For practical purposes, most analytical potentials reported in the literature were approximated by a sum of Yukawa terms [196, 443, 800]. Despite its simplicity, the greatest disadvantage of the Yukawa potential is that it is bound to physically unrealistic density distributions (8.22a) because of the singularity at the origin.

Table 8.1: Weighting coefficients γ_i and exponents λ_i for the presently concise atomic densities and static potentials based on a sum of Slater $1s$ orbitals. Equivalently, on may define the atomic decaying radii $a_i = 1/\lambda_i$. They were fitted on top of the results from the Hartree-Fock calculations of Koga [522]. The smallest exponents in the last columns were imposed as $\lambda_{\min} = \sqrt{8I}$ [522, eq.(10f)] from ionisation potentials I of homonuclear diatomic molecules and noble gas atoms.

Atom (Z)	$\gamma_{i=}$ / $\lambda_{i=}$	1	2	3	4	5
$N^{\ddagger}_{(2)}$ (7)		0.3268	−0.2569	0.6556	0.2744	
		13.03	5.434	2.678	2.141	
N¶ (7)		0.2820	−0.1910	0.9090		
		13.84	4.656	2.453		
$O^{\ddagger}_{(2)}$ (8)		0.2397	−0.038 90	0.7987	0.000 558 0†	
		15.99	6.783	2.442	1.884	
O¶ (8)		0.2500	−0.1150	0.8650		
		15.84	6.439	2.710		
Ne (10)		0.2295	−0.1523	0.7819	0.1409	
		19.90	9.791	3.706	2.522	
Ar (18)		0.083 10	2.850	-5*	2.710	0.3568
		36*	5.688	4.489	3.653	2.153

‡ Only used for diatomic molecules.
¶ Taken from Pacios [726, p.415:table II].
† The abnormally low value is due to the imposition of $\lambda_4 = \sqrt{8I_{O_2}}$, which is $I_{O_2} = 12.07\,\text{eV}$.
* Those values were constrained to obtain the fit for argon.

In the present work, we decided to follow the philosophy of Pacios [726]. We use a simple exponential distribution $\rho_X \equiv \rho_{1s}$ and the resulting potential V_X to represent atomic targets. Its advantage is that ρ_{1s} may correspond to a physically valid distribution while still being mathematically simple to decompose in harmonics for diatomic potentials. The full expression derived from (8.17) is given by:

$$V_{1s}(r) = -Z \sum_{i=1}^{n_\rho} \gamma_i (1 + \frac{\lambda_i r}{2}) \frac{e^{-\lambda_i r}}{r} \tag{8.23}$$

The weights γ_i and exponents λ_i are the same as mentioned earlier and are summarised in table 8.1. For atomic nitrogen and oxygen, we use directly the 3-term fit of Pacios [726] whereas for neon and argon we decided to refit the static potential with one more term. In the fitting process, we had the choice to fit either the electronic density ρ or the numerically-computed static potential V_s. For atoms, the density can be accurately described by Koga's [522] analytical fits while for molecules, we expected the density to be distorted from the chemical bond. As a consequence, it would not make sense to try to obtain accurate fits of densities. Thus, we decided fit the parameters in table 8.1 in order to reproduce the static potential of atoms obtained from the density of Koga [522].

We applied constraints to the weighting coefficients to verify the conservation of charge: $\sum_i \gamma_i = 1$. We also constrained the exponents λ_i in a monotonically decreasing series as $2Z > \lambda_1 > \cdots > \lambda_{n_\rho} = \sqrt{8I}$. The upper boundary $2Z$ comes from Kato's cusp condition [480] and the last exponent λ_{n_ρ} was imposed to correspond to the ionisation potential I, from the asymptotic

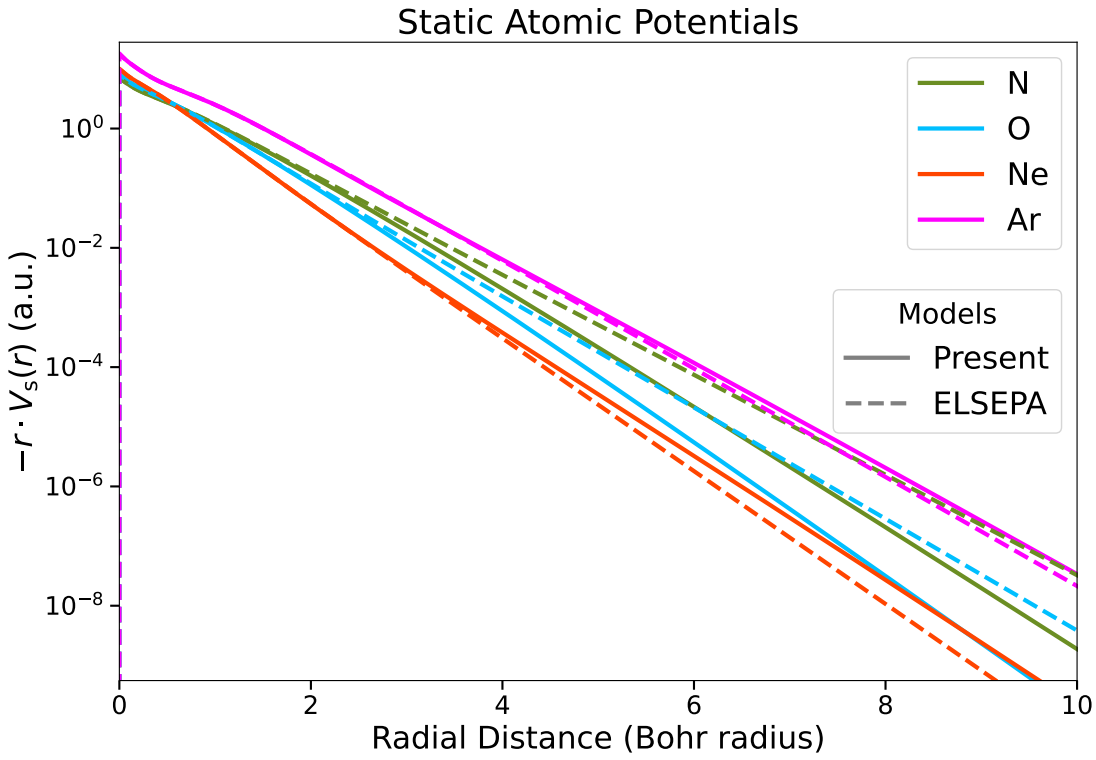

Figure 8.1: Comparison of the present model static potential (—) (8.23) with parameters reported in table 8.1, to the one calculated by ELSEPA (- - -) for four atoms. For N and O, the fit is from Pacios [726] for which the asymptotic decay rate λ_3 has not been constrained according to the ionisation potential.

behaviour of bound orbitals [382, eq.(32)]. For N and O as constituent atoms in molecules, this ionisation potential I was taken from N_2 (15.58 eV) and O_2 (12.07 eV) respectively. Since we did not attempt to obtain fits directly from Hartree-Fock molecular potentials, we did not consider it worth distinguishing the static potential of N (O) when in N_2 (O_2) or NO. We nonetheless constructed the present fit in table 8.1 in order to have a different model to study the sensitivity of the DCS on the static potential. This sensitivity is illustrated in figure 10.9 of section 10.3.1 on page 353.

A comparison of the static atomic potentials obtained is available on figure 8.1 (multiplied by r to remove the singularity at the origin), where the dashed lines (- - -) show the potentials calculated by ELSEPA [803]. The main differences arise at larger distances $r > 2a_0$, and are due to the smallest exponent λ_{n_ρ}.

The intention of the present fit in table 8.1 was to have (i) a compact, mathematically manipulable and reasonably accurate analytical expression; (ii) a constrained asymptotic tail $\propto \sqrt{8I}$ and (iii) a model to compare with and check the sensitivity of DCS on the model used. When it comes to diatomic molecules, the limitations of the independent atom model are far more restrictive than the model used for the atomic potential.

Diatomic Molecules

As mentioned before, to represent the potential of diatomic molecules, we first superpose the densities of the constituent atoms located at $\mathbf{R}_A = +\mathbf{R}/2$ and $\mathbf{R}_{A'} = -\mathbf{R}/2$ as in sketch 8.2. This corresponds to the independent atom model (IAM) applied to the description of the target molecule. There exist analytical corrections to the IAM that account for the chemical bonding of N_2 and O_2 as given in Fink and Bonham [285, p.119:table 1.]. We have not explored this option due to limitations both in time and information, since the exact atomic potentials to which the corrections are proposed are not disclosed. Instead, we corrected the IAM with a simple analytical expression for the asymptotic potential due to permanent multipoles of the molecule.

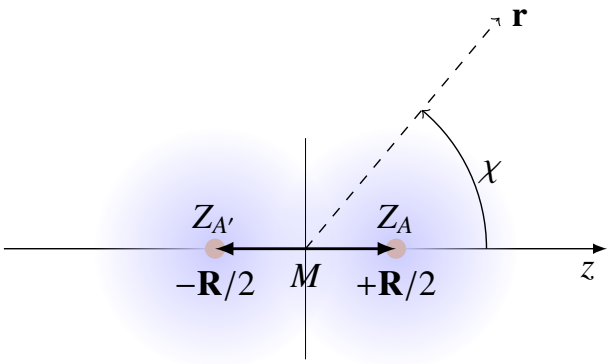

Figure 8.2: Representation of a diatomic molecule according to the independent atom model superposing the unperturbed densities of its constituent atoms A and A'.

For any distribution of charge $\rho(\mathbf{r})$, the n^{th} multipole is a tensor of rank n with $2n+1$ independent components given by [398, eq.(F.7)]:

$$Q_{nm} = \frac{\sqrt{4\pi}}{\sqrt{2n+1}} \int Y_{nm}(\chi,\varphi)\rho(\mathbf{r})r^n \,\mathrm{d}^3\mathbf{r} \,. \tag{8.24}$$

The function $Y_{nm}(\chi,\varphi)$ is the spherical harmonic of degree n and projection m on the z-axis defining the polar angle χ and around which the azimuthal angle φ revolves. From the axial symmetry of diatomic molecules, there is only one independent component for each multipole. In the frame where the z axis is aligned with the principal interatomic axis (fig. 8.2), only the $m = 0$ components are non-zero and we may replace in (8.24) $Y_{n0}(\chi) = \sqrt{(2n+1)/(4\pi)}P_n(\chi)$ [956, p.133:§5.2:eq.(1)], where P_n is the Legendre polynomial of degree n. The components Q_{n0} are unambiguously referred to as the multipole moments. The dipole D and quadrupole Q moments, in particular, are defined as:

$$D \equiv Q_{10} = \iint r\cos\chi\,\rho(\mathbf{r})r^2\,\mathrm{d}r\sin\chi\,\mathrm{d}\chi\,2\pi \,, \tag{8.25}$$

$$Q \equiv Q_{20} = \iint r^2\frac{(3\cos^2\chi-1)}{2}\rho(\mathbf{r})r^2\,\mathrm{d}r\sin\chi\,\mathrm{d}\chi\,2\pi \,. \tag{8.26}$$

with χ being the angle between the running point $\mathbf{r}$ and the z axis (see fig. 8.2). The static potential produced by the n^{th} multipole M_n behaves asymptotically as [908, p.150]:

$$V_{n,\infty}(\mathbf{r}) \sim \frac{M_n}{r^{n+1}}P_n(\chi) \,. \tag{8.27}$$

This stems from the Legendre expansion of $(1/|\mathbf{r}-\mathbf{r}'| = \sum_n r_<^n/r_>^{n+1}\,P_n)$ in (8.20), the addition theorem of Legendre polynomials [219, eq.(14.18.2)] and the definition of multipoles (8.24).

To eliminate the unphysical singularity at $r = 0$ of multipole static potentials (8.27), one can introduce cutoff radii r_{d}, r_{q} [197, 945, p.496:§3, p.3252:§III.B]. For finite (3D-integrable) charge distributions $\rho(r')$ regular at the origin, the static potential from the n^{th} multipole from (8.20) annihilates as $\sim r^n$. Therefrom, we decided to use the following analytical expressions for dipole and quadrupole potentials:

$$V_{\mathrm{d}}(\mathbf{r}) = -D\frac{r}{r^3 + r_{\mathrm{d}}^3}\cos\chi\ , \tag{8.28}$$

$$V_{\mathrm{q}}(\mathbf{r}) = -Q\frac{r^2}{r^5 + r_{\mathrm{q}}^5}\frac{3\cos^2\chi - 1}{2}\ . \tag{8.29}$$

Tentatively, we set the cutoff radii to two-thirds of the internuclear equilibrium separation R: $r_{\mathrm{d}} = r_{\mathrm{q}} = (2/3)\,R$. We did not attempt to adjust this value to obtain better agreement with experimental data. Values in atomic units of quadrupoles Q and NO dipole D are reported in table 8.3.

Altogether, we construct the static potential of diatomic molecules in the following way: two decentred unperturbed atomic potentials and the adapted multipole potentials.

$$V_{\mathrm{s}}(\mathbf{r},\mathbf{R}) = V_{A,1s}(|\mathbf{r} - \frac{\mathbf{R}}{2}|) + V_{A',1s}(|\mathbf{r} + \frac{\mathbf{R}}{2}|) + V_{\mathrm{d}}(\mathbf{r}) + V_{\mathrm{q}}(\mathbf{r})\ . \tag{8.30}$$

The coordinate system proper to the diatomic molecule is represented in sketch 8.2, where χ is the angle between $\mathbf{r}$ and $\mathbf{R}$. In this frame, the molecular potential can be decomposed into a sum of harmonics: $V_{\mathrm{s}}(\mathbf{r},\mathbf{R}) = \sum_{l=0}^{\infty} V_l(r)P_l(\cos\chi)$ [906, p.222:eq.(4.3)]. This will be very useful in the single-centre expansion of the scattering equation from which partial waves emerge (sec. 8.4). The harmonic V_l of degree l of the potential (8.30) can be obtained numerically as the projection:

$$V_l(r) = \frac{2l+1}{2}\int_0^{\pi} V_{\mathrm{s}}(\mathbf{r})P_l(\cos\chi)\sin\chi\,\mathrm{d}\chi\ . \tag{8.31}$$

If $V_{\mathrm{s}}(\mathbf{r})$ results from shifted central potentials $V_{1\mathrm{s}}(|\mathbf{r} \pm \mathbf{R}/2|)$ as in (8.30), then one can use the addition theorem of the function represented by $V_{1\mathrm{s}}$. For instance, the addition theorem of a shifted Yukawa potential is well known from the decomposition of modified spherical Bessel functions of the first ι_l and second κ_l kinds [3, 618, p.107 or p.445:eq.(10.2.35)]:

$$\frac{\mathrm{e}^{-\lambda|\mathbf{r}-\frac{\mathbf{R}}{2}|}}{|\mathbf{r} - \frac{\mathbf{R}}{2}|} = \lambda\sum_{l=0}^{\infty}(2l+1)\iota_l(\lambda r_<)\kappa_l(\lambda r_>)P_l(\cos\chi)\ , \tag{8.32}$$

where we can immediately recognise the harmonic components V_l. The radii $r_{\lessgtr}$ are the lesser ($r_<$) and greater ($r_>$) of the two radii $|\mathbf{r}|$ and $|\mathbf{R}/2|$. The two kinds of modified spherical Bessel functions are defined as [3, 219, §10.2, eqs.(10.47.7–9) and (10.52.5–6)]:

$$\begin{cases} \text{first kind}: & \iota_l(x) = \sqrt{\dfrac{\pi}{2x}}I_{l+1/2}(x) = (-\mathrm{i})^l\,\mathrm{j}_l(\mathrm{i}x) \sim \dfrac{\mathrm{e}^x}{2x} & (8.33) \\ \text{second}^{\dagger}\text{ kind}: & \kappa_l(x) = \sqrt{\dfrac{\pi}{2x}}K_{l+1/2}(x) = \dfrac{\pi}{2}(-)^{l+1}\sqrt{\dfrac{\pi}{2x}}\left(I_{l+1/2}(x) - I_{-l-1/2}(x)\right) \sim \dfrac{\pi}{2}\dfrac{\mathrm{e}^{-x}}{x} & (8.34) \end{cases}$$

They are derived from the modified Bessel function $I_{l+1/2}$ and $K_{l+1/2}$ or the spherical Bessel function j_l which will be reminded later on page 301. Given their opposite asymptotic trends $\sim \exp(\pm r)/r$ at $r \to \infty$, it is easy to remember which of the lesser/greater radii $r_{\lessgtr}$ goes as argument to ι_l/κ_l.

The addition theorem for Slater-type functions was unravelled in Weniger and Steinborn [979, p.(4.31–2)]. It becomes more involved and the individual harmonic components V_l are obtained from a sum of modified spherical Bessel functions ι_l and κ_l. For instance, the harmonic expansion of a negative exponential function is:

[†]In older textbooks [3, p.443], it is rather called of the "third" kind.

$$\mathrm{e}^{-|\mathbf{r}-\frac{\mathbf{R}}{2}|} = \sum_{l=0}^{\infty}(-)^l \frac{2}{\pi}(2l+1)\left(\lambda r_> \iota_l(\lambda r_<)\kappa_{l-1}(\lambda r_>) - \lambda r_< \iota_{l+1}(\lambda r_<)\kappa_l(\lambda r_>)\right) P_l(\cos\chi) \tag{8.35}$$

$$\text{the term for } l=0 \;:\; \mathrm{e}^{-\lambda r_>}\left(\frac{\sinh(\lambda r_<)}{\lambda r_<}\left(1+\frac{1}{\lambda r_>}\right) - \frac{\cosh(\lambda r_<)}{\lambda r_>}\right) \tag{8.36}$$

Thus, if we apply both exponential (8.35) and Yukawa (8.32) decompositions to the static potential $V_\mathrm{X} = \frac{\lambda}{2}\mathrm{e}^{-\lambda r} + \mathrm{e}^{-\lambda r}/r$, we obtain*:

$$V_\mathrm{X}(|\mathbf{r}-\frac{\mathbf{R}}{2}|) = -Z\sum_{i=1}^{n_\rho}\gamma_i \sum_{l=0}^{\infty} V_{\mathrm{X},l} P_l(\cos\chi)\,, \tag{8.37}$$

$$\text{with } V_{\mathrm{X},l} = \frac{2}{\pi}\lambda(2l+1)\left[\iota_l(\lambda r_<)\kappa_l(\lambda r_>) + \frac{(-)^l}{2}\left(\lambda r_>\iota_l(\lambda r_<)\kappa_{l-1}(\lambda r_>) - \lambda r_<\iota_{l+1}(\lambda r_<)\kappa_l(\lambda r_>)\right)\right], \tag{8.38}$$

$$\text{and } V_{\mathrm{X},0} = \frac{\lambda}{2}\mathrm{e}^{-\lambda r_>}\left(\frac{\sinh(\lambda r_<)}{\lambda r_<}\left(1+\frac{3}{\lambda r_>}\right) - \frac{\cosh(\lambda r_<)}{\lambda r_>}\right) \tag{8.39}$$

The oppositely shifted $\pm\mathbf{R}/2$ potentials V_A and $V_{A'}$ have supplementary polar angles (see sketch 8.2) meaning that χ for atom A is replaced by $\pi-\chi$ for atom A' and thus $\cos\chi$ is replaced by $-\cos\chi$. As expected from the symmetry of Legendre polynomials $P_l(-\cos\chi) = (-1)^l P_l(\cos\chi)$, homonuclear molecules $A = A'$ only have even l non-zero harmonics. The harmonics of the potential may be observed on figure 8.3. There, we see that the nuclear singularity requires a sufficiently high harmonic degree to be represented with fair accuracy.

8.2.2 Exchange

As seen above in (8.9), the indistinguishability of electrons entails a non-local interaction potential $\int W_{\alpha\alpha}(x,x_j)\psi_\alpha(x_j)\,\mathrm{d}x_j$. Here, we note $x = (\mathbf{r}, s)$ the position $\mathbf{r}$ and spin s of the scattering electron. First, we note that exchange terms are non-null only between electron states of identical spin projection. Then, the exchange term coupling the spatial orbitals of two (spin-aligned) electrons may be approximated by a local interaction through an expansion in $\mathbf{r}_j$ about the point $\mathbf{r}$. This expansion may be applied on the scattering wavefunction $\psi_\alpha(\mathbf{r}_j)$ [as in 775, eq.(6)], the bound orbital $\phi_j(\mathbf{r}_j)$ in the exchange kernel (8.13), or to both [following 309].

This approximation is known as the **S**emi**C**lassical (SC) exchange potential. Succinctly, the expansion in $\mathbf{r}_j$ leads to a $\exp((\mathbf{r}_j-\mathbf{r})\cdot\nabla_j)$ term, which, when integrated over the exchange kernel, transforms into a term inversely proportional to the Laplacian; i.e. the energy of the electron(s) [100, p.235:eqs. (3.17–8)]. We retained two versions of the SC model; the original one where the expansion applies to ψ_α only [775, eq.(8)]:

$$V_{\mathrm{ex,SC}}(\mathbf{r}) = \frac{1}{2}(\varepsilon_0 - V_\mathrm{s}(\mathbf{r})) - \sqrt{(\varepsilon_0 - V_\mathrm{s}(\mathbf{r}))^2 + 4\pi\rho(\mathbf{r})}\,; \tag{8.40}$$

and the modified one which also expands the bound orbital [325, eq.(9) and (18)] leading to:

$$V_{\mathrm{ex,SCF}}(\mathbf{r}) = \frac{1}{2}(\varepsilon_0 - V_\mathrm{s}(\mathbf{r}) + \frac{3}{10}(3\pi^2\rho(\mathbf{r})^{2/3}) - \frac{1}{2}\sqrt{\left((\varepsilon_0 - V_\mathrm{s}(\mathbf{r}) + \frac{3}{10}(3\pi^2\rho(\mathbf{r})^{2/3})\right)^2 + 4\pi\rho(\mathbf{r})}\,. \tag{8.41}$$

*Note that the γ_i and λ_i parameters to be used in (8.38–8.39) are to be found in table 8.1 in the rows with the N, O atoms marked with a ‡ superscript.

The inclusion of the $\frac{3}{10}(3\pi^2\rho(\mathbf{r})^{2/3})$ term stems from the approximation of the bound electron's kinetic energy as given by the free electron gas model (see E.3) for why we labelled it "SCF": semi-classical free-[electron-gas]).

Strictly speaking, these equations (8.40 and 8.41) are valid for targets with no singly occupied orbitals. For N, O and NO, one would need to differentiate the spin up ($|\uparrow\rangle$) and spin down ($|\downarrow\rangle$) densities $\rho_\uparrow$, $\rho_\downarrow$ which would give slightly different exchange potentials for the spatial states associated to spin up and spin down states of the unpolarised scattering electron beam.

The overall effect of the exchange potential (local or not) is to lower the total energy of the electron-molecule system due to "fermionic repulsion" which reduces the overlap of wavefunctions for identical spin projection. The exchange potential is therefore negative (attractive).

In a later section 10.3.2, we compare three semi-empirical local exchange potentials for argon and molecular oxygen. Limited by the inaccuracy of diatomic static potentials modelled by (8.30), we observed that using the least attractive $V_{\text{ex,SCF}}$ (8.41) (least negative of all models on fig. 10.10) yielded the least disagreeable results for N_2, O_2 and NO. Regarding Ar, it seems (from figure 10.11) that another model $V_{\text{ex,FEG}}$ (10.39), based on the free electron gas, is best suited for yielding accurate DCS. For N and O, we had no means of determining which model would perform best due to lack of experimental data. As a result, we used the original $V_{\text{ex,SC}}$ (8.40) which is an intermediary between $V_{\text{ex,FEG}}$ and $V_{\text{ex,SCF}}$. These choices are summarised in table 8.2.

8.2.3 Distortion

Due to the external electric field generated by the scattering electron, the state of the molecule or atom is slightly affected. From earlier, we remember that this perturbation may be modelled through an expansion (8.6) of excited states $|\Phi_\alpha\rangle$ to each of which a particular scattering wavefunction $|\psi_\alpha\rangle$ is associated. The close-coupling approximation selects a limited number of such states, which leads to a system of N_α coupled equations [413]. A simplification step consists in bypassing the system of coupled equations by finding an approximate polarised wavefunction [925] which represents a state of virtual excitation induced by the presence of the scattering electron. Formally, one can encompass the perturbation as an effective potential defined by the total energy difference of the electron-molecule system with and without distortion of the molecule at the position x (including spin projection) [674, §II.A:eqs.(1–3)]:

$$V_{\text{pol}}(x) \equiv \langle\Psi(x_m;x,\mathbf{R})|H|\Psi(x_m;x,\mathbf{R})\rangle - \langle\Psi_0(x_m;\mathbf{R})|H_0|\Psi_0(x_m;\mathbf{R})\rangle \tag{8.42}$$

The ground-state molecular wavefunction $\Psi_0(x_m;\mathbf{R})$ is linked to the unperturbed Hamiltonian H_0, with x_m being a shorthand notation for all bound electronic coordinates (spatial and spin) and $\mathbf{R}$ is the internuclear separation of diatomic molecules. The semicolon (;) separates the coordinates that are integrated (x_m) from those that are parametric* ($\mathbf{R}$ and x). In its most complete form, the total Hamiltonian H comprises the kinetic operators of all nuclei and electrons and the two-particle interaction potentials. As we saw earlier, the obtention of the total system's wavefunction Ψ is the crux the whole scattering theory.

There are numerous ways in which one can obtain an approximate effective polarisation potential from (8.42). First, exchange effects may be treated separately into an exchange potential

*Technically, the polarisation potential could also be integrated over the nuclear separation vector $\mathbf{R}$. Nonetheless, in practice this leads to an intractable expression in the scattering electron's position x because it is usually assumed on the contrary that the nuclei do not budge while the electron scatters (see section 8.5.2), so that the averaging is done later on the scattering amplitude [551, eq.(32)] under the adiabatic nuclei approximation in 8.5.2.

Table 8.2: Overview of the present optical potential model used for our targets.

N_2	O_2	NO	Ar	O	N
V_s (8.30)			V_{1s} (8.23)		
$V_{ex,SCF}$ (8.41)			$V_{ex,FEG}$ (10.39)	$V_{ex,SC}$ (8.40)	
V_{co+pol} (8.53)			V_{cop} (8.55)		
$V_{abs,bcFEG}$ (8.58–8.63)					

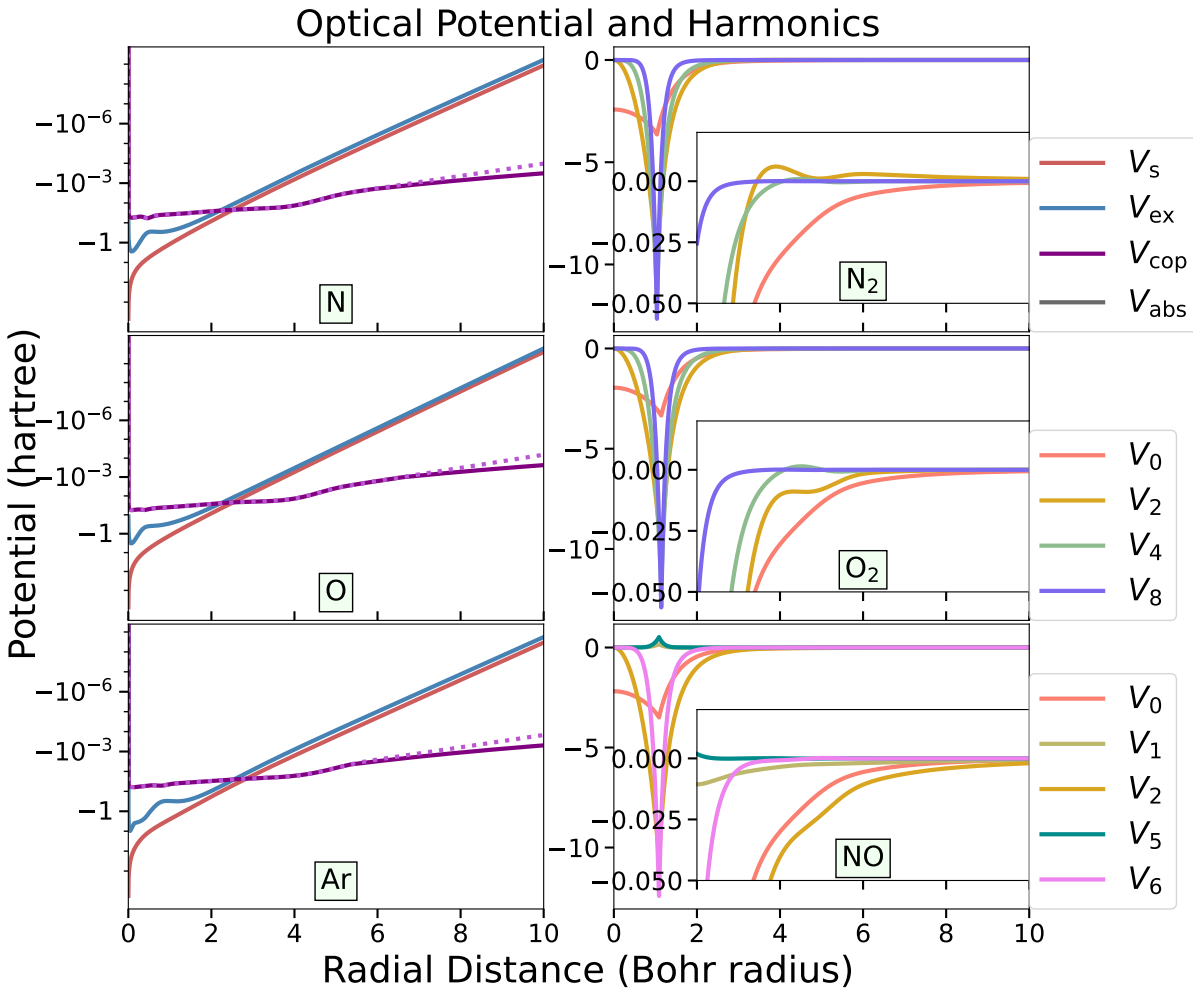

Figure 8.3: An overview of the optical potential constructed for six targets perceived by an electron at $k_0 = 2$ a.u. ~ 50 eV. On the left column: the four parts static, exchange, correlation-polarisation and absorption represented for atoms. The orchid dotted line is the pure correlation potential which is in (8.55) superseded by the polarisation long-range potential. On the right column: the potential harmonics V_l of the full molecular potential. The inset shows the influence of the long-range quadrupole and dipole potentials. For NO, the orientation is chosen so that z points from O to N, *opposite* to the dipole ($\overrightarrow{{}^{\ominus}\mathrm{NO}^{\oplus}}$), which is why the odd harmonics are positive.

which was described in the previous section. One can therefore only focus on perturbation due to purely Coulombic repulsion and replace x by $\mathbf{r}$. Then, further approximations may be taken, namely that the coupling to other (inelastic) channels is weak compared to the elastic channel, that the response of the molecule is adiabatic (instantaneous) [672, 946] or the Born approximation for estimating the coupled terms [137, 524, eq.(8), eq.(2.24)]. A brief overview of numerical techniques for finding a tractable expression for the complicated polarisation potential may be found in Čarský and Čurík [156, chapter 2.3].

In essence, the perturbation potential (8.42) is composed of a real and an imaginary part [524, 880, eq.(24)]. The latter represents a loss of flux into open reaction channels and forms the absorption potential described in the last section 8.2.4. The real part represents virtual excitations, i.e. couplings with closed channels, and may be separated into long- and short-range components:

- Polarisation acting on long ranges distorts the electronic molecular cloud and thereby induces multipoles [138].
- Correlation acts on short ranges when the scattering electron penetrates the cloud which forms a positive "Coulombic hole" around it [742, §II.C].

Below, we briefly describe what those components are and how they are consolidated together.

Polarisation – long range

When the scattering electron is far from the target molecule or atom, its wavefunction does not overlap. In the ideal case when the electron may be represented by a singly localised point charge, the distortion of the electronic cloud may be modelled as an expansion of induced multipole moments. The proportionality coefficient between the induced charge moment and the external electric field is known as the polarisability $\underline{\alpha}$. It depends on the relative orientation of the molecule and the electric field. In general, the polarisability $\underline{\alpha}_n$ is a tensor of rank $n+1$ which defines an induced multipole of degree n given an electric field $\mathbf{E}$.

For a diatomic molecule, the polarisability tensor has only two independent components: one for the induced multipole component when the electric field is oriented along the principal axis $\alpha_\parallel$ and the other $\alpha_\perp$ perpendicular to that axis. Combined together, the induced dipole $\tilde{D}$ may be decomposed into an isotropic $\alpha_{\mathrm{d},0}$ and anisotropic component $\alpha_{\mathrm{d},2}$ [834, p.19:eq.(25)]:

$$\frac{|\tilde{\mathbf{D}}|}{|\mathbf{E}|} = \alpha_{\mathrm{d}}(\cos\chi) = \alpha_\parallel \cos^2\chi + \alpha_\perp \sin^2\chi = \underbrace{\frac{(\alpha_\parallel + 2\alpha_\perp)}{3}}_{\alpha_{\mathrm{d},0}} + \underbrace{\frac{2(\alpha_\parallel - \alpha_\perp)}{3}}_{\alpha_{\mathrm{d},2}} \mathrm{P}_2(\cos\chi)\,. \tag{8.43}$$

The angle χ spans between the direction of the electric field $\mathbf{E}$ and the z axis (principal molecular axis, see 8.2). The same can be done with higher order multipoles such as the quadrupole polarisability α_{q}.

At closer distances near the target molecule, dynamic effects perturb the ideal static polarisation described above. As the incident velocity of the electron v_0 increases and the distance r decreases, the response of the molecule becomes less adiabatic. Non-adiabaticity can be introduced by considering the higher-order polarisability coefficients which are moments $S(\mu)$ of the dipole (or multipole) oscillator strength distribution of the atomic target [229, p.L701]:

$$\alpha_\mathrm{d} \equiv 2^2 S(-2) = \sum_n \frac{f_{\mathrm{d},0\to\mathrm{n}}}{(\mathcal{E}_n - \mathcal{E}_0)^2} + \sum_i \int_0^\infty \frac{\mathrm{d}f_{\mathrm{d},i}}{\mathrm{d}\varepsilon_2 + I_i} \frac{1}{(\varepsilon_2 + I_i)^2}\,\mathrm{d}\varepsilon_2 \,, \tag{8.44a}$$

$$\beta_\mathrm{d} \equiv 2^3 S(-3) = \sum_n \frac{f_{\mathrm{d},0\to\mathrm{n}}}{(\mathcal{E}_n - \mathcal{E}_0)^3} + \sum_i \int_0^\infty \frac{\mathrm{d}f_{\mathrm{d},i}}{\mathrm{d}\varepsilon_2 + I_i} \frac{1}{(\varepsilon_2 + I_i)^3}\,\mathrm{d}\varepsilon_2 \,, \tag{8.44b}$$

$$\gamma_\mathrm{d} \equiv 2^4 S(-4) = \sum_n \frac{f_{\mathrm{d},0\to\mathrm{n}}}{(\mathcal{E}_n - \mathcal{E}_0)^4} + \sum_i \int_0^\infty \frac{\mathrm{d}f_{\mathrm{d},i}}{\mathrm{d}\varepsilon_2 + I_i} \frac{1}{(\varepsilon_2 + I_i)^4}\,\mathrm{d}\varepsilon_2 \,. \tag{8.44c}$$

The $S(\mu = -2, -3, -4)$ refer to the standard notation [427, §3.3] of the energy moments of the **d**ipole (optical) oscillator strength distribution over discrete (excitation) states n ($f_{\mathrm{d},n}$) and continuum (ionisation) states i ($\mathrm{d}f_{\mathrm{d},i}/\,\mathrm{d}\varepsilon_2$) with the energy ε_2 of the ejected electron and the ionisation threshold I_i to the ionic state i. More information can be found later in chapter 11 section 11.5 and in the appendix D.1. Please note that the current definitions are adapted to the atomic units using the hartree energy $\mathcal{E}_\mathrm{h} = 2\mathrm{Ryd}$ and differ slightly from the original ones [229, 824, eq.(1.10-2), p.L701] due to the absorption of powers of 2 coming from the Rydberg unit system traditionally used.

Then, the non-adiabatic asymptotic expansion of the long-range polarisation potential of an atomic target is given by [824, eq.(1.9)]:

$$V_\mathrm{pol}^\infty \sim -\frac{\alpha_\mathrm{d}}{2r^4} - \frac{\alpha_\mathrm{q}}{2r^6} + \frac{3\beta_\mathrm{d}}{2r^6} + \frac{6\gamma_\mathrm{d}\mathrm{v}_0^2}{2r^6} + O\left(\frac{1}{r^7}\right) . \tag{8.45}$$

For diatomic molecules, one must include anisotropic effects by considering that the polarisabilities vary with χ as explained above (8.43).

As one can see, the multipolar expansion collapses as $r \to 0$ near the singularity regions of the atomic nuclei. The importance of high-order terms increases very rapidly and to remove the singular behaviour, it is necessary to use cutoff functions just as for permanent multipoles (8.27). One may choose to use a different function for each of the orders in (8.45) as in Gianturco *et al.* [329], or alternatively, regard the terms in (8.45) as part of a Taylor expansion of an analytical function as suggested by Onda and Truhlar [719].

We use two different analytical expression for the non-adiabatic polarisation potential with attenuation at close encounters $r \to 0$.

The first is the Buckingham potential (for atoms):

$$V_\mathrm{b} = -\frac{\alpha_\mathrm{d}}{2(r^2 + r_\mathrm{b}^2)^2} . \tag{8.46}$$

The second is the exponentially damped polarisation (for diatomic molecules):

$$V_\mathrm{pol,exp} = -\frac{\alpha_\mathrm{d}}{2r^4} \exp\left(-\frac{r_\mathrm{d}^2}{r^2}\right) . \tag{8.47}$$

In principle, one could calculate all coefficients $\beta_\mathrm{d}, \gamma_\mathrm{d}$ from (8.44b, 8.44c) and find α_q from Dykstra [254] or approximate it through Dalgarno and Lewis [209, §4:eq.(33)]. To match (8.45), the curbing r_b and damping r_d would then be related:

$$r_\mathrm{d}^2 = 2r_\mathrm{b}^2 = \frac{3\beta_\mathrm{d} + 6\gamma_\mathrm{d}\mathrm{v}_0^2 - \alpha_\mathrm{q}}{\alpha_\mathrm{d}} . \tag{8.48}$$

Nonetheless, there are presently two issues that may arise with this procedure (which is why we crossed the second equation):

I. $3\beta_d - \alpha_q \ll \alpha_d$: in that case the value of r_b at $v_0 \sim 0$ would be too small ($r_b \ll a_0$) resulting in an improper polarisation potential near the molecule/atom at lower energies.

II. $6\gamma_d \gg \alpha_d$: then the damping due to dynamic effects at $v_0 > 1$ would be too strong and this results, to the contrary, in an underestimation of the polarisation potential near the molecule/atom at higher energies.

A later section 10.3.3 is dedicated to illustrate this problem in figures 10.15 and 10.18b. What results from this, is that because the importance of higher-order ($\sim 1/r^{n>6}$) perturbation terms in (8.45) rises fast with decreasing r, the outer region where only the zeroth $1/r^4$ and first $1/r^6$ order terms dominate is restricted to large radii $r \gtrsim 3a_0$. This impedes one from recurring to (8.48) as a valid representation of non-adiabatic effects. This problem was already discussed by Gianturco *et al.* [329] for noble gases and addressed with correction (cutoff) functions.

There are many studies that endeavoured to map radially the polarisation potential from *ab initio* calculations of the perturbed target wavefunction. Models included: an adiabatic approach with the electron as a static point charge [257, 672], a non-penetrating approximation in the electronic cloud [332], an estimation of non-local effects through a Gaussian charge distribution of the scattering electron [276, 277], an inclusion of dynamic effects from the gradients and Laplacian of the electron's density [638]. An overview of perturbative methods can be found in Valone *et al.* [955], who also proposes semi-empirical approximations based on the *local* kinetic energy of the scattering electron (unlike v_0 which is asymptotic).

In all studies, the polarisation potential takes the shape of a smoothly damped curve at small distances. In adiabatic models [638, 672, 674, figs. 1-6, fig. 1], the maximum of the potential is situated at the origin and resembles the Buckingham potential (8.46); while in non-adiabatic models, V_{pol} goes through a maximum in the inner region of the molecule and annihilates at the origin [276, 332, fig. 1-2, fig. 4], like the shape of (8.47). Morrison *et al.* [674, eq.(21)] give an analytical fit to their non-adiabatic potential which basically is a damped modified Buckingham potential.

In any case, when the electron's wavefunction significantly overlaps the region occupied by bound electrons, the interaction is more suitably described by correlation forces rather than the description given by polarisation of the electronic cloud. We describe those below.

Correlation – short range

As the incident electron penetrates the region occupied by bound electrons, its Coulomb repulsion causes restructuration of the electronic density in the space surrounding the incident electron which we now qualify as 'invading' electron. The change of total energy of the system due to the restructuration of the electronic density is commonly known as the correlation energy from which an effective potential may be derived.

The correlation potential felt by an electron situated inside an electronic cloud, is the perturbation to the electrostatic potential generated by the cloud's fixed charge distribution. The electrons in the cloud adapt to the presence of the invading electron by forming a 'positive hole' around the current position $\mathbf{r}$ occupied by that electron. Here, we assume that the formation of the positive hole is immediate, meaning that the correlation is *adiabatic*. However, in practice, the response is non-adiabatic when the invading electron's velocity is large.

The density functional theory (DFT) consists in giving an estimation of this correlation potential based on the local electron density $\rho(\mathbf{r})$ at $\mathbf{r}$. A more detailed introduction into DFT models of correlation is given later in section 10.3.3. Based on the overviews of Gianturco and Rodriguez-Ruiz [327, 328], we selected the local kinetic density formulation (KDF) of Lee *et al.* [567] which stems from the model of Colle and Salvetti [185]. Concisely, this model estimates

the Hartree-Fock kinetic energy density (which depends on individual electron orbitals) from the Thomas-Fermi free electron gas model (E.5) [567, §III].

In the Thomas-Fermi model, the local kinetic density of the free electron gas filling the momentum space can be directly derived from the local density as $\propto (\rho(\mathbf{r}))^{5/3}$ (see E.5 in appendix E). To this simple formula, some corrections may be introduced taking into account the gradient $\nabla\rho(\mathbf{r})$ of the density [468, eq.(4)]. Lee *et al.* [567] expanded the Laplacian of the second-order Hartree-Fock reduced density matrix in terms of the gradient of the single particle density, to wit:

$$\triangle\rho_2(\mathbf{r},\Delta\mathbf{r})|_{\Delta\mathbf{r}=0} \cong \frac{3}{10}(3\pi^2)^{2/3}(\rho(\mathbf{r}))^{5/3} + \left[\frac{W(\mathbf{r})}{9} + \frac{\triangle\rho(\mathbf{r})}{18}\right] - 2W(\mathbf{r}) \,, \tag{8.49}$$

where $W(\mathbf{r})$ is a kinetic density functional based on von Weizsäcker [965]:

$$W(\mathbf{r}) = \frac{1}{8}\left(\frac{|\nabla\rho(\mathbf{r})|^2}{\rho(\mathbf{r})} - \triangle\rho(\mathbf{r})\right) . \tag{8.50}$$

After insertion in the expression of the correlation energy $\mathcal{E}_{\text{co}}$ and taking the functional derivative with respect to the density ρ, Lee *et al.* [567] determined a formula for the correlation potential V_{co}, which we have condensed here in a more convenient form for numerical implementation:

$$\begin{aligned} V_{\text{co,KDF}}(\mathbf{r}) = \frac{-a}{\rho^{1/3}+d}\Bigg\{\rho^{1/3}\left(1+\frac{d}{\rho^{1/3}+d}\right) + b\mathrm{e}^{-c\rho^{-1/3}}\Bigg[\frac{3}{10}(3\pi^2)^{2/3}\left(\frac{\rho^{1/3}}{3}(dF+c)+1\right) \\ + \frac{|\nabla\rho|^2\rho^{-3}}{216}\left(7(2d^2F^2+2cdF+c^2) - 3\rho^{1/3}(5\rho^{1/3}+13(dF+c))\right) \\ + \frac{\rho^{-5/3}}{36}\triangle\rho(7(dF+c)+3\rho^{1/3})\Bigg]\Bigg\} \end{aligned} \tag{8.51}$$

The parameters a, b, c, d were obtained as a fit to match the calculated energy of the Helium atom from a Hartree-Fock description. They were initially determined by Colle and Salvetti [185]. Later, Gianturco and Rodriguez-Ruiz [327, p.107] updated those values as: $a = 0.0578$; $b = 0.062$; $c = 0.253$; $d = 0.543$, which we use in our current implementation. The function $F(\rho)$ is defined as:

$$F(\rho) = \frac{1}{1+d\rho^{-1/3}} \tag{8.52}$$

In (8.51), the dependence on the position $\mathbf{r}$ is tacit; gradients ∇ and Laplacians $\triangle$ operate on the space coordinate $\mathbf{r}$ on which the density $\rho(\mathbf{r})$ depends. Analytical expressions for density gradients and Laplacians can be found in section 14.1 for Yukawa–14.1.1 and Exponential–14.1.2 distributions.

If the target has open shells, meaning that some orbitals are half occupied, the correlation potential depends on the local density of the orbitals with spin up $\rho_\uparrow$ and spin down $\rho_\downarrow$, which are different. This further description should be applied to nitric oxide, oxygen and nitrogen atoms. Given the limitations of our approach, we did not implement this spin-distinguished density. Inclusion of spin-related effects would also imply to adapt the exchange model above to open-shell targets.

Although more involved than simpler free electron gas models of Perdew and Zunger [742] or Padial and Norcross [728], the kinetic energy density functional correlation potential (8.51) was observed, in a comparison study conducted in section 10.3.3, to give more agreeable results at smaller angles for diatomic molecules and at lower energies for argon.

Correlation-Polarisation

The full potential accounting for the electron-molecule perturbation must somehow conciliate the long-range polarisation with the short-range correlation. For simplicity, many authors [569, 617, 728] chose to stitch them together at their outer intersection radius. In chapter 10, we explore different ways to represent a global correlation-polarisation potential. There exists not any straightforward solution that would yield accurate results over a very wide range of energies from eV to keV. The greatest issue is that the correlation potential (8.51) is adiabatic and therefrom independent of the electron's energy. It becomes unusable at high energies > keV and must be scaled down heuristically. The most elegant way we found in the literature was proposed by Salvat [801] and implemented in the program ELSEPA [803] for calculating DCS. It consists in taking the maximal (least negative) value between correlation and polarisation in the inner region below their intersection, if it exists. In this way, correlation gradually vanishes as the energy increases thanks to the growth of the curbing radius (8.48) with k_0^2, decreasing the value of V_b (8.46) at the origin.

We did not take this option because we obtained DCS in better agreement at small angles when using the kinetic density functional correlation (8.51). Acknowledging that finding an adequate yet simple expression for the combined correlation-polarisation potential for diatomic molecules and atoms is far beyond the reach of this thesis, we resolved to use the following distinct expressions for atoms and diatomic molecules respectively:

$$\text{Diatomic Molecules :} \qquad V_\mathrm{co+pol} = V_\mathrm{co,KDF}(\mathbf{r}) - \frac{\alpha_{\mathrm{d},0} + \alpha_{\mathrm{d},2}\mathrm{P}_2(\cos\chi)}{2r^4}\exp\left(-\frac{r_\mathrm{d}^2}{r^2}\right) \tag{8.53}$$

$$\text{and } r_\mathrm{d}^2 = \max\left(2a + 6k_0^2, R^2\right) \tag{8.54}$$

$$\text{Atoms :} \qquad V_\mathrm{cop} = \begin{cases} V_\mathrm{co,KDF}(r) & r < r_\mathrm{t} \\ V_\mathrm{b}(r) = -\dfrac{\alpha_\mathrm{d}}{(r^2 + r_\mathrm{b}^2)^2} & r \geq r_\mathrm{t} \end{cases} \tag{8.55}$$

$$\text{and } r_\mathrm{b}^2 = a + 3k_0^2 \tag{8.56}$$

We remind here that, in atomic units, velocities and wavenumbers are alike: $\mathrm{v}_0 \equiv \mathrm{k}_0$ a.u.. One may thus compare the electron's wavelength ($1/\mathrm{v}_0 \gtrless 1$?) to the atomic size in expressions where the velocity appears (e.g. 8.45, 8.58). The radius r_t is taken as the outermost intersection between the polarisation and correlation potential. An illustration of the junction at r_t is given by the darkred curves in figures 10.14 (although the potentials used are not exactly the same, the analogy applies: —V_cop, ···$V_\mathrm{co,KDF}$ and - - -V_b). At higher energies, we had to choose an energy at which the correlation and polarisation would be replaced altogether by a Buckingham potential. This is explained on page 396 in the results chapter 11.

The values for the parameters involved can be found in table 8.3. For the curbing radii r_b and r_d, the original theoretical relation (8.48) was heuristically modified in order to make the polarisation potential usable over a wide range of energies. In particular, we replaced γ_d by $\alpha_\mathrm{d}/2$ (this is not true but convenient). We did not attempt to fit r_b nor r_d in order to get good agreement. The value for a in (8.54) and (8.56) was simply deduced from what $(3\beta_\mathrm{d} - \alpha_\mathrm{q})/\alpha_\mathrm{d}$ would be as given by equation (8.48). A theoretically founded estimation of the curbing radius which would yield accurate long-range polarisation potentials is a desideratum for the future.

Table 8.3: Internuclear separation R, permanent multipole moments D, Q, polarisabilities $\alpha_{\rm d}$ and parameter a for the curbing radius of atoms and diatomic molecules to be used in (8.53–8.56). Last row gives the minimal excitation thresholds $\Delta\mathcal{E}_{\rm min}$ selected for the absorption potentials (8.58–8.70).

	N_2	O_2	NO	Ar	O	N
R (a_0)	2.074[a,g]	2.281[a,g]	2.175[a,g]	–	–	–
D ($e\,a_0$)			0.0625[a]			
Q ($e\,a_0^2$)	-1.13[a]	-0.29[a]	1.78[f]	–	–	–
$\alpha_{\rm d,0}$ (a_0^3)	11.74[a]	10.67[a]	11.47[a]	11.08[b]	5.412[c]	7.423[c]
$\alpha_{\rm d,2}$ (a_0^3)	3.131[d]	4.93[e,d]	3.78[d]	–	–	–
a (a.u.)	2.27	2.92	4.3	2.43	2.29	3.07
$\Delta\mathcal{E}_{\rm min}$ (eV)	6.17[g]	4.26[g]	5.48[g]	11.55[h]	1.97[h]	2.38[h]

[a] Khristenko *et al.* [499, p.25–26:table 2.1 for R, p.81:table 4.4 for Q, p.83:table 4.6 for $\alpha_{\rm d}$ and p.74 for D]
[b] Inokuti *et al.* [426, p.244:table 1]
[c] Miller [648]
[d] Bridge *et al.* [108] and Padial and Norcross [728, p.347, p.1743:table I.]
[e] Hirschfelder *et al.* [403] and Machado *et al.* [617, p.1200]
[f] Tejwani *et al.* [924]
[g] Linstrom and Mallard [601]
[h] Kramida *et al.* [539]

8.2.4 Absorption

Formally, an absorption potential represents the imaginary part of the perturbation potential obtained above for modelling the correlation-polarisation effects. It is negative imaginary everywhere, corresponding to a localised leak of electron current probability density* at the position $\mathbf{r}$ from the *elastic* channel [147, p.292:eq.(7.5)]. The absorption probability per unit time of an electron at $\mathbf{r}$ submitted to the absorption potential $V_{\rm abs}(\mathbf{r})$ is given by:

$$\text{Flux loss rate}: \frac{2}{\hbar}\Im\{V_{\rm abs}(\mathbf{r})\}\,. \tag{8.57}$$

Ideally, absorption should be derived directly from the potential perturbation given by the general equation (8.42) from the previous subsection [as in 525, appendix eq.(A.21)]. However, the correlation-polarisation model introduced above does not account for inelastic reactions.

- On the one hand, the polarisation potential (8.45) stems from long-range interactions whereas absorption is a rather short-range potential since it depends on a more intensified interaction with the bound electrons.
- On the other hand, the correlation potential (8.51) represents the local perturbation to the static potential created by the formation of a Coulomb hole around an electron in an electronic cloud of density $\rho(\mathbf{r})$. This hole is conservative; it vanishes when the electron moves away from the cloud.

*This stems from the non-hermiticity of the Hamiltonian which has a complex potential. The proof is a good exercise for undergraduate students.

Thus, usually another approximation is necessary to estimate absorption. If inelastic reactions are approximated as binary collisions of cross section $\sigma_{\rm bc}$ between the incident and a bound electron in a gas of density $\rho(\mathbf{r})$, then the absorption potential may be constructed as a probability of colliding per unit time [877, eq.(1)]:

$$V_{\rm abs} = \frac{\hbar}{2}\mathrm{v}(\mathbf{r})\rho(\mathbf{r})\sigma_{\rm bc}(\varepsilon,\rho,\Delta\mathcal{E}_{\rm min})\ . \tag{8.58}$$

The *local* velocity $\mathrm{v}(\mathbf{r})$ and local energy ε of the incident electron are determined from the asymptotic energy ε_0 and the static-exchange potential:

$$\varepsilon = \varepsilon_0 - V_{\rm s}(\mathbf{r}) - V_{\rm ex}(\mathbf{r}) \tag{8.59}$$

$$\mathrm{v} = \sqrt{1-\left(\frac{m_{\rm e}c^2}{\varepsilon+m_{\rm e}c^2}\right)^2} \cong \underbrace{\sqrt{2\varepsilon/m_{\rm e}}}_{\text{Non-relativistic : } \varepsilon\ll m_{\rm e}c^2} \tag{8.60}$$

In a *local* binary collision, the invading electron of initial energy ε (locally) transfers a momentum $\mathbf{q} = \mathbf{k}_- - \mathbf{k}_+$ and an amount $\Delta\varepsilon$ of energy to a bound electron. This energy $\Delta\varepsilon$ must be superior to a minimal excitation threshold $\Delta\mathcal{E}_{\rm min}$ of the inelastic process. The momenta of the invading electron before $\mathbf{k}_- \equiv \mathbf{k}$ and after $\mathbf{k}_+$ the local collision, separated by an angle θ, are sketched in 7.2 (with a different notation: $\mathbf{k}_- \equiv \mathbf{p}_i$ and $\mathbf{k}_+ \equiv \mathbf{p}_f$). We may define the recoil energy as [801, eq.(A2): but missing a factor 2 in front of 'E']:

$$\frac{\hbar^2q^2}{2m_{\rm e}} = \frac{\hbar^2k_+^2}{2m_{\rm e}} + \frac{\hbar^2k_-^2}{2m_{\rm e}} - 2\frac{\hbar^2\sqrt{k_-k_+}}{2m_{\rm e}}\cos\theta = 2\varepsilon - \Delta\varepsilon - 2\sqrt{\varepsilon(\varepsilon-\Delta\varepsilon)}\cos\theta\ . \tag{8.61}$$

If the bound electrons are modelled as a free electron gas (FEG) of local density $\rho(\mathbf{r})$, both ejected and scattered electrons must have a final energy beyond the local Fermi energy $\varepsilon_{\rm F} = \dfrac{k_{\rm F}^2}{2} = \dfrac{1}{2}(3\pi^2\rho(\mathbf{r}))^{2/3}$ (E.3). Due to the indistinguishability of both electrons, the maximal energy lost is reduced by half [801, eq.(A24)]. These requirements and the one for the inelastic excitation are summarised as:

$$\Delta\varepsilon > \Delta\mathcal{E}_{\rm min}\ , \tag{8.62a}$$

$$\varepsilon - \Delta\varepsilon > \varepsilon_{\rm F} \Rightarrow \varepsilon > \Delta\mathcal{E}_{\rm min} + \varepsilon_{\rm F}\ , \tag{8.62b}$$

$$\Delta\varepsilon < \frac{1}{2}(\varepsilon - \varepsilon_{\rm F}). \tag{8.62c}$$

The difficulty now resides in calculating the binary cross section $\sigma_{\rm bc}$ for the inelastic process. We defer this discussion to a later section 10.3.4 where different models are compared. Presently, we implemented the binary cross section of Salvat [801] which relies on the first Born-Ochkur* approximation and the dielectric theory of Lindhard [595] for the electronic cloud modelled as a free electron gas.

With the following dimensionless variables:

$$\text{Local initial energy : } \xi_\varepsilon = \frac{\varepsilon}{\varepsilon_{\rm F}}\ ,$$

$$\text{Transferred energy : } \xi = \frac{\Delta\varepsilon}{\varepsilon_{\rm F}}\ ,$$

$$\text{Momentum transfer : } \zeta = \frac{1}{2}\sqrt{\frac{\hbar^2q^2}{2m_{\rm e}\varepsilon_{\rm F}}}\ ;$$

*Ochkur and Brattsev's approximation [711] accounts for exchange

the binary cross section is obtained from the integration of the differential cross section of an electron scattering in a FEG:

$$\sigma_{\mathrm{bc,FEG}} = \int_{\Delta\mathcal{E}_{\min}/\varepsilon_{\mathrm{F}}}^{(\varepsilon/\varepsilon_{\mathrm{F}}-1)/2} \frac{\mathrm{d}\sigma_{\mathrm{bc}}}{\mathrm{d}\xi}\,\mathrm{d}\xi\,, \tag{8.63}$$

$$\frac{\mathrm{d}\sigma_{\mathrm{bc}}}{\mathrm{d}\xi} = \frac{2\pi}{\varepsilon\varepsilon_{\mathrm{F}}}\int_{\zeta_-}^{\zeta_+}\frac{1}{\xi\zeta}\underbrace{\frac{6}{16\pi X^2}\frac{\xi\zeta^2X^2f_2(\zeta,\xi)}{(\zeta^2+X^2f_1(\zeta,\xi))^2+X^4f_2^2(\zeta,\xi)}}_{\text{Generalised oscillator strength of the FEG}}\underbrace{\left[1-\frac{4\zeta^2}{\xi_\varepsilon-\xi}+\frac{16\zeta^4}{(\xi_\varepsilon-\xi)^2}\right]}_{\substack{\text{Exchange correction}\\ \text{(Born-Ochkur)}}}\mathrm{d}\zeta\,, \tag{8.64}$$

$$\text{where } f_2(\zeta,\xi) = \begin{cases}\pi\xi/8\zeta & \text{if } |\zeta+\xi/4\zeta|\le 1\,,\\ \pi[1-(\zeta-\xi/4\zeta)^2] & \text{if } |\zeta\pm\xi/4\zeta|\gtrless 1\,,\\ \approx 0 & \text{if } |\zeta-\xi/4\zeta|\ge 1\,;\end{cases} \tag{8.65}$$

$$\text{and } f_1(\zeta,\xi) = \frac{1}{2}+\frac{1}{8\zeta}(1-w_-^2)\ln\left|\frac{w_-+1}{w_--1}\right|+\frac{1}{8\zeta}(1-w_+^2)\ln\left|\frac{w_++1}{w_+-1}\right|\,. \tag{8.66}$$

We introduced the shorthand $w_\pm \equiv \zeta \pm \xi/4\zeta$. To alleviate the notation, the 'FEG' index of the cross sections (referring to the free electron gas), will be implicit in the rest of this section.

The integral operates over the subspace of kinematically allowed collision outcomes (by conservation law 8.62c, where the factor 1/2 comes from the electron indistinguishability):

$$\xi_{\min} = \frac{\Delta\mathcal{E}_{\min}}{\varepsilon_{\mathrm{F}}} \quad \text{to} \quad \xi_{\max} = \frac{1}{2}\frac{(\varepsilon-\varepsilon_{\mathrm{F}})}{\varepsilon_{\mathrm{F}}} \equiv \frac{1}{2}(\xi_\varepsilon-1)\,, \tag{8.67}$$

$$\zeta_\pm = \frac{1}{2}\overset{\min}{\max}\left(\sqrt{\xi_\varepsilon}\pm\sqrt{\xi_\varepsilon-\xi},\sqrt{\xi+1}\pm 1\right)\,; \tag{8.68}$$

and in the region where the generalised oscillator strength of the FEG for a momentum and energy transfer (q, $\Delta\varepsilon$) is not null [801, eq.(A26)]. This region is determined by $f_2 > 0$ (8.65), through the second value appearing in the parenthesis of $\zeta_\pm$'s equation (8.68).

The integrals (8.63) and (8.64) must be computed numerically. Nonetheless, at high energy transfers, the generalised oscillator strength in (8.64) may be approximated by a Dirac peak (delta function $\delta(\xi-4\zeta^2)$) centred on $\zeta = \sqrt{\xi}/2$ (i.e. $q \approxeq \sqrt{2m_{\mathrm{e}}\Delta\varepsilon}/\hbar$) and the integration on ξ and ζ yields [801, eqs.(A30–1)]:

$$\sigma_{\mathrm{bc}} \approxeq \frac{\pi}{\varepsilon^2}\left[\frac{\varepsilon-2\Delta\mathcal{E}_{\min}}{\Delta\mathcal{E}_{\min}(1-\Delta\mathcal{E}_{\min}/\varepsilon)}-4\frac{\varepsilon_{\mathrm{F}}\varepsilon}{\varepsilon^2-\varepsilon_{\mathrm{F}}^2}-\ln\left(\frac{\varepsilon-\varepsilon_{\mathrm{F}}}{\varepsilon+\varepsilon_{\mathrm{F}}}\frac{\varepsilon-\Delta\mathcal{E}_{\min}}{\Delta\mathcal{E}_{\min}}\right)\right]\,. \tag{8.69}$$

As a simpler alternative, we also adapted a fully analytical absorption potential based on the quasi-free ('qf') potential of Staszewska *et al.* [877] but with the use of the local electron energy in the cross section as suggested but incorrectly implemented by Blanco and García [81]:

$$\begin{aligned}\sigma_{\mathrm{bc,qf}} =& \frac{4\pi}{5k_{\mathrm{F}}^3k^2}\mathrm{h}(k_{\mathrm{b}}^2-k_{\mathrm{F}}^2-2\Delta\mathcal{E}_{\min})\times\\ &\left[\frac{1}{2\Delta\mathcal{E}_{\min}}-\frac{k_{\mathrm{b}}^2-\frac{3}{5}k_{\mathrm{F}}^2}{(k_{\mathrm{b}}^2-k_{\mathrm{F}}^2)^2}+\mathrm{h}(2k_{\mathrm{F}}^2+2\Delta\mathcal{E}_{\min}-k_{\mathrm{b}}^2)\frac{2(2k_{\mathrm{F}}^2+2\Delta\mathcal{E}_{\min}-k_{\mathrm{b}}^2)^{5/2}}{5k_{\mathrm{F}}^3(k_{\mathrm{b}}^2-k_{\mathrm{F}}^2)^2}\right]\,.\end{aligned} \tag{8.70}$$

Heaviside's step function is noted:

$$\mathrm{h}(x) = \begin{cases}1\forall x\ge 0\\ 0\forall x<0\end{cases}\,.$$

The momentum k_b at $\mathbf{r}$ results from the counterbalance between the energy gained by the incident electron from the potential of the target V and the local binding energy V_b of a bound electron:

$$\frac{k_\mathrm{b}^2(\mathbf{r})}{2} = \varepsilon_0 - V(\mathbf{r}) + V_\mathrm{b}(\mathbf{r}) \tag{8.71}$$

$$V_\mathrm{b}(\mathbf{r}) = -\frac{1}{|\mathbf{r}-\frac{\mathbf{R}}{2}|} + \frac{(Z_A-1)}{Z_A}V_A(|\mathbf{r}-\frac{\mathbf{R}}{2}|) - \frac{1}{|\mathbf{r}+\frac{\mathbf{R}}{2}|} + \frac{(Z_{A'}-1)}{Z_{A'}}V_{A'}(|\mathbf{r}+\frac{\mathbf{R}}{2}|) \tag{8.72}$$

However, due to the first term in (8.70) $\propto 1/\Delta\mathcal{E}_\mathrm{min}$, this model is rather sensitive to the choice of the inelastic threshold $\Delta\mathcal{E}_\mathrm{min}$ which introduces some arbitrariness since this inelastic threshold is supposed to represent the onset of a continuum of excitations. We dedicated section 10.3.4 to a critical review and comparison of various absorption models.

Now that we have assembled a local optical potential from 8.2.1 through 8.2.4, which may be visualised in figure 8.3 for our six targets, we may return to the one-electron Schrödinger equation in the next section.

8.3 Operator formalism

Thanks to the optical potential, the elastic scattering of electrons off molecules, originally a coupled system (8.9), may now be charmingly represented as a single-electron equation in the centre of mass reference frame:

$$-\frac{1}{2\mu}\bigtriangleup\psi(\mathbf{r}) + V(\mathbf{r})\psi(\mathbf{r}) = \varepsilon_0\psi(\mathbf{r})\ , \tag{8.73}$$

where the final energy of the electron is equal to its incident value: $\varepsilon' = \varepsilon_0$, thus $k' = k_0$. The reduced mass $\mu = Mm_\mathrm{e}/(M+m_\mathrm{e}) \approx m_\mathrm{e}$ may be taken as the electron's rest mass due to the heaviness of the target atoms or molecules $M \gg m_\mathrm{e}$.

We recall that for calculating differential cross sections, we are not interested in the wavefunction $\psi(\mathbf{r})$ *per se*, but in its asymptotic angular dependence $f(\Omega)$ at far distances $\mathbf{r} \to \infty$.

It would be convenient to possess a formalism that would extract this angular dependence alone from the wavefunction. For this matter, we introduce here some fundamentals of scattering from the perspective of operators (see for instance Rodberg *et al.* [782, chapter 6.1]) starting with:

$$H|\psi\rangle \equiv (H_0+V)|\psi\rangle = \varepsilon|\psi\rangle\ , \tag{8.74}$$

which is the same equation (8.73), but with operators acting in the vectorial space of scattering states; H_0 being the Hamiltonian of a free state and V is now a (potential) operator instead of a function in space*.

We consider the Green's operators of H_0 and H as noted by $G_0(\varepsilon\pm\mathrm{i}\epsilon)$ and $G(\varepsilon\pm\mathrm{i}\epsilon)$ respectively in a complex space of the real energy ε and an arbitrarily small imaginary part $\pm\epsilon$ which is useful to bypass singularities on the real axis (we will see shortly soon how the $\pm$ distinction is manifested). Those operators "revert" the Hamiltonians so that [922, p.129:§8-a]:

$$G(\varepsilon \pm \mathrm{i}\epsilon)\,(\varepsilon \pm \mathrm{i}\epsilon - H) = 1\ , \tag{8.75}$$

for values of $\varepsilon \pm \mathrm{i}\epsilon$ outside the spectrum of H which is continuous on the positive real axis†.

*The operator formalism does not require that V be local nor that the state correspond to single-channel scattering. It can also be applied to the multi-channel case, albeit with more complications (see [922, chapter 16] or [147, chapter 9.2])

†Despite the fact that H is non Hermitian when the imaginary absorption potential is non zero, its spectrum remains real. That is a restrictive condition on the absorption potential [147, eq.(10.101)].

We remember that the electron's state $|\psi\rangle$ can be seen as a superposition of its incident wave $|\mathbf{k}_0\rangle$ with a scattered wave $|\psi_\mathrm{s}\rangle$. The latter's asymptotic form (7.27) contains the information about the scattering amplitude. Replacing in (8.74) and after some manipulations, we obtain Lippman-Schwinger's equations [797, 922, p.133:eqs.(8.4&5), p.380:eq.(7.1.6)]:

$$G = G_0 + G\,V\,G_0 = G_0 + G_0\,V\,G\ , \tag{8.76}$$

$$|\psi\rangle = |\mathbf{k}_0\rangle + \underbrace{G_0(\varepsilon_0 \pm \mathrm{i}\epsilon)\,V|\psi\rangle}_{=|\psi_\mathrm{s}\rangle} = |\mathbf{k}_0\rangle + \underbrace{G(\varepsilon_0 \pm \mathrm{i}\epsilon)\,V|\mathbf{k}_0\rangle}_{=|\psi_\mathrm{s}\rangle}\ . \tag{8.77}$$

We identified the scattered wave with either of the two projections: $G_0\,V|\psi\rangle$ or $G\,V|\mathbf{k}_0\rangle$. The very last equation (8.77) unveils an interesting operator $\Omega^\pm$, called Møller operator [147, §4.1.4], that takes as input a plane wave and transforms it into the unknown scattering wavefunction:

$$|\psi\rangle = \Omega^\pm(\varepsilon \pm \mathrm{i}\epsilon)|\mathbf{k}_0\rangle = (1 + G(\varepsilon \pm \mathrm{i}\epsilon)\,V)|\mathbf{k}_0\rangle = (1 - G_0(\varepsilon \pm \mathrm{i}\epsilon)\,V)^{-1}|\mathbf{k}_0\rangle\ , \tag{8.78}$$

where the last equality was obtained through the first equality in (8.77). As one can see, there are actually two Møller operators: a forward Ω^+ and a froward Ω^-, whose significance is given below.

The expression for G is unknown, but $G_0(\mathbf{r},\mathbf{r}')$ in configuration space takes the known form [147, eq.(4.37)]:

$$\lim_{\epsilon\to 0^+}\langle\mathbf{r}|G_0(\varepsilon \pm \mathrm{i}\epsilon)|\mathbf{r}'\rangle = \frac{2m_\mathrm{e}}{\hbar^2}\frac{1}{4\pi}\frac{\mathrm{e}^{\pm\mathrm{i}k|\mathbf{r}-\mathbf{r}'|}}{|\mathbf{r}-\mathbf{r}'|}\ , \tag{8.79}$$

with $\hbar^2k^2/2m_\mathrm{e} = \varepsilon$ and where ϵ was taken as a positive arbitrarily small real number. The singularity branch on the positive real axis signifies that the waves generated from $|\psi_\mathrm{s}^\pm\rangle = G_0^\pm V|\psi^\pm\rangle$ (with the $\pm\epsilon$ distinction) are associated to outgoing (+) and incoming (−) spherical waves respectively [797, p.382]. In the forthcoming discussion, we shall preserve now this ± distinction and label $G^\pm$, $G_0^\pm$. In the context of scattering, we are mostly interested in the $|\psi^+\rangle$ solution which represents the stationary state corresponding to a radially outgoing flux (and transmitted wave).

With (8.77) and the expression of $G_0^\pm(\mathbf{r},\mathbf{r}')$ (8.79), one can confirm, in configuration space, the asymptotic $\mathbf{r}\to\infty$ behaviour of $\psi_\mathrm{s}(\mathbf{r})$ (7.27). Since the potential V is of finite range, there is exists a maximal radius beyond which its decay is stronger than $\sim 1/(r')^{2*}$ [697, p.337:eq.(12.21)]. For $|\mathbf{r}| \gg |\mathbf{r}'|$ we may approximate $|\mathbf{r}-\mathbf{r}'|$ as $r - \mathbf{r}\cdot\mathbf{r}'/r$ in (8.79) and obtain asymptotically [797, eq.(7.1.33)]:

$$\begin{aligned}\langle\mathbf{r}|\psi_\mathrm{s}^\pm\rangle = \langle\mathbf{r}|G_0^\pm\,V|\psi^\pm\rangle &= \int G_0^\pm(\mathbf{r},\mathbf{r}')V(\mathbf{r}')\psi^\pm(\mathbf{r}')\,\mathrm{d}^3\mathbf{r}' \\ &= -\frac{\mathrm{e}^{\pm\mathrm{i}kr}}{r}\frac{2m_\mathrm{e}}{\hbar^2 4\pi}\int \mathrm{e}^{\mp\mathrm{i}\mathbf{k}\cdot\mathbf{r}}V(\mathbf{r}')\psi^\pm(\mathbf{r}')\,\mathrm{d}^3\mathbf{r}' = \frac{\mathrm{e}^{\pm\mathrm{i}kr}}{r}f^\pm_{\mathbf{k}\leftarrow\mathbf{k}_0}(\Omega)\ .\end{aligned} \tag{8.80}$$

*The dipole potential (8.28) is borderline from this perspective. Its long-range effect introduces a divergence in the traditional partial wave expansion [186, p.470:§low]. An analysis involving rotational excitations shows that actually this divergence is caused only by rotational excitations $\Delta J = \pm 1$ whereas the cross section for purely elastic scattering due to the dipole vanish [198, p.185:eq.(18)]. This means that at forward angles, the cross section involves an energy gain or loss and thus the divergence of the DCS disappears thanks to a change in the kinetic momentum of the electron $k' \neq k_0$. Fortunately, NO's dipole is quite small and the distortion at large radii is not as dramatic as for H_2O for instance [616, p.470]. Thus, we allow ourselves to overlook the non-strictly limited-range potential of NO.

The outgoing wavector $\mathbf{k}$ was naturally identified with the direction of observation $\mathbf{k} \equiv k\hat{\mathbf{r}}$. We recognise now an expression for the scattering amplitude $f^{+}_{\mathbf{k}\leftarrow\mathbf{k}_0}$ which can be expressed formally as a vector biprojection of the operator potential V:

$$f_{\mathbf{k}'\leftarrow\mathbf{k}_0}(\Omega) = -\frac{(2\pi)^3}{4\pi}\frac{2m_\mathrm{e}}{\hbar^2}\underbrace{\langle\mathbf{k}'|V|\psi^+\rangle}_{\equiv T_{\mathbf{k}',\mathbf{k}_0}}, \tag{8.81}$$

where the $(2\pi^3)$ factor comes from the normalisation of plane waves (7.22).

With the help of the forward Møller operator Ω^+, we can introduce a transition operator T between two outgoing $\mathbf{k}'$ and incident $\mathbf{k}_0$ plane waves [922, eq.(3.8)]:

$$f_{\mathbf{k}'\leftarrow\mathbf{k}_0}(\Omega) = -2\pi^2\frac{2m_\mathrm{e}}{\hbar^2}\langle\mathbf{k}'|\underbrace{V\Omega^+}_{\equiv T}|\mathbf{k}_0\rangle \equiv -4\pi^2 T_{\mathbf{k}',\mathbf{k}_0}\ \text{a.u.} \tag{8.82}$$

The advantage is that now, instead of a 'biprojection', the scattering amplitude may be interpreted as the matrix element $T_{\mathbf{k}',\mathbf{k}_0}$ of the operator T in the basis of plane waves. We note of interest the symmetry $(\Omega^-)^\dagger V = T = V\Omega^+$.

As the potential V vanishes, so does the transition operator T and thereby the scattering amplitude. The part of electron flux which is not accounted by the transition matrix is the transmitted (unscathed) incident wave. Mathematically, it is interesting to have an operator which conserves the electron flux, i.e. which is *unitary*. This is the scattering operator S which formally expresses the probability that an incident wave (whatsoever) will be cast out into an outgoing wave. This is where intervenes the froward Møller operator Ω^-: given an outgoing plane wave, the projection $\Omega^-|\mathbf{k}\rangle = |\psi^-\rangle$ rewinds back to the scattering state of the electron as a spherically converging state. The scalar product $\langle\psi^-|\psi^+\rangle$ of the converging and diverging waves gives the likelihood that the incident wave $|\mathbf{k}_0\rangle$ related to $|\psi^+\rangle$ evolve into the outgoing wave $|\mathbf{k}'\rangle$ related to $|\psi^-\rangle$ scattered or not ($\mathbf{k}' \stackrel{?}{=} \mathbf{k}_0$):

$$\langle\psi^-|\psi^+\rangle = \langle\mathbf{k}'|\underbrace{(\Omega^-)^\dagger\Omega^+}_{\equiv S}|\mathbf{k}_0\rangle \tag{8.83}$$

One can also define a reactance operator K related to S by the Caley transform [697, p.157]:

$$K \equiv \mathrm{i}(1-S)(1+S)^{-1} \tag{8.84}$$

The scattering amplitudes are constructed from the matrix elements of the T, S or K operators in momentum space. Below we summarise all pertinent relations between their matrix elements* [697, p.188]:

$$T_{\mathbf{k}_0,\mathbf{k}'} = \frac{\delta(\mathbf{k}_0-\mathbf{k}') - \delta(\varepsilon_0-\varepsilon')S_{\mathbf{k}_0,\mathbf{k}'}}{2\pi\mathrm{i}} = -\frac{1}{\pi}\frac{K_{\mathbf{k}_0,\mathbf{k}'}}{\mathbb{1}-\mathrm{i}K_{\mathbf{k}_0,\mathbf{k}'}}, \tag{8.85a}$$

$$S_{\mathbf{k}_0,\mathbf{k}'} = \delta(\mathbf{k}_0-\mathbf{k}') - 2\pi\mathrm{i}\delta(\varepsilon_0-\varepsilon')T_{\mathbf{k}_0,\mathbf{k}'} = \frac{\mathbb{1}+\mathrm{i}K_{\mathbf{k}_0,\mathbf{k}'}}{\mathbb{1}-\mathrm{i}K_{\mathbf{k}_0,\mathbf{k}'}}, \tag{8.85b}$$

$$K_{\mathbf{k}_0,\mathbf{k}'} = \mathrm{i}\frac{\mathbb{1}-S_{\mathbf{k}_0,\mathbf{k}'}}{\mathbb{1}+S_{\mathbf{k}_0,\mathbf{k}'}} = \frac{-\pi T_{\mathbf{k}_0,\mathbf{k}'}}{\mathbb{1}-\pi\mathrm{i}T_{\mathbf{k}_0,\mathbf{k}'}}; \tag{8.85c}$$

where the shorthand $\mathbb{1} = \delta(\mathbf{k}_0-\mathbf{k}')$ is the identical operator in the momentum space base.

*Different conventions exist among various authors. Here we follow Canto and Hussein [147], Newton [697], and Taylor [922]

Note that when one considers an expansion of those operators into multiple coupled channels, as in the partial wave method in the next section 8.4, the above relations must be understood as matrix operations between different channels.

When the Hamiltonian H of the scattering electron is Hermitian, the scattering operator S is unitary. Additionally, if H is invariant under rotation and translation, then the S matrix is symmetric in momentum space [922, p.282]. This implies that the K matrix is both real and symmetric which is why it is numerically convenient to compute the T matrix used from the K matrix. Unfortunately, with the optical potential used here, this advantage may not be exploited.

Because of the imaginary negative absorption potential, the K matrix in our model will be complex and thus the S matrix will not be unitary.

This is a logical consequence from the loss of elastic scattering flux into inelastic channels.

Still, the relations (8.85) enable to calculate the T matrix from either the S or K matrix elements. Then the scattering amplitude is obtained from (8.82). These matrices are presently expressed in the momentum space. Nevertheless, they may be expressed in any complete vectorial basis to be chosen for our convenience according to the symmetry of the system's Hamiltonian. Then, the scattering amplitude between $\mathbf{k}_0$ and $\mathbf{k}'$ will have to be reconstructed from partial spherical waves of which plane waves are composed of. This is the topic on the next section.

8.4 Partial Waves

In principle, one could directly solve (8.73) by imposing the required boundary conditions (8.3). Nevertheless, a significantly more accurate and economic method is to decompose the problem into an adequate basis of functions. The method of partial waves in the *single-centre expansion* [330] is perhaps the most popular example due to the familiarity of the basis used: spherical harmonics $Y_{\ell m}$ and spherical Bessel functions of the first j_ℓ and second y_ℓ kinds.

The scattering electron's wavefunction is then expanded into [147, p.137:eqs.(4.180a)]:

$$\psi(\mathbf{r}) = \frac{1}{(2\pi)^{3/2}} \sum_{\ell=0}^{\infty} \sum_{m=-\ell}^{\ell} 4\pi \mathrm{i}^\ell \frac{u_\ell(kr)}{kr} Y^*_{\ell m}(\hat{\mathbf{k}}_0) Y_{\ell m}(\hat{\mathbf{r}}) \tag{8.86}$$

This state is associated to the full Hamiltonian with an energy $\varepsilon = \hbar k^2/2m_\mathrm{e}$ and initial momentum $\mathbf{k}_0$. The normalisation of $\psi(\mathbf{r})$ comes from the projection (where $k \equiv |\mathbf{k}|$):

$$\langle \mathbf{r}|\mathbf{k}\rangle \equiv \mathrm{e}^{\mathrm{i}\mathbf{k}\cdot\mathbf{r}} = \int \mathrm{d}\varepsilon \sum_{\ell,m} \langle \mathbf{r}|k,\ell,m\rangle\langle k,\ell,m|\mathbf{k}\rangle \,, \tag{8.87}$$

and the closure of the free wave basis $|k,\ell,m\rangle$ which forms a complete representation of the eigenstates of the free particle Hamiltonian. Its projections on space $\langle \mathbf{r}|k,\ell,m\rangle$ and momentum $\langle k,\ell,m|\mathbf{k}\rangle$ may be found in Sakurai [797, p.398:eq.(7.5.21)]. This decomposition is known as the Bauer expansion for a free plane wave [147, p.50:eq.(2.43)]:

$$\mathrm{e}^{\mathrm{i}\mathbf{k}\cdot\mathbf{r}} = 4\pi \sum_{\ell=0}^{\infty} \sum_{m=-\ell}^{\ell} \mathrm{i}^\ell \mathrm{j}_\ell(kr) Y^*_{\ell m}(\hat{\mathbf{k}}) Y_{\ell m}(\hat{\mathbf{r}}) = \sum_{\ell=0}^{\infty} \mathrm{i}^\ell (2\ell+1) \mathrm{j}_\ell(kr) P_\ell(\hat{\mathbf{k}}\cdot\hat{\mathbf{r}}) \,, \tag{8.88}$$

where we remind the important connection between Legendre polynomials P_ℓ and spherical harmonics $Y_{\ell m}$ through their addition theorem [956, p.164:§5.17.2:eq.(9)] valid for any two unit-norm vectors $\hat{\mathbf{x}}$, $\hat{\mathbf{y}}$:

$$P_\ell(\hat{\mathbf{x}}\cdot\hat{\mathbf{y}}) = \frac{4\pi}{2\ell+1} \sum_{m=-\ell}^{\ell} Y^*_{\ell m}(\hat{\mathbf{x}}) Y_{\ell m}(\hat{\mathbf{y}}) \,, \tag{8.89}$$

It is also not inopportune to remind the definition [956, 133:§5.2:eq.(1)]:

$$Y_{\ell m}(\theta,\varphi) = \sqrt{\frac{2\ell+1}{4\pi}\frac{(\ell-m)!}{(\ell+m)!}} P_\ell^m(\cos\theta)\mathrm{e}^{\mathrm{i}m\varphi} \,, \tag{8.90}$$

with associated Legendre polynomials P_ℓ^m of degree ℓ and order m [3, p.332:eq.(8.1.2)].

Everything seems orderly until we replace (8.86) into the Schrödinger equation (8.73) and ask about what reference frame are we in. Then, the whole illusion about obtaining a charming one-electron equation unravels again, because the potential V is (parametrically) dependent on the orientation of the molecule through the internuclear separation vector $\mathbf{R}$. Much worse, the orbital angular momentum operator L^2 and projection L_z do not commute with the non-central optical potential of the diatomic molecule. This means that neither ℓ nor m are good quantum numbers: the matrix of the one-electron Hamiltonian cannot be diagonalised in the basis of spherical harmonics. This means that the decomposition (8.86) of $\psi(\mathbf{r})$ into spherical harmonics will inevitably lead to a system of coupled equations between different partial waves u_ℓ.

A transition between various orbital angular momentum implies also a transfer of angular momentum to the molecule, thus rotational excitations. Although we have eliminated the worrisome expansion in excited electronic states through the optical potential, we must reconsider the electron-molecule system as a whole from a kinematic perspective. Given a frame of reference, the total angular momentum of the electron and molecule $\boldsymbol{\mathcal{L}} = \mathbf{L} + \mathbf{J}$ and its z projection $\mathcal{M} = m + M$ are constants of motion [835, p.130:§4.2.1].

Then, we can develop *partial* total wavefunctions* $\psi^{\mathcal{LM}}_{\ell_0 m_0, J_0}$ at determined $\mathcal{L}$ and $\mathcal{M} = M_0 + m_0$, and which are solutions associated to the initial conditions of molecule of rotational momentum J_0, M_0 and of an incident electron at an angular momentum ℓ_0 and projection m_0 in the chosen reference frame [147, 442, eq.(9.165), p.5:eqs.(8–9)]:

$$\psi^{\mathcal{LM}}_{\ell_0 m_0}(\mathbf{r}) = \frac{4\pi}{(2\pi)^{3/2}}\frac{1}{k_0}\sum_{J,\ell} \mathrm{i}^\ell \frac{u^{\mathcal{L}}_{\ell J}(r)}{r} Y^*_{\ell_0 m_0}(\hat{\mathbf{k}}_0)\mathcal{Y}^{\mathcal{LM}}_{\ell J}(\hat{\mathbf{r}},\hat{\mathbf{R}})\chi_v(R) \,, \tag{8.91}$$

$$\mathcal{Y}^{\mathcal{LM}}_{\ell J}(\hat{\mathbf{r}},\hat{\mathbf{R}}) = \sum_{m,M} C^{\mathcal{LM}}_{\ell m, JM} Y_{\ell m}(\hat{\mathbf{r}}) Y_{JM}(\hat{\mathbf{R}}) \,. \tag{8.92}$$

These functions ψ serve to reconstruct the full scattering wavefunction Ψ in (8.99). They are composed of partial radial functions $u^{\mathcal{L}}_{\ell J}$ of the electron and vibrational wavefunctions of the atomic nuclei $\chi_v(R)$. Inclusion of vibrational states $v' \neq v$ would have led to vibrational close-coupling [394]. The angular momenta of the electron ℓ and molecule J are coupled together by the Clebsch-Gordan coefficients $C^{\mathcal{LJ}}_{\ell m, JM}$ to form the function $\mathcal{Y}^{\mathcal{LM}}_{\ell J}$ [908, p.113:§2:eq.(4)]. We remind the interpretation of Clebsch-Gordan coefficients as [956, p.235:§8.1.1]:

> $|C^{\mathcal{LM}}_{\ell m, JM}|^2$ corresponds to the probability that two subsystems of angular momenta (projection on z axis) $\ell(m)$ and $J(M)$ couple to form a total system whose total angular momentum is $\mathcal{L}$ ($|\ell - J| \leq \mathcal{L} \leq \ell + J$) and projection $\mathcal{M} = m + M$.
> The phase of $C^{\mathcal{LM}}_{\ell m, JM}$ is conventionally fixed so that the coefficients are all real.

*There are many terms that intervene in the definition of the total wavefunction Ψ in (8.99), and thus one may choose to group the terms differently when expanding in partial waves. In this section, we did not follow exclusively one author but took inspiration from a variety of authors to produce a coherent notation. Our main sources are Canto and Hussein [147, §9.3], Itikawa and Mason [442], Lane [551] and Takayanagi and Itikawa [908]. We kindly ask forgiveness to the reader who will have to juggle between those references to reconstruct the formulae that we present.

Furthermore, if the target molecule has a non-zero spin, one would also need to consider different electron-molecule spin coupling schemes [as in 551, eq.(60) or (66)]. Despite the fact that in their ground states, $O_2(^3\Sigma_g^-)$ is a triplet, $NO(^2\Pi)$ is a (degenerate) doublet, $N(^4S^o)$ is a quadruplet and $O(^3P)$ is a triplet, we will utterly overlook the effect of spin coupling in the rest of the thesis. The approximations made on the optical potential are far worse than negligence of spin couplings.

Each system of total wavefunction $\psi^{\mathcal{LM}}$ is uncoupled to other total angular momenta $\mathcal{L}'\mathcal{M}'$. However, each partial wave $u^{\mathcal{L}}_{\ell J}$ of a system satisfies an equation for vibrationally elastic transitions $v \to v$ [442, eq.(12)]:

$$\left[\frac{\mathrm{d}^2}{\mathrm{d}r^2} - \frac{\ell(\ell+1)}{r^2} + k_J^2\right] u^{\mathcal{L}}_{\ell J}(r) = 2\sum_{\ell' J'} \langle \ell J v|V|\ell' J' v\rangle^{\mathcal{L}} u^{\mathcal{L}}_{\ell' J'}(r)\ , \tag{8.93}$$

which couples different ℓ' and J' through the potential matrix elements [908, p.114:eq.(8)]:

$$\langle \ell J v|V(r)|\ell' J' v\rangle^{\mathcal{LM}} = \int \mathcal{Y}^{\mathcal{LM}*}_{\ell J}(\hat{\mathbf{r}},\hat{\mathbf{R}}) V(\mathbf{r},\mathbf{R}) \mathcal{Y}^{\mathcal{LM}}_{\ell' J'}(\hat{\mathbf{r}},\hat{\mathbf{R}}) |\chi_v(R)|^2 \,\mathrm{d}^2\hat{\mathbf{r}}\,\mathrm{d}^3\mathbf{R}\ . \tag{8.94}$$

We remark their residual dependence on the radial coordinate r, and the integration over the angular space spanned by the $\hat{\mathbf{r}}$ direction. Due to the rotational symmetry of the whole electron-molecule system, the potential matrix elements are independent of the total projection $\mathcal{M}$, which justifies the suppression of this index from the partial waves $u^{\mathcal{LM}}_{\ell J}$ as well. The partial wave equation (8.93) was obtained from the projection of Schrödinger's equation (8.73) on the coupled functions $\mathcal{Y}^{\mathcal{LM}}_{\ell J}$. The wavenumber k_J in the rotational channel J is obtained from the energy conservation law as on the right-hand side of (8.9):

$$\frac{k_J^2}{2} + \mathcal{E}_J = \underbrace{\frac{k_0^2}{2}}_{\equiv\varepsilon_0} + \mathcal{E}_{J_0} \Leftrightarrow \frac{k_J^2}{2} = \varepsilon_0 - \Delta\mathcal{E}_{J_0\to J}\ , \tag{8.95}$$

where the transition energy $\Delta\mathcal{E}_{J_0\to J} = \mathcal{E}_J - \mathcal{E}_{J_0}$ is obtained from the rotational energy levels of the molecule (given concretely later in chapter 11.2).

Each system (8.93) possesses as many different solutions as there are partial wave functions $u_{\ell J}$ spanned in the discrete $\ell \times J$ space which are energetically allowed ($k_J^2 > 0$ in 8.95). As mentioned before, the independent set of solutions is formed by imposing different initial conditions (labelled by the initial angular momenta ℓ_0 and J_0). The radial function $u^{\mathcal{L}}_{\ell J,\ell_0 J_0}$, bound to the initial state ℓ_0, J_0, satisfies the boundary condition which comprises either the T, S or K matrix elements. Here, we give the often-used S matrix asymptotic condition [675, eq.(27)]:

$$\lim_{r\to\infty} u^{\mathcal{L}}_{\ell J,\ell_0 J_0}(r) = \frac{\mathrm{i}}{2}\left(\delta_{\ell\ell_0}\delta_{JJ_0}\hat{h}^-_{\ell_0}(k_0 r) - \sqrt{\frac{k_0}{k_J}} S^{\mathcal{L}}_{\ell J,\ell_0 J_0}\hat{h}^+_{\ell}(k_J r)\right)\ , \tag{8.96}$$

which involve the Riccati-Hankel* functions of progressing $\hat{h}^+$ and recessing $\hat{h}^-$ kinds, constructed from spherical (Riccati)-Bessel functions. These functions (except j_ℓ) have different conventions scattered in the literature. We chose to follow [139, p.198–200 for j_ℓ and y_ℓ and p.203 or $\mathrm{h}^\pm_\ell$] whose sign convention is revealed by their asymptotic behaviour for $x \to \infty$:

*In the literature, not only do these functions have different conventions but even their names are misspelled: '~~Ricatti~~' and '~~Haenkel~~'. With a `pdfgrep`, one can easily spot who got confused.

$$\mathrm{j}_\ell(x) = \frac{\hat{j}_\ell(x)}{x} = \sqrt{\frac{\pi}{2x}} J_{\ell+1/2}(x) \qquad \sim \frac{\sin(x - \frac{\pi}{2}\ell)}{x} = \mathrm{j}_{\ell=0}(x) \tag{8.97a}$$

$$\mathrm{y}_\ell(x) = \frac{\hat{y}_\ell(x)}{x} = \sqrt{\frac{\pi}{2x}} Y_{\ell+1/2}(x) \qquad \sim -\frac{\cos(x - \frac{\pi}{2}\ell)}{x} = \mathrm{y}_{\ell=0}(x) \tag{8.97b}$$

$$\mathrm{h}^\pm_\ell(x) = \frac{\hat{\mathrm{h}}^\pm_\ell(x)}{x} = -\mathrm{y}_\ell(x) \pm \mathrm{i}\,\mathrm{j}_\ell(x) \qquad \sim \frac{\mathrm{e}^{\pm \mathrm{i}(x - \frac{\pi}{2}\ell)}}{x} = \mathrm{h}^\pm_{\ell=0}(x)\,. \tag{8.97c}$$

The conventions for the normalisation of the partial waves $u^{\mathcal{L}}_{\ell J,\ell_0 J_0}$ are many. Since (8.93) is homogenous, one may multiply $u^{\mathcal{L}}_{\ell J,\ell_0 J_0}$ by an arbitrary complex constant. What remains invariant is the construction of the full scattering function Ψ (8.99) from which the scattering amplitude is extracted at the asymptotic boundary condition. Compared to most references, we decided to follow closely the convention of Canto and Hussein [147, eq.(4.180) and (9.101)]. The partial components of the T matrix can be obtained from (8.81) with the decomposition of $\langle \mathbf{k}'|$ and $|\psi^+\rangle$ into partial waves in (8.88) and in (8.91) [147, eq.(9.191)]*:

$$T^{\mathcal{L}}_{\ell J,\ell_0 J_0} = \frac{1}{\pi\sqrt{k_J k_0}} \sum_{\ell' J'} \int \hat{\mathrm{j}}_\ell(k_J r) \langle \ell, J, v|V(\mathbf{r},\mathbf{R})|\ell', J', v\rangle^{\mathcal{L}} u^{\mathcal{L}}_{\ell' J',\ell_0 J_0}(r)\,\mathrm{d}r\,. \tag{8.98}$$

The (rotational) close-coupling is noticeable from the sum on all $\ell' J'$ states that emerged from the initial conditions $\ell_0 J_0$ and which have to "transit" to the final ℓJ. This is just a mark away from the vibrational close-coupling which would also include a sum on various v' states [compare to, for instance, 671, eq.(35)].

In the end, the full wavefunction which scatters from a molecule initially at J_0, M_0 is given by the sum of all possible $\mathcal{L}$ and $\mathcal{M}$ states and initial electron states ℓ_0, m_0 [29, eq.(11)]:

$$\Psi_{J_0,M_0}(\mathbf{r}) = \sum_{\mathcal{L}\mathcal{M}}^{\infty} \sum_{\ell_0,m_0}^{\infty} C^{\mathcal{L}\mathcal{M}}_{\ell_0 m_0, J_0 M_0} \psi^{\mathcal{L}\mathcal{M}}_{\ell_0 J_0}(\mathbf{r},\mathbf{R})\,. \tag{8.99}$$

Whence, one can get scattering amplitudes for rotational excitations $J_0, M_0 \to J, M$ [442, eq.(15)]:

$$f_{J_0 M_0 \to JM}(\mathbf{k}_0, \mathbf{k}_J) = \frac{2\pi\mathrm{i}}{\sqrt{k_0 k_J}} \sum_{\mathcal{L}\mathcal{M}} \sum_{\ell_0 m_0,\ell} \mathrm{i}^{\ell_0 - \ell} Y^*_{\ell_0 m_0}(\hat{\mathbf{k}}_0) C^{\mathcal{L}\mathcal{M}}_{\ell_0 m_0, J_0 M_0} \left(\delta_{\ell_0 \ell}\delta_{J_0 J} - S^{\mathcal{L}}_{\ell J,\ell_0 J_0}\right) \sum_m C^{\mathcal{L}\mathcal{M}}_{\ell m, JM} Y_{\ell m}(\hat{\mathbf{k}}_J)\,. \tag{8.100}$$

Most of the time, one fixes the reference frame so as to align $\mathbf{k}_0$ with the z axis, which sets $m_0 = 0$ (all other projections from $Y_{\ell_0 m_0 \neq 0}$ are zero). We kept the general expression to preserve a coherent perspective on the physical interpretation of all terms gathered in (8.100).

At last, the differential cross section which is of interest experimentally should be averaged (isotropically) on M_0 and summed over M to give [442, eq.(25)]:

$$\frac{\mathrm{d}\sigma_{J \leftarrow J_0}(\mathbf{k}_0 \to \mathbf{k}_J)}{\mathrm{d}\Omega} = \frac{1}{2M_0 + 1} \sum_{M_0=-J_0}^{J_0} \sum_{M=-J}^{J} \frac{k_J}{k_0} |f_{J_0 M_0 \to JM}(\mathbf{k}_0, \mathbf{k}_J)|^2\,. \tag{8.101}$$

At the beginning of this chapter we stated that we shall not mingle with wavefunctions. Indeed, from (8.100), our objectives of computing differential cross sections can be met just with the S (or T or K) matrix. Now that we understand the decomposition of partial waves, we present in chapter 9 a practical way to compute directly S matrix elements at a chosen distance $r \ggg a_0$ from a system of coupled ordinary differential equations of the first order.

*We must advise the diligent reader who will check the references, that this relation depends on the normalisation of the radial wave $u_{\ell J,\ell_0 J_0}$. For the choice (8.96), we obtain the T matrix element. A distinct choice [671, eq.(11)⇒eq.(35)] would have led to the K matrix of Morrison and Sun [675, p.154:eq.(55)].

8.4.1 Phase shifts

The most treated case in textbooks is when the potential $V(r)$ is central as can be approximated for atomic targets. For a central potential, the scattering is purely elastic implying $k_0 = k = k'$. Also, the potential matrix elements are all diagonal in ℓ because of the orthonormality of spherical harmonics. In other words, there is no coupling between u_ℓ functions with $\ell \neq \ell'$. Each partial wave satisfies an individual ordinary differential equation [834, p.30:eq.(51)]:

$$\left[\frac{\mathrm{d}^2}{\mathrm{d}r^2} - \frac{\ell(\ell+1)}{r^2} + k^2 - 2V(r)\right] u_\ell(r) = 0 \,. \tag{8.102}$$

Consequently, all matrices defined previously are diagonal in angular momenta which leads to the definition of phase-shifts δ_ℓ for each partial wave u_ℓ as linked by [906, eq.(4.15)]:

$$S^{\mathcal{L}\ell\,\mathcal{M}m}_{\ell\ell_0,\mathcal{L}0,\mathcal{M}0} = \delta_{\ell\ell_0}\mathrm{e}^{\mathrm{i}2\delta_\ell} \,, \tag{8.103}$$

$$K_{\ell\ell_0} = \delta_{\ell\ell_0}\tan\delta_\ell \,. \tag{8.104}$$

The phase shifts δ_ℓ (not to be confused with the Kronecker symbol $\delta_{\ell\ell_0}$) are extracted from the boundary conditions of the u_ℓ partial waves which, in accordance with the normalisation chosen in the previous subsection (8.91 and 8.96), are expressed as [147, 906, eq.(4.14), eq.(2.39)]:

$$\lim_{r\to\infty} u_\ell(r) = \mathrm{e}^{\mathrm{i}\delta_\ell}\cos\delta_\ell\left(\hat{\mathrm{j}}_\ell(kr) - \tan\delta_\ell\hat{\mathrm{y}}_\ell(kr)\right) \sim \mathrm{e}^{\mathrm{i}\delta_\ell}\sin(kr - \frac{\pi}{2}\ell + \delta_\ell) \,. \tag{8.105}$$

With a given set of phase shifts, the scattering amplitude is expressed very simply in a familiar form [26, eq.(2)]:

$$f(\theta) = \frac{\mathrm{i}}{2k}\sum_{\ell=0}^{\infty}(2\ell+1)(1-\mathrm{e}^{\mathrm{i}2\delta_\ell})P_\ell(\cos\theta) = \frac{1}{k}\sum_{\ell=0}^{\infty}(2\ell+1)\sin\delta_\ell\mathrm{e}^{\mathrm{i}\delta_\ell}P_\ell(\cos\theta) \,. \tag{8.106}$$

This expression may be obtained from (8.100) by noticing that since J, J_0, M, M_0 are zero, $k_0 = k_J$ and the Clebsch-Gordan coefficients impose: $C^{\mathcal{L}\mathcal{M}}_{\ell m,00} = \delta_{\ell\mathcal{L}}\delta_{m\mathcal{M}}$ and so $\ell_0 = \ell$ and $m_0 = m$. All that is left is the addition theorem of spherical harmonics (8.89) which gives the Legendre polynomials P_ℓ.

The square of this amplitude involves mixed ℓ, ℓ' terms which may be reorganised into a series of Legendre polynomials L according to the relationship [956, p.144:§5.6.2:eq.(9) with $m_1 = m_2 = M = 0$]:

$$P_\ell(\cos\theta)P_{\ell'}(\cos\theta) = \sum_L (C^{L0}_{\ell 0,\ell' 0})^2 P_L(\cos\theta) \tag{8.107}$$

The differential, integral and momentum-transfer cross sections become [26, 127, eq.(22–24), eq.(7)]:

$$\frac{\mathrm{d}\sigma}{\mathrm{d}\Omega}(\theta) = \frac{1}{4k^2}\sum_{L=0}^{\infty}P_L(\cos\theta)\sum_{\ell,\ell'}(2\ell+1)(2\ell'+1)(C^{L0}_{\ell 0,\ell' 0})^2(1-\mathrm{e}^{\mathrm{i}2\delta_\ell})(1-\mathrm{e}^{-\mathrm{i}2\delta^*_{\ell'}}) \,, \tag{8.108}$$

$$\sigma = \frac{4\pi}{k^2}\sum_{\ell=0}^{\infty}(2\ell+1)\sin\delta_\ell\,\sin\delta^*_\ell\mathrm{e}^{-2\Im\{\delta_\ell\}} \,, \tag{8.109}$$

$$\sigma_{\mathrm{m}} = \frac{4\pi}{k^2}\sum_{\ell=0}^{\infty}(\ell+1)\left(\mathrm{e}^{\mathrm{i}\delta_\ell}\sin\delta_\ell - \mathrm{e}^{\mathrm{i}\delta_{\ell+1}}\sin\delta_{\ell+1}\right)\left(\mathrm{e}^{-\mathrm{i}\delta^*_\ell}\sin\delta^*_\ell - \mathrm{e}^{-\mathrm{i}\delta^*_{\ell+1}}\sin\delta^*_{\ell+1}\right) \,. \tag{8.110}$$

All the above cross sections are defined for elastic (or rotational) collisions. Since we model electronically inelastic scattering with an absorption potential, our phase-shifts δ_ℓ obtained by integrating (8.102) will be complex. This aspect is included in the formulae above (8.108–8.110) by the intervention of the complex conjugate δ_ℓ^* of the phase shifts. From the imaginary part of the phase shifts, one can calculate the absorption cross section representing electronically inelastic scattering by [139, Chapter 18, p.133:eq.(23–24)]:

$$\sigma_{\mathrm{a}} = \frac{4\pi}{(2k)^2} \sum_{\ell=0}^{\infty} (2\ell+1)(1 - \exp(-4\Im\{\delta_\ell\})) \; . \tag{8.111}$$

This relation is very useful to test the consistency of the model used for the absorption potential. One can compare it to the sum of all electronic and ionisation cross sections of a given target (this is done in fig. 11.3 on page 394).

8.5 Approximations

In the theoretical sections above, we presented a general treatment: using total wave functions, operators and partial-wave decompositions which, in principle, should give an exact or accurate description of the scattering of an electron by the molecule. Even the methodology behind the optical potential [922, p.383–8:§19-d] may exactly represent the coupling between N_α different equations, if calculated properly. Nevertheless, there is no secret that without taking approximations, one can never get close to obtaining a result in a practical way*. In this section, we present several approximations that will be exploited, in different ways, to generate our cross sections. We start with the most popular one.

8.5.1 Plane-Wave Born

If we glance back at section 8.3 and steal (8.76), we can notice a recurrence relation between the Green's operator G of the full interaction Hamiltonian and G_0 of the free Hamiltonian:

$$G = G_0 + G_0VG = G_0 + G_0VG_0 + G_0V(G_0VG_0) + G_0V(G_0V(G_0VG_0)) + \dots \; , \tag{8.112}$$

which can be developed at will to an infinitely large number of terms. This corresponds to the Born series [96], the truncation of which to a desired order yields the first, second, .. n^{th} Born approximation ($G = G_0$ would be the zeroth order whereby no scattering occurs.).

To derive the scattering amplitude in the Born series, we recall that the T operator is defined as:

$$T = V\Omega^+ = V(1 + G^+V) = V(1 + G_0T) \; , \tag{8.113}$$

which we can unfold into the series:

$$T = \underbrace{\underbrace{\underbrace{V}_{\text{First Born approx.}} + V(G_0V)}_{\text{Second Born approx.}} + V(G_0V(G_0V))}_{} + \dots \tag{8.114}$$

*English has the advantage of permitting such semantically redundant utterances because of its two-sided etymological lexicon.

When restricting to the first term only, the T operator is merely replaced by the potential V so that the scattering amplitude (8.82) in the first Born approximation* is:

$$\tilde{f}_{\mathbf{k}'\leftarrow\mathbf{k}_0}(\Omega) = -4\pi^2\langle\mathbf{k}'|V|\mathbf{k}_0\rangle = -\frac{1}{2\pi}\int \mathrm{e}^{-\mathrm{i}\mathbf{k}'\cdot\mathbf{r}}V(\mathbf{r})\mathrm{e}^{\mathrm{i}\mathbf{k}_0\cdot\mathbf{r}}\,\mathrm{d}^3\mathbf{r}\,. \tag{8.115}$$

In the last term, we see that instead of the scattering wavefunction ψ^+, the electron's state is approximated by an unperturbed plane wave $\mathbf{k}_0$ which is why the first Born approximation for elastic scattering is rightfully called the "plane-wave Born approximation" (PWBA) in the literature [504, 911]. This terminology is contrasted with the distorted wave Born approximation which uses waves distorted by the main part of a potential to calculate the scattering amplitude from an auxiliary part of a potential [511]. A more distant cousin to the PWBA is the Glauber or eikonal approximation [147, §5.2.1] which assumes that the trajectory of the electron in the potential follows a straight line and the scattering amplitude is obtained as an integral over the impact parameter and the straight distance through the potential. This approximation has given fair results for atoms [137] and molecules [326] even at intermediate energies, though we have not exploited it presently.

The (conjugate) product of two plane waves in (8.115) clears out an important dependence of the amplitude, which is solely based on the momentum transfer: $\mathbf{q} \equiv \mathbf{k}_0 - \mathbf{k}'$. The transition matrix in the first Born approximation is thus equivalent to the Fourier transform of the potential (in $-\mathbf{q}$) [147, eq.(5.12–13)]:

$$\tilde{T}_{\mathbf{k}'\mathbf{k}_0} = \langle\mathbf{k}'|V|\mathbf{k}_0\rangle = \frac{1}{(2\pi)^3}\int \mathrm{e}^{\mathrm{i}\mathbf{q}\cdot\mathbf{r}}V(\mathbf{r})\,\mathrm{d}^3\mathbf{r} \tag{8.116}$$

The plane-wave Born approximation is not restricted to potential scattering and may be used in multi-channel collisions [147, §11.1.1] to represent the first-order transition matrix element from an initial $|\mathbf{k}_i\rangle\times|\Psi_i\rangle$ to a final state $|\mathbf{k}_f\rangle\times|\Psi_f\rangle$:

$$f_{f\leftarrow i}(\mathbf{k}_i,\mathbf{k}_f) = \sum_s \int \Psi_f^*(x_m,\mathbf{R},s)\mathrm{e}^{-\mathrm{i}\mathbf{k}_f\cdot\mathbf{r}'}V(\mathbf{r}',\mathbf{r};s,x_m,\mathbf{R})\mathrm{e}^{\mathrm{i}\mathbf{k}_i\cdot\mathbf{r}}\Psi_i(x_m,\mathbf{R},s)\,\mathrm{d}^{3N}x_m\,\mathrm{d}^3\mathbf{r}\,\mathrm{d}^3\mathbf{r}'\,\mathrm{d}^3\mathbf{R}\,. \tag{8.117}$$

One may include non-local interactions $\mathbf{r}' \neq \mathbf{r}$, the internal coordinates of the bound electrons x_m, the internuclear separation $\mathbf{R}$ and different spin projections $s = \pm 1/2$ when the electron's spin couples with the target's to form a total spin $\mathcal{S}$; as required by the full interaction potential (8.2). This expression (8.117) will serve as a starting point for the modelling of electronically inelastic collisions as described in chapter 11 sections 11.4.1 and 11.5.1. One may consult the introduction in Shimamura and Takayanagi [834, chapter 1:§6.2] for further information about the first Born's approximation for inelastic channels.

The validity of Born's approximation is discussed in chapter 10.1. It assumes that the interaction is qualitatively "weak". The distortion effect of the potential on the electron's wavefunction will be smaller (relatively) when the energy (wavenumber) of the electron is high ($\varepsilon_0 \gg V$) and when the momentum-transfer is small ($q \ll k$). Thus, Born's approximation (any) tends to be by default a high-energy approximation. Nonetheless, the partial-wave decomposition discussed previously enables one to delineate situations where the electron's wavefunction gets weakly distorted by the potential due to the strongly repulsive centrifugal potential $+\ell(\ell+1)/r^2$ for $\ell > 0$ waves which reduces the amplitude of the scattered wave in the region where the interaction

*In the rest of this thesis, all (but not exclusively all) quantities based on the first Born approximation will be noted with a tilde ˜ as $\tilde{f}$.

potential is strongest. This justifies also the use of Born's approximation at very low energies for rotational scattering as proposed by Gerjuoy and Stein [323].

This partial wave decomposition opens the way to a *partial* use of the plane-wave Born approximation in (8.98) by replacing those radial functions $u^{\mathcal{L}}_{\ell' J',\ell_0 J_0}$, whose distortion is weaker, by their free-wave analogues $\delta_{\ell'\ell_0}\hat{\mathrm{j}}_{\ell_0}$. Weak distortion naturally betokens little change from a wave's initial conditions, setting thereby $\ell_0 = \ell'$. The plane-wave-Born-approximated $\tilde{T}_{\ell\ell_0}$ partial-wave matrix element reads [671, p.2536:eq.(A2)]:

$$\tilde{T}_{\ell J,\ell_0 J_0} = \frac{2}{\pi\sqrt{k_J k_0}} \int \hat{\mathrm{j}}_\ell(k_J r)\langle \ell J v|V|\ell_0 J_0 v\rangle \hat{\mathrm{j}}_{\ell_0}(k_0 r)\,\mathrm{d}r\ . \tag{8.118}$$

This approximation can be used to compute matrix elements between weakly coupled channels when $\ell \neq \ell_0$ and $\ell \gg 0 \vee \ell_0 \gg 0$. Of interest, many integrals involving spherical Bessel functions and polynomials are developed in Bloomfield *et al.* [85].

Central Potential

In the simple case of a central potential, the plane-wave Born approximation takes a very simple form. The scattering amplitude (8.115) reduces to (8.88) [799, eq.(5)]:

$$\tilde{f}_{\mathbf{k}'\leftarrow\mathbf{k}_0}(\Omega) = -\frac{2\mu}{\hbar^2 q}\int_0^\infty \sin(qr)V(r)r\,\mathrm{d}r\ . \tag{8.119}$$

The phase shifts are obtained from (8.118), remembering that $T_{\ell\ell} = (1 - S_{\ell\ell})/2\pi\mathrm{i}$ as [147, eq.(2.72)]:

$$\left.\begin{aligned} \frac{1-\mathrm{e}^{\mathrm{i}2\tilde{\delta}_\ell}}{-2\mathrm{i}} = \mathrm{e}^{\mathrm{i}\tilde{\delta}_\ell}\sin\tilde{\delta}_\ell &= \\ \sin\tilde{\delta}_\ell &\simeq \\ \tilde{\delta}_\ell &\approx \end{aligned}\right\} -2k\int_0^\infty V(r)\mathrm{j}_\ell^2(kr)r^2\,\mathrm{d}r\ . \tag{8.120}$$

Consistence with (8.119) is maintained [680, p.89:V§2] if (8.120-top) is directly inserted into (8.108) (replacing $\mathrm{e}^{\mathrm{i}\delta_\ell}\sin\delta_\ell$ by $\mathrm{e}^{\mathrm{i}\tilde{\delta}_\ell}\sin\tilde{\delta}_\ell$). It is interesting to note that if one tries to resolve $\tilde{\delta}_\ell$ from the topmost equality in (8.120), the imaginary part of $\tilde{\delta}_\ell$ (if the potential is real) will be negative. This, implies unphysical creation of scattering flux. Consequently, the differential cross section derived from the Born approximation will overall lie in overestimation ($\tilde{\sigma}$ too large, figure 10.3 is a very good example). There are many ways to interpret this. For instance, that the effect of distortion is to conserve the flux in scattering. An electron would be accelerated in the potential of the target and thus have a local wavenumber k superior to the incident k_0, which would reduce the overestimated phase shifts in (8.120) (introduce a dependence of $k(r) \neq k_0$ in $\mathrm{j}_\ell(k(r)\,r)$), and the amplitude in (8.106). Since (differential) cross sections obtained from the plane wave Born approximation are systematically overestimated, we could try to scale them down in order to improve the applicability of the PWBA [505, 911]. We will exploit this multiple times in chapter 11.

When the integral in (8.120) surpasses 1 (far beyond the region of validity of the PWBA), one can use the approximation on the last row, which will guarantee that the phase shift $\tilde{\delta}_\ell$ stay real for a real potential (prevent mathematically-allowed trespassing in the complex domain).

For direct applications of the Born approximation for DCS, scattering amplitudes and phase shifts on atomic potentials, please consult chapter 14 of part III.

8.5.2 Adiabatic Nuclei

The plane wave Born approximation simplifies considerably the calculation of scattering amplitudes and matrix elements. There are, however, two main criticisms to be addressed. First, this simplification is too crude to obtain worthy results at intermediate energies of several tens of eV. Second, despite the crudity, the dread lurking behind the calculation of the potential matrix elements $\langle \ell' J' v | V | \ell J v \rangle$ (8.94), still looms over us in equations (8.118) and (8.93). To be sure, Born's approximation is practical but not pertinent to our needs.

What is mostly relevant, much more than approximating the scattered wave by the free wave, is that the motion of nuclei is much slower than the flyby time of the electron in the scattering region. An electron above 5 eV will scatter in less than $\sim 10^{-15}$ s whereas the vibrational period of molecules is around 10^{-14} s and the rotational period is even longer $\sim 10^{-12}$ s [834, p.497:§2.1]. Thus, one may assume that during the collision, the nuclei stay fixed. This is in essence the adiabatic nuclei approximation* introduced by Chase [173]. Lane [551, eq.(32–33)] distinguishes two stages of the approximation: the fixed-nuclei and then the adiabatic-nuclei. First, the scattering amplitude (or T matrix) is calculated for an immobile molecule. Then, those are averaged over the internuclear separation vector $\mathbf{R}$. Mathematically, these two stages are clearly marked on equation (8.127) below. Succinctly:

> The adiabatic nuclei approximation replaces rovibrational coupling by averaging.

Its validity relies upon three conditions [551, p.35:bottom-right]:

1. The electron's incident energy is much larger than the excitation threshold of the rovibrational transition ($\varepsilon \gg \Delta\mathcal{E}_{J_0 \to J}$);
2. The long-range potential is not too strong nor too extended;
3. The scattering is nonresonant.

Under these conditions, the electron's angular momentum $\boldsymbol{\ell}$ does not couple with the rotational quantum J, but it couples with the orientation of the internuclear axis $\hat{\mathbf{R}}$ to define the projection:

$$\Lambda \equiv \boldsymbol{\ell} \cdot \hat{\mathbf{R}} \,, \tag{8.121}$$

which becomes a new constant of motion.

To take advantage of this approximation, one can define and calculate the partial waves $u^{\Lambda}_{\ell,\ell_0}$ in the molecular body frame of reference where the molecular axis $\hat{\mathbf{R}} \parallel z$ as represented in 8.2 [442, eq.(18)].

$$\left[\frac{\mathrm{d}^2}{\mathrm{d}r^2} - \frac{\ell(\ell+1)}{r^2} + \frac{k^2}{2}\right] u^{\Lambda}_{\ell,\ell_0} = \sum_{\ell'} \langle \ell | V | \ell' \rangle^{\Lambda} u^{\Lambda}_{\ell',\ell_0} \,. \tag{8.122}$$

The potential matrix elements are now obtained as [671, eq.(20)]:

$$\langle \ell | V | \ell' \rangle^{\Lambda} = \int Y^*_{\ell\Lambda}(\hat{\mathbf{r}}) V(\mathbf{r}) Y_{\ell'\Lambda}(\hat{\mathbf{r}}) \, \mathrm{d}\hat{\mathbf{r}} = \sum_{l=0}^{\infty} V_l(r) \sqrt{\frac{4\pi}{2l+1}} \underbrace{\int Y^*_{\ell\Lambda}(\hat{\mathbf{r}}) Y_{l0}(\hat{\mathbf{r}}) Y_{\ell'\Lambda}(\hat{\mathbf{r}}) \, \mathrm{d}\hat{\mathbf{r}}}_{\equiv (-)^{\Lambda} G(l,0;\ell,-\Lambda;\ell',\Lambda)} \,, \tag{8.123}$$

*also called "(sudden-)impulse" approximation.

with $V_l(r)$ defined in (8.31) and where the addition theorem (8.89) and $Y_{\ell 0}(0,0) = \sqrt{(2\ell+1)/(4\pi)}$ from (8.90) have been used. The integral of three spherical harmonics is known as the Gaunt coefficient $G(l,\mu;\ell,m;\ell,m')$ and equals [956, p.148:§5.9:eq.(6)]:

$$\int Y_{\ell m}(\Omega) Y_{\ell' m'}(\Omega) Y_{l\mu}(\Omega)\,\mathrm{d}\Omega = \sqrt{\frac{(2l+1)(2\ell+1)(2\ell'+1)}{4\pi}} \begin{pmatrix} l & \ell & \ell' \\ 0 & 0 & 0 \end{pmatrix} \begin{pmatrix} l & \ell & \ell' \\ \mu & m & m' \end{pmatrix}, \tag{8.124}$$

with the Wigner-3j coefficients related to the Clebsch-Gordan coefficients as [956, p.236:§8.2.1]:

$$\begin{pmatrix} L & \ell & \ell' \\ M & m & m' \end{pmatrix} \equiv \frac{(-)^{M+(\ell-\ell')}}{\sqrt{2L+1}} C^{L-M}_{\ell m, \ell' m'} . \tag{8.125}$$

From the properties of those coefficients, we can already edict the following rules applying on the potential matrix elements:

The l harmonic of the potential matrix element $\langle \ell | V_l P_l | \ell' \rangle^{\Lambda} \neq 0$ if :

$$\ell + \ell' + l \text{ is even} \Rightarrow \langle \ell | V | \ell' \rangle^{\Lambda} = \langle \ell | V | \ell' \rangle^{-\Lambda} ,$$
$$|\ell - \ell'| \leq l \leq \ell + \ell' .$$

Because of the first selection rule, the potential matrix element is independent of the sign of Λ. Also, for homonuclear diatomic molecules, since l is always even (see p. 284), this means that their potential couples angular momenta ℓ, ℓ' of the same parity. For homonuclear diatomic molecules, one can therefore distinguish two independent S matrices: $S^{\Lambda g}_{\ell,\ell_0}$ and $S^{\Lambda u}_{\ell,\ell_0}$ which respectively couple even g ("gerade") and uneven u ("ungerade") ℓ, ℓ_0 pairs.

The system of equations (8.122) is similar to (8.93) but simpler to evaluate. Once the T matrix elements in the body frame have been evaluated, they have to be transformed back into the laboratory frame (where $z \parallel \hat{\mathbf{k}}_0$) [551, 835, p.38:eq.(40), p.137:eq.(94)] where the total state $\mathcal{LM}$ of the electron-molecule system will be decomposed again into the rotational state J, M of the molecule and the ℓ, m angular-momentum state of the electron as in (8.98).

Rotational (and optionally vibrational Onda and Truhlar [718, eq.(11)]) dynamics are then introduced during the frame transformation of the T matrix. This makes the value of the wavenumber k in the body-frame equation (8.122) ambiguous. Morrison *et al.* [671, p.2524] proposed to take $k = \sqrt{k_0 k_J}$ in order to respect the threshold law of the $J_0 \to J$ cross section at low electron energies.

The transformation [675, p.151:eq.(37)] of the body frame T-matrix to the laboratory frame involves two steps: (1) rotation of the molecular axis $\hat{\mathbf{R}}$ to the axis of the initial electron's direction $\hat{\mathbf{k}}_0$ [551, p.38:eq.(40)] and (2) integrating over the initial (v_0, J_0, M_0) and final (v, J, M) rovibrational states of the molecule [551, eqs.(32–33)]:

$$T^{\mathcal{LM}}_{\ell J, \ell_0 J_0} = \underbrace{\int Y^*_{JM}(\hat{\mathbf{R}}) \chi^*_v(R) \underbrace{\sum_{\Lambda} D^{\ell}_{m\Lambda}(\hat{\mathbf{R}}) T^{\Lambda}_{\ell,\ell_0} D^{\ell_0 *}_{\Lambda 0}(\hat{\mathbf{R}})}_{\text{Fixed-Nuclei approx.}} \chi_{v_0}(R) Y_{J_0 M_0}(\hat{\mathbf{R}})\,\mathrm{d}^3\mathbf{R}}_{\text{Adiabatic nuclei approx.}} . \tag{8.127}$$

The $D^{\ell}_{mm'}$ functions are Wigner-D matrices for a transformation between the body frame to the lab frame coordinates [see 784, p.52].

Putting all things together, the scattering amplitude for the process $J_0 M_0 \to JM$ in the adiabatic nuclei approximation is [551, eq.(44–5)]:

$$f_{JM\leftarrow J_0M_0}(\mathbf{k}_0,\mathbf{k}_J) = \frac{-(2\pi)^2}{\sqrt{k_0k_J}} \sum_{\ell\ell_0 m} \mathrm{i}^{\ell_0-\ell} Y^*_{\ell_0 0}(\hat{\mathbf{k}}_0) Y_{\ell m}(\hat{\mathbf{k}}_J) \tag{8.128}$$
$$\times \underbrace{\sum_{\mathcal{L}} C^{\mathcal{L}M_0}_{\ell_0 0, J_0 M_0} C^{\mathcal{L}M_0}_{\ell m, JM}}_{\text{Lab decoupling: } \mathcal{L}\mathcal{M}\to JM,\ell m} \underbrace{\sum_{\Lambda} \frac{\sqrt{(2J_0+1)(2J+1)}}{(2\mathcal{L}+1)} C^{\mathcal{L}\Lambda}_{\ell_0\Lambda, J_0 0} C^{\mathcal{L}\Lambda}_{\ell\Lambda, J0} T^{\Lambda}_{\ell\ell_0}}_{\text{Body}\to\text{Lab coupled}} .$$

When computing the differential cross section for the rotational sum and average (8.101), and summing over all transitions $J_0 \to J$ for any J, a simplification arises from the Clebsch-Gordan coefficients coupling J with ℓ. Neglecting the variation of k_J with J, one obtains the compact form for the differential cross section for all rotational processes which is independent of J_0 [673, eqs.(2.19–23)]:

$$\frac{\mathrm{d}\sigma}{\mathrm{d}\Omega}(\theta) = \frac{4\pi^2}{4k^2} \sum_{L=0}^{\infty} P_L(\cos\theta) \sum_{\ell_0,\ell} \sum_{\ell'_0,\ell'} \frac{\sqrt{(2\ell_0+1)(2\ell'_0+1)(2\ell+1)(2\ell'+1)}}{2L+1} \mathrm{i}^{\ell_0-\ell}(-\mathrm{i})^{\ell'_0-\ell'}$$
$$\times C^{L0}_{\ell_0 0,\ell'_0 0} C^{L0}_{\ell 0,\ell' 0} \sum_{\Lambda,\Lambda'} C^{L\Lambda'-\Lambda}_{\ell_0-\Lambda,\ell'_0\Lambda'} C^{L\Lambda'-\Lambda}_{\ell-\Lambda,\ell'\Lambda'} T^{\Lambda}_{\ell,\ell_0} (T^{\Lambda'}_{\ell',\ell'_0})^* . \tag{8.129}$$

This equation is the master equation that we used to compute our vibrationally elastic DCS for diatomic molecules. In later chapters, we will abbreviate this DCS by "ℓCC" and refer to it as the angular-momentum (ℓ) **c**lose **c**oupling (in the adiabatic nuclei approximation). The $T^{\Lambda}_{\ell,\ell_0}$ matrix elements correspond to the ones calculated in the body frame. Those are obtained from an algorithm presented in section 9.1.2.

8.5.3 Multiple scattering

The adiabatic-nuclei approximation with angular-momentum coupling in the body-frame is a powerful approximation because it considerably simplifies the treatment without sacrificing the accuracy of the cross sections obtained. Nevertheless, to build the DCS from the T matrix in (8.129) requires a long loop of sums that, even when optimised, can take very long. As the electron energy increases, this gets worse as more partial waves ℓ participate to the scattering. On top of that, when the wavelength of the electron is reduced, one also needs to resolve better the nuclear singularities; thus requiring higher potential harmonics (increase l). In that case, it is better to find an alternative way to build the elastic scattering amplitude and DCS.

At higher energies, the T matrix becomes quite sparse and coupling of angular momenta is reduced to a few only. Physically, when the electron's wavelength becomes smaller than the internuclear separation, one may imagine another kind of approximation that is based on the coherent interference between waves that are scattered at different nodes corresponding to the position of atomic nuclei surrounded by their diffuse electron cloud. This is named intramolecular multiple or multicentre scattering.

Just like the Born approximation, multicentre scattering can be developed in a series [526, eq.(13)]. One can separate the diatomic potential into two contributions representative of each atom A and A': $V(\mathbf{r}) = V_A(\mathbf{r}) + V_{A'}(\mathbf{r})$. If one injects this decomposition into (8.113), one gets:

$$T = V_A + V_{A'} + V_A G_0 V_A + V_A G_0 V_{A'} + V_{A'} G_0 V_A + V_{A'} G_0 V_{A'} + \ldots \tag{8.130}$$

The atomic potential would not necessarily have to be central or non-overlapping. However, as we saw in 8.4.1, there is considerable ease to work with spherically symmetric potentials, in

which case the scattering amplitude can be solved exactly. If one supposes that V_A and $V_{A'}$ are unperturbed central atomic potentials centred around $\pm\mathbf{R}/2$. One can perform a resummation in equation (8.130), of all terms that involve only V_A or $V_{A'}$ but no mixing. We can write:

$$T = T_A + T_{A'} + \underbrace{T_{A'}G_0T_A}_{\equiv T^1_{A'A}} + \underbrace{T_AG_0T_{A'}}_{\equiv T^1_{AA'}} + \dots \tag{8.131}$$

which is now a series extending only with mixed terms. We see that we replaced V_A by T_A in the first-order mixed terms, which regroup all terms that scattered about A up to 'infinite times' ($\sum_{n=0}^{\infty} V_A(G_0V_A)^n$). This procedure is akin to the distorted wave Born approximation where the waves injected for calculating T matrix elements are waves scattered from individual atoms, instead of plane waves as in the first Born approximation. However, as opposed to the distorted wave approach where stronger emphasis is put on one part of the potential (V_1 more important than V_2), in multicentre scattering, there is equal participation of waves distorted by each of the $V_{A,A'}$ potentials. We see indeed that if we project $\langle\mathbf{k}'|$ and $|\mathbf{k}_0\rangle$ on the resummed T matrix (8.131), and recalling the link between the Møller operator(s) and the T operator (8.82), we would obtain [390, eq.(29)]:

$$\langle\mathbf{k}'|T|\mathbf{k}_0\rangle = \langle\mathbf{k}'|V_A|\psi_A\rangle + \langle\mathbf{k}'|V_{A'}|\psi_{A'}\rangle + \langle\psi^-_{A'}|V_{A'}G_0V_A|\psi_A\rangle + \langle\psi^-_A|V_AG_0V_{A'}|\psi_{A'}\rangle\ , \tag{8.132}$$

where $|\psi_{A,A'}\rangle = \Omega^+|\mathbf{k}_0\rangle$ (and $\langle\psi^-_{A,A'}| = \langle\mathbf{k}'|(\Omega^-)^\dagger$) are wavectors obtained from the scattering of an incident (outgoing) plane wave $|\mathbf{k}_0\rangle$ ($\langle\mathbf{k}'|$) on the atoms A, A' centred at $\pm\mathbf{R}/2$:

$$\langle\mathbf{r}|\psi_{A,A'}\rangle = \mathrm{e}^{\pm\mathrm{i}\frac{\mathbf{R}}{2}\cdot\mathbf{k}_0}\psi_{A,A'}(\mathbf{r}\mp\mathbf{R}/2)\ . \tag{8.133}$$

The multiplication by a shifted phase comes from the incident plane wave which changes the initial conditions of scattering about A or A'. This shifting will provoke the emblematic coherent interference pattern in multicentre scattering through the matrix element:

$$\langle\mathbf{k}'|V_A|\psi_A\rangle = \int \frac{\mathrm{e}^{-\mathrm{i}\mathbf{k}'\cdot\mathbf{r}}}{(2\pi)^{3/2}}V_A(\mathbf{r}-\frac{\mathbf{R}}{2})\psi_A(\mathbf{r}-\frac{\mathbf{R}}{2})\mathrm{e}^{+\mathrm{i}\mathbf{k}_0\cdot\frac{\mathbf{R}}{2}}\,\mathrm{d}^3\mathbf{r} \tag{8.134}$$

$$= \frac{\mathrm{e}^{\mathrm{i}(\mathbf{k}_0-\mathbf{k}')\cdot\frac{\mathbf{R}}{2}}}{(2\pi)^{3/2}}\underbrace{\int \mathrm{e}^{-\mathrm{i}\mathbf{k}'\cdot(\mathbf{r}-\frac{\mathbf{R}}{2})}V_A(\mathbf{r}-\frac{\mathbf{R}}{2})\psi_A(\mathbf{r}-\frac{\mathbf{R}}{2})\,\mathrm{d}^3\mathbf{r}}_{\equiv -f_A/4\pi^2}\ , \tag{8.135}$$

where we see the appearance of the momentum-transfer's shifted projection $\mathbf{q}\cdot\mathbf{R}/2 = (\mathbf{k}_0-\mathbf{k}')\cdot\mathbf{R}/2$. The potential V_A projected in space is defined as the function that takes as argument the relative position with respect to the atom A located at $+\mathbf{R}/2$.

To obtain the DCS from the T matrix we recall so far that:

- In a close-coupling approximation, the DCS would be obtained by the matrix elements between final and initial states of the total electron-molecule system [147, p.418:eq.(9.192)];
- In the first Born approximation, ... by integration of the first order T matrix ($\equiv V$) over the "electron×molecule" initial and final states (8.118);
- In the adiabatic nuclei approximation, ... by integrating T matrix elements over the molecular rovibrational state;
- And in the present multicentre scattering, ... by averaging the DCS (i.e. the square $|T_{\mathbf{k}'\mathbf{k}_0}|^2$) over the molecular orientation.

The distinction is subtle, but essential. With adiabatic-nuclei, the electron transfers instantaneously an amount of kinetic momentum which prongs the molecule from an initial J_0 to a final J state. To obtain the total elastic cross section, one has to sum over all allowed J final states. In multiple scattering, there is virtually no deposition of kinetic momentum, it is like an oriented mini-crystal (of two atoms) giving a scattering pattern which must be then averaged over the isotropic distribution of the mini-crystal. This is why the averaging over $\mathbf{R}$ is performed on the fixed-nuclei DCS and not over the T-matrix as in (8.127). Having said that, the multicentre isotropically averaged DCS may be organised as [920, eq.(10)]:

$$\frac{\mathrm{d}\sigma}{\mathrm{d}\Omega} = \underbrace{I_{\mathrm{S}} + I_{\mathrm{SS}}}_{\mathrm{IAM}} + I_{\mathrm{SD}} + I_{\mathrm{D}} + I_{\mathrm{DD}} + \dots \tag{8.136}$$

The labelled terms represent[390, eq.(32)]:

$$\text{Single Pure :} \qquad I_{\mathrm{S}} = \int \frac{\mathrm{d}\hat{\mathbf{R}}}{4\pi} |f_A|^2 + |f_{A'}|^2$$

$$\text{Single Interference :} \qquad I_{\mathrm{SS}} = \int \frac{\mathrm{d}\hat{\mathbf{R}}}{4\pi} 2\Re\{ f_A \mathrm{e}^{+\mathrm{i}\frac{\mathbf{R}}{2}\cdot\mathbf{q}} f^*_{A'} \mathrm{e}^{-(-\mathrm{i})\frac{\mathbf{R}}{2}\cdot\mathbf{k}_0} \}$$

$$\text{Single-Double Interf. :} \qquad I_{\mathrm{SD}} = \frac{1}{-4\pi^2} \int \frac{\mathrm{d}\hat{\mathbf{R}}}{4\pi} 2\Re \Big\{ (f_A \mathrm{e}^{\mathrm{i}(\mathbf{k}_0-\mathbf{k})\cdot\frac{\mathbf{R}}{2}} + f_{A'} \mathrm{e}^{\mathrm{i}(\mathbf{k}_0-\mathbf{k})\cdot\frac{-\mathbf{R}}{2}})^* \times \left(\int \mathrm{d}^3\mathbf{k} \underbrace{(-4\pi^2)\langle \psi^-_{A'} | V_{A'} | \mathbf{k} \rangle}_{= f_{A'} \exp(\mathrm{i}(\mathbf{k}-\mathbf{k}')\cdot\frac{\mathbf{R}}{2})} \underbrace{\langle \mathbf{k} | G_0 | \mathbf{k} \rangle}_{= (\varepsilon_0 + \mathrm{i}\epsilon - \frac{k^2}{2})^{-1}} \underbrace{(-4\pi^2)\langle \mathbf{k} | V_A | \psi_A \rangle}_{= f_A \exp(\mathrm{i}(\mathbf{k}_0-\mathbf{k})\cdot\frac{\mathbf{R}}{2})} + \big[A \leftrightarrow A' \big] \right) \Big\}$$

and so on ... Notice the striding $(-4\pi^2)$ factor coming from the conversion between T matrix elements and scattering amplitudes $f_{A,A'}$.

The simplest approximation to multiple scattering is called the independent atom model (IAM) (8.136) which regroups the sum of separate atomic cross sections $I_{\mathrm{S}} = |f_A|^2 + |f_{A'}|^2$ and their coherent interference term I_{SS}.

Originally, the averaging is made on the molecule's orientation. If one wants to include vibrational motion, an average on the internuclear separation can be used as well using the first vibrational level solution of the simple harmonic oscillator [264, p.221–5:table 6-1]. Those functions are scaled with the vibrational angular frequency ω and reduced mass $\bar{M} = M_A M_{A'}/(M_A + M_{A'})$ of the diatomic molecule. The integration yields [526, p.1917:eq.(34)]:

$$\begin{aligned} I_{\mathrm{SS}} &= 2\Re \left\{ f_A\, f^*_{A'} \int \frac{\mathrm{d}^3\mathbf{R}}{4\pi} \underbrace{\sqrt{\frac{\omega\bar{M}}{\hbar\pi}} \exp(-\frac{\omega\bar{M}}{\hbar}(R-\bar{R})^2)}_{\approx |\chi_{v=0}(R)|^2} \mathrm{e}^{\mathrm{i}\mathbf{q}\cdot\mathbf{R}} \right\} \\ &= 2\Re\{ f_A\, f^*_{A'} \} \int_{-\infty}^{\infty} \mathrm{e}^{-x^2} \mathrm{j}_0 \left(q(\frac{x\sqrt{\hbar}}{\sqrt{\omega\bar{M}}} + \bar{R}) \right) \frac{\mathrm{d}x}{\sqrt{\pi}} \simeq 2\Re\{ f_A f^*_{A'} \} \mathrm{j}_0(q\bar{R}) \exp\left(-\frac{\hbar^2 q^2}{2\bar{M}} \frac{1}{2\hbar\omega} \right) \end{aligned}$$

Thence, the explicit formula of the independent atom model for scattering from a diatomic molecule of equilibrium separation $\bar{R}$ and with a momentum transfer $q = 2k\sin\theta/2$ is [420, eq.(2)]:

$$\boxed{\frac{\mathrm{d}\sigma_{\mathrm{IAM}}}{\mathrm{d}\Omega} = |f_A(\theta)|^2 + |f_{A'}(\theta)|^2 + 2\Re\{ f_A(\theta)\, f^*_{A'}(\theta) \} \mathrm{j}_0(q\bar{R}) \exp\left(-\frac{q^2}{4\bar{M}\omega} \right),} \tag{8.137}$$

in atomic units; and for homonuclear molecules $f_A = f_{A'}$ the compact form [419, eq.(11)]:

$$\text{Homonuclear IAM} : 2|f_A|^2\left[1+\frac{\sin(qR)}{qR}\exp\left(-\frac{q^2}{4\bar{M}\omega}\right)\right] . \tag{8.138}$$

The IAM (8.137) starts to give valid DCS at energies above $\gtrsim 150\,\text{eV}$. Those latter need, however, to be scaled down by a screening correction s which decreases with the incident electron's energy (see table 11.3 on p. 402). This is due to the fact that the IAM, although yielding qualitatively good DCS shapes, does not obey the optical theorem (7.29) [526, 1915:eq.(10–11)].

8.5.4 Relativistic

Normally, in the relativistic domain of energies, instead of solving Schrödinger's equation, one should solve Dirac's equation which involves the 4-component spinor of the electron [804, §3.2]. The wavenumber k is relativistically related to the kinetic energy ε_0 and velocity v as:

$$\hbar k = m_\text{e}\text{v}\gamma = \frac{\beta}{c}(\varepsilon_0 + m_\text{e}c^2) \quad \text{or} \quad k = \frac{\beta\gamma}{\alpha}\,\text{a.u.} \;\Rightarrow\; k^2 = \frac{\gamma^2-1}{\alpha^2}\,\text{a.u.} \tag{8.139}$$

Since the relativistic DCS differs from the classical Rutherford scattering only by a factor of γ^2 and by $(1-\beta^2\sin^2\frac{\theta}{2})$ for the relativistic spin correction [716, p.902–3:eq.(1A-102–3)], we use a convenient conversion factor between a non-relativistic to an approximately relativistic DCS:

$$\frac{\mathrm{d}\sigma_\text{rel}}{\mathrm{d}\Omega}(\theta) = \frac{\mathrm{d}\sigma_\text{non-rel}}{\mathrm{d}\Omega}(\theta)\left(\frac{\varepsilon_0}{m_\text{e}c^2}+1\right)^2(1-\beta^2\sin^2\frac{\theta}{2}) . \tag{8.140}$$

We do not consider recoil effects nor nuclear form factors which start affecting the DCS at large angles above 100 MeV [803a, p.165].

8.5.5 Inter-Electron scattering

The scattering of two individual electrons is not an approximation *per se*. Nevertheless, it is used in binary-encounter models to represent the local interaction of the impinging electron with a bound electron. This is used in the absorption model 8.2.4 and for approximating the ionisation cross section 11.5.3. Therefore, we cover here the basic formulae giving the differential cross sections of two colliding electrons in different reference frames and in the relativistic domain.

Expressed in the centre of mass frame, the scattering into an angle of θ between two frontally colliding electrons of relative velocity* $\overleftrightarrow{\text{v}}$ (in atomic units $\hbar/a_0 m_\text{e}$) and arbitrary spin orientation (unpolarised beams) is given by Mott and Fowler's [679] formula [680, p.302:eq.(25-26)]:

$$\frac{\mathrm{d}\sigma}{\mathrm{d}\omega} = \frac{a_0^2}{\overleftrightarrow{\text{v}}^4}\left(\frac{1}{\sin^4\theta/2}+\frac{1}{\cos^4\theta/2}-\frac{\cos(\frac{1}{\overleftrightarrow{\text{v}}}\log(\tan^2(\theta/2)))}{\sin^2\theta/2\,\cos^2\theta/2}\right) \tag{8.141}$$

The solid angle $\mathrm{d}\omega = \sin\theta\,\mathrm{d}\theta\,\mathrm{d}\varphi$ is expressed in the centre of mass frame. The first term in the cross section represents classical Rutherford scattering whereas the second term invokes the possibility that the two electrons exchange places due to their indistinguishability. The last term represents an interference due to the fact that the wave functions (scattering amplitudes) of the two electrons are summed coherently before being brought to their square modulus as in (8.5).

*This is in Galilean kinematics the difference in velocities of the electrons, but **not** the velocity in the relative frame! In that latter case, a factor 16 would appear next to the velocity as given in some references [821, p.350:eq.(15.5.36)] and their eq.(15.5.35) which lacks a 1/4 coefficient somewhere.

Equivalently, this cross section can be expressed differentially with respect to the energy ε_2 of the secondary electron assumed initially at rest in the fixed frame. This implies that the momentum transfer $q = 2k_\mathrm{r}\sin\theta/2$ (in the relative frame) is directly converted into kinetic energy pertaining to the ejected electron: $\varepsilon_2 = \hbar^2 q^2/2m_\mathrm{e}$. Since the initial momentum k of the primary electron is twice its value k_r in the relative frame, $k = 2k_\mathrm{r}$ we have:

$$\varepsilon_2 = \frac{(\hbar 2k_\mathrm{r})^2}{2m_\mathrm{e}}\sin^2\frac{\theta}{2} = \varepsilon_0\sin^2\frac{\theta}{2} \Rightarrow \mathrm{d}\varepsilon_2 = \varepsilon_0\frac{1}{2}2\sin\frac{\theta}{2}\cos\frac{\theta}{2}\mathrm{d}\theta = \frac{\varepsilon_0}{2}\sin\theta\,\mathrm{d}\theta \tag{8.142}$$

Replacing this relation into (8.141) and integrating over the azimuthal angle φ yields the alternative expression in the fixed frame [412, 605, eq.(1), eq.(7)]:

$$\begin{aligned}\frac{\mathrm{d}\sigma}{\mathrm{d}\varepsilon_2} &= \frac{2\pi a_0^2}{(2\varepsilon_0/\mathcal{E}_h)^2}\frac{2}{\varepsilon_0}\left(\frac{\varepsilon_0^2}{\varepsilon_2^2} + \frac{\varepsilon_0^2}{(\varepsilon_0-\varepsilon_2)^2} - \frac{\varepsilon_0^2\cos(\sqrt{\frac{\mathcal{E}_h}{2\varepsilon_0}}\log(\varepsilon_2/(\varepsilon_0-\varepsilon_2)))}{\varepsilon_2(\varepsilon_0-\varepsilon_2)}\right)\\ &= \frac{4\pi a_0^2}{(\varepsilon_0/\mathrm{Ryd})}\mathrm{Ryd}\left(\frac{1}{\varepsilon_2^2} + \frac{1}{(\varepsilon_0-\varepsilon_2)^2} - \frac{\cos(\sqrt{\frac{\mathrm{Ryd}}{\varepsilon_0}}\log(\varepsilon_2/(\varepsilon_0-\varepsilon_2)))}{\varepsilon_2(\varepsilon_0-\varepsilon_2)}\right)\end{aligned} \tag{8.143}$$

The presence of the Rydberg unit (Ryd) absorbs the factor 2 associated to the conversion between velocities and energies (hartree: $\mathcal{E}_h$) expressed in atomic units.

The cosine function in the numerator of the interference term is usually designated as $\phi(\theta;\overleftrightarrow{\mathrm{v}})$ in the relative frame or $\phi(\varepsilon_2;\varepsilon_0)$ in the fixed frame:

$$\phi(\theta;\overleftrightarrow{\mathrm{v}}) = \cos\left(\frac{1}{\overleftrightarrow{\mathrm{v}}}\ln(\tan^2\frac{\theta}{2})\right) \tag{8.144a}$$

$$\phi(\varepsilon_2;\varepsilon_0) = \cos\left(\sqrt{\frac{\mathrm{Ryd}}{\varepsilon_0}}\ln\frac{\varepsilon_2}{\varepsilon_0-\varepsilon_2}\right) \tag{8.144b}$$

This function $\phi(\varepsilon_2;\varepsilon_0)$ is plotted for various incident energies ε_0 in figure 8.4a between $\varepsilon_2/\varepsilon_0 = 10^{-6}$ and 0.5; the upper limit of ε_2 beyond which the formula is symmetrical due to exchange. Essentially, as $\varepsilon_2 \to 0$ the function oscillates between ±1, with slower oscillations as $\varepsilon_0 \gg$ Ryd until they become almost imperceptible. Typically, this formula is applied when $\overleftrightarrow{\mathrm{v}} \gg 1$ (or $\varepsilon_0 \gg$ Ryd) so that the cosine in the numerator is replaced by 1 in most expressions in the literature [412, 507, 508, 968, eq.(26), eq.(3), eq.(1)]. For direct comparison, we also show in figure 8.4b the interference function between a free and a pseudo-free electron bound by an energy B in an atomic orbital. This case will be treated later in sections 10.2.2 and 11.5.2.

Generalised to the relativistic domain, Mott's cross section is named after Møller [657, eq.(74)]*:

$$\frac{\mathrm{d}\sigma_\mathrm{Møller}}{\mathrm{d}\omega} = \left(\frac{a_0\alpha^2(1+\beta_\mathrm{r}^2)}{4\gamma_\mathrm{r}\beta_\mathrm{r}^2}\right)^2\left[\frac{1}{\sin^4\frac{\theta}{2}} + \frac{1}{\cos^4\frac{\theta}{2}} - \frac{1}{\sin^2\frac{\theta}{2}\cos^2\frac{\theta}{2}} + \left(\frac{2\beta_\mathrm{r}^2}{1+\beta_\mathrm{r}^2}\right)^2\left(1+\frac{1}{\sin^2\frac{\theta}{2}\cos^2\frac{\theta}{2}}\right)\right]. \tag{8.145}$$

All relativistic Lorentz factors γ_r and β_r are expressed in the relative (centre of mass) frame. The appearance of the fine-structure constant α is due to the (inverse of the) speed of light expressed in atomic units (see 7.38).

*There is a mistyped exponent in Schwabl [821, eq.(15.5.34)], the last term should be a $1/\sin^2$ instead of ~~$1/\sin^4$~~

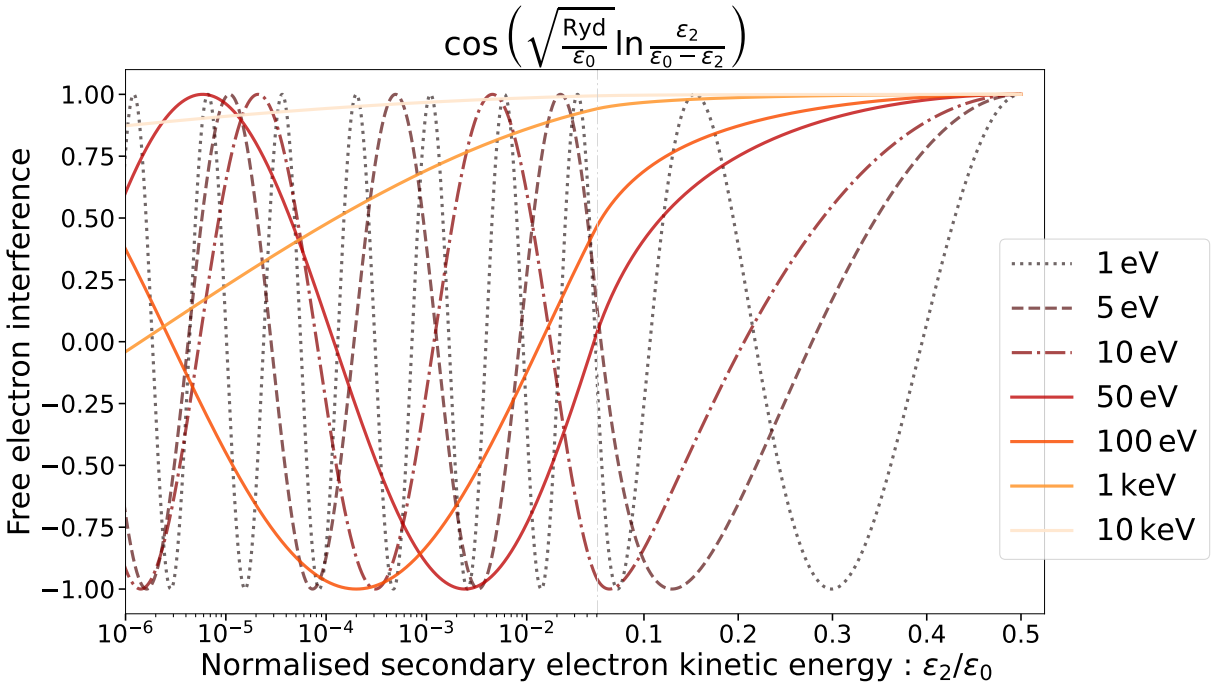

(a) Coulomb-wave interference function from Mott's scattering between free electrons. Oscillations are stretched as the incident velocity ε_0 increases. The middle-line of the graph at $\varepsilon_2/\varepsilon_0 = 0.05$ separates logarithmically scaled low values from linearly scaled values up to one half.

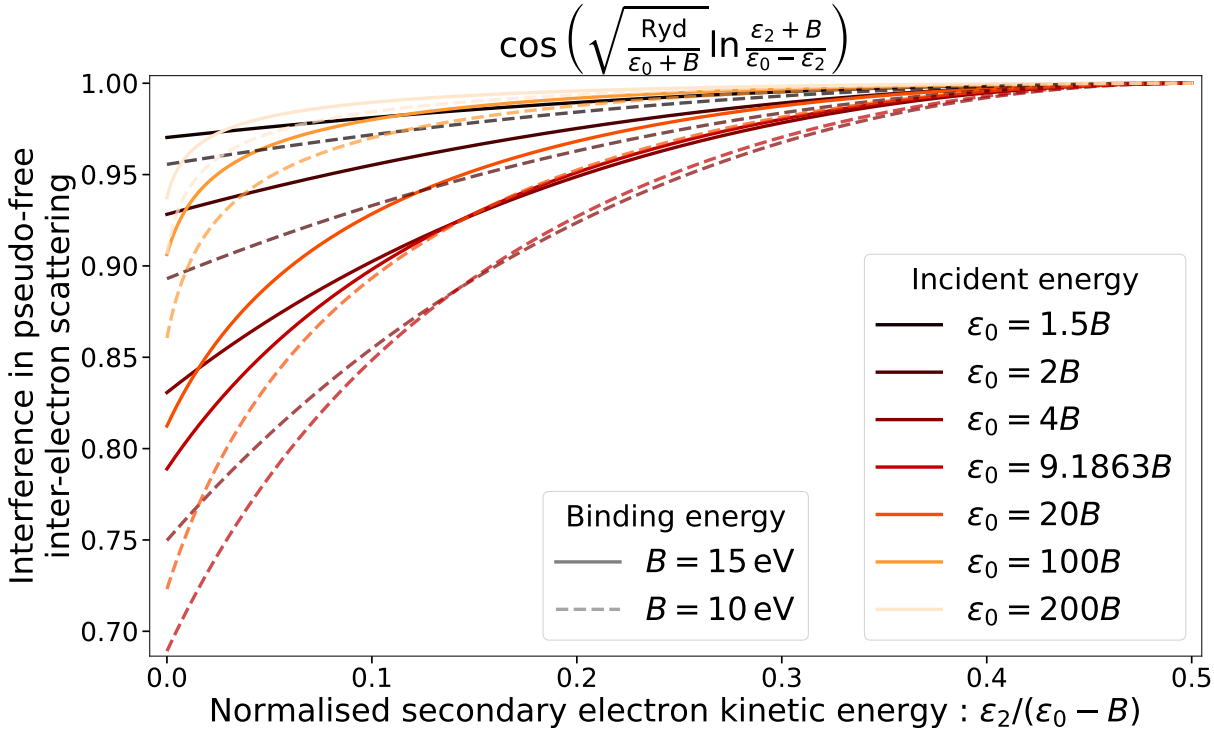

(b) Coulomb-wave interference function from modified Mott's scattering between free and pseudo-free (bound) electrons. No oscillations are observed for $B \gtrapprox 0.6656\,\text{eV}{=}B_{\text{co}}$, the critical binding energy. The function is monotonically increasing and reaches a minimum at $\varepsilon_0 \approx 9.1863\,B = \varepsilon_{\phi,\text{min}}$.

Figure 8.4: Coulomb-wave interference functions between two electrons.

As opposed to Mott's cross section (8.141) which is based on an exact treatment of the Coulomb wave interference in a non-relativistic, Møller's cross section (8.145) is expressed in the first Born approximation using thus Dirac plane-waves instead of relativistic Coulomb waves. The difference is that the interference function $\phi(\theta, \overleftrightarrow{\mathrm{v}})$ was replaced by 1; its asymptotic value for $(\overleftrightarrow{\mathrm{v}}) \to \infty$.

Again, one can choose to express this cross section in terms of the energy of the secondary electron (in the fixed frame where it is initially at rest). The relation (8.142) can be shown to hold relativistically as well, an elegant way is to remember that the kinetic energies of the 'primary' and 'secondary' electron which are equal in the centre of mass, transform in opposite ways with respect to the momentum in the relative frame (see Lorentz transformation in appendix A-(A.6&A.7)), this implies that their difference is purely due to the momentum exchange $2p_r \sin\frac{\theta}{2}$, which is an invariant of the collision [58, p.324].

When moving to the fixed frame, from equation (A.6) in the appendix A of the previous part (using $\vec{\mathcal{V}} \cdot \mathbf{p} = -m_\mathrm{e}\mathrm{v}_\mathrm{r}^2\gamma_\mathrm{r}$), we can convert:

$$\beta_\mathrm{r}^2 = \frac{\gamma - 1}{\gamma + 1} \quad \text{and} \quad \gamma_\mathrm{r}^2 = \frac{\gamma + 1}{2} \,, \tag{8.146}$$

which leads to a more aesthetic presentation [58, 605, eq.(81.14), eq.(13)]:

$$\frac{\mathrm{d}\sigma_{\text{Møller}}}{\mathrm{d}\varepsilon_2} = \frac{2\pi a_0^2\alpha^2}{\beta^2}\left[\frac{1}{\varepsilon_2^2} + \frac{1}{(\varepsilon_0 - \varepsilon_2)^2} - \frac{1}{\varepsilon_2(\varepsilon_0 - \varepsilon_2)} + (\frac{\gamma - 1}{\gamma})^2(\frac{1}{\varepsilon_0^2} + \frac{1}{\varepsilon_2(\varepsilon_0 - \varepsilon_2)})\right], \tag{8.147}$$

$$= \frac{2\pi a_0^2\alpha^2}{\beta^2}\left[\frac{1}{\varepsilon_2^2} + \frac{1}{(\varepsilon_0 - \varepsilon_2)^2} - \frac{2\gamma - 1}{\gamma^2\varepsilon_2(\varepsilon_0 - \varepsilon_2)} + \frac{1}{(\varepsilon_0 + m_\mathrm{e}c^2)^2}\right]. \tag{8.148}$$

In case the notation is not explicit enough, β and γ are now linked to the incident kinetic energy ε_0 in the fixed frame.

Chapter 9

Numerical algorithms

The present chapter regroups various numerical methods that are used in order to compute the quantities necessary for the generation of differential cross sections (DCS). In particular, we describe concretely how we obtain in the partial-wave decomposition: the phase shifts δ_ℓ for central potentials and the S-matrix for diatomic potentials.

9.1 Variable Phase Method

We start with the simplest case of central potentials. For constructing the DCS one only requires the knowledge of the phase shifts δ_ℓ. In principle, they are obtained from the asymptotic behaviour of the radial functions $u_\ell(r)$ at $r \to \infty$. However, there exists a more efficient and accurate way to calculate those phase shifts, as described in detail in Calogero [139], through their generalisation as variable phase functions of the radial coordinate $\delta_\ell(r)$. They are defined such that [139, p.8–10:eqs.(3, 6&11)]:

$$u_\ell(r) = A(\hat{\mathrm{j}}_\ell(kr) - \hat{\mathrm{y}}_\ell(kr)\tan\delta_\ell(r)) \;, \tag{9.1}$$

$$\text{Asymptotically}: \lim_{r\to\infty}\delta_\ell(r) = \delta_\ell \;, \tag{9.2}$$

$$\text{At the origin}: \lim_{r\to 0}\delta_\ell(r) = 0 \;; \tag{9.3}$$

with the normalisation factor A defined in (8.105). If one introduces this form into the second order differential equation satisfied by $u_\ell(r)$ (8.102), after some manipulations, one arrives to the heart of the differential equation satisfied by the variable phase [139, p.11:eq.(14–5)]:

$$\frac{\mathrm{d}\delta_\ell(r)}{\mathrm{d}r} = -\frac{2}{k}V(r)\left(\cos\delta_\ell(r)\hat{\mathrm{j}}_\ell(kr) - \sin\delta_\ell(r)\hat{\mathrm{y}}_\ell(kr)\right)^2 \;, \tag{9.4}$$

$$\text{which, for } \ell = 0 \;:\; \frac{\mathrm{d}\delta_0(r)}{\mathrm{d}r} = -\frac{2}{k}\sin^2(kr + \delta_0(r)) \tag{9.5}$$

with the simple boundary condition (9.3). Since, as k increases for higher electron energies, the spherical Bessel waves have shorter oscillations, we use a different variable of integration: $x \equiv kr$. In this space ($\check{\delta}_\ell(kr) = \delta_\ell(r)$):

$$\frac{\mathrm{d}\check{\delta}_\ell(x)}{\mathrm{d}x} = -U(r)\left(\sin\check{\delta}_\ell(x)\hat{\mathrm{j}}_\ell(x) - \sin\check{\delta}_\ell(x)\hat{\mathrm{y}}_\ell(x)\right)^2 \;, \tag{9.6}$$

with the reduced potential: $U(x) \equiv V(x/k)2/k^2$.

9.1.1 Asymptotics

The behaviour of spherical Bessel functions near the origin is given by:

$$\mathrm{j}_\ell(x) \sim \frac{x^\ell}{(2\ell+1)!!} \sim \frac{x^\ell}{\sqrt{2}(\frac{2\ell+1}{\mathrm{e}})^{(\ell+1)}} \text{ for } x \ll 1 \tag{9.7}$$

Considering Stirling's approximation $n! \sim \sqrt{2\pi n}(n/\mathrm{e})^n$, the double factorial when $\ell \gg 1$ approaches:

$$(2\ell+1)!! \sim \frac{\sqrt{2\pi(2\ell+1)}\,((2\ell+1)/\mathrm{e})^{2\ell+1}}{\sqrt{2\pi\ell}\,(\ell/\mathrm{e})^\ell} \sim \sqrt{2\mathrm{e}}\left(\frac{2\ell+1}{\mathrm{e}}\right)^{\ell+1}, \tag{9.8}$$

within 5% for $\ell > 3$ and 2% for $\ell > 8$.

We can thus derive a rapid evaluation of an outer radius r_ℓ below which $\mathrm{j}_\ell(kr_\ell) < \epsilon\ ;\ \forall r < r_\ell$:

$$\frac{(kr_\ell)^\ell}{(2\ell+1)!!} < \epsilon \Rightarrow kr_\ell < (\epsilon\sqrt{2\mathrm{e}})^{1/\ell}\left(\frac{2\ell+1}{\mathrm{e}}\right)^{1+1/\ell} \tag{9.9}$$

The actual value $\mathrm{j}_\ell(kr_\ell)$ will always be smaller for all $\ell > 0$ than any desired ϵ, and will decrease drastically for large ℓ.

We use (9.9) for various purposes.

1. If we want to compute the phase shift for the ℓ partial wave, we integrate the differential equation starting from r_ℓ instead of 0.

2. To estimate the maximal $\ell_{\max}$ order beyond which we use the analytical Born approximation for $\tilde{\delta}_\ell$. We first calculate a maximal $r_{\max}$ radius beyond which the potential V_{seoa} without polarisation is negligible ($<10^{-12}$). Then, we invert (9.9) where we replace r_ℓ by $r_{\max}$ and search (dichotomically) for the minimal ℓ for which the inequality is satisfied.

3. The phase shift due to the polarisation potential can be calculated accurately and analytically by the Born approximation (14.43). Nevertheless, the formula for the Buckingham potential $-\alpha_\mathrm{d}/2(r^2+r_\mathrm{b}^2)^2$ (10.52), presents a difficulty when $kr_\mathrm{b} \to \infty$ because:

$$\begin{cases} \mathrm{K}'_{\ell+\frac{1}{2}}(kr_\mathrm{b}) \xrightarrow{kr_\mathrm{b}\to\infty} \infty \\ \mathrm{I}_{\ell+\frac{1}{2}}(kr_\mathrm{b}) \xrightarrow[kr_\mathrm{b}\to\infty]{} 0 \end{cases},$$

   so that their product is numerically undefined in (14.43). We circumvent this by using the formula (10.17b) for the asymptotic $-\alpha_\mathrm{d}/2r^4$ polarisation where $r_\ell > 5r_\mathrm{b}(k)$ with r_ℓ corresponding this time to:

$$\frac{\alpha_\mathrm{d}}{2r_\ell^4} \cdot \frac{(kr_\ell)^\ell}{(2\ell+1)!!} = 1 \tag{9.10}$$

   In this case, we require that ℓ be at least 5.

9.1.2 Multi-channel variable matrix

The variable phase method can be generalised as in Martinazzo *et al.* [632] to the angular-momentum close-coupling method for electron scattering off diatomic molecules. One defines a *variable* function $S^{\mathcal{L}}_{\ell J,\ell_0 J_0}(r)$ for each matrix element such that:

$$u^{\mathcal{L}}_{\ell J,\ell_0 J_0}(r) = \delta_{\ell\ell_0}\delta_{JJ_0}\hat{\mathrm{h}}^-(k_0 r) + \sqrt{\frac{k_0}{k_J}}\hat{\mathrm{h}}^+(k_J r) S^{\mathcal{L}}_{\ell J,\ell_0 J_0}(r)\ . \tag{9.11}$$

Because $k_J \approx k_0$ in the range of energies of interest ($> 30\,\mathrm{eV}$), we take $k \equiv k_0 = k_J$ and use the same dimensionless variable $x = kr$ as before.

The differential equation satisfied by the S matrix is [632, p.198:bottom]:

$$\frac{\mathrm{d}S^{\Lambda}_{\ell,\ell_0}(x)}{\mathrm{d}x} = \frac{\mathrm{i}}{2}\sum_{i,j=0}^{\ell_{\max}} \left(\delta_{\ell i}\hat{\mathrm{h}}^-_i(x) - S^{\Lambda}_{\ell,i}(x)\hat{\mathrm{h}}^+_i(x)\right) U^{\Lambda}_{ij}(x) \left(\delta_{j\ell_0}\hat{\mathrm{h}}^-_{\ell_0}(x) - \hat{\mathrm{h}}^+_j(x) S^{\Lambda}_{j,\ell_0}(x)\right)\ . \tag{9.12}$$

It is a product of square $\bar{\ell}_{\max}\times\bar{\ell}_{\max}$ matrices, one for each Λ projection symmetry. For homonuclear diatomic molecules, we recall (see p. 307) that the S matrices may also be separated into two independent sub-matrices for even (g) and odd (u) parity of ℓ, ℓ_0 pairs. We therefore integrate (9.12) separately for each $0 < \Lambda \le \bar{\ell}_{\max}$ and for each parity (g, u) if the molecule is homonuclear.

The (reduced) potential matrix U^{Λ}_{ij} is defined as (8.123):

$$U^{\Lambda}_{ij}(x) = \frac{2}{k^2}\sum_{l=|i-j|}^{l=\min(l_{\max},i+j)} V_l(x/k)\underbrace{(-)^{\Lambda}\sqrt{(2\ell+1)(2\ell'+1)}\begin{pmatrix} l & \ell & \ell' \\ 0 & 0 & 0\end{pmatrix}\begin{pmatrix} l & \ell & \ell' \\ 0 & -\Lambda & \Lambda\end{pmatrix}}_{\text{Precalculated}}\ . \tag{9.13}$$

For efficiency, we precalculated all the multipliers of V_l and stored them in a $[\Lambda \le \bar{\ell}_{\max};\, l \le l_{\max};\, \ell \le \bar{\ell}_{\max};\, \ell' \le \bar{\ell}_{\max}]$ matrix file.

The boundary condition for the S-matrix at the origin is $S(0) = 1$. Nevertheless, one cannot proceed to integrate (9.12) from $x = 0$ because the Riccati-Hankel functions $\hat{\mathrm{h}}^{\pm}_{\ell}$ defined in (8.97c) are irregular at the origin due to the Riccati-Bessel function $\hat{\mathrm{y}}_\ell$ (8.97b). Martinazzo *et al.* [632] proposed instead to integrate the K-matrix through:

$$\frac{\mathrm{d}K^{\Lambda}_{\ell,\ell_0}}{\mathrm{d}x} = -\sum_{i,j=0}^{\ell_{\max}} \left(\delta_{\ell i}\hat{\mathrm{j}}_\ell(x) - K^{\Lambda}_{\ell i}(x)\hat{\mathrm{y}}_i\right) U^{\Lambda}_{ij}(x) \left(\delta_{j\ell_0}\hat{\mathrm{j}}_{\ell_0}(x) - \hat{\mathrm{y}}_j(x) K^{\Lambda}_{j,\ell_0}(x)\right)\ , \tag{9.14}$$

and subsequently calculate the S matrix (8.85) at the asymptotic boundary $x = x_{\max}$, when the K matrix has converged.

The problem now is that every once in a while, the K matrix may go through singularities when the potential is strong and the accumulated 'phase shift' between j_ℓ and y_ℓ passes through $\pi/2$. Each time this happens, one would need to inverse the K matrix and continue integration on the K^{-1} matrix. Still, this does not exclude the very improbable but not impossible situation where the K^{-1} and K matrices possess singularity points which lie very close on the radial axis.

Thus we settled on the following procedure:

1. Integrate $\boldsymbol{K}(x)$ starting from $\boldsymbol{K} = 0$ at $x = 0$ until its trace $|\sum_{\ell=0}^{\bar{\ell}_{\max}} K^{\Lambda}_{\ell,\ell}| \ge 2$;
2. Convert to the S matrix (8.84):

   $$S^{\Lambda}_{\ell,\ell_0}(x) = (\boldsymbol{I} + \mathrm{i}\boldsymbol{K})\cdot(\boldsymbol{I} - \mathrm{i}\boldsymbol{K})^{-1}$$

   (using matrix operations and where $\boldsymbol{I} = \delta_{\ell\ell_0}$ is the identity matrix)
3. Continue the integration with the $\boldsymbol{S}(x)$ matrix-function up to $x_{\max}$ (9.12).

9.1.3 Integration

We need integration at two different levels: calculate the potential and solve the first order differential equations.

Potential

All central potentials used presently pose no problem to implement since they are analytical, except for the absorption potential from the free electron gas (FEG) oscillator in section 8.2.4. There are two integrations: one on the $\xi = \Delta\varepsilon/\varepsilon_\mathrm{F}$ variable representing the ratio of the energy transfer on the Fermi energy of the FEG; and one the $\zeta = q/2k_\mathrm{F}$ variable representing the momentum transfer q relative to the Fermi momentum.

- $\int \ldots \mathrm{d}\zeta$: As suggested by Salvat [801, p.16], we use an adaptative Gauss-Legendre quadrature of 32 points. Those correspond to the roots p_n of the Legendre polynomial $P_{32}(x)$ of order 32 weighted by [884, p.178–180]:

$$w_\mathrm{n} = \frac{2}{(1-p_n)^2}\left[\left.\frac{\mathrm{d}P_{32}(x)}{\mathrm{d}x}\right|_{x=p_n}\right]^2 . \tag{9.15}$$

  The corresponding ζ_n samples are adapted to the segment extending from ζ_- to ζ_+ as $\zeta_n = r_n\,(\zeta_+ - \zeta_-)/2 + (\zeta_+ + \zeta_-)/2$.

- $\int \ldots \mathrm{d}\xi$: we take 80 linearly spaced values between ξ_min and ξ_max. Also, to reduce the strain on the computational effort, we subsample the radial points x_n so as not to exceed 10000 points for which double integration is performed.

- Analytical (8.69) : is used when $\Delta\mathcal{E}_\mathrm{min}/\varepsilon_\mathrm{F} < 100(4\zeta_\mathrm{p}(\zeta_\mathrm{p}+1))$ where $\zeta_\mathrm{p} \approx 1/\sqrt[3]{4\pi k_\mathrm{F}}$ is an approximate value for the plasmon cutoff momentum [801, eq.(A15&A17)]. We recall that $\Delta\mathcal{E}_\mathrm{min}$ represents the minimal loss of energy in the inelastic collision.

For diatomic potentials, we use the analytical decomposition (8.31) for the static part. For the other potentials, we use another Gauss-Legendre quadrature of 64 points which are reduced to 32 points only when we exploit the symmetry for homonuclear molecules.

Differential Equations

For integrating (9.6), (9.14) and (9.12), we discretise the radial coordinate $x = kr$ into N_x points spanning from $x = 0$ to $x = x_\mathrm{max}$ with a logarithmic spacing as follows:

Atoms : from $x = 10^{-9}$ to x_max and then replacing by $x = 0$ at the origin.

Molecules : symmetrical logarithmic spacing about the singularity point located at $r = R/2$. This is done by stitching together two logarithmically-spaced vectors $(x)_n$ (from $x = 10^{-9}$ to $x = R/2$) as: $R/2-(x)_n$ and $R/2+(x)_n$ and concatenated with $R/2$ at their junction. Then we continue a logarithmic spacing up to x_max.

The maximal radius is estimated as follows:

$$
\begin{aligned}
x_{\max} &= k\ \cdot \max(r_0, r_{\rm cf}, 3r_{\ell_{\max}}) \qquad (9.16)\\
\text{Where}\ \ r_0\ &:\ |V_{l=0}(r)| < \epsilon\ ;\ \forall r > r_0\ ,\\
r_{\rm cf}\ &:\ \left|\frac{2V_{l=0}(r)r^2}{\ell_{\max}(\ell_{\max}+1)}\right| < \epsilon\ ;\ \forall r > r_{\rm cf}\\
r_{\ell_{\max}} &\equiv r_\ell \text{ for } \ell = \ell_{\max} \text{ in (9.9)}
\end{aligned}
$$

The potential $V_{l=0}$ is the isotropic real potential comprising static, exchange, and polarisation effects. The maximal partial-wave order $\ell_{\max}$ is estimated from $r_{\rm sr}$ as:

$$
\begin{aligned}
r_{\rm sr}\ &:\ V_{\rm sr}(r, \theta = 0^\circ) < \epsilon\ ;\ \forall r > r_{\rm sr}\ ,\\
\ell_{\max}\ &:\ \mathrm{j}_\ell(kr) < \epsilon\ ;\ \forall \ell > \ell_{\max} \text{ and } \forall r < r_{\rm sr}\ .
\end{aligned}
$$

It is important to note that this estimation is based on the range of the short-range (static) potential $V_{\rm sr}$ alone, but not including the long-range multipole nor polarisation potentials for which the integrals can be calculated analytically from the Born approximation as will be explained in section 9.2.1.

Our current parameters were set by default to:

$$\epsilon = 10^{-10} \qquad\qquad N_x = 200000$$

With these, we obtain overall (this varies with k):

$$100a_0 < r_{\max} < 800a_0 \qquad \text{and} \qquad 72 < \ell_{\max} < 120$$

For molecules, we note that we use two different $\bar{\ell}_{\max} = 35 \neq \ell_{\max}$. The first $\bar{\ell}_{\max}$ is the maximal order used in the angular-momentum close-coupling S matrix, whereas the second $\ell_{\max}$ is for the remainder of the diagonal S matrix with phase shifts.

With the discretised space of radial coordinates, we use the popular fourth-order explicit Runge-Kutta quadrature [431, p.38–41:§3.2:eq.(3.5)]. We denote the function derivative $F(x, y)$. (This is applicable to a scalar equation: $\mathrm{d}y/\mathrm{d}x = F(x, y)$ (9.6) as well as for a matrix equation: $\mathrm{d}A/\mathrm{d}x = F(x, A)$ (9.14) or (9.12).) Given the value of $y(x)$ at a point x, the value $y(x + \Delta x)$ at the next radial step $x + \Delta x$ is obtained from:

$$
\begin{aligned}
y(x+\Delta x) =& y(x) + \frac{\Delta x}{6}\left(F^{(0)} + 2F^{(1)} + 2F^{(2)} + F^{(3)}\right) \qquad (9.17)\\
\text{With}:\ F^{(0)} &= F(x, y(x)) \qquad (9.17a)\\
F^{(1)} &= F\left(x + \frac{\Delta x}{2}, y(x) + \frac{\Delta x}{2}\cdot F^{(0)}\right) \qquad (9.17b)\\
F^{(2)} &= F\left(x + \frac{\Delta x}{2}, y(x) + \frac{\Delta x}{2}\cdot F^{(1)}\right) \qquad (9.17c)\\
F^{(3)} &= F\left(x + \Delta x, y(x) + \Delta x\cdot F^{(2)}\right) \qquad (9.17d)
\end{aligned}
$$

The value of $y(x_{\max})$ is the value of our converged quantity (phase shift or S matrix). In the next section, we explain how we build the scattering amplitudes and cross sections from those phase shifts and S matrices.

9.2 Building Cross Sections

Once the phase shifts and S matrices are obtained, they can be put into the two formulae used for the elastic differential cross sections (atoms 8.106) and (molecules 8.129). The major difficulties lies in (i) the infinite sum which must be truncated to $\ell_{\max}$ and (ii) an efficient handling of the multiple sums through the symmetry or sparsity properties of the T matrix and Clebsch-Gordan coefficients featuring in (8.129).

Starting with (ii) the 7-folded sum in (8.129), our approach is inspired from the suggestions in Morrison [664, §7.3:p.179–182]. We first eliminate matrix elements whose value is below 10^{-12} and estimate the number d of (non-principal) diagonals that are spanned. Then, we proceed through the sum in the following way for each coefficient A_L of the corresponding Legendre polynomial P_L:

- ℓ : $\max(0, L - \bar{\ell}_{\max}) \dots \bar{\ell}_{\max}$
- ℓ' : $|L - \ell| \dots \min(\bar{\ell}_{\max}, L + \ell)$ by steps of 2 from the requirement that $\ell + \ell' + L$ be even
- ℓ_0 : $\max(\ell\%p, \ell - p \cdot d, L - \bar{\ell}_{\max} + \bar{p}) \dots \min(\bar{\ell}_{\max}, \ell + p \cdot d)$.

  The parity p determines the steps of ℓ_0 in virtue of the requirement that $\ell + \ell_0$ be even for homonuclear molecules ($p = 2$); which does not affect heteronuclear molecules ($p = 1$). The correction: $\bar{p} = 1$ if the parities $\ell\%p \neq (L - \bar{\ell}_{\max})\%p$, and $\bar{p} = 0$ otherwise.
- ℓ'_0 : $\max(|L - \ell_0|, \ell' - p \cdot d) \dots \min(\bar{\ell}_{\max}, L + \ell_0, \ell' + p \cdot d)$ by steps of 2.
- Λ : $0 \dots \min(\ell, \ell_0, \Lambda_{\max})$
- Λ' : $0 \dots \min(\ell', \ell'_0, \Lambda_{\max})$

Because of :

▷ the symmetry property: $C^{L\mathcal{M}}_{\ell-\Lambda,\ell'\Lambda'} = (-)^{\ell+\ell'-L} C^{L-\mathcal{M}}_{\ell\Lambda,\ell'-\Lambda'}$,

▷ from the Wigner-3j coefficient: $\ell + \ell' + L$ is even,

▷ the independence of $T^{\Lambda}_{\ell\ell_0} = T^{-\Lambda}_{\ell\ell_0}$ on the sign of Λ;

we may sum only positive Λ and take the twice the value for each additive $\Lambda + \Lambda'$ and subtractive $\Lambda - \Lambda'$ terms. Care must be taken so that terms for which either or both $\Lambda = 0 \vee \Lambda' = 0$, be not counted twice [664, p.182:eq.(7.19)]. For summing the elements, we separate in advance the real $\mathfrak{R}^{\Lambda}_{\ell\ell_0}$ and imaginary $\mathfrak{I}^{\Lambda}_{\ell\ell_0}$ parts of the T matrix and execute:

$$A_L += \left(\mathfrak{R}^{\Lambda}_{\ell\ell_0}\,\mathfrak{R}^{\Lambda'}_{\ell'\ell'_0} + \mathfrak{I}^{\Lambda}_{\ell\ell_0}\,\mathfrak{I}^{\Lambda'}_{\ell'\ell'_0}\right)\sqrt{(2\ell_0+1)(2\ell'_0+1)(2\ell+1)(2\ell'+1)}(-)^{\frac{\ell_0-\ell+\ell'-\ell'_0}{2}}$$
$$\times \begin{pmatrix} \ell & \ell' & L \\ 0 & 0 & 0 \end{pmatrix}\begin{pmatrix} \ell_0 & \ell'_0 & L \\ 0 & 0 & 0 \end{pmatrix} C^{L\Lambda'-\Lambda}_{\ell-\Lambda,\ell'\Lambda'} C^{L\Lambda'-\Lambda}_{\ell_0-\Lambda,\ell'_0\Lambda'}$$

For rapidity, we use the `wigxjpf` library. Naturally, for an efficient handling, we precompute the coefficients independent of Λ, Λ' before summing on these.

Currently we used the following truncation:

$$\bar{\ell}_{\max} = 35 = \Lambda_{\max} \qquad\qquad l_{\max} = 24$$

These limits were chosen after a convergence study in section 10.4 conducted in the range of energies where the angular-momentum coupling is used. The shortcomings that arise at smaller wavelengths (higher energies) require to raise both $\bar{\ell}_{\max}$ (deeper penetration in the centrifugal barrier) and $l_{\max}$ (more resolution at the nuclear singularities). The limitations of $l_{\max}$ are palliated by replacing the computation of DCS with the independent atom model (8.137) described in sec. 8.5.3. Using atomic potentials makes affordable the promotion of $\bar{\ell}_{\max}$ to a higher $\ell_{\max}$.

9.2.1 Born Completion

As mentioned above, all the summations are truncated to a maximal $\bar{\ell}_{\max}$ or $\ell_{\max}$. Truncation at high partial waves usually only clips the forward scattering slope as illustrated in 9.1. Luckily, the higher partial waves are only affected by the long-range potential which is easy to model analytically [274, eq.(11)] (8.45 for polarisation). Then, the scattering amplitude may be calculated analytically with the Born approximation $\tilde{f}$ (8.115) [e.g. 430, eq.(8)], whose decomposition in partial-wave phase shifts $\tilde{\delta}_\ell$ can also be computed analytically (8.120) [e.g. 430, eq.(9)] (or numerically if need be). It is important to remind that:

> The amplitude $\tilde{f}$ and $\tilde{\delta}_\ell$ must proceed consistently from the same potential, and in virtue of the first Born approximation, can be added from the constituent parts of composite potentials (e.g. static + polarisation)

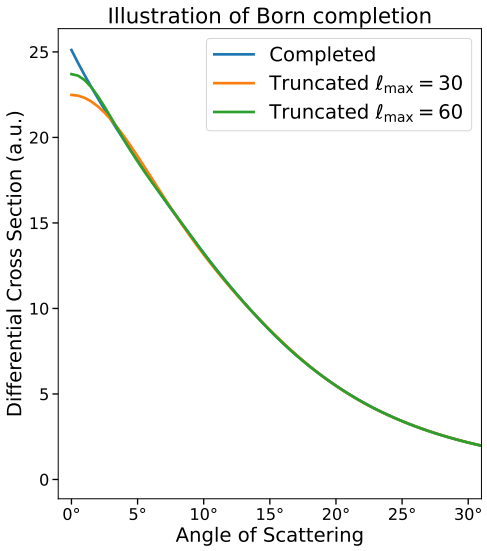

Figure 9.1: Effect of DCS truncation to $\ell_{\max}$ illustrated on atomic oxygen at 100 eV.

For practical purposes, we regrouped the analytical plane wave Born amplitudes $\tilde{f}$ and associated phase-shifts $\tilde{\delta}_\ell$ for various simple potentials in a dedicated chapter 14 of part III.

The philosophy of the Born completion or closure is to encompass the trailing terms in the infinite sum in a compact analytical expression [799, eq.(8)]:

$$\mathring{f}(\theta) = \frac{1}{2\mathrm{i}k}\sum_{\ell=0}^{\ell_{\max}}(2\ell+1)P_\ell(\cos\theta)\left[\underbrace{(\mathrm{e}^{\mathrm{i}2\delta_\ell}-1)}_{\text{Exact}} - \underbrace{\mathrm{i}2\tilde{\delta}_\ell}_{\text{Approx.}}\right] + \underbrace{\frac{1}{2\mathrm{i}k}\sum_{\ell=0}^{\infty}(2\ell+1)P_\ell(\cos\theta)\mathrm{i}2\tilde{\delta}_\ell}_{\equiv\tilde{f}(\theta)} . \tag{9.18}$$

The formula (9.18) above is specifically designed for scattering amplitudes from spherically symmetric potentials. In diatomic molecules, the DCS is obtained as an average (and summation) upon the initial (and final) rotational momentum projection M_0 (and M). Then, the Born completion ought to be performed on the DCS rather than the scattering amplitude [430, eq.(14–17)]. In this case, we use the expressions of the potentials centred on the molecule [430, eq.(7)] (not on the individual atoms) to calculate the diagonal T matrix elements $\ell = \ell_0$. Using (8.108), we can subtract from the calculated T matrix the analytical diagonal elements and add separately the analytical expression $|\tilde{f}(\theta)|^2$ of the differential cross section.

Combining with what we said earlier at the beginning of this section 9.2:

$$\begin{aligned}\frac{\mathrm{d}\sigma}{\mathrm{d}\Omega} &= \frac{1}{4k^2}\sum_{L=0}^{2\bar{\ell}_{\max}} P_L(\cos\theta)\sum_{\ell}\sum_{\ell'}\sum_{\ell_0}\sum_{\ell'_0}\sqrt{\cdots}\begin{pmatrix}\ell & \ell' & L\\ 0 & 0 & 0\end{pmatrix}\begin{pmatrix}\ell_0 & \ell'_0 & L\\ 0 & 0 & 0\end{pmatrix}\\ &\times\left\{\left[\sum_{\Lambda}\sum_{\Lambda'}\left(\Re^{\Lambda}_{\ell\ell_0}\,\Re^{\Lambda'}_{\ell'\ell'_0}+\Im^{\Lambda}_{\ell\ell_0}\,\Im^{\Lambda'}_{\ell'\ell'_0}\right)C^{L\Lambda'-\Lambda}_{\ell-\Lambda,\ell'\Lambda'}C^{L\Lambda'-\Lambda}_{\ell_0-\Lambda,\ell'_0\Lambda'}\right](-)^{\frac{\ell_0-\ell+\ell'-\ell'_0}{2}}-\frac{\delta_{\ell\ell_0}\delta_{\ell'\ell'_0}}{4\pi^2}(1-\mathrm{e}^{\mathrm{i}2\tilde{\delta}_\ell})(1-\mathrm{e}^{-\mathrm{i}2\tilde{\delta}_{\ell'}})\right\}\\ &+\underbrace{\frac{1}{k^2}\left(\sum_{\ell}^{\infty}(2\ell+1)P_\ell(\cos(\theta))\tilde{\delta}_\ell\right)^2}_{\equiv\tilde{f}(\theta)}\end{aligned}\tag{9.19}$$

Note that this expression does not include the higher potential harmonics $> l_{\max}$ which are more adequately included by the independent atom model (IAM). In Schmalzried *et al.* [812, Appendix A], we proposed how to separate the contribution of each partial scattering amplitude f_l. Which means that we could also add the IAM to (9.19) and subtract all contributions from $l = 0$ to $l_{\max}$ harmonics. Nevertheless, our selected $l_{\max} = 24$ is high enough that this additional (IAM) correction is completely negligible and not worth including.

Although the present methodology only exploits the diagonal elements of the T matrix for high partial waves, the Born completion can be made for any T matrix element as done in the work of Feldt and Morrison [274, §II.D]. Given our inaccurate modelling of the molecular harmonics, it was not worth considering non-diagonal elements beyond the $\bar{\ell}_{\max}\times\bar{\ell}_{\max}$ block.

Libraries

At last, we would like to credit the libraries of codes we used.

- Wigner 3j coefficients (Clebsch-Gordan coeff.) were computed with `pywigxjpf`, a python package from the algorithm Johansson and Forssén [459]
- Analytical atomic wavefunctions of Koga *et al.* [523]: we used them to fit our coefficients of 1s-Slater densities in table 8.1 and for estimating kinetic densities in orbitals. The package we used comes from `https://github.com/JFurness1/AtomicOrbitals`. We subsequently modified this code according to our needs.

Apart from these two packages, all other packages we used in Python come from the PyPi library. The list without dependencies can be found in the `requirements.txt` file on the repository: `https://doi.org/10.5281/zenodo.8190461`.

Calculating molecular or atomic potentials, integrating S (or T) matrix elements, and constructing differential cross sections are the main preoccupations targeted by our algorithms. Those having been exposed in the present chapter, we may now move to a critical perspective toward the various models that we encountered on our way to obtain results. The following chapter 10 is supposed to enlighten the choices we made and the difficulties that crossed our way when building our own model.

Chapter 10

Critical review

Although very outspoken, it is not unfounded to say that one can very easily be mislead or deceived in the realm of quantum mechanics. Since the beginning, quantum effects brought into light by specific experiments did not cease to arouse surprise and amazement. Anyone who followed an elementary course in this field has heard about some turning points about the undulatory nature of elementary particles in Young's double slit experiment, Stern-Gerlach's experiment on spin-magnetic field interaction or the spectroscopic structure of atoms unveiled first by Franck and Hertz' cathode rays in mercury vapour.

Similarly, many important discoveries took place within the more specific field of electron-molecule collisions. Such is the case of resonant scattering which had been imagined in the very burgeoning days of quantum physics [300] before experimental evidence [372, 819] emerged in the well studied case of electron-nitrogen scattering. Another example is the existence of rotational rainbows in high-energy electron-diatom scattering [1009] which demonstrates that backscattering is most probably accompanied by a large rotational transition [534, figure 9] $\Delta J \gtrsim 8$, whereas a first Born approximation analysis at low energies [323] only reveals a preponderance of quadrupole-type transitions $\Delta J = 2$, thus little energy transfers.

From an exterior perspective, the search for an unequivocal explanation to physical observations of collision cross-sections often appears as a slowly convergent series of over- then under-compensations of effects. An illustrious example exposed in Robertson *et al.* [780] is the "long-standing mystery" of why the simpler quadrupole Born approximation of Gerjuoy and Stein [323] explained better experimental data than more elaborate studies [208, 266] including polarisation effects. This is caused by the many cancellations that can occur within a more rigorous description including effects of similar order of magnitude: long-range polarisation, short-range exchange and correlation, wave-distortion. A concrete example of cancellation of different orders in the incident wavenumber k^n is given in section 10.1.5 as represented in figures 10.6-10.7. A similar observation was found in Iga *et al.* [419] in intramolecular multiple scattering order decompositions where an alternation of sign contribution could be observed between double-scattering as calculated in Hayashi and Kuchitsu [390] and higher-order scattering terms.

In general, one could say that the ultimate purpose behind calculations in quantum physics, is to obtain an accurate solution to the Schrödinger equation from which measurable quantities can be derived in order to validate the model used; ascertain its underlying values, discover further corrections to be inserted into the model or even bring the assumptions and the theory under trial. In this sense, computing interaction cross sections is a fundamental way to explore how, in the current case, electrons interact with matter and shape our understanding of molecular and atomic structure.

Unfortunately, this honourable endeavour lies beyond the scope of this thesis which just sought after generating cross sections in order to "fill in" consistently some missing input data into our electron swarm simulations. Nevertheless, as I scoured through the literature in urge to find an efficient yet reliable and above all – respectable – way of producing my own cross sections to model electron-molecule interactions, my attention got especially caught at the enchanting character by which simple, elegant and comprehensible models could compete with treatments of utmost sophistication beyond facilitated implementation and easier understanding.

The greatest challenge I struggled with while delving in the realm of quantum physics computation, is that, as opposed to "classical" physics where one would expect a gradual and smooth reconciliation of theory and experiment; the models used in quantum physics to obtain resulting cross sections are very fragile. At first, an encouraging result can be obtained from extremely simple models or crude approximations. Then, if one seeks improvement from little amendments, the whole model crumbles and yields completely aberrant results. Instead, as dictated by the law of diminishing returns, one is forced to spend endless time in looking for more accurate models that require a hecatuplated (100×) effort for a shockingly marginal improvement at best, or at worst the introduction of more annoyingly indelible inaccuracies.

For this reason, due to the very low effort/gain ratio in quantum computations, the discouraged soul succumbs to the temptation of resorting to semi-empirical models that teem in the literature. Of indispensable pragmatic use, semi-empirical models form a very dangerous and deceiving trap for scientific investigation because they often deteriorate the link between a parameter or a model and its physical significance.

> The strength of semi-empirical models often lies rather in *ad hoc* adjustments of loose physical justification than in the inclusion of complex effects credited in the model.

As a consequence, I decided to devote this chapter to some of the many deceptions that I (almost) fell victim to, while trying to generate differential cross sections in elastic scattering. It is segmented into four sections. The first discusses some inexact statements about the (in)validity of approximations. The second criticises some *a posteriori* derivations and incorporation of more complex effects in formerly simple models. The third is a short review of semi-empirical models for higher-order (perturbation) effects in electron-molecule scattering. The fourth is an illustration of the mathematical complexity underlying the construction of differential cross sections.

10.1 Use of Approximations

A perfect place to start with, is the purpose behind taking approximations in quantum mechanics calculations.

A Nowadays, an approximation would be most likely understood as an easier way to produce results that are not far from the ideally expected value that an "exact" (i.e. a more accurate) treatment would yield. This means that "approximations" are used as a tool of convenience. Their justification often lies in the assertion that the difference of the result from a more involved/costly/cumbersome method can be reduced below a certain threshold by exploiting a simpler method, so that it is not worth going through the strain of doing it "the proper way". Usually, a quantitative value is given; 15 % being the probably the maximally subjectively acceptable threshold depending on the uncertainty of experimental values which can be quite large. Anything lesser than 1% is perceived as insignificant.

B After the ideal limit of an approximation has been established, one can try to "de-approximate" that is: try to grossly estimate the cause and value of the $n\%$ difference that is not included in the approximation. For instance, if we had neglected spin or exchange effects in the approximation of the cross sections, we might try to find a way to roughly estimate their contribution and possibly augment the approximation with a supplementary effect.

C Oftentimes we may encounter ourselves stuck in front of an insurmountable barrier due to various limitations: time, resources, knowledge, data, etc. In this case, adopting an "approximation" can be understood as finding an alternative route, a way around in order to obtain a result. In burgeoning times of a particular field of science, approximations are indeed rather an indispensable recourse to obtain results, whatever they were, to have something to compare experimental data with. I quote this passage from Inokuti's [427] review (section 3.5 p.321 left column lower half):

> At the outset, one usually assumes the Born-Oppenheimer separation between the electronic and nuclear motions simply because of lack of better alternatives. The assumption is perhaps justifiable for the ground electronic state, but is in general questionable for excited electronic states, especially for higher states that involve near crossings of different molecular terms. Therefore, the schematic nature of the treatment below should be always borne in mind.

I would like to emphasize on the "simply because of lack of better alternatives". It is indeed quite important to realise that many approximations not necessarily stem from a wilful decision of the investigator to frame the problem in a certain perspective where it is expected to yield reliable results. A notorious example is the usage of the independent atom model (IAM) for complex polyatomic molecules at intermediate energies (~20–100 eV) [83]. Another example that fits this purpose are empirical or semi-empirical formulas. Those are introduced in order to obtain agreeable results with experiments. This way of using approximations for their effectiveness can be very pragmatic but it can be unfortunately utterly deceptive.

D Finally, getting back to the first point, an "approximation" can simply consist in setting a practical limit to an otherwise indefinite problem. If the problem faced can be expanded in a convergent series of decreasing effects (orders), then, an approximation may be understood as a truncation. It resembles very closely the first point **A** above but it may still differ in the sense that some series can be summed exactly and thus, approximations **A** need not be truncations if a clever expansion is used.

From the aforementioned points, we may identify four sides to what we commonly refer to as an "approximation":

A Approach an ideal/correct result;

B Flee an invalid/incorrect/inaccurate result;

C Move on, continue, proceed with a calculation;

D Truncate an abysmal problem.

This section deals with the most common meaning **A** attributed to "approximation". The ensuing sections illustrate themes **B**, **C** and **D**

10.1.1 Born Approximations

Although there are various approximations that fall under the "Born" category [146, p.166, p.187]: Glauber, distorted-wave and higher-order; the most commonly used Born approximation is the first order with plane waves (PWBA) [146, 922, p.159, p.147:eq.(9.6)] that we presented in section 8.5.1 and of which we remind the scattering amplitude $\tilde{f}$:

$$\tilde{f}(\theta) = -2\pi^2 \frac{2\mu}{\hbar^2} \frac{1}{(2\pi)^3} \int \mathrm{e}^{-\mathrm{i}\mathbf{k}_+\cdot\mathbf{r}} V(\mathbf{r}) \mathrm{e}^{\mathrm{i}\mathbf{k}_-\cdot\mathbf{r}} \,\mathrm{d}^3\mathbf{r} = -\frac{2\mu}{\hbar^2} \frac{1}{4\pi} \int \mathrm{e}^{\mathrm{i}\mathbf{q}\cdot\mathbf{r}} V(\mathbf{r}) \,\mathrm{d}^3\mathbf{r} \,. \tag{10.1}$$

The incoming $\mathbf{k}_-$ and outgoing $\mathbf{k}_+$ wavectors are used to represent the incident and emerging plane waves. The approximation relies on the reduced distortion effect of the interaction potential $V(\mathbf{r})$ on the incident wave which is assumed to remain plane. The equation is formally expressed in the centre of mass with $\mu \approx m_\mathrm{e}$ as the reduced mass of the electron and the scattering target.

A key quantity in the Born approach to a scattering event is the momentum transfer* $\mathbf{q} \equiv \mathbf{k}_- - \mathbf{k}_+$ whose norm is connected to the angle of scattering θ as:

$$q^2 = k_+^2 + k_-^2 - 2k_-k_+ \cos\theta \cong \left(2k \sin\frac{\theta}{2}\right)^2 \,, \tag{10.2}$$

where $k_\pm$ represent respectively the wave number after (+) and before (−) the scattering event. In pure elastic scattering $|\mathbf{k}_+| = |\mathbf{k}_-| \equiv k$.

A very important implication of the Born approximation (10.1) is that the scattering amplitude (and thus the differential cross section) at for zero momentum transfer $q = 0$ corresponding to forward elastic scattering ($\theta = 0°$) is constant; independent of the incident energy ε_+ [147, §5.1.1:p.160]. This is not true at relativistic energies though.

As the most ubiquitous approximation in quantum approach to scattering, it has often been pulled afar from its region of validity to serve the demands of Monte Carlo simulations eagerly looking for analytical formulations to electron-molecule scattering [497, 677, 713, 830].

Its alliance to the screened Wentzel [980] potential of atomic targets: $V(r) = -Z\dfrac{e^{-r/a}}{r}$, gave birth to the legendary screened Rutherford expression recalled here:

$$\frac{\mathrm{d}\sigma_\mathrm{SR}}{\mathrm{d}\Omega} \propto \frac{1}{(1 - \cos\theta + 2\eta)^2} \,, \tag{10.3}$$

which involves the screening parameter $\eta \equiv 1/(2ka)^2$, linked to the decay radius a of the electronic cloud. The great benefit of this formula is its simplicity and the fact that its cumulative integral may be inverted analytically in order to sample the scattering angle θ in Monte Carlo codes as in [238, 677, 683, 896].

Our starting point of our enquiry of the Born approximation, will therefore be the screened Rutherford formula applied to elastic scattering treated in the following subsection.

10.1.2 Elastic

One very straightforward way to verify the applicability of Born's approximation for elastic scattering, is to compare data from differential scattering cross sections (DCS) at different energies [287, §IV:fig. 10]. From (10.1), one can see that the key dependence is on the momentum transfer $q = 2k\sin\theta/2$ and is independent from the incident energy. This stems from the fact that no distortion was taken into account and that the incident and outgoing electron waves are plane.

*The momentum transfer is often labelled $\mathbf{K}$ in the literature. In the more recent formalism of scattering theory, K is reserved for the *reactance* matrix or sometimes used also for the kinetic operator of the free electron.

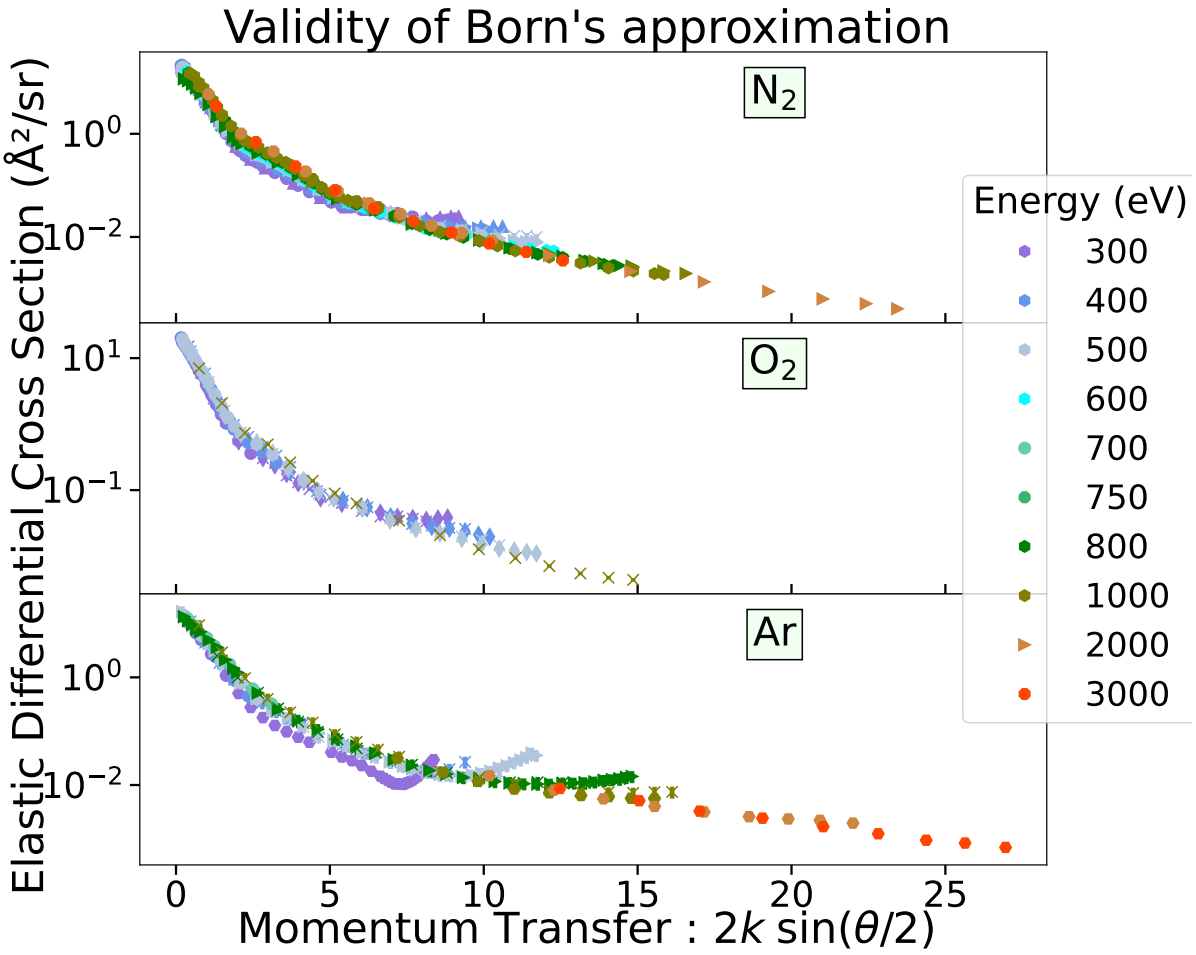

Figure 10.1: Stacks of experimentally measured differential cross sections at high energies. The first Born approximation (plane wave) in (10.1) is valid when the DCS depends exclusively on the momentum transfer $q = 2k\sin(\theta/2)$ regardless of the incident energy ε. For N_2, O_2 and Ar, the Born approximation 'looks' valid starting from 500 eV when the momentum transfer is not too large for angles scattered below ~90°.

In figure 10.1, we stacked DCS measurements for three targets at energies above 300 eV. From the qualitative agreement in alignment of the DCS at energies as low as 500 eV, we see that the first Born's approximation should hold at least at moderate momentum transfer values. This agreement improves with increasing energy.

It may thus seem surprising that several sources [316, 603, §IV, §V] pointed out that the Born approximation would not be valid even at energies as high as 5 keV. For noble gases, the integral elastic cross section in the Born approximation can be found to be twice the experimental value at 1 keV and still 20 % off at 4 keV [708, p.2546]. This disagreement worsens with the heaviness Z of the atom due to increased distortion effects (stronger potentials).

Later, it was found [317] that the discrepancy with experimental data was partly due to unaccounted contributions from forward scattering in the transmission method for measuring total cross sections, which is not due to the invalidity of the Born approximation.

In order to examine the importance of properly accounting for forward angle scattering, we plot in figure 10.2b DCS from a variety of analytical models representing the static potential V_s

shown on figure 10.2a of an atom, which in the present situation was selected to be nitrogen. This is equivalent to modelling the radial density distribution $\rho(r)$ of nitrogen. We have separated the models into two categories:

1. Thomas-Fermi (TF) potentials [680, p.460–4] represented as a simple (or a sum of) Yukawa $V_{\rm TF}(r) = -\dfrac{Z\mathrm{e}^{-r/a}}{r}$ potentials, which are based on some correction/adjustment to the Fermi radius $a \simeq a_{\rm F}$ [862, eq.(12)] (see end of appendix E).

   ▷ Fermi : simply the Fermi radius $a_{\rm Fermi} \equiv a_{\rm F} = 0.8853Z^{-1/3}$ as defined in (E.8);

   ▷ Nigam : the adapted formula of Nigam *et al.* [702, eq.(67a)] for the Thomas-Fermi potential, $a_{\rm Nigam} = a_{\rm F}/1.12 \approx 0.79a_0Z^{-1/3}$;

   ▷ Berkes&Demeter : the screening derived from experimentally fitted DCS of Berkes and Demeter [61, p.433-bottom] at very high energies, $a_{\rm Berkes\&Demeter} = 1.195a_0Z^{-1/3}\,(Z/Z-1)^{2/3}$

   ▷ Molière : the Thomas-Fermi potential as fitted by Moliere [656],

$$V_{\rm Molière}(r) = \sum_{i=1}^{3} a_i \mathrm{e}^{-b_i\, r/a_{\rm F}} \quad \left[\begin{array}{ccc} a_1 = 0.1 & a_2 = 0.55 & a_3 = 0.35 \\ b_1 = 6 & b_2 = 1.2 & b_3 = 0.3 \end{array}\right]; \tag{10.4}$$

   ▷ Jackson : given in Jackson [446, p.641:eq. (13.54)], $a_{\rm Jackson} = 1.4a_0Z^{-1/3}$;

   ▷ Mott&Massey : given in Mott and Massey [680, p.463:eq.(18)], $a_{\rm Mott\&Massey} = a_{\rm F}/0.66 \approx 1.34a_0Z^{-1/3}$;

2. Hartree-Fock (HF) potentials for which analytical representations have been given in terms of Yukawa or Slater functions (for the electron density).

   ▸ Reference : the only one which is numerical and yielded by the ELSEPA routine `elscata.exe` into the file `scfield.dat` [803] from the multiconfiguration Dirac-Fock program of [215].

   ▸ Present : our present fit to the HF densities of Koga [522] given previously in section 8.2.1 table 8.1.

   ▸ Salvat : Yukawa 2 or 3 term potentials as given by Salvat *et al.* [800, eq.(12) and table I] based on Dirac Hartree Fock Slater self-consistent field calculations.

   ▸ Pacios : Sum of exponentials (Slater 1s orbitals) representing the electron density from HF analysis as given by Pacios [726, eq.(1) and table II].

   ▸ Cox&Bonham : 6 Yukawa terms from Cox and Bonham [196, eq.(2.3) and table I] based on tabulated HF atomic wavefunctions of Clementi [183].

In the DCS (fig. 10.2b), the 'Reference' is an exact calculation of the DCS based on partial-wave phase shifts from the numerical HF potential. Despite the fact that it is well known and repeatedly advised that the Thomas-Fermi model is neither suitable for light atoms ($Z < 27$), especially noble gases and alkali metals [680, p.461], this did not prevent its eager use in Monte Carlo simulations [238, eqs.(5–11)]. One can see that:

1. The tail of the static potential at $r > a_0$ is strongly under- or over-estimated by the Thomas-Fermi model for a light atom such a nitrogen.

2. This tail directly translates into an over- or under- estimation of the forward scattering peak in the Born approximation.

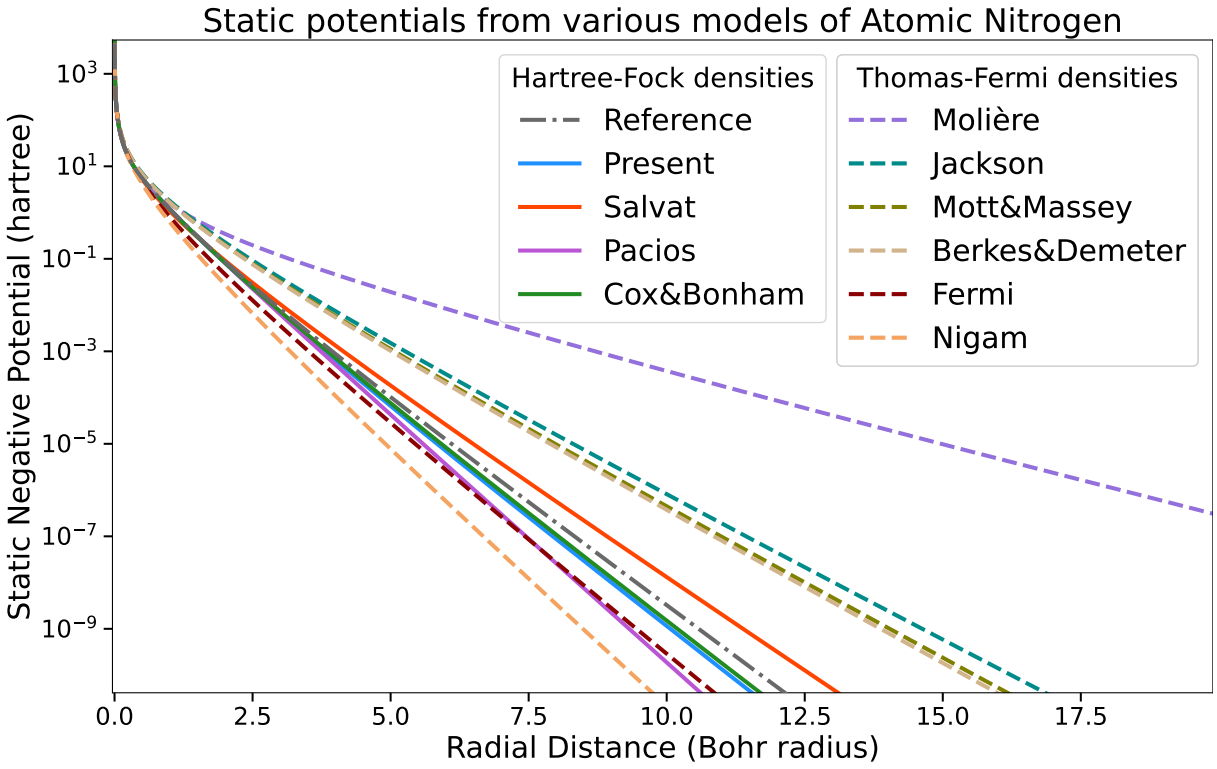

(a) Comparison of static potentials for atomic nitrogen from various Hartree-Fock and Thomas-Fermi densities.

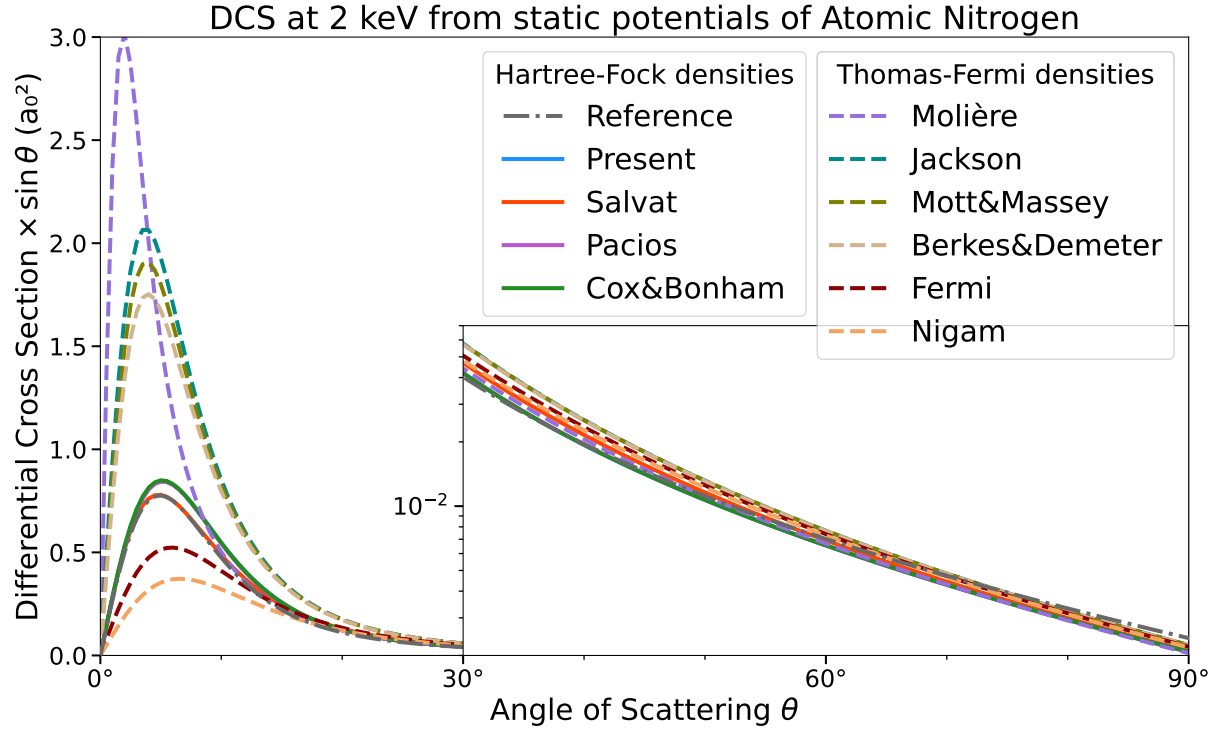

(b) DCS calculated in the plane-wave Born approximation from static potentials given in 10.2a, and compared to a partial-wave calculated DCS based on ELSEPA's HF static potential [803].

Figure 10.2: Importance of forward angle scattering at high energies and its strong dependence on the representation of the static potential.

Compact	$a < a_0$	More screening	Less forward scattering
Diffuse	$a > a_0$	Less screening	More forward scattering

A more diffuse potential will scatter more the electron (higher momentum transfer cross section) albeit preferably at smaller angles. A more compact potential will scatter less overall, but will not be as forward-peaked.

1. As the incident energy increases $\varepsilon \gg 1\,\mathrm{keV}$, the majority of the scattering is due to the tail of the potential (static and polarisation) from high order phase shifts.

2. At higher energies, the electron becomes less sensitive to the falloff radius a of the static potential which governs the scattering at intermediate angles.

This means that the exact value of the falloff radius a is not critical at high energies where the Born approximation is valid. This is also why there can be a significant disparity in the value of a from various sources as given above, depending on how the DCS is regarded: its integral, its shape or the momentum transfer. We will illustrate this in the next chapter when using the Born approximation to represent scattering at high energies (sec. 11.1.4).

What figure 10.2b shows, is that the question of the validity of the Born approximation, when comparing with experimental data, might be significantly blurred or masked by the very representation of the potential used. For instance, the Born approximation applied to the bi-Yukawa potential of Salvat *et al.* [800] gives a DCS nicely following the reference curve of ELSEPA (which is calculated from exact partial waves). Naturally, ELSEPA does not exactly use the same potential as Salvat *et al.* [800], actually the static potential of Cox and Bonham [196] is much closer to the reference, yet its Born-approximated DCS differs more than Salvat *et al.* [800] at small scattering angles. Similarly, one might find a model whose integrated DCS in the Born approximation is close to the correct one. Nevertheless, if one regards all aspects: integral, shape and momentum transfer; then fortuitous agreement cannot be maintained throughout.

In order to explore more rigorously the question of first Born approximation's validity, we calculate the phase shifts from the same atomic potential. For four atoms (N $Z = 7$, Ne $Z = 10$, Ar $Z = 18$, Kr $Z = 36$), we display on figure 10.3 the relative error percentage committed by the first Born approximation with respect to an accurate partial wave calculation on the integral cross section σ (ICS), momentum transfer (MT) CS σ_m and average cosine $\langle\cos\theta\rangle = 1 - \sigma_\mathrm{m}/\sigma$ for elastically scattered electrons above 100 eV. The model used includes static, exchange, polarisation and absorption as described in the previous chapter 8.2. Here, we see that for all atoms considered $Z \geq 7$, Born's plane wave approximation would be valid at least from 5 keV but not below. The irregularities close to 10 keV come from our imposed limitations to compute phase shifts not lower than 10^{-6}, this introduces some artifacts due to the necessity to include more phase shifts of lower value and higher orders as the energy increases.

From a theoretical perspective, Born's approximation should be valid if all phase shifts from the partial waves are small $\delta_\ell \ll 1$. Since the most important phase shift in general (outside resonances) comes from the isotropic wave $\ell = 0$, the first Born's approximation requires that [680, Chapter V§2:p.89:eq.(12)]:

$$\tilde{\delta}_0 = -\frac{2m_\mathrm{e}k}{\hbar^2}\int_0^\infty V(r)\mathrm{j}_0^2(kr)r^2\,\mathrm{d}r \ll 1 \tag{10.5}$$

Given the fact that atomic potentials decay asymptotically as Yukawa potentials $V(r) \sim Z\mathrm{e}^{-r/a}/r$, the equation above reduces to [219, 347, §6.612(3), eq.(14.5.7)] :

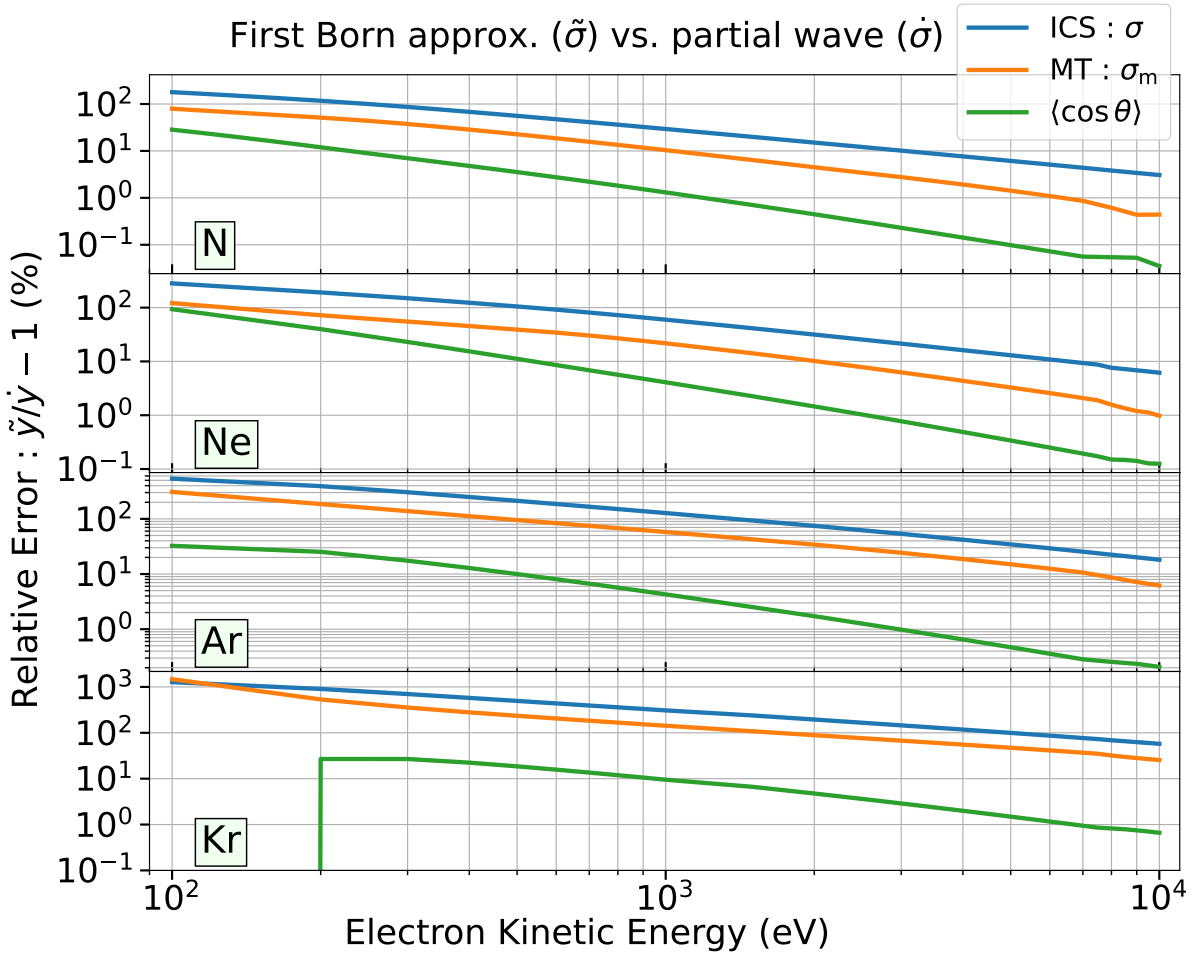

Figure 10.3: Error of the first Born approximation ($\tilde{\sigma}$) relative to a partial wave calculation ($\dot{\sigma}$) for various atoms (N, Ne, Ar, Kr): $\frac{\tilde{\sigma}}{\dot{\sigma}} - 1$. The invalidity of the first Born approximation increases with Z (Ar and Kr versus N and Ne). This implies that the energy threshold $\varepsilon_{\text{Born}}$ beyond which the approximation is valid (error $< 1\,\%$) is pushed toward higher values.

$$k\tilde{\delta}_0 \cong 2\int_0^\infty \frac{Z\mathrm{e}^{-r/a}}{r}\sin^2(kr)\,\mathrm{d}r = ZQ_0\left(1+\frac{2}{(2ka)^2}\right) = \frac{Z}{2}\ln(1+(2ka)^2) \tag{10.6}$$

One therefore often finds that the validity of Born's approximation is conditioned by [680, 716, p.111:eq.(89), p.903:(1)a]:

$$\frac{Za}{\mathrm{v}} = \frac{\alpha Za}{\beta} \ll 1\,, \tag{10.7}$$

expressed in the incident velocity v (or reduced velocity $\beta = \mathrm{v}/c$) of the electron. The range a of the potential is not always included explicitly since it is assumed to be not far from the atomic Bohr radius $a_0 = 1$.

From (10.7), we should expect that the energy ε_{B} beyond which the first Born approximation is valid, scales with the atomic number Z of the target. This can be seen indeed on figure 10.3, as heavier targets have a higher relative error with respect to the Born approximation at a given energy.

Physically, the relevant quantity in elastic scattering is the momentum transfer cross section σ_{m}. If we require that the error exceed not 1 %, we can derive the following validity thresholds $\varepsilon_{\mathrm{Born}}$ for our three atoms N,O and Ar:

N (Z=7)	O (Z=8)	Ar (Z=18)
6.5 keV	8 keV	20 keV

According to this criterion ($\tilde{\sigma}_{\mathrm{m}}/\dot{\sigma}_{\mathrm{m}} - 1 < 1\,\%$), we have $\alpha Z/\beta < 1/3$. From the trend seen above for light elements, we can formulate a "magical" rule of thumb:

> The validity of the first Born approx. for a light atomic target $Z < 20$ starts from $\sim Z$ keV.

Let us glance a second time at figure 10.3. This time, we consider only the average deviation cosine (green line) which conveys information about the *shape* of the DCS:

$$\langle \cos\theta \rangle \equiv \frac{\int_0^\pi \frac{\mathrm{d}\sigma}{\mathrm{d}\Omega} \cos\theta \sin\theta \,\mathrm{d}\theta}{\int_0^\pi \frac{\mathrm{d}\sigma}{\mathrm{d}\Omega} \sin\theta \,\mathrm{d}\theta}$$

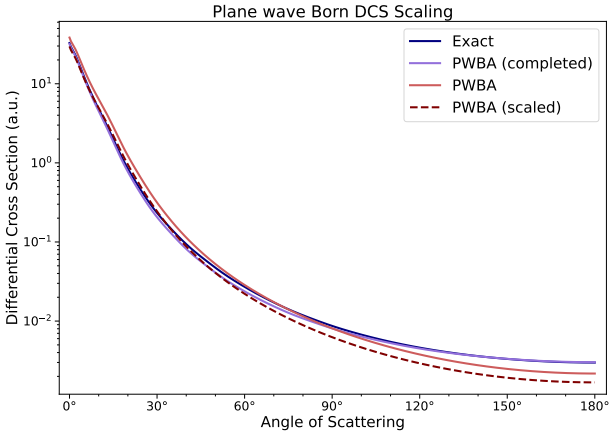

Figure 10.4: Scaling of the first Born approximation's DCS. The dashed red (- - -) and dark blue (—) curves have the same integral value.

We see now that in principle, the agreement in shape can be found at lower energies. If a difference of 1 % in $\langle \cos\theta \rangle$ may be forgiven, then the shape from Born's approximation could be used from 2 keV for light atoms (N and O). The absolute value of the DCS may then be subsequently scaled down in order to reduce the disagreement in the integral and momentum-transfer cross sections. An example is shown on the side in fig. 10.4. Significant differences at large angles > 60° are observed only where the DCS is negligible (3.5 orders of magnitude below the forward peak). This qualitative agreement explains why the plane-wave Born approximation (PWBA) looked valid from 500 eV from the experimental data stacked on figure 10.1 for small momentum transfers. In the following section and particularly in the next chapter section 11.4.2, we will see that scaling DCS from the PWBA can be used to our advantage when modelling inelastic CS from electronic excitations and ionisation [911]. Also of interest, we included the formula for a completed PWBA when the Born-calculated phase shifts $\tilde{\delta}_\ell$ are inserted in (9.18), which considerably improves the applicability of Born's approximation.

The scaling of the PWBA can be pushed to extremes even when the approximated DCS does not agree in shape. To illustrate this, we plot in figure 10.5, the elastic cross section for O_2 from various experiments and compare it with our constructed elastic CS (blue) obtained from a total CS with all inelastic processes subtracted (see part I p.115). A Born expansion (red—):

$$\tilde{\sigma}_{\mathrm{Born}}(\xi) = \frac{\pi a_0^2}{\xi}(\tilde{A} + \tilde{B}/\xi + \tilde{C}/\xi^2)\,, \qquad \text{with } \xi = \frac{1}{m_{\mathrm{e}} v^2 + K}\,; \tag{10.8}$$

was fitted to our data with four free parameters ($\tilde{A}$,$\tilde{B}$,$\tilde{C}$,K), the last one K playing the role of scaling. This expression is used later in the next chapter 11.1.4 for extrapolating elastic ICS at high energies (11.9). A screened Rutherford (SR) with only one parameter (the decay radius a), was also fitted for comparison (yellow—).

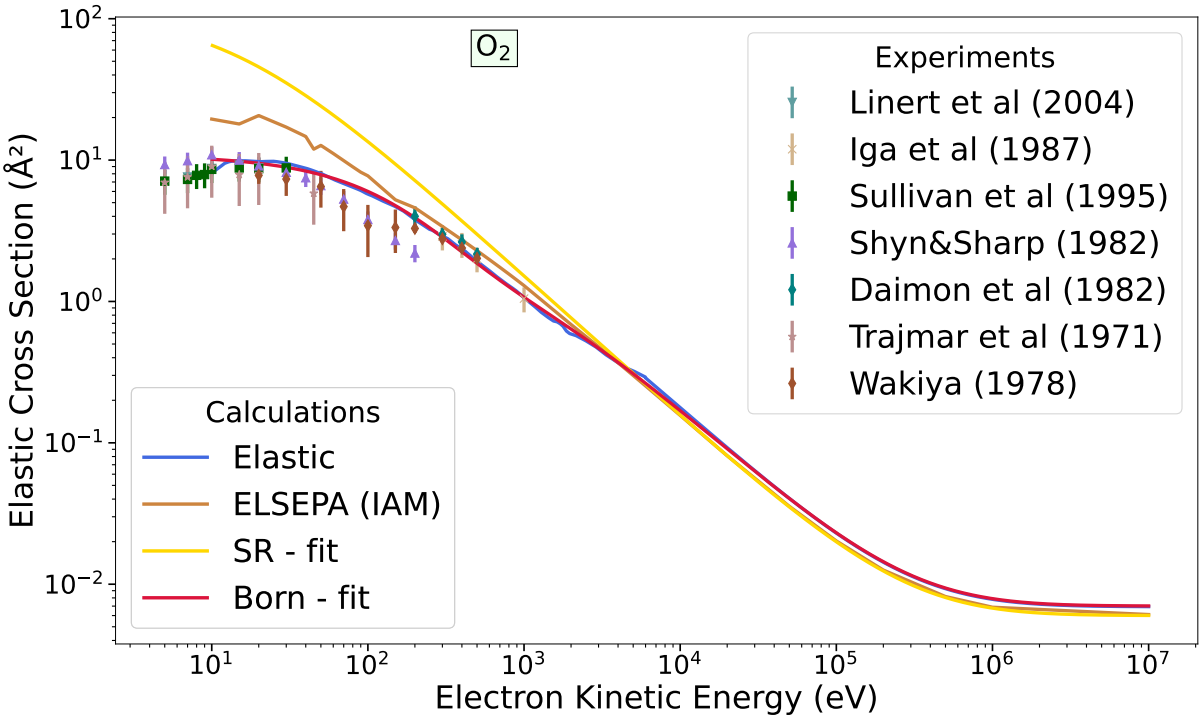

Figure 10.5: Elastic cross section for O_2 from various experiments and calculations: "Elastic" – inelastic processes subtracted from a constructed total cross section (4.5); ELSEPA [803] – independent atom model; SR – fitted screened Rutherford (to the blue curve); Born – fitted scaled Born expansion (10.8). Experiments: ▼ [598], × [418], ■ [893], ▲ [842], ♦ [206], ★ [938] and ♦ [972].

Before we close this subsection, we should mention about the extension of Born's approximation for diatomic molecules. In that case, the situation is more complicated because of the non-spherical potential. As a matter of fact, if the Born approximation is valid, so should be the independent atom model (IAM – which is exactly the PWBA applied to decentred multiple isotropic potentials). Therefore, if a discrepancy arises at very high energies, it is imputable to the imperfect representation of the potential rather than the use of the Born approximation [602, fig. 4]. For H_2 and N_2, the effect of chemical bonding, unaccounted for by the IAM, was shown by Fink *et al.* [286, 287] to be observable at small angle scattering. This is related to the long-range quadrupole potential which affects high-order phase shifts. It is therefore irrelevant to consider the validity of PWBA for diatomic molecules based on agreement at forward angles if one uses the IAM; i.e. the approximation might be valid, whereas the chemical bonding cannot be neglected for DCS calculated below 5° [287, figs.8–9].

On the other hand, the independent atom model yields DCS whose shape agrees qualitatively well with experimental data at non-small angles (> 5°). Again, with a scaling factor, we exploit this agreement in order to use the IAM for calculating DCS of diatomic molecules at energies above 200 eV even when the PWBA is not valid. On figure 10.3, one sees that the DCS data from ELSEPA [803] which relies on the IAM, can be scaled down from 100 eV with an appropriate factor in order to obtain agreeable CS values.

10.1.3 ~~Inelastic >< Elastic~~

Cross sections may be expressed differentially in the momentum-transfer $\mathrm{d}q$ or scattered angle $\mathrm{d}\theta$ through the following equivalence obtained by differentiating (10.2) [427, eq(2.5)§(2.6)]:

$$q\,\mathrm{d}q = k_- k_+ \sin\theta\,\mathrm{d}\theta\ . \tag{10.9}$$

Furthermore, the expression of the inelastic DCS may also be written through a quantity known as the generalised oscillator strength (GOS) $F_\mathrm{i}(q)$ (described in more detail in section 11.4.1) [834, p.61:eq.(158)]:

$$\frac{\mathrm{d}\sigma_\mathrm{i}}{\mathrm{d}\Omega} \propto \frac{F_\mathrm{i}(q)}{q^2}\ , \tag{10.10}$$

A miscorrespondence of (10.9) blurred further by the formulation (10.10), seems to have misled a part of the community [377, 454, 896] in Monte-Carlo simulations to believe that inelastic scattering scales as $\propto 1/q^2$ instead of the correct Born-Rutherford expression $\propto 1/q^4$. This is strange because one ought to expect analytical continuity between a very weakly inelastic scattering and a purely elastic scattering as the inelastic energy loss $\Delta\mathcal{E} \ll \varepsilon$ becomes negligible in comparison to the incident kinetic energy ε.

This is probably due to the fact that the notation used throughout various references might be confusing. Below is an excerpt from Inokuti [427], Mott and Massey [680], and Shimamura and Takayanagi [834] of the same equation (careful about the different notations used!):

K. Takayanagi, Electron-molecule collisions (1984), p. 60

$$q(av \to a'v') = \frac{k'}{k}\left(\frac{2\mu e^2}{\hbar^2 K^2}\right)^2 \int \frac{d\hat{\mathbf{R}}}{4\pi}\left|\iint \sum_j \exp(i\mathbf{K}\cdot\mathbf{r}_j)\chi_a^{v'}(R)\phi_a^{*}(\mathbf{r}_m,\mathbf{R})\,\chi_a^{v}(R)\phi_a(\mathbf{r}_m,\mathbf{R})dR\,d\mathbf{r}_m\right|^2. \tag{151}$$

M. Inokuti, Inelastic Collisions of Fast Charged Particles with Atoms and Molecules—the Bethe Theory Revisited (1971), p. 299

$$d\sigma_n = 4\pi z^2 (Me^2/\hbar^2)^2 k^{-2} K^{-4}\,|\,\epsilon_n(K)\,|^2 d(K^2). \tag{2.6}$$

Mott and Massey, The Theory of Atomic Collisions (1965), p. 477

$$I_{mn}(K)\,dK = \frac{128\pi^5 m^2 e^4}{k^2 h^4}\frac{dK}{K^3}|\epsilon_{mn}(K)|^2, \tag{84}$$

In the first equation (151) above*, "$q(av \to a'v')$" is the DCS $\mathrm{d}\sigma/\mathrm{d}\Omega$ for an inelastic excitation from state av to $a'v'$. The second (2.6) is the same but the excitation is noted with the index "n" and the differential operator has been moved to the right side. The term "$|\epsilon_n(K)|^2$" is the inelastic form factor (defined more in detail in 11.49). The squared integral in the first equation (151) is the expression of $|\epsilon_{av\to a'v'}|^2$ for a diatomic molecule. Finally, in the third equation (84), the inelastic differential cross section given in Mott and Massey [680, XVI§7p.477:eq(82)] (noted "I_{mn}" in their work) reads according to the present notation :

$$\frac{\mathrm{d}\sigma_\mathrm{i}(q)}{\mathrm{d}q}\,\mathrm{d}q = \frac{8\pi m^2 e^2}{\hbar^4}\frac{|\epsilon_i(q)|^2}{q^3}\,\mathrm{d}q \tag{10.11}$$

*The vertical bar in red is a correction of the misplaced bar in Shimamura and Takayanagi [834, p.60] as given by Inokuti [427, eq.(3.48)]

Thus, in order to obtain the integral cross section, one ought directly integrate on $\mathrm{d}q$ in this formula as given by Mott and Massey [680, p.477:eq.(86)] which should give a $\propto 1/q^4$ expression. Nevertheless, this detail was overlooked in some works [454, §2.2] whose mathematical trail we reproduce below:

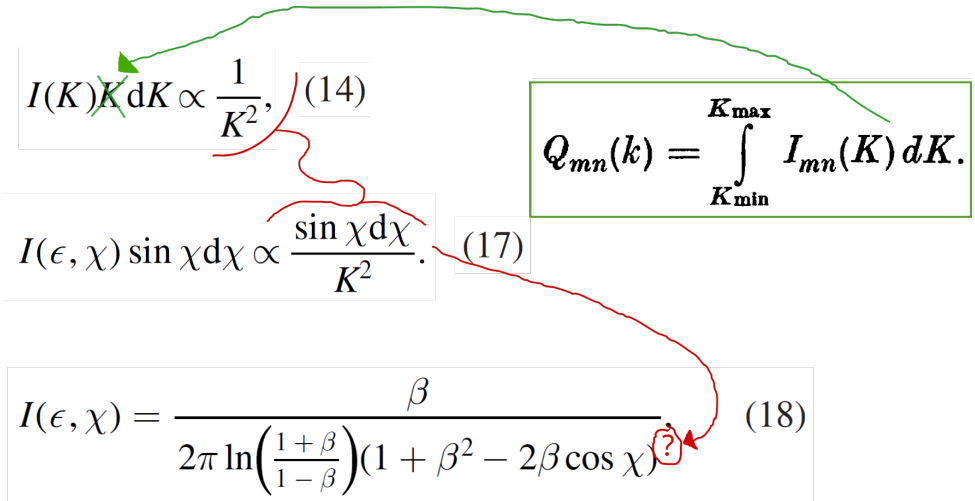

The green squared equation is the correct original equation from Mott and Massey [680, p.477:eq.(86)]. The green arrow shows that "$I(K)$" should have been integrated directly on "$\mathrm{d}K$" ($\mathrm{d}q$ in our notation) and not "$K\,\mathrm{d}K$" as the correspondence (10.9) would suggest. This mistake is the same as if one wrote plainly:

$$\sigma = \int \frac{\mathrm{d}\sigma}{\mathrm{d}q}\underbrace{\sin\theta\,\mathrm{d}\theta}_{\neq \mathrm{d}q} \tag{10.12}$$

This is exactly what happened when jumping from equation (14) in the excerpt above to equation (17). Finally the red arrow points to the fact that this naturally led to the omission of the square exponent in equation (18) the denominator of the standard screened Rutherford scattering.

This confusion would not likely have taken place in the "more modern" notation $\mathrm{d}\sigma/\mathrm{d}\Omega$ as written in Tanaka *et al.* [911, eq.(4a)] but also in Green and Dutta [348, eq.(3)]; because one sees directly which differential the cross section is: $\mathrm{d}q$ or $\mathrm{d}\Omega$, and so integration is straightforward.

In summary, the confusion arises from the fact that DCS are more typically expressed like the extracted (151) in differential forms of $\mathrm{d}\Omega = q\,\mathrm{d}q/(2k_+k_-)$. Truly, if one wishes to obtain the expression for $\mathrm{d}\sigma/\mathrm{d}\Omega$, then a $1/q$ is needed on both sides of (10.11= extracted 84). Then, the DCS can take its standard familiar form :

$$\frac{\mathrm{d}\sigma_i(q)}{q\,\mathrm{d}q}2k_+k_- \equiv \frac{\mathrm{d}\sigma_i(\theta)}{\mathrm{d}\Omega} \equiv \frac{\mathrm{d}\sigma_i(\theta)}{\sin\theta\,\mathrm{d}\theta d\phi} = \frac{8\pi m^2e^2}{\hbar^4}\frac{k_+}{k_-}\frac{|\epsilon_i(q)|^2}{q^4} \tag{10.13}$$

In other words, taking the original notations from the references, the connection between equations (151), (2.6) and (84) is:

$$\text{« } \quad I_{mn}(K)dK \equiv \mathrm{d}\sigma_n(K) \equiv q(av \to a'v')2\pi\frac{KdK}{2kk'} \quad \text{ »}$$

Note the 2π factor in the last term because integration of the azimuthal angle φ is implicit in I_{mn} and $\mathrm{d}\sigma_n$, as specified by Inokuti [427, p.299] :

> "Further, since K is independent of φ, one implies integration over φ when one expresses $\mathrm{d}\sigma_n$ in terms of $\mathrm{d}K$."

Moreover, one might argue that the GOS for optically forbidden transitions converges toward zero for small momentum transfers [855, fig.1-3]. Since it is always positive, it therefore has to pass through a maximum before decreasing again at large momentum transfers [712, fig.2&3]. This means that there should be a range of angles for which the DCS for optically forbidden excitations does not decrease steadily as prescribed by the Rutherford $\propto 1/q^4$ trend. This can be best seen by comparing how fast the DCS (optically allowed) in figures 5&7 from Wakiya [972] decrease compared to figures 2-4 in Wakiya [973] (forbidden).

Nonetheless, when one examines the extremal values of q for $\theta = 0°$ and 180°:

$$q_{\min} \simeq \frac{\mathcal{E}_i}{4\mathrm{Ryd}}\frac{1}{\varepsilon} + o\left(\frac{1}{\varepsilon}\right), \tag{10.14}$$

$$q_{\max} \simeq \frac{4\varepsilon}{\mathrm{Ryd}} - \frac{2\mathcal{E}_i}{\mathrm{Ryd}} + o\left(\frac{1}{\varepsilon}\right); \tag{10.15}$$

then, one sees that the interval $[q_{\min}, q_{\max}]$ expands rapidly [427, eqs.(2.16-2.18)] with increasing kinetic energy $\varepsilon = (\hbar k)^2/2m_e$. Therefore, the range in which the GOS rises and decays gets quickly compressed into a small angular range and outside this range, the Rutherford trend should be recovered.

In the end, the consequences borne by this confusion are not catastrophic. They just generate perplexity [497, 713], introduce limited inaccuracy in Monte-Carlo codes [218, 677, 896, eq.(19), eq.(12), §2.1] and create a myth on the Born approximation for inelastic scattering [377, 454, eq.(24), eq.(18)].

10.1.4 ~~Ionisation~~

Of interest, the plane wave Born approximation was also tried by Tahira and Oda [904] for describing electron scattering in impact ionisation collisions. As one knows, a remarkable property of the plane wave Born approximation is that it yields the exact cross section for Rutherford scattering [474] between two charged particles (see also p. 558):

$$\frac{\mathrm{d}\sigma_{\mathrm{R}}}{\mathrm{d}\Omega} = \frac{Z^2}{16\varepsilon_{\mathrm{r}}^2 \sin^4(\theta/2)} \tag{10.16}$$

The energy ε_{r} represents here the kinetic energy in the relative centre of mass frame (practically equal to electron energy in electron-nucleus scattering).

It seems, therefore, interesting to compare the performance of a plane wave Born approximation for describing electron impact ionisation of atoms and molecules. Foremost, we must clarify what exactly are we comparing:

* Total ionisation cross section
* Singly differential CS in secondary electron energy
* Double differential CS in secondary energy and scattering angle
* Triply differential CS in secondary energy and angle and primary angle

Those four different concepts are explained more in detail in section 11.5.4. What is important to realise here, is that the applicability of the plane wave Born approximation depends on the detail level at which we characterise the ionisation (total cross section or differential).

Total and Single: When only describing the total cross section (simply accounting for whether the ionisation takes place or not), the plane wave Born approximation may yield agreeable results down to 30 times the ionisation threshold [605, p.16:§2.2.3]. As one can imagine, at lower energies, the distortion effect of the ionic potential on the outgoing electron becomes more important and the use of a *distorted wave* Born approximation becomes necessary [605, §2.2.3]. This approach can give accurate results down to 15 times the ionisation threshold.

Another way around, is to use a so called "scaling" method which remarkably brings the simply calculated results from the plane wave Born approximation into accurate values throughout the whole range of energies down to ionisation threshold. This was well exploited by Kim and Rudd's [507] model which we propose to revisit in chapter 11.5. It can be shown that this Born scaling yields good estimations of singly differential cross sections as well (see [503, p.272]).

Double and Triple: Despite the encouraging results of the scaled Born approximation obtained by [904, §2.2:eq.(14)] for doubly differential scattering cross sections describing the angular emission of secondary electrons, there still remains much room for improvement. A semi-empirical analytical model is often preferred [790] instead of a modification based on the scaled Born approximation and the binary encounter theory [see 904, fig 5&6].

Alone, the Born approximation (planar or distorted) gives not reliable cross sections for inelastic collisions near the threshold. For ionisation, the fact that two electrons are ejected complicates further the topic, with more interference terms, especially in the situation where the available kinetic energy is equally split among the fleeing electrons.

10.1.5 Low-energy Approximations

Technically, the plane-wave Born approximation (PWBA) is applicable only at energies high enough where the higher-order perturbations on the incident plane wave may be disregarded in (8.114). Nonetheless, in some cases, the PWBA can be useful even at low energies.

This is for example the case of rotational excitation cross sections with homonuclear diatomic molecules, in which the interaction at low energies comes mainly from the long-range permanent quadrupole potential of the molecule. Gerjuoy and Stein [323] justified that distortion effects could be neglected in the region far from the molecule and that, due to the centrifugal potential of $\ell > 0$, the electron at decreasing energies is less affected by the stronger short-range potential.

As mentioned in the previous subsection 10.1.4, the next improvement is the distorted wave approximation for rotational excitation as was done by Takayanagi and Geltman [905]. The distorted wave is obtained by including only diagonal elements of the potential matrix in the angular decomposition (no angular-momentum coupling). Then, the off-diagonal elements of the scattering matrix are calculated from the first Born approximation with the distorted wave.

Later, it was shown by Robertson *et al.* [780], that apparently, the success of a simple plane wave Born approximation for rotational excitation and momentum transfer cross sections at very low energies < eV was mostly a coincidental feature from the complex cancellation of distortion effects from short-range potentials whose contribution is in principle non-negligible.

In a similar fashion to Geltman and Takayanagi [322], we tried ourselves to apply the distorted-wave approximation to calculate off-diagonal elements for elastic scattering at intermediate energies ~50 eV to cope with the failure of the independent atom model. We obtained very misleading* results showing that it is in general hard to derive any sensible physical interpretation from the application of the Born approximation outside its range of validity. Angular close-coupling brought into better light our investigations.

*"Misleading" in the sense that more accurate-looking results were obtained from less accurate models.

Despite the dangers linked to the Born approximation where distortion, multiple scattering and coupling effects are important, the plane wave Born approximation still remains a very practical tool. In general, it can be used for calculating the asymptotic contribution of a matrix element in a region beyond a certain radius $r_{\max}$ where distortion of the wave is thought to have little effect on the exact integral [671, Appendix]. Such procedure is sometimes called "Born completion" [430] or "Born closure"[671, §IV.B.3]. All in all, we conclude and recommend that:

> An *a posteriori* safety check for the applicability of the Born (plane or distorted) approximation, is to ensure that the value calculated (phase-shift 10.5 or matrix element 8.118) be small $\lesssim 0.1$; otherwise the distortion may not be treated as a first order perturbation.

Below, we remind a low-energy method that conciliates the deficiency of the Born approximation to properly account for both long-range and short-range potentials in a consistent way.

Modified effective range theory

Undeniably the most prominent and widespread approximation for elastic (differential) cross sections at low-energies $k \to 0$ is the modified effective range theory (MERT) [668, 836, p.7–8:§V] which assumes that the dominant force acting at low-energies is the polarisation potential [168, 710]. This hypothesis is supported by the recent successful application of MERT [272], to noble gas atoms and a few molecules to energies as high as 20 eV, by encompassing the effect of short-range potentials into four fitted parameters only.

Assuming an asymptotic decay of $V_p(r) \sim -\alpha_{\rm d}/2r^4$ with the **d**ipole polarisability $\alpha_{\rm d}$, the phase shifts (sec. 8.4.1) from such *isotropic* potential are defined by [168, 709, eq.(2.3), eqs.(4-5)]*:

$$\frac{1}{k}\tan\delta_0 = -A - \frac{\pi}{3}\alpha_{\rm d}k - \frac{4\pi}{3}\alpha_{\rm d}Ak^2\log(k) - \underbrace{\left(\frac{4}{3}\alpha_{\rm d}A\log(1.23\sqrt{\alpha_{\rm d}}) + \frac{\pi}{3}\sqrt{\alpha_{\rm d}}(A-\alpha_{\rm d}) + \frac{r_0}{2}A\right)}_{\equiv C}k^2 + O(k^3)\,, \tag{10.17a}$$

$$\frac{1}{k}\tan\delta_\ell = \frac{\pi\alpha_{\rm d}k}{(2\ell+3)(2\ell+1)(2\ell-1)} + A_\ell k^{2\ell} + O(k^3)\,. \tag{10.17b}$$

The very definition of the scattering length A is [147, p.71:eq.(2.120)]:

$$A \equiv -\lim_{k\to 0}\frac{\tan\delta_0}{k}\,, \tag{10.18}$$

which can be extended for $\ell > 0$ to define the lengths A_ℓ (usually $A_{\ell=1}$ only). This theory is named after the parameter r_0, known as the *effective range* of the (full) potential [710, eq.(5.5)]:

$$\frac{r_0}{2} \equiv \int_0^\infty (\tilde{u}_0^2 - u_0^2)\,{\rm d}r \tag{10.19}$$

where the free solution $\tilde{u}$ of the Schrödinger equation with $V(r) = \alpha_{\rm d}/2r^4$ is expressed in the limit $k \to 0$:

$$\tilde{u}_0\,(\sqrt{\alpha_{\rm d}}/r) \equiv \sin(\sqrt{\alpha_{\rm d}}/r) + (\sqrt{\alpha_{\rm d}}/A)\cos(\sqrt{\alpha_{\rm d}}/r) \tag{10.20}$$

*Note the missing square on A in Chang [168, eq.(4)] and the fact that A_ℓ in his eq.(5) should be accompanied by $k^{2\ell+1}$ instead of k^3 which applies to $\ell = 1$ only.

The function u_0 is the solution to the Schrödinger equation with the full potential in the limit of zero energy. All in all, $r_0 \sim a_0$ is expected to be a small multiple of Bohr's radius [168, p.894-bottom] and is thus not necessary to include in (10.17a) as $k \to 0$.

When extending to a molecule [268], the ensemble of rotational transitions $J \to J'$ of the molecule must be included [168]. After summation and neglect of the kinetic energy gain/loss due to rotational de/excitation, the differential [668, eq.(100)] and integrated cross sections [168, eq.(18)] for total scattering (d)σ_{tot} can be expanded (presently to second $\sim k^2$ order) as:

$$\frac{\mathrm{d}\sigma_{\text{tot}}}{\mathrm{d}\Omega} \cong A^2 + \frac{4Q^2}{45} + \pi k(\alpha_{\text{d}} A + \frac{\alpha_2 Q}{30})\sin(\theta/2) + \frac{8\alpha_{\text{d}}}{3}A^2 k^2 \ln k + \left[\left(\sin\frac{\theta}{2}\frac{\pi\alpha_{\text{d}}}{2} + 4kA\ln k\frac{\alpha_{\text{d}}}{3}\right)^2 - A^4 + 2AC\right]k^2 + O(k^3) \tag{10.21}$$

$$\sigma_{\text{tot}} \cong 4\pi A^2\left[1 + \frac{4Q^2}{45A^2} + \frac{2\pi}{3}k(\alpha_{\text{d}}A + \frac{\alpha_2 Q}{30}) + \frac{8\alpha_{\text{d}}}{3}k^2\ln k + \left(\frac{\pi^2\alpha_{\text{d}}^2}{8A^2} + \frac{8\alpha_{\text{d}}}{3}\ln(1.23\sqrt{\alpha_{\text{d}}}) + \frac{\pi}{3}\sqrt{\alpha_{\text{d}}}(A - \frac{\alpha_{\text{d}}}{A}) - A^2 + Ar_0\right)k^2 + O(k^3)\right] \tag{10.22}$$

The coefficient C in (10.21) encompasses the order k^2 in 10.17a. The following sum on Legendre polynomials was used [709, eq.(2.6)]*:

$$-\frac{2}{3} + \sum_{\ell=1}^{\infty}\frac{2P_\ell(\cos\theta)}{(2\ell+3)(2\ell-1)} = -\sin\frac{\theta}{2} \tag{10.23}$$

The issue when applying the above MERT equations on molecules, is that the coefficients of the higher order k^2, k^3 terms might actually be quite large ($\gtrsim 100$) [168, eq.(23)]. Hence, their negligibility as $k \to 0$ might be justified only at lower energies $\lesssim 10\,\text{meV}$ than what is achievable with atoms [836, table I] (up to a few eVs) [709, §IV].

Worse is the applicability on DCS from the expansion (10.21), rather than by using the phase shifts (and matrix elements [168, eq.(6)]) from (10.17a–10.17b). The leading backscattering shape should be due to $\sin\theta/2$ according to (10.21). Nevertheless, the probings of elastic scattering from N_2 at 0.1 eV from Sohn *et al.* [863] show some inadequacy in figure 10.6b. This means that their curve could not have possibly been plotted with (10.21) as claimed in Morrison [668, fig 13].

Furthermore, the agreement on figure 10.6b between the DCS from phase shifts and the expansion to order k^3 is misleading. The phase-shift DCS does not include the quadrupole Q whereas the expansion (10.21) does. The agreement is merely fortuitous because the negative isotropic contribution of order k^4 is more or less of the same magnitude as that of $4/45Q^2$ at 0.1 eV. At a lower energy of 0.01 eV plotted on fig. 10.7, the fortuitous agreement disappears.

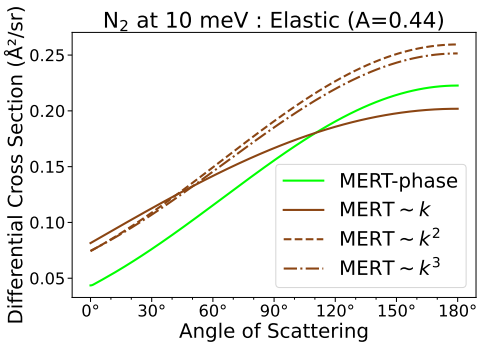

Figure 10.7: Disagreement reveals itself at a lower energy (10 meV)

This instance is a tree among a jungle of examples showing how obtaining shape agreement in DCS calculated in the framework of quantum mechanics in a particular situation, can be largely arranged by fortuity and thus is often a misleading factor when comparing results from different models.

We will now move on to a different kind of "approximative" method.

*I was not able to find an identity in reference books for this relation.

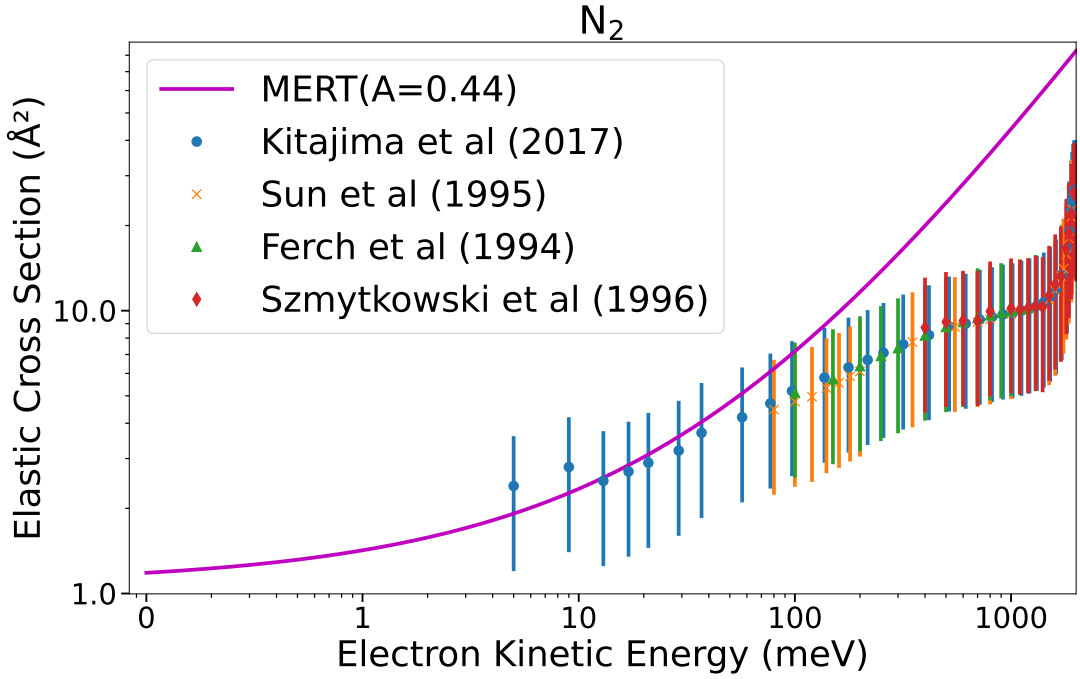

(a) MERT performance comparison between (10.22) and the phase-shift constructed CS (10.17 with 8.109).

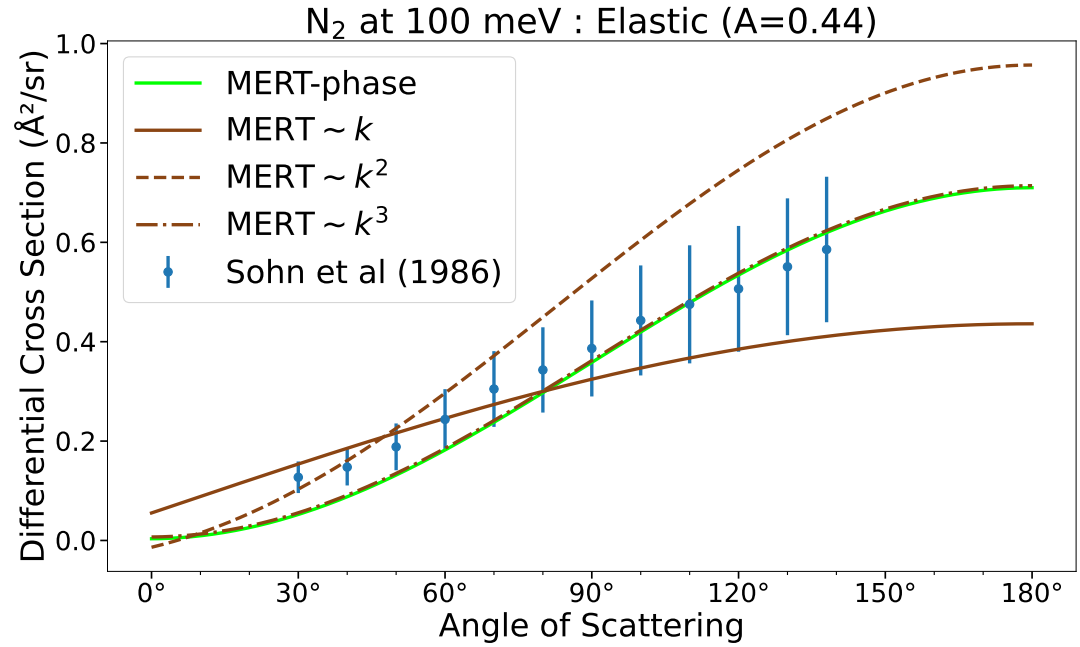

(b) MERT comparison on the adjusted(1.2) data of Sohn *et al.* [863] using directly (10.21) to various orders in k and the phase-shift constructed DCS (10.17 with 8.108).

Figure 10.6: MERT performance compared between DCS and ICS of elastic scattering with N_2, the applicability for low k orders on DCS is irresolute.

10.2 Appeal to Generalisations

It is not easy to propose a universal classification of approximations in physics. The habitual appearance of an "approximation" is that from a general and often incalculable expression, the parts that pose difficulty are encompassed in an order of magnitude that is shrunk to some desired smallness while the rest is calculated with ease. This was presented in the former section with the wavenumber k of the incident electron as one of the parameters determining the overall imprecision made.

The result obtained may be seen as an idealisation of a real phenomenon, such as assuming that the interaction with an ion $+Z$ is entirely Coulombic $\propto +Z/r$ or that the polarisation is indefinitely intense as we get closer to an atom $\propto \alpha/2r^4$.

Usually, one is aware that the reality is more complex and that some additional terms (multipoles, interferences, etc.) would be needed in order to paint more truthfully the physical situation. The approximation consists in discarding those terms and looking at the most important one.

So an approximation is basically bringing the real toward an ideal situation.

$$\text{Approximation} \ : \ \text{Real} \longrightarrow \text{Ideal}$$

On the other hand, one might decide to start from an ideal case which is known to be treated exactly and therefrom try to adapt to represent a real situation. Undoubtedly, philosophers must have a proper terminology for this alternative "approximation" which actually proceeds in the opposite way of our usual approximation. This is usually designated by the vague term of *ad hoc* modification, adjustment or approximation, signifying that it was introduced *a posteriori*, in a loosely justified manner, in order to get the desired behaviour. This denomination is, however, unclear because any subsequent modification or correction of a formula (ideal or approximate) may be qualified as being *ad hoc*. Here, I propose a different terminology and name the converse of an "approximation": an "approculation" (from an idealised case), "procul" meaning "afar" in Latin.

$$\text{Approculation} \ : \ \text{Real} \longleftarrow \text{Ideal}$$

The underlying idea of an "approculation" is not to get closer toward an ideal but away from it by introducing a change that leads toward more realistic values. Approximation, or approculations alike, might be justified, founded or *ad hoc*.

This distinction will surely seem obscure and futile to the readership. However, the pith of an approximation is to project reality onto an ideal (like in Born's plane-wave approximation, imagining that the incident electron's wave stays plane), whereas an approculation aims to get back toward reality by disguising the ideal as we shall exemplify below.

Perhaps another way to look at it (albeit still in the Latin perspective) is to say that the starting point taken by the approximations introduced in the previous subsection 10.1 was *ab initio*. In this subsection, we would like to illustrate what happens when we proceed inversely: *ab fine*; the "ending point" being the exact solution in a mathematically ideal situation.

We will cover the following approculations:

1. Adapting a (classical) differential dipole strength oscillator to a (quantum) expression accounting for the indistinguishability of the incident and target electrons.

2. Generalising Mott's cross section between free electrons to a pseudo-free situation where one of the electrons is initially bound to an atom.

3. Extending a cross section at slow velocities to the relativistic domain.

10.2.1 Dipole Oscillator

The dipole oscillator strength (DOS) of a target molecule/atom represents the overall intensity linked to a transition induced by an inelastic collision. In ionising collisions it is expressed differentially with respect to the energy ε_2 of the secondary electron $\mathrm{d}f_\mathrm{i}/\mathrm{d}\varepsilon_2$, which is formerly bound by B to the target. The corresponding ionisation singly differential cross section (SDCS) from the DOS is [427, eq.(4.22)]:

$$\frac{\mathrm{d}\sigma_\mathrm{d}}{\mathrm{d}\varepsilon_2} = \frac{4\pi a_0^2}{\varepsilon_0/\mathrm{Ryd}}\left(\frac{\mathrm{Ryd}}{\varepsilon_2+B}\frac{\mathrm{d}f_\mathrm{i}}{\mathrm{d}\varepsilon_2}\ln(4\check{c}_\mathrm{i}\varepsilon_0/\mathrm{Ryd}) + \frac{\mathrm{Ryd}}{\varepsilon_0}\frac{\mathrm{d}\check{\gamma}_\mathrm{i}}{\mathrm{d}\varepsilon_2} + O(1/\varepsilon_0^2)\right) , \tag{10.24}$$

where the function $\check{c}_\mathrm{i}(\varepsilon_2)$ and $\mathrm{d}\check{\gamma}_\mathrm{i}(\varepsilon_2)/\mathrm{d}\varepsilon_2$ are derived from the more generic "generalised oscillator strength density" (see dedicated section 11.5).

One enigmatic aspect of $\mathrm{d}f_\mathrm{i}/\mathrm{d}\varepsilon_2$ in approximate treatments of collisions involving fast electrons, is the inclusion of indistinguishability between the incident and target electrons which enables their exchange.

Under Born's approximation the differential oscillator strength is asymptotically independent from the incident kinetic energy ε_0 and is a property intrinsic to the target atom/molecule. In Bethe's [65] theory, exchange comes into play [427, p.333:§below-eq.(4.63)] not from the DOS itself but by limiting integrations over the kinetic energies to $(\varepsilon_0 - B)/2$, thereby defining the primary versus the secondary electron. Thus, exchange intervenes only when expressing *integral* cross sections.

Nevertheless, as we know, Born's approximation usually holds only at higher energies ($\varepsilon_0 \gg B$). As the energy decreases, there is a departure from the asymptotic expression of the DOS which becomes affected by ε_0.

In the analytical approximation proposed by Kim and Rudd [507, eq.(46&50)] as suggested by Inokuti [911, eq.(21)], the differential oscillator strength linked to the ejection of electrons bound by B is expressed as:

$$\frac{\mathrm{d}f}{\mathrm{d}\varepsilon_2} \propto \frac{1}{(\varepsilon_2+B)^2} + \underbrace{\frac{(\varepsilon_2+B)}{(\varepsilon_0-\varepsilon_2)^3}}_{\text{exchange}} . \tag{10.25}$$

The term highlighted is the contribution that would make the singly differential cross section for ionisation (10.24) symmetric with respect to the exchange of the incident and ejected electrons which corresponds to the replacement :

$$\varepsilon_2 \leftrightarrow \varepsilon_1 \equiv \varepsilon_0 - \varepsilon_2 - B , \tag{10.26}$$

in which the primary ε_1 is swapped with the secondary ε_2 energy. As mentionned by Kim and Rudd [507, p.3958:right column-top], this symmetrisation is not important at higher energies (>100 eV) where the probability of exchange is very low. Nevertheless, since the dipole oscillator strength is asymptotically defined without taking into account the possibility for exchange, it is not straightforward to understand [507, 508, p.3958 vs. p.3] whether this symmetrised term should be included or not when $\varepsilon_0 \gtrsim B$.

Later, we will see in figure 10.8, that comparison with experimental data shows that, *a priori*, better agreement is found most of the time when ignoring the exchange symmetric term in (10.25).

The reason for this, to be discussed much later in section 11.5.3, is probably not physical but mathematical.

10.2.2 Pseudo-free Binary-encounter

When two free electrons scatter, their exchange is treated in the interference term of Mott and Fowler's cross section averaged over the spin direction for unpolarised beams (8.141) [679]. If now one electron is subjected to the binding energy to its atom, there arise some complications with respect to the way to treat the problem as a whole.

If we interest ourselves only on the (single) ionisation channel, we may define the following *asymptotic* quantities (i.e. far away from the ion/atom):

ε_0	Kinetic energy of the incident electron
ε_1	Higher kinetic energy after ionisation (primary)
ε_2	Lower kinetic energy after ionisation (secondary)

The energy conservation binds all those energies together with the ionisation potential B (binding energy):

$$\boxed{\varepsilon_0 = \varepsilon_2 + \varepsilon_1 + B} = \underbrace{(\varepsilon_2 + \frac{B}{2}) + (\varepsilon_1 + \frac{B}{2})}_{\textbf{II.}\ \text{eq.(10.30)}} = \underbrace{(\varepsilon_2 + B) + (\varepsilon_1)}_{\textbf{I.}\ :\ \text{Kim and Rudd [507]}} \tag{10.27}$$

Two possibilities (among many) of grouping kinetic energies with the binding energy are represented in (10.27). This is because it is unclear how the potential of the ion affects the fleeing electrons. This relation applies on the macroscopic (asymptotic) scales but it gives no insight on what happens locally.

If we choose to conceptualise the interaction as given by Møller's cross section (8.145), we must now zoom onto the place of encounter: at the orbital. On its way, the incoming electron gained a certain amount of kinetic energy K due to the attractive potential of the atom. At the 'time of the collision', we now have an electron of energy $\varepsilon_0 + K$ that will interact with a bound electron.

In the simplest case of a hydrogen atom, an electron initially at rest located at infinity from a proton will gradually accelerate to reach a kinetic energy of $U + B = 2B$ from the virial theorem. If by any luck, it loses a B amount of energy, it will stay bound to the proton on an orbital with a kinetic energy U and a total negative energy $-|B|$ signifying its bound state.

Based on this analogy, we may apply the same reasoning for a more complex atom. As we know, the bound electron has a certain *average* initial kinetic energy $U \neq B$ (not necessarily equal to its binding energy) associated to the orbital on which it dwells. This electron will be classically able to escape only if its kinetic energy is augmented by the binding energy B to a total of $U + B$. Thus, we may reckon that at the outcome of a local collision leading to ionisation, the lowest kinetic energy of any of the two electrons must be above $B + U$ in order for them to be able to escape from the ion. The term $U + B$ can be understood as an energy gain or acceleration in the ionic potential.

We now differentiate two extreme situations:

I The incident energy ε_0 is large and only a fraction is given to $\varepsilon_2 \ll \varepsilon_1$.

II The energy share is fair and $\varepsilon_1 \simeq \varepsilon_2$.

I. $\varepsilon_2 \ll \varepsilon_1$ In this case, we may imagine that the incident electron deposited $\Delta\varepsilon$, a small proportion of its energy to the bound electron and left rapidly. Such scenario is widely used in approximate treatments of interactions and is generically known as the *impulse approximation*.

In this picture, the primary escapes at a local speed corresponding to $\varepsilon_0 + K - \Delta\varepsilon$ and will trade K back to the atom to seek leave. In the meantime, the bound electron has now a *local* kinetic energy $U + \Delta\varepsilon$, which is augmented by the energy transfer $\Delta\varepsilon = \varepsilon_2 + B$. In order to escape, it will have to give away $B + U$ and remain with the asymptotic ε_2.

The *local* kinetic energies to be used in Møller's DCS expressed in kinetic energy (8.148) are:

$$\begin{aligned} \varepsilon_0 + K - \Delta\varepsilon &= \varepsilon_0 + K - (\varepsilon_2 + B) && \text{Local kinetic energy of the primary} \\ \Delta\varepsilon + U &= \varepsilon_2 + B + U && \text{Local kinetic energy of the secondary} \end{aligned}$$

This would lead to the following *modified* (M) Møller singly differential cross section (SDCS):

$$\begin{aligned} \frac{\mathrm{d}\sigma_{\mathrm{M,I}}}{\mathrm{d}\Delta\varepsilon} = \frac{\mathrm{d}\sigma_{\mathrm{M,I}}}{\mathrm{d}\varepsilon_2} = \frac{2\pi a_0^2 \alpha^2}{\beta^2} \Bigg[& \frac{1}{(\varepsilon_2 + B \cancel{+U})^2} + \frac{1}{(\varepsilon_0 + K - \varepsilon_2 - B - U)^2} \\ & - \frac{2\gamma - 1}{\gamma^2 (\varepsilon_2 + B \cancel{+U})(\varepsilon_0 + K - \varepsilon_2 - B - U)} + \frac{1}{(\varepsilon_0 + K + m_\mathrm{e}c^2)^2} \Bigg] . \end{aligned} \tag{10.28}$$

As could be imagined, there is a problem with this reasoning and we have purposefully barred the '$+U$' in the terms related to the secondary electron. The problem is that Møller's formula in the form (8.148), is expressed in a reference frame where the secondary electron is initially at rest, whereas here it possesses an initial kinetic energy U.

If we return to the appendix A in part I dealing with collision kinematics and consult sketch A.1a, we see that for identical outgoing kinetic energies, there is a continuum of possible momentum transfers $\mathbf{p}_0 - \mathbf{p}_1$ due to the relative rotation of the momenta in the outgoing plane compared to the incident plane, about the symmetry axis z aligned with $\mathbf{\Pi}$: the total momentum involved in the collision. As highlighted by Vriens [966, p.14], this means that the relationship between the momentum transfer q and the kinetic energy transfer $\Delta\varepsilon$ is no longer univalent as in the two extreme cases (secondary initially at rest vs. centre of mass frame). One must therefore decide how to express the cross section: in terms of momentum transfer or energy transfer?

In collisions with bound electrons, in many cases, we are only interested in determining the kinetic energies of the outgoing electrons; their direction will follow an angular distribution to be characterised thereafter. The cross section that is obtained is thus an integration over the transfer momenta q corresponding to a fixed energy transfer $\Delta\varepsilon$. Ideally, one would need to describe the momentum distribution of the electron in its orbital and perform an average.

For an isotropic distribution in the bound orbital over a sphere at an average square orbital momentum $\langle p^2 \rangle = 2m_\mathrm{e}U$, Vriens [966, eq.(21)] obtained the formula for binary encounters σ_be in which it is the energy transferred $\Delta\varepsilon$ that intervenes in the denominator of the Mott scattering cross section. In our notation we have:

$$\frac{\mathrm{d}\sigma_\mathrm{be}}{\mathrm{d}\Delta\varepsilon} = \frac{4\pi a_0^2 \mathrm{Ryd}^2}{\varepsilon_0} \left(\frac{1}{(\Delta\varepsilon)^2} + \frac{1}{(\varepsilon_0 - U - \Delta\varepsilon)^2} - \frac{\phi_B}{\Delta\varepsilon(\varepsilon_0 - U - \Delta\varepsilon)} + \frac{4U}{3} \left[\frac{1}{(\Delta\varepsilon)^3} + \frac{1}{(\varepsilon_0 - U - \Delta\varepsilon)^3} \right] \right) \tag{10.29}$$

where ϕ_B is the Coulomb interference term defined in (11.118). One may compare this simple generalisation with the particular case in which $U = 0$ given by (8.143). The difference now is that ε_2 has been replaced by $\Delta\varepsilon$. To obtain the relativistic form (10.28), we approculated* (10.29) and got rid of the binary encounter term $\propto \dfrac{4U}{3}$, not because it is negligible but because it is used in a different term when fully describing the ionisation (see section 11.5.3).

*Meaning that we add relativistic terms based on analogy but not on rigorous derivation. See p. 341

Here in principle, β and γ relate to $\varepsilon_0 + K$ ($\gamma - 1 = (\varepsilon_0 + K)/m_e c^2$). Since usually $K \ll m_e c^2$, it does not really affect γ, though it should not be neglected in β if it is comparable to ε_0; this is at the core of the binary-encounter model [507, eq.(7)] (cf. section 11.5).

If we now want to apply the *exchange principle*, the SDCS should be symmetric in the exchange ($\leftrightarrow$) of the kinetic energies of the ejected electrons on two different scales:

$$\begin{cases} \text{Locally}: & \varepsilon_0 + K - \Delta\varepsilon \leftrightarrow U + \Delta\varepsilon \\ \text{Globally (asymptotically)}: & \varepsilon_1 \leftrightarrow \varepsilon_2 \end{cases}$$

Locally, (10.28) is *de facto* symmetric with exchange of $\Delta\varepsilon \leftrightarrow \varepsilon_0 + K - \Delta\varepsilon$ but not globally (asymptotically$= \varepsilon_2 \leftrightarrow \varepsilon_0 - \varepsilon_2 - B$). There is however a way to fix this by imposing:

$$\text{“}K \equiv B + U\text{”}$$

By doing so, we follow the path taken by Kim and Rudd [507, §II.B] and obtain their equation (6). This corresponds to the grouping **I.** as labelled in (10.27). Physically, it implies that the ionic potential is the same as of the neutral atom/molecule.

We must remark that, it is not uncommon to stumble nowadays in the literature (e.g. [911, §1.a:p.10]) into a contradictory argument whereby the primary electron's initial energy ε_0 would be incremented by $+B+U$ in the leading denominator of (10.28), but would mysteriously be only augmented by $+B$ in the bracket terms in order to get the right formula in the end.

The presence of U in (10.28) from (10.29) is fundamental to preserve a sensible physical explanation. This was already remarked in Rudge's review [793, §4.3:p.585-6], noting that the analysis of Burgess [133] and Vriens [966] did not coincide. We recommend the reader to return to Vriens' original work [966, 967], where all the details are disclosed about getting the Mott scattering formula in an arbitrary reference frame where neither of the colliding electrons are initially at rest.

II. $\varepsilon_2 \simeq \varepsilon_1$ We now take the opposite perspective and imagine that the two electrons confusedly try to escape the ionic potential at similar speeds, figuratively shoving one another. For further reference, this corresponds to what is known as ‘post-collision interaction’ mentioned later on page 495.

There is an overall toll of $K + B + U$ that both electrons have to pay in common to escape the ion. If we suppose that the system is isotropic, there is no reason that the local energies of the electrons differ much locally if they match asymptotically. Hence, this time we can suppose that they decide to split the toll equally:

$$\begin{aligned} \varepsilon_0 + K - \Delta\varepsilon &= \varepsilon_0 + K - (\varepsilon_2 + (K + B - U)/2) && \text{Local kinetic energy of the primary} \\ U + \Delta\varepsilon &= \varepsilon_2 + (K + B + U)/2 && \text{Local kinetic energy of the secondary} \end{aligned}$$

We recall that if $\Delta\varepsilon$ represents the kinetic energy transfer (exclusively between two electrons), then the local kinetic energy of the secondary is $U + \Delta\varepsilon$. This electron will have to give up $(K + B + U)/2$ (half of the toll) to attain ε_2 asymptotically, hence the second equation above.

Again, going back to the origins, we take (10.29) and welcome another guest to the collection of approximate SDCS:

$$\frac{\mathrm{d}\sigma_{\mathrm{M,II}}}{\mathrm{d}\Delta\varepsilon} = \frac{\mathrm{d}\sigma_{\mathrm{M,II}}}{\mathrm{d}\varepsilon_2} = \frac{2\pi a_0^2 \alpha^2}{\beta^2}\left[\frac{1}{(\varepsilon_2 + \frac{K+B-U}{2})^2} + \frac{1}{(\varepsilon_0 - \varepsilon_2 + \frac{K-B-U}{2})^2}\right. \\ \left. - \frac{2\gamma - 1}{\gamma^2(\varepsilon_2 + \frac{K+B-U}{2})(\varepsilon_0 - \varepsilon_2 + \frac{K-B-U}{2})} + \frac{1}{(\varepsilon_0 + K + m_e c^2)^2}\right]. \tag{10.30}$$

We see that if we set $B+U \equiv K$ as in the previous case **I**, we get identical equations (10.30≡10.28). Nonetheless, this time, the exchange principle applies both locally and asymptotically if we replaced $\varepsilon_2 \leftrightarrow \varepsilon_0 - \varepsilon_2 - B$. Thus, we may choose K however we wish. Since we are certain that $K < B+U$ (this would be the energy gain of an electron impinging on the singly charged ion), we may parametrise:

$$K = \iota B + \kappa U \ , \tag{10.31}$$

in terms of some fractions $0 < \iota, \kappa < 1$.

We may expect that for fast electrons, the energy partition is unequal most of the time, so that $\mathrm{d}\sigma_{\mathrm{M,I}}$ should give a better approximation. On the contrary, slow electrons $\varepsilon_0 \lesssim 2B$ are most likely obliged to share their energy fairly with the ejected electron and modelled rather through $\mathrm{d}\sigma_{\mathrm{M,II}}$ with an adequate value of $K < B+U$.

The literature [911, §1.a] is not clear whether introducing $\varepsilon_0 + B(+U?)$ in (10.28) is mainly due to the kinetic acceleration [793, §4.3] of the electron or due to the necessity of symmetrising [605, p.8] Møller's formula when extending to scattering with a pseudo-free electron. This logical incoherence was touched upon in §1 above.

Here, we showed that if it is for the latter reason (exchange), then there is not only one way to symmetrise Møller's formula but many different ways as shown by the introduction of ι and κ in (10.31). On the other hand, it is hard to conceive that the acceleration of the electron in the atom/molecule's potential would be systematically represented by $B+U$.

A more formal justification to setting $K \approx B+U$ as a scaling factor for ε is evoked in Tanaka *et al.* [911, §1.a]. Formally, for *open-shell* atoms, the incident electron would temporarily be coupled with an orbital of binding energy B if electron correlation and spin alignment were disregarded. In the simplest case of the hydrogen atom, the incident electron's wavefunction is coupled to $1s$ and higher hydrogenic states with their appropriate binding energies [217].

In Born's approximation, the appearance of $q^2 + 4B^2$ in the denominator is even more conspicuous. Bound states decay as $\exp(-2\sqrt{B}r)$, so that the plane-wave Born matrix element of the *static* interaction potential automatically introduces the screening by B (cf. screened Rutherford in section 10.1.2). Still, this picture holds only in the Born approximation ($\varepsilon_0 \ggg B$) when exchange, polarisation, correlation effects can be overlooked.

From this analysis we may retain that setting $K = B+U$ is somewhat justified for fast electrons. Of course, one could enter into an endless debate of how the energy partition in the modified Møller equation (10.30) should be handled. It could be thus imagined that the parameter K would be a function $K(\varepsilon_2, \varepsilon_0)$ of the incident and secondary energies tending toward B as $\varepsilon_2 \ll \varepsilon_0$.

Nevertheless, such endeavour would be paved with delusions, for one cannot separate the role played by the target atom/molecule on the outgoing electron waves. An *ab initio* approach would be considerably more desirable instead.

For the purpose of demonstration, we now combine the SDCS from the dipole oscillator with the modified Møller of the previous section in order to define two types of integrated SDCS:

$$\sigma_{\mathrm{I}}(\varepsilon_0) \equiv \int_0^{\frac{\varepsilon_0 - B}{2}} \left[(2-Q) \frac{\mathrm{d}\sigma_{\mathrm{M,I}}}{\mathrm{d}\varepsilon_2} + Q \frac{\mathrm{d}\sigma_{\mathrm{d-sym}}}{\mathrm{d}\varepsilon_2} \right] \mathrm{d}\varepsilon_2 \ , \tag{10.32i}$$

$$\sigma_{\mathrm{II}}(\varepsilon_0; K) \equiv \int_0^{\frac{\varepsilon_0 - B}{2}} \left[(2-Q) \frac{\mathrm{d}\sigma_{\mathrm{M,II}}(K)}{\mathrm{d}\varepsilon_2} + Q \frac{\mathrm{d}\sigma_{\mathrm{d-asym}}}{\mathrm{d}\varepsilon_2} \right] \mathrm{d}\varepsilon_2 \ . \tag{10.32ii}$$

An adjustable parameter to the combined model is Q, which is linked to the integral of the differential oscillator strength (11.108) from $\varepsilon_2 = 0$ to ∞. Its value is at most 1. All the relevant information linked to this combination can be found in the next chapter section 11.5.3. When $Q = 1$, σ_{I} is called the relativistic binary-encounter-Bethe model (RBEB) [507, 508].

We must highlight here the very important distinction:

$\sigma_{\rm I}$ includes the symmetric term of (10.25),

$\sigma_{\rm II}$ does **not** include the symmetric term of (10.25).

The objective in doing so, is to compare in figure 10.8 the effects of the dipole term and the modified Møller terms. We plot the cross sections models for various elements of air, fixing $Q = 1$ to have a fair comparison. The solid curves show the overall performance of $\sigma_{\rm I}(\varepsilon_0; Q = 1)$ (10.32i-darkblue) and $\sigma_{\rm II}(\varepsilon_0; Q = 1, K)$ (10.32ii-pink). Each time, the chosen value for K (for $\sigma_{\rm II}$) is displayed. Provocatively, we show that by fiddling with the value of K, by setting it to a certain fraction of B and U, one can almost compensate the effects of the symmetric term in the dipole term and make $\sigma_{\rm I}$ and $\sigma_{\rm II}$ agree more or less.

As mentioned before, setting $K = B + U$ amounts to equalling $\mathrm{d}\sigma_{\rm M,II}$ with $\mathrm{d}\sigma_{\rm M,I}$. Therefore, the difference at $K = B+U$ between $\sigma_{\rm I}$ (darkblue —) and $\sigma_{\rm II}(K = B+U)$ (pink –·–) is purely due to the removal of the symmetric term in (10.24). Overall, this symmetric term mostly contributes at $\varepsilon_0 < 200\,\mathrm{eV}$ and results indicate that it is in general better to discard the symmetric term in the dipole oscillator to obtain closer agreement with the cross section. This is not true for argon, whose shell structure complexity might compromise the accuracy of the model.

For illustration, we also show in figure 10.8, the contribution to $\sigma_{\rm I}$ of the dipole term only (darkblue - - -). This is done by an artifice $\sigma_{\rm I}(Q = 2)/2$ which annihilates the contribution at small impact parameters from the modified Møller cross sections (cf. 10.32). Here, we see that even if the magnitude were to be adjusted through Q, the shape would not match the theory as well. This is due to the fact that higher order terms in the Bethe theory become important at intermediate energies $\varepsilon_0 \lesssim 500\mathrm{eV}$.

The purpose behind this section, is to illustrate through figure 10.8, a typical and most hated situation in scientific debate when the approximations taken are so many that no sound physical conclusion can be harvested from the work done. We have stalled in a ditch. Any attempt at finding a justification will be densely paved with thick and bumpy cobbles of delusion. There are uncountable ways one could be lured into. One could:

- ⊠ introduce a dependence of $Q(\varepsilon_0)$ with the incident energy with $\lim_{\varepsilon_0 \to \infty} Q(\varepsilon_0) = 1$;
- ⊠ imagine that $K(\varepsilon_2)$ in (10.30) be a function in secondary energy which is equal to $B + U$ when ε_2 is zero and decreases toward a certain value as ε_2 grows;
- ⊠ choose a different generic shape for $\mathrm{d}f/\mathrm{d}\varepsilon_2$ than (10.24);
- ⊠ revise the scaling applying to β^2 in the leading denominator [359]
- ⊠ include an exact treatment of the interference term due to exchange [358]

Anyhow, the RBEB model embodied in (10.32) was designed only by conferring a common asymptotic $\varepsilon_0 \ggg B$ behaviour of the cross section, which is readily seen by the convergence of all curves at higher energies on figure 10.8. Ascribing a physical relevance of the cross sections nearer the threshold $\varepsilon_0 \gtrsim B$ is dubious. The binary-encounter-dipole model briefly inserted here is a marvellous example of simple and approximative models in quantum physics that work astonishingly well* for a great variety of atoms and molecules [415], yet whose success remains to be elucidated based on a rigorous physical justification.

*in fact sometimes much better than more cumbersome calculations based on distorted-waves [507, figures:1-7]

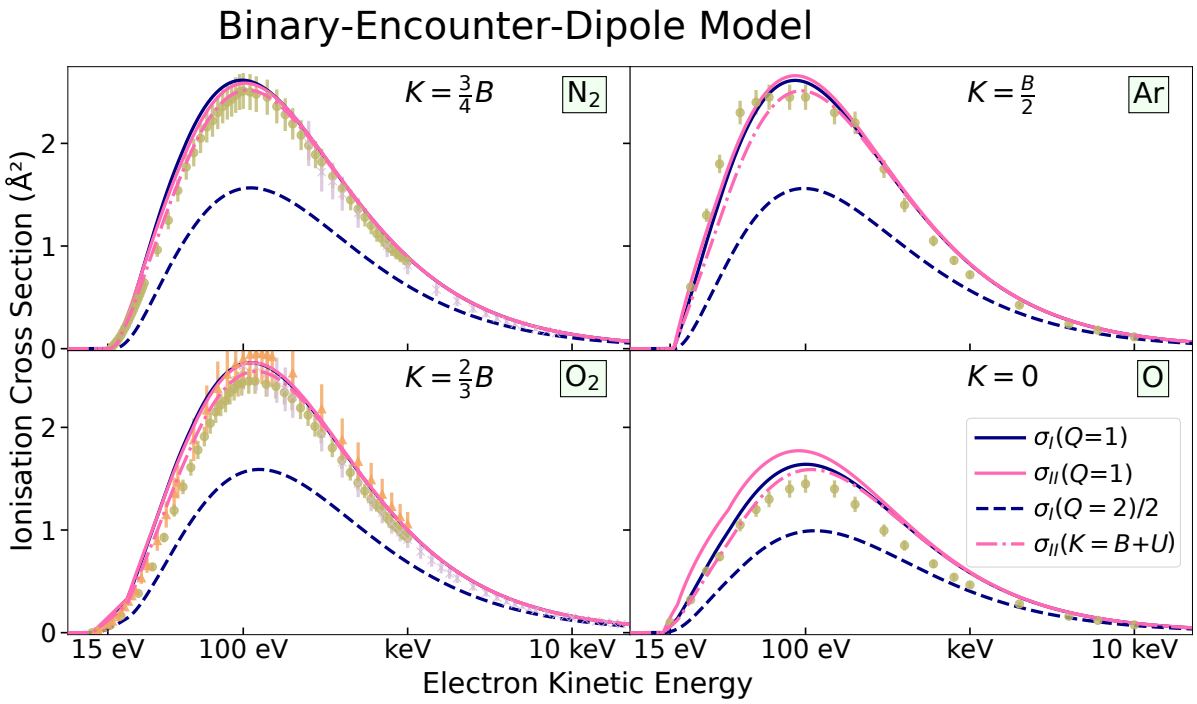

Figure 10.8: Variants of the RBEB model (11.5) defined in (10.32) compared with evaluated databases found in Inokuti *et al.* [425] (for Ar and O) and Lindsay and Mangan [596] (for N_2 and O_2). The parameter K (energy gain) affects only σ_{II}. When $K = B + U$, the difference between σ_I and σ_{II} is only due to the neglection of the exchange term in the dipole oscillator strength (10.25). The curve $\sigma_I(Q = 2)/2$ is an artifice to show only the contribution of the dipole term in (10.32i).

It is hard to believe that, given the numerous approximations of the model, the agreement with experimental data be coincidental for so many different molecules. Nonetheless, as will be shown in the next chapter section 11.5.3, trying to revise the RBEB is unrewarded, by deterioration of the former agreement with experimental data.

Once again, when performing *ad hoc* modifications (as illustrated here above by models I and II) instead of *ab initio* analysis to model a certain phenomenon, one should not attach too much importance to the exactness or meaning of the results obtained. A heuristic approach in quantum mechanics is rewarded with encouraging results more often than not, because finer effects wont to compensate among themselves.

History is full of examples of "lucky" guesses that were not rigorously introduced from the outset, but that later revisits elucidated what compensations in the higher order effects validate the simple result. Such had been the case of the classical Rutherford cross section [147, chapter 3] and the introduction of the electron's spin [345, 929], among many other cases.

At the end of section 11.5.3, we take the risk of interpreting the success of the binary-encounter-dipole model of Kim and Rudd [507] by comparing with the terms from Bethe theory as reviewed by Inokuti [427]. The essence of the argument is embodied in equations (11.127) and (11.128). There are still some open questions left regarding the correspondence among the higher order terms.

10.2.3 Relativistic Forms

When extending a formula to relativistic energies, one must pay attention not only to mathematical correspondence in the limit $c \to \infty$ (infinite speed of light), but also to respect physical consistency. Below, we transcribe the current [358, 508] appearance of the relativistic binary-encounter (RBE) model (without the dipole):

$$\frac{\mathrm{d}\sigma_{\mathrm{RBE}}}{\mathrm{d}\varepsilon_2} \neq \frac{4\pi a_0^2 \alpha^2 2\mathrm{Ryd}^2}{\beta_0^2+\beta_B^2+\beta_U^2}\left[\frac{1}{(\varepsilon_2+B)^2}+\frac{1}{(\varepsilon_0-\varepsilon_2)^2}+\frac{1}{(\varepsilon_0/2+m_\mathrm{e}c^2)^2}\right. \tag{10.33}$$

$$\left.-\frac{m_\mathrm{e}c^2(m_\mathrm{e}c^2+2\varepsilon_0)}{(m_\mathrm{e}c^2+\varepsilon_0/2)^2}\frac{\cos\left(\sqrt{\dfrac{\alpha^2}{(\beta_0^2+\beta_B^2)}}\ln\dfrac{\beta_0^2}{\beta_B^2}\right)}{(\varepsilon_2+B)(\varepsilon_0-\varepsilon_2)}\right]. \tag{10.34}$$

The fuzzy parts and differences with (10.28) introduced previously are highlighted. To each coloured group, we address a critique. The reduced velocities β_0, β_B, β_U are defined respectively from the initial kinetic energy of the inciden electron ε_0, the binding B and kinetic U energies of an electron bound to the atom/molecule (see the correspondences on the right hand side of 10.36 below).

⊠ Acceleration term: In the non-relativistic binary-encounter model (see 11.79 in section 11.5.2) the incident energy in the denominator is rescaled as:

$$\bar{\sigma}_0 \propto \frac{1}{\varepsilon_0} \text{ replaced by } \frac{1}{\varepsilon_0+U+B}, \quad \text{or equivalently : } \quad \text{replaced by } \tilde{\sigma}_0 \tag{10.35}$$

where U is the average kinetic energy of the target electron bound by B to its orbital. This addition is supposed to represent the kinetic energy gained by the incident electron in the attractive potential of the target atom/molecule [507, §VI.].

If that is so, then generalisation to relativistic energies implies formally to replace the total (incident + gained) kinetic energy by its classical expression of the squared velocity, which is the pertinent quantity in the interaction (not the kinetic energy *per se*). We thus introduce the reduced velocity:

$$\tilde{\beta}^2 \equiv 1-\left(\frac{m_\mathrm{e}c^2}{\varepsilon_0+U+B+m_\mathrm{e}c^2}\right)^2 \not\equiv \beta_0^2+\beta_B^2+\beta_U^2 = 1-\frac{m_\mathrm{e}c^2}{\varepsilon_0+m_\mathrm{e}c^2}+1-\frac{m_\mathrm{e}c^2}{B+m_\mathrm{e}c^2}+1-\frac{m_\mathrm{e}c^2}{U+m_\mathrm{e}c^2}, \tag{10.36}$$

which is fundamentally different than the denominator (10.34) from Kim *et al.* [508, p.4:eq.(19)]. Of course, mathematically the difference is ridiculous because in general $B, U \lll m_\mathrm{e}c^2$, except for K-shells (n=1) of heavy atoms. Nonetheless, an expression summing $\beta^2+\beta_B^2+\beta_U^2$ should be viewed as a physical aberration* (what if $\beta^2 > 0.9$ and $\beta_U^2+\beta_B^2 > 0.1$?). This concern was raised in Wang *et al.* [974, p.10-11:eq.(19-21)], though only to change the prefactor to $1/\beta_0^2$...

*Otherwise, electrons that penetrate to the K-shell of Uranium would surpass the speed of light!

☒ Inaccelerated velocity: In the cosine of the logarithmic term appears a 1/v factor for the velocity of the incident electron. A glance at Mott's cross section (8.141) reveals that this velocity is formally the same as the velocity of relative motion $\overleftrightarrow{\mathrm{v}}$ that appears in the denominator of the magnitude. Based on the correspondence between Mott and Møller's cross sections (8.141 & 8.145), we get the following relationship*:

$$\left(\frac{m_e a_0}{\hbar}\right) \overleftrightarrow{\mathrm{v}} = \frac{\tilde{\beta}}{\alpha} \sqrt[4]{\frac{2\tilde{\gamma}^2}{\tilde{\gamma}+1}} \,. \tag{10.37}$$

This velocity can exceed the speed of light, an intriguing aspect, but not unphysical since it is not a velocity of a particle, but a relative velocity for an observer sitting right in both electrons' centre of mass frame. The Lorentz factors in (10.37) would be defined as:

$$\tilde{\gamma} = \left(\frac{\varepsilon_0 + U + B}{m_e c^2}\right) + 1 \quad \text{and} \quad \tilde{\beta}^2 = 1 - \frac{1}{\tilde{\gamma}^2} \,, \tag{10.38}$$

though this is purely conjectural, as one would need to make a calculation with Coulomb waves in the relativistic frame of Dirac's equation instead of Schrödinger's equation.

☒ Momentum transfer: the fraction β^2/β_B^2 as argument to the logarithm in (10.34) is a distortion from its original *non-relativistic* expression (8.141):

$$\tan^2 \frac{\theta}{2} = \frac{(\varepsilon_2 + B)}{(\varepsilon_0 - \varepsilon_2)} \,,$$

where we have also expressed the angle of deviation θ in the *centre-of-mass* frame. This ratio has the same origin as the $1/(\varepsilon_2 + B)$ terms in Møller's cross section: it is related to the momentum transfer. One's mind can be refreshed in (8.142) in section 8.5.5 which is valid relativistically.

There are in essence two mistakes that distorted an energy fraction into a velocity fraction: First, the expression (10.2.3) was replaced [358, eqs.(7-9)] by its value at $\varepsilon_2 = 0$ because of a recommendation from Vriens [966, eq.(24)] who could not use an exact analytical average as in (11.88) because he included the initial kinetic energy U in the electron's bound orbital.

Second, the kinetic energies were mistakenly replaced by ratios of velocities, hence the conversion of a former 'ε' to a 'β'.

In summary, the physical interpretation of the Coulomb-wave interference in the logarithm (10.2.3) is not a velocity ratio but an *energy ratio* between the secondary and the primary electrons.

☒ Mutation to half: the passage from Mott to Møller's cross section (8.143 to 8.148) is accompanied by the appearance of a term preceded by:

$$\left(\frac{\gamma - 1}{\gamma}\right)^2 = \frac{\varepsilon_0^2}{(\varepsilon_0 + m_e c^2)^2} \,,$$

in which there is no trace of a division $\varepsilon_0/2$. The curious mind may notice in the excerpt below from Kim *et al.* [508], that this factor made its appearance in equation (19) whereas

*This is merely a comparison, not a derivation. I do not dare plunge into a formal derivation of Møller's cross section with Coulomb waves instead of plane waves!

it was not yet present in their equation (15) which is the same pseudo-free Møller cross section as used here.

$$\left(\frac{d\sigma}{dw}\right)_{\text{Møller}} = \frac{4\pi a_0^2 \alpha^2 N(R/B)}{\beta_t^2}\left[\frac{1}{(w+1)^2} + \frac{1}{(t-w)^2} + \frac{b'^2}{(1+t')^2} - \frac{1}{(w+1)(t-w)}\frac{1+2t'}{(1+t')^2}\right], \quad (15)$$

$$\left(\frac{d\sigma}{dW}\right)_{\text{RBED}} = \frac{4\pi a_0^2 \alpha^4 N}{(\beta_t^2+\beta_u^2+\beta_b^2)2b'}\left\{\frac{(N_i/N)-2}{t+1}\left(\frac{1}{w+1}+\frac{1}{t-w}\right)\frac{1+2t'}{(1+t'/2)^2} + [2-(N_i/N)]\left[\frac{1}{(w+1)^2}+\frac{1}{(t-w)^2}+\frac{b'^2}{(1+t'/2)^2}\right]\right. \quad (19)$$

This '/2' never left the stage once it became immortalised in the RBED model. In principle, the lone ε_0 of (10.2.3) should have been augmented to $\varepsilon_0 + B + U$, by virtue of the usual replacement (10.35) representing the acceleration in the target's potential.

The corrections introduced here could be considered as a mere cavilling at physical inconsistencies in *ad hoc* adaptations of a formula (Møller scattering in this case). Mathematically, the differences highlighted may luckily take negligibly small values in the usual range of application of the formula. Nevertheless, we consider such remarks as important since they point out at a general problem in scientific investigation: automated repetition of conceptual mistakes. This problem might represent the tip of an iceberg, that even a field which we would expect to have the virtue of constantly refining itself, may be sullied by inconspicuous mechanisms of degeneration.

10.3 Semi-Empirical Models

An empirical model corresponds to a mathematical formulation that matches closely all the available experimental data disregarding a justification or interpretation of the parameters involved. The promotion to "semi"-empirical entails that a certain guidance is given over the parameters used, the shape of the function, the asymptotic or near-threshold behaviour based on theoretical modelling or physical reasoning.

The purpose of the present section is to compare and comment DCS from different semi-empirical models of the optical potential.

Purely empirical models are usually provisional, since they spur scientific minds to quickly find a physical reason, mechanism to shed light upon the nature of the underlying function to which the data would abide.

Often, semi-empirical models start from a known asymptotic ideal behaviour of a function, valid in ideal and simple cases (static, adiabatic, unperturbed, high-energy, etc.) and try to extend the applicability over the whole domain of the function.

In this process, the heuristic approach is the supreme recourse. The primitive function might become unruly in certain ranges: possess singularities. The first step always consists in checking that all such singularities are well controlled or screened away either through the application of an exponential decay or the removal of the singularity through a scale parameter b. Mathematically, in case of an inversely decaying function $\propto 1/x^\alpha$, this implies :

$$\frac{1}{x^\alpha} \longrightarrow \begin{cases} \dfrac{\exp(-(b/x)^\beta)}{x^\alpha} \\ \dfrac{1-\exp(-(x/b)^\beta)}{x^\alpha} \\ \dfrac{1}{(x^{\frac{\alpha}{\beta}}+b^{\frac{\alpha}{\beta}})^\beta} \end{cases}$$

The scale b controls the approximate position where one needs the function to ebb, while the exponent β tunes the strength of the transition; large (small) β produces an abrupt (smooth) ebbing. Rarely is β left as an adjustable parameter, one is usually content with setting an integer value $1 < \beta < 7$ once and for all.

The example given here above was actually applied to semi-empirical models of the polarisation potential. Below, we will comment two particular semi-empirical models for representing optical potentials in electron-molecule scattering: polarisation-correlation and absorption potentials. Before that, for the sake of inclusion, we will graze over semi-empirical exchange potentials.

10.3.1 Static

In order to draw meaningful observations, before we can compare semi-empirical models of the optical potential, it is important to check that the sensitivity of calculated DCS on the existing models for atomic electronic densities [196, 726, 800, 803] is smaller than the differences arising from second-order contributions to the optical potential: exchange, polarisation and absorption.

This preliminary check is represented in figure 10.9a for atomic oxygen at 10 eV. This is the target for which our fit deviates most from the other models and thus should illustrate the worst case differences, which, as seen, can be quite significant. Nonetheless, the influence of the semi-empirical models is even more conspicuous in the forward scattering range.

The effect of the static model is smaller for other atoms as shown in the figure 10.9b below for argon. The curve from our model is practically superposed with the fit of Pacios [726].

In the case of atomic nitrogen and oxygen, one must however not attach too much relevance to the exact DCS. First, there is no available experimental data to compare with. Second, the presence of open-shells is not taken into account. Third, the accuracy of the optical potential model is poor in the energy range close to ionisation threshold. In the following study, we shall thus attach more importance to well-known targets such as argon and will highlight significant differences due to the semi-empirical model used.

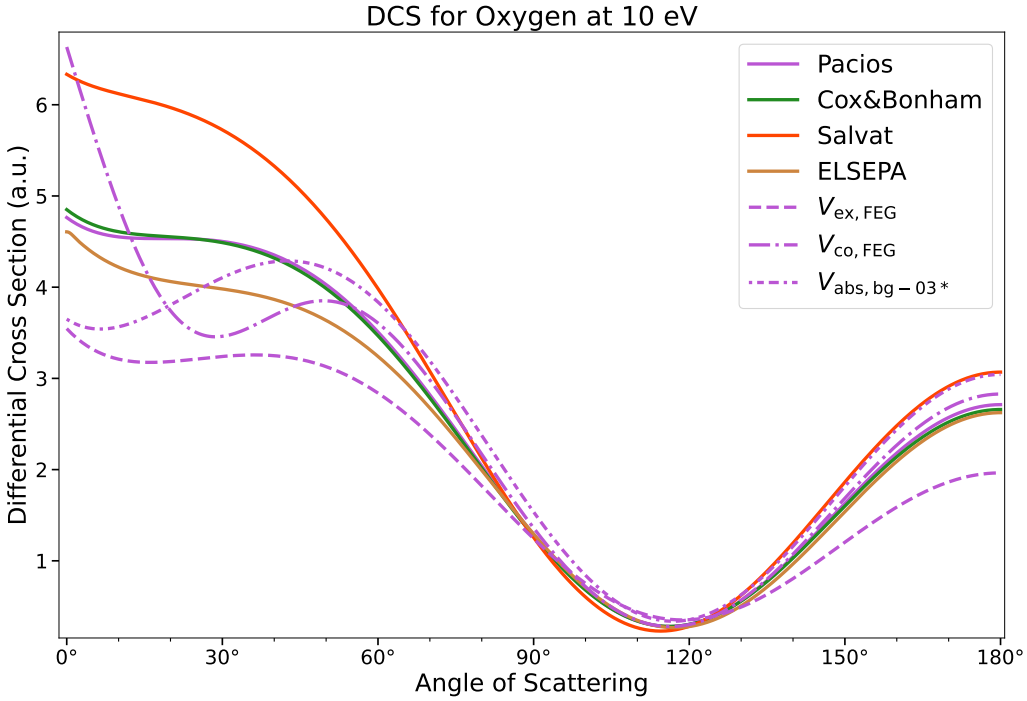

(a) Comparison of DCS for atomic oxygen at 10 eV. Subsequently, we also show the DCS arising from a different choice of semi-empirical potentials for exchange (10.39), correlation (10.61) and absorption (10.73) which are discussed in the following subsections.

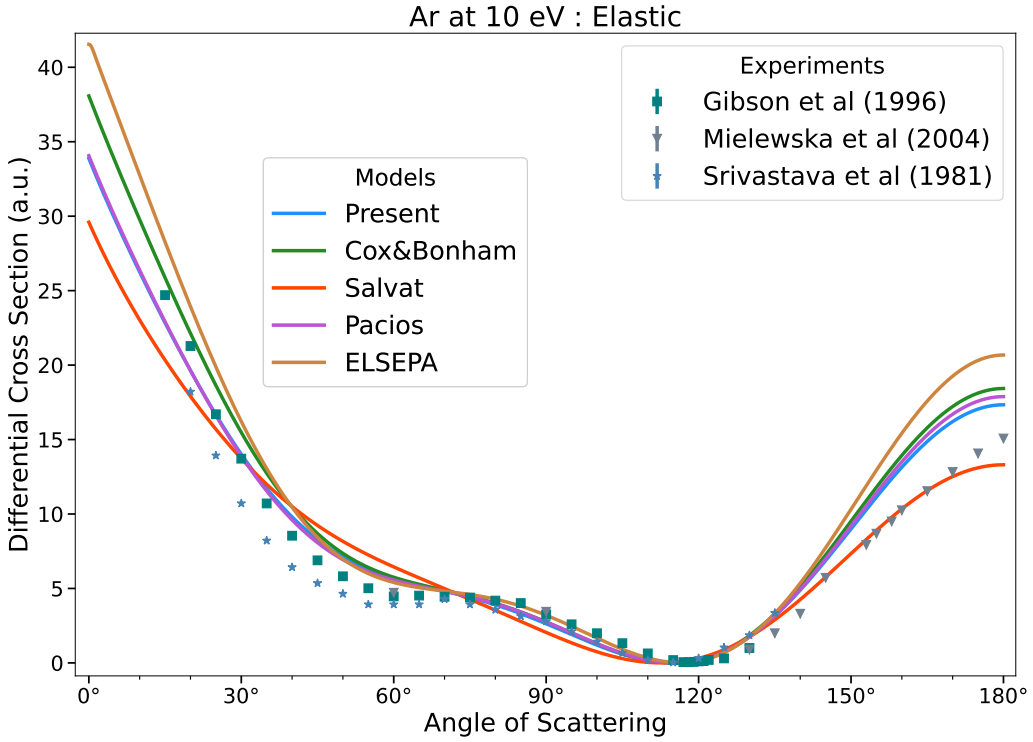

(b) Comparison of DCS for argon at 10 eV.

Figure 10.9: Effect of the static potential on the DCS from four different models of electronic density: our model (p.280 and (8.23)), Cox and Bonham [196], Salvat *et al.* [800] and Pacios [726]; and ELSEPA [803].

10.3.2 Exchange

We recall from (8.13) that the exchange potential comes from the necessity that the wavefunction of the total electron-molecule system be antisymmetrical with respect to interchange of the scattering electron with any of the bound electrons. This leads to the introduction of nonlocal potentials which, at each point $\mathbf{r}$, require the knowledge of the overlap interaction integral of the scattering wave $\psi(\mathbf{r})$ with a bound orbital $\phi_j(\mathbf{r})$. To circumvent this, there have been numerous propositions of *local* approximations for the exchange potential that may be classified into two categories:

1. Free electron gas (FEG) : stemming from Slater's [856] proposition of modelling the target locally as a free electron gas for including exchange in *bound* electron orbitals.

2. Semi classical (SC) : from Furness and McCarthy [309] where the local kinetic energies of the bound electrons are assumed negligible compared to the intruding electron's kinetic energy.

The free electron gas model was later adapted by Hara [384] to electron scattering problems to take the generic form:

$$V_{\text{ex,FEG}}(\mathbf{r}) = -\frac{2}{\pi} k_{\text{F}}(\mathbf{r}) \left(\frac{1}{2} + \frac{1-\eta}{4\eta} \ln \left| \frac{1+\eta}{1-\eta} \right| \right) , \tag{10.39}$$
$$\text{where } \eta = \frac{k(\mathbf{r})}{k_{\text{F}}(\mathbf{r})} .$$

The FEG basically represents all electronic wavefunctions (bound or free) as plane waves with a local wavenumber $k(\mathbf{r})$ (10.40) for the scattering electron and $k_{\text{F}}(\mathbf{r})$ (10.41) corresponding to the Fermi energy level for all bound electrons (see appendix E eq.(E.3)).

$$k(\mathbf{r}) = \sqrt{2(\varepsilon_0 - V_{\text{s}}(\mathbf{r}))} , \tag{10.40}$$
$$k_{\text{F}}(\mathbf{r}) = \left(3\pi^2 \rho(\mathbf{r})\right)^{1/3} . \tag{10.41}$$

Those wavenumbers depend on the static potential $V_{\text{s}}(\mathbf{r})$ and the electron density $\rho(\mathbf{r})$, of which analytical expressions were given in section 8.2.1.

As very well explained in Morrison and Collins [669, §III], those wavenumbers are assumed constant when performing the overlap exchange integrals, but vary with the position $\mathbf{r}$ when used in the local potential (10.39). In our vocabulary, (10.39) is a marvellous example of:

1. An approximation (the dependence of $\mathbf{k}$ on $\mathbf{r}$ is neglected):

$$\psi(\mathbf{r}) = \exp(\mathbf{k}(\cancel{\mathbf{r}}) \cdot \mathbf{r}) , \tag{10.42}$$
$$\phi_j(\mathbf{r}) = \exp(\mathbf{k}_j(\cancel{\mathbf{r}}) \cdot \mathbf{r}) , \tag{10.43}$$

2. followed by an approculation (the dependence of $\mathbf{k}$ on $\mathbf{r}$ is reincorporated *a posteriori*) :

$$k \text{ not constant :} \qquad k(\mathbf{r}) = 10.40 \tag{10.44}$$
$$k_{\text{F}} \text{ not constant :} \qquad k_{\text{F}}(\mathbf{r}) = 10.41 \tag{10.45}$$

Hence, the dialectic notion of 'approxi' and 'approcul' is supposed to convey the idea of 'forth' and 'back'. Its adoption, would, in the author's opinion, clarify how a model is constructed*. Different variants appeared [669, 775, §II.A.2, fig.3] depending on the value adopted for the local potential $V(\mathbf{r})$ for calculating the wavenumber $k(\mathbf{r})$ (10.40) of the scattering electron at position $\mathbf{r}$. The different versions were unified by Kutz and Meyer [546, eq.(7)] into a parametric form depending on the ionisation energy potential I:

$$k^2(\mathbf{r};g) = k_0^2 + k_{\mathrm{F}}^2(\mathbf{r}) + \frac{(2-g)\,k_{\mathrm{F}}^2(\mathbf{r})2I}{(2-g)\,k_{\mathrm{F}}^2(\mathbf{r}) + g\,2I}\ ,\ \text{with } 0 \le g \le 2\ . \tag{10.46}$$

A comparison of the performance from various FEG models of local exchange potentials was done by Riley and Truhlar [775] for He and Ar; and Morrison and Collins [669] for H_2 and N_2. The conclusion was that an intermediate model with an adjustable $g \neq 0$ or 2 would be the most appropriate representation for reproducing similar phase shifts as when the exchange is treated exactly.

The second category (historically) of approximate local exchange potentials is the semiclassical (SC) potential which was generalised by Riley and Truhlar [775, §II.A.1:eqs.(8–9)]:

$$V_{\mathrm{ex,SC}}(\mathbf{r}) = \underbrace{\frac{1}{2}(\varepsilon_0 - V_{\mathrm{s}}(\mathbf{r}))}_{\equiv k(\mathbf{r})} - \frac{1}{2}\sqrt{(\varepsilon_0 - V_{\mathrm{s}}(\mathbf{r}))^2 + 4\pi\rho(\mathbf{r})}\ . \tag{10.47}$$

The assumptions are less restrictive than for the free electron gas. They rely on the fact that the bound orbitals $\phi(\mathbf{r})$ are slowly varying functions of $\mathbf{r}$ [775, eq.(5–6)] compared to the wavefunction of the scattering electron $\psi(\mathbf{r})$. Physically, this is equivalent to neglecting the kinetic energy of the bound electrons compared to $\varepsilon_0 = k_0^2/2$:

$$\triangle\,\phi(\mathbf{r}) \ll \varepsilon_0\ . \tag{10.48}$$

In an attempt to include the kinetic energy of the bound orbitals, Gianturco and Scialla [324] proposed to add the kinetic energy of a free electron gas (E.4) to the local kinetic energy of the scattering electron in (10.47) giving the model presented earlier in (8.41).

At very high energies, where $\varepsilon_0 \gg V_{\mathrm{s}}(\mathbf{r})$, both FEG and SC models converge† to [775, eq.(11) and §II.B]:

$$V_{\mathrm{ex},\varepsilon\nearrow} = -\frac{\pi\rho(\mathbf{r})}{\varepsilon_0 - V_{\mathrm{s}}(\mathbf{r})}\ , \tag{10.49}$$

which is equivalent to the Born-Ochkur [711] approximation when $V_{\mathrm{s}}(\mathbf{r})$ is removed.

The two approximation classes (FEG and SC) for the exchange potential are represented in figure 10.10, with the hybrid semiclassical Fermi version (SCF) from Gianturco and Scialla [324], the high-energy approximation (10.49) and the effect of g on the $V_{\mathrm{ex,FEG}}$ in (10.39). We see that in general, the free electron gas (FEG) gives a markedly stronger attractive exchange potential than the semiclassical (SC) model for argon but that the effect of the g tuning parameter (10.40) in FEG for O_2 is more or less of the same magnitude as the difference with the SC model.

*We remind that presently, one would describe this procedure either by the vague "*ad hoc*" or by a more correct "*a posteriori*" that does not however convey that we are somehow "undoing" the assumption made for the approximation.

†The demonstration is an excellent exercise in an undergraduate exam of quantum physics. It requires to expand the logarithm $\ln((1+\eta)/|1-\eta|)$ up to the third Taylor order in $2/(\eta-1)$ and prove that the zeroth and first orders in $1/\eta$ in (10.39) cancel and only a $\sim 1/(3\eta^2) + O(1/\eta^3)$ remains.

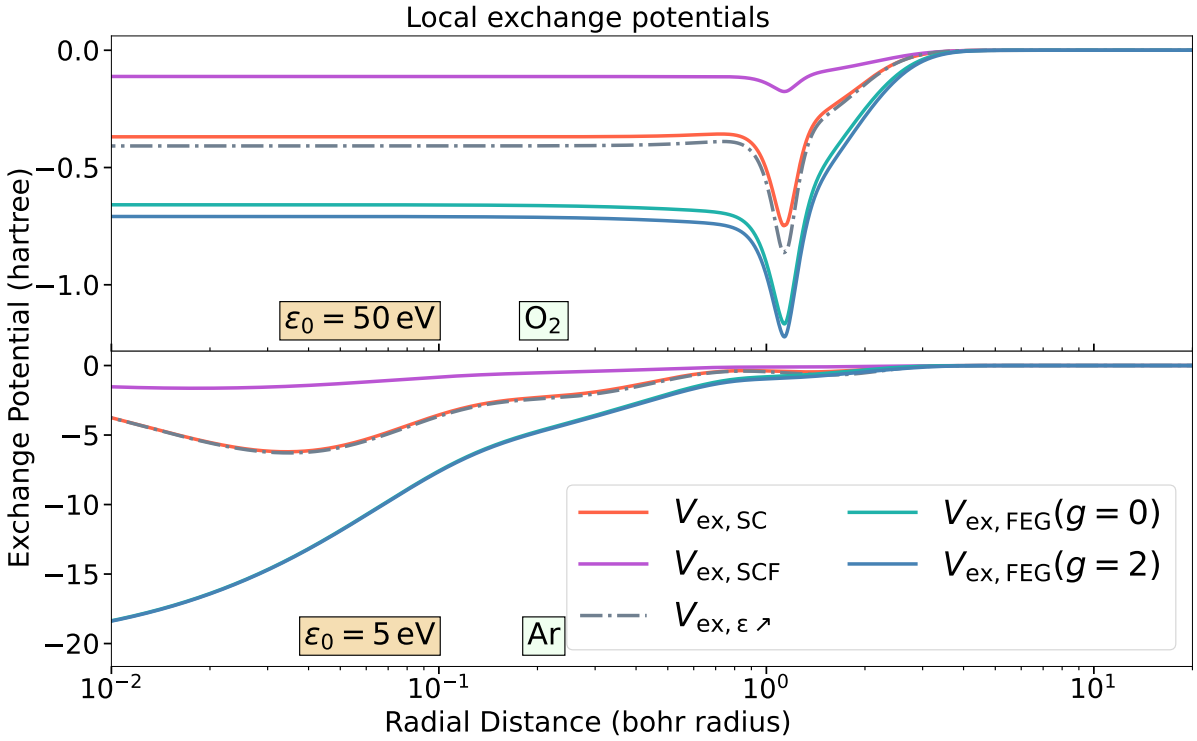

Figure 10.10: Comparison of exchange potentials for argon and molecular oxygen for an electron at 200 eV and 50 eV respectively.

The inclusion of the bound kinetic energy in the SCF (8.41) systematically reduces the effect of exchange.

As regarding the recommended model to be taken in calculations, on the one hand, according to [794, p.5224 and §VI], the semiclassical model alone is too attractive (negative) for N_2 at lower energies. From our analysis, the results with the SC alone for diatomic molecules were indeed somewhat worse than with the SCF. On the other hand, our own calculations for argon at low energies (< 10 eV) revealed on figure 10.11 that the FEG (whatever $0 < g < 2$) performed more agreeably than the SC, while the SCF gave significant disagreement. It is absolutely incongruous to conclude that the FEG model for exchange is more accurate, since alluring results can also be obtained by tinkering with the polarisation potential (in the next subsection) and the SC exchange [4, p.11:fig. 1B and p.22:graph 5].

This strange inversion of performance may be related to our poor modelling of diatomic potentials. For diatomic molecules, we adopted the semiclassical Fermi (SCF) model presented in section 8.2.2 which was initially used for CH_4 [324, eq.(18)]. For atoms however, we preferred the use of the FEG for argon and the SC for N and O.

There have been numerous studies comparing previous local exchange models and proposing new ones (e.g. [275]), we did not attempt to delve further in this matter. In the next section we will concern ourselves with the important potential of polarisation accounting for perturbations induced by the presence of the scattering electron.

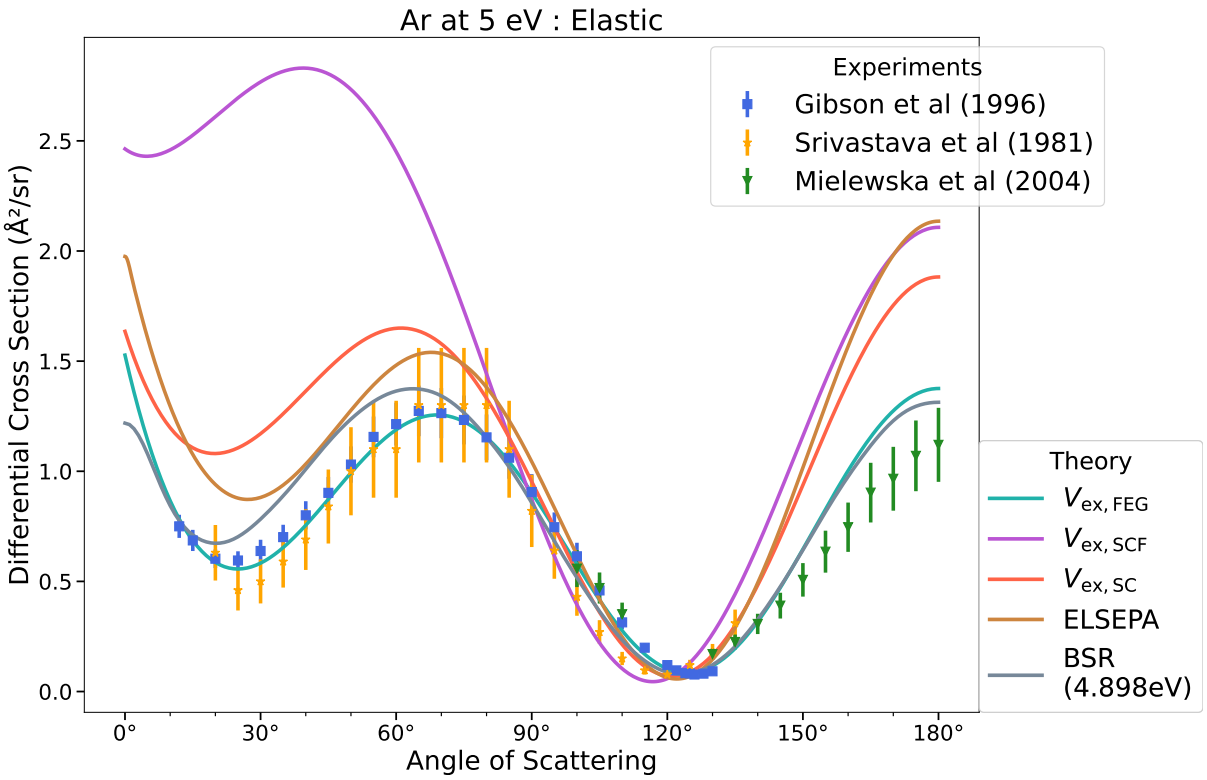

Figure 10.11: Comparison of DCS for an electron scattering off argon at 5 eV from three different local exchange potentials $V_{\text{ex,FEG}}$ (10.39), $V_{\text{ex,SCF}}$ (8.41) and $V_{\text{ex,SC}}$ (10.47). The static potential is obtained from Koga's [522] analytical HF density, while the correlation polarisation is V_{kob} (10.71) below. Other theoretical curves are from ELSEPA [803] and BSR calculations from Zatsarinny and Bartschat [998] and Zatsarinny *et al.* [1002] extracted from `lxcat.net/bsr`. Experimental data are from ■ [331], ⋆ [871] and ▼ [644].

10.3.3 Polarisation

It is well known [824, eq.(1.9)] that the dipole polarisation potential of any atomic target behaves adiabatically and asymptotically as $V_{\text{pol}}^{\infty}(r) = -\alpha_{\text{d}}/2r^4$ for $r \to \infty$. The factor α_{d} is the **d**ipole polarisability of the atom or molecule expressing the deformation of the electronic cloud under a static and homogeneous electric field. This situation corresponds ideally to an extremely slow electron (~eV) and far from the atom ($\gg a_0$). Such premise allows us to assume that the electronic cloud polarises instantly due to the outer presence of the scattering electron without any overlap of their respective wave functions.

The base of this image crumbles when the electron is near the target (small $r \lesssim a_0$) and at fast velocities (ε ~keV) [327, p.100-1]. At closer distances, the molecule polarises to higher orders than the dipole (lowest order) [257]. At faster velocities, the molecule does not have enough time to polarise fully. Those invalidating situations are actually connected by the fact that the electron is not positioned definitely but is spread over a region determined by its wavefunction. This implies that the response of the bound electrons is non-local and dynamic [524, eq.(11)] which leads to the necessity of treating the potential non-adiabatically [332]. Here, we briefly review the attempts of emulating non-adiabatic effects at small radii and/or high velocities through fully- or semi- empirical modifications. We then select a few of those, compare them and assess their performance at intermediate (~ 50 eV) and high (~ keV) energies for atoms and molecules.

History

As seen from the figure 10.12 beside, there is a practical need to abate the unphysical $1/r^4$ abyss of the polarisation potential at small radii. In principle, the radial Schrödinger equation can be solved exactly for a $1/r^n$ potential [710, §2.A]. This is usefully exploited in the modified effective range theory (MERT, see sec 10.1.5) at low energies, when the centrifugal barrier at $\ell > 0$ prevents the electron from penetrating into the region at small radii. The phase shift δ_0 for the s-wave when $n = 4$, can also be defined and converges to a finite value at zero energy. This analytic property has been exploited by Fedus *et al.* [272] with a simple $1/r^4$ potential, who fitted the three lowest phase shifts $\ell \leq 2$ for argon with six parameters (two for each ℓ). Those parameters accounted for all complicated short-range potentials. Agreeable results could be obtained for energies up to 10 eV.

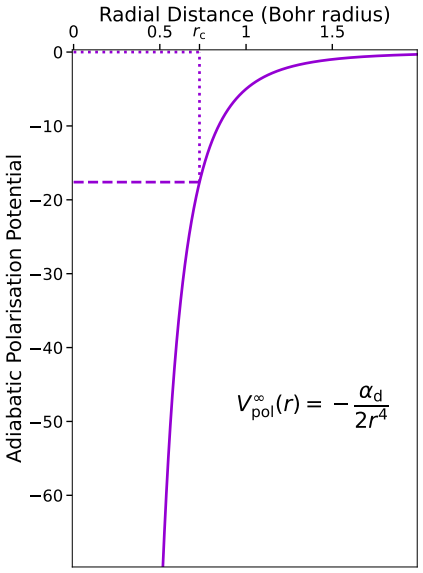

Figure 10.12: Illustrative adiabatic dipole polarisation potential with $\alpha_{\rm d} = 10\,a_0^3$

Nonetheless, at higher energies, when the electron's partial waves may penetrate deeper into the molecular/atomic region where the short-ranged potentials of the molecule dominate, it is clear that the $1/r^4$ trend of the polarisation potential must be somehow corrected.

It is impossible to make in just the preamble of a section, a comprehensive review of how to characterise polarisation forces beyond the asymptotic adiabatic (static) dipole decay. In this subsection, we focus on the most widely used semi-empirical models that roughly try to encompass the complicated nature of polarisation as the electron nears the target.

In early studies, the adiabatic polarisation would either be saturated [905, eq.(5a)] to a definite radius $r_{\rm c}$ (i.e. $1/r_{\rm c}^4 \;\forall\, r \leq r_{\rm c}$, dashed - - -line on figure 10.12) or simply sharply quelled to zero (dotted ··· line) [103, eqs.(28-31)].

A smoother, popular empirical correction is to introduce cutoff functions [197, 572, 946, §3., eq.(4), eq.(13)] to the adiabatic dipole polarisation potential:

$$V_{\rm pol}(r) = V^{\infty}_{\rm pol}(r) \cdot C_{\rm p}(r) = -\frac{\alpha_{\rm d}}{2r^4} C_{\rm p}(r)\ , \tag{10.50}$$

of which the exponential with the exponent 6 [551, 834, p.51:eq.(147), p20:eq.(26)]:

$$C_{\rm p,cut}(r) = (1 - \exp((-r/r_{\rm c})^6))\ , \tag{10.51}$$

was the most widespread [135, 166, 389, eq.(41), eq.(4.1), eq.(1)] before it was superseded in the 80s' with *ab initio* approaches [257, 332, 672]. The cutoff radius $r_{\rm c}$ was usually matched heuristically in order to reproduce a specific feature in the cross section, such as the position of a resonance peak [127, eq.(13)]

In the meantime, more polished ways of incorporating non-adiabatic curbing at small r was through the Buckingham potential [126]:

$$V_B(r) = -\frac{\alpha_{\rm d}}{2(r^2 + r_{\rm B}^2)^2}\ . \tag{10.52}$$

This formula was also frequently used for permanent quadrupole and dipole potentials [197, §3]. Its principal advantage is that it lends itself easily to analytical treatment under the first

Born approximation [397, eq(2)]. It was thus used as an empirical model to fit exponentially decaying DCS [114, 115, fig.3, 4] at very small angles (θ <10°) and high energies (ε > 200eV) corresponding to small momentum transfers ($qa_0 \ll 1$). The parameter r_b could then be adjusted to match the decaying slope in semi-logarithmic scale [453, eq(21)] as : $\lim_{k\to 0} \mathrm{d}\sigma \sim \exp(kr_\mathrm{B})\,\mathrm{d}\Omega$.

When comparing the value of r_B at various energies, an empirical law [653, eq.(8-9)] of its dependence with energy could be obtained [801, eqs.(4-5)]:

$$r_\mathrm{B}^2 = \frac{\alpha_\mathrm{d}}{2} Z^{-1/3} b_\mathrm{pol}^2 \quad \text{with} \quad b_\mathrm{pol}^2 = \max\left[\frac{\varepsilon_0 - 50\,\mathrm{eV}}{16\,\mathrm{eV}}, 1\right] \tag{10.53}$$

Other variants of the Buckingham potential with an empirically parametrised cutoff radius $r_\mathrm{b}(\varepsilon)$ were also explored [4, 470, 729]. The results are seductively deceiving because the sensitivity of the DCS on the cutoff radius is such that one can always obtain alluring agreement despite the crude simplicity of the polarisation potential used. An alternative way to incorporate non-adiabaticity was to assume that the polarisability $\alpha_\mathrm{d}(\mathrm{v}_0/r)$ depended on the electron's incident v_0 or local v velocity and distance r from the molecule [389]. At large v/r ratios (fast and/or close) this apparent polarisability would differ from its static value α_d [453, table 12]. This could be also effectively done through a semi-classical down-scaling [955, §V-VI]: $1/f(r,\varepsilon_0)\cdot\alpha_\mathrm{d}/2r^4$.

We note additionally, that some studies [53, 469, 729, 772, eqs.(1-2), eq.(4), eq.(1), eq.(4)] proposed to adjust the exponents in the Buckingham potential that led to a generic form $V_\mathrm{B,gen} \sim r^n/(r^m + r_\mathrm{b}^m)^{(4+n)/m}$, in order to cancel the value at $r = 0$ like with the exponential cutoff (10.51).

More formally, non-adiabatic* effects are found to behave asymptotically as $\sim -c/r^6 + O(1/r^7)$ for hydrogen [229, eq.(10)], atoms [824, eq.(1.9)] and also for molecules albeit in more complex manners (angular dependence) due to anisotropic effects. It is noteworthy to mention that a derivation based on the eikonal (or Glauber [337]) approximation at high-energies leads to an opposite sign of c [137, eq.(2.26)], when the potential is deduced from the inverse Fourier transform of the scattering amplitude [137, eq.(2.24)] in the second Born approximation. This may signify an inconsistency when mixing terms in the first and second Born approximation (the scattering amplitude was of second order but the derived potential was based on a first order!).

In the correct derivation, the coefficient c of the r^{-6} term is a weighted sum of (i) the quadrupole polarisability α_q, the inverse (ii) third $\propto \Delta\mathcal{E}^{-3}$ and (iii) fourth $\propto \Delta\mathcal{E}^{-4}$ momenta of the (dipole) optical oscillator strength distribution.

Some proposals separated each asymptotic power into a series of Buckingham-like potentials [496, eqs.(24-28)], which we call the "augmented Buckingham":

$$V_\mathrm{B,aug} = -\frac{\alpha_\mathrm{d}}{2(r^2 + r_\mathrm{B}^2)^2} + \frac{cr^2}{(r^2 + r_\mathrm{B}^2)^4} \tag{10.54}$$

Getting rid of empirical corrections, there were also other damping functions f_n proposed [329, eq.(13)] each applying to their respective power of $1/r^n$:

$$V_\mathrm{damp} = -\frac{\alpha_\mathrm{d}}{2r^4} f_4(r) - \frac{c_6}{2r^6} f_6(r) - \frac{c_7}{2r^7} f_7(r) - \frac{c_8}{2r^8} f_8(r) + \ldots \tag{10.55}$$

The expansion coefficients c_n as well as the damping functions are obtained from the average unperturbed density distribution of the target.

Nevertheless, the decomposition into $\propto -a/r^4 + c/r^6 + \ldots$ can be actually taken as the asymptotic expansion of a single whole function. This was the philosophy of Onda [717, eqs.(51-a&b)] who proposed two other cutoff functions, to be replaced in (10.50), which yield the desired $1/r^6$ term at $r \gg a_0$:

*We recall that 'non-adiabatic' means that the response of the molecular cloud is not instantaneous and thus that the energy of the system is correlated to the invading electron's kinetic energy and position [138, §I]

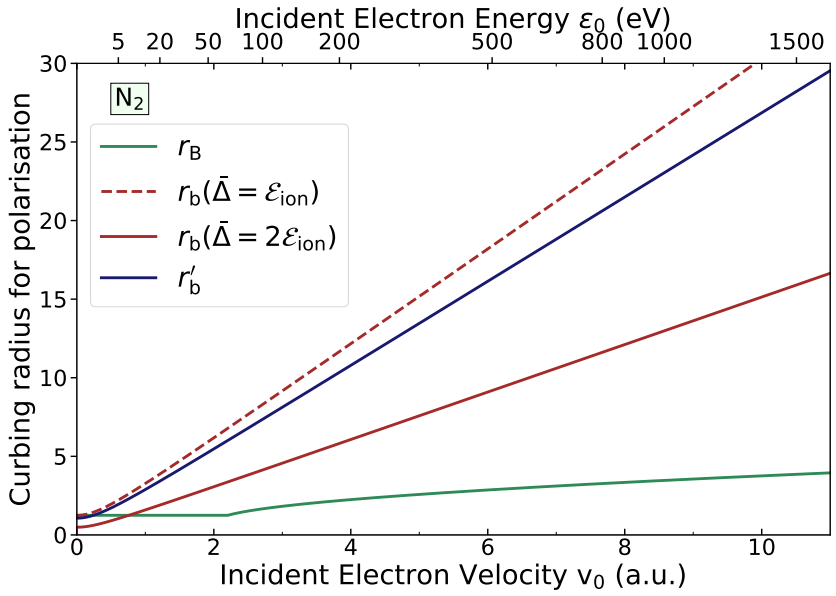

Figure 10.13: Curbing radii used by different models for the Buckingham potential (10.53,10.57) or in the polarisation cutoff functions (10.56). The present issue is that the purely empirical formulae for r_B gives a more reasonable elongation of the curbing radius with incident velocity v_0 than any of the semi-empirical attempts r_d to incorporate non-adiabatic effects. In particular, r'_d is based on an approximate estimation of the higher-order dipole moments (8.44a–8.44c).

$$\left.\begin{aligned} C_{\mathrm{p,exp}} &= \exp\left(-\frac{r_\mathrm{d}^2(v_0)}{r^2}\right) \\ C_{\mathrm{p,inv}} &= \frac{1}{1+r_\mathrm{d}^2(v_0)/r^2} \end{aligned}\right\} \sim 1 - \left(\frac{r_\mathrm{d}(v_0)}{r}\right)^2 \quad \text{for } r \gg r_\mathrm{d}\,. \tag{10.56}$$

Non-adiabaticity resides in the behaviour of the **d**iabatic radius r_d in the electron's incident velocity v as [719, eq.(5-6)]:

$$r_\mathrm{d}^2(v_0) = \frac{(3\bar{\Delta} + 6v_0^2)}{\bar{\Delta}^2} - \frac{\alpha_\mathrm{q}}{\alpha_\mathrm{d}}\,. \tag{10.57}$$

This expression comprises an average excitation energy $\bar{\Delta}$ (in hartrees) which needs to be determined in virtue of either the third or fourth inverse momenta of the oscillator strength distribution. It is expected to rove above the ionisation threshold $\bar{\Delta} \gtrsim \mathcal{E}_\mathrm{ion}$ of the target [719, §II.A]. The term added in blue represents the ratio of the quadrupole α_q on the dipole α_d polarisabilities. It was not present in the original works [717, 719, eq.(32), eq.(5)], we tentatively restored it in analogy with the polarisation potential of atomic targets [824, eq.(1.9)].

Recently, we proposed [812, eqs.(9-10) see also §II.D(iii)] to unite the cutoff functions to the Buckingham potential to represent the non-adiabatic $1/r^6$ expansion as:

$$V_\mathrm{b}(r) = -\frac{\alpha_\mathrm{d}}{(r^2 + r_\mathrm{b}^2)^2} \quad \text{with} \quad r_\mathrm{b}^2 \equiv \frac{1}{2} r_\mathrm{d}^2(v_0) \quad \text{from eq.(10.57)}\,, \tag{10.58}$$

instead of the other two forms (10.56). The introduction of a new $r_\mathrm{b} = r_\mathrm{d}/\sqrt{2}$ is just related to the fact that $1/(1+\epsilon^2)^2$ expands as $\sim 1 - 2(\epsilon^2) + 3(\epsilon^4)\ldots$ for $\epsilon \ll 1$.

Originally [812, p.3-top-right], we had defined the average excitation energy parameter $\bar{\Delta}$ as the ionisation threshold: $\bar{\Delta} \equiv \mathcal{E}_\mathrm{ion}$. Later, we realised that the curbing radii $r_\mathrm{b}(v)$ from formula (10.57) are too large at intermediate energies > 20 eV (could be a factor 2 or 10 depending on

v_0 see figure 10.13) which causes a premature extinction of polarisation at intermediate energies (the polarisation potential becomes underestimated from 100 eV onward). Here, after noticing that our $r_b(v_0)$ from (10.57) grows much faster than $r_B(v_0)$ from (10.53), we tentatively risked setting $\bar{\Delta} = 2\mathcal{E}_{ion}$. This is an arbitrary empirical adjustment so as to soften the slope of r_b with the electron energy (see figure 10.13). We will see below that although this gives agreeable results for molecules within the limits of the approximations taken, it is an unsound guess for argon (figs. 10.15&10.18b). This is a sign that non-adiabatic effects are more complicated than what can be conveyed through a simple Buckingham potential.

A similar definition to (10.57) was used for the cutoff radius [470, 495, eq.(2b)], though for a modified Buckingham potential made to annihilate at the origin and which does not yield the proper coefficient for the asymptotic decay.

There were other suggestions [1008, eq.(3)] for fixing r_d, not in regard of the asymptotic behaviour of $V_b(r)$, but at smaller radii in relation to the *correlation* potential V_{co} which we briefly present below.

Correlation

As mentioned earlier in this subsection, the potential perceived by the invading electron due to the perturbed molecular cloud is *non-local*. This implies that the interaction V_{int} would have to be modelled through an integral:

$$\text{non-local interaction : } \int_{\mathbf{r}'} V_{int}(\mathbf{r},\mathbf{r}')\psi(\mathbf{r}')\,\mathrm{d}^3\mathbf{r}' \,, \tag{10.59}$$

with the wavefunction $\psi(\mathbf{r}')$ of the invading electron.

Since the wavefunction of the invading electron is unknown, including non-local interactions must in principle be done iteratively. Nonetheless, a first way to emulate non-local correlation effects is to represent the invading electron by a diffuse Gaussian spherical distribution with a certain spread [98]. As a first-order approximation, one can then calculate the energy perturbation on the molecular or atomic wavefunction from the coulomb interaction of the electron at $\mathbf{r}$ spread over a certain region [276]. Nevertheless, this requires accurate knowledge of the target's wavefunction and computing the overlap integral at each point $\mathbf{r}$. It is therefore desirable to obtain a local approximation to the correlation potential.

The idea underlying the local density approximation (LDA) [327], is to approximate this correlation through a local potential V_{co} based on the average electron density $\rho(\mathbf{r})$ at the position $\mathbf{r}$. This approximation builds upon the framework of the density-functional theory (DFT) to which quick and extensive introductions can be respectively found in Jones [467] and Iadonisi *et al.* [416]. If $\mathcal{E}_{co}$ represents the total energy due to inter-electron correlation, then the potential V_{co} can be derived as a functional derivative of the density [327, 527, eq.(2.7), eq.(24a)]:

$$V_{co}(\mathbf{r}) = \frac{\partial \mathcal{E}_{co}}{\partial \rho(\mathbf{r})} \,. \tag{10.60}$$

Although models stemming from the density-based approach rely more or less on a similar set of fundamental equations, there may be many different analytic expressions for the correlation potential scattered in the literature. Their difference depends on the assumptions taken to represent the pair correlation function [416, 467, p.10:§3.5, p.599:§6.2.3]. The most used models are those for which an analytic expression for this pair correlation was proposed [185, 304, 567, 742].

The most popular expressions for the density-based correlation potential rely on the free electron gas approximation [728, 742], whose best fit is believed to be given by Perdew and Zunger [742, p.5075:appendix C. and table XII.] from Ceperley and Alder's [165] parameters:

$$V_{\rm co,FEG}(\mathbf{r}) = \begin{cases} (0.0311 + \frac{2}{3}0.002 r_{\rm s})\ln r_{\rm s} - 0.0084 r_{\rm s} - (0.048 + \frac{0.0311}{3}) & \text{if} \quad r_{\rm s} < 1 \\ -1.423 \dfrac{1 + \frac{7}{6}\beta_1\sqrt{r_{\rm s}} + \frac{4}{3}\beta_2 r_{\rm s}}{(1 + \frac{7}{6}\beta_1\sqrt{r_{\rm s}} + \frac{4}{3}\beta_2 r_{\rm s})^2} & \text{if} \quad r_{\rm s} \geq 1 \end{cases} \qquad (10.61)$$

$$\text{with} \quad \beta_1 = 1.0529 \ \text{ and } \ \beta_2 = 0.3334 \,,$$

expressed in terms of the average inter-electron distance $r_{\rm s}$ in the gas:

$$r_{\rm s}(\mathbf{r}) \equiv \sqrt[3]{\frac{3}{4\pi\rho(\mathbf{r})}} \,. \qquad (10.62)$$

Caution is advised when consulting this formula dispersed in the literature. It is rare to find it unstained by an error sign either in the $r_{\rm s} < 1$ expression [494, 801, 803a, eq.(7a), eq.('46a'), eq.(7)] or in the $r_{\rm s} > 1$ one [327, eq.('44'):$\gamma \not> 0$].

A more elaborate correlation potential appeared later [567] which considers also the kinetic energy density of the electrons based on their local density. This potential $V_{\rm co,KDF}$ (for **k**inetic **d**ensity **f**unctional) was introduced earlier in chapter 8 in section 8.2.3. We do not recall it here but we continue our description of the combined polarisation-correlation model.

Critique

As explained before, the polarisation potential $V_{\rm pol} \propto \alpha_{\rm d}/2r^4$ of an atom/molecule in the presence of a point charge (the electron) is ill-defined when this intruding electron mingles with the electronic cloud of the target. For this reason, a complete description of the perturbation potential (correlation+polarisation) was contrived [728] in which one uses $V_{\rm co}$ at radial distances below $r_{\rm t}$ and $V_{\rm pol}$ beyond [328, 753, eq.(16),]:

$$V_{\rm cop} = \begin{cases} V_{\rm co}(\mathbf{r}) & \text{for} \quad \|\mathbf{r}\| < r_{\rm t} \\ V_{\rm pol}(\mathbf{r}) & \text{for} \quad \|\mathbf{r}\| \geq r_{\rm t} \end{cases} \,. \qquad (10.63)$$

For molecular targets, one has to consider a harmonic expansion of the potential as in chapter 8 equation (8.31). Then, for each harmonic order $l = 0, 1, 2 \ldots$, the corresponding transition radius $r_{\rm t}^{(l)}$ is implicitly defined as the outermost value at which $V_{\rm co}^{(l)}(r_{\rm t}^{(l)}) = V_{\rm pol}^{(l)}(r_{\rm t}^{(l)})$. Usually, for homodiatomic molecules only the isotropic $l = 0$ component of the (asymptotic) polarisation is considered, so that $r_{\rm t} \equiv r_{\rm t}^{(0)}$ is determined only for that case $l = 0$.

In principle, any combination of $V_{\rm co}$ and $V_{\rm pol}$ is possible. If the polarisation is chosen as the non-adiabatic $V_{\rm b}$ expression which depends on the electron's incident velocity v_0 via the radius $r_{\rm b}(\mathrm{v}_0)$ from (10.58&10.57), then inevitably the transition radius $r_{\rm t}(\mathrm{v}_0)$ will also depend on the incident velocity and will have to be recalculated for each electron energy.

This non-adiabatic aspect had been overlooked in studies which considered that $r_{\rm t}$ was invariant. For instance, Zhang *et al.* [1008] proposed to use a Buckingham potential with the curbing radius $r_{\rm B}$ chosen so that $V_{\rm B}(r = 0) = -\alpha_{\rm d}/2r_{\rm B}^4 = V_{\rm co}(r = 0)$, and so the efforts in including non-adiabatic effects (at faster velocities) are lost.

A major issue with the correlation potential is that it remains exclusively and entirely an intrinsic property to the atom or molecule without the deranging presence of the intruding electron. It indeed was originally conceived as a correction potential [527, eqs.(2.5–7)] accounting

for inter-electronic correlation in space which is overlooked when integrating the total density $\rho(\mathbf{r})$ in the electronic Coulomb repulsive potential:

$$\text{Overestimated inter-electron Coulomb interaction } : \frac{1}{2}\int \frac{\rho(\mathbf{r})\rho(\mathbf{r}')}{|\mathbf{r}-\mathbf{r}'|}\,\mathrm{d}^3\mathbf{r}\,\mathrm{d}^3\mathbf{r}' \,. \tag{10.64}$$

Exchange plays also its role in correcting this overestimation. In any case, $V_{\mathrm{co}}(\mathbf{r})$ ought to be interpreted as the corrective potential that any electron located at $\mathbf{r}$ would feel because of the "Coulombic hole" which it causes for being there [185]. This supposes that V_{co} can be seen as a local modification of the overall static potential V_{s} given by the ground-state distribution of charges ρ [527]. Normally, the "size" of this hole depends on the local velocity of the electron [185, eqs.(2, 12&14)]. This velocity is assumed to be derivable on the basis of the local kinetic energy as a functional of the density [567, eq.(8)]:

$$\text{local kinetic energy (Weizsacker)} : \frac{1}{8}\left[\frac{|\nabla\rho(\mathbf{r})|^2}{\rho(\mathbf{r})} - \triangle\rho(\mathbf{r})\right] . \tag{10.65}$$

From this analysis, we may suppose that the correlation potential as used in *scattering* problems is expected to be not severely invalid under two assumptions:

1. The invading electron has a *local* velocity similar to the host electrons from the molecule.
2. The alteration of the local electron density $\rho(\mathbf{r})$ of the target under the presence of the invading electron is small enough to be considered as a correction.

Again, our problem is that non-adiabatic effects might appear when the incident electron is very fast ($> 10\,\mathrm{keV}$). In those cases, one should also consider scaling down V_{co}. One usually assumes that the short-range effects of polarisation dwindle as the electron becomes faster so that V_{co} can be discarded altogether leaving only the asymptotic tail $-\alpha_{\mathrm{d}}/2r^4$.

A very effective method of attenuating correlation forces for fast electrons was introduced by Salvat [801, eq.(9)], where instead of (10.63), a more subtle transition is operated between polarisation and correlation at $r < r_{\mathrm{t}}$:

$$V_{\mathrm{cop,max}} = \begin{cases} \max\{V_{\mathrm{co,FEG}}(\mathbf{r}), V_{\mathrm{B}}(\mathbf{r})\} & \text{for } \|\mathbf{r}\| < r_{\mathrm{t}} \,, \\ V_{\mathrm{B}}(\mathbf{r}) & \text{for } \|\mathbf{r}\| \geq r_{\mathrm{t}} \,. \end{cases} \tag{10.66}$$

Since both polarisation and correlation are attractive (negative), this means that only the values of $V_{\mathrm{co,FEG}}$ which are higher (closer to zero) than V_{B} are effectively included in the joint potential. At high enough energies so that $V_{\mathrm{B}}(r) > V_{\mathrm{co,FEG}}(r)\ \forall\, r < r_{\mathrm{t}}$, then this amounts to completely discarding $V_{\mathrm{co,FEG}}$. This has proven to be a major improvement not only to incorporate non-adiabatic effects but also to overcome the inadequacy of the free electron gas correlation potential at larger radii [327, p.111-2]. This version of the correlation-polarisation was implemented in the code ELSEPA [803a] to which results will be compared in the next subsection.

Additionally, an alternative way to derive the correlation-polarisation potential is via its relation to the absorption potential V_{abs} [879, eq.(1)] (presented in the next section 10.3.4). The advantage is that absorption and correlation/polarisation would be treated in a coherent way in regard of the eigenvalues of the molecule's Hamiltonian, though this would require to have a good knowledge of the absorption potential in the first place. Finally, we ought to mention that polarisation effects may be incorporated *ab initio* as in the polarised orbital [925] and close-coupling [413] approaches. We did not explore these last possibilities which are too complex to be compared with semi-empirical models.

Below, we illustrate how the correlation-polarisation potential affects the differential scattering cross section of electrons at higher (> 200 eV) and intermediate (> 2 Ryd) energies for various selected targets. In the case of argon, we risked exploring the validity of semi-empirical potentials at low energies.

Comparison

For this mini-study, we selected four different correlation-polarisation potentials among the ones introduced above:

- Exponential cutoff :

$$V_{\mathrm{p,cut}}(r) = V^{\infty}_{\mathrm{pol}}(r) \cdot C_{\mathrm{p,cut}}(r) = \alpha_{\mathrm{d}} \frac{(1 - \exp(-(r/r_{\mathrm{c}})^6))}{2r^4} \,, \tag{10.67}$$

- Non-adiabatic Buckingham :

$$V_{\mathrm{B}}(r) = \frac{\alpha_{\mathrm{d}}}{(r + r^2_{\mathrm{B}}(\varepsilon_0))^2} \,, \tag{10.68}$$

- Free electron gas correlation polarisation :

$$V_{\mathrm{cob}}(r) = \begin{cases} V_{\mathrm{co,FEG}}(r) & \text{for } \; r < r_{\mathrm{t}}(\varepsilon_0) \\ \dfrac{\alpha_{\mathrm{d}}}{2(r^2 + r^2_{\mathrm{b}}(\varepsilon_0))^2} & \text{for } \; r \geq r_{\mathrm{t}}(\varepsilon_0) \end{cases} \,, \tag{10.69}$$

- Kinetic correlation polarisation

$$V_{\mathrm{ko+p}}(r) = V_{\mathrm{co,KDF}}(r) + V_{\mathrm{pol}}(r) \cdot C_{\mathrm{p,exp}}(r) = V_{\mathrm{co,KDF}}(r) + \frac{\alpha_{\mathrm{d}} \exp\left(-2\dfrac{r^2_{\mathrm{b}}(\varepsilon_0)}{r^2}\right)}{2r^4} \,. \tag{10.70}$$

All radii $r_{\mathrm{b}}(\varepsilon_0)$ (10.57) with $\bar{\Delta} = 2\mathcal{E}_{\mathrm{ion}}$ (twice the ionisation potential), $r_{\mathrm{B}}(\varepsilon_0)$ (10.53), functions of the incident energy ε_0 (or velocity $\mathrm{v}_0 \cong \sqrt{2m_{\mathrm{e}}\varepsilon_0}$) have been defined previously except r_{c} which is set to $1.592a_0$ for N_2 [135, p.1706:above eq.(42)]. Note that this radius r_{c} was often used as a parameter adjusted to fit experimental DCS at different energies, so that $r_{\mathrm{c}} = 3.1a_0$ [863, p.4022] was found to be convenient at lower energies (~eV). An arbitrary value of 1.7 a_0 will be used of Ar. We did not attempt to adapt r_{c} according to the incident velocity v_0. Differences in agreement at different energies will serve to emphasise the importance of non-adiabatic effects.

Finally, the comparison with ELSEPA [803] will highlight the importance of properly combining polarisation and correlation; at lower energies, by not letting polarisation override correlation effects; and at higher energies, by abating the free electron gas correlation $V_{\mathrm{co,FEG}}$ as done in (10.66) instead of (10.69).

Those potentials are represented on figures 10.14 for O_2 and Ar. At higher energies, non-adiabatic Buckingham potentials V_{B} and V_{b}, comprised by V_{cob}, decrease as a result of the expansion of the respective curbing radii r_{B} (10.53) and r_{b} (10.57). The transition radius r_{t} defined implicitly in (10.69) also expands as a consequence. One can see that the free electron gas model $V_{\mathrm{co,FEG}}$ (10.61) in V_{cob} overestimates correlation compared to the kinetic density model $V_{\mathrm{co,KDF}}$ (8.51) in $V_{\mathrm{ko+p}}$ at any radial distance.

At lower energies (<20 eV), the values of curbing radii r_{b} and r_{B} are too small and this causes a spurious overestimation of polarisation forces at small radii as seen on figure 10.14c. As a consequence, we have to relinquish the idea of promoting the Buckingham potential to a

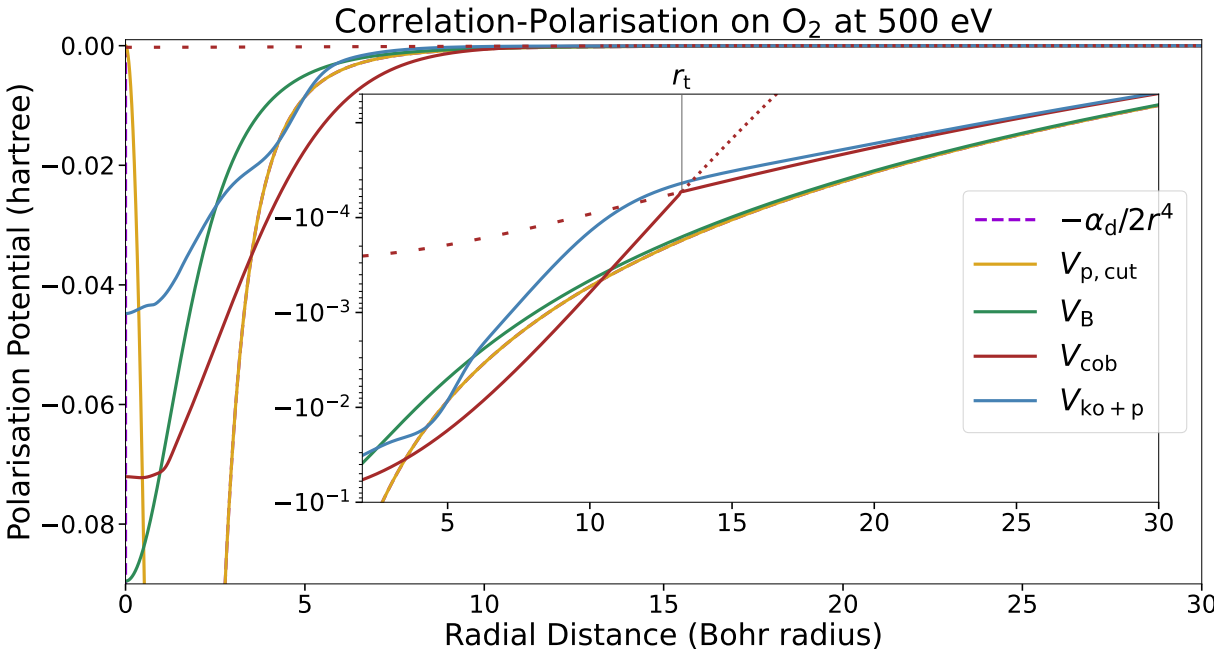

(a) Non-adiabaticity at higher energies can be seen as the gradual decrease of the Buckingham potentials V_B (green) and V_b (red) due to the increase of the curbing radii r_B and r_b, while the other (adiabatic) potentials, $V_{p,cut}$ and V_{co}, remain fixed.

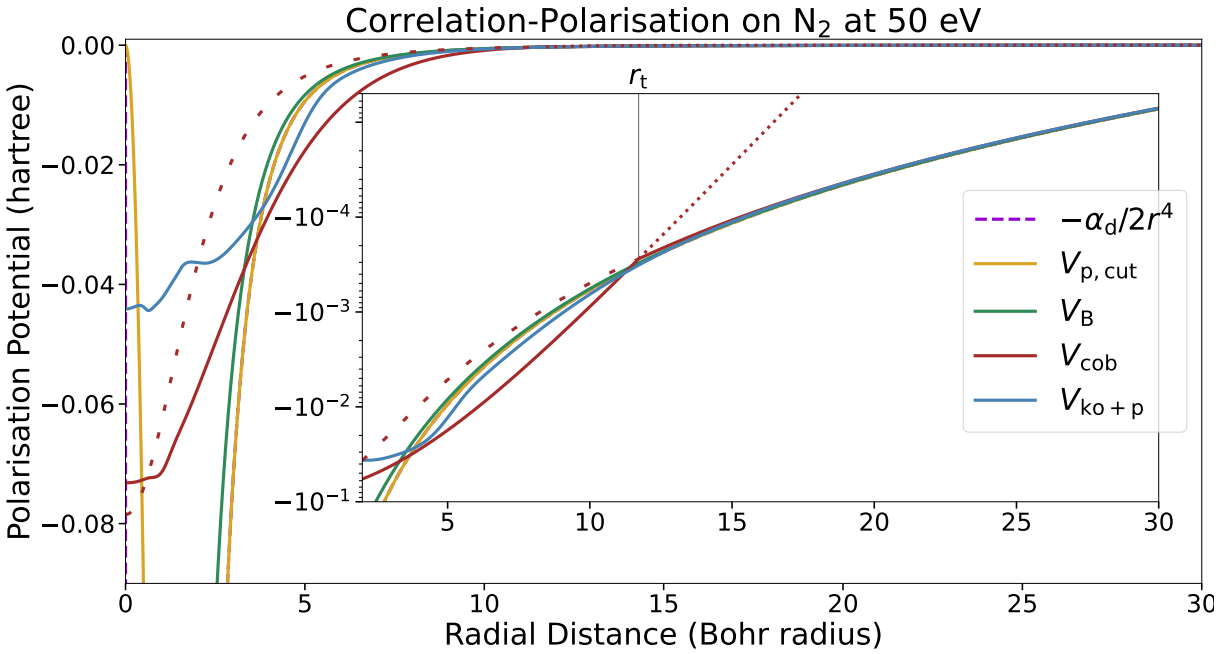

(b) At intermediate energies, non-adiabatic effects are lessened from the shrinkage of the radii r_B and r_b of the Buckingham potentials (sparse dashed - - - and solid —). As a result, the transition radius r_t for the V_{cob} model is also shorter. To be noted additionally is the swelling of V_{ko+p} — from the exponentially damped polarisation in eq. (10.70).

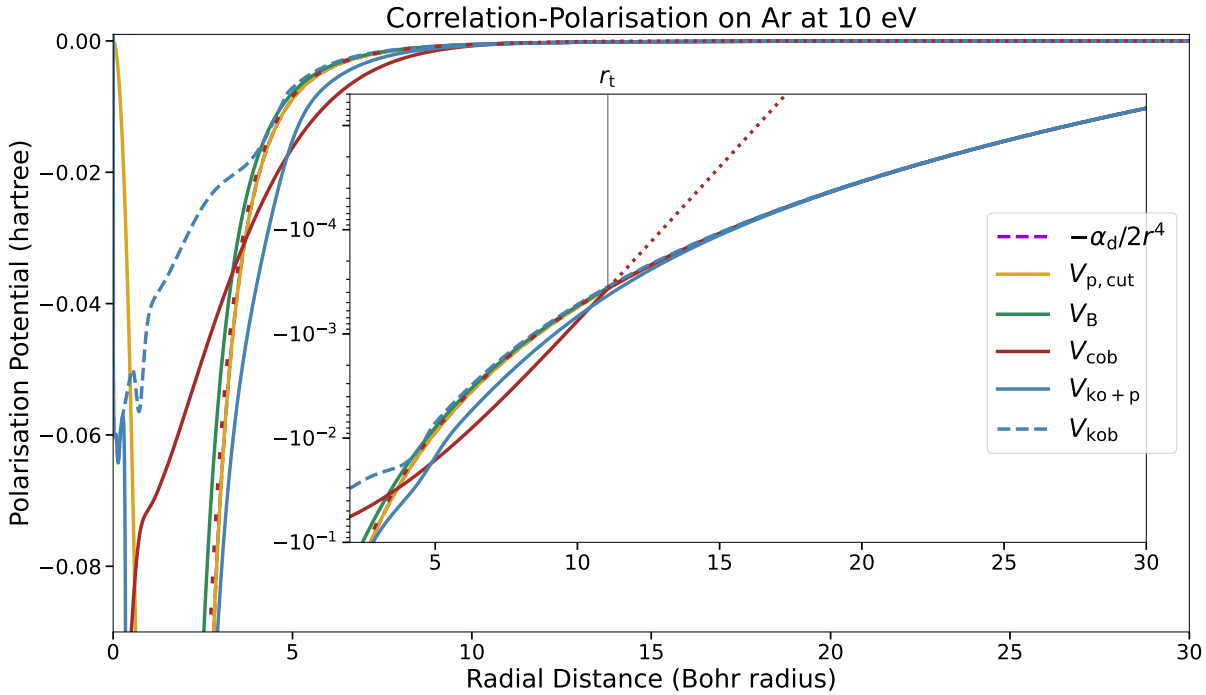

(c) At lower energies, the Buckingham potential V_B (green) may greatly exceed the correlation potential estimated at small distances. The shrinkage of r_b is so intense that the polarisation in V_{ko+p} — completely overpowers the KDF correlation in (10.70). The amended potential V_{kob} - - - shows the more sensible combination of correlation and polarisation from (10.71). The potential that clings most onto the asymptotic $-\alpha_d/2r^4$ --- potential is $V_{p,cut}$ — given by the exponential cutoff function (10.51).

Figure 10.14: Selected correlation-polarisation potentials expounded on p.364 for molecular oxygen (top), nitrogen (middle) and argon (bottom) at descending incident energies of the scattering electron. Dotted ($V_{co,FEG}$:eq.10.61) and sparsely dashed (V_b:eq.10.58) lines show the continuation of the stitched V_{cob} potential. The equivalent potential implemented in the program ELSEPA[803] can be visually seen as the highest (closest to zero) of the two V_B (—) and $V_{co,FEG}$ (—) before they meet at r_t.

slightly-more-than-semi-empirical model through the formula (10.57) for r_b. We checked that due to the higher order terms $O(1/r^7)$ in the asymptotic and non-adiabatic expansion of the polarisation potential, the behaviour of the Buckingham potential may not be constrained well over a wide range of energies with the simple non-empirical formula proposed for the curbing radius r_b in (10.57). Instead, an empirical scaling of the type $r_d^2(v_0) = a + bv_0^2$ (as 8.54) with a, b as adjustable parameters, is still sadly needed. The value of those parameters is actually quite arbitrary if one stitches correlation to polarisation at r_t as in (10.63). For illustration, we show in figure 10.18b that with rather arbitrary values ($a = 2.43$, $b = 3$), the amended potential:

$$V_{kob}(r) \equiv \begin{cases} V_{co,KDF}(r) & r < r_t \ , \\ V_b(r, r_b = \dfrac{2.43 + 3v_0}{2}) & r \geq r_t \ ; \end{cases} \tag{10.71}$$

as displayed by the dashed (- - -) line in figure 10.14c, yields a DCS in significantly better agreement with experimental data at lower energies than V_{ko+p} (10.70).

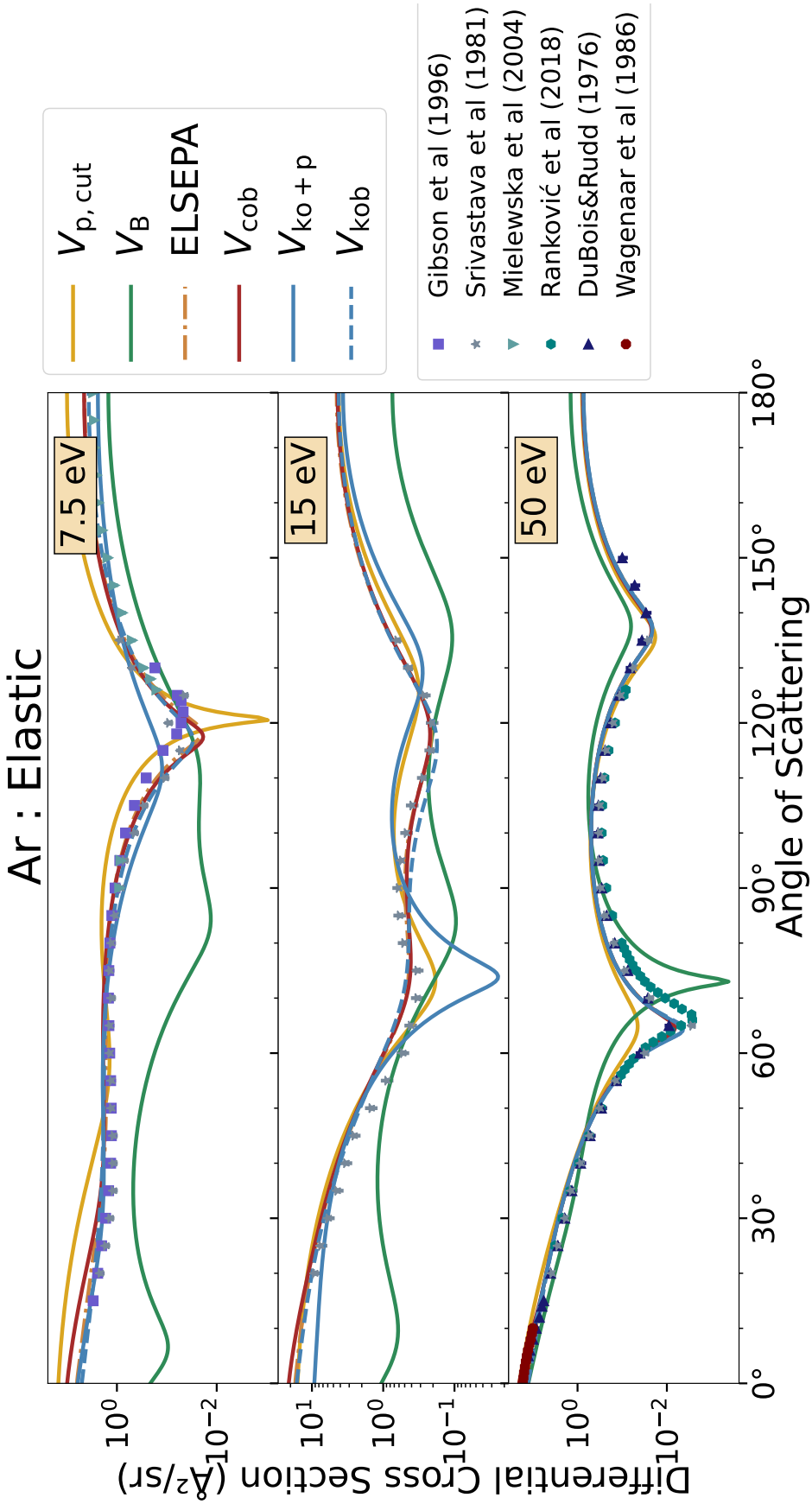

Figure 10.15: Differential cross section for electron elastic scattering by argon.

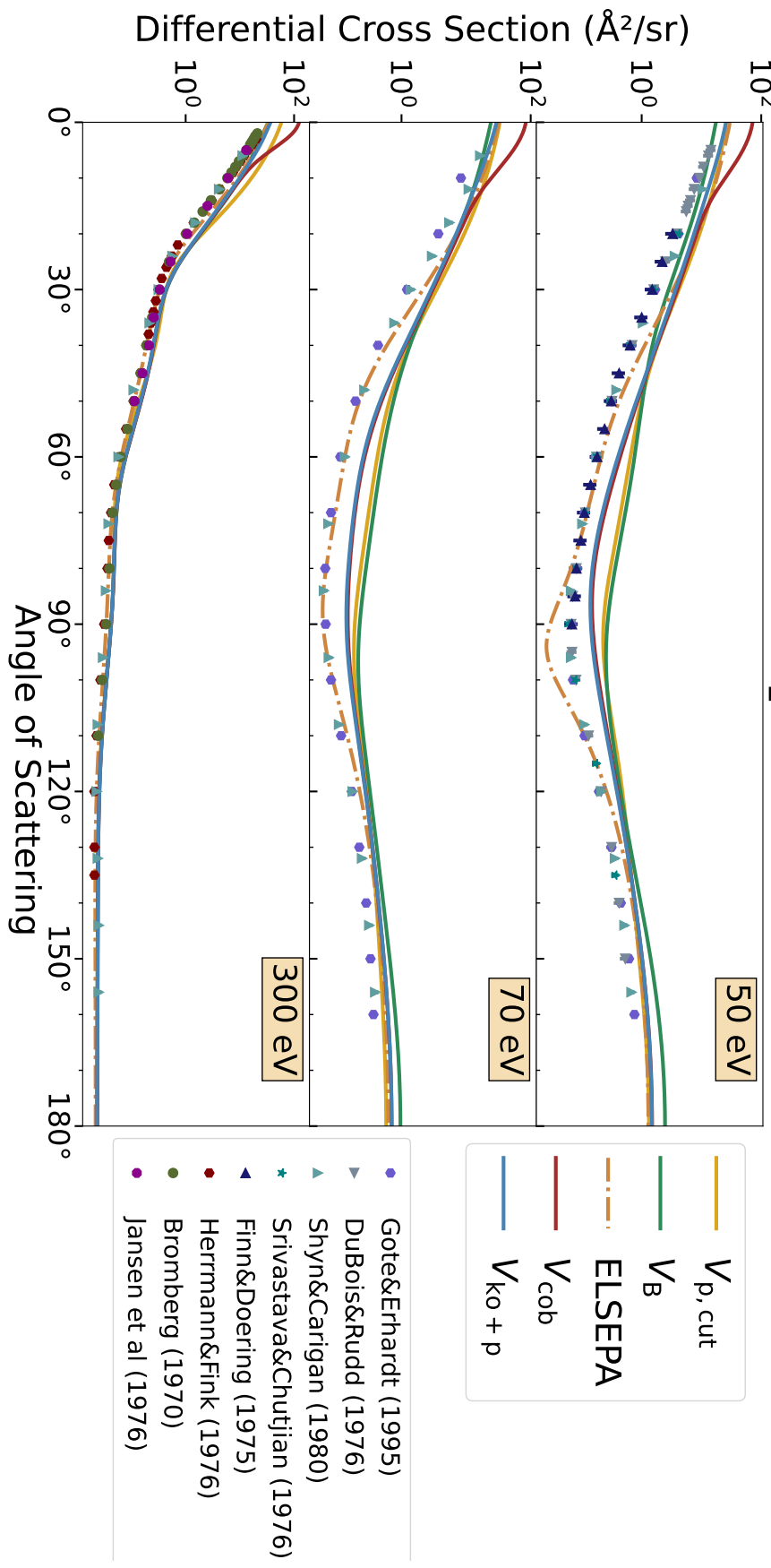

Figure 10.16: Differential cross section for electron elastic scattering by molecular nitrogen.

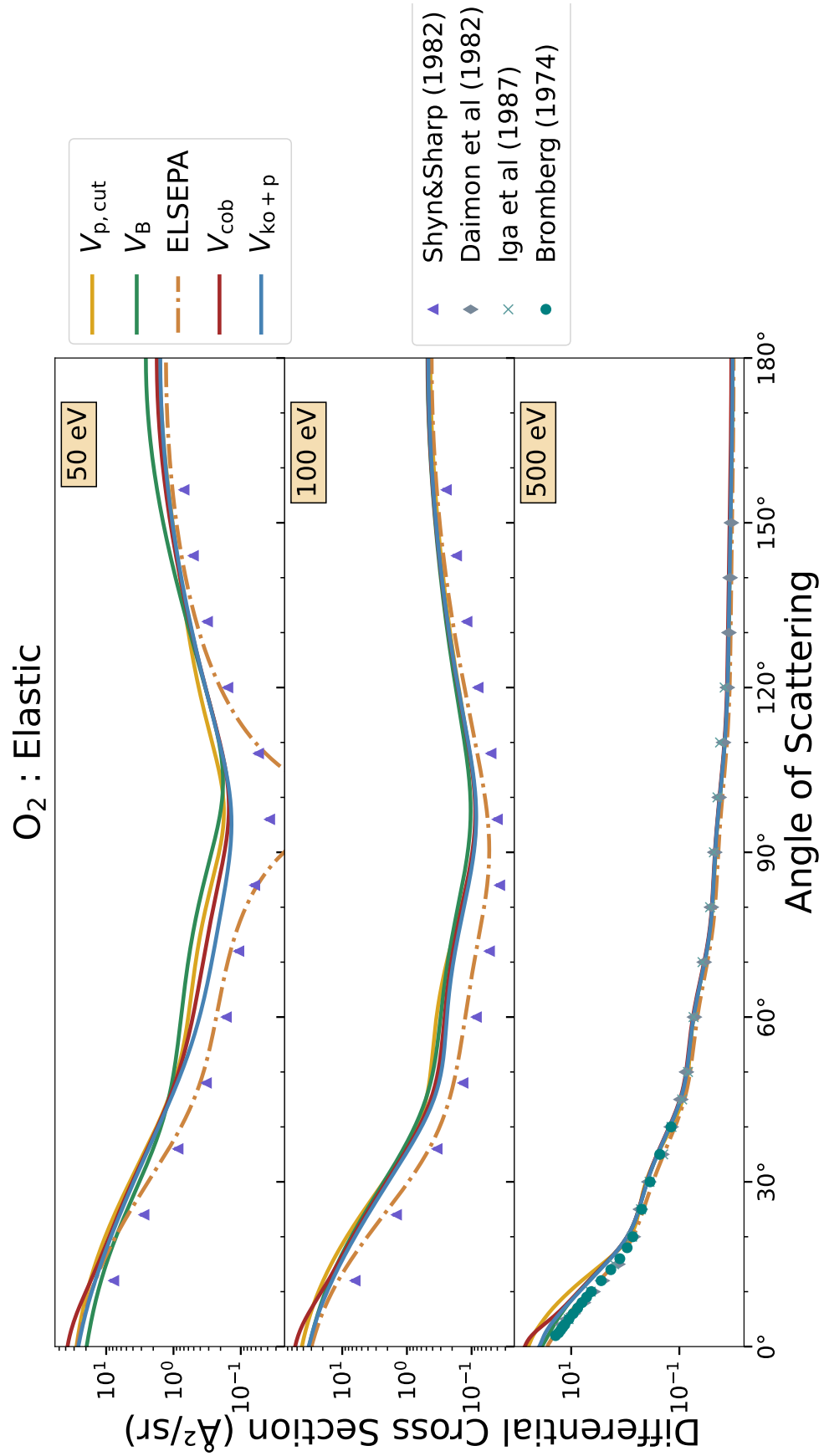

Figure 10.17: Differential cross section for electron elastic scattering by molecular oxygen.

The results for the differential cross section obtained from the four models described above for argon, molecular nitrogen and molecular oxygen are displayed in figures 10.15-10.17. The models differ solely on the implementation of the semi-empirical correlation+polarisation potential. For molecules, the reference program ELSEPA uses the independent atom model whereas our curves are generated through a combination of molecular isotropic and atomic potentials [812].

Argon as an atom, offers the most straightforward comparison between the models because the atomic potential is isotropic. As a preliminary remark, we can see that the accuracy of the results is highly sensitive to the correlation and polarisation models adopted which is why the literature offers an abundance of theoretical studies on electron scattering with noble gases (to cite only a few: [298, 373, 383, 638, 729, 753, 772] and references therein). Since they are the most experimentally studied atoms in the gas phase for electron scattering, they constitute a very fertile field for testing the validity of semi-empirical potential models.

From figure 10.15, we can see that a great malleability is conferred to the DCS shape by the correlation-polarisation potential. For instance, the Buckingham V_{B} or the exponential cutoff models $V_{\mathrm{p,cut}}$, which *a priori* give the least accurate results, could be used in conjunction with a better adjustment of their curbing radius r_{c} and r_{B} to match the experimental data [729]. This is a heavily criticised aspect of semi-empirical models, but quite irresistible given their simplicity and the success that they promise.

As a few examples, [997] obtained good agreement with experimental DCS using a simple Buckingham potential and correlation potential for neon, argon, krypton and xenon by adjusting r_{B} at each energy. Another study [753], using practically the same potential as V_{cob}, obtained somewhat more compelling results than our red curves on figure 10.15, but at the cost of using an empirical modification to the free-electron-gas exchange model of [384, eq.(21)]. With a quenched version of the Buckingham potential at the origin $r = 0$, Reid and Wadehra [772] showed that good agreement could be found for all five noble gases from He to Xe. In general, we may say that the DCS of argon at the energies considered (<50 eV) mainly stems from the first three partial waves ($\ell = 0, 1, 2$), so that if one finds a suitable way to match the calculated phase shifts to some reference [729], then the DCS are almost guaranteed to match accordingly. They can even be more accurate than more costly *ab initio* calculations, as, for instance, the many-body effects from Kohn-Sham density functional [373] and R-matrix (electronic state close-coupling) calculations [298].

Taking now a critical look at the performance of the presently studied compilation of models, we derive the following observations:

- Exponential cutoff $V_{\mathrm{p,cut}}$ (10.67) : The cutoff radius r_{c} is worthless if it is not adjusted at each energy. The value of this model is purely pragmatic but of low theoretical significance. The importance of non-adiabatic effects increases with energy and manifests itself at small angle scattering as can be seen on figure 10.18a.

- Non-adiabatic Buckingham V_{B} (10.68) : The random aspect of the output from this model bespeaks the invalidity of the Buckingham potential at small radii. If the agreement improves slightly with energy, it is only due to the attenuation of polarisation as r_{B} extends with $\varepsilon \to \infty$ as seen on figure 10.13. At high energies ~keV, V_{B} concords with ELSEPA, which is specialised in scattering at intermediate to high (even relativistic) energies. Thus, the empirical formula (10.53) for r_{B} is unreliable below 100 eV. The use of correlation (through eq.10.66) is vital to obtain accurate results. The Buckingham potential was used by Yousif and Matthew [997] to obtain good results at 3 eV with $r_{\mathrm{B}} \sim 2$ a.u. whereas our value (10.53) would be at 1.2 a.u. and yield discouraging results as in figure 10.18b.

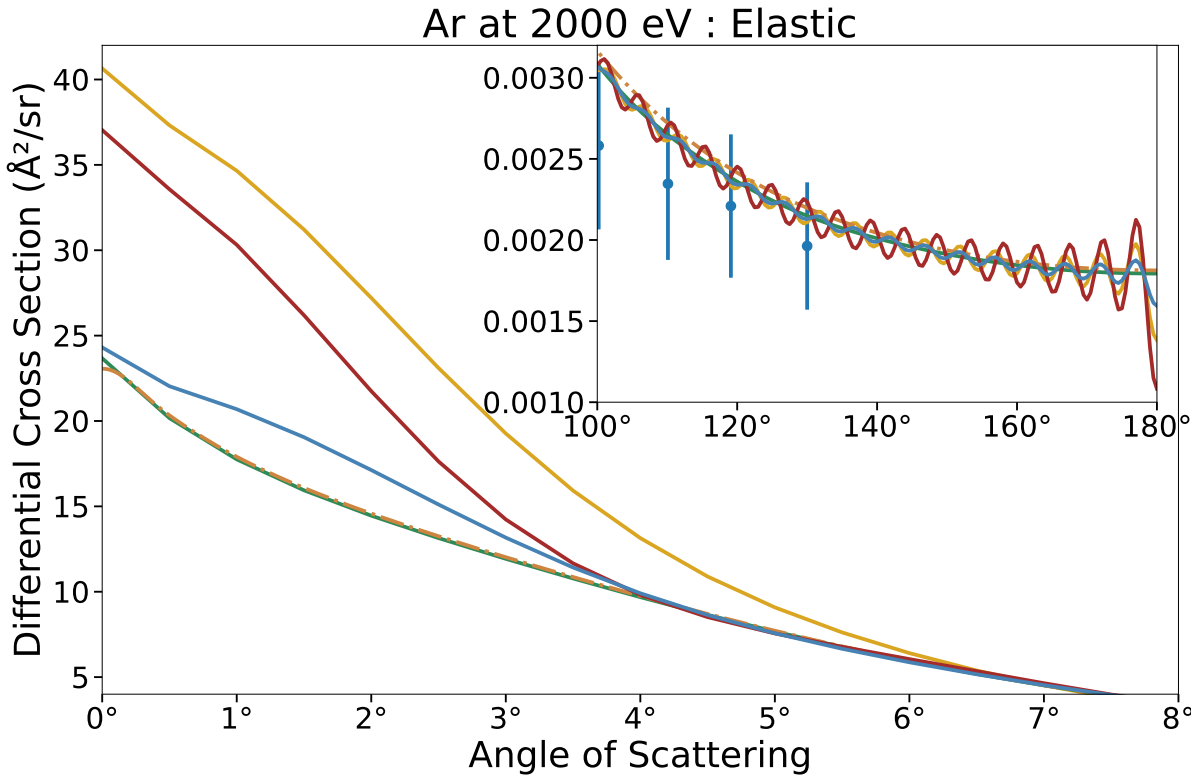

(a) Negligence of non-adiabatic effects at higher energies introduce two principal artifacts in DCS: overestimation at small angles and unphysical wobbling at large angles.

(b) Overestimation of correlation potentials at low energies can completely distort the shape of the DCS which relies principally on only two phase shifts: $\ell = 0$ & $\ell = 1$.

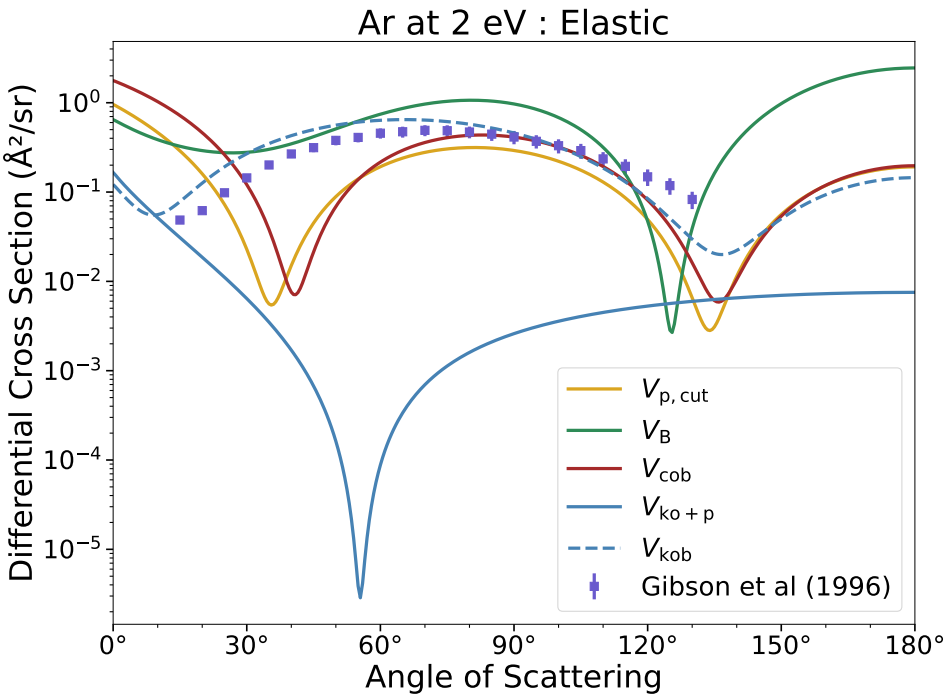

Figure 10.18: Tracing effects from incorrect behaviour of the correlation-polarisation potentials in argon at low and high energies.

- FEG correlation $V_{\rm cob}$ (10.69) : This gives the most agreeable results of all models over a wide range of energies and similar to ELSEPA as expected (the only difference lies in that the polarisation is replaced by correlation at $r < r_{\rm t}$ à la eq.10.63 instead of eq.10.66). The criticism we can make here is at high energies where the fact that the correlation potential is not attenuated poses a problem. First, we may notice that this non-adiabaticity introduces an overestimation ("a bump") at small angles as seen on figure 10.18a. This has another artificial effect at backscattering angles which is the emergence of ripples as seen on the inset of the same figure. Those ripples are not due to unconvergence of the phase shifts but to the correlation potential at small radii which ought to be attenuated at higher energies, a criticism that was discussed previously. The only models that do not introduce ripples at high energies are $V_{\rm B}$ and ELSEPA (which are actually equivalent because $V_{\rm B} > V_{\rm co,FEG}$ at all radii for $\varepsilon_0 \gtrsim$ keV).

- kinetic correlation $V_{\rm ko+p}$ (10.70) : This model fails to give accurate results at intermediate energies and performs most terribly of all at low energies (see fig. 10.18b). The main reason for this is the problem of quenching the polarisation potential at small radii. The assumption that $\bar{\Delta} \stackrel{?}{=} 2\mathcal{E}_{\rm ion}$ in (10.57) is wrongly founded for argon. It gives unreasonably low values of $r_{\rm d}$ at low energies and this spoils the correlation potential as seen on figure 10.14c by the unphysical lump on the blue curve. This expresses the major difficulty in conciliating the asymptotic polarisation with short-range correlation potentials.

- Kinetic+Buckingham $V_{\rm kob}$ (10.71:- - -) : We provide a quickfix for the invalidity of the previous model by stitching the polarisation potential from $V_{\rm b}$ instead of adding $V_{\rm p,exp}$ (as done in $V_{\rm ko+p}$) which spoils the accuracy of the model at low energies. This gives a DCS in significantly better accord with experimental data throughout a wide range of energies. We thus support the recommendation given by Gianturco and Rodriguez-Ruiz [328] that the potential $V_{\rm co,KDF}$ (8.51) based on kinetic and density functionals [567] gives an accurate representation of correlation forces for noble gases.

Molecular Nitrogen has also been studied intensely as in [448, 571] with a method based on multicentre scattering. Almost identical results were obtained using both an exponential cutoff (10.67) with $r_{\rm c} = (R/2+1)a_0$ and an augmented Buckingham (10.54). Presently, in figure 10.16, we show that an agreement in shape can be obtained with $V_{\rm ko+p}$ and $V_{\rm cob}$ but due to the violation of the optical theorem, all cross sections have a systematic overestimation. This may be semi-empirically corrected through a "screening" correction as done in Schmalzried *et al.* [812], which is simply a scaling factor close to 0.5 at energies below 50 eV. Unlike in our published article [812], we show our results without this additional correction.

A more accurate correction is to solve the Schrödinger equation with a proper expansion of the molecular potential in spherical harmonics and solve the system of equations coupled in angular momenta for various symmetries of the electron scattering off the molecule [894, §III.A]. Then a significant change affects the DCS: all are scaled down, the underestimation of the polarisation by $V_{\rm ko+p}$ vanishes and issues related to the modelling of the molecular static potential emerge. These differences will be expounded moreover in the next section 10.4.

Originally, we thought that using the correlation potential $V_{\rm co,FEG}$ of the free electron gas was justified. It artificially improved our agreement with experimental data because the polarisation potential was greatly underestimated when using $\bar{\Delta} = \mathcal{E}_{\rm ion}$ in (10.57). As a result, the lumping artifact of the red curve from $V_{\rm cob}$ somehow compensated for the underestimation of forward scattering due to polarisation forces.

Molecular Oxygen on figure 10.17 supports this premise that using $V_{\text{co,FEG}}$ would tend to improve results at intermediate energies. Nevertheless, we restate that the validity of the simple method of resolution does not allow us to draw safe conclusions even if the agreement in shape for V_{cob} (red curve) is very alluring. More pertinent is the observation at higher energies $> 100\,\text{eV}$, that V_{cob} yields an overestimation of correlation forces that must be somehow quenched non-adiabatically. Salvat [801, eq.(9)] had proposed to use the maximal value given by (10.66). This may be done using the density functional kinetic model of [567] as well. Thus, it is not straightforward to determine which of the two correlation potentials ($V_{\text{co,FEG}}$ or $V_{\text{co,KDF}}$) is more suitable.

Discussion

This section was meant as an introductory discussion about the use(fulness) of semi-empirical models for correlation and polarisation forces in electron-atom or -molecule scattering. From a formal point of view, those forces arise from the perturbation that the presence of the scattering electron induces on the molecular or atomic cloud of electrons. Although difficult to treat exactly, those forces may be modelled with some average simple analytical formula estimating this perturbation according to the electron's position $\mathbf{r}$ but also velocity v.

After a brief review of some of the models used in the literature, we conducted a small study by comparing differential cross sections (DCS) for argon, nitrogen and oxygen. We confirmed the generally accepted trend that the polarisation potential primarily affects DCS at small angles and low-energies [see the references in 329, 524, 801, p.3227, p.27, p.7:§IV]. Overall, the sensitivity of the results to the parameters of the model is high enough to obtain accurate results from heuristic rather than rigorous adjustments.

> The perturbation approach of polarisation collapses very quickly near the target because the importance of higher order terms (multipoles, hyperpolarisabilities, dynamic distortion, multi-body correlation) grows all at once. A crudely simple semi-empirical approximation, if properly adjusted, can yield more accurate results than a more rigorous attempt to truncate a perturbative series.

The comparison with argon revealed why semi-empirical models are irresistible in scattering calculations. Despite their simplicity, the differential cross section presents enough sensitivity [672, §IV] to the correlation-polarisation potential used that one could easily try to find an empirical adjustment to obtain accurate results over a wide range of energies [4, 729, 753, 997].

For molecules, the problem is rendered more complex due to the necessity to treat non-spherically symmetric potentials. Here, the use of semi-empirical models is even more deceiving because by tinkering with a series of over-then-under compensations, an accurate result that reproduces experimental data can still be obtained. In essence, many other studies [332, 672] showed that the great manifold of effects standing behind an accurate treatment of perturbation by the scattering electron can be more or less incorporated into simple semi-empirical models.

Unfortunately, the great force of semi-empirical models resides in the "empirical" part rather than the "semi" part which sometimes plays only a decorative role. Indeed, we have seen that agreement usually stems rather from ad hoc adjustments (especially the curbing radius r_{B} 10.53 in conjunction with $V_{\text{co,FEG}}$) than from derived results based on theoretical consideration (like the diabatic radius r_{d} 10.57 which had to be amended empirically for argon in 10.71). Dramatically, more rigorous attempts to improve the accuracy of DCS by incorporating higher-order terms through a perturbation expansion of the polarisation are, very often, unfruitful [276, 329, fig. 5, figs 6–8].

For now, we may state that one can be easily mislead into fallacious conclusions concerning the validity of the correlation-polarisation potential for diatomic molecules and even atoms. Nevertheless, at energies high enough to enable the applicability of the independent atom model, results show the necessity to include non-adiabatic effects into the short-range correlation potential which is *a priori* independent of the scattering electron's energy. The importance of non-adiabatic effects was already highlighted by Fink *et al.* [286] for H_2 at energies above 100 eV through comparison with accurate measurements at small scattering angles. Even then, Fink *et al.* [287] and Liu [602] showed that discrepancies imputable to the use of the independent atom model spoil the accuracy of calculated DCS at small angles from N_2. The effect of chemical bonding is observable at high energies >1 keV in very precise small-angle measurements. Thus we see that due to the shortcomings of modelling a molecule as if it were two individual atoms placed side-by-side, any discussion over the precision and pertinence of semi-empirical correlation-polarisation potentials becomes shrouded.

A simple, universal, parameterless yet accurate model for a unified treatment of correlation and polarisation forces is still to be discovered. More complex methods like the multi-channel variational approach [611], convergent close coupling [51] or polarised orbital [638, 925] constitute a potential source for benchmarking and comparing against semi-empirical models.

In the meantime, the use of semi-empirical models in elastic scattering should be taken with great caution especially when they rely on *ad hoc* adjustments without proper comparison with more accurate *ab initio* computations.

10.3.4 Absorption

The absorption part in elastic scattering is certainly a crux in the potential scattering. Its sole purpose is to represent reduction in the output flow of the elastic collision due to migration of scattering events into inelastic channels from electronic excitations. It proved to be a very powerful model to bring DCS from partial-wave expansions into agreement with experimental data [307, 570], particularly with noble gases [80, 878].

Notwithstanding, this part of the model is undoubtedly the most tentative and as a consequence is also one of the most disputed issues when it comes to get agreeable results.

We recall from (8.58) in section 8.2.4, that the absorption potential is defined as $V_{\mathrm{abs}} \equiv -\frac{\hbar}{2}\mathrm{v}\rho\sigma_{\mathrm{b}}$, depending on the *local* velocity v and electron density ρ, where the key element in the model is the binary-collision cross section σ_{b} representing the collision between the incoming electron and a target electron which would lead to a durable (non-virtual) excitation of the target.

In the second chapter of this part (8.2.4), we presented two distinct models for the absorption: namely the quasifree [877] and the dielectric oscillator [801]. The former received repetitive attention throughout many years and we recall here the generic form of its binary cross section σ_{b} [877, 879, eq.(4), eq.(11)]:

$$\sigma_{\mathrm{b}} \equiv \frac{1}{p}\int \mathrm{d}\mathbf{k} N_k(\mathbf{k}, k_{\mathrm{F}})|\mathbf{p}-\mathbf{k}| \int d\hat{\mathbf{p}}_r \frac{\mathrm{d}\sigma_{\mathrm{Mott}}}{\mathrm{d}\Omega}(p_r, \mathbf{p}_r\cdot\mathbf{p}'_r) H(p'-\beta)H(k'-\alpha)H(k_{\mathrm{F}}-k) \quad (10.72)$$

which, after integration gives :

$$\sigma_{\mathrm{b}} = \frac{4\pi}{5k_{\mathrm{F}}^3 p^2} H(p^2+k_{\mathrm{F}}^2-\alpha-\beta)\left[\frac{1}{\alpha-k_{\mathrm{F}}^2} - \frac{p^2-\beta+\frac{2}{5}k_{\mathrm{F}}^2}{(p^2-\beta)^2} + H(\alpha+\beta-p^2)\frac{2(\alpha+\beta-p^2)^{5/2}}{5k_{\mathrm{F}}^3(p^2-\beta)^2}\right] \quad (10.73)$$

Here are represented the momenta of the target $\mathbf{k}$ and incident $\mathbf{p}$ electrons before the collision, and after as $\mathbf{k}'$ and $\mathbf{p}'$. Their values in the relative centre of mass frame of the two electrons is

noted with a subscript $\mathbf{p}_r = -\mathbf{k}_r$. The momentum k_F of the Fermi sphere populated uniformly by $N_k(k, k_\mathrm{F})$, corresponds to the minimally occupied momentum of the local free electron gas (see appendix E).

The differential cross section $\mathrm{d}\sigma_\mathrm{Mott}$ is normally the one from Mott [679] but it may be eventually replaced by the classical Rutherford to make the integrals more feasible analytically. Finally, the Heaviside threshold functions $\mathrm{h}(x-a)$ are simply equal to 1 for $x > a$ and 0 below. The first two quantities α and β are the restrictions on the outgoing momenta of the target and incident electrons respectively and are referred-to as "Pauli-blocking conditions". Initially [877, 878, eqs.(12–3)], they were devised as functions of the Fermi momentum k_F and the excitation threshold Δ as:

$$\alpha = k_\mathrm{F}^2 + 2\Delta \,, \tag{10.74a}$$

$$\beta = k_\mathrm{F}^2 \,, \tag{10.74b}$$

but were tweaked into multiple variants later on.

This formulation (10.73) of the binary cross sections allows us to see how the Pauli-blocking restrictions remain after the integrals have been performed. The quasifree model was modified multiple times by different authors. We start first by introducing its history before commenting and questioning some of the modifications brought to the model.

History

The quasifree model [877], introduced in 1983 by Staszewska *et al.*, brought a new insight into how to approximately account for excitation processes other than through an extension to the polarisation potential. The idea was to model the target electrons as a free electron gas according to the local density at a certain point. Collisions by the incoming electron that resulted in outgoing momenta beyond the Fermi sphere determined from the local density, were considered to participate in the inelastic open channels and thus formed part of the binary cross section σ_b leading to excitation events.

No later than the following year, Staszewska *et al.* [878] proposed already two other versions of her model by noticing that the behaviour of the absorption potential close the nuclei at small radii ($r \lesssim a_0$) should be shallower to raise underestimated elastic DCS at large angles and high energies [878, p.3085:top§]. The potential in farther regions (large r) affects the overall absorption cross section (8.111). Subsequently, the Pauli-blocking conditions representing the allowed subspace for the outcome of a binary collisions were modified heuristically to try to take into account the acceleration of the incoming electron in the atomic field and the ionisation continuum.

Rapidly, the model was tried on more complex molecules, as in Jain [449] for methane. Two major modifications were proposed so as to make a more consistent connection between the absorption and the polarisation potential. The distorted electron density due to polarisation replaced the static density in the absorption model, and the excitation threshold was taken as an *average* excitation linked to the static dipole-polarisability α_d of the molecule. This model was applied to many different molecules in the ensuing years [450] together with a higher-order multiple scattering theory based on the independent atom model. To avoid having to calculate the average excitation energy, it was proposed to replace it by the *ionisation threshold* which gives a more or less close value for most molecules.

The model got revisited a decade later by Blanco and García [80]. The improvement sought after a better approximation of Mott's cross section for two indistinguishable particles in Coulombic interaction [680, p.300:eq.(20)]. In that revision, an error of a misplaced factor was detected in Staszewska *et al.* [877, eq.(11)] who perhaps confused the expression of Rutherford cross section when expressed with kinetic energy: $\propto 4/\varepsilon^2$ versus velocity: $\propto 1/\mathrm{v}^4$ whose appearances understandably differ by a factor four.

Used now for more involved calculations, Lee and Iga [569] tried the third variant of the original quasifree model [878, eq.(22)] together with the average excitation energy [450, table II:Δ] for N_2 in a combined Schwinger-variational and distorted-wave approach. They later made in Lee *et al.* [570] a comparison of four variants of the model from the different authors: namely Staszewska, Jain and two from Blanco. They uncovered serious discrepancies in the DCS showing that models might have been mishandled when implemented (on whose side ever it was).

Moving next toward O_2, Raj and Kumar [763] pointed out that the model performed quite miserably at higher energies, because its excitation threshold is lower than 1 eV. To decrease the effect of absorption at higher energies as it ought to, they simply added a $1/k$ factor to the absorption and obtained significantly better results.

Getting still more attention, adjustments were proposed by Blanco and García [79, 81] to get better results for various noble gases and diatomic molecules. The new features included:

1. a more adapted choice of the excitation threshold which for some molecules gave the risk of overestimating the absorption to unreasonable results;

2. a symmetrical Pauli-blocking condition for both ejected electrons since they are indistinguishable;

3. a screening of inner regions to account for electrons that already interacted inelastically in outer regions (and thus are not eligible to excite again);

4. relativistic corrections for electrons impinging on heavy atoms as they get near the nucleus;

5. accounting for multi-body processes according to the probability of interacting with any of the target electrons within the distance of one local wavelength of the intruded electron.

At last, the original author published three articles the same year where she attempts to bring together and compare all the existing variants dispersed in the literature of the quasifree model [879]; then studies the effect of empirical scaling factors [881]; and finally demonstrates [880] that a completely different empirical model that nevertheless binds absorption and polarisation potentials in a coherent way gives accurate and consistent results for Helium and Neon, but inevitably relies upon adjustment of the free parameters. In their comparative study Staszewska *et al.* [879] discusses comprehensively the deficiencies of each version and how they affect integrated and differential cross section in distinct energy and angular ranges. Also, various polarisation potentials are combined with the absorption in order to reduce the bias of the real part of the model on the results. The overall conclusion is that all three versions from the original author perform well but in different aspects (energy, angle, or absorption cross section) and that the energy dependence of both polarisation and absorption potential should be studied more in detail in the future.

There may have been a continuation in the more recent years to this model, but most investigations on more complex molecules settled on the fact that many empirical modifications to the *ab initio* model gave satisfactory results and thus did not attempt to explore furthermore. Others [383, 494] turned toward another non-empirical model proposed by Salvat [801].

Critique

Having given an overview about the evolution of the quasifree model, I would like to point out some inconsistencies introduced during some revisions. If I may be pardoned for my obnoxious subjectiveness, the history of how the quasifree model was handled, embodies, for me, an archetypical example of empirical fiddling. Having myself played with it in my own model, I can ascertain that it is almost impossible to get agreeable results for a wide range of energies, at all angles and for various targets without tinkering and adjusting the model in order to obtain presentable curves. For that matter, I dedicate to each *ad hoc* adjustment an explanatory paragraph arguing why I think it is unfounded (which is why the titles are crossed out).

~~Local momentum~~: At the time when the first empirical corrections were proposed to the model [878, p.3085:eq.(21-22)], it was known that the absorption rate was overestimated at small radii. Absorption rates are not expected to be important in the deeper layers of an atom, where the electrons are more tightly bound to their orbitals. Blanco and García [79, p.180, left-middle§] commented that the excitation threshold, labelled Δ, should ideally be a monotonically decreasing function of the radial position r from the nuclei, basically repeating what Staszewska *et al.* [878, p.3081:2nd§] had remarked for the blocking restrictions. To raise α and β at small r, Staszewska *et al.* [878, eq.(21-22)] proposed to adjust (10.74) as (changes in red):

$$\alpha = k_\mathrm{F}^2 + 2\Delta - 2V_\mathrm{se}(r) \tag{10.75a}$$
$$\beta = k_\mathrm{F}^2 - 2V_\mathrm{se}(r) \tag{10.75b}$$

In one of the two modifications, a different offset is taken instead of 2Δ and the factor 2 is removed before the static-exchange potential $V_\mathrm{se}(r)$. In both cases, the physical meaning to such correction was allegedly attributed to the "local increase in kinetic energy of the incident electron" [878, p.3085:§between (22)&(23)]. The problem is that this reasoning is ambiguous. Since V_se is negative, one should expect that this increase would on the contrary permit the incident electron to kick off electron in deeper shells more easily. What Staszewska *et al.* probably meant is that, if the incident electron shall be given the chance to escape again, its outgoing momentum should lie at least $-2V_\mathrm{se}$ above the Fermi sphere. Such reasoning would indeed explain why V_se is added negatively to α and β instead of p.

Nonetheless, if we imagined that a $p = 0$ electron was brought in the vicinity of the atom, it would indeed have a $-2V_\mathrm{se}$ and that should be interpreted as the minimum energy an electron ought to have if is not to stay trapped forever inside the atom. Therefore, in my opinion, a more sound condition would have been the following:

$$\alpha = k_\mathrm{F}^2 + 2\Delta \tag{10.76a}$$
$$\beta = \max(k_\mathrm{F}^2 + 2\Delta, -2V_\mathrm{se}(r)) \tag{10.76b}$$

Such conditions would effectively reduce the probability of absorption in atoms nearer the nucleus ($r \lesssim a_0$) when we look at the ratio $k_\mathrm{F}^2/(-2V_\mathrm{se})$ in figure 10.19 for three different targets. If the polarisation potential were used as well, the condition (10.76) would be even more stringent. This would however not have any effect with the isotropic potential of molecules because the atomic singularities are averaged into finite values.

In the previous case, I do not know what would be a correct physical interpretation requiring that at any point r, the energy of the intruded electron be $-V_\mathrm{se}(r)$ above the local Fermi energy $E_\mathrm{F}(r)$ as expressed by (10.75).

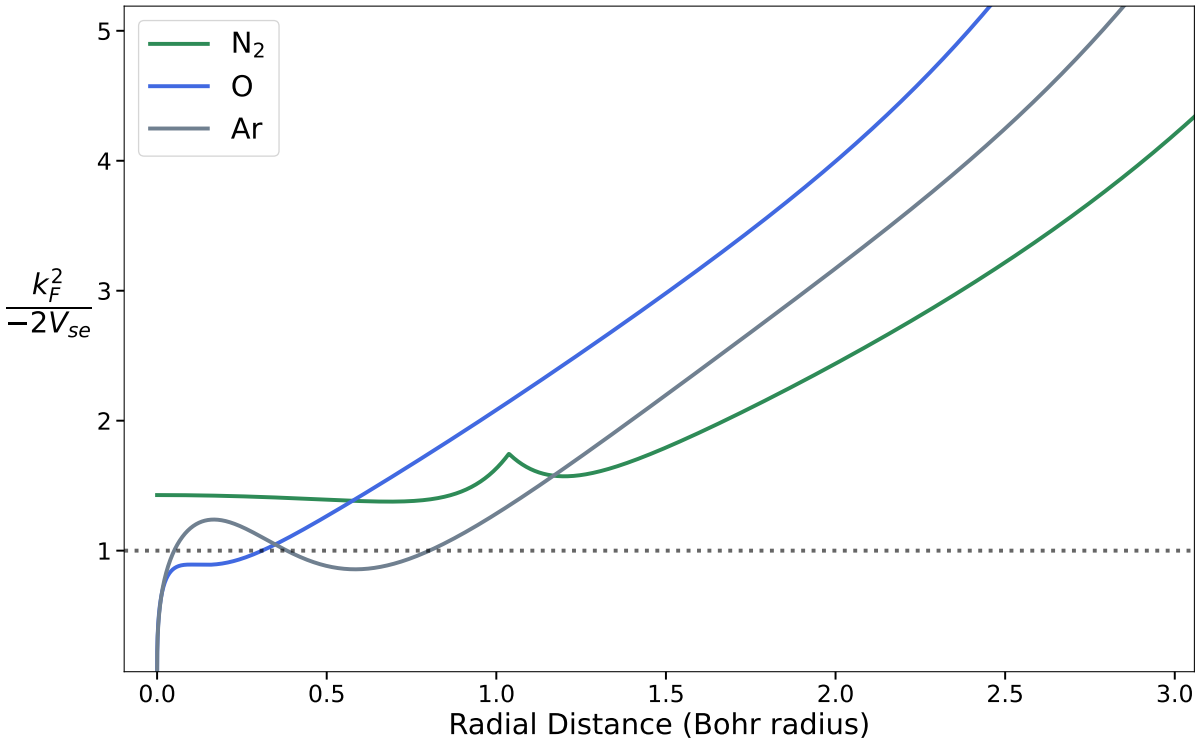

Figure 10.19: Comparison of Fermi energy $k_{\mathrm{F}}^2/2$ with the local static-exchange potential V_{se} according to the radial distance r for Oxygen, Argon and molecular Nitrogen (in which latter case the potential is the spherically averaged one). This shows that a Pauli-blocking position based on V_{se} as in (10.76) would be more stringent in the inner region of atomic targets, but not in the averaged potential of molecules.

This puzzle was solved differently by Blanco and García. In Blanco's first article [80], he knew that taking the local momentum in the absorption would thwart the model's results. Using the asymptotic value p instead of $p - 2V_{\mathrm{se}}(r)$ in (10.73) was initially justified [80, p.150:left-bottom§] as a way to incorporate "screening of the inner electrons by the outermost ones". In his next article, another interpretation had to be given so as to make room for the new modification proposed. This time, keeping the asymptotic momentum was due to the excitation threshold Δ which ideally should be a function with higher values in the inner region. Finally, both forms of justifications were revoked in his third publication [81], and an average local binding energy $V_b(r)$ was proposed that would restrict the excitations allowed even when taking into account the local increase in kinetic energy of the incident electron.

~~Local binding energy~~: The potential V_b seen by one of the target electrons due to the nucleus and the remaining $Z-1$ electrons can be estimated in a mean-field approximation as [81, II.A]:

$$V_b(r) \approxeq V(r)\frac{Z-1}{Z} - \frac{1}{r} \tag{10.77}$$

The second term of the right side is to put back again the Coulomb attraction of a proton that was removed together with one electron in the first term $(Z-1)/Z$.

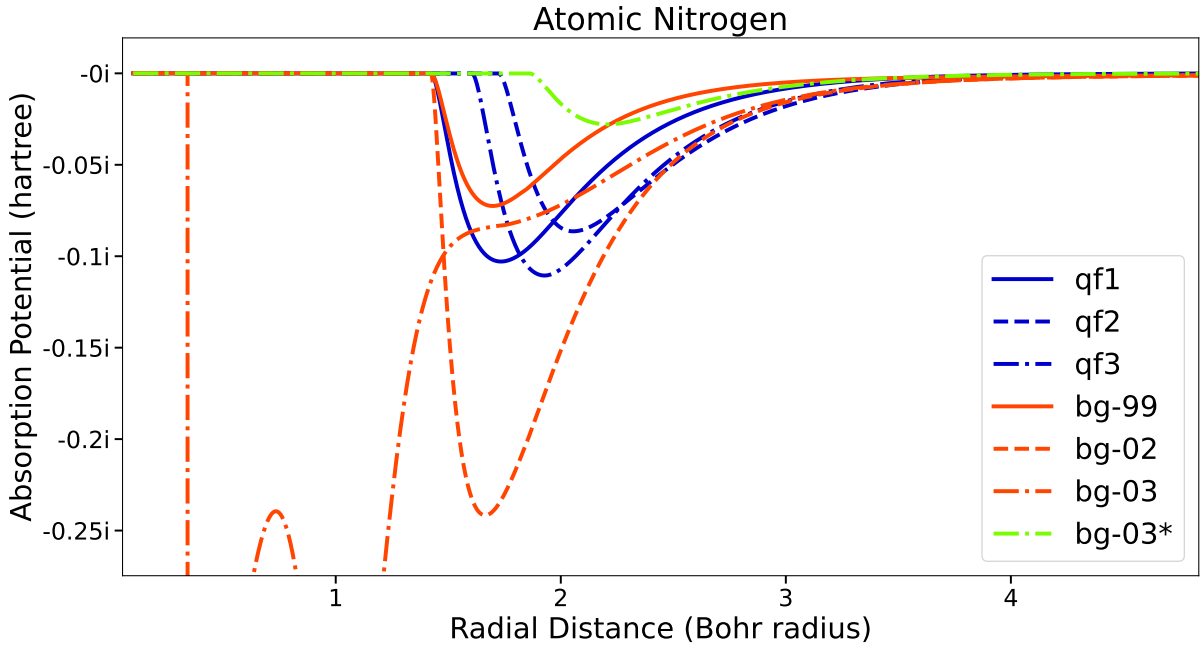

Figure 10.20: Comparison of absorption potentials for atomic nitrogen with excitation threshold at Δ =10.326 eV and incident electron energy of 40 eV. Legend : "qf{1,2,3}" = Quasifree model [879, §3.2.{1, 2, 3}] version {1,2,3}; bg-?? = modified in (19)99 [80], (20)02 [79] and (20)03 [81]; bg-03* = presently corrected version from last modification with Pauli-blocking condition $\beta(r) = k_{\mathrm{F}}^2 - 2V_{\mathrm{b}}(r)$.

Unfortunately, this binding energy was improperly incorporated into the absorption model as Staszewska *et al.* [879, p.62] pointed out. This considerably deepens and widens the potential before cutting it discontinuously at small r as can be observed for "bg-03" in figure 10.20.

The present version "bg-03*", whose equation (8.70) is given on page 294 (that correctly includes the binding energy into the Pauli-blocking conditions as : $\beta(r) = k_{\mathrm{F}}^2 - 2V_b(r)$), shows a neat difference and reduction in the absorption as needed to improve the model. The full comparison shows all three versions of the original quasifree model [879, §3.2.1-3], the three modified versions [79–81], and the presently corrected version (8.70).

The first modification in 1999 [80] only included the correction due to interference term in Mott's scattering cross section which lowers the absorption well, due to less scattering at 90°. The next two modifications in [79, 81] attempted to symmetrise the Pauli-blocking conditions by setting $\alpha = \beta = k_{\mathrm{F}}^2 + \Delta$, and introduce more 'corrections' that we tackle below.

~~Indistinguishability~~: One typical concern is that the ejected electrons with momenta $\mathbf{k}'$ and $\mathbf{p}'$ in (10.73) after the binary collision are indistinguishable from each other with respect to where they came from. This led Blanco and García [79, p.179:right column] to symmetrise the original Pauli-blocking conditions (10.74) into (removal of the factor '2' from eq. 10.74a in red):

$$\alpha = \beta = k_{\mathrm{F}}^2 + \cancel{2}\Delta \tag{10.78}$$

This caused the potential in (10.20) to deepen by more than two-folds, mostly because of replacing the first term in σ_{b}: $1/2\Delta$ by $1/\Delta$. Although it is undeniable that the electrons are indistinguishable, this only implies that the definition of the primary electron after the collision is

arbitrary. If we assume that the electron (whichever of the two) associated to the final momentum $\mathbf{p}'$ is the one that shall be retained in the asymptotic expression for the scattered wave, then, it would be more logical to require that $p' \geq k'$ and the Pauli-blocking conditions would become:

$$\alpha = k_{\mathrm{F}}^2 + 2\Delta \,, \tag{10.79a}$$

$$\beta = k'^2 \tag{10.79b}$$

Omission to restrict $p' \geq k'$, in my opinion, is the greatest inconsistency of the quasifree model and was never addressed properly in any of the revisions. If we compare to the successful model of Salvat [801, p.15:eq.(A24)], there, the primary electron is correctly taken as the one possessing the highest energy of the two ejected electrons. This does not howsoever violate the principle of indistinguishability.

Exchange effects are directly taken into account in Mott's cross section [680, p.300:eq(20)]. If in the aftermath of the collision one defines $p' > k'$ as the outgoing momenta of the primary > secondary electrons, the exchange effects are also accounted-for, since Mott's DCS was normalised to 2. This relieves one from having to divide the DCS by 2 [80, §3:eq.(11)] before integrating (10.73) so as not to double the estimated binary cross section.

Related to this issue, it is often wrongly thought (e.g. [383, p.4:eq(20)§(21)]) that the factor $1/2$ in $\hbar/2\mathrm{v}\rho(r)\sigma_{\mathrm{b}}$ is due to exchange effects. As Salvat [801, eq.(12)§] points out, this factor is only due to the interpretation of $2V_{\mathrm{abs}}/\hbar$ as an absorption rate. This confusion probably stems from Staszewska *et al.* [878] which uses half of the Rutherford cross section for binary collisions between two electrons to roughly account for the quantum interference term maximal at 90° of scattering (in the centre of mass frame) from the Mott's corrected formula.

~~Screening~~: Blanco and García [79] conjecture that the part of the incident electron flux that has been absorbed while going through the outer shell at large radii, should be removed from the rate of possible inelastic scattering and thus should reduce the absorption potential at smaller radii deeper in the atomic shell. The screening coefficient that reduces the absorption is:

$$C_{scr}(r) \equiv \exp\left(\int_r^{\infty} \frac{-2V_{\mathrm{abs}}(t)}{\mathrm{v}(t)} \frac{t}{\sqrt{t^2 - r^2}} dt\right) . \tag{10.80}$$

This screening measures the average flux reduction based on the local velocity of the projectile electron $\mathrm{v} = \sqrt{p^2 - 2V_{\mathrm{se}}(r)}$ and the path it traces in a spherically symmetric absorption potential $V_{\mathrm{abs}}(r)$. This reasoning is intuitively correct, though deceptive. One has to get back to how the absorption potential is used. It serves to define an absorptive component in the one-electron Schrödinger equation of the scattering problem:

$$\triangle\psi(\mathbf{r}) - (V_{\mathrm{sep}}(\mathbf{r}) + iV_{\mathrm{abs}}(\mathbf{r}))\psi(\mathbf{r}) + \frac{\hbar^2 p^2}{2m_{\mathrm{e}}}\psi(\mathbf{r}) = 0$$

To get a physical insight, we take the simplest case of s-waves and constant potential barrier $V_{\mathrm{sep}} + iV_{\mathrm{abs}}$ non-zero only between r_0 and r_1; and define $u_0(r) \equiv r\psi(r)$. Since we know that $V_{\mathrm{abs}} < 0$, with the requirement that $u_0(r) \xrightarrow{r\to 0} 0$ and the asymptotic relation $u_0(r) \xrightarrow{r\to\infty} \sin(pr + \delta_0)$ with δ_0 being the asymptotic phase-shift, the amplitude probability of the wavefunction adapts itself according to the potential barrier in $[r_0, r_1]$ and shrinks as seen on the graph (10.21) on the right. The effect of the complex potential is to lift the nodes of u_0 away from zero and shrink the amplitude. The probability distribution beyond $r > r_1$ now never vanishes because of the complex phase-shift δ_0.

In summary, the "screening" effect of a potential is to effectively reduce the flux of the wave-function in regions where the absorption is important. This effect readily operates on the wavefunction itself. I do not conceive well what significance would bear an absorption potential that includes a screening of itself as given by Blanco and García [81, eq.(1b)] (10.80). In particular, the equation solved above is of the time-independent type, thus barring the notion of flux and penetration; the wavefunction rather permeates the space and gets reduced in classically forbidden regions.

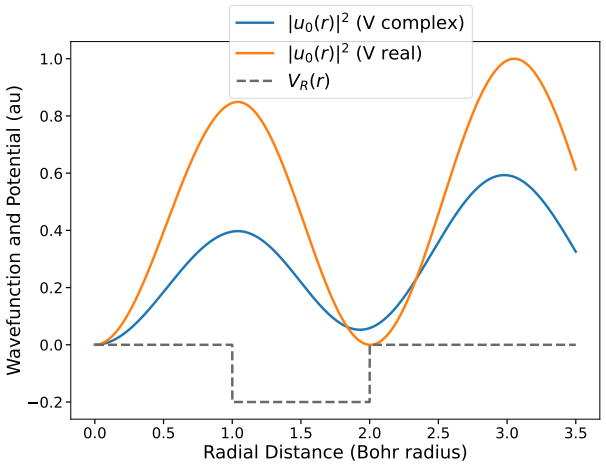

Figure 10.21: Dummy example of an s-wave in a small complex potential barrier $V = 0.2 - 0.3i$.

~~**Many-body interactions:**~~ Another correction introduced in Blanco and García [81, p.3:right column] is the probability that the projectile electron interact with the Z atomic electrons once in the atom's vicinity. There, it is argued that if $\rho(r)/Z$ represents the probability density of one electron to be at r, then the probability of interaction with at least one electron within a small region of the extent of the projectile's local wavelength λ is : $1-(1-\lambda^3\rho(r)/Z)^Z$, in other words: the complementary probability that no electron is found in that region λ^3. Once again, intuitive thinking misled. We must recall that the density function $\rho(r)$ comes ideally from the full atomic properly antisymmetrised wavefunction $\Psi(r_1,\ldots,r_Z)$ [416, eq.(6.1)]:

$$\rho(\mathbf{r}) \equiv Z \int |\Psi(\mathbf{r},\ldots,\mathbf{r}_Z)|^2 \,\mathrm{d}^3\mathbf{r}_2 \ldots \mathrm{d}^3\mathbf{r}_Z$$

In this case, $\rho(r)/Z$ corresponds to the probability density of finding any electron near r. There shouldn't be any effect of interaction with more than one electron involved since this information is inaccessible due to the integration over the other $Z-1$ electrons. It is true, though, that in density functional theory (DFT) [398, §10.3:eq.(10.37)] , $\rho(r)$ is obtained through a sum of individual orbitals $\varphi_i(\mathbf{r})$:

$$\rho_{\mathrm{DFT}}(\mathbf{r}) = \sum_{i=1}^{Z} |\varphi_i(\mathbf{r})|^2$$

Notwithstanding, the orbitals $\varphi(\mathbf{r})$ are still obtained through the one-electron Schrödinger equation in a self-consistent way which includes the repulsive Coulomb and exchange terms among electrons. This implies that $\rho_{\mathrm{DFT}}(r)$ should still be viewed as a whole expressing the probability to find any electron in a system of Z electrons. One should not regress to think that the Z electrons are all equally and independently distributed over a $\rho(r)/Z$ distribution. This thinking is erroneous since the individual density of electrons is in principle known for each of them : $|\varphi_i(\mathbf{r})|^2 \neq \rho(\mathbf{r})/Z$. Taking multi-electron effects by assuming that all follow $\rho(r)/Z$ is therefore not well founded because it does not acknowledge that $\rho(r)$ was obtained from a Slater determinant which already comprises spin correlations.

Added on top of that, if one really needs to estimate the joint probability of finding any pair of electrons at positions $\mathbf{r}$ and $\mathbf{r}'$, then one must make use of the correlation function $h(\mathbf{r},\mathbf{r}')$ which includes exchange and formation of a Coulomb hole (as discussed in the previous subsection 10.3.3) around an electron due to its presence at $\mathbf{r}$ [416, §6.2.3]:

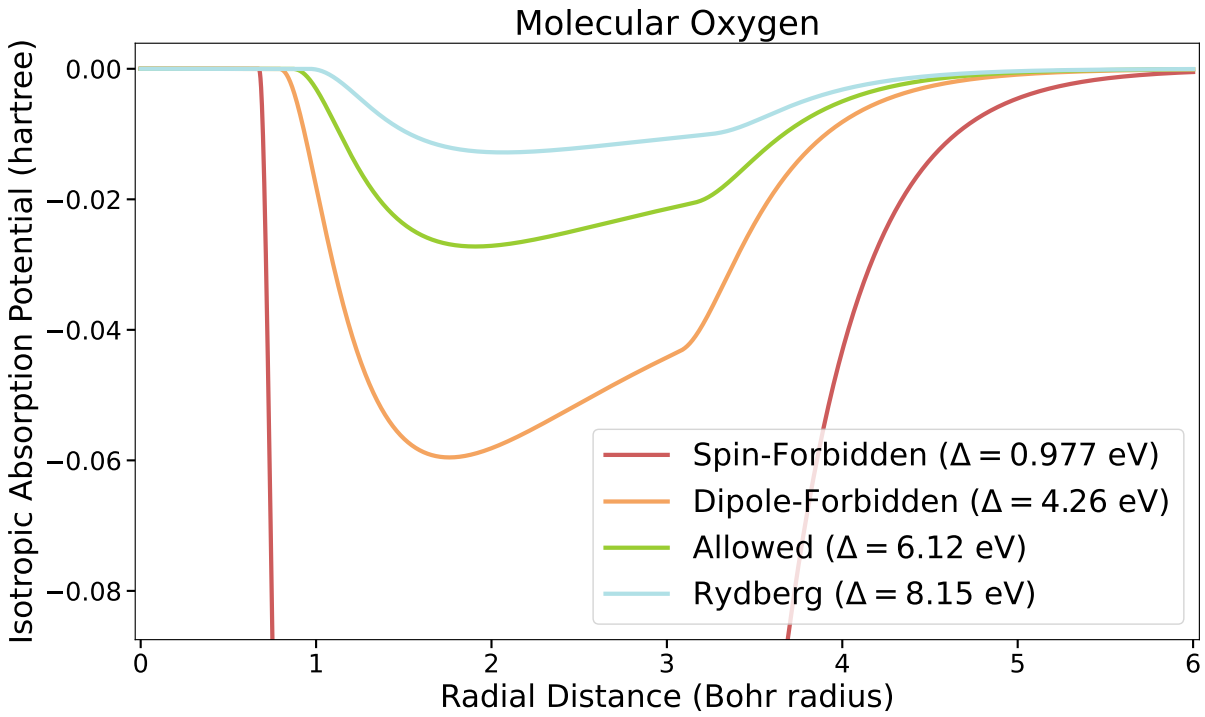

Figure 10.22: Influence of the excitation energy threshold Δ used in the quasifree model (10.73). The four values taken correspond to the lowest excitation state for O_2 (which is spin-forbidden), the first dipole-forbidden, dipole-allowed and Rydberg state.

$$\rho_2(\mathbf{r},\mathbf{r}') = \frac{\rho(\mathbf{r})\rho(\mathbf{r}')}{2}\left(1 + h(\mathbf{r},\mathbf{r}')\right) . \tag{10.81}$$

Therefore, in particular when $\mathbf{r} \approxeq \mathbf{r}' \Rightarrow h(\mathbf{r},\mathbf{r}') \not\approx 0$, the pair probability may not be modelled as a simple independent single particle density probability product due to Coulomb correlation effects.

~~Optically allowed threshold~~ Δ: It is clear that the excitation threshold parameter Δ has a tremendous influence on the depth of the quasifree absorption potential as can be observed from figure 10.22. For this reason, taking systematically the lowest excitation state for every target might not always give reasonable absorption potentials. A suggestion by Blanco and García [81, §II.C] was to take the first optically-allowed excitation threshold (or the ionisation potential [79, p.180] in a previous model).

A more consistent reasoning is to remember that any excitation with an energy loss exceeding Δ will be allowed and counted in the binary CS (10.73). That is, the binary collision approach models a continuum instead of a discrete spectrum. Each target's energy-loss spectrum have unique characteristics, some are more regular, others sparse; some figures can be found in the section (11.4) devoted to electronic excitations (11.32 and 11.35). The illustrious examples of O_2 and N_2 show two very opposite trends: N_2 spectrum is dense directly starting from its lowest threshold at 6.17 eV, whereas O_2 is much deserted between 1.62 eV and 7 eV where the Schumann-Runge continuum starts and all the Rydberg states. Due to the arbitrary nature of selecting Δ to represent an onset of a continuum, it seems reasonable that this parameter be left to the decision of the user according to the target modelled.

Comparisons can be seen in numerous studies about the effect of absorption as complex optical potential models. For citing a few, an extensive study of the major semi-empirical absorption models derived from the quasifree model was conducted by Staszewska *et al.* [879] for neon, the conclusion of which led to preferring the "qf-2" and "qf-3" versions. In another study, "bg-03" and "bg-02" have been compared against "qf-2" and "qf-3" for methane in Lee *et al.* [570]. The same author had implemented "qf-3" for molecular nitrogen [569] with good agreement down to 30 eV. The highest score was obtained by "qf-3" when the "threshold" Δ was used according to Jain and Baluja's [450] interpretation as a "mean excitation energy" of the order of the ionisation threshold. Without comparing, Raj and Kumar [763] altered "qf-2" to their taste to improve the applicability of the model for molecular oxygen. The general effect of absorption is to lower differential cross section (loss of flux) at intermediate energies and large angles [878, V(i)].

Although the agreement obtained from the various *ad hoc* alterations to the quasifree model was presented in the best of lights, we presently deplore the heuristic nature of the model which needs quickfixes and a bit of wand wielding to give desired results for each target. Instead, we prefer to resort to the model proposed by Salvat [801] and presented earlier in section 8.2.4. The ultimate alternative would have been to delve into the realm of multi-channel scattering [101].

10.4 Convergence Matters

When assessing the accuracy of a numerical result ξ, a fundamental concept at play is the convergence toward a certain value $\dot{\xi}$ which is believed to be the 'true' value obtained with infinitely fine precision. Given a certain computational methodology, we may approach this value with consecutive values from a series $(\xi)_n$ $n \in \mathbb{N}$. The index n reflects the degree of (numerical) resolution and/or complexity involved in obtaining the n^{th} estimate. Formally, convergence $(\xi)_n \overset{n\to\infty}{\longrightarrow} \dot{\xi}$ is defined as:

$$\exists! \dot{\xi} \in \mathbb{R} \ : \forall \epsilon \in \mathbb{R}^+ \, \exists N_{\text{cp}} \in \mathbb{N} : |\xi_n - \dot{\xi}| < \epsilon \quad \forall n \geq N_{\text{cp}}$$

Vulgarly, convergence of a series concerns whether (1) $\dot{\xi}$ exists, is unique ("$\exists!\dot{\xi}$") and finite; (2) at a certain point, improving the resolution n beyond N_{cp} will always bring us closer to $\dot{\xi}$ to an arbitrarily small difference ϵ (precision). If that is true, thence the notions of resolution and precision coincide. When the convergence is well understood, one can better assess the errors made when truncating the series $(\xi)_n$ to the $(N_{\text{lim}})^{\text{th}}$ term $(\xi)_{N_{\text{lim}}}$, which otherwise converges to the ideal value $\dot{\xi}$ reached at $n \to \infty$.

A proper understanding and assessment of convergence is so fundamental that it is often taken for granted that it has been taken care of properly when publishing results for calculated differential cross sections (DCS). In the context of the angular-momentum close-coupling formalism which is the one adopted in the thesis, due attention to this issue was given by Morrison and Sun [675, p.146–8] and their group [see for instance 274, 430, 669, 894, §IV:p.925–7, §IV:1237–9]. We recall here three ingredients as defined by Morrison [666, §IV.A:p.34]:

1. What quantity converges? →DCS
2. When is it converged? →a convergence criterion C_{lim}
3. How does it converge? →number of parameters in the convergence N_{cp}

To ensure proper convergence, the criterion C_{lim} must be checked for globally and not locally. This is done by considering how little the DCS differs if one includes $K > 1$ more parameters [773, p.34-35:eqs(4.1-2)]:

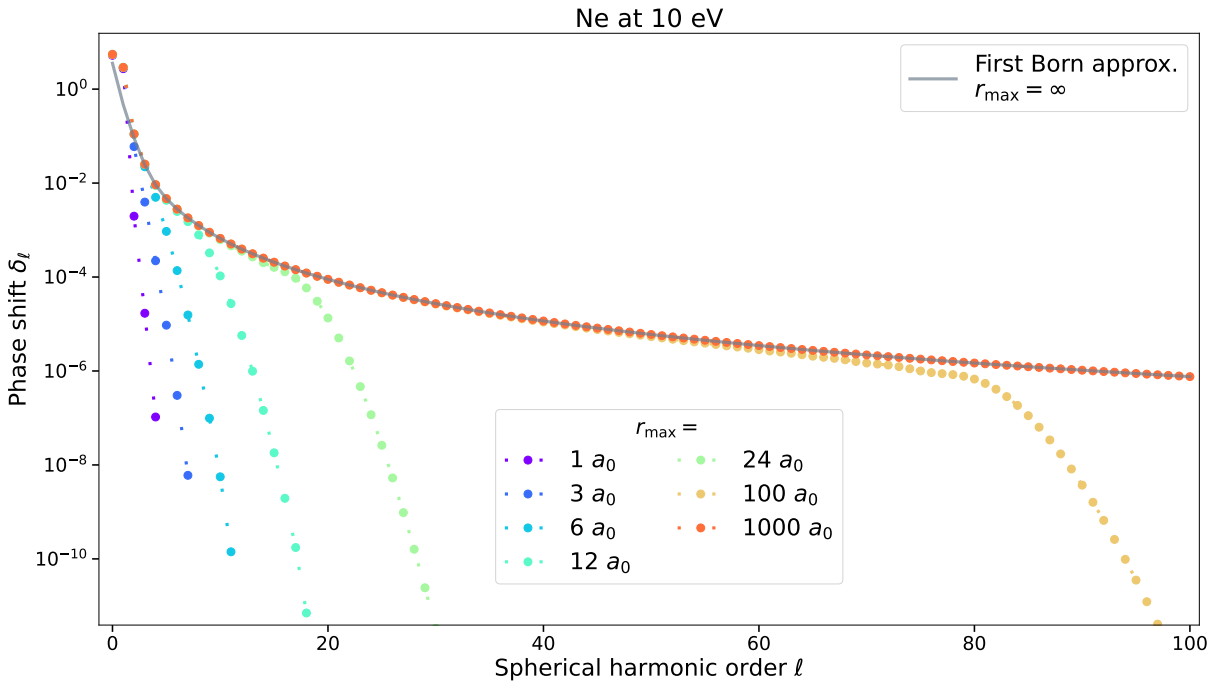

Figure 10.23: Convergence of the phase shift $\delta_\ell(r_{\max})$ according to the maximal radius $r_{\max}$ of integration of the equation (9.4).

$$\left|\frac{\mathrm{DCS}(N_{\mathrm{cp}}) - \mathrm{DCS}(N_{\mathrm{cp}} - K)}{\mathrm{DCS}(N_{\mathrm{cp}})}\right| < C_{\mathrm{lim}} \; ; \; \begin{cases} K \simeq 6 & : \text{ Global convergence} \\ K = 1 & : \text{ Local convergence} \end{cases} \tag{10.82}$$

In this thesis, we conducted convergence studies in order to ensure that our results were not missing out a significant 'chunk' of values due to an improper handling of the computation methods. This is to ensure that all discrepancies observed may be safely imputed to the limitations of our model and approximations; and not to an incomplete calculation of numerical nature. In this section, we will briefly expose what parameters intervene (and how) in the convergence of computed DCS.

Without detailing thoroughly the procedure of checking convergence, we illustrate in this section how unconverged DCS appear in various situations through the number of partial waves included $\ell_{\max}$ or the symmetries of the potential $l_{\max}$ and the projections $\Lambda_{\max}$ on the internuclear axis. We first start with the partial waves for spherically symmetric potentials representing the interaction with atoms.

10.4.1 Phase shifts

When solving the phase-shift equation (9.4) numerically from $r = 0$ to $r_{\max}$, one needs to ensure, somehow, that the algorithm yielding asymptotic phase-shifts has properly converged and is well resolved enough.

One very efficient way to do this is to test the convergence of $\delta_\ell(r_{\max})$ to $\tilde{\delta}_\ell(\infty)$, the Born approximation for the analytical expression of phase shifts. This is represented in figure 10.23 for scattering off neon at 10 eV for phase shifts from $\ell = 0$ to $\ell = 100$. As the maximal radius $r_{\max}$ is extended for the integration of $\delta_\ell(r)$ in (9.4), the phase shifts properly converge and for high $\ell > 6$, they also converge to the theoretical value from the first Born approximation (8.120).

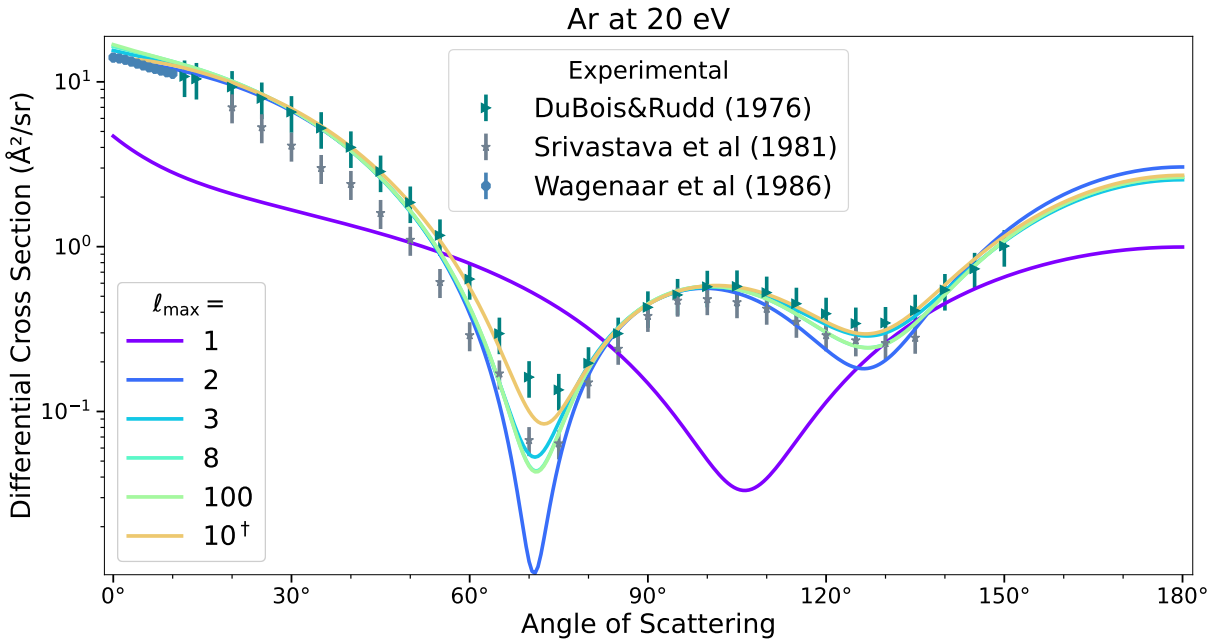

Figure 10.24: Convergence of the DCS with partial waves and the effect of Born completion. All phase shifts beyond the ℓ_{max} are calculated from the analytical Born approximation for the static and Buckingham polarisation potential: $\forall\, \ell > \ell_{max} : \delta_\ell \equiv \tilde{\delta}_\ell$. This enables to use the analytical scattering amplitude $\tilde{f}$ for completion (9.18). The curve labelled with a dagger $\ell_{max} = 10^{\dagger}$ has no Born completion, implying that the scattering amplitude is only the sum of 11 terms ($\ell = 0..10$). An uncompleted DCS can seem to favour agreement with one set of experimental data (▸ [232]) over another (⋆ [871]).

Since lower ℓ orders converge faster with r_{max} while higher orders converge faster to the Born approximation, it is possible in practice as Morrison *et al.* [671, eq.(38–39)] proposed, to select a maximal radius $r_{max} = 10\, a_0$ beyond which the remaining integral to $r = \infty$ for the phase shift is completed through the Born approximation.

10.4.2 Partial Waves

The previous subsection was concerned about integration of each phase shift: that is radial truncation r_{max}. Here, we treat the partial wave order truncation ℓ_{max} for a spherical potential and how to ensure that a DCS has properly converged.

In the previous chapter, we presented a very convenient way of circumventing the limitations of truncation through completion of the infinite sum by the analytical Born approximation of the scattering amplitude. This is commonly known as Born completion or closure [274, 430]. In figure 10.24, we show that if such completion is used for all δ_ℓ beyond ℓ_{max}, one can safely take $\ell_{max} = 5$ when the energy is not too high. As the energy increases, higher order partial waves may penetrate into the short-range region containing exchange, correlation and absorption potentials which are not accounted by the analytical Born amplitude (they would have to be calculated by numerical integration). At the same time, those three potentials shrink as the energy increases, so that in general, imposing $\ell_{max} = 5$ poses no significant risk. The uncertainty introduced thus is of the same order as the very modelling of the target through the optical potential.

An analogous illustration of analytical Born completion but for diatomic molecules is available in Feldt and Morrison [274, figs. 2&4] in which $\ell_{max} = 2$ is a safe choice for H_2 and $\ell_{max} = 3$ for

N_2. This boundary is pushed slightly higher when considering inelastic vibrational excitations. We continue our convergence investigation for diatomic molecules in the next subsection.

10.4.3 Angular Momentum Close Coupling

For non spherically symmetric potentials, the scattering matrix $S_{\ell_0\ell}$ has non diagonal elements that must be included to construct the DCS. We study here in figure 10.25 the convergence of the DCS for N_2, NO and O_2 from the perspective of the number of harmonics used. An example of a convergence study for the DCS of N_2 at low energies can be found in Morrison *et al.* [674, III.C:table II].

Partial Waves When it comes to coupling, the illustration for N_2 at 40 eV in 10.25a shows that a difference of $|\ell_0 - \ell| < 12$ is usually sufficient at the energies considered. The remaining differences arise from the diagonal elements of the S matrix with $\ell > 12$, principally affecting the forward scattering. Also, most high-order elements $\ell_0, \ell > 4$ can be safely calculated from the Born approximation [274, 671, p.2530:§IV.B.2, fig. 4 and tab. II]. In our calculations, we took $\bar{\ell}_{\max} = 35$ for the S matrix as in Fujimoto and Lee [307, p.4762], and assumed that the S matrix were purely diagonal for $\ell > 35$.

Potential Harmonics The number of potential harmonics is the most critical parameter in convergence studies because of the necessity to properly represent the static potential singularities located at the two decentred atoms. The larger the interatomic distance R, the slower the convergence of the DCS in $l_{\max}$ will be. We show this slow convergence on figure 10.25b for NO at 30 eV which has both odd and even l orders. As explained in Morrison [666, pp. 156–7], the relevance of l is technically limited to $2\ell_{\max}$ due to the triangular relation. In some cases an $l_{\max} = 36$ is recommended [186, p.480:left–middle§]. Presently, we adopted $l_{\max} = 24 = 2 \times 12$ from the convergence seen for $\ell_{\max}$.

Angular Projection Symmetries At last, we know that the S matrix may be decomposed in symmetries of the projection $\Lambda_{\max}$ of the electron's angular momentum on the internuclear axis. As illustrated in figure 10.25c, it seems that quite a few symmetries are needed to properly converge the DCS at all angles. Actually, this observation is biased by the size of the S matrix considered. For large $\ell > 12$, one can roughly consider that the scattering matrix S becomes independent of the projection Λ and therefore, one may sum over all Λ for those higher order ℓ in order to obtain the diagonal contribution of higher orders which actually account for the difference seen at forward angles between $\Lambda_{\max} = 8$ and $\Lambda_{\max} = 35$. If one has established a $\ell_{\max}$, one should not arbitrarily restrict $\Lambda_{\max}$, as all projections should be summed in order to get the full contribution from all orientations of the molecule. The only difference is that this sum can be made more systematic if one assumes an ℓ_Λ beyond which the scattering matrix is fairly independent of Λ. Following our decision above, we used $\Lambda_{\max} = \ell_{\max} = 35$.

Nevertheless, in order not to waste computational time on minute matrix elements, we required that the minimal value of $|S^\Lambda_{\ell_0\ell}| > 10^{-10}$ and neglected all smaller contributions.

Although our current parameters for constructing our DCS are far from optimal, we contented ourselves with these values for the purpose of the present study whose objective was to complete the DCS database of elastic cross sections where experimental data were lacking.

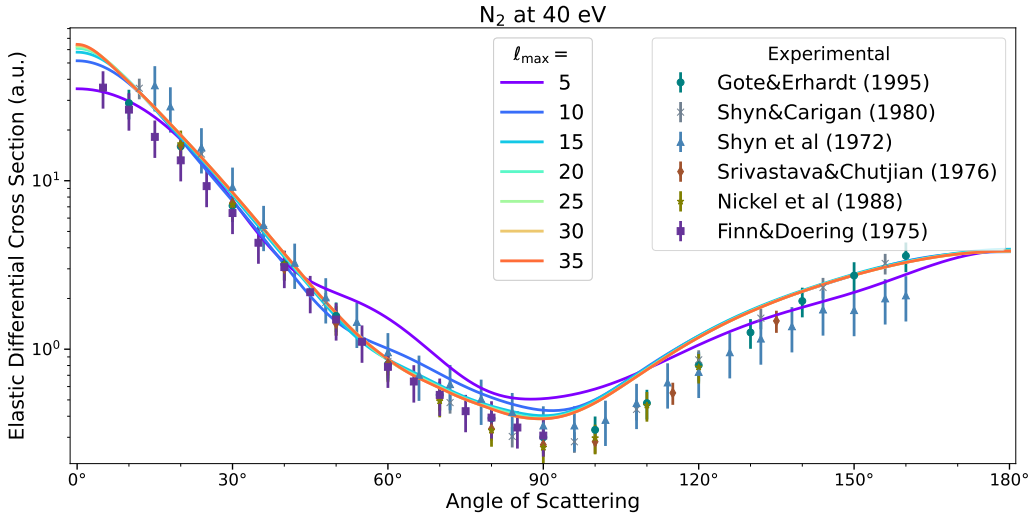

(a) Convergence in the size ($\ell_{\max} \times \ell_{\max}$) of the S matrix: in orbital angular quanta.

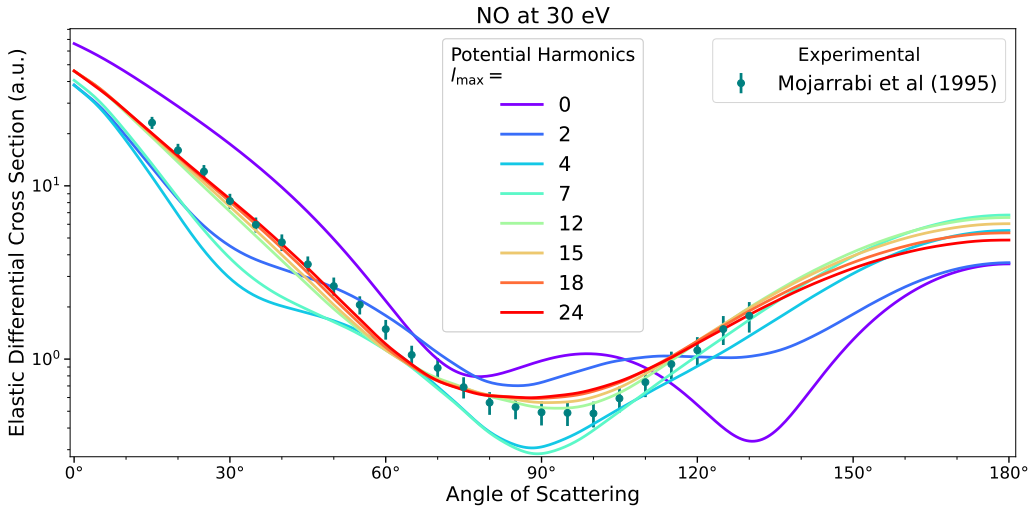

(b) Convergence in $l_{\max}$: the number of potential spherical harmonics.

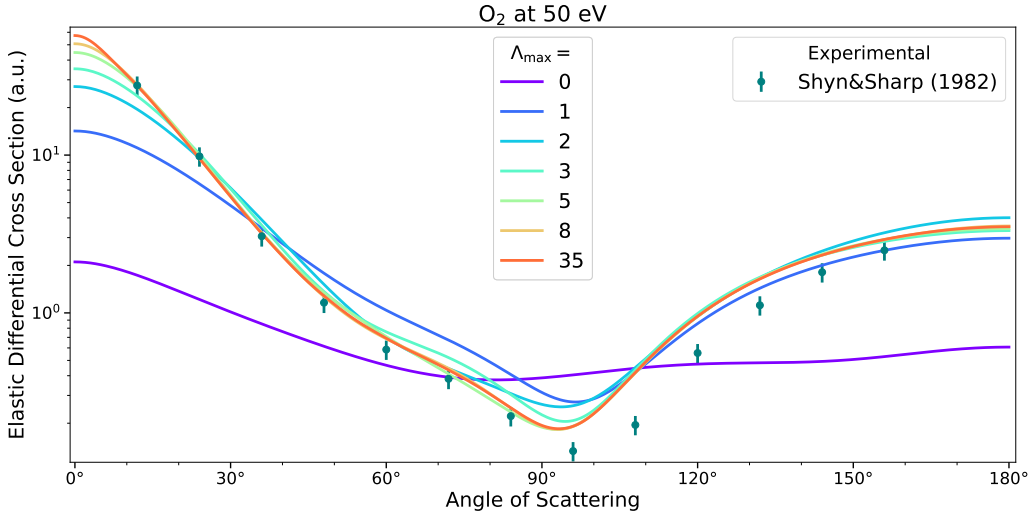

(c) Convergence in $\Lambda_{\max}$: the angular projection symmetries.

Figure 10.25: Convergence of DCS in the angular-momentum close coupling calculations. Excluding the parameter varied in the series, the calculations are done at $\ell_{\max} = 35$, $l_{\max} = 24$ and $\Lambda_{\max} = 35$.

Apology

The issue of convergence forms a whole field on its own in computational physics and applied mathematics. Studying the convergence of a series enables us to see clearly whether our efforts are vain or not, whether our approach is efficient or sloppy. It also enables us to highlight the importance of each term $(\xi)_{n+1} - (\xi)_n$ involved and helps to bring about new ways of computing/estimating results. There is a fine line demarcating the investigations that highlight convergence of their results from those that pass over the subject as a mere formality to be crammed in a paragraph to be lost somewhere in the methodology section. The contrast is as stark as between a cultivator that comes year round and the reaper who pops up just on the day of harvest. May I be excused, despite my efforts, to take more after the latter than the former in the approach to this thesis. At the very least, we may safely assert that the results for the elastic DCS produced in this thesis stem from the limitations imposed by our optical potential model and not by some negligence in the numerical calculation. This is a minimal requirement for those DCS to have relevance in scientific investigation.

Chapter 11

Application to (Differential) Cross Sections

In the previous four chapters we have:

7 : introduced the topic of (differential) cross section for electron-molecule collisions;

8 : introduced the quantum theory of electron-molecule collisions and focussed on the elastic scattering for which we selected some incommensurably helpful approximation;

9 : gathered the numerical methods that we implemented in order to calculate the quantities of relevance to the scattering process;

10 : elaborated on the nature use and validity of approximations, generalisations, semi-empirical models and touched upon the issue of numerical convergence.

Now:

This chapter presents the underlying models and the resulting cross sections for elastic and various inelastic (rotational, vibrational, attachment, electronic and ionisation) processes. Our database is made accessible through this Digital Object Identifier: 10.5281/zenodo.8190461 and will be hosted on LXCat.

11.1 Elastic Collisions

An electron that scatters elastically from a target, does not lose kinetic energy in the centre of mass frame of the collision. From a kinematic perspective, such collisions were treated in the appendix A of the previous part I. Here, we discuss the probabilistic part which is comprised of (i) the differential cross section (DCS) $\mathrm{d}\sigma/\mathrm{d}\Omega$ giving a density probability to scatter the electron into the direction Ω per infinitesimal solid angle $\mathrm{d}\Omega$; and (ii) the integrated cross section (ICS) σ which relates to the probability that the collision occur. The ICS is obtained from the DCS as (7.4) $\sigma = \int (\mathrm{d}\sigma/\mathrm{d}\Omega)\ \mathrm{d}\Omega$.

From the previous chapters we already know that various approximations used to describe elastic scattering, apply on different energy ranges. This is why, in order to build our database, we have partitioned the energy space for each target in the following way as detailed in table 11.1. This partitioning may be qualitatively understood as represented below:

Very low	Low	Intermediate	High	Very high	Relativistic
Below resonance	Resonant and/or below ionisation	Above ionisation	Beyond ionisation peak	asymptotic energy dependence	$\gamma \gtrsim 2$
Modified effective range theory	R-matrix	Adiabatic nuclei	Independent atom model	plane wave Born approx.	relativistic Born approx.
MERT 10.1.5 [710]	~~8.4~~ [134]	BF-AN 8.5.2 [671]	IAM 8.5.3 [572]	PWBA 8.5.1 [799]	RB 8.5.4 [716]
$\lesssim 0.1$ eV	0.5—15 eV	20—100 eV	0.2—8 keV	10—100 keV	$\gtrsim 0.5$ MeV

In each regime, we give an indicative energy range, we highlight the physical nature of the scattering and associate an adequate model for computing DCS, with a cross-reference in this thesis and a bibliographic reference (out of a plethora). The only theory which we have not broached in this thesis is the R-matrix, which defines various regions of space where (electronic, vibrational, rotational) close-coupling apply. It is a titanic and leading-edge topic in the field, please consult Burke [136] and Descouvemont and Baye [216] for more information.

Evidently, the qualitative partitioning presented may depend on the target. For instance the MERT method is inapplicable for atomic nitrogen at 0.1 eV while it seems satisfactory for molecular nitrogen (see 11.1). In the low- and high- energy limits, we used the same models (MERT and PWBA respectively), for different targets, with parameters given in tables 11.2 and 11.13). In the middle-energy range, the models varied depending on the target. The rest of this section describes these models from low to high energies

Table 11.1: Partitioning of the construction of our present DCS database according to the electron incident energy.

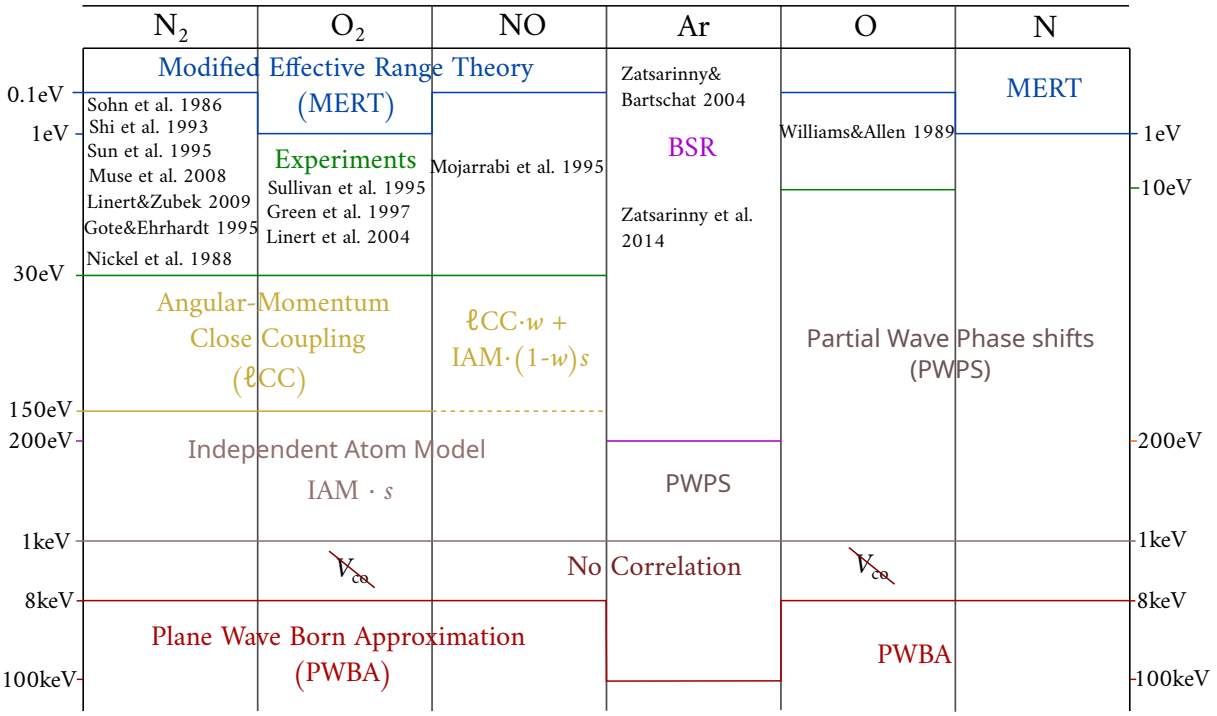

Table 11.2: Parameters used in MERT (10.21) in atomic units of the Bohr radius a_0.

	N_2	O_2	NO	Ar	O	N
A (a_0)	0.44	0.3	0.75	-1.37	0.63	0.6
$\alpha_{d,0}$ (a_0^3)	11.74	10.67	11.47	11.08	5.412	7.423
$\alpha_{d,2}$ (a_0^3)	3.131	4.93	3.78			
Q (ea_0^2)	-1.13	-0.29	1.78			

11.1.1 Very low energy

In the sub-eV domain, the modified effective range theory (MERT) is has proven to be a very powerful tool for computing DCS for noble gases [272] and molecules [429]. Nevertheless, the application of the "classical" MERT, whose equations (10.21) were exposed in section 10.1.5, is limited. For molecules, Isaacs and Morrison [429] show that because of the underlying adiabatic nuclei approximation (which is not valid at very low energies near the threshold of rotational excitations), the scattering length A ought to be extracted from rigorous close-coupling calculations so as to make the MERT (10.22) 'fit' the calculated cross sections. For atoms, in order to make the MERT applicable up to 1 eV, one requires the inclusion of a few additional parameters to be fitted. A notable difficulty in the MERT is the relatively high sensitivity of the scattering length A when derived to fit a DCS or from total cross section at the zero energy limit. Deriving A from calculations is even more prohibitive [892, p.7] because of the significant dependence of the s-wave phase shift on correlation, polarisation and exchange at very low energies [999, p.1244 and fig. 2].

Since we wanted to preserve a unified and simple handling of very-low-energy DCS for atoms and molecules, we did not attempt to pursue any of the advanced MERT implementations which would require to deal with the body-frame K-matrix [268] or a more advanced parametrisation of the phase shifts [272, eq.(7)]. Therefore, we only produced simple MERT DCS (10.21) and (10.17a–10.17b).

The parameters used are summarised in table 11.2, we purposefully privileged values of the scattering length A most recently derived from total cross sections [545]. Disgracefully, for some targets we had to resort to ballpark estimates for A. Concretely, the values were obtained:

- N_2 : 0.44 from Chang [168] and Fabrikant [269, p.899:§3.2, p.4229:§4.2];
- O_2 : 0.3 from Zecca *et al.* [1006, p.116:1st§] with $A = \sqrt{\sigma(\varepsilon = 0)/4\pi - 4Q^2/45}$;
- NO : 0.75 guessed from the $\sigma(\varepsilon = 0) = 3 \times 10^{-20}\,\mathrm{m}^2$ extrapolated to zero from the cross sections calculated by Laporta *et al.* [557];
- Ar : -1.37 taken from Kurokawa *et al.* [545, p.7:table II];
- O : 0.63 derived from Zatsarinny *et al.* [999, fig.2] and in agreement with Tayal and Zatsarinny [921, fig.1] giving $\sigma(\varepsilon = 0) \approx 5a_0^2$;
- N : 0.6 from a MERT fit to the integral cross sections of Wang *et al.* [975] for data below 0.01 eV.

Note that, as remarked by Isaacs and Morrison [429, p.709], the scattering length A for molecules must be derived in conjunction with the quadrupole contribution $(16\pi/45)Q^2$ to the zero-energy cross section if the approximation used is that of the adiabatic nuclei.

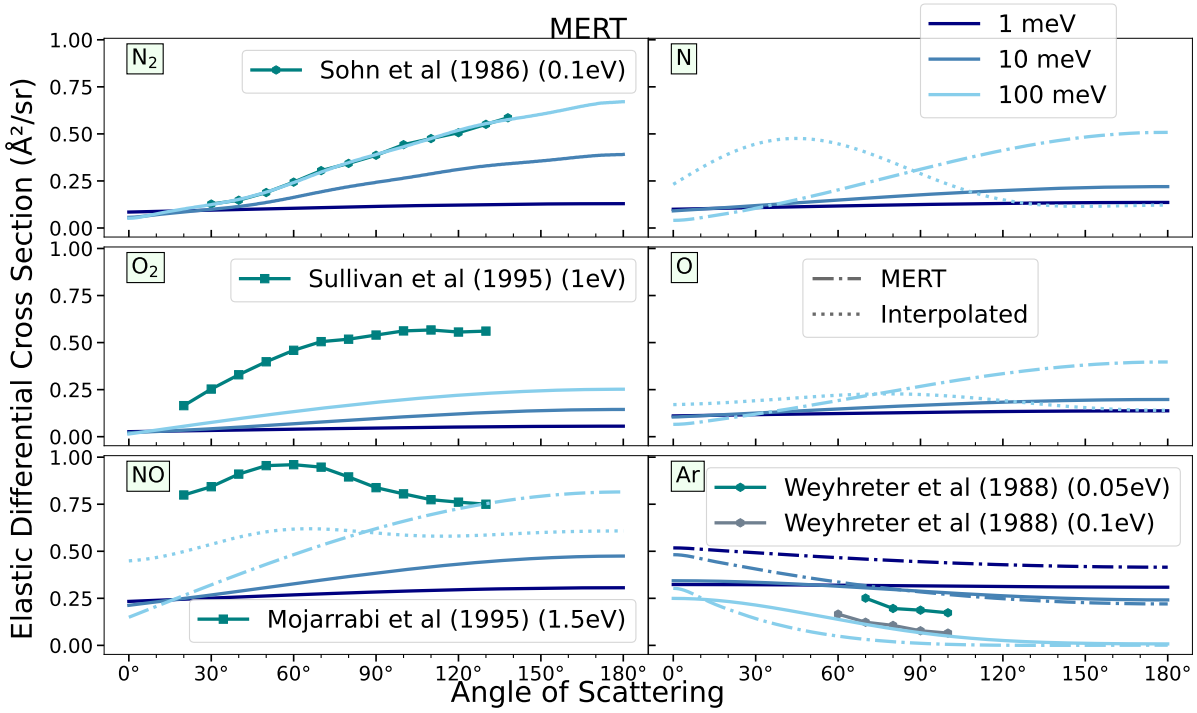

Figure 11.1: Very low energy DCS at three lowest energies (1 meV, 10 meV and 100 meV) for six targets using the MERT when deemed applicable; otherwise through logarithmic interpolation (...) between the highest MERT DCS and the lowest experimentally available DCS.

A comparison of very-low-energy DCS in our database with MERT and experimental DCS, when available, is displayed in figure 11.1. The selected DCS in the database (—solid) are compared with MERT (–•–), when both differ. Dotted lines (···) show DCS interpolated logarithmically between two energies when the used approximations are inapplicable to compute a DCS at a given energy in our database. To be more explicit: we did not compute a DCS for N, O and NO at 0.1 eV. The dotted DCS shown (···) is obtained from a logarithmic interpolation between 0.01–1 eV and 0.54–1.5 eV respectively.

A noteworthy exception in our database is argon for which the BSR calculation of Zatsarinny [1000] and Zatsarinny *et al.* [1002] has been made available on LXCat in the 0.001–200 eV range.

We now move to the low through intermediate to high energy range of the DCS for which we separate the treatment for atoms and diatomic molecules.

11.1.2 Atoms

For each atom, as seen on the summary representation 11.1 the generation of DCS in the low-mid-high energy range reflected the differences in availability of data.

Argon

As a noble gas, argon has been honoured by a plethora of both theoretical and experimental databases. Thus we deemed wise to build from the existing B-spline R-matrix database of Zatsarinny and Bartschat [998] and Zatsarinny and Bartschat [1001]. Since the DCS spanned 1 meV to 200 eV, we completed the set for energies beyond 200 eV with our own calculations that we checked against ELSEPA [803]. A comparison at 200 eV is shown on figure 11.2 to wit the agreement between all three theoretical sources.

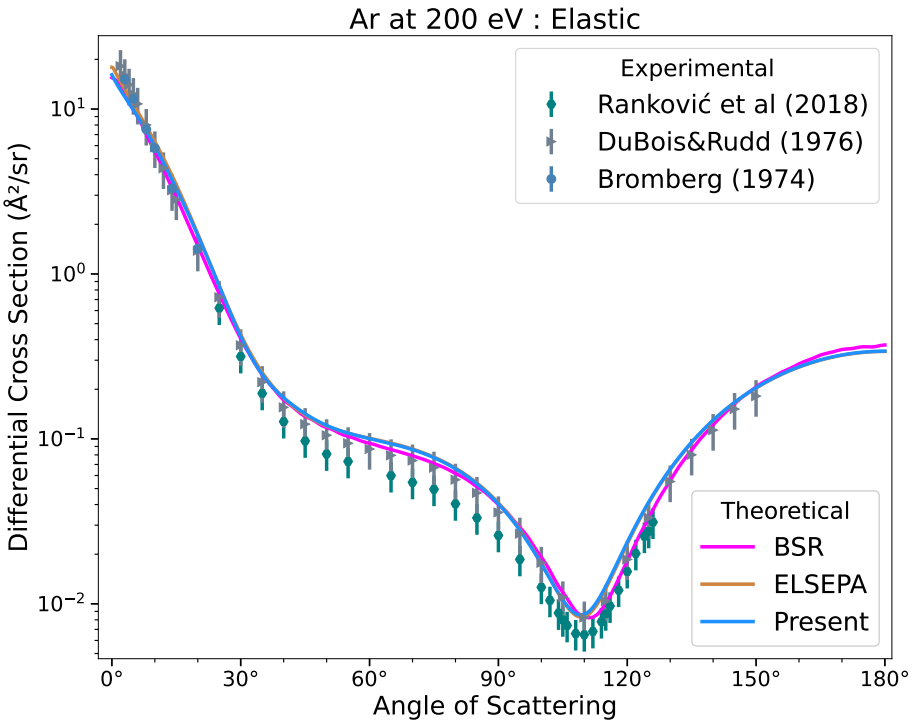

Figure 11.2: A comparison of BSR [1000] and our calculations practically superposed with ELSEPA [803] for electron-argon elastic DCS at 200 eV. Experiments: ⬡:[766], ▸:[232], ●:[116]

Overall, all three DCS are in agreement except perhaps that ours (and ELSEPA's) slighlty overestimate the DCS in some angular ranges. We think this might be related to a strong underestimation of absorption as can be seen on figure 11.3. More absorption would consistently raise the calculated inelastic cross section while decreasing the elastic DCS.

Of further interest, we note that, the actual BSR database for integral elastic cross sections has been updated more recently than the one for differential CS. For this reason, there are some slight inconsistencies at low energies as can be seen on figure 11.4 if one compares the integrated DCS with the given CS. Also, there is a discontinuity at 0.017 eV in the shape of the DCS as can be seen from the momentum transfer CS on the right. Even though the MERT CS seems to fit the most recent data of Kurokawa *et al.* [545] well, we did not attempt to resolve this inconsistency with the MERT DCS due to the quite large difference with the BSR DCS even at very low energies.

Atomic oxygen

So far, we have access only to one source of experimental DCS for atomic oxygen in the low energy range 0.5–10 eV [984]. The construction of the DCS has been challenged by the discord at forward scattering angles between experimental data [984] and theoretical calculations [999]. Regardless, we decided to use the phase shifts determined experimentally by Williams and Allen [984] to build the DCS below 10 eV and then completed the DCS to higher energies with our own calculations. Similarly to Zatsarinny *et al.* [999, fig. 4], the DCS calculated by ELSEPA on figure 11.5 also predicts less prominent forward scattering than the measurements. Our DCS have even less forward scattering which is due to the less precise static potential for atomic oxygen that we use in table 8.1.

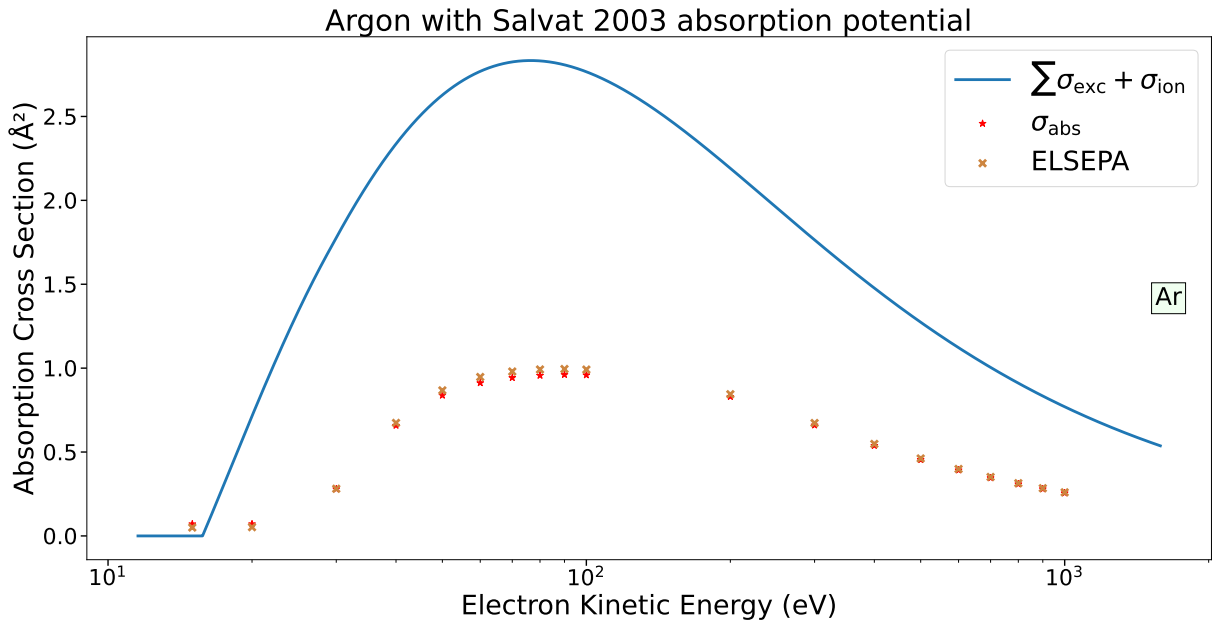

Figure 11.3: Absorption cross section (8.111) from the imaginary part of the phase shifts obtained with the central potential for argon based on (8.58–8.64). The consistency of our calculations is verified with ELSEPA [803] which uses the same model for absorption. Nevertheless, an overall underestimation of a factor of 3 is observed throughout the energy range covered.

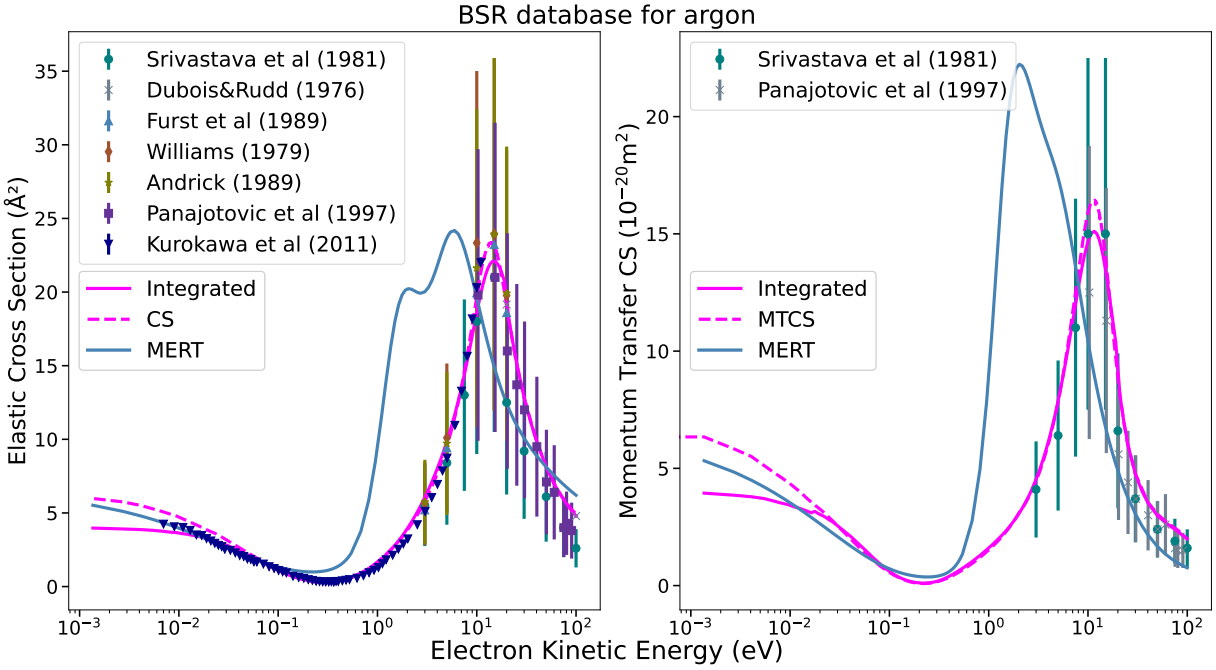

Figure 11.4: Electron-argon elastic integral CS (left) and momentum-transfer CS (right) of the BSR database (pink) [998, 1002] and calculated with the MERT (10.22) (blue) with parameters from table 11.2. The MERT seems valid only below 0.1 eV. Solid (—) curves are integrated from the DCS [1001] and dashed (- - -) are from the ones published in [1002].
Experiments: •:[871], ×:[232], ▲:♦ ★:[310, tab. IV], ■:[731], ▼:[545]

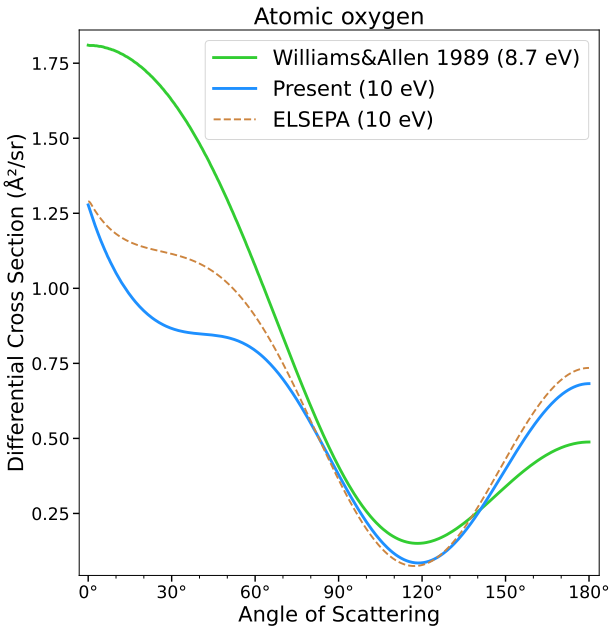

Figure 11.5: Discrepancy at forward angles between Williams and Allen [984] data at 8.7 eV and theoretical calculations (at 10 eV).

Atomic nitrogen

Due to the utter absence of experimental data for elastic scattering, our calculations for atomic nitrogen are completely blind. There are several theoretical studies [928, 975], however, no DCS data were made available in tabulated format. As for oxygen, a general agreement with ELSEPA's calculations was our only guide in building the DCS.

For the *integral* elastic cross section (ICS), Wang *et al.* [975] published their results on LXCat. Together with the calculations of ELSEPA, they are displayed on figure 11.6. Good agreement of our ICS is found for all energies beyond 20 eV. Below this point, it gradually deteriorates to a terrible disagreement in the region of resonance at 0.08 eV.

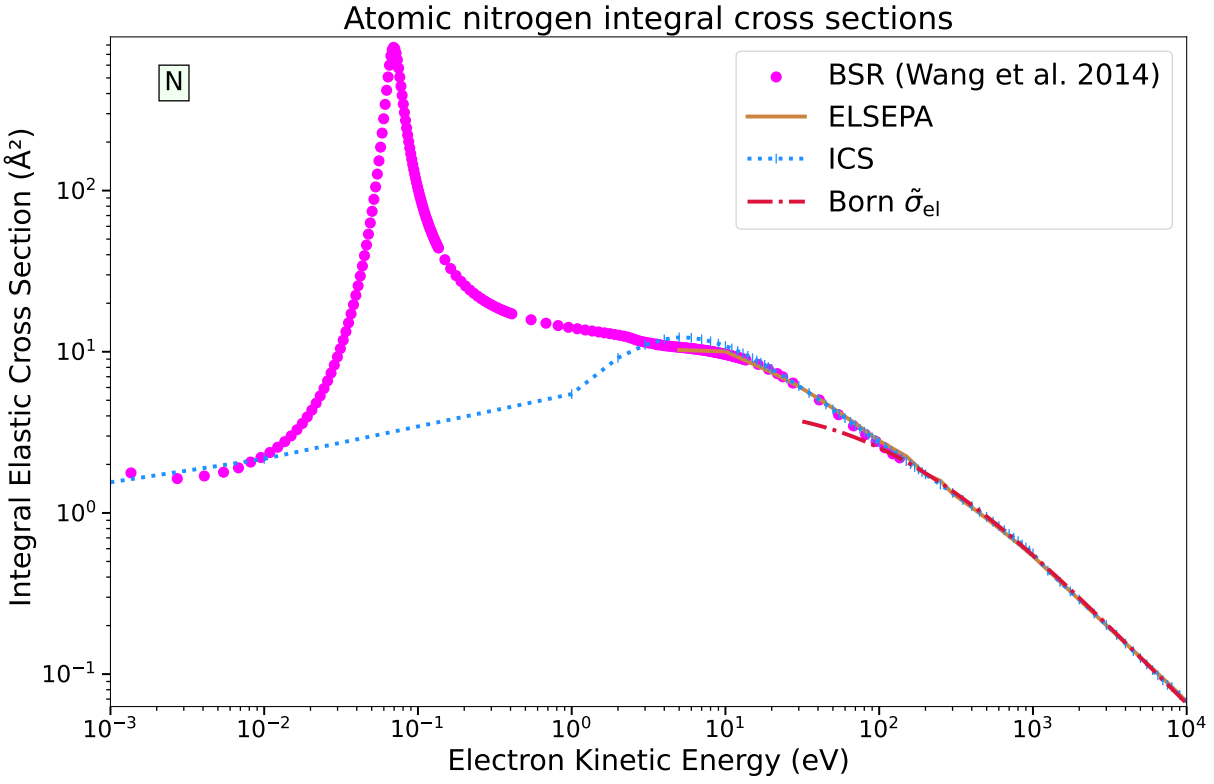

Figure 11.6: Integral cross sections for N obtained from the DCS of Wang *et al.* [975] (•), our calculations ('ICS' ···) and those of ELSEPA [803] (—). As explained in section 11.1.5, the present database of elastic cross sections for atomic nitrogen is generated by extending the BSR data of Wang *et al.* [975] with our ICS from 140 eV. The Born fit (–·–) is obtained from (11.9).

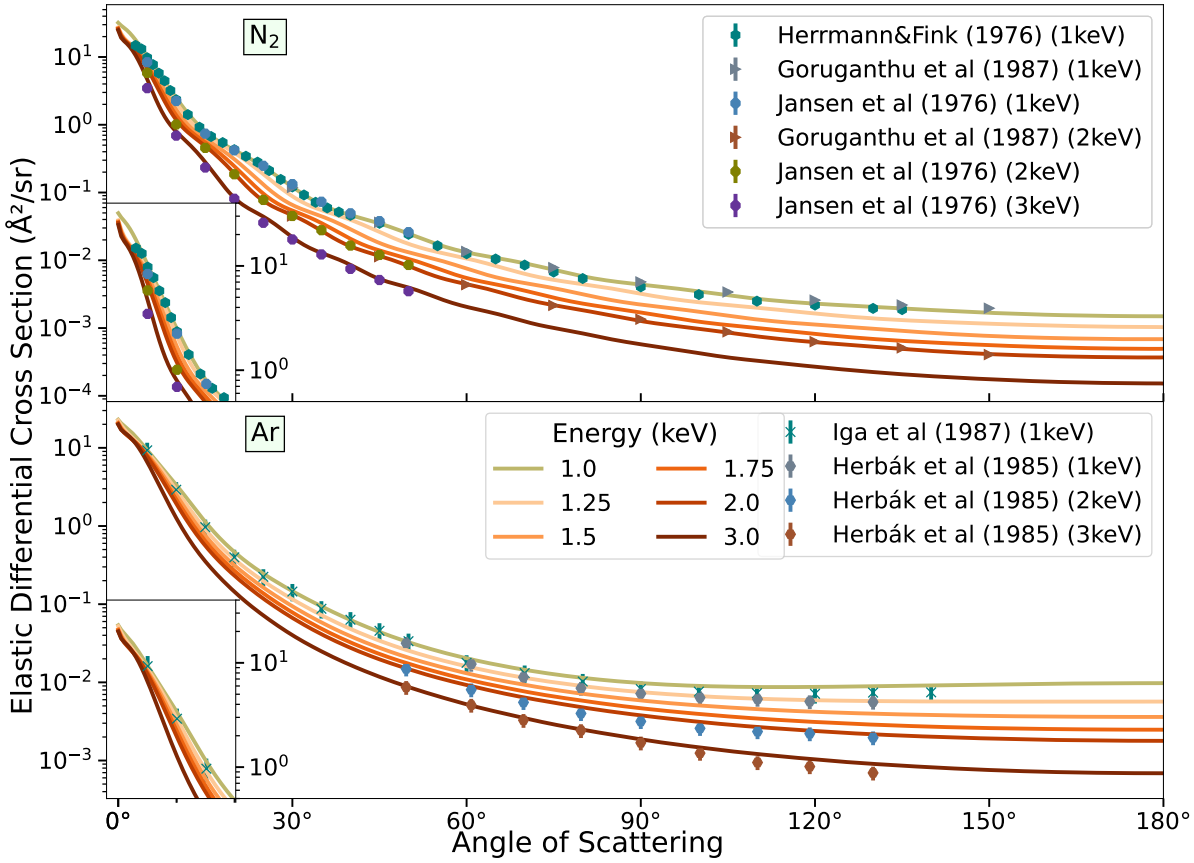

Figure 11.7: Transitions of the DCS between 1 and 2 keV represented by the replacement (11.1) of the kinetic density functional correlation potential $V_{\mathrm{co,kdf}}$ by the Buckingham potential V_{b}. Experiments: N_2 – ⬡:[397], ▷:[343], ⬡:[453]. Ar – ×:[418], ⬡:[396].

Correlation at high energies

As we discussed in the previous chapter 10.3.3, as the energy of the incident electron increases, the polarisation (and correlation) effects should decrease due to the non-adiabatic response of the atomic electronic cloud. For all atoms, the long-range polarisation potential is combined with the short-range kinetic density functional (KDF) correlation potential $V_{\mathrm{co,kdf}}$ through (8.55) by a junction at their outer intersection radius r_{t}. This is graphically visible on figures 10.14. Non-adiabatic scaling of the long-range polarisation is done by growth of the curbing radius $r_{\mathrm{d}}(\mathrm{v})$ (8.56) with the incident velocity, but has no equivalent for short-range correlation.

The correlation potential given by the KDF model (8.51) has in fact a significantly longer range than the static-exchange, and should rather be considered a "mid-range" potential (see violet—curves in the left panel of figure 8.3). This means that at high energies, correlation will mostly affect scattering at small angles as we demonstrated on figure 10.18a of section 10.3.3.

As we mentioned on earlier occasions, the determination of a correct DCS at very small angles at high energies is unclear for at least two reasons.

1. The experimental probing of small angle scattering is difficult even at high energies. The experimental data available is not sufficiently diverse and resolved in angle to allow to discriminate one model potential versus another.

2. For molecules, the DCS at small angles is affected by deficiency of the independent atom model which does not account for long-range multipole potentials emerging from the chemical bond [287, 602, figs. 8–10, fig. 4].

3. In addition to this, in practical applications of plasma physics, the scattering at very small angles might come from regions of space ($> 20a_0$) where the electron is affected by other forces than those attributable to the scattering target.

Since we have not found any evident way of reducing correlation effects at higher energies (otherwise than empirically), we resorted to replace the KDF correlation above 1 keV for all targets (atoms and molecules alike) by the Buckingham potential which crudely mimics it, but resorbs with energy. Mathematically:

$$\text{Below 1 keV included :} \qquad V_{\text{cop}}(r) = \begin{cases} V_{\text{co,KDF}}(r) & r < r_{\text{t}} \\ V_{\text{b}}(r) & r \geq r_{\text{t}} \end{cases} \tag{11.1a}$$

$$\text{Above 1 keV :} \qquad V_{\text{cop}}(r) = V_{\text{b}}(r) = -\frac{\alpha_{\text{d}}}{(r^2 + r_{\text{b}}(\varepsilon)^2)^2} \tag{11.1b}$$

The curbing radius r_{b} was adjusted so as to enable a smooth transition of the DCS between 1 keV and 2 keV. This is represented on figure 11.7. The transition is almost imperceptible for argon, because its polarisation is relatively small compared to its static potential; whereas for molecular nitrogen, we can see in the inset of the top graph in figure 11.7 how switching off correlation removes a 'lump' at very small $< 2°$ angles where experimental data are nought.

11.1.3 Diatomic Molecules

An overview of the presently constructed DCS for diatomic molecules was displayed on table 11.1 which is separated into low, intermediate and high-energy regions.

Low energy (< 30 eV)

Low-energy scattering with diatomic molecules is very complex and requires top-edge methodologies to model. Even then, there are some discrepancies that emerge in some angular ranges [915, fig.1], mostly forward scattering as can be seen for N_2 on figure 11.8 comparing the theoretical –•–curve of Sun *et al.* [894, tables III and VII] with the bulk of experimental data. Fortunately, for N_2 and somewhat for O_2, the database of experimentally measured DCS is rich and one can resort to fitting techniques, as illustrated (see fig. 13.3) in a dedicated chapter 13 of part III.

In order to obtain coherent fits, we had to select some experiments and discard others based on reviews [124, 941] and comments from more recent studies [17, 353, 600]. The sources in each column of table 11.1 were retained in the fitting procedure. For cross referencing, those sources are given below (with the ones disregarded, crossed):

N_2	O_2	NO
Allan [17], Gote and Ehrhardt [344], Linert and Zubek [600], Muse *et al.* [684], Shi *et al.* [832], Sohn *et al.* [863], and Sun *et al.* [894]	Green *et al.* [353], Linert *et al.* [598], and Sullivan *et al.* [893]	Mojarrabi *et al.* [654]
~~Shyn *et al.* [844],Shyn and Carignan [838] Srivastava *et al.* [870],Brennan *et al.* [105]~~	~~Trajmar *et al.* [938],Woste *et al.* [989] and Shyn and Sharp [842],~~	

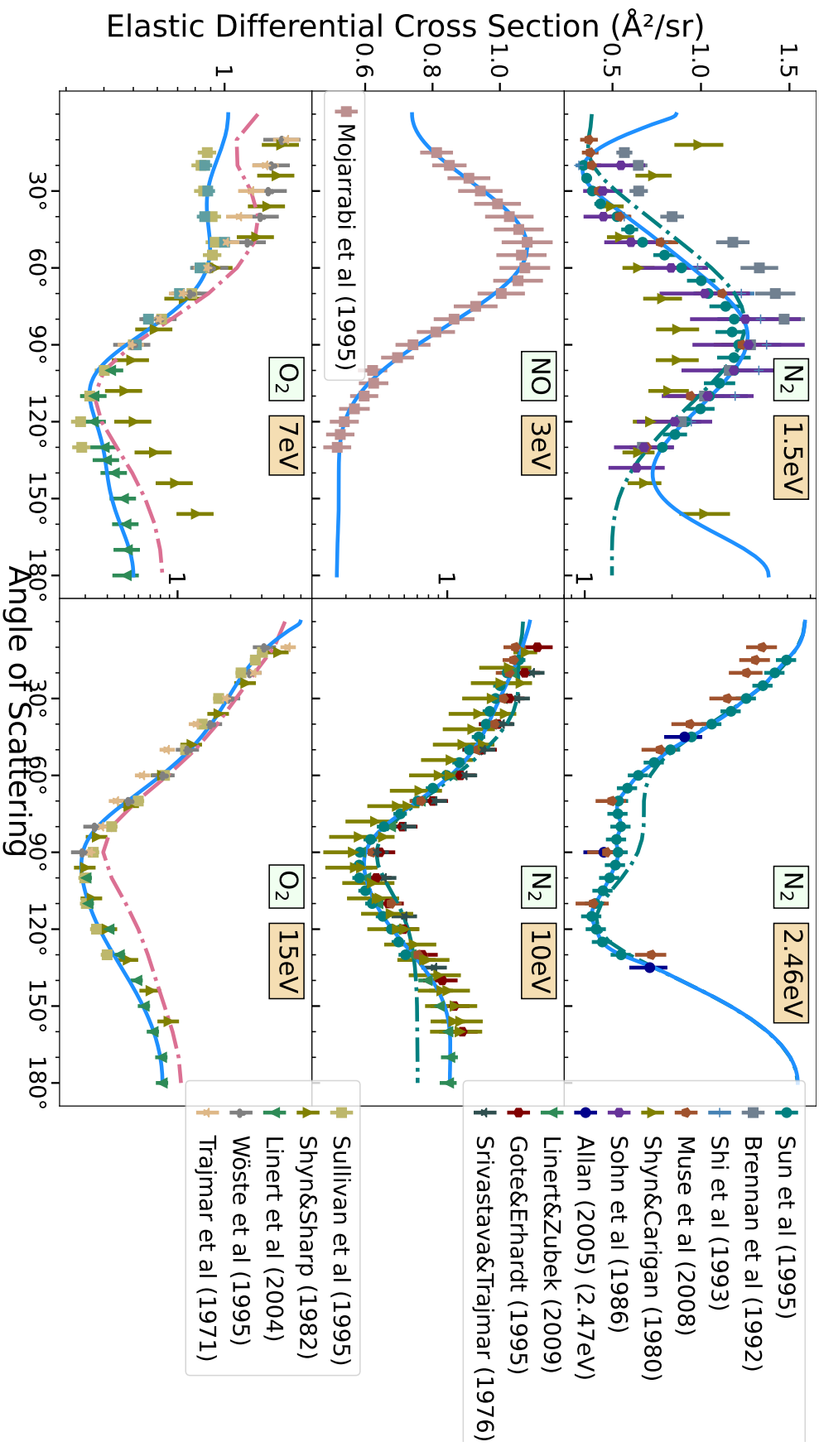

Figure 11.8: Examples of fitted DCS to experimental data for diatomic molecules at various energies below 30 eV. The blue curve — shows the present database and can be compared to the dash-dotted -·- curve of Sun *et al.*'s [894] theoretical calculations for N_2 when available.

For more information about the sources, the reader may consult section **??** in a later chapter, which comments about eventual adjustments that we made on some experimental data.

The graphs shown on figure 11.8, for all three molecules N_2, O_2 and NO, are examples of fits used in our database. Concretely, we have juggled with a combination of:

- Least-squares Legendre polynomial fit of order $L_{\max}$ between 3 to 7 depending on the energy and the necessity of including steep DCS slopes at forward angles.
- Molecular phase-shift analysis (MPSA) as initiated by Boesten and Tanaka [87] and reminded in equation (13.5b) in section 13.1.1. This method exploits the calculation of high-order phase shifts from the plane-wave Born approximation to long-range potentials and leaves the first few phase shifts in 8.108 as free parameters. Its advantage is that the fit will be guaranteed to be positive and reduce the number of parameters while keeping high the maximal degree of the Legendre expansion of the DCS. Unfortunately, as one can imagine, the use of MPSA is purely speculative since molecules do not have a diagonal S matrix and thus the "phase shifts" fitted are convenient parameters with an unclear physical significance (in which frame does the S matrix diagonalise since it is supposed to be unitary? what about absorption and coupling?). As a result, our success in obtaining agreeable MPSA fits was very limited (O_2 at 7 eV on 11.8 is an example of MPSA fit).
- Available theoretical calculations from Sun *et al.* [894]. We did not find other sources for which the agreement would be compelling (e.g. Machado *et al.* [617] for O_2).

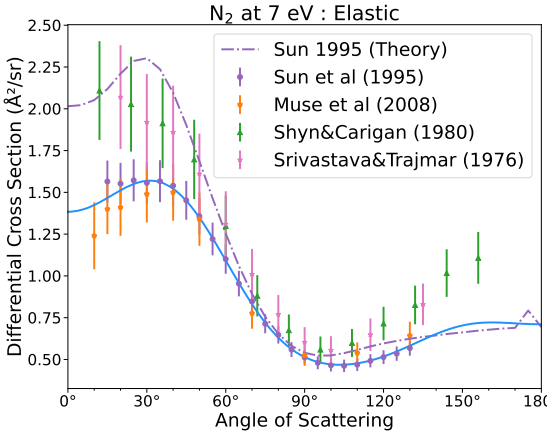

Figure 11.9: Constraining the backward angle DCS with theoretical results at 180°.

In some cases, we mixed the three methods at a same energy to obtain better agreement with a set of experimental data. In order to better constrain the extrapolation to large angles up to 180°, we aggregated results from theoretical calculations Fujimoto and Lee [307], Machado *et al.* [616], Sun *et al.* [894], and Tashiro *et al.* [915] at 180° when performing a least squares or MPSA fit. This can be seen on the figure 11.9 where we disregarded experimental data [838, 870] while privileging the theoretical backscattering trend* [894, table VII]. In a few cases, we performed a fastidious adjustment of our DCS. This is neatly seen for N_2 at 2.46 eV, where we stitched theoretical calculations [894] at forward and backward angles while using a least squares fit at intermediate angles.

At energies beyond 15 eV the shape of the DCS starts to be prominent at forward scattering angles . Unfortunately, our modelling of molecular potentials did not enable us to use angular-momentum close-coupling results below 30 eV (see how bad the grey dash-dotted –·– curve looks on figure 11.11 for NO at 20 eV, while being acceptable at 30 eV). Thus in the energy range 15–25 eV, we used a combination of a screened Rutherford formula complemented by a residual backscattering Legendre polynomial expansion. This trick is the remnant of our original methodology in Schmalzried and Luque [811, §2.4] which produced empirical fits of DCS based on an adaptation of the Rutherford screening parameter η in (14.9) for all energies above 15 eV.

*This figure 11.9 reveals the mistyped value '0.793' at 7 eV and 175° which should be corrected to '0.693'

Intermediate energies (30 eV $\leq \varepsilon \leq$ 100 eV)

Originally, in Schmalzried *et al.* [812], we had designed a way to extend the validity of the independent atom model (IAM) to this intermediate energy range by performing a different separation of the molecular potential: two atomic unperturbed potentials and a central isotropic molecular potential. With a partial-wave decomposition based on the Born approximation, we estimated a way to subtract that part of the scattering amplitude f_A that participated to the scattering from the isotropic centre of the molecule. This technique enabled us to obtain DCS in fair agreement with experimental data, yet only involving scattering amplitudes from three central potentials (two atomic and one molecular isotropic).

In yearn of improving our DCS, we decided to implement the angular-momentum close coupling (ℓCC) methodology in the body-frame as described in 8.5.2 and embodied in equation (8.129). The results may be observed on figure 11.10 for N_2 and O_2, and on figure 11.11 at a few selected energies. Since the validity range of the simple IAM overlaps with the applicability range of the ℓCC, we did not use our methodology [812] to construct our elastic DCS database.

N_2 The results for N_2 on the left column of figure 11.10 are fairly in agreement with experimental data, except at intermediate angles between 60° to 120°. We deem that a more accurate treatment the static molecular potential as in Lee and Iga [569], would remove this overestimation. Nevertheless, at energies below 40 eV, it seems that their results [569] also present slight overestimation in the mid-angular range. This could be imputable to a limited modelling of correlation-polarisation and absorption effects. Perhaps, the FEG $V_{\mathrm{co,feg}}$ (10.61) correlation potential (—) that they use is too strong (deep) compared to the KDF $V_{\mathrm{co,kdf}}$ (8.51) (—) as can be seen best on figure 10.14b in the previous chapter on pages 364–373.

For O_2 and NO which both have open shells, we were confronted with more difficulties.

O_2 For O_2, a comparison of our calculations is shown on the right column of fig. 11.10 with the Schwinger-variational distorted-wave calculations of Machado *et al.* [617] (–•–) and experimental data of Shyn and Sharp [842]. Very surprisingly, despite our crude modelling of oxygen's diatomic potential, our results differ little with Machado *et al.*'s in the intermediate energy range. However, it seems that both our and their [617] calculations, despite their more accurate modelling of static and exchange potentials, overestimate the experimental DCS in the mid-angular range. Here, the discrepancy may either come from the absorption potential, which improperly accounts for the coupling with the low-lying inelastic transitions to a $^1\Delta_g$ and b $^1\Sigma_g^+$ states of O_2, or rather be likely due to a bias in Shyn and Sharp's [842] experimental results which are the only ones available at intermediate energies. Indeed, one can find on the right column in fig. 11.12 a quite noticeable discrepancy of a factor exceeding 1.3 with Daimon *et al.* [206] at 200 eV whose data is favoured by both our ℓCC calculations and those of Machado *et al.* [617, table II]. This is also consistent with the difference at 30 eV with Sullivan *et al.* [893] in fig. 11.10-top-right.

NO However, the same conclusion cannot be drawn for NO. A comparison of Mojarrabi *et al.*'s measurements [654] with the calculations of Fujimoto and Lee [307, figs. 3&4] show excellent agreement at 30 and 40 eV*, while ours (ℓCC–•–) on figure 11.11 dramatically overestimate scattering at intermediate 70°–130° angles. They [307] used the FEG correlation potential $V_{\mathrm{co,feg}}$ (10.61) with the quasifree absorption $V_{\mathrm{abs,qf}}$ of Jain and Baluja [450, eq.(7–8)] but treated the static and exchange potentials exactly and properly averaged the cross section according to the spin triplet and singlet couplings with the single 2π electron of NO. We therefore surmise that the present discrepancy in our calculations for NO arises from our very limited modelling of static molecular diatomic potentials and no account for the deformation of the valence orbitals from the chemical bonding, nor inclusion of spin-dependent cross sections.

*They unfortunately did not provide digitised data at those energies.

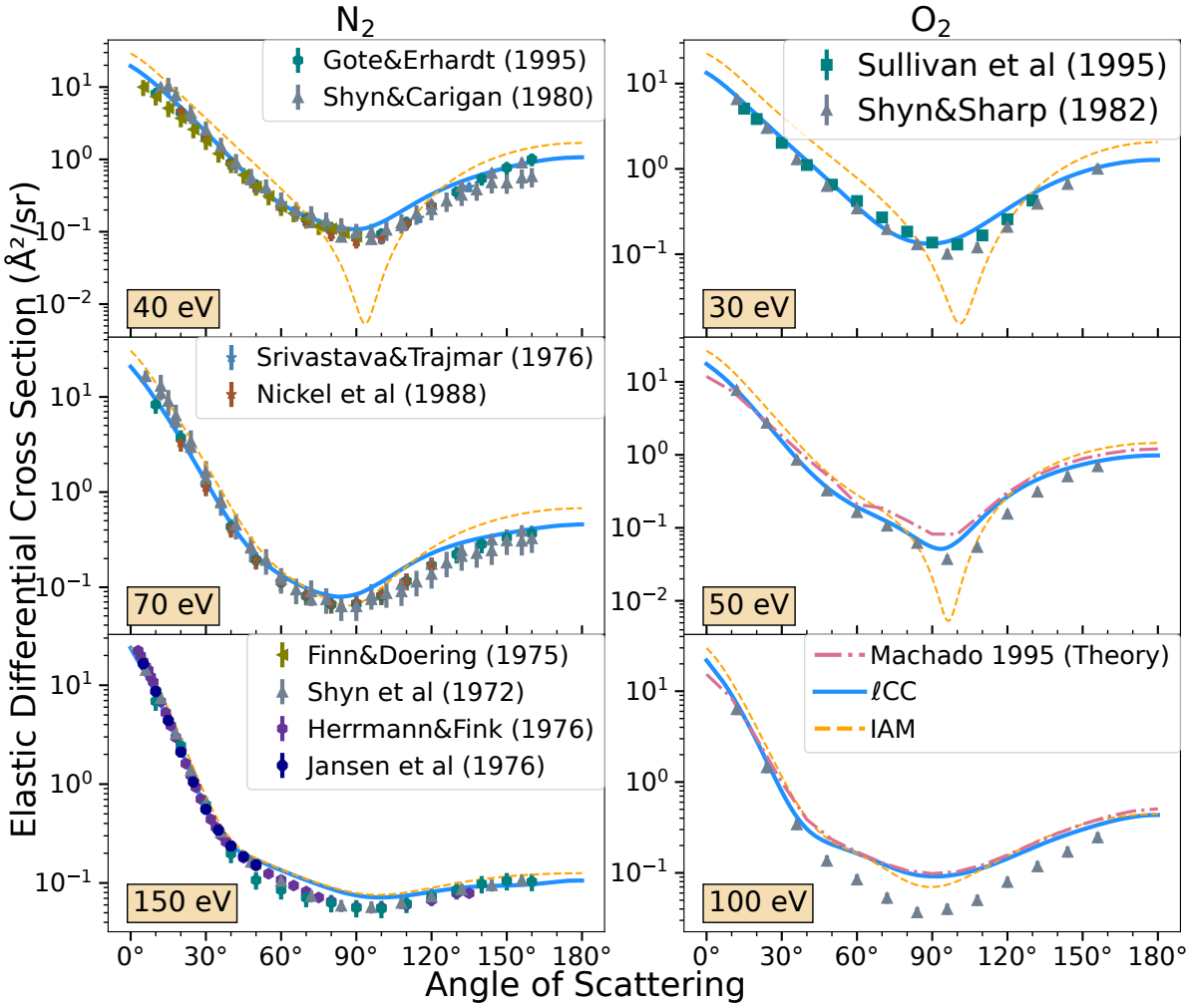

Figure 11.10: DCS calculated from angular-momentum close-coupling (ℓCC-8.129) and compared with various experimental data [288, 344, 397, 453, 700, 838, 842, 844, 870, 893] in the intermediate energy range. Also shown are the curves (- - -) from the independent atom model (IAM-8.137). The general issue is that our calculations overestimate the DCS at large angles. Also shown are the theoretical calculations of Machado *et al.* [617] (-·-).

As a matter of fortunate coincidence, the independent atom model (IAM) on the other hand has a dip in that angular range (- - -curve on fig. 11.11) due to the negligence of multiple intramolecular scattering. For pragmatic purposes, to palliate our modelling flaws and salvage our endeavour of building an elastic DCS database, we decided to use a weighted sum of ℓCCand IAM DCS for NO in the following way:

$$\frac{\mathrm{d}\sigma_{\mathrm{NO}}}{\mathrm{d}\Omega} = w\frac{\mathrm{d}\sigma_{\ell\mathrm{CC}}}{\mathrm{d}\Omega} + (1-w)s\frac{\mathrm{d}\sigma_{\mathrm{IAM}}}{\mathrm{d}\Omega}\ . \tag{11.2}$$

The parameter $w \leq 1$ is a weight and $s \leq 1$ is a screening correction to scale down the IAM which violates the optical theorem (and thus overestimates the overall DCS). Both w and s decrease with energy as given in table 11.3. We decided not use weighting w for N_2 nor O_2; the improvement of their calculated DCS will be left for the future.

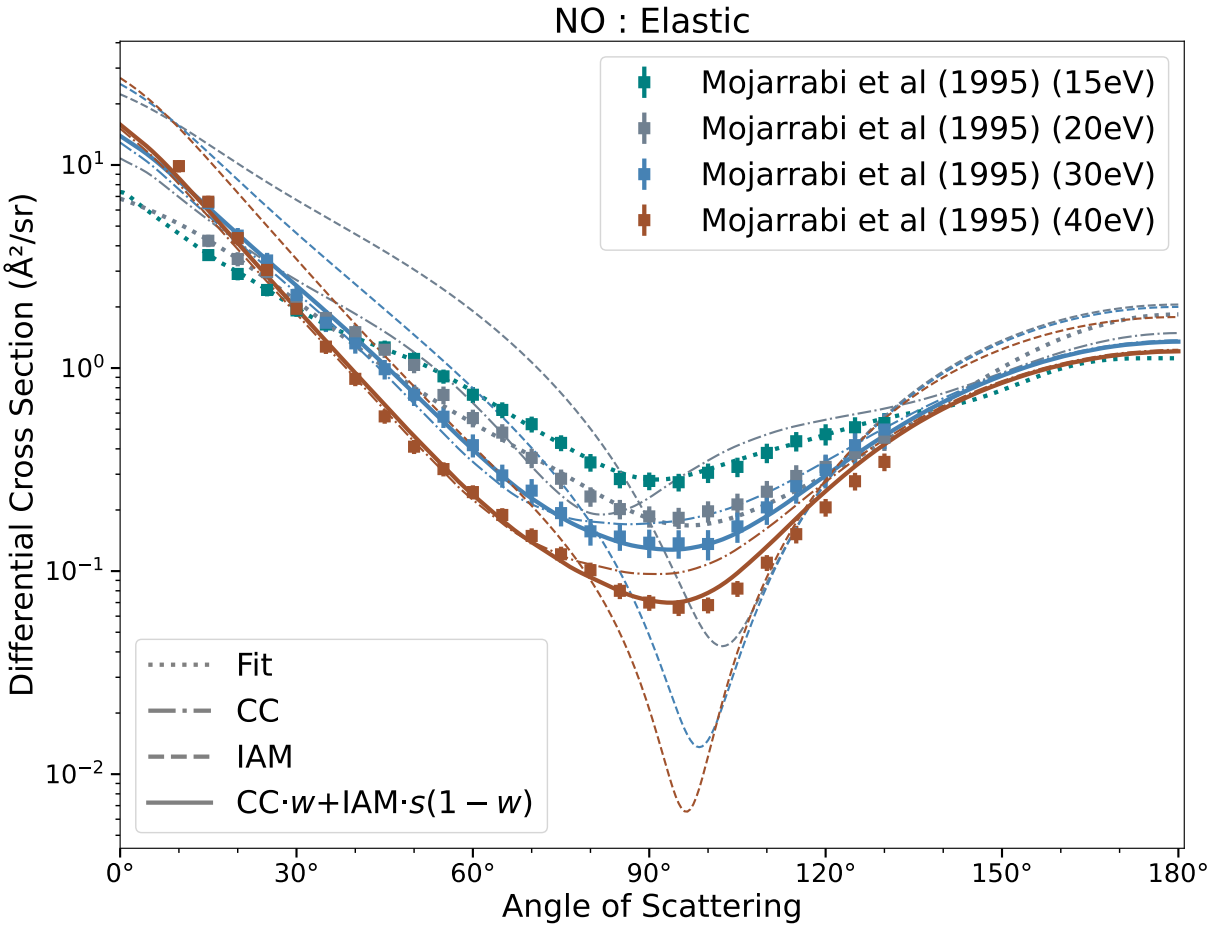

Figure 11.11: ↑ DCS calculated for NO from a least squares Legendre polynomial fit ···, from angular-momentum close-coupling –•–(ℓCC-8.129), from the independent atom model - - -(IAM-8.137) and their weighted sum —(11.2). The experimental data are from Mojarrabi *et al.* [654].

Table 11.3: Empirical weight w (for NO only) and screening correction s for constructing DCS from angular-momentum close-coupling and independent atom models as through (11.2). The cells highlighted lightly in green correspond to cases where the DCS could be compared to experimental data. All other cells are therefore "blind" interpolations. →

Energy (eV)	N_2	O_2	NO	
	s	s	w	s
30	–	–	0.7	0.65
40	–	–	0.675	0.65
70	–	–	0.6	0.66
100	–	–	0.375	0.68
150	–	0	0	0.7
200	0.85	0.85	0	0.75
300	0.85	0.87		0.8
400	0.85	0.9		0.85
500	0.85	0.92		0.9
600	0.85	0.93		0.91
700	0.85	0.93		0.92
800	0.86	0.94		0.93
900	0.87	0.94		0.94
1000	0.9	0.95		0.95
2000	1	1		1

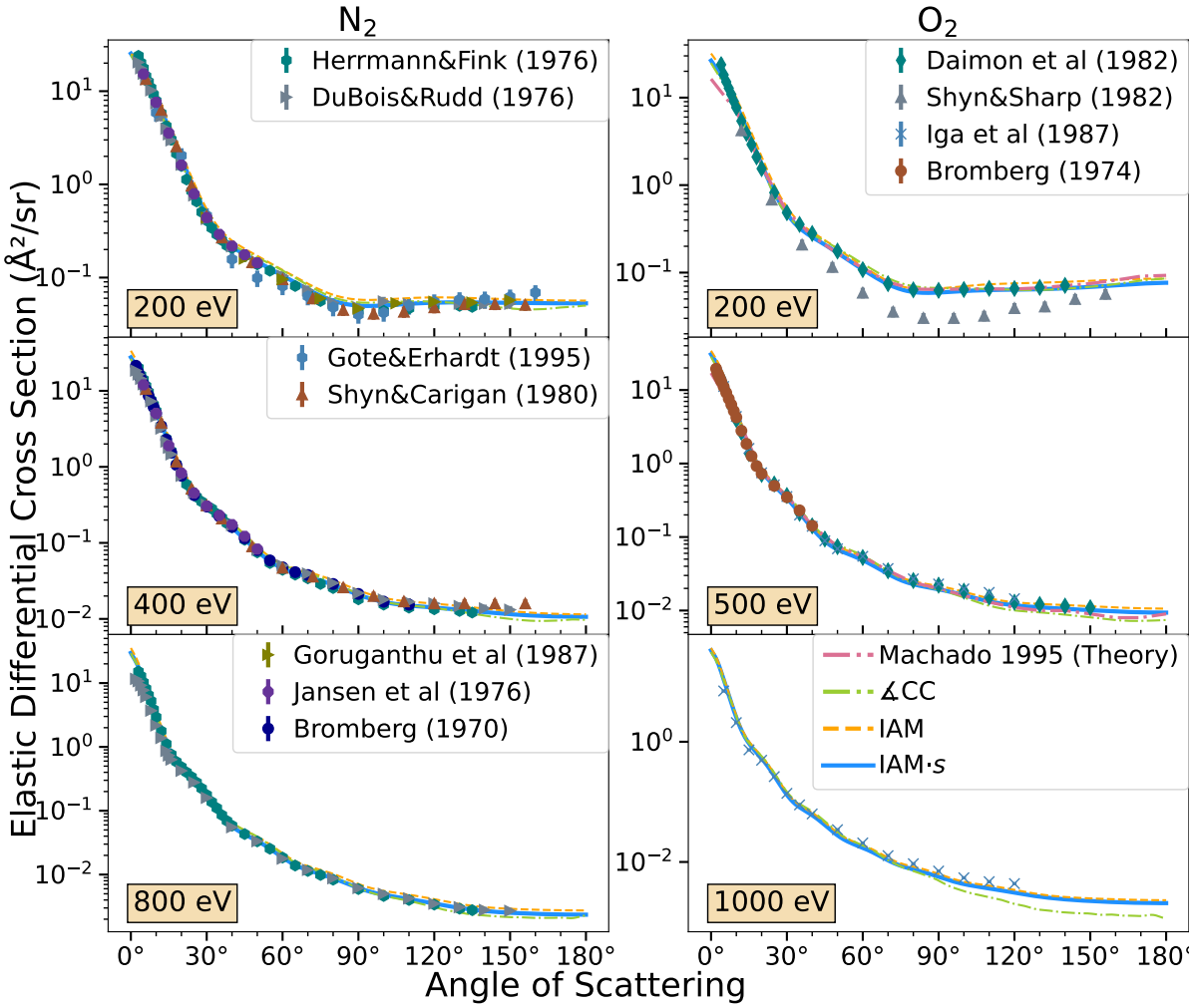

Figure 11.12: Present DCS constructed with scaled independent atom model (IAM·s) with the screening correction s given in table 11.3. The angular-momentum close coupling (–·–ℓCC) is still a valid, albeit increasingly costly way to compute DCS. For O_2 at 200 eV we decided to favour Daimon *et al.*'s [206] (♦) experimental results over Shyn and Sharp [842] (▲) for reasons developed on page 574 of part III.

High energies (> 150 eV)

The angular-momentum close coupling is used up to 150 eV included for all three diatomic molecules. Beyond that energy, we use a scaled independent atom model (IAM) DCS (8.137) with a screening correction s: $\mathrm{d}\sigma_{\mathrm{IAM}}/\mathrm{d}\Omega \cdot s$. There have been several propositions to estimate s semi-empirically through a thorough geometrical approach as in Jiang *et al.* [458] and Zecca *et al.* [1007] or through a loosely justified empirical law as in Blanco and García [83] which we corrected in Schmalzried *et al.* [812, eq.(35)] for a factor 4 which had no apparent justification. We have nonetheless left those formulae aside and adjusted s to our experimental database as reported in table 11.3.

The reason for this is that we could have continued using angular-momentum close coupling (ℓCC–·–) at high energies to calculate DCS as can be seen on the graphs of figure 11.12. There are however two computational issues that deterred us from doing so. First, IAM calculations are much faster (20 seconds versus 2 hours).

Second, the ℓCC DCS were contaminated by oscillations of the Hankel functions (8.97c), which are denser at higher energies, at backward scattering angles due to our limitations of the radial discretisation in the integration (9.17) as can be observed on figure 11.12.

In the end, manually-scaled IAM do not differ significantly from a well-converged angular-momentum close coupling calculation as seen on figure 11.12. The IAM calculations are performed with atomic potentials except that we use molecular parameters in table 8.3 for polarisability and excitation thresholds. Following Salvat *et al.* [803a, eq.(94)], each atom carries a proportion of the molecular isotropic polarisation according to the atomic polarisability.

11.1.4 Very high energy

We have seen in previous chapters that many useful approximations can be used when the electron energy ε is high "enough". In chapter 8 section 8.5.1, we introduced the plane wave Born approximation (PWBA) which is of fundamental importance in high energy scattering. The determination of what "high enough" is, was the purpose of section 10.1, where we estimated the error committed by the PWBA compared to a more accurate calculation of phase shifts. As a result, all our DCS beyond 8 keV were calculated with plane wave Born phase shifts as in (8.120) whose analytical expressions are to be found in chapter 14. Those phase shifts $\tilde{\delta}_\ell$ were then used in the Born closure of the scattering amplitude (9.18) to replace the exact phase shifts δ_ℓ. Note that this procedure is slightly better than the direct use of the Born scattering amplitude $\tilde{f}$ of (8.115), as can be seen on figure 10.4.

In addition to the PWBA we include a corrective relativistic factor as explained in section 8.5.4. This implies that the DCS at forward angles does <u>not</u> saturate to a constant value when the energy increases as implied by (8.115). On the contrary, it rises to absurdly high values due to the extremely forward-peaked DCS at relativistic energies. This poses no physical incoherence because the integral cross section (ICS) saturates to a constant value (fig. 11.13a) while the momentum transfer cross section (MTCS) decreases steadily as seen on figure 11.13b.

This behaviour is due to the screening parameter η related to the wavenumber k and range a of atomic static potentials:

$$\eta = \frac{1}{(2ka)^2} = \left(\frac{\alpha}{2a\beta\gamma}\right)^2 = \frac{\alpha^2}{4a^2(\gamma^2-1)} \,, \tag{11.3}$$

together with the saturation of the electron's speed $\beta < 1$ in relativistic units. We remind that the range a of an atomic static potential is the inverse of the exponential average decay rate $a = 1/\lambda$. Of course, since there are more than one decay rate λ_i, the effective potential range $a(\varepsilon)$ is, in fact, an energy-dependent average between the different a_i.

Notwithstanding, beyond 10 keV for the present targets, one might desire to determine a single energy-independent $\bar{a}$ value that fits the DCS with a simple screened-Rutherford expression:

$$\frac{\mathrm{d}\tilde{\sigma}_{\mathrm{SR}}}{\mathrm{d}\Omega} = \frac{\sigma}{2(k\bar{a})^2}\frac{1+\bar{\eta}}{(1-\cos\theta+2\bar{\eta})^2} \,, \quad \text{with } \bar{\eta} \equiv \frac{1}{(2k\bar{a})^2} \,. \tag{11.4}$$

This is because this expression can be analytically inverted when sampling the scattering angle in Monte Carlo simulations (see eq. 3.11 in chapter 3 of part I). One must, however, choose what to fit $\bar{a}$ to: the ICS, MTCS or $\langle\cos\theta\rangle$? Most references logically choose the momentum transfer cross section (MTCS) which is the physically relevant quantity. In our case, since we provide Born fits to the ICS (see eq. 11.9 below), in order to obtain the correct MTCS σ_{m}, one must properly fit the average cosine $\langle\cos\theta\rangle$ so as to verify:

$$\tilde{\sigma}_{\mathrm{m}} = \tilde{\sigma}(\varepsilon)(1-\langle\cos\theta\rangle(\varepsilon)) \tag{11.5}$$

Table 11.4: The shape parameter $\bar{a}$ (single Yukawa exponential decay radius) used for (11.4) adjusted from the average cosine on figure 11.13c from 100 eV. The uncertainty on $\bar{a}$ was quite large due to the relative low sensitivity of the average cosine $\langle\cos\theta\rangle$ on the exact value of $\bar{a}$.

	N_2	O_2	NO	Ar	O	N
$\bar{a}$ ($\langle\cos\theta\rangle$)	0.6052	0.5677	0.6039	0.4533	0.4875	0.5546

Thus, by fitting the DCS shape and the ICS separately, we can reconstruct a coherent MTCS which depends on 4+1 parameters ($4 - \tilde{A}, \tilde{B}, \tilde{C}, K -$ from the ICS and only $1 - \bar{a} -$ from the DCS). This is much better than trying to fit the MTCS directly with 5 parameters.

The parameter $\bar{a}$ required by (11.4) was fitted to the average cosines represented on figure 11.13-c). The fitted values are reported in table 11.4.

At very high energies, leading terms in the integral and momentum-transfer cross sections from a Slater 1s potential (8.23) are respectively from (14.33) and (14.34) of chapter 14.1.2:

$$\begin{aligned}\lim_{k\to\infty}\sigma_{\mathrm{SX}}(k) &= \lim_{k\to\infty}\frac{2\pi Z^2a_0^2\gamma^2}{k^4}\left\{\frac{6\eta(2\eta+3)+7}{6\eta(1+\eta)^3}-\frac{\beta^2}{2}\left[\frac{1-\eta(\eta(\eta+9)+6)}{6(1+\eta)^3}+\ln\left(\frac{1+\eta}{\eta}\right)\right]\right\}\\ &= \frac{2\pi Z^2a_0^2\alpha^4\gamma^2}{(\gamma^2-1)^2}\left\{\frac{14(\gamma^2-1)a^2}{3\alpha^2}+3-\frac{\gamma^2-1}{2\gamma^2}\left[\frac{1}{6}+\ln\left(1+\frac{4(\gamma^2-1)a^2}{\alpha^2}\right)\right]\right\}\\ &\sim \frac{2\pi Z^2a_0^2a^2\alpha^2}{\beta^2}\left(\frac{14}{3}+\frac{3}{k^2a^2}-\frac{\alpha^2}{12a^2\gamma^2}\ln(1+\frac{4(\gamma^2-1)a^2}{\alpha^2})\right), \qquad (11.6)\\ \lim_{k\to\infty}\sigma_{\mathrm{m,SX}}(k) &= \lim_{k\to\infty}\frac{2\pi Z^2a_0^2\gamma^2}{k^4}\left[\frac{1}{1+\eta}-\frac{1}{2}(1-\frac{\eta^2}{(1+\eta)^2})-\frac{1}{3}(1-\frac{\eta^3}{(1+\eta)^3})-\frac{\beta^2}{3}\frac{4\eta+3}{(1+\eta)^3}+\ln\left(\frac{1+\eta}{\eta}\right)\right]\\ &= \frac{2\pi Z^2a_0^2\alpha^4}{\beta^4\gamma^2}\left[\frac{5}{6}-\beta^2+\ln\left(1+\frac{4\gamma^2\beta^2a^2}{\alpha^2}\right)\right]\\ &\sim \frac{2\pi Z^2a_0^2\alpha^4}{\beta^4\gamma^2}\left[2\ln\left(2\frac{\gamma\beta a}{\alpha}\right)+\frac{5}{6}-\beta^2\right]. \qquad (11.7)\end{aligned}$$

We see on the right-hand side of figure 11.13 that while the integral cross section saturates at an asymptotic rate $\sim 1/\beta^2(\text{cst.}+\beta^2\eta\ln(1+1/\eta))$, the momentum transfer cross section keeps decreasing roughly as $\sim\ln(\gamma)/\gamma^2$. We also see a nice continuity between the asymptotic values of the ICS according to the target's effective atomic number, which is $\bar{Z}\equiv\sqrt{Z_A^2+Z_{A'}^2}$ for diatomic molecules. From (11.6), one could generalise the traditional $\tilde{\sigma}_{\mathrm{el}}=\pi a_0^2k^{-2}(A+Bk^{-2}+Ck^{-4}+Dk^{-6})$ Born expansion from Inokuti and McDowell [424, eq.(13)] to a relativistic expression:

$$\tilde{\sigma}_{\mathrm{el}}=\frac{\pi a_0^2\gamma^2}{k^2}\left(A+\frac{B}{k^2}+\frac{C}{k^4}+\underbrace{\frac{B'\beta^2}{k^2}\ln(1+4\bar{a}^2k^2)}_{\text{Relativistic and spin correction}}\right) \qquad (11.8)$$

Nonetheless in practice, the logarithmic term is never important: neither at high energies where it is shrunk by the $\frac{1}{k^2}$ prefactor, nor at lower energies where it is muted by β^2. On the other hand, more critical is the quenching of the terms inversely proportional to k when $k\to 0$ at lower energies. This can be done by adding an acceleration' energy K to the incident kinetic energy ε of the electron (see p. 343). As a result, we devised a scaled relativistic Born expansion in the following way:

$$\tilde{\sigma}_{\rm el} = \frac{\pi a_0^2 \tilde{\gamma}^2}{\tilde{k}^2}\left(\tilde{A} + \frac{\tilde{B}}{\tilde{k}^2} + \frac{\tilde{C}}{\tilde{k}^4}\right), \qquad (11.9)$$

$$\text{where } \tilde{\gamma} = 1 + \frac{\varepsilon + K}{m_e c^2} \quad \text{and} \quad \tilde{k} = \frac{\tilde{\gamma}\tilde{\beta}}{\alpha} \text{ a.u.}$$

In order to avoid possible confusion with parameters in the MERT expansion (sec. 10.1.5), we note the Born coefficients $\tilde{A}, \tilde{B}, \tilde{C}$ with a tilde (following the nomenclature of Born-related quantities). More on the physical explanation behind this 'acceleration' K was elaborated – picturesquely – in the previous chapter 10.2.2 through (10.31). We shall come back again to this very useful scaling in inelastic scattering in sections 11.4.2 and 11.5.3. For a review of this method, we recommend Tanaka *et al.* [911]. Most examples of the Born scaling in the literature are applied to inelastic scattering. It would be surprising, nonetheless, that a formula similar to (11.9) would not have been proposed already by other researchers for elastic CS. In any case, examples of the curve from (11.9) adjusted to our ICS database can be seen as red dot-dashed curves (–•–) on the upper graphs of figures 11.14. The adjusted Born parameters to our ICS database are displayed in table 11.13 in the last section 11.6.2 where they are used for computing the total scattering cross section at high energies together with Bethe parameters (for inelastic scattering).

11.1.5 Integral cross sections

In principle, integral elastic cross sections should be straightforwardly obtained from the DCS with (7.4). These are plotted on figure 11.14. Nonetheless, there is no guarantee that the sum of all elastic and inelastic cross sections (as detailed in the following sections 11.2–11.5) adds up to the measured total scattering cross section as in transmission beam experiments (see section 7.3.3 p.254). This is why for the purpose of creating a consistent database of cross sections we define a:

$$\text{Residual (Vibrationally) Elastic Cross Section}: \quad \sigma_{\rm re} \equiv \sigma_{\rm tot} - \sum_{i \in (\not{e} \setminus \{\rm rot\})} \sigma_i \,, \qquad (11.10)$$

which is the total cross section minus all inelastic processes ($\not{e}$) excluding pure rotational excitations (rot).

This unfortunately means that we must resign to following inconsistency of which the user of our database should be alerted:

> The integral and momentum-transfer cross sections in our database are <u>not</u> obtained from the differential cross sections reported, but as residual products through (11.10) from the total scattering cross section.

The atomic nitrogen and oxygen were exempted from this inconsistency because there is no or not enough data available in order to construct the "grand" total scattering cross section. The differences between the residual (——) and integral (- - -) cross sections may be observed on figures 11.14 for N_2, O_2, NO and Ar.

From the *residual* elastic cross section $\sigma_{\rm re}$ we may also derive the equivalent:

$$\text{Residual Momentum-Transfer Elastic Cross Section}: \quad \sigma_{\rm rm} \equiv \sigma_{\rm re}(1 - \langle\cos\theta\rangle) \,, \qquad (11.11)$$

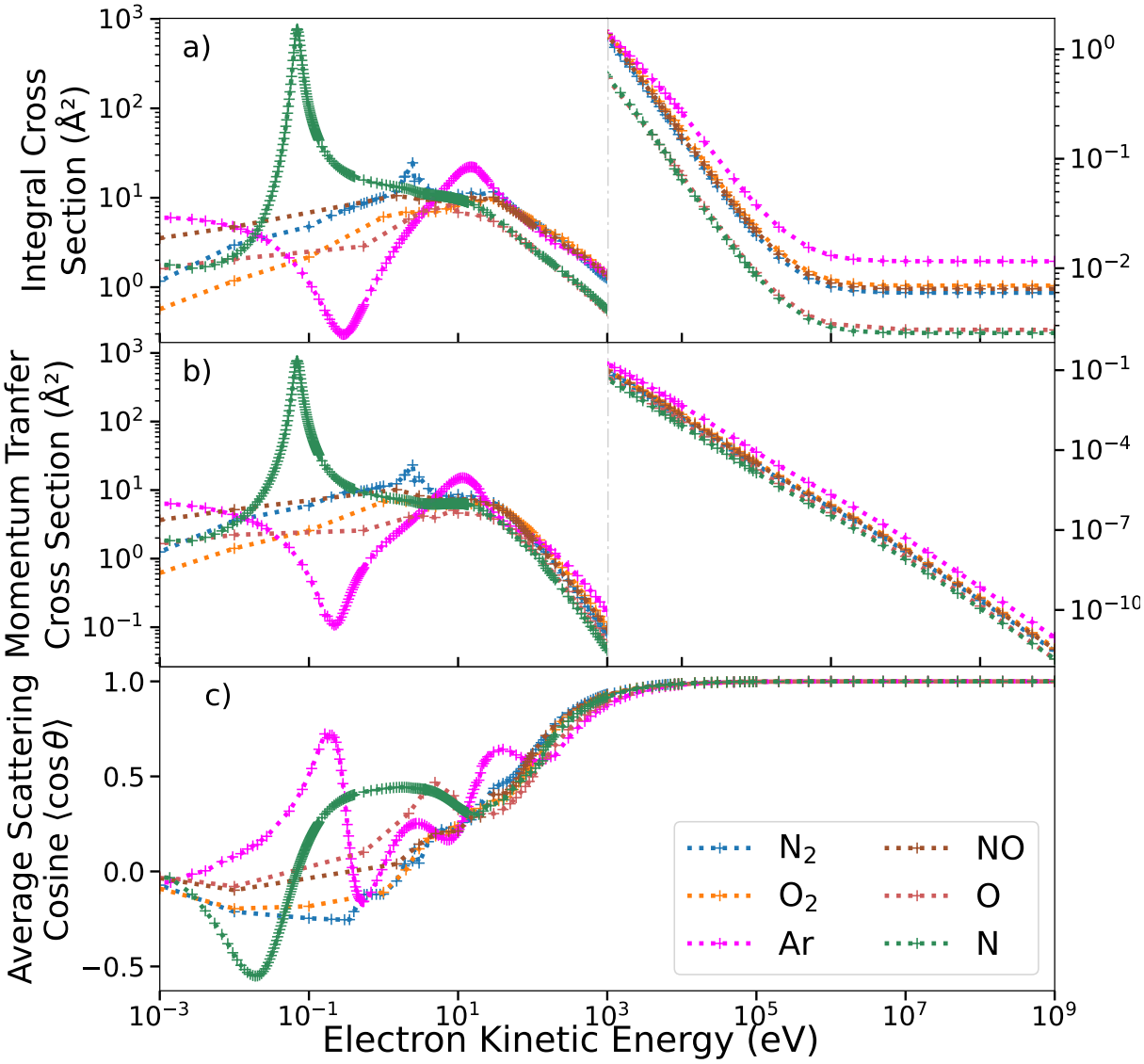

Figure 11.13: a) Integrated differential cross sections (ICS) b) momentum transfer cross sections (MTCS) and c) average cosine deviation $\langle \cos\theta \rangle$ obtained from our DCS database for all six atmospheric gas targets.

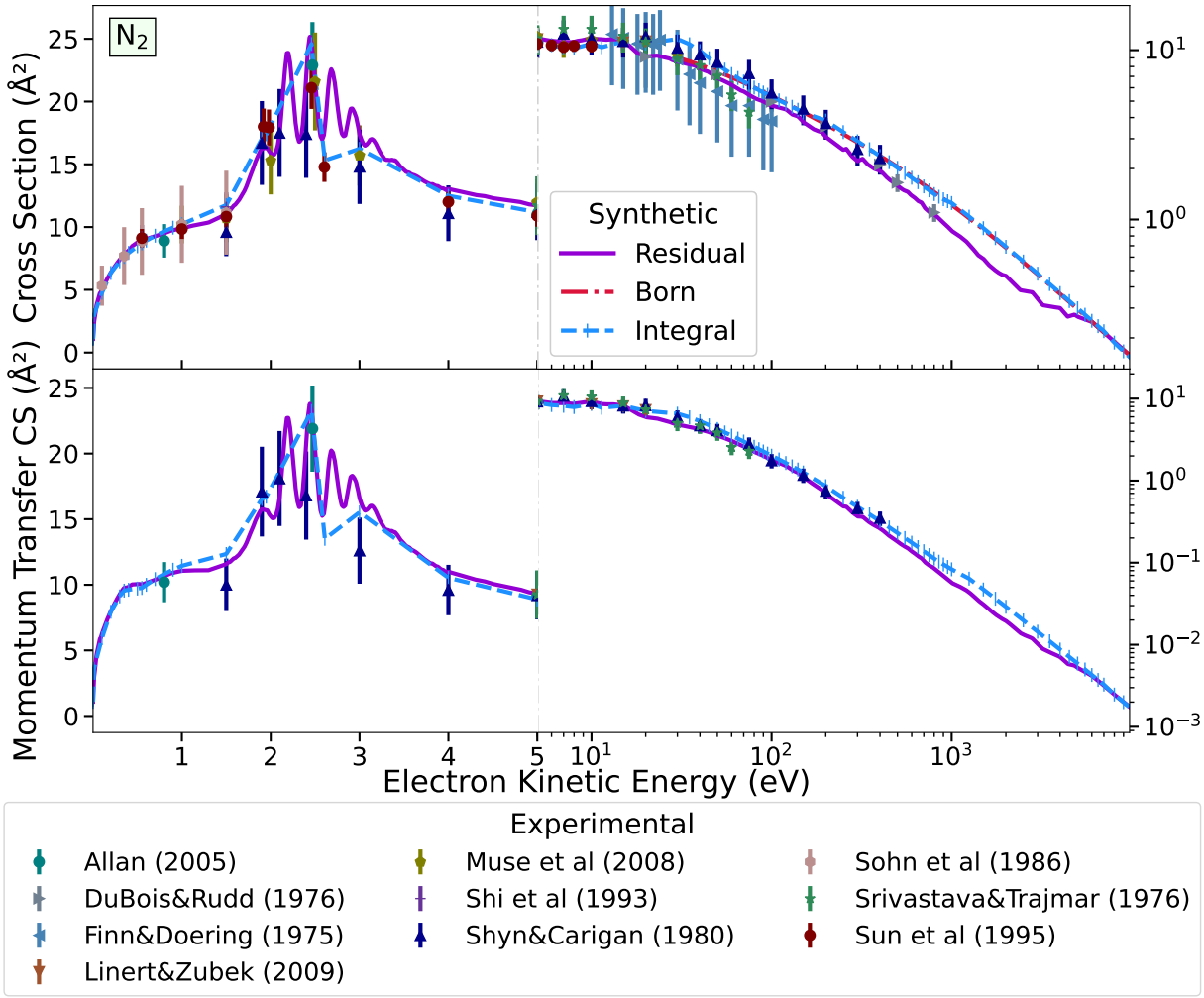

(a) Most trusted experimental data are from Allan [17], Linert and Zubek [600], Muse *et al.* [684], Shi *et al.* [832], and Sun *et al.* [894], less trusted from DuBois and Rudd [232], Shyn and Carignan [838], Sohn *et al.* [863], and Srivastava *et al.* [870] and untrusted from Finn and Doering [288] because they measured DCS up to 90° only (hence the large error bars on top-right graph).

Figure 11.14: Difference between the integrated cross sections (7.4) and the residual cross sections as defined through (11.10) for molecular nitrogen, molecular oxygen, nitric oxide and argon. A fit (-·-) of the Born expansion (11.9) to the residual (purple) curves is represented for higher energies.

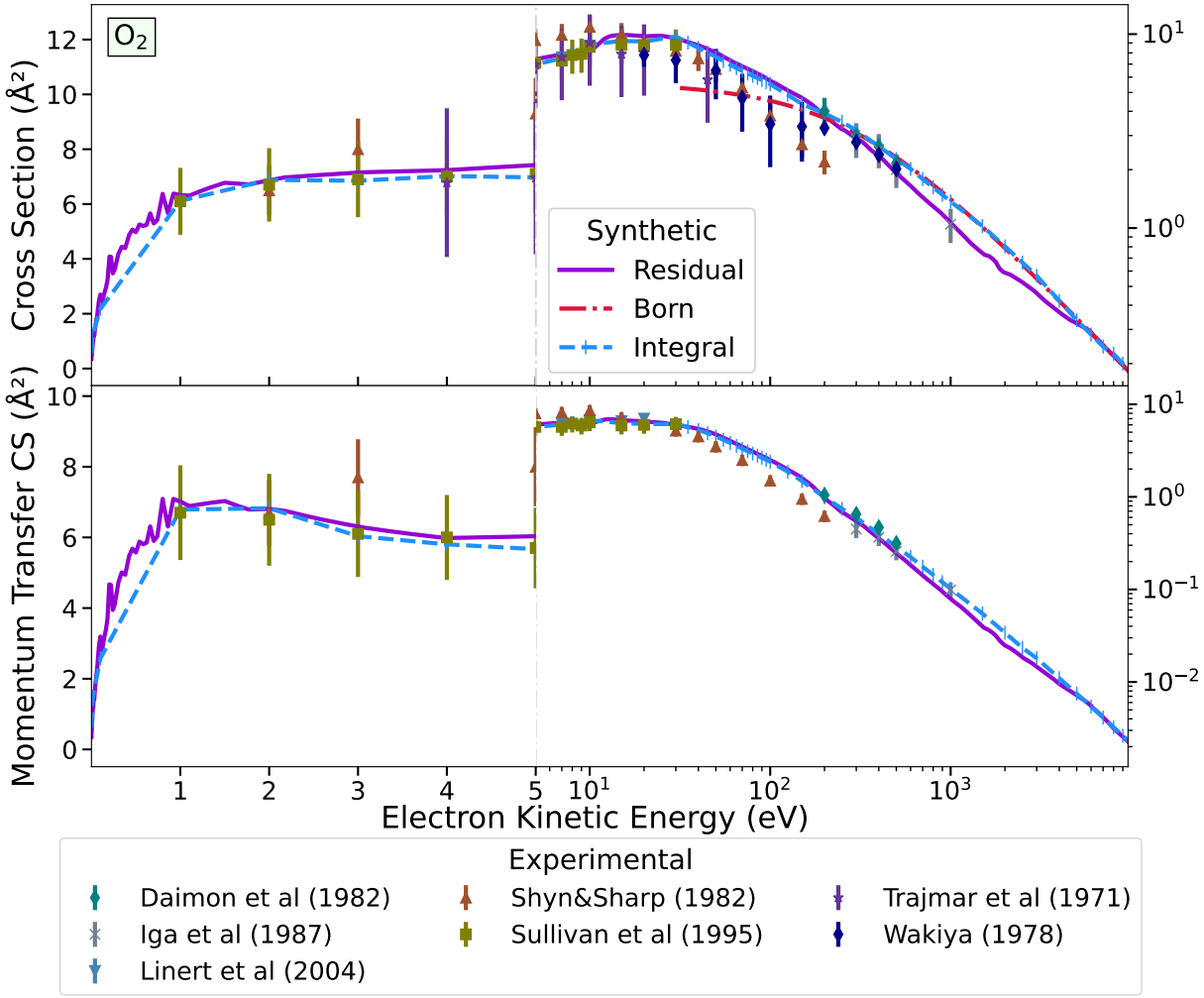

(b) (continued from 11.14) Most trusted experimental data are from Daimon *et al.* [206], Iga *et al.* [418], Linert *et al.* [598], Linert and Zubek [600], and Sullivan *et al.* [893], less trusted from Trajmar *et al.* [938] (older) and untrusted from Shyn and Sharp [842] and Wakiya [972] because of the discrepancies discussed above on page 400 and also 574.

where we remind that the average cosine $\langle \cos\theta \rangle$ is obtained from the DCS as:

$$\langle \cos\theta \rangle \equiv \frac{\int_0^\pi \frac{\mathrm{d}\sigma}{\mathrm{d}\Omega}(\varepsilon,\theta) \cos\theta \sin\theta \,\mathrm{d}\theta}{\int_0^\pi \frac{\mathrm{d}\sigma}{\mathrm{d}\Omega}(\varepsilon,\theta) \sin\theta \,\mathrm{d}\theta} \,. \tag{11.12}$$

The residual momentum-transfer elastic cross section σ_{rm} is useful for comparing consistently results from kinetic solvers with Monte Carlo simulations (see previous part I sections 2.3.2 and 4.3.2).

This concludes the output of our investigations on the elastic scattering of electrons from atmospheric atoms and molecules. We remind that those (differential) cross section include all rotational excitations (modelled in the adiabatic nuclei approximation 8.5.2). In the next section, we develop how individual rotational excitation cross sections may be calculated or approximated.

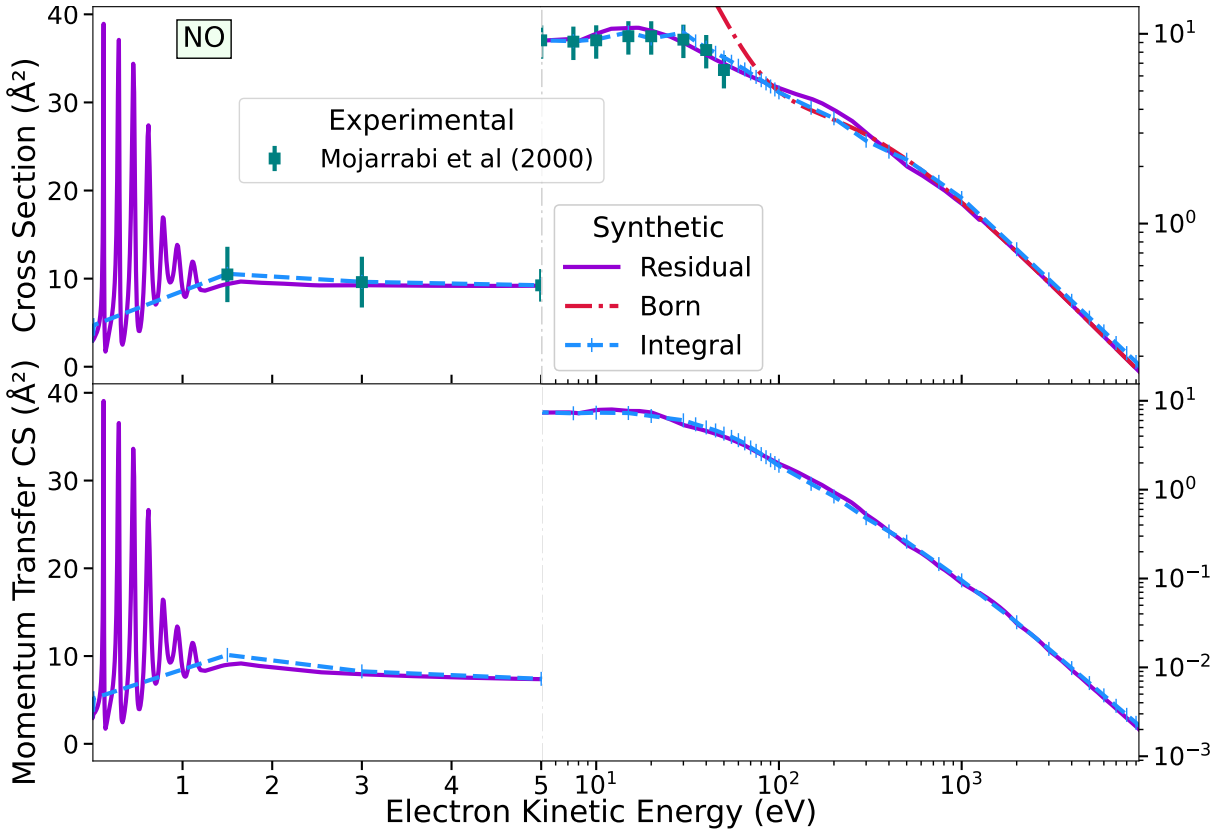

(c) (continued from 11.14) Only (available) experimental data are from Mojarrabi *et al.* [654]. Note the very narrow resonance peaks below 1 eV from the calculations of Laporta *et al.* [557].

11.2 Rotational Excitations

Classically, when a projectile impacts a rigid rod at a point distinct from its centre of mass, a certain angular momentum $\hbar\mathbf{J}' = \omega_{\text{rot}} I_{\text{rot}}$ is induced on the rod which starts turning at a velocity ω_{rot} determined by its moment of inertia I_{rot}. The (dimensionless) angular momenta of the initial $\mathbf{J}$ and final $\mathbf{J}'$ states obey the addition rule:

$$\hbar\mathbf{J}' = \hbar\mathbf{J} + \hbar\mathbf{J}_{\text{t}} \,, \tag{11.13}$$

for a transfer of $\hbar\mathbf{J}_{\text{t}}$ angular momentum. The parallel and anti-parallel alignments of $\mathbf{J}$ and $\mathbf{J}_{\text{t}}$ delimit the range of values taken by the norm $J' \equiv \|\mathbf{J}'\|$:

$$|J - J_{\text{t}}| \leq J' \leq J + J_{\text{t}} \,. \tag{11.14}$$

This fundamental inequality is known as the triangular relation between angular momentum and is symmetric with respect to permutation of any pair between J, J' and J_{t}.

The projection of $\mathbf{J}$ on the axis z is traditionally denoted as $M = \mathbf{J} \cdot \hat{\mathbf{z}}$ and verifies:

$$-J \leq M \leq +J \,. \tag{11.15}$$

The values of J, J', J_{t} and their projections M, M', M_{t} may only take integer values (i.e. all momenta and projections are multiples of $\hbar$). Thus M may take only $2J+1$ values and J' only $2\max(J, J_{\text{t}}) + 1$ values.

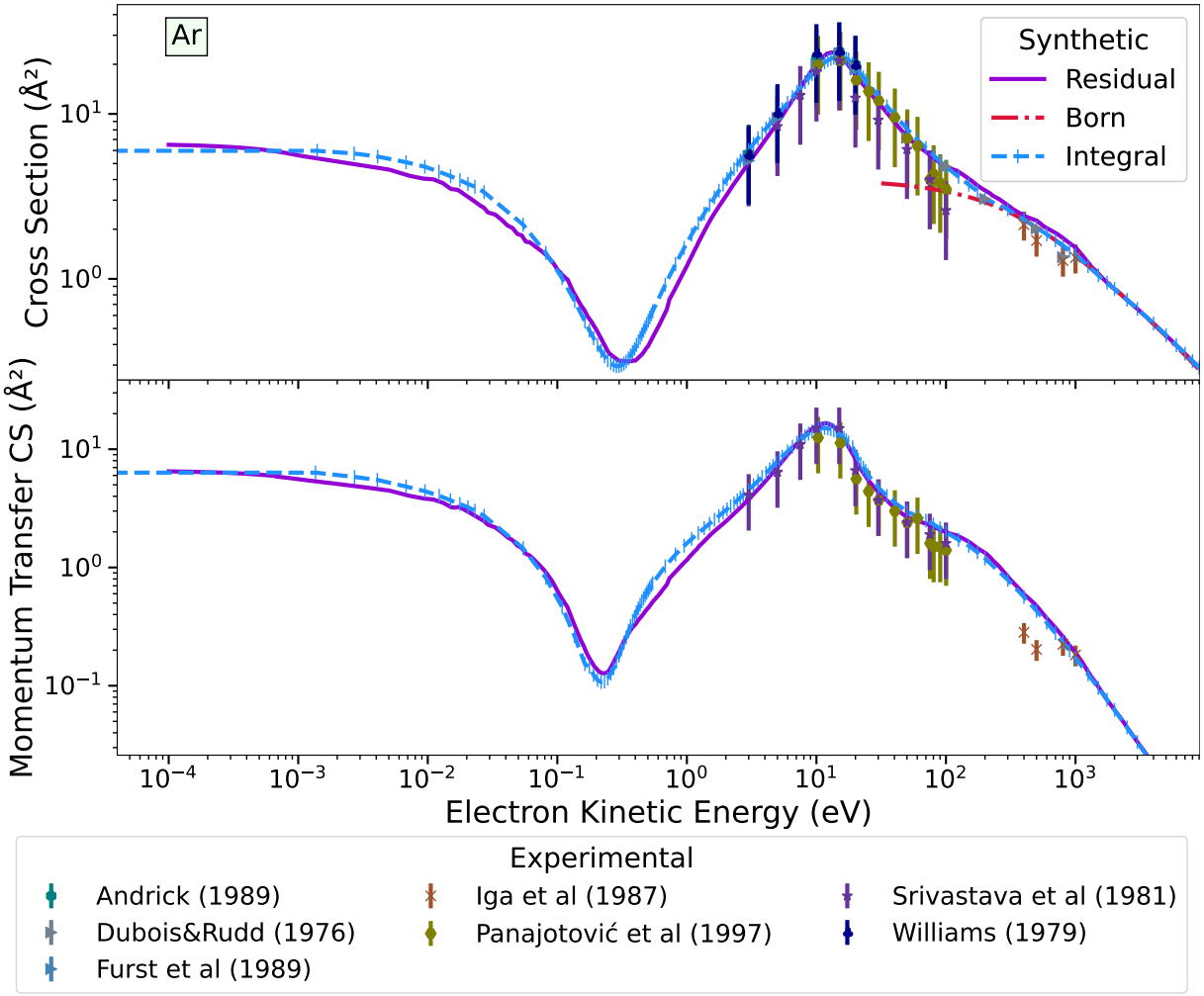

(d) (continued from 11.14) Trusted experimental data are from DuBois and Rudd [232], Furst *et al.* [310], Panajotović *et al.* [731], Srivastava *et al.* [871], and Williams and Willis [985]. Less trusted are from Iga *et al.* [418]. The 'Residual' purple curve actually follows exactly the most recent measurements for total scattering with argon of Kurokawa *et al.* [545] (not represented because superposed).

The energy $\mathcal{E}_{\rm rot}$ and angular velocity $\omega_{\rm rot}$ of a rotating *rigid* molecule are connected to its momentum quantum J by the rotational constant $B_{\rm rot} = \hbar^2/2I_{\rm rot}$ [399, §3.3.2:p.153]:

$$\mathcal{E}_{\rm rot} = B_{\rm rot} J(J+1) \quad \text{and} \quad \omega_{\rm rot} = \sqrt{\frac{2\mathcal{E}_{\rm rot}}{I_{\rm rot}}} = \frac{2B_{\rm rot}}{\hbar}\sqrt{J(J+1)}\,. \tag{11.16}$$

This may be generalised to a non-rigid rotator which involves elongation of the molecule under the centrifugal force from the rotation [399, 676, eq.(13), §3.3.6:eq.(3.54)].

11.2.1 Long Range PWBA

We recall from chapter 8 section 8.4 that the angular-momentum close-coupling method yields scattering amplitudes (8.100) for a rotational transition from state J_0, M_0 to J, M:

$$\frac{\mathrm{d}\sigma_{J_0\to J}}{\mathrm{d}\Omega} = \frac{(2\pi)^2}{4k_0^2}\sum_{M_0,M}\frac{(2\mathcal{L}+1)}{(2J_0+1)}\left|\sum_{\ell\ell_0}(2\ell_0+1)(4\pi)Y^*_{\ell_0 m_0}(\hat{\mathbf{k}}_0)Y_{\ell m}(\hat{\mathbf{k}}_J)\mathrm{i}^{\ell_0-\ell}T_{JM\ell m,J_0M_0\ell_0m_0}\right|^2 , \tag{11.17}$$

$$T_{JM\ell m,J_0M_0\ell_0m_0} = \sqrt{(2J+1)(2J_0+1)}\sum_{\mathcal{L}}\frac{1}{2\mathcal{L}+1}\sum_{\Lambda}C^{\mathcal{L}\mathcal{M}}_{JM,\ell m}C^{\mathcal{L}\mathcal{M}}_{J_0M_0,\ell_0m_0}C^{\mathcal{L}\Lambda}_{J0,\ell\Lambda}C^{\mathcal{L}\Lambda}_{J_00,\ell_0\Lambda}T^{\Lambda}_{\ell\ell_0} \tag{11.18}$$

where the leading $(2\pi)^2$ factor comes from the definition (8.85a) of the T matrix involving a $1/(2\pi\mathrm{i})$ coefficient. Optionally, the squared sum in the first (11.17) may be expanded into a Legendre polynomial series [908, p.114:eq.(11)] to obtain the formula of Arthurs *et al.* [29, p.542:eqs.(18–20)] involving Racah coefficients.

This way of calculating rotational DCS for each single $J_0 \to J$ transition is extremely costly and one might wish to possess a faster, albeit approximative, way to do so [323]. This can be done for instance in the first Born approximation which equals [812, 908, eq.(21), eq.(22)]:

$$\frac{\mathrm{d}\tilde{\sigma}_{J_0\to J}}{\mathrm{d}\Omega} = \frac{4k_J}{k_0}\sum_{l=0}^{\infty}\frac{2J+1}{(2l+1)^2}\left[C^{l0}_{J_00,J0}\right]^2\left|\int_0^\infty \mathrm{j}_l(qr)V_l(r)r^2\,\mathrm{d}r\right|^2 \tag{11.19}$$

This relation comes from the fact that the Bauer expansions (8.88) of the incident and outgoing planar waves may be combined to be expressed only in the momentum transfer $q^2 = k_J^2 + k_0^2 - 2k_Jk_0\cos\theta$. We recall that V_l is the l^{th} harmonic of the interaction potential (8.31).

The great advantage of (11.19) is that one may completely separate the parts that depend on the rotational quanta J_0, J from the actual shape of the DCS stemming from the potential harmonics V_l. The major contribution to rotational excitations in the Born approximation comes from long-range multipoles (induced or static). Assuming that the short-range contribution of the potential to the DCS is negligible for $l > 0$, one may replace V_l by the multipolar asymptotic decay $\sim -M_l/r^{l+1}$ (8.27) and exploit the following analytic integral [347, p.684:eq. (6.561.14)]:

$$\int \mathrm{j}_\ell(qr)\frac{r^2}{r^n}\,\mathrm{d}r = \sqrt{\pi}\frac{q^{n-3}}{2^{n-1}}\frac{\Gamma(\frac{l-n+3}{2})}{\Gamma(\frac{l+n}{2})} . \tag{11.20}$$

$\Gamma(x)$ is the Gamma function [3, p.255:eq.(6.1.1)] which can be reduced, in the present case, to either a factorial or double factorial depending on the parity of $l+n$.

From there, one obtains the first Born approximation for rotational excitations from long range potentials [21, 323, 908, p.116:eq.(22), p.1674:eq.(20), p.119:eq.(27)].

$$\frac{\mathrm{d}\tilde{\sigma}_{J_0\to J}}{\mathrm{d}\Omega} = \frac{4k_J}{k_0}\sum_{l=0}^{\infty}\left[C^{l0}_{J_00,J0}\right]^2\left(\frac{M_l}{q^{2-l}(2l-1)!!}\right)^2 ; \tag{11.21}$$

$$\frac{\mathrm{d}\sigma_{J_0\to J_0+1}}{\mathrm{d}\Omega} = \frac{k'}{k_0}\frac{4}{3}\frac{J_0+1}{2J_0+1}\left\{\frac{D}{q}+O(M_{l>2})\right\}^2 , \tag{11.21a}$$

$$\frac{\mathrm{d}\sigma_{J_0\to J_0+2}}{\mathrm{d}\Omega} = \frac{k'}{k_0}\frac{6}{5}\frac{(J_0+1)(J_0+2)}{(2J_0+1)(2J_0+3)}\left\{\frac{Q}{3}+\frac{\alpha_{\mathrm{d},2}}{2}\frac{\pi q^2}{16}+O(M_{l>3})\right\}^2 . \tag{11.21b}$$

The inverse $J_0 \leftarrow J$ transitions may be obtained from the direct $J_0 \rightarrow J$ excitation through the detailed balance (7.6) [836, p.8:eq.(16)]:

$$\varepsilon_J(2J+1)\frac{\mathrm{d}\sigma_{J_0\leftarrow J}}{\mathrm{d}\Omega}(\varepsilon_J) = \varepsilon_0(2J_0+1)\frac{\mathrm{d}\sigma_{J_0\rightarrow J}}{\mathrm{d}\Omega}(\varepsilon_0)\ . \tag{11.22}$$

with $\varepsilon_J = \varepsilon_0 + B\left(J_0(J_0+1) - J(J+1)\right)$.

The higher-order $l > 2$ multipoles of diatomic molecules are weak, thus one may assume that, in the first Born approximation, rotational excitations are reduced to transitions $J - J_0 = \pm 1$ due to dipole D and $J - J_0 = \pm 2$ due to quadrupole Q and anisotropic polarisation $\alpha_{\mathrm{d},2}$. Dipolar transitions are by nature very forward peaked $\propto 1/q^2$ [21] whereas quadrupolar transitions are almost fully isotropic ($\perp\!\!\!\perp q$) [323] with an eventually weak backscattering due to anisotropic polarisation [208]. These trends are verified experimentally at low energies as can be seen on figure 11.15 extracted from Jung *et al.* [473]. The slight angular variation stems mostly from the resonant part of the excitation in this energy region as pointed out by Wong and Dubé [988].

The first Born approximation for rotational excitation is a very powerful tool, nonetheless it might not yield accurate results at intermediate energies when the electron's p and d waves penetrate deeper in the molecule and when the scattering is resonant. Actually, outside of resonances, we do not need the Born approximation to efficiently estimate rotational cross sections at higher energies. Under certain assumptions, one may relate any rotational excitation $J_0 \rightarrow J$ from a known set of $J_0 = 0 \rightarrow \Delta J$ of elementary transitions. This is the topic of the next section.

11.2.2 Sudden Impulse Approximation

At an ambient temperature of 300 K, the rotational states of N_2 are typically populated to some $J = 12$. With the constant $B_{\mathrm{rot}}(N_2) \approx 0.25\,\mathrm{meV}$ the maximal rotational velocity of a nitrogen atom would be $\sim 500\,\mathrm{m/s}$; a velocity that even a slow electron of 1 meV would surpass by two orders of magnitude. Therefore, it is customary to assume that the momentum transfer from the electron to the molecule is an instant process [908, p.107].

This assumption is commonly known as the sudden [834, Chapter 2:§3.2], impulse or adiabatic nuclei approximation [173]. It implies that:

- The rotational energy of the molecule is neglected, the Hamiltonian H_{rot} is removed from the Schrödinger equation;
- The coordinates of the nuclei are fixed during the scattering process;
- There is no coupling between the rotational states of the molecule and the scattering wave of the electron.

These assumptions, however, are only valid if the energy lost by the electron from the rotational excitation $\Delta\mathcal{E}_{\mathrm{rot}}$ is a negligible fraction of its incident energy ε_0:

$$\varepsilon_0 \gg \Delta\mathcal{E}_{\mathrm{rot}} = B_{\mathrm{rot}}\left(J(J+1) - J_0(J_0+1)\right)\ . \tag{11.23}$$

Different scaling laws were proposed in order to enable the use of the abiabatic nuclei approximation near threshold such as the scaling from first Born approximated T matrix elements [273].

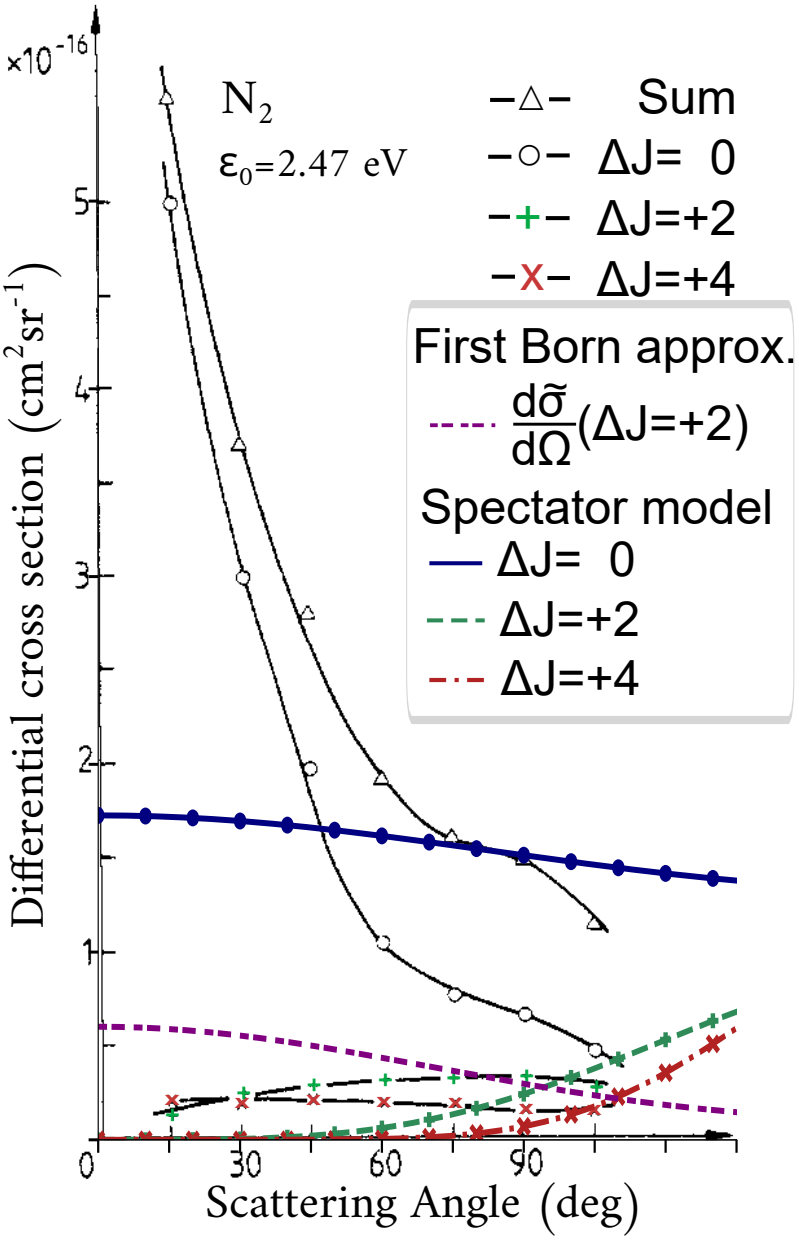

Figure 11.15: Experimentally measured DCS for rotational excitations of N_2 at (500 ± 30) K for various rotational transitions ΔJ. The figure is adapted from Jung *et al.* [473, fig. 5]. Superposed on the figure are rescaled DCS from the first Born approximation (11.21b) and from the spectator model (11.35).

Supposing one possesses a set of differential cross sections for excitations: $0 \to \Delta J$, one may construct the DCS for an arbitrary transition $J_0 \to J$ as:

$$\frac{\mathrm{d}\sigma_{J_0\to J}}{\mathrm{d}\Omega} = \frac{k_J}{k_0} \sum_{\Delta J=|J-J_0|}^{J+J_0} \left[C^{J0}_{J_0 0,\Delta J 0}\right]^2 \frac{k_0}{k_{\Delta J}} \frac{\mathrm{d}\sigma_{0\to\Delta J}}{\mathrm{d}\Omega} \,. \tag{11.24}$$

The wavenumbers are related by conservation of the total the energy in a determined channel (rotational transition), namely [835, p.116:eq.(62)]:

$$\frac{k_0^2}{2} = \frac{k_{\Delta J}^2}{2} + \mathcal{E}_{\Delta J} \qquad\qquad \frac{k_0^2}{2} + \mathcal{E}_{J_0} = \frac{k_J^2}{2} + \mathcal{E}_J \,. \tag{11.25}$$

One may check easily that the plane wave Born rotational cross sections presented above in (11.21) verify the scaling law (11.24) as an immediate consequence of the Clebsch-Gordan relation [956, p.245:§8.4.3]:

$$C^{J0}_{J_0 0,\Delta J 0} = (-)^{J_0} \sqrt{\frac{2J+1}{2\Delta J+1}} C^{\Delta J 0}_{J_0 0, J 0} \tag{11.26}$$

Also, since $\sum_J \left[C^{J0}_{J_0 0,\Delta J 0}\right]^2 = 1$ [956, p.259:eq.§8.7.2(9)], one may relate the probability $\mathcal{P}_{J_0\to J}(\varepsilon,\Omega)$ that an excitation from an initial rotational state J_0 comes out into the state J for a scattering event at an incident energy ε and solid angle Ω:

$$\mathcal{P}_{J_0\to J}(\Omega) \simeq \sum_{\Delta J} \left[C^{J0}_{J_0 0,\Delta J 0}\right]^2 \mathcal{P}_{0\to\Delta J} \,, \tag{11.27}$$

$$\text{where } \mathcal{P}_{0\to\Delta J} = \frac{\frac{\mathrm{d}\sigma_{0\to\Delta J}}{\mathrm{d}\Omega}}{\sum_J \frac{\mathrm{d}\sigma_{0\to J}}{\mathrm{d}\Omega}} \,, \tag{11.28}$$

a logical consequence from the first equation (11.24) when $J_0 = 0 \Rightarrow C^{J0}_{00,\Delta J 0} = \delta_{J\,\Delta J}$.

From now on, all that we miss is a way to determine the DCS $\mathrm{d}\sigma_{0\to\Delta J}/\mathrm{d}\Omega$. Since our modelling of molecular static potentials is poor, we did not dare to produce our own rotational elementary DCS through (11.17). On the other hand, the first Born approximation in the previous section is not of much help because it only allows for $\Delta J = 2, 1, 0$ transitions whereas we are looking for larger momentum-transfer reactions. Such reactions of large ΔJ may be approximated according to the model presented in the next section.

11.2.3 Spectator Model

This model introduced by Korsch *et al.* [535] imagines that the electron, when impacting the diatomic molecule, transfers part of its momentum only to one of the two atoms. The other atom acts then as a "spectator" in the collision, hence the model's name.

The assumptions of this model [534, §2.1.2] rely, in addition to those underlying the sudden approximation, that (i) the interaction potential possesses only even harmonics and (ii) there is no multiple scattering of the electron among the constituent atoms, i.e. that the electron interacts independently with each atom. Therefore, the spectator model may be seen as the *independent atom model* applied to rotational excitations of *homonuclear* diatomic molecules. It is by nature a *high energy approximation*.

This extremely simple model is actually independent of the interaction potential. Thus, it should not be expected to be accurate at low or even intermediate energies.

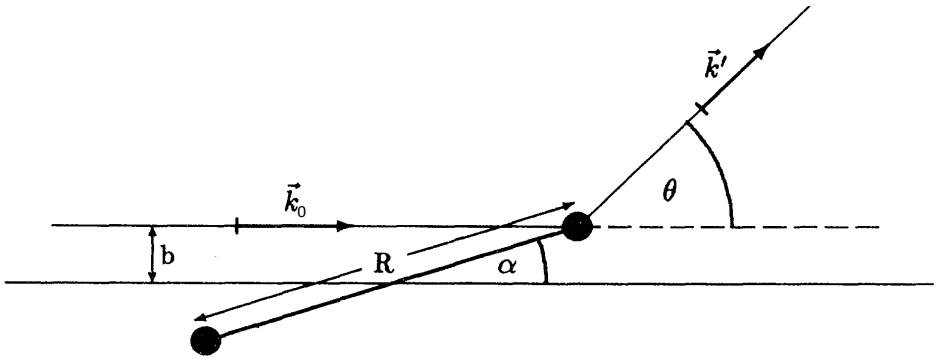

Figure 11.16: Classical sketch of the spectator model whereupon the electron impinges on one of the two atoms and transfers its momentum exclusively to that one. Extracted from Kutz and Meyer [546, p.3822:fig. 2].

The rotational angular momentum change ΔJ of the molecule, as depicted in sketch 11.16, is geometrically related to the momentum transfer of the electron by:

$$\Delta J = kR \sin\frac{\theta}{2} \sin\alpha = \frac{qR}{2} \sin\alpha \,. \tag{11.29}$$

The interatomic distance R of a few diatomic molecules can be found in table 2.2. The angle α describes the orientation of the molecule with respect to the z axis aligned in the direction of incidence and θ is the usual scattering angle. In quantum mechanics, naturally, the transition ΔJ is discretised over a certain set of values.

At $\alpha = 90°$, the quantity $J_\mathrm{R} = kR\sin\theta/2$ defines a *rotational rainbow parameter** [535, eq.(7)]. At a fixed energy ε and scattering θ, J_R determines the rotational excitation for which the probability is maximal. This rainbow mechanism of excitation has been confirmed experimentally at high energies above 100 eV from the study of Gote and Ehrhardt [344, fig. 7] whose figure is reproduced in 11.17.

Rotational rainbow excitations at high energies are particular because they allow larger transfers of energy than expected through a resonant interaction at low energies [473, §3.1].

From the rainbow parameter J_R, the spectator model gives the branching ratio to excite a molecule initially at rest to a ΔJ rotational quantum:

$$\mathcal{P}_\mathrm{spectator}(0 \to \Delta J, \varepsilon, \theta) = \bar{C}(2\,\Delta J + 1)\mathrm{j}^2_{\Delta J}(kR\sin\frac{\theta}{2}) \,, \tag{11.30}$$

where j_n is the spherical Bessel function of degree n and $\bar{C}$ is a normalisation factor such that $\sum_{\Delta J=0}^{\infty} \mathcal{P}(0 \to \Delta J) = 1$.

For heteronuclear molecules, since $\sum_{n=0}^{\infty} \mathrm{j}_n^2(J_\mathrm{R})(2n{+}1) = 1$ [3, 219, p.440:eq.(10.1.45), eq.(10.60.12)], the normalisation is automatic and $\bar{C} = 1$. However, for homonuclear molecules, only pair ΔJ transitions are permitted and thus $1/\bar{C} = \sum_{m=0}^{\infty} \mathrm{j}^2_{2m}(J_\mathrm{R})(4m+1) = (1 + \sin(2J_\mathrm{R})/(2J_\mathrm{R}))/2$.
We may thus summarise the relative rotational transition probabilities in the spectator model:

$$\text{Homonuclear :} \qquad \mathcal{P}(0 \to \Delta J) = \frac{2(2\Delta J + 1)\mathrm{j}^2_{\Delta J}(kR\sin(\theta/2))}{1 + \sin(2kR\sin\theta/2)/2kR\sin\theta/2} \,; \quad \Delta J \text{ even}, \tag{11.31}$$

$$\text{Heteronuclear :} \qquad \mathcal{P}(0 \to \Delta J) = (2\Delta J + 1)\mathrm{j}^2_{\Delta J}(kR\sin(\theta/2)) \,; \quad \Delta J \in \mathbb{N}_0 \tag{11.32}$$

*The terminology comes from 'rainbow' scattering [147, §1.4.2] where the scattering is enhanced at large angles, itself called in relation to the wonderful light scattering in water droplets giving birth to rainbows.

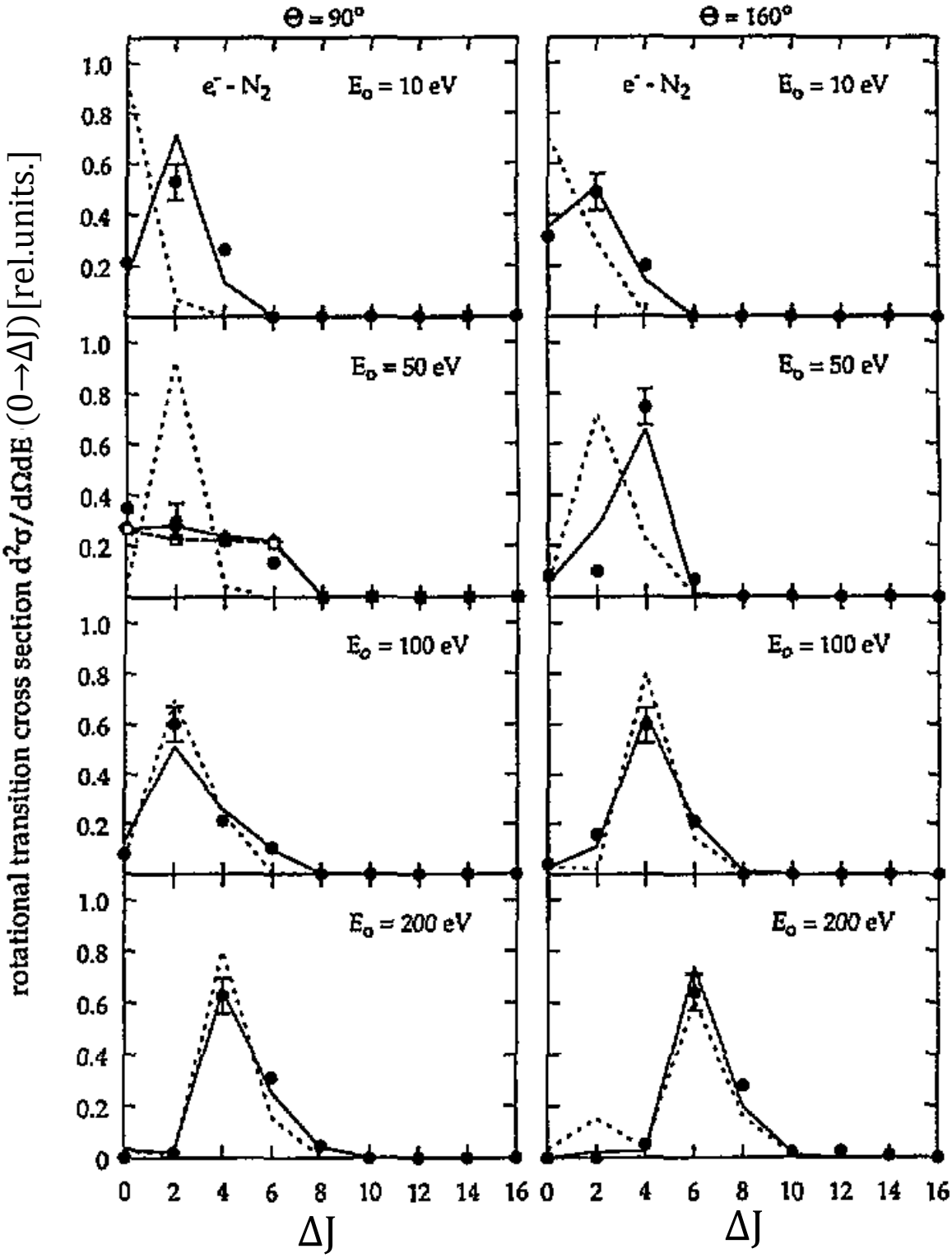

Figure 11.17: Rotational rainbows related to important momentum transfers giving rise to rotational transitions with larger quantal differences $\Delta J > 2$ for electrons scattering off nitrogen molecules at energies above 100 eV. The DCS are normalised so that the sum of all ΔJ transitions give unity at a given energy and angle. The experimental data of Gote and Ehrhardt [344] (•) are compared to close-coupling calculations of Kutz and Meyer [546] (—) and the spectator model (- - -). The figure has been extracted from Gote and Ehrhardt [344, fig. 7]

To obtain the DCS, since the spectator model is a geometrical model disregarding the interaction potential, one needs to manually set the norm with the help of the following integral:

$$\bar{\varsigma}_n = \int_0^\pi \mathrm{j}_n^2(kR\sin\theta/2)\sin\theta\,\mathrm{d}\theta = \left(\frac{2}{kR}\right)^2 \frac{\pi}{2}\int_0^{kR} J^2_{n+\frac{1}{2}}(J_\mathrm{R})\,\mathrm{d}J_\mathrm{R} \tag{11.33}$$

$$= \left(\frac{2}{kR}\right)^2 \left[\bar{\varsigma}_{n-1} + \mathrm{j}^2_{n-1}(kR)\left(\frac{(kR)^2+2n-1}{2n}\right)\right.$$

$$\left. + kR\mathrm{j}_{n-1}\left(\frac{n-1}{n}\mathrm{j}_{n-2}(kR) - \mathrm{j}_n(kR)\right) - \frac{(kR\mathrm{j}_{n-2}(kR))^2}{2n}\right] \tag{11.33a}$$

$$\text{With}: \bar{\varsigma}_0 = \left(\frac{2}{kR}\right)^2 \frac{1}{2}(\ln(2kR) + \gamma_\mathrm{e} - \mathrm{Ci}(2kR)) \tag{11.33b}$$

$$\bar{\varsigma}_1 = \left(\frac{2}{kR}\right)^2 \frac{1}{2}\left(\mathrm{j}_0(kR)[\mathrm{j}_0(kR) - kR\,\mathrm{j}_1(kR)] + \ln(2kR) + \gamma_{\mathrm{e-m}} - \mathrm{Ci}(2kR) - 1\right) \tag{11.33c}$$

The finite integral in the first line must be computed from the indefinite integral series of Bloomfield *et al.* [85, eq.(46)], which gives a second order recurrence relation (11.33a). The terms introduced include the cosine integral [219, eq.(8.21.7)]:

$$\mathrm{Ci}(x) \equiv -\int_x^\infty \frac{\cos w}{w}\,\mathrm{d}w = \gamma_{\mathrm{e-m}} + \ln(x) + \int_0^x \frac{\cos w - 1}{w}\,\mathrm{d}w\,, \tag{11.34}$$

and the Euler-Mascheroni constant:

$$\gamma_{\mathrm{e-m}} = \lim_{n\to\infty}\left(\sum_{k=1}^{n}\frac{1}{k} - \ln(n)\right) \approx 0.577216\,.$$

Finally, the DCS could be normalised from known integral CS $\sigma_{0\to\Delta\mathrm{J}}$:

$$\frac{\mathrm{d}\sigma_\mathrm{spectator}}{\mathrm{d}\Omega}(0\to\Delta J,\varepsilon,\theta) = \frac{\sigma_{0\to\Delta J}}{2\pi\bar{\varsigma}_{\Delta J}}\mathrm{j}^2_{\Delta J}(kR\sin\frac{\theta}{2})\,, \tag{11.35}$$

such as $\sigma_{\Delta\mathrm{J}}$ theoretically calculated by Kutz and Meyer [546] or Morrison *et al.* [665] and Morrison *et al.* [674] for example. Note, however, that this would override the scaling set by the model between the relative probabilities $\mathcal{P}_\mathrm{spectator}$ (11.30).

In principle, with this set of DCS, in conjunction with the impulse approximation (11.24), one could now generate rotational DCS between any arbitrary pair $J_0 \to J$ of rotational states. Nevertheless, despite the mathematical and analytical seductiveness of the spectator model, it is evidently not suitable for modelling rotational excitations at low impact energies as can be seen from the disagreement on figure 11.15 at 2.47 eV. We shall keep in mind that at low energies, the spectator model overall underestimates the rotational excitation probabilities as seen on figure 11.17 from [344, figure 7]. On the other hand, the DCS from the first Born approximation (11.21) are not suitable either in the resonant region of scattering (which is ~ 2–4 eV for N_2). Since we could not find a proper way to unify the rotational excitations at low, resonant, intermediate and high energies respectively, and due to a lack of experimental and theoretical data, we did not attempt to construct more accurate representations of rotational excitations.

For future investigations, it would be desirable to elucidate how to astutely exploit approximations and accurate calculations so as to produce a smooth set of rotational DCS throughout the whole electron energy range. Leaving that aside, we introduce now, in the following section, vibrational excitations in the light of resonant scattering.

11.3 Vibrational Excitations

The vibrational excitation of a diatomic molecule 'AB', characterised by the transition of vibrational quanta v to v', can be formally separated into two processes: direct and resonant.

$$e^- + \mathrm{AB}(v) \rightarrow \mathrm{AB}(v') + e^- \qquad \text{direct} \qquad \text{(V1)}$$
$$e^- + \mathrm{AB}(v) \rightarrow \mathrm{AB}^-(v'') \rightarrow \mathrm{AB}(v') + e^- \qquad \text{resonant} \qquad \text{(V2)}$$

In this section, a set of cross sections for vibrational excitations is assembled by combining accurate calculations for resonant scattering of Laporta *et al.* [552, 554, 557] with available experimental measurements outside the resonances modelled.

The direct channel (V1) constitutes in most cases a minor contribution (unless $v' = v$ which corresponds to elastic scattering). In this reaction, the electron would transfer in a short time a significant kinetic momentum to a nucleus in order to excite the molecule to a higher vibrational level. Due to the very low electron-to-atom mass ratio $\lesssim 4 \times 10^{-5}$ for N and O, the transfer of a large amount of kinetic energy, enough to induce a vibrational excitation, is improbable at low electron energies and classically impossible [834, p.191–2].

Therefore, the nature of vibrational excitations must be radically different from a classical kinetic view of hard spheres. In particular, vibrational excitations of multiple quanta $v' - v > 1$ are almost exclusively due to 'resonances' [91, 834, p.363, §VI]. What formally occurs, is the formation of a negatively charged electron-molecule compound AB^- vibrating at v'', which is unstable and decays after a certain time. The lifetime of this compound is variable depending on the molecule's electronic affinity and the potential curves of the compound and the molecule.

A concrete illustration for O_2 is given in figure 11.18. Excited anion states $O_2^-(X\,^2\Pi_g, v'')$ for $v'' \leq 3$ are stable (indefinite lifetimes) which means that they will not detach unless if given energy through a collision with another molecule (or a free electron). For $O_2^-(X\,^2\Pi_g, v'' = 4)$, the lifetime is very long $\sim 10^{-10}$ s [820, p.470], exceeding by 4 to 5 orders of magnitude the fly-by time spent in a non-resonant collision. In human terms, this would mean a fateful overlay of 30 years instead of 1 day at a transit airport.

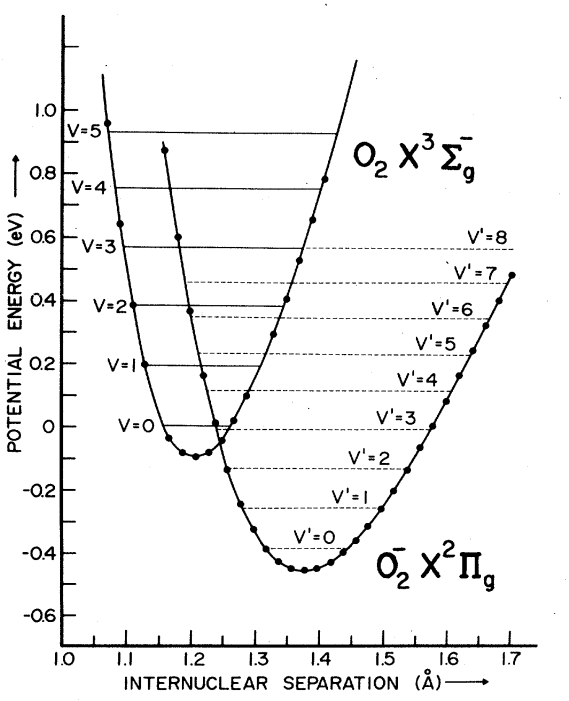

Figure 11.18: Potential curves of oxygen and its anion in their ground states taken from Schulz [820]. The vertical difference between the vibrational ground levels of $O_2^-(v'' = 0)$ and of $O_2(v = 0)$ corresponds to the electronic affinity which equals $\simeq 0.44$ eV[820, §VI.A.1:p.468]. All $O_2^-(v'' = 0..3)$ levels are below $O_2(v = 0)$ which means they are stable and will detach only through endothermic collisions.

As a result, the lifetime of the compound formed during collision may be a large fraction or exceed the period of diatomic molecular vibration which is of the order of $\sim 10^{-14}$ s [820, p.427]. This possibilitates the transition to a different vibrational state not through instantaneous

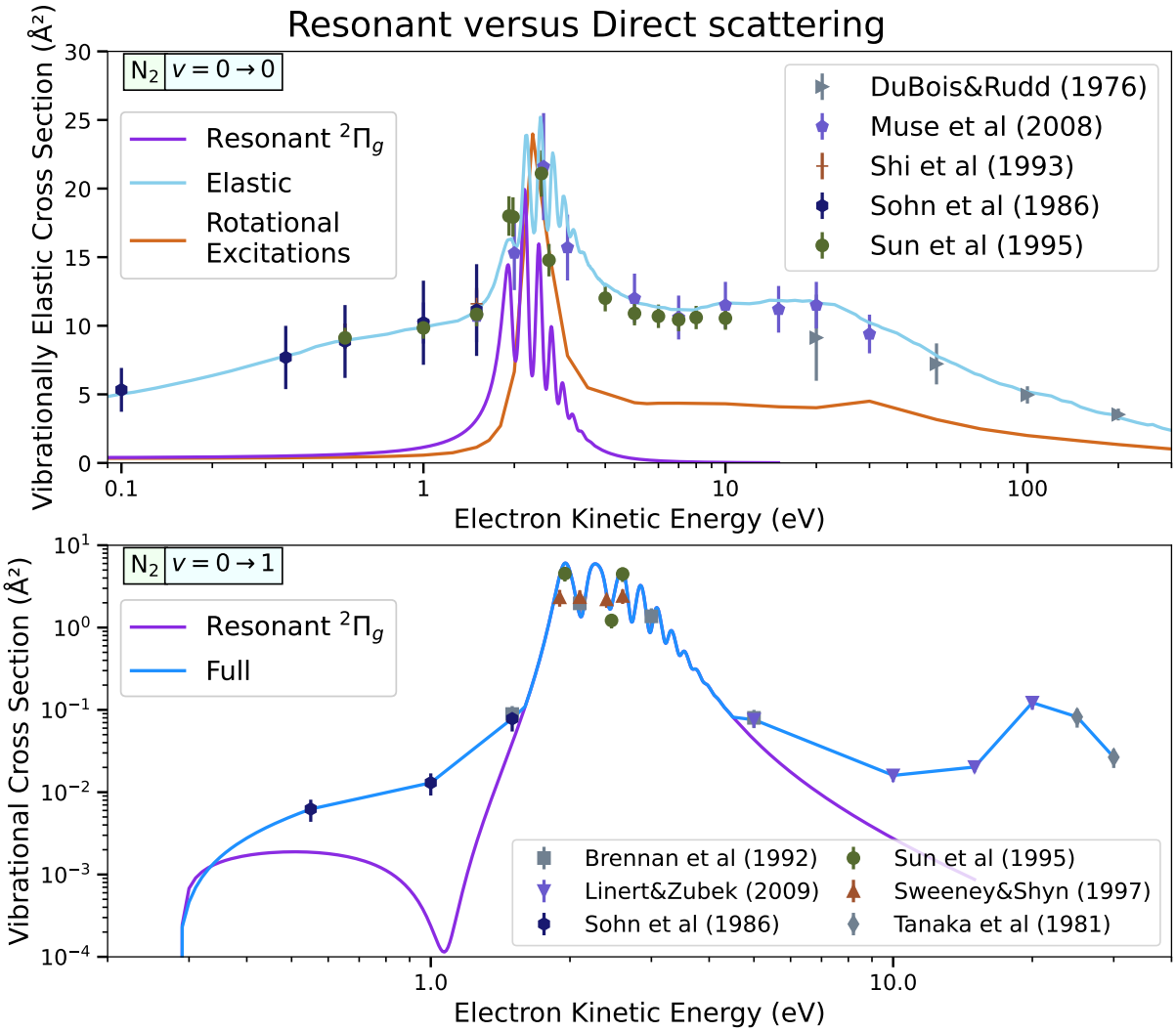

Figure 11.19: Comparison of resonant versus full (non-resonant and resonant) scattering from molecular nitrogen. One can see that the N_2^- $^2\Pi_g$ resonance mainly takes place for incident electrons between 1.5–4 eV and is the dominant process for the $v = 0 \rightarrow v' = 1$ channel (bottom). For elastic scattering (top), the rotational excitations (with $\Delta J \neq 0$) were calculated from the theoretical cross sections of Kutz and Meyer [546, fig. 7] and averaged over a Maxwellian distribution of initial J_0 states at 300 K. The curves for resonant scattering in the $^2\Pi_g$ symmetry are obtained from Laporta *et al.* [554]. The second mound between 15–30 eV is principally due to another (excited) configuration of the negative ion: N_2^- $^2\Sigma_u^+$ [600, §3.3:p.6].

transfer of momentum but through a prolonged perturbation of the Coulomb field acting upon the nuclei [834, chapter 3:§2.5]. The formation of the compound is due to the temporary trapping of the incoming electron in the potential of the molecule. This process is referred to as a resonance. The importance of resonant scattering can be assessed by comparing full (resonant+direct) and resonant curves on figure 11.19.

Below, we talk briefly about resonances, mainly directing towards some references in the field and illustrating the concept. Then, we present the cross sections used for vibrational scattering and attachment, which is also a resonant process.

11.3.1 Resonances

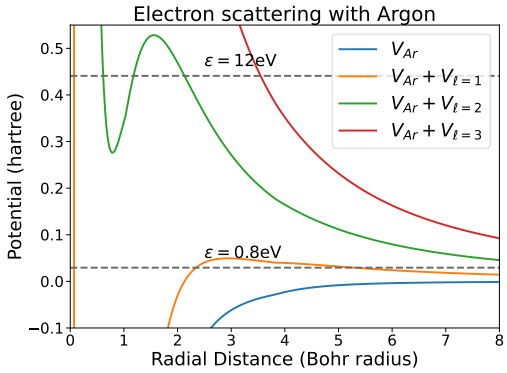

Figure 11.20: Illustration of possible shape resonances due to trapping of an incident electron in the potential of argon and centrifugal barriers of $\ell = 1, 2, 3$.

Resonances occur when the potential of the molecule (or atom), combined with the centrifugal potential of harmonic waves with $\ell > 0$, presents a classical barrier that the electron of a lower energy (than the maximum of the barrier) has to cross. This is illustrated besides (fig. 11.20) for electrons in the central potential of argon, modelled with the optical potential (without absorption), described in section 8.2 and outlined in table 8.2. We see that an electron below approximately 1 eV could be trapped in the centrifugal potential of angular momentum $\ell = 1$ which presents a low but wide barrier. A similar situation occurs for electrons between 7–14 eV for $\ell = 2$ waves with however a narrower and peaked barrier. The partial waves beyond $\ell = 3$ do not present any resonances.

If the electron is trapped in the potential given by the ground state of the molecule, we have a *shape* resonance [820, VII.A]. When the incoming electron interacts with a bound electron so that both become trapped in the potential of an electronically excited compound, it corresponds to a *core-excited* resonance. The state that the molecule would be in if the most energetic (if in different orbitals) of the electrons were removed, is known as the parent state. Core-excited resonances may be of two types:

Type I : the total energy of the compound lies below the energy of the molecule in the electronically excited state. Then it cannot decay into the parent excited state, the channel is closed. The decay process requires electronic rearrangement and is usually slow, implying longer lifetimes. This is also known as a Feshbach resonance [280].

Type II : the total energy of the compound lies above the threshold of electronic excitation from ground to the parent state. Then, the electronic excitation to the parent state is a possible outcome of the resonant collision. This is equivalent to a shape resonance but with an excited state instead of a ground state. Shape resonances tend to have shorter lifetimes.

When the excited state (parent) is in a Rydberg orbital, the two excited electrons may be seen as wandering about in the field of a core ionic state (grandparent).

Each resonance is characterised by an energy $\mathcal{E}_{\text{res}}$ and a width Γ that characterises the decay at a rate given by $\tau = \hbar/\Gamma$ [399, §6.5.2]. In the helpful image of a particle (the scattering electron) trapped in a potential well (see fig. 11.20), the energy $\mathcal{E}_{\text{res}}$ is related to the de Broglie wavelength of the electron at which successive reflections on the "walls" of the potential add constructively and thereby enhance the amplitude of the electron's wavefunction inside the well. The width Γ is interpreted as the leakage rate through the barrier. For more insight, we recommend the introduction given in chapter 3 section 2 of Shimamura and Takayanagi [834, p.201-220].

At a resonance $\mathcal{E}_{\text{res}}$, the phase shift of one specific partial wave ℓ_{r} varies abruptly over a small range Γ of energies, while other phase shifts $\delta_{\ell\neq\ell_{\text{r}}}$ can be considered approximately constant or weakly (linearly) dependent on energy. More generally, for non-spherical potentials, this abrupt variation could apply to one particular element of the scattering matrix $S^{\Lambda}_{\ell_0\ell}$ of a symmetry Λ. Mathematically, this abrupt variation comes a pole in the scattering matrix $S(\varepsilon)$ at the complex energy $\tilde{\mathcal{E}}_{\text{res}} \equiv \mathcal{E}_{\text{res}} - \mathrm{i}\frac{\Gamma}{2}$. The smaller Γ, the closer the pole is to the real axis and thus the more abrupt (narrow) the resonance is [399, 834, §2.4, eq.(6.124)].

What results from this, is that the cross section (differential or integrated) for the process considered can be locally approximated near $\varepsilon \simeq \mathcal{E}_{\text{res}}$ as the renowned Breit-Wigner profile[834, p.355:eq.(6)]:

$$(\mathrm{d})\sigma(\varepsilon) \cong \left| C + A\frac{\Gamma/2}{(\varepsilon - \mathcal{E}_{\text{res}}) + \mathrm{i}\Gamma/2} \right|^2 \tag{11.36}$$

The non-resonant (background) term C may present a slight variation in energy to the first order as : $C(\varepsilon) = C_0 + C_1(\varepsilon - \mathcal{E}_{\text{res}})$, near the resonance. If applied to the differential cross section, then angular dependence through Legendre polynomials is included in C and A. An equivalent expression, when the square modulus is applied in (11.36), can be obtained after a rearrangement of the terms which leads to the famous [270] profile [26, eq.(13)]:

$$(\mathrm{d})\sigma \cong (\mathrm{d})\sigma_{\text{min}} + \frac{(\epsilon + q)^2}{(1+\epsilon^2)(1+q^2)}(\mathrm{d})\sigma_{\text{res}}\,, \tag{11.37}$$
$$\text{with } \epsilon \equiv \frac{(\varepsilon - \mathcal{E}_{\text{res}})}{\Gamma/2}\ ;$$

which determines a minimum value σ_{min} and a resonance amplitude σ_{res}. The shape parameter q, sometimes called the "profile index", may vary from $-\infty$ to $+\infty$. Depending on the relative phasing and amplitude of A and C, the Fano profile may either show a perfectly symmetric peak, dip or a general asymmetric ripple. As C vanishes, the profile converges to a Lorentzian. For illustration, please consult Hertel and Schulz [398, p.370:fig 7.10 and eq.(7.74)].

We may now restate the relationship between the lifetime of a resonant state and the corresponding breadth observed in the peak structure of a given cross section in a given channel:

- Sharp, narrow peaks are related to resonant states with long lifetimes (small Γ): a typical example is the $O_2^-\ ^2\Pi_g$ resonance on figure 11.21a.
- Broad, flatter knolls are related to short-lived resonant states (large Γ): those are characteristic in the $H_2^-\ ^2\Sigma_u^+$ resonance on figure 11.21b.

Typically, the lifetime of a resonance is compared with a vibrational period $\sim 10^{-14}$ s of the compound. Lifetimes are considered short if the compound decays no longer than after a quarter of a period has elapsed [834, p.225]. Longer lifetimes imply that the compound has time to vibrate even up to several cycles and therefore individual vibrational peaks may be identified in the cross section. The compound $N_2^-\ ^2\Pi_g$ lies just in the middle between short-lived and long-lived resonances with a lifetime of approximately one vibrational period [72, fig. 2], which explains the wobbly shape of resonances peaks with flat tops in figure 11.19.

In general, Feshbach resonances are long-lived whereas shape resonances are short-lived. Of course, this is not a strict rule as the $O_2^-\ ^2\Pi_g$ compound (shape resonance) has a very long lifetime $\sim 10^{-10}$ s. The fine spectroscopy of Okumura *et al.* [714] even permits to distinguish the non-degeneracy of the O_2^- anion with Hund's coupling case (a) [399, §3.6.4] : $\Omega = 1 \mp \frac{1}{2}$ from $\Lambda = 1$ and $\Sigma = \frac{1}{2}$ for the $^2\Pi_g$ symmetry.

An example of sharp Feshbach resonance peaks associated to multiple NO^- excited states (labelled a,b,c,d,d') is shown in figure 11.22b. For N_2, one can visualise in figure 11.22a the Feshbach resonance linked to the $N_2^-(\mathrm{R}\,^2\Sigma_g^+)$ state observed as a notch in the total cross section [512, fig. 5] and compare it to the core-excited shape resonance linked to the $N_2(\mathrm{E}\,^3\Sigma_g^+)$ parent in the inset [407, fig. 14].

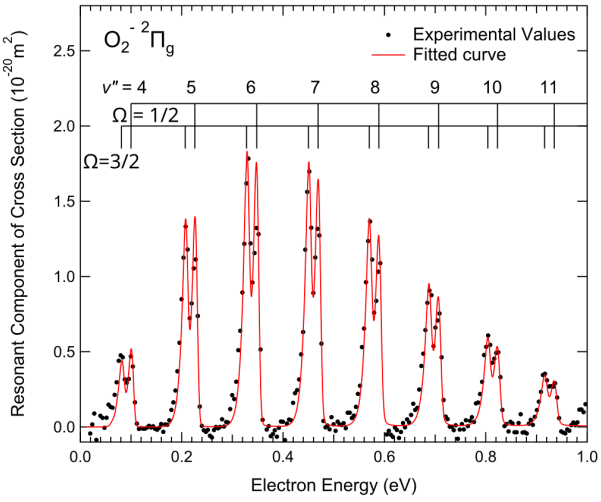

(a) Example of sharp resonance peaks for long-lived compounds ($O_2^-\ ^2\Pi_g$) from [714, fig. 3].

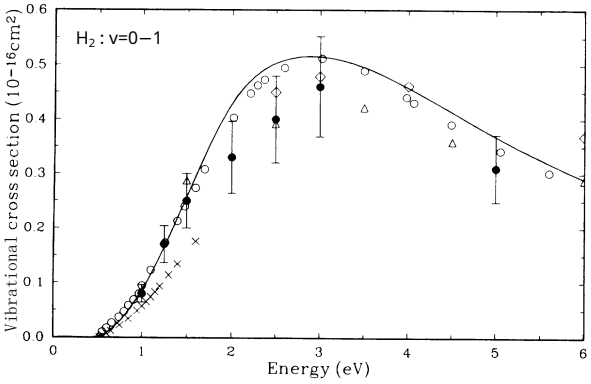

(b) Example of broad resonance bump for short-lived compounds ($H_2^-\ ^2\Sigma_u^+$) adapted from Buckman *et al.* [130, fig.2]

Figure 11.21: Comparison of long-lived and short-lived resonant states and the resulting structure in the vibrational excitation cross section.

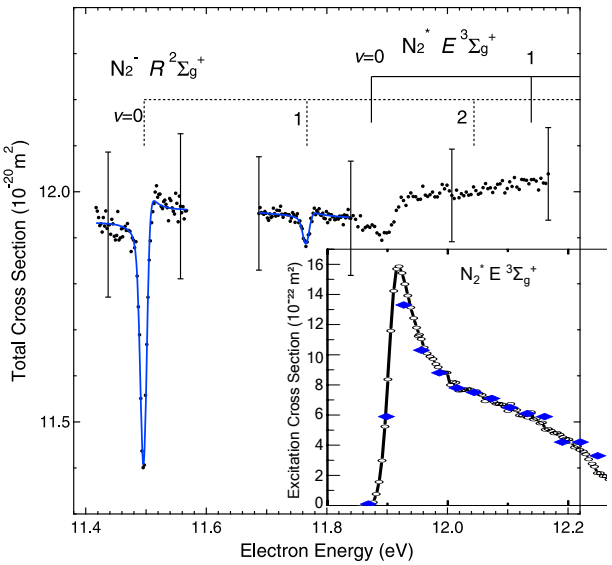

(a) Core-excited Feshbach and shape resonances (inset) linked to the $E\ ^3\Sigma_g^+$ parent state of N_2, total cross section from [512, fig. 5] and excitation cross section in inset from [407, fig. 14]

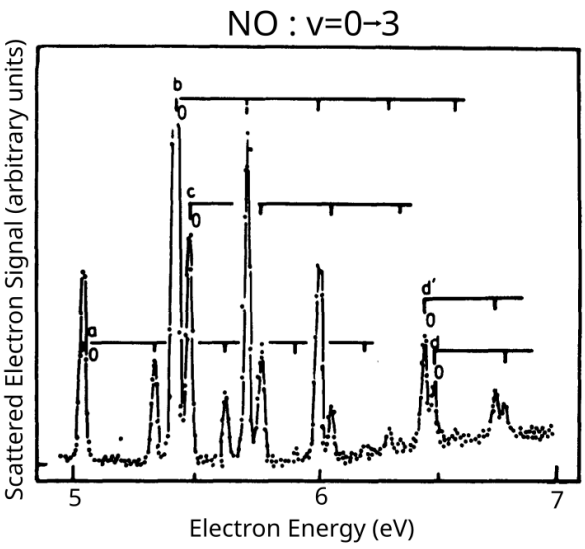

(b) Feshbach resonance bands (a,b,c,d,d') linked to various low-lying excited states of NO from [355].

Figure 11.22: Narrow profiles from Feshbach resonances: a very fine spectroscopic resolution is needed to resolve bands from long-living resonant states.

In practice, the simple image of resonance shapes with Fano profiles (11.37) can be enriched with several considerations, in particular when applied to molecules.

Peak. The position of the Fano profile peak, not necessarily located at $\mathcal{E}_{\text{res}}$, may vary with the scattering angle [124, p.281]. This variation [17, p.3663-4:figs. 6-10] ($\mathcal{E}_{\text{res}}$ stays fixed) comes from the coherent superposition of the direct C and resonant components in (11.36) [832]. The peak may be shifted or shrunk depending on the relative phase of C. Therefore, the peaked structure of DCS (if observable) may be blurred when considering the integral cross section at a given energy. As a result, comparison with experimental data is made difficult in the resonance region [894, §V] due to the convention used to slice the two-dimensional space where the DCS varies in energy and scattering angle.

Width. The resonance width $\Gamma(\varepsilon, R)$ varies with the electron's incident energy ε and the internuclear separation R. Since the resonance width $\Gamma(\varepsilon, R)$ represents the probability rate of escaping through the potential barrier, it is natural that Γ be considered a function of both the incident electron's energy ε and the internuclear separation R [72]. From the illustrative example 11.20, varying the electron energy changes the height (and thus the width) at which the barrier must be crossed. If it represented the potential of a diatomic molecule, a dependence on R would roughly stretch and compress the landscape if the Born-Oppenheimer approximation (separation of electronic and vibrational wavefunctions) is valid.

Interference. If there are resonant poles which lie close to each other in the $\mathcal{E}_{\text{res}} - \mathrm{i}\Gamma/2$ complex energy space, then the Breit-Wigner formula (11.36) will be composed by coherent superposition of multiple resonant profiles. The resultant cross section may be composed of multiple peaks (if narrow resonance widths as in fig. 11.21a) or a mixed broader profile (as in fig. 11.19-lower graph in the region 15–30 eV which lies above the ionisation potential of N_2 are where multiple closely spaced configurations are thought to participate in the resonance [740]).

Averaging. Depending on the duration of the resonance, the cross sections should be obtained from vibrational and rotational averaging in order to be compared with experimental ones. An efficient yet reliable calculation of the cross sections depends on the lifetime of the resonant state. For durations longer than the order of a rotational period $\gtrsim 10^{-12}$ s, the rotation of the molecule must be taken into account (coupled) to the resonant state. Rotational motion strongly affects the resonant shape of the differential scattering cross section [820, fig. 66]. When the duration is shorter than the rotation of the molecule but still longer than a vibrational period, the cross section may be averaged on the orientation of the molecule but the electron and vibrational wavefunctions remain coupled. For a short-lived resonance ($\ll 10^{-14}$ s), the impulse approximation may be used to compute the cross section [834, p.266-8]. Rotational and vibrational averaging over the internuclear separation distance R (and orientation $\hat{\mathbf{R}}$) are performed by taking the (ro)vibrational wavefunctions of the final and initial states of excitation.

Resonant scattering is, of course, not limited to vibrational excitations. As seen in (V2) the first step consists in the formation of the resonant compound. The following step is the decay of the compound into a final state accessible by an open reaction channel. Elastic scattering, rotational excitations (see fig. 11.19-bottom), electronic excitations (see red curve on fig. 11.30), dissociation are also subject to resonances. Evidently, attachment is an exclusively resonant process due to the necessity to form the compound state. We may distinguish the three following compound decay outcomes:

A. Auto-detachment: after a while, the electron detaches from the compound and leaves the molecule in its initial or in an excited (rotationally, vibrationally, electronically) state AB^*. The detachment happens in the internuclear distance range where the potential curves of the compound and neutral molecule overlap (see fig.11.18).

B. Attachment: if the lifetime of the compound is longer than the average time of collisions between molecules in the gas, the compound may communicate its excess of energy to another molecule and deexcite to one of the stable states ($v'' \in \{0..3\}$ for O_2 and $v'' = 0$ for NO). This corresponds to the *three-body* attachment which affects electric discharges in air as described in the first part of this thesis.

C. Dissociative Attachment: when the energy of the electron is sufficiently high, above the last vibrational level of the compound (>4.02 eV for $O_2^-\ ^2\Pi_g$ [558, table 1] and >5.074 eV for $NO^-\ ^3\Sigma^-$ [441, eq.(6a)]), this compound may dissociate into its individual atoms, to one of which the electron stays attached.

More illustrations and information about resonant scattering can be found in the early comprehensive review given by Schulz [820] for the main diatomic molecules usually encountered in air. In the following subsections, we will describe how we assembled the cross sections for vibrational excitations and attachment.

11.3.2 Differential Cross Sections

As mentioned earlier, resonance occurs when the scattering electron gets trapped in a potential well that is formed by the attractive potential of the target and repulsive centrifugal potential. This electron somehow "settles in" an orbital of the compound state, whence it eventually escapes with a wave corresponding to the symmetry and angular momentum of the orbital.

For instance, electrons escaping from the $^2\Pi_g$ symmetries of N_2^- and O_2^- will flee through a $d\pi$ wave because of the former $3d\pi_g$ orbital they occupied [820, p.448:§III.A]. Nevertheless, the shape of the differential cross section will not necessarily reflect the symmetry determined by the wave unless four conditions are verified [820, p.458]:

- Background scattering (term C in eq.11.36) is negligible.
- The resonance is dominated by only one electronic configuration.
- The lifetime of the compound is much shorter than the rotational period: $\tau_{\text{res}} \ll 10^{-12}\,\text{s}$.
- The electronic and vibrational parts of the wavefunction are separable.

Under these conditions, the theory of angular distribution for resonant scattering [770, §6:eq(9)&tab 4] may be applied. For a single partial wave characterised by $\ell\lambda$, the DCS equals:

$$\frac{\mathrm{d}\sigma_{\text{res}}}{\mathrm{d}\Omega} = \sigma_0 \sum_n A_n P_n(\cos\theta)\ , \tag{11.38}$$

$$A_n = (2n+1)\begin{pmatrix} \ell & \ell & n \\ 0 & 0 & 0 \end{pmatrix}\left\{\begin{pmatrix} \ell & \ell & n \\ \lambda & -\lambda & 0 \end{pmatrix}^2 + p\begin{pmatrix} \ell & \ell & n \\ \lambda & \lambda & -2\lambda \end{pmatrix}^2\right\}\ . \tag{11.39}$$

The parameter $p = 1$ when the states are doubly degenerate ($\Lambda \geq 1$ symmetries) and $p = 0.5$ for non-degenerate Σ symmetries (which can either be + or −, see appendix C). The proportionality coefficient σ_0 is related to the norm of the cross section.

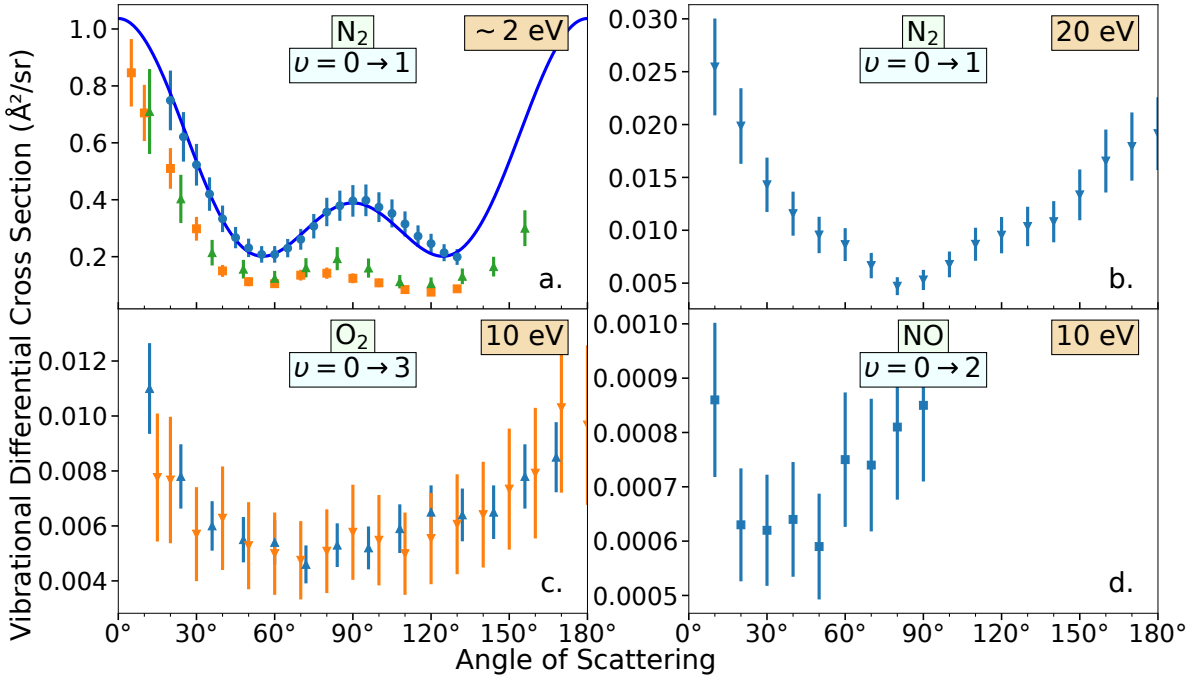

Figure 11.23: DCS for vibrational excitations of diatomic molecules. At low energies, the DCS shape can be plainly characterised as a $d\pi$ wave (11.40) only for N_2. At intermediate energies, the interference between different configurations of the resonant anion make the shape harder to interpret. Experimental data from a:[105, 894, 898], b:[600], c:[599, 846] and d:[654].

The most conspicuous example of such uniquely shaped resonant scattering are the DCS of $N_2(v \to v')$ excitations in the $^2\Pi_g$ resonance region for which a $d\pi$ wave [17, p.3669]:

$$\frac{\mathrm{d}\sigma_{d\pi}}{\mathrm{d}\Omega} = \sigma_0 \left(1 - 3\cos^2\theta + \frac{14}{3}\cos^4\theta\right) \tag{11.40}$$

was plotted on figure 11.23a. Note that if the vibrational excitation is accompanied by a rotational transition $\Delta J \neq 0$, the shape of the DCS is considerably affected, to the point that it becomes roughly isotropic [473, fig. 4-5]. At higher energies (fig. 11.23b), more than one configuration participates in resonant scattering and so the shape at 20 eV is more complex.

For O_2 at low energies, because of long lifetimes, the DCS cannot be simply averaged over the rotational levels. In figure 11.23c we show the measurements of Linert and Zubek [599] for the $O_2(v = 0 \to v' = 3)$ excitation at 10 eV. There are two oversights in [599, p.4088&4091] when citing Allan's work [12]. Firstly, the autodetachment width of O_2^- around 9 eV is actually *narrow* which implies that the resonance is *longer*-lived. Secondly, the expected $p\sigma$ wave seems to be contaminated by a small contribution of a $d\sigma$ wave on figure 11.23c. The DCS is then presumably determined by the relative proportion of two waves, and may be somewhat rotationally blurred thus resulting in a relatively flat bed. Since Allan's [12] measurements, we do not know of any theoretical work that addressed this question for that specific excitation.

Finally, we show in figure 11.23d the measurements of [654] for NO at 10 eV. In the shape resonance below 2 eV the DCS results from a mixture of a dominant $p\pi$ (from $NO^-\ ^3\Sigma^-$) and a minor $d\pi$ wave (from $NO^-\ ^1\Sigma^+$ and $NO^-\ ^1\Delta$) [16, fig. 10]. Above 2 eV, the DCS results from higher-lying configurations [557, §3].

To model approximately the scattering from vibrational excitations at low energies, we recommend taking a $d\pi$ wave for N_2 below 5 eV and resort to isotropic scattering for O_2 and NO.

11.3.3 Cross sections

As seen in the previous section, computing cross sections from resonant scattering requires a solid model of the target molecule to which the bound and continuum states of the scattering electron are coupled. Among the bound states in previously unoccupied orbitals, resonances are observed at certain energies and with a certain width (which varies also with the internuclear separation). The resonant vibrational cross sections are then obtained from the transition matrix between internuclear (vibrational) wavefunctions of the compound ξ and final $\chi_{v'}$ states of the molecule and electron. There may be several compound states participating to the cross section at a given electron energy. Potential curves of the three diatomic molecules and some lower anion states have been put together in figure 11.24. Those potentials intervene in the Schrödinger equation verified by the compound internuclear wavefunction. Another term accounts for the probability of capturing the incident electron given the initial molecular state χ_v [553, eqs.(4-6)].

Comparison between calculations and experiments, as done in figure 11.19, enables to identify regions where direct, or resonant processes from other symmetries not included in the theoretical model (e.g. $N_2^-\ ^2\Pi_u$), participate to vibrational excitation. The data from theoretical calculations are downloadable from Laporta's database on LXCat [732]. Putting together both sources, we obtain the sets on figure 11.25 (in solid) for N_2, O_2 and NO. The dashed curves show the calculated CS beyond the range of energies where they are adopted.

N_2 : This molecule has the most replete experimental database for vibrational excitation, especially in the $^2\Pi_g$ resonance region between 1.8–4 eV. There, the cross section is taken from Laporta *et al.* [554] and compared with Allan [17], Brennan *et al.* [105], Sun *et al.* [894], and Sweeney and Shyn [898]. The high-resolution measurements of [778, 962] are not shown though good agreement was found in [554, fig. 3]. Surprisingly, there is an absence of experimental integral cross sections for higher excitations $v \to v' > 1$ beyond the resonance region. The present constructed CS shown on figure 11.25-top is basically the same as the one from Kawaguchi *et al.* [482, fig. 1] except for two adjustments explained below.

i. Below 1.6 eV, we interpolate the data of Sohn *et al.* [863], rescaled by us ($\times$1.3, 1.4 and 1.5 at 0.55 eV, 1 eV and 1.5 eV) as explained in part III section 15.1.1. The outlying point is from Allan [17] whose measurements are accurate and which could eventually be inserted in the interpolation grid.

ii. Above 4.5 eV, there are only data for $v = 0 \to v' = 1$: from Tanaka *et al.* [910] and Linert and Zubek [600]. Between 15–30 eV there is a second resonance bump due to the $N_2^-(\ ^2\Sigma_u^+)$ configuration [600, p.6]. There, we privileged the more recent data [600] and used the former [910] above 21 eV only, as opposed to Kawaguchi *et al.* [482] (who used [910] only).

O_2 : The comparison with experimental data shows qualitative agreement in the position of the sharp $^2\Pi_g$ peaks below 2 eV and also for the broad knoll at 10 eV. The experimental data is essentially based on the compilation of Itikawa [440] who adopted Shyn and Sweeney's [846] measurements above 5 eV. The agreement of the theoretical results from Laporta *et al.* [552] is best at 10 eV; the only energy at which Linert and Zubek's [599] measurements are available. The shift to lower magnitudes for $v \to v' > 1$ excitations is in disagreement with Allan's [12] absolute measurements at 90°. Presently, it is not possible to determine whether the disagreement above and below 10 eV is due to errors in extrapolation and/or normalisation of vibrational DCS from Shyn and Sweeney [846], or whether the theoretical calculations underestimate the contribution of other (resonant or non-resonant) vibrational channels. As a result, we did not alter the CS and use Laporta *et al.*'s [552] original complete set of vibrational cross sections.

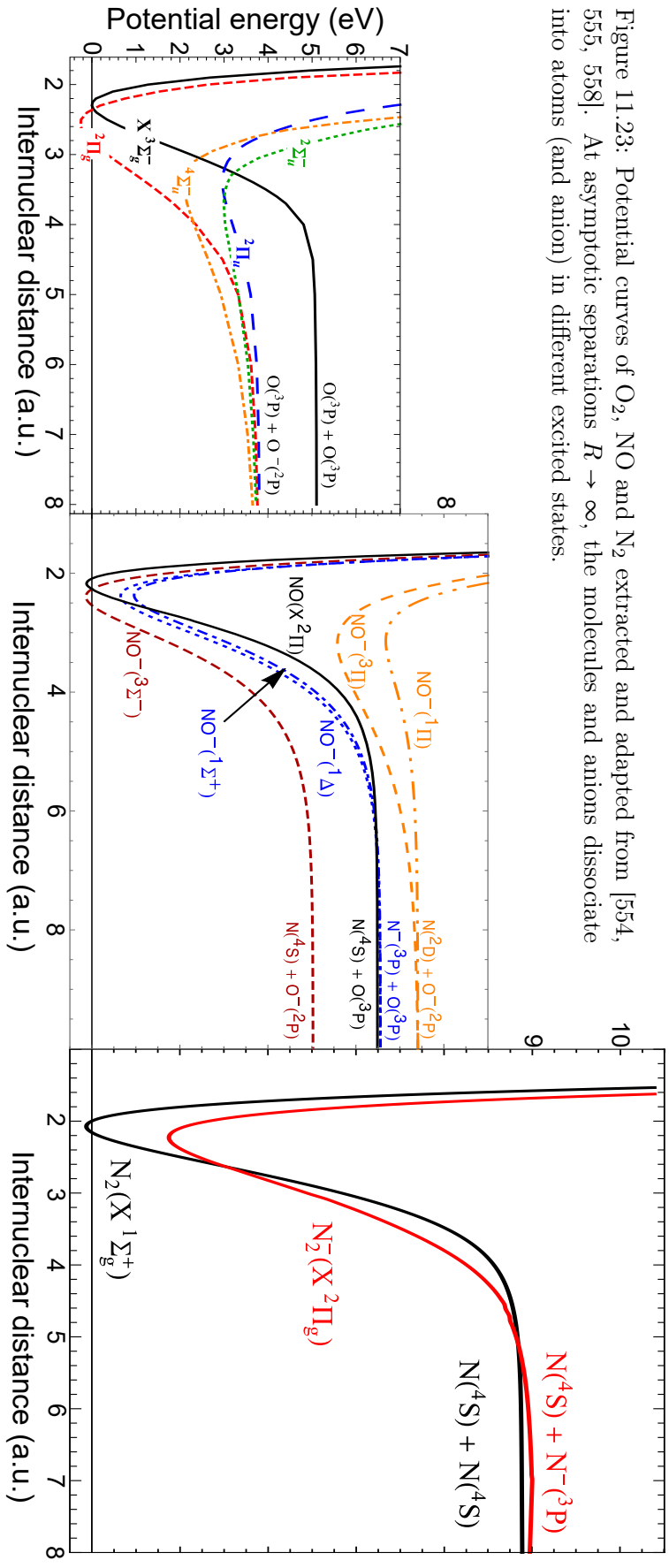

Figure 11.23: Potential curves of O_2, NO and N_2 extracted and adapted from [554, 555, 558]. At asymptotic separations $R \to \infty$, the molecules and anions dissociate into atoms (and anion) in different excited states.

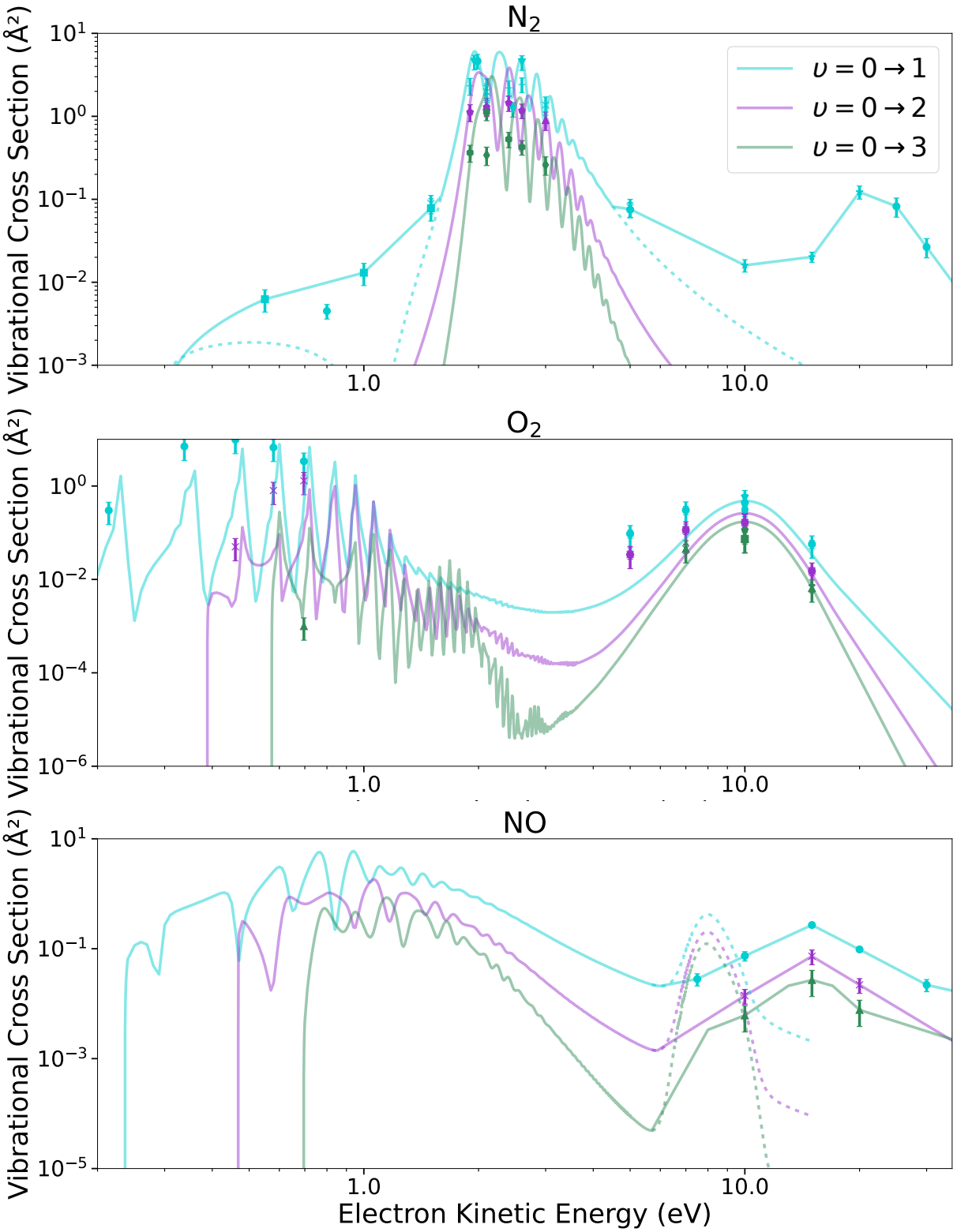

Figure 11.25: Constructed CS for the first three vibrational excitations of N_2, O_2 and NO. The smooth curves in the main resonant regions are based on the calculations by Laporta *et al.* [552, 554, 557]. The dashed lines (- - -) demarcate the theoretical calculations in the region where a log-log interpolation (in solid —) between selected experimental data is used instead.

NO : The vibrational excitation of NO is dominant in the 0.1–2.5 eV range where resonant collisions take place in the NO^-: $^3\Sigma^-$, $^1\Delta$ and $^1\Sigma^+$ symmetries, increasing in energy (see fig. 11.24). There, the contribution of direct excitation is negligible [944]. Below 2 eV, the calculations of Laporta *et al.* [557] are in good agreement with the shapes measured by Allan [16].

The region between 3–7 eV is devoid of resonances and therefore the cross section (from direct excitation) is low. Then, the CS rises again and spreads over a broad bump between 10–25 eV mainly due to the $^3\Pi$ shape resonance [557, p.2:§3]. The only available experimental data > 7 eV are from Mojarrabi *et al.* [654], which had to be extrapolated beyond 90° and have thus a large ~30 % uncertainty. On figure 11.25-bottom, there is a miscorrespondence between the theoretically predicted knoll beyond 6 eV which is narrower and at lower energies than what measurements show [557]. This could be from the participation of even higher-lying (>6 eV) symmetries of the NO^- anion which were not included in the calculation of Laporta *et al.* [557]. Given the limited available knowledge of vibrational excitations, we interpolate data from Mojarrabi *et al.* [654] beyond 6 eV. The connection point has been placed at the energy where the theoretical CS goes through a minimum.

Neutral Dissociation

In the extreme case where the resonant state is excited beyond the dissociation threshold of the molecule ($\mathcal{E}_{\text{diss}}$ in table 2.2), the nuclear wavefunction may diverge and the atoms, in their respective ground states, are ejected into the kinetic continuum. This can be visualised on the black curves of figure 11.24 when the internuclear separation is large ($R > 8$ a.u.). In neutral dissociation, the electron flees away from the anion as it dissociates. If it stays bound to one of the atoms, the situation corresponds to dissociative attachment presented below.

Cross sections for resonant neutral dissociation of N_2, O_2 and NO into the vibrational continuum have been computed by Laporta *et al.* [554, 556, 558]. They are displayed in figure 11.26.

This channel is negligible for N_2. Dissociation of NO involves mainly the NO^- $^3\Pi$ and $^1\Pi$ symmetries, with a contribution of the ground state $^3\Sigma^-$ giving the flat slope beyond 11 eV [556, fig. 2] on the green (—) curve of figure 11.26. For O_2^-, the extended broad dissociation CS is shared between $^2\Pi_u$ (lower energies, higher peak) and $^4\Sigma_u^-$ (higher energies, flatter hump) symmetries [558, fig. 4a].

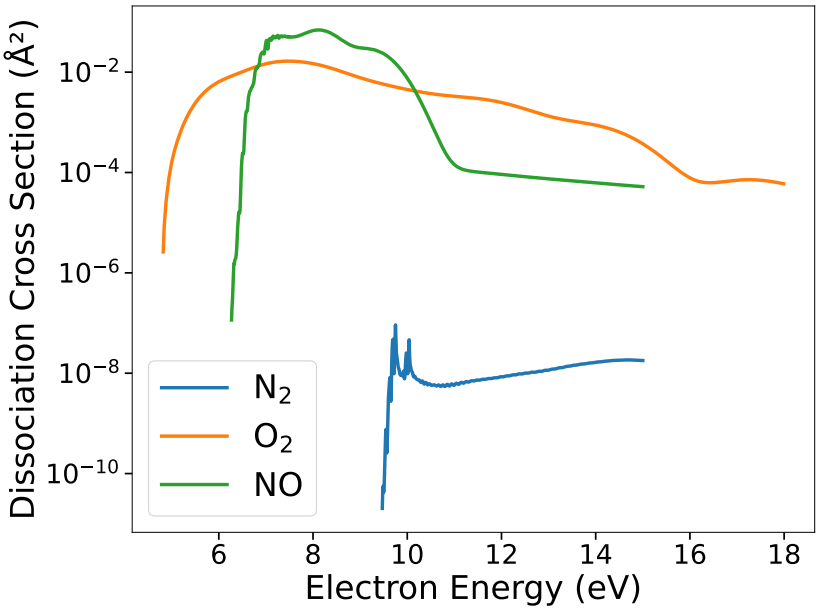

Figure 11.26: Cross sections for neutral dissociation through resonant scattering in diatomic molecules from Laporta *et al.* [554, 556, 558]. This channel of dissociation is mainly important for O_2 and NO while negligible for N_2.

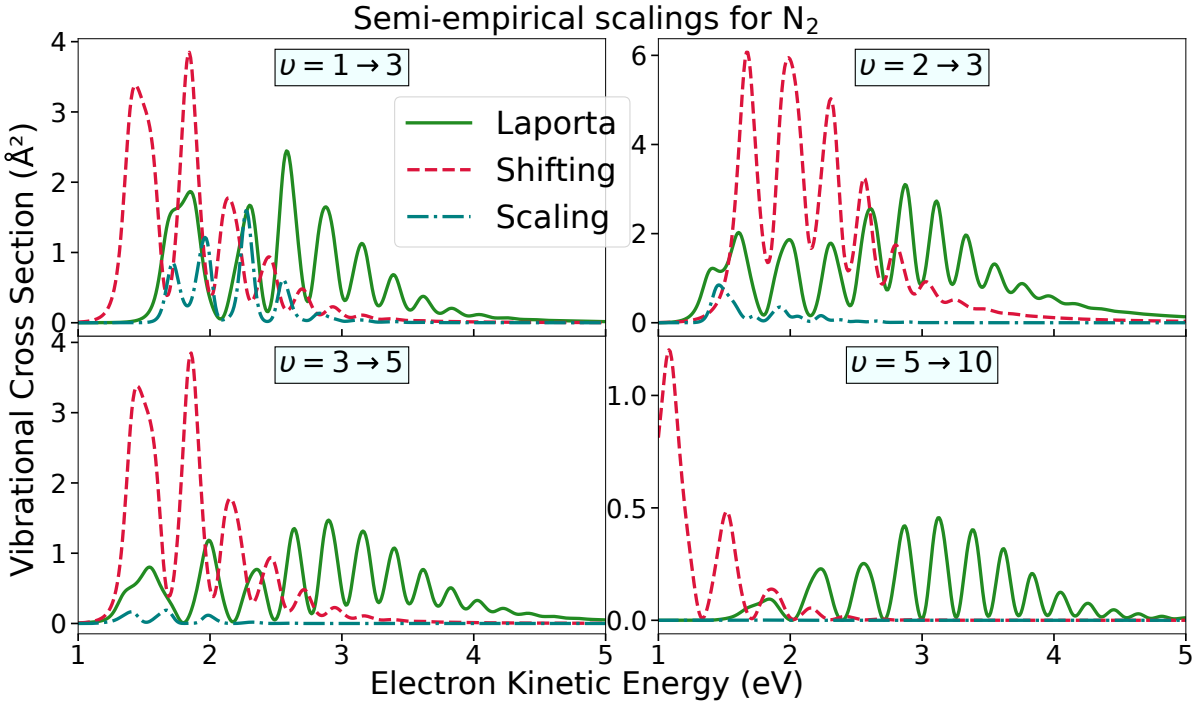

Figure 11.27: Inaccurate semi-empirical scaling methods for estimating vibrational excitation cross sections from vibrationally excited states of N_2. The equations "Shifting"-(11.41) and "Scaling"-(11.42) are compared to the calculations of Laporta *et al.* [554]

Scaling laws

Before accurate theoretical calculations of vibrational cross sections were available, modellers made use of scaling laws in order to derive cross sections for electron collisions with vibrationally excited states based on the excitations from ground level. In kinetic models, if an electron energy distribution is assumed (Maxwellian), then the scaling may be applied directly to reaction rates instead of individual electron-molecule collisions [187]. The resulting electron distribution obtained depended strongly on the set of cross sections used [253].

To stress the importance of using a reliable set of vibrational cross sections in electron-molecule collisions, we present two elementary scaling laws for vibrational cross sections.
The first, widely used in earlier studies [609, p.22], is [187, eq.(3)]:

$$\text{Shifting}: \quad \sigma_{v v'}(\varepsilon) = \sigma_{0|v'-v|}(\varepsilon - \Delta\mathcal{E}) \tag{11.41}$$

where $\Delta\mathcal{E} = (\mathcal{E}_{v'} - \mathcal{E}_v) - \mathcal{E}_{v'-v}$ for $v' > v$.
The second scaling law, used in [758], is based on arguments for resonant scattering [645, eq.(9)]:

$$\text{Scaling}: \quad \sigma_{v v'}(\varepsilon) = \frac{\varepsilon + \mathcal{E}_v}{\varepsilon} \frac{\sigma_{0v}(\varepsilon + \mathcal{E}_v)\sigma_{0v'}(\varepsilon + \mathcal{E}_v)}{\sigma_{00}(\varepsilon + \mathcal{E}_v)}, \tag{11.42}$$

For both (11.41) and (11.42), the vibrational energy levels $\mathcal{E}_v$ and the set of CS were taken from [554]. The comparison on figure 11.27 shows that resonant scattering is too complex to be modelled by simple semi-empirical formulae. While shifting (11.41) tends to overestimate the $0 < v \rightarrow v'$ cross section, the scaling in (11.42) strongly underestimates the CS. One can therefore surmise that the results of previous studies which used semi-empirical scalings [253, 609, 758] would be affected if a proper set of vibrational cross sections were used instead [149, 187].

11.3.4 Attachment

As mentioned previously, attachment is a resonant process in which the electron does not autodetach. When the compound anion is formed, two possibilities occur.

If the molecule has a positive electron affinity, then it may transit to a stable anion after it deexcites in a collision with an atom or a molecule in the gas. This process is known as three-body attachment. It is possible to form $O_2^-(v'' = 0, 1, 2, 3)$ and $NO(v'' = 0)$ anions, provided the resonant state has a long enough lifetime in the pressure conditions of the gas. In principle, a radiative deexcitation of the anions could also lead to attachment. However, this theoretically conjectured possibility has a very low probability and has been measured experimentally. The reactions for three-body attachment in air are:

$$e \; + \; NO \; + \; M \longrightarrow NO^- \; + M \, , \tag{A1}$$

$$e \; + \; O_2 \; + \; M \longrightarrow O_2^- \; + M \, . \tag{A2}$$

An alternative scenario for electrons at energies above the dissociation limit of the compound is called dissociative attachment. If the compound is excited beyond its last vibrational level, the nuclear wavefunction is purely divergent and the atoms separate; one of them keeps the electron attached.

$$e^- \; + \; O_2 \longrightarrow O_2^-(^2\Pi_u) \longrightarrow O^-(^2P) + O(^3P) \tag{D1}$$

$$e^- \; + \; NO \longrightarrow NO^* \longrightarrow N + O^- \tag{D2}$$

$$e^- \; + \; N_2 \longrightarrow N_2^-(A\ ^2\Pi_u) \longrightarrow N^-(^3P) + N(^4S^o) \longrightarrow e + N + N \tag{D3}$$

Between those two contrasted (dissociative and three-body) attachment mechanisms, there is a third intermediate possibility; dissociation and attachment to 'Van der Waals' molecules [833]:

$$e + (O_2)_2 \longrightarrow O_2 + O_2^- \tag{B1}$$

$$e + (NO)_2 \longrightarrow NO + NO^- \tag{B2}$$

Those 'molecules' are weakly bound molecular aggregates by intermolecular forces caused by mutual polarisation (perturbation) of bound electronic clouds. A common name for those binary aggregates is a 'dimer' ('two-parts' in Ancient Greek). The presence of dimers requires high concentrations of molecules in the gas. Effects of 'dis-mer-ing' attachment are most important at lower temperatures where they supplant three-body attachment rates.

Three-body attachment

Measurements of three-body attachment usually proceed from swarm experiments measuring the output signal of molecular anions. Attachment and detachment rate coefficients were measured for NO by Parkes and Sugden [734] and for O_2 by Shimamori and Fessenden [833]. A measurement of the reaction rate based on electron energy for oxygen was performed by Spence and Schulz [868], showing a quadratic dependence on molecule density. A theoretical estimation of three-body attachment requires to know:

1. σ_{res} : the total collision cross section for the formation of the resonant compound
2. τ_{res} : the lifetime (inverse autodetachment rate) of the resonant compound

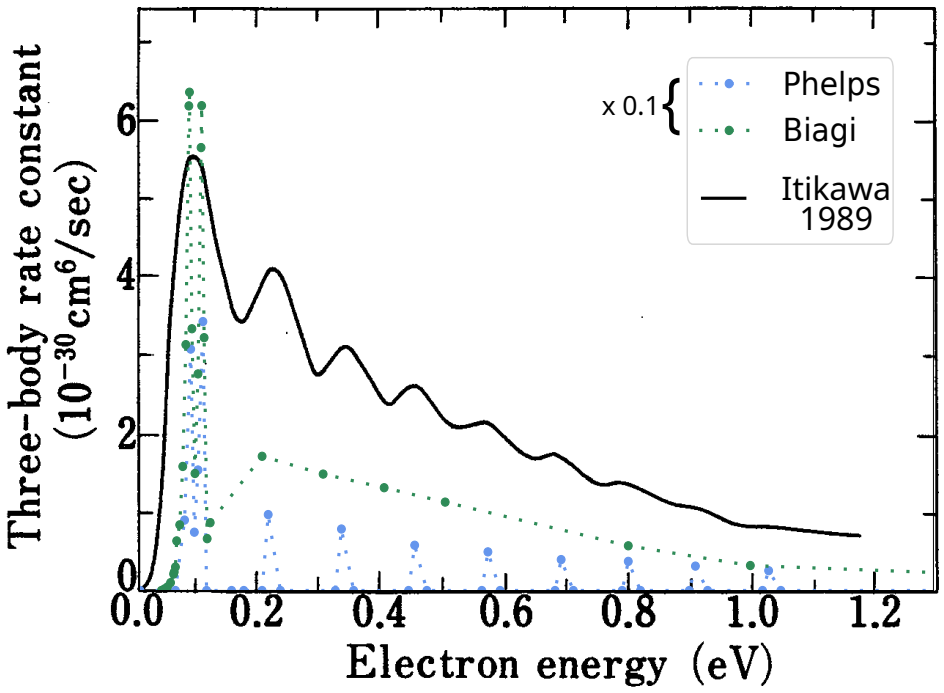

Figure 11.28: Unknown discrepancy between three-body rates drawn from `Biagi` and `Phelps` databases on LXCat (which are presently scaled to one-tenth for clarity) and the data of Itikawa *et al.* [438, fig. 8.3] based on Spence and Schulz [868, fig. 5].

3. σ_{AM} the total collision cross section between the anion (A) and a neutral molecule (M)
4. $\xi(v'' \to v''')$: the branching ratio of the A + M collision to a vibrational state v''' of the anion situated below the ground state of the molecule.

Then, the ansatz for the three-body attachment cross section is [694, eq.(62–3)]:

$$\sigma_{3\mathrm{B}} \cong \sigma_{\mathrm{res}} \tau_{\mathrm{res}} \bar{\mathrm{v}}_{\mathrm{M}} n_{\mathrm{M}} \sigma_{\mathrm{AM}} \xi \,, \tag{11.43}$$

with the density of molecules n_{M} and average inter-molecule velocity $\bar{\mathrm{v}}_{\mathrm{M}}$ at the given gas temperature. If we take the total cross section $0.5 \times 10^{-20}\,\mathrm{m}^2$ from Okumura *et al.* [714, fig. 3] at the resonance peak 0.1 eV for the $v'' = 4$ vibrational state of O_2^- with an average lifetime of $\tau_{v''=4} = \hbar/\Gamma_{v''=4} \approx 25\,\mathrm{ps}$ and roughly estimate the average inter-oxygen velocity at 300 K, hard sphere collision cross section $\sim \pi(3R_{O_2})^2$ and assuming a univalent branching ratio $\xi = 1$, we get the three-body attachment cross section $\approx 3.3 \times 10^{-37}\,\mathrm{cm}^2\,\mathrm{cm}^3$ for an electron at expressed as an effective cross section for a gas at a density of 1 molecule/cm^3. For comparison, Spence and Schulz [868, p.728] reported value at 0.09 eV is $3.1 \times 10^{-37}\,\mathrm{cm}^2\,\mathrm{cm}^3$.

Nevertheless, the three-body attachment cross section values only available in `Biagi` and `Phelps` databases on LXCat are about one order of magnitude higher than in Spence and Schulz [868, fig.5], from figure 11.28. A more agreeable estimate could be obtained from the resonant cross sections reported by Okumura *et al.* [714, fig. 3] put into the tentative derivation (11.43).

In the end, we surmise that elastic and vibrational resonant cross sections in the $^2\Pi_g$ resonance of O_2^- should be somewhat quenched by three-body attachment process at higher molecular densities and lower gas temperatures. We did not pursue this route of investigation any further. A more rigorous derivation of three-body attachment cross sections, like the one described in Spence and Schulz [868, §V], would be desirable in the future.

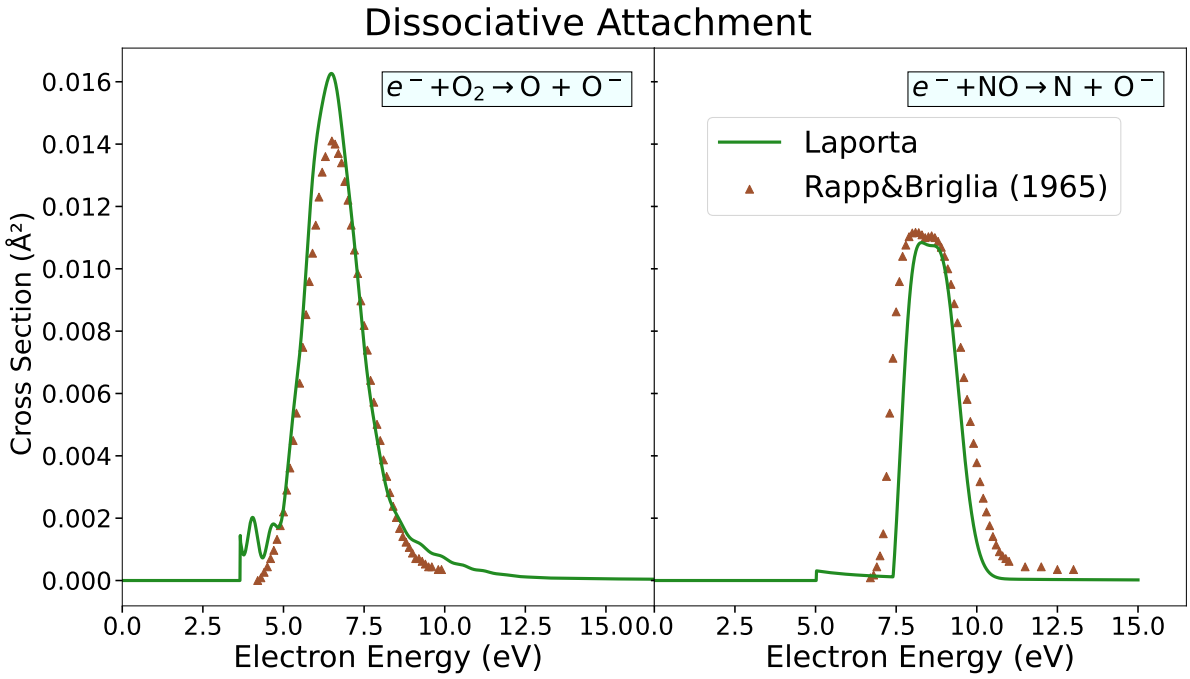

Figure 11.29: Electron impact dissociative attachment from resonant collisions with O_2 (mainly $O_2^-\,{}^2\Pi_u$) and NO (mainly $NO^-\,{}^3\Pi$ and ${}^1\Pi$) calculated from Laporta *et al.* [555, 558] and measured by Rapp and Briglia [767].

Dissociative attachment

An overview of the resonances and thresholds for dissociative attachment is given in table 11.5. Various dissociation processes from different resonant anion symmetries can be found on at the asymptotic ends of the potential curves in figure 11.24.

For O_2, the major contribution to dissociative attachment comes from the ${}^2\Pi_u$ resonant anion state [558, 820, p.475, fig. 2]. Other symmetries participate at lower (${}^2\Pi_g$) and higher (${}^4\Sigma_u^-$) energies. All the present dissociation channels lead to production of $O\,{}^3P$ and $O^-\,{}^2P$.

NO may dissociate into several channels:

$$e^- + NO \longrightarrow NO^-({}^3\Sigma^-) \longrightarrow N({}^4S^o) + O^-({}^2P)\,, \tag{DA1}$$

$$e^- + NO \longrightarrow NO^-({}^1\Delta, {}^1\Sigma^+) \longrightarrow N^-({}^3P) + O({}^3P)\,, \tag{DA2}$$

$$e^- + NO \longrightarrow NO^-({}^3\Pi, {}^1\Pi) \longrightarrow N({}^2D) + O^-({}^2P)\,, \tag{DA3}$$

$$e^- + NO \longrightarrow NO^-(*) \longrightarrow N({}^2P) + O^-({}^2P)\,. \tag{DA4}$$

The most important channel comes from resonance symmetries ${}^3\Pi$ and ${}^1\Pi$ [555, figs. 4-5]. The other channels have a lesser contribution, the formation of N^- in particular is negligible and information about the production of $N({}^2P)$, possibly related to some of the higher excited symmetries of NO [574], is missing in the most recent reviews [441, 555, 865]. The contribution of the shape resonance $NO^-({}^3\Sigma^-)$ rises with the initial vibrational state v of NO. The threshold levels for each process are given in table 11.5. In figure 11.29, one can compare the importance of total dissociative attachment cross sections for O_2 [558] and NO [555] and the good agreement with experimental results from Rapp and Briglia [767].

Formally speaking, dissociative attachment applies also to the core-excited shape resonance of $N_2^-({}^2\Pi_u)$ linked to the $N_2(A\,{}^3\Sigma_u)$ parent state [834, p.378-383:chapter 5-§2.7]. The unstable

$N^-(^3P)$ anion has a short lifetime $\sim 2.5 \times 10^{-14}$ s [635]. Therefore this process (D3) is comprised in the total dissociation cross section into neutral products [193].

Table 11.5 Dissociative attachment thresholds $\mathcal{E}_{\mathrm{DA}}$, from Laporta *et al.* [558, §I] (O_2), Itikawa [441] and Laporta *et al.* [555, eq.(6), tab. 1] (NO) and [834, p.380] (N_2). These are the dissociation limits of different anion states on fig. 11.24 with respect to the neutral molecule ground state.

Compound	O_2^-	NO^-				N_2^-
Resonance	$^2\Pi_u$ ($^2\Pi_g$, $^4\Sigma_u^-$, $^2\Sigma_u^-$)	$^3\Sigma^-$	$^1\Delta, ^1\Sigma^+$	$^3\Pi, ^1\Pi$	$*$	$^2\Pi_u$
$\mathcal{E}_{\mathrm{DA}}$ (eV)	3.64	5.074	6.55	7.457	8.65	9.83

11.4 Electronic Excitations

When the incident electron approaches a molecular or atomic target, it perturbs the electrons bound to the target which are repelled by Coulomb interaction. In some cases, this perturbation may be significant enough to "shove" a bound electron into another orbital. If this new electronic orbital configuration is stable, it maintains itself even after the incident electron has left, this leads to an electronic excitation into a discrete state.

The cross sections for electronic excitations form an important energy loss for incident electrons not far above the ionisation threshold of the target. For molecules: rotational, vibrational and electronic excitations combine together to form "rovibronic" bands with regularly spaced vibrational peaks (rotationally broadened) that fill the probability space in which an incident electron may lose part of its energy (see figures 11.32,11.35 below).

The present section provides analytical expressions for electronic excitation cross sections with N_2, O_2, NO, Ar, O and N. Those are obtained based on semi-empirical corrections to the plane-wave Born approximation (11.61-11.64), fitted to a presently reviewed database of experimental measurements in tables (11.6-11.11).

As of today, the database in electronic excitations is very rich. Experiments were conducted early [158, 938] from the 70's and some groups still perform active research either theoretically [889] or experimentally [493, 624, 897]. One of the major reasons for ongoing investigation is the persisting discrepancies between various measurements for some electronic states [479], especially near threshold [463]. It is not unusual that recommended values present large uncertainties [121, 439, 440] above 30%.

The reason for this is that there are several ways to obtain integral cross sections: through time-of-flight analysis of electrons or excited species [633], detection of radiative de-excitations from principal emission bands for optically-allowed transitions [9, 452], swarm experiments on electron energy loss spectra [289, 490] or direct integration of differential cross section measurements [158] extrapolated through the whole angular range. Since these experiments may rely on different reference values, fitting methods, instrumental calibration procedures or normalisation, it is not straightforward to obtain good agreement. Nevertheless, most reliable values for the cross sections are obtained when various techniques agree well for the same excitation considered [124, figure 37(b)].

Theoretical calculations of electronic excitations are cumbersome because they require an accurate description of the wave functions associated to each excited state and their dependence on the internuclear separation. Then, the resolution is befitted by a close-coupling treatment involving various (or rather many) excited target states [914, 916].

Setting these complex methods aside, our approach for representing inelastic cross sections is based on two powerful tools:

1. The "generalised oscillator strength" formulation from Bethe [64] relying on the plane-wave Born approximation.

2. A semi-empirical correction to the above formulation called the "scaled plane-wave Born approximation" introduced by Kim [504].

In the next two sections, we first introduce in 11.4.1 the generalised oscillator strength as reviewed by Inokuti [427] and then, in 11.4.2, we present an adaptation of the scaled-Born method to our modelling of electronic excitations.

11.4.1 Generalised Oscillator Strength

We start from the plane-wave Born approximation (8.117) for the scattering amplitude f of an electron scattered with momentum transfer $\mathbf{q} = \mathbf{k} - \mathbf{k}'$ with a reduced mass μ for a transition of a diatomic $^1\Sigma$ molecule from a state a, v, J, M to a state a', v', J', M', assuming the Born-Oppenheimer separability of nuclear and electronic motions [907, p.58:eq.(145)]:

$$f(a,v,J\to a',v',J') = -\frac{2\mu}{\hbar^2 4\pi}\iiint R^2\,\mathrm{d}R\,\mathrm{d}\hat{\mathbf{R}}\,\mathrm{d}\mathbf{r}_m\,\mathrm{d}\mathbf{r}\times \tag{11.44}$$
$$\underbrace{\mathrm{e}^{-\mathrm{i}\mathbf{k}'\cdot\mathbf{r}}\phi^*_{a'}(\mathbf{r}_m,\mathbf{R})\frac{\chi^{v',J',*}_{a'}(R)}{R}Y^*_{J',M'}(\hat{\mathbf{R}})}_{\text{final state}}\underbrace{V(\mathbf{r}_m,\mathbf{R},\mathbf{r})}_{\text{interaction}}\underbrace{\mathrm{e}^{\mathrm{i}\mathbf{k}\cdot\mathbf{r}}\phi_a(\mathbf{r}_m,\mathbf{R})\frac{\chi^{v,J}_a(R)}{R}Y_{J,M}(\hat{\mathbf{R}})}_{\text{initial state}},$$

with R being the interatomic separation and orientation $\hat{\mathbf{R}}$; $\mathbf{r}_m$: all internal electronic coordinates of the molecule; ϕ, χ/R and Y: the electronic, vibrational and rotational (spherical harmonic) functions; and the interaction potential constructed from Coulomb static interaction and other local approximations $\tilde{V}(\mathbf{R},\mathbf{r})$ [907, eq.(147)]:

$$V(\mathbf{r}_m,\mathbf{R},\mathbf{r}) = \sum_A \frac{-Z_A e^2}{|\mathbf{r}-\mathbf{R}_A|} + \sum_{j\in m}\frac{e^2}{|\mathbf{r}-\mathbf{r}_j|} + \tilde{V}(\mathbf{R},\mathbf{r})\,. \tag{11.45}$$

Considerable simplifications arise when the scattering is electronically inelastic : $a \neq a'$. Since ϕ_a is orthogonal to $\phi_{a'}$ through integration over $\mathbf{r}_m$, all potential terms independent of $\mathbf{r}_m$ can be discarded and one may cunningly exploit [427, p.299:eq(2.3)] (as justified originally in Bethe [64]):

$$\int \frac{e^2}{|\mathbf{r}-\mathbf{r}_j|}\exp(\mathrm{i}\mathbf{q}\cdot\mathbf{r})d\mathbf{r} \to \frac{4\pi e^2}{q^2}\exp(\mathrm{i}\mathbf{q}\cdot\mathbf{r}_j)\,. \tag{11.46}$$

In practical applications, the differential cross section as obtained through $|f|^2\,k'/k$ is summed over final J', M' and averaged over initial M rotational states and under the sudden impulse approximation (fixed molecular orientation and k' independent of J'), it is independent of J. After calculations, it can be expressed as [834, p.60:eq(151)]* :

*Note that there is a typo in eq(151), the averaging over $\hat{\mathbf{R}}$ should be done outside of the modulus bar | as in, for instance, Takayanagi [906, p.221:eq(3·5)]

$$\frac{\mathrm{d}\sigma}{\mathrm{d}\Omega}(av \to a'v') = \frac{k'}{k}\frac{(2\mu/m_\mathrm{e})^2}{(a_0 q^2)^2}\int \frac{\mathrm{d}\hat{\mathbf{R}}}{4\pi}\left|\iint \sum_{j\in m} \mathrm{e}^{\mathrm{i}\mathbf{q}\cdot\mathbf{r}_j}\phi^*_{a'}(\mathbf{r}_m,\mathbf{R})\chi^{v'}_{a'}(R)\phi_a(\mathbf{r}_m,\mathbf{R})\chi^v_a(R)\,\mathrm{d}R\,\mathrm{d}\mathbf{r}_m\right|^2 . \tag{11.47}$$

Under the first Born approximation, the term in modulus brackets ("inelastic scattering form factor") is seen not to depend on the impacting electron's energy. This leads to the definition of the generalised oscillator strength* for a transition between two energy levels $\mathcal{E}_{av} \to \mathcal{E}_{a'v'}$:

$$F_{av,a'v'}(q) \equiv \frac{\mathcal{E}_{a'v'} - \mathcal{E}_{av}}{\mathrm{Ryd}}\frac{\langle|\epsilon_{av,a'v'}(\mathbf{q})|^2\rangle_{\hat{\mathbf{R}}}}{a_0^2 q^2}\,, \tag{11.48}$$

where Ryd ≈ 13.606 eV is the Rydberg energy unit and $\langle|\epsilon_{av,a'v'}(\mathbf{q})|^2\rangle_{\hat{\mathbf{R}}}$ stands for the spherically-averaged (as above in 11.47) squared form factor ϵ defined as :

$$\epsilon_{av,a'v'} \equiv \iint \sum_{j\in m} \exp(\mathrm{i}\mathbf{q}\cdot\mathbf{r}_j)\phi^*_{a'}(\mathbf{r}_m,\mathbf{R})\chi^{v'*}_{a'}(R)\phi_a(\mathbf{r}_m,\mathbf{R})\chi^v_a(R)\,\mathrm{d}R\,\mathrm{d}\mathbf{r}_m\,. \tag{11.49}$$

It is also known [911, §1] as the molecular or atomic *matrix element*. Under the dipole approximation (cf. appendix D.1), it is rather called the *dipole* matrix element; when $\|\mathbf{q}\|a_0 \ll 1$, so that the exponential may be limited to its lowest order in $\mathbf{q}\cdot\boldsymbol{r}$.

Furthermore, the combination of the Born-Oppenheimer approximation with the impulse approximation, enables to separate the integral (11.49) over electronic $\mathbf{r}_m$ and nuclear $\mathbf{R}$ parts so as to factorise $\epsilon_{av,a'v'}$ as:

$$|\epsilon_{av,a'v'}|^2 \simeq \underbrace{\left|\int \chi^{v'*}_{a'}(R)\chi^v_a(R)\,\mathrm{d}R\right|^2}_{\equiv C_{aa'}(v\to v')}\left|\int \sum_{j\in m}\exp(\mathrm{i}\mathbf{q}\cdot\mathbf{r}_j)\phi^*_{a'}(\mathbf{r}_m,\mathbf{R})\phi_a(\mathbf{r}_m,\mathbf{R})\,\mathrm{d}\mathbf{r}_m\right|^2 , \tag{11.50}$$

thus defining a transition probability $C_{aa'}(v \to v')$ between the v and v' vibrational levels of the electronic states a and a' respectively. This probability is known as the *Franck-Condon factor*, which is presented in appendix D.2.

The "generalised" oscillator strength (11.48) takes its name after its relationship to the *optical* dipole oscillator strength [398, see §4.3.4 and §5.2.2] $f_{av,a'v'}$ at small momentum transfers [427, p.300:eq(2.12)] $q \to 0$:

$$\lim_{q\to 0} F_{av,a'v'}(q) = f_{av,a'v'}\,, \tag{11.51}$$

which can be derived from the expansion of $\exp(-\mathrm{i}\mathbf{q}\cdot\mathbf{r}) = 1 - \mathrm{i}\mathbf{q}\cdot\mathbf{r} + (-\mathrm{i}\mathbf{q}\cdot\mathbf{r})^2/2 + \ldots$ in (11.47), and noting that the zeroth term disappears due to the orthogonality of electronic states $a \neq a'$. More information about this optical oscillator strength is to be found in appendix D.1.

This connection of the generalised to the optical oscillator strength implies that it also satisfies the Bethe sum rule [64] $\sum\!\!\!\!\!\!\int_{a'v'} F_{av,a'v'}(q) = \sum_A Z_A = N$, amounting to the total number of electrons (N) in the molecule. The "sum" over all states $a'v'$ should be understood as including the ionisation continuum of states as well (see section 11.5).

*The conventional notation for molecules [834, Chapter 1:§6.5.2] is $F_{aa'}$ whereas for atoms [427] it is $f_{aa'}$. In this thesis, however, regardless of atom or molecule, we take the *capital* letter F for the *generalised* OS whereas the *lower* case f is for the *optical* OS in the limit $q \to 0$

The generalised oscillator strength (GOS) is an idealised property of any target molecule at high scattering energies $ka_0 \gg 1$, where the Born approach is valid, and is a measurable quantity proportional to the differential cross section :

$$\frac{\mathrm{d}\sigma}{\mathrm{d}\Omega} \underset{k\to\infty}{=} \frac{k'}{k}\frac{(2\mu/m_\mathrm{e})^2\mathrm{Ryd}}{\mathcal{E}_{a'v'}-\mathcal{E}_{av}}\frac{F_{av,a'v'}(q)}{q^2} \,. \tag{11.52}$$

This relation can however be preserved down to energies even where the Born approximation is not valid [563], to the cost of having an additional dependency on the projectile's initial momentum k : $F_{av,a'v'}(q) \overset{ka_0\lesssim 1}{\longrightarrow} F_{av,a'v'}(q,k)$. In this case, $F(q,k)$ is called the *apparent* GOS [911, eq.(11a)]:

$$F_{av,a'v'}(q,k) \equiv \frac{k}{k'}q^2\frac{\mathcal{E}_{a'v'}-\mathcal{E}_{av}}{(2\mu/m_\mathrm{e})^2\mathrm{Ryd}}\frac{\mathrm{d}\sigma}{\mathrm{d}\Omega} \,. \tag{11.53}$$

For electrons scattering off molecules and atoms, $\mu \cong m_\mathrm{e}$ and we may drop this term in the rest of this section. The knowledge of the GOS enables an easy integration of any cross section as [834, p.62:eq(159)]:

$$\sigma_{\mathrm{av,a'v'}}(\varepsilon) = \int \frac{\mathrm{d}\sigma_{\mathrm{av,a'v'}}}{\mathrm{d}\Omega}\,\mathrm{d}\Omega = \frac{2\pi}{k^2}\frac{4\mathrm{Ryd}}{\mathcal{E}_{a'v'}-\mathcal{E}_{av}}\int_{|k-k'|}^{k+k'}\frac{F_{av,a'v'}(q,k)}{q}\,\mathrm{d}q \,. \tag{11.54}$$

The integration over q was deduced from $q^2 = k'^2 + k^2 - 2k'k\cos\theta$ giving the differential relationship $q\,\mathrm{d}q = k'k\sin\theta\,\mathrm{d}\theta\mathrm{d}\theta$, and noting that $\mathrm{d}\Omega = \sin\theta\,\mathrm{d}\theta\,\mathrm{d}\phi$.

The asymptotic behaviour of inelastic cross sections at energies considerably higher than the excitation threshold: $\varepsilon \gg \Delta\mathcal{E} = \mathcal{E}_{a'v'} - \mathcal{E}_{av}$, can be predicted according to whether the transition is optically allowed ($f_{av,a'v'} \neq 0$) or forbidden ($f_{av,a'v'} = 0$) through the electric dipole operator. To alleviate the notation, we now use the subscript $x \equiv av, a'v'$ to denote the e**x**citation transition.

Starting with the simplest case of optically forbidden transitions, $f_x = 0$ enables to extend the lower bound $|k - k'| \simeq 0$ in (11.54) without committing much error when $k \gg \Delta\mathcal{E}$. Then, asymptotically [427, p.328:eq(4.28)] using $k^2a_0^2 = m_\mathrm{e}\mathrm{v}^2/2\mathrm{Ryd}$:

$$\sigma_x(\varepsilon) = \frac{4\pi a_0^2\mathrm{Ryd}}{m_\mathrm{e}\mathrm{v}^2/2}\left(b_x + O\left(\frac{\mathrm{Ryd}}{m_\mathrm{e}\mathrm{v}^2}\right)\right) \,. \tag{11.55}$$

The parameter b_x is a moment of the GOS given by [427, eq.(4.21)]:

$$b_x \equiv \int_0^\infty \frac{2\mathrm{Ryd}}{\Delta\mathcal{E}}\frac{F_x(q)}{q}\,\mathrm{d}q \tag{11.56}$$

For optically allowed transitions $f_x \neq 0$, the decrease at higher energies ($\varepsilon \gg \Delta\mathcal{E}$) is slightly slower [427, p.328:eq(4.26)] :

$$\sigma_x(\varepsilon) = \frac{4\pi a_0^2\mathrm{Ryd}}{m_\mathrm{e}\mathrm{v}^2/2}\left(M_x^2\left[\ln\left(\frac{2m_\mathrm{e}\mathrm{v}^2\gamma^2}{\mathrm{Ryd}}c_x\right) - \frac{\mathrm{v}^2}{c^2}\right] + O\left(\frac{\mathrm{Ryd}}{m_\mathrm{e}\mathrm{v}^2}\right)\right) \,. \tag{11.57}$$

M_x is known as the dipole matrix element related to the optical oscillator strength $f_x = M_x^2\Delta\mathcal{E}_x/\mathrm{Ryd}$ (see appendix D.1 and equation (D.2)). The other coefficient c_x is a constant related to some integral of the GOS for the given transition x. It is analogous to the definition of the $\check{c}_\mathrm{i}(\varepsilon_2)$ parameter for impact ionisation (p.464), replacing the differential GOS ($\mathrm{d}F_i/\mathrm{d}\varepsilon_2$) by the GOS ($F_x$) in equations (11.74) and (11.76).

Those two expressions above (11.55&11.57) are given in terms of the electron velocity v instead of its kinetic energy ε so as to remain relativistically correct as noted by Bethe [64] and Inokuti [427, p.299 and eq.(2.27)].

Alternatively, the cross section σ_x (allowed or not) can be expressed [504, eq.(1)] in terms of the *collision strength** $\Omega_x(\varepsilon)$:

$$\sigma_x = \frac{4\pi a_0^2}{g\,\varepsilon/\mathrm{Ryd}}\Omega_x(\varepsilon) \tag{11.58}$$

The coefficient g represents the statistical weight (energy degeneracy) associated to the initial state [154, eq.(2)].

For practical purposes of performing integrals, the GOS can be expanded [562] in the following series [505, §C:eq(9)]:

$$F_x(q) = \frac{1}{(1+\xi)^{\ell+\ell'+5}}\left(f_x + \sum_{m=1}^{\infty}\frac{a_m\xi^m}{(1+\xi)^m}\right), \tag{11.59}$$

where ξ is defined with the ionisation (binding) energy B of the electron in its initial orbital, which will be subsequently left excited by the amount $\Delta\mathcal{E}_x$, as [968, p.100:right column]:

$$\xi = \left(\frac{qa_0}{\sqrt{B}+\sqrt{B-\Delta\mathcal{E}_x}}\right)^2. \tag{11.60}$$

The integers ℓ and ℓ' represent the orbital angular numbers of the excited electron in its initial and final configurations. They may be well defined in atoms, but as soon as one moves to a poly-atomic description, their definition is more involved as discussed by Kim [505, §C]. The coefficients a_m are to be determined by fitting or can be derived as explained by Klump and Lassettre [513, p.889:left column] from the expansion of the exponential in the electronic form factor in (11.49).

The literature giving such fits of GOS for various transitions is rich [563, 604, 968] and in many cases, equation (11.59) may be reduced to just one term and give a sufficiently accurate fit as shown in Kim [505, eq(10-14)].

Note that for dipole-forbidden transitions $f_x = 0$ implies that the series starts at least from the first power in ξ at $m = 1$. Moreover, higher degrees of forbiddance [513, eq.(27-30)] can lead to $a_m = 0 \,:\, \forall m \geq M$. This gives a leading term of $\xi^M/(1+\xi)^{\ell+\ell'+5+M}$ in (11.59). For $M > 1$ this implies that $b_x = 0$ in (11.55) and thus the corresponding cross section decreases at faster rates than $1/\varepsilon$.

In spin-forbidden transitions ($\Delta S \neq 0$, refer to appendix D.1), the change in total spin results most probably from the *exchange* of the incoming electron with a shell electron of opposite spin [834, p.11 lower half]. This situation preferably happens at slow incoming velocities and implies that the cross section rises steeply at low energies [399, p.463] but decreases fast $\sim 1/\varepsilon^3$ (see the "$d = 3$" curves on fig. 11.30) as reported in Inokuti [427, p.341:left column lower half] from the exchange approximation of Ochkur and Brattsev [711].

Depending on the nature of the electronic transition, the cross section, in the framework of Born's approximation, will decay at an asymptotic rate of $1/\varepsilon^d$ for forbidden transitions and $(\ln\varepsilon)/\varepsilon$ for optically-allowed ones. We will call the exponent d the "*forbiddance degree*" because it describes how much a transition is forbidden (dipole, quadrupole, spin). The value $d = 0$ is reserved for optically-allowed transitions.

*Different conventions can apply to the definition of the collision strength. Some authors [154, 395, §V., eq.(2)] prefer the connection to the momentum k in the DCS which after integration gives a $4\pi a_0^2/(2k)^2$ factor. Others [427, 504, eqs.(4.26-28), eq.(1)] absorb the $1/4$ factor in Ω to keep the $4\pi a_0^2$ magnitude. We shall adopt here the latter convention.

In practice, nothing impedes the cross sections from decaying as $1/\varepsilon^{\alpha}$ at some intermediate non-integer α rates [973, §2.2:(iii)], because the contribution to the process may not entirely depend on one mechanism (exchange, magnetic/electric dipole, etc.). Sometimes, a cross section can also correspond to various transitions lumped together as in the broad peaks of O_2. Nonetheless, in the next section describing semi-empirical fits, we shall impose the asymptotic decay $1/\varepsilon^{d}$ with $d \in \mathbb{N}$ an integer, in order to constrain the optimisation and prevent unphysical behaviour in the extrapolated high-energy region.

11.4.2 Scaled Plane-wave Born Cross Section

Despite the possibility of integrating cross sections through the generalised oscillator strength seen before, we are interested in taking a shortcut and directly provide reliable fits to integral cross sections. Such attempts were already made multiple times in the farther [350] and recent [27, 902] past as new and revised sets of experimental data were released.

Here, we are looking for compact formulae that asymptotically behave as (11.57) and (11.55), that annihilate at the threshold $\Delta\mathcal{E}$ and present enough flexibility to match the typical cross section gently/steeply rising to maximum and slowly/steadily decreasing for optically allowed/-forbidden transitions.

For this, we make use of the scaling correction proposed by Kim [504] to the Born approximation. This procedures amounts to replacing the $1/\varepsilon$ dependence in (11.57) by $1/(\varepsilon+\varepsilon_{\mathrm{o}})$, where the offset $\varepsilon_{\mathrm{o}} \simeq \Delta\mathcal{E} + I$ is linked to the excitation threshold $\Delta\mathcal{E}$ and the ionisation potential I of the molecule. This scaling was originally intended and successfully applied [27, 604] only for dipole-allowed transition CS [911, p.14:§2.a].

> To extend the application of Born-scaling to forbidden transitions, we presently propose to offset the denominator $1/\varepsilon^{d} \dashrightarrow 1/(\varepsilon+\varepsilon_{\mathrm{o}})^{d}$ even for stricter degrees of forbiddance ($d > 1$).

The second correction is what Green and Stolarski [350] describe as "low-energy modifiers" so that the fitted CS behaves well near the excitation threshold $\Delta\mathcal{E}$. For allowed transitions, the annihilation at threshold energy can be inserted in the logarithmic part [350, eq.(9)] of (11.57). For forbidden transitions, this can be done most naturally through $(\varepsilon - \Delta\mathcal{E})^{b}$ as a numerator [349, eq.(1)]. Still, as explained in Hertel and Schulz [399, §7.2.7], the behaviour near threshold may undergo a very rapid change over a very short range of energies. Forbidden transitions are known to rise steeper than allowed ones. In order to enable a better flexibility for this rising portion, the generic form $(1-(\Delta\mathcal{E}/\varepsilon)^{a})^{b}$ seen in many reports[348, 350, 444, 549, eq.(7), eq.(1)] can be used*. It enables to separate the near-threshold behaviour from the fast rising portion of the graph. Nevertheless, the near-threshold behaviour usually remains unrevealed by experimental data. So it is better to fix $a = 1$ and leave b as a free parameter. Furthermore, due to the introduction of the offset in the scaling correction, the description with $(1-(\Delta\mathcal{E}/\varepsilon)^{a})^{b}$ and $(\varepsilon^{a}-(\Delta\mathcal{E})^{a})^{b}$ as numerators are no longer equivalent as they were in the original work of Green and Dutta [348]. In order to cope with this, we decided to privilege $(\varepsilon-\Delta\mathcal{E})^{a}/(\varepsilon+\varepsilon_{\mathrm{o}})^{a+d}$ over $(1-\Delta\mathcal{E}/\varepsilon)^{a}/(\varepsilon+\varepsilon_{\mathrm{o}})^{d}$. The former expression could fit experimental data better than the latter (cf. sec. 13.1.2 fig. 13.7).

Finally, touching the dangerous border of overfitting, we indulged into adding another factor $[(\varepsilon-\Delta\mathcal{E})^{a'}+c']$ to the expression to form a six-parameter adjustable function when deemed necessary. The reason why the exponent features inside the bracket is to produce sharper inflexion

*A square root could be imposed ($b = 0.5$) if s-waves ($\ell = 0$) are allowed in the outgoing channel Wigner [982, §III.A]. This law near threshold does however not hold well over a large range of energies.

points around c' to follow given data trends. More insight about this choice of functions is given in the third part in the section 13.1.2 devoted to commenting fitting procedures.

The elementary generic functions s_{exc} for fitting electronic excitation cross sections take the following forms expressed in the dimensionless variable $w \equiv (\varepsilon/\Delta\mathcal{E} - 1)$:

$$s_{\text{exc}} = \begin{cases} \dfrac{4\pi a_0^2}{\Delta\mathcal{E}/\text{Ryd}} \dfrac{M}{b} \dfrac{\ln((\frac{4w\Delta\mathcal{E}}{\text{Ryd}}\, c)^b + 1)}{(w+C)} & ; \quad \text{allowed transition} \qquad (11.61a) \\ \dfrac{4\pi a_0^2}{(\Delta\mathcal{E}/\text{Ryd})^d} M \dfrac{((w+1)^a - 1)^b}{(w+C)^{d+ab+a'}} [w^{a'} + c'] & ; \quad \text{forbidden transition} \qquad (11.61b) \end{cases}$$

In those expressions, M, a, a', b, c, c' and C are free parameters. In particular, a', c' can be fixed to zero, and a to one, to decrease the parametric form of s_{exc} in forbidden transitions that present simple enough trends.

In contrast, the forbiddance degree $d \geq 1$ should be determined in advance as discussed toward the end of the previous section:

- dipole-forbidden : $d = 1$
- quadrupole-forbidden: $d = 2$
- spin-forbidden: $d = 3$

Furthermore, a comparison with the asymptotic Bethe equations (11.55–11.57) shows that the following correspondences should be found with the Bethe parameters [427, eq.(4.15&4.20)]:

$$\text{For } \varepsilon \gg \Delta\mathcal{E} \text{ (or } w \gg 1) : \begin{cases} M \to b_x & \text{in forbidden } s_{\text{exc}} \\ M \to M_x^2 = f_x \cdot \text{Ryd}/\Delta\mathcal{E} \quad \text{and} \quad c \to c_x & \text{in allowed } s_{\text{exc}} \end{cases}$$

If the Bethe parameters are known (or oscillator strengths for allowed transitions), they can serve to check the pertinence of the fitted parameters, as initial input values or simply fixed constraints for the fitting procedure. For atomic transitions, the optical oscillator strengths can be well constrained. However, in molecular transitions, these can vary much with the particular rovibronic transition.

Also, the parameter C is related to the scaling correction $\varepsilon_{\text{o}} \simeq \Delta\mathcal{E} + I$ mentioned above as $C = \varepsilon_{\text{o}}/\Delta\mathcal{E} + 1$. Therefore, we should in principle have: $C \simeq 2 + I/\Delta\mathcal{E}$. This relation is however overshadowed by the introduction of the low-energy modifier (parameters a and b).

For allowed transitions, the expression (11.61a) can be generalised to relativistic energies to follow a formula similar to Bretagne *et al.* [106, eq.(5)]:

$$s_{\text{rel}}(\varepsilon) = \frac{4\pi a_0^2}{\Delta\mathcal{E}/\text{Ryd}} \frac{M}{b} \frac{\ln\big((w'\gamma^2\, 4c\Delta\mathcal{E}/\text{Ryd})^b + 1\big) \cancel{\beta^2}}{w' + C} \qquad \text{with } w' = \frac{\beta^2 m_{\text{e}} c^2}{2\Delta\mathcal{E}} - 1\,, \qquad (11.62)$$

where w' represents the generalisation of the reduced kinetic energy above threshold w in the relativistic regime.

Originally, Bretagne *et al.* [106, eq.(7)] used an empirical modification to make the relativistic expression valid down to threshold $\varepsilon \to \Delta\mathcal{E}$. Here, we decided to embed the near-threshold behaviour more naturally inside the logarithmic term. Due to this choice, we had to drop the β^2 crossed out* in the numerator of (11.62). Nevertheless, we resigned to drop it because it

*By crossing it out, we remind the reader that we are aware of its presence in the relativistic expression.

annoyingly makes the cross section become almost imperceptibly negative near threshold. One would need find a more pleasing way to modify the relativistic expression near threshold [as in 106, eq.(7)].

In the rare cases where a resonance peak (or feature) in a cross section was well resolved experimentally, we provided an additional function $s_{\rm res}$ as suggested by Andrick [26, eq.(21)] following a Fano profile [270] :

$$s_{\rm res} = A_{\rm res}\frac{\cos 2\alpha_{\rm r} - w'\sin 2\alpha_{\rm r}}{(1+w'^2)} \tag{11.63}$$

The dimensionless energy parameter $w' \equiv (\varepsilon - \mathcal{E}_r)/(\Gamma/2)$, depends this time on the energy position of the resonance $\mathcal{E}_r$ and the resonance width Γ. $A_{\rm res}$ and $\alpha_{\rm r}$ are parameters related to the amplitude (normalised by a factor $4\pi a_0^2$) of the resonance and background phase-shift of the dominant partial wave respectively. Further information about the emergence this profile can be found in the previous section 11.3.1

Resonances are characterised by abrupt changes in the scattering matrix over a short energy range producing a transient feature whose validity is *local* only. For spin-forbidden transition, the decay $\propto 1/\varepsilon^3$ is stronger than a Fano profile which decays at most as $\gtrsim 1/\varepsilon^2$. Therefore, if we took a simple addition $s_{\rm exc}+s_{\rm res}$, the tail of the Fano profile would eventually ruin the asymptotic expression of the whole at large energies above the resonance region. This is why, we thought it be wise to factorise the cross section in a 'slowly' varying $s_{\rm exc}$ and a local enhancement $1+s_{\rm res}$. The total profile for excitation cross section was then constructed as a product:

$$s_{\rm aug} \equiv s_{\rm exc}(1+s_{\rm res})\ . \tag{11.64}$$

By choosing adequate bounds (refer to sec. 13.3), the parameters from (11.61) could be easily determined for each transition from a least-squares fit to experimental data weighted by their uncertainties. However, because of the factorisation in (11.64), one may not rigorously attribute the usual significance to the parameters obtained when fitting $s_{\rm res}$ in (11.63).

We illustrate in figure 11.30 our use of the variants $s_{\rm exc}$ for four different excitation cross sections with N_2 : one allowed ($b\,^1\Pi_u$), a simply-forbidden ($a''\,^1\Sigma_g^+$) and two spin-forbidden ($B\,^3\Pi_g$) and ($E\,^3\Sigma_g^+$) with a resonance peak fitted by $s_{\rm res}$.

To obtain more flexibility, other authors like Tabata *et al.* [902] used linear combinations of modified forms of Green and McNeal [349, eq.(1)]. Although the fits presented there reproduced well the data sets considered, we prefer in our case to curtail the number of free parameters in order to elude the great fear of overfitting discussed in section 13.1. For detailed information about our reasoning and challenges encountered during the fitting process, we redirect the reader to the chapter 13 in the third part.

Additionally, as we shall see below, many experimental sets present poor agreement (sometimes higher than 50%) beyond the uncertainty of the reported values. This is why we do not think it wise to put stress upon obtaining close cross section fits. Rather, simple considerations of near-threshold and asymptotic behaviour should suffice for constructing a reliable database. Additionally, the purpose of providing simple analytical fits as compared to tabulated values is to permit quick amendments when new experimental evidence emerge, according to the philosophy of Green and Stolarski [350] and Inokuti *et al.* [426].

For each molecule, we present our assembled database of electronic excitation cross sections that served to construct our fits and very briefly discuss the main reviews in the field. Details relevant to the fitting procedure are explained and illustrated in chapter 13 of the third part. For more information about how the database was assembled and comments of eventual renormalisations made, please refer to the subsection for the corresponding molecule/atom in the subsequent chapter 15.

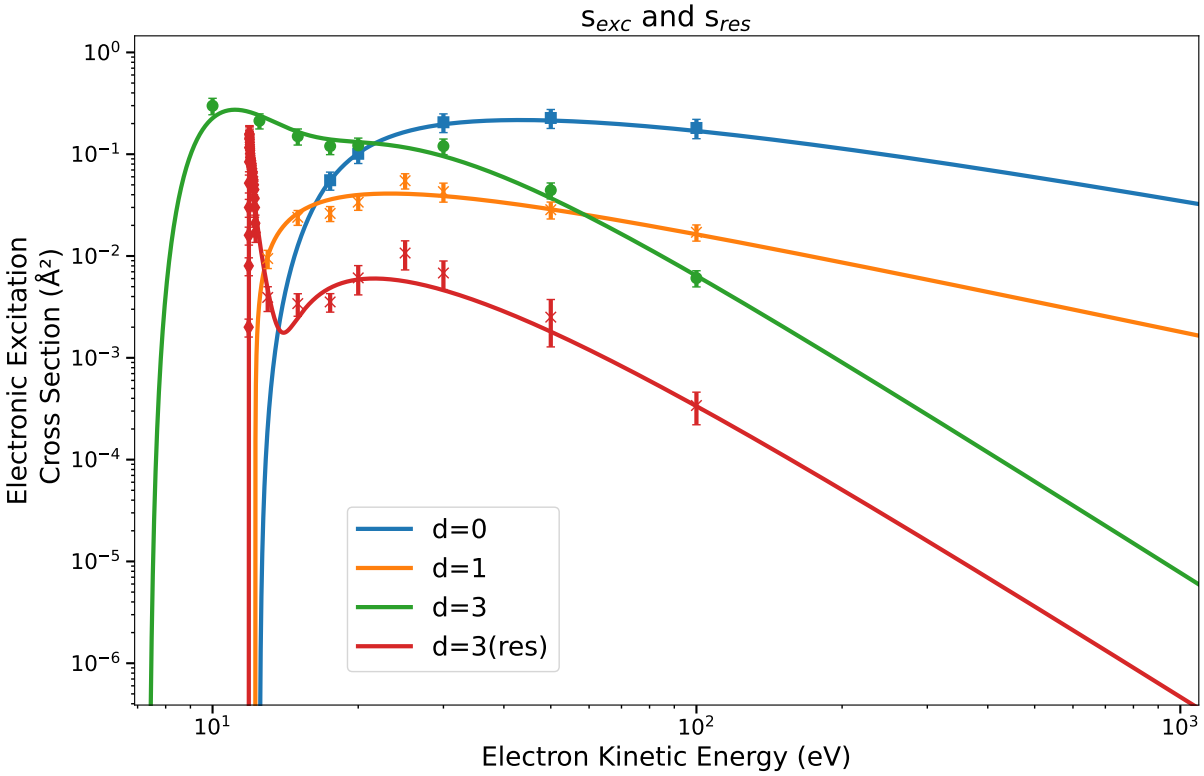

Figure 11.30: Representative fits of s_{exc} (11.61) for N_2 electronic excitations to allowed $b\,^1\Pi_u$ ($d = 0$, ■-Malone *et al.* [624]) and forbidden $a''\,^1\Sigma_g^+$ ($d = 1$, ×-Malone *et al.* [622]), $B\,^3\Pi_g$ ($d = 3$, ○-Johnson *et al.* [463]) and $E\,^3\Sigma_g^+$ ($d = 3$, ×-Malone *et al.* [622]) with the peak (◇-Hoffmann *et al.* [407]) fitted by s_{res} (11.63) and combined smoothly in s_{aug} (11.64).

Also, the excitations listed altogether might not fully account for the losses endured by electron in inelastic non-ionising collisions. We explain in chapter 15, how to compensate for these missing losses. This played a decisive role when validating our set of cross sections in the first part, chapters 4 and 5.

As a last warning, it must be stated that :

> The present fits with 11.61 were conceived as a convenient and simple way to express cross sections.
> The only parameter of clear physical significance is the leading magnitude coefficient M which, for dipole-allowed transitions, is related to the oscillator strength $f = M\,\Delta\mathcal{E}\text{Ryd}$.
> For the other parameters, it is unsafe to try to derive a physical meaning from the values obtained.

With more insight about the near-threshold behaviour (a, b) and the physical significance of the scaling parameter C by Kim [504], the fits below could be better constrained physically.

Meanwhile, we dare not qualify our fits with the noble status of "analytical representation" whose cause Inokuti *et al.* [426, p.216] defends.

11.4.3 Molecular Nitrogen

As the most common diatomic molecule in atmospheric physics, the experimental database for electronic impact excitation cross sections is replete. Nevertheless, for some transitions at certain energies, discrepancies among different research groups persist.

A summary of electronic states, their energy thresholds $\Delta\mathcal{E}$ [439, 493, table 7, table I], allowance/forbiddance, ranges of most probable vibronic excitations (v' range), branching ratios for predissociation η_{pd} [193, 620, 624, 1011, table 2, table III, table 1] and experimental sources is given in table 11.6. See also the comprehensive report from Lofthus and Krupenie [607]. Predissociation and spontaneous emission rates from deexcitation (Eintein coefficients) can be found in Capitelli *et al.* [150, p.157:table 9.1].

The transition probabilities $\mathcal{P}_{X,a'}(0 \to v')$ to a vibronic level v' in a band (X, a') from ground state X to excited state a' were taken from [492, 493, table II, table I]. Those probabilities can be, but are not necessarily, equal to the corresponding Franck-Condon factors (FCF) defined in (D.5) or (11.50). Based on those probabilities $\mathcal{P}_{X,a'}(0 \to v')$, the most probable range of vibronic bands (v' range) is loosely defined as one standard deviation around the mean value of the vibrational excitation level. The definition is loose in the sense that if a vibronic level lies initially beyond one standard deviation but its transition probability differs not by more than 90% of its direct neighbour in the range, then it is also included in the range.

An overview of potential curves for lower electronically excited states of N_2 is displayed in figure 11.31 from the calculations of Tashiro and Morokuma [914]. Since the extensive experimental results of Cartwright *et al.* [159] for lower and Chutjian *et al.* [181] for higher states, more recent detailed comparisons of cross sections were conducted by Johnson *et al.* [463] for valence states and Malone *et al.* [624] for Rydberg states.

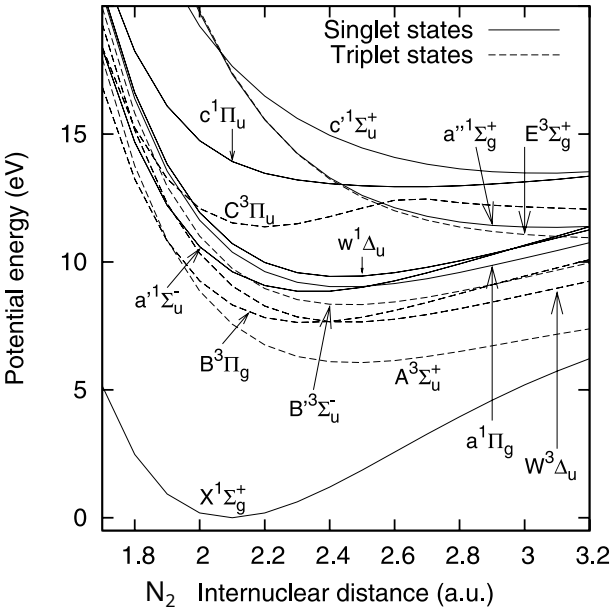

Figure 11.31: from Tashiro and Morokuma [914]

The three forbidden states $\mathrm{C}\,^3\Pi_u$, $\mathrm{E}\,^3\Sigma_g^+$ and $\mathrm{a''}\,^1\Sigma_g^+$ were most recently studied by Malone *et al.* [622]. For $\mathrm{E}\,^3\Sigma_g^+$ in particular, the near-threshold resonance peak was well resolved by Hoffmann *et al.* [407] in very good agreement with Brunger *et al.* [123].

There may eventually be observable narrow or broad resonance peaks not too far from threshold energies on integrated cross section of other forbidden transitions.

Recent theoretical R-matrix calculations [889, 914] predict that $\mathrm{A}\,^3\Sigma_u^+$, $\mathrm{B}\,^3\Pi_u$ and $\mathrm{C}\,^3\Pi_u$ should have a "bump" around 12 eV (for A and B) and 17 eV (for C). The main contributions to these features come [914, §III.B:p.3-5] from $N_2^-\ ^2\Pi_u$, $1\ ^2\Delta_g$ and $^2\Sigma_u^+$ shape resonances respectively. Other symmetries have a smaller participation. Although the agreement between various R-matrix calculations is good [333, 889], they rely on identical assumptions: particularly the fixed-nuclei approximation which may not be valid below 15 eV in the resonance region.

Experimentally, resonance peaks are observed at lower energies than predicted theoretically. In spectroscopic measurements [834, p.378-383:fig. 16], the peak from the $^2\Pi_u$ resonance linked to the N_2 A parent state is seen at slightly lower energies $\lesssim$10 eV, which supports the maximum observed at 10 eV in Johnson *et al.* [463, fig. 2].

The presence of resonance peaks is difficult to confirm though, because (1) the scatter of measured CS near threshold is quite chaotic and (2) measurements are too sparse (jump to fig. 16.3 on p.592). Exceptions are the E $^3\Sigma_g^+$ and the C $^3\Pi_u$ states, both fitted with $s_{\rm aug}$ (11.64). The C $^3\Pi_u$ state was clearly delineated experimentally by Zubek [1012] with a prominent bump around 14 eV (lower than the predicted 17 eV). We used Zubek's data renormalised by [622].

For most excitations, we privileged the recent data of Johnson *et al.* [463], Malone *et al.* [622], and Malone *et al.* [624] and our renormalisation of Cartwright *et al.* [159]. Procedures for normalisation and stabilisation of the signal in DCS from which the ICS derive, were carried over meticulously [492, 493, 623].

The only data which did not lend themselves easily to be fit by $s_{\rm exc}$ with 4 parameters were the ones for w $^1\Delta_u$ because of a very sharp rise near-threshold and a damped fall-off tail. We did not venture to use a resonant shape $s_{\rm res}$ as it would overfit the data. This case is addressed in section 13.3 (fig 13.13).

Some experimental reports had to be rejected from our database for fitting. The data from Campbell *et al.* [141] were based on a phase-shift extrapolations from 10°–90° measurements of Brunger and Teubner [122] and thus were contaminated by a too large uncertainty to be used presently. The detection of metastable a $^1\Pi_g$ by Mason and Newell [633] was criticised [463, §34-36] to suffer from contamination by other excited states and to have been normalised to outdated data.

Dissociation. At the end of the table 11.6, we also give the expression – based on an optically allowed transition – for the *residual* dissociation cross section $\sigma_{\rm rd}$. It is obtained from the total dissociation $\sigma_{\rm diss}$ into neutral nitrogen atoms recommended by Cosby [193], after subtracting all the contributions from predissociation given by the branching ratios $\eta_{\rm pd}$ as prescribed by Itikawa [439, p.51:eq.(8)]:

$$\sigma_{\rm rd}(\varepsilon) \equiv \sigma_{\rm diss}(\varepsilon) - \sum_i \eta_{{\rm pd},i}\sigma_i(\varepsilon) \ . \tag{11.65}$$

The predissociation ratios $\eta_{\rm pd}$ can be found in table 11.6 for N_2 whose dissociation threshold is at 9.753 eV [193, p.9550]. The values for most states were taken from James *et al.* [452] and from Malone *et al.* [624, p.7&11] for the b $^1\Pi_u$ (88 %) and b $^1\Sigma_u^+$ (96 %) states.

For the C $^3\Pi_u$ state, the value of 50 % in Majeed and Strickland [620, table 1] could not be found anywhere else in the cited literature. According to Lofthus and Krupenie [607, p.167:§8.5], all higher $v' > 4$ vibrational levels from C $^3\Pi_u$ predissociate. From the FCF of Malone *et al.* [623, table I], this would correspond to only 0.39 % on the whole, which is the value that we take.

The values with question marks are the ones for which we did not find a precise numerical value in the literature, but suggestions thereof. Some branching ratios are assumed to be close to 100 % because the emission bands of those states are either very faint [10] or were never observed (for the G $^3\Pi_u$ and F $^3\Pi_u$ states) [193, p.9550:right column]. For the c_4' $^1\Sigma_u^+$ state, the predissociation is "certainly nonzero" [624, p.13:right column] (contrary to the assumption of Ajello *et al.* [9]). Although not confirmed by more recent experiments, we took the original value of 15 % reported in Zipf and McLaughlin [1011, table 2].

Table 11.6: Electronic transitions from Nitrogen molecule ground state. Optically allowed (↕) are distinguished from forbidden (‡) transitions characterised by their asymptotic $1/\varepsilon^d$ trend d in brackets. Also given are the energy threshold $\Delta\mathcal{E}$ to $v' = 0$, the range of most probable vibronic v' excitations and the predissociation rate $\eta_{\rm pd}$. The next four columns give the parameters of the Born-scaled equations (11.61–11.64) fitted to the experimental data given in the last column. The middle horizontal line separates valence from Rydberg states although $\mathrm{b}\,^1$ and $b'\,^1$ are high-lying valence states.

(d) to $N_2(X\,^1\Sigma_g^+)$		$\Delta\mathcal{E}$ (eV)	v' range	$\eta_{\rm pd}$ (%)	Fitting Parameters $M\,\Delta\mathcal{E}$/Ryd	C	$a\,\vert\,c$	b	Experiments
‡ (3)	$A\,^3\Sigma_u^+$	6.169	4-14		1.06 ± 0.34	5.23 ± 1.62	1	0.5 ± 0.36	
‡ (3)	$B\,^3\Pi_g$	7.353	0-6	†	0.481 ± 1	0.82 ± 7	1.63 ± 25	5.64 ± 18	
‡ (3)	$W\,^3\Delta_u$	7.362	4-13		0.311 ± 0.049	0.403 ± 0.118	1	9.51 ± 2.56	
‡ (3)	$B'\,^3\Sigma_u^-$	8.165	4-12		0.19 ± 0.071	0.561 ± 0.422	1	7.54 ± 5.38	[159, 463]
‡ (2)	$a'\,^1\Sigma_u^-$	8.398	4-12		0.026 ± 0.006	0.227 ± 0.286	1	10 ± 12	
‡ (1)	$a\,^1\Pi_g$	8.549	1-7	12	0.102 ± 0.05	0.99 ± 2.7	1.75 ± 9	2.368 ± 0.584	
‡ (1)	$w\,^1\Delta_u$	8.895	3-11	✠	0.686 ± 2.25	0.551 ± 0.094	0.942 ± 0.031	6.79 ± 3.42	
‡ (3)	$C\,^3\Pi_u$	11.032	0-2	0.39	0.476 ± 0.071	1.384 ± 0.116	1	1.203 ± 0.062	[159, 623,
	resonance param.		$s_{\rm res}$: $A_{\rm res}$, $\alpha_{\rm r}$, $\mathcal{E}_{\rm r}$, Γ		2.682 ± 0.253	-0.336 ± 0.03	13.72 ± 0.06	2.11 ± 0.135	1012, 1013]
‡ (3)	$E\,^3\Sigma_g^+$	11.877	0-1		0.048 ± 0.013	1.38 ± 0.21	1	1.15 ± 0.125	[123, 141, 159,
	resonance param.		$s_{\rm res}$: $A_{\rm res}$, $\alpha_{\rm r}$, $\mathcal{E}_{\rm r}$, Γ		1000	0.027 ± 0.007	11.9 ± 0.01	0.128 ± 0.028	407, 622]
‡ (1)	$a''\,^1\Sigma_g^+$	12.255	0-1		0.041 ± 0.008	1.301 ± 0.428	1	0.851 ± 0.19	[622, 1013]
↕	$b\,^1\Pi_u$	12.500	1-8	96	0.144 ± 0.055	1.53 ± 5.63	0.5 ± 1.2	2.29 ± 2.31	
‡ (3)	$G\,^3\Pi_u$	12.810	0-2	100?	3.484 ± 3.625	5.35 ± 3.74	1	0.61 ± 0.566	
‡ (3)	$D\,^3\Sigma_u^+$	12.841	0	100?					
↕	$b'\,^1\Sigma_u^+$	12.854	0-2,8-9	88	0.105 ± 3.7	2.88 ± 164	0.3 ± 41.5	0.89 ± 9.72	
↕	$c_3\,^1\Pi_u$	12.912	0-2	100	0.098 ± 0.06	0.18 ± 2.69	0.18 ± 0.0915	2 ± 2.48	[181, 624]
↕	$c_4'\,^1\Sigma_u^+$	12.934	0-1	15?	0.131 ± 0.086	4.1 ± 22	0.28 ± 1.19	1.66 ± 1.25	
‡ (3)	$F\,^3\Pi_u$	12.985	0-2	100?	1.288 ± 1.2	3.53 ± 2.36	1	1.06 ± 0.74	
↕	$o_3\,^1\Pi_u$	13.103	1-4	100	0.084 ± 0.144	10 ± 101	0.7 ± 12.4	1.11 ± 6.28	
↕	N+N	9.75¤			0.583 ± 14.4	9.21 ± 100	1	3 ± 242	[193]

† The state $B\,^3\Pi_g$ was fitted with 6 parameters in (11.61b) with $a' = 4.56 \pm 1.57$ and $c' = 1.168 \pm 0.323$ as shown in fig. 13.12.

✠ The equation used for fitting $w\,^1\Delta_u$ was a variant corresponding to (13.4c) described in chapter 13 and shown in fig. 13.13.

¤ The onset of the residual dissociation (without predissociation) is located at 12.5 eV (use $w = \varepsilon/12.5\,\mathrm{eV} - 1$ in (11.61a)).

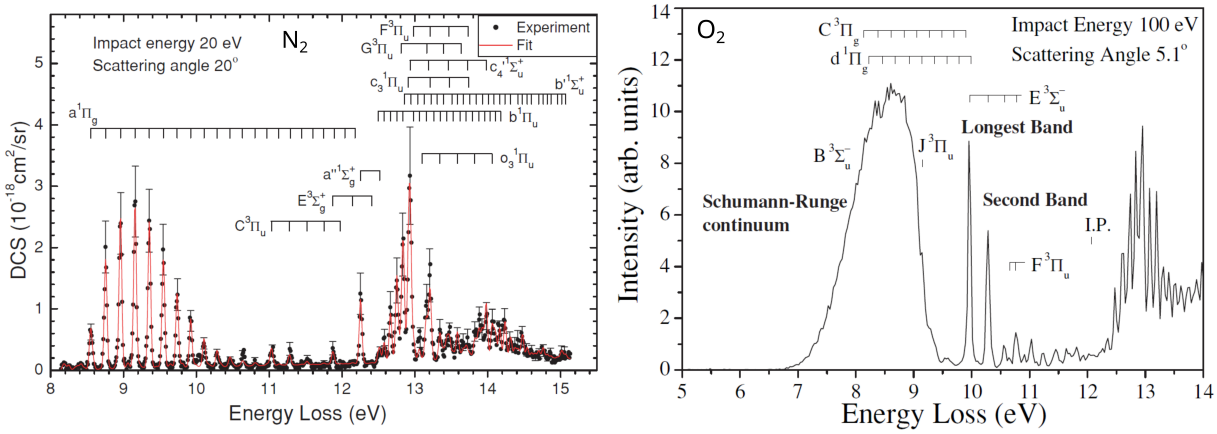

(a) N_2 from Kato *et al.* [479] (b) O_2 from Suzuki *et al.* [897]

Figure 11.32: Electron energy loss spectra from inelastic scattering by the most common molecules in air. The very neat spiky structure in nitrogen (a) is markedly different from broad peaks, bands and the continuum displayed in oxygen (b).

11.4.4 Molecular Oxygen

Compared to nitrogen, the database for excitations with oxygen lacks completion. This was repeatedly emphasised in different reviews [124, 440] and motivated further research [27]. A representation of the internuclear potential curve for various electronic bound and repulsive states of O_2 is shown in figure 11.33.

The most well-defined and studied transitions are the two first low-lying levels [938] of $a\,^1\Delta_g$ (0.977 eV) and $b\,^1\Sigma_g^+$ (1.627 eV). Theoretical calculations [916, fig.3] predict a resonance peak (for both states) located around 8 eV due to the $O_2^-\,^2\Pi_u$ compound state. This resonance can be clearly observed when looking at the energy dependence of DCS at a fixed scattering angle [12], but its shape varies with the angle. Currently, there is still no consensus whether this peak persists in the integrated DCS or whether it is averaged down when the calculations included nuclear motion into account, as a long-lived resonant scattering would require so.

Experimental evidence of such peak [643] in the ICS is disputed in reviews, with Rescigno *et al.* [773, §6:p.149] being in favour of the peak and Itikawa [440, §7.1] doubtful. For transitions to higher states [352], such peak was not observed either. Presently, I followed the advice of Itikawa [440] to disregard this peak since the uncertainty of the experimental ICS is large due to the necessity of extrapolating [642] beyond 90°.

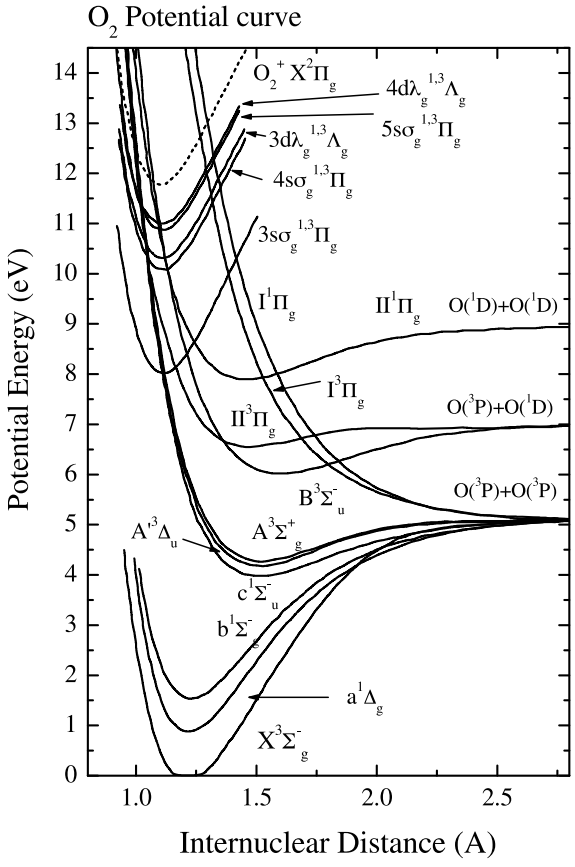

Figure 11.33: from Tanaka *et al.* [911, p.29:fig.21(b)]

One of the principal difficulty of characterising other electronic excitations of oxygen is the presence of broad bumps in the energy-loss spectrum seen on figure 11.32b, compared to the very non-overlapping narrow peaks of nitrogen.

This has motivated some studies [847] to try to deconvolve the enmeshed bands of the trio [438] $c\,^1\Sigma_u^-$ (4.05 eV), $A'\,^3\Delta_u$ (4.262 eV) and $A\,^3\Sigma_u^+$ (4.340 eV) forming the Herzberg Pseudo-continuum(II, III and I) [540, §3.4–7]. Nevertheless, most of the works in the literature [351, 923, 973] give the cross section summed over all three systems lumped together. The three electronic states c,A′&A, whose potential curves lie very close to each other on figure 11.33, are characterised by closely spaced vibrational levels, none with prominent excitation probability as can be checked from their Franck-Condon factors in Campbell *et al.* [145, table 1]. This is because their vibrational states lie outside of the Franck-Condon region [438, §7.2.a] as can be apprehended in figure 11.33 (see fig. D.1 on p. 521 for a visual explanation). An imaginary vertical excitation line from the ground state would intersect at a position of any of the three c,A and A′ states which is above the first dissociation threshold of O_2 (this corresponds to the situation a–c in the middle-top graph of figure D.1). This explains why the Herzberg Pseudo-continuum is mostly composed of energy losses in the 4.5–6.1 eV range [351, fig. 1] which lead to the dissociation when above 5.116 eV [438, tab. 2.1]:

$$e \,+\, O_2\,(X\,^3\Sigma_g^-) \longrightarrow e \,+\, O_2^*\,(c,\,A,\,A') \longrightarrow e \,+\, O(^3P) \,+\, O(^3P)\,. \tag{HPC}$$

In our fitting procedure, we thus left the threshold energy as a free parameter between 4 and 7 eV just to avoid overestimating the near-threshold behaviour of the cross section. The bulk of the energy losses are however situated in the range 4.5–6.1 eV.

The true continuum known as Schumann-Runge (SR) starts around 7 eV and is due to the dissociation of molecular oxygen either directly or through predissociation of an excited state whose vibronic bands may be seen as a superposition of sharper peaks [560] on figure 11.32b. The main contribution to the bands is due to the first optically allowed transition to $B\,^3\Sigma_u^-$ from ground. The continuum is formed by direct dissociation from excitation to repulsive states : $1\,^3\Pi_u$, $1\,^1\Pi_u$, $1\,^5\Pi_u$, $2\,^3\Sigma_u^+$ whose potential curves cross with $B\,^3\Sigma_u^-$ and cause predissociation [472]. Minor contributions to the SR come from the peaks of higher optically-forbidden transitions of Rydberg states ($C\,^3\Pi_g$, $d\,^1\Pi_g$, etc.) [937]. The upper limit of the SR is arbitrary as other isolated bands emerge in the spectrum, it was assigned to 9.7 eV by Wakiya [972]. We modelled the energy-loss spectrum of the SR continuum with a very simple mound between two boundaries $\mathcal{E}_0$ and $\mathcal{E}_1$ moulding the shape*:

$$f_{\text{SR}}(\mathcal{E}) = C_{\text{norm}}(\mathcal{E}-\mathcal{E}_0)^s(\mathcal{E}-\mathcal{E}_1)^2\,, \tag{11.66}$$

$$\text{with}\ \begin{cases} \mathcal{E}_0 = 6.12\,\text{eV} & \text{Onset of } B\,^3\Sigma_u^- \\ \mathcal{E}_1 = 9.7\,\text{eV} & \text{arbitrary, from Wakiya [972, p.3922–3]} \\ \mathcal{E}_{\max} = 8.6\,\text{eV} & \text{peak position, from Suzuki } \textit{et al.} \text{ [897, fig. 1] in fig. 11.32b} \end{cases}$$

$$\text{hence}\quad s = -2\frac{\mathcal{E}_{\max}-\mathcal{E}_0}{\mathcal{E}_{\max}-\mathcal{E}_1} \approx 4.51\,; \tag{11.67}$$

where $\mathcal{E}_{\max}$ represents the energy at which the energy-loss in the Schumann-Runge continuum is maximal. The normalisation C_{norm} is arbitrary and unimportant since the shape f_{SR} is used in part I eq. (3.12) to sample the *probability* of loosing an energy $\mathcal{E}$ in the continuum.

*We could not find a tabulation of energy-loss spectra in the SR, thus we took a simple shape with three fairly-well-defined parameters: two boundaries and a maximum position.

The energy-loss spectrum in the Herzberg pseudo-continuum has been modelled similarly using (11.66) with the following parameters: $\mathcal{E}_0 = 4.5\,\mathrm{eV}$, $\mathcal{E}_{\max} = 6.1\,\mathrm{eV}$, $\mathcal{E}_1 = 7\,\mathrm{eV}$ and thus $s \approx 3.55$. Those values were based on the curve displayed in Wakiya [972, figure 2]. It is not incompatible that it overlaps with the SR.

Beyond the SR lie the prominent optically-allowed bands of $\mathrm{E}\,^3\Sigma_u^-$ known as the *longest band* (LB) for $v' = 0$ and *second band* (2B) for $v' = 1$ as assigned by Yoshimine *et al.* [995]. Nevertheless, the nature of these bands was debated for long and the results of Shyn *et al.* [848] indicate that those bands might actually be a mixture of dipole-allowed and forbidden transitions (thus to different states). The latest study by Suzuki *et al.* [897] on those bands does, however, not mention any composite structure and in their introduction, they implicitly assume that the bands belong to $\mathrm{E}\,^3\Sigma_u^-$ exclusively. Due to the relatively recent identification of this state, it is not labelled uniformly in the literature. For instance, we could not establish a correspondence with the states mentioned in Krupenie [540, §3.9], the identification came indeed later [995]. Also, the $\mathrm{E}\,^3\Sigma_u^-$ state seems to correspond to the state labelled "B'$\,^3\Sigma_u^-$" in Cosby [194]. We suppose that the predissociation rate of $\mathrm{E}\,^3\Sigma_u^-$ mentioned in Huber and Herzberg [410, p.494:footnote b.] is nearly 100%.

Unlike for nitrogen, higher lying states have been studied very little so far. Bands from $\mathrm{E}\,^3\Sigma_u^-$ $v' > 1$ are of a considerably lower magnitude [460] and other systems are of even lesser importance. Current information about those high states is regrouped in Huber and Herzberg [410, p.492–4]. The ionisation continuum of oxygen starting from 12.07 eV superposed with excitation bands of ionised oxygen make the major energy-loss contribution to electron impact.

An interesting aspect of oxygen, is that the idealisation of well defined distinct electronic states as imagined for a molecule, is broken due to non-negligible perturbation [573] terms in the Hamiltonian (such as rotational, vibrational, and spin-orbit coupling in the description of the electronic states). For N_2 the peaks in the energy-loss spectrum can each be associated to a distinct molecular state. Here, for O_2, the SR continuum and the peaks beyond, all bespeak strong valence-Rydberg state interferences [584]: the molecule's "real" state could be more accurately described by a linear combination of individual states [882, §5.7]. Therefore, the bands belonging to the same system do not scale as predicted by Franck-Condon factors [509]. This interference makes the theoretical study of excitations in the SR, LB, and 2B difficult and accounts for the vacuum in the literature [897, p.2].

The excited states of molecular oxygen with their threshold energies [440, 897, table 7,], most probable vibronic transition range [145, table I], and grouped together when not resolved are summarised in table 11.7. A row is left out in the SR continuum for repulsive (e.g. $1\,^1\Pi_g$) and unclassified states in the 7-9.7 eV region [849] which could correspond those labelled in [410, p.494]. The vibronic bands v' of trio states from the Herzberg pseudo-continuum which lie above the dissociation threshold (5.116 eV) lead to direct dissociation. The states in the Schumann-Runge continuum, and presumably all Rydberg states beyond, predissociate entirely*.

*The rates are faster than spontaneous emission rates

Table 11.7: Electronic transitions from Oxygen molecule ground state. Optically allowed (↕) are distinguished from forbidden (‡) transitions characterised by their asymptotic $1/\varepsilon^d$ trend d in brackets. Also given are the energy threshold $\Delta\mathcal{E}$ to $v' = 0$ and the bulk of most probable vibronic bands v'. The next four columns gives parameters for $s_{\rm exc}$ fitted with the experimental data given in the last column regroups the experimental data available. The dashed line separates the states that lead to dissociation of the molecule for which it is assumed that the predissociation ratio $\eta_{\rm pd}$ is very close to 100 %. All states in the Schumann-Runge continuum (SR) and above are strongly perturbed by valence-Rydberg state interference. The perturbation is so strong for the $\mathrm{E}\,^3\Sigma_u^-$ state, that its first and second vibrational levels are markedly distinct from a Franck-Condon ratio (see eq.D.4). They are designated as the longest (LB:$v' = 0$) and second (2B:$v' = 1$) bands [897, §1].

	(d) to $O_2(X\,^3\Sigma_g^-)$		$\Delta\mathcal{E}$ (eV)	v' range	$\eta_{\rm pd}$	Fitting Parameters $M\,\Delta\mathcal{E}$/Ryd	C	$a\,\vert\,c$	b	Experiments
	‡ (3)	$a\,^1\Delta_g$	0.977	0		0.187 ± 1.084	12.12 ± 2.59	0.1	2.281 ± 0.358	[221, 593,
	‡ (3)	$b\,^1\Sigma_g^+$	1.627	0		0.026 ± 0.28	8.03 ± 1.83	0.1	1.415 ± 0.308	642, 845,
HPC	‡ (3)	$c\,^1\Sigma_u^-$	4.05	6–18	93.11♦	0.008 ± 0.055	0.067 ± 13	7 ± 47.5	10	938, 973]
HPC	‡ (1)	$A'\,^3\Delta_u$	4.262	6–12	97.71♦					[352, 973]
HPC	‡ (2)	$A\,^3\Sigma_u^+$	4.340	7–12	98.47♦					
SR	↕	$B\,^3\Sigma_u^-$	6.12	1–8	<100	0.085 ± 0.096	6.072 ± 14.7	7.536 ± 72	4.925 ± 10^8	[897]
SR		...	7–9.7		100?					
SR	‡ (1)	$C\,^3\Pi_g$	8.15	0–2	100?					
SR	‡ (3)	$d\,^1\Pi_g$	8.595	0	100?					
LB,	↕	$E\,^3\Sigma_u^-$	9.97	$v' = 0$	>0	0.007 ± 0.016	10^{-20}	1.171 ± 10.7	3.961 ± 55.3	[848, 897]
2B,	↕	$E\,^3\Sigma_u^-$	10.28	$v' = 1$	>0	0.006 ± 0.113	3.922 ± 102	0.787 ± 77	0.844 ± 15	

♦ This is not a predissociation but a *direct* dissociation ratio obtained by subtracting from 1 the sum of Franck-Condon factors reported in Campbell *et al.* [145, table I].

11.4.5 Nitric Oxide

This molecule produced in atmospheric discharges is recognised to play an important role in auroral emissions [140] and as a catalyser for the destruction of the ozone layer [143]. In our model, NO intervenes marginally as it is formed in non-overheated (~ 3000–6000 K) leader cores (consult our table 2.1 in part I section 2.1). Still, it is thought that it might be present up to a ratio of ~10% in that temperature range.

NO displays a great abundance of electronic states below ionisation threshold (9.26 eV) with some potential curves represented on figure 11.34 from Song *et al.* [865, fig.1]. Except from optical emission cross sections, the only comprehensive study of excitation cross section was made by Brunger *et al.* [120] for 28 states* between 15 and 50 eV. The most recent review by Song *et al.* [865, §2.7, p.11] found that there is a shortage of about four times the sum over all those 28 electronic states between 15 to 40 eV to match the total scattering cross section with the given elastic and ionisation cross sections. This means that a major part of the electron energy loss in NO is currently unrepresented by the set of electronic excitations summarised in table 11.8. As explained in the third part p. 577, we chose to patch this deficiency with a cross section for losses beyond 9 eV which we reckon remained unprocessed† in the energy-loss spectrum of Mojarrabi *et al.* [655], reproduced in figure 11.35.

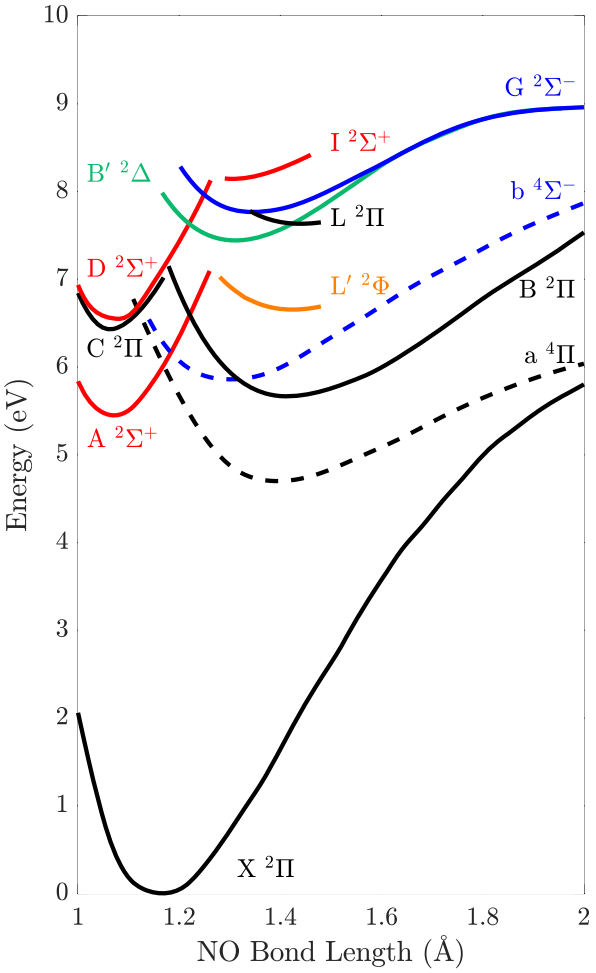

Figure 11.34: from Song *et al.* [865, fig.1]

An atypical CS was measured for L′ $^2\Phi$ which, with the scaling correction at 50 eV (cf. sec 15.1.3), displays a cusp at 30 eV instead of a bump. It is reported [119, §2.5] that the extrapolation of higher vibrationally excited contributions to that band introduced significant uncertainties in the derivation of the DCS. Because no reasonable fit can be obtained for such a dataset, we regrouped it with the energetically nearest state D $^2\Sigma^+$.

The result of our fits to the reported data is given in table 11.8. To reduce the number of individual states having to be modelled in Monte Carlo simulations, some fits are presented for the sum of energetically close-lying states, either because they were reported thus or because we chose to group them together. Though we have not found any concrete information about predissociation rates, we surmise that all branching ratios for predissociation above the dissociation threshold at 6.534 eV [865, tab. 1] are very high ≳90 %.

*10 states were lumped by three or two to present combined cross sections

†Actually, we lack of formal information and chose this threshold arbitrarily just by looking at the overall deconvolution of the energy-loss spectra

Table 11.8: Electronic transitions from Nitric Oxide ground state. Optically allowed (↕) are distinguished from forbidden (↨) transitions characterised by their asymptotic $1/\varepsilon^d$ trend d in brackets. Also given are the energy threshold $\Delta\mathcal{E}$ to $v' = 0$ and the most probable vibronic bands v'. Valence states are separated from Rydberg states by the dashed line, except for $A\,^2\Sigma^+$ and $C\,^2\Pi$ which are low-lying Rydberg states. The last four columns gives parameters for s_{exc} exclusively fitted to the experimental data of Brunger *et al.* [120]. Keep in mind that the flag signalling overfitting is raised; for only 5 data points were available at each excitation.

(d)		$\Delta\mathcal{E}$	v' range	Fitting Parameters			
to NO($X\,^2\Pi$)		(eV)		$M\,\Delta\mathcal{E}$/Ryd	C	$a \,\vert\, c$	b
↨ (3)	$a\,^4\Pi$	4.747	6–10	0.322 ± 1	4.5 ± 16	1	3.2 ± 11
↕	$A\,^2\Sigma^+$	5.484	0–3	0.004 ± 0.009	0	0.34 ± 4	2.6 ± 16
↕	$B\,^2\Pi$	5.642	10–21	0.0036 ± 0.02	0	0.384 ± 11	2.9 ± 15
↨ (3)	$b\,^4\Sigma^-$	5.718	1–6	0.133 ± 0.137	0.36 ± 3	1	16 ± 135
↕	$C\,^2\Pi$	6.499	0–3	0.016 ± 0.019	0	0.24 ± 0.42	2.23 ± 9
↨ (1)	$L'\,^2\Phi$	6.6	9–>30	0.044 ± 1.4	0	0.06 ± 3	1.2 ± 13
↕	$D\,^2\Sigma^+$	6.617	0–3				
↕	$B'\,^2\Delta$	7.442	2–8	0.0082 ± 0.044	0	0.64 ± 16	5
↕	$E\,^2\Sigma^+$	7.58	0–2	0.0018 ± 1.6	3.6 ± 6470	0.284 ± 918	1
↕	$F\,^2\Delta$	7.722	0–3	0.008 ± 3.5	2.43 ± 6920	0.17 ± 267	1.38 ± 322
↕	$L\,^2\Pi$	7.751	6–12	0.21 ± 22	4.6 ± 4880	0.12 ± 69	1.47 ± 81
↕	$H\,^2\Sigma^+$	7.833	0–3	0.0078 ± 0.017	0	0.27 ± 1	2.3 ± 19
↕	$H'\,^2\Pi$	7.856	0–3				
↕	$K\,^2\Pi$	7.977	0–3	0.012 ± 0.034	0	0.208 ± 0.38	2.14 ± 10
↕	$M\,^2\Sigma^+$	8.017	0–4				
↕	$S\,^2\Sigma^+$	8.324	1–2	0.0058 ± 0.0072	0	0.35 ± 3	3 ± 19
↕	$N\,^2\Delta$	8.383	0–2				
↕	$O'\,^2\Pi$ / $O\,^2\Sigma^+$	8.43	0–2	0.0061 ± 0.016	0	0.23 ± 0.32	2.3 ± 12
↕	$Q\,^2\Pi$	8.515	0–4	0.0078 ± 0.027	0	0.18 ± 0.5	2.11 ± 8
↕	$T\,^2\Sigma^+$	8.674	1–>3	0.0009 ± 0.002	0	0.42 ± 6	2.9 ± 23
↕	$U\,^2\Delta$	8.705	0–>3				
↕	5f	8.718	0–3				
↕	$W\,^2\Pi$	8.784	1–>2	0.008 ± 0.01	0	0.29 ± 0.47	2.3 ± 10
↕	$Y\,^2\Sigma^+$	8.876	0–2				
↕	$Z\,^2\Sigma^+$	8.814	0–1	0.0031 ± 3	6.5 ± 3810	0.046 ± 126	0.67 ± 34
↕	$6d\delta$	8.86	0–>2				
↕	6f	8.885	1–>2				

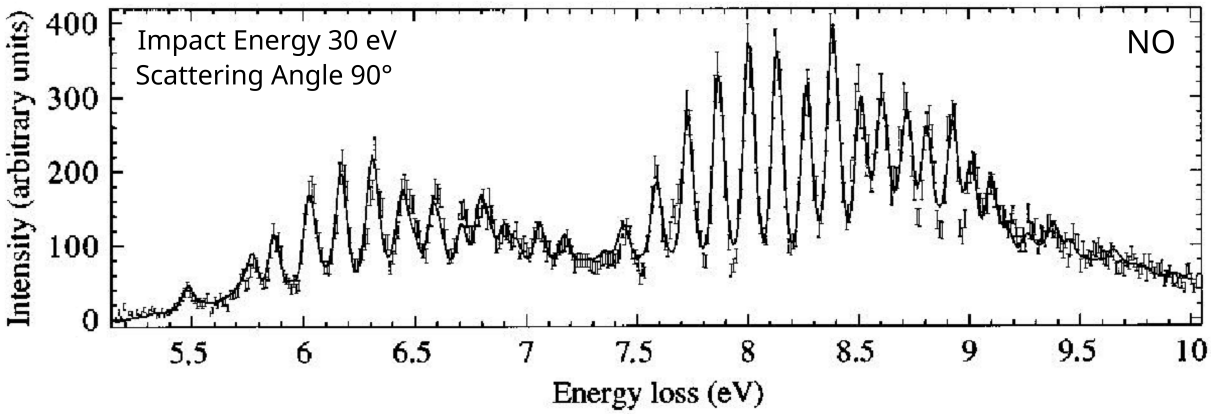

Figure 11.35: Electron energy-loss spectrum in NO at 30 eV of impacting energy scattered at 90°, extracted from Mojarrabi *et al.* [655, fig.1:bottom plot]

11.4.6 Argon

As a fundamental gas in noble-gas discharges and lasers, the database for Argon is maybe the most replete [89, p.348] after Helium. Because noble gases offer accessible assessment of cross sections both theoretically and experimentally, the number of publications about argon spans over more than a century. The colossal work of compiling existing cross sections and giving recommended values was made by Hayashi in 2003 [388]. The most recent review from Gargioni and Grosswendt [319] gives practical information about where to find databases online [30, 732], how to inspect experimental data, analytical expression for fitting cross-sections and a comparison of the most recent data. For detailed information about the renormalisation presently made to generate analytical fits, please refer to part III section 15.1.4.

From the theoretical side, argon was studied profusely [283, table 2]. We shall only retain here (i) the recent B-spline R-matrix calculations from Zatsarinny *et al.* [1002] which were uploaded to the LXCat [732] database and compared to the most recent experimental data [175, 491, 883]; and (ii) Gangwar *et al.* [313] as an example, out of a plethora, of distorted-wave studies.

The ground state electronic configuration of Argon is : $(1s^2\,2s^2\,2p^6\,3s^2\,3p^6)\,{}^1S_0$. Its lowest excited states are structured as represented in the energy diagram in figure 11.36 according to the progression of the excited electron into the orbitals $4s$, $4p$, $3d$, $5s$, etc.

As explained in the review of Boffard *et al.* [89, §2.1:p.321], the spin-orbit coupling in Ar is important in the $(3p^5)$ ion core, as well as the electrostatic interaction with the excited electron. Thus, two rivalling coupling schemes (LS and jj, cf. C.1) interplay under the total angular momentum $\mathbf{J} = \mathbf{L}_c + \mathbf{S}_c + \boldsymbol{\ell}_e + \mathbf{s}_e$ between the Ar^+ core (c) and the excited electron (e). As a result, the sublevels seen for each of the orbitals on figure 11.36 are non-degenerate and can all be resolved within a tenth of an electron-Volt. Most importantly, as opposed to the spectra of N_2 and NO for which there is virtually no mixing between different molecular states within the same peak, excitation lines of Ar can correspond to a *mixture* of singlet and triplet states with the same total angular momentum J (intermediate coupling). This is why, sometimes, it is not possible to attribute a definite ${}^{2S+1}L_J$ configuration (see appendix C) for every excited state [89, p.354-364]. Instead, the Racah notation is used [388, consult table 1 at the end]: $nl[K]^o_J$, where $\mathbf{K} = \mathbf{L}_c + \mathbf{S}_c + \boldsymbol{\ell}_e$ is the coupling momentum without the spin of the excited electron occupying the nl orbital. Since the Ar^+ core can either be ${}^2P_{3/2}$ or ${}^2P_{1/2}$, a shortcut prime is added as $nl'[K]^o_J$ when the core is ${}^2P_{1/2}$.

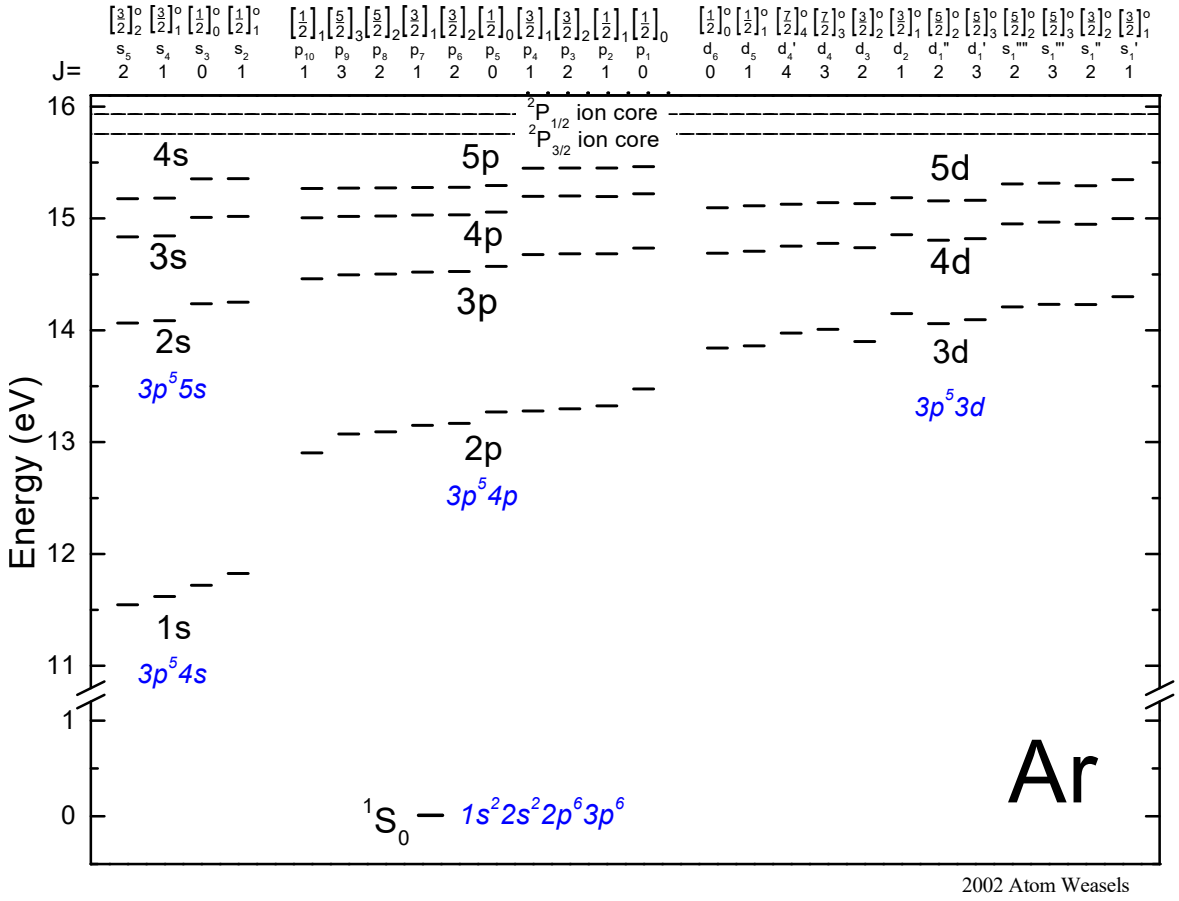

Figure 11.36: Energy diagram of excited levels of Argon

There are four distinct ns at each $n > 3$. Two are allowed (and mixed): $^1P_1$ and $^3P_1$; the other two are dipole-forbidden [89, p.322]: $^3P_2$ and $^3P_0$. The 4s configuration [89, §5.1.2] was most recently studied by Khakoo *et al.* [491]. Cross sections from optical emissions for the two $J = 1$ allowed states of 4s were reported by Ajello *et al.* [8] and for all four 5s states by Stewart *et al.* [883].

The np states [89, §5.1.4] form a suite of ten levels. All involve a mixture of different S and L configurations for $J = 0, 1, 2$ except the state $J = 3$, which is uniquely defined by the $^3D_3$ triplet to which transition from ground is spin-forbidden. Despite being all forbidden at least due to parity violation ($\ell = p \nrightarrow p$), practically all 4p cross section derived from the optical emissions of Chilton *et al.* [175] exhibit a high-energy tail not decaying as fast as predicted by the Born-Bethe approximation. This is a defect due to the important contribution of cascades beyond 100 eV. It implies that the direct cross sections are derived as differences between two large values with sometimes overlapping uncertainties, and thus cannot be used reliably*. When available, we privileged using Chutjian and Cartwright [180] renormalised results from relative-flow measurements rather than optical emissions (see sec. 15.1.4 p. 577 for details about renormalisation).

$\mathbf{L}_c(=P) + \boldsymbol{\ell}_e(=p)$				
S	P	D		
$^1S_0$	$^1P_1$	$^1D_2$	0	$\mathbf{S}_c$
$^3S_1$	$^3P_0$	$^3D_1$	1	+
	$^3P_1$	$^3D_2$	1	$\mathbf{s}_e$
	$^3P_2$	$^3D_3$	1	

*Actually, in some cases [176], the cascade contribution is measured higher than the apparent emission and thus their difference would yield negative direct cross section values.

Table 11.9: Electronic transitions from Argon ground state. Optically allowed (↕) are distinguished from forbidden (‡) transitions characterised by their asymptotic $1/\varepsilon^d$ trend (d) in brackets. Also given are the energy threshold $\Delta\mathcal{E}$. The last four columns gives parameters for $s_{\rm exc}$ exclusively fitted with the experimental data of Ajello *et al.* [8], Chilton *et al.* [175], Chilton and Lin [176], Chutjian and Cartwright [180], Filipović *et al.* [282, 283], Khakoo *et al.* [491], and Stewart *et al.* [883]. Keep in mind that the flag signalling overfitting is raised; the $4p$ and $3d$ were sometimes fitted with only 4 data points [180].

(d)		$\Delta\mathcal{E}$	Fitting Parameters			
	to Ar($X\,^1S_0$)	(eV)	$M\,\Delta\mathcal{E}$/Ryd	C	$a\,\vert\,c$	b
‡ (3)	$(4s)[3/2]\,^3P_2^o$	11.55	0.041 ± 0.0064	0.3 ± 0.12	1	4.25 ± 1.9
↕	$(4s)[3/2]\,^3P_1^o$	11.62	0.06 ± 0.03	0.26 ± 0.9	0.1 ± 0.13	0.99 ± 0.77
‡ (3)	$(4s')[1/2]\,^3P_0^o$	11.72	0.0086 ± 0.0016	0.26 ± 0.12	1	5.43 ± 2.7
↕	$(4s')[1/2]\,^1P_1^o$	11.83	0.233 ± 0.07	0.28 ± 0.7	0.11 ± 0.054	1.2 ± 0.5
‡ (1)	$4p$	12.91	0.13 ± 0.08	0.73 ± 4.26	1	0.74 ± 6.43
‡ (1)	$(4p)[1/2]1$	12.91	0.00073 ± 0.01	0.12 ± 27	1.24 ± 64	9.14 ± 2070
‡ (3)	$(4p)[5/2]\,^3D_3$	13.08	0.14 ± 0.34	1.4 ± 32	8 ± 663	0.5 ± 31
‡ (1)	$(4p)[5/2]2$	13.09	0.021 ± 0.009	0.11 ± 1.26	1	10 ± 115
‡ (1)	$(4p)[3/2]1$	13.15	0.0041 ± 0.0047	0.1 ± 17	1.08 ± 18	5.2 ± 917
‡ (1)	$(4p)[3/2]2$	13.17	0.021 ± 0.0087	1.74 ± 3.38	1	0.34 ± 1.2
‡ (1)	$(4p)[1/2]0$	13.27	0.014 ± 0.0082	0.1 ± 3.2	1	5 ± 170
‡ (1)	$(4p')[3/2]1$	13.28				
‡ (1)	$(4p')[3/2]2$	13.3	0.016 ± 0.009	0.1 ± 1.74	1	10 ± 168
‡ (1)	$(4p')[1/2]1$	13.33	0.002 ± 0.0033	0.1 ± 15	1.1 ± 14	10 ± 1050
‡ (1)	$(4p')[1/2]0$	13.48	0.3 ± 45	0.1 ± 6.77	0.1 ± 21	1.1 ± 33.9
‡ (1)	$3d + 5s$	13.84	0.37 ± 0.48	1.2 ± 29	10 ± 855	0.5 ± 26
‡ (3)	$(3d)[1/2]^3P_0^o$	13.84	0.308 ± 0.17	0.92 ± 1.15	1	1.53 ± 3.13
‡ (3)	$(3d)[1/2]1^o$	13.86	0.1 ± 0.02	0.63 ± 0.15	1	2.8 ± 0.62
‡ (3)	$(3d)[3/2]2^o$	13.9	0.23 ± 0.12	0.62 ± 0.82	1	2.61 ± 4.54
‡ (3)	$(3d)[7/2]^3F_4^o$	13.98	0.221 ± 0.29	0.1 ± 6.7	0.85 ± 7.9	9 ± 559
‡ (1)	$(3d)[7/2]3^o$	14.01	0.0032 ± 0.0031	0.13 ± 6.6	1.17 ± 9.9	10 ± 475
‡ (3)	$(3d)[5/2]2^o$	14.06	0.0094 ± 0.0023	0.27 ± 0.1	1	2.46 ± 1.07
‡ (1)	$(3d)[5/2]3^o$	14.09	0.0104 ± 0.0034	2.38 ± 1.7	1	0.8 ± 0.4
↕	$(3d)[3/2]1^o$	14.153	0.083 ± 0.39	10 ± 44	0.16 ± 4.3	0.5 ± 0.7
‡ (1)	$(3d')[5/2]2^o$	14.21	0.0017 ± 0.0026	0.68 ± 2.97	3.1 ± 19	4.56 ± 8.16
‡ (1)	$(3d')[5/2]3^o$	14.24	0.0077 ± 0.002	1.8 ± 1.52	1	0.113 ± 0.3
‡ (1)	$(3d')[3/2]2^o$	14.23	0.028 ± 0.008	0.882 ± 0.26	1	0.97 ± 0.49
↕	$(3d')[3/2]1o$	14.3	0.093 ± 0.33	7 ± 102	0.4 ± 13	1.04 ± 6.5
‡ (3)	$(5s)[3/2]^3P_2^o$	14.07	0.106 ± 0.034	1.35 ± 0.52	1	0.533 ± 0.45
↕	$(5s)[3/2]P_1^o$	14.09	0.026 ± 0.007	0.3 ± 6.4	0.18 ± 0.16	1.45 ± 4.44
‡ (3)	$(5s')[1/2]^3P_0^o$	14.241	0.025 ± 0.0055	1.39 ± 0.31	1	0.56 ± 0.23
↕	$(5s')[1/2]P_1^o$	14.255	0.011 ± 0.053	1.97 ± 6	0.1 ± 1.8	0.5 ± 0.24

Finally, nd states, for which only $n = 3$ is considered, can be combined into twelve levels most of which were reported in Chilton and Lin [176] and Chutjian and Cartwright [180]. Only two states are pure triplets: $^3P_0$ and $^3F_4$; the others are mixtures of singlet and triplets. For some states – $(3d)[3/2]2^\circ$ – the asymptotic decay matched rather $d = 3$ than $d = 1$; bespeaking little participation of the $^1D_2$ singlet in the mixture.

$\mathbf{L}_c(=P) + \boldsymbol{\ell}_e(=d)$				
P	D	F		
$^1P_1$	$^1D_2$	$^1F_3$	0	$\mathbf{S}_c$
$^3P_0$	$^3D_1$	$^3F_2$	1	+
$^3P_1$	$^3D_2$	$^3F_3$	1	$\mathbf{s}_e$
$^3P_2$	$^3D_3$	$^3F_4$	1	

In a similar fashion to the relativistically correct analytical expressions from Bretagne *et al.* [106], we attempted to fit the excitation cross sections for Argon given in table 11.9. Since the levels lie close to each other, we grouped for convenience all $4p$ and $3d + 5s$ excitations into a summed cross section highlighted in grey. The sum of individual fits was checked to be consistent with the global fit. For allowed transitions from higher excited states, Bretagne *et al.* [106, table 1] constructed a more exhaustive set of analytical excitation cross sections, albeit based on optical oscillator strengths (OOS) from Lee and Lu [568]. Since then, the set of OOS has not been significantly updated. Thus, we did not attempt any revision for those higher electron-impact excitations.

11.4.7 Oxygen

No less important is the role that atomic oxygen plays in hot gas channels. Its major impact consists in catalysing chemical reactions. In gas discharges, it manifests its presence through the $\mathrm{O}(3p\ ^5P) \rightarrow \mathrm{O}(3s\ ^5S^o)$ transition located at a magical number $\sim 777\,\mathrm{nm}$. This strong dipole-allowed line may be seen from space to track optical emissions from lightning activity [e.g. 74, figs. 1-2], but also in laboratory sparks in order to infer the temperature inside the ionised channel [e.g. 500, §4.2]. As for collisions with electrons, atomic oxygen offers an important cooling mechanism in the ionosphere and plasmas in space [437, table 5.1]. Therefore, an accurate assessment of $\mathrm{O}(3p\ ^5P)$ and other excitations are vital when modelling electron swarms in hot ionised plasma discharge channels.

The experimental setup for measuring cross sections with atomic oxygen is made difficult by the need of dissociating a parent oxygen molecule (usually O_2 or NO) through a microwave discharge and then deriving the signals related to O transitions relative to the parent molecule. Of primary importance is to ensure that the dissociation fraction in the beam is stable in order to properly deconvolve the energy-loss spectrum.

An example from Kanik *et al.* [476, fig 2] is shown on figure 11.37. The dissociation fraction is derived by comparing the ratios of the summed longest, second and third bands of molecular oxygen when the discharge was on and off. Such experiment was carried by Stone and Zipf [887] for the first time, measuring however optical emissions instead of energy-loss spectra which can result in high uncertainties on the derived results due to the difficulty related to normalisation and proper exclusion of all cascading contributions.

The numerous theoretical and experimental investigations that ensued, were comprehensively reviewed by Laher and Gilmore [549]. The contemporaneous report by Itikawa and Ichimura [437] also included elastic and photon emission and absorption cross sections. The most recent update was made by Johnson *et al.* [462] to incorporate the advances made by later experiments [227, 461, 476]. It seems that no other experiment has been reported after 2005, despite Johnson *et al.*'s [462, §8] call for new measurements.

On the other hand, as for other atoms in general, oxygen has been actively studied theoretically. The latest report from Tayal and Zatsarinny [921] incorporated the largest amount of pseudostates in the (B-spline) R-matrix method. The excellent agreement for some states is con-

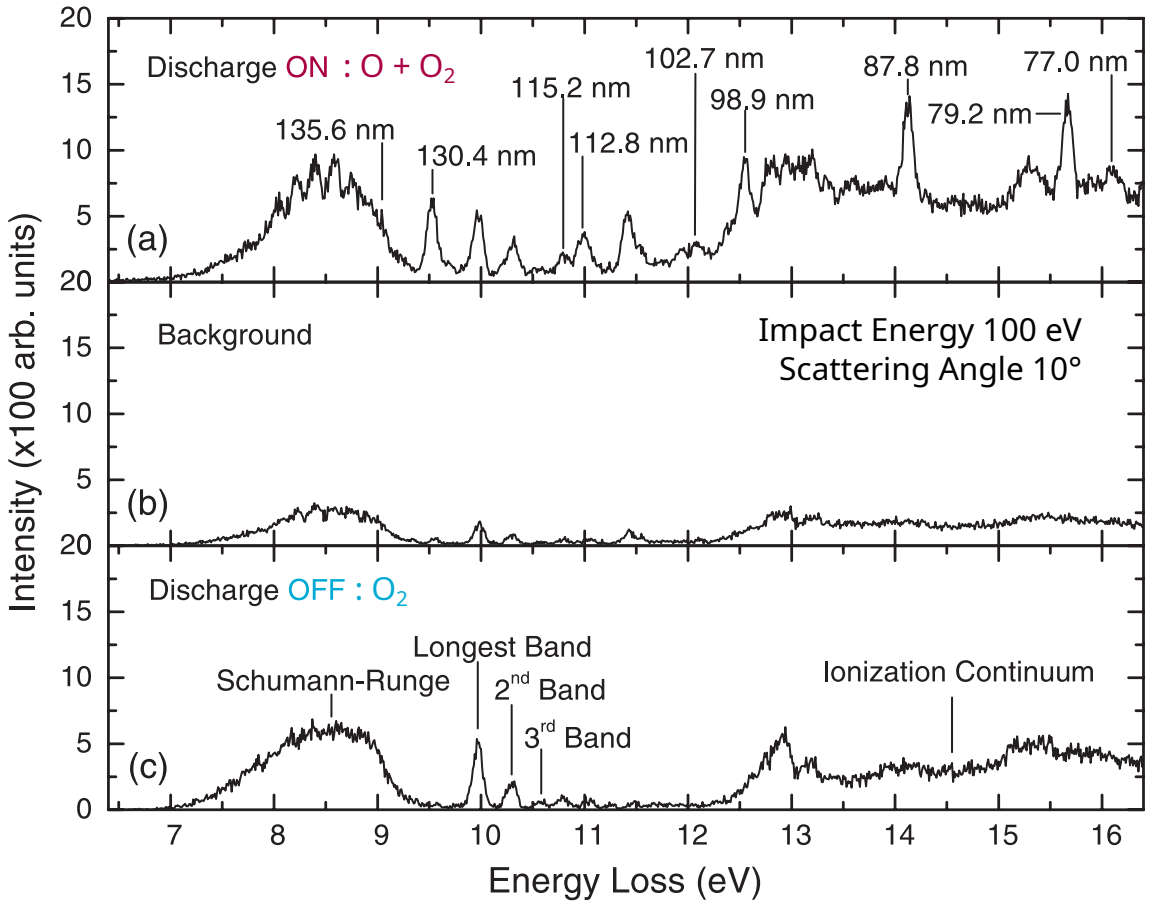

Figure 11.37: Electron energy-loss spectrum (at 100 eV and 10°) in an oxygen-nitrogen (19:1) mixture during and without sustained microwave discharge, adapted from Kanik *et al.* [476, fig 2]. Nitrogen is used as a buffer gas in order to raise the oxygen dissociation fraction (reduce recombination). The atomic bands must be fitted to derive their intensity (area) and then be compared against the molecular bands.

trasted with unsystematic discrepancies for other transitions where even experimental evidence cannot lucidate*.

As a light atom, the states of atomic oxygen can be well described by LS-coupling (cf. appendix C.1). Its ground state configuration is $2s^2\,2p^4 : {}^3P_2$ which is non-degenerate in $J = 2, 1, 0$ in decreasing (rising) order of binding (potential) energy.

Unsurprisingly, there is a complete experimental void of data on those fine-structure split states [462, 549]. All information rely on theoretical considerations [154]. Following Itikawa and Ichimura [437], we took the more recent calculations of Berrington [63] near threshold for collision strengths that we converted into cross sections with $a = 3$ and $b = 0.5$ in $s_{\rm exc}$ (11.61) so that $\sigma \sim \varepsilon^{3/2}$ farther from the threshold as prescribed [63, see fig.1 and p.1086§3.].

There are two other valence states which are metastable : ${}^1D_2$ and ${}^1S_0$. The most recent reports come from Doering [220], Doering and Gulcicek [224], Shyn *et al.* [839], and Shyn and Sharp [843] with middling agreement and high uncertainty rates. Both excitations are spin-forbidden $\Rightarrow$ $d = 3$, however, this asymptotic trend is not conspicuous in the experimental data

*'Lūcĭdāre' = bring light, enlighten; it would have been nice if 'lucidate' were the intransitive version of the transitive 'elucidate'. However, as Latin became vulgarised, its use became slacker.

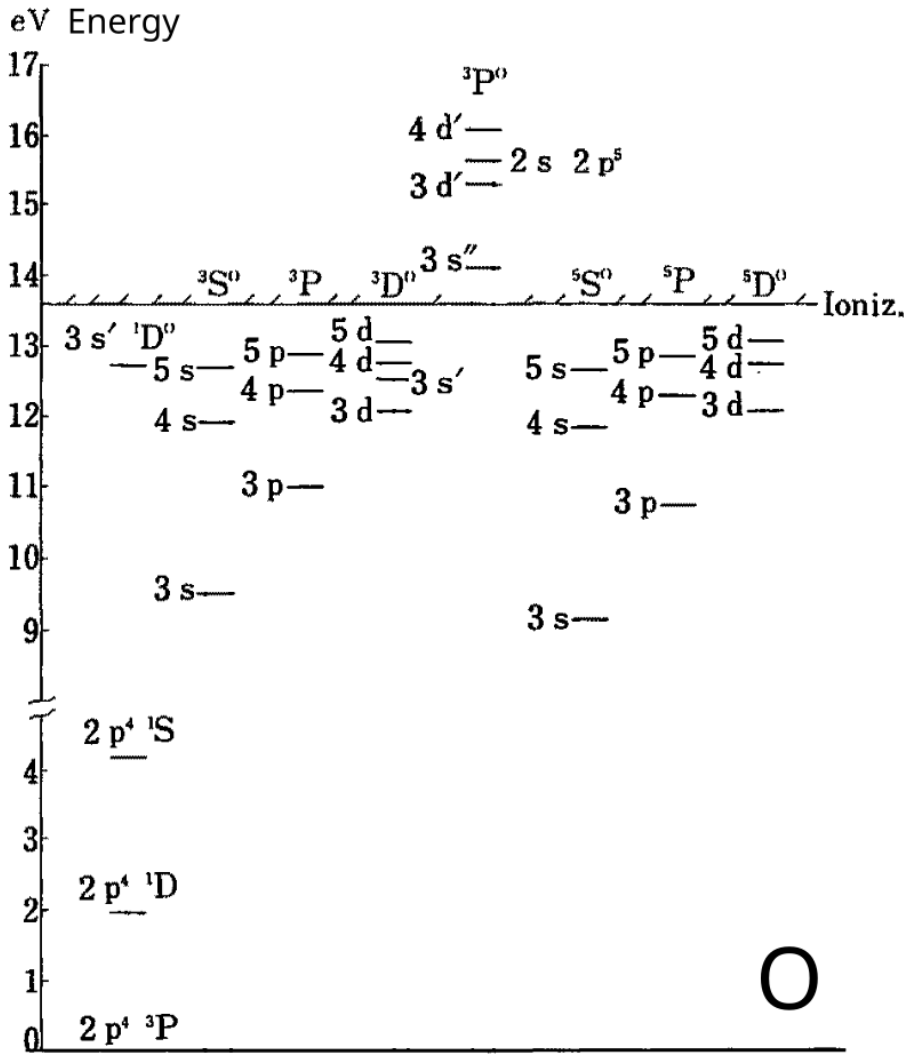

Figure 11.38: Energy diagram of excited levels of atomic Oxygen adapted from Itikawa and Ichimura [437, fig 2.1]. Levels lying above the ionisation continuum are autoionising states.

[437, fig. 5.2]. As a result, the fit to $^1D_2$ had no other choice than to be forceful (meaning that additional constraints on the parameters had to be imposed in order to get pleasing results cf. 13.2:fig. 13.9).

The Rydberg states populate the $n(spdf)\ldots; n \geq 3$ orbitals displayed on the diagram 11.38. All np series are dipole-forbidden ^3P (or spin-forbidden ^5P) while ns and nd series give rise to allowed ($^3S^o$, $^3D^o$) and spin-forbidden ($^5S^o$, $^5D^o$) transitions from ground. The single (nl') and double (nl'') primed notations refer to the state of the ion core $(2s^2\,2p^3)\,^2D^o$ and $^2P^o$, which ordinarily is $^4S^o$ when unprimed (all $2p$ have parallel spin projections) [462, p.590].

Best known is the $(3s)\,^3S^o$ state [461, 476, 958]. Some discrepancies in later measurements [227, 360] that revealed larger cross sections were pointed out by Kanik *et al.* [476, p.2662-2663] and dismissed for an improper extrapolation of smaller angles and thereby an overestimation of the forwardly peaked DCS.

For the other states: nd series [960], np series [361], $3s'$ state [959] and autoionising states [960], data is comparatively scarcer and uncertain.

The trend underlined by the $nd\,^3D^o$ series [476, 960] is queer. As an allowed transition, it

should follow a slow logarithmic falloff. Nevertheless, a peaked structure at 50 eV precludes a close fit like the one shown in Vaughan and Doering [960, figure 3]. Laher and Gilmore [549, p.286:§2.3.d] decided to stitch a logarithmic tail above 100 eV.

Presently, we deem this is because all $nd\,^3D^o$ are inevitably contaminated by their spin-forbidden sibling $nd\,^5D^o$ which lies at most 10 meV below, and therefore could not be possibly resolved within the 50 meV spectral resolution of the detectors [476, p.2651]. Spin-forbidden transitions should indeed present sharply peaked and decaying CS usually located in the immediate threshold's vicinity > 12 eV, thus around 20–30 eV. Kanik *et al.*'s [476, figure 3, table 4] data indeed suggest that this peak would be located below 30 eV, as opposed to Vaughan and Doering [960, table 4]. Reluctantly, taking these considerations into account, we decided to lump all nd transitions [960] together, disregard their peak at 50 eV and let the fit take a maximum nearer threshold at 12.09 eV for all transitions.

Autoionising states reported by Vaughan and Doering [960] had somewhat peaked structures that could not be fitted simply with the expression (11.61). We allowed a supplementary term according to the Bethe theory decaying as $1/\varepsilon^2$ and fixed $C = 1$ and $M = f_x\mathrm{Ryd}/\Delta\mathcal{E}$ from the optical oscillator strength [225, table 2] f_x and the excitation threshold $\Delta\mathcal{E}$:

$$s'_a \equiv 4\pi a_0^2 \frac{f_x}{\Delta\mathcal{E}/\mathrm{Ryd}} \frac{(1-(\Delta\mathcal{E}/\varepsilon)^a)^b}{\varepsilon/\mathrm{Ryd}} \left[\ln\left(4\frac{\varepsilon}{\mathrm{Ryd}}c\right) + \frac{c'}{\varepsilon/\mathrm{Ryd}}\right] . \tag{11.68}$$

Experimental data for $\geq 4s, 4p$ is absent and Laher and Gilmore [549, §2.2] suggested a scaling method based on the knowledge of fits for lower states and energy level distribution from quantum defects. We used the optical oscillator strengths of $4s\,^3S^o$ to scale its CS from $3s\,^3S^o$. As for forbidden transitions, they are lower in magnitude and scaling is less straightforward; thus we omitted them.

A summary of the excitation thresholds and cross section fitted presently is available in table 11.10.

11.4.8 Nitrogen

In molecular form, we started with the most studied target in electron collisions and end presently with one of the least studied light atoms : nitrogen. So few is the experimental data that it did not even deserve its own section in Zecca *et al.*'s centennial review [1006, p.139:§5.3] nor in Inokuti *et al.* [425].

Although its study in laboratory for impact excitation from optical measurements preceded that of oxygen by one year [886], the low signal-to-noise ratio of crossed-beams experiments on atomic nitrogen is very prohibitive. The reason for this, as Doering and Goembel [222] explain, is because the dissociation yield of N in microwave discharges is very low ~ 5%, and also because the signal can get contaminated by metastable excited states produced in the discharge.

The ground state electronic configuration of N is a quadruplet : $2p^3\,^4S^o_{3/2}$. Of the two spin-forbidden transitions only the lowest lying $^2D^o$ was experimentally studied by Yang and Doering [992]. The other two previous experiments probed the allowed $2p^2\,3s\;^4P$ [222] and $2s\,2p^4\;^4P$ [223]. The $3s\;^4P$ transition possesses a core-excited Feshbach-like resonance structure near threshold at 10.33 eV [867], for which unfortunately not enough data are available in order to provide a reliable fit.

In contrast, theoretical investigations on atomic nitrogen are bountiful. From early variational matrix studies for low-energy scattering [928] to Born approximated GOS at high energies [312], to name just a few examples. Again, we shall retain here the most recent BSR calculations [975], particularly because their results are readily available on LXCat.

Table 11.10: Electronic transitions from atomic Oxygen ground state. Optically allowed (↕) are distinguished from forbidden (↨) transitions characterised by their asymptotic $1/\varepsilon^d$ trend (d) in brackets. Also given are the energy threshold $\Delta\mathcal{E}$. The last four columns gives parameters for s_{exc} (11.61). The three excitations below the dashed line are autoionising states.

(d)		$\Delta\mathcal{E}$		Fitting Parameters		
	to O($2p^4\ ^3P_2$)	(eV)	$M\,\Delta\mathcal{E}$/Ryd	C	$a\,\vert\,c$	b
↨ (1)	$(2p^4)\ ^3P_1$	0.0196	1.123×10^{-4}	1	3	0.5
↨ (1)	$(2p^4)\ ^3P_0$	0.0281	6.351×10^{-5}	1	3	0.5
↨ (1)	$(2p^4)\ ^3P_0$	0.0095	3.5×10^{-6}	1	3	0.5
↨ (3)	$(2p^4)\ ^1D$	1.967	0.324 ± 29	11.35 ± 16	0.1 ± 21	0.5 ± 4.1
↨ (3)	$(2p^4)\ ^1S$	4.19	0.063 ± 0.07	3.03 ± 3.3	1	1.72 ± 2
↨ (3)	$(3s)\ ^5S^o$	9.146	0.007 ± 0.015	1 ± 2	10 ± 1040	2.43 ± 966
↕	$(3s)\ ^3S^o$	9.521	0.048 ± 0.12	2.3 ± 14	0.25 ± 2.3	0.844 ± 0.78
↨ (3)	$(3p)\ ^5P$	10.74	5.89 ± 605	4.97 ± 8.9	0.1 ± 24	0.5 ± 2
↨ (1)	$(3p)\ ^3P$	10.99	0.001 ± 0.001	0.84 ± 0.15	5.15 ± 2.62	5.85 ± 2.9
↕	$(nd)\ ^3D^o$	12.09	0.017 ± 0.15	1 ± 36	1.6 ± 78	$9.782 \pm 5 \times 10^{-6}$
↕	$(3s')\ ^3D^o$	12.54	0.061 ± 0.11	1.1 ± 33.1	0.108 ± 0.5	0.98 ± 7.8
↕	$(3s'')\ ^3P^o$	14.12	0.086 ± 0.21	0 ± 32	0.18 ± 1.94	2 ± 21
↕	$(2s2p^5)\ ^3P^o$	15.66♠	0.07 ± 2.75	1 ± 0.733	0.1 ± 10	10 ± 357
↕	$(4d')\ ^3P^o$	16.11	0.02 ± 0.014	1 ± 11	0.27 ± 1.2	10 ± 421

♠ This autoionising state had to be fitted to [960] using (11.68) with $a = 3.1 \pm 70$ and $c' = 10 \pm 170$ (upper bound constraint)

We decided, for practical purposes, to fit the missing cross sections [$(2p^3)\ ^2P^o$, ($3p$), ($3d$), ($4p$) states and $(4s)\ ^4P$] based on calculations provided by Wang *et al.* [975]. All transitions to $3p$, $3d$ and $4p$ orbitals, whose excitation thresholds lie close together, were summed and fitted into one compound cross section per orbital. A summary of our results is presented in table 11.11.

Table 11.11: Electronic transitions from atomic Nitrogen ground state. Optically allowed (↕) are distinguished from forbidden (↨) transitions characterised by their asymptotic $1/\varepsilon^d$ trend (d) in brackets. Also given are the energy threshold $\Delta\mathcal{E}$. The last four columns gives parameters for $s_{\rm exc}$ (11.61).

(d)		$\Delta\mathcal{E}$		Fitting Parameters		
to N($2p^3\ {}^4S^o_{3/2}$)		(eV)	$M\,\Delta\mathcal{E}$/Ryd	C	$a\,\vert\,c$	b
↨ (3)	$(2p^3)\ {}^2D^o$	2.39	0.213 ± 0.228	3.12 ± 4.1	1	2.28 ± 3.27
↨ (3)	$(2p^3)\ {}^2P^o$	3.58	0.07 ± 0.036	1.82 ± 5	5.1 ± 36.2	1.329 ± 0.986
↕	$(3s)\ {}^4P$	10.33	0.271 ± 0.139	1 ± 14	0.39 ± 1.6	10 ± 0.00415
↕	$(2s2p^4)\ {}^4P$	10.93	0.085 ± 0.64	5.3 ± 75	10 ± 727	6.7585 ± 0.0011
↨ (1)	$3p$	11.84	0.11 ± 0.053	2.26 ± 4.8	1	0.41 ± 1.23
↕	$3d$	13	0.075 ± 0.072	7.106 ± 30	0.477 ± 2	1.085 ± 1.64
↕	$(4s)\ {}^4P$	12.85	0.027 ± 0.024	9.5 ± 37	1.8 ± 18	1.3 ± 11
↨ (1)	$4p$	13.24	0.068 ± 1.51	1.3 ± 12	0.1 ± 4.8	0.5 ± 2.6

11.5 Impact Ionisation

Impact ionisation is the dominant process by which high-energy electrons interact with matter. As consequence, a variety of empirical, semi-empirical and approximative theoretical methods were developed in order to model impact ionisation (see for instance Hahn *et al.* [380, p.3-128..9]). The early review of Rudge [793] highlights how much attention the subject was given and summarises the various approximations and empirical models at the time. A more recent review, more focused on concrete calculations and results was conducted by Llovet *et al.* [605].

When an electron collides with a molecule and induces ionisation, a secondary or ejected electron is freed from the molecular shell and both outgoing electrons are formally defined by Coulomb waves in the potential of the ion.

The theoretical difficulty is that the primary electron is now coupled to an ionic target with a continuum of states for the ejected electron [102, eq.(17-18)]. In practice, close-coupling expansions make use of a large number of pseudo-states whose density is used to approximate the continuum [662].

Instead of proceeding to a direct resolution of Schrödinger's coupled equations of the target and incident electron, the problem can again be circumvented with an approximation valid at high-energies and extended down to threshold by means of artful adjustments.

Perhaps the most advanced treatment is given by the distorted-wave Born approximation [97] which uses the incident electron wave distorted by the potential of the neutral target in the interaction with a target electron. This treatment also properly includes the effect of electron exchange at lower energies. Despite the complexity of this approach, it was shown many times in the literature [97, 793, 911] that the major correction provided by the distorted-wave can be encapsulated effectively in a *scaling* factor of the cross section which offsets the incident electron's energy ε_0 by a certain gain of kinetic energy. As a result, considerably simpler methods using the plane-wave Born approximation with an adequate scaling proved to be invaluable tools to model ionisation cross sections with great accuracy.

In this section, we present a betterment of the to relativistic binary-encounter Bethe model of Kim *et al.* [508] that consist in two major revisions:

1. The inclusion of high-order effects in the dipole term through a coefficient C_d
2. For ionisation from ejection of an electron in *valence* orbitals, the reformulation of the partial ionisation cross sections not in binding energies B_o to the (valence) orbital o of the initial state, but in terms of energy thresholds I_i to excited ionic states i.

For *core* orbitals, we still use the binding energy B. To keep a coherent notation, we will keep the notation "B" for denoting either a binding energy or an ionisation potential.

To start on steady grounds in the following two sections (11.5.1 and 11.5.2), we first remind the two complementary models of the dipole (Bethe [64]) and the binary encounter (Vriens [967]) approximations to the impact ionisation of electrons on molecules. The revision and concise review starts in section 11.5.3. Finally, the results for practical applications are best summarised in table 11.12 of section 11.5.4.

11.5.1 Generalised Oscillator Strength Density

In this subsection, we underline the fundamental concepts applicable to electron impact ionisation in the revisited formulation of Inokuti [427]. The notation is adapted to match with the convention taken in this thesis.

In Bethe's [64] theory, the concept of GOS for discrete excitations is extended to the "dGOS": *density* of generalised oscillator strength [427, eq.(2.21)] :

$$\frac{\mathrm{d}F_i(q,\varepsilon_2)}{\mathrm{d}\varepsilon_2} \equiv \frac{\varepsilon_2 + I_i}{\mathrm{Ryd}} \sum_{\Omega_2} \frac{|\epsilon_{\varepsilon_2,\Omega_2}(q)|^2}{(qa_0)^2} \,, \tag{11.69}$$

where q is the momentum-transfer of the primary electron as usual, ε_2, Ω_2 represent the kinetic energy and direction of the secondary electron and I_i is the ionisation potential to the state i of the ion (it may be an excited state or a multiply ionised state in which case, one must also account for the other ejected electrons). The Rydberg Ryd and Bohr radius a_0 are given in section 7.5.

With this further generalisation of the notion of generalised oscillator strength density over a continuum of states, the Bethe sum rule seen previously (section 11.4.1), traditionally noted $S(0)$ implying the 'zeroth' momentum of the dipole oscillator strength distribution, can now be written explicitly [911, eq.(16)]:

$$S(0) \equiv \lim_{q\to 0} \sum_{a'v'} F_{a'v'}(q) + \sum_i \underbrace{\int_0^\infty \frac{\mathrm{d}F_i(q,\varepsilon_2)}{\mathrm{d}\varepsilon_2} \mathrm{d}\varepsilon_2}_{N_i} = \sum_A Z_A = N \,. \tag{11.70}$$

This result is independent of the value of the momentum transfer q which is maintained constant in the process of summation/integration.

Moving onward, the doubly* differential ionisation cross section (DDCS) is similarly related to the GOS density as for discrete excitations (11.47):

$$\frac{\mathrm{d}\sigma_i}{\mathrm{d}\Omega_1\,\mathrm{d}\varepsilon_2} = \frac{4a_0^2}{\varepsilon/\mathrm{Ryd}} \frac{\mathrm{d}F_i(q,\varepsilon_2)}{\mathrm{d}\varepsilon_2} \frac{\mathrm{Ryd}}{\varepsilon_2 + I_i} \frac{kk'}{q^2} \,. \tag{11.71}$$

The kinetic energy of the incident electron is denoted ε. This theoretical DDCS should not be confused with experimental DDCS (p. 492) which are typically in the secondary electron's energy ε_2 and direction Ω_2. Integration through Ω_1 (or q equivalently) gives the ionisation cross section singly differential in ejected electron energy ε_2 which behaves asymptotically as a dipole-allowed transition. The relativistically correct version is:

$$\frac{\mathrm{d}\sigma_i}{\mathrm{d}\varepsilon_2} = \frac{4\pi a_0^2 \mathrm{Ryd}}{m_\mathrm{e}c^2\beta^2/2} \left[\frac{\mathrm{Ryd}}{\varepsilon_2 + I_i} \frac{\mathrm{d}f_i(\varepsilon_2)}{\mathrm{d}\varepsilon_2} \left(\ln\left(\frac{2m_\mathrm{e}c^2\beta^2\gamma^2}{\mathrm{Ryd}} \check{c}_i(\varepsilon_2) \right) - \beta^2 \right) + \frac{\mathrm{d}\check{\gamma}_i(\varepsilon_2)}{\mathrm{d}\varepsilon_2} \frac{\mathrm{Ryd}}{\varepsilon_2} \right] . \tag{11.72}$$

The *differential* optical oscillator strength $\mathrm{d}f_i(\varepsilon_2)/\mathrm{d}\varepsilon_2$ is obtained from (11.69) at the limit $q \to 0$:

$$\frac{\mathrm{d}f_i(\varepsilon_2)}{\mathrm{d}\varepsilon_2} \equiv \left.\frac{\mathrm{d}F_i(q,\varepsilon_2)}{\mathrm{d}\varepsilon_2}\right|_{q=0} \,. \tag{11.73}$$

The Bethe parameters for the ionisation continuum $\check{c}_i(\varepsilon_2)$, $\check{\gamma}_i(\varepsilon_2)$ which are functions of ε_2, are defined in Inokuti [427, eqs.(4.12, 14&19)]:

*in direction of the primary electron Ω_1 and in kinetic energy of the ejected electron ε_2. Adding the distribution of the direction taken by the secondary electron Ω_2 would lead to the triply differential cross section (p. 495).

$$\ln \check{c}_i(\varepsilon_2) = 2\ln\left[(\bar{q}_i a_0)\frac{\mathrm{Ryd}}{I_i+\varepsilon_2}\right], \tag{11.74}$$

$$\frac{\mathrm{d}\check{\gamma}_i}{\mathrm{d}\varepsilon_2} = -\frac{m_\mathrm{e}}{2\mu}\frac{\mathrm{d}f_i(\varepsilon_2)}{\mathrm{d}\varepsilon_2} - \frac{\varepsilon_2+I_i}{4\mathrm{Ryd}}\left.\frac{\mathrm{d}^2F_i(q,\varepsilon_2)}{\mathrm{d}\varepsilon_2\,\mathrm{d}(q^2)}\right|_{q=0}. \tag{11.75}$$

The average momentum transfer $\bar{q}_i$, linked to the ionisation process i, is defined as:

$$\frac{\mathrm{d}f_i}{\mathrm{d}\varepsilon_2}\ln(\bar{q}_i a_0) = \int_0^\infty \frac{\mathrm{d}F_i(q,\varepsilon_2)}{\mathrm{d}\varepsilon_2}\,\mathrm{d}[\ln qa_0] - \int_{-\infty}^0 \left(\frac{\mathrm{d}f_i}{\mathrm{d}\varepsilon_2} - \frac{\mathrm{d}F_i(q,\varepsilon_2)}{\mathrm{d}\varepsilon_2}\right)\mathrm{d}[\ln qa_0]\,. \tag{11.76}$$

If one is not interested in the partial but only in the total ionisation σ_ion cross section, then it suffices to sum over all possible i (final ionic states):

$$(\mathrm{d})\sigma_\mathrm{ion} = \sum_i (\mathrm{d})\sigma_i \tag{11.77}$$

In principle, we could thus use the same empirical low-energy modifiers (11.61) on the Bethe ionisation cross sections and fit the parameters as in the previous section for optically allowed excitations. This methodology was followed in early times [608, eq.(4)] after measurements of ionisation cross sections became available.

We do however not choose to proceed to parametric fitting for three main reasons. First, as we saw in the previous section 11.4.2 for discrete excitation, there is too much arbitrariness introduced by the parameters, which are not always well constrained (large variance). Second, ionisation is the dominant energy loss process for incident electrons above the ionisation threshold. We must not allow any form of arbitrariness contaminate the cross sections asymptotically (through a magnitude parameter like M in eq.11.61b). Third, ionisation requires as input the *differential* cross section in secondary electron energy which is not only difficult to fit (because of its 2D character) but also not necessarily well probed experimentally for all targets considered. In brief, we seek a *consistent* theoretical model that would enable us to characterise ionisation for any of the atmospheric gases considered in this work.

Alternatively, we choose to describe ionisation with two simpler models [503, p.265-6:§2] that derive from the general Bethe theory.

1. Dipole oscillator ↦ soft collisions

2. Binary encounter ↦ hard collisions

The dipole oscillator is a straightforward approximation from the generalised oscillator when the momentum transfer is small $qa_0 \ll 1$ associated with *soft* collisions, in which case all matrix elements are calculated from the dipole operator (cf. appendix D.1). The binary encounter [969] emerged as an impulse approximation from close interaction (small impact parameters) between the incident and target electrons which involves a significant transfer of energy, associated with *hard* collisions.

We will see later in this chapter that a proper alliance of the binary-encounter with the dipole oscillator models yields remarkably satisfactory results of the total ionisation cross section for a very broad variety of targets over the whole range of energies. We proceed now by introducing the binary-encounter model.

11.5.2 Binary Encounters

When both incident and ejected electrons move fast compared to the kinetic energy of electrons in bound orbitals, their interaction may be viewed as isolated from their environment. In this framework, the following assumptions are equivalent:

$$\left.\begin{array}{l}\text{Impulse Approximation:}\\ \text{Small Impact Parameter:}\\ \text{Pseudo-Free Binary-Encounter:}\end{array}\right\}\ \text{the energy } \Delta\varepsilon \text{ lost by the incident electron is transferred } \left\{\begin{array}{c}\text{instantly}\\ \text{locally}\\ \text{entirely}\end{array}\right\}\ \text{to the secondary electron.}$$

This approach takes its roots already from Bohr [90] and Thomson [931]. The energy of the free incident electron is ε_0. The target electron is initially in a bound orbital with an average kinetic energy $U \equiv \langle \boldsymbol{p}^2 \rangle / 2m_\mathrm{e}$ and a binding energy $B > 0$. The energies $\varepsilon_1 > \varepsilon_2$ of the outgoing primary and secondary electrons are bound by the conservation of kinetic energy (neglecting kinetic energy communicated to the ion):

$$\varepsilon_0 = \varepsilon_2 + \varepsilon_1 + B \tag{11.78}$$

During the collision, it is assumed that a kinetic energy $\Delta\varepsilon \gg B$ is (exclusively) transferred to the secondary electron. In this framework, the process may be modelled by a modified Mott cross section (cf. eq.(8.143) in §8.5.5) between a free and pseudo-free electron [507, eq.(14)]:

$$\frac{\mathrm{d}\sigma_\mathrm{eBe}}{\mathrm{d}\varepsilon_2} = \frac{4\pi a_0^2 \mathrm{Ryd}^2}{\varepsilon_0 + \kappa U + \iota B} \left[\underbrace{\overbrace{\frac{1}{(\varepsilon_2+\Delta_2)^2}}^{\text{direct}} + \overbrace{\frac{1}{(\varepsilon_1+\Delta_1-U)^2}}^{\text{exchange}} - \overbrace{\frac{\phi_B(\varepsilon_2;\varepsilon_0)}{(\varepsilon_2+\Delta_2)(\varepsilon_1+\Delta_1-U)}}^{\text{interference}}}_{\text{pseudo-free Mott}} + \underbrace{\frac{4U}{3}\left(\frac{1}{(\varepsilon_2+\Delta_2)^3} + \frac{1}{(\varepsilon_1+\Delta_1-U)^3}\right)}_{\text{target electron in motion}} \right] \tag{11.79}$$

The modifications introduced roughly account for the potential of the atom/molecule and the initial kinetic energy U of the bound electron in its orbital [969]:

- The most important one is the quenching of the denominator at low energies:

  $$\varepsilon_0 \text{ replaced with } \varepsilon_0 + \kappa U + \iota B \,,$$

  where the offset $K \equiv \kappa U + \iota B$ represents the acceleration of the electron in the target potential [605, eq.(8)].

- The kinetic energy $\Delta\varepsilon$ transferred from the incident to the secondary electron may be decomposed as $\Delta\varepsilon \equiv \varepsilon_2 + \Delta_2$. The offset $\Delta_2 + U$ represents the energy that will be lost by the secondary electron after it escapes from the ion.

- Similarly, the primary, which locally has an energy $\varepsilon_1 + \Delta_1$, will lose Δ_1 after escaping. The difference is that the initial energy U of the bound electron is subtracted from the primary in the exchange and interference terms, instead of appearing in the direct term.

- Altogether, the energy required for liberating the two (incident and bound) electrons from the potential of the ion amounts to $\Delta_1 + \Delta_2 + U = K + B + U = (1+\iota)B + (1+\kappa)U$. The offset Δ_2 may be obtained from the requirement of exchange symmetry $\varepsilon_1 \leftrightarrow \varepsilon_2$ between $(\varepsilon_2 + \Delta_2)$ and $(\varepsilon_1 + \Delta_1 - U)$ giving:

$$\varepsilon_2 + \Delta_1 - U = \varepsilon_2 + \Delta_2 \Leftrightarrow (1+\iota)B - (1-\kappa)U = 2\Delta_2 \tag{11.80}$$

  Thus, in the square brackets, Mott's cross section between free electrons is now offset by:

$$\varepsilon_2 + \Delta_2 \equiv \varepsilon_2 + \frac{1-\iota}{2}B - \frac{1-\kappa}{2}U\ , \tag{11.81}$$

$$\varepsilon_1 + \Delta_1 - U \equiv \varepsilon_0 - \varepsilon_2 - \frac{1-\iota}{2}B - \frac{1-\kappa}{2}U\ . \tag{11.82}$$

- The additional term behind $4U/3$ represents the fact that the bound electron is not motionless but has an initial (average) kinetic energy $U \neq 0$ so that its final energy corresponds not exactly to the recoil energy due to momentum transfer $(\hbar q)^2/2m_\mathrm{e}$ [427, eqs.(4.82–9)].

- ϕ_B is a Coulomb-wave interference term from the Mott scattering (see sec. 8.5.5) between a free and a pseudo-free electron bound by $-|B|$ to the molecule.

Presently, in (11.79), we took the liberty of introducing two corrective parameters $0 < \kappa \leq 1$ and $0 < \iota \leq 1$, following the discussion presented in the previous chapter section 10.2.2. They underline the fact that $\iota B + \kappa U = K$ are supposed to represent the gain K in kinetic energy by the incident electron from the attractive potential of the neutral atom/molecule.

Tacitly, this gain was assumed [133] in some binary-encounter theories to be equal to B, putting $\iota = 1$, $\kappa = 0$. Such assumption relies on the plane-wave Born approximation applied to static potentials of the target with negligible motion of electrons in their bound orbitals ($\varepsilon_0 \gg U$) and when all other exchange, correlation, polarisation effects can be ignored.

The additional introduction of U in the leading denominator of (11.79) was proposed by Vriens [967, §II.B:eq.(9)] based on the fact that, setting $\iota = 1 = \kappa$, this acceleration is exact for the electron bound to the hydrogen atom. It [κU] has physically nothing to do with the $4U/3$ term inside the square bracket! For more information please consult section 10.2.2 and Vriens [966, 967].

Furthermore, for atoms beyond the second row (heavier than Neon), Huo and Kim [412, §III.B:p.1234] suggested that $\kappa \equiv 1/n$ for $n > 2$ where n stands for the principal quantum number of the orbital considered. When treating with molecules, this applies only to atomic (core) orbitals.

To highlight the conjectural nature of these scalings:

> we write ι, κ in (11.79) to remind the reader that the scaling of the incident energy through $\varepsilon_0 + \kappa U + \iota B$ is purely speculative [793, §4.3] and that numerous corrections and revisions have been proposed in order to seek improvement [359, 412]. The prefactors ι and κ are certainly not intended to act as fitting parameters. They serve as a visual guide for unifying the representations of different variants of the binary encounter model.

Coulomb-wave interference ϕ_B The numerator of the interference term in (11.79) comprises a function ϕ_B originally stemming from interference between the phases of Coulomb-waves from two outgoing electrons in (8.144b). Vriens [966] originally introduced it rigorously from the momentum transfers q and $\tilde{q} = |\mathbf{k}_2 - \mathbf{k}_0|$ (called the 'exchange momentum transfer'). Unfortunately, it may not be averaged analytically over an isotropic distribution of initial secondary momenta $\mathbf{k}_{-2}$. This means that an average value of ϕ_B must be somehow estimated. Notwithstanding, the presence of ϕ_B in (11.79) is controversial since the binary encounter is valid for large momentum transfers implying $\varepsilon_2 \gg U$. Thus the interference term in (11.79) might rigorously be a more complicated term whose form is both uncertain but also irrelevant due to the approximative nature of the binary-encounter model between a free and a pseudo-free electron.

To stay consistent with all the changes introduced in the pseudo-free Mott cross section, namely $\varepsilon_2 \rightarrowtail \varepsilon_2 + \Delta_2$ and $\varepsilon_0 \rightarrowtail \varepsilon_0 + K$, we currently approculate $\phi_B(\varepsilon_2;\varepsilon_0)$ as [793, eq.(4.19)]:

$$\phi_B(\varepsilon_2;\varepsilon_0) \equiv \cos\left(\sqrt{\frac{\mathrm{Ryd}}{\varepsilon_0 + \iota B + \kappa U}}\ln\frac{\varepsilon_2 + (\iota+1)B/2 - (1-\kappa)U/2}{\varepsilon_0 - \varepsilon_2 - (1-\iota)B/2 - (1-\kappa)U/2}\right). \tag{11.83}$$

The function (with $\iota = 1,\ \kappa = 1$) is plotted in figure 8.4b on page 313 in the section 8.5.5 where the Mott scattering was introduced. For binding energies in atmospheric targets ($B \gtrsim \mathrm{Ryd}$), we can see that the image of ϕ_B is situated between ~0.75 and 1, with all minima at $\varepsilon_2 = 0$. If we try to determine the value of ε_0 which minimises $\phi_B(\varepsilon_2 = 0;\varepsilon_0)$, we arrive at a transcendental equation:

$$\ln\sqrt{x} - 1 - \frac{1}{x} = 0 \ \Rightarrow\ x = \frac{\varepsilon_0}{B} \approx 9.1863\ldots\,, \tag{11.84}$$

that we solved through a simple non-linear root-finder (such as Newton-Raphson's method [706, p.274-8, p.633-5]). At this specific energy almost ten times above threshold, the minimal value of ϕ_B is given by:

$$\min_{\varepsilon_0}\phi_B(0;\varepsilon_0) = \min_{\varepsilon_0}\cos\left(2\frac{\sqrt{\mathrm{Ryd}(\varepsilon_0+B)}}{\varepsilon_0}\right) = \cos\left(2\sqrt{\frac{\mathrm{Ryd}}{B}}\frac{\sqrt{x+1}}{x}\right) \ \text{ at } x \approx 9.1863\,. \tag{11.85}$$

From this value, we can also determine the minimal threshold B_{co} below which the interference is no longer monotonically increasing in ε_2. This corresponds to $B_{\mathrm{co}} = 4\mathrm{Ryd}(x+1)/(x\pi)^2 \approx 0.6656\,\mathrm{eV}$.

Since for most targets considered $B \sim \mathrm{Ryd} \gg B_{\mathrm{co}}$ and the fact that the binary encounter requires $\varepsilon_0 \gg B$, the assumption $\phi_B(\varepsilon_2;\varepsilon_0) \simeq 1$ is tacitly taken in most binary-encounter models [412, 507, eq.(13-14), eq.(1)].

The great advantage by defining ϕ_B as (11.83), is that the interference term in (11.79) can be easily integrated analytically:

$$\int_0^{\frac{\varepsilon_0-B}{2}} \frac{\phi_B(\varepsilon_2;\varepsilon_0)}{(\varepsilon_2 + (\iota+1)B/2 - (1-\kappa)U/2)(\varepsilon_0 - \varepsilon_2 - (1-\iota)B/2 - (1-\kappa)U/2)}\,\mathrm{d}\varepsilon_2 \tag{11.86}$$

$$= \frac{\sin\left(\sqrt{\frac{\mathrm{Ryd}}{\varepsilon_0 + \iota B + \kappa U}}\ln\frac{\varepsilon_0 - (1-\iota)B/2 - (1-\kappa)U/2}{(1+\iota)B/2 - (1-\kappa)U/2}\right)}{\sqrt{\mathrm{Ryd}(\varepsilon_0 + \iota B + \kappa U)}}\,, \tag{11.87}$$

which will prove useful in the next subsection for studying total ionisation cross sections. For this, we introduce also the average of the pseudo-free Coulomb-wave interference:

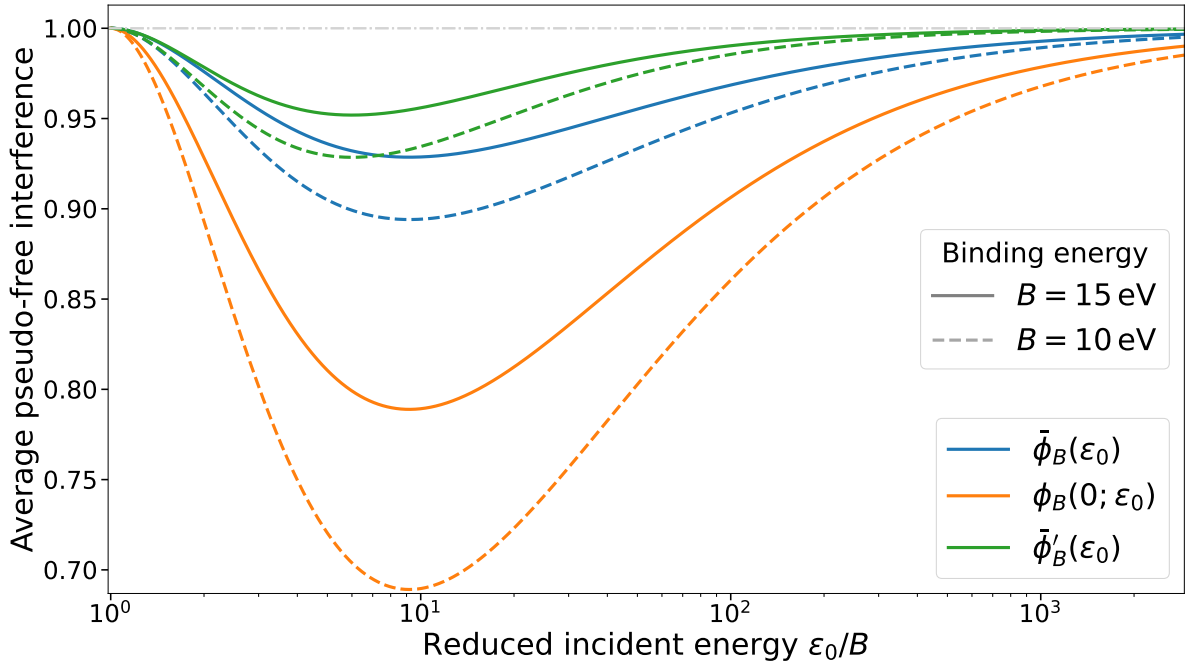

Figure 11.39: Comparison of the true average numerator of the interference term $\bar{\phi}_B(\varepsilon_0)$ from (11.88) and the value used by Vriens [966, eq.(24)] $\phi_B(0;\varepsilon_0)$ from (11.83). Also shown in green is the weighted average ϕ'_B as defined in (11.100) for the binary-encounter-dipole model.

$$\bar{\phi}_B(\varepsilon_0) \equiv \frac{\int_0^{\frac{\varepsilon_0-B}{2}} \frac{\phi_B(\varepsilon_2;\varepsilon_0)}{(\varepsilon_2+B)(\varepsilon_0-\varepsilon_2)}\,\mathrm{d}\varepsilon_2}{\int_0^{\frac{\varepsilon_0-B}{2}} \frac{1}{(\varepsilon_2+B)(\varepsilon_0-\varepsilon_2)}\,\mathrm{d}\varepsilon_2} = \frac{\sin\left(\sqrt{\frac{\mathrm{Ryd}}{\varepsilon_0+B}}\ln\frac{\varepsilon_0}{B}\right)}{\sqrt{\frac{\mathrm{Ryd}}{\varepsilon_0+B}}\ln\frac{\varepsilon_0}{B}}\,. \tag{11.88}$$

This had not been exploited in the past [358, 966, eq.(24), eq.(4)], where a 'recommended' constant value was given but not rigorously calculated, equal to $\cos(\sqrt{\frac{\mathrm{Ryd}}{\varepsilon_0+B}}\ln\frac{\varepsilon_0}{B})$, which actually corresponds to $\phi_B(0;\varepsilon_0)$: the minimum but not the average. As shown in figure 11.39, this systematic underestimation has a slow asymptotic convergence toward 1. This will exaggerate the effect of the interference term [358] which later in figure 11.42 will be shown to be completely irrelevant in the total ionisation cross section given the approximations taken in the binary encounter model.

Although very successful at intermediate energies, the binary-encounter model cannot reproduce the correct energy dependence of the total ionisation cross section at high energies. This is due to the fact that it lacks the dipole interaction which is characterised by small momentum transfers. In the next section, we proceed to combining the advantages of both approaches.

11.5.3 Binary-Encounter-Dipole

Dipole (11.69) and binary-encounter (11.79) interactions are two complementary ways to conceptualise electron impact ionisation on molecules. The former (dipole) describes the global response of the electronic cloud behaving as a dipole under a perturbation from an external electric field, whereas the latter (binary-encounter) idealises a local and sudden impact of the incident electron onto one particular bound electron. Their complementarity can be summarised as:

Theory	Impact Parameter b	Incident Velocity v_0	Momentum Transfer q
Dipole Oscillator	Far	Fast	Small
Binary Encounter	Near	Fast	Large

We see already that both theories rely on the common assumption of fast incident electrons, that is with energies much greater than the average kinetic energies U of the bound electrons: $\varepsilon_0 \gg U$. Inokuti [427, §4.4] showed that both models actually derive (in the specific case of electrons as projectiles) as particular cases to Bethe's theory [64] based on the generalised oscillator strength density $\mathrm{d}F(q,\varepsilon_2)/\mathrm{d}q\,\mathrm{d}\varepsilon_2$.

The dipole approximation assumes $qa_0 \ll 1$ while on the contrary the binary-encounter is based on $(\hbar q)^2/2m_\mathrm{e} \gg B$ with a target electron in an orbital at an energy $-B < 0$.

There have been many early attempts [451, eqs.(7-9)] at constructing a hybrid binary-encounter + dipole-oscillator model for electron impact ionisation. Although their success was encouraging, their empirical nature remained an unattractive part. Later, a parameterless model proposed by Kim and Rudd [507] was able to ally simplicity with effectiveness. The results obtained were satisfactory for a great variety of atomic [506] and molecular [415] targets. In this section, we present and elaborate on the foundation of this model.

All the present discussion here applies specifically to a subshell containing N electrons each with an average kinetic energy U, in an atomic/molecular orbital of a binding energy $B > 0$. Generalisation to the whole target is straightforward through a summation of those partial cross sections for each subshell o:

$$\sigma_\mathrm{ion} = \sum_o \sigma_o(N_o, B_o, U_o) \;, \tag{11.89}$$

Construction

To begin with, the binary-encounter-dipole (BED) singly differential cross section (SDCS) for ionisation $\mathrm{d}\sigma_\mathrm{bed}$ can be viewed asymptotically ($\varepsilon_0 \gg B$) as composed of the dipole oscillator (11.72) and pseudo-free Mott (11.79) cross sections with different coefficients C_d and C_M:

$$\frac{\mathrm{d}\sigma_\mathrm{bed}}{\mathrm{d}\varepsilon_2} \sim \underbrace{\frac{4\pi a_0^2}{\varepsilon_0/\mathrm{Ryd}}}_{\equiv\bar{\sigma}_0} \left[\underbrace{\frac{\mathrm{Ryd}}{(\varepsilon_2+B)}\frac{\mathrm{d}f_\mathrm{d}}{\mathrm{d}\varepsilon_2}}_{\text{dipole}} \left(\ln\frac{\varepsilon_0}{B} + C_\mathrm{d} \right) \right.$$
$$\left. + C_\mathrm{M} N \mathrm{Ryd} \underbrace{\left(\frac{1}{(\varepsilon_2+B)^2} + \frac{1}{(\varepsilon_0-\varepsilon_2)^2} - \frac{\phi_B(\varepsilon_2;\varepsilon_0)}{(\varepsilon_2+B)(\varepsilon_0-\varepsilon_2)} \right)}_{\text{pseudo-free Mott}} \right] . \tag{11.90}$$

In line with the main forms encountered in the literature, we follow the assumption $\iota = \kappa = 1$ for the pseudo-free Mott cross section (11.79) discussed in the previous subsection, which we recall (see 10.2.2) is the soundest approximation when $\varepsilon_0 \ggg B$ and $\varepsilon_1 \gg \varepsilon_2$ in the framework of binary encounters.

We have exposed the simpler *non-relativistic* form, as the procedure does not change when generalising to relativistic energies (exposed in subsection 11.5.3). In the original work [507], C_d was not included, which we add presently to the model. The leading magnitude factor intervenes in all expressions and will be designated henceforth as $\bar{\sigma}_0 = 4\pi a_0^2 \mathrm{Ryd}/\varepsilon_0$. After analysis, $\bar{\sigma}$ will be replaced by the rescaled magnitude $\tilde{\sigma}$ as used in the binary-encounter model [133, 969], which we define here for later reference:

$$\tilde{\sigma}_0 \equiv \frac{4\pi a_0^2 \mathrm{Ryd}}{\varepsilon_0 + U + B} \,, \tag{11.91}$$

in order to account (roughly) for the acceleration of the incident electron in the potential of the molecule/atom.

In (11.90), the binary-encounter contribution $4U/3$ was excluded because it constitutes a higher-order term in the expansion at large momentum transfers [427, eq.(4.87)] which (i) may not be valid in general and (ii) could actually be included mathematically in the dipole term as we will see in later.

Direct comparison with the asymptotic expression from Bethe's theory (10.24) shows that ideally:

$$\begin{aligned} C_\mathrm{d} &\stackrel{?}{=} \ln(4\check{c}(\varepsilon_2)B/\mathrm{Ryd}) \,, \\ C_\mathrm{M} N \frac{\mathrm{d}\sigma_\mathrm{M}}{\mathrm{d}\varepsilon_2} &\stackrel{?}{=} \frac{\mathrm{d}\check{\gamma}}{\mathrm{d}\varepsilon_2}\frac{1}{\varepsilon_0} + O(1/\varepsilon_0^2) \,? \end{aligned}$$

This does however not bring any help, because the functions $\check{c}(\varepsilon_2)$ and $\mathrm{d}\check{\gamma}(\varepsilon_2)/\mathrm{d}\varepsilon_2\,\mathrm{d}q$ depend on the density of the generalised oscillator strength (dGOS): $\mathrm{d}f(\varepsilon_2,q)/\mathrm{d}\varepsilon_2$, which remains unbeknownst to us. Furthermore, the dependence of $\check{c}(\varepsilon_2)$ on ε_2 would force C_d to become a function of ε_2 which goes against our principles. Also, the pseudo-free Mott cross section involves a term $1/(\varepsilon_2+B)^2$ which is independent from ε_0 and so may not be matched to the $1/\varepsilon_0$ term in (11.72). In other words, no sound conclusion can be drawn from the comparison of the SDCS (11.90) and (11.72). This is quite logical, otherwise we would have directly used Bethe's expression, and would not need to approximate it by a dipole and binary-encounter contribution.

An easier path is to take advantage of Bethe's parameters and sum rules (11.70), and proceed instead by comparing the *total* σ_i and *stopping-power* σ_si cross sections from ionisation. In Bethe's theory, they amount asymptotically ($\varepsilon_0 \gg B$) to:

$$\sigma_\mathrm{i} = \int_0^{\frac{\varepsilon_0-B}{2}} \frac{\mathrm{d}\sigma_\mathrm{i}}{\mathrm{d}\varepsilon_2}\,\mathrm{d}\varepsilon_2 \sim \bar{\sigma}_0 \left[(M_\mathrm{i}^2 - O(\frac{1}{\varepsilon_0^{3.5}})) \ln\left(\frac{\varepsilon_0 4c_\mathrm{i}}{\mathrm{Ryd}}\right) + O(\frac{1}{\varepsilon_0}) \right] \tag{11.92a}$$

$$\begin{aligned} \sigma_\mathrm{si} &= \int_0^{\frac{\varepsilon_0-B}{2}} \frac{(\varepsilon_2+B)}{\mathrm{Ryd}} \frac{\mathrm{d}\sigma_\mathrm{i}}{\mathrm{d}\varepsilon_2}\,\mathrm{d}\varepsilon_2 \\ &\sim 2\bar{\sigma}_0 \left[(N_\mathrm{i} - O(\frac{1}{\varepsilon_0^{2.5}})) \ln\left(\frac{\varepsilon_0}{\tilde{B}}\sqrt{\frac{\mathrm{e}}{2}}\right) + \frac{\overline{\Delta N_\mathrm{i}}}{2} \ln\left(\frac{\varepsilon_0(\varepsilon_0-B)}{B^2}\frac{\mathrm{e}}{2}\right) + O(\frac{1}{\varepsilon_0}) \right] \end{aligned} \tag{11.92b}$$

We have introduced the following Bethe parameters which emerge by definition of the differential oscillator strength. They are reminded here [427, eq.(4.30-1)]:

$$N_\mathrm{i} \equiv \int_0^\infty \frac{\mathrm{d}f}{\mathrm{d}\varepsilon_2}\,\mathrm{d}\varepsilon_2 \neq N \tag{11.93}$$

$$M_\mathrm{i}^2 \equiv \int_0^\infty \frac{\mathrm{Ryd}}{\varepsilon_2+B}\frac{\mathrm{d}f}{\mathrm{d}\varepsilon_2}\,\mathrm{d}\varepsilon_2 \tag{11.94}$$

$$\ln c_\mathrm{i} \equiv \frac{1}{M_\mathrm{i}^2}\int_0^\infty \frac{\mathrm{Ryd}}{\varepsilon_2+B}\frac{\mathrm{d}f}{\mathrm{d}\varepsilon_2}\ln\check{c}_\mathrm{i}(\varepsilon_2)\,\mathrm{d}\varepsilon_2 \tag{11.95}$$

$$\ln\left(\frac{\bar{B}}{\mathrm{Ryd}}\right) \equiv \frac{1}{N_\mathrm{i}}\int_0^\infty \frac{\mathrm{d}f}{\mathrm{d}\varepsilon_2}\ln\left(\frac{\varepsilon_2+B}{\mathrm{Ryd}}\right)\mathrm{d}\varepsilon_2 \tag{11.96}$$

Since the integrals in (11.92) do not run to ∞ but stop at $(\varepsilon_0-B)/2$, the asymptotic tail [769] of $\mathrm{d}f/\mathrm{d}\varepsilon_2 \sim 1/(\varepsilon_2)^{3.5}$ may be rigorously removed from N_i and M_i^2. For c_i, this tail is put aside in the $O(1/\varepsilon_0)$ garbage term (this is because of eq.11.127 on page 485 from [427, eq.(4.89)]). The factor 2 in (11.92b) comes from the contributions of $\check{c}(\varepsilon_2)$ after integration [427, eqs.(4.60-3)]. Also, the integral of the dGOS (N_i) does not fully amount to N, because it does not include the discrete excitations which are in principle necessary to complete Bethe's sum rule (11.70). Finally, the residual $\overline{\Delta N_\mathrm{i}}$ represents an average of the dGOS over the kinematically allowed space:

$$\overline{\Delta N_\mathrm{i}}(\varepsilon_0)\cdot\ln\left(\frac{\varepsilon_0(\varepsilon_0-B)}{B^2}\frac{\mathrm{e}}{2}\right) \cong \int_{\ln(\frac{B^2}{4\varepsilon_0\mathrm{Ryd}})}^{\ln(\frac{\varepsilon_0-B}{\mathrm{Ryd}})}\left[-N_\mathrm{i}+\int_0^{\frac{\varepsilon_0-B}{2}}\frac{\mathrm{d}F}{\mathrm{d}\varepsilon_2\,\mathrm{d}q}\,\mathrm{d}\varepsilon_2\right]\mathrm{d}q \tag{11.97}$$

This accounts roughly for the fact that, as the energy due to momentum transfer q becomes larger than the electron binding energy $\hbar^2q^2/2m_\mathrm{e} > B$, the probability of ionisation predominates over discrete excitations. This implies that the Bethe sum when performed at such q is actually very near N: the actual number of bound electron. The factor e/2 (Euler number/2) is a correction that incorporates the effect of electron exchange as indicated in Inokuti [427, eq.(4.63)-§below]. At threshold and asymptotically, this average is constrained as:

$$0 \xleftarrow{\varepsilon_0\simeq B} \overline{\Delta N_\mathrm{i}}(\varepsilon_0) \xrightarrow{\varepsilon_0\gg B} N-N_\mathrm{i}\,. \tag{11.98}$$

It is nevertheless not straightforward to estimate what shape does $\overline{\Delta N_\mathrm{i}}(\varepsilon_0)$ have. One could at first guess a typical $(N-N_\mathrm{i})(1-(B/\varepsilon_0)^a)$ trend, but this is unrigorous and unproven.

At this point, it is important to highlight the notation presently used:

> The Bethe parameters in eqs.(11.93–11.96) are specifically linked to single ionisation events for the N electrons that are bound by B. This does not include multiple ionisation nor ionisation through electrons situated on a different subshell (i.e. with binding energies $\neq B$).
> Their present definition is thus less general than in Inokuti [427] which applies to all ionisation events.

If we now insert the BED (11.90) into those definitions of σ_i and σ_si, we obtain:

$$\sigma_\mathrm{bed} \simeq \bar{\sigma}_0\left[(M_\mathrm{i}^2-O(1/\varepsilon_0^2))\left(\ln(\frac{\varepsilon_0}{B})+C_\mathrm{d}\right)+C_\mathrm{M}N\mathrm{Ryd}\left(\frac{1}{B}-\frac{1}{\varepsilon_0}-\bar{\phi}_B(\varepsilon_0)\frac{\ln(\varepsilon_0/B)}{\varepsilon_0+B}\right)\right] \tag{11.99a}$$

$$\sigma_\mathrm{s,bed} \simeq \bar{\sigma}_0\left[(N_i-O(1/\varepsilon_0))(\ln(\frac{\varepsilon_0}{B})+C_\mathrm{d})+C_\mathrm{M}N\left(\ln\left[\frac{(\varepsilon_0+B)^2}{4B\varepsilon_0}\right]+1-\frac{B}{\varepsilon_0}-\bar{\phi}'_B\ln(\frac{2\varepsilon_0}{\varepsilon_0+B})\right)\right] \tag{11.99b}$$

The weighted average $\bar{\phi}'_B$ is defined as:

$$\bar{\phi}'_B \ln(\frac{2\varepsilon_0}{\varepsilon_0+B}) = \int_0^{\frac{\varepsilon_0-B}{2}} \frac{\phi_B(\varepsilon_2;\varepsilon_0)}{(\varepsilon_0-\varepsilon_2)}\,\mathrm{d}\varepsilon_2\,, \tag{11.100}$$

from the interference term in (11.90) and the multiplication by (ε_2+B) in the stopping-power (11.92b). It is displayed on figure 11.39, where we observe that $\bar{\phi}'_B(\varepsilon_0) > \bar{\phi}_B(\varepsilon_0)$, as could be expected from the multiplication by (ε_2+B) in (11.100). Although $\bar{\phi}'_B$ is not analytical, we can see that it differs at most 5% from 1 and converges rapidly to 1, so applying $\varepsilon_0 \ggg B$ we may safely replace $\bar{\phi}'_B$ by 1 in (11.99b).

The attractiveness of (11.99) as opposed to (11.92) is that the cross sections properly annihilate at threshold $\varepsilon_0 = B$ (M_i^2 is annihilated by the $O(1/\varepsilon_0^2)$ term), and higher orders up to $1/\varepsilon_0$ are included explicitly. In order to proceed to matching (11.99) to (11.92), the BED model splits the leading logarithmic term into two parts:

$$\ln\left(\frac{\varepsilon_0 4c_\mathrm{i}}{\mathrm{Ryd}}\right) = \underbrace{\ln\left(\frac{\varepsilon_0}{B}\right)}_{\text{known}} + \underbrace{\ln\left(\frac{4c_\mathrm{i}B}{\mathrm{Ryd}}\right)}_{\text{unknown}}\,. \tag{11.101}$$

As mentioned before, c_i is problematic and is put to the side. Then, the main contribution to the cross sections in the asymptotic region is bequeathed [507, eq.(34)] to $\ln(\varepsilon_0/B)$. In the limit $\varepsilon_0 \gg B$, it is found that the $1/(\varepsilon_2+B)^2$ term of the pseudo-free Mott cross section stemming from (11.90) has a non-overlookable contribution only in the stopping-power CS. We then arrive to the wedding ceremony of the binary-encounter and dipole models. When all terms that do not vanish with $\varepsilon_0 \gg B$ are included, we equate terms from the Bethe theory (terms on the left) and the BED (terms on the right) :

Integral ionisation CS $\lim\limits_{\varepsilon_0 \ggg B} \sigma_\mathrm{i}(\varepsilon_0)$:

$$M_\mathrm{i}^2\left(\ln(\frac{\varepsilon_0}{B}) + \ln(\frac{4Bc_\mathrm{i}}{\mathrm{Ryd}})\right) = M_\mathrm{i}^2(\ln(\frac{\varepsilon_0}{B}) + C_\mathrm{d}) + C_\mathrm{M}N\frac{\mathrm{Ryd}}{B} \tag{11.102}$$

Ionisation Stopping-Power $\lim\limits_{\varepsilon_0 \ggg B} \sigma_\mathrm{si}(\varepsilon_0)$:

$$\begin{aligned} &2N_\mathrm{i}\left(\ln(\frac{\varepsilon_0}{B}) + \ln(\frac{B}{\bar{B}}) + \frac{1}{2} - \frac{\ln 2}{2}\right) + \overline{\Delta N_\mathrm{i}}(\varepsilon_0)\left(2\ln(\frac{\varepsilon_0}{B}) + 1 - \ln 2\right) \\ &\quad = N_\mathrm{i}\left(\ln(\frac{\varepsilon_0}{B}) + C_\mathrm{d}\right) + C_\mathrm{M}N\left(\ln(\frac{\varepsilon_0}{B}) + 1 - 3\ln 2\right) \\ &\Leftrightarrow (2N - N_\mathrm{i})\ln(\frac{\varepsilon_0}{B}) + 2N_\mathrm{i}\ln(\frac{B}{\bar{B}}) + N(1-\ln 2) = N_\mathrm{i}C_\mathrm{d} + C_\mathrm{M}N\left(\ln(\frac{\varepsilon_0}{B}) + 1 - 3\ln 2\right) \end{aligned} \tag{11.103}$$

From the stopping-power cross section (11.103) we get the constraints:

$$\ln(\frac{\varepsilon_0}{B})\text{ term :} \qquad C_\mathrm{M} = 2 - \frac{N_\mathrm{i}}{N} \tag{11.104}$$

$$\text{Constant term :} \qquad C_\mathrm{d} = 2\ln\frac{B}{\bar{B}} + 1 - \frac{N}{N_\mathrm{i}} + \left(5\frac{N}{N_\mathrm{i}} - 3\right)\ln 2 \tag{11.105}$$

But from the integral cross section, we get a questioned equivalence:

$$\ln(\frac{4c_\mathrm{i}B}{\mathrm{Ryd}}) \stackrel{?}{=} 2\ln\frac{B}{\bar{B}} + 1 - \frac{N}{N_\mathrm{i}} + \left(5\frac{N}{N_\mathrm{i}} - 3\right)\ln 2 + (2N - N_\mathrm{i})\frac{\mathrm{Ryd}}{BM_\mathrm{i}^2}\ ? \tag{11.106}$$

The definition of $C_\mathrm{M} = 2 - N_\mathrm{i}/N$ was already established in Kim and Rudd [507, eq.(41)]. Their questioned equivalence [508, eqs.(27-31)] is different from ours (11.106) due to the present inclusion of the parameter C_d.

Analytical Dipole-Oscillator-Strength

In principle, the above equations from the binary encounter model can be applied to any target molecule/atom if the dipole oscillator strength $\mathrm{d}f/\mathrm{d}\varepsilon_2$ is provided. In practice, this DOS is known with great accuracy only for a few light atoms: H and He in particular. For more complex atoms, one needs to proceed numerically or build upon known hydrogenic DOS [974]; although this reduces the attractiveness of the binary encounter model as easily treated analytically.

As a result, Kim and Rudd [507, eq.(47)] proposed a simple analytical approximation:

$$\frac{\mathrm{d}f_Q}{\mathrm{d}\varepsilon_2} = QNB\left[\frac{1}{(\varepsilon_2+B)^2} + \underbrace{\frac{(\varepsilon_2+B)}{(\varepsilon_0-\varepsilon_2)^3}}_{\text{symmetric}}\right], \tag{11.107}$$

which is properly normalised so that its integral gives $\int_0^\infty \mathrm{d}f_Q = N_\mathrm{i}$. The function f_Q is parametric in Q, which is defined by [507, eq.(49)]:

$$Q \equiv \frac{N_\mathrm{i}}{N} \leq 1\ ,\ \text{since } N_\mathrm{i} \leq N\ . \tag{11.108}$$

Various integrals of $\mathrm{d}f_Q/\mathrm{d}\varepsilon_2$ intervening in the integral and stopping CS can now be calculated exactly:

$$\int_0^{\frac{\varepsilon_0-B}{2}} \frac{\mathrm{d}f_Q}{\mathrm{d}\varepsilon_2}\,\mathrm{d}\varepsilon_2 = QN\left(1+\frac{B}{2\varepsilon_0}\left(1-\frac{B}{\varepsilon_0}\right)-\frac{2B}{\varepsilon_0+B}\right) = N_{\mathrm{i},Q} + O\left(\frac{1}{\varepsilon_0}\right) \tag{11.109}$$

$$\int_0^{\frac{\varepsilon_0-B}{2}} \frac{\mathrm{Ryd}}{\varepsilon_2+B}\frac{\mathrm{d}f_Q}{\mathrm{d}\varepsilon_2}\,\mathrm{d}\varepsilon_2 = Q\frac{N\mathrm{Ryd}}{2B}\left(1-\frac{B^2}{\varepsilon_0^2}\right) = M_{\mathrm{i},Q}^2 + O\left(\frac{1}{\varepsilon_0^2}\right) \tag{11.110}$$

$$\begin{aligned}\int_0^{\frac{\varepsilon_0-B}{2}} \frac{\mathrm{d}f_Q}{\mathrm{d}\varepsilon_2}\ln\left(\frac{\varepsilon_2+B}{\mathrm{Ryd}}\right)\mathrm{d}\varepsilon_2 &= N_{\mathrm{i},Q}\ln\frac{\bar{B}_Q}{\mathrm{Ryd}} + O\left(\frac{\ln\varepsilon_0}{\varepsilon_0}\right) \\ &= N_{\mathrm{i},Q}\underbrace{\left(1+\ln\frac{B}{\mathrm{Ryd}}\right)}_{=\ln(\bar{B}_Q/\mathrm{Ryd})}\left(1+\frac{B}{2\varepsilon_0}\right) + \frac{N_{\mathrm{i},Q}B}{\varepsilon_0+B}\left[\frac{1}{2}\ln\frac{\varepsilon_0}{B} - 2\ln\left(\frac{\varepsilon_0+B}{2\mathrm{Ryd}}\right) - 3\right] - N_{\mathrm{i},Q}\frac{B^2}{2\varepsilon_0^2}\ln\frac{B}{\mathrm{Ryd}}\end{aligned} \tag{11.111}$$

From the last line we find a simple proportionality relationship:

$$\bar{B}_Q = \mathrm{e}B\ , \tag{11.112}$$

that could be verified if the true differential optical oscillator strength were known and inserted into the definition (11.96) of the 'mean ionisation energy' [427, eq.(4.62)].

The questioned equivalence (11.106) now takes a more concrete form:

$$\ln(\frac{4c_\mathrm{i}B}{\mathrm{Ryd}}) \stackrel{?}{=} -\frac{1}{Q}\left(1+Q-(5-3Q)\ln 2\right) + \frac{2(2-Q)}{Q} = \frac{1}{Q}\left(3(1-Q)+(5-3Q)\ln 2\right)\ ? \tag{11.113}$$

We see better now how Q could be adjusted to match the unknown c_i Bethe parameter. If we took $Q = 1$ that would imply:

$$c_\mathrm{i} \stackrel{?}{=} \frac{\mathrm{Ryd}}{B}\ ; \tag{11.114}$$

a relationship that should not be too difficult to examine in practice for a wide range of targets.

Relativistic Model

The formula presented in (11.90) can be generalised to the relativistic domain through the adaptation of the Møller cross section (8.148) to scattering with a pseudo-free electron as done previously with the Mott cross section. The details of converting from the classical to relativistic domain are covered in section (10.2.3), where critiques are addressed to the original [508, eq.(19)] and modified [358, eq.(10)] formulae in the literature. The present version, noted RBED*, takes the form:

$$\frac{\mathrm{d}\sigma_{\text{RBED*}}}{\mathrm{d}\varepsilon_2} = \frac{4\pi a_0^2\alpha^2}{\tilde{\beta}^2}\mathrm{Ryd}\left[\frac{1}{\varepsilon_2+B}\frac{\mathrm{d}f_\mathrm{d}}{\mathrm{d}\varepsilon_2}\left(\ln\left(\frac{m_\mathrm{e}c^2\beta_0^2\gamma_0^2}{2B}\right)-\beta_0^2+C_\mathrm{d}\right)\right. \tag{11.115}$$
$$\left.+(2N-N_\mathrm{i})\left(\frac{1}{(\varepsilon_2+B)^2}+\frac{1}{(\varepsilon_0-\varepsilon_2)^2}+\frac{1}{(m_\mathrm{e}c^2\tilde{\gamma})^2}-\frac{(2\tilde{\gamma}-1)\phi_B(\varepsilon_2;\varepsilon_0)}{\tilde{\gamma}^2(\varepsilon_2+B)(\varepsilon_0-\varepsilon_2)}\right)\right] .$$

The parameter C_d has been defined earlier (11.105). As mentioned before, a crucial aspect of the binary-encounter model (11.90) is rescaling the denominator (11.91) as proposed initially by Burgess [133]. In the relativistic regime, the incident electron *accelerated* in the static atomic potential $\varepsilon_0+U+B \gtrsim$MeV, ideally possesses a velocity linked to the Lorentz parameters:

$$\tilde{\gamma} = 1+\frac{\varepsilon_0+U+B}{m_\mathrm{e}c^2} \quad \text{and} \quad \tilde{\beta}^2 = 1-\frac{1}{\tilde{\gamma}^2} . \tag{11.116}$$

In contrast, the *dipole* interaction is considered to act at *long ranges* where the electron is not so affected by the molecular potential. Therefore, the Lorentz factors involved in the dipole term correspond only to the (unaccelerated) incident energy ε_0:

$$\gamma_0 = 1+\frac{\varepsilon_0}{m_\mathrm{e}c^2} \quad \text{and} \quad \beta_0^2 = 1-\frac{1}{\gamma_0^2} . \tag{11.117}$$

The generalisation of the interference function to the relativistic domain is less certain (cf. section 10.2.3), although it is not crucial, since $\phi_B \to 1$ for fast electrons. We actually recommend taking $\phi_B = 1$ because this effect is irrelevant in the model discussed. The approximation underlying the binary encounter model is far worse that neglecting ϕ_B, this can be checked through the two practically superposed negative dotted curves on figure 11.42. Nevertheless, to soothe the minds that cannot withstand the removal of ϕ_B from the interference in the Mott's modified cross section, we propose*:

$$\phi_B(\varepsilon_2;\varepsilon_0) = \cos\left(\frac{\alpha}{\tilde{\beta}}\sqrt[4]{\frac{\tilde{\gamma}+1}{2\tilde{\gamma}^2}}\ln\frac{\varepsilon_2+B}{\varepsilon_0-\varepsilon_2}\right) . \tag{11.118}$$

The slow $\tilde{\gamma}$ dependence ensures that the velocity does not saturate to $1/\alpha$, which would break the convergence of $\phi_B \to 1$ at extreme $\varepsilon_0 \ggg m_\mathrm{e}c^2$.

*Keeping the ϕ_B in the notation is at least useful for distinguishing wilful negligence from unaware omission

Applying the analytical model seen in the previous subsection with the parameter Q, we may introduce the RBEQ* model:

$$\frac{\mathrm{d}\sigma_{\mathrm{RBEQ*}}}{\mathrm{d}\varepsilon_2} = \frac{4\pi a_0^2 \alpha^2 N}{\tilde{\beta}^2}\mathrm{Ryd}\left[\left(\frac{QB}{(\varepsilon_2+B)^3}+\frac{QB}{(\varepsilon_0-\varepsilon_2)^3}\right)\left(\ln\left(\frac{m_\mathrm{e}c^2\beta_0^2\gamma_0^2}{2B}\right)-\beta_0^2+C_\mathrm{d}\right)\right. \tag{11.119}$$
$$\left.+(2-Q)\left(\frac{1}{(\varepsilon_2+B)^2}+\frac{1}{(\varepsilon_0-\varepsilon_2)^2}+\frac{1}{(m_\mathrm{e}c^2\tilde{\gamma})^2}-\frac{(2\tilde{\gamma}-1)\phi_B(\varepsilon_2;\varepsilon_0)}{\tilde{\gamma}^2(\varepsilon_2+B)(\varepsilon_0-\varepsilon_2)}\right)\right].$$

$$\sigma_{\mathrm{RBEQ*}} = \frac{4\pi a_0^2 \alpha^2 N}{\tilde{\beta}^2}\frac{\mathrm{Ryd}}{B}\left[\frac{Q}{2}\left(1-\frac{B^2}{\varepsilon_0^2}\right)\left(\ln\left(\frac{m_\mathrm{e}c^2\beta_0^2\gamma_0^2}{2B}\right)-\beta_0^2+C_\mathrm{d}\right)\right. \tag{11.120}$$
$$\left.+(2-Q)\left(1-\frac{B}{\varepsilon_0}+\frac{B(\varepsilon_0-B)/2}{(m_\mathrm{e}c^2\tilde{\gamma})^2}-\frac{(2\tilde{\gamma}-1)\bar{\phi}_B(\varepsilon_0)B}{\tilde{\gamma}^2(\varepsilon_0+B)}\ln(\frac{\varepsilon_0}{B})\right)\right].$$

The dipole coefficient $C_\mathrm{d}(Q)$ is obtained through (11.105) and (11.111) as :

$$C_\mathrm{d}(Q) = \frac{-1}{Q}\left(1+Q-(5-3Q)\ln 2\right) \tag{11.121}$$
$$\Rightarrow C_\mathrm{d}(Q=1) = -2(1-\ln 2) \approx -0.6137 \tag{11.122}$$

The average of the Coulomb-wave interference $\bar{\phi}_B(\varepsilon)$ results from applying to (11.88) the replacement of $\sqrt{\mathrm{Ryd}/(\varepsilon_0+B)}$ by $\alpha/\tilde{\beta}\sqrt[4]{(\tilde{\gamma}+1)/2\tilde{\gamma}^2}$ as in (11.118).

Discussion

In total, the (relativistic) binary-encounter-dipole introduced by Kim and Rudd [507] and Kim *et al.* [508] and presently revised has three declinations depending on the choice for dipole oscillator term f:

RBED	RBEQ	RBEB
f_d	f_Q	$f_{Q=1}$
?	(11.107)	(11.107) with $Q=1$

Good knowledge of f_d is only available for atomic Hydrogen and Helium. We will not use here any differential dipole oscillator strength for the atmospheric targets presently studied. This aspect may be deferred to future investigation. Thus, we restrict ourselves to studying the RBEQ and RBEB sub-models.

There are a number of uncertainties linked to the marriage as declared through (11.103-11.106). All of them emerge from the fact that the contract was established asymptotically ($\varepsilon_0 \ggg B$), but nothing guarantees satisfaction over the whole domain of incident energies*

In the original RBED model [507]:

1. Kim and Rudd [507, eq.(29)] used the total stopping power cross section including all inelastic processes instead of the exact (11.92b) stopping power cross section due to ionisation only. The reasons for this are (i) the unknown behaviour of $\overline{\Delta N_\mathrm{i}}$ (11.97) and (ii) the fact that ionisation is the dominant process at high energies implying $N \approx N_\mathrm{i}$.

2. C_d had been totally ignored

3. $\bar{B}$ had been silently substituted by B in (11.103) which actually is its lower boundary.

*This is one of the major causes of discrepancies in physical hybrid models: a miscorrespondence between asymptotic and ordinary behaviour.

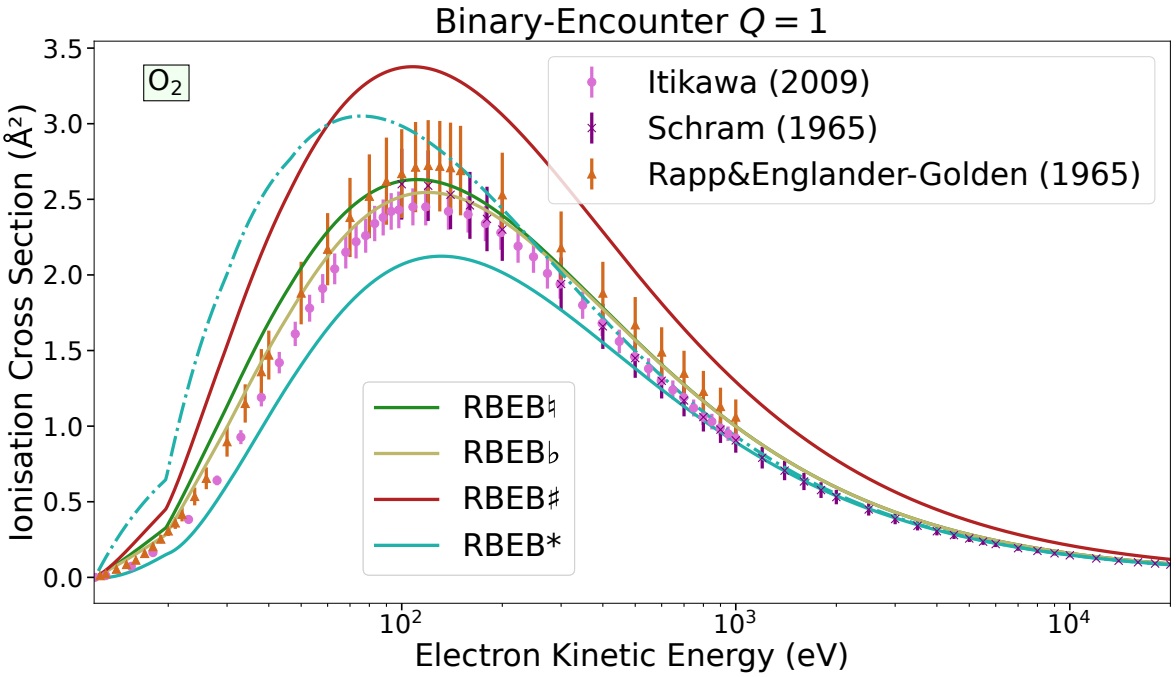

(a) The two original RBEB♮ and asymmetric RBEB♭ models are satisfactory at intermediate energies whereas the revised RBEB* are more accurate asymptotically (the dot-dashed –·–tries to include higher orders $O(1/\varepsilon_0)$). The utter failure of RBEB♯ signifies that f_Q as defined by (11.107) is very well suited.

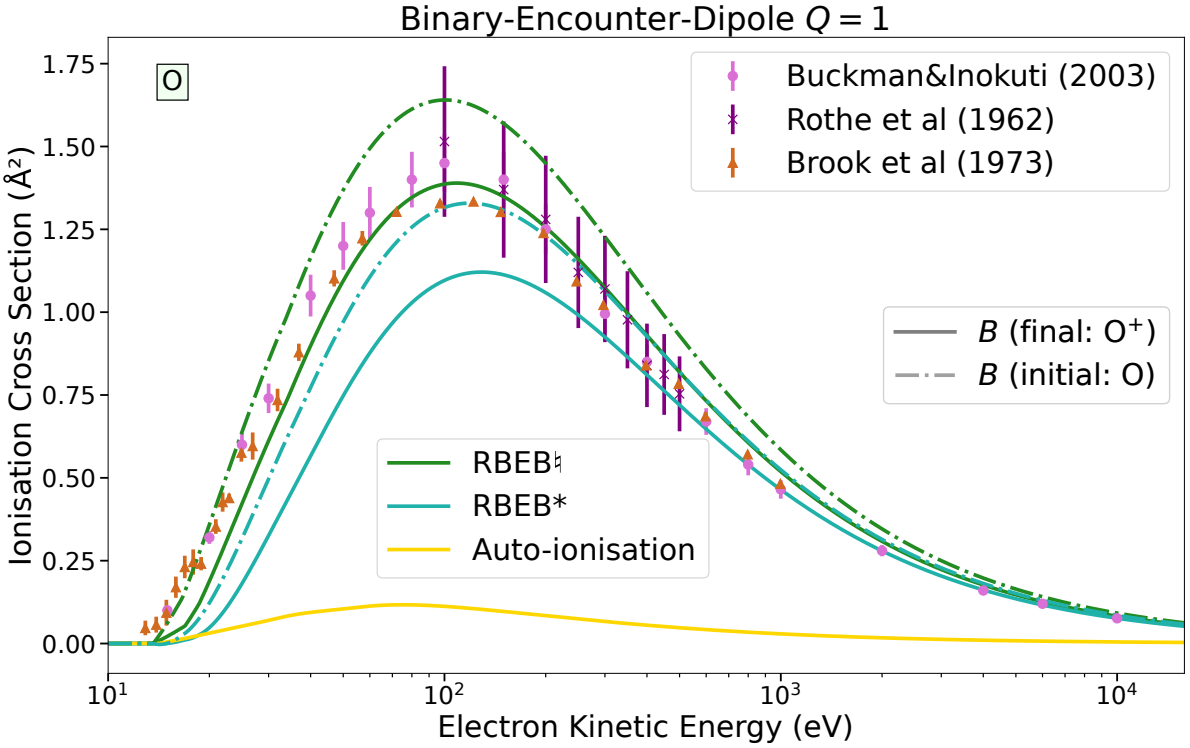

(b) The RBEB are compared when using the original orbital binding energies B (dot-dashed –·–) linked to the initial state of the O neutral atom; and when using the revised ionisation potentials (solid ---) linked to the final excited state of the O^+ ion. The contribution of auto-ionising excited states of O* are also represented (from the fits in table 11.10 below the dashed divider).

Figure 11.40: Comparison of the RBEB sub-model variants for molecular (top) and atomic (bottom) oxygen. The limitations of the RBEB model is due to the imposition of $Q = 1$.

4. It is not clear whether $\mathrm{d}f/\mathrm{d}\varepsilon_2$ should be symmetric with respect to exchange in order to bring better accord of the CS near threshold.

5. The analytical approximation to $\mathrm{d}f/\mathrm{d}\varepsilon_2$ in (11.107) might not be correct asymptotically. Formally, it seems that [769]:

$$\lim_{\varepsilon_2\to\infty}\frac{\mathrm{d}f}{\mathrm{d}\varepsilon_2}\sim\frac{1}{(\varepsilon_2+B)^{7/2}}\,, \tag{11.123}$$

   whereas the DOS as defined in (10.25) behaves as $1/(\varepsilon_2+B)^2$ asymptotically. This results in a mismatch of the higher-order correction terms of M_i^2 and N_i as can be compared in (11.109 vs. 11.92b) (11.110 vs. 11.92a).

6. In general, all higher order $O(1/\varepsilon_0^n)\ :\ n\geq 1$ terms in (11.99a) are not guaranteed to correspond properly to the Bethe theory (11.92a).

7. Minor details were disregarded such as Coulomb-wave interference which was approximated by $\phi_B\to 1$ and generalisation to relativistic energies. This was discussed in section 10.2.3.

Presently, we have tried to push the consistency of the model one step further by using the symmetric form of the DOS and incorporating a correction stemming from a multiplicative constant in the logarithmic term in incident energy: $(\ln(\varepsilon_0/B)+C_\mathrm{d})$ in (11.90) and determined by (11.105). In the list above, these corrections correspond to addressing points 2,3,4 and 7.

In figure 11.40, we show what effect do these corrections bear on the model in the case of O_2 and O. Here, we compare four different versions of the RBEB sub-model with the analytical DOS (11.107) and Q set to 1.

- RBEB$_\natural$ represents the original unaltered* RBEB of Kim *et al.* [508] with the symmetrised version (including exchange) of the DOS (11.107), addressing only point 4 above.

- RBEB$_\flat$ represents the non-symmetrised version (excluding exchange) of the DOS (11.107), addressing none of the points above. The flat $\flat$ was chosen because the symbol does not have a symmetric shape and that the values taken by the cross sections are systematically, albeit slightly, lower than with the symmetrised DOS version.

- RBEB$_\sharp$ represents the model linked to a

$$\frac{\mathrm{d}f}{\mathrm{d}\varepsilon_2}=\frac{N_\mathrm{i}(5/2)}{B}\left[\frac{1}{(\varepsilon_2/B+1)^{7/2}}+\frac{1}{(\varepsilon_0/B-\varepsilon_2/B)^{7/2}}\right], \tag{11.124}$$

  DOS in accordance with Rau and Fano [769] and Inokuti [427, eq.(3.31)], which addresses the points 4 and 5 above. The sharp $\sharp$ was chosen because the symbol is (can be idealised as) symmetric and that it yields higher values of the cross section at lower energies <100 eV.

- RBEB* is the version including both C_d and the symmetric shape of the DOS, addressing points 2,3,4&7 above. The asterisk * is just a way to represent that the model is newer (but not necessarily better) and perhaps more cumbersome.

- A dash-dotted –•– line is a variant of the preceding RBEB*, in which $\bar{B}(\varepsilon_0)$ is allowed to be a function of ε_0 according to the integral (11.111), and thus making $C_\mathrm{d}\nrightarrow C_\mathrm{d}(\varepsilon_0)$ also dependent on ε_0. This corresponds, very loosely, on probing point 6 in the list.

*hence the "bécarre" $\natural$ symbol

We can observe on figure 11.40a that all expressions rapidly converge asymptotically except RBEB♯ because of an unreasonable choice for $\mathrm{d}f/\mathrm{d}\varepsilon_2$ in shape, though we tried to incorporate its predicted asymptotic behaviour. This results in an overestimation of the coefficient M_i^2 multiplying $\ln \varepsilon_0/B$ in (11.92a).

Then, above 300 eV, the best performance is obtained by RBEB∗ thanks to the inclusion of C_d. The collapse of the Born approach in Bethe theory at energies nearing threshold is seen by the utter separation of the dash-dotted (–•–) and solid aquamarine (—) curves which respectively include and neglect the monotonically increasing behaviour of $C_\mathrm{d}(\varepsilon_0)$ with incident energy in virtue of (11.105) through $\bar{B}(\varepsilon_0)$ in (11.111). Although the allowance of $C_\mathrm{d}(\varepsilon_0)$ as a function (dash-dotted –••–) gives the best agreement down to 300 eV, its departure from accuracy at low energies is caused by an improper treatment of higher order terms of $1/\varepsilon_0$ in (11.99).

The least unsatisfactory models below 300 eV are the original RBEB♮ and non-symmetric RBEB♭. The latter, which from a formal point of view is the crudest of all models, is slightly better than the former. This is because taking $Q = 1$ is prone to instigate overestimation of the CS everywhere and especially at low energies. Hence, removing the symmetrical contribution from the DOS (11.107) will mathematically reduce this overestimation.

Which of those models is the best? This is an ill question from the outset since all of them are compared with the assumption that $Q = 1$ which is certainly not true for O_2 due to the very important presence of the Schumann-Runge continuum (optically allowed) in the electron energy loss spectrum (cf. figure 11.32b of previous chapter). This entails that a non-negligible contribution in the Bethe sum of the GOS (11.70) is occupied by electronic excitations making N_i only a fraction of $N = 16$ at $\varepsilon_0 \gtrsim B$.

Furthermore, when comparing to experimental results, there can also arise differences due to the contribution of:

a) Auto-ionisation from states above the first ionisation threshold. This occurs when sub-valence orbital electrons are excited to a Rydberg orbital or to the valence orbital if it is not fully occupied. This contribution is represented for atomic oxygen by the sunny yellow line (—) in figure 11.40b. It more or less accounts for the underestimation of the RBEB♮ sub-model.

b) Ionisation to excited ionic states that are not accounted by ionisation from a subshell. This could be for example ionis/excit-ations to either one of the B,D or C states of N_2^+ because all of them are assumed (from the electron configuration table of Lofthus and Krupenie [607, p.121]) to be mixtures involving at least one state with the $1\pi_g$ orbital occupied*. For atomic oxygen, this effect (expounded later) can be best apprehended by comparing the solid (—) and dash-dotted (–•–) lines on figure 11.40b. An example of partial contributions from excited ionic states of atomic nitrogen is given by the dashed (- - -) lines in figure 11.41a.

c) Ionisation from low lying metastable states present in the gas beam. This is typically the case of atomic nitrogen data, as seen on figure 11.41, from the contribution of the $\mathrm{N}\,^2D^o$ metastable state, believed to be present in Brook *et al.*'s [117, table 5] experiment due to the method used to produce atomic beams. Apparently, the contamination of metastable states for oxygen is not as high [930, 1010] and thus good agreement (cf. fig. 11.40b) can be obtained just by using ionisation from its ground ^3P state.

Kim and Desclaux [506] considered these three additional aspects when comparing the RBEB to the measured total cross sections for ionisation of C,N and O atoms (see fig. 11.41b).

*N_2 ground state's last occupied orbital is $3\sigma_g < 1\pi_g$.

Once again, compelling agreement was obtained within the framework of the approximation and the uncertainty of the experimental conditions. This result is nonetheless at the cost of complexifying the model which now has to involve a weighted sum of excitations that lead to a different excited state of the ion.

For a fixed electronic configuration, the final state of the ion may correspond to a certain LS coupling (total ionic orbital and spin momentum, see appendix C.1). Assuming that the probability of excitation to one of the states is proportional to its multiplicity $(2L+1)(2S+1)$, the weighted sum of the direct ionisation (not including auto-ionisation) is [506, eq.(2&3)]:

$$\sigma_{\text{direct}} = \frac{1}{N_{\text{mult}}} \sum_{LS} (2L+1)(2S+1)\sigma_{LS} \,, \tag{11.125}$$

where $N_{\text{mult}} = \sum_{LS}(2L+1)(2S+1)$ is the summed multiplicity of all ionic states with a different LS state.

As an example, we take atomic nitrogen [506, table I] which can be ionised in the three following ways (five if fine-structure is taken into account) for the $(2s^2\,2p^2)$ configuration:

$$\mathrm{N}(2s^2\,2p^3)\,{}^4S^o_{3/2} \rightarrow \mathrm{N}^+(2s^2\,2p^2) \begin{cases} {}^3P_0\,(14.53\,\mathrm{eV}),\ {}^3P_1\,(14.54\,\mathrm{eV}),\ {}^3P_2\,(14.55\,\mathrm{eV}) \\ {}^1D_2\,(16.43\,\mathrm{eV}) \\ {}^1S_0\,(18.59\,\mathrm{eV}) \end{cases} \tag{11.126}$$

At the same time, the orbital structure of the N ground-state atom is [506, table II]:

Orbital	B (eV)	U (eV)	N
$1s_{1/2}$	425.469	598.726	2
$2s_{1/2}$	25.828	65.656	2
$2p_{1/2}$	15.439	51.094	1.0025
$2p_{3/2}$	14.534	51.034	1.9975

Originally, Kim and Desclaux [506] used the ionisation potentials of the excited states in (11.126) as B and the U and N values in the table above. It is nonetheless not clear whether the only orbital used was $2p_{3/2}$ (with B replaced) or whether inner orbitals $1s$, $2s$ were also included, and what was done with the $2p_{1/2}$ orbital (included, modified, discarded?).

In order to bring clarification and simplification of this procedure, we propose to restructure the input values in the RBEB model. First, we quote a fundamental aspect of the model:

Kim and Desclaux [506, §II.B]

> [...] the target data [B, U, and N] used in [the RBEB model] are those for the initial state only. No final-state data are used explicitly, except indirectly through the ionization energy B.

As a consequence, we decide to reverse the logic of the model and take the point of view of the final ionic state. Instead of viewing a target (atom or molecule) as a structured set of electrons bound in orbitals with different average kinetic energies, we propose to conceptualise it as a set of *open-channels* with different activation thresholds B that lead to a determined *final* state of the ion.

This interpretation is the correct one regarding the dipole oscillator strength: the B in (11.90) now corresponds to the ionisation potential I_i as defined and used in the original Bethe theory (11.72). For the binary-encounter model this represents a shift of perspective:

Upon meeting a bound electron, the incident electron asks:
~~Initial-state~~ →"~~What is the price of your freedom (B_o) ?~~"
Final-state →"What should I pay (I_i) in order to leave your ion in tranquillity ?"

We see that the question of ionisation is now posed to the target as a whole, instead of a single electron. This is a more pertinent question since the ion may be left only in a determined state. In case of molecules, this may even lead to a vibrationally excited state! Thus it is not important to know necessarily the structure of the initial state rather than the open-channels that lead to ionisation.

To reinstate this new perspective into the RBEB model we propose to use the statistical multiplicity $(2L+1)(2S+1)/N_{\text{mult}}$ as the new factor determining the number of electrons N in a virtual subshell. Therefore, we now have:

Orbital Transition	B (eV)	U (eV)	N
$1s_{1/2}$	425.469	598.726	2
$(2s)^{-1} \rightarrow \mathrm{N}^+\ {}^5S^o$	20.34	65.656	$\frac{(1)\cdot 5}{40}\cdot 2 = \frac{1}{4} = 0.25$
$(2s)^{-1} \rightarrow \mathrm{N}^+\ {}^3D^o$	25.97	65.656	$\frac{(2\cdot 2+1)\cdot 3}{40}\cdot 2 = \frac{3}{4} = 0.75$
$(2s)^{-1} \rightarrow \mathrm{N}^+\ {}^3P^o$	28.08	65.656	$\frac{(2\cdot 1+1)\cdot 3}{40}\cdot 2 = \frac{9}{20} = 0.45$
$(2s)^{-1} \rightarrow \mathrm{N}^+\ {}^1D^o$	31.42	65.656	$\frac{(2\cdot 2+1)\cdot 1}{40}\cdot 2 = \frac{1}{4} = 0.25$
$(2s)^{-1} \rightarrow \mathrm{N}^+\ {}^3S^o$	33.78	65.656	$\frac{(1)\cdot 3}{40}\cdot 2 = \frac{3}{20} = 0.15$
$(2s)^{-1} \rightarrow \mathrm{N}^+\ {}^1P^o$	35.22	65.656	$\frac{(2\cdot 1+1)\cdot 1}{40}\cdot 2 = \frac{3}{20} = 0.15$
$(2p)^{-1} \rightarrow \mathrm{N}^+\ {}^3P$	14.545	51.094	$\frac{(2\cdot 1+1)\cdot 3}{15}\cdot 3 = \frac{9}{5} = 1.8$
$(2p)^{-1} \rightarrow \mathrm{N}^+\ {}^1D$	16.43	51.034	$\frac{(2\cdot 2+1)\cdot 1}{15}\cdot 3 = \frac{15}{15} = 1$
$(2p)^{-1} \rightarrow \mathrm{N}^+\ {}^1S$	18.59	51.034	$\frac{1\cdot 1}{15}\cdot 3 = \frac{1}{5} = 0.2$

This perspective is now tested on figure 11.41a to be compared against the original perspective reference 11.41b below. Two differences arise. First, the $\mathrm{N}^+(2s^1\,2p^3)$ contribution in our version 11.41a, seems to have been lumped together in the 'Partial, $\mathrm{N}^+(^3P)$' of Kim and Desclaux's figure on 11.41b-right [506]. Second, we used a very crude approximation to account for auto-ionisation from the $\mathrm{N}(2s2p^4)\,{}^2D$ state which systematically underestimates the one in figure 11.41b-left. Besides these differences, the correspondence is quite good. We may thus conclude that the change in perspective (final-state instead of initial-state) is a useful shortcut since it is mathematically equivalent though conceptually different.

We recommend thus that the orbital structure of targets be now interpreted with regards to the probability of producing an ion in a certain final state. This very simplistic perspective overlooks the complexity of determining which orbital did the ejected electron come from and whether the interaction perturbed other neighbouring electrons to the point of switching orbitals and/or flipping their spin, and whether they could have exchanged places with the incident electron, etc. In brief, it completely bypasses the realm of quantum physics as unfolded through Schrödinger's equation of the electron-molecule compound.

Overall, we must recall that the binary-encounter-dipole model is only defined so as to annihilate at threshold ($\varepsilon_0 = B$) and adjusted to decay asymptotically ($\varepsilon_0 \gg B$) as predicted by the Bethe theory. Therefore, the gap in the region of interest $\varepsilon_0 \gtrsim B$ is filled in a completely blind manner! Yet, the original model works astonishingly well even when none of the aforementioned issues are addressed duly. Notwithstanding the success of the RBEB sub-model, it was repeatedly apprised in Kim and Desclaux [506] and Kim *et al.* [508, §II.D, §II.B&C] that it is not clear how the simplicity of the model might compromise the exactitude of results obtained.

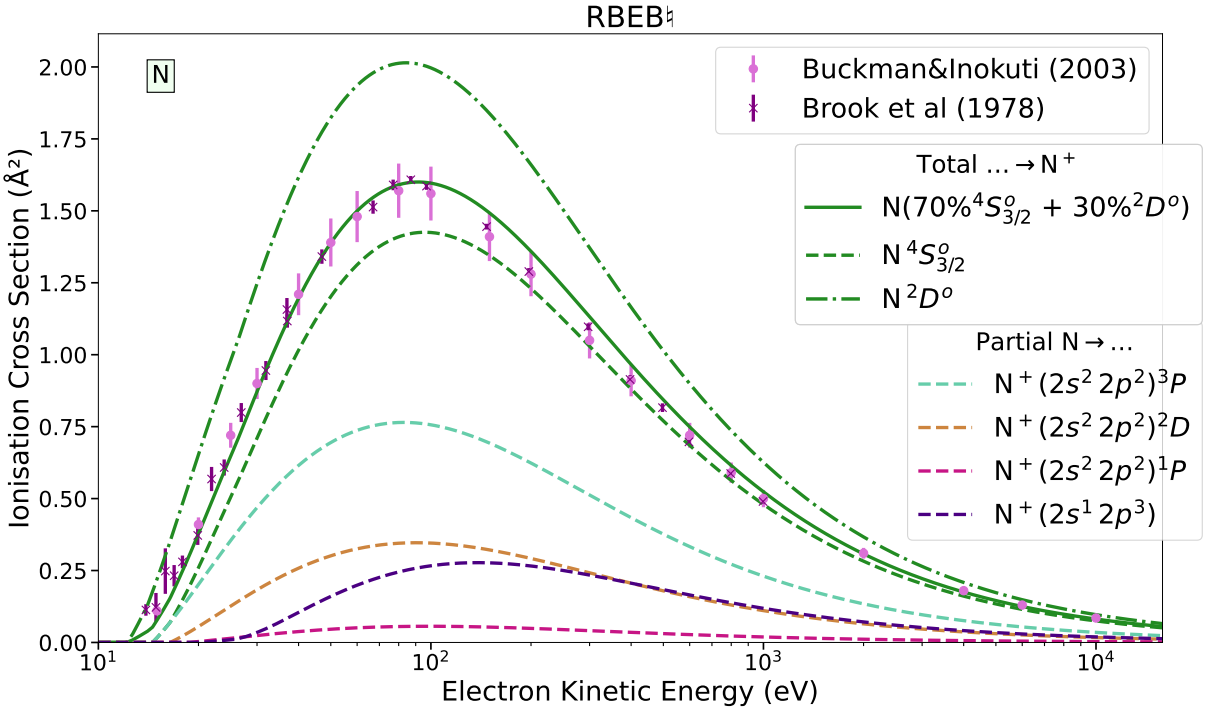

(a) Final-state perspective: Reinstated RBEB$_\natural$ model where B corresponds now to ionisation potentials that lead to a particular ionic state LS and N to its statistical ratio.

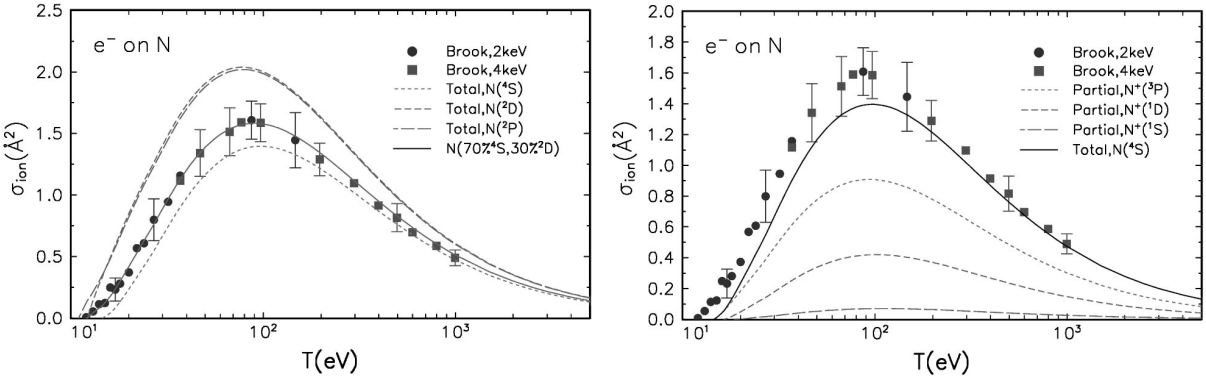

(b) Initial-state perspective: Data from Kim and Desclaux [506] where a weighted sum (11.125) of different final ionic states LS is used.

Figure 11.41: Comparison of the original RBEB$_\natural$ with experimental for atomic nitrogen which is believed to contain a 70% N $^4S^o_{3/2}$ and 30% N $^2D^o$ mixture due to the production method used. The N$^2D^o$ also includes auto-ionisation from the N$(2s2p^4)\,^2D$ state.

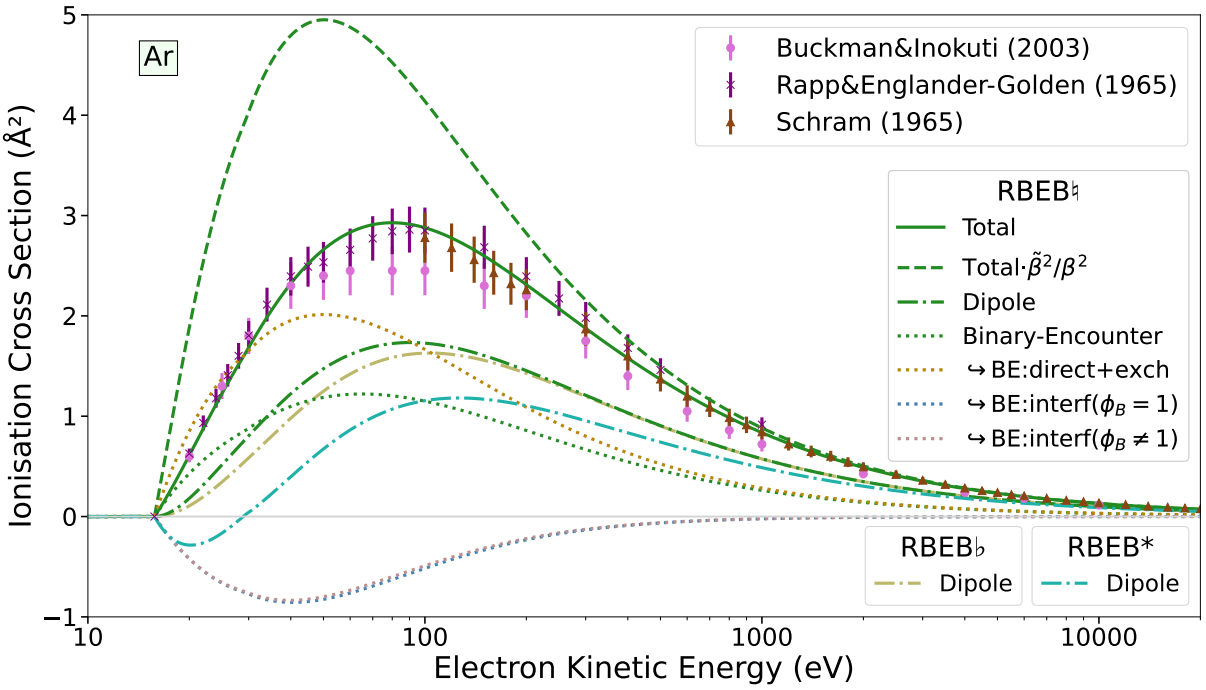

Figure 11.42: Decomposition of the RBEB model illustrated for Argon. The dashed (- - -) line shows the effect of rescaling the leading denominator through (11.91) or (11.116). The dipole contribution (–•–) is separated from the binary-encounter (BE ···). The main effect of the RBEB* revision is to change the shape of the dipole term through the C_d coefficient (11.105) added to the logarithm $\ln \varepsilon_0/B$ in (11.120). The binary-encounter contribution (···) is further decomposed in the direct+exchange terms of the pseudo-free Mott cross section (11.79) and the interference where the effect of ϕ_B (11.118) is of lowest importance.

Conversely, as we saw with our revisions, the search for deeper accuracy through corrective terms can unravel the simplicity of the model, its attractiveness and even its accuracy. We may already formulate a pre-conclusion:

> Imposing $Q = 1$ severely restrains the improvements that can be made on the binary-encounter-dipole model and the physical conclusions that can drawn from its practical application.

If we wish to preserve the present improvements proposed so far, we must explore the concealed secrets behind the success of the RBEB model. To this end, we first decompose the equation (11.120) underlying the model as shown in figure 11.42. We see that the most important ingredient is the rescaling of the cross section's denominator through (11.91) or (11.116). Next, the dipole and binary-encounter terms are complementary: the former dominates asymptotically while the latter determines the near-threshold behaviour. The binary-encounter is moderated by the (negative) interference term. A synthetic view of the RBEB model is given below.

Incident velocity	Main ingredient, lowers the CS at $\varepsilon_0 \lesssim 4(U+B)$ by more than 80 %.
rescaling	Critical for proper near-threshold behaviour.
Dipole	Slow asymptotic tail of the cross section ($\varepsilon_0 \sim 10\,\mathrm{keV} \ggg B$)
	Sign of derivative at threshold determined by C_d.
Binary-encounter	Dictates the behaviour at threshold

Direct :	$1/\varepsilon_0$ asymptotic tail.
Exchange :	$1/\varepsilon_0^2$ asymptotic tail.
Interference :	negative $\ln(\varepsilon_0)/\varepsilon_0^2$ asymptotic tail.

Finally, our revised RBEB* model implies a significant reduction of the dipole term through $C_\mathrm{d} < 0$ which even induces negative values near threshold. We recall here from (11.121) that $C_\mathrm{d}(Q)$ is a monotonically decreasing function in the range $Q \in [0,1]$ taking its minimum $\min C_\mathrm{d} \approx -0.6137$ at $Q = 1$ and annihilating at $Q \approx 0.8$ as shown here-against (fig.11.43).

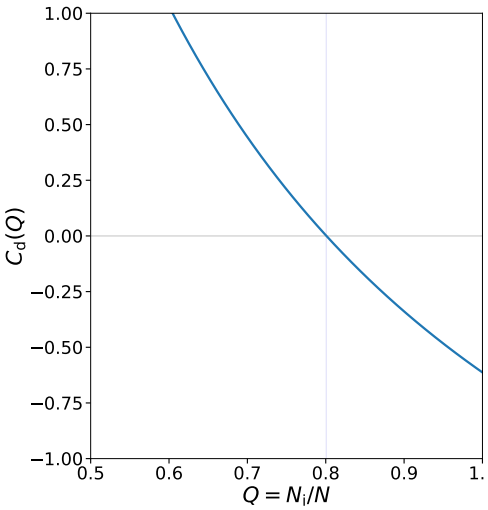

Figure 11.43: $C_\mathrm{d}(Q)$ dipole offset in RBEQ* model from (11.121) as a function of Q.

This demonstrates already that the distinction between dipole and binary-encounter contributions is blurred at low energies. The behaviour of $C_\mathrm{d}(Q)$ as a function of Q is crucial in determining the effect of Q on the RBEQ sub-model.

We illustrate how the partial ionisations from different shells scale with Q in two comparative graphs in figure 11.44a for RBEQ$\natural$ and 11.44b for RBEQ* models. At first sight, it would seem that the RBEQ$\natural$ and RBEB* react oppositely to the adjustment of Q. A closer inspection reveals that this is not inherently true because they both increase near threshold and decrease asymptotically when $Q \to 0$ is tuned down. Their radical difference lies in the crossing point ε_Q at which the curves switch trends with Q. For RBEQ$\natural$ this point $\varepsilon_Q \simeq 2B$ is much lower than for RBEQ* ($\varepsilon_Q >$ keV). This time, if we compare qualitatively the matching of experimental data by the shapes, we see that the revised RBEQ* has a much better adjustability to the single non-dissociative ionisation of N_2 than the original RBEQ$\natural$. We can also deduce that there is not a univocal correspondence between the orbital ionised and the dissociative ionisation. Explicitly, some ionisation events from the $2\sigma_u$ subshell of N_2 lead to dissociation while others not. There is a branching ratio associated with each ionic excitation channel involved. The dissociation energy [228] of N_2^+ is at ≃15.58+8.72=24.30eV. In the experimental data [596, p.62-3:table 5.1.44] shown on 11.44, the onset of dissociative ionisation starts around ~30 eV. This dissociative process may either be direct or come from predissociation (cf. appendix D). For core K-shells (1σ), dissociation is systematic due to an "Auger shower" and "Coulombic explosion" to put it in Berkowitz's [62, p.216:bottom] terms.

From this analysis, we can conclude that taking $Q \simeq 1$ might not necessarily be a good assumption since the RBEQ* sub-model is sensitive to Q and as opposed to the original RBEQ$\natural$, the missing percentage to the completion of $Q = N_\mathrm{i}/N$ is directly reflected on the value of the cross section. For molecules which have a manifold of optically allowed excitations including auto-ionising states, the contribution of ionisation (i.e. N_i from 11.93) can be an underwhelming fraction of N, the total electrons in a subshell that figuratively participate in a set of open-channel reactions. This will clarified in the next section.

In order to ensure that all partial cross section be positive near threshold, we need to make an additional amendment regarding $C_\mathrm{d}(Q)$. In principle, $Q < 0.8$ will guarantee that all cross sections are positive. However, this restriction on Q is unfounded and cannot be applied.

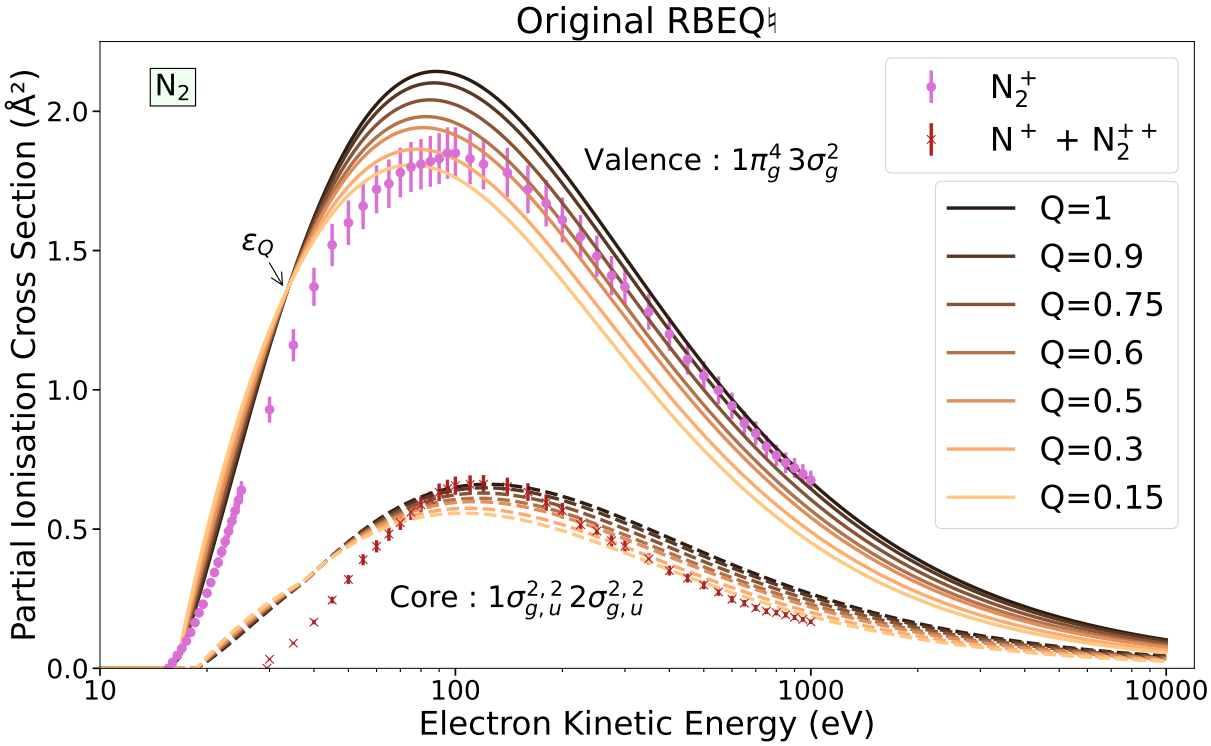

(a) The magnitude of the cross section from the RBEQ♮ sub-model shrinks with Q. Only a small portion below the crossing point $\varepsilon_Q \simeq 30\,\text{eV}$ inflates very slightly as Q decreases. Although the shapes do not match the partial ionisation cross sections, their sum reproduces more or less the total cross section.

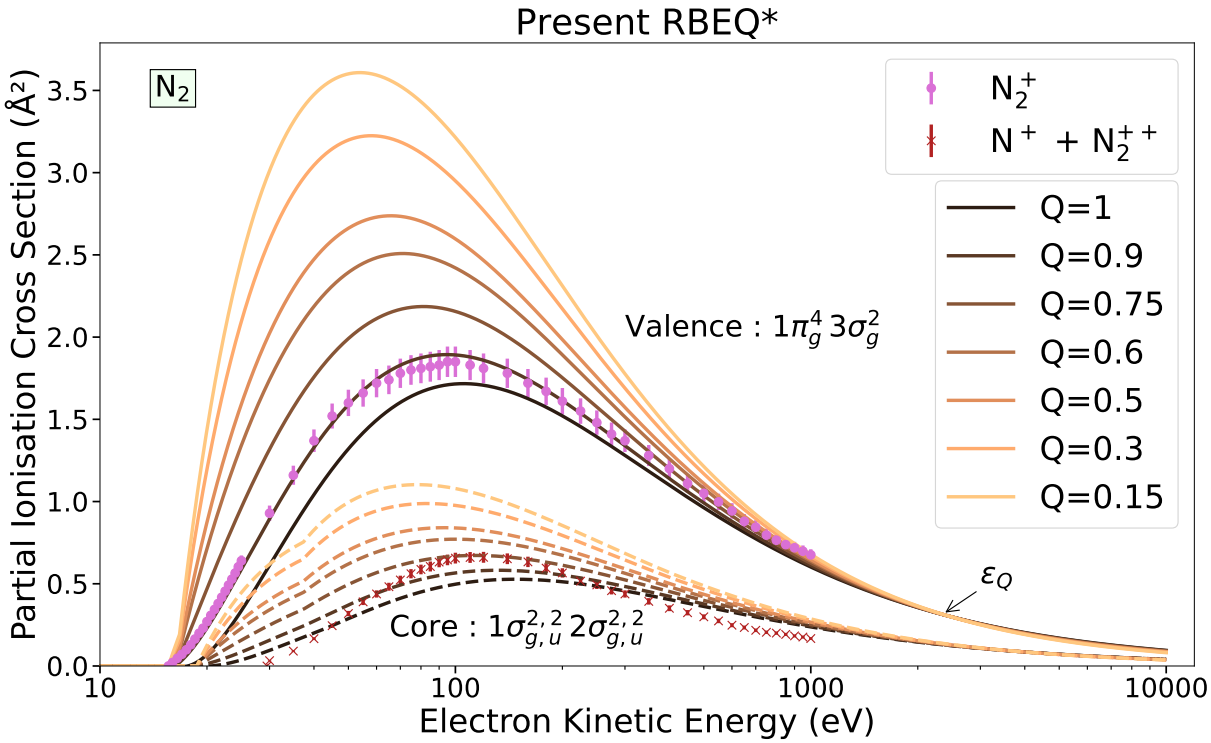

(b) The RBEQ* sub-model is quite sensitive to Q and its maximum increases as Q decreases. This trend reverses at the crossing point ε_Q beyond 1 keV.

Figure 11.44: Behaviour of RBEQ with the parameter Q for two shell groups of molecular nitrogen. Those are compared to experimental data for partial (single and dissociative+double) ionisation from Lindsay and Mangan [596, table 5.1.44].

There are only two options that are at our disposal for the time-being.

i. C_d be multiplied by a quenching factor $\to C_\mathrm{d}\cdot(1-b(B/\varepsilon_0)^a)$, where a and b would need to be determined.

ii. The total dipole + binary-encounter cross section be enforced to zero where otherwise it would be negative.

Option i. is intuitive but is not flawless, and its *ad hoc* character is somewhat deterring. Here lies an opportunity to reconcile the ionisation threshold law of the RBEQ* model with the Wannier [976] theory that may be examined in future investigations. Presently, since all considerations were based asymptotically, we do not recommend to succumb to the empiricist's secret weapon of *ad hoc* magic. We simply recognise that the limitative aspect of our approach at low energies and decide to opt for the amendment ii. For total ionisation cross sections, this will not pose any problem since the constraints require that the summed cross section be positive. However, when applying to a subshell by subshell analysis, there are some unforeseen risks that have to be tackled.

Before we close this section, we now unveil what property made the RBEB$\natural$ an unbeatable opponent in simplistic yet accurate modelling of electron impact ionisation. In his seminal review, Inokuti [427, eq.(4.25) and (4.89)] discloses the fundamental behaviour of the unknown $\ln\check{c}_\mathrm{i}(\varepsilon_2)$ parameter seen previously in (11.72):

$$\boxed{\frac{\mathrm{Ryd}}{\varepsilon_2+B}\frac{\mathrm{d}F}{\mathrm{d}\varepsilon_2}\ln\check{c}_\mathrm{i}(\varepsilon_2)\sim N\left(\frac{\mathrm{Ryd}}{(\varepsilon_2+B)}\right)^2.} \tag{11.127}$$

This formula clearly expounds the connection point and complicity between the dipole and binary-encounter models. To strike the minds of the readership, the mathematical layout (11.128) can help.

$$\begin{aligned}\frac{\mathrm{d}\sigma_\mathrm{i}}{\mathrm{d}\varepsilon_2}=\frac{4\pi a_0^2}{\varepsilon_0/\mathrm{Ryd}}\Bigg(&\underbrace{\frac{\mathrm{Ryd}}{\varepsilon_2+B}\frac{\mathrm{d}F}{\mathrm{d}\varepsilon_2}\left(\ln\frac{\varepsilon_0}{B}+\ln\frac{4B}{\mathrm{Ryd}}\right)}_{\downarrow}+\underbrace{\frac{\mathrm{Ryd}}{\varepsilon_2+B}\frac{\mathrm{d}F}{\mathrm{d}\varepsilon_2}\ln\check{c}_\mathrm{i}(\varepsilon_2)}_{\downarrow}+\underbrace{\frac{\mathrm{d}\check{\gamma}_\mathrm{i}(\varepsilon_2)}{\mathrm{d}\varepsilon_2}\frac{\mathrm{Ryd}}{\varepsilon_0}}_{?\downarrow?}+O(\frac{1}{\varepsilon_0^2})\Bigg)\\ &\underbrace{\frac{\mathrm{Ryd}}{\varepsilon_2+B}\frac{\mathrm{d}f_\mathrm{d}}{\mathrm{d}\varepsilon_2}\left(\ln\frac{\varepsilon_0}{B}+C_\mathrm{d}\right)}_{\text{dipole}}+\underbrace{\frac{N\mathrm{Ryd}}{(\varepsilon_2+B)^2}}_{\text{binary-encounter}}+\underbrace{\frac{N\mathrm{Ryd}}{(\varepsilon_2+B)(\varepsilon_0-\varepsilon_2)}}_{\text{interference}}\end{aligned} \tag{11.128}$$

We now get to another corner of the binary-encounter-dipole model, where one doesn't know well what to do with the $\overline{\Delta N_\mathrm{i}}$ residue as defined by (11.97) which is necessary to patch the correct integral total (11.102) and stopping-power (11.103) cross sections for ionisation. This is to say that although asymptotic relations are well determined, there is much leeway left in the region of interest $\varepsilon_0\gtrsim B$. Why does the binary-encounter seem to complement well the dipole term even in non-asymptotic regions is subject to further questioning. Likely, it stems from the fact that at lower energies, the partition of energy is more equal between the secondary and primary electron, which validates the use of the binary-encounter cross section meant to be used at large energy transfers $\varepsilon_2\lesssim(\varepsilon_0-B)/2$ (also see discussion in 10.2.2).

There are still many ways one could try to deepen the consistency of the binary-encounter-dipole model, nevertheless, it is not certain whether this would lead to a significant and systematic improvement over the results obtained; given the number of approximations and *ad hoc* modifications introduced...

11.5.4 Cross Sections

We now quietly leave the realm of scientific pondering and go back to practical purposes: the determination of total, singly and doubly differential ionisation cross sections.

We provide total (11.120) and singly differential (11.119) cross sections by our revised RBEQ* model, with all parameters tabulated in table 11.12.
For simulating angular scattering of the secondary electron $\Omega_2 = (\theta_2, \varphi_2)$, we propose a provisional sampling method (11.132).
Angular scattering of primary electrons $\Omega_1 = (\theta_1, \varphi_1) = (\theta_+, \varphi_+)^a$ is deterministic (in θ_1) according to the relativistic binary encounter model (2.60) but neglecting the kinetic momentum of the bound electron.

[a] Notations differ slightly between part I and part II

Total cross sections were determined from the RBEQ* model represented by (11.120). A constrained fit on Q_o was performed for each subshell/open-channel o of the atomic or molecular target. The constraints imposed were the following:

a) $Q_{o=1} = 1$

b) $0.1 \leq Q_o \leq 1 \quad \forall o > 1$

c) $\min N_\mathrm{i} \leq \sum_o N_o \cdot Q_o \leq \max N_\mathrm{i}$

Here, all K-shells are represented by $o = 1$, their contribution to ionisation is so minimal that it is not pertinent to try to perform a fit on the $Q_{o=1}$ parameter involved. Besides, if a very unlikely K-shell excitation happens, it is most probably going to lead to ionisation. It is hard to imagine that an electron that came from a K-shell would be stuck in a Rydberg state, since the instability of the hole in the K-shell would inevitably cause (multiple) auto-ionisation and dissociation in molecules. In general, $Q_o = 1$ for core o orbitals.

For the remaining subshells, the lower boundary 0.1 of Q is arbitrary. Even though it is evident that such a low value is unlikely, for practical purposes, it is safer to leave the algorithm realise itself that such a value would give an absurd result.

The sum on the product of Q_o and N_o is the most effective of the constraints. The values $\min N_\mathrm{i}$ and $\max N_\mathrm{i}$ reflect the knowledge we have about Bethe sums of a given molecule or atom. Those values are determined from the optical oscillator strengths tabulated in Berkowitz [62]. The maximum $\max N_\mathrm{i} = N - \sum_x f_x$ is simply the subtraction of the discrete excitations f_x from the total electron number N in the target. The minimum $\min N_\mathrm{i} = \int \mathrm{d} f_\mathrm{i}(q, \varepsilon_2)$ is the derived integral of the differential oscillator strength over a region of probed energies.

For atoms, an even finer constraint on Q_o was possible by subtracting the sum of oscillator strengths f_x pertaining to excitations from a given orbital configuration. For argon, the sum of f_x for excitations from the $3p$ orbital is at least 0.8. Since, the $3p$ subshell is populated by 6 electrons, we constrained its Q value as $(16.53 - 12)/6 < Q_{3p} < (6 - 0.8)/6$. The lower boundary comes from the minimal value of the oscillator strength from ionisation and the twelve electrons in lower $< 3p$ shells. An overview of subshell constraints for O and N is given in the descriptive list below.

With these constraints, we performed a least-squares minimisation algorithm on the most recommended experimental values of ionisation for all the atmospheric gas targets. A summary of the fits is presented in table 11.12 and displayed in figure 11.45. The table also includes the revisited orbital/open-channel structure described in the discussion of the previous section.

A glossary of the bibliographic sources for each element is given below. Most of these data are also available online on Kramida *et al.* [539].

N_2 B – Lofthus and Krupenie [607, p.198:table 3] : average of observed values

U – Hwang *et al.* [415, p.2958:tab. I] and Santos *et al.* [805, p.4215:tab. 1] for core K-shell

N_i – Berkowitz [62, p.100:table 9]

O_2 B – (1σ) [565], $(2\sigma_g)$ [318], Edqvist *et al.* [259, p.27:table I] for the rest

U – Hwang *et al.* [415, p.2958:tab. I] and Santos *et al.* [805, p.4215:tab. 1] for core K-shell

N_i – Berkowitz [62, p.107:table 11]

NO B – (1σ, 2σ and 3σ) averages from Davis and Shirley [211] and Edqvist *et al.* [260, table 2]; for the rest, representative values of the band onsets

U – Hwang *et al.* [415, p.2958:table I] and respective U from O_2 (1σ) and N_2 (2σ) for deepest core.

N_i – Berkowitz [62, p.113:table 14]

Ar B – Jolly *et al.* [464, p.444] ($2s$ and $2p$) and Williams [983]; average over orbitals as $B(np) = \frac{1}{3}B(np_{1/2}) + \frac{2}{3}B(np_{3/2})$.

U – Santos *et al.* [805, p.4215:table 1] for K-shell and calculated averages $\langle|-i\hbar\nabla\Psi(\mathbf{r})|^2\rangle/2m_e$ from analytical Slater orbitals $\Psi(r)$ of Koga *et al.* [523].

N_i – Berkowitz [62, p.84:table 3]

O B – Kim and Desclaux [506, p.6:table II] ($1s$ and $2s$) and Moore [658] for $2p$ open channels

U – Kim and Desclaux [506, p.6:table II] for $2p$ open channels the values are arbitrarily chosen from $2p_{1/2}$ and $2p_{3/2}$ orbitals*.

N_i – Doering *et al.* [225, p.84:table 3] and Tayal and Zatsarinny [921, table II] optical oscillator strengths

$(2s\,2p^5)\,^3P^o$	= 0.07		$O^+(^4P)$	
$(3s'')\,^3D^o$	= 0.086	subtracted	$O^+(^2P^o)$	
$(3s')\,^3D^o + (4s')\,^3D^o$	= 0.071	from the	$O^+(^2D^o)$	channel
$(3s)\,^3S^o + (4s)\,^3S^o + (3d)\,^3D^o + (4d)\,^3D^o$	= 0.093		$O^+(^4S^o)$	

N B – Kim and Desclaux [506, p.6:table II] ($1s$ and $2s$) and Moore [658] for $2p$ open channels

U – Kim and Desclaux [506, p.6:table II] for $2p$ open channels the values are arbitrarily chosen from $2p_{1/2}$ and $2p_{3/2}$ orbitals*.

N_i – Goldbach *et al.* [338] optical oscillator strengths

$(2s\,2p^4)\,^4P$	= 0.085	subtracted from the	$2s$	orbital
$(3s)\,^4P + (4s)\,^4P + (3d)\,^4P$	= 0.373		$N^+(^3P)$	channel

In principle, the RBEQ* model can also be applied for metastable excited states of the gases covered here. However, the knowledge of the oscillator strengths from excited states is very reduced. In that case, it might be more desirable to recur to the RBEB model with $Q = 1$ as done by Laricchiuta *et al.* [561].

*The exact value is irrelevant, we recall that U is an *ad hoc* representation of the acceleration of the incident electron in the potential of the atom.

The only case where the contribution of ionisation from a metastable specie is non-negligible in experimental data is with atomic nitrogen as seen from the least agreeable result on figure 11.45-bottom-right. Since the specie mixture is unknown in the experiment of Brook *et al.* [117], we do not presently try to fit the RBEQ* model because of (i) the ambiguous dependence of the cross section both on Q, (ii) the mixture percentage and (iii) possibly non-negligible contribution from auto-ionisation [506, §III.B]. Therefore, the Q values for N in table 11.12 are not least-squares fits but subtractions from known optical oscillator strengths [338] of discrete excitations below the ionisation potential. The interested reader may like to consult recent R-matrix calculations of impact ionisation of atomic nitrogen [182, 465].

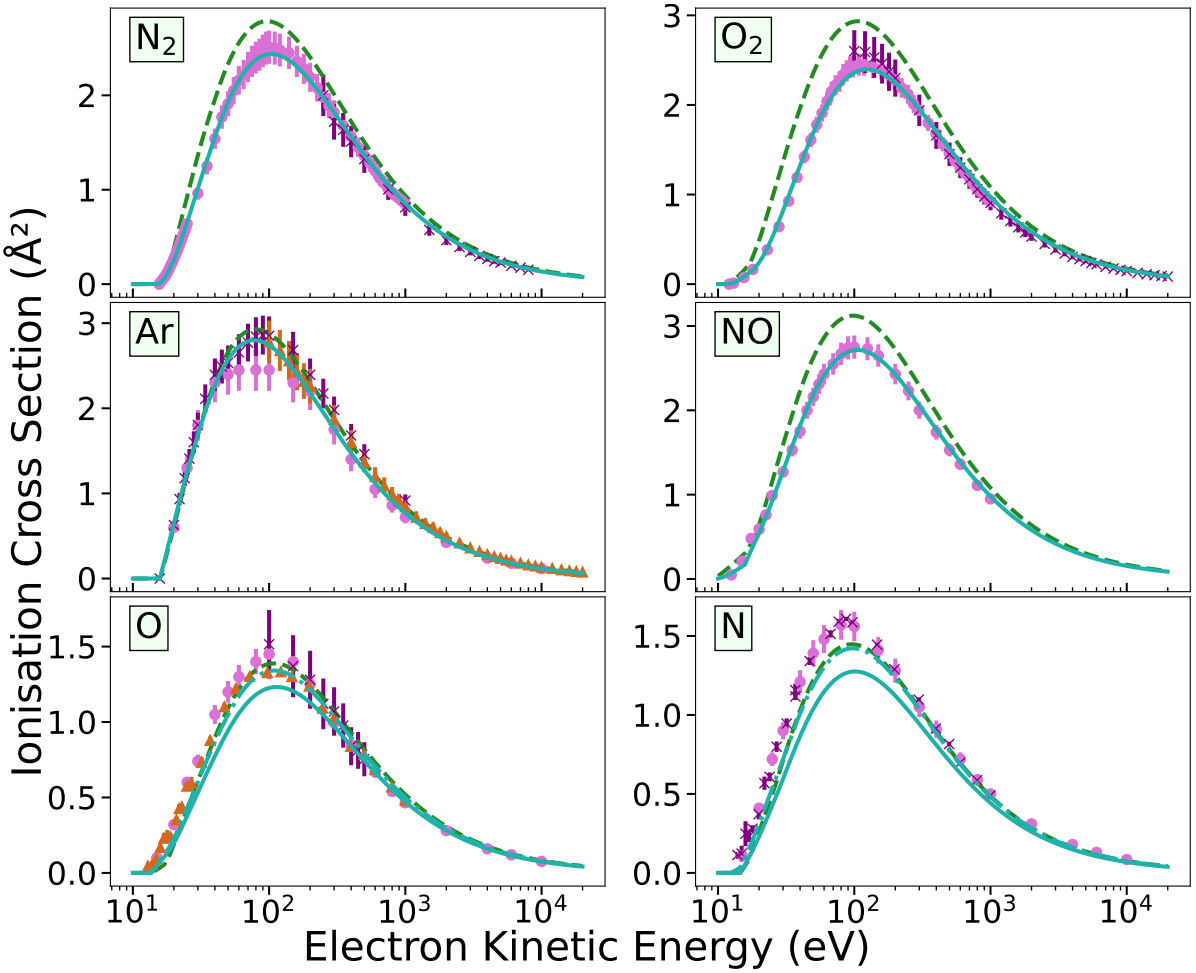

Figure 11.45: Ionisation cross sections yielded by the RBEQ* model (solid) calculated with the parameters in table 11.12 and compared to the RBEB$_\natural$ model (dashed - - -). For atomic oxygen, the dash-dotted (-·-) line shows the sum with the auto-ionising states, and for atomic nitrogen: the weighted sum of the N $^2D^o$ metastable state including its auto-ionisation. Experimental data are extracted from Inokuti *et al.* [425, p.65-6:tables 2.6.5, 6] and Lindsay and Mangan [596, p.60-1, 62–4, 67-8:tables 5.1.42, 44, 46] for the circles (•), from Shen *et al.* [831] (N_2), Brook *et al.* [117] (N,O) and Schram *et al.* [814, 815] for the crosses (×) and Rapp and Englander-Golden [768] for the triangles (△).

Table 11.12: Ionisation parameters for the revised RBEQ* model described in section 11.5.3 and equations (11.119-11.120). B : Binding energy, U : Average kinetic energy, N : effective number of electrons in the orbital or reaction, $Q = N_\mathrm{i}/N$: OOS ratio of ionisation / excitations.

subshell/open-channel	B (eV)	U (eV)	N	Q
N_2 ($X\,^1\Sigma_g^+$)		$12.512 \le N_\mathrm{i} \le 12.84$		$= 14 - \underbrace{0.682}_{b\,^1\Pi_u} - \underbrace{0.471}_{b'\,^1\Sigma_u^+}$
1σ	409.50	603.30	4	1
$2\sigma_g$	37.30	71.13	2	0.76 ± 0.19
$(2\sigma_u)^{-1} \to N_2^+(B\,^2\Sigma_u^+)$	18.72	63.18	2	1.00 ± 0.05
$(1\pi_u)^{-1} \to N_2^+(A\,^2\Pi_u)$	16.74	44.30	4	0.938 ± 0.014
$(3\sigma_g)^{-1} \to N_2^+(X\,^2\Sigma_g^+)$	15.58	54.91	2	0.792 ± 0.011
O_2 ($X\,^3\Sigma_g^-$)		$15.784 \le N_\mathrm{i} \le 15.801$		$= 16 - \underbrace{0.179}_{\mathrm{SR}} - \underbrace{0.020}_{\mathrm{Rydberg}}$
1σ	543.80	796.20	4	1
$2\sigma_g$	40.33	79.73	2	0.96 ± 0.27
$2\sigma_u$	27.05	90.92	2	1.00 ± 0.21
$(3\sigma_g)^{-1} \to O_2^+(B\,^2\Sigma_g^-)$	20.30	71.84	2	1.00 ± 0.11
$(1\pi_u)^{-1} \to O_2^+(A\,^2\Pi_u)$	17.08	59.89	4	1.00 ± 0.02
$(1\pi_g)^{-1} \to O_2^+(X\,^2\Pi_g)$	12.07	84.88	2	0.9314 ± 0.0021
NO ($X\,^2\Pi_r$)		$\underbrace{1.413}_{\text{Auto-ionisation}}$	$+12.759 =$	$14.172 \le N_\mathrm{i} \le 15$
1σ	543.26	796.2	2	1
2σ	410.26	603.3	2	1
3σ	40.56	76.55	2	1.00 ± 0.29
$(4\sigma)^{-1} \to NO^+(c\,^3\Pi,\ B\,^1\Pi)$	21.848	77.04	2	1.00 ± 0.26
$(5\sigma)^{-1} \to NO^+(b\,^3\Pi,\ A\,^1\Pi)$	18.370	55.37	4	1.00 ± 0.09
$(1\pi)^{-1} \to NO^+(a\,^3\Sigma^+,\ w,\ b', \dots)$	15.730	62.25	2	0.60 ± 0.08
$(2\pi)^{-1} \to NO^+(X\,^1\Sigma^+)$	9.260	65.27	1	0.970 ± 0.004
Ar ($X\,^1S$)		$16.53 \le N_\mathrm{i} \le 17.173$		$= 18 - \underbrace{0.827}_{11.623\text{–}15.755\mathrm{eV}}$
$1s$	3203.00	4229.00	2	1
$2s$	326.30	683.10	2	1
$2p \quad (= \frac{1}{3}2p_{1/2} + \frac{2}{3}2p_{3/2})$	249.13	651.00	6	1
$3s$	29.30	$\frac{103.5\,\mathrm{a}}{3}$	2	0.85 ± 0.15
$3p \quad (= \frac{1}{3}3p_{1/2} + \frac{2}{3}3p_{3/2})$	15.76	$\frac{78.03\,\mathrm{a}}{3}$	6	0.804 ± 0.009
O ($X\,^3P_2$)	$\underbrace{7}_{\text{Arbitrary}}$	$\le N_\mathrm{i} \le 7.69$	$= 8 -$	$\underbrace{0.154}_{3s, 3s', 4s, 3d, 4d} - \underbrace{0.156}_{\text{Auto-ionisation}}$
$1s$	562.878	796.1890	2	1.0
$2s$	33.913	84.7620	2	0.965 ± 0.035
$(2p)^{-1} \to O^+(^2P^o)$	18.630	70.8825	1.2	0.928 ± 0.005
$(2p)^{-1} \to O^+(^2D^o)$	16.932	68.5050	2.0	0.9645 ± 0.0035
$(2p)^{-1} \to O^+(^4S^o)$	13.610	69.1400	0.8	0.6^b

Table 11.12: Ionisation parameters for the revised RBEQ* model described in section 11.5.3 and equations (11.119-11.120). B : Binding energy, U : Average kinetic energy, N : effective number of electrons in the orbital or reaction, $Q = N_\mathrm{i}/N$: OOS ratio of ionisation / excitations.

subshell/open-channel	B (eV)	U (eV)	N	Q
N ($\mathrm{X}\,^4S^o_{3/2}$)	$\underbrace{6}_{\text{Arbitrary}} \le N_\mathrm{i} \le 6.542$		$= 7 - \underbrace{0.271}_{3s} - \underbrace{0.085}_{2s\,2p^4} - \underbrace{0.027}_{4s} - \underbrace{0.075}_{3d}$	
$1s$	425.469	598.726	2	1.0000
$2s$	25.828	65.656	2	0.9575
$(2p)^{-1} \to \mathrm{N}^+(^1S)$	18.590	51.100	0.2	1.0000
$(2p)^{-1} \to \mathrm{N}^+(^1D)$	16.430	51.094	1.0	1.0000
$(2p)^{-1} \to \mathrm{N}^+(^3P)$	14.544	51.034	1.8	0.7930

[a] division by principal quantum number, see Huo and Kim [412, §III.B:p.1233-4] and Tanaka *et al.* [911, eq.(29)]

[b] the algorithm converged to 0.4 ± 0.04, which seems too low. Due to the uncertainty on the contribution of auto-ionising states, we selected the value manually while maintaining Q fixed for the other open-channels.

Singly Differential Cross Sections

The formula (11.119) represents the cross-sectional distribution in secondary electron kinetic energy ε_2 for a given incident energy ε_0, commonly known as the singly differential cross section (SDCS). Since the two emerging electrons after ionisation are indistinguishable, they should have the same distribution. The function (11.119) is indeed symmetric around the mirror energy at $\varepsilon_2 = (\varepsilon_0 - B)/2 = \varepsilon_1$. The energy distribution of the primary electrons ε_1 is obtained through the reflection:

$$\frac{\mathrm{d}\sigma_\mathrm{i}}{\mathrm{d}\varepsilon_1}(\varepsilon_1, \varepsilon_0) = \frac{\mathrm{d}\sigma_\mathrm{i}}{\mathrm{d}\varepsilon_2}(\varepsilon_2 = \varepsilon_0 - B - \varepsilon_1, \varepsilon_0)\ . \tag{11.129}$$

A comparison with experimental data [343, 721, 837] is given in figure 11.46 for N_2.

Experimentally, SDCS are obtained by angular integration of doubly differential CS (DDCS) displayed in the next subsection on figure 11.47. Those DDCS are hard to probe at large and small angles [343, p.543:right-bottom]. In order to derive pertinent SDCS, a good angular resolution of the DDCS is required or assistance from a smoothing procedure based on semi-empirical models to extrapolate the DDCS throughout the whole angular range. This is problematic partly due to enhanced backscattering [792, eq.(10)] which is due to dipole interaction [503, p.269:§4] and subsequent recoil of the secondary from the ion.

As discussed in the following subsection p. 492, the data of Opal *et al.* [721] at low $\varepsilon_0 \lesssim 50\,\mathrm{eV}$, are dubious at small and large angles θ_2 of the secondary electron. As a result, there is a systematic discrepancy of about 50 % lower than the data reported by Shyn [837] as shown by the purple triangles (▲) on figure 11.46. Nonetheless, at higher energies $\varepsilon_0 \gtrsim 200\,\mathrm{eV}$, the agreement between Goruganthu *et al.* [343] and Opal *et al.* [721] is good.

For an adequate comparison with the experimental data, the energy of primary electrons ε_1 had to be blended seamlessly into the distribution of the secondaries which are summed over all partial ionisation SDCS:

$$\frac{\mathrm{d}\sigma_\mathrm{i}}{\mathrm{d}\varepsilon_2} = \sum_o \frac{\mathrm{d}\sigma_{B_o}}{\mathrm{d}\varepsilon_2}\ . \tag{11.130}$$

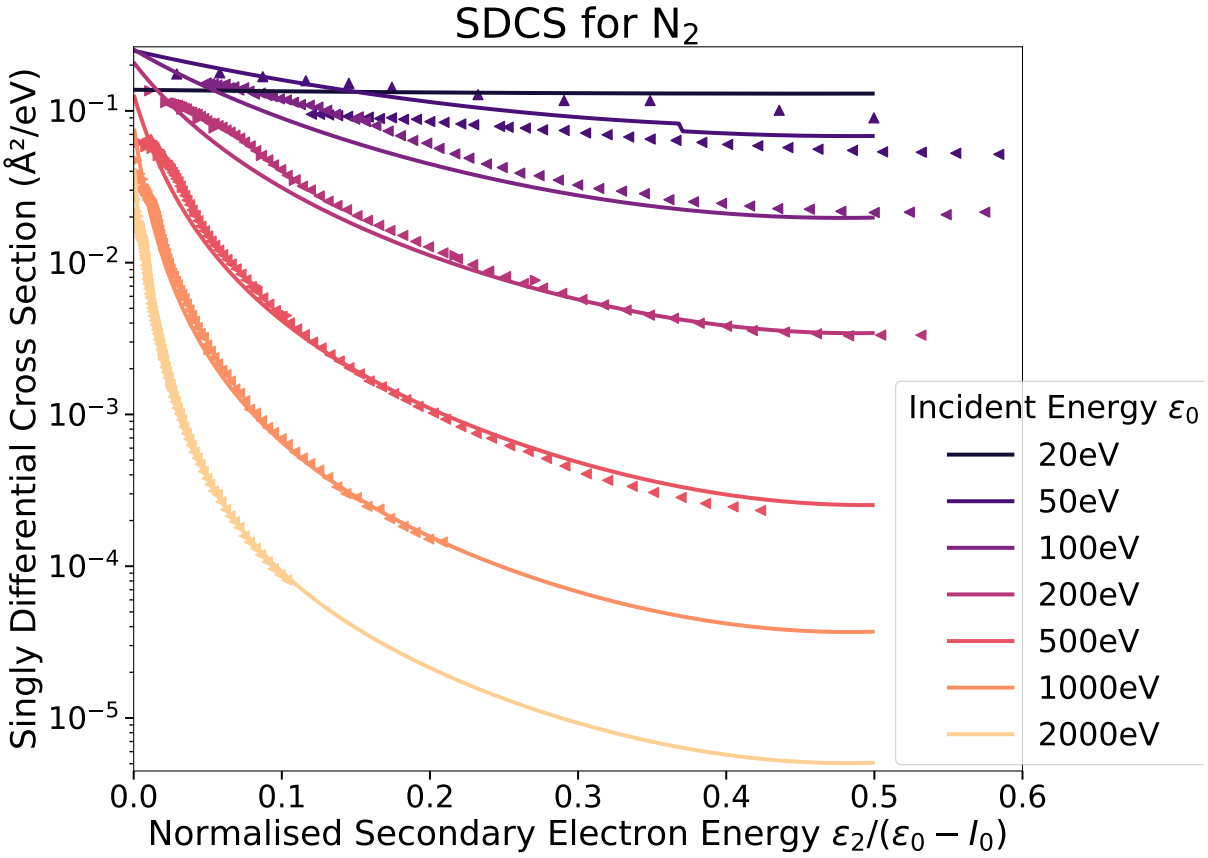

Figure 11.46: Singly differential cross section for molecular nitrogen at different incident electron energies ε_0. For synopsis, the energy of the secondary electron ε_2 on the abscissa is normalised according to the available energy $\varepsilon_0 - I_0$, with the ionisation threshold at $I_0 = 15.58\,\text{eV}$. Energies beyond 0.5 simply correspond to energies of primary electrons $\varepsilon_1 > \varepsilon_2$. Solid curves are calculated with dRBEQ* (11.119) and compared with Goruganthu *et al.* [343] (▸), Shyn [837] (▲) and Opal *et al.* [720] (◂).

The binding energies B_o for each orbital o (or rather ionisation channel) are tabulated in 11.12. One must therefore beware that signals of primary electrons which underwent a higher-lying ionisation event $B_o > I_0$ than the ionisation threshold $I_0 = 15.58\,\text{eV}$ are included in the region $\varepsilon_2/(\varepsilon_0 - I_0) < 0.5$. For instance, primary electrons which emerge from excitations to the $A^2\Pi_u$ (16.74 eV) and $B^2\Sigma_u^+$ (18.72 eV) states of N_2^+ are counted in the region below $(\varepsilon_0 - 15.58\,\text{eV})/2$. The discontinuity at 50 eV around 0.37 in figure 11.46 comes from the impossibility of having ionisation events from the inner orbital $2\sigma_g$ with $B_{2\sigma_g} = 37.3\,\text{eV}$ with $\varepsilon_1 > 12.7\,\text{eV}$. The experimental data does not reveal such a drop, implying perhaps that the ionisation from this inner shell is presently overestimated.

The trends of the SDCS with respect to the incident ε_0 and secondary ε_2 energies are quite simple. At small impact energies $\varepsilon_0 \lesssim 3I_0$, a flat distribution signify an overall even repartition of kinetic energy. For higher ε_0, the curves decrease steeper as ε_2 rises, implying that the energy is split unevenly. Most of the energy is kept by the primary and a small part is given to the secondary. This is very compatible with the Bethe theory comprising far-range dipole and close-range binary-encounter interactions as given by the RBEQ* model (11.119). Departures from this model are obvious as ε_0 and ε_2 become small, i.e. a few times the ionisation threshold. This is discussed more in detail in the following subsections p. 492–495.

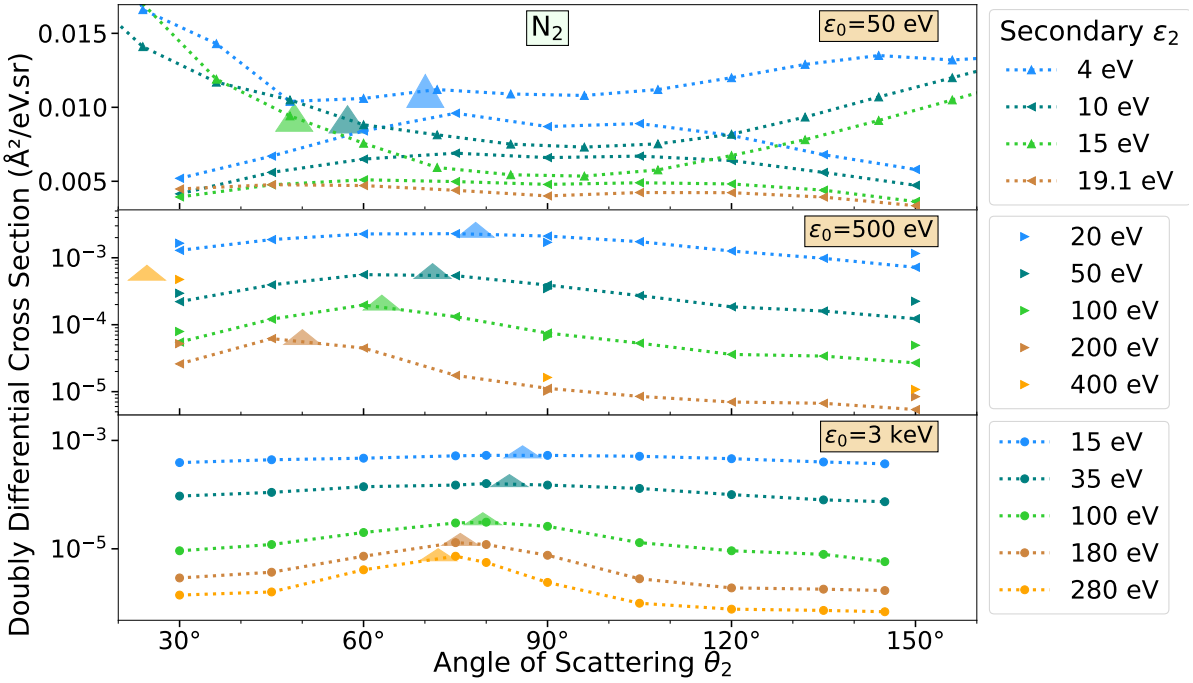

Figure 11.47: Double differential scattering cross sections in secondary electron energy ε_2 and polar angle θ_2 for N_2 at various energies of the incident electron ε_0. Experimental data come from ◂–[721]; ▲–[837] and ●–[177]. When ε_2 becomes appreciable, above the ionisation threshold, the binary encounter model may be identified as a local maximum on a broad bump. The translucid triangles give the exact location classically determined by the binary encounter model from the kinematic relationship (11.131) between a free and a pseudo-free electron.

Doubly Differential Cross Sections

At a fixed emitted energy ε_2, we may choose to observe the direction of the primary Ω_1 or of the secondary electron Ω_2. The former is bound to the generalised oscillator strength density as described at the beginning of section 11.5.1. Experimentally though, it is easier to observe the latter, ejected electrons' angular distribution (in Ω_2), since we need to measure ε_2. These secondary DDCS reveal two main features (see 11.47):

- the 'binary encounter' peak ($\varepsilon_2 \gg I$): corresponding to a simple kinematic relation between two free electrons once their energies after collision ε_1, ε_2 are known (see also chapter 2 on 66),

$$\cos\theta_2 = \frac{\varepsilon_2 + I/2}{\sqrt{\varepsilon_0 \varepsilon_2}} \; ; \tag{11.131}$$

- a "backward rise" ($\varepsilon_2 \lesssim I$): may be due to dipole interaction or more complex effects, such as interference, exchange or intensified interaction and correlation with the ion core.

Those features do not always appear both on the same graph at a fixed ejected energy ε_2. The binary peak is more prominent when ε_2 is high above the ionisation threshold I, where the binary collision assumption is more valid. On the other hand, the "backward" rise corresponding to recoil scattering (see next subsection p. 495) increases as ε_2 decreases below I. The trends are well explained and summarised in Ehrhardt [261].

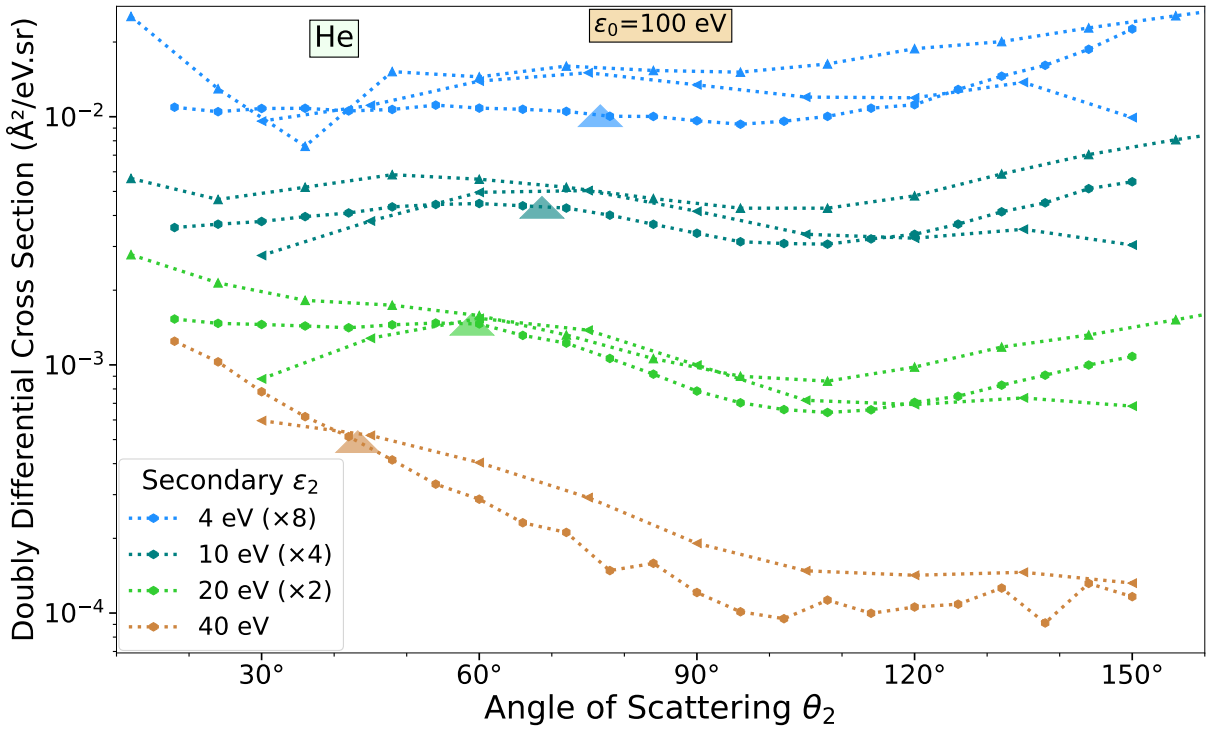

Figure 11.48: Double differential scattering cross sections in secondary electron energy ε_2 and polar angle θ_2 for helium at an incident energy of $\varepsilon_0 = 100\,\text{eV}$ which is roughly 4 times above the ionisation threshold $I_{\text{He}} \approx 24.6\,\text{eV}$. There are two types of discrepancies between the data of Opal *et al.* [720, p.216] (◂), Shyn and Sharp [840] (▲) and Müller-Fiedler *et al.* [681] (⬡): one comes from normalisation to an absolute scale [840, p.560:right column], the other by inaccuracy at small and large angle scattering (away from 90°) [791].

Data for doubly differential cross sections are mainly available for helium [31, 262, 342, 681, 817, 840]. The first survey over various target gases (He,N_2,O_2, noble gases, important diatomic and some polyatomic molecules) was made by Opal *et al.* [721] and tabulated in [720]. Nevertheless, a subsequent survey by DuBois and Rudd [233] revealed serious discrepancies at low incident energies ε_0 and forward and backward scattering angles (away from 90°). These can be seen on figure 11.47&11.48 where the data of Opal *et al.* [721] (◂) are compared with Shyn [837] and Shyn and Sharp [840] (▲), DuBois and Rudd [233] (▸) and Müller-Fiedler *et al.* [681] (⬡). Rudd and DuBois [791, p.29-30] attributed this discrepancy to an inadequate estimation of the electron-gas interaction volume and to the low angular resolution (10°–15°) in the experiment. At higher energies $\varepsilon_0 > 200\,\text{eV}$ this disagreement is reduced and the results may be compared well with theory, in particular with the Born approximation above 1 keV [233, fig. 3].

Examples of prominent binary peaks can be seen when both $\varepsilon_0, \varepsilon_2 \gg I$; on figure 11.47 for N_2 on the lower curves in the middle ([721]–◂) and bottom ([177]–●) graphs . The validity of the binary encounter is confirmed by a correct alignment of the predicted central position of the peak (coloured triangles) from equation (11.131).

Gradually, as ε_2 diminishes, the binary peak drowns into a meagre knoll [343, fig. 3], and the angular distribution becomes almost isotropic (upper curves on fig. 11.47), which invalidates the binary encounter model.

In the region where the incident electron's energy is just a few times above the ionisation threshold $\varepsilon_0 \lesssim 4I$, there is a transition from binary (higher ε_0) to backward (lower ε_0) scattering regimes. This can be seen on figure 11.48 for helium at an incident energy of $\varepsilon_0 = 100\,\mathrm{eV} \simeq 4I_{\mathrm{He}} = 4 \times 24.6\,\mathrm{eV}$. The exact position of the supposed maximum from the binary collision is however difficult to establish, due to the important scatter among the experimental data. Although a peak is visible somewhere at intermediate angles (50°–70°), it may not be simply attributed to binary kinematics as through (11.131), which would predict a more pronounced peak, as seen by the coloured triangle patches on figure 11.48. The inter-electron repulsive Coulomb force actually increases this angle between the outgoing electrons and causes the secondary electron to be scattered more toward 90°. This is known as 'post-collision interaction' and is illustrated by the shift in scattering angle on figure 11.49 in the following subsection p. 495 as well.

At lower ε_2, backward scattering is well enhanced for He in figure 11.48 on Müller-Fiedler *et al.*'s (⬡ [681]) and Shyn and Sharp's (▲ [840]) measurements but absent in Opal *et al.*'s (◂ [720]) due to the discrepancy discussed above. The same can be said about N_2 (fig. 11.47-top) at ε_0 =50 eV, were this discrepancy is the most striking.

Ab initio calculations of the angular distribution from ionisation events is complicated by the coupling of the scattered electron's wave with the states of ionisation continuum (comprising the ejected electron). On the other hand, use of approximative methods is quite restrictive [996, §4.2.1.1]. Due to the long-range Coulomb interaction with the ion, the wavefunction of the scattered electron is significantly distorted. Only at high energies (≳30×the ionisation threshold), may this distortion be neglected by use of the plane wave Born approximation. Furthermore, one can then make use of a distorted wave instead of a plane wave to get reasonable agreement [605, §2.2.3]. Still, the improvement is lowered down to at most 15 times the ionisation threshold but does not yield reasonable results at lower energies.

This is why semi-empirical or fully empirical formulae are widely used in order to represent DDCS. Tahira and Oda [904] compared the results from a pure plane wave approximation, a binary-encounter model and a scaled Born approximation; the latter giving the least disagreeing results.

A simple analytical yet accurate formula is still greatly sought after, in order to model angular distributions from impact ionisation. The two features described above can be empirically modelled by Lorentzian profiles [790] for the binary-encounter peak and a simple $\propto \cos^2\theta$ term for the backward rise [503, eq.(20)]. Experimental angular distributions complemented by theoretical calculations were tabulated for helium by Kim [502]. Similar data could exist for other targets (depending on the availability of experimental data).

Although we did not explore any further, we surmise that there could exist more developed models for computing DDCS from impact ionisation [177, §3]. For instance, some authors of experimental studies provide coefficients of Legendre polynomials that fit their experimental data [343, 681, tab. 13, tab. IX]. We leave the search for analytical DDCS up to future investigation.

In the mean time, for Monte Carlo simulations we will use a crude averaging:

$$\cos\theta_2 = \frac{\varepsilon_2}{\varepsilon_2 + B}\frac{\varepsilon_2 + B/2}{\sqrt{\varepsilon_2\varepsilon_0}} + \frac{B}{\varepsilon_2 + B}(1 - 2x)\,, \tag{11.132}$$

where B is the binding energy of the secondary electron and x represents a sample of a random variable uniformly distributed on $[0, 1]$. The resulting distribution is simply a square window (shifted toward larger angles) that shrinks as $\varepsilon_2 \gg B$.

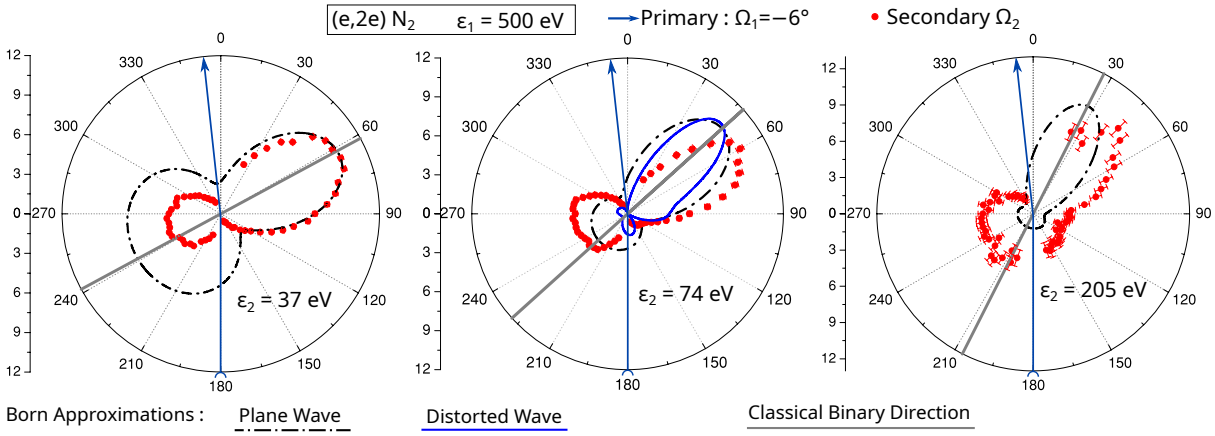

Figure 11.49: Triply differential cross section from impact ionisation of molecular nitrogen's outer valence shell ($1\pi_u$, $3\sigma_g$ and also the deeper $2\sigma_u$) for electrons scattered at an angle of $-6°$ and at an energy of $\varepsilon_1 = 500\,\text{eV}$ after the event (adapted from Lahmam-Bennani *et al.* [550, fig. 1]). The consecutive plots show how the angular distribution of the ejected electron ($\mathrm{d}\sigma(\Omega_2;\varepsilon_2)$) varies with respect to its energy ε_2. The main lobes experimentally observed correspond to the ideal situations of electron binary-encounter peak and recoil (back)scattering from the ion core.

Triply Differential Cross Sections

The ideal full description of the ionisation process should be given by the triply differential cross section in secondary energy ε_2, angle Ω_2 and primary angle Ω_1 from which all quantities can be derived [503, p.264:eqs.(1-5)]:

$$\frac{\mathrm{d}\sigma_{\mathrm{DDCS}}}{\mathrm{d}\varepsilon_2\,\mathrm{d}\Omega_2} = \int \frac{\mathrm{d}\sigma_{\mathrm{TDCS}}}{\mathrm{d}\varepsilon_2\,\mathrm{d}\Omega_2\,\mathrm{d}\Omega_1}\,\mathrm{d}\Omega_1 \tag{11.133}$$

$$\frac{\mathrm{d}\sigma_{\mathrm{SDCS}}}{\mathrm{d}\varepsilon_2} = \int \frac{\mathrm{d}\sigma_{\mathrm{DDCS}}}{\mathrm{d}\varepsilon_2\,\mathrm{d}\Omega_2}\,\mathrm{d}\Omega_2 \tag{11.134}$$

$$\sigma_{\mathrm{ion}} = \int \frac{\mathrm{d}\sigma_{\mathrm{SDCS}}}{\mathrm{d}\varepsilon_2}\,\mathrm{d}\varepsilon_2 \tag{11.135}$$

As usual, the primary (1) and secondary (2) electrons are conventionally defined as $\varepsilon_1 > \varepsilon_2$. Probing the TDCS requires a very sophisticated experimental apparatus correlating detections of primary and secondary electrons that emerged from the same ionisation event. The resolution and accuracy of measurements greatly improved over time [263, 550, 810, 817], in particular at small scattering angles of the primary electron $\theta_1 < 10°$.

Triply differential cross sections provide an invaluable means of probing the momentum distribution in electronic orbitals of atoms and molecules [978]. This is done by measuring TDCS in a symmetric configuration where $\varepsilon_1 = \varepsilon_2$ and varying the azimuthal φ (non-coplanar) and/or polar θ (coplanar) angle [996, Chapter 4:§4.2].

An example of recent TDCS for impact ionisation of N_2 is shown in figure 11.49 from Lahmam-Bennani *et al.* [550]. As an important update to the introductory discussion in subsections 11.5.1–11.5.3, when considering angular distributions, impact ionisation may actually be categorised [550] into three regimes:

- Dipole interaction : q, Ω_1, and ε_2 all small
  Weak interaction of the incoming electron classically dashing by at large distances.

- Binary-Encounter peak : $\mathbf{q} \simeq \mathbf{k}_2$
  Local interaction between a free and a pseudo-free electron, this corresponds to the 'Bethe ridge'.

- Recoil peak : q, Ω_1 small but ε_2 large, i.e. $q < k_2$
  This implies that the recoil momentum $\mathbf{k}_\mathrm{i}$ of the ion is comparable to $-\mathbf{k}_2$.

The first two regimes (also referred to as 'soft' and 'hard') are relatively well understood and described in the previous sections. The binary lobe (oval shape in forward scattering on figure 11.49) is useful to derive information about the momentum distribution of electrons that are ejected from a certain orbital [996, §4.2.2:p.111–117]. Additionally, a binary lobe corresponding to ejection of an electron coming from a *np* orbital will be split into two sub-lobes.

Recoil scattering on the other hand remains poorly understood other than the fact that it results from complex interaction with the ion whereby a significant momentum of the secondary is imparted to the ion which 'recoils' with k_i. The ejected electron is then backscattered at $\theta_2 > 90°$ which defines the 'recoil lobe' on figure 11.49. It must not be understood as a regime not fully comprised by the now-classical soft dipole and hard binary models. Recoil concerns mostly what happens with the secondary electron after the primary has left. Although the Born approximation (upon which the dipole and binary encounters are founded) does predict a recoil lobe, it is nevertheless quantitatively off the experimental chart, as seen by dash-dotted –•–lines on figure 11.49. Most impressive is to see some apparent contradictions about the magnitude of the recoil lobe derived from experimental surveys.

At earlier times it was observed in general that:

Ehrhardt [261, p.191:§iii.]

> For high $\varepsilon_2 \geq 20\,\mathrm{eV}$ the binary peak represents a very high portion of the cross section. The recoil peak practically vanishes.

whereas recent experimental investigations reveal rather that:

Lahmam-Bennani *et al.* [550, p.5:§(i)]

> For the outer orbital of N_2, [...] the experiments reveal the opposite, i.e. an increasing [recoil-to-binary] ratio with increasing ejected electron energy ε_2.

To clarify this, we may draw a "territory" chart 11.50 in a ε_0, q^2 map that delimits the applicability of each of the three (dipole, binary, recoil) domains above. At each point, there are two supplementary degrees of freedom that delineate a subspace: namely the secondary electron's kinetic energy ε_2 and the momentum transferred to the ion k_i. These degrees of freedom, which are also critical for delimiting the different regimes, blur the boundaries defined and tune the respective contributions of the binary and recoil lobes.

The dipole approximation is a Born approximation (high energies $\varepsilon_0 \ggg B$) with small momentum transfers $q \ll 1$. At larger q, the untruncated oscillator strength in the Bethe theory should be used (higher multipoles) and this description encompasses the impulse approximation, as discussed previously 11.5.3 and in Inokuti [427, §4.4].

The impulse approximation is embodied by the binary encounter with larger momentum transfers that exclusively correspond to the ejected electron's kinetic energy ε_2 (this third dimensional aspect is missing in 11.50). Nevertheless, as ε_2 increases and becomes comparable to the energy of the primary ε_1, the electrons interact for a longer time during their escape. This

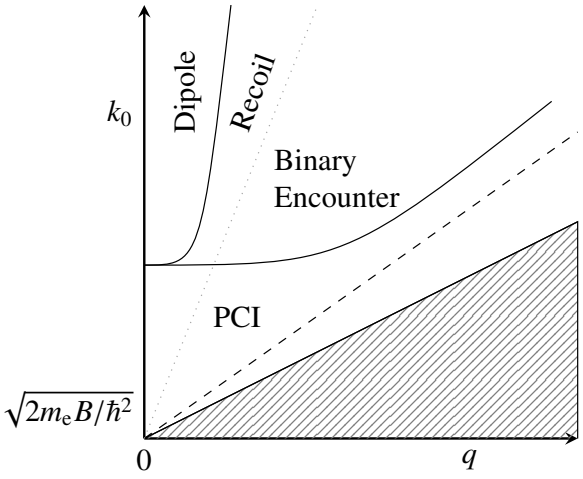

Figure 11.50: Domains of different regimes of electron impact ionisation with atoms and molecules in a map showing the incident momentum k_0 and the momentum transfer q. The shaded area is physically unreachable ($q > 2k_0$). The dashed line represents the limit of symmetric scattering $k_1 = k_2$ at $q^2 = (k_0^2 - 2m_eB/\hbar^2)/2$. 'PCI' stands for 'Post-Collision Interaction' between the two outgoing electrons repelling each other when they flee at similar velocities in the electric field of the ion core. In the ideal case when inelastic losses are negligible compared to the incident energy, constant scattering angles θ_1 would be drawn as straight lines with the inclination $q = 2k_0 \sin(\theta_1)$. This idealisation may be applied to the upper left corner of the graph but is irrelevant elsewhere.

overall widens the angle between them both, and produces a shift of the binary lobe compared to the classical direction as can be seen on figure 11.49 for the plots in the middle and especially on the right. This inter-electronic repulsion is technically designated as "post-collision interaction" (PCI) implying that this shift results from long-range coulomb repulsion even far away after the ionisation has taken place [200]. PCI effects are most important when both electrons flee at similar velocities, thus in symmetric scattering conditions.

Conceptually opposite to PCI, recoil is characterised by small angle scattering but comparable momenta of ejected electron and ion core : $k_2 \simeq k_i$. This corresponds to an enhanced interaction of the secondary electron with the ion whereas the primary has left the scene. It is impossible to delimit a region in the (k_0^2, q^2) space alone which would strictly pertain to binary or recoil scattering since both are present over a broad range of ε_2 with variable amplitudes. The binary lobe is enhanced when ε_2 increases but while q remains substantial. If, on the contrary, the primary angle of scattering θ_1 becomes too small, then the binary model collapses and the recoil lobe takes importance [996, p.117]. This is the situation represented in figure 11.49. We remark that this is where the contradiction [261, p.191:§i] vs. [550, p.5:§i] dwells.

At low incident energies, the interaction is more complex and the bilobed binary-recoil structure of the TDCS vanishes. We do not know what terminology applies to this situation, but it physically corresponds to a complex ternary electron-electron-ion interaction with various coupled channels and interferences.

Although variably successful methods of calculations exist for computing the TDCS [936], even under the Born approximation, it is out of the scope of the present thesis to include those as a modelling of impact ionisation.

11.6 Total scattering cross section

The five sections of this chapter, about elastic, rotational, vibrational/resonant, electronic and ionisation collisions enable us to culminate our research so far to the construction of "grand total" cross sections of electrons with six atmospheric gas targets.

11.6.1 Low-energy : experiments

In order to make the set consistent with experimental data of total cross sections, we remind that in 11.1.5, we constructed what we call a *residual* elastic cross section σ_{re} (encompassing rotational excitations) so as to sum, together will all other inelastic processes, to the grand total cross section σ_{tot}. The latter has been obtained from a weighted average of carefully selected measurements from the most up-to-date experiments available. The results can observed on the graphs of figure 11.51.

We selected experimental data based on the extensive reviews of Brunger and Buckman [124] and Zecca *et al.* [1006] and also from more specific reviews [865] for NO. Once selected, the total cross section σ_{tot} was averaged on a logarithmically spaced (but rounded to three significant digits) array of kinetic energies according to the uncertainties s_m of the measurements m:

$$\sigma_{\mathrm{tot}}(\varepsilon) = \frac{\sum_m \sigma_m / s_m^2}{\sum_m 1/s_m^2} \tag{11.136}$$

These are the purple curves (—) shown in graphs of figure 11.51. Measurements are available usually up to a few keVs. Beyond a certain point at $\varepsilon_>$, one needs to find a way for extrapolation.

11.6.2 High-energy : theory

At high energies, the total cross section may be approximated by the sum of the inelastic cross section in the Bethe theory as revisited by Inokuti [427, §4.3:eqs. (4.55–6)] and the elastic cross section in the Born approximation (11.9) to combine into a well-known Born-Bethe expression [424, 428, eq.(13), eqs.(1–2)]:

$$\tilde{\sigma}_{\mathrm{tot}}(\varepsilon) = \underbrace{\tilde{\sigma}_{\mathrm{inel}}}_{\text{Bethe-Inokuti}} + \underbrace{\tilde{\sigma}_{\mathrm{el}}}_{\text{Born-Inokuti}} \tag{11.137}$$

$$= \frac{8\pi a_0^2}{m_{\mathrm{e}}\mathrm{v}^2/\mathrm{Ryd}} \left(M_{\mathrm{tot}}^2 \left[\ln\left(\beta^2\gamma^2\, 4c_{\mathrm{tot}} \frac{m_{\mathrm{e}}c^2}{2\mathrm{Ryd}} \right) - \beta^2 \right] + \frac{\gamma_{\mathrm{tot}}}{m_{\mathrm{e}}\mathrm{v}^2/(2\mathrm{Ryd})} \right) + \frac{2\pi a_0^2}{m_{\mathrm{e}}\tilde{\mathrm{v}}^2/\mathrm{Ryd}} \left(\tilde{A} + \frac{\tilde{B}}{m_{\mathrm{e}}\tilde{\mathrm{v}}^2/(2\mathrm{Ryd})} + \frac{\tilde{C}}{(m_{\mathrm{e}}\tilde{\mathrm{v}}^2)^2/(2\mathrm{Ryd})^2} \right) \tag{11.138}$$

$$= \frac{4\pi a_0^2 \alpha^2}{\beta^2} \left(M_{\mathrm{tot}}^2 \left[2\ln(2k) + \ln c_{\mathrm{tot}} - \beta^2 \right] + \frac{\gamma_{\mathrm{tot}}\alpha^2}{\beta^2} \right) + \frac{\pi a_0 \alpha^2}{\tilde{\beta}^2} \left(\tilde{A} + \frac{\tilde{B}}{\tilde{k}^2} + \frac{\tilde{C}}{\tilde{k}^4} \right) \tag{11.139}$$

Born parameters in the last rows of table 11.13 are fits to integral cross sections of elastic scattering as explained earlier in section 11.1.4.

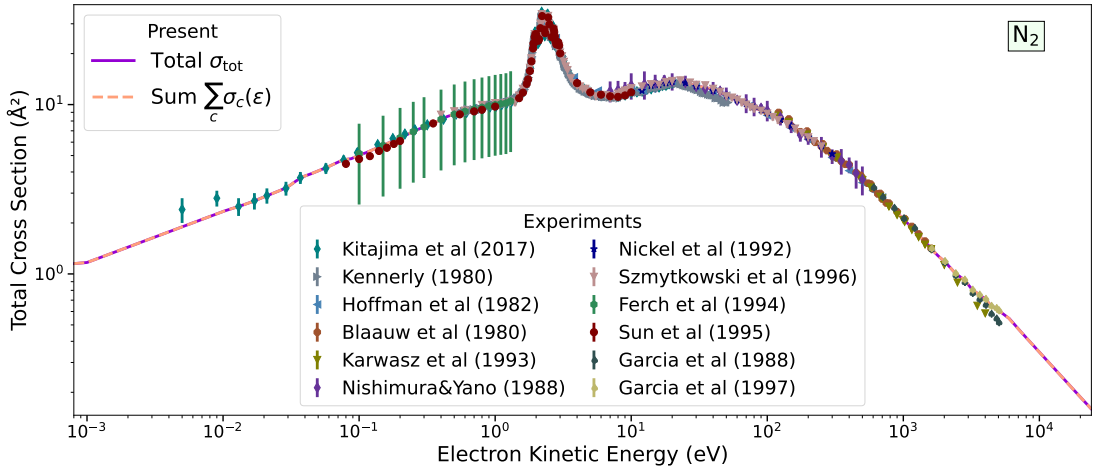

(a) Used for average : ♦ [512], ▸ [488],● [894], ⬡ [124, p.279:tab.15:Ferch&Jost], ▼ [900], ⋆ [699], ♠ [317]; Unused : ◂ [405], ◇ [705], ◯ [75, 207], ▼ [478], ♠ [316].

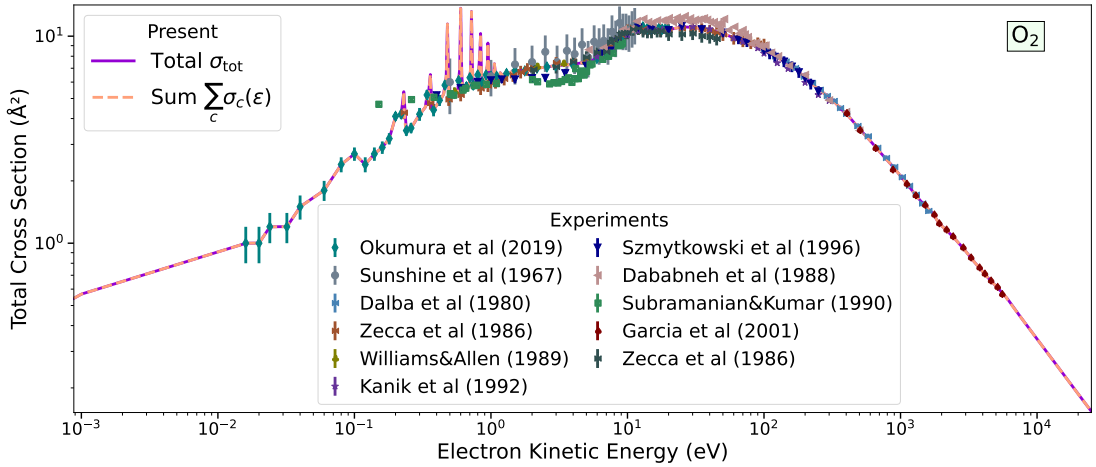

(b) Used for average : ♦ [714], ★ [477], ⋈ [1003], ▼ [900], ⋈ [207], ♠ [315]; Unused : ● [895], ■ [890], ◂ [205], ♣ [984].

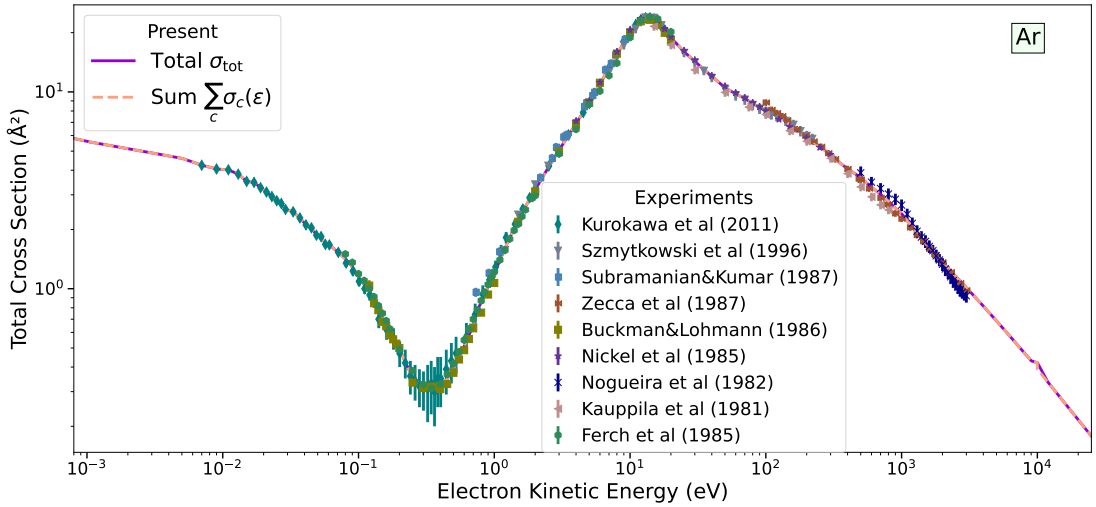

(c) Used for average : ♦ [545], ▼ [900], , ■ [891], ⋈ [1004], ■ [129], ★ [701], × [708], ⬡ [278]; Unused : ◂ [481] .

Figure 11.51: Total cross sections constructed from weighted averages of selected experimental data (N_2, O_2, Ar) and from a patchwork of recommended values and calculations (NO, O, N).

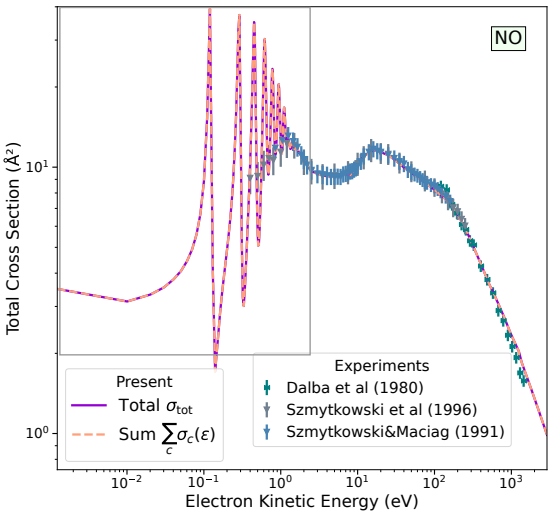

(d) Constructed from [557, 865] and based on ⋈ [207] ▼ [899] ▼ [900]. Zoom of the grey squared area is represented on the figure 11.51e here to the right.

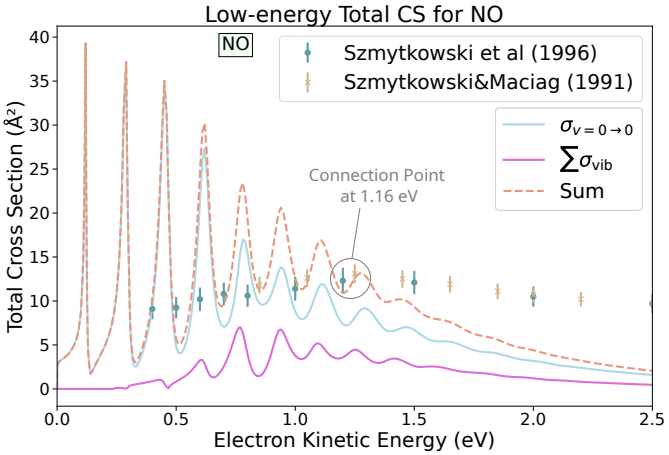

(e) The data of Laporta *et al.* [557] (at T_{vib} = 300 K) are used below 1.16 eV whereas the recommended values of Song *et al.* [865] are used from 1.25 eV. The connection between both sets is made with the data of Szmytkowski *et al.* [900].

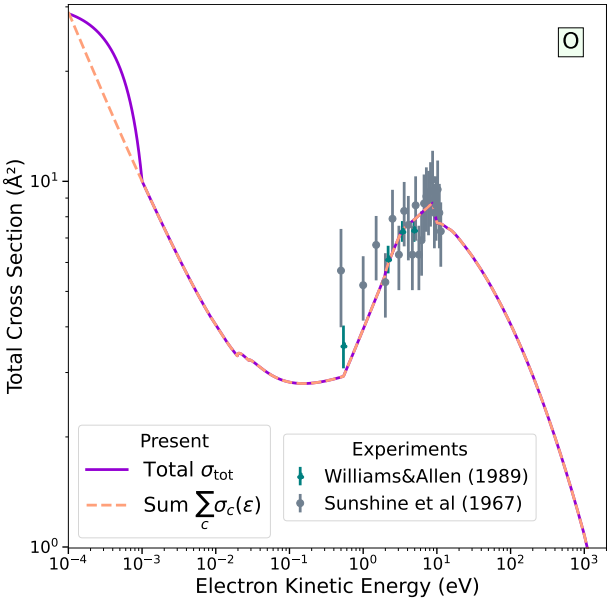

(f) The rise at very small energies is due to the fine-structure $O(^3P_{0,1}) \to O(^3P_2)$ transitions. The linear interpolation scheme of the purple curve (—) causes the bump (The next data point below 1 meV is 0).

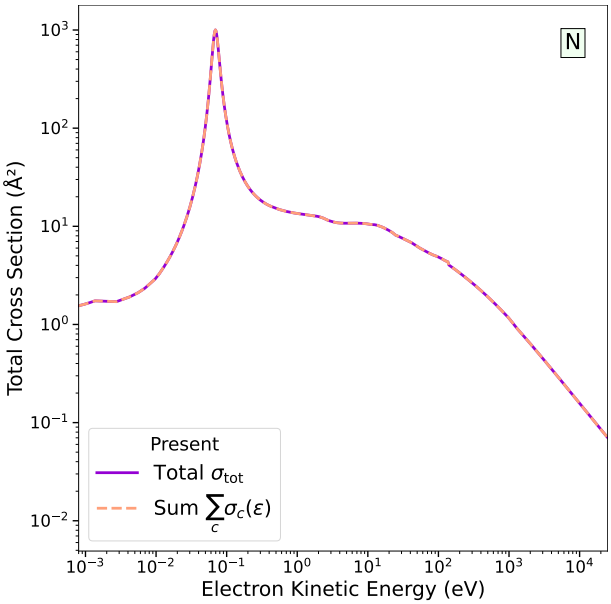

(g) This cross section comes mainly from the BSR calculations of [975] up to 200 eV, apart from some inelastic excitations and ionisation (see sec. 11.4.8).

Table 11.13: Bethe and Born parameters, separated in the middle by a vertical line, for atmospheric species. The last column is the energy $\varepsilon_>$ at which junction is made between the asymptotic expression and the actual value of the total CS.

	$M^2_{\rm tot}$	$\ln c_{\rm tot}$	Z	$\ln \bar{B}$	$\tilde{A}$	$\tilde{B}$	$\tilde{C}$	K (eV)	$\varepsilon_>$ (keV)
N_2	4.70	0.400	14	9.70	129	−271	74 900	342	6
O_2	4.40	−0.0900	16	11	149	−381	167 000	412	6
NO	4.29	0.0765	15	10.3	139	−296	24 900	296	1.25
Ar	4.33	−0.400	18	35.6	246	−530	4 340 000	1910	10
O	2.15	0.111	8	11.6	57.7	−116	8250	238	10
N	2.26	0.334	7	9.96	54.3	−111	4340	180	10
Air	4.63	0.295	14.5	10.1	134	−296	136 000	372	–

The Bethe parameters, gathered in the first rows of table 11.13, are obtained from analytical parameters describing impact ionisation and electronic excitations (allowed and forbidden) in the following way [427, eqs.(4.42, 43&52)]:

$$M^2_{\rm tot} = \sum_i M^2_{{\rm i},i} + \sum_a M_{\rm a} \,, \tag{11.140a}$$

$$M^2_{\rm tot} \ln c_{\rm tot} = \underbrace{\sum_i M^2_{{\rm i},i} \ln c_{{\rm i},i}}_{\text{Ionisation}} + \underbrace{\sum_a M_a \ln c_a}_{\text{allowed}} + \underbrace{\sum_b M_b}_{\text{dipole forbidden}} \,, \tag{11.140b}$$

$$\gamma_{\rm tot} \simeq -\frac{3}{4} Z + Z\left(\ln(\bar{B}\alpha^2/\beta^2) - 1\right) \,. \tag{11.140c}$$

The number $Z \equiv \sum_i N_i$ represents the total number of electrons in the molecule (all atoms comprised).

Ionisation The dipole matrix elements from ionisation $M^2_{{\rm i},i}$ and the parameter $\ln c_{{\rm i},i}$, for each partial ionisation channel indexed by i, can be found from the RBEQ* model in section 11.5.3 which we remind here:

$$M^2_{{\rm i},i} = \frac{Q_i N_i {\rm Ryd}}{2B_i} \tag{11.141}$$

$$\ln c_{{\rm i},i} = \ln \frac{\rm Ryd}{4B_i} + \frac{1}{Q_i}\left(3(1-Q_i) + (5-3Q_i)\ln 2\right) \tag{11.142}$$

The values of the ionisation number Q_i, the number of bound electrons N_i, the binding energy B_i; all parameters of the RBEQ* model, are to be found in table 11.12 on page 490. The definition of the "average binding energy" $\bar{B}$ in the last equation (11.140c) is unclear from its sudden apparition in Inokuti [427, eq.(4.52)]. We would need to rederive the original formula to confirm whether it can merely be taken as the average:

$$\bar{B} \stackrel{?}{=} \frac{1}{Z} \sum_i N_i B_i \,,$$

which is the value that we used and reported in table 11.13.

Allowed The oscillator strength f_a of an allowed excitation is linked to the magnitude factor M_a as through the excitation threshold $\Delta\mathcal{E}_a$ as :

$$f_a = M_a {\rm Ryd}/\Delta\mathcal{E}_a \,.$$

Tabulated values of this magnitude as well as the parameter c_a for allowed excitations are dispersed throughout the tables (11.6,11.7,11.8,11.9,11.10,11.11) in section 11.4. (Look for the rows headed by the symbol $\updownarrow$ for optically allowed transitions.)

Forbidden Only dipole-forbidden transitions contribute to the second parameter c_{tot} (11.140b) through their magnitude M_b coefficient also found in the tables mentioned above. (Look for the rows headed by the symbol $\updownarrow$ and a forbiddance degree $d = 1$)

Bethe parameters from a gas mixture are combined through a sum of the parameters in (11.140) weighted by the ratio x_g of each species g in the mixture.

11.6.3 Connection

To extend the cross sections to high energies $\gtrsim 5\,\text{keV}$, where measurements are unavailable, we added a connection point with the expression for the total cross section from Bethe's theory. There are two possible choices of for the junction located at $\varepsilon_>$ which may be visualised on figure 4.3 in the chapter 4 of the previous part page 118:

- $\sigma_{\text{tot}}(\varepsilon_>) = \tilde{\sigma}_{\text{el}}(\varepsilon_>) + \sigma_{\text{inel}}(\varepsilon_>)$: replace only the elastic CS σ_{el} by the Born approximation $\tilde{\sigma}_{\text{el}}$ but leave the inelastic CS as the exact sum of individual processes : $\sigma_{\text{inel}} = \sum_i \sigma_i$.

  In this way, the elastic cross section is replaced by the Born approximation (11.9) at $\varepsilon_>$, but the inelastic cross sections are kept as their exact sum.

- $\sigma_{\text{tot}}(\varepsilon_>) = \tilde{\sigma}_{\text{el}}(\varepsilon_>) + \tilde{\sigma}_{\text{inel}}(\varepsilon_>)$: replace both the elastic and the inelastic by their high-energy approximations (Born-Inokuti 11.9 and Bethe-Inokuti 11.139).

  Then, the total cross section may be fully extrapolated analytically from $\varepsilon_>$ but it will not exactly match the sum of all processes (elastic and inelastic).

For the purpose of Monte Carlo simulations of electron swarm in the first part of this thesis, it is primordial to preserve the correspondence between the total cross section and the sum of all cross sections. Thus, we used the first choice for junction which corresponds to the last row in the tabulated values of the total cross sections available here. More on this issue is discussed in part I section 4.1.2, in particular on pages 118–120.

The construction of the total scattering cross section concludes the investigation we have done so far. The fruit of our efforts consists in a creation of a new database of cross sections which is compared and assessed in greater detail in chapter 16 of part III. In the last chapter of this part, we summarise and overview our work.

Chapter 12

Synthesis

Throughout this second part, our objective was to revisit the differential and integral cross sections between electrons and neutral atoms/molecules present in atmospheric gases; namely:

1. Molecular Nitrogen : N_2
2. Molecular Oxygen : O_2
3. Nitric Oxide : NO
4. Argon : Ar
5. Atomic Oxygen : O
6. Atomic Nitrogen : N

Our study is motivated by the presence of those species at different temperatures (see table 2.1 on page 41) which ideally correspond to different evolution stages of electric discharges in air described in the first part of this thesis.

In this chapter, we bring together the results obtained and highlight the main points of the database constructed.

After an introductory chapter 7 discussing the basic notions related to scattering (sec. 7.2), how cross sections are obtained experimentally through a very diverse palette of methods (sec. 7.3), how the calculation of cross sections relies on the marvels of quantum physics (sec. 7.4.2), we delved into an overview of the theoretical models used to calculation cross sections in chapter 8. After commenting on the difficulty of solving Schrödinger's equation from the most general approach (sec. 8.1), we oriented ourselves toward the widely used potential scattering method (sec. 8.2) in which we adopted an independent atom-based description of molecular potentials due to lack of access to more accurate models (sec. 8.2.1).

Using the partial wave approach (sec. 8.4), we combined various relevant approximations (sec. 8.5) at different energy domains to compute differential cross sections for elastic scattering 11.1 over a wide range of energies, except at low energies where we resorted to deriving differential cross sections (DCS) from a database of carefully selected experiments at each energy. A useful graphical overview of our procedure is rendered on table 11.1.

In chapter 9, we presented the algorithms used to compute matrix elements of the partial-wave method (sec. 9.1) and subsequently to assemble the differential cross section (sec. 9.2). On our path, we were faced with many doubts and issues that we expose in a dreadful chapter 10.

There, in an attempt to make a coherent review, we discuss the applicability of approximations (sec. 10.1) and criticise some *ad hoc* corrections for which we propose a dialectical terminology to qualify them and distinguish them from *ab initio* approximations (sec. 10.2). At last, we offer a walk through semi-empirical models upon which the potential scattering model relies (sec. 10.3) and conclude with a mini-study on the numerical convergence of our results (sec. 10.4).

After putting those efforts in setting up the stage, the fruit of our labour is presented in chapter 11. There, we scoured the literature in order to gather a complete set of cross sections for electron-molecule collisions. We strived to build cross sections based on available experimental data represented by simple yet adequate theoretical formulae. Chapter 11 is structured into five sections, each associated to a specific collision process:

11.1 Elastic Scattering: a patchwork of experimentally fitted DCS at low energies and theoretical calculations at intermediate and high energies.

- 11.1.1 Modified effective range theory (MERT–sec. 10.1.5) to calculate DCS at very low energies < eV based only on the scattering length A and static dipole polarisability $\alpha_{\mathrm{d},0}$ of atoms and molecules.
- 11.1.4 Plane-wave Born approximation (PWBA–sec. 8.5.1) to calculate DCS at very high energies > 10 keV based on the exponential decay radii a_i of atomic Slater-1s type orbitals (tab. 8.1).
- 11.1.5 Integrated and "residual" elastic cross sections obtained from the DCS and total cross sections respectively.

11.2 Rotational Excitations: a summary of three approximations used to calculate rotational DCS in different energy domains.

- 11.2.2 Sudden impulse approximation enables to derive DCS for any rotational transition $J_0 \to J'$ from a basic set of $J = 0 \to J'$ DCS at energies far from the excitation threshold and resonances.
- 11.2.1 First Born approximation enables to calculate DCS at *very low* energies (< eV) for:
  - (11.21a) $J \to J+1$ transitions from the static *dipole* D of heteronuclear diatomic molecules;
  - (11.21b) $J \to J+2$ transitions from the static *quadrupole* Q and anisotropic polarisability $\alpha_{\mathrm{d},2}$ of homonuclear diatomic molecules.
- 11.2.3 Spectator model approximates rotational DCS at *higher* energies (> 50 eV) only based on a geometric perspective relying on the internuclear separation R.

11.3 Vibrational Excitations and Attachment

- 11.3.1 Some elementary notions about resonant scattering
- 11.3.2 recommended vibrational DCS in the shape resonance regions ($d\pi$ wave for $N^-\ ^2\Pi_g$, isotropic for $O^-\ ^2\Pi_g$ and $NO^-\ ^3\Sigma^-$)
- 11.3.3 Cross sections of vibrational excitation obtained from the combination of accurate calculations in the local-complex-potential approach [553] and experimental data.
- 11.3.4 Dissociative attachment from theoretical calculations [555, 558] and semi-empirical law for three-body attachment.

11.4 Electronic Excitations represented by fully analytical formulae based on a semi-empirical model constructed from:

11.4.1 theoretical cross sections for dipole-allowed transitions based on the generalised oscillator strength F_n from Bethe's theory connected to the optical oscillator strength f_n of the same transition.

11.4.2 first Born approximation *scaled* semi-empirically to account for the acceleration of the scattering electron in the attractive field of the molecule

11.4.3–11.4.8 mini-review of most recent experimental data for electronic excitations with N_2, O_2, NO, Ar, O and N targets, to which our variant (11.61) of the scaled plane-wave Born approximation was fitted. The physical parameters of the fit are the "forbiddance degree" d of the transition and the optical oscillator strength f_n for optically (dipole) allowed transitions. The remaining 2 to 5 parameters are semi-empirical.

11.5 Impact Ionisation represented by an analytical model emerging from the complementation of two approximations:

11.5.1 dipole approximation of the Bethe theory described by the generalised oscillator strength density $\mathrm{d}F_i/\mathrm{d}\varepsilon$, which is accurate at small momentum transfers $qa_0 \ll 1$ and large impact parameters.

11.5.2 binary encounter approximation between the incident and a bound electron valid at large momentum transfers and small impact parameters.

11.5.3 together, both approximations were joined in Kim and Rudd [507] and Kim *et al.* [508] to which we propose a revision consisting of : (1) a higher-order correction $\propto 1/\varepsilon_0$ in the incident electron energy ε_0 and (2) a reinterpretation of the parameters used in partial ionisation cross sections.

11.5.4 most accurate and up-to-date experimental ionisation cross sections are fitted with the resulting model which relies on one parameter Q_i physically related to the integral of the oscillator strength density in each specific ionisation channel i. Furthermore, an assessment of differential ionisation cross sections is performed.

11.6 at last, we constructed a total cross section from zero to relativistic energies bridging the gap (in sec. 11.6.3) between accurate experimental measurements at low energies (sec. 11.6.1) and the asymptotic trends predicted by the Born-Bethe-Inokuti approximation for elastic and inelastic scattering of fast electrons (sec. 11.6.2).

In complementation of the summary given here, we give, in the next section, a succinct overview of the cross sections obtained for each gas target.

12.1 Anagraphs per target

For each target, we summarise the main points on the integral cross sections (ICS) and differential cross sections (DCS) obtained. For a visual and more detailed comparison of the cross sections with experimental data and other databases, the interested reader may consult chapter 16 in the third part.

Below, we first remind the notation we use and underlying models.

- σ_{tot} : Total CS, constructed as explained in the previous subsection 11.6 from experimental data up to a few keV and Bethe parameters $S(-1) \equiv M_{\text{tot}}$ and $\ln c_{\text{tot}}$.

- $\mathrm{d}\sigma_{\text{e}}/\mathrm{d}\Omega^{*}$: (vibrationally) elastic DCS (comprising all rotational transitions) obtained either from:

  1. Mean-effective-range theory (MERT sec. 10.1.5) (very low energies $\leq 0.1\,\text{eV}$)
  2. Extrapolation of experimental data (low energies 1—20 eV)
  3. Partial wave calculations in potential scattering (intermediate and high energies 30 eV to 10 keV) from (8.129) with (9.19)
  4. Born approximation to polarisation and static atomic potentials (very high energies $> 10\,\text{keV}$) from formulae gathered in chapter 14

- σ_{e} : Elastic ICS, integrated from the DCS:

$$\sigma_{\text{e}} \equiv 2\pi \int_0^{\pi} \frac{\mathrm{d}\sigma_{\text{e}}}{\mathrm{d}\Omega} \sin\theta \,\mathrm{d}\theta \;.$$

- σ_{re} : Residual rotational-elastic CS, obtained from the total CS after subtracting all inelastic (except rotational) cross sections:

$$\sigma_{\text{re}} \equiv \sigma_{\text{tot}} - \sum_i \sigma_i \;.$$

- σ_{m} : elastic momentum-transfer CS obtained from σ_{re} through:

$$\sigma_{\text{m}} = \sigma_{\text{re}}(1 - \langle\cos\theta\rangle) \;,$$

  with

$$\langle\cos\theta\rangle = \frac{2\pi}{\sigma_{\text{e}}} \int_0^{\pi} \frac{\mathrm{d}\sigma_{\text{e}}}{\mathrm{d}\Omega} \cos\theta \sin\theta \,\mathrm{d}\theta \;.$$

- σ_{rot} : rotational excitation CS. Obtained from a set of elementary $J_0 = 0 \to J$ rotational excitations, and extended to arbitrary transitions $J_0 \neq 0 \to J'$ with the sudden impulse approximation (11.24).

- σ_{vib} : vibrational excitation CS. Obtained from the local-complex-potential calculations of Laporta *et al.* [552, 553] and extended with experimental measurements for a few $v = 0 \to v'$ transitions.

- σ_{att} : dissociative attachment CS for O_2 and NO. Obtained from the local-complex-potential calculations of Laporta *et al.* [555, 558] and experimental data of Rapp and Briglia [767].

- σ_{elc} : electronic excitation CS. Analytical fits to most recent experimental data. Transitions are categorised according to their "forbiddance degree" d determined by the transition matrix element in the Born approximation:

  $d = 0$: Optically (dipole) allowed transitions (11.62)

  $d = 1$: Electric dipole forbidden transitions (11.61b)

*The subscript 'e' is implicit in the thesis

$d = 2$: Electric quadrupole forbidden transitions (or magnetic dipole forbidden) (11.61b)

$d = 3$: Spin forbidden transitions (11.61b)

Some transitions may contain a resonance peak fitted by (11.63).

- σ_{ion} : total or partial ionisation cross sections determined by a revised analytical relativistic binary encounter and dipole approximation called RBEQ* (11.120). It relies on one adjustable parameter Q (11.108) of physical interpretation linked to the integral of the optical oscillator strength density for a given partial ionisation channel (11.109) and (11.93). Q is adjusted with constraint to match most recommended experimental data by Lindsay and Mangan [596].

N_2

σ_{tot} The number of experimental data their agreement and resolution are very good and enable an accurate estimation of the total CS up to 2 keV. Data above 2 keV are contaminated with noise. The Bethe parameter M_{tot} is in agreement with previously reported values [62, p.100:table 9].

$\frac{\mathrm{d}\sigma_{\text{e}}}{\mathrm{d}\Omega}$ Below 30 eV, experimental results agree well and an accurate extrapolation is possible. The DCS may be extended with the MERT below 0.1 eV where it agrees well with the results of Sohn *et al.* [863].

Above 30 eV, angular-momentum close-coupling calculations with an optical potential give acceptable results except at intermediate angles 70–120°, where the DCS is overestimated. This can be corrected with a more accurate representation of the static potential from the Hartree-Fock variational method.

σ_{m} Elastic momentum transfer cross section (MTCS) is in excellent agreement with experimental data in the two regions of 0.1–2 eV and 4–200 eV. In the vicinity of the N_2^- $^2\Pi_g$ resonance, it needs considerable improvement from the DCS. Above 200 eV, there is a large experimental uncertainty over scattering at wide angles.

σ_{rot} The theoretical calculations of Kutz and Meyer [546] may be used to derive rotational CS in the sudden impulse approximation.

σ_{vib} The calculations of Laporta *et al.* [554] provide accurate CS in the N_2^- $^2\Pi_g$ resonance region. Above 5 eV, the CS must be extended with experimental data [600, 910] available only for $v = 0 \rightarrow 1$.

σ_{elc} Analytical fits to recent experimental data [463, 622, 624] were obtained. Fits to optically allowed excitations are very accurate. For forbidden transitions, experimental results not agree well, especially in the region near threshold where the data is also sparse. Thus, fits to forbidden transitions are average.

Two notable exceptions : accurate measurements of the transitions to the C $^3\Pi_u$ [623, 1012] and E $^3\Sigma_g^+$ [123, 407, 622] states enabled to give close fits using (11.64) including the resonance peak.

σ_{ion} The RBEQ* analytical fit to the data recommended by Itikawa [439] and recently measured by Shen *et al.* [831] is accurate to within 3 %.

O_2

$\sigma_{\rm tot}$ Up to 100 eV experimental data are not in good agreement and one must choose carefully which measurements to favour in certain regions over others. Above 100 eV the agreement is very satisfactory. The Bethe parameter $M_{\rm tot}$ is in slightly below the one reported in [62, p.107:table 11].

$\frac{{\rm d}\sigma_{\rm e}}{{\rm d}\Omega}$ Below 30 eV, some sets of experimental results agree better [353, 598, 893] than others, an accurate extrapolation to 180° is possible at some energies. The DCS does not agree well with the MERT at 1 eV and the extrapolation below 1 eV is very uncertain.

Above 30 eV, angular-momentum close-coupling calculations with an optical potential give fair results except at intermediate angles 70—120°, where the only available experimental DCS is overestimated [842]. This can be improved, albeit not totally corrected, with a more accurate representation of the static potential from the Hartree-Fock variational method. There is a discrepancy at 200 eV between experimental data at large angles and the unadjusted absorption potential of the optical model favours one set of data [206] over the other [842].

$\sigma_{\rm m}$ Good agreement between 1—10 eV but strong overestimation over a factor of 2 beyond 30 eV. This discrepancy may be partly imputable to the underestimated experimental data and partly to the overestimation of the mid-angle DCS and intermediate energies.

$\sigma_{\rm rot}$ Utter absence of reliable rotational theoretical or experimental cross sections. These are affected by the very narrow O_2^- $^2\Pi_g$ resonance. The first Born quadrupole approximation gives insufficient CS.

$\sigma_{\rm vib}$ The calculations of Laporta *et al.* [552] provide accurate CS in the O_2^- $^2\Pi_g$ resonance region. The agreement in the $^4\Sigma_u^-$ resonance (mainly) at 10 eV with experimental data is qualitatively good but deviates strongly at 5 eV.

$\sigma_{\rm att}$: Exclusively from theoretical calculations [558] which agree well with experimental data [767].

$\sigma_{\rm elc}$ Experimental data for low forbidden transitions (a $^1\Delta_g$ and b $^1\Sigma_g^+$) are numerous but scattered. The fit is difficult to constrain asymptotically. Old and recent experimental data for higher excitations are in considerable disagreement. We privileged the recent study of Suzuki *et al.* [897] which the fits follow closely.

$\sigma_{\rm ion}$ The RBEQ* analytical fit to the data recommended by Itikawa [440] is accurate to within 4 % and within 8 % with the data of [814] at high energies > keV.

NO

$\sigma_{\rm tot}$ Experimental data are few but agree well. We copied the recommended data of Song *et al.* [865, table 2] and used theoretical calculations of Laporta *et al.* [554] below 1.16 eV. There is a great gap in the (Bethe) sum of oscillator strengths of optically-allowed excitations (11.70) which is also seen in [62, p.113:table 14].

$\frac{{\rm d}\sigma_{\rm e}}{{\rm d}\Omega}$ Below 30 eV the DCS is extrapolated from only one set of data [654]. DCS below 1 eV extrapolated with the MERT are expected to be inaccurate due to the permanent dipole of NO.

Above 30 eV, angular-momentum close-coupling calculations with an optical potential are mixed with the independent atom approximation to give a close match with experimental data in the mid-angular range. Accurate results could be obtained with a more rigorous calculation using a representation of the static potential from the Hartree-Fock variational method. There is to experimental data to compare with above 50 eV, calculations from the optical potential are blind.

σ_{rot} No experimental nor theoretical data, the first Born dipole approximation is the best guess.

σ_{vib} The calculations of Laporta *et al.* [557] at energies below 5 eV were complemented with experimental [654] in the NO^- $^3\Pi$ resonance region near 15 eV whose position is shifted about twice farther in energy than predicted theoretically.

σ_{att} Below 6 eV from theoretical calculations [555] above from experimental data [767].

σ_{elc} Experimental data are scarce [120] and the description of the inelastic energy losses is incomplete. Nonetheless, most excitations are optically-allowed with no resonance feature and the fits to the unique data are usually good.

σ_{ion} The accuracy of the RBEQ* analytical fit to the data recommended by Itikawa [441] is better than 2 % but the disagreement with other data [768] exceeds 12 %.

Ar

σ_{tot} Experimental data agree very well on a broad range of energies except from 400 eV where a small (~8 %) disparity appears probably imputable to strong forward angle scattering. The Bethe sum of oscillator strengths (11.70) is incomplete. Also, due to missing ionisation losses, the M_{tot} Bethe parameter is greatly underestimated compared to the reported value [62, p.84:table 3].

$\frac{\mathrm{d}\sigma_{\mathrm{e}}}{\mathrm{d}\Omega}$ Below 200 eV, accurate BSR calculations of Zatsarinny *et al.* [1002] give DCS in good agreement with a lavish database of experimental DCS.

Above 200 eV, calculations from our implementation of the optical potential scattering join smoothly with the BSR DCS and agree well with experimental data at high energies.

σ_{e} & σ_{m} The miscorrespondence between the ICS and the MTCS σ_{m} at energies below 5 eV deteriorates the accuracy of the latter near the Ramsauer-Townsend minimum around 0.23 eV. Beyond 10 eV, both ICS and MTCS are accurate although disagreement persists with experimental DCS in specific energy regions.

σ_{elc} Experimental data from optical methods [175, 176] disagree significantly with cross-beam integrated DCS [180, 491]. The fine-structure splitting of Ar excited states may not be resolved well for all states. Our fits to experimental data are essentially good for $4s$ excited states and fair for the ensemble of $4p$ states grouped together. Fits to optically-allowed excitations are well constrained with measurements of optical oscillator strengths, but lack good constraint for forbidden excitations. Excitations to Rydberg states above the $5s$ orbital are difficult to resolve and must be lumped together.

σ_{ion} There is a surprisingly large disparity (>15 %) in the experimental data for ionisation. The RBEQ* analytical fit matches selected measurements [321, 768] to within 4 %. Nevertheless, the corresponding Bethe parameters $M^2_{\mathrm{i},Q}$ are greatly underestimated because the model distinguishes not partial ionisations to excited ionic states.

O

σ_{tot} Experimental data are few and very noisy.

$\frac{\mathrm{d}\sigma_{\mathrm{e}}}{\mathrm{d}\Omega}$ Below 10 eV only one set of experimental DCS is available [984]. It does not join smoothly neither with the MERT below 1 eV nor with our partial-wave DCS from an optical potential above 10 eV. The fact that atomic oxygen has two singly occupied orbitals requires to improve significantly the exchange and correlation potentials based on the spin-up and spin-down average electron densities.

σ_{elc} There is no data for transitions between the low lying fine-structure levels of the atomic oxygen ground state. The CS are based on purely theoretical conjectures [63]. For other excitations, several experiments were conducted to measure inelastic cross sections and oscillator strengths. The fits are not always constrained well. There are four excitations to fully auto-ionising states.

σ_{ion} The RBEQ* model may not be directly fitted to experimental cross sections because of autoionising states modelled separately. Without autoionisation, the analytical fit is 10 % the experimental CS for total ionisation.

N

σ_{tot} Data is absent.

$\frac{\mathrm{d}\sigma_{\mathrm{e}}}{\mathrm{d}\Omega}$ Experimental data is absent. We use our own partial wave calculations in the whole range of energies, except below 1 eV which is calculated by the MERT. Calculations are coherent with the optical potential CS of ELSEPA.

σ_{e} Calculations of Wang *et al.* [975] are used up to 150 eV. The derived MTCS σ_{m} are probably inaccurate below 5 eV.

σ_{elc} Very few experimental data. Many transitions, for which experimental data is absent (e.g. $\mathrm{N}^*\ {}^2P^o$), are fitted to the calculations of Wang *et al.* [975].

σ_{ion} Available experimental data are probably contaminated with ionisation CS from metastable $\mathrm{N}^*\ {}^2D^o$ states released in the microwave discharge producing nitrogen atoms from dissociation of N_2 [117]. The RBEQ* is not fitted to the data but the Q values are derived from known oscillator strengths to optically-allowed excitations. The resulting CS agrees well with the theoretical conjecture of Kim and Desclaux [506].

12.2 Conclusions

The interaction of electrons with molecules is paved with endlessly fascinating characteristics. The outcome of a collision is determined by the outgoing electron energy, deflection and the final state of the molecule. For each different final state, one defines a reaction channel of the collision. Within the same channel, the angular distribution of the outgoing electron is encompassed by a differential scattering cross section whose integration over all angle of the unit sphere gives a very practical quantity of the dimension of a surface area named the integral cross section.

A cross section linked to a specific channel may be physically interpreted as the "apparent size" of the molecule seen by electrons that are shot like arrows on an archery target. A cross section is thus a bridge between the deterministic and probabilistic description of a collision. The possession of cross sections for all possible reaction channels enables, in principle, a complete description of the interaction of electrons in gaseous media. In this second part of the present thesis, we sought after such endeavour.

From low to high kinetic energies of the colliding electron, the outcome of the interaction reflects very distinct traits.

At low energies and at far impact parameters (distant interaction), polarisation forces dominate;	At high energies and close distances, the electrostatic force between electrons and the screened nucleus dominates.

Fast electrons at far distances introduce an electromagnetic perturbation on the electronic cloud similar to that of a photon. This perturbation can be approximated by a swinging dipole whose amplitude is determined by the dipole matrix moment between the ground and electronic excited state. This is why in the limit of very high energies and small momentum-transfers (insignificant deviation), the cross section for inelastic scattering may be related to photoabsorption cross sections through the optical oscillator strength. At closer distances, fast electrons impinge on bound electrons in a fashion assimilable* to billiard balls. The interaction is described as a binary encounter with large amounts of momentum transferred to the bound electrons.

Slow electrons at far distances perturb the electronic cloud almost adiabatically; meaning that the cloud distorts in response to the quasi-electrostatic field of the slow electron. The distortion induced may be parameterised by the static polarisability coefficients of the molecule. Moreover, except for s-waves (frontal collisions) slow electrons do not penetrate the inner layers of atoms and molecules due to the centrifugal barrier. This implies that the interaction may be restricted to a zone of the size of the molecule's effective range. For very slow electrons, a development in orders of the electron's velocity leads to the modified effective range theory.

In the **intermediate** range of energies, the interaction is complex and intricate. The scattering electron invades the space occupied by the electronic cloud and becomes almost part of the molecule, forming thereby an anion compound. The compound formed is unstable and decays after a certain time. Formation of the compound is favoured at certain electron energies which emulate electronic configurations of the anion. The specific energies and decay times characterise the phenomenon of resonance. Resonant interaction manifests itself very conspicuously by rapid changes in the cross section according to the electron energy.

In a wave mechanics perspective, the propagation of a free electron is described in terms of plane waves (or rather packets of these), whereas the interaction with a target involves harmonic spherical waves. The correspondence between planar waves and spherical waves makes the whole description of scattering mathematically challenging to grasp though beautifully interlaced. Interference patterns between different spherical waves create, far from the scattering target, a distribution pattern of scattering probabilities describing the angular differential cross section of the scattered electrons. Understanding the correspondence between incoming spherical waves and outgoing spherical waves which incurred phase shifts, enables to encompass the information of the electron-molecule interaction into the differential cross section.

The purpose of the second part of this thesis was to gather available knowledge about electron-molecule scattering in order to construct an extended set of cross sections for various types of interactions with atmospheric atoms and molecules.

*"assimilare": to make like, make similar. The modern meaning, of integrating into a community or adopting an idea/tradition, is a derivation.

Our goal was reached within the limits of our possibilities owing to the great amount of open research available in the scientific literature. The advance of science and availability of data enabled us to undertake a study similar to the one conducted by Brusa *et al.* [125] for noble gases, but extended to diatomic molecules with several major improvements which we highlight below.

- ▷ The description of elastic scattering through an optical potential based on the model of Salvat [801], extended presently with more recent semi-empirical models, and the S-matrix in the angular-momentum close-coupling approximation from Martinazzo *et al.* [632].
- ▷ Extension of the scaled Born approximation to obtain new analytical fits to the asymptotical integral elastic cross sections calculated with from atomic potentials based on the Hartree-Fock-Slater approximation.
- ▷ Use of the sudden impulse approximation to scale rotational excitations to arbitrary transitions $J_0 \to J$ as summarised by Shimamura [836].
- ▷ Combination of most recent experimental data [598, 600, 654] and accurate theoretical calculations from Laporta *et al.* [552, 553] in order to produce a set of cross section for vibrational excitations and attachment to oxygen and nitric oxide.
- ▷ Improved analytical formulae of cross sections for electronic excitations based on the semi-empirical scaling model of Kim [504].
- ▷ Constraint of the electronic excitations according to their forbiddance degree and optical oscillator strengths (if allowed).
- ▷ Partial ionisation cross sections from an improved model of the relativistic binary-encounter Bethe model of Kim *et al.* [508].
- ▷ Constraint of the partial ionisation based on only one physically meaningful parameter Q, related to the integral of the generalised oscillator strength density.
- ▷ The asymptotical total cross section is not fitted but results from the sum of the Born and Bethe parameters related to the analytical elastic and inelastic cross sections respectively.
- ▷ The total cross section was constructed from a selected set of most up-to-date experimental measurements.
- ▷ As done in the study [125], the residual elastic cross section has been obtained as the difference between the total and the sum of inelastic cross sections.

The cross sections obtained are physically enrooted through well defined parameters which are:

- ◦ A : the scattering length
- ◦ α_{d} : the static dipole polarisability
- ◦ D : dipole and Q : quadrupole moments
- ◦ f_x : Optical oscillator strengths
- ◦ M_i^2 : Bethe parameters
- ◦ I_i : Partial ionisation thresholds

This is a first step in producing a database which contains both information and knowledge.

12.3 Perspectives

There are many ways in which our cross sections would need to be improved. Their current state reflects the limitations inherent to a doctoral thesis isolated from the community of quantum physics electron-molecule interactions.

Starting from the least demanding to the most difficult improvements we list:

* Use more advanced versions [272, 668] of the modified effective range theory to improve the elastic cross sections at very low energies.
* Apply the analytical Born completion [274, 676] to diatomic molecules to calculate accurate rotational cross sections near threshold.
* Search for the most recent updates on the sum of oscillator strengths of optical allowed excitations pertaining to each vibronic band of a molecular excited state.
* Obtain accurate Hartree-Fock representations of static potentials of diatomic molecules. We could start with analytical corrections to the independent atom model [285].
* Build a robust semi-empirical to calculate three-body attachment cross sections from resonant vibrational excitation CS.
* Find a simple yet universal parameterisation of the generalised oscillator strength to use in the RBEQ* model and discrete excitations.
* Devise a semi-empirical fit to inelastic DCS based on the generalised oscillator strength.
* Extend the RBEQ* model to represent doubly differential cross section for impact ionisation.
* Move away from semi-empirical models of the optical potential to the more general R-matrix calculation of DCS.

Further investigations on the experimental side are always welcome, however, we think we should better manage the resources that are at our disposal rather than ask for more onerous projects.

The present study revealed that the resources available are endlessly bountiful and exceed our ability to assimilate those into coherent sets of information. We would therefore like to encourage the centralisation of parameters of physical relevance, such as multipole moments, polarisabilities, oscillator strengths, Franck-Condon factors, scattering lengths, etc. which are scattered throughout the literature and are not always regrouped for modellers' convenience.

As a note to the side, investigation in the future will certainly focus and exploit the potential offered by machine learning to construct cross sections from trained algorithms [885]. Although, we think that diversification of methods always enriches the field of science, it also poses a danger that some methods fall out of use due to the extensive shift to others. Some methods have proven themselves more powerful than others without any doubt. Nevertheless, ascent in power is most often accompanied by more onerous needs. It is thus good to have a palette of possibilities each affordable and open to everyone's means.

The philosophy of the present cross sections was to make them accessible and understandable to the users. We wish that the future will bring us with sources of data both open in their information content but also significantly less obscure in the knowledge they rely on.

Appendix C

Atomic and Molecular Structure

C.1 Atoms

The qualitative shell structure of electrons around nuclei is well-known and perhaps too basic to be included here. Every elementary textbook on quantum mechanics (e.g. Eisberg *et al.* [264, §7-5:p.239-242 and §9-7:p.331-336] or Hertel and Schulz [398, §3.1:p.137-142]) explains why the electron's wave function in bounds states can be characterised by four quantum numbers : (n, ℓ, m_ℓ, m_s). Those represent the principal quantum number (essentially for the radial part of the wave function), the orbital angular momentum $\hbar\ell(\ell+1)$, its projection $\boldsymbol{\ell}\cdot\hat{\mathbf{z}}$ on the reference z-axis m_ℓ (known as the magnetic number) and the spin projection $m_s = \pm 1/2$ on z. All *orbitals* with an identical n form an atomic *shell* composed of $\ell = 0 \dots n-1$ *subshells*.

Arguably the most fundamental principle (after quantisation) to the structure of matter is the Pauli exclusion principle which states that the set of quantum numbers in a system are unique to each electron. This leads to the regular filling of orbitals in the periodic system of elements.

With the familiar spectroscopic notation $\ell = 0, 1, 2, 3, \cdots \equiv s, p, d, f, \dots$, the electronic configuration of an atom is represented as an ordered set of orbitals with their occupation number as a superscript. The three atoms studied presently N, O, Ar, have a ground-state ("X") configuration [539] :

N - $1s^2\,2s^2\,2p^3$: X $^4S^\circ_{3/2}$

O - $1s^2\,2s^2\,2p^4$: X $^3P_2$

Ar - $1s^2\,2s^2\,2p^6\,3s^2\,3p^6$: X $^1S_0$

Besides the configuration, the *state* of the atom can be described by the *total* (orbital and spin) angular momenta of its constituent electrons with the following notation $^{2S+1}L_J$. The pre-superscript $2S+1$ gives the multiplicity of the state due to the total spin S. Then, a capital letter is used $S, P, D, \dots$ for total orbital momenta $L = 0, 1, 2, \dots$. Finally, the value for the combined orbital+spin angular momentum $\mathbf{J} = \mathbf{L} + \mathbf{S}$ is written as a subscript. This type of coupling is known as Russel-Saunders or "LS"-coupling which applies to atoms with smaller Z (typically all before Neon). More explanations can be found in Hertel and Schulz [398, §6.2.6:p.301-303].

For heavier atoms, the spin-orbit $\mathbf{j} = \boldsymbol{\ell} + \mathbf{s}$ coupling between a group of electrons (ionic core or shell) or even for each individual electron becomes important. In this case, the total orbital L and spin S momenta may no longer describe unambiguously the state of the atom and only J becomes pertinent. This situation is known as the "jj"-coupling illustrated in Hertel and Schulz [398, p.512-9:§10.4].

In addition to J, regardless of the dominant coupling scheme, the inversion symmetry (parity) of the wave function is signalled as $^\circ$ for negative (odd) parity states. This property can be derived from the number (odd/even) of electrons in open shells of *odd* ℓ angular orbitals inherent from symmetry properties of spherical harmonics.

For more insight about atoms and various perturbations altering the simple image of their shell structure, I recommend consulting Morrison *et al.* [670, especially chapters 8&9].

C.2 Molecules

In molecules, the orbital structure observed in atoms must be amended. Molecular orbitals (MO) can be roughly seen as a linear combination of atomic orbitals (LCAO) in order to establish an identification pattern. When two atoms are brought close together, the orbital angular momentum number ℓ loses its goodness (the $\boldsymbol{\ell}$ operator does not commute any more with the Hamiltonian due to the breakdown of spherical symmetry). This means that a new set of quantum numbers must be chosen to describe molecular orbitals. One such number is the orbital angular momentum's projection on the internuclear z-axis : $\lambda = \boldsymbol{\ell}\cdot\hat{\mathbf{z}}$, labelled with Greek letters $\lambda = 0, 1, 2, \cdots \equiv \sigma, \pi, \delta, \ldots$ in analogy to $s, p, d, \ldots$ atomic orbitals.

For *homonuclear* atoms, depending whether the atomic orbitals a, a are combined constructively $(a + a)$ or subtractively $(a - a)$, the resulting molecular orbital is endowed with different symmetry properties ($\pm$ parity). For positive = "even" = "gerade" = g parity, the wave function $\Psi(\mathbf{r})$ is symmetric in space inversion ($\mathbf{r} \leftrightarrow -\mathbf{r}$) about the internuclear midpoint. Negative = "odd" = "ungerade" = u parity is antisymmetric. In shorthand :

$$\Psi_g(\mathbf{r}) = +\Psi_g(-\mathbf{r}) \qquad \text{whereas} \qquad \Psi_u(\mathbf{r}) = -\Psi_u(-\mathbf{r}) \tag{C.1}$$

A useful notion (but not a quantum number) to the MO is the *bonding* character of an orbital related to the overlap integral. Simply put, the electronic density of a bonding orbital does not annihilate on the internuclear axis, as opposed to antibonding orbitals which are marked with an * superscript. Below, we indicate how the first $1s$, $2s$ and $2p$ orbitals from *homonuclear* atoms merge to give molecular orbitals

$$\begin{aligned} 1s + 1s &\to 1\sigma_g & \qquad 1\sigma_u^* &\leftarrow 1s - 1s \\ 2s + 2s &\to 2\sigma_g & \qquad 2\sigma_u^* &\leftarrow 2s - 2s \\ 2p_{x,y} + 2p_{x,y} &\to 1\pi_u & \qquad 1\pi_g^* &\leftarrow 2p_{x,y} - 2p_{x,y} \\ 2p_z + 2p_z &\to 3\sigma_u^* & \qquad 3\sigma_g &\leftarrow 2p_z - 2p_z \end{aligned}$$

The first numeral quantum number merely counts the orbitals in an ordered manner rising with energy for each projection type. In LCAO from *heteronuclear* atoms, parity ceases to exist and thus what were originally $1\sigma_g, 1\sigma_u^*, 2\sigma_g, 2\sigma_u^*, \ldots$ have to be relabelled as $1\sigma, 2\sigma^*, 3\sigma, 4\sigma^*, \ldots$.

In a similar fashion to atoms, the state of a *linear* molecule is designated by $^{2S+1}\Lambda$, where the *projection* on the molecular z-axis $\Lambda = \mathbf{L}\cdot\hat{\mathbf{z}}$ of the *total* orbital angular momentum $\mathbf{L}$ operator is used instead; with $\Lambda = \Sigma, \Pi, \Delta, \ldots$ for $\Lambda = 0, 1, 2, \ldots$. As before, $2S + 1$ denotes the multiplicity due to the molecule's spin projections on $\hat{\mathbf{z}}$. For *homonuclear* molecules (or symmetric-top), the state can additionally be characterised by its parity (g/u) defined by the properties in (C.1).

For $\Sigma :\equiv \Lambda = 0$ states *only* but also applicable to *heteronuclear* molecules, an additionally quantum number noted as a superscript $^\pm$, characterises the *reflection* symmetry property by an arbitrary plane containing the molecular axis $\hat{\mathbf{z}}$.

We can now introduce the notation that characterises the *ground* state of our three main diatomic molecules N_2, O_2 and NO as [399, 540, 607, p.121, p.426, p.217]:

N_2 - $1\sigma_g^2\,1\sigma_u^2\,2\sigma_g^2\,2\sigma_u^2\,1\pi_u^4\,3\sigma_g^2$: X $^1\Sigma_g^+$

O_2 - $1\sigma_g^2\,1\sigma_u^2\,2\sigma_g^2\,2\sigma_u^2\,3\sigma_g^2\,1\pi_u^4\,1\pi_g^2$: X $^3\Sigma_g^-$

NO - $1\sigma^2\,2\sigma^2\,3\sigma^2\,4\sigma^2\,1\pi^4\,5\sigma^2\,2\pi^1$: X $^2\Pi$

In summary we have here perfect examples of a singlet (N_2), a doublet* (NO) and a triplet (O_2) for diatomic molecules in their ground states.

Readers interested in more quantitative information can consult Hertel and Schulz [399, Chapter 3, section 3.5.4] discussing molecular orbitals built from LCAO. Particularly, the attentive reader will find why there is an inversion between $3\sigma_g$ and $1\pi_u$ orbital energies from N_2 to O_2 (as correctly listed above) in their figures 3.36 and 3.37 [399]. Finally, [399, sections 3.6 and 3.7] study respectively homonuclear and heteronuclear diatomic molecules.

Both for atoms and molecules, all filled inner orbitals corresponding to a certain principal quantum number are called *core* orbitals whereas the last level is known as the *valence* orbitals. Core orbitals participate weakly to chemical bonding and remain fairly unperturbed when atoms are grouped into molecules as opposed to molecular valence orbitals which get deformed from their original atomic shape and define the molecular bond strength. All outer orbitals $s, p, ...$ pertaining to the same principal quantum number n form the valence shell.

Excitations. When a shell electron excites, it switches to a previously unoccupied orbital or flips its spin if it may. If this new configuration remains still within the same valence shell, it is referred-to as a *valence state*. If however the electron jumps to a higher orbital with a different principal quantum number, a *Rydberg state* is created. Rydberg states of molecules resemble the Rydberg progression in atoms where the excited *Rydberg electron* sees a screened central potential. They play a fundamental role in core-excited resonance scattering and molecule predissociation.

Finally, from spectroscopic tradition, all ground states are preceded by and "X" and electronically excited states form (ro)vibronic bands named with letters $A, B, C, \ldots, a, b, c, \ldots$ with an eventual single $'$ or double prime $''$ and a numeral subscript $2, 3, 4, \ldots$ for Rydberg states indicating the principal quantum number of the excited electron.

Valuable information about the electronic configuration of ground and excited states can be found in the reports of Lofthus and Krupenie [607] (N_2) and Krupenie [540] (O_2).

*Actually, the spin-orbit interaction of the lone electron in 2π splits the degenerate state into $^2\Pi_{1/2}$ and $^2\Pi_{3/2}$

Appendix D

Vibronic Transitions

When an electron excites a molecule to a different electronic state, the molecule's potential curve with respect to the internuclear separation R changes also. This is illustrated on figure D.1. As a consequence, the final state can settle into a different vibrational level of the excited electronic state. Thus, electronic and vibrational transitions are most often mixed together and known as "vibronic" transitions. However, because the nuclei are considerably heavier than electrons, the vibrational motion and electronic transitions can be handily separated in their mathematical treatment.

When the energy is sufficiently high, vibronic excitations can eventually lead to dissociation of the molecule. There are essentially five ways in which this can occur [834, p.67:figure 12] (excluding the role of subsequent collisions).

1. The molecule is directly excited to a *repulsive* state. The nuclei move away from each other as they roll down the internuclear potential curve (fig D.1-iii). This is considered as a *direct dissociation*.

2. The vibrational level of the excited state lies beyond the highest bound state (fig D.1-ii transition $a \rightarrow c$). In this case, if the molecule cannot lose more energy through de-excitation, it dissociates as well. This is known as *dissociative excitation* and is not a strictly direct excitation in the sense that the process can be *resonant*[*] [558].

3. There is a crossing point between an electronic bound state and a repulsive state (fig D.1-ii point p). As it vibrates, the molecule can also change its state at this crossing point and veer apart in a mechanism known as *predissociation*.

4. The unstable intermediary state of the electron-molecule anion has a lifetime longer than its vibrational period which may lead to *dissociative attachment* [834, p.276] (fig D.1 (vvv) or transition $a \rightarrow c$ on (vv))

5. For energies above the ionisation threshold, *dissociative ionisation* corresponds to (direct or pre-)dissociation of an ion most often when left in an excited state. This is particularly the case when the ejected electron comes from a core orbital.

[*] and thus not obeying the Franck-Condon principle described below

Figuratively, those scenarios of molecule dissociation by electron impact could be parodied by a child running and accidentally kicking into a towering stack of lumber whereupon:

1. the stack collapses on the spot;
2. the stack wiggles while collapsing;
3. the stack tilts to one side, to the other, gives a sign of ebbing then suddenly collapses long after the child has run away in terror;
4. the unfortunate child actually clings onto the stack which slowly falls down;
5. one log got swiftly kicked away, causing subsequent instability of the stack.

The point is, that while the stack is tilting, an adult can try to intervene and resorb the swaying to prevent collapse.

Formally, back to the atomic world, a collision with another molecule or a spontaneous photon emission can prevent the dissociation of a excited bound state. Also, analogous to the concept of predissociation, the phenomenon where excited states above the ionisation threshold subsequently ionise on their own is known as *autoionisation*. This mechanism applies to atoms as well.

In summary, the future of a (super-)excited molecule (state $a'v'$) is torn between the competing probability rates of spontaneous emission $A_{a'v'}$ (to any allowed lower state), autoionisation $I_{a'v'}$ (if applicable), predissociation $P_{a'v'}$ or collisional quenching $Q_{a'v'}$. Given the conditions (gas density, temperature, composition), predissociation is characterised by a *branching ratio* η_{pd} which determines the overall probability that an electronically (a') and vibrationally (v') excited state lead to dissociation [1011, eq.(1)]:

$$\eta_{\mathrm{pd}} = \frac{P_{a'v'}}{A_{a'v'} + I_{a'v'} + P_{a'v'} + Q_{a'v'}} \tag{D.1}$$

When determining this ratio experimentally, a distracting enemy is the optical thickness of the medium [1011, p.450:right column] which gives the impression that predissociation rates are higher due to a lower apparent emission (detection) rate of optical signals.

For an introduction into electron-diatomic molecule collision processes, we recommend reading Chandra and Joshi [167, p.2-11] from which the figure D.1 was extracted and remastered. Below, we offer a slight reminder of how and why electron-impact electronic excitations are affected by selection rules applying to optical transitions and then explain how the vibrational part can be treated separately from the electronic part in the calculation of inelastic differential cross sections.

D.1 Dipole approximation

An introduction to optical transitions (absorption/emission) due to induced electric-dipole oscillations in atoms and molecules can be found in Hertel and Schulz [398, chapter 4]. Here, we just need to express the basic formula of the dipole approximation to which the (optical) oscillator strength is closely tied. Since the electromagnetic perturbation's wavelength around the optical domain is much longer than the size of the target molecule : $k \cdot a_0 \ll 1$, only the linear term in the expansion of the plane wave exponential phase is used:

$$\exp(\mathrm{i}\mathbf{k}\cdot\mathbf{r}) = 1 + (\mathrm{i}\mathbf{k}\cdot\mathbf{r}) + \frac{1}{2!}(\mathrm{i}\mathbf{k}\cdot\mathbf{r})^2 + o(\mathbf{k}\cdot\mathbf{r})^2$$

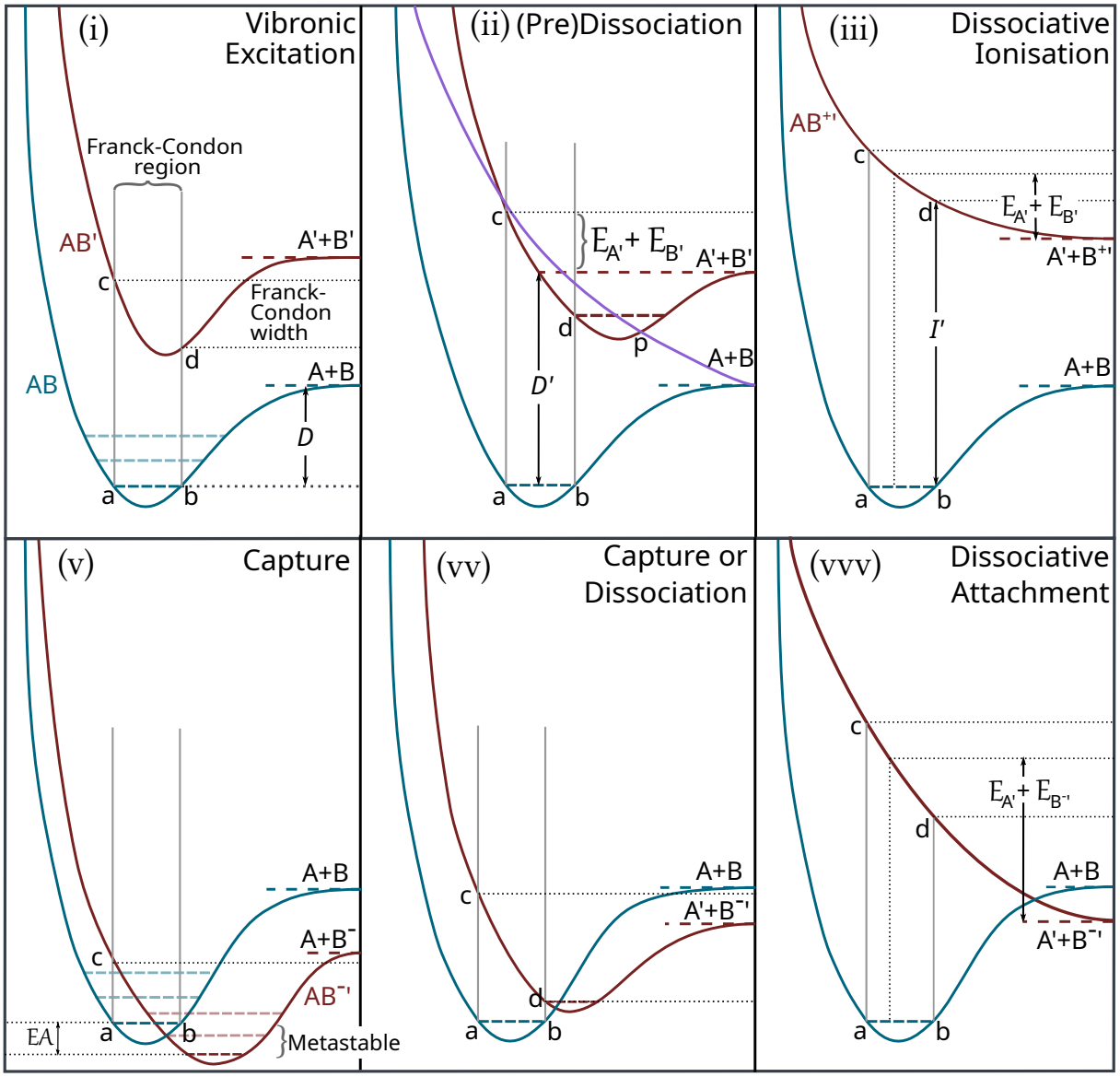

Figure D.1: Vibronic impact excitations can be visualised, according to the Franck-Condon principle (D.4-D.5), as vertical transitions intersecting two different potential curves. The internuclear separation does not change much during such transition and the probability to reach a certain vibrational sublevel can be interpreted visually as related to the probabilities of finding a molecule stretched at an initial separation value R_0. The six different situations illustrate various possible outcomes in inelastic excitations.

The three top figures represent the possibility that the molecule be (i) excited; (ii) excited or dissociated (either directly or from predissociation); (iii) directly dissociated (with or without anterior ionisation).

The bottom figures cover the possibilities that incident electron (v) be captured (attach); (vv) attach and-or dissociate the molecule; (vvv) attach dissociatively to the molecule.

Displayed on the figure are: D energy (from ground) for dissociation into atomic fragment in their ground state; D' energy for dissociation into excited fragments; $E_{A'}$ kinetic energy of the dissociated excited atomic fragment A'; EA electronic affinity of the anion AB^-; p a connection point from which predissociation is triggered. (Readapted from Chandra and Joshi [167, figure 2])

The form factor $\epsilon_{AB}(q)$ in inelastic transitions (11.49) becomes approximated by the dipole matrix element M_{AB} between two states A, B of a molecule comprising N electrons [399, 427, eq.(2.11), §3.4:eq.(3.63)] :

$$M_{AB} \equiv \langle \int \phi_A^*(\mathbf{x}_1..\mathbf{x}_N, \mathbf{R}) \sum_{j=1}^{N} \mathbf{r}_j \cdot \hat{\mathbf{e}} \phi_B(\mathbf{x}_1..\mathbf{x}_N, \mathbf{R}) \, \mathrm{d}\mathbf{x}_1.. \, \mathrm{d}\mathbf{x}_N \, \mathrm{d}\mathbf{R} \rangle_{\hat{\mathbf{e}}} \,, \tag{D.2}$$

where $\hat{\mathbf{e}}$ is an arbitrarily oriented vector used to represent light polarisation over which we perform an average ($\langle \ldots \rangle_{\hat{\mathbf{e}}}$), assuming the target molecules are isotropically oriented ($\hat{\mathbf{R}}$). The wavefunctions ϕ_A, ϕ_B depend of the shell electrons' generalised coordinates $\mathbf{x}_j = (\mathbf{r}_j, s_j)$ of configuration space $\mathbf{r}_j$ and spin s_j, and the nuclear separation vector $\mathbf{R}$.

If $M_{AB} = 0$, the transition $A \nleftrightarrow B$ is qualified as "forbidden" in the dipole approximation. Terms such as "(electric) dipole-forbidden" or "optically-forbidden" are equivalent terminologies. If this is the case, then, one must search for higher-order terms of interaction. These can stem from higher electric multipole moments (quadrupole, octupole, etc.) or from weaker coupling effects between the magnetic moment from the total electron orbital angular momentum $\mathbf{L}$ and the spin $\mathbf{S}$ (commonly known as "LS coupling", Hertel and Schulz [see section 6.2 of 398]).

If the total spin S of the multi-electron configuration changes between states A and B, only including the spin-orbit interaction (fine structure) can enlighten the possibility of such transition. In absence of coupling, because the matrix element (D.2) annihilates due to spin orthogonality, such transition is particularly qualified as "spin-forbidden".

Selection rules can quickly indicate how the transition between a state A and B is allowed or forbidden. They can be derived from symmetry arguments of the dipole matrix element (D.2) and conservation laws of total angular momentum. The spin carried by a photon is 1. Thus defining j and j' as the initial and final total momenta of the target: the triangular relation $|j - j'| \leq 1 \leq j + j'$ must be satisfied (with $j = 0 \nleftrightarrow j' = 0$). We summarise the following rules of interest in diatomic and monatomic molecules:

- The product of ϕ_A and ϕ_B must not be symmetric with respect to the inversion of $\mathbf{r}_j$ coordinates for all j. Thus in *homonuclear* diatomic molecules transitions between: $u \leftrightarrow g$ states are allowed but $u \nleftrightarrow u$ and $g \nleftrightarrow g$ not. In atoms, the parity must change also (odd $\leftrightarrow$ even).
- In Σ states, other considerations prohibit the change of the reflection symmetry, implying: $\Sigma^+ \leftrightarrow \Sigma^+$ or $\Sigma^- \leftrightarrow \Sigma^-$ but $\Sigma^+ \nleftrightarrow \Sigma^-$.
- The total angular momentum *projection* conservation logically implies that $|\Delta\Lambda| \leq 1$, since a single photon cannot induce a momentum-transfer change superior to 1.
- When spin-orbit coupling is neglected, the total spin S must be preserved. Transitions between states of different spin multiplicities $\Delta S \neq 0$ are thus spin-forbidden.
- In atoms, where the orbital angular momentum is well defined, the parity rule of spherical harmonics together with the conservation of the total angular momentum imposes that $\ell + \ell' + 1$ be even. Thus only $\Delta\ell = \ell' - \ell = \pm 1$ are allowed, $\Delta\ell = 0$ is forbidden. This is valid when only one electron switches orbitals, multiple reconfigurations are not allowed in optically induced transitions.

Those selection rules are introduced and discussed in Hertel and Schulz [399, p.309-312:especially table 5.1] for diatomic molecules and in Hertel and Schulz [398, p.196-203] for atoms. For more details and mathematical insight, refer to Steinfeld [882, p.87].

D.2 Franck-Condon Principle

When the target is a diatomic molecule, electronic transitions also involve vibrational and rotational excitations. The latter ones have negligible thresholds at energies where electronic transitions are permitted so that they are averaged over the initial and summed over the final rotational states. The transition integral as used in (11.47) for the differential cross section depends on the initial χ_a^v and final $\chi_{a'}^{v'}$ vibrational wave functions of the electronic transitions $a \to a'$ considered.

Similarly to the adiabatic approximation underlying rotational averaging, in *non-resonant* scattering, the Franck-Condon principle states that the electronic transition is faster than the vibrational period of the molecule [834, §6.5.4]. Thus, if we represent the potential curves $V_{a,a'}(R)$ of the final a' and initial a states with respect to the internuclear separation R, a transition can be conceptualised as a "vertical jump" connecting two specific vibronic states a, v and a', v' (as schematised in figure D.1, from point a→c or b→d or any intermediate pair).

Mathematically, the Franck-Condon principle is represented by taking the approximation [427, §3.5:p.321] that in orientationally-averaged DCS integral of (11.47) the electronic parts $\phi_{a'v'}(\mathbf{r}_m, \mathbf{R})$ vary slowly with R compared to the vibrational functions $\chi_{a'}^{v'}$ so that an equilibrium R_e separation can be fixed for $\phi_{a'v'}(\mathbf{r}_m, \mathbf{R}_e)$ and the remaining integral over R now proceeds only on the vibrational functions $\chi_{a,a'}^{v,v'}$:

$$\int \frac{\mathrm{d}\hat{\mathbf{R}}}{4\pi} \left| \iint \sum_{j \in m} \exp(-\mathrm{i}\mathbf{q}\cdot\mathbf{r}_j) \phi_{a'}^*(\mathbf{r}_m, \mathbf{R}) \chi_{a'}^{v'}(R) \phi_a(\mathbf{r}_m, \mathbf{R}) \chi_a^v(R)\, \mathrm{d}R\, \mathrm{d}\mathbf{r}_m \right|^2 , \tag{D.3}$$

$$\approxeq \left| \int \chi_{a'}^{v'}(R) \chi_a^v(R)\, \mathrm{d}R \right|^2 \int \frac{d\hat{\mathbf{R}}}{4\pi} \left| \int \sum_{j \in m} \exp(-\mathrm{i}\mathbf{q}\cdot\mathbf{r}_j) \phi_{a'}^*(\mathbf{r}_m, \mathbf{R}_e) \phi_a(\mathbf{r}_m, \mathbf{R}_e)\, \mathrm{d}\mathbf{r}_m \right|^2 . \tag{D.4}$$

The Franck-Condon factor $C_{\mathrm{FC}}(av, a'v')$ is defined as the squared integral [834, p.63:eq.(164)]:

$$C_{\mathrm{FC}}(av, a'v') \equiv \left| \int \chi_{a'}^{v'}(R) \chi_a^v(R)\, \mathrm{d}R \right|^2 . \tag{D.5}$$

This factor primarily governs the relative intensities of vibronic peaks corresponding to the same electronic $a \to a'$ transition [563]. There are however many cases in which this scaling law is not satisfied [509] as for example the $\mathrm{X}\,^3\Sigma_g^- \to \mathrm{B}\,^3\Sigma_u^-$ and $\mathrm{E}\,^3\Sigma_u^-$ systems of O_2.

Appendix E

Free electron gas

This model introduced by Fermi, is widely known and used in problems of quantum mechanics and can be consulted in many reference books as Eisberg *et al.* [264] and Hertel and Schulz [398, p.400-406, p.103-107]. Nonetheless, we think a basic reminder for our purpose might be useful here, especially since many derivations of the Fermi momentum found on the internet are erroneous.

The fundamental idea is to find the most compact energy distribution taken by a number of electrons confined in a small volume of space. In a cube element of volume $V = L^3$, the solutions of the 3-dimensional Schrödinger equation are standing waves verifying the following wave-number equation:

$$k^2 = \left(\frac{2\pi}{2L}\right)^2 (n_x^2 + n_y^2 + n_z^2) \quad \text{with } n_x + n_y + n_z \in \mathbb{N}^+ \tag{E.1}$$

Those are multiples of the maximal wavelength $2L$, twice the size of the box.

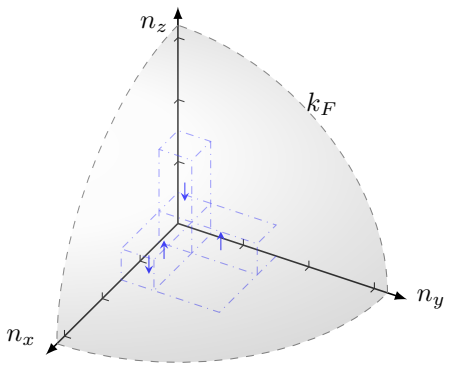

Figure E.1: Occupied cells in the momentum space of a free electron gas with spin degeneracy

Each cell is characterised by a unique set (n_x, n_y, n_z), and can host two degenerate substates due to the electron's spin $\pm\frac{1}{2}$. An illustration is given in figure E.1, with three cells, populated by electrons of spin-up or spin-down (either or both). For a given number of electron N_e inside that cubic volume element L^3, one starts populating the levels from the lowest energy. The highest occupied level when all sublevels are occupied is known as the Fermi energy ε_F straightforwardly related to the Fermi momentum k_F: $\varepsilon_\mathrm{F} = \dfrac{\hbar^2 k_\mathrm{F}^2}{2m_\mathrm{e}}$.

For a given electron density $\rho(r)$ in configuration space, one can deduce at each point the corresponding Fermi energy if we imagine that electrons coexist locally as a free gas. When the number of electrons is sufficiently high, we can move toward a statistical description of the Fermi sphere making $n_{x,y,z}$ continuous positive numbers. The overall number of vacant cells in a radius of $r \equiv \sqrt{n_x^2 + n_y^2 + n_z^2}$ is given by the octant: $\frac{1}{8}4\pi r^3/3$. By equating the number of vacancies (twice the number of cells for spin degeneracy) to the number of electrons $N_e \equiv \rho(r)L^3$, we get the Fermi radius r_F:

$$\frac{2}{8}\frac{4\pi r_\mathrm{F}^3}{3} = N_e = \rho(r)L^3 \Leftrightarrow r_\mathrm{F} = L\sqrt[3]{\rho(r)3/\pi}\,. \tag{E.2}$$

The Fermi momentum-transfer corresponds to this radius as in virtue of (E.1):

$$k_\mathrm{F} = \frac{2\pi}{2L} r_\mathrm{F} = \sqrt[3]{3\pi^2 \rho(r)} \,. \tag{E.3}$$

The present derivation of the Fermi momentum is simplistic but holds the line. I strongly advise the reader to be suspicious of derivations hosted on official websites of universities where the wave-number is magically set to $\mathbf{k} = \cancel{2\pi} / L \, (n_x, n_y, n_z)$ then the volume $4\pi k_\mathrm{F}^3/3$ is compared to the erroneously derived volume occupied by a single state, to get in the end the correct formula.

From the Fermi distribution, uniform in a spherical volume of radius k_F, the average classical kinetic energy at a position $\mathbf{r}$ is given by the integral in momentum space:

$$\left\langle \frac{\hbar^2 k^2(\mathbf{r})}{2m_\mathrm{e}} \right\rangle = \oint \frac{\hbar^2 k^2}{2m_\mathrm{e}} \frac{3}{4\pi k_\mathrm{F}^3} 4\pi k^2 \, \mathrm{d}k = \frac{3}{10} \frac{\hbar^2 k_\mathrm{F}^2}{2m_\mathrm{e}} = \frac{3}{10} (3\pi^2 \rho(\mathbf{r}))^{2/3} \text{ a.u.} \tag{E.4}$$

At a position $\mathbf{r}$, the local kinetic energy density $\mathrm{d}\varepsilon(\mathbf{r})$ in a volume element $\mathrm{d}^3\mathbf{r}$ is the average kinetic energy (E.4) times the local electron density $\rho(\mathbf{r})$:

$$\mathrm{d}\varepsilon(\mathbf{r}) = \oint_{k_\mathrm{F}} \frac{\hbar^2 k^2}{2m_\mathrm{e}} \frac{\rho(\mathbf{r}) \, \mathrm{d}^3\mathbf{r}}{\frac{4\pi}{3} (\hbar k_\mathrm{F})^3} \, \mathrm{d}^3(\hbar\mathbf{k}) = \frac{3}{5} \frac{\hbar^2 k_\mathrm{F}^2}{2m_\mathrm{e}} \rho(\mathbf{r}) \, \mathrm{d}^3\mathbf{r} = \frac{3}{10} (3\pi^2)^{2/3} (\rho(\mathbf{r}))^{5/3} \, \mathrm{d}^3\mathbf{r} \,. \tag{E.5}$$

When the free electron gas is applied not to a boxed space but to the Coulomb potential given by a point-like nucleus $V_0(r) = -Z/r$, one obtains the Thomas-Fermi model for an atom described in Hertel and Schulz [398, §10.1.5:p.501–2]. Now, the electrons in the gas are subject to a total potential V_TF determined by the nuclear potential and electronic density distribution ρ. If one assumes that the Fermi energy directly relates to the potential at a point r: $\varepsilon_\mathrm{F} = -V_\mathrm{TF}(r)$, then the potential V_TF may be determined from the Poisson equation and the link between the Fermi energy (or momentum eq. E.3) and the electronic distribution ρ [398, eq.(10.21)]:

$$\triangle V_\mathrm{TF}(r) = e^2 \frac{\rho}{\epsilon_0} = -\frac{e^2}{\epsilon_0} \left(\frac{2m_\mathrm{e}}{\hbar^2} \right)^{3/2} \frac{1}{3\pi^2} |V_\mathrm{TF}(r)|^{3/2} \,. \tag{E.6}$$

The solution of this equation with the boundary constraints yields:

$$\begin{cases} \lim\limits_{r\to\infty} V_\mathrm{TF}(r) = 0 \,, \\ \lim\limits_{r\to 0} r V_\mathrm{TF}(r) = Z \,, \end{cases} \quad \Rightarrow V_\mathrm{TF}(r) = -\frac{Ze^2}{4\pi\epsilon_0} \Phi_\mathrm{TF}(r/a_\mathrm{F}) \,, \tag{E.7}$$

where the Fermi radius a_F is defined as:

$$a_\mathrm{F} = \frac{1}{4} \left(\frac{3\pi}{\sqrt{2}} \right)^{2/3} Z^{-1/3} \cong 0.8853 Z^{-1/3} \,. \tag{E.8}$$

The Thomas-Fermi screening function Φ_TF is not exactly a decaying exponential function, though there are many analytical fits which are expressed as a weighted sum of exponentials [443] or a polynomial expansion of a denominator [564]. For exponential fits, the exponents may be scaled either in Bohr radii a_0 or Fermi radii a_F.

Part III

Building a cross sections database

Epilogue

A scientific investigation journey, when it ends, if it ends, is torn by the dilemma:

¿To share or not to share?

Historically, we know that knowledge is power and it is often assumed that withholding the former will preserve the latter. If it has not been obviated by the two previous parts of this thesis, a scientist may often feel powerless compared to (I) the enormity of the phenomenon studied and (II) the bolting advancement of theory and experiment. Not sharing data only empowers the feeling of powerlessness.

There is nothing to gain from withholding information, but is there anything to lose?

While it is very rare that experimental studies do not share concrete values of their measurements in numerical tables or supplementary files; this is quite the opposite for theoretical studies even if their results look fantastic in their plots. I would say there are two main reasons why there could be some reticence about sharing theoretical data.

Time. Disclosing data requires an extra effort than just showing the data. Since experimental data always primes over theoretical data, one could fear that the effort invested in preparing theoretical data be a waste of time.

Vulnerability. There is a fundamental difference between experimental and theoretical data.

- Errors on experimental data may be classified into systematic biases and noise.
  - When systematic, errors can sometimes be corrected by a scaling factor or a recalibration.
  - Noise, on the other hand, cannot be corrected. However, if one measurement is an outlier, it does not necessarily compromise the rest of the data.

  In brief, there are ways to salvage experimental data if one understands better what errors contaminate the data. One does not necessarily have to redo the measurements.
- Unless stochastic, as in Monte Carlo models, errors in theoretical calculations are systematic in the sense that an imprecision in the model will affect all results to a certain degree. Although in principle one can try to salvage inaccurate theoretical results with *ad hoc* corrections, these are very unwelcome.

Since theoretical results are never perfectly in agreement with experimental data, modellers might be content with showing their results but discouraged to share them (as concrete numerical values).

Then, we arrive at a crux. Contemporary science is mainly propelled by data*. Data are indispensable inputs to modelling. As a consequence, there is a growing and insatiable hunger for data because:

A. Quantity: experimental data are never enough, and we unanimously ask for more,

B. Quality: theoretical data are too often not deemed to be accurate enough, and we often disregard them.

*This sounds almost like a tautology, but anthropologists could argue that, in the past, science was driven by aesthetics, ideas or more dangerously: ideologies.

There is only one way to consolidate the best of both worlds: through synthesis. The action of synthesising is difficult because it requires to make the connection, between experimental and theoretical worlds, look seamless. This process heavily relies on the judgement aptitudes of the scientist. The mind of the scientist is assaulted by questions which require a firm decision:

- Which data are to be trusted?
- How to put weights on the data?
- Where does a model stop to be valid?
- Should a model be adjusted to data?, how?
- How to correct data to resolve a discrepancy?
- How to join smoothly two sets of data?
- Should the data privilege accuracy or traceability?

The last question deserves more explanation. Concretely, in scattering experiments, data cover a certain range of incident electron energies and angles. Synthesis is about representing the values of many experimental data, but also at energies and angles where data is absent. A theoretical model typically gives partial agreement: good agreement at some energies and angles, but less good elsewhere. If experimental evidence is compelling, one has to decide whether to adjust (tweak) the model or whether to preserve the reproducibility of the data.

¿To adjust or not to adjust?

- Adjustment of a model or the data itself may improve accuracy but kills the scientific soul of the results because it jeopardises reproducibility. Thus, adjusted data can either be taken in or thrown out but they cannot be recycled.

■ Raw data output by an algorithm or a model will inevitably contain "imperfections". Nonetheless, if the algorithm and the model are well documented, there is a spark of hope that the data could be revised in the future by improving the algorithm or the model.

This dilemma resembles the historic transition of science in the 'enlightenment' age and in the 'industrial' age. I strongly recommend the essay of Daston and Galison [210] about the objectivity of scientific images. There, they explain that, where atlases used to show stereotypical pictures of animals, plants, the human body; the advent of photography suddenly froze our perception of reality into raw pictures with shocking realism. The images would become presented not aesthetically, but in their crude raw unsynthesised form with minimal intervention of human judgement and/or perception.

At the time, raw data from photographs or measurements from machines were very prestigious because of their rarity and the difficulty to obtain them. Therefore, there were regarded as tokens that nobody would ever think about 'touching' them howsoever. In contrast, now, times have changed significantly and we are literally flooded with data produced by machines; we must synthesise them.

Back to our situation, we decided to respond to the need for updated electron-molecule cross sections by creating a database from the investigation that we conducted about electron-molecule collisions in part II. This database could not rely only on pure theoretical calculations and we had to intervene in many cases to obtain agreeable results.

This third part contains chapters that complement the work realised in part II which was subsequently used as input to the research conducted in part I.

- chapter 13 explains how experimental (differential) cross sections were fitted by analytical expressions, how they were constrained and how we assessed them.
- chapter 14 regroups a collection of formulae obtained in the framework of the plane-wave Born approximation in order to model elastic scattering at high energies above 10 keV.
- chapter 15 presents the database constructed. The first section 15.1 explains how some experimental data were updated and how we coped with missing data. The second section 15.2 explains how to access and use the database.
- chapter 16 compares the database presented in the previous chapter with cross sections from other databases and experimental data. It then assesses the accuracy of the new database from electron swarm transport parameters calculated by a kinetic solver of the Boltzmann equation.

At the end, I added two other chapters about the conclusions I drew, not about the content of the science produced, but about the process of scientific investigation from an anthropological perspective.

- chapter 17 very briefly stresses how important language is for a steady foundation of science, why English has been a judicious *provisional* choice and why we, the scientific community, should seriously consider adopting a new language in the near present*.
- chapter 18 is a collection of thoughts about the thesis and why I felt the need to make it so long...

At the beginning of the doctoral study, I shared the illusion† that with time, experimental data will be better matched with more sophisticated theoretical models. Today, at the end, I think that human intervention will always remain an essential ingredient to the generation of information.

*¿Kial ne nun? `https://esperanto.net/`

†In French and English, 'illusion' is imbued with pejorative connotation of a false belief or idea. Here, I invite the reader to see it from the Spanish perspective 'ilusión' which is a dream, an idea that does not exist, yet brings hope and motivation.

Chapter 13

The Art(ifice) of Fitting

> *"Analytic forms which are good over broad energy ranges can provide compact and accurate means of communicating information,"*
>
> — Green & Stolarski*, 1972, J. Atmos. Terr. Phys. 34-1716*

When introduced for the first time in mathematics classes, functions are dreaded for being so mystical objects. The fact that they could represent (almost) anything that binds two variables makes them somewhat difficult to appraise. With time and habit, they become the most coveted friends of (data-)scientists because of their potential of concisely representing tabulated datasets.

In the most fortunate cases, the functions underlying a physical model of reality are mathematically known objects. They can be part of a parametric family whose few parameters need to be determined according to some given information. A dummy example is the exponential growth rate of an electron population as treated in this thesis. Given a certain number of points, one can infer from semi-logarithmic plots, the offset and slope related to the initial number of electrons and their growth rate with respect to the variable (space or time).

A more elaborate example are the spherical harmonics Y_ℓ^m which appear anytime one is interested in working with spherical coordinates for solving the Schrödinger's equation of a particle in a potential. If the angular distribution of a molecular potential is known at a certain radial distance, one can try to find the coefficients linearly applied to Y_ℓ^m that reproduce the angular shape. In this case, one needs also to known how many of such harmonics are needed; to choose an upper $L \geq \ell$ limit.

In less fortunate cases, the functions that would provide structure to the given data points are not known at all. This situation is probably the most common that data-scientists are faced with at first sight. Our intuition is trained to see curves that link points together. Interpolating unidentified data can be mathematically embodied in the most basic of all functions : polynomials, of which the simple linear regression is part. However, this intuitive approach fails when measurements are sparse or look erratic. Evidently, the lesser data points one has, the lesser information is known about the problem faced. The worst comes when we try to extrapolate the trends beyond the lower and higher boundaries. Consider two restricted sets of measurements shown in figure 13.1.

The first figure on the left shows some experimental data for an excitation of nitrogen by electron impact. Luckily, the data points look very well aligned and our eye can imagine a smooth curve going through all the points. The problem is that our imagination would draw a curve that does not bend much beyond the rightmost point, it would either continue growing slowly or curb and halt toward a threshold. Here our imagination comes into conflict with our intuition that tells us that all cross sections must somehow decrease and fade at higher electron energies, but how? The situation on the right panel is different. The points look erratic although they display a hooked shape with a slightly decreasing slope on the right. In this case, our imagination stalls

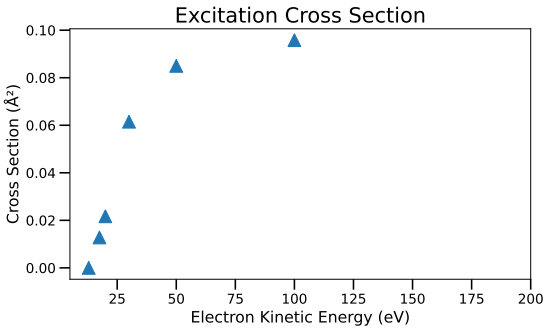

(a) A sparse dataset for an electron impact excitation of nitrogen from Johnson *et al.* [463]

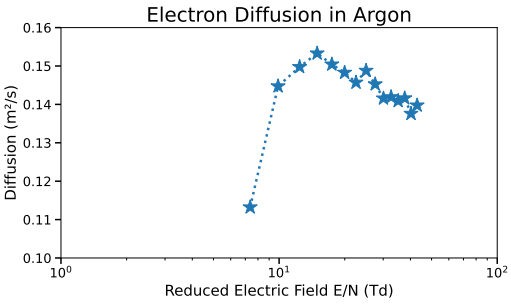

(b) An incomplete dataset for electron diffusion coefficient in Argon at ground density from Haefliger and Franck [375]

Figure 13.1: Illustration of issues linked to sparse or restricted sets of measurements. It is difficult to imagine a physically founded trend to the data.

and it seems helpful to underline graphically the connection between the points with dotted lines. Our intuition is also mesmerised, should an electron swarm diffuse less at lower electric fields? Or should it actually diffuse more, due to scattering that is more isotropic at lower energies?

In general, we are interested in inferring trends from experimental data when we try to build a model that relies on it as an input source. If one has no knowledge of eventual physical models that can roughly complement the available data, then one has to find clever ways to make the data usable as input to the *actual* problem that one is concerned with. Interpolation is rarely an issue. Most scientists find it acceptable to link data points by straight lines: the comforting linear interpolation. It is however when making extrapolations that one is doomed trying to find a discrete way to get around the inquisitive gaze of the scientific suspicion.

This was my first concern when I worked on my first article [811]. I tried to make the input differential cross section for electron scattering look consistent as they were both extrapolated at small and large angles and toward higher energies. This article is a perfect example showing how much fiddling is involved in fitting curves. It is understandable that the human eye is craving after perfection embodied in nicely smooth curves. However, the subjective ugliness in the analytic expressions obtained may be a source of disappointment to the user.

In the rest of this chapter, I would like to illustrate two common problems linked to fitting. The first is overfitting and the second is ad hoc forcing.

13.1 Overfitting

It is well known that if we throw tens dots onto a surface and ask a child to join them by one uninterrupted line, we may get theoretically an infinitely continuous number of curves that satisfy the requirements. Selecting our preferred curve would inevitably invoke our arbitrariness. Even if we impose that the curve must belong to a mono-valued continuous and infinitely derivable function, the field of possibilities remains large.

To reduce subjectivity and personal bias, algorithms can be used that define criteria and constraints on the curve to be obtained. The most celebrated method is the "least squares" which strives to find the curve giving minimal sum of distance to the points weighted by the uncertainty of their values. Other constraints can define the asymptotic behaviour of the function beyond data boundaries, some desired property of the function (e.g. positive, monotonic, etc.),

or some reasonable range given to each adjustable parameter. The concept of least-squares can be generalised into a minimisation problem of a cost function that can penalise any kind of undesired behaviour.

Overfitting occurs when various curves that score all very closely on the criteria given and satisfy all constraints still differ significantly in some parts. It thus introduces arbitrariness again.

For the purpose of illustration, we shall reintroduce here the following functions used in the context of fitting excitation cross section in part II sec.11.4.2. We label them here as f_4 and f_6:

$$f_4(w) = c_0\frac{((w+1)^a-1)^b}{(w/C+1)^{d+ab}} \qquad f_6(w) = c_0\frac{((w+1)^a-1)^b((w/c')^{a'}+1)}{(w/C+1)^{d+ab+a'}} \tag{13.1}$$

$$f_3(w) = f_4(w; a=1) \qquad f_5(w) = f_6(w; a=1) \tag{13.2}$$

The variable w represents the relative electron energy (ε) difference from the reaction threshold (Δ): $w = \varepsilon/\Delta - 1$. The forms f_4 and f_6 can both be reduced to f_3 and f_5 by fixing the parameter $a \equiv 1$. The parameter d is not free, it is determined by the type of transition considered, I will call it the "asymptotic strength" because it represents how much the denominator overpowers the numerator at high energies $w \to \infty$.

The numerator in all expressions is based on Green and Stolarski [350, eq.(7)] for correctly encompassing behaviour at threshold. The exponent a controls the sharpness of the transition at threshold, while b curbs it. When used in the form $(w/c')^{a'}+1$, this can lead to the occurrence of local extrema near c'. We exploited this property by creating the 6-parameter form f_6 to be able to "twist" in the region $w \simeq c'$.

After we introduced the Bethe scaling from Kim [504] which offsets the denominator $\varepsilon/\Delta = w+1$ to $w+C$, we were faced with the dilemma of what to do with the numerator. Should we echo this offset or not? For this we decided to compare the differences between $(w+1)^a-1$ (normal), $1-1/(w+1)^a$ (original) and $(w/C+1)^a-1$ (offset) as the numerators based on the low-energy modifier in Green and Stolarski [350, eq.(7)]'s original expressions. We denote those functions as f° and $f^{\circ\circ}$:

$$f_4^\circ(w) = c_0\frac{((w/C+1)^a-1)^b}{(w/C+1)^{d+ab}} \qquad f_6^\circ(w) = c_0\frac{((w/C+1)^a-1)^b((w/c')^{a'}+1)}{(w/C+1)^{d+ab+a'}} \tag{13.3a}$$

$$f_4^{\circ\circ}(w) = c_0\frac{(1-\frac{1}{(w+1)^a})^b}{(w/C+1)^{d}} \qquad f_6^{\circ\circ}(w) = c_0\frac{(1-\frac{1}{(w+1)^a})^b((w/c')^{a'}+1)}{(w/C+1)^{d+a'}} \tag{13.3b}$$

We also explored other possible functions by departing from the canonical expression of Green and Dutta [348] and adding more flexibility in other places. We denote by f' (13.4a), the versions that have enhanced "twisting" capabilities instead of an adjustable near-threshold slope. They can have up to 7 parameters to point-out how quickly can overfitting arise (even when the number of points is over 30).

$$f_5'(w) = c_0\frac{w^b((w/c)^a+1)}{(w+C)^{d+b+a}} \qquad f_7'(w) = c_0\frac{w^b((w/c)^a+1)((w/c')^{a'}+1)}{(w+C)^{d+b+a+a'}} \tag{13.4a}$$

$$f_4'(w) \equiv f_5'(w; a=2) \qquad f_6'(w) \equiv f_7'(w; a'=2) \tag{13.4b}$$

$$f_4''(w) = c_0\frac{((w+1)^a-1)^b}{((w/C)^{d+ab}+1)} \qquad f_6''(w) = c_0\frac{((w+1)^a-1)^b((w/c')^{a'}+1)}{((w/C)^{(d+ab+a')}+1)} \tag{13.4c}$$

Finally, Tabata *et al.* [902] as inspired by the earlier formula from Green and McNeal [349, eq.1] proposed to exploit sharp transitioning in the *denominator* to give f_4'' and f_6'' (13.4c). This

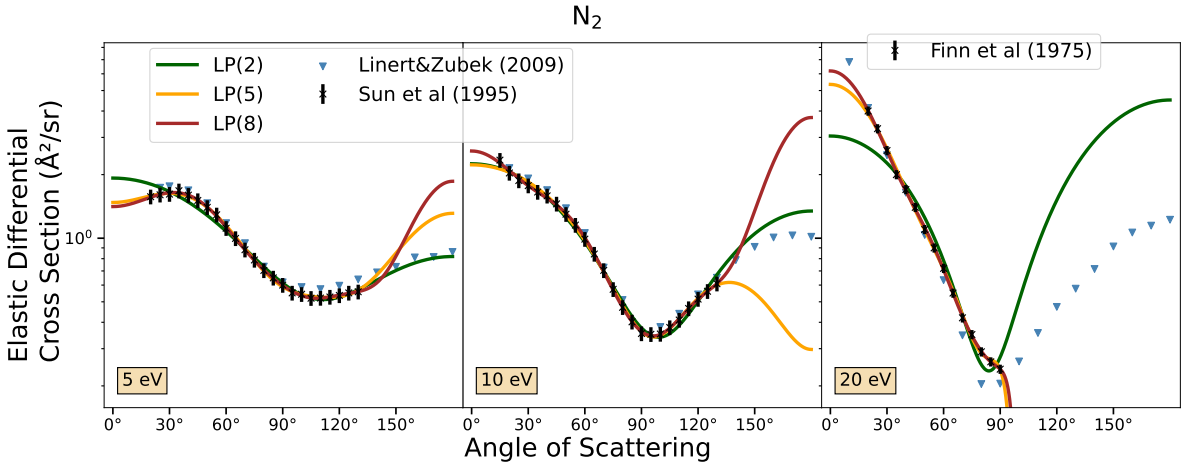

Figure 13.2: (Over)fitting electron-N_2 differential cross sections with Legendre polynomials (LP). At each selected energy (5, 10 and 20 eV) Legendre polynomials of degrees 3, 5 and 8 are fitted in least-squares to experimental data points [288, 894] in black. The results of Linert and Zubek [600] in blue triangles which cover the range of large angle scattering are shown so that one may observe how far off are the fitted results in the extrapolated regions.

contrasts the prescription by Kim [504] who offsets the denominator only *linearly* by a factor C. However, this form for the denominator can fit sharper structures as for example resonance peaks, in which case the exponent e in $(w/C)^e$ should in principle be equal to 2, though such restriction has not been imposed.

With this set of functions, together with other basic functions, I exemplify overfitting in two ways. Although they are two sides of the same coin, on one side I focus on how allowing too many free parameters spoils the fit; whereas on the other side, I show that for the same number of parameters involved, some functions adapt more easily (because of their nature) to a set of data than others.

13.1.1 Too many parameters

It is well known that any N pairs of data coordinates (x_i, y_i) can be perfectly joined with a polynomial of degree $N-1$. Although very tempting, this solution is strongly deprecated because offers no control over the values that the obtained fit takes between and beyond the data given. This undermines the purpose of the fit which tries to find a regular curve implied by the points.

A very conspicuous place to start is the problem of fitting differential cross sections to obtain a fit covering the full angular range 0°–180°. This is a ubiquitous problem in all cross-beamed studies which try to derive integrated cross sections from incomplete measurements [120, 141]. In figure 13.2 we show how naively applying a least squares algorithm to find the best matching Legendre polynomial can give utterly erroneous results beyond the angular scope of the measured data especially at large angles. A comparison is shown with the late experimental data of Linert and Zubek [600] in which the magnetic angle changer technique [1014] permitted to probe backscattering angles. The point is that the results of a 3 parameter fit (2^{nd} degree) can overall surpass the mediocrity of higher-degree polynomials even though they do not follow exactly the curve undertraced by the points in all of its meanders as the other fits. On the rightmost graph at 20 eV, the cusp of the DCS is deep and it would require a higher degree Legendre polynomial to be properly fitted for all angles. Nevertheless, DCS which merely extend to 90° are very difficult to extrapolate and that the parity of the highest degree of polynomial can have a severe

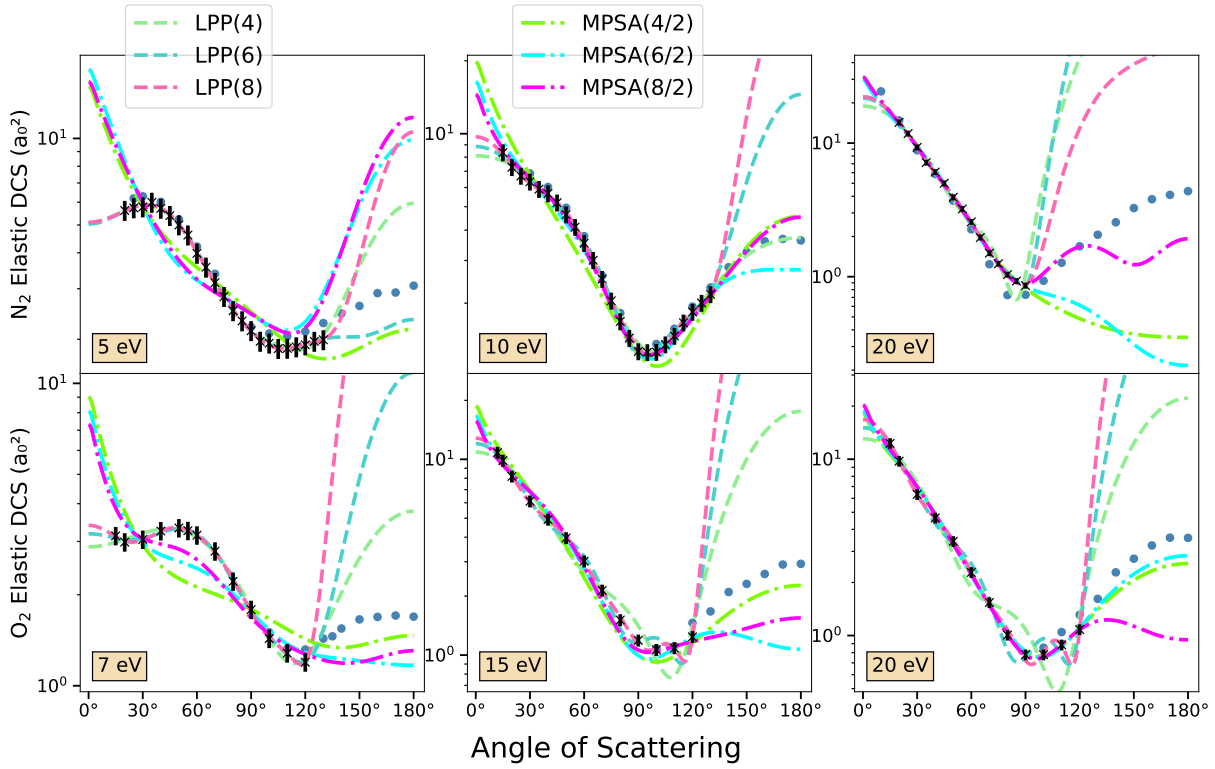

Figure 13.3: The phase-shift (MPSA-eq 13.5b, flashy colours, dash-dotted) analysis [87] is compared to a penalised (anti-negative and lower coefficients for high degrees) least-squares fit (LPP-eq 13.5a, mild colours, dashed) of Legendre polynomials. The degrees $L = 4, 6, 8$ of the fits are always the same but the phase-shift analysis only involves $L/2 + 1$ free parameters (δ_l). The black points show experimental data used for the fits [288, 893, 894] and blue triangles show backscattering measurementsLinert *et al.* [598] and Linert and Zubek [600].

impact on the fitted result. The decomposition of DCS in partial waves (13.5b) described in the previous part section 8.4.1 implies that the highest degree of the Legendre polynomial should always be even. If odd degrees are left unchecked, it is not uncommon that negative values are obtained in the range of extrapolated angles!

The art of extrapolating DCS over the full angular range called for new fitting techniques such as the famous phase-shift analysis of Boesten and Tanaka [87]. This consists of exploiting the assumption that DCS for molecular targets averaged over their orientation can be modelled by phase shifts much alike in central potentials seen in the previous part section 8.4.1.

$$\mathrm{DCS}(\theta) = \begin{cases} \sum_{l=0}^{L} a_l P_l(\cos\theta) \quad > 0 \quad \forall\theta \in [0,\pi] & \text{(13.5a)} \\ \frac{1}{(2k)^2} \left| \sum_{l=0}^{L/2} (2l+1)(e^{2i\delta_l} - 1) P_l(\cos\theta) \right|^2 & \text{(13.5b)} \end{cases}$$

In figure 13.3, we compare a more cautious Legendre fitting based on penalisation (cost function - LPP 13.5a) and molecular phase-shift analysis (MPSA 13.5b). The main message is that the MPSA can both prevent the DCS from being negative and can significantly reduce the

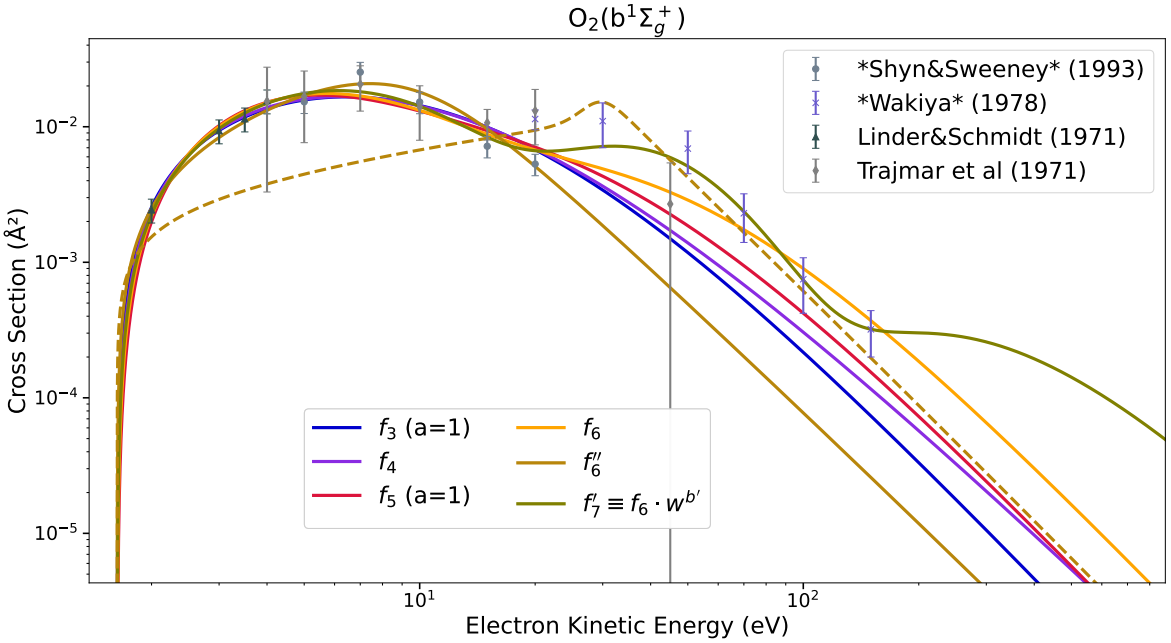

Figure 13.4: Generic functions defined in eqs (13.1-13.4) are fitted to an ill-looking collection of excitation cross-sections for oxygen. Increasing the number of parameters makes the fit more vulnerable to overfitting.

number of free parameters while the more traditional fitting with cost function does almost never extrapolate reasonably, getting worse at intermediate energies which are characterised by steeper curves and deeper cusps. Nevertheless, at energies closer to resonances, it gets more difficult to handle the MPSA because the initial guess for the phase-shifts is only based on the (molecular isotropic) polarisation potential which is valid rather at higher energies and higher phase-shifts. Again, adding more parameters does not always help improve the fit. Sometimes, the fits with the lowest number of parameters yield the most desirable results. This is because the optimisation algorithm is unguided adequately and thus searches almost blindly for a solution. In some cases when the angular range is very limited (<90°), it is necessary to explore the variable space of the MPSA and perform an averaging [141, figure 1].

As mentioned, the MPSA assumes that the scattering matrix (S-matrix) of a rotationally-averaged interaction with a molecule is mainly diagonal. At lower energies and lower partial-waves, this is not true and a deeper physical analysis is required; with off-diagonal elements calculated through a first Born approximation [274] as described in Sun *et al.* [894, §VII.A].

Fitting DCS is an example where the extrapolation range is limited, when moving to CS, the energies are in principle unlimited and thus, one must watch over the asymptotic trend of the fit. Another example of overfitting due to too many free parameters is shown in figure 13.4

At this stage, it is instructive to first observe the progression of functions f involving from 3 to 7 free parameters. The shape beyond 30 eV looks magnetically attracted to the somewhat up-shifted data of Wakiya [973] (which we renormalised, cf. sec 15.1.2). The question, more difficult to answer here is: at what point can we consider that we are overfitting? Clearly the f_7' form is the over the top. What about $f_3 \lessdot f_4 \lessdot f_5 \lessdot f_6$ (with $a \lessdot b$ as "b slightly better than a")? Could we consider that the two points at 100 and 200 eV are trustworthy and should we thus privilege $f_{5,6}$ over $f_{3,4}$?

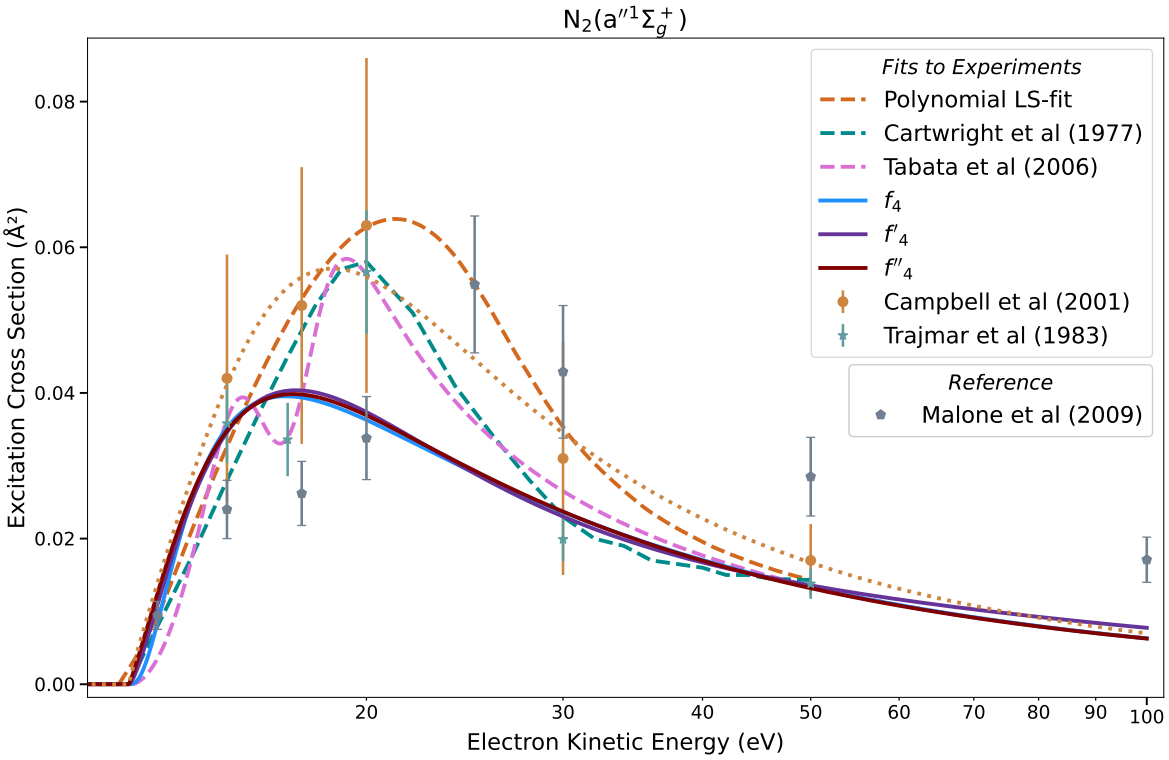

Figure 13.5: Various fits to the experimental data reported by Trajmar *et al.* [941] (dark cyan) and Campbell *et al.* [141] (light brown). The polynomial fits (dashed) synthesised by Brunger *et al.* [121] and Cartwright *et al.* [159] have a higher cross section than the present fits (solid) between 15—40 eV. The very large error bars ($\gtrsim 40\%$) of Campbell *et al.* [141] may have not been incorporated in the least-square fit (dashed light brown), since the dotted line fitting only those data shows also a prominent bump in the CS.

Perhaps the aftershock of looking at completely aberrant fits of DCS (fig 13.2) might affect our judgement. As a matter of fact, the functions (13.1) chosen to describe CS are much better constrained than the Legendre polynomials which we may mangle however we please. This leads us to the next section discussing the problem of flexibility in a fit.

13.1.2 Too much flexibility

Polynomial expansions are very powerful mathematical tools because they offer a virtually unlimited flexibility to represent functions. Physically though, one should not expect to get much answers while using them as a fitting basis.

For DCS, figure 13.3 showed previously how reducing the flexibility over the allowed space of polynomial coefficients as expressed through the difference between equations (13.5a) vs. (13.5b), can reduce the aberration of a polynomial fit in the extrapolated region. As a complement, figure 13.5 compares polynomial fits ([121, 159, §6.4.5.2.13, fig.1]) and a fraction fit [902] to the data of Trajmar *et al.* [941] and Campbell *et al.* [141]. Our set of generic functions f, f', f'' (13.1,13.4a,13.4c) is fitted to the same data. The most recent measurements of Malone *et al.* [622] are displayed as an exterior reference. There is a striking difference between the set of polynomial fits which all display a prominent bump between 15—40 eV, and our fits which remain low.

The difference can be explained at least by two factors. First, by comparing the curves, one could surmise that that the least-squares polynomial fit [121, §6.4.5.2.13] must have comprised an at least third degree (1×2) numerator and maybe a first degree denominator raised to the power of four (the asymptotic strength $d = 1$). Second, the closest reproduction of the "Polynomial LS" fit obtained with the 4-parametric f'_4 is given as a dotted line based solely on Campbell *et al.* [141] data though. The great difference in error bars between the two data sets indicates that those were probably not accounted-for properly in the polynomial fit, since the difference between the solid lines (fitting both sets) and the dotted line is quite significant.

Here again we face the question of where lies the boundary between overfitting. This can become a philosophical question: are we trying to link sporadic measurements with a smooth curve (like the dashed curves in fig. 13.5), or are we trying to derive the generic shape that would be in accordance with the Born approximation? The unused data of Malone *et al.* [622, §4.4] bring more material to the discussion. Without them, the dashed fits look much more convincing than our solid-line fits. Nevertheless, the experimental discrepancy near threshold casts a doubt on the previously reported polynomial fits. The reason for this discord is because of the narrower angular range of the measurements involved in Campbell *et al.* [141] which implies a wide uncertainty on the derived ICS. As a result, we deem that the bumped dashed lines on figure 13.5 are overfitting the data in the sense that they either do not consider the wide uncertainties in the least-squares fit, or endow too much flexibility to the polynomial function used (which is pitifully not reported).

We further illustrate how the shape of the function chosen can severely affect the risk of overfitting even if the number of parameters is kept constant.

First, we explore the concept of vulnerability to outliers. Without constraining the parameters, we unleash the optimisation algorithm on a dataset with one point amiss for the $(4p)[5/2]\,^3D_3$ state of Argon (cf. comment 15.1.4) and observe the curves obtained on figure 13.6a. We see that f''_4 is definitely attracted by the outlier at 30 eV and its natural propensity to peak would wrongfully judge the last of the four points at 100 eV to be the outlier. From here, we can already place a doubt on the generic form of f''. The rest of the generic functions completely ignore the outlier, however, the lack of points near threshold permits the exposure of two kinds of singular behaviours caused by $b \to 0$ for f_3, f'_4; and by $C \to 0$ for f_4 and $f_4^{\circ\circ}$ in (13.1). We shall see later how such marginal behaviours are duly addressed.

In the second figure 13.6b for $N_2(G\,^3\Pi_u)$, f'_4 shows too much sensitivity to the first point in the series. Its vulnerability is exhibited due to the factor $(w/c)^a + 1$ in (13.4a). Conversely, f''_4 is unable to adapt itself to the trend because of its inherently asymmetrical shape with a sharper falloff beyond $w > C$ due to the denominator $1/((w/C)^e + 1)$ with $e > d = 3$ in (13.4c).

Next, we consider fits of N_2—$B\,^3\pi_g$ for f, f', f'' are presented in figure 13.7-top (left:logarithmic and right:linear scales). Each time, the competing formulae have the same number (6) of parameters so that they stand in principle on equal footing when discussing mismatching issues, the f'$_4$ is shown for comparison.

This set from Johnson *et al.* [463, §4.2]'s measurements shows a wavy pattern, also called a "shoulder", about 20 eV. On the contrary to the example of $b\,^1\Sigma_g^+$ state of O_2 on figure 13.4 which also presents a wave due to juxtaposition of different experiments, the present data comes from the same experiment and it is reasonable to assume that the shoulder observed is therefore not an artifact. Another sound observation is to notice the fact that this "irregularity" happens close to threshold ($\simeq$7.353 eV) as opposed to the data in 13.4 which appears an order of magnitude above threshold (lower at $\simeq$1.627 eV). Therefore, we deem that even though we fit 8 points of N_2 (fig 13.7-top) with 6 parameters, the curves for O_2 (fig 13.4) with 22 points are clearly more overfitted by 6 parameters.

Nonetheless, since only one database is used it is difficult to decide which of f_6 and f_6' best represent the data. Their shape near threshold is too sensitive to the first point of the data set which shows a large (absolute) uncertainty.

Concerning the underfits, f_4' and f_6'', it is quite obvious that their shape is not adequate for the data selected. The sharper transition in the f'' variant given its by denominator $(w^e + C)$ creates a three-segmented bow with marked changes in the first derivative. Probably a sounder variant would be to consider $(w^2 + C)^e$ in reminiscence of Breit-Wigner resonance peaks.

A sum of two f_6'' would be needed to represent the data. Actually, two f_4'' would suffice. This is because the theoretical capability of f_6'' to twist like its siblings f_6 and f_6' seems inhibited by the traumatisingly sharp form chosen for the denominator. Once the $w = C$ threshold is passed, it is impossible for the numerator to catch up and induce a wobble, the asymptotic strength ($d = 3$) prohibits such option.

The use of f_4'' as generic function [349, eq.(1)] comes from pragmatic but definitely not physical considerations. When combined in sums as was the case in the original publication [902, eq.(ii-iii)], each component can fit one bump and thereby produce a wavy pattern like the dashed-pink curve seen on fig 13.5. The decomposition of the bumps can be also seen on 13.4 where the solid and dashed light-brown curves, when summed, would in principle be also able to link the points continuously. These examples illustrate, in my opinion, why choosing a cutoff denominator $1/(w^e + C)$ with $e > 2$ does not make much physical sense and should therefore be avoided (even if it may be convenient for creating sharp peaks near threshold as in fig 13.17 presented later).

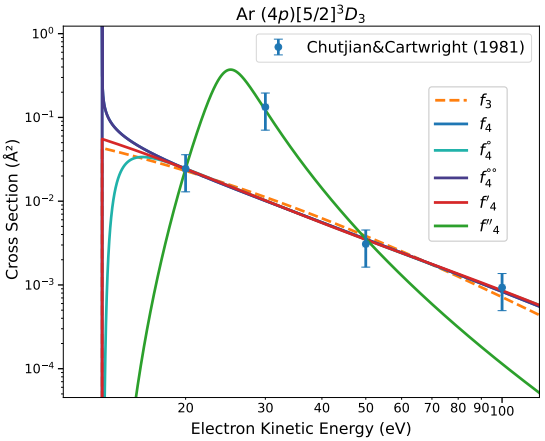

(a) Vulnerability on outliers is tested on the generic functions. Only f_4'' gets caught in the net, while f_4 and $f_4^{\circ\circ}$ outstretch their singular behaviour near threshold due to $a \to 0$ in (13.1).

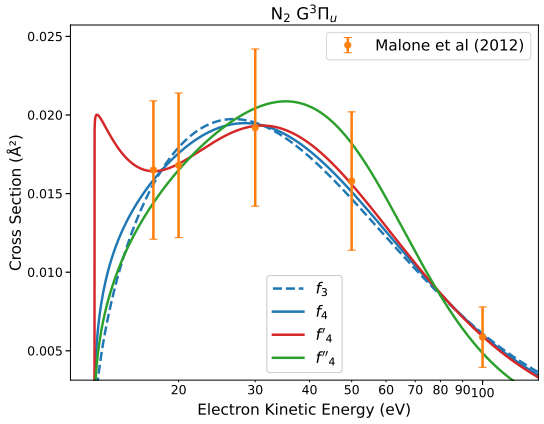

(b) In this case, f_4' suffers from overflexibility while f_4'' from underflexibility. A low $b < 0.05$ and its ability to twist around c causes f_4' (13.4a) to squeeze its near-threshold shape because of the first data point.

Figure 13.6: Vulnerability on outliers is tested on the generic functions.

Moving back to Argon again, we present another set of fits to the $(4p)[1/2]1$ state in the middle row of figure 13.7. This time, f_4 keeps a decent shape, while f_4° and $f_4^{\circ\circ}$ display a singular behaviour near threshold. The dotted line shows the unconstrained singularity $C, b \to 0$, which is attenuated on the solid lines when C, b are bounded minimally.

The reason for the apparent versatility of f_4 is due to the asymptotic strength which was $d = 3$ (spin-exchange excitation) for the $(4p)[5/2]3$ state in fig. 13.6 while being $d = 1$ (dipole-forbidden) for the present $(4p)[1/2]1$ state. In many cases, the behaviours of the f, f°, $f^{\circ\circ}$ saga are indistinguishable (e.g. bottom graph of fig. 13.7). This occurs when $C \simeq 1$, whereby all forms are equivalent. These three variants are distinguished when $C \to 0$, as provoked by the measurements for $(4p)[1/2]1$, where $C = 0.16$ for f_4 and would be even smaller for $f_{\circ}$ and $f^{\circ\circ}$.

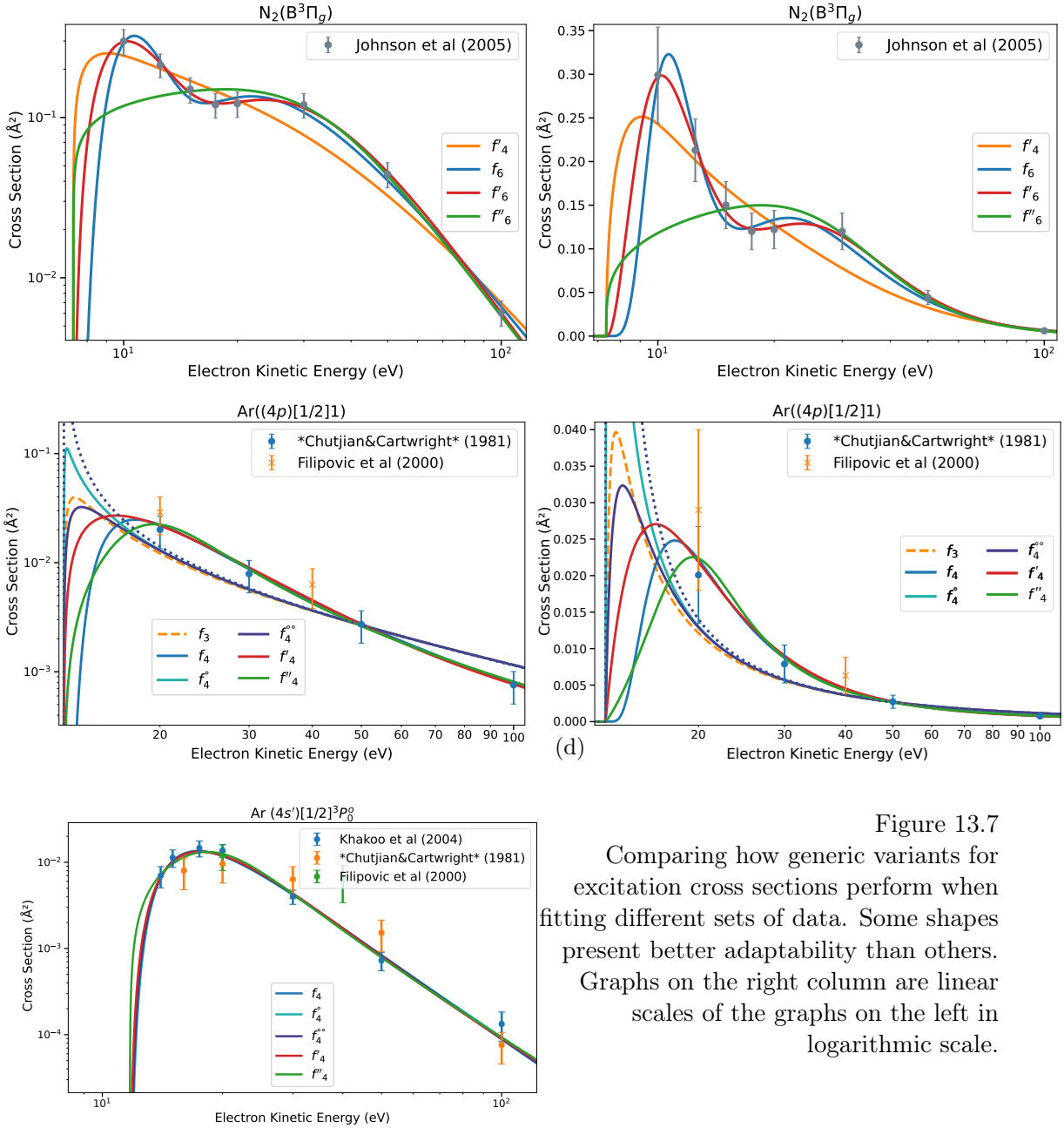

Figure 13.7
Comparing how generic variants for excitation cross sections perform when fitting different sets of data. Some shapes present better adaptability than others. Graphs on the right column are linear scales of the graphs on the left in logarithmic scale.

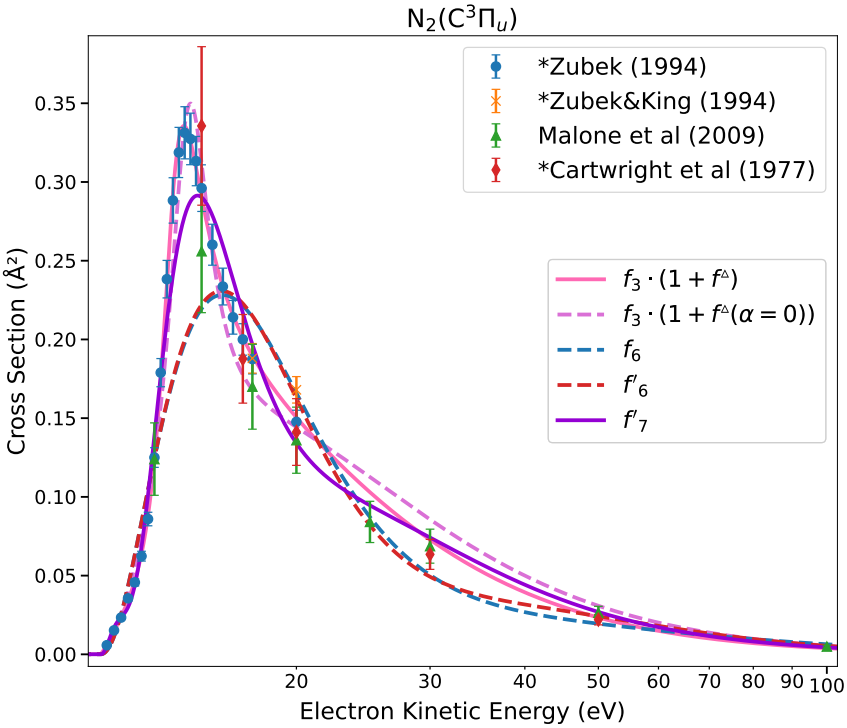

Figure 13.8: The near-threshold resonant peak of $C\,^3\Pi_u$ cannot be fitted with any of the generic forms presented earlier in (13.1-13.4a). The function f must be augmented with a Fano profile $f_{\rm res}$ (13.6) in order to produce a satisfactory result. All dashed lines use 6 parameters, and full lines use 7.

13.2 Ad hoc Fitting

So far, the fitting procedure we have covered was based on open exploration. We presented a functional space in which the fits could be built and optimised in that space and sometimes to its fringes. When the intrinsic characteristics of a function could not enable a pertinent fit to a set of data, which most stereotypically was the case of f'' in figures 13.7-top or 13.6, and f°, $f^{\circ\circ}$ in figure 13.7-middle; then we would simply discard it and favour the other successful variants.

Sometimes, a function might be regarded as too precious by its creator and it would hurt too much to discredit its use. And so, several ways might be tried in hope of salvaging that poor function.

In my personal case, that would apply to the f_4 and f_6 I have so fervently dedicated time and effort. So when there arises, somewhere in the database, an instance of data that cannot be fitted well by the f family, I had to urgently find a way to preserve its use which was satisfactory in 96% of the instances. I augmented f to its 'super-peaky-power' form :

$$\begin{aligned} f_{\rm aug}(w) &\equiv f_3(w)\cdot(1+f_{\rm res}(w')) \\ &= M\frac{w^b}{(w+C)^{b+d}}\left(1+A\frac{\cos(2\alpha)-\sin(2\alpha)w'}{(w')^2+1}\right) \qquad ;\ \text{with } w'=\frac{\varepsilon-\varepsilon_r}{\Gamma/2} \end{aligned} \tag{13.6}$$

This augmented form distinguishes a "slow" background shape f_3 on which is superposed a resonant asymmetric Fano-profile $f_{\rm res}$ introduced in Andrick [26, eq.(21)]. One can see how the $f_{\rm aug}$ overwhelms all other forms f_6, f_6' and f_7' on figure 13.8.

In this case, the augmentation is semi-justified by the fact that there most likely is a resonance peak for $C\,^3\Pi_u$ somewhere near 13 eV which also features in R-matrix calculations (but at 16 eV, cf. 11.4.3). Also, the profile of shape resonances is well described theoretically and I didn't need to recur to a far-fetched modification.

In more unfortunate cases, lack of knowledge may prevent us from finding a physical explanation and subsequently derive a modified formula that matches well the results. I call "ad hoc" fitting, any kind of amendment that augments a formula based on a tentative (or simply put: flimsy) physical justification. In my personal point of view, a non-overlookable percentage of scientific research is imbued by *ad hoc* 'improvements'.

The problem with *ad hoc* fitting is not necessarily about its pragmatism but rather about how it is presented and treated. In my example above (13.6), some parameters have a physical meaning, while others do not (or at the very least it is blurred).

- M : it is related to the b_i (or γ_i or higher-order) coefficient in Bethe-Born theory of inelastic collisions (cf. 11.4.1-eq.11.55)
- C : is the empirical coefficient proposed by Kim [504], it lost its "semi" status as I liberated it into a free parameter.
- d : is the "forbiddance degree" of the transition which is fixed. Other authors [482] might have chosen to give it some leeway since some transitions can be partly dipole permitted and partly quadrupole.
- a and b : control the near-threshold bump and slope, but are physically-unbound mere mathematical parameters.
- ε_r : would be the resonance centroid energy position. It could be known, just like the excitation threshold. For $\mathrm{C}\,^3\Pi_u$, the maximum is reported by many experiments [1012] to be located at 14.1 eV. But this needs not correspond to the centroid ε_r because it is superposed on the function f_3 which also peaks in that region. The present fit (fig 13.8) was obtained with $\varepsilon_r = 13.7$ eV.
- Γ : would be the resonance width fitted to $\simeq$2 eV.
- A : would be related to the resonance amplitude
- α : would be the background phase-shift at the resonance of the dominant partial-wave.

Notice the difference between which parameters <u>are</u> and which <u>would be</u> their correspondent. Unfortunately, the formula f_{aug} is an *ad hoc* modification to my favourite profile for forbidden transitions. Normally, the resonance is considered as a *local* feature in the cross section. If the reader did not wince when reading that $\Gamma = 2$ eV was the resonance width, he or she is probably not acquainted with typical resonance widths [407] which are expressed in the order of meV. The safer interpretation is to admit that (13.6) is an *ad hoc* modification based on resonance profiles that was required in order to fit the feature peak seen for $\mathrm{C}\,^3\Pi_u$. If one starts diverging toward physical arguments, one will tread on swampy grounds. The cross section presented is the sum over the first three vibronic bands and the bump fitted with f_{aug} may correspond to contributions due to various symmetries of the N_2^- compound [914, p.5]. In informal words, I have no idea whether this feature should be considered officially as a 'resonant peak' or a 'residual resonant bump' and I use the Fano-profile as a convenient way to fit its shape. It would have been dishonest to stay with the justificative paragraph written above the list.

A somewhat similar augmentation was introduced in Laher and Gilmore [549, eq.(2)] where the original shape [444, eq.(1)] was modified for spin-forbidden transitions:

$$f'_{aug} = \frac{M}{1+\gamma(w+1)^2}\,\frac{(1-\frac{1}{(w+1)^a})^b}{w+1} \tag{13.7}$$

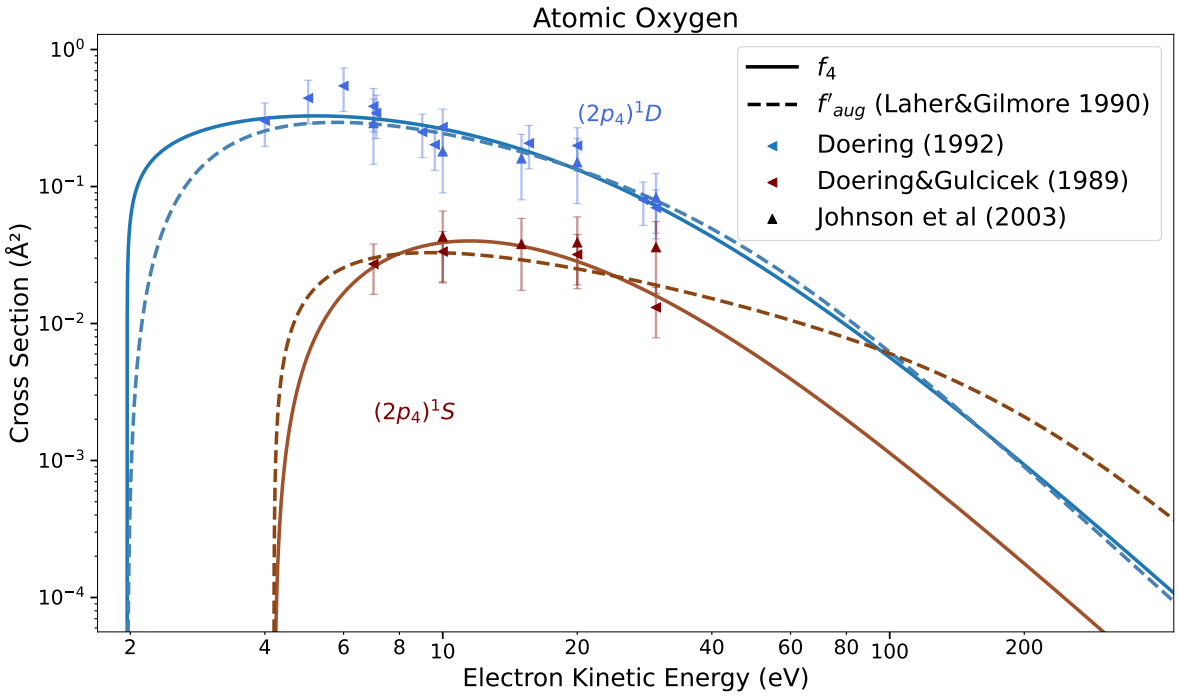

Figure 13.9: The two low-lying spin-forbidden transitions in atomic oxygen (^1D 1.97 eV and ^1D 4.19 eV) require an asymptotic decay $1/\varepsilon^3$. This trend is however not underlined by the experimental data. The formula adopted for the fit presents significant variations outside the range of experimental values.

This form cannot peak like f_{aug} (13.6) but bends around $\sqrt{\gamma}(w+1) = 1$. It was introduced after the observation that O $^3P \rightarrow {}^1D, {}^1S$ transitions in atomic oxygen are spin-forbidden and thus must decay $\sim 1/\varepsilon^3 \sim 1/w^3$ at "high-energies" (>200 eV) [549, p.282]. However, this trend is not evinced experimentally [437, see figure 5.2]. In figure 13.9, we show how mismatching trends between experimental values and predicted asymptotic decay affect the fitted function in the near-threshold and high-energy regions. The bent form f'_{aug} (13.7) seems convenient for ^1D but somewhat inappropriate for ^1S. Our generic form f_4 (13.1) has trouble keeping a and b at reasonable values ($a \sim 1$ and $b > 0.5$) in the former case because of the steep rise near threshold predicted theoretically [395, fig 3]. Trying to adjust carefully the formulae to the experiments would be another example of *ad hoc* fitting. Ultimately, this lack of determination calls for further experimental investigation [462, §8].

The literature is rich in examples of *ad hoc* fittings and one should always be wary that:

> Conclusions based on assessments of *ad hoc* constructs are of little scientific value.

Therefore, one should not be tempted to seek physical meaning under every *ad hoc* adjustment being made to match data. I list:

- The "screening correction" that I use to adjust my DCS for elastic scattering in chapter 11.1, should not be interpreted as a compensation for the hiding of one atom behind another in a molecule [82]. It is a mere convenience for scaling down the independent atom approximation which does not verify the optical theorem.

- The "screening factor" in the screened Rutherford expression should not be systematically linked to the electronic density profile around atomic nuclei, especially when it is used to fit below ~100 eV. Beside my own fit [811] which certainly holds no other than a pragmatic value, Jackman and Green [445, eq.(4)]'s expression has a screening factor $a = 0.11$ which is constant with energy; an absolute physical inconsistency!

- The restless "scaling factor" for the absorption potential [881] is a correction that merely compensates the overestimation of absorption rates at higher energies. The numerous other ways [79–81, 878] that this shortcoming can be compensated with, attaches an inseparable arbitrariness to this correction. It should not be considered as a physically founded effect as implied in Raj and Kumar [763].

A very responsible way of introducing an *ad hoc* adjustment is given by Kim [504, p.2] to explain the introduction of C in (13.9) below:

Kim [504, p.2]

> In the absence of more fundamental understanding of the origin of the BE scaling, the combination $[I + \Delta\mathcal{E}]$ in the BE scaling should not be taken literally as a rigid rule, but only as an indicator of the order of magnitude of a constant shift to be added to $[\varepsilon]$.

It is good to state that the fundamental justification to such adjustment is not clear and may derive from various causes. Also, this is applied only for *dipole-allowed* transitions; I presently used it as a fitting parameter for any transition (forbidden or allowed). With the low-energy modifier $((w+1)^a - 1)^b$, this parameter C in 13.1 loses any physical significance it may have borne before.

13.3 Constraining

In the two previous sections, we underlined the issues that paved the world of fitting. The present section is dedicated to the indispensable caution with which fitting ought to be approached.

The risk of overfitting can be reduced and brute forcing can be alleviated when properly constraining the fitting procedure. When we look at an unsatisfactory fit (as in figures 13.7,13.4), we immediately know what has gone wrong. Giving proper constraints can discard such results and facilitate the process of optimisation.

We illustrate this with three basic considerations: preliminary treatment of data, choosing a proper analytical variant and applying rigid bounds to the parameters. More advanced aspects such as inclusion of cost functions and the optimisation search algorithm, though very important as well, will not be covered here. We will show that significant improvement can already be attained starting with the most basic of considerations below.

Data Presentation

It goes without saying that the first step to take in data analysis is to *look* at the data. Even while the field of machine learning is booming and works sometimes miraculously well without prior checking, it is vital to acquaint oneself with the characteristics of the data (magnitude, range, regularity, trends, source, etc.). After all, "machine learning" operates subliminally in ourselves as well.

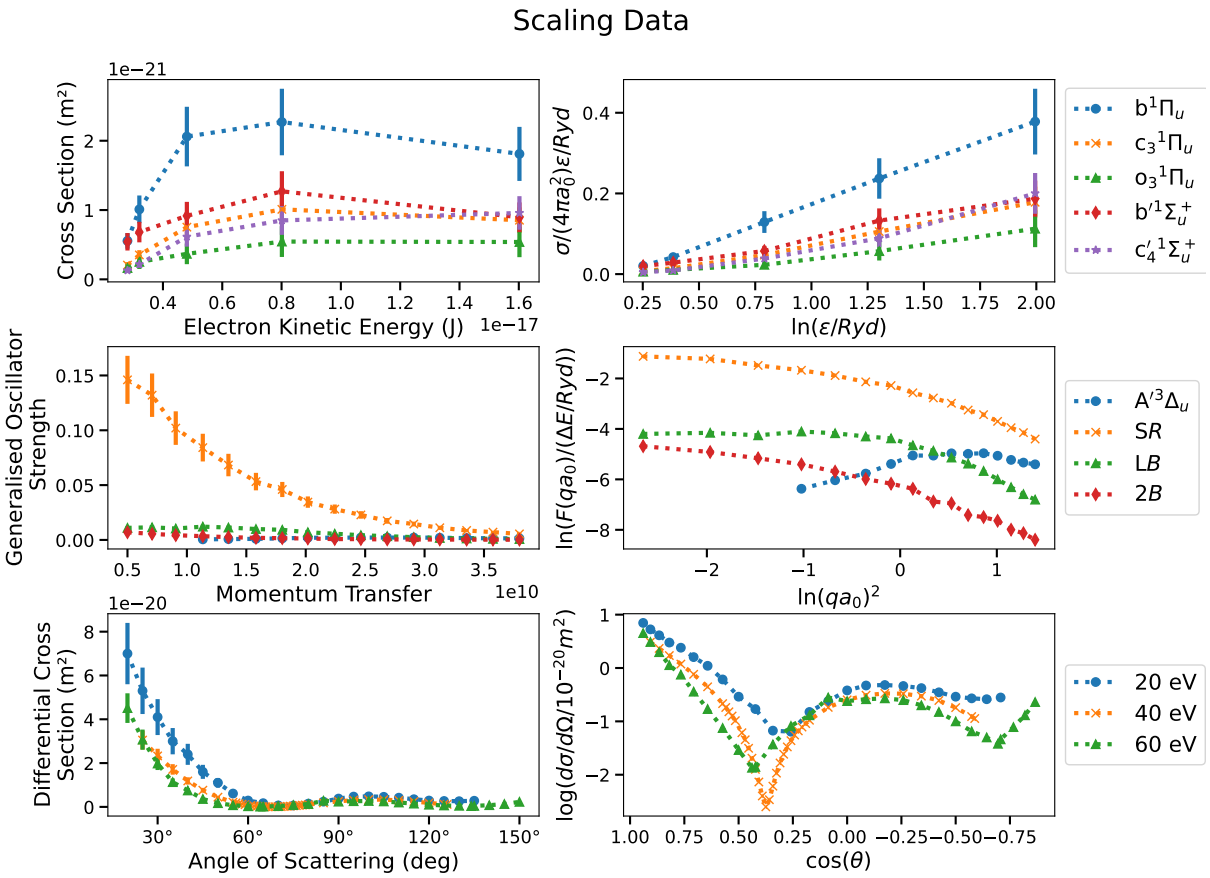

Figure 13.10: The comparison between left and right columns illustrate the process of inspecting a set of data and choosing appropriate scales for x and y-axis. Top row shows cross sections for dipole-allowed transitions of N_2, middle row shows generalised oscillator strengths for optically allowed O_2 excitations and bottom row is a set of elastic differential cross sections with Ar.

There are many directives for treating data whatsoever and a branch of science dedicated on data analysis. Here, I shall just restrict myself to highlight some important preliminary steps to get acquainted with data.

The first place to start when given data is to inquire about the units and scale the problem to a range of values easier to grasp for our mind. Determine the extrema, the amplitude they span, their sign. If non-zero and homo-signed, determine their ratio and check the magnitude range. Choose an appropriate unit to express them altogether. In our case, energies might be expressed in eV, keV, MeV, GeV,... or Rydbergs, Hartrees (atomic unit system). Cross sections might be barns ($=10^{-28}\,\mathrm{m}^2$), squared Bohr radius ($\simeq 2.8\times10^{-21}\,\mathrm{m}^2$), squared Angströms ($=10^{-20}\,\mathrm{m}^2$) or any round magnitude in the 10^{-19}–$10^{-26}\mathrm{m}^2$ range. The choice might depend strongly on the domain of research: nuclear, atomic/molecular, plasma, high-energy physics etc.

From the perspective of machines, it is sounder to normalise the data either to the maximal absolute value, or the mean/median when appropriate. In rare cases where one doesn't know at all what is being observed, it might help to subtract the mean/median, divide by one standard-deviation/interquartile-range and sneak a peek on a plot. This enables to properly constrain the values observed.

If one has a trained eye or brain, then knowledge about the data characteristics comes into play. Regular data could be turned into their spectral component, power laws viewed in a log-log scale and exponentials or logarithms in a semi-log scale.

In our case, cross sections are viewed on a log-log scale to observe the predicted asymptotic Bethe trend. For more complex trends, as for allowed transitions (cf. section 11.4.2), one speaks of a "Fano plot" ([427, p.329:fig. 17-18]) or "Bethe line" ([476, p.2662]), while naming it "Bethe plot" ([450, p.215]) or "Born-Bethe plot" ([865, p.4:fig. 3]) when looking at total scattering; there the cross section is multiplied by the electron kinetic energy $\sigma/(4\pi a_0^2) \times \varepsilon/\mathrm{Ryd}$ and displayed against $\log(\varepsilon/\mathrm{Ryd})$.

When looking at differential cross sections, the relevant quantity is the momentum transfer q. One may choose to plot generalised oscillator strengths against [851, fig 1-2] $(qa_0)^2$ or its logarithm [427, p.324:fig 13]. A comparative illustration of how to prescale data for visualisation and treatment is shown on the graphs of figure 13.10. Clearly, setting an adequate format for prescaling data is essential to grasp their structure, detect inconsistencies and check trends.

It is important to keep in mind that how data are prescaled will affect the optimisation process for finding a suitable fit. In particular, if one is fitting an exponential function or a power law on raw data, the result may be greatly affected by outlying or misplaced points with higher values. To spread more evenly the importance among the points x_i, y_i used for fitting a function f, one may choose to apply the least-square method scaled to the *relative* $|f(x_i) - y_i|/y_i$ instead of the absolute displacement.

Linked to this issue of sensitivity to data points is the knowledge about the *uncertainty* associated to each point. This is where we ought to turn toward the *source* of the data and go through the painstaking process of examination. The minimal requirement (necessary but certainly not sufficient) for a report to be reliable, is to include a section dedicated to a quantified error analysis of reported data. Those may come as relative uncertainties in percents applying to a wide range of values, or absolute error estimates accompanying each individually tabulated value.

Nevertheless, the hardest error to guess from an exterior point of view, is about the reported data themselves. This would be the "meta-error" or the trust we attribute to a particular value reported in a study. The purpose of many articles is actually to address the reliability of reported values, characterise this meta-error.

As an example, the raw data of Chutjian and Cartwright [180] for excitations with Argon are given in figure 13.11 for the lowest two (4p) excitations. An unidentified [106, p.766] typo in Chutjian and Cartwright [180] table IV at 30 eV misplaced the data units by an order of magnitude higher causing Puech's database to become spoiled for those two excitations. A comparison with Hayashi's database on the right shows that this typo had been properly identified in other reviews.

There may be many other spurious inconsistencies in reported values of DCS and CS hidden in the literature. I address some of them later in this part in the chapters 15&16 describing the databases. The one for Argon is the most prominent and obvious which is why I showed it here. For some molecules, there is an ongoing disagreement among reported measurements. Surely, the normalisation procedure may play a major role in those discrepancies. The process of rewinding the reported work and trying to untie the knot can be dreadfully time-consuming and often fruitless, which is why it not addressed enough. Nevertheless, solving discrepancies is one of the major endeavour in scientific research, and this starts by getting acquainted with the data being presented to us.

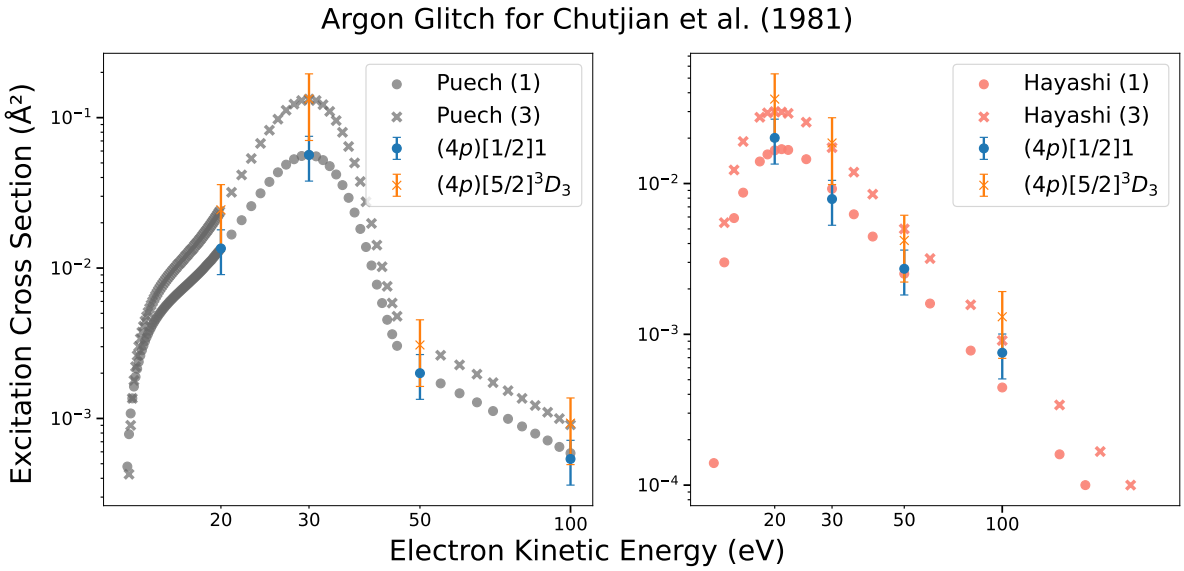

Figure 13.11: Two unidentified mistyped orders of magnitude in the columns of Chutjian and Cartwright [180, table IV]. On the left: uncorrected typo. On the right: same data with typo corrected. Comparison with other databases (e.g. `Hayashi` on the right) or measurements can serve to spot them out easily.

Analytic Variants

Equivalent functions can be expressed in different forms; which one should be chosen? Depending on the algorithm used, or the desired shape, one might prefer a variant over another. In general, it is recommended that all the parameters vary within a "reasonable" magnitude range.

As described above, it is important to start by setting an adequate order of magnitude M. Thus, if one fits cross sections $\sim a_0^2$ that are of the order of a squared Bohr radius, it is natural to prepend a magnitude factor a_0^2 to the function as in 11.4.2 eq.(11.61). If the magnitude is not set properly, the optimisation algorithm might run back and forth running through a great range of values of M and might even give up. A concrete example is given below.

Next, one must face the hard choice of fixing the generic expression for the core of the function when multiple parameters are involved. Typically, this has to do with factorisation. As implied above, it is not the same to ask an algorithm to fit $b\exp(-ax)$ or $-ax+\log(b)$.

We first consider the very simple cases of the three-parametric variants :

$$\frac{Mx^b}{(x+C)^{b+d}} \text{ versus } \frac{Mx^b}{(x/C+1)^{b+d}}$$

The difference affects again the magnitude coefficient M which varies as $1/(C)^{b+d}$ between the left and the right expressions. In this particular case, the functions all annihilate at the root $x = 0$ and the characteristic magnitude is obtained at their maximum when $x = C\,b/d$ which gives:

$$\frac{M}{(\frac{C\,b}{d})^d(1+d/b)^{b+d}} \text{ versus } \frac{M(C)^b}{(\frac{b}{d})^d(1+d/b)^{b+d}}$$

In the limit of $C \to 0$, the left expression would need to respond by $M \to 0$ to maintain the magnitude, whereas the expression on the right would bring $M \to \infty$ to catch up. Since it is preferable for a parameter to be well bounded, the left expression seems a better candidate for feeding an optimisation algorithm.

Table 13.1: Least-squares optimisation on various N_2 electronic excitation cross sections. In each cell are listed the number of (function calls ; iterations) for a Nelder-Mead simplex algorithm [314] The first function form is better suited for such purposes. In * , the algorithm did not even converge.

Fit Function	$a\,^1\Pi_g$	$a'\,^1\Sigma_u^-$	$a''\,^1\Sigma_g^+$	$B'\,^3\Sigma_u^-$	$B\,^3\Pi_u$
$Mx/(x+C)^{b+d}$	196 ; 111	269 ; 462	340 ; 190	343 ; 197	289 ; 165
$Mx/(x/C+1)^{b+d}$	311 ; 176	2000^* ; 3411	401 ; 228	1281 ; 748	361 ; 206

This hypothesis is tested on a few sets of excitation cross section data in table 13.1. We see that the Nelder-Mead simplex algorithm has to run on average lesser times to converge to an identical result with $(x+C)^{b+d}$ as a denominator. Sometimes, when C is menacingly low, the algorithm might not even converge within the limit number of iterations as has happened with the $N_2(a'\,^1\Sigma_u^-)$ database.

The bottom line is that even if $1/(x/C+1)^b$ expressions in (11.61) are more friendly from our perspective, to imply strictly that $C>0$, they might not be suited to the fitting procedure.

This duality of having a parameter featuring as $1/c$ versus $c/1$ is ubiquitous when giving form to a particular generic function. If any of the parameters in a fit are put out abnormally high or low, it signifies most probably that the problem was not constrained well.

The careful process of checking that parameters in a function can all be restricted to a reasonable range of values is what makes our interaction with machines more civilised rather than appealing to brute force. After having applied this principle on equation (13.1), the task of optimising is greatly eased with the following recipe:

$$f_{4[6]}(w) = \frac{M}{(w+C)^d}\left(\frac{(w+1)^a-1}{(w+C)^a}\right)^b\left[\frac{w^{a'}+(c')^{a'}}{(w+C)^{a'}}\right] \tag{13.8}$$

If we are sure that we want a certain parameter to be confined within a certain range of values (e.g. $C>0$ in 13.8); rather than making it implicit in the form chosen for the function, it is always better to tell it explicitly by providing bounds as presented in the next section.

Bounds

Parameters intervening in a function do evidently not all play the same role. Some (e.g. exponents) are more critical than others (e.g. coefficients of higher orders) to which the fit is less sensitive. Often, each parameter is expected to vary in a decently restricted range of values. For instance, magnitude coefficients and exponents of fixed denominators ought not be negative. In general, exponents shouldn't exceed 12, otherwise, a better suited function (exponential, Lorentz profile) can be chosen for the steep slopes of the fit.

In some instances, the shape of the four-parameter function f_4 might not be adequate to fit the data given. Then, it is important to properly constrain the range of values that the parameters can take, in order to avoid getting discontinuous or marginal behaviour.

In (13.8) The pair a,b of exponents represents the near-threshold rising portion. For $a,b>1$ the derivative at the root value $w=0$ is zero but then rises steeply. When $a<1$ and $b>1$, the transition is smoother but still steady. Non-zero derivatives are obtained for $b\leq 1$, with sloppy $a<1$ or faster $a>1$ convergence toward one for $w\gg C$. Clearly, a cliff is obtained when $b\to 0$ and $a\to\infty$, which we must prevent from forming. Physically, it is doubtful that $b<0.5$ which is the limiting case of near-threshold from s-wave excited transitions [982]. We show on figure 13.12 that setting $b\geq 0.5$ wards cliffs away from threshold.

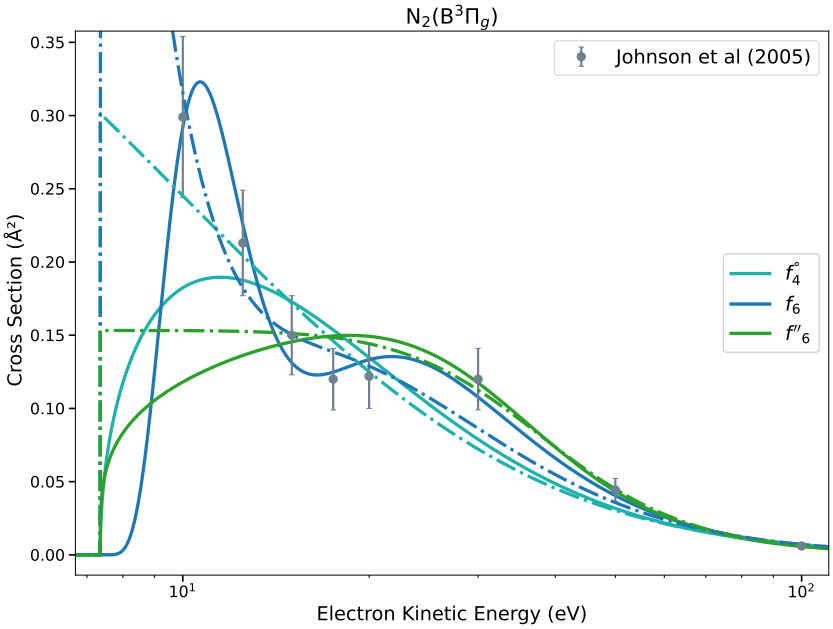

Figure 13.12: Constraining $b \geq 0.5$ in (13.8) prevents the generic functions defined in (13.8) from exposing their cliffing capability from the singularity $b \to 0$ combined with $a \to \infty$ at threshold. Solid curves are constrained ($b \geq 0.5$) while dot-dashed are unconstrained

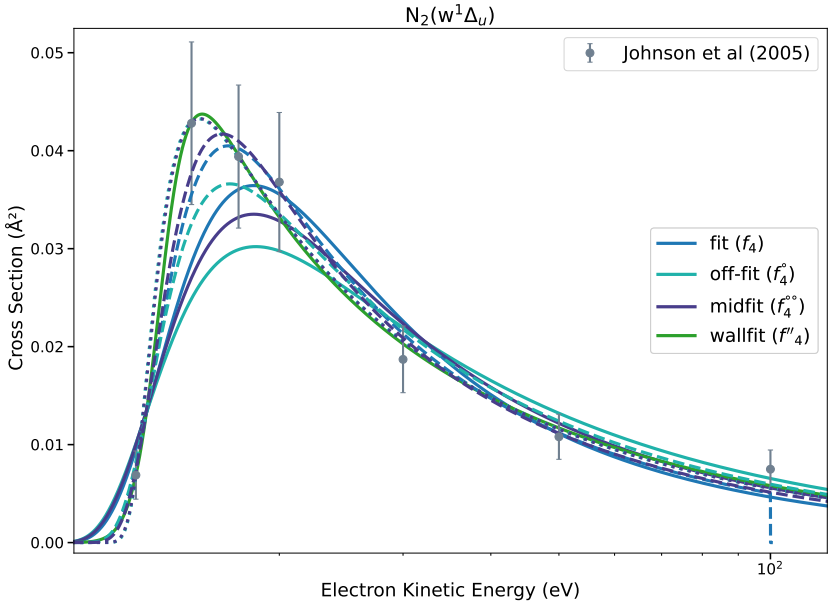

Figure 13.13: The upper bound of b in (13.8) controls the steepness of the slope close after threshold. The solid ($b \leq 10$), dashed ($b \leq 50$) and dotted ($b \leq 1000$) show how the peaking capabilities differ among the three variants presented in (13.1-13.3). In particular, peaking is natural (unforced) for a $1/(x^b+c)$ denominator, but forced (abnormally high b) for the other functions f_4 and f_4'.

Figure 13.14: Finding appropriate fitting functions for excitation cross sections among the possible candidates.

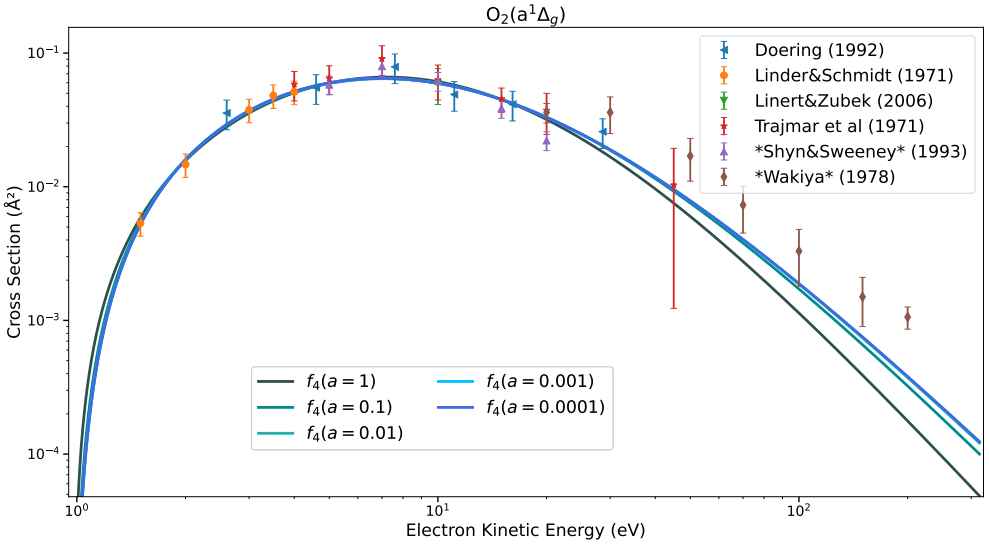

Figure 13.15: Low values of a introduce a slowly rising portion of the graph that can fit broad plateaus. Here, the algorithm is trapped into getting its tail closer to Wakiya [973]'s results at high energies. It is accompanied by a divergence of $M \to \infty$; its value goes from 0.2, 2.6,480, 1.3×10^5 up to 3.4×10^7 at the lowest value of $a = 0.0001$. To prevent this ill-conditioned fit, one must impose a lower bound on a in (13.8).

The other extreme $b \to \infty$ while a can take any value, creates a displaceable wall. It is not as discontinuous as the previously seen cliff because it must gradually rise from a zero derivative, which makes a bend at the foot of the wall. Physically, this trend would not be necessarily unfounded as some data display very sharp onsets (see figure 13.13). In this case, constraining the upper bounds for b and a prevents generic functions from surpassing their capabilities. It is a precaution against overfitting. As a general rule, we impose $a, b < 10$ and when the optimisation reaches this ceiling, we look at why the shape of the data calls for a sharp peak or steep slope. Generally, such structure can result from a local resonance (as for N_2-E $^3\Sigma_g^+$), in which case we prefer to augment the fit with a generic $1/((2x/\Gamma)^2 + 1)$ Breit-Wigner profile (13.6).

If we now examine the last case where $a \to 0$ while b stays finite, we obtain a gradual fading in amplitude of the low-energy modifier with an initial step followed by a very slowly rising slope. This occurs when the function requires a flat and broad plateau as for instance with a $^1\Delta_g$ of oxygen in figure 13.15. It shows a series of extremely slowly convergent curves as $a \to 0$ which all try to desperately raise their high-energy tail. This behaviour is naturally accompanied by a $C \gg 1$. The parameter suffering most from this sloppiness is the magnitude M which will shoot up $M \to \infty$, to try to maintain the level of the plateau. Since we chose $b < 10$, we decided to impose $a > 0.1$ so that their product ab can be at least unity if needed.

The offset C is due to Kim [504]'s BEf scaling and would represent the local increase in kinetic energy of the electron incident in an attractive potential. It is clear that the asymptotic trend emerges only after $w > C$ which implies that one should not expect C to be much larger than the ratio of the energy at CS maximum to the threshold $\Delta\mathcal{E}$. It can happen that a given set of data probes only the rising portion of a CS as represented in figure 13.16. In this case, the upper bound of C is endangered as the optimisation process may try to shove C as far as possible toward high energies. Physically, C is not expected to be many folds of the excitation energy, so that we chose $C < 10$ as an upper bound.

Table 13.2: Parameters for forbidden (13.8) and allowed (13.9) generic functions.

Parameter	M	C	a	b	a'	c'
Effect	Magnitude	Fall-off (position)	Cliff/Plateau (height/breadth)	Wall (onset)	Wriggle (bump)	Wriggle (position)
Bounds	$]0,\infty[$	$]0,12]$	$]0.1,10]$	$[0.5,10]$	$[1,10]$	$]1,10]$

The lower bound of C cannot go below 0 for the obvious concern of not introducing a singularity at $w + C = 0$. Theoretically, from BE-scaling (see section11.4.2), C should at least be > 1 so that the cross section decreases with $1/\varepsilon^d$ as the inverse of the kinetic energy. There are nonetheless some situations that demand a peak with a fall-off nearer threshold. One may visualise that $\lim_{c\to 0} 1/(w/c+1)$ moves the singularity closer toward the threshold $w = 0$ and thus brings steeper fall-off slopes at $w = 0$ corresponding to $-w/c$. In figure 13.13, the fall-off portion is situated slightly below twice the energy threshold of the transition ($\Delta\mathcal{E}$=8.895 eV) which demands $C \cong 0.85 < 1$ for an optimal fit given the bound constraints. For this reason, we didn't dare to impose an inferior bound higher than 0.

The same argument about C applies to allowed transitions whose generic expression is recalled here as well :

$$g_4(w) = \frac{M}{(w+C)} \log((w \cdot a)^b + 1) \tag{13.9}$$

Its behaviour near threshold shows that a, b play the same role (derivative, flatness) as in (13.8).

For most allowed transitions with NO, as shown in figure 13.17, the optimisation converged preferably toward $C \simeq 0$ just because the last data point (at 50 eV) in Brunger *et al.* [120] measurements systematically demands a sharper fall-off even when it is corrected for normalisation (cf. section 15.1.3). The opposite trend, when the fall-off is demanded to be slow, C swings toward higher values as seen in figure 13.16.

A brief summary of the parameters treated presently and their bounds is given in table 13.2.

The constraints over the wriggle $[(w/c')^{a'} + 1]$ in (13.8) come from the fact that this feature is usually farther from threshold thus $c' \geq 1$ and $a' \not< 1$ is because the wriggle cannot appear unless the transition at $w = c'$ is sharp.

13.3.1 Diagnostics

So far, we have presented very binary and qualitative means of assessing whether a fit is well constrained or not. We have determined that if the parameters are permitted to vary over a broad range, the fitting is not well constrained either because of the function chosen, or the data available.

There is another very important quantitative indicator assessing how well (or unwell) are the parameters suited to the data to be fitted. It is the *variance* of the parameters involved (or its square root giving the standard deviation). It gives an estimation of the uncertainty over the optimum obtained. The covariance of the parameters is very rarely disclosed because its values can be frighteningly large. As can be imagined, most of the fits presented above are actually very poorly conditioned. This is because the near-threshold behaviour is scarcely probed by measurements. This implies that a and b of (13.8) in particular, are not known with exactitude and that the algorithm will try to adjust them over broad ranges for minute improvements (as for example in figure 13.15).

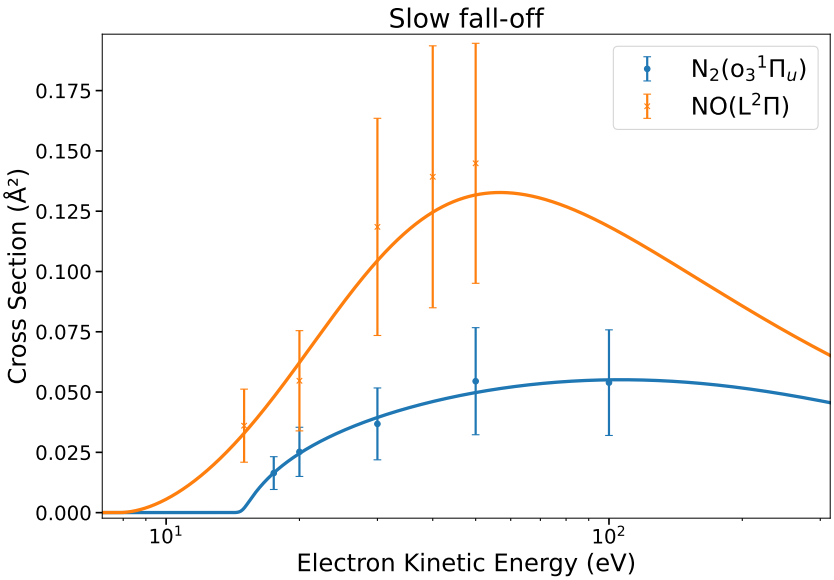

Figure 13.16: An unrevealed falling off portion from the measurements of Malone *et al.* [624] (N_2) and Brunger *et al.* [120] (NO) pushes the parameter C in (13.9) toward higher values: C = 11.4 and 4.1 respectively.

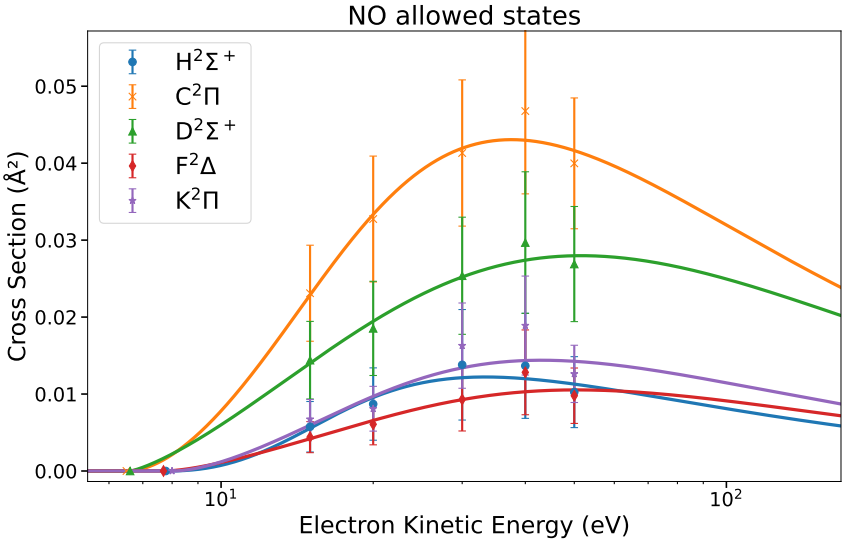

Figure 13.17: A systematic over/under estimation at 40/50 eV for NO in the data of Brunger *et al.* [120] crushes the parameter C to 0 in eq. (13.9) for allowed excitations, in order to obtain the steepest falloff between 40–50 eV.

A concrete example is given in figure 13.18, comparing how the low-energy modifier b, though similar in value (≃2.6), is fitted with larger uncertainty for an excitation with argon (bottom graph) than with nitrogen (top graph). This is because of the presence of a data point [159] at low values and near the excitation threshold of a $^1\Pi_g$ highlighted as a red dot at 10 eV. By artificially imposing different values for $b \in [1.5\,;8]$, one can see how the shapes of the CS fits evolve. While on the bottom graph, the least-square distance to the 4 data points is weakly affected by the behaviour near-threshold, the situation is quite different on the top graph where the distancing of the curve to the red dot is impactfully penalising the result of the fit.

Unfortunately, there are very few cases where the data is enough to constrain well the parameters a and b. For most of our fits, their uncertainty can even exceed their nominal value! At first, this could discredit the quality of the fits presented. In practice, this only means that the parameters a and b cannot, for most of the cases, be given pertinent significance. The most important parameter remains the magnitude M linked to the physical Bethe-Born parameter b_i (or γ_i for forbidden transitions) given in sec. 11.4.1 eq. (11.55). When disclosing parameters in a publication, such diagnosis helps to distinguish crucial parameters from flexible ones.

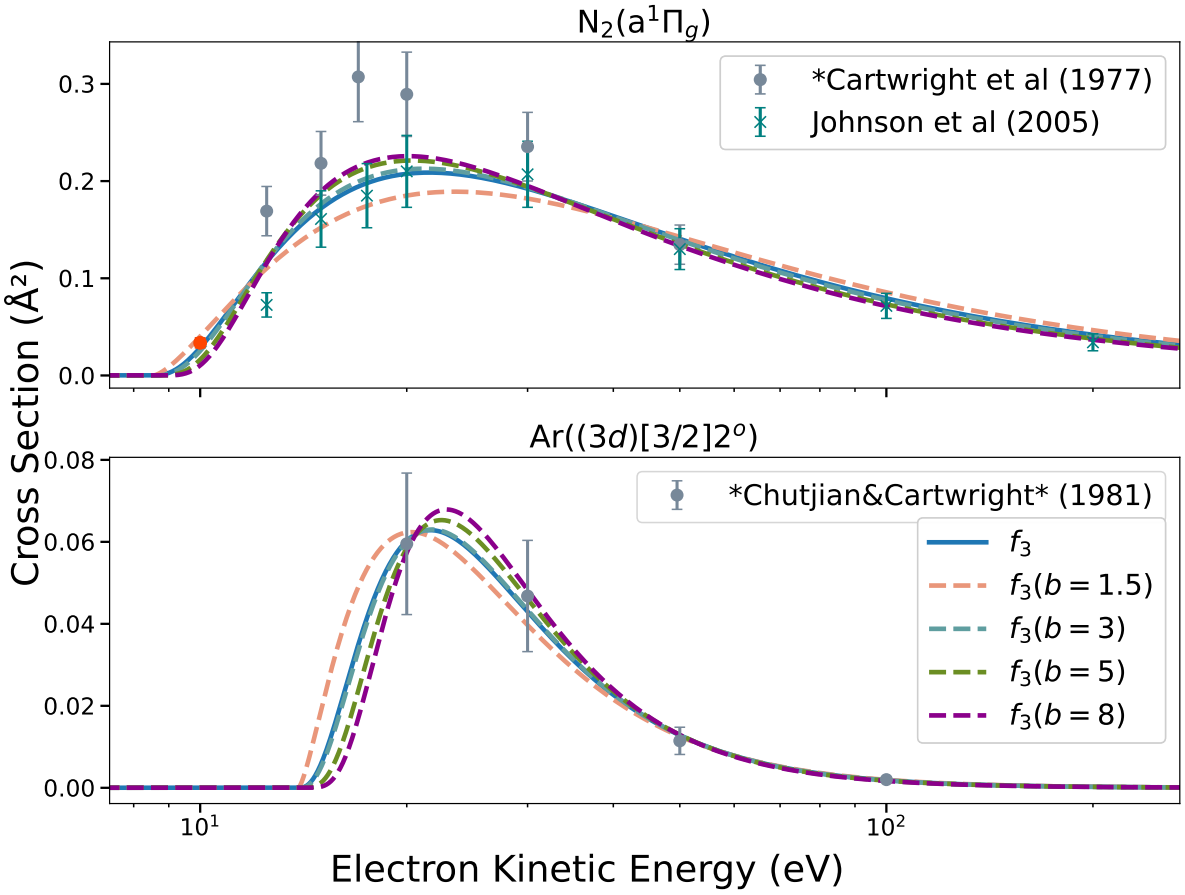

Figure 13.18: Near-threshold behaviour for N_2-a $^1\Pi_g$ (top) better constrained than for Ar-$(3d)[5/2]2^o$ (bottom). The red dot at 10 eV from Cartwright *et al.* [159] (renormalised) is crucial in constraining properly the b parameter in (13.8). It is estimated at 2.553 ± 0.517 for N_2(top) versus 2.61 ± 4.54 for Ar (bottom).

13.4 Closing Remarks

There are many more aspects to be covered when fitting data. Data science forms an entire field on its own and many treaties can be found in a variety of textbooks. The least-squares optimisation method used presently is covered for example in Kendall [487], and concrete numerical methods can be found in Nocedal [706].

Besides being didactic, one of the purposes of this chapter was to bring a qualitative justification (i.e. "how I came up with") for the choice of generic functions used to fit excitation cross sections in part II section 11.4.2. Such complementary information about the scientist's intuitive thinking could be disclosed more often in supplementary files to published articles, or at least in public reports, like the ones of Phelps and Pitchford [750]. It enables to inspect more easily the quality of fitted data and most importantly, opens the way for further improvement.

We showed that the risk of overfitting is lurking practically everywhere. One can easily overfit not only when one set of data is considered (fig 13.5) but also when one combines data from different sources (fig 13.4). Although one might not be acquainted enough with each molecule's electronic state characteristics and eventual resonances, the behaviour of a generic function

when fitting a set of cross section data can help to indicate whether that set is consistent or not. For individual cases, the variance of the parameter is a key indicator to the pertinence of the parameters used.

If the function must writhe and contort itself, push its parameters toward their limits to try to match a shape it means that either:

A. The data is inconsistent

B. The fitting function is wrongly chosen

Identifying which of the two conclusions is the sounder, is part of the art of fitting. Failure to identify any of the two, disregard the discrepancy and force an extrapolated shape through tuning would rather be called the *artifice* of fitting. Pitifully, both are needed in a science which craves after results.

In its most virtuous application, fitting permits to reconcile fragmented pieces of a theory to experimental data. One can ideally draw physical conclusions about the nature of a phenomenon. In the present example, fitting the tail of cross sections from unidentified transitions could help to unveil the forbiddance degree d and understand whether this transition is spin-forbidden or not, or a mixture of states, etc. Nevertheless, one should never confuse fits whose purpose is to derive a value for a physically well-defined parameter, with fits destined to trace curves. In particular, we should refrain from giving in to the perilous temptation of doing science with results derived from *ad hoc* fits.

In the current state of the scientific literature, fits are undeniably under-regarded. It is less and less common to have access to the generic function or the value of the parameters [121, 482, 902], let aside their uncertainty. Paradoxically, machine learning, which is a direct descendent to the art of fitting, attracts an explosively obsessive attention from the scientific community. Could it be because the (older) basics are assumed well-mastered? Whereas on the contrary, I believe they become forlorn.

In Inokuti *et al.* [426, p.216]'s own words :

> [...] the systematization of physical data into an analytic expression sometimes leads to a deeper understanding[...] Once a reliable form of analytic representation is established, we can sometimes use it to judge the correctness of data given in the literature or even to predict cross-section values. To emphasize the importance of sound reasoning in choosing an appropriate form of analytic expression, we use the term *analytic representation* and distinguish it from the data fitting often practiced by engineers.
>
> The topic of analytic representation has not received the attention that its importance warrants.

In the end, fitting, when not an art, is unfortunately a heuristic process, or more informally: a disgraceful loss of time in a scientist's life.

Chapter 14

Plane-Wave Born Scattering

"Les mathématiques sont la poésie des sciences."

— Léopold Sédar Senghor.

The majority of analytical expressions for differential cross sections (DCS) are based on the plane-wave Born approximation (PWBA) which was presented in the section 8.5.1 of part II. They are used in Monte Carlo (MC) simulations for modelling elastic scattering of electrons off molecules in gases [218, 445, 542, 713, 896].

We devoted some effort into investigating the validity of the plane-wave Born approximation at the beginning of chapter 10. There, we determined that, overall, for the atoms considered ($Z > 7$), the PWBA could be used from about ~10 keV.

Regardless, many MC simulations in the past used analytical DCS from the PWBA either because of limited availability of experimental data for DCS or because of convenience. It is indeed very convenient to sample the scattering angle analytical from a reverse formula (3.11) than to construct a bilinear interpolation of many experimental data collected and extrapolated manually.

In the ever-growingly digitised world of today, access to well maintained numerical databases is key for facilitating further research. We strived to create a database of elastic differential cross sections synthesised from both experimental and theoretical sources. The next chapter 15 explains how to access and use this database.

Notwithstanding, we acknowledge that accurate analytical representations are superior to numerical tables in their capability to encompass a physical model and because there is no loss of information due to discretisation. In this chapter, we present succinctly the expressions relevant to elastic scattering at high energies.

> The analytical representation of electron-molecule differential cross sections in the plane-wave Born approximation is only valid at high energies. We recommend to use it only above 10 keV.

The bias introduced in MC simulations by modelling elastic scattering from PWBA DCS at energies lower than 10 keV can be assessed. Many studies demonstrated that the effect of elastic scattering on the electron energy distribution function is large [169, 811]. In particular, Janssen *et al.* [454] compared electron transport in argon from various analytic DCS models to DCS from precise quantum calculations of Zatsarinny and Bartschat [998]. They concluded that: (i) no simple analytical DCS may accurately represent elastic scattering at large angles and (ii) transport parameters are significantly affected by anisotropic scattering above 100 Td.

In the following sections, we gather various quantities related to the elastic scattering of electrons at high energies: differential (DCS), integral (ICS), cumulative (CCS), momentum-transfer (MTCS) cross sections, scattering amplitudes and phase shifts; all calculated from the

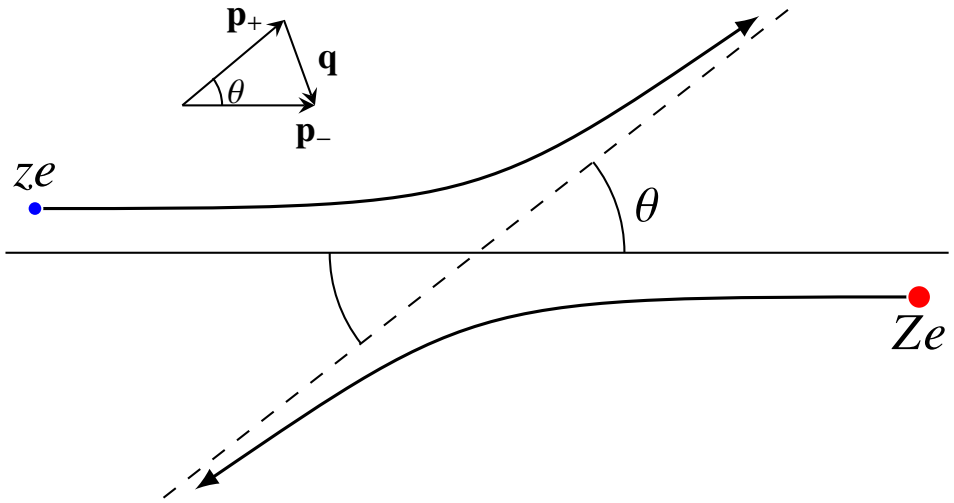

Figure 14.1: Scattering of two structureless charged particles ze and Ze in their centre of mass frame with a reduced mass μ. The deflection by an angle θ is accompanied by a momentum transfer $\mathbf{q}$ between the two particles.

first Born approximation applied to a spherically symmetric potential representing the static potential of an atomic target. Consult Canto and Hussein [147, p.57:eq.(2.72) and p.160:eq.(5.18)] for more information.

As a prerequisite, we remind first the Rutherford scattering formula between two charged particles Ze and ze forming a system of reduced mass μ:

$$\frac{\mathrm{d}\sigma_{\mathrm{R}}}{\mathrm{d}\Omega} = \left(\frac{e^2}{4\pi\epsilon_0}\frac{Zz2\mu}{q^2}\right)^2 \tag{14.1}$$

where q is the momentum transfer linked to the deflection angle θ as $|\mathbf{q}| = 2p\sin\theta/2$. The modulus of the kinetic momentum in the centre of mass frame $p = |\mathbf{p}_+| = |\mathbf{p}_-|$ remains unchanged before ($\mathbf{p}_-$) and after ($\mathbf{p}_+$) the collision. The situation is sketched in 14.1.

We now present the screened Rutherford formulae obtained from a Yukawa and a Slater $1s$ potential. These are used for modelling static atomic potentials in section 8.2.1 in part II.

14.1 Static (Screened Rutherford)

Considering an electron of wavenumber k, one usually defines a:

$$\boxed{\text{Screening Parameter : } \eta \equiv \frac{1}{(2ka)^2}\,.} \tag{14.2}$$

14.1.1 Yukawa : $Z\exp(-r/a)/r$

Potential

$$V_{\mathrm{Y}}(r) = -\frac{Z\mathrm{e}^{-r/a}}{r}\left(\frac{e^2}{4\pi\epsilon_0}\right)\,. \tag{14.3}$$

Electronic Density

$$\rho_{\mathrm{Y}}(r) = \frac{1}{4\pi a^2}\frac{Z\mathrm{e}^{-r/a}}{r}\ \text{a.u.} \tag{14.4}$$

Gradient :

$$\nabla\rho_{\mathrm{Y}}(r) = -\hat{\mathbf{r}}\frac{Z}{4\pi a^2}\frac{(1+r/a)\mathrm{e}^{-r/a}}{r^2}\,\text{a.u.} \tag{14.5}$$

Laplacian :

$$\triangle\rho_{\mathrm{Y}}(r) = \frac{Z}{4\pi a^2}\frac{\mathrm{e}^{-r/a}}{ra^2}\,\text{a.u.} \tag{14.6}$$

Phase-shifts From (8.120) and with [347, 6.612:eq.(3)]:

$$\delta_{\mathrm{SR},\ell} = 2k\int_0^\infty Z\frac{\mathrm{e}^{-r/a}}{r}\mathrm{j}_\ell^2(kr)r^2\,\mathrm{d}r = \frac{Z}{k}Q_\ell\left(1+\frac{1}{2(ka)^2}\right) = \frac{Z}{k}Q_\ell(1+2\eta)\,, \tag{14.7}$$

with the Legendre polynomial of the second kind Q_ℓ as defined in [3, p.332:eq.(8.1.3)].

A. The Golden Screened Rutherford

Plane-Wave Scattering Amplitude

$$f_{\mathrm{SR}} = -\left(\frac{2\mu}{\hbar^2}\right)\int_0^\infty \frac{-Z\mathrm{e}^{-r/a}}{r}\frac{\sin(qr)}{qr}r^2\,\mathrm{d}r = \frac{2Z}{q^2+\dfrac{1}{a^2}} = \frac{Z}{k^2}\frac{1}{1-\cos\theta+\underbrace{2\eta}_{2/(2ka)^2}} \tag{14.8}$$

Plane-Wave DCS

$$\frac{\mathrm{d}\sigma_{\mathrm{SR}}}{\mathrm{d}\Omega} = |f_{\mathrm{SR}}|^2 = \frac{4Z^2}{(q^2+\frac{1}{a^2})^2} = \frac{Z^2}{k^4}\frac{1}{(1-\cos\theta+2\eta)^2} \tag{14.9}$$

Plane-Wave CCS

$$\acute{\sigma}(\theta)_{\mathrm{SR}} = 2\pi\int_0^\theta \frac{\mathrm{d}\sigma_{\mathrm{SR}}}{\mathrm{d}\Omega}(\theta)\sin\theta\,\mathrm{d}\theta = \frac{2\pi Z^2}{k^4}\left(\frac{1}{2\eta}-\frac{1}{1-\cos\theta+2\eta}\right) \tag{14.10}$$

Plane-Wave ICS

$$\sigma_{\mathrm{SR}} = \int_0^{2\pi}\int_0^\pi \frac{\mathrm{d}\sigma_{\mathrm{SR}}}{\mathrm{d}\Omega}(\theta)\sin\theta\,\mathrm{d}\theta\,\mathrm{d}\varphi = \frac{2\pi Z^2}{k^4}\frac{1}{2\eta(\eta+1)} = \frac{4\pi Z^2a^2}{k^2}\frac{1}{1+\frac{1}{(2ka)^2}} \tag{14.11}$$

Plane-Wave MTCS

$$\sigma_{\mathrm{m,SR}} = \int_0^{2\pi}\int_0^\pi \frac{\mathrm{d}\sigma_{\mathrm{SR}}}{\mathrm{d}\Omega}(\theta)(1-\cos\theta)\sin\theta\,\mathrm{d}\theta\,\mathrm{d}\varphi = \frac{2\pi Z^2}{k^4}\left[\ln\left(\frac{1+\eta}{\eta}\right)-\frac{1}{1+\eta}\right] \tag{14.12}$$

B. The Relativistic Screened Rutherford

Relativistic Scattering Amplitude

$$f_{\mathrm{SR}+} = \frac{Z\alpha^2a_0}{\gamma\beta^2}\frac{\sqrt{1-\beta^2\sin^2\frac{\theta}{2}}}{1-\cos(\theta)+2\eta} \tag{14.13}$$

Relativistic CCS with $\mu = \sin^2\frac{\theta}{2}$

$$\acute{\sigma}_{\mathrm{SR}+}(\theta) = \left(\frac{Z\alpha^2 a_0}{\gamma\beta^2}\right)^2 \frac{\mu + \beta^2\eta\left[\mu - (\mu+\eta)\ln(1+\frac{\mu}{\eta})\right]}{2\eta(\mu+\eta)}\,, \tag{14.14}$$

Relativistic ICS

$$\sigma_{\mathrm{SR}+} = \left(\frac{Z\alpha^2 a_0}{\gamma\beta^2}\right)^2 \left[\frac{1}{2\eta(1+\eta)} - \frac{\beta^2}{2}\left(\ln(1+1/\eta) - \frac{1}{1+\eta}\right)\right]. \tag{14.15}$$

Relativistic MTCS

$$\sigma_{\mathrm{m,SR}+} = \left(\frac{Z\alpha^2 a_0}{\gamma\beta^2}\right)^2 \left[(1+2\beta^2\eta)\ln(1+1/\eta) - \frac{1+\beta^2(1+2\eta)}{1+\eta}\right]. \tag{14.16}$$

Relativistic $\langle\cos\theta\rangle$

$$\langle\cos\theta\rangle_{\mathrm{m,SR}+} = 1 + 2\eta\left[2 - \frac{1+(1+\eta)\ln(1+1/\eta) - \beta^2}{1+\beta^2\eta(1-(1+\eta)\ln(1+1/\eta))}\right]. \tag{14.17}$$

C. The Generalised Screened Rutherford

Potential

$$V(r) = -Z\sum_i g_i \frac{\mathrm{e}^{-r/a_i}}{r}\left(\frac{e^2}{4\pi\epsilon_0}\right). \tag{14.18}$$

Generalised Scattering Amplitude Define $\eta_i \equiv 1/(2ka_i)^2$.

$$f_{\mathrm{SR}*} = \frac{Z\alpha^2 a_0}{\gamma\beta^2}\sqrt{1-\beta^2\sin^2\frac{\theta}{2}}\sum_i \frac{g_i}{1-\cos(\theta)+2\eta_i} \tag{14.19}$$

Generalised CCS

$$\begin{aligned}\acute{\sigma}_{\mathrm{SR}*} = \frac{Z\alpha^2 a_0}{\gamma\beta^2}\Bigg\{&\sum_i g_i^2\left[\frac{1}{1+2\eta_i} - \frac{1}{1-\mu+2\eta_i} + \frac{\beta^2}{2}\left(1 - \frac{2\eta}{1-\mu+2\eta} - \ln\left(\frac{1-\mu+2\eta}{2\eta}\right)\right)\right]\\ &-2\sum_{i<j}\frac{g_i g_j}{\eta_i-\eta_j}\left[\ln\left(\frac{1-\mu+2\eta_i}{1-\mu+2\eta_j}\frac{\eta_j}{\eta_i}\right) + \beta^2\left(\eta_i\ln\left(\frac{1-\mu+2\eta_i}{2\eta_i}\right) - \eta_j\ln\left(\frac{1-\mu+2\eta_j}{2\eta_j}\right)\right)\right]\Bigg\}.\end{aligned} \tag{14.20}$$

Generalised ICS

$$\begin{aligned}\sigma_{\mathrm{SR}*} = \frac{Z\alpha^2 a_0}{\gamma\beta^2}\Bigg\{&\sum_i g_i^2\left[\frac{1}{2\eta(1+\eta)} - \frac{\beta^2}{2}\left(\ln(1+1/\eta) - \frac{1}{1+\eta}\right)\right]\\ &-2\sum_{i<j}\frac{g_i g_j}{\eta_i-\eta_j}\left[\ln\left(\frac{(1+\eta_i)}{(1+\eta_j)}\frac{\eta_j}{\eta_i}\right) + \beta^2\left(\eta_i\ln(1+1/\eta_i) - \eta_j\ln(1+1/\eta_j)\right)\right]\Bigg\}.\end{aligned} \tag{14.21}$$

Generalised MTCS

$$\sigma_{\mathrm{m,SR}*} = \frac{Z\alpha^2 a_0}{\gamma\beta^2}\left\{\sum_i g_i^2\left[\ln(1+1/\eta) - \frac{1}{1+\eta} - \frac{\beta^2}{2}\left(2 + \frac{2\eta}{\eta+1} - 4\eta\ln(1+1/\eta)\right)\right]\right. \tag{14.22}$$
$$\left. +2\sum_{i<j}\frac{g_i g_j}{\eta_i - \eta_j}\left[\left(\eta_i \ln(1+1/\eta_i)(1+\beta^2\eta_i) - \eta_j\ln(1+1/\eta_j)(1+\beta^2\eta_i)\right) - \beta^2(\eta_i - \eta_j)\right]\right\}.$$

14.1.2 Exponential (Slater) : $(1 + r/2a)\exp(-r/a)/r$

Potential

$$V_{\mathrm{SX}}(r) = -\left(1 + \frac{r}{2a}\right)\frac{Z\mathrm{e}^{-r/a}}{r}\left(\frac{e^2}{4\pi\epsilon_0}\right). \tag{14.23}$$

Electronic Density

$$\rho_{\mathrm{SX}}(r) = \frac{Z}{8\pi a^3}\mathrm{e}^{-r/a}\ \text{a.u.} \tag{14.24}$$

Gradient:

$$\nabla\rho_{\mathrm{SX}}(r) = -\hat{\mathbf{r}}\frac{Z}{8\pi a^3}\frac{\mathrm{e}^{-r/a}}{a} \tag{14.25}$$

Laplacian:

$$\triangle\rho_{\mathrm{SX}}(r) = \frac{Z}{8\pi a^3}\frac{(r/a-2)\,\mathrm{e}^{-r/a}}{ar} \tag{14.26}$$

Phase-shifts From (8.120) and with [347, 6.612:eq.(3)]:

$$\delta_{\mathrm{SX},\ell} = 2k\int_0^\infty\left(1+\frac{r}{2a}\right)\frac{Z\mathrm{e}^{-r/a}}{r}\mathrm{j}_\ell^2(kr)r^2\,\mathrm{d}r = \frac{Z}{k}\left[Q_\ell(1+2\eta) + \frac{1}{(ka)^2}\sum_{l=\ell+1}^{\infty}\left(l+\frac{1}{2}\right)Q_l(1+2\eta)\right], \tag{14.27}$$

with the Legendre polynomial of the second kind Q_ℓ as defined in [3, p.332:eq.(8.1.3)]. In practice, the sum can be truncated to $\ell_{\max} = 100$, for instance.

A. The Golden Screened Slater

Plane-Wave Amplitude

$$f_{\mathrm{SX}} = -\left(\frac{2\mu}{\hbar}\right)\int_0^\infty -\left(1+\frac{r}{2a}\right)\frac{Z\mathrm{e}^{-r/a}}{r}\frac{\sin(qr)}{qr}r^2\,\mathrm{d}r = \frac{Z}{k^2}\left(1+\frac{2\eta}{1-\cos\theta+2\eta}\right)\frac{1}{1-\cos\theta+2\eta}. \tag{14.28}$$

Plane-Wave DCS

$$\frac{\mathrm{d}\sigma_{\mathrm{SX}}}{\mathrm{d}\Omega} = \left(\frac{Z}{k^2}\right)^2\left(1+\frac{2\eta}{1-\cos\theta+2\eta}\right)^2\frac{1}{(1-\cos\theta+2\eta)^2}. \tag{14.29}$$

B. The Relativistic Screened Slater

Relativistic Amplitude

$$f_{\mathrm{SX}+} = \frac{Z\alpha^2}{\gamma\beta^2}\left(1+\frac{2\eta}{1-\cos\theta+2\eta}\right)\frac{\sqrt{1-\beta^2\sin^2\frac{\theta}{2}}}{1-\cos\theta+2\eta}. \tag{14.30}$$

Relativistic DCS

$$\frac{\mathrm{d}\sigma_{\mathrm{SX}+}}{\mathrm{d}\Omega} = \left(\frac{Z\alpha^2}{\gamma\beta^2}\right)^2 \left(1 + \frac{2\eta}{1-\cos\theta+2\eta}\right)^2 \frac{1-\beta^2\sin^2\frac{\theta}{2}}{(1-\cos\theta+2\eta)^2}\,. \tag{14.31}$$

Relativistic CCS Let: $\mu \equiv \cos\theta$ and $\xi \equiv \dfrac{2\eta}{1-\mu+2\eta}$

$$\acute{\sigma}_{\mathrm{SX}+} = \left(\frac{Z\alpha^2}{\gamma\beta^2}\right)^2 \left[\frac{(7/3-\xi-\xi^2-\xi_i^3/3)}{2\eta} + \frac{\beta^2}{2}\left(\frac{2\eta^2-9\eta(\mu-1)+3(\mu-1)^2}{3(2\eta)^2\xi^3} - \frac{1}{6} + \ln\xi\right)\right] \tag{14.32}$$

Relativistic ICS Let $\zeta \equiv \eta/(1+\eta)$

$$\sigma_{\mathrm{SX}+} = \left(\frac{Z\alpha^2}{\gamma\beta^2}\right)^2 \left[\frac{6\eta(2\eta+3)+7}{6\eta(1+\eta)^3} - \frac{\beta^2}{2}\left(\frac{1}{6}\left(1 - \frac{\eta(\eta(\eta+9)+6)}{(\eta+1)^3}\right) - \ln\zeta\right)\right] \tag{14.33}$$

Relativistic MTCS

$$\sigma_{\mathrm{m,SX}+} = \left(\frac{Z\alpha^2}{\gamma\beta^2}\right)^2 \left[\ln\zeta + 1 - \zeta - \frac{1-\zeta^2}{2} - \frac{1-\zeta^3}{3} - \beta^2\left(\frac{4\eta+3}{3(\eta+1)^3}\right)\right] \tag{14.34}$$

C. The Generalised Screened Slater

Potential

$$V_{\mathrm{SX}*}(r) = \sum_i g_i - \left(1 + \frac{r}{2a_i}\right)\frac{Z\mathrm{e}^{-r/a_i}}{r}\left(\frac{e^2}{4\pi\epsilon_0}\right)\,. \tag{14.35}$$

Generalised Scattering Amplitude

$$f_{\mathrm{SX}+} = \frac{Z\alpha^2}{\gamma\beta^2}\sum_i g_i\left(1 + \frac{2\eta_i}{1-\cos\theta+2\eta_i}\right)\frac{\sqrt{1-\beta^2\sin^2\frac{\theta}{2}}}{1-\cos\theta+2\eta_i}\,. \tag{14.36}$$

Generalised DCS

$$\begin{aligned}\frac{\mathrm{d}\sigma_{\mathrm{SX}*}}{\mathrm{d}\Omega} &= \left(\frac{Z\alpha^2}{\gamma\beta^2}\right)^2 \left(1-\beta^2\sin^2\frac{\theta}{2}\right)\sum_i g_i^2\left(1+\frac{2\eta_i}{1-\cos\theta+2\eta_i}\right)^2\frac{1}{(1-\cos\theta+2\eta_i)^2} \\ &= 2\sum_{i<j}\frac{g_i g_j}{(1-\cos\theta+2\eta_i)(1-\cos\theta+2\eta_j)}\left(1-\frac{2\eta_i}{1-\cos\theta+2\eta_i}\right)\left(1-\frac{2\eta_j}{1-\cos\theta+2\eta_j}\right)\,.\end{aligned} \tag{14.37}$$

Generalised CCS Let: $\mu \equiv \cos\theta$ and $\xi_i \equiv \dfrac{2\eta_i}{1-\mu+2\eta_i}$

$$\begin{aligned}\acute{\sigma}_{\mathrm{SX}*} = \left(\frac{Z\alpha^2}{\gamma\beta^2}\right)^2 \Bigg\{&\sum_i g_i^2\left[\frac{(7/3-\xi_i-\xi_i^2-\xi_i^3/3)}{2\eta_i} + \frac{\beta^2}{2}\left(\frac{2\eta_i^2-9\eta_i(\mu-1)+3(\mu-1)^2}{3(2\eta_i)^2\xi_i^3} - \frac{1}{6} + \ln\xi_i\right)\right] \\ &+ 2\sum_{i<j}\frac{g_i g_j}{(\eta_i-\eta_j)}\Bigg[\left(1-\frac{\eta_i\eta_j}{(\eta_i-\eta_j)^2}\right)\ln\left(\frac{\xi_i}{\xi_j}\right) \\ &\quad - \frac{1}{2(\eta_i-\eta_j)}\left((1+\beta^2\eta_i)(\eta_i-2\eta_j)(1-\xi_i) + (1+\beta^2\eta_j)(\eta_j-2\eta_i)(1-\xi_j)\right) \\ &\quad + \frac{\beta^2}{2(\eta_i-\eta_j)^2}\left((\eta_i^2(\eta_i-3\eta_j)\ln\xi_i - \eta_j^2(\eta_j-3\eta_i)\ln\xi_j)\right)\Bigg]\Bigg\}\end{aligned} \tag{14.38}$$

Generalised ICS Let $\zeta_i \equiv \dfrac{\eta_i}{(1+\eta_i)}$

$$\begin{aligned}\sigma_{\mathrm{SX}*} = \left(\frac{Z\alpha^2}{\gamma\beta^2}\right)^2 \Bigg\{ \sum_i g_i^2 \left[\frac{6\eta_i(2\eta_i+3)+7}{6\eta_i(1+\eta_i)^3} - \frac{\beta^2}{2}\left(\frac{1}{6}\left(1 - \frac{\eta_i(\eta_i(\eta_i+9)+6)}{(\eta_i+1)^3}\right) - \ln\zeta_i\right)\right] \\ + 2\sum_{i<j} \frac{g_i g_j}{\eta_i - \eta_j}\left[\left(1 - \frac{\eta_i\eta_j}{(\eta_i-\eta_j)^2}\right)\ln\left(\frac{\zeta_i}{\zeta_j}\right)\right. \\ - \left(\frac{(\eta_i - 2\eta_j)(1+\beta^2\eta_i)}{2(\eta_i-\eta_j)(1+\eta_i)} + \frac{(\eta_j - 2\eta_i)(1+\beta^2\eta_j)}{2(\eta_i-\eta_j)(1+\eta_j)}\right) \\ \left. + \frac{\beta^2}{2(\eta_i-\eta_j)^2}\left(\eta_i^2(\eta_i - 3\eta_j)\ln\zeta_i - \eta_j^2(\eta_j - 3\eta_i)\ln\zeta_j\right)\right]\Bigg\} \end{aligned} \tag{14.39}$$

Generalised MTCS

$$\begin{aligned}\sigma_{\mathrm{m,SX}*} = \left(\frac{Z\alpha^2}{\gamma\beta^2}\right)^2 \Bigg\{ \sum_i g_i^2 \left[\ln\zeta_i + 1 - \zeta_i - \frac{1-\zeta_i^2}{2} - \frac{1-\zeta_i^3}{3} - \beta^2\left(\frac{4\eta_i+3}{3(\eta_i+1)^3}\right)\right] \\ + 2\sum_{i<j}\frac{g_i g_j}{(\eta_i-\eta_j)^2}\left[(\zeta_i(\eta_i - 2\eta_j) + \zeta_j(\eta_j - 2\eta_i))\right. \\ - \frac{\left(\eta_i^2(\eta_i - 3\eta_j)\ln\zeta_i - \eta_j^2(\eta_j - 3\eta_i)\ln\zeta_j\right)}{(\eta_i - \eta_j)} \\ \left. + \beta^2\left(\frac{2(\eta_i\eta_j)^2}{\eta_i - \eta_j}\ln\left(\frac{\zeta_j}{\zeta_i}\right) + 1 - (\zeta_i\eta_i(\eta_i - 2\eta_j) + \zeta_j\eta_j(\eta_j - 2\eta_i))\right)\right]\Bigg\} \end{aligned} \tag{14.40}$$

14.2 Multipole : $\sim 1/r^n$

14.2.1 Polarised : $\sim 1/r^4$

Potential

$$V_{\mathrm{b}} = -\frac{\alpha_{\mathrm{d}}}{2(r^2 + r_{\mathrm{b}}^2)^2} \tag{14.41}$$

Phase-shifts From (8.120) and with [347, 6.541(1-2)]:

$$\tilde{\delta}_{\mathrm{b},\ell} = 2k\int_0^\infty \frac{\alpha_{\mathrm{d}}}{2(r^2+r_{\mathrm{b}}^2)^2}\mathrm{j}_\ell^2(kr)r^2\,\mathrm{d}r = \frac{\alpha_{\mathrm{d}}\pi k}{2r_{\mathrm{b}}}\left(\mathrm{I}_{\ell+\frac{1}{2}}(kr_{\mathrm{b}})\mathrm{K}'_{\ell+\frac{1}{2}}(kr_{\mathrm{b}}) + \frac{1}{2kr_{\mathrm{b}}}\right) \tag{14.42}$$

$$= -\frac{\alpha_{\mathrm{d}}\pi k}{2r_{\mathrm{b}}}\left(\mathrm{I}'_{\ell+\frac{1}{2}}(kr_{\mathrm{b}})\mathrm{K}_{\ell+\frac{1}{2}}(kr_{\mathrm{b}}) - \frac{1}{2kr_{\mathrm{b}}}\right) \tag{14.43}$$

with modified Bessel functions of the first ($\mathrm{I}_{\ell+\frac{1}{2}}$) and second ($\mathrm{K}_{\ell+\frac{1}{2}}$) kinds [3, p.374:§9.6]. The $K'(x)$ means the derivative in x. There is a 'k' missing in the numerator of [812, eq.(B4)]

Scattering amplitude From (8.115) and [347, 6.565(3)], (see also [572, eq.(24)]):

$$\tilde{f}_{\mathrm{b}} = -\left(\frac{2\mu}{\hbar^2}\right)\int_0^\infty \frac{-\alpha_{\mathrm{d}}}{2(r^2+r_{\mathrm{b}}^2)^2}\frac{\sin(qr)}{qr}r^2\,\mathrm{d}r = \frac{\alpha_{\mathrm{d}}\pi}{4r_{\mathrm{b}}}\mathrm{e}^{-qr_{\mathrm{b}}} = \frac{\alpha_{\mathrm{d}}\pi}{4r_{\mathrm{b}}}\mathrm{e}^{-2k\sin\frac{\theta}{2}r_{\mathrm{b}}} \tag{14.44}$$

Chapter 15

The IAA Database

"A database is never finished, only abandoned."

— As was said by many others, in their own wor(l)ds...

When it comes to cross sections, one could perhaps establish the following hierarchy :
Study ≪ Multiple study ≪ Compilation ≪ Review ≪ Database

A study just publishes a set of cross section measurements at various energies, whereas a multiple study presents several ones measured with the same apparatus (for instance elastic along with vibrational or various electronic transitions). A compilation regroups different studies but does not present much critique by comparing data such as in reviews. Finally, a database gives a practical recommendation based on reviews and structures clearly the data into easily transcribable tables and eventually regroups them into a file readily readable by a program.

The purpose of the present chapter is to expose the cross sections assembled in chapter 11 and turn it into a database. Comparison to experimental data and other databases is made in the next chapter 16.

We would like to baptise the present database of electron-molecule cross sections as the "IAA database" in honour of the *Instituto de Astrofísica de Andalucía* which has generously provided its resources to the realisation of the present thesis.
This chapter is devoted to the description of the present – IAA – database which is hosted on the server `https://doi.org/10.5281/zenodo.8190461`.

Our IAA database, is distinguished from other ones in seven respects:

I. – It is mostly *independent* from all other databases but not totally unrelated either.

By this, we mean that we have not directly used the values of the CS featuring in other databases but we gleaned experimentally measured and theoretically calculated CS available in the literature with an emphasis on the most recent ones. The only places where our database coincides exactly point-by-point with another one, is when it relies on theoretically calculated CS for a particular species in a specific energy range from either the BSR calculations of Zatsarinny [1000] or the local-complex-potential resonant CS of Laporta *et al.* [552, 553].

II. – It possesses, in addition to integral cross sections, a grid of differential cross sections (DCS) for *elastic scattering* sampled on angles spanning 0° to 180° with an interval of 0.5° (361 values at each energy).

The energy grid is the union of all energies probed experimentally, with presently made theoretical calculations on a grid of rounded energy values in eV. The only exception is the DCS of argon up to 200 eV for which we resampled the more accurate DCS computed by Zatsarinny and Bartschat [998].

For inelastic scattering, it uses linear interpolation of various experimental data collected into a common file.

III. – The elastic momentum-transfer CS is the product of a three-step chain:

i. Determine the total CS and all inelastic CS (sec. 11.6);

ii. Deduce the residual elastic CS from the subtraction of all inelastic CS (sec. 11.1.5);

iii. Derive the momentum-transfer CS from the average cosine $\langle \cos\theta \rangle$ given by the shape of the DCS (see eq. (11.11)).

This was a choice motivated by the availability of abundant, accurate, well-resolved and updated measurements of the total scattering cross section. The other way around would be physically more relevant, but also unfortunately too risky because of the larger uncertainties and lesser availability of data of elastic momentum-transfer CS.

IV. – It extends on an unequalled wide range of energies from 0 eV to 1 GeV thanks to the extrapolation through relativistically valid analytical formulae.

V. – The extrapolation of the CS at both extremes of the energy range is based on physically meaningful parameters:

◁ At low energies : the scattering length A, static (dipole) polarisability α_d and quadrupole Q (for molecules only)

▷ At high energies : Bethe parameters moments of the oscillator strength distribution for inelastic CS (M^2, $\ln c$) and parameters from a Born expansion for elastic scattering $\tilde{A}$, $\tilde{B}$, $\tilde{C}$ and a cutoff energy K for the Born-scaling.

VI. – The inelastic cross sections are enhanced with more precise information on the electron energy loss such as Franck-Condon factors (or transition probabilities) for discrete vibronic bands of diatomic molecules, distribution over a bump for continuum losses (molecular oxygen) and partial ionisation based on core orbitals and valence-state excitations of the ion.

VII. – It is unadjusted to match transport coefficients when used by a two-term Boltzmann kinetic solver.

In lieu of adjustment, the CS are complemented with an inelastic cross section from unknown losses based on the complementary to the Thomas-Reiche-Kuhn sum rule of oscillator strengths from optically-allowed excitations and ionisation. The big exception is molecular nitrogen, for which the CS had to be complemented with losses from forbidden excitations based on the database of Kawaguchi *et al.* [482].

The known weaknesses of our database depend on each target, but are generally all linked to elastic cross sections at energies below 1 eV because of three reasons:

i) Elastic CS were derived from integral total scattering cross section measurements instead of momentum-transfer cross sections deduced from swarm experiments.

ii) The DCS at very low energies < 1 eV are computed from a too basic model (the MERT described in 10.1.5). The correspondence between integral and momentum-transfer cross sections might thus be inaccurate at low energies.

iii) Because of the two previous limitations, the resolution (number of data points) at low energies is very sparse. Only 3 points are given: 1 meV, 10 meV and 100 meV.

We could not find a reliable way to compute three-body attachment coefficients to molecular oxygen. This process significantly affects transport in O_2 at low electric fields < 100 Td.

For atomic oxygen and nitrogen, the cross section might be very inaccurate, especially elastic scattering due to little availability and lower reliability of experimental data.

Nevertheless, we estimate that the present database reflects electron-molecule interactions in atmospheric gases to the best of our knowledge. The rest of this chapter is divided into two sections. In the first 15.1, we give additional information on how the data was manipulated besides all the explanations given throughout part II. In the second 15.2, we give practical information on how to retrieve and use our data.

15.1 Metadata

In this section, we redirect the reader looking for specific information to the appropriate place in the thesis. Most of the information on how (differential) cross sections were constructed is available in chapter 11, organised in sections according to the collision type. The table 15.1 contains hyperlinks to figures, tables and equations for each target according to the collision type of the cross section. A detailed account of how we used fitting to synthesise data from a large experimental database was given in the previous chapter 13. A commented summary of the results from the physical point of view is presented in section 12.1 organised per gaseous species.

Instructions about how to use our cross sections in Monte Carlo simulations are given in section 15.2 and additional prescriptions in section 4.1. For sampling the outcome or the occurrence of a collision, instructions are given in section 3.2.

An overview of the performance of our cross sections and comparison with other databases is the topic of the next chapter 16.

In the rest of this section, for each target we explain how we dealt with:

A. Outdated experimental data $\Longrightarrow$ **Renormalisation**

B. Missing experimental data $\Longrightarrow$ **Completion**

Renormalisation

Any measurement of a physical quantity requires a calibration of the instrument so as to match the output signal of the instrument to an absolute physically meaningful value. Since a full calibration is such a tedious process, many experimental measurements rely on benchmarks [132] which are a consensus over either very precise experimental values or very accurate theoretical calculations.

Table 15.1: Overview of information about cross sections scattered throughout this thesis for each gaseous target. Next to the number of the section are displayed the page numbers. Both are hyperlinked. To navigate easily back and forth, use `Alt+←`, or check the equivalent shortcut on your pdf browser to come back to this page. In the printed distribution, here is a good page to place your bookmark.

Target		N_2	O_2	NO	Ar	O	N
Anagraph		p.507	p.508	p.508	p.509	p.510	p.510
Transport		fig.16.5	fig.16.10	fig.16.14	fig.16.18	fig.16.21	fig.16.23
References		tab. 16.1	tab. 16.2	tab. 16.3	tab. 16.4		
Total	σ_{tot}	fig.11.51a	fig.11.51b	fig.11.51d	fig.11.51c	fig.11.51f	fig.11.51g
Elastic DCS	$\frac{\mathrm{d}\sigma}{\mathrm{d}\Omega}$	fig.11.9 figs.	11.10,11.12,11.8	fig.11.11	fig.11.2,11.7	fig.11.5	
ICS	σ_{e}			fig.11.13			fig.11.6
MTCS	σ_{m}	fig.11.14a	fig.11.14b	fig.11.14c	fig.11.14d	fig.16.19	
Residual	σ_{re}	fig.16.1	fig.16.6	fig.16.11	fig.16.15	×	×
MTCS	σ_{rm}					×	×
Rotational	σ_{rot}	eq.(11.24)	eq.(11.21b)	eq.(11.21a)			
Vibrational	σ_{vib}	fig.11.19	fig.11.25,11.23				
Attachment	σ_{att}			fig.11.29			
Electronic	σ_{elt}	fig.16.3	fig.16.8	fig.13.17	fig.16.17	fig.13.9	
		tab.11.6	tab.11.7	tab.11.8	tab.11.9	tab.11.10	tab.11.11
		eq.(11.64)		eqs.(11.61),(11.62)		eq.(11.68)	
Ionisation	σ_{ion}	fig.16.4	fig.16.9	fig.16.13	fig.16.16	fig.16.20	fig.16.22
				eq.(11.120)	fig.11.45	tab.11.12	
SDCS	$\frac{\mathrm{d}\sigma_{\text{i}}}{\mathrm{d}\varepsilon_2}$	fig.11.46			eq.(11.119)		

Benchmarking serves to bridge the gap between the instrument signal and the measurement value by using a known quantity about a standard object. In scattering experiments, these are typically resonance peaks and cross sections in helium or argon. To know how benchmarks are used to facilitate subsequent measurements of cross sections, please refer to sections 7.3.5&7.3.6. As instrumental or theoretical accuracy improves with time, new benchmarks [e.g. 14] are brought about every decade or so. Therefore, we may say that a set of experimental data becomes outdated when the benchmark it relies on, has been replaced by a more recent one.

One of the great usefulnesses of reviews, is not only to gather information under a coherent ensemble, but also to keep it updated as was done throughout the years [124, 388, 941]. Nonetheless, updating data from someone else's measurements without their assistance is exacting. If original values of the raw measurements are not disclosed, it is all the more risky. This is why, most reviews prefer to update the measurements performed by their group only [941].

In our case, we decided, notwithstanding, to update some of the older sets of measurements based on evidence gleaned from the literature. There are mainly two reasons for this: first, using outdated data to construct a database would compromise the coherence of the database; second, there would be no point in proposing a new database if we decided to overlook this aspect.

For those studies that were not revised for their normalisation to outdated references, we proceeded to a **coarse** renormalisation corresponding to the second case in the equation of point **2**. in section 7.3.5 of the previous part.

By coarse, we mean that instead of properly selecting a benchmark differential cross section (DCS) at each individual energy, calculate all the ratios to the older reference DCS and then applying those ratios to all other concerned DCS (not to mention extrapolation to 0° and 180°); we only proceeded to renormalisation directly from reported integrated DCS (ICS). This assumes that all DCS actually perfectly agree in shape, and that there is only one calibration factor to be adjusted at each energy. This, of course, is not necessarily verified. Nonetheless, normalising through the DCS would require to deal with extrapolation, which may be risky or daunting for the purpose of the present thesis. The renormalisation we present for each target is thus based on an *average* of ICS values.

All experimental which have been renormalised by us are labelled with an asterisk * placed before the author name in our figures.

For instance, data from Zubek [1012] renormalised for N_2 are displayed as "*Zubek (1994)" in figure 16.3.

Completion

An often understated issue of cross section databases is their completeness. It is difficult to obtain a set of cross sections which completely accounts for all the losses endured by electrons in their collisions with molecules. We explain here how we compensate missing cross sections from unknown or unmeasured inelastic processes in our database.

Let us refresh our minds and jump to* figure 11.32a on page 447. Yon figure showed a snapshot of the electron energy-loss spectrum (EELS) for an electron originally at an energy of $\varepsilon_0 = 20\,\mathrm{eV}$ after being inelastically scattered at an angle of 20°. If we were to integrate this spectrum over all angles Ω and all energy-losses ε, we should be able to retrieve the total cross section of interaction:

$$\sigma_{\mathrm{tot}} = \oint_{\Omega} \int_{0}^{\varepsilon_0} \frac{\mathrm{d}\sigma_{\mathrm{EELS}}}{\mathrm{d}\varepsilon\,\mathrm{d}\Omega}\,\mathrm{d}\varepsilon\,\mathrm{d}\Omega\,. \tag{15.1}$$

If we have good spectroscopic knowledge, we may group energy losses according to the (rotationally-broadened) vibronic band pertaining to one identical electronic configuration of an excited state of the molecule. This is a tedious process since, as seen well on figure 11.32a, we would need to fit each peak of a band with a Voigt or Lorentz profile then take the integral value of the fit and sum all integrals to obtain the differential cross section of that electronic excitation at the observed angle of scattering.

Notwithstanding, even with good spectroscopic knowledge, we may not classify all bands; and particularly not those which are drowned in the noise. In relation to this limitation, we would like to quote an astute observation:

Song *et al.* [865]

> The resultant electronic excitation cross sections, however, should be understood as a whole only to provide realistic energy loss of electrons passing through the gas, and in fact, unique determination of individual cross sections will not be possible as long as there is no additional information.

*On a typical .pdf reader press `Alt+←` to promptly navigate back here to the previous page.

This means, that even with the greatest of all care, there will always be a part of the electron energy-loss spectrum unaccounted in our database.

> "Completion" of a set of inelastic cross sections is the attempt to include all unidentified losses in the electron energy-loss spectrum into complementary cross sections which may be seen as virtual electronic states at certain average energy levels.
> For molecules, completion also comprises the construction of a set of rotational cross sections.

There are essentially three ways to create the complementary cross section:

I. Sum rules: The preferred way is to exploit the Thomas-Reiche-Kuhn sum rule (11.70) when the sum of optical oscillator strengths from dipole-allowed excitations (f_x) and ionisation (f_i) does not amount exactly to the number of electrons (N) in the target molecule. We may then very straightforwardly define a complementary optically-allowed excitation whose oscillator strength f_o is determined by the parameters of our analytical fits from chapter 11:

$$f_o = N - \sum_x M_x \frac{\Delta\mathcal{E}}{\mathrm{Ryd}} - \sum_i Q_i N_i \ . \tag{15.2}$$

[Please mind the notation in the above equation (15.2): x index for discrete excitation, i index for ionisation channel (ground, ionic excitation and/or multiple ionisation). Namely, forgive the potentially confusing notation $N_{\mathrm{i},i} = Q_i N_i$ (roman 'i' subscript stands for **i**onisation, whereas italic i is the index for ionisation channel). The $N_{\mathrm{i},i}$ quantity ("active number of electrons in the ionisation channel i") was defined in (11.93) and more specifically in (11.108). The Q_i and N_i parameters are to be found in each row (indexed by i) of table 11.12.]

If this sum (15.2) is already complete (i.e. $f_o = 0$), then, one must seek for other sum rules or higher moments of the oscillator strength sum rule [319, §IV.C].

II. Total inelastic CS: An alternative way is to derive directly the missing cross section from the difference between the total CS for electronic excitations σ_{exc} and the sum from the CS σ_c in the current database.

$$\sigma_{\rhd}(\varepsilon) = \sigma_{\mathrm{exc}}(\varepsilon) - \sum_{c\in\mathrm{exc}} \sigma_c(\varepsilon)$$

The disadvantage is that one does not always have access to the total inelastic CS and if so, the accuracy might not be good enough. One then obtains an (ugly) tabulation of the complementary CS whose accuracy is marginal.

III. Blind adjustment : When none of the solutions above are within reach, one must surrender to the ultimate empiricist's tool: *ad hoc* adjustments.

The concept of completion is tightly linked to the adjustment of cross sections so as to match experimental transport coefficients of an electron swarm in a given gas at a certain electric field. The complementary inelastic cross section represents major electron energy losses besides the ionisation which, normally, is well characterised. One may then scale an arbitrarily chosen cross section upwards until the Townsend's first ionisation coefficient α_{i} (or other reaction coefficients) match well the experimental data of electron swarms in discharge gas tubes.

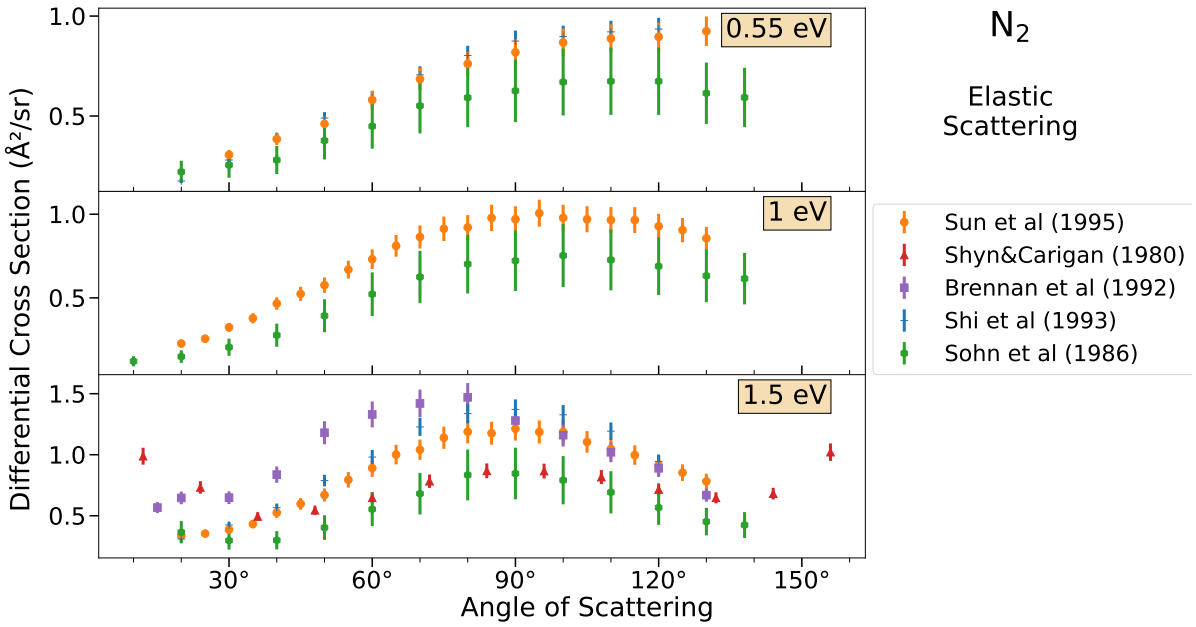

Figure 15.1: Experimental electron elastic differential cross section with N_2 at 0.55, 1 and 1.5 eV. ▲ - Shyn and Carignan [838]; ■ - Brennan *et al.* [105]; •- Sun *et al.* [894]; + - Shi *et al.* [832]; ⬡ - Sohn *et al.* [863]. Earlier data [838, 863] are lower than more recent data [832, 894].

Completion is not a new concept, but its denomination is not standard. Many databases on LXCat possess such a complementary cross section. For instance, for N_2, `Phelps` (and also `IST-Lisbon`) has one named "sum of singlet states" which represents the bulk of all electronic excitations lying beyond $a''\ ^1\Sigma_g^+$ at 12.25 eV. `Biagi` also possesses a "sum of singlets" but it is hard to guess which states it comprises because the b, b′, c_3, c_4' and o_3 singlet states are all already present in the database.

We recommend that "completion"* be added as a fourth criterion to the list of Itikawa [435].

15.1.1 N_2 – updates

Renormalisation

The accuracy of elastic DCS of molecular nitrogen improved with time. As an example, several discrepancies [832, fig. 1-2] at low energies got resolved after more recent experiments [894] elucidated the DCS with a deepened comparison with theoretical values and calibration to a well established absolute reference, usually Helium [693, 771]. Such disagreement is shown in 15.1 at 0.55, 1 and 1.5 eV, where the earlier measurements of Sohn *et al.* [863] and Shyn and Carignan [838] are challenged by Sun *et al.* [894] and Shi *et al.* [832].

Although Sohn *et al.* [863] mentioned that all their results were underestimated by calculations and other experimental results, they did not expound their calibration and normalisation procedure. Albeit not systematic, an upward correction by ~1.2, 1.25, 1.3, 1.4 and 1.5 to Sohn *et al.* [863, table 2] at 0.1, 0.35, 0.55, 1 and 1.5eV brings their data into better agreement both with [832, 894] and even the most recent total CS of Kitajima *et al.* [512]. Consequently, we used these factors to scale up all their [863, table 2-3] elastic and vibrational CS.

*"completion of the representation of inelastic losses of electrons in a gas through a discrete set of cross sections".

In the $^2\Pi_g$ resonance region, comparison between theory and experiment and even among different measurements is intricately difficult. This stems from the fact that the energy position of the resonance feature (peaks or dales) varies with the angle of scattering [17, p.3664-5:table 2]. Thus, it is not straightforward to understand whether the energies reported are consistent between different experiments. Instead, it is desirable to take a reverse approach [832, table 2] and compare DCS by adjusting the incident electron energy to remain at the peak position while maintaining the angle fixed [894, 1240-2:table I].

In general, it is observed that Shyn and Carignan [838]'s DCS (also for other molecules [842]) report higher rates of forward and backward scattering than the majority of other experiments [894, figs. 6–8]. This might point toward a systematic contamination of the signal at small and large angles in their apparatus [939, §V:p.82]; a concern that was addressed already many times and that should be reminded to those who use the data for modelling. This is also true for doubly differential cross section from impact ionisation as discussed in section 11.5.4 p.492 in the previous part II (see the triangles ▲ in figures 11.47–11.48).

At higher energies, the agreement between measurements is much better due to an accurate calibration of the absolute DCS [114]. Herrmann *et al.* [397] performed measurements over an extended range of energies (90–1000 eV) but used approximate IAM calculations to normalise their data. They did provided scaling factors [397, table II] to bring their DCS in agreement with Bromberg [114] and Jansen *et al.* [453] on absolute scale. After rechecking those original factors from averaged ratios, we determined that those are valid and should be applied for correcting their reported DCS.

Some measurements published during the 70's were updated due to more accurate results for the values of the DCS used as a reference. This was the case of Cartwright *et al.* [158] and Chutjian *et al.* [181] which were renormalised later by Trajmar *et al.* [941] with the data of Srivastava *et al.* [870] revised. Nevertheless, at the lower energies $\varepsilon < 15$ eV, the latter DCS is higher at small and large angles than more recent measurements as observed in figure 15.2. In contrast, Brunger and Teubner [122, §III.B] relied on the measurements of Shyn and Carignan [838], which they found to lie in better agreement with their own results.

Since the most recent measurements of Linert and Zubek [600] and Allan [17] probed a wide range of angles even up to 180°owing to the magnetic angle changer technique [510], we performed our own quick renormalisation of Cartwright *et al.* [158] DCS using Linert and Zubek [600] below 21 eV and Shyn and Carignan [838] at higher energies. The overall agreement with Johnson *et al.* [463] was slightly improved compared to Trajmar *et al.* [941]. This freshly renormalised set of data was used along with the most recent measurements to obtain fits for the integral cross sections in section 11.4.3 of the previous part.

The difficulty with measurements [910] based on normalisation from the relative ratio to Helium published in Srivastava *et al.* [870, table II] is that they are not guaranteed to be consistently accurate at all angles and all energies. Indeed, uncertainty is introduced twice, when multiplying by the ratio N_2/He and then by the absolute He DCS. In order to obtain newly renormalised sets, one would have to revert the process of normalisation at all angles, multiply by a trusted set of absolute N_2 DCS and extrapolate at small and large angles before finally integrating. We did not choose to pursue this daunting task and decided to simply put less weight on older measurements that could not be renormalised in a straightforward way.

Malone *et al.* [622] reported re-integrated values of Zubek and King [1013] for the $C\,^3\Pi_u$, $E\,^3\Sigma_g^+$ and $a''\,^1\Sigma_g^+$ states. Subsequently, we scaled down Zubek [1012]'s ICS for $C\,^3\Pi_u$ by a factor of 1.28* in order to bring his formerly reported value of 24×10^{-18} cm^2 at 17.5 eV in agreement with the newly calculated value of 18.8×10^{-18} cm^2 by Malone *et al.* [622].

*Malone *et al.* [622, figure 1] had hinted a factor of 1.32

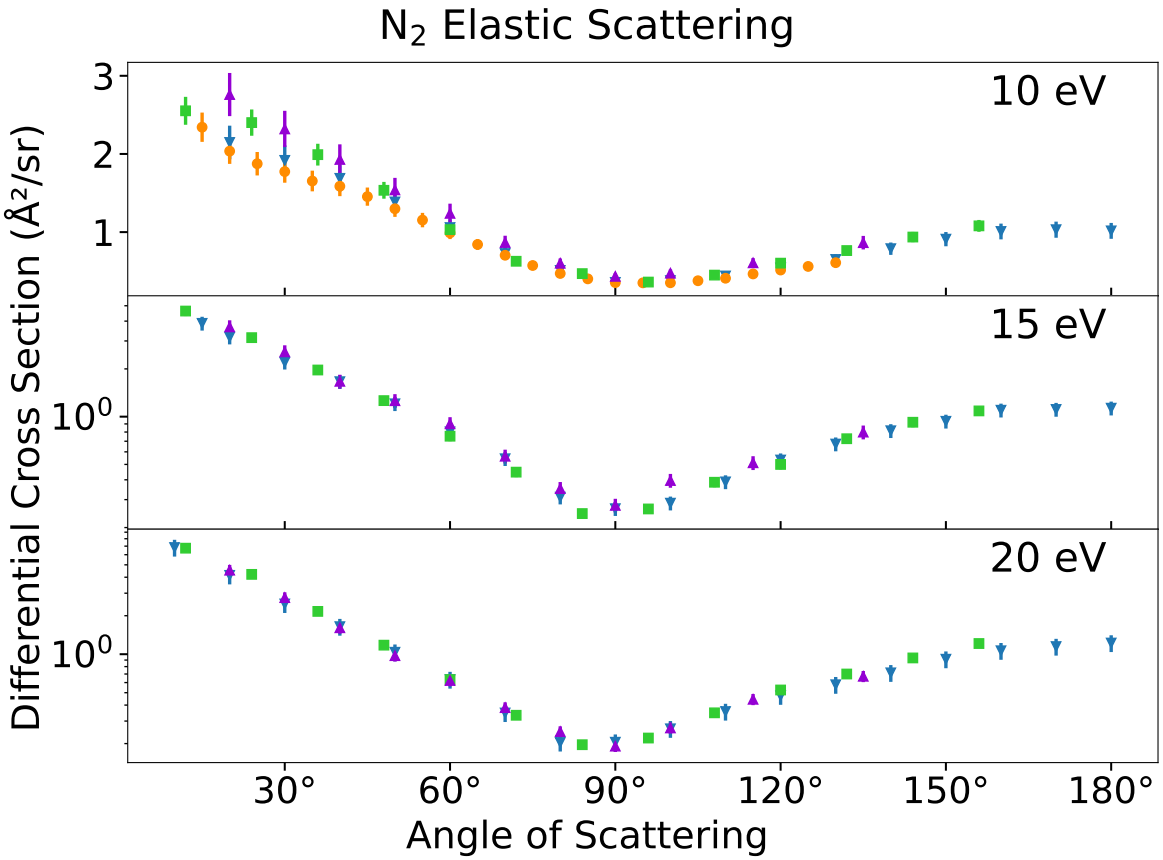

Figure 15.2: Experimental electron elastic differential cross section with N_2 at 10, 15 and 20 eV. ▲ - Srivastava *et al.* [870] renormalised by Trajmar *et al.* [941]; ■ - Shyn and Carignan [838]; •- Sun *et al.* [894]; ▼ - Linert and Zubek [600]. At lower energies, the data of Srivastava *et al.* [870] lead to a slight overestimation of the integral cross section.

Completion

Despite the differences between all other databases of N_2, what mostly distinguishes our – incomplete – database is that its total inelastic cross section (for N_2) lies systematically below any of the other databases as can seen on the bottom graph of figure 16.2.

We checked that the sum Thomas-Reiche-Kuhn sum amounts to ~14 in our database:

$$\text{OOS completion for } N_2 : \quad \not{\sum_x} f_x = \underbrace{\sum_x f_x \frac{\Delta\mathcal{E}}{\text{Ryd}}}_{=1.145} + \underbrace{\sum_i Q_i N_i}_{=12.856} = 14.01 \; ; \tag{15.3}$$

so the difference cannot be imputed to a missing dipole-allowed excitation.

Strangely, we also include the residual dissociation cross section σ_{rd} as defined in (11.65). It is obtained as the remaining dissociation cross section by subtracting the contribution of predissociation to Cosby's [193] cross section for neutral (i.e. non-ionising) dissociation of nitrogen molecules. This "residual" dissociation cross section, together with all other identified electronic states, is also present in the most recently updated database for N_2 by Kawaguchi *et al.* [482] but our total inelastic CS is systematically lower than theirs (compare - - - with ··· in fig. 16.2–bottom).

Thus, the only possibility is that we underestimate the cross sections from *forbidden* excitations. This is confirmed by looking at figure 16.3, for four excitation CS of optically-forbidden transitions. Most of the databases show higher peaks, whereas we decided not to follow strictly outlying points in our analytical fits on table 11.6.

We also know from our study of transport coefficients at the end of chapter 4 p. 137, that it is our database which is deficient since it overestimates Townsend's ionisation coefficient α_i by over a factor of 2 (fig. 4.17a–right panel), and the mobility coefficient μ_e by roughly 10 %. Thus, we may reasonably suppose that there are some missing resonance peaks of spin-forbidden excitations which could explain the discrepancy with the ionisation coefficient.

Due to the present lack of information and resources, we opted for the method II. consisting in completing from the total sum of inelastic CS of a known and trusted source. Among the databases listed in the next chapter section 16.1, the "`Muroran`" database of Kawaguchi *et al.* [482] showed the greatest diligence in assembling the cross sections. Therefore, we patched our database with the differences observed between our incomplete (dark blue dashed - - -) database and the dark purple short-dotted curve ··· in figure 16.2–bottom. Then, we split the cross section into two regions: one with a loss at 7 eV and the other at 14 eV. The difference between our incomplete and complete sets can be observed on figure 16.2–bottom, where the complete set is superposed with the purple dotted curve (···) of "`Muroran`" from Kawaguchi *et al.* [482].

Concerning rotational losses relevant at low electric fields <1 Td, we constructed the set of rotational cross section for $J_0 \to J'$, using the sudden-impulse approximation (11.24), with the four elementary transitions: $J = 0 \to 0$, $J = 0 \to 2$, $J = 0 \to 4$ and $J = 0 \to 6$ which we digitised from the figures of Kutz and Meyer [546, fig. 7a].

15.1.2 O_2 – updates

Renormalisation

The data from Wakiya [972, 973] and Shyn and Sweeney [845, 847] and Shyn *et al.* [848, 849] were normalised to an elastic cross section that was later found to be in disagreement with more recent and improved experiments [206, 353, 598, 893] as can be seen in figure 15.3. We thus took the initiative of renormalising their data assuming that their DCS overall shape was reasonably correct. Unfortunately, the measurements of Shyn and Sharp [842] showed systematic overestimation at large angles [893, §3:p.4321-2, fig 1&2] and small energies. Brunger and Buckman [124, §3.3.2.2:p.317] believes that this is caused by error contamination of Shyn's measurements at backward angles (> 110°). In addition to this, the data of Shyn and Sharp [842] systematically underestimate DCS at 30 eV in comparison with the data of Sullivan *et al.* [893] and at 200 eV by 30–100 % with those of Daimon *et al.* [206]. This could be due to a bias in the absolute normalisation of the DCS.

The reference data for renormalisation was essentially composed of Linert *et al.* [598] (update of Sullivan *et al.* [893]) at low energies and of Daimon *et al.* [206] at high energies which we extrapolated with our own IAM calculations from the previous part. Currently, there is no other available experimental data from 40–150 eV than that of Shyn and Sharp [842]. Therefore, we have no sound way to assess the accuracy of the DCS and ICS in that range. This discrepancy and uncertainty might somehow affect the inelastic DCS outside of the 10–30 eV range.

The two (original vs. renormalised) are compared in figure 15.3. The data from Shyn and Sharp [842] are all lowered, especially < 10 eV due to spurious backward scattering, whereas Wakiya [972]'s values are all raised in the renormalised version. A dotted line represents the data gathered from other sources [221, 352, 897, 938].

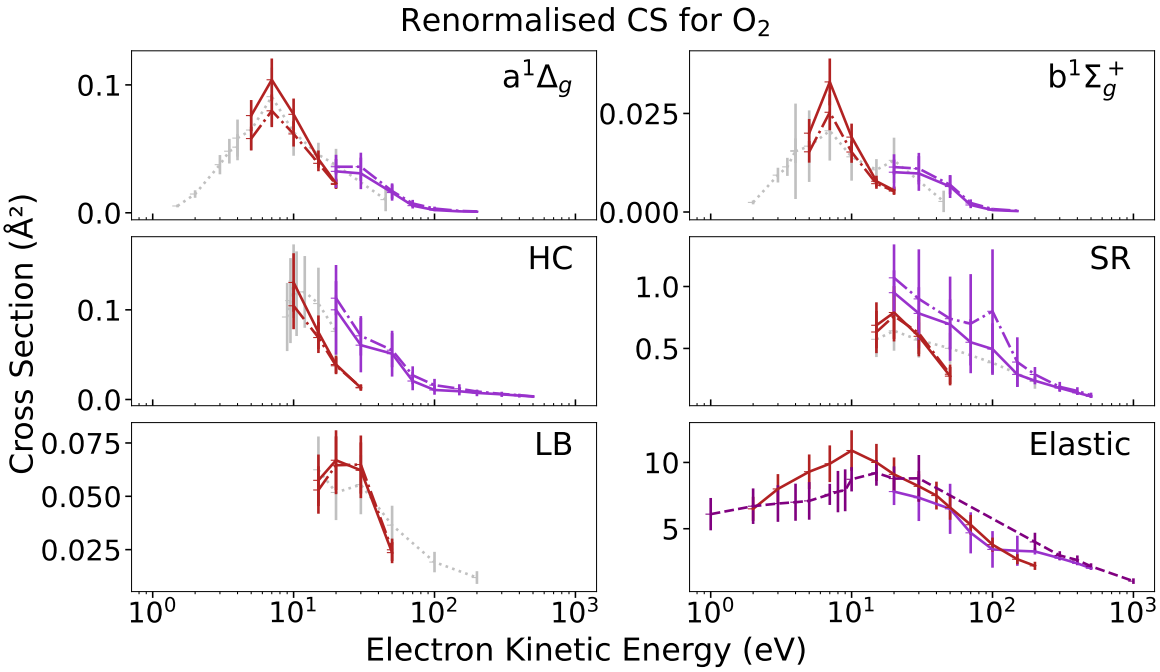

Figure 15.3: Renormalised set of cross sections of Wakiya [972, 973] (in violet) and Shyn and Sweeney [845, 847] and Shyn *et al.* [848, 849] (in red) for electronic excitations of O_2. Solid-dotted (–•–) lines represent renormalised data according to the ratios of the elastic cross sections represented on the bottom right panel. There, the purple dashed (- - -) is our built reference for the integral elastic cross section. Light-grey dotted lines represent data points from other sources in the literature.

Unfortunately, the improvement in experimental concordance with our renormalisation is quite marginal. Wakiya's elastic data was lower than our reference and raising the values actually worsens the trend seen at large energies yielding significant overestimation. A possible cause would be that the inelastic-to-elastic ratios had large uncertainties. A survey of inelastic scattering beyond 50 eV would be desirable in order to check Wakiya [972, 973]'s results. The overlap [599, fig.2] between ground state vibrational levels $v' = 5$ and $a\ ^1\Delta_g$, and $v' = 9$ and $b\ ^1\Sigma_g^+$ could potentially explain a slight overestimation in Wakiya's result below 50 eV but it cannot explain discrepancies above 50 eV, where vibrational losses are typically negligible. Shyn's data are overall brought into better agreement with renormalisation, although the bulk of the data situated in the interval 10–30 eV is luckily in the region where Shyn and Sharp [842]'s elastic CS do not differ much from the reference (cf. fig 15.3 bottom right).

Completion

See the explanation on p.569 about the concept underlying "completion", in particular point I..

If we sum the oscillator strengths from allowed excitations on table 11.7 and from ionisation 11.12, we get:

$$\text{OOS completion for } O_2 : \ \oint\!\!\!\!\!\!\sum_x f_x = \underbrace{\sum_x M_x \frac{\Delta\mathcal{E}}{\text{Ryd}}}_{=0.1232} + \underbrace{\sum_i Q_i N_i}_{=15.7828} = 15.906 < 16 \ . \tag{15.4}$$

Thus, we took $f_o \approx 0.1$ and $\Delta\mathcal{E}_o = 11\,\text{eV}$. The parameters for (11.61a) are fixed by: $M_o = f_o\text{Ryd}/\Delta\mathcal{E}_o$, $C_o = 3$, $b_o = 1 = c_o$. Hence, we do not make any adjustments on C_o, b_o, c_o. The interested user is invited to do so if he/she finds it convenient.

Another aspect, often tacit, is that inelastic cross sections σ_x associated to a given energy threshold $\Delta\mathcal{E}_x$ might not represent accurately the actual inelastic electron energy loss spectrum (EELS) in the gas. This is particularly true for molecules, whose vibronic bands can extend over several eVs and even more for O_2 because of the broad continuous bumps in the EELS forming the Herzberg pseudo-continuum (HC) and Schumann-Runge (SR) continuum spanning altogether from about 4.5 eV up to roughly 9.7 eV. While in the Monte Carlo approach, we are free to sample the actual energy loss from a discrete (vibronic peaks) or continuous (bump) distribution; this is not (usually) the case of kinetic solvers which are based on a single threshold $\Delta\mathcal{E}$. As a result, it is not correct to set the loss in the HC or SR to the threshold value; rather, one should set it to the *average* value $\mathcal{E}_\text{m}$:

$$\mathcal{E}_\text{m} = \frac{\int_{\Delta\mathcal{E}}^{\mathcal{E}_\text{max}} \frac{\text{d}\sigma}{\text{d}\varepsilon}\varepsilon\,\text{d}\varepsilon}{\int_{\Delta\mathcal{E}}^{\mathcal{E}_\text{max}} \frac{\text{d}\sigma}{\text{d}\varepsilon}\,\text{d}\varepsilon}\,, \tag{15.5}$$

where the upper boundary $\mathcal{E}_\text{max}$ is determined from the EELS (sometimes arbitrarily). Thus, as done in the `Phelps` database, we presently set the centroid $\mathcal{E}_\text{m}$ in the Herzberg pseudo-continuum to 6 eV; whereas in the Schumann-Runge continuum, to 8.6 eV (a small part was left at 6.12 eV for the onset of the SR, which, for practical purposes, can be merged into the HC if one wishes).

For rotational cross sections, we could not find any experimental nor theoretical data. Lacking such information, we used the quadrupole and anisotropic polarisation Born approximation in (eq. 11.21b, p. 412), as given in Takayanagi and Itikawa [908, eq.(38)] from Dalgarno and Moffett [208]. Bluntly put, these rotational cross sections are but a "better than nothing" addition. They are expected to be severely inaccurate since rotational scattering off O_2 should be strongly affected by the $O_2^-\ ^2\Pi_g$ resonance.

In order to fit transport parameters in O_2 from Nelson and Davis [691] below 0.1 Td, Alves *et al.* [24] had to use a value (1.4 a.u.) for the permanent quadrupole Q more than four times higher that the actual experimental value ($Q \simeq -0.29$ a.u.). This confirms the invalidity of the quadrupole Born approximation for electron rotational scattering off O_2.

15.1.3 NO – updates

Renormalisation

The elastic cross section used for normalisation [654] was corrected by Brunger *et al.* [120, table 3] before they presented their integrated cross sections (ICS) for electronic excitations. Nevertheless, the value at 50 eV must have been extrapolated because this energy was not measured in Mojarrabi *et al.* [654]. Since the theoretical ICS by Fujimoto and Lee [307, table 1] were all in good agreement with the experimental data at lower energies, Itikawa [441, table 2] recommended to use their results for $\varepsilon \geq 50$ eV. As a result, all values from Brunger *et al.* [120] at 50 eV were presently raised by a factor 7.88/6.444, which, to our relief, improves the agreement of fitted s_{exc} functions at that energy for all cross sections. We interpret this as a clue that the extrapolated [120, table 3] $6.444 \times 10^{-20}\,\text{m}^2$ at 50 eV is underestimated. Sadly, this slight inconsistency was not noticed by any of the most recent reviews [441, 865], we hereby recommend to multiply all the reported ICS at 50 eV by 1.223 for electronic excitations of NO.

Completion

The completion of NO is even more important than for O_2 or N_2. Song *et al.* [865, p.11–2:fig. 13] reports that the sum of all electronic impact excitation CS from Brunger *et al.* [120] is a factor of five below total electronic CS derived from swarm experiments.

This, we confirm from the complementary oscillator strength $f_o = 0.571$ deduced from:

$$\text{OOS completion for NO}: \quad \cancel{\sum_x} f_x = \underbrace{\sum_x M_x \frac{\Delta\mathcal{E}}{\text{Ryd}}}_{=0.2587} + \underbrace{\sum_i Q_i N_i}_{=14.17} = 14.429 < 15\,. \tag{15.6}$$

Due to the low ionisation potential of NO at 9.26 eV, we took $\Delta\mathcal{E}_o = 9\,\text{eV}$ giving thus $M_o = f_o\text{Ryd}/\Delta\mathcal{E}_o \approx 0.8636$ and the remaining parameters are fixed as for O_2 ($C_o = 3$, $b_o = c_o = 1$).

When we include this complementary cross section, our complete set agrees better with the swarm results of Song *et al.* [865, fig. 13] and are about a factor of five higher than our incomplete set as observed from the large difference between the solid and dashed dark blue curves in figure 16.12.

NO has a permanent dipole of $D \approx 0.0625ea_0$ [924]. In the Born approximation, rotational excitation CS for NO may be expressed with (11.21a) [442, eq.(39)]. We used this simple formula to compute a set of $J_0 \to J_0 + 1$ cross sections, up to 20 eV, which are the dominant modes of rotational excitation in NO at low energies. Be wary that these cross sections might be inaccurate in the resonance region between 0.2 eV and 1.5 eV.

15.1.4 Ar – updates

Renormalisation

As with the previous cases, the older data from Chutjian and Cartwright [180] could benefit from renormalisation due to the differences observed between their reference elastic cross section [871] and newer measurements [310, 731]. In his recommendation, Hayashi [388] must have been aware of this because his reported values are much better matched by renormalised data of Chutjian and Cartwright [180]. In his earlier report, Hayashi [387, p.4-5] mentions that he indeed renormalised some of the data with the then recent measurements for elastic scattering with Helium from Register *et al.* [771]. Strangely, Srivastava *et al.*'s measurements were actually normalised on that aforementioned set of Helium data. Perhaps in 2003, another set of reference data was used for renormalisation of subsequent cross section with argon.

Ironically, Srivastava *et al.* [871] in their table IV add a footnote saying that their results from phase-shift analysis are less reliable than from the normalisation, though the former were found in better agreement with all experimental data in those energy ranges [310, p.39-40]. We used the renormalised data based on Furst *et al.* [310] values ≤20 eV and Panajotović *et al.* [731] above, to produce our recommended analytical cross sections. Still today, many sources [313, 319, 383, 491, 1002] do not consider renormalisation when they compare their calculated results. This is probably because no review of argon's CS specifically addressed the daunting task of correctly renormalising DCS and then proceed to integration once more.

Another renormalisation was pointed out in Allan's measurements [14, p.2:bottom right] concerning the most recent data of Khakoo *et al.* [491] for 4*s* excited states at 15 eV only. They say a division by a factor of 1.45 brings Khakoo *et al.*'s results in agreement with their absolute DCS at 135°. We checked that Khakoo *et al.* [491] DCS at 15 eV indeed show an awkward lump for all four 4*s* states that is not attributable to a resonance but to the normalisation used. We then used the 1/1.45 reduction for those data (at 15 eV only) in our collected database.

Another important deduction is that the units of DCS at 30 eV in table IV of Chutjian and Cartwright [180] were manifestly mistyped to an order of magnitude larger:

20		30		50	
5 (10^{-19})	6 (10^{-19})	5 (10^{-19}) -20	6 (10^{-19}) -20	5 (10^{-20})	6 (10^{-20})
5.20	1.01	39.0	69.0	8.40	110
2.95	0.780	29.5	43.5	4.82	44.5

This caused Puech and Torchin [760]'s database on LXCat to grow two jolly bumps (cf. figure 13.11 behind) to try to match the erroneous data for $4p[1/2]_1$ and $4p[5/2]_3$ that was fitted in Bretagne *et al.* [106, p.766:table 2].

We surmise that there are two other typographical errors in Chutjian and Cartwright [180]: for the magnitude of level '3' ($^3P_0$) in table III at 100 eV which should be 10^{-22} and level '21' ($(4d')[5/2]2°$) in table IX at 100 eV which should be 10^{-21}. This gives indeed a very good agreement both with the theoretical $1/\varepsilon$ decrease for forbidden transitions but also with Khakoo *et al.* [491] and Chilton and Lin [176] respectively. The first typo could not be identified in Hayashi [388] because no suitable comparison was available at that time.

At the time in 1986, the availability of other databases was scarce and even a typo of an order of magnitude can pass through examination if no comparison can evince the queerness. I used this example in chapter 13 section 13.3 to stress the importance of inspecting thoroughly given information.

Completion

See the explanation on p.573 about the concept underlying "completion", in particular point I..

In case of argon, completion was not obtained through the complementary to the sum of oscillator strengths (OOS). This is because there is almost $f_o = 1$ missing to complete the sum (15.2), which is an implausibly large portion:

$$\text{Missing OOS in Ar}: \quad \not\sum_x f_x = \underbrace{\sum_x M_x \frac{\Delta\mathcal{E}}{\text{Ryd}}}_{=0.505} + \underbrace{\sum_i Q_i N_i}_{=16.532} = 17.037 < 18\,. \tag{15.7}$$

Furthermore, as we commented in chapter 12 p.509, the RBEQ* model to ionisation could be improved by specifying each particular channel leading to partial ionisation from the $3p$ orbital. Then, the integration of oscillator strength densities from the ionisation continuum could become higher than the actual value (16.53) which corresponds to the minimum reported in Berkowitz [62, p.84:table 3]. We also note that the current Bethe parameter from the RBEQ* fit ($M_{\text{i},Q} = 2.662 < M_\text{i} \simeq 3.52$) is significantly below its reported value M_i. We therefore think that a great portion of the missing (complementary) oscillator strength in Ar is imputable to an imprecise modelling of losses in the ionisation continuum.

In lieu of completion, the complementary oscillator strength in the complete database is obtained from the sum of OOS of allowed excitations to higher states than to $5s$ orbitals (e.g. $4d$, $6s$, etc.) as collected by Gargioni and Grosswendt [319, p.477:table XI].

$$\text{Complementary OOS in Ar}: \quad \sum_{x>5s} f_x = 0.293 = f_o\,. \tag{15.8}$$

These are supposed to encompass loss from 14.7 eV up to the ionisation threshold (15.76 eV). We therefore set $\Delta\mathcal{E}_o = 15$ eV giving $M_o = 0.2678$.

Besides the inclusion of f_o, the complete database for argon is also a finer database in the sense that the excitations to $4p$, $3d$ and $5s$ orbitals are fitted individually, whereas in the "incomplete" database they are grouped together in a singly fitted CS as represented by the gray-shaded lines on table 11.9. Those differences can be observed on the four graphs of figure 16.17, where a true sum of CS ("complete" —) is compared to an overall fit ("incomplete" - - -).

15.1.5 O – updates

Renormalisation

The data of Kanik *et al.* [476] were normalised at each angle and energy based on summed DCS Johnson and Kanik [460] for molecular oxygen, which themselves were normalised based on inelastic excitations of He and Ne. A more recent survey from Suzuki *et al.* [897] probed the same excitation DCS (for O_2) but normalised to the elastic DCS of He. Both sets agree within their uncertainties except at 100 eV where Suzuki *et al.* [897] are systematically a factor of $\simeq 1.25$ higher. Thus, we decided to multiply all values from Johnson and Kanik [460] and Kanik *et al.* [476] by 1.25 at 100 eV. This correction systematically improves agreement with Vaughan and Doering [959, 960]'s measurements.

Completion

See the explanation on p.569 about the concept underlying "completion", in particular point I..

As for molecular oxygen, the set for atomic oxygen was complete with the complementary oscillator strength:

$$\text{OOS completion for O}: \quad \cancel{\sum_x} f_x = \underbrace{\sum_x M_x \frac{\Delta\mathcal{E}}{\text{Ryd}}}_{=0.3} + \underbrace{\sum_i Q_i N_i}_{=7.4526} = 17.037 < 8\,, \tag{15.9}$$

giving $f_o = 0.247$. We chose the threshold of 13 eV below ionisation, and thus $M_o = 0.2585$.

Many of these complementary states are auto-ionising and we could have chosen a higher threshold. Nevertheless, when we fitted the RBEQ* on p.488, we only included known (i.e. fitted) auto-ionising states: $3s''\,{}^3P^o$, $2s2p^5\,{}^3P^o$, and $4d'\,{}^3P^o$. Therefore, it is not very clear which auto-ionising states form part of the RBEQ* and which not.

15.1.6 N – updates

Renormalisation

There are not many data about atomic nitrogen, so the discussion about renormalisation is limited. We only detected one potential systematic bias in the data of Doering and Goembel [222, 223] at 30 eV which was normalised to Chutjian and Cartwright [180, table III] excitation to $(4s')[1/2]_1^o$ of Argon, lying about ~1.45 below the more recent Khakoo *et al.* [491, figure 6(d)] and most of the theoretical curves. We multiplied thus Doering and Goembel [222] data at 30 eV by 1.45. Raising this outlying point on Wang *et al.* [975, figure 4-mid] improves the agreement with the most recent theoretical calculations.

Measurements at higher energies were based on the well established values for Helium ${}^1S_0 \rightarrow {}^1P$ from Register *et al.* [771], and we could not find any relevant correction applying there.

Completion

The sum rule (15.2) may be applied to any electronically inelastic excitation, including ionisation. In case of atomic nitrogen, we decided to apply the sum rule for completion on the Q parameter of the RBEQ* model instead of fitting it to ionisation CS as was done for the other targets.

This is because, as Kim and Desclaux [506, §III.B] explain, in the experiments of Brook *et al.* [117], the ionisation CS for atomic nitrogen were performed on a mixture including the lowest metastable state $^2D^o$. Thus, if one wishes to derive the ionisation CS for the ground $^4S^o$ state, one needs to adjust also the proportion of the metastable state.

Since we did not wish to make such speculations, we used the known oscillator strengths for electronic excitations from Goldbach *et al.* [338] that pertain to the $\mathrm{N} \to \mathrm{N}^+(^3P)$ channel:

$$\text{OOS completion for N} : f(\mathrm{N} \to \mathrm{N}^+(^3P)) = 1.8 - 0.373 = 1.427 \,,$$

and ionisation from the $2s$ orbital:

$$\text{OOS completion for N} : f(\mathrm{N} \to \mathrm{N}^+(2s\,2p^3) = 2 - 0.085 = 1.915 \,,$$

From there, the $Q = N_\mathrm{i}/N$ parameter of the RBEQ* was derived straightforwardly (see explanatory paragraph on page 490).

15.2 Instructions for use

There are essentially two perspectives in which we anticipate our database can be used:

1. Opaque : As input data to electron swarm calculations at moderate to high electric fields.
2. Transparent : As a basis data for future investigation on electron-molecule interaction.

These objectives reflect those of part I and part II of the thesis.

15.2.1 Opaque : pragmatic

If you are looking for raw numerical data of cross sections to be plugged into a kinetic solver or a basic Monte Carlo code, we provide a file available on:

`https://doi.org/10.5281/zenodo.8192503`

which respects the input format of the standard two-term solver BOLSIG+. We advise the users to use a log-log interpolation of the energy and cross sections as explained on p.111, particularly at high energies.

Elastic differential cross sections (DCS) are to be found in separate folders (one per target molecule) at:

`https://doi.org/10.5281/zenodo.8190461`

which also includes our own reading module written in Python for parsing cross sections and differential cross sections in various formats. The interpolation of DCS can in principle be bilinear, nonetheless, we prefer the following scheme:

$$\frac{\mathrm{d}\sigma}{\mathrm{d}\Omega}(\theta) = \frac{(S[i,j](x-x[i+1])(y-y[j+1]) + S[i+1,j+1](x-x[i])(y-y[i]))}{(x[i+1]-x[i])(y[j+1]-y[j])} - \frac{(S[i+1,j](x-x[i])(y-y[j+1]) + S[i,j+1](x-x[i+1])(y-y[j]))}{(x[i+1]-x[i])(y[j+1]-y[j])} ;$$

$$\text{with} \begin{cases} S[i,j] = \dfrac{\mathrm{d}\sigma}{\mathrm{d}\Omega}(\varepsilon[i], \theta[j]) , \\ x[i] = \log(\varepsilon[i]) , \\ y[j] = \sin\dfrac{\theta[j]}{2} , \end{cases}$$

which is a bilinear interpolation in transformed spaces of the electron energy (logarithmic) and scattering angle (sine).

A more robust reader also written in Python, but only for integral cross sections, is included in the package `bolos` (`https://github.com/aluque/bolos`) authored by Alejandro Luque, the director of this thesis.

We list below some important points:

Extrapolation: Cross sections of inelastic processes are typically tabulated up to 1 keV. For extrapolation, you will have to use the analytical formulae given in chapter 11.

Scattering: Electron scattering beyond 10 keV can be safely sampled analytically from the inverse of a single screened Rutherford expression (3.11) on page 94 using the average decay radius $\bar{a}$ tabulated in table 11.4 on page 405.

Rotational Excitations: A common issue for molecules, is to distinguish purely elastic (non-rotational) losses from rotational excitations. The sum total cross section of rotational excitations $J_0 \to J$ varies with the temperature of the gas, because the proportion population of initial rotational states at J_0 changes according to the Boltzmann distribution (see appendix B.2 in part I). The problem is that "elastic" momentum-transfer cross sections are determined experimentally at a given temperature and comprise actually both elastic and rotational losses. They are more formally called "vibrationally elastic" cross sections.

In solvers like BOLSIG+, if you give as input both state-to-state rotational excitations and the elastic momentum-transfer cross section σ_m, there will be a discrepancy because momentum losses will be overestimated due to being counted twice. The solution is to provide an "effective" momentum-transfer cross section which is the sum of σ_m and all inelastic CS. Then, at each gas temperature, the rotational cross sections will be subtracted from the "effective" CS and the remaining CS will determine the momentum-losses which are purely due to elastic scattering.

Thus, for each molecule, we provide an "effective" momentum-transfer cross section that should be used in BOLSIG+. The elastic σ_m is given but in comments.

Resonances: In very narrow resonant scattering, the duration of the collision may have a visible impact on the transport parameters. This is why accurate vibrational cross sections do not entail accurate modelling of electron transport if this "temporal period of attachment" is not considered. We did not investigate this effect in this thesis, but we surmise it should be important in O_2 and NO but negligible in N_2.

In that case, paradoxically, you might wish to use less accurate cross sections that have been adjusted to transport parameters for your needs. Ours have not been adjusted.

Inelastic Losses: The exact position of the energy thresholds for electronic excitations is relatively unimportant compared to the magnitude of the cross section. This is because losses are actually distributions over a discrete band of vibronic states or over a continuum as in molecular oxygen. Ionisation losses are typically underestimated as well, because partial ionisation to excited ionic states may be significantly above the ionisation threshold, albeit the cross section is also much smaller than ionisation to the ground ionic state.

If you are unsatisfied with the accuracy of the cross section database, consider first adjusting the energy threshold of each electronic excitation to the centroid of the vibronic band or continuum.

We did this already for molecular oxygen which makes a significant difference when setting the loss in the Herzberg pseudo-continuum at 6 eV (true threshold is around 4.5 eV) and the Schumann-Runge continuum at 8.1 eV (threshold would be below 7 eV).

In short: tweak the energy loss, not the cross section magnitude.

Atomic oxygen: Oxygen's ground state is split in fine-structure spectroscopy into three very low-lying states: $^3P_2$, $^3P_1$ and $^3P_0$ (separated by some ~20 meV). This is above but still comparable to gaps between rotational states of diatomic molecules. Since oxygen in atomic form appears in gases at high temperatures, oxygen atoms in plasmas must be distributed over their fine-structure states.

From a purely computational perspective, these states may be treated in a kinetic solver just as rotational excitations of molecules, so that their abundance ratio be adjusted according to the temperature. In our database, they are labelled as "ROTATION" (obviously they are electronic excitations). Thus, please do not let yourself be surprised when you check the list of collision types for atomic oxygen.

15.2.2 Transparent : scientific

If you are interested in our cross sections for scientific investigation, in order to improve their accuracy, we recommend you to download the `elmolcs` package on CodeBerg*:

`https://codeberg.org/aschmalz/elmolcs.git`

or the frozen version hosted on a DOI server: `https://doi.org/10.5281/zenodo.8190461`.

With the reader module that we provided, use the routines `loadCS` and `loadDCS` for loading cross section (CS) and differential cross section (DCS) databases respectively.

To load our CS database, use:

```
>>> cs = loadCS('N2','iaa*')
```

and replace `'N2'` by O2, NO, Ar, O or N for other targets. This will load all the analytical fits to electronic excitations and the RBEQ* model for impact ionisation from the `cscoll` module. The `cs` object is a dictionary of cross sections classified according to their collision type:

- `'TOTAL'` : total scattering (integral)
- `'ELASTIC'` : integral and momentum-transfer
- `'EXCITATION'` : only electronic and dissociation

*CodeBerg is an open-source platform for hosting projects, not owned by a private organisation. Feel free to visit it at `https://docs.codeberg.org/getting-started/what-is-codeberg/`

- `'VIBRATIONAL'` : only $v = 0 \rightarrow v' < 4$ transitions
- `'ROTATIONAL'` : elementary $J_0 = 0 \rightarrow J'$ transitions
- `'ATTACHMENT'` : only dissociative attachment
- `'IONIZATION'` : total impact ionisation

To save space, we did not include two copies of our full set of numerical cross sections. For rotational and vibrational cross sections, this means that if you want access to the full numerical values of the CS, you should load:

```
>>> cs = loadCS('N2','iaa')
```

which loads CS from the file presented in the previous section 15.2.1. This is because:

i) Rotational CS are constructed from elementary transitions ($J_0 = 0 \rightarrow J'$) using the sudden-impulse approximation (sec.11.2.2).

ii) Vibrational CS are constructed from the theoretical calculations of Laporta *et al.* [552, 553] which are stored in voluminous files describing rovibrational transitions $J_0, v_0 \rightarrow J', v'$. We decided not to include those files nor the routines to read and process them.

In addition to our database, we provide all the resources from other databases and experiments that we used in our investigation. To load them, replace the `'iaa*'` argument above by any of:

Databases hosted on LXCat

- `'phelps'` : Phelps' database
- `'biagi'` : Biagi's database
- `'ist'` : IST-Lisbon [22]
- `'itikawa'` : Itikawa's reviews (only molecules)
- `'hayashi'` : Hayashi database (only Ar and NO)
- `'flinders'` : Flinders database (only molecules)
- `'bsr'` : BSR database [1000] (only atoms)
- `'muroran'` : from Kawaguchi *et al.* [482] (N_2 only)

Collected experimental data

- `'total'` : Total scattering and ionisation CS
- `'elastic'` : Elastic integral and momentum-transfer CS
- `'excitation'` : Electronic excitations mostly
- `'vib'` : vibrational excitations for O_2 only
- `'rotational'` : Theoretical rotational excitations for N_2 only

If you wish to compare and handle a large database of cross sections together, you can use the `CS_Data` object in the following way:

```
>>> csdata = CS_Data()
>>> csdata.add_database('O2','total')
>>> csdata.add_database('Ar',['hayashi','excitation'])
>>> csdata.add_database(['N2','NO'],'itikawa')
>>> selection,errors = csdata.select(['N2','O2'],['itikawa','Szmytkowski'])
```

This will output two `DataFrame` objects from the `pandas` package, one for the values of the cross sections for the selected criteria (target, source), and the associated uncertainties. All our plots for cross sections were generated using this selection routine.

For differential cross sections, call the routine:

```
>>> dcs,_ = loadDCS('N2','iaa')
```

This will load a `DCS_Data` object in the `dcs` variable of elastic scattering from our database.

As for integral CS, we also made an extensive tabulation of experimental DCS for elastic and inelastic scattering. To access them, call:

```
>>> elast,inel = loadDCS('N2','exp')
```

Elastic DCS (`elast`) are distinguished from all inelastic processes stored in a dictionary of `DCS_Data` objects (`inel`) mapped by keys of the final excitation state of the process. All our DCS were plotted using the `DCS_Data` objects, which stores two `DataFrames`:

```
>>> dcs = elast.data
>>> err = elast.error
```

representing the DCS values and uncertainties respectively on an angle-by-energy array (angles on rows, energies on columns).

Minimal bibliographic information accompanies the data loaded by our routines. If you want to retrieve the original articles, you may either: (1) search for the article (and its DOI link) in the `references.bib` file provided (using a reference management program) or (2) peek into the source files classified in the `Data` folder according to the gas target.

The files are relatively easy to read and contain headers with full bibliographic information and DOI links to the articles. There, you will also find more detailed comments about how cross sections were adapted from experimental data in a given energy range.

If our database receives positive and enthusiastic feedback, we hope to be able to incorporate it to the LXCat server.

Chapter 16

Comparison with Previous Databases

> *"The manipulation of cross-section sets weakens the predictive power of the simulation technique because of its arbitrary nature."*
>
> — *Blevin&co-workers as reported by* Brunger & Teubner*, 1990, Phys Rev A:41-1425*

In the previous chapter we introduced our database of cross sections, overviewed how it has been constructed and gave instructions on how to use it. Here, we are only interested in comparing databases, the creation of which requires a tremendous amount of effort. We make two types of comparisons:

- Direct comparison of cross sections with selected experimental measurements based on our own judgement.
- Comparison of electron transport parameters calculated by the two-term Boltzmann kinetic solver BOLSIG+ [378] which we introduced in part I section 4.3.2 on page 4.3.2.

We do not compare differential cross sections (DCS) because currently, there does exist any proper database of DCS. At best, there are collections of experimental and theoretical data, but no attempt to make a full description of scattering throughout a large scale of electron energies. The consistent modelling of DCS in Monte Carlo simulations is left to the discretion of each author. Instead, in the next chapter 14, we dress a catalogue of analytical DCS expressions based on the first Born approximation to model elastic scattering at high energies.

Most databases presented are hosted by the outstandingly useful LXCat server [732]. Nevertheless, its main focus is for *kinetic solvers* rather than Monte Carlo simulations. As a result, we believe that addition of other databases might significantly enhance the scope of the LXCat project.

A noteworthy example is the cross section set proposed by Kawaguchi *et al.* [482] which we refer to as the `Muroran`* database. Its wealthy collection of references prompted us to conduct our own independent assemblage of cross sections (from primary sources), which we described in chapter 11, only to be compared in the forthcoming sections.

Separate from and complementary to the LXCat server is the (Japanese) National Institute for Fusion Science: NIFS [682] which compiles a very wide set of measurements, calculations and evaluations of cross sections for atoms (AMDIS) and molecules (AMOL). The NIFS also hosts the most complete compilation work of collision cross sections between electrons and atoms or molecules which was conducted by Hayashi at the beginning on the new century. This colossal work regroups all the bibliographic references for 17 atoms and 51 molecules from 1906, i.e. since the discovery of the electron, to the beginning of the 21st century. Those reports are available

*It is an unofficial name, we call it thus because the authors are all affiliated to the Muroran institute of technology.

at `http://dpc.nifs.ac.jp/hayashi/`. Furthermore, Hayashi also prepared some recommended sets of cross sections [387] for noble gases, four diatomic molecules and CO_2 readily available as input into Boltzmann solvers or Monte-Carlo codes. Some of them are available on LXCat, whereas others are hosted by the Institute of Electrical Engineers of Japan and are available to download at `http://dpc.nifs.ac.jp/DB/IEEJ/`. Some recommendations have been updated since then.

The rest of this chapter is structured in six sections dedicated to the six atmospheric gas species studied. Comparisons of cross sections and transport parameters are preceded by an introduction and overview of the selected databases.

16.1 N_2

As the most prominent diatomic molecule in atmospheric physics, the database for nitrogen is lush and numerous reviews were published especially in the early 2000. A compilation of cross sections was released as early as 1966 by Takayanagi and Takahashi as cited in Itikawa's 1986 seminal review [436].

Today, a vast number of databases are available on LXCat. They are, however, not all independent works and a certain lineage can be established by looking at table 16.1. We offer a short description of each database below.

`Phelps` The most ancestral database (on LXCat) is the one from Phelps and Pitchford [749] and retranscribed from the JILA report [750]. Some databases (not shown) are direct copies of this data. The CS were adapted from available experimental and theoretical results in order to bring the transport coefficients of the two-term Boltzmann kinetic approach into agreement with experimental data. At low energies $< 7\,\text{eV}$, (elastic) momentum-transfer cross sections are derived from swarm experiments [266]. At higher energies, elastic scattering is derived from integrated DCS of beam experiments. They also derive the integral elastic CS and the average deviation cosine (11.12). Rotational excitations are modelled according to the single-level approximation described in the appendix of Hake and Phelps [381]. Vibrational and electronic excitations from a variety of sources [159, 740, 819] were adjusted so as to yield reaction coefficients in agreement with experimental results.

`IST-Lisbon` We could say that the direct successor of `Phelps` database is the `IST-Lisbon` database whose main differences are (i) interpolation on a finer grid of values, (ii) update of the ionisation cross section with partial ionisation cross section from Isola *et al.* [433] and (iii) extension with a rotational set of quadrupole transition ($\Delta J = 2$) cross sections from Gerjuoy and Stein [323].

`Biagi` This is the most obscure database as it is the least documented of all. There is no publication associated to it and no reference specific to any of the processes included. Its origin comes from the Fortran program of Stephen Biagi [71] called MAGBOLTZ hosted by the CERN. Most probably, it is based on the `Phelps` database, albeit with notable differences.

`Itikawa` Very well documented in Itikawa *et al.* [436] and Itikawa [439] and mostly based on the massive compilation of cross sections in 2003 [434] where Itikawa was the editor. This is the only database on LXCat which has not been adjusted in order to yield good results for the transport parameters calculated by a two-term Boltzmann kinetic solver. When using

with BOLSIG+, one needs to ensure to subtract predissociation from the total dissociation cross section.

`Flinders` Comprises only vibrational and electronic excitations as measured by the research group in Flinders' University Campbell *et al.* [141, 142]

`Tabata` Analytical fits by Tabata *et al.* [902], to experimental data mainly from the reviews of Itikawa *et al.* [436] and Majeed and Strickland [620] and the data from Campbell *et al.* [141] as in the `Flinders` database.

`Laporta` Vibrational cross sections exclusively from the N_2^- ($X\,^2\Pi_g$) resonant state using accurate local-complex-potential calculations as published in Laporta *et al.* [554].

`Muroran` Most recently published database in Kawaguchi *et al.* [482] which proposes new fits to the latest experimental studies [463, 622, 624]. It incorporates the calculations of Laporta *et al.* [554] as well.

We owe the authors of this publication the discovery of the most recent references relevant to the cross sections with nitrogen molecules. Our work brings an update to their contribution.

To-date, the databases which give swarm transport parameters most in accord with experimental measurements are the `IST-Lisbon` from Loureiro and Ferreira [609] and the `Muroran` from Kawaguchi *et al.* [482]. The comparison was done in part I, section 4.3.3. It is therefore, very instructive, albeit exhausting, to compare how cross sections sets may differ yet give similar transport parameters when used in a two-term Boltzmann kinetic solver (see p. 81 and sec. 4.3.2).

Comparisons

Using the renormalised data when applicable (all preceded by an asterisk when labelled in legends as : " *Zubek "), we now display comparisons of cross section sets against experimental measurements. At the very end, in figure 16.5, we compare the transport coefficients obtained for each (complete) database when used by the two-term kinetic solver BOLSIG+ [378].

Elastic CS fig. 16.1

1. At very low energies < 0.1 eV, we both need to improve the momentum-transfer cross section given from the MERT method (see sec.10.1.5) and use swarm-derived measurements such as Haddad [374].

2. In the $N_2^-\ ^2\Pi_g$ resonance region ($2\,\text{eV} < \varepsilon < 4\,\text{eV}$), the "`Muroran`" momentum-transfer CS has been scaled upward [482, p.4] so as to closely match the electron-drift experimental measurements in the 1–100 Td region.

3. At intermediate energies above the $N_2^-\ ^2\Pi_g$ resonance region ($4\,\text{eV} < \varepsilon < 15\,\text{eV}$), there are two classes of measurements, those of Shyn and Carignan [838] and Srivastava *et al.* [870] of higher momentum-transfer and the more recent from Linert and Zubek [600] about 10–20 % lower. The databases tend to either follow one set or the other with a crossing point at 15 eV where the trends revert (overestimate ⇌ underestimate).

Table 16.1: Databases of electron collision cross sections with molecular nitrogen. First half represents the ones hosted on LXCat, the second half are incomplete or separate databases. Names in quotes are unofficial denominations. In the columns we regroup the references to the experimental data upon which the database are constructed. If it exists, the reference to the publication which describes each database is under the column "Origin".

Database	Year	Origin	Total	Elastic	Vibrational	Electronic	Ionisation
IAA (Present)	2023	11	[124, 317, 488, 512, 699, 894, 900]	[344, 600, 684, 700, 832, 863, 894]	[554, 600, 863, 910]	[123, 407, 463, 622, 624, 1012]	[768, 831, 888]
Phelps	1985	[749]	[266]	[113, 288, 453, 838, 870]	[819]	[159, 1011]	[768, 814]
Itikawa	2006	[436, 439]	[478, 488, 699, 894]	[105, 232, 832, 838, 863, 870, 894]	[105, 863, 894, 910]	[123, 141, 289, 333, 633, 757, 941, 1013]	[768, 888]
Biagi	2012						
IST-Lisbon	2014	[22]	[749]		[609, 819]	[159, 1011]	[433, 768]
Flinders	2001-4				[142]	[141]	
"Tabata"	2006	[902]	[105, 316, 405, 699, 705]	[105, 436, 832]	[436]	[9, 123, 159, 289, 452, 1012]	[768, 888, 932]
Laporta	2014	[554]					
"Muroran"	2021	[482]	[512]	[232, 600, 684, 838, 863, 870, 894]	[554, 600, 863, 910]	[141, 407, 463, 622, 624]	[888]

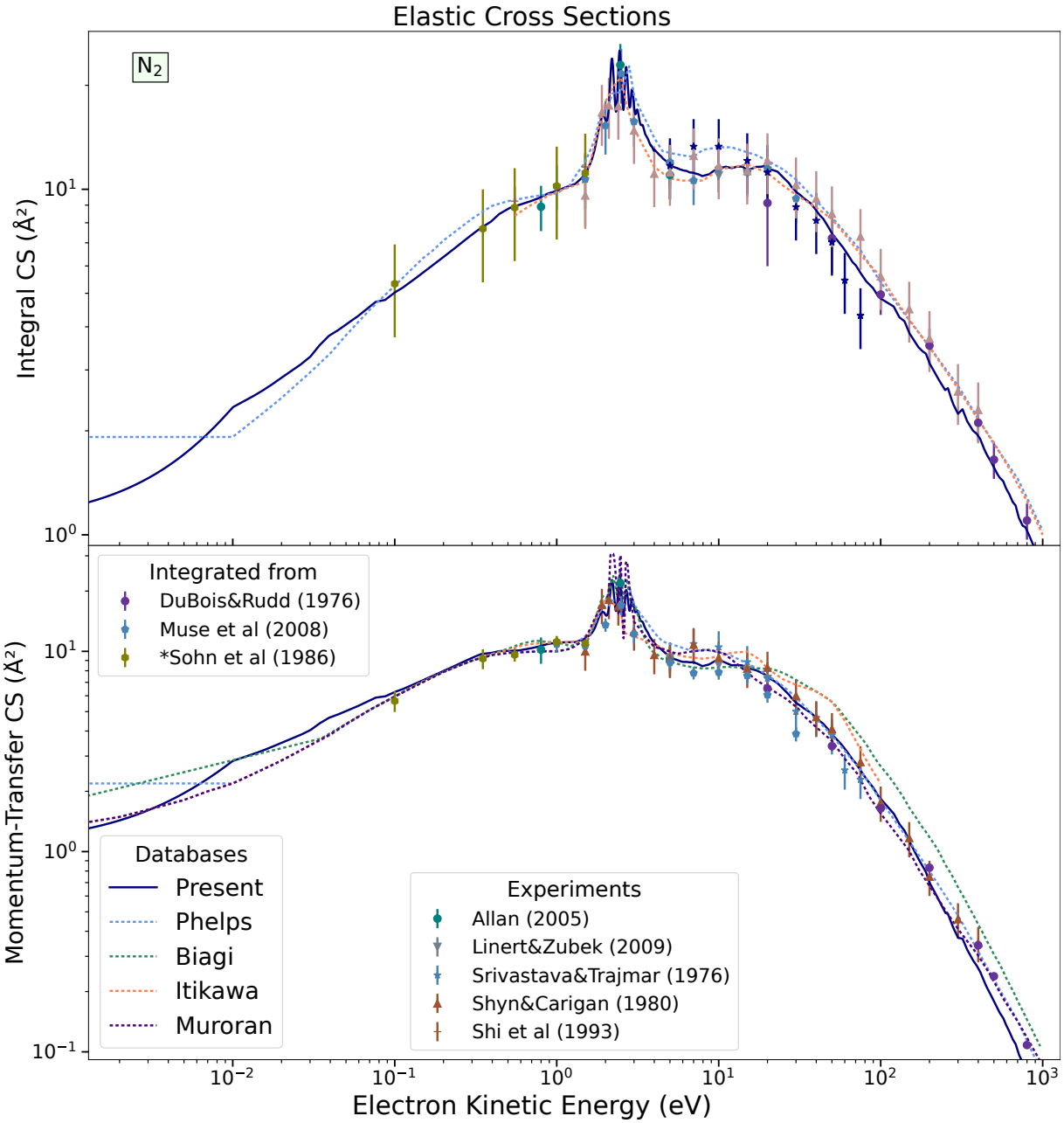

Figure 16.1: Comparison of elastic integral and momentum-transfer cross sections for molecular nitrogen.

Inelastic CS fig. 16.2

- Vibrational CS : $\sum_{v'} \sigma_{v=0\to v'}$

  1. First resonance $^2\Pi_g$ 2–4 eV: similar for all databases except Itikawa [439], who purposefully recommended only the $v = 0 \to 1$ transition, since updated experimental data for all other transitions is missing.
  2. Second resonance $^2\Sigma_u^+$ ~23 eV [600, p.6] (broad shape resonance): two sets of measurements, the former from Tanaka *et al.* [910] and more recent from Linert and Zubek [600], explain the difference between our and other databases.
  3. Outside resonances: databases manage the CS differently. Some use linear-linear interpolation which creates the skipping aspect of the pink ··· and green ··· dotted curves on figure 16.2-top; when a database uses linear interpolation instead of logarithmic (power-law) interpolation to between sparse data points.

- Electronic CS : $\sum_{a'} \sigma_{0\to a'}$

  △ Resonance peaks of spin-forbidden transitions < 12 eV : most databases have higher peaks near threshold, in particular `Flinders` and `Itikawa` (orange ··· and beige ··· dotted curves on fig 16.2-bottom) because they follow Campbell *et al.*'s [145] measurements as seen on the individual electronic CS in figure 16.3.

  △ Missing tail : at energies above 30 eV our incomplete cross sections (- - -) are systematically below the others. We did include the residual dissociation CS σ_{rd} obtained from eq. (11.65); i.e. fitted to the data of Cosby [193] after subtracting all contributions from predissociation (see p. 445). Notwithstanding, the uncertainty on the total dissociation into neutral products is large as seen from the error bars on fig. 16.2-bottom. Also, our incomplete (- - -) CS intersects with the total dissociation CS at the last measurement at 200 eV, which should not be the case since some excitations do not lead to dissociation.

  This missing tail is the reason why we decided to patch our database with the remaining difference to "`Muroran`" curve (purple dotted ···) from Kawaguchi *et al.* [482].

Electronic CS fig. 16.3

1. In general, the measurements of Campbell *et al.* [145] (comprised in the `Flinders` database) tend toward indicating the presence of tall peaks of dipole- and spin-forbidden transitions near threshold. Most databases try to follow those peaks, except ours which used resonance profiles only for well-resolved measurements as, for example, from Zubek [1012] for the C $^3\Pi_u$ state (fig. 13.8).

2. The high-energy decaying tail is not well constrained in any of the databases, except in ours (from the imposed integer d in (11.61) determining the $\sim 1/\varepsilon^d$ decay) and in `Muroran` [482]. This has however no observable effect on the swarm transport coefficients.

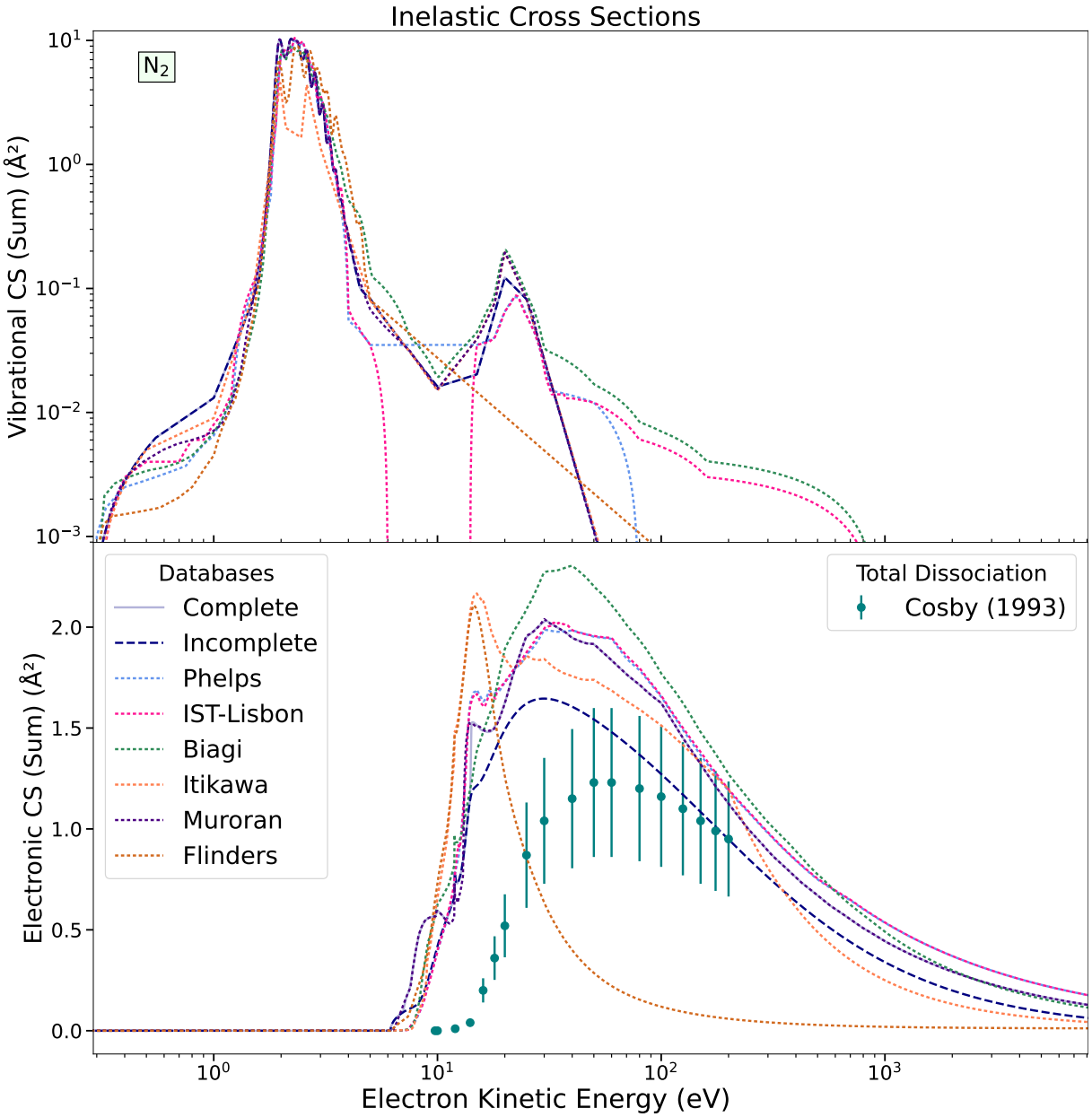

Figure 16.2: Comparison of the sum of vibrational and electronic impact excitation cross sections for molecular nitrogen. The "Complete" curve is superposed with the dotted purple curve labelled "Muroran".

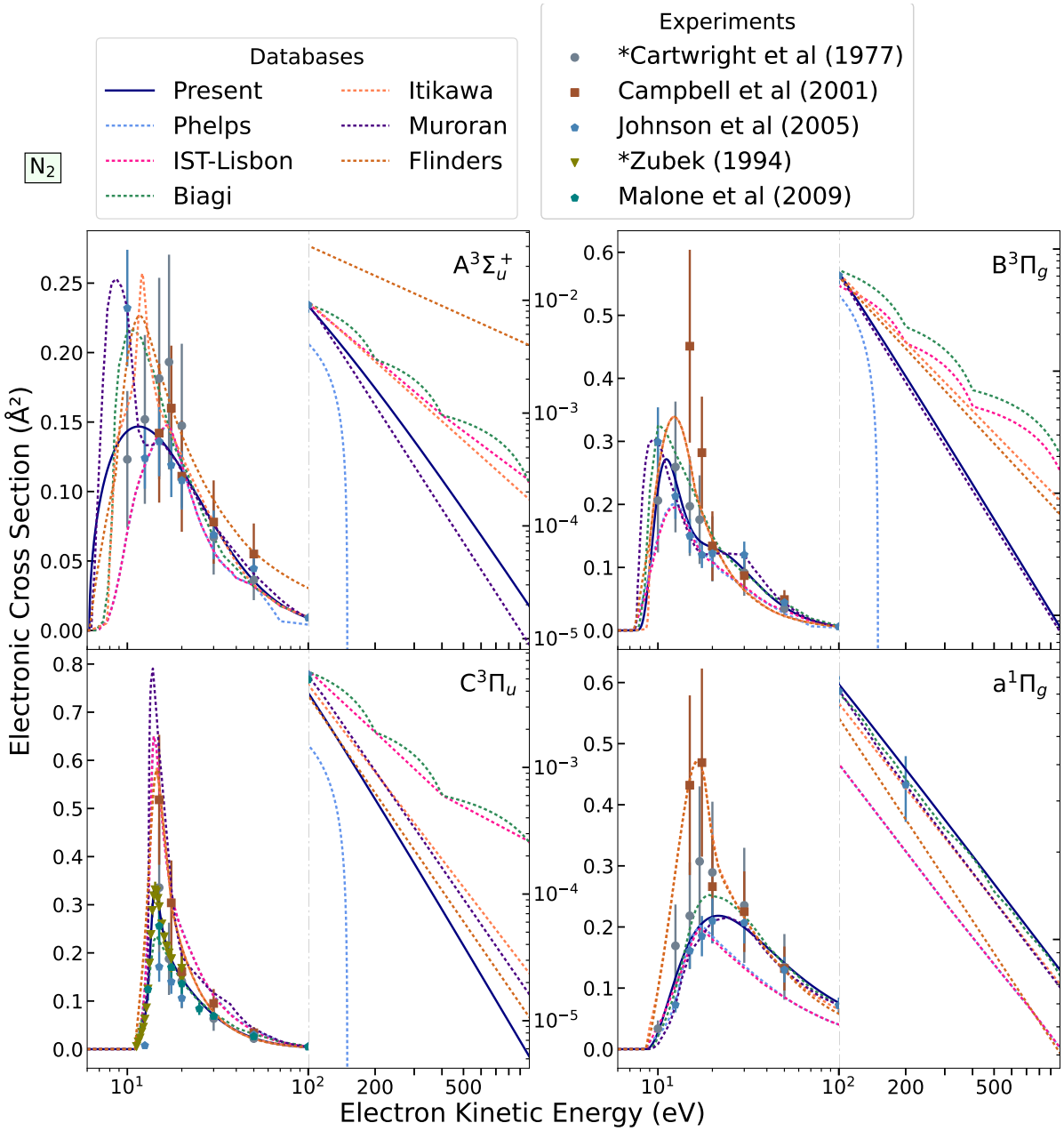

Figure 16.3: Comparison of selected electronic impact excitation cross sections for molecular nitrogen.

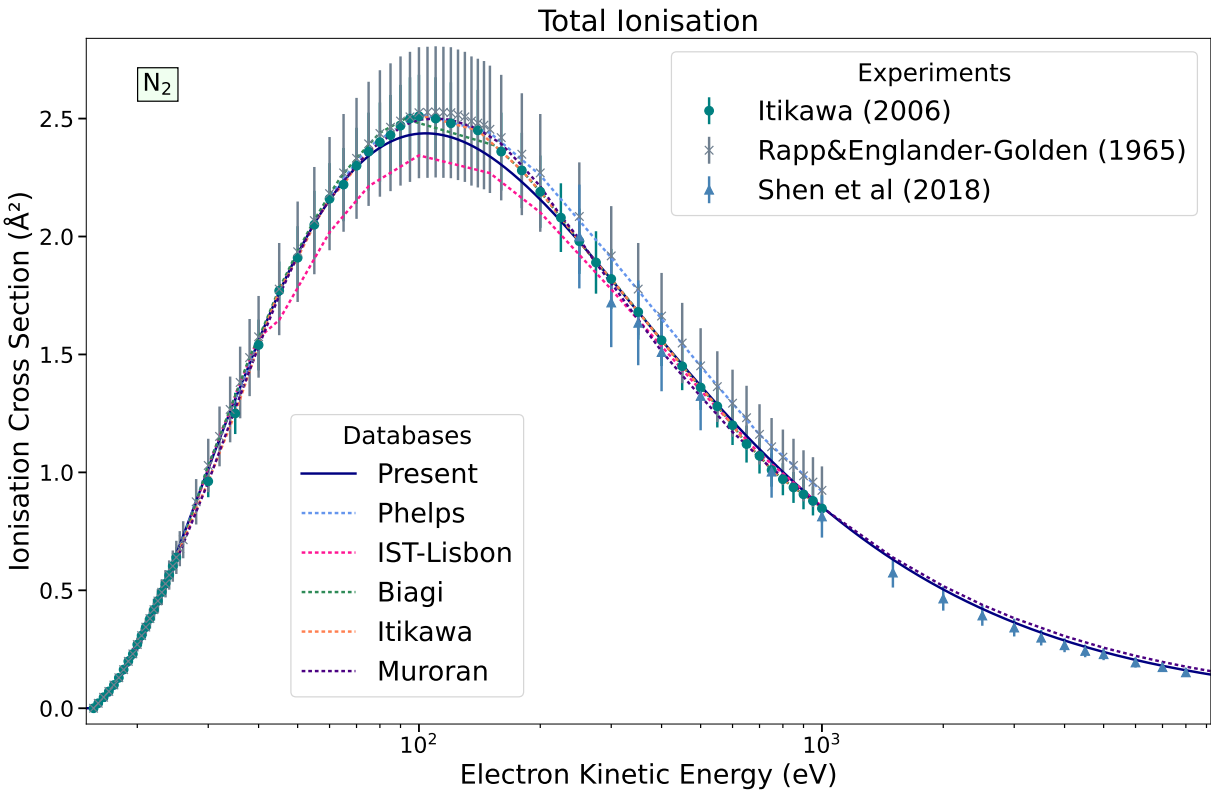

Figure 16.4: Comparison of impact ionisation cross sections for molecular nitrogen.

Ionisation CS fig. 16.4

- All databases follow the measurements of Rapp and Englander-Golden [768] below 50 eV and the values of Straub *et al.* [888] (renormalised in Lindsay and Mangan [596]) at higher energies.
- Our analytical RBEQ* fit misses about ~3 % on the peak.
- The data of `IST-Lisbon` [433] are surprisingly lower than the rest. This is due to retraction of the N_2^+ B $^2\Sigma_u^+$ ionic excitation, which is treated separately, but even when included, does not sum to the total ionisation.

Transport Coefficients fig. 16.5

- Below < 2 Td : Transport is dominated by rotational excitation. Both sets of Gerjuoy and Stein [323] in `IST-Lisbon` and of Kutz and Meyer [546] in our `IAA` database bring mobility into accord with experiments. For diffusion in particular, the set in our database gives more accurate results. The influence of rotational cross sections on transport in N_2 was elaborated in Ridenti *et al.* [774].

  Note that the comparison with `Muroran` is not fair because we did not include the rotational set. Nevertheless, the results are practically identical to `IST-Lisbon` below 0.5 Td so that the difference between `IST-Lisbon` (`---`) and `Muroran` (`---`) highlights the importance of rotational excitations.

- Between 0.6–6 Td : we predict a mobility about 10 % higher than most experiments (except Pack and Phelps [727] which is lying above). This difference is hard to explain but we surmise that it is because our elastic MTCS is lower than for other databases in the energy region 0.1–1 eV surrounding the characteristic energy $\langle\varepsilon\rangle$ and especially at the onset of the resonance region at 1.5 eV. Part of this difference could also be due to rotational excitations but this does would affect only values below ~ 5 Td. `Muroran` has an even lower elastic CS, but then compensates with a MTCS scaled upwards in the resonance region. Given the very close similarity of our `IAA` database with `Muroran`, we attribute our overestimation of the mobility to an underestimation of momentum loss in particular in the resonance region.

- Between 5–100 Td : The average electron kinetic energy $\langle\varepsilon\rangle$ is nearing toward the N_2 $^2\Pi_g$ resonance region. The separation of `Itikawa` transport curves is due to the absence of vibrational excitations higher than the $v = 0 \rightarrow 1$ transition in that set.

- α_i : Ionisation coefficient in decreasing order `IAA`>`Muroran`> `IST-Lisbon`> `Phelps`> `Itikawa`. `Biagi` crosses from first to last as the electric intensifies. This is explained by a late but higher loss of energy in electronic excitations (fig. 16.2). `Itikawa`'s lowest α_i is due, on the contrary, to an early peaked electronic inelastic CS (at lower energies).

16.2 O_2

In comparison to N_2, molecular oxygen is much less studied. As a reactive gas, it is difficult to make accurate measurements. An early review of cross sections was done, again, by Itikawa *et al.* [438] and updated two decades later [440].

Because of its high electron affinity (see sec. 11.3, fig. 11.18), the electron interaction with O_2 at low sub-eV energies is sprouted with a series of sharp narrow and very tall resonance peaks from the $O_2^-(X\,^2\Pi_g)$ symmetry (fig. 11.25). Proper visualisation of those peaks require precise and highly resolved measurements which became possible only recently [128, 714].

Those peaks seem to be better characterised now. Nonetheless, according to the most recent survey of Szmytkowski and Możejko [901, fig. 4], there is an ongoing "disaccord" of measurements beyond 1 eV in the total scattering cross section.

An overview of the principal databases for O_2 is laid out in table 16.2, for each of which we give an individual description below.

`Phelps` This database predates the one for N_2 and was described in the appendix C of Lawton and Phelps [566] and tabulated in Phelps and Pitchford [751]. The elastic momentum-transfer of Hake and Phelps [381] was modified below 1 eV so as to yield good results in agreement with Nelson and Davis [691] at electric fields < 1 Td, together with the single-level approximated rotational cross section at a loss of 20 meV (as for N_2). Three-body attachment cross section are adapted from Spence and Schulz [868] with regular peaks coinciding with the shape resonance of the O_2^- ($^2\Pi_g$) anion. Dissociative attachment was adapted from Schulz [818]. Apart from the two lowest electronic states $a\,^1\Delta_g$ and $b\,^1\Sigma_g^+$, electronic excitations of higher states are grouped into losses at 4.5 eV, 6 eV and 8.4 eV.

`Itikawa` Documented in depth in Itikawa [440] which updates the former review [438]. The cross sections are principally taken from the massive compilation of Itikawa [434]. The major difference with our database is that Itikawa privileged data from Shyn *et al.*'s laboratory [842, 845, 846, 848, 849], whereas we shunned those data due the availability of more recent results and also to Brunger and Buckman's observation in Brunger and Buckman

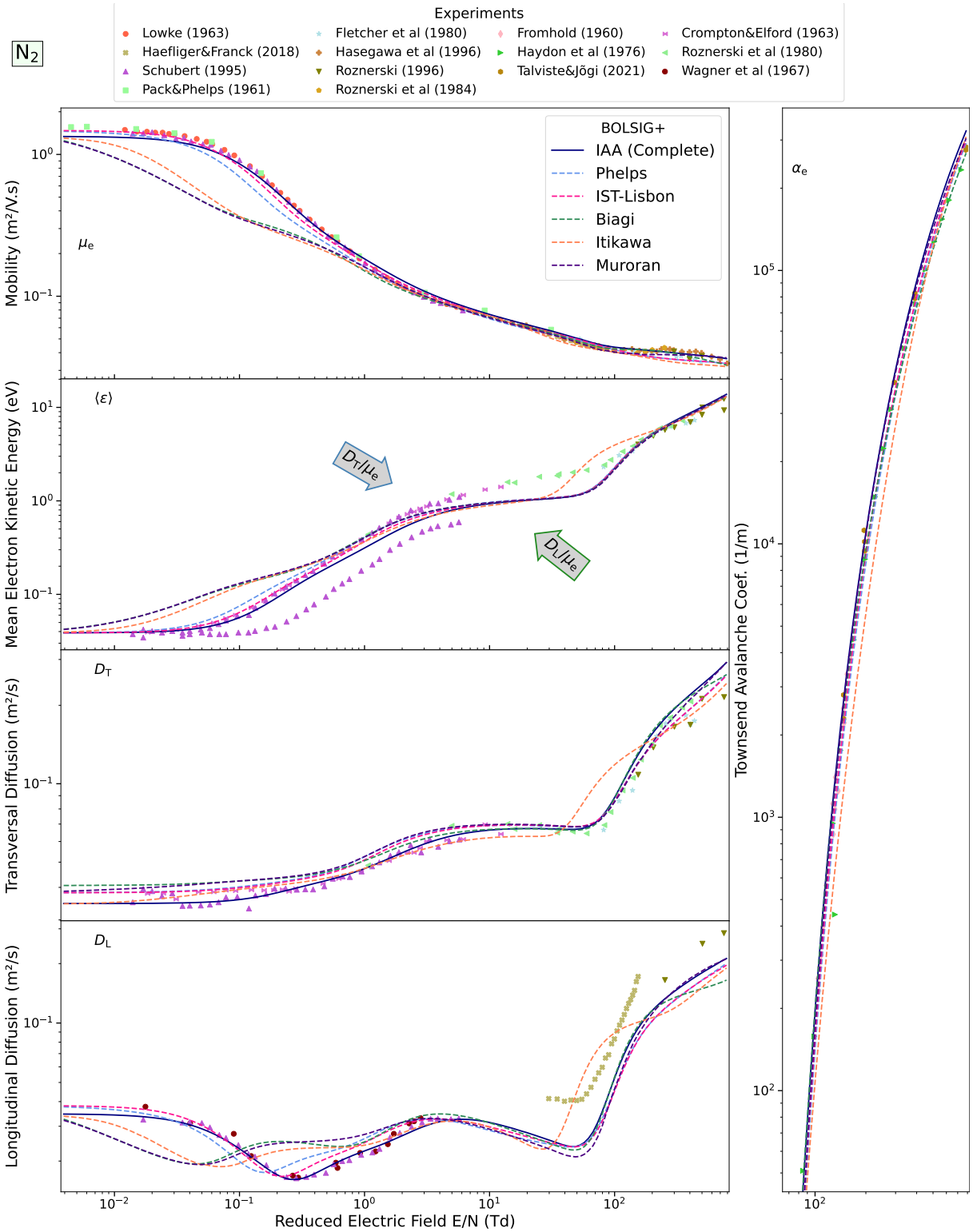

Figure 16.5: Transport coefficients in molecular nitrogen as calculated by BOLSIG+ for different cross section sets and compared with a variety of experimental data.

Table 16.2: Databases of electron collision cross sections with molecular oxygen. Middle rows represent the ones hosted on LXCat, the last rows are incomplete databases. In the columns we regroup the references to the experimental data upon which the database are constructed. If it exists, the reference to the publication which describes each database is under the column "Origin".

Database	Year	Origin	Total	Elastic	Vibrational	Electronic	Ionisation	Attachment
IAA (Present)	2023	11	[207, 315, 477, 714, 900, 1003]	[353, 598, 893]	[552]	[352, 845, 848, 897, 972, 973]	[768, 814, 815, 888]	[558]
Phelps	1978	[566]		[381]	[593, 987]	[593] ...	[917]	[818, 868]
Itikawa	2009	[438, 440]	[205, 207, 477, 798, 890, 900, 1003]	[598, 842, 893, 938]	[12, 401, 599, 846]	[845, 848, 849]	[888]	[767]
Biagi	2012		same as `Phelps` + 14 eV exc.					
IST-Lisbon	2016	[24, 346]						
Flinders	2014				[467]	[897]		
Laporta	2013	[552]		[552]	[552]			[558]

[124, p.317]. Careful that the energy thresholds for the longest (LB) and second (2B) as re-transcribed on LXCat should be modified to 9.97 eV and 10.29 eV respectively (instead of put 6.12 eV which is for the Schumann-Runge continuum). Also, do not use the total dissociation cross section when input to BOLSIG+.

`Biagi` See note for N_2 in the previous section 16.1.

`IST-Lisbon` It is practically the same as the `Phelps` database, except that it includes an additional electronic excitations lumped together at a loss of 14 eV as the last table in the report of Phelps and Pitchford [751]. Also, in Alves *et al.* [24], it was extended with a set of rotational cross sections as calculated with the quadrupole Born approximation of Gerjuoy and Stein [323], albeit with a highly contrived value of the quadrupole $Q = 1.4\,\mathrm{ea}_0^3$ which is more than four times the actual value $Q = -0.29$ a.u. reported in Khristenko *et al.* [498, p.81]. This was changed in order to fit closely the transport coefficients of Nelson and Davis [691] at low energies.

`Flinders` Vibrational and electronic excitations as reported in the cross-beam measurements of Jones *et al.* [466] and Suzuki *et al.* [897].

`Laporta` Resonant vibrational excitation and attachment cross sections from local-complex-potential calculations of Laporta *et al.* [552, 558] and used in Laporta *et al.* [559] to estimate vibrational relaxation in oxygen plasmas.

Comparisons

Elastic CS fig. 16.6

1. Very low energies < eV : no data from beam experiments, only swarm data [e.g. 381], though they have been modified in `Phelps` [566, Appendix C:(1)] so as to match transport coefficients from Nelson and Davis [691]. Our values directly result from Okumura *et al.*'s measurements [714] scaled by $1 - \langle \cos\theta \rangle$ from the MERT DCS (cf. fig. 11.1).

   Also, hard to determine is the momentum-transfer CS in the resonance peaks.

2. Low-to-intermediate $1\,\text{eV} < \varepsilon < 30\,\text{eV}$: our momentum-transfer CS and `Itikawa` faithfully meander between the two most trusted results of Linert *et al.* [598] and Sullivan *et al.* [893], whereas the other databases go through a "roller-coaster" of over-then-under-estimations.

3. Intermediate $30\,\text{eV} < \varepsilon < 200\,\text{eV}$: unadjusted angular-momentum close-coupling calculations (see chapter 9). We know from Brunger and Buckman [124, §3.3.2.2:p.317] and our own observations that Shyn and Sharp's results [842] most probably have a systematic error, so that we cannot rely on those. The same is true about Trajmar *et al.* [938] as noted by Lawton and Phelps [566, p.(1065):§C(1)]. Systematic errors could be due to contact potential changes* since O_2 is a reactive gas as Green *et al.* [353] say so in their conclusion.

4. High energies > 200 eV : our CS dashes (accompanied by the hopping `Biagi` CS) between the beam measurements of Daimon *et al.* [206] and Iga *et al.* [418], whereas `IST-Lisbon` and `Phelps` go their own clearly distinct way.

Inelastic CS fig. 16.7

- Vibrational CS : $\sum_{v'} \sigma_{v=0\to v'}$

  1. First resonance $O_2^- \, {}^2_\Pi g < 1.2\,\text{eV}$: our tall skewed peaks come entirely from Laporta *et al.* [552]. Of very important note :

     > The first vibrational resonance peak strongly affects the electron mobility in O_2 between 1—10 Td. Reducing this peak both in our and `Biagi`'s CS would considerably improve agreement with experimental mobilities (see fig. 16.10).

     What about modelling the delay in electrons resonantly scattering from O_2? This could also lower the discrepancy observed in the mobility while keeping the CS intact.

  2. Second broad resonance (mainly ${}^4\Sigma_u^-$) 7—14 eV : we follow theoretical calculations, whereas other databases interpolate experimental measurements [846, 938, 987].

  3. Between resonances 1.2—4 eV : participation of other electronic configurations to the excitation to higher vibrational levels [552, p.6:§5]

- Electronic CS : $\sum_{a'} \sigma_{0\to a'}$

  △ Schumann-Runge (SR) $\gtrsim 8.6\,\text{eV}$: cliff discontinuity for `IST-Lisbon` and `Phelps` because they do not include losses to the SR below 8.6 eV. Overestimation due to Wakiya [972], see fig. 16.8-left-bottom.

*I am not an experimentalist, so behold my words like an umbrella repelling rain.

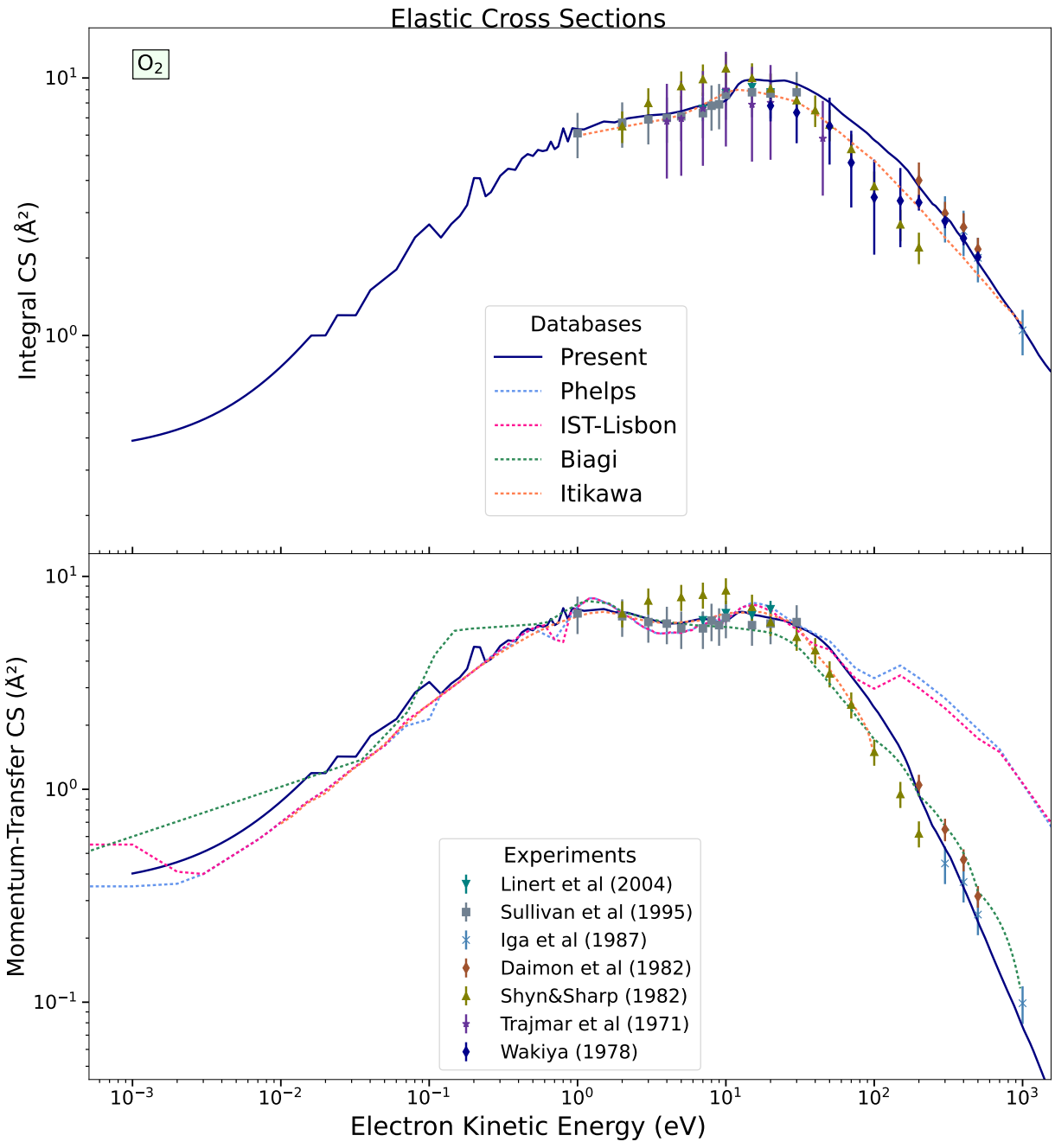

Figure 16.6: Comparison of elastic integral and momentum-transfer cross sections for molecular oxygen.

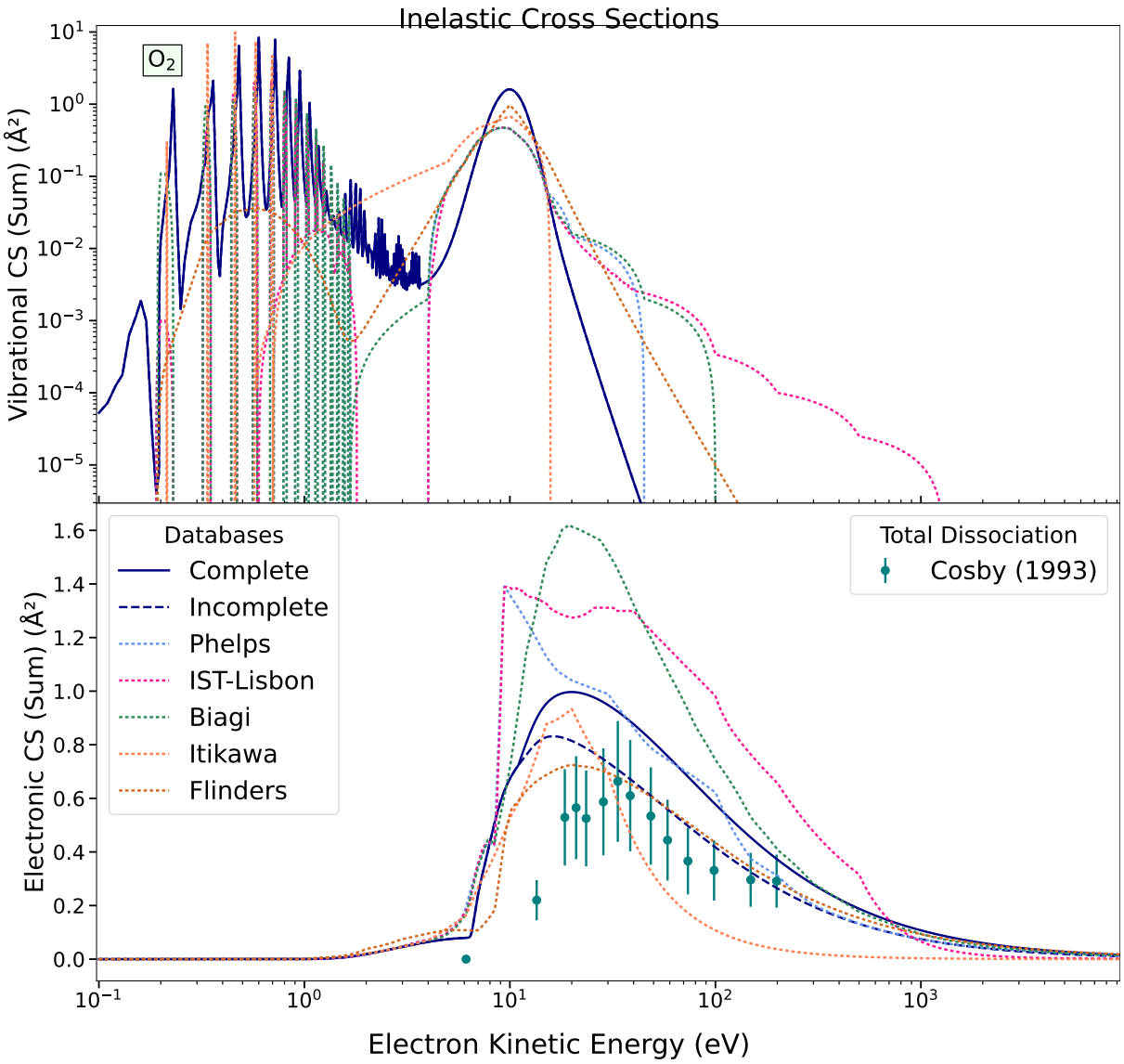

Figure 16.7: Comparison of the sum of vibrational and electronic impact excitation cross sections for molecular oxygen.

△ Losses beyond the SR > 10 eV : Our incomplete CS (- - -) are complemented with an unknown loss from an optically allowed excitation of $f_o = 0.1$ oscillator strength which increases the total CS to the solid dark blue curve —.

It is very unlikely that the states from the complementary CS would not predissociate. Nevertheless, these losses are not part of the neutral dissociation of Cosby [194]. Therefore, we think that these losses are most probably from *auto-ionising* excitations not comprised in the ionisation RBEQ* model.

`Itikawa`'s database does not provide extrapolation beyond 50 eV (which is why the tail drops at high energies).

Supplementary losses in `IST-Lisbon` and `Biagi` are unreasonably overestimated.

Electronic CS fig. 16.8

1. Forbidden low-lying a $^1\Delta_g$: the peak is sharper than our fit can follow.
2. Herzberg Pseudo-continuum (HC) : `Phelps, IST-Lisbon` and `Biagi` overestimate the peak but underestimate the tail.
3. Schumann-Runge continuum (SR) : Wakiya's results [972] are about twice the values of Suzuki *et al.* [897] and Shyn *et al.* [849], this is the first cause of too high CS of `Phelps, IST-Lisbon` and `Biagi`.
4. Longest and Second bands (LB+2B) : origin of overestimation same as for SR.

Ionisation CS fig. 16.9

- More recent : `Itikawa` and our database following Straub *et al.* [888] and Schram *et al.* [814, 815].
- Older : `Phelps, Biagi` following Rapp and Englander-Golden [768]
- Outlying : `IST-Lisbon` below 200 eV overestimates the ionisation CS for no apparent reason. It is supposed to be identical to the `Phelps` database [346].

Transport Coefficients fig. 16.10

- Three-body Attachment : Only included in `Biagi`'s curve. The effect is high below 20 Td and extreme at any field below 0.7 Td. This effect is only shown for illustration of the importance that three-body attachment has at low electric fields.
- Dissociative Attachment : Our and `Itikawa`'s CS for dissociative attachment are identical. The differences in the reduced Townsend coefficient $\eta_a = \nu_a/v_d$ for attachment are thus entirely due to the differences in the electron energy distribution function. The same can be said about the ionisation coefficient α_i.
- Below < 5 Td : The good matching between `IST-Lisbon` and Nelson and Davis [691] is due to an adjustment of the rotational set of cross sections calculated in the Born approximation setting the quadrupole of O_2 to a value of 1.4 atomic units which is more than 4 times its true value. Our rotational cross sections were calculated with the experimental value $Q = -0.29$ atomic units and are manifestly too small. The adjustment of Q serves as a scaling factor of the rotational CS which are mostly flat. This indicates that rotational scattering off oxygen ought to be strongly enhanced by low-energy resonant scattering, of which a proper study would be highly valued.
- Between 0.5–15 Td : Region dominated by vibrational resonant collisions linked to O_2^- $^2\Pi_g$ (lowest threshold ~20 meV). This can be seen by the glitchy behaviour of `Itikawa` curves (μ_e and D_L) whose vibrational CS are very sharp and very tall (fig. 16.7–top). The wider the peaks, the smoother the curve is, but the larger the deviation. Our and `Biagi`'s transport coefficients are strongly affected by the resonant vibrational CS which are wider and taller than used in `Phelps` and `IST-Lisbon`.

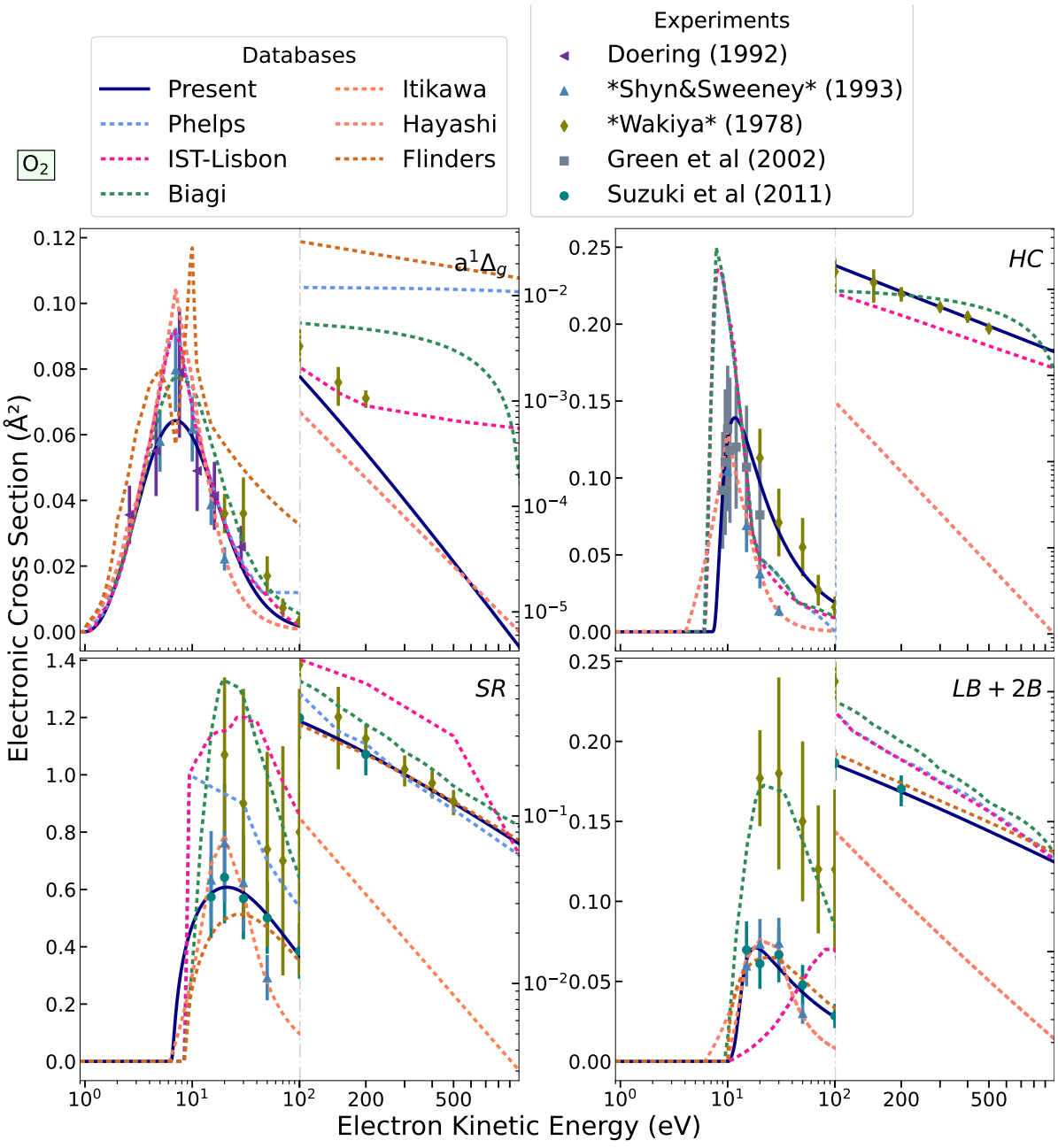

Figure 16.8: Comparison of selected electronic impact excitation cross sections for molecular oxygen.

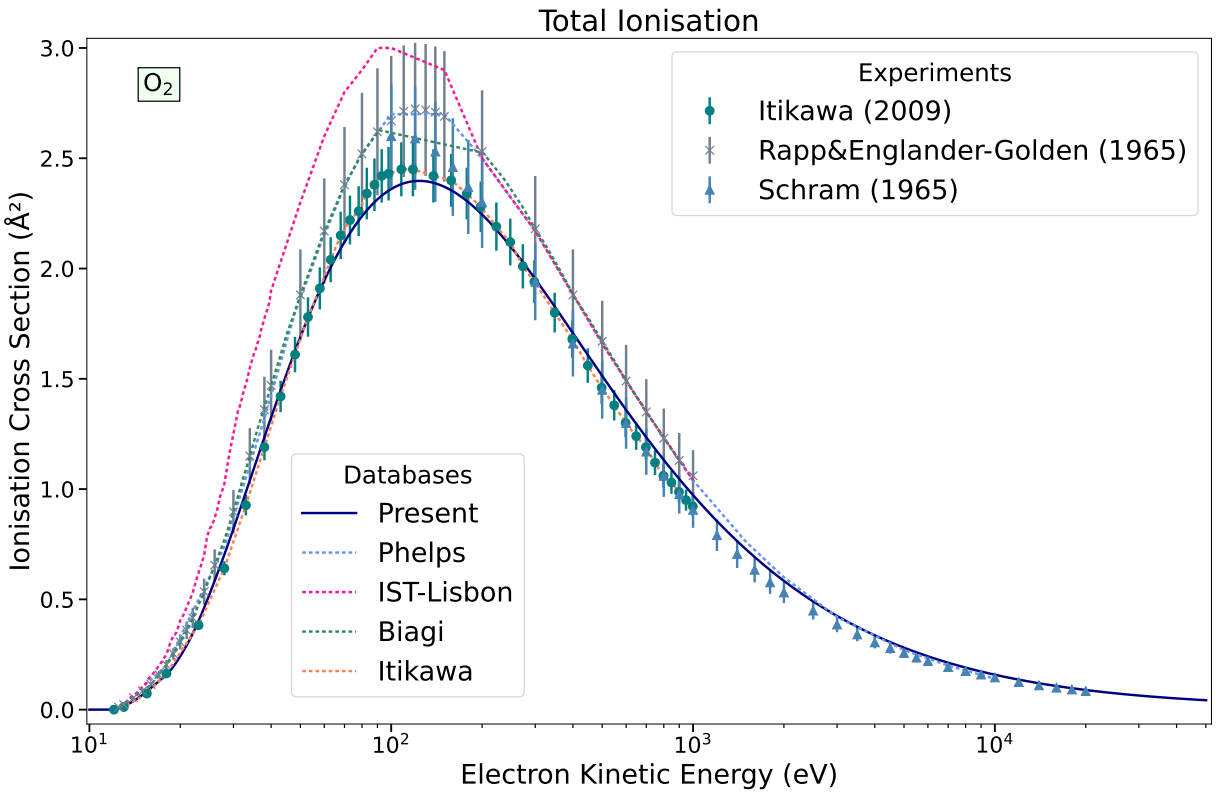

Figure 16.9: Comparison of impact ionisation cross sections for molecular oxygen.

- Above 200 Td lowest inelastic losses in electronic excitations in `Itikawa` (fig. 16.7) explain why transport and ionisation are enhanced at higher electric fields.
- α_i : Ionisation coefficient in the following order : `Itikawa>IAA>Phelps>IST-Lisbon`. `Biagi` crosses through. This can be explained by initially low elastic MTCS (fig. 16.6) and low inelastic CS (fig. 16.7). Then, the ionisation rate decreases as the inelastic losses in electronic excitations rise and peak highest than all other databases.
- `IST-Lisbon` : has the lowest α_i but highest σ_{ion}. This is because it has to compensate for the overestimation of losses in electronic excitations (fig. 16.7).

16.3 NO

Interest in nitric oxide is more recent than for other diatomic molecules since it is absent in the list of recommended CS of Hayashi [387]. In the near past, the interest in studying NO has been spurred due to its presence in auroral emissions from the Earth's ionosphere where it is formed by recombination of nitrogen and oxygen atoms as dissociated products from UV radiation [144]. More recently, it received further attention due to its production in discharges [743], or as a byproduct of fossil fuel combustion, in order to assess its climatological impact.

It has been reviewed twice in recent years. Once by Itikawa [441] which was then extended by Song *et al.* [865] about three nitrogen oxides. Nitric oxide is usually included in studies of electrons scattering off diatomic molecules together with the unmissable hydrogen, nitrogen and oxygen diatomic molecules. [207, 768, 900].

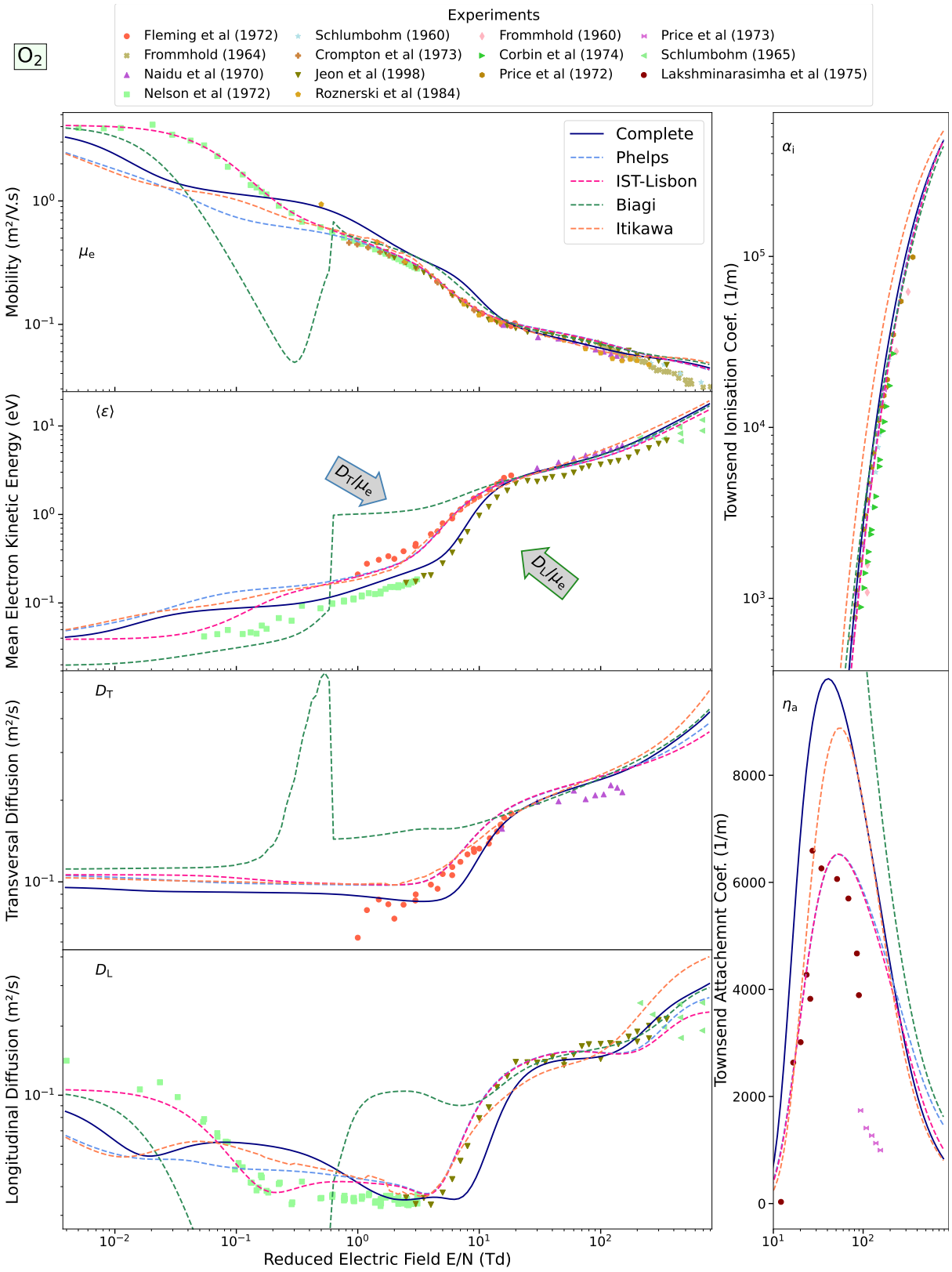

Figure 16.10: Transport coefficients in molecular oxygen as calculated by BOLSIG+ for different cross section sets and compared with a variety of experimental data.

Nevertheless, the database of elastic and inelastic scattering of electrons off NO is nearly reduced to the studies from the group of Brunger *et al.* [120]. In particular, the database of elastic DCS for NO is restricted to the single study of Mojarrabi *et al.* [654]. We could not access the measurements of Kubo *et al.* [541], though they lie roughly in agreement with Mojarrabi *et al.* [654, figs. 2–3]. Also, at low energies below 1.5 eV, there is a strong resonant structure in electron-NO scattering [944, figs. 1–2], which makes the establishment of elastic DCS prohibitive there.

In table 16.3, we offer an overview of current databases of cross sections with NO, which we briefly describe below.

`Phelps` This database seems to be even older than the one from N_2 and O_2. It has been updated only once for its ionisation cross section from Lindsay and Mangan [596, p.5-60]. The documentation regarding the determination of the remaining cross sections is unavailable.

`Hayashi` Database from Hayashi's massive compilation of electron-molecule cross sections. It was privately communicated to the JILA centre.

`Itikawa` From the recent review of Itikawa [441]. The cross sections are principally taken from the massive compilation of Itikawa [434]. For inelastic (vibrational and electronic) excitations, the cross sections are the same as in the `Flinders` database.

`Flinders` Vibrational and electronic excitations as constructed in Campbell *et al.* [144] from the cross-beam measurements of Cartwright *et al.* [157], Jelisavcic *et al.* [456], and Mojarrabi *et al.* [654].

`Laporta` Resonant vibrational excitation and attachment cross sections from local-complex-potential calculations of Laporta *et al.* [553, 555, 556] and used in Laporta *et al.* [557] to investigate electron transport in non-equilibrium nitrogen-oxygen plasmas.

"`Song`" Most recent review in Song *et al.* [865] principally based on the previous review from Itikawa [441]. The main differences are (i) the total scattering cross section has been corrected at high energies to follow the Born-Bethe scaling, (ii) the elastic momentum-transfer has been updated from swarm measurements, (iii) the electronic excitations are completed with Born-scaled analytical fits as described in Kim [505]. Also, (iv) the new review includes transitions between the fine-structure spin-orbit split states of the ground configuration $^2\Pi_{1/2}$ and $^2\Pi_{3/2}$ from Allan [15].

This latest review served as a basis for the creation of the present set of cross sections.

Comparisons

Elastic CS fig. 16.11

1. Resonance region NO^- $^3\Sigma^-$ < 1.5 eV : vibrationally-elastic data of Laporta *et al.* [557].

2. Low to intermediate energies 2–50 eV : cross-beam ICS from Mojarrabi *et al.* [654] (corrected in [120, tab. 3]). Our ICS are taken from the total CS recommended by Song *et al.* [865, table 2] and the subtraction of the sum of all inelastic CS. The inclusion of the complementary inelastic CS improves the agreement with the measured ICS below 20 eV but is underestimated beyond.

Table 16.3: Databases of electron collision cross sections with nitric oxide. Middle rows represent the ones hosted on LXCat, the last rows are incomplete databases. In the columns we regroup the references to the experimental data upon which the database are constructed. If it exists, the reference to the publication which describes each database is under the column "Origin".

Database	Year	Origin	Total	Elastic	Vibrational	Electronic	Ionisation	Attachment
IAA (Present)	2023	11	[865]	[654]	[557, 654]	[120]	[597]	[555]
Phelps	1969		unpublished					
Hayashi	1987							
Itikawa	2016	[441]	[207, 899, 900, 1005]	[654]	[456, 654]	[120]	[597]	[767]
Flinders	2004				[144]	[157, 655]		
Laporta	2013	[553]		[553]	[553]			[555]

3. Momentum-transfer CS : The complete database lies systematically in better agreement with the momentum-transfer CS integrated from the DCS of Mojarrabi *et al.* [654] and the recommendation of Song *et al.* [865, fig. 6]. The data recommended by Itikawa [441] are somewhat lower than the rest.

   The data of `Phelps` are outdated (and were actually never published).

4. Above 500 eV : the lowering correction from the tail of the complementary inelastic cross section is too strong and could be reduced.

Inelastic CS fig. 16.12

- Vibrational CS : $\sum_{v'} \sigma_{v=0 \to v'}$

  1. Below 2 eV : vibrational excitation CS from Laporta *et al.* [557] mainly from NO^- $^3\Sigma^-$ (0.2–1.5 eV) resonant state.
  2. Between 5–15 eV : double peak is an artifact due to the mismatch in the position of the dominant $^3\Pi$ resonance between theoretical calculations [557] (~ 8 eV) and measurements (~ 15 eV) [144, 654] synthesised by the `Flinders` database (light brown dotted ···).

- Electronic CS : $\sum_{a'} \sigma_{0 \to a'}$

  △ A significant portion of the electronic excitation CS is missing from the survey of excitations by Brunger *et al.* [120]. The total sum of inelastic CS for electronic excitations must be completed with four times its value in order to bring calculations from a kinetic solver in agreement with experimental swarm transport parameters [865, §2.7].

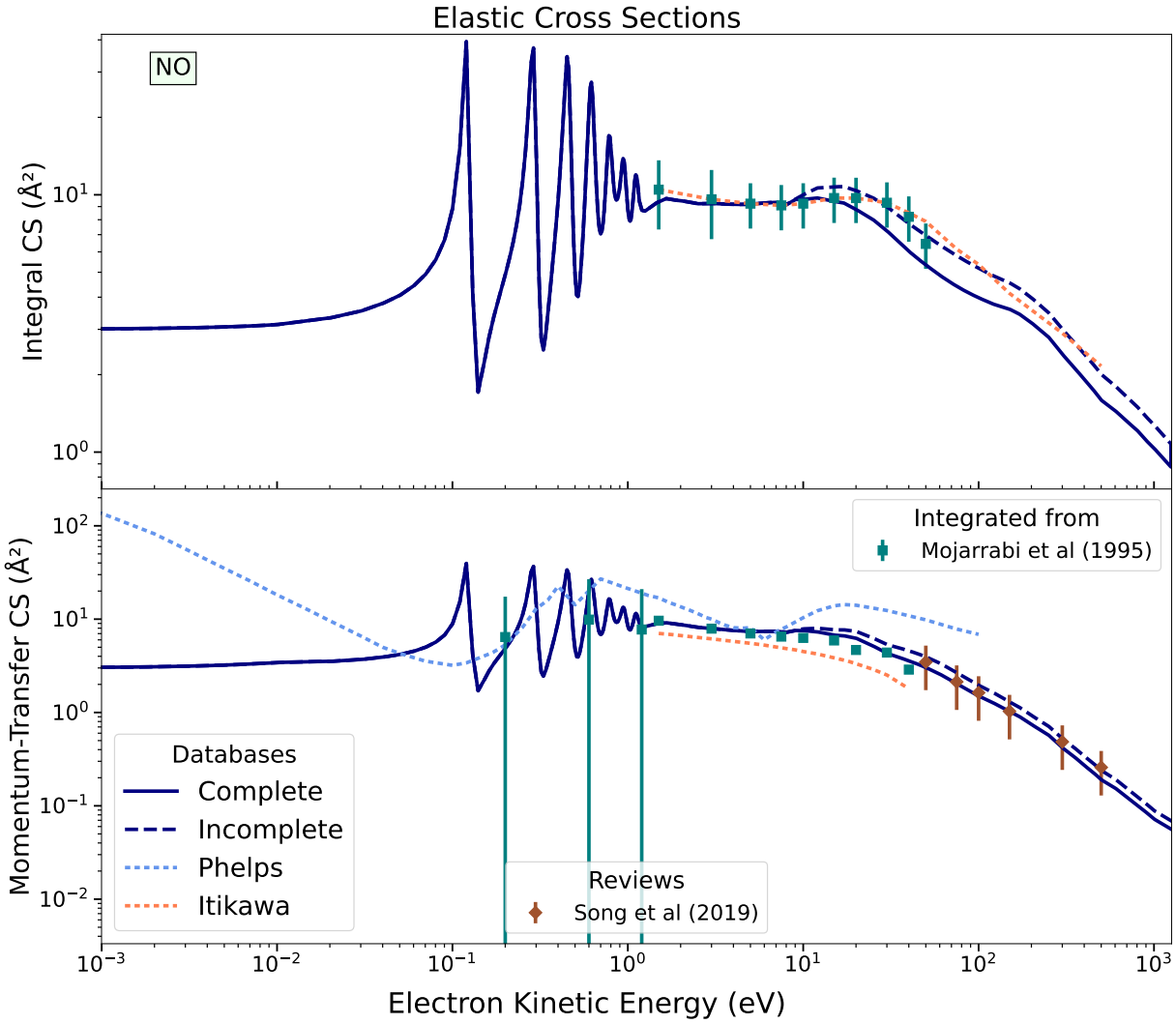

Figure 16.11: Comparison of elastic integral and momentum-transfer cross sections for nitric oxide. No curve could be obtained from `Hayashi` because the subtraction of inelastic CS from the reported 'total' cross section gives negative values above 10 eV.

△ The significant difference between the complete (—) and incomplete (- - -) CS might be due to the non-ionising dissociation CS of NO which is expected to be large, although concrete experimental data is missing [865, §2.8].

Ionisation CS fig. 16.13

Transport Coefficients fig. 16.14

- Our and `Itikawa` sets differ substantially, it is therefore not surprising to see almost a complete discord among the calculated transport coefficients.
- The effect of rotational cross sections at electric fields <1 Td is very strong and completely governs the transport of electrons in that region. This was already observed in CO by Vialetto *et al.* [961]. NO's dipole is about 1.5 times stronger than CO's.

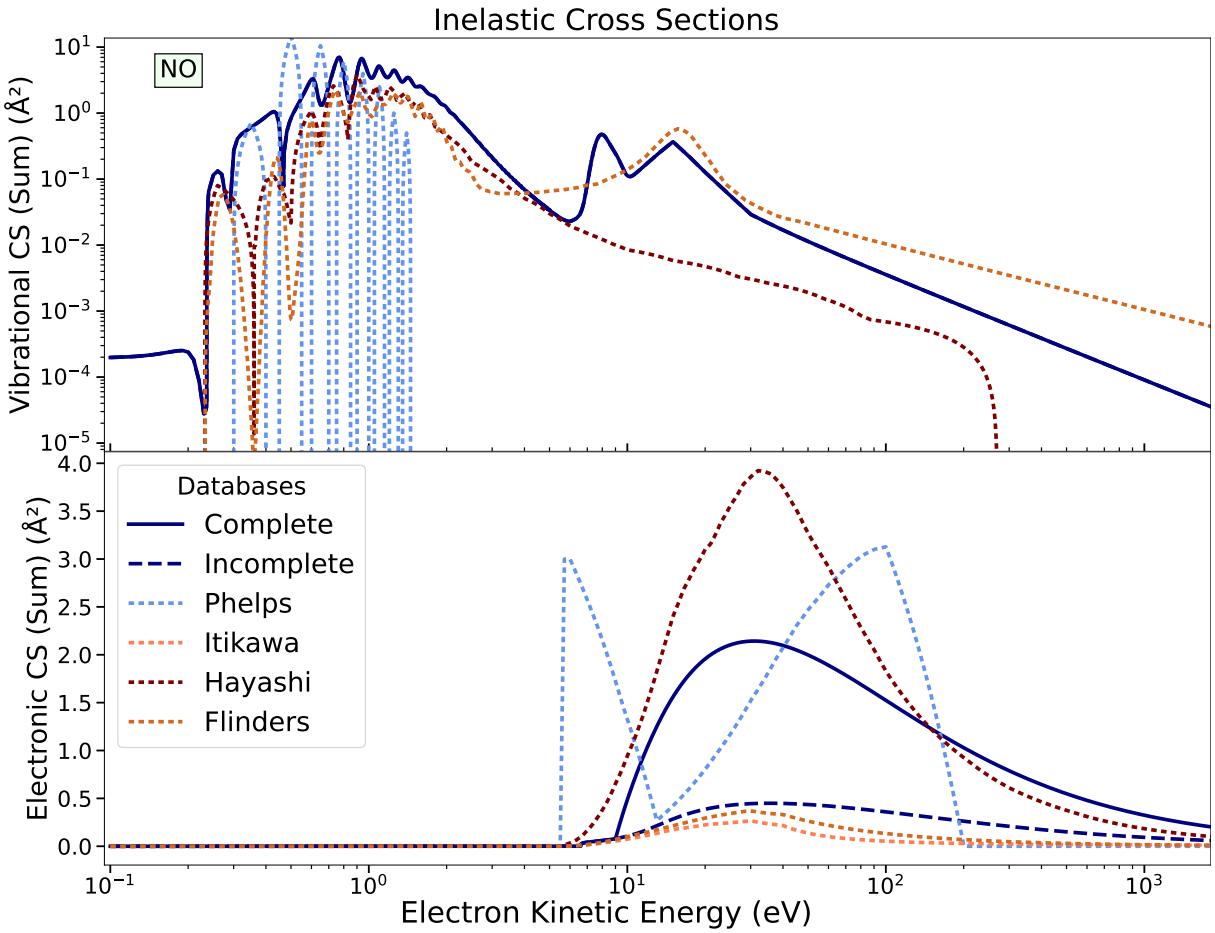

Figure 16.12: Comparison of the sum of vibrational and electronic impact excitation cross sections for nitric oxide.

- Below < 40 Td : Transport in `Hayashi` is eased by a lower vibrational CS (fig. 16.12–top) and absence of the $^3\Pi$ resonance around ~ 8–12 eV.
- Above > 40 Td : Inversion of trends due to acute inelastic losses in `Hayashi` total electronic CS (fig. 16.12–bottom).

16.4 Ar

There are many reviews about noble gases in general. Argon is the second most studied noble gas after helium. An early set of recommended cross sections was given in Hayashi's report [387]. Later came many other reviews, which sometimes cover also other noble gases. Brusa *et al.* [125] gave analytical fits to elastic, electronic excitation and ionisation cross sections of electrons colliding with noble gases.

Most recently, Boffard *et al.* [89] reviewed electron-impact excitations of noble gases including from metastable states. Then, Gargioni and Grosswendt [319] performed a more detailed review specific to argon including the verification of the consistency of optical oscillator strength measurements and sum rules. The construction of our database was mainly based on the information reviewed in those two recent studies [89, 319].

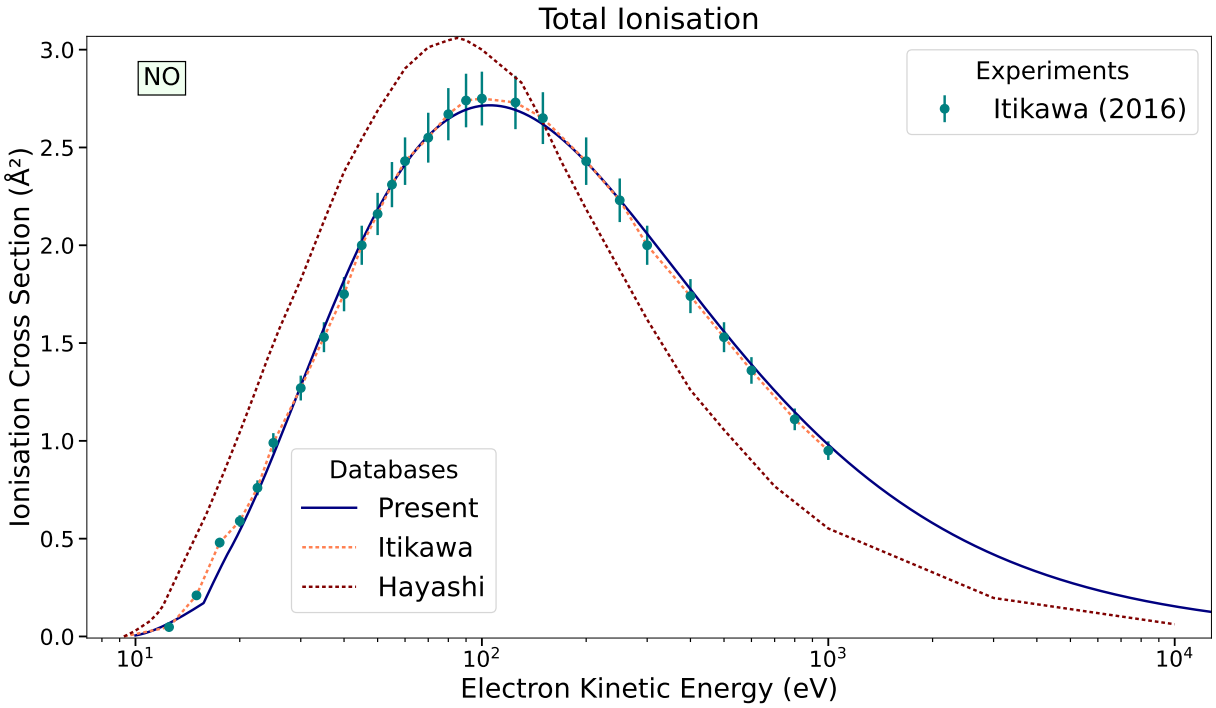

Figure 16.13: Comparison of impact ionisation cross sections for nitric oxide. We exclusively follow the recommendation of Itikawa [441] from the review of Lindsay and Mangan [596]. Data in `Hayashi` database were communicated privately to the JILA centre and are available on LXCat only.

Regarding cross section databases, argon is perhaps one of the targets most replete with sets of data. A review and comparison of databases hosted on LXCat for argon was conducted by Pitchford *et al.* [752]. It is actually the first of the review trilogy for noble gases continued in Alves *et al.* [23] and Bordage *et al.* [95]. Extensive comments to each database of LXCat are given in appendices of that review [752], we invite the reader to consult them there and offer only a tabular overview, for practical purposes, of the argon database in table 16.4 below.

Comparisons

Elastic CS fig. 16.15

1. Very low energies < 0.01 eV : the elastic cross sections of each database converge to a difference value $\sigma_e(\varepsilon = 0) = \pi A^2$ corresponding to the scattering length A. Ours is based on the value most recently deduced by Kurokawa *et al.* [545, p.7:table II].

2. Low energies < 10 eV : Purely elastic scattering, ICS identical to total CS of Kurokawa *et al.* [545] the `BSR` calculations of Zatsarinny and Bartschat [998] are slightly different.

3. Momentum-transfer (MT) : obtained from ICS with the $\langle \cos\theta \rangle$ given by the `BSR` DCS. Thus, the differences in σ_m between our and all other databases are a consequence of the slight mismatch between the `BSR` and the ICS. The calculated average cosine $\langle \cos\theta$ is too large in the Ramsauer-Townsend minimum at ~ 0.23 eV

4. From 10–100 eV : our ICS and MTCS are closer to the values of DuBois and Rudd [232] and Panajotović *et al.* [731] than all other database.

NO

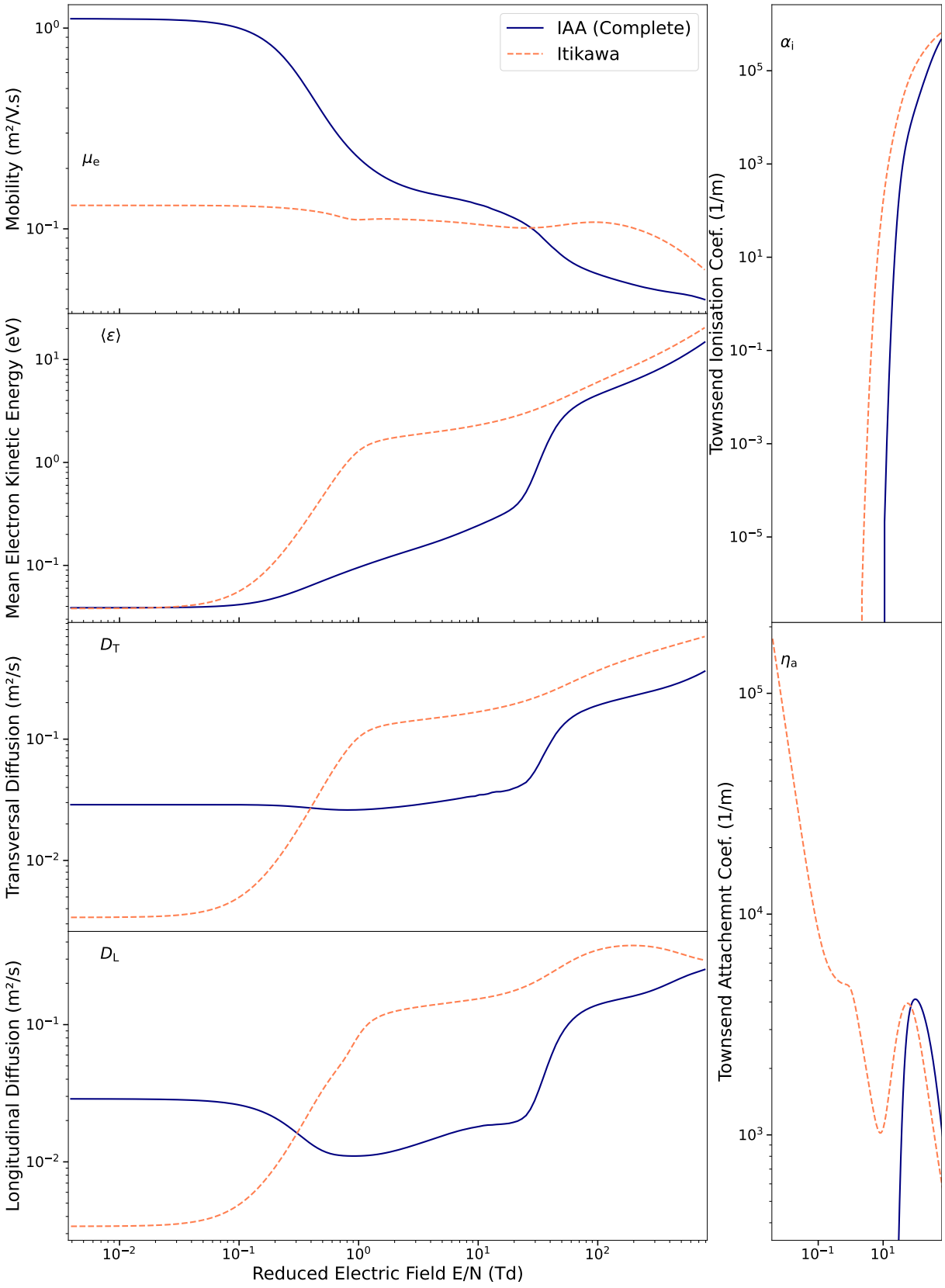

Figure 16.14: Transport coefficients in nitric oxide as calculated by BOLSIG+ for different cross section sets. We could not retrieve any experimental data in NO, consult Laporta *et al.* [557, fig.9] on which our set is based.

Table 16.4: Databases of electron collision cross sections with argon hosted on `https://www.lxcat.net/`. In the columns we regroup the references to the experimental data upon which the database are constructed. If it exists, the reference to the publication which describes each database is under the column "Origin".

Database	Year	Origin	Elastic	Electronic				Ionisation
				$4s$	$4p$	$3d$, $5s$	other	
IAA (Present)	2023	11	[129, 278, 545, 701, 708, 891, 900, 1004]	[8, 180, 282, 283, 491]	[180]	[180]	[319]	[321, 768, 814, 815, 869]
Phelps	1983	[306, 903]	[295, 650]	Schaper and Scheibner [809]				[861]
Puech	1986	[760]	[306, 650]	[106, 107, 180]				[106]
Hayashi	1991	[388]	Hayashi [388, p.200–9]					
IST-Lisbon	2005	[993]	[991]	[491]	[175]	[388]	[568, 977]	[768]
Biagi	2011	[752, app.A]	[689, 746]	[14, 319, 504, 505]				[768, 888]
BSR	2014	[998]	Zatsarinny *et al.* [1002]					

5. Above > 100 eV : the trends inverse. Our database lies closer to `Hayashi`'s and `BSR`, whereas `Biagi` and `IST-Lisbon` are lower.

6. At 1 keV : All database intersect and coincide with the last measurement of Iga *et al.* [418] except `Phelps` which has been straying away from 150 eV.

7. Completion : the complete database has a roughly constant correction ratio of −8 %.

Inelastic CS fig. 16.16

- Electronic CS : $\sum_{a'} \sigma_{0\to a'}$
  - △ Below < 200 eV : All databases peak differently. `Hayashi` and `Biagi` have a broad and tall peak, `BSR` has a flat and low plateau, `IST-Lisbon` and our incomplete database have sharper peaks, and `Phelps` has a tall pointy peak with only one excitation at 11.55 eV
  - △ Above 200 eV : our complete database is well in agreement with `Hayashi, Biagi, BSR` and `Phelps IST-Lisbon` coincides with our incomplete database.
- Ionisation CS :
  - – Below < 100 eV : All databases follow Rapp and Englander-Golden [768] except `BSR` [1002] which misses a large portion. Ours analytical fit cannot swerve awkwardly between 50–70 eV.
  - – Above > 100 eV : Two groups:

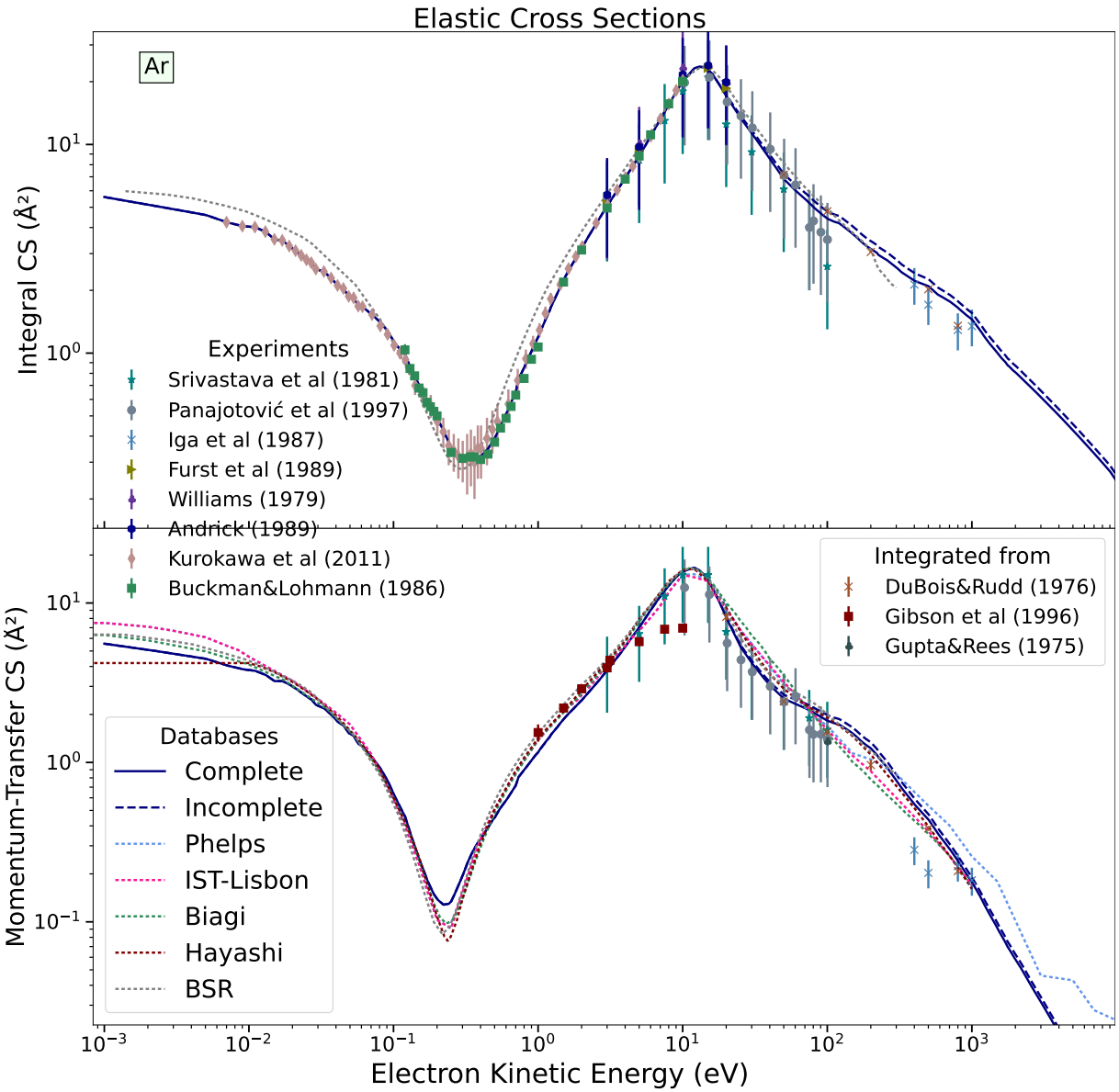

Figure 16.15: Comparison of elastic integral and momentum-transfer cross sections for argon.

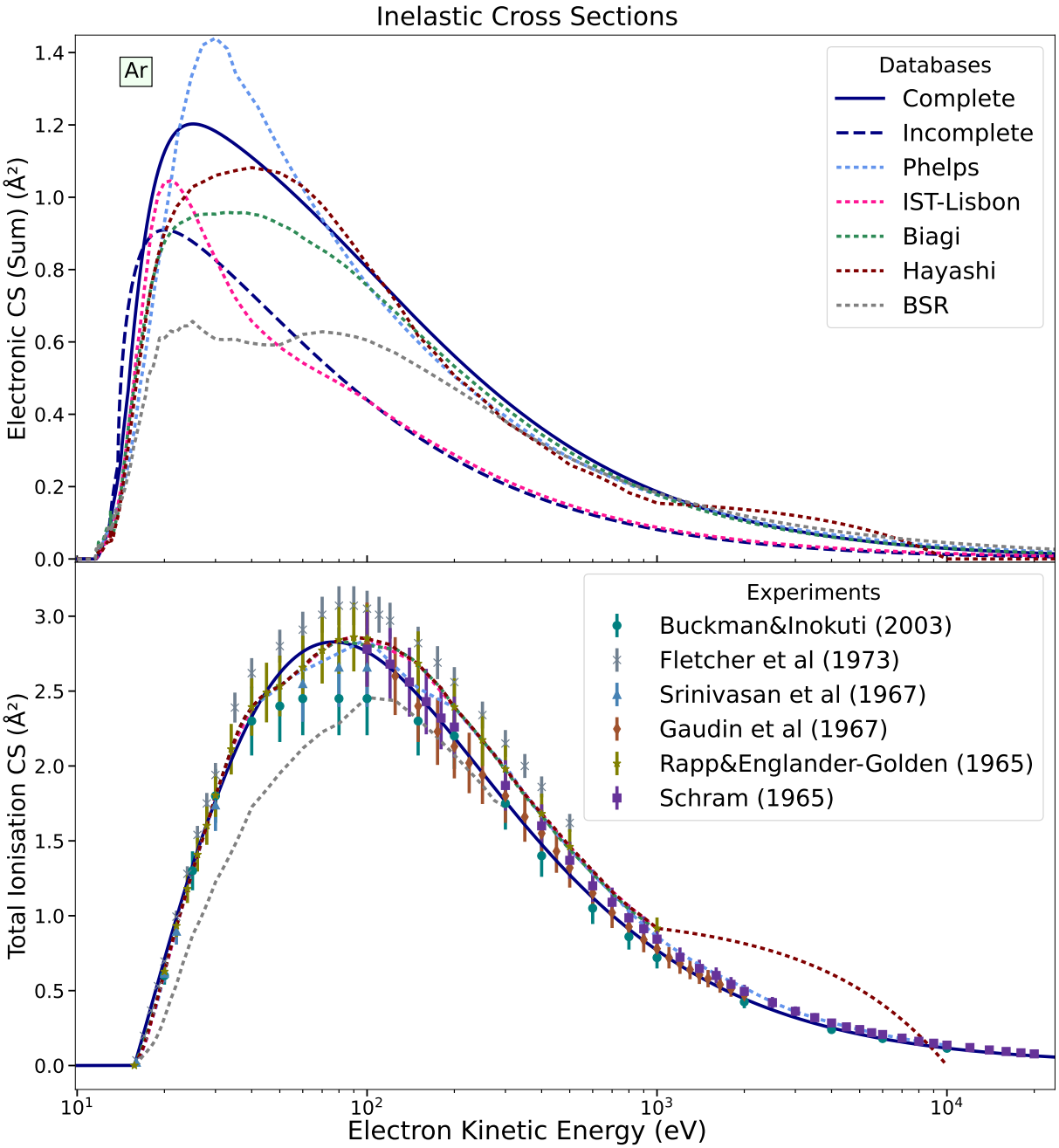

Figure 16.16: Comparison of the sum of electronic impact excitation and ionisation cross sections for argon. The weird bump on the `Hayashi` curve is due to a linear interpolation from 1 keV to 10 keV where the CS is forced to zero.

A. Followers of Rapp and Englander-Golden [768] : `IST-Lisbon`, `Phelps`, `Biagi` and `Hayashi`.

B. Followers of Gaudin, Albert and Hagemann, Robert [321], Inokuti *et al.* [425], and Schram *et al.* [814] : our database (`IAA`) and `BSR`.

Electronic CS fig. 16.17

1. Completion : The dashed curves "incomplete" `---` are direct fits to the data plotted, whereas solid curves — and dotted curves **cdots** are sums over the states mentioned.

2. Allowed $4s$ ($^3P_1^o$ and $^1P_1^o$) : When renormalised, Chutjian and Cartwright [180] and Filipović *et al.* [282] seem to indicate the presence of a peak between 40–50 eV, which is only followed by `Hayashi`. The most recent cross-beam measurements of Khakoo *et al.* [491] show the opposite. Theoretical `BSR` [1002] calculations follow neither trends, and `IST-Lisbon` is about half the updated CS estimate.

3. $4s$ forbidden ($^3P_0^o$ and $^3P_2^o$) : peaked CS in the following order : `IST-Lisbon` > Present > `Hayashi` > `BSR`. Our CS follow most Khakoo *et al.* [491] and Filipović *et al.* [283]. `Hayashi` follows Chutjian and Cartwright [180] when renormalised, we suspect he did his own renormalisation when constructing his recommended data in Hayashi [387].

4. $4p$ (9 dipole-forbidden + 1 pure spin-forbidden): `IST-Lisbon` follows closely Chilton *et al.* [175], whereas we and `Hayashi` preferred to follow Chutjian and Cartwright [180] after renormalisation. The `BSR` database misses a significant portion of the CS below < 100 eV.

5. $3d + 5s$ (mixture of allowed, dipole forbidden and spin-forbidden transitions, 12 in total) : Here is where lumping together the cross sections in a single fit ('Incomplete': `---`) is inaccurate compared to a sum of individual fits ('Complete': —). `IST-Lisbon` is practically superposed with `Hayashi` which is located between Chutjian and Cartwright [180] when renormalised and Chilton and Lin [176]. Our full curve is a fit to individual CS from various sources: Chilton and Lin [176] and Stewart *et al.* [883] and Chutjian and Cartwright [180] renormalised. One can see in the inflexion points of the curve, the regions where forbidden and allowed transitions dominate respectively. Again, `BSR` underestimates the CS in the peak region.

Transport Coefficients fig. 16.18

See Pitchford *et al.* [752] for a detailed comparison of transport in argon and explanation of each cross section database. Here, we only highlight differences with the present database.

- Below < 5 Td : Differences are entirely imputable to the momentum-transfer CS (fig. 16.15–bottom).
  - 0.005–0.1 Td : Diffusion coefficients governed by the depth of the Ramsauer-Townsend minimum at 0.23 eV. Our MTCS is certainly less accurate in that minimum than all other databases.
  - D_L at 3 Td : Two groups in the sharp bend: `IST-Lisbon, Phelps` and all others. This demarcation may only be explained by the lower elastic MTCS for those two databases between 5–12 eV (fig. 16.15).
- Above > 10 Td : mean kinetic energy $\langle\varepsilon\rangle \gtrsim 5$ eV, influence of electronic excitations starts building up.
  - μ_e around ~ 10 Td : Difference in the mobility is probably also due to the elastic MTCS; separation again of `Phelps, IST-Lisbon` from the rest (fig. 16.15).

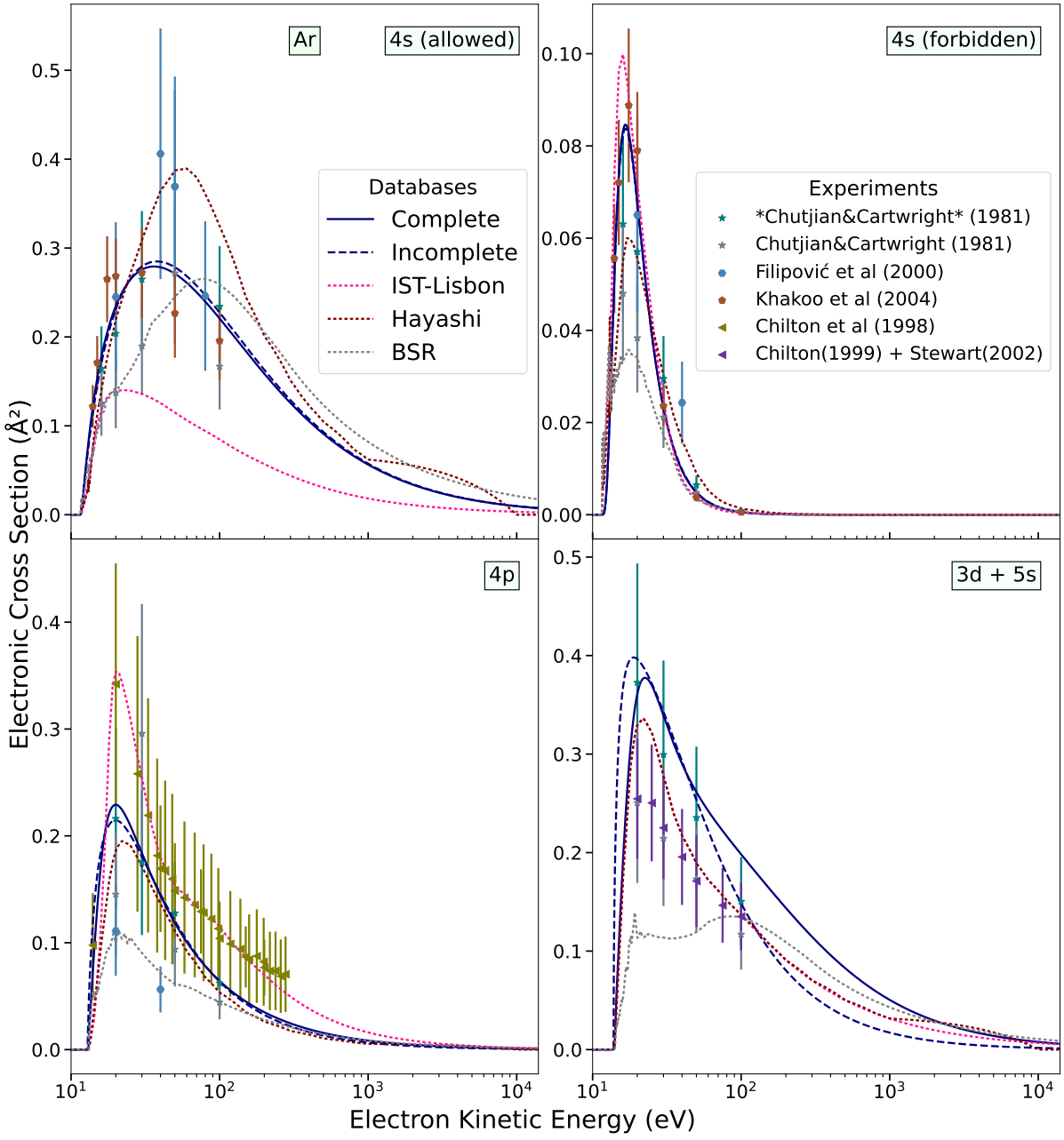

Figure 16.17: Comparison of selected electronic impact excitation cross sections for argon.

  - α_{i} : neatly ordered values of the ionisation coefficient from highest to lowest: `Phelps` > `Hayashi` > `Biagi` ~ `BSR` > `IST-Lisbon` > `IAA`.

    It is very probable that our RBEQ* to the ionisation CS is too low at the peak around ~100 eV and should be raised. This is not obvious from the experimental data shown on figure 16.16–bottom.

- Above 100 Td : difference in transport of the `BSR` database due to underestimation of inelastic losses (fig. 16.16).

16.5 O

Atomic oxygen was mainly studied by Vaughan and Doering in a series of articles [220, 227, 958–960].

More recently, Johnson *et al.* [462] made a survey of the available experimental and theoretical cross sections for O.

Two databases exist for atomic oxygen: `IST-Lisbon` who reinterpolated the data reported in the former survey of Laher and Gilmore [549] and `BSR` from the calculations in Tayal and Zatsarinny [921]. The latter are unfortunately not disclosed on LXCat, so we could not compared our results to `BSR`.

Comparisons

Elastic CS fig. 16.19

1. Below < 0.5 eV : our CS are calculated with the MERT (sec. 10.1.5).
2. Between 0.5 10eV : we closely stick to the only experimental results available of Williams and Allen [984].
3. Above 10 eV : all our CS are obtained from partial wave calculations off the optical potential. They differ significantly from the ones of `IST-Lisbon` for increasing energies.

Inelastic CS fig. 16.20

- Electronic CS : $\sum_{a'} \sigma_{0\to a'}$
  - △ Below < 20 meV : our CS are dominated by superelastic collisions between the fine-structure states of O: ${}^3_P0^o$, ${}^3_P1^o$ and ${}^3_P2^o$ (ground). These were obtained by pure conjecture based on the theoretical calculations of Berrington [63] and scaled according to the Boltzmann distribution at 300 K.
  - △ From > 20 meV : we see two bumps due to excitations from the ground to fine structure states.
  - △ At > 2 eV we see excitations to the two lowest spin-forbidden excitations to valence states: $2p^4\ {}^1D$ and $2p^4\ {}^1S$ (fig. 13.9), which are a bit lower in `IST-Lisbon` from Laher and Gilmore [549].
  - △ Beyond > 10 eV : Large bump due to all other electronic excitations. The complementary cross section is significant and its relevance is supported by the tall peak seen in `IST-Lisbon`.

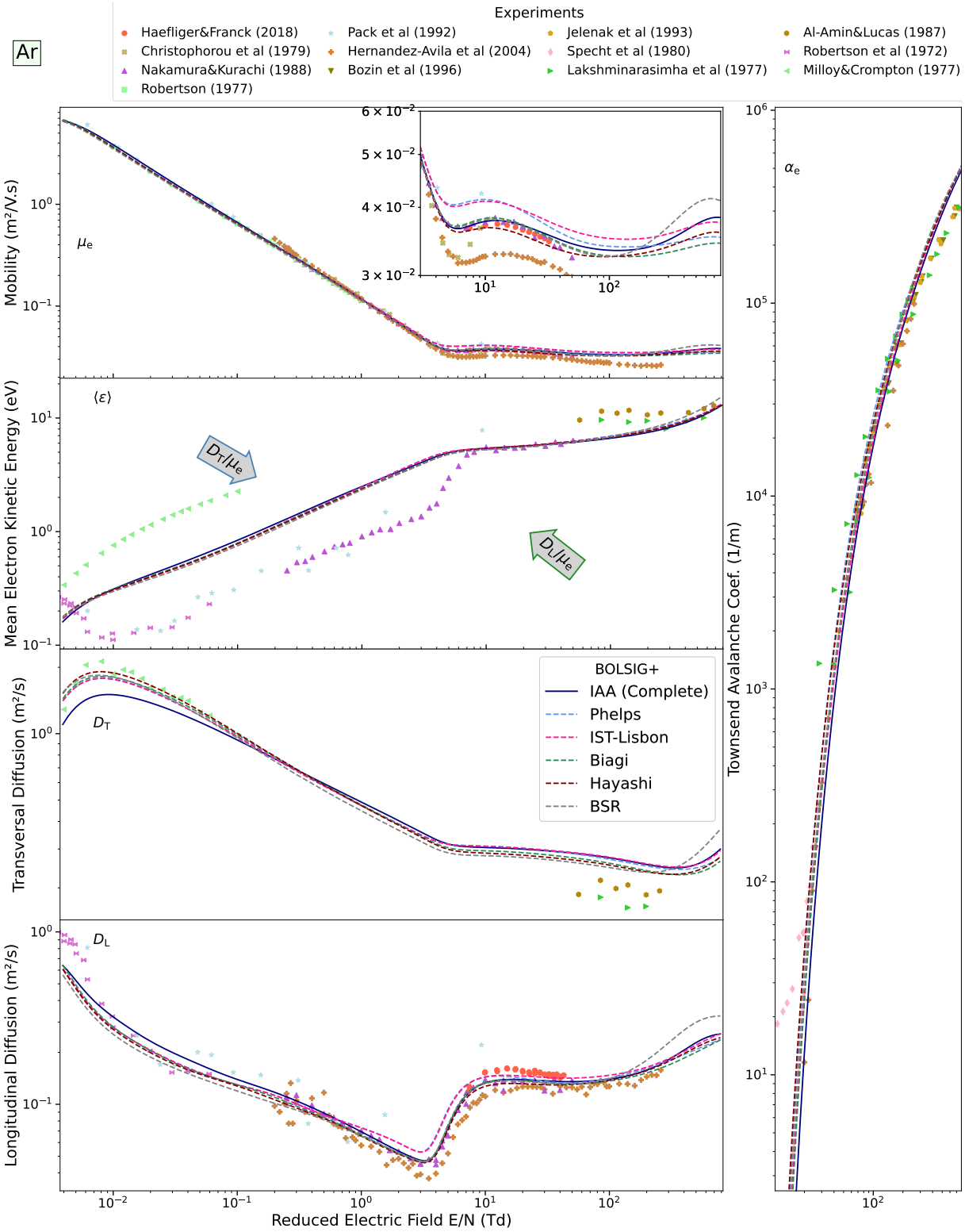

Figure 16.18: Transport coefficients in argon as calculated by the two-term Boltzmann solver BOLSIG+ for different cross section sets and compared with a variety of experimental data.

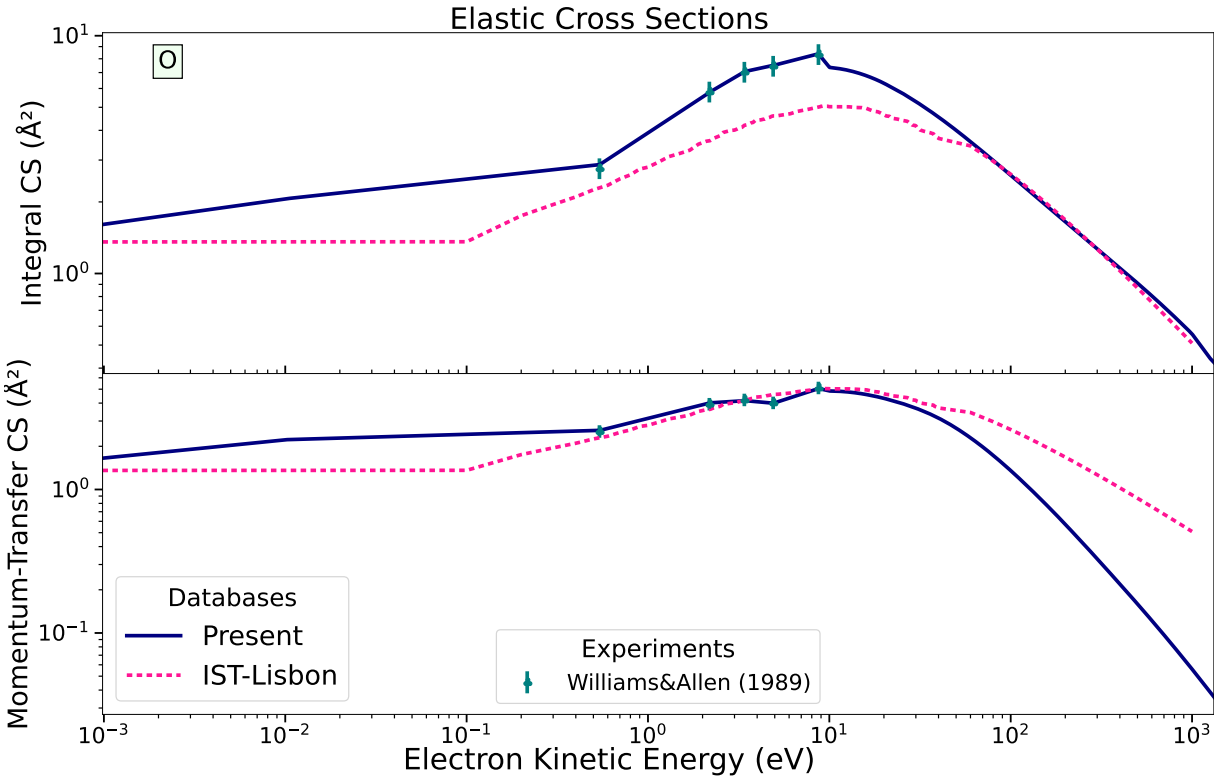

Figure 16.19: Comparison of elastic integral and momentum-transfer cross sections for atomic oxygen.

- Ionisation CS : The main difference between our database and `IST-Lisbon` is that we treat three auto-ionising states ($3s''\ ^3P^o$, $2s2p^5\ ^3P^o$, and $4d'\ ^3P^o$) separately from the total ionisation cross section. This explains why our CS is lower that experimental measurements.

Transport Coefficients fig. 16.21

- Below < 1 Td : Electron transport is dominated by the inelastic spin-forbidden transitions between the fine-structure spin-orbit states of O : ${}^3_P2$, ${}^3_P1$ and ${}^3_P0$.

  Trick : when given as input to BOLSIG+, these three inelastic transitions are treated as 'rotational' excitations, so that the program scales the superelastic transitions according to the temperature (300 K).

- Between 0.5–50 Td : Mean kinetic energy of `IST-Lisbon` is higher due to lower inelastic CS (fig. 16.20) higher ionisation rate due to higher ionisation CS.

- Above > 100 Td : Transport trends inverse, probably due to the difference in ionisation and perhaps also due to CS divergence of momentum-transfer CS between `IST-Lisbon` and our database above 20 eV (fig. 16.20).

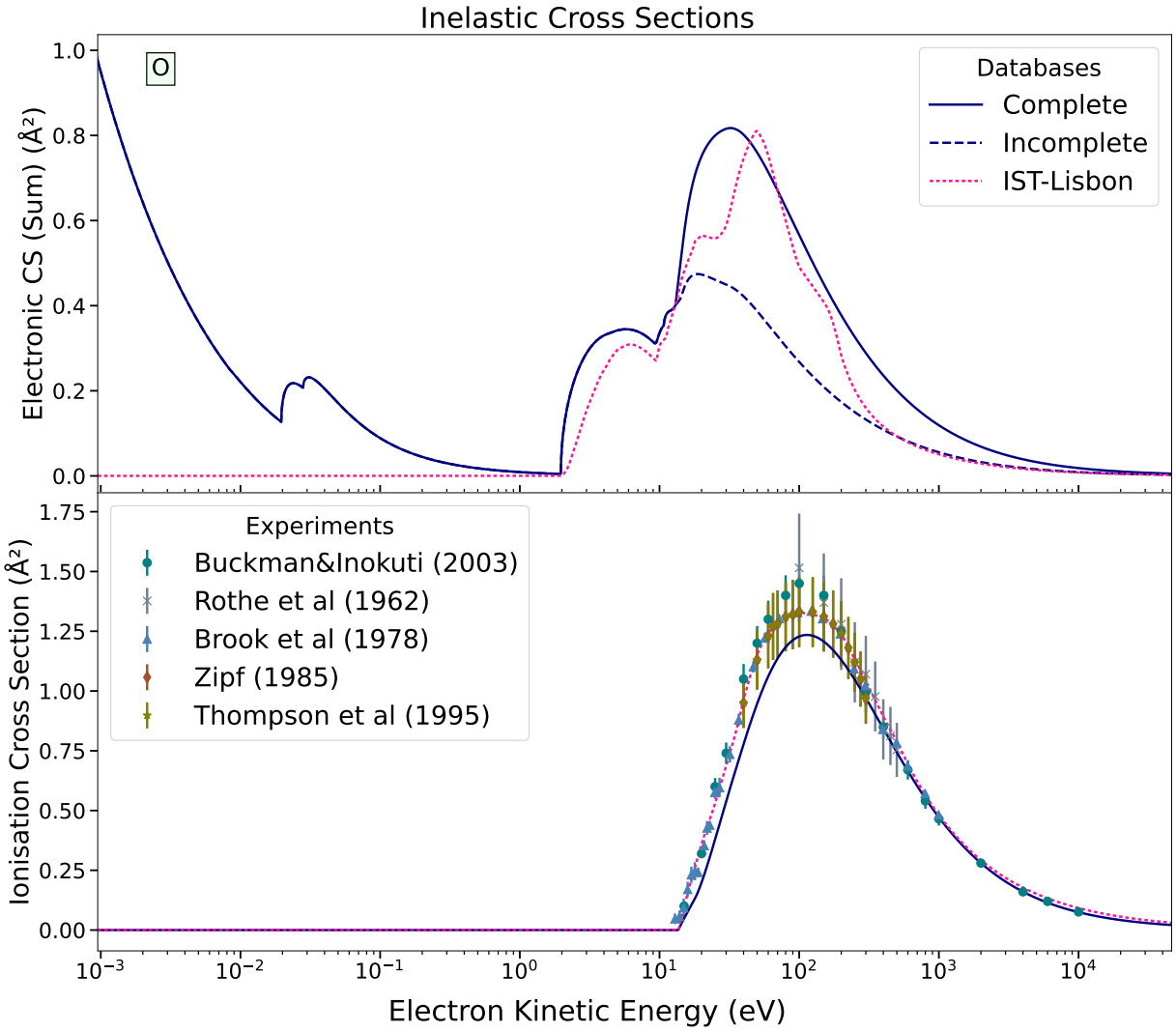

Figure 16.20: Comparison of the sum of electronic impact excitation and ionisation cross sections for atomic oxygen.

16.6 N

Cross sections for atomic nitrogen were mainly measured by the group of Doering and Goembel [222, 223, 992].

From the theoretical perspective, the most recent calculations were conducted by Wang *et al.* [975] from which two databases derive : the `BSR` and the `IST-Lisbon` which can be seen as reduced and reinterpolated version of the former.

Comparisons

Elastic CS fig. 11.6

- Below 140 eV : we use calculations from Wang *et al.* [975] (`BSR` database)
- Beyond 140 eV : our calculations of partial wave from the optical potential merge smoothly with the `BSR` data.

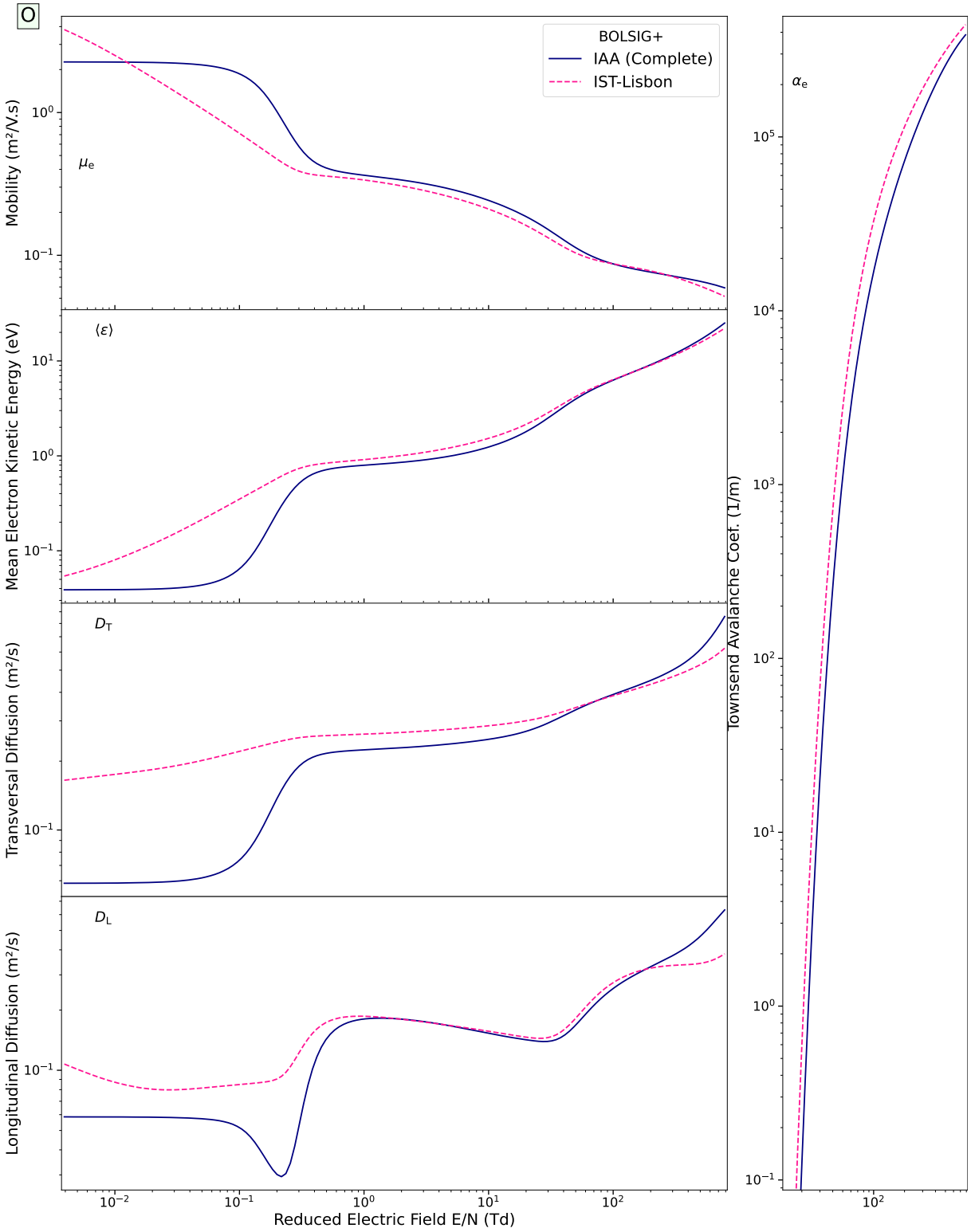

Figure 16.21: Transport coefficients in atomic oxygen as calculated by the two-term Boltzmann solver BOLSIG+ for different cross section sets at a temperature of 300 K.

Inelastic CS fig. 16.22

- Electronic CS : $\sum_{a'} \sigma_{0\to a'}$, three peaks :
  - △ First peak < 10 eV : due to spin-forbidden low-lying excitations ($2p^3\ ^2D^o$ and $2p^3\ ^2P^o$). The BSR calculations predict a sharp rise, whereas we fitted a curve rising more slowly to the data of Yang and Doering [992].
  - △ Middle peak ~ 12 eV : mainly from $2s\,2p^4\ ^4P$ allowed excitation and a small participation from $3p$ dipole-forbidden states.
  - △ Third peak > 40 eV : mostly from allowed $3s\ ^4P$ excitation and small participation of higher allowed excitations ($4s$ and $3d$).
  - △ In BSR, the two last peaks are merged into a mound. We find this a more 'natural' shape for the electronic CS in nitrogen.
  - △ IST-Lisbon does not include higher states than the lowest two spin-forbidden from BSR.
- Ionisation CS : We recall that we did not perform a fit with the RBEQ* model but derived the Q parameter based on the sum rule of oscillator strengths (see previous page 580). Worthy to note, the BSR calculations [975] seem to fit well the ionisation of Brook *et al.* [117] without taking into account metastable states, whereas Kim and Desclaux [506] obtained a good fit corresponding to a 70:30% ratio of $\mathrm{N}\,^4S^o$:$\mathrm{N}\,^2D^o$. To be continued...

Transport Coefficients fig. 16.23

- Below < 1 Td : Electron transport is identical in all databases since most is due to elastic scattering.
- Above > 1 Td : Mean kinetic energy and ionisation in our database is superior to the BSR, as expected from the higher electronic CS of the latter.
- Above > 100 Td : The effect of higher excitations than forbidden states (second bump on figure 16.22–top) is significant as can be seen by the divergence of the IST-Lisbon from the BSR database. Since the former does not include higher electronic excitations.

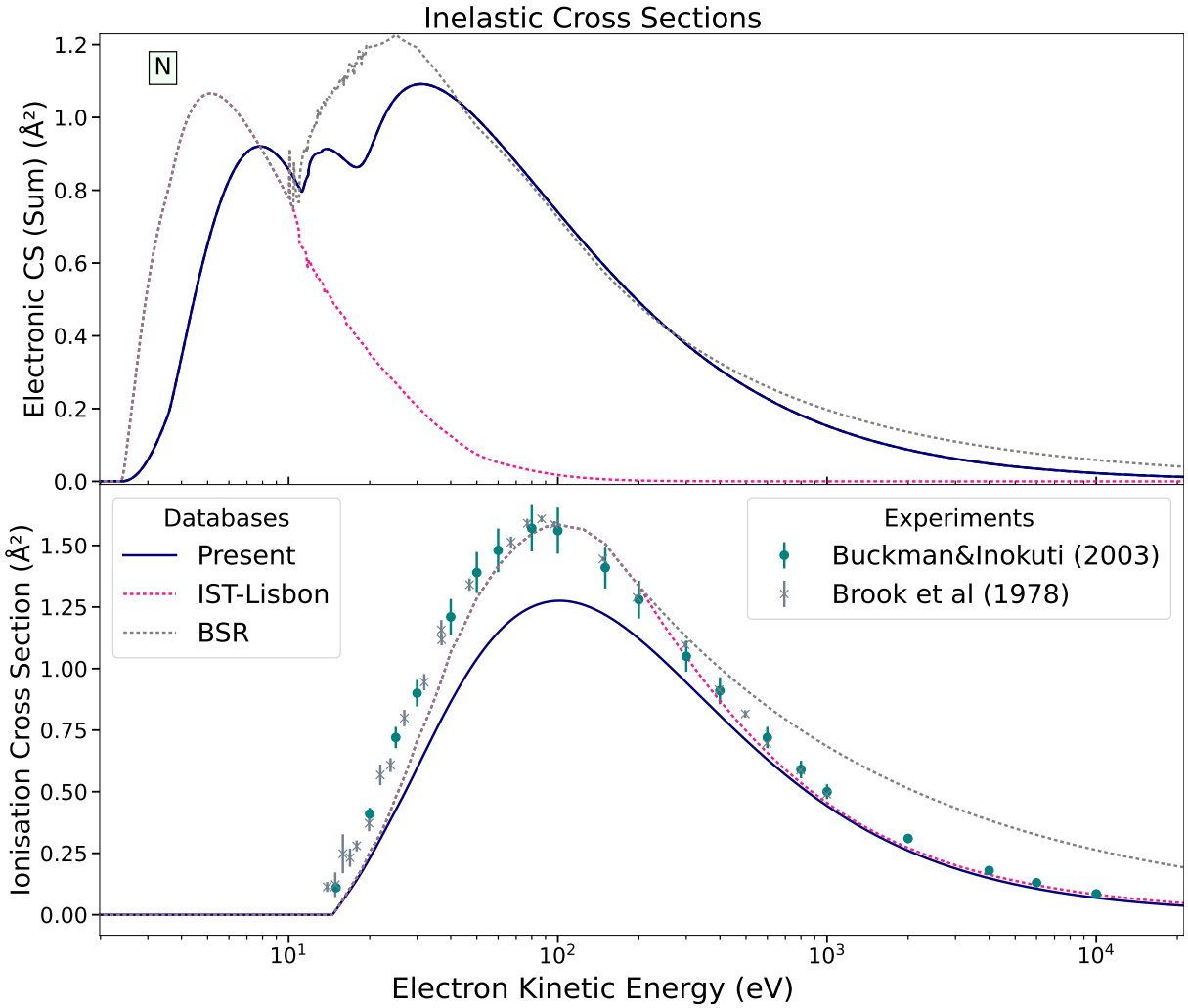

Figure 16.22: Comparison of the sum of electronic impact excitation and ionisation cross sections for atomic nitrogen.

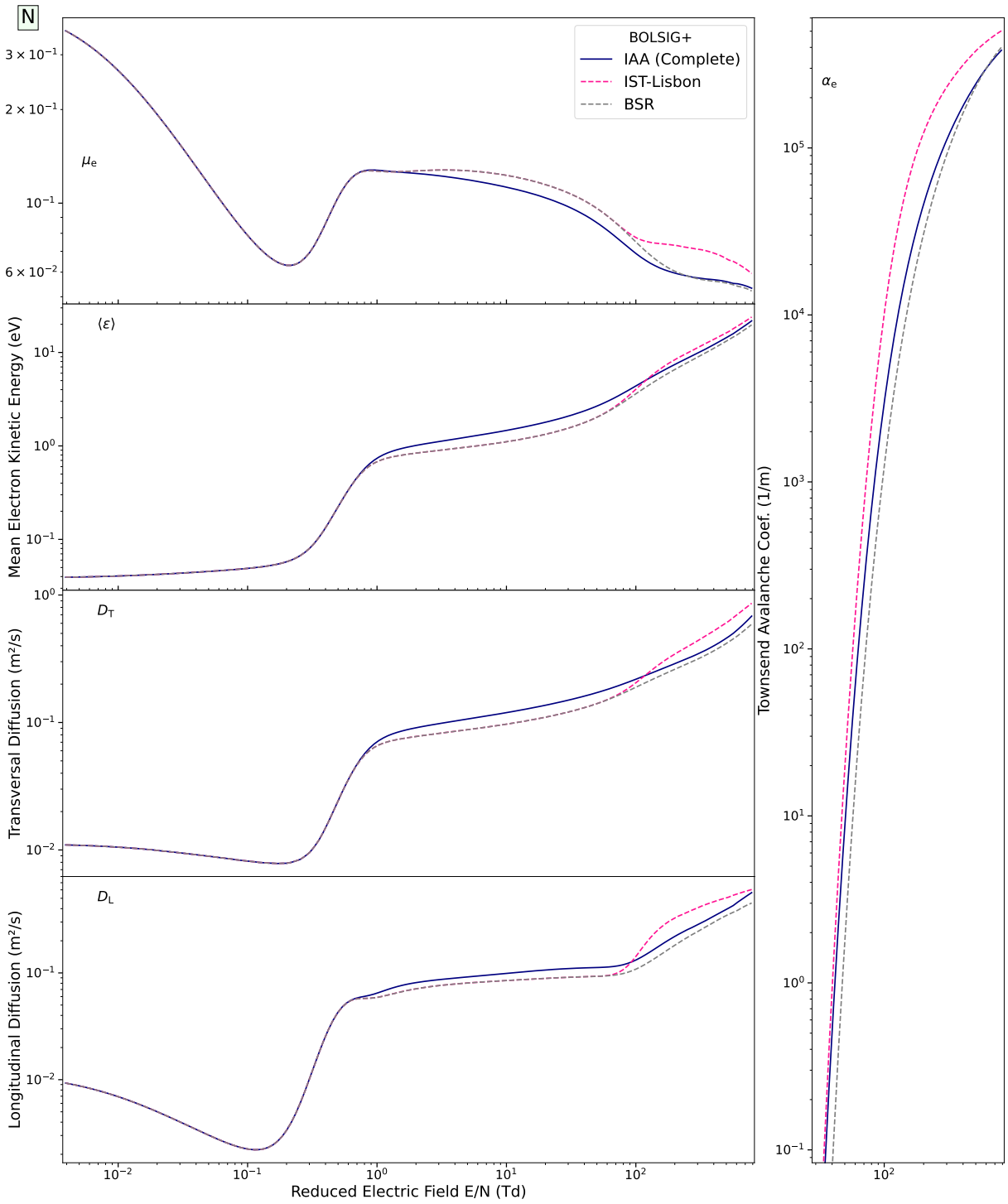

Figure 16.23: Transport coefficients in atomic nitrogen as calculated by the two-term Boltzmann solver BOLSIG+ for different cross section sets at a temperature of 300 K.

Chapter 17

Scientific Language

> *"Les langues sont faites pour être parlées,*
> *l'écriture ne sert que de supplément à la parole..."*
>
> — Jean-Jacques Rousseau, *Prononciation*

In his "*Traité des systèmes*" (1749), the French philosopher Étienne Bonnot de Condillac asks rhetorically:

> *Voulez-vous apprendre les sciences avec facilité?*

and answers provocatively:

> *Commencez par apprendre votre langue.*

Certainly, language is an essential element to the foundation of knowledge or at least its transmission. Cognitive sciences are arduously debating whether knowledge is possible without a language, but this is a completely other topic.

Transmission of knowledge heavily relies on its vector: a scientific language. Since science keeps not only refining but also revolving itself, an ideal scientific language must:

(i) be prepared to evolve alongside,

(ii) possess the most generic infrastructure possible to build knowledge from elementary cognitive bricks,

(iii) and have a consistent intrinsic logic that can only be defied by philosophers.

During a very long epoch, Latin, constructed on Ancient Greek foundations, was the primary vector of knowledge and profoundly influenced all languages on the European continent. Originally, Latin (and Greek) was used as the language of sciences and was indissociable from scientific education. It possessed all the vocabulary and grammar to be able to engage into philosophical debate.

After the fall of the Roman empire, the use of Latin was maintained for over a millenary, especially in administrative texts, treaties and scientific monographs. Then, Renaissance was not only a rebirth of aesthetic and humanitarian values, but also an enlivenment of European vernaculars* into scientifically active languages. The massive importation and resurrection of Latin words into European vernaculars at the time happened throughout the 16^{th} century. Next, the shift from Latin to vernaculars in scientific literature took place in the late 17^{th} century as prominent scientists, such as Galileo or Newton, started to publish in their own languages

*A vernacular is the language most commonly spoken in a region. In modern times, we are accustomed that vernaculars are official languages of the state. Historically, this was and still is not always the case.

and therefrom, the rest followed. The benefit of this shift was that there was consequentially much less obstruction to the access to knowledge by individuals. However, on the downside, the spread of knowledge between different countries would be significantly restrained and the scientific community feared the "Babelisation" of science [77].

At the time, there was a spirited discussion about creating a new international language for the scientific community. The society at the Renaissance was very earnest to recover the legacy of the Greek schools of philosophy and to search after a truthful description of nature. There were various attempts of creating a perfect language for science. However, the quest in search of absolute clashed with the imperfection inherent to human language and so, the idea that a perfect language for science could exist faded out.

Notwithstanding, the scientific community at the time continued to use Latin as a base for international communication. Scientific vocabulary was almost completely shaped by the Greco-Latin infrastructure of words, with their somewhat obscure radicals and various prefixes. Many words of Latin or Greek origin were converted in vernaculars and then used in scientific discourse. As a few examples:

- 'molecule' was derived in the 17^{th} century as the diminutive of 'moles' : 'mass' in Latin, to signify a tiny part of physical bodies.

- 'electron' was proposed by the Irish physicist G. Stoney in 1891 as the elementary unit of electric charge. The word 'electric', introduced in 1600, is of Greco-Latin origin for the material 'amber' because of its charge-separation properties when rubbed.

- 'interference' was used for wave mechanics in 1802 by T. Young from an earlier nominalisation of the verb in Old English 'enterferen' which was passed down from Old French constructed on Latin.

None of these terms actually existed in Latin, but were constructed on, or derived from, Latin roots. The creation of those terms was enabled by an agglutination of a root and an affix (prefix or suffix). A similar example was given in the first chapter p. 14 with the 'an-ion' and 'cat-ion' based on Greek prefixes (ana/cata) and Latin root (ion).

However, what is most stunning about all these terms, is that none originally bore the meaning that we ascribe them today. Nobody knew what molecules could be, how small nor even how big they could be! An 'electron' was not thought of as a particle, but a unit! Not to mention that a cation would turn out to be a molecule missing an electron. As for the verb 'to interfere', it was a sound analogy of cancelling contributions of waves, but still far from the phases of complex numbers.

The emergence of scientific terms conceals a complex history of analogies, derivations from concepts or words that philosophers of the past spent much time to construct. 'Molecule' for instance, was discussed by Le Gallois in the 17^{th} century, more than a century before Avogadro finally attached to it, the physical meaning of today. It is bemusing to think that philosophers whisper to the ears, the words that scientists crave to describe what they find or what they perceive.

Strange isn't it, to think that language after all, is not merely a means of communication, not just a vector of information, but a also a cognitive framework, a matrix for building knowledge. Stranger it was, how the shift toward this perspective of language – as a cultural soul, a cognitive capacity of a society – nourished loathsome supremacist ideologies which would later become newborn 'racisms'. The book of Olender [715] develops further on this issue.

As time passed, the usage of Latin, at least as a base, declined severely during the 19th century. Perhaps, to study machines was too busying to have time to learn an obsolete language. And after the turn to the 20th century, new terminologies in science had roots directly stemming from the official languages:

* 'Bremsstrahlung' by Sommerfeld for "braking radiation",
* 'spin', due to an ardent discussion about the fourth quantisation of the electron's state in atoms (maybe remembered from L. Thomas' article [929])
* and, of course, 'runaway', which was reportedly first used by Eddington [258, p. 32:left-bottom§] in reference to Wilson's article [986].

'Runaway', in this context, referred to the fact that these [run-away] electrons would accelerate in the electric field to such high energies until they start radiating rays of energy comparable to subatomic processes. Later, when interest in nuclear fusion was brought about, the term 'runaway' was perhaps based on an analogy of trains whose speed runs out of control, until they eventually derail or result in a train wreck; 'runaway' was the common term to describe such phenomenon*.

What is very interesting to note is that, perhaps, the 19th brought a baggage of tools, concrete insightful measurements, experimental evidence, that the scientists would turn away from books, literary studies, as they did traditionally; and start a new exciting era of science which was much more enrooted experimentally than ever before. It seems thus understandable that the concepts that emerged then – 'bremsstrahlung', 'spin', 'runaway', etc. – would not have been given abstract and abstruse Latin terms whose origin and meaning not many would fathom. This transition is natural, as one would attempt to describe what one sees or foresees in his or her own language.

For a short while, before the outbreak of WWII, it seemed as if German would ascertain its place as an international language of science. The turn of dismal events did not pursue this route, however. Today, English is considered the prime language of scientific discourse, and we may inspect it from a closer perspective in the following section.

17.1 English

According to sociologists, when an institutional power weakens and cedes to the emergence of smaller competing parties, the period traversed is known as a "critical juncture" [151]. Specific to scientific languages in Europe, the first linguistic critical juncture came in the late 17th century with the obsolescence of Latin as we mentioned above.

Then, a lively competition arose between European languages as to which one would become the new *lingua franca*. For a while, French had ascended to that position, albeit precariously. Toward the end of the 19th century, the European continent was linguistically tri-polar: French–for diplomacy, German–for sciences and English–for commerce.

The latter is today, the ongoing winner of that competition and the interested reader may find in Crystal [201], a detailed narration of how this came to be†. Briefly, the rise of English can be explained by (i) geo-political factors, in a first wave; and then echoed by (ii) socio-cultural aspects in a second stage, especially in the second half of the 20th century.

*It was used in the 16th century to speak about horses that would run out of control of their harness.

†It is reputed to be one of the few objective narrations of the rise of English without the "triumphalist tone which is unfortunately all too common when people write on English in English".

It is however not the aim to go over the global perspective, encompassing the press, advertising, broadcasting, cinema and music; tourism, travelling, politics, business, industry, technology and the many aspects which follow from the global stance of English. Here, I wish not to diverge on the multi-faceted aspect of English, but would like, instead, to refocus on the primary concern: English as a language for science.

Shortly, we may summarise the most-cited advantages of using English in science:

- Morphological simplicity : no genders, almost no conjugation, practically no declination.
- Concision : interchange of word classes.
  - Gerund↔*noun* : an electron scattering off a molecule ↔ electron *scattering* is a complex topic.
  - Verb↔ *noun*: electrons spread isotropically ↔ the electrons' *spread* is isotropic.
  - Adjective↔ *noun*: runaway electrons are scarce ↔ electron *runaway* rarely occurs.
  - Adverb↔ *adjective*: slow electrons scatter fast ↔ *fast* electrons scatter less

  Interchanging word classes enables to formulate concise phrases in English*.
- Grammatical flexibility : English is grammatically not a 'pure' language but a hybrid with Anglo-Saxon, Germanic, Nordic and Latin roots. As a result, it offers much flexibility when formulating a sentence.
  - Anglo-Saxon: "There are more issues to talk about."
  - Nordic (V2): "Never have we talked about so many issues."
  - French-like (SVO): "We ought to talk about more issues."
  - Latin-like (OSV): "About these issues, we must talk."

  Certainly, there is some subtle variation in the meaning conveyed by each of these sentences. The last line, would be a "declamative" English; to put more stress.
- Lexicon: Because of the innumerable importations and loans of foreign words during its evolution, English probably possesses the largest – scientific – vocabulary of all languages in the world. A few examples:
  - from German: Ansatz – initial guess to a mathematical problem
  - from Norse: Bulk – originally the cargo of a ship; now the most of an object, a volume, a size...
  - from Dutch: Trigger – to pull
  - from French: Evanescent† – another word for "vanishing"
  - from Latin: Equilibrium – balance
- Neologism : forming new words in English is fairly simple. This follows from the three points above.

*Compare with: "L'alternance entre les classes grammaticales des mots permet de formuler des phrases concises en anglais" in French.

†I tried to take an example different from the full encyclopedia of words imported into English during the Norman invasion.

  - Compound : 'isotropically-averaged' differential cross section (run-away is another example)
  - Inflection : 'thermalisation' (from 'thermal')
  - Loan : 'intershock' (I just made it up from French)

  It is difficult to find a French word used in science that is not already present in English.

- Outreach : Currently, no other language has a global outreach as expanded as English.

These advantages may well support the use of English in sciences, but may not, in any case, bring justification. The use of English today, in sciences, has little to do with any linguistic or cognitive trait, but, as had always been the case historically, is tightly bound to the ascension of English-speaking countries to power over the globe.

Understandably, English has also evolved considerably since it ascended to the position of a global international language. This, however, poses several problems from the perspective of English qs still participating to the cultural identity of a nation. Since it is the language most spoken today by non-native speakers, it is also, as a result, the language which is currently changing at the fastest rate. As Crystal [201] puts it clearly in his first chapter, a global language may not be 'owned' or claimed as property to a single nation, but must be shared throughout the world.

Although I enjoy imitating a pure Anglo-Saxon way of forming sentences, my (ab)use of English is noticeable in this thesis. I liken English to a linguistic playground because it is, to put it in delicate terms, striving to maintain a resemblance of coherence*. English has spread much faster than it was able to gather a coherent and even consistent grammatical structure. And this utter lack of consistency makes it, in my opinion, a language ill-suited to the communication of scientific knowledge. Below, I list some inconsistencies:

Spelling: This is probably the first issue as a global language; English spelling is not phonetic but an unkempt ensemble of unassimilated loan words. There are and have been many propositions to reform the spelling of English. Nevertheless, there are too many homophones in English that prevent a systematic solution in a spelling reform ('sight' clashes with 'site', 'red' with the past tense of 'read', 'write' with 'right', etc.)

Pronunciation: The next problem is directly related to the former, English pronunciation has been deformed very significantly over time to the point where no pronunciation can be considered 'standard'. With respect to the problem of spelling, it would be much simpler to change the way we speak and pronounce words so as to revert the shift in vowels that took place in the 17^{th} century. Words such as 'disappearance' would have to respect the "ea" sound in "stead". Again, such a change would be cataclysmic because we grew so accustomed to hearing non-standard English† in the media, that trying to revert the pronunciation would turn it into an (even more) unintelligible language.

Word morphology: There are too many exceptions to "general rules" to speak rightfully in terms of exceptions and rules. Here I give a few example of opposites:

- Coherent: ~~uncoherent~~ but 'incoherent'
- Balance: 'Imbalance' (noun) and 'unbalance' (verb)

*Coherency?

†American English is non standard from a linguistic perspective: vowels are absent in the alphabet (they are diphthongs) and the only vowel 'E' is mispronounced as 'ɪː' ...

- Stable: ~~instable~~ but 'unstable' though 'instability' not ~~unstability~~
- Tractable: 'intractable' or 'untractable' ?*

Then, there also exist words that are, from a semantic point of view, concealed double negations:

- 'Impaired' and 'unimpaired'
- 'Impeded' and 'unimpeded'

At times, it is hard to figure out when the preposition is a negation or an "enabling":

- Inflammable = flammable
- Invalidate >< validate
- Inhabitable = habitable
- Incapacitate = "discapacitate" but invigorate = "envigorate"

The Latin prefix 'in' is ambiguous because it can either indicate inward or negate. Better would be to drop it and use only 'un' and 'en' instead, just as in 'enable' and 'unable' which are both very clear. Imagine having to deal with 'inable'... As a result, it is not unimpossible to avoid misunderstandings in English...

The third problem is that there is no systematic way of distinguishing words from verbs. There are some terminations that are exclusive to verbs ("-ize", "-ate") and to nouns ("-tion", "-ence", "-ment") but most of the time, it is wearisome to guess if a word is a verb or a noun.

- Postposition: phrasal verbs are always separate (e.g. break down) whereas nouns or adjectives are in one word (e.g. breakdown)
- Preposition: there is no rule – act → 'enact' (verb), break → 'outbreak' (noun)

Subjunctive: in a scientific field, it is of primal importance to distinguish which assertions are hypothetical or depend from† their subject and which ones are objective. With the decline of subjunctive in English, this is not possibilitated any more.

In British English, the use of subjunctive was still fairly common and I have checked that all authors of British origin always used the correct form [680, 793, 922, p.301, p.585:eq.(4.22)]:

> "The probability that [an electron] <u>be</u> [backscattered] is [high,low,negligible]"

In American English, some authors would use "should be" like Slater [856, p.387:§III]; while in International English, this subtlety is washed away altogether. At times, I made correct use of subjunctive in this thesis, as I would have if I had written it in Spanish. But most of the time, I decided not to abuse of the correct use of subjunctive in order to avoid upsetting the readership. I made a compromise.

Negation: it is not possible to negate non-auxiliary verbs without putting emphasis on the negation with the verb 'to do'. This makes negation pointlessly cumbersome: ~~The electron scatters not isotropically~~ → The electron <u>does</u> not scatter isotropically Cumbersome negation is an argument against the assertion that English is concise. The most concise languages I know of, are either Slavic or Asian.

*go check Collins' dictionary, you will be surprized.

†See the "Phrasal verbs" bullet point on p. 630

Grammar: Once again, there may not be a coherent way to encompass English grammar. Linguistically, one of the most despised and unpardonable aspect of English grammar is the confusion of participles (passive voice) with the past tense (active voice):

- ✓ Write: 'wrote' (past) and 'written' (passive)
- × Increase: 'the energy increased' (active) and 'the increased energy' (passive), then what about our energy-increased electron (compound-word adjective) ?
- ? Prove: has anyone *proved* that English is a suitable language for global communication? Or does it remain to be *proven*?*

The second problem is about the transitivity† of verbs:

- Scatter : 'electrons scatter in the gas' (intransitive) but 'the gas molecules scatter electrons too' (transitive)
- Decrease : 'the electric field decreases' (intransitive) but 'accumulation of space charges decreases the electric field behind ionisation waves'‡ (transitive).
- Accelerate : electrons accelerate (intransitive) but the electric field accelerates electrons♪ (transitive)

Transitivity is a problem for parsing scientific articles outside of one's field. There is no easy way to resolve this issue. I sense that archaic verbs would distinguish transitivity with the preposition 'be' as in 'befit' and 'bescatter' (which are exclusively transitive). The subject of those verbs transforms the object into a state which is given by the root. An archaic example is 'darken' (e.g. the skin) and 'bedarken' (someone who causes it to darken).

Sometimes, there are very big surprises about the (in)transitivity of verbs such as 'to obtain' which, most of the time is transitive (obtain something) but also exists weirdly as an intransitive:

> "Such a situation actually obtains when the incident particle is heavy ($M \gg m$) and at least moderately fast." [427, p.334:§4.4]

The transitivity is partly smeared because English lost the presence of *reflexive* verbs. In other European languages, reflexivity unambiguously determines the intransitivity of a verb. Compare in French ("disperser" = "to scatter"):

- "Les électrons se dispersent" (intransitive reflexive)
- "Les molécules dispersent les électrons" (transitive non-reflexive)

Semantic: Because of a queer grammar, the semantic aspect of English can, at times, become absurd. The very way we coin new terms can illustrate, not only how unaware we are of the linguistic aspect of languages, but also how many thoughtlessly abide by a new terminology.

> "Cognitive science" ... Which sciences are not cognitive?

*Check your dictionary, this case is very interesting!

†By the way: transitiveness?

‡A correct formulation is : "The electric is decreased by ..." or replace "decreases" by "screens".

♪I tried to privilege the formulation "electrons accelerate in the field"

'Cognitive' relates to the process of forming knowledge and understanding. Is it possible for us to have a branch of science totally unrelated to our cognitive aspects? I understand it is supposed to be: "the branch of science that studies (human) cognition". But then, it should be named "Cognology"*.

Certainly, this is not a problem exclusive to English but to virtually all language to confuse the trait with the purpose. However, in English, this is greatly facilitated as illustrated below:

- Gerunds: "Dining table", "drinking fountain", "sleeping mattress"... yes, those all express the purpose of the object, but why the gerund? A "staggering achievement" is it an achievement so unstable that it staggers until it crumples?
- Phrasal verbs: "depend on" is constructed in analogy to "rely on" but the image is incorrect. It should be "depend of" or "depend from" as in all other Romance languages.

Confusion: Because of the reasons exposed above, I think that English is confusing from the outset. One requires an immense amount of drilling, inhibition of logical reasoning and effort to grow accustomed to the way English is used by fluent speakers.

In the following examples, I find it difficult to find the verb in the sentence when we parse it in a first run:

- "Coronas from objects on the ground limit the electric field there to typically 0.1 to 1 $\times 104$ V m^{-1}." [764, p.84]
- "Polling at the time suggested Salmond accurately gauged the popular mood on the Queen" press release
- "The slight shift of the M3DW-OAMO results from the θ_K direction was discussed [previously] and is due to the fact that this model includes final state electron–electron post-collision interactions." [550, p.5]

All in all, the lack of firm grammatical structure in English makes it a profuse language in garden-path sentences. I really have to strive hard to avert creating such ambiguous syntactical structures. The solution proposed is often to make shorter sentences, or use more punctuation. I think, however, that the problem is more profound than that. I liken the native way of speaking English to a gradual laziness to communicate plainly in written form. Most of the time, I cannot distinguish between the levels of written and spoken English.

Any article taken at random written by a contemporary speaker, has examples of syntactical structures that bespeak how English speakers are deprived of alternative ways of expressing themselves. On an article featuring on the front page of the journal nature:

> "But in practice, people still dispute precisely what needs reining in, how risky AI is and what actually needs to be restricted."

I can understand that "needs reining in" is a contraction of "what needs to be reined in" and thus, that English speakers hail the conciseness of English. I also understand that the author already uses "needs to be" at the end of the sentence, and thus thought it would be nicer to use a different syntactical structure in the first clause so as not to make the sentence too repetitive. But I also cannot believe that this syntactical structure is universal. I assume

*Unfortunately though, this term is just the name of a parading private business company.

I would be severely reprimanded for saying: “I need processing data” or “Their measurements needed revising”, “should we talk planning the project?”, etc.

I think these syntactical problems are deeply enrooted in the former abuse of English word classes. Namely, that gerunds are too often employed as nouns for continuing processes, and that speakers cannot distinguish between both uses.

It may help, in the short term, to endorse the training in English language skills by:

- instilling English as early as possible in the minds of the younger generation,
- by continuing to discriminate against foreign learners who do not have the knack for speaking in the queer zeitgheist of the contemporary anglophone community,
- or by continuing to debilitate the use of other languages in science to prevent scientists from thinking and sharing their work in other languages than English.

However, I do not find any attractiveness in any of the solutions mentioned, nor do I find myself capable of shrouding the emotional heaviness of the way I formulated those three options.

I cannot disagree anyhow with Wilhelm von Humbolt when he said:

On Language, On the Diversity of Human Language Construction and its Influence on the Mental Development of the Human Species.

> “Language is, as it were, the outer appearance of the spirit of a people; their language is their spirit, and their spirit is their language; we can never think of them sufficiently as identical.”

The only way I was able to overcome my strong aversion against the use of English in science, was to reconnect with the spirit of past geniuses that once contributed to the construction of knowledge as we have inherited it. To anyone that traverses internal strife about having English as the global language, I recommend reading articles written before WWII, where I found a very pleasing and personal tone to English as in the articles of Eddington [258] and Mott [678]. Outside the scientific sphere, the English literature of the past is very rich. Fortunately, being able to choose my own way of spelling and enjoying the freedom of resurrecting archaic words such as “whence”, “yon”; filled my time writing this thesis with delight and rediscovery both of the language and the science I gathered.

I would not dare advocating that English should be dethroned from the status of a global language. However, if it is to maintain that prestige, then the “native” community of English must inevitably relinquish their ownership or rightfulness over the language. The way we choose to speak and write English should be much more free so as to prevent unilateral thinking and create a chasm between fluent and not fluent speakers; which I foresee is happening nowadays.

This is a very complex issue because one cannot dissociate easily a language from its cultural background or even its spirit as W. von Humbolt put it. This is why there is maybe another, more desirable and indisputably more just alternative solution for the future, which I present in the following section.

17.2 Esperanto

I had heard of this mysterious artificial language before, at secondary school, but shared the same prejudice that all learners of foreign languages have: why should we learn a language whose speaking community is so small and that is not even an official language at a national level?

This is because we often think of a language in the traditional way: a mere tool of communication, a vector of information. However, throughout my university studies, I realised that language bears also a cognitive dimension and that thinking in a different language can have an impact on scientific investigation. It is fair to have a common language to relay information, but it is certainly not fair that the burden of relaying information in a common language be carried by scientists alone.

During the writing of my thesis, I suddenly got curious to know more about the story behind Esperanto and consulted various sources. I became immediately astounded by the many positive aspects of this artificial language. I will distinguish pure technical linguistic aspects from humanitarian and cultural traits.

Humanitarian. Esperanto was created with the hope of bringing humanity under a common union. Its originator, L.L. Zamenhof, yearned to bring a peaceful end to the conflicts that scarred the many different communities living under a common imperial rule in Europe. He came from a Jewish family living in Poland under the rule of the Russian empire. He travelled a lot, learned many languages and realised that learning a new language would not have to be necessarily difficult if the learner did not have to assimilate the cultural and historical traits which the language bore.

He was not the only one of his time to share this dream. Actually, the beginning of the 20^{th} century was marked by a simultaneous emergence of many artificial languages due to the competition between French, English and German to take the position of a *lingua franca*. However, he was the only one not conceited to the point of wanting to hold a firm grasp over the future of his language. Instead, he founded an international committee with various members which would discuss matters about the language and make polls among the speaking community for changes or amendments proposed to the language.

Thanks to this, Esperanto was able to survive as the only artificial language still spoken today. Because it reflected the democratic values of our modern society. More information about the history of Esperanto can be found in Garvía [320].

Grammar. The construction of Esperanto reflects a consistent logic befitting a scientific language. It is genderless and its conjugation is not pronominal but only based on tenses. There are no irregularities in its spelling and it is fully phonological. All grammatical classes are unambiguously defined:

- Substantives (nouns): all end with the letter 'o' (e.g. 'energio' for energy)
- Adjectives: end with 'a' (e.g. 'energia' for energetic)
- Verbs: end with 'i' (e.g. 'ŝanĝi' for the verb 'to change')
- Adverbs: end with 'e' (e.g. 'energie' for energetically)

Other classes such as pronouns, numbers, conjunctions and prepositions are concise and easy to remember. Notably the correlatives are very logically organised in a matrix which maps beginnings (for demonstrative, interrogative, negative,...) to endings (for place, time, people, quantity, cause,...).

Then, the morphology is also very clear. One may either add a prefix or a suffix to the root of the word like in most Indo-european languages. Prefixes include 'dis', 'pra', 'ek' indicating in all directions, long ago, suddenly. Suffixes are plentiful and specify whether the word is an actor, a container, an action, a group, etc.

A succinct introduction to Esperanto's grammar is available on `https://lernu.net/gramatiko`.

Culture. Virtually, Esperanto is like a cultural whiteboard. It is the language currently most devoid of cultural bias, because it bears no history of idiomatic expressions. At the same time, it has the potential of being the most culturally rich language because it has native speakers scattered around the globe issued from many different local cultures. Learning Esperanto would enliven the scientific community of today as much as prominent scientists of the Renaissance had the delight of rediscovering, but also reinventing their own vernacular language.

Several scientists mentioned about the usefulness of Esperanto as a scientific language [357, 663]. These prospects were stifled by the stirring political contentions in the course of the 20^{th} century and still distracting us today. Sadly, no one seems to consider seriously the possibility of promoting the use of Esperanto in science nowadays. I hope this will gradually change with time.

In brief, of all the languages I know, if there is one language better suited for science it is definitely Esperanto. Out of many reasons, I name three:

- Clarity: the purity of Esperanto's grammar would greatly facilitate the learning and mastery of that language. This would be a relief to the stress and injustice of learning and mastering English.
- Flexibility: as science evolves, it is important to have a language whose infrastructure is solid yet flexible enough to adapt to the new discoveries made in science. Such is the case of Esperanto.
- Ethics: Having Esperanto as a language for science would promote building a scientific community whose values are reflected by the language it speaks.

As an illustration of what Esperanto looks like, I translated and corrected the English abstract into Esperanto at the beginning of the thesis on page xi. I hope I will be able to improve my skills of Esperanto in the future and explore better its possibilities.

Notwithstanding, the most beautiful fact about Esperanto, is not its grammatical coherence but that it has never been used as a means of domination...

Chapter 18

Some Retrospection

"I would prefer not to."

— Bartleby, the Scrivener*, 1853, A Story of Wall Street*

I would have liked to conclude this thesis in due manner but I find myself unable to gather the words to do so. I was astounded by the difference I see myself now, compared to when I had just started. Of all the many things I have learned, during my doctoral journey, there is one thing I certainly did not learn:

Concision

Although it is too late to try to do so after hundreds of loquacious pages, I would like to share – in a few words – some personal thoughts in retrospect to my work.

18.1 Toward a Deontology of Science?

If translated into English, "deontology" based on $\delta\epsilon o\nu$+$\lambda o\gamma o\varsigma$ from Ancient Greek, could mean the "discourse about what ought to be done" or the science of duty and moral bindings.

Although I did not work on living beings nor did anybody directly depend on my work, I still believe there are some issues about how we relate to science and how we work as scientists. I cannot give this issue the full importance that it deserves, nonetheless, I feel adequate to find some place for it at the end of this thesis.

In the following, I write a few sentences on different aspects of science nowadays*.

In the next section, I offer a few advices to future students. And to conclude the thesis, I end with acknowledgements.

Self-plagiarism In this thesis, I absolutely avoided recycling any phrases, paragraphs from my previous publications.

To me, I strongly share the view of Kafka about the imperfection of language. There are endlessly better ways in which to reformulate one's assertions. Nonetheless, there are several disappointing examples of authors that reused some of their texts from previous publications without quoting them.

*Some things were too upsetting to write black on white, so I buried them in white font...

I can understand that it may be a burden to try to reformulate something that we have been working on for the past ten years. But this betokens another problem: that we gradually become incapable of innovating, taking a different perspective and correcting our previous mistakes. Self-plagiarism is okay only if it is clearly indicated (e.g. we requote our work: " ... "). However, this is probably not going to be a problem in the future with automated generation of texts...

Referencing In the majority of the citations in this thesis, I strived to place the exact page, equation, figure or paragraph to the source I was referring to, in order to facilitate the traceability of my work.

It is a great strain to look for the exact formula that we are thinking about or the exact plot that we remember we have seen once. However, it is not only useful to the community but to ourselves. Science is very fragile and mistakes may slyly slip into typographical errors at any time. It is therefore important to take the time to be sure about what exactly we are referring.

Doubts I strongly believe that doubt is an inseparable part of knowledge. I tried to create a special place for my doubts in this thesis so that they would not subvert the relevance of my work, but at the same time that they enlighten the path toward open questions.

Science is a continuing open debate about our understanding of nature. The assertions we built are founded on our premises and we should always make sure to put them together when we present our results. That was the idea about the framed list on p. 149. Multiple times, I would also remind the reader to vigilance, about the limitations of the model and my doubts about the importance of other effects that would significantly distort the results presented. I admire authors who, with very few words, express their surprise at an unknown discrepancy and resist the temptation to fit in an explanation. Good examples of open discussions are Khakoo *et al.* [491], Kim and Rudd [507], and Zatsarinny *et al.* [999, p.13–4, p.3958:right§, last§].

Self-Critique This is the direct continuation of the previous paragraph. Even if I did not have the resources to palliate the limitations of my work, I tried to explore the limits of my model and from there, estimate a range of validity.

A deductive approach in science is only possible in the negative: the ability to disprove a hypothesis but not to prove. When we propose a model, adopt a premise or reach a conclusion, we should not only already have in mind a possible counter-example or method of falsification, but we should also find the courage to expose it in our publications. It is one of the toughest problems I find in science, to find the balance between self-criticism and confidence.

It is true that at first, this exposes us to the risk of being refuted, but science progresses through funerals and we should not identify our efforts to the models that we build. There is no vanity in ephemerity, there is no progress without failures. I respect the views of the Atomic Collisions Group from the University of Wisconsin's, who humoursomely set up a "hall of failures" on their homepage* to illustrate how much serious research is paved with mistakes thwarting scientific output.

Peer-reviewing All my experiences with peer-reviewing, turned out (ultimately) to be positive ones. I received many pertinent comments and suggestions from my first reviewers that I shall duly thank in the very last section of this thesis. Luckily, it was not until my third paper that I

*`http://raptor.physics.wisc.edu/fail/`

got confronted with the contentious archetypical personality who had difficulty in concealing his complacency at discrediting my work.

Those were tough times but I made a great effort in addressing all the critiques that had some foundations in them. Nonetheless, it also spurred a great wave of angst at the level of disrespect that can be put under guise in the peer-reviewing process.

What I disapprove about the peer-reviewing is the anonymity. The reviewer, when he or she does a good job, should be duly recognised because it requires much effort to understand someone else's work and bring a critical improvement to its quality. On the counter part, not benefiting of anonymity would also prevent deplorable traits of unnecessary disrespect and the ridiculous need for reviewers to earn recognition by being bribed with more citations.

From my perspective, my most useful reviewers were people who knew me and who had accepted to review my work. I think peer-reviewing is an ingenious collaborative implementation of Hegel's Thesis, Anti-thesis, Synthesis pillars. I strongly support that articles be published with two columns: authors alongside reviewers. It would also greatly relieve the burden to prove our productivity to the exterior.

Sharing Data It was very important to me not to finish my thesis until I had something to share. In a data-driven scientific era, there is no better way to contribute than to disclose data in a safely guarded repository.

Today, this is possible with the digital object identifier and the generosity of public organisations to host massive servers supporting open science. Unfortunately, stress is almost exclusively put on paper output. Paradoxically, advance in science is at the present time mostly boosted by sharing common pools of data or codes. Notwithstanding, there is little or no recognition to the work done in compiling databases and making them available in machine-readable files.

This thesis would have never come into being without the existence of servers such as LXCat and NIFS. Still, even though it would benefit everyone, there are publications that list the data they used from sources scattered in all corners of the literature but did not choose to take on the responsibility to make them available to the rest of the community.

Given the critical importance of data, we should think about reviewing numerical databases and treating data as the primary contribution of a scientific output and not as a bonus to research.

Time A critical turning point during my thesis is when I started working for results and not for time. Although I believe it is the way it ought to be, it brought many troubles. In retrospect, I do not think it is possible to revert this problem. Time is the ultimate emperor, and we should abide by its rule...

18.2 A different epoch

Looking now not at the immediate past, but much before I came into existence, I find myself in utter admiration of the legacy of our scientific predecessors. The lens of time is a highly distorting one, but there is no other glass to look into the past. I have little notions of anthropology but there are some traits I venture to identify.

Bibliography One of the major differences about articles published at the beginning of the 20^{th} century and today is the number of citations that they contain. In the past, twelve could be a sufficient number of references. Nowadays, it seems there are never enough references to give credit to every one. Even now, with over a thousand references, I am still anxious about having overlooked the work of some pertinent source to the field I broached.

The problem with such an immense number of references is that one has no time to really understand and read them in depth. I have my favourite references that I would read *en long et en large* such as Inokuti [427], Itikawa [439], and Takayanagi and Itikawa [908]. But the vast majority, I only took a glimpse at them. The problem is complex because, with reference management software, we may generate an indefinite amount of bibliographic references at no cost.

I imagine that in the past, scientists had much better knowledge of each other's work. In contrast, they had also much less overview and hindsight than we do today. I found the re-transcription of Goudsmit's talk (`https://lorentz.leidenuniv.nl/history/spin/goudsmit.html`) very insightful in this respect. About how it was like to work in science in the 1920s'.

Archive On the other hand, our access to worldwide research, recent or far in the past has never been so facilitated. I must duly thank my department's librarian for finding references for me and access to many journals. Furthermore, I acknowledge the indispensable helpfulness of open-access hubs. I hope that we could bring more support to open-access science **not** by paying golden access to the paperless paper industry, but by officially supporting projects like:

- sci-hub `https://www.sci-hub.st/`
- the internet archive `https://archive.org/`
- the arXiv `https://arxiv.org/`
- CodeBerg `https://codeberg.org/`
- Zenodo `https://zenodo.org/`
- LXCat `https://nl.lxcat.net` (specific to our community)

I think the ratio of value/investment surpasses the one we spend in other resources by at leat one order of magnitude. Our money should reflect our will, not our fears. I have come to use all of those resources and found them much more resourceful than payed services.

Yet, despite this advantage at our disposal, there is a feeling of anxiety indissociable from browsing through archives. The further we dig, the more our hopes of finding what we are looking for erode. There is always a limit to the things that are documented, no matter how much or deeply they are documented. We may stumble onto a formula, whose notation we have no means to decrypt. We may debouch onto an article outside our comprehension, intellectually or linguistically. Or we may stumble into a dead end such as a "private communication" or a number that has manifestly popped out from nowhere. This impression, Derrida and Prenowitz [214] call it "Mal d'Archive" translated as "Archive Fever". Derrida explores in great depth, beyond science, the importance and impact of archives on sociocultural identity, on granting authority, on justification, etc.

I find his analyses very timely and relevant, especially today where we have constructed the biggest archive in human history and where a strife happens not merely for the access to information but for the protection against disinformation. What we can most remember is that archives are a double-edge sword: on the one hand they are used as a foundation for truth, justification; while on the other hand, they are subject to interpretation and manipulation.

Communication Another great difference is the immediacy of the system of communication today. From my understanding, scientific journals were really like journals: i.e. a relay of information, updates, suggestions, ideas, notes... When I consult, for instance, Eddington [258], Franck and Grotrian [300], and Wilson [986] I see a very interesting style of writing. An account of one's insights, about possibilities, about observations in experiments with a few figures when obtainable.

Today, we are conferred the possibility to speak, to express ourselves in many more ways. However, in a world where everyone is given a voice, only the loudest will be overheard. Now that we have access to this incommensurable amount of information, instantaneously, I find it harder to engage into a scientific debate.

Thankfully, anthropologists take the time to study the evolution of human conditions and its impact on society. I found particularly useful the work of Virilio [963] about the "tyranny of velocity" in our modern times.

Media Im*media*tely related to the ease of communication, is the overwhelming mediatisation of science. Since the progress in our society is essentially driven by technology, too much emphasis is put on science to the point that the mass media seems incapable of differentiating the complex peripeteia of scientific investigation from the episodes of an entertainment series. It is most deplorable to me to hear everywhere the expressions of "selling your science" or "make your research a breakthrough over the world".

These expressions have so much exacerbated my attitude to science that I would start seeing articles as advertisements for formulae and methodologies full of defects. Certainly, there are some dubious behaviour I saw in many articles, about some strange bias in how they selected their sources, about their omission to disclose the values of the (semi-)empirical parameters they fitted, about their staged figures comparing their results with other references...

From my perspective, I am wary of how the content of scientific investigation is distorted by the mediatic coverage they receive. The visibility that we are conferred through the number of articles we publish is distracting us from our primary concern. There is no further need for "breakthroughs", we have broken enough already. Let us gather the remaining pieces while they are still here...

Authorship It is good to know the source of one's information. It is important for tracing knowledge and giving due recognition. It could be, that in the past, individual contributions to a scientific study were well defined, or it could also be that not. Regardless, today it is even more blurry. Leading-edge research now depends on the collaboration of gigantic international groups working together on different aspects of the research. Some of those aspects may still be acknowledged in the form of publications, but a non-overlookable contribution lacks a proper recognition.

I understand that scientific research has evolved at a bewildering rate over a short interval of time, but so have changed the ways to produce scientific output. This was probably already true before, but it is even truer today: science relies heavily on the contribution of individuals which are not given due recognition in the scientific field.

There is certainly a part in innovation, improvement of existing models, but to be successful, science requires a lot of bookkeeping, handling databases, technical software development and student supervision... Those are not low-level tasks and can be much more exhausting and challenging than to produce new results. An overweighted emphasis on authorship has, from a personal point of view, also stimulated a decrease in scrupulousness.

I think science is, both at a personal and at a societal level, a sufficiently rewarding endeavour, that it needs not be distracted with an output metric that reflects the structure of a worldwide videogame.

Objectivity Although the objective of natural sciences is to give an objective description of reality, the objectivity of science is subject to much subjectivity.

The greatest limitations that were imposed on my thesis came from a lack of time and resources. I had to impose them myself and this did not stem from an objective decision. It is very hard to find out which physical effects are relevant or not in the research conducted and which are less relevant. The relevance can be estimated only once the problem is framed. And the very framing of the problem is an entirely subjective process.

I was also impressed to see how the objectivity of science evolved over time as analysed by anthropologists. This can been observed in the evolution of atlases by Daston and Galison [210], how the advent of photography and machine-produced graphs suddenly imposed themselves as new standards of objectivity. Since now, much of our results rely of the output of machines, we might be tempted to see ourselves closer to our ideal of objective science. However, there is always some intervention when we present the data to make it intelligible to us, as Lynch and Edgerton [614] argues. The scales, the colours, the processing algorithms, the resolution, the sampling... In many cases, it is hard to reach a consensus about what we are measuring. In scattering experiments near resonances, do we choose to stay on the peak energy while varying the angle or do we maintain the energy fixed? In forward scattering, how do we emulate non-adiabatic effects at high energies in semi-empirical models?

There are millions of instances where scientifically "objective" output requires human intervention which, by nature, is subjective. Fleck [294] reminds us how perilous it is to grant scientific results an objective status and therefrom use it as a justification for political decisions. In the same way as archives need interpretation to derive meaning, so does information extracted from contemporary scientific conclusions.

Overall, I would say that the information we obtain is objective; it is a measurement or an indicator that was extracted from reality. The hardest part is to unveil its relationship to reality, where does it come from, how does it emerge? Knowledge enables us to interpret information, to relate it with other observations.

However, the way we see this relation depends on us, our perception. I "know" electrons interact through their electric field, but my colleagues will tell me they interact through quantas of virtual photons they emit. Will anyone prove they interact through a distortion of the space around them?

I would say that a good scientific study maintains a balance between (i) the information it gathered/produced and (ii) the knowledge about how this information was produced, what it signifies and what can it be related to other information. In a simple formula:

$$\underbrace{\text{Information}}_{\sim\text{Objective}} + \underbrace{\text{Knowledge}}_{\sim\text{Subjective}} = \text{Science}$$

Of course, this equation, though eloquent, looks really too simplistic to be taken on serious grounds.

And this, I hope,

will

at the individual level

beyond our attachment

prompt us to acknowledge that

science

a visage

takes

at a societal level

that reflects

our culture.

Agradecimientos

Acknowledging is too little. I wish to *thank*.

I bethank my two supervisors Alejandro and Nikolai. Thank you for your support, your advice and your patience. This thesis was really a challenge and would never have been possible without your guidance. Thank you Alejandro for saving my work in the most critical moments that had erupted overnight, for always being able to figure out a reasonable solution and keep a straight path. Thank you Nikolai for teaching me how constructive and powerful can critical thinking be. You both helped me to find clearer ways of formulating my thoughts. And most importantly, thank you for your faith.

I thank my reviewers, those who helped me significantly improve the quality of my publications as well as those who taught me to hone better my weapons for the war we wage against our ignorance. I especially wish to thank the jury for accepting to review and assess my thesis. You have had a profound influence on my work.

I thank my colleagues from the IAA, those I met at the beginning as well as toward the endless(-like) ending of the thesis. Thanks to you, the institute, which looks like a prison from the outside, felt like home from the inside. Thank you for all the adventures we went through together, Miguel, Ny, Ricardo, Mike, Manuel, Ban, Estef, Florian, Azaymi, Denis, Beth and all the gang of new students that suddenly refilled the institute with a great atmosphere after a long and sad period of crisis.

Muchas gracias al personal del instituto, los que me habéis permitido extender mi estancia, los que me habéis ayudado a resolver los problemas, los que me habéis abierto la reja a cualquier hora del día o de la noche, a nuestra archivista y bibliotecaria que me ayudó a acceder a los artículos los más inencontrables del mundo.

I thank my flat and house mates that made me it difficult for me to leave Granada. Thank you Florian for all those nice moments together, for all the fun and for sharing your spirit for adventures. Thanks to those who made my stay possible in Norway. Kine, Mads, Nikolai, thank you for the good times spent there.

Thank you very much Greg and María for saving me from the hustle of the city and letting me find tranquillity. I also appreciate a lot that you shared your passion with me and included me as a family. Thank you especially for helping me to recover during my toughest times. Gracias María por compartir tu experiencia de la vida y por tu sonrisa indeleble.

Luego, muchas gracias a Gerardo y Julio, mis compis guapis del IAA. Gracias por darme otro techo en la recta final de varios meses. Me habéis permitido dar lo mejor de mí. Gracias por vuestra generosidad y la buena convivencia, los momentos graciosos e incluso serios compartidos.

Děkuji mé rodině, at' jsem se vracel kdy jsem se vracel, vždy jste mě přivítali a podpořili v mé práci jak jste kdo mohl. Díky za všechny veselé doby a prázdniny spolu strávené, které mě osvobodili z mích bujných myšlenek.

Les agradezco a mis maestros de taiji, a Kamala, Fernando, Sundari, y todos mis compañeros. Gracias por vuestra paciencia y por acogerme cuando apenas había llegado a Granada con sólo un poquito de español en los labios. Gracias por enseñarme con generosidad vuestros conocimientos y por vuestra confianza en mí.

Gracias a mis profesores de baile, Rosa, Vladi, Eli, por compartir el buen gusto de bailar con sencillez y alegría. Gracias a Granada por todo lo bueno que ofrece, a las ecotiendas a la cultura, al buen gusto de vivir.

謝謝我台灣朋友.你們讓我打開眼界. 讓我多認識世界也認識自己.

My last but unleast of all thanks,

謝謝妳愛眉. 沒有妳沒有愛, 有了妳眉有愛.

Merci pour m'avoir partagé

Thank you for

everything.

Bibliography

Programs, Codes, Databases and Electronic Resources

30. *Atomic and Molecular Numerical databases*, National Institute for Fusion Science (`https://dbshino.nifs.ac.jp/nifsdb/`) (453).

71. Biagi, *Fortran program MAGBOLTZ cross-sections* (`https://magboltz.web.cern.ch/magboltz/`) (586).

215. (a) Desclaux, "A multiconfiguration relativistic DIRAC-FOCK program", *Comput Phys Commun* **9**, 31–45 (1975); (b) "Erratum notice", *Comput Phys Commun* **13**, 71 (1977), 328.

219. Olver, Olde Daalhuis, Lozier, *et al.*, *NIST Digital Library of Mathematical Functions*, Release 1.1.3 of 2021-09-15 (`http://dlmf.nist.gov/`) (282–283, 330, 416, 418).

378. (a) Hagelaar, Pitchford, "Solving the Boltzmann equation to obtain electron transport coefficients and rate coefficients for fluid models", *Plasma Sources Sci. Technol.* **14**, 722 (2005); (b) Hagelaar, *BOLSIG+*, version 12/2019, Laboratoire Plasma et Conversion d'Energie (`http://www.bolsig.laplace.univ-tlse.fr/index.html`), 79, 84, 86–87, 132, 146, 585, 587.

432. *ISO-80000-2 : Mathematics*, International Organization for Standardization, 2019 (xvi).

539. Kramida, Ralchenko, Reader, NIST ASD Team, *NIST Atomic Spectra Database (version 5.9)*, English, [Sat May 28 2022], National Institute of Standards and Technology (`https://physics.nist.gov/asd`) (292, 487, 515).

601. Linstrom, Mallard, *NIST Chemistry WebBook*, National Institute of Standards and Technology (`https://webbook.nist.gov/chemistry/`) (292).

732. Pancheshnyi, Bordage, Chaudhury, *et al.*, *LXCat*, Plasma Data Exchange Project (`https://www.lxcat.net/`) (427, 453, 585, 610).

803. (a) Salvat, Jablonski, Powell, "ELSEPA—Dirac partial-wave calculation of elastic scattering of electrons and positrons by atoms, positive ions and molecules", *Comput Phys Commun* **165**, 157–190 (2005); (b) Salvat, Fernández-Varea, "radial: A Fortran subroutine package for the solution of the radial Schrödinger and Dirac wave equations", *Comput Phys Commun* **240**, 165–177 (2019); (c) Salvat, Jablonski, Powell, "ELSEPA—Dirac partial-wave calculation of elastic scattering of electrons and positrons by atoms, positive ions and molecules (New Version Announcement)", *Comput Phys Commun* **261**, 107704 (2021), 277, 281, 291, 311, 328–329, 333, 352–353, 357, 362–364, 366, 392–395, 404.

950. *U. S. Standard Atmosphere*, Washington, D.C: COESA, 1976 (40).

Electron Swarms and Discharges (Part I)

1. Abbasi, Abe, Abu-Zayyad, *et al.*, "The bursts of high energy events observed by the telescope array surface detector", *Phys Lett A* **381**, 2565–2572 (2017) (21, 23–24).
2. Abbasi, Abu-Zayyad, Allen, *et al.*, "Gamma Ray Showers Observed at Ground Level in Coincidence With Downward Lightning Leaders", *J. Geophys. Res.: Atmos.* **123**, 6864–6879 (2018) (vii, ix, xi, 22–23).
5. Agafonov, Bogachenkov, Chubenko, *et al.*, "Observation of hard radiations in a laboratory atmospheric high-voltage discharge", *J. Phys. D: Appl. Phys.* **50**, 165202 (2017) (27).
6. Agafonov, Bagulya, Dalkarov, *et al.*, "Observation of Neutron Bursts Produced by Laboratory High-Voltage Atmospheric Discharge", *Phys. Rev. Lett.* **111**, 115003 (2013) (19, 27).
7. Agafonov, Oginov, Rodionov, *et al.*, "Hard bremsstrahlung from a high-voltage atmospheric discharge and its anisotropy", *arXiv e-prints*, arXiv:1807.07675 (2018) (28).
11. Aleksandrov, Bazelyan, "Ionization processes in spark discharge plasmas", *Plasma Sources Sci. Technol.* **8**, 285–294 (1999) (11, 156, 208).
20. Alnussirat, Christian, Fishman, *et al.*, "Simultaneous space-based observations of terrestrial gamma-ray flashes and lightning optical emissions: Investigation of the terrestrial gamma-ray flash production mechanisms", *Phys. Rev. D* **100**, 083018 (2019) (24).
25. Al-Amin, Lucas, "Time of flight measurements of the ratio of radial diffusion coefficient and mobility for electron swarms in helium, argon, neon and krypton at high E/N", *J. Phys. D: Appl. Phys.* **20**, 1590 (1987) (142).
33. Babich, "Generation of neutrons in giant upward atmospheric discharges", *JETP Lett.* **84**, 285–288 (2006) (27).
34. Babich, "Analysis of a laboratory experiment on neutron generation by discharges in the open atmosphere", *Phys. Rev. C* **92**, 044602 (2015) (27).
35. Babich, Bochkov, Kutsyk, "Lightning initiation mechanism based on the development of relativistic runaway electron avalanches triggered by background cosmic radiation: Numerical simulation", *J Exp Theor Phys+* **112**, 902–909 (2011) (34).
36. Babich, Bochkov, Kutsyk, "Mechanism of generation of runaway electrons in a lightning leader", *JETP Lett.* **99**, 386–390 (2014) (29, 32, 196, 201, 224).
37. Babich, Bochkov, Kutsyk, Rassoul, "Analysis of fundamental interactions capable of producing neutrons in thunderstorms", *Phys. Rev. D* **89**, 093010 (2014) (27).
38. Babich, Bochkov, Kutsyk, *et al.*, "A model for electric field enhancement in lightning leader tips to levels allowing X-ray and γ ray emissions", *J. Geophys. Res. : Space Phys.* **120**, 5087–5100 (2015) (29, 40, 222).
39. Babich, Bochkov, Kutsyk, *et al.*, "Analyses of electron runaway in front of the negative streamer channel", *J. Geophys. Res. : Space Phys.* **122**, 8974–8984 (2017) (16, 29, 32, 37, 40, 196, 215, 217, 225).
40. Babich, Donskoy, Il'kaev, *et al.*, "Fundamental parameters of a relativistic runaway electron avalanche in air", *Plasma Phys Rep* **30**, 616–624 (2004) (31, 34, 37, 48, 71, 190).
41. Babich, Donskoy, Kutsyk, *et al.*, "Comparison of relativistic runaway electron avalanche rates obtained from Monte Carlo simulations and kinetic equation solution", *IEEE Trans. Plasma Sci.* **29**, 430–438 (2001) (34).

42. Babich, Kutsyk, Donskoy, Kudryavtsev, "New data on space and time scales of relativistic runaway electron avalanche for thunderstorm environment: Monte Carlo calculations", *Phys Lett A* **245**, 460–470 (1998) (34, 37, 190).

43. Babich, Bochkov, "Electron runaway rate in air", *J. Phys. D: Appl. Phys.* **54**, 465205 (2021) (32, 37, 182, 637).

44. Babich, Bochkov, "Numerical simulation of electric field enhancement at the contact of positive and negative streamers in relation to the problem of runaway electron generation in lightning and in long laboratory sparks", *J. Phys. D: Appl. Phys.* **50**, 455202 (2017) (28–29, 32, 37).

45. Babich, Kutsyk, Bochkov, *et al.*, "General processes responsible for the space leader birth in streamer coronas of negative leaders", *Plasma Res. Express* **3**, 045003 (2021) (17).

46. Babich, "Analysis of a new electron-runaway mechanism and record-high runaway-electron currents achieved in dense-gas discharges", *Phys.-Uspekhi* **48**, 1015–1037 (2005) (37).

47. Babich, Bochkov, Donskoi, Kutsyk, "Source of prolonged bursts of high-energy gamma rays detected in thunderstorm atmosphere in Japan at the coastal area of the Sea of Japan and on high mountaintop", *J. Geophys. Res. : Space Phys.* **115** (, 2010) (21).

48. Babich, Bochkov, Kutsyk, Roussel-Dupré, "Localization of the source of terrestrial neutron bursts detected in thunderstorm atmosphere", *J. Geophys. Res. : Space Phys.* **115** (, 2010) (27).

49. Babich, Roussel-Dupré, "Origin of neutron flux increases observed in correlation with lightning", *J. Geophys. Res.: Atmos.* **112** (, 2007) (27).

50. Bakhov, Babich, Kutsyk, "Temporal characteristics of runaway electrons in electron-neutral collision-dominated plasma of dense gases. Monte Carlo calculations", *IEEE Trans. Plasma Sci.* **28**, 1254–1262 (2000) (71, 182).

52. Bauer, "Physics of High-Temperature Air: Part I, Basics", tech. rep. D-487 (Institute for Defense Analyses, 1990) (46).

54. Bell, Pasko, Inan, "Runaway electrons as a source of red sprites in the mesosphere", *Geophys Res Lett* **22**, 2127–2130 (1995) (23).

56. Belz, Krehbiel, Remington, *et al.*, "Observations of the Origin of Downward Terrestrial Gamma-Ray Flashes", *J. Geophys. Res.: Atmos.* **125**, e2019JD031940 (2020) (24).

57. Benilov, Naidis, "Modelling of low-current discharges in atmospheric-pressure air taking account of non-equilibrium effects", *J. Phys. D: Appl. Phys.* **36**, 1834 (2003) (44, 156, 209).

59. Berger, Anderson, Kroninger, "Parameters of lightning flashes", *Electra* **80**, 23–37 (1975) (13).

60. Berger, Inokuti, Anderson, *et al.*, "Stopping Powers for Electrons and Positrons", tech. rep. 37 (69–70).

67. Bethe, Heitler, Dirac, "On the stopping of fast particles and on the creation of positive electrons", *Proc. R. Soc. London A.* **146**, 83–112 (1934) (70).

68. Biagi, Uman, Hill, Jordan, "Negative leader step mechanisms observed in altitude triggered lightning", *J. Geophys. Res.: Atmos.* **119**, 8160–8168 (2014) (18, 210).

69. Biagi, Uman, Hill, *et al.*, "Observations of stepping mechanisms in a rocket-and-wire triggered lightning flash", *J. Geophys. Res.: Atmos.* **115** (, 2010) (17–18).

70. Biagi, Uman, Hill, Jordan, "Observations of the initial, upward-propagating, positive leader steps in a rocket-and-wire triggered lightning discharge", *Geophys Res Lett* **38** (, 2011) (12).

76. Blackman, "Vibrational relaxation in oxygen and nitrogen", *J Fluid Mech* **1**, 61–85 (1956) (44).

78. Blanc, Lefeuvre, Roussel-Dupré, Sauvaud, "TARANIS: A microsatellite project dedicated to the study of impulsive transfers of energy between the Earth atmosphere, the ionosphere, and the magnetosphere", *Adv Space Res* **40**, 1268–1275 (2007) (21).

84. Blaton, "On a Geometrical Interpretation of Energy and Momentum Conservation in atomic Collisions and Disintegration Processes", *Matematisk-Fysiske Meddelelser* **24** (, 1950) (227–228).

86. Bochkov, Babich, Kutsyk, "Dependence of the Generation Rate of High-Energy Electrons in Helium on the Electron Angular Scattering Model", *Plasma Phys Rep* **47**, 1027–1041 (2021) (37).

88. Boeuf, Marode, "A Monte Carlo analysis of an electron swarm in a nonuniform field: the cathode region of a glow discharge in helium", *J. Phys. D: Appl. Phys.* **15**, 2169–2187 (1982) (56, 67).

92. Boozer, "Theory of runaway electrons in ITER: Equations, important parameters, and implications for mitigation", *Phys Plasmas* **22**, 032504 (2015) (50).

93. Boozer, "Runaway electrons and magnetic island confinement", *Phys Plasmas* **23**, 082514 (2016) (50).

94. Boozer, "Runaway electrons and ITER", *Nucl Fusion* **57**, 056018 (2017) (50).

99. Bowers, Smith, Kelley, *et al.*, "A Terrestrial Gamma-Ray Flash inside the Eyewall of Hurricane Patricia", *J. Geophys. Res.: Atmos.* **123**, 4977–4987 (2018) (21).

104. Breizman, Aleynikov, Hollmann, Lehnen, "Physics of runaway electrons in tokamaks", *Nucl Fusion* **59**, 083001 (2019) (37).

109. Briels, Kos, Winands, *et al.*, "Positive and negative streamers in ambient air: measuring diameter, velocity and dissipated energy", *J. Phys. D: Appl. Phys.* **41**, 234004 (2008) (11, 16).

110. Briggs, Fishman, Connaughton, *et al.*, "First results on terrestrial gamma ray flashes from the Fermi Gamma-ray Burst Monitor", *J. Geophys. Res. : Space Phys.* **115** (, 2010) (22).

111. Briggs, Connaughton, Wilson-Hodge, *et al.*, "Electron-positron beams from terrestrial lightning observed with Fermi GBM", *Geophys Res Lett* **38** (, 2011) (27).

112. Briggs, Xiong, Connaughton, *et al.*, "Terrestrial gamma-ray flashes in the Fermi era: Improved observations and analysis methods", *J. Geophys. Res. : Space Phys.* **118**, 3805–3830 (2013) (26).

118. Brunetti, Cecchini, Galli, *et al.*, "Gamma-ray bursts of atmospheric origin in the MeV energy range", *Geophys Res Lett* **27**, 1599–1602 (2000) (23).

148. Capitelli, Armenise, Bisceglie, *et al.*, "Thermodynamics, Transport and Kinetics of Equilibrium and Non-Equilibrium Plasmas: A State-to-State Approach", *Plasma Chem Plasma P* **32**, 427–450 (2012) (222).

149. Capitelli, Colonna, D'Ammando, *et al.*, "The role of electron scattering with vibrationally excited nitrogen molecules on non-equilibrium plasma kinetics", *Phys Plasmas* **20**, 101609 (2013) (210, 431).

152. Carlson, Lehtinen, Inan, "Constraints on terrestrial gamma ray flash production from satellite observation", *Geophys Res Lett* **34** (, 2007) (23).

153. Carlson, Lehtinen, Inan, "Neutron production in terrestrial gamma ray flashes", *J. Geophys. Res. : Space Phys.* **115** (, 2010) (27).

155. Carnevale, Carey, Larson, "Ultrasonic Determination of Rotational Collision Numbers and Vibrational Relaxation Times of Polyatomic Gases at High Temperatures", *J. Chem. Phys.* **47**, 2829–2835 (1967) (44).

160. Célestin, Pasko, "Soft collisions in relativistic runaway electron avalanches", *J. Phys. D: Appl. Phys.* **43**, 315206 (2010) (66).

161. Célestin, Pasko, "Energy and fluxes of thermal runaway electrons produced by exponential growth of streamers during the stepping of lightning leaders and in transient luminous events", *J. Geophys. Res. : Space Phys.* **116** (, 2011) (32–33, 37, 196, 215, 217, 222).

162. Célestin, Pasko, "Compton scattering effects on the duration of terrestrial gamma-ray flashes", *Geophys Res Lett* **39** (, 2012) (22, 36–37).

163. Célestin, Xu, Pasko, "Terrestrial gamma ray flashes with energies up to 100 MeV produced by nonequilibrium acceleration of electrons in lightning", *J. Geophys. Res. : Space Phys.* **117** (, 2012) (32–33).

164. Célestin, Xu, Pasko, "Variability in fluence and spectrum of high-energy photon bursts produced by lightning leaders", *J. Geophys. Res. : Space Phys.* **120**, 10, 712–10, 723 (2015) (33, 36, 201).

169. Chanrion, Bonaventura, Bourdon, Neubert, "Influence of the angular scattering of electrons on the runaway threshold in air", *Plasma Phys Contr F* **58**, 044001 (2016) (vii, ix, xi, 32, 557).

170. Chanrion, Bonaventura, Çinar, *et al.*, "Runaway electrons from a 'beam-bulk' model of streamer: application to TGFs", *Environ Res Lett* **9**, 055003 (2014) (28, 32, 37).

171. Chanrion, Neubert, "Production of runaway electrons by negative streamer discharges", *J. Geophys. Res. : Space Phys.* **115** (, 2010) (28, 32, 37, 196, 222).

172. Chanrion, Neubert, "A PIC-MCC code for simulation of streamer propagation in air", English, *J Comput Phys* **15**, 7222–7245 (2008) (161).

174. Chilingarian, Daryan, Arakelyan, *et al.*, "Ground-based observations of thunderstorm-correlated fluxes of high-energy electrons, gamma rays, and neutrons", *Phys. Rev. D* **82**, 043009 (2010) (27, 36).

179. Chubenko, Antonova, Kryukov, *et al.*, "Intensive X-ray emission bursts during thunderstorms", *Phys Lett A* **275**, 90–100 (2000) (20).

184. Coleman, Dwyer, "Propagation speed of runaway electron avalanches", *Geophys Res Lett* **33** (, 2006) (34, 37).

188. Connaughton, Briggs, Xiong, *et al.*, "Radio signals from electron beams in terrestrial gamma ray flashes", *J. Geophys. Res. : Space Phys.* **118**, 2313–2320 (2013) (24).

190. Cooray, Arevalo, Rahman, *et al.*, "On the possible origin of X-rays in long laboratory sparks", *J. Atmos. Sol. Terr. Phys.* **71**, 1890–1898 (2009) (18, 29).

191. Cooray, Becerra, Rakov, "On the electric field at the tip of dart leaders in lightning flashes", *J. Atmos. Sol. Terr. Phys.* **71**, 1397–1404 (2009) (28).

192. Cooray, Cooray, Rubinstein, Rachidi, "Ionization Waves Enhance the Production of X-rays during Streamer Collisions", *Atmosphere* **12** (, 2021) (32, 37).

195. Cotton, Bryan, van den Heever, in *Storm and Cloud Dynamics*, ed. by Cotton, Bryan, van den Heever (Academic Press, 2011), vol. 99, pp. 315–454 (9).

202. Cummer, Zhai, Hu, *et al.*, "Measurements and implications of the relationship between lightning and terrestrial gamma ray flashes", *Geophys Res Lett* **32** (, 2005) (24).

203. da Silva, Millan, McGaw, *et al.*, "Laboratory Measurements of X-Ray Emissions From Centimeter-Long Streamer Corona Discharges", *Geophys Res Lett* **44**, 11, 174–11, 183 (2017) (28, 44, 46).

204. da Silva, Pasko, "Dynamics of streamer-to-leader transition at reduced air densities and its implications for propagation of lightning leaders and gigantic jets", *J. Geophys. Res.: Atmos.* **118**, 13, 561–13, 590 (2013) (40, 45).

213. Delong, Beňo, Břeň, Kulhánek, "Notes on the relativistic movement of runaway electrons in parallel electric and magnetic fields", *Phys Plasmas* **23**, 094504 (2016) (50).

218. Diniz, Rutjes, Ebert, Ferreira, "Cold Electron Runaway Below the Friction Curve", *J. Geophys. Res.: Atmos.* **124**, 189–198 (2019) (vii, ix, xi, 32, 71, 163, 182, 336, 557).

230. Dreicer, "Electron and Ion Runaway in a Fully Ionized Gas. I", *Phys. Rev.* **115**, 238–249 (1959) (31).

231. Dreicer, "Electron and Ion Runaway in a Fully Ionized Gas. II", *Phys. Rev.* **117**, 329–342 (1960) (31).

234. Dujko, Markosyan, White, Ebert, "High-order fluid model for streamer discharges: I. Derivation of model and transport data", *J. Phys. D: Appl. Phys.* **46**, 475202 (2013) (86).

235. Dujko, Ebert, White, Petrović, "Boltzmann Equation Analysis of Electron Transport in a N_2–O_2 Streamer Discharge", *Jpn J Appl Phys* **50**, 08JC01 (2011) (115, 220).

236. Dwyer, "A fundamental limit on electric fields in air", *Geophys Res Lett* **30** (, 2003) (31, 33, 35, 37, 71).

237. Dwyer, "The initiation of lightning by runaway air breakdown", *Geophys Res Lett* **32** (, 2005) (35).

238. Dwyer, "Relativistic breakdown in planetary atmospheres", *Phys Plasmas* **14**, 042901 (2007) (36–37, 326, 328).

239. Dwyer, Rassoul, Al-Dayeh, *et al.*, "A ground level gamma-ray burst observed in association with rocket-triggered lightning", *Geophys Res Lett* **31** (, 2004) (13, 23–24, 26).

240. Dwyer, Rassoul, Al-Dayeh, *et al.*, "Measurements of X-ray emission from rocket-triggered lightning", *Geophys Res Lett* **31** (, 2004) (27).

241. Dwyer, Rassoul, Al-Dayeh, *et al.*, "X-ray bursts associated with leader steps in cloud-to-ground lightning", *Geophys Res Lett* **32** (, 2005) (27).

242. Dwyer, Rassoul, Saleh, *et al.*, "X-ray bursts produced by laboratory sparks in air", *Geophys Res Lett* **32** (, 2005) (27–28).

243. Dwyer, Saleh, Rassoul, *et al.*, "A study of X-ray emission from laboratory sparks in air at atmospheric pressure", *J. Geophys. Res.: Atmos.* **113** (, 2008) (27–28).

244. Dwyer, Schaal, Rassoul, *et al.*, "High-speed X-ray images of triggered lightning dart leaders", *J. Geophys. Res.: Atmos.* **116** (, 2011) (27–28, 33).

245. Dwyer, Smith, "A comparison between Monte Carlo simulations of runaway breakdown and terrestrial gamma-ray flash observations", *Geophys Res Lett* **32** (, 2005) (22–23, 35–36).

246. Dwyer, "The relativistic feedback discharge model of terrestrial gamma ray flashes", *J. Geophys. Res. : Space Phys.* **117** (, 2012) (21, 24, 26, 35–37, 201, 635).

247. Dwyer, Babich, "Low-energy electron production by relativistic runaway electron avalanches in air", *J. Geophys. Res. : Space Phys.* **116** (, 2011) (34–35).

248. Dwyer, Cummer, "Radio emissions from terrestrial gamma-ray flashes", *J. Geophys. Res. : Space Phys.* **118**, 3769–3790 (2013) (24, 36).

249. Dwyer, Grefenstette, Smith, "High-energy electron beams launched into space by thunderstorms", *Geophys Res Lett* **35** (, 2008) (27).

250. Dwyer, Smith, Cummer, "High-Energy Atmospheric Physics: Terrestrial Gamma-Ray Flashes and Related Phenomena", *Space Sci Rev* **173**, 133–196 (2012) (20, 30, 34, 71, 635).

251. Dwyer, Smith, Hazelton, *et al.*, "Positron clouds within thunderstorms", *J Plasma Phys* **81**, 475810405 (2015) (27).

252. Dwyer, Uman, Rassoul, *et al.*, "Energetic Radiation Produced During Rocket-Triggered Lightning", *Science* **299**, 694–697 (2003) (vii, ix, xi, 13, 23).

255. Eack, Beasley, Rust, *et al.*, "Initial results from simultaneous observation of X-rays and electric fields in a thunderstorm", *J. Geophys. Res.: Atmos.* **101**, 29637–29640 (1996) (20–21).

256. Eack, Suszcynsky, Beasley, *et al.*, "Gamma-ray emissions observed in a thunderstorm anvil", *Geophys Res Lett* **27**, 185–188 (2000) (21).

267. Enoto, Wada, Furuta, *et al.*, "Photonuclear reactions triggered by lightning discharge", *Nature* **551**, 481–484 (2017) (vii, ix, xi, 13, 27).

271. Faraday, "On electro-chemical decomposition", *Philosophical Transactions of the Royal Society* (, 1834) (14).

281. Fierro, Moore, Yee, Hopkins, "Three-dimensional kinetic modeling of streamer propagation in a nitrogen/helium gas mixture", *Plasma Sources Sci. Technol.* **27**, 105008 (2018) (88).

291. Fishman, Bhat, Mallozzi, *et al.*, "Discovery of Intense Gamma-Ray Flashes of Atmospheric Origin", *Science* **264**, 1313–1316 (1994) (13, 21, 23).

292. Fishman, Briggs, Connaughton, *et al.*, "Temporal properties of the terrestrial gamma-ray flashes from the Gamma-Ray Burst Monitor on the Fermi Observatory", *J. Geophys. Res. : Space Phys.* **116** (, 2011) (22).

296. Flitti, Pancheshnyi, "Gas heating in fast pulsed discharges in N_2–O_2 mixtures", *The European Physical Journal-Applied Physics* **45** (, 2009) (44–45, 159).

297. Foley, Fitzpatrick, Briggs, *et al.*, "Pulse properties of terrestrial gamma-ray flashes detected by the Fermi Gamma-Ray Burst Monitor", *J. Geophys. Res. : Space Phys.* **119**, 5931–5942 (2014) (22).

299. Francisco, Teunissen, Bagheri, Ebert, "Simulations of positive streamers in air in different electric fields: steady motion of solitary streamer heads and the stability field", *Plasma Sources Sci. Technol.* **30**, 115007 (2021) (10–11).

301. Frankel, Highland, Sloan, *et al.*, "Observation of X-rays from spark discharges in a spark chamber", *Nuclear Instruments and Methods* **44**, 345–348 (1966) (28).

303. Freedman, Diaconis, "On the histogram as a density estimator:L2 theory", *Zeitschrift für Wahrscheinlichkeitstheorie und Verwandte Gebiete* **57**, 453–476 (1981) (97).

305. Frost, Phelps, "Rotational Excitation and Momentum Transfer Cross Sections for Electrons in H_2 and N_2 from Transport Coefficients", *Phys. Rev.* **127**, 1621–1633 (1962) (43, 252).

308. Fuller, "Photonuclear reaction cross sections for ^{1}2C, ^{1}4N and ^{1}6O", *Phys. Rep.* **127**, 185–231 (1985) (26).

311. Gallimberti, Bacchiega, Bondiou-Clergerie, Lalande, "Fundamental processes in long air gap discharges", *Cr Phys* **3**, 1335–1359 (2002) (11, 16–18, 46, 210).

334. Gjesteland, Østgaard, Collier, *et al.*, "Confining the angular distribution of terrestrial gamma ray flash emission", *J. Geophys. Res. : Space Phys.* **116** (, 2011) (23).

335. Gjesteland, Østgaard, Connell, *et al.*, "Effects of dead time losses on terrestrial gamma ray flash measurements with the Burst and Transient Source Experiment", *J. Geophys. Res. : Space Phys.* **115** (, 2010) (22–23).

336. Gjesteland, Østgaard, Bitzer, Christian, "On the timing between terrestrial gamma ray flashes, radio atmospherics, and optical lightning emission", *J. Geophys. Res. : Space Phys.* **122**, 7734–7741 (2017) (24).

340. Gorin, Levitov, Shkilev, presented at the IEE Conference Publication, vol. 143, pp. 274–278 (11, 17–18, 224).

341. Gorin, Shkilev, "Development of the electric discharge in long gaps subjected to positive voltage impulses", *Electricity*, 29–38 (1974) (11–12, 16).

354. Grefenstette, Smith, Dwyer, Fishman, "Time evolution of terrestrial gamma ray flashes", *Geophys Res Lett* **35** (, 2008) (22–23).

356. Griffiths, Phelps, "A model for lightning initiation arising from positive corona streamer development", *J. Geophys. Res. (1896-1977)* **81**, 3671–3676 (1976) (11).

362. Gurevich, Antonova, Chubenko, *et al.*, "Strong Flux of Low-Energy Neutrons Produced by Thunderstorms", *Phys. Rev. Lett.* **108**, 125001 (2012) (27).

363. Gurevich, Carlson, Medvedev, Zybin, "Generation of electron–positron pairs in runaway breakdown", *Phys Lett A* **275**, 101–108 (2000) (35).

364. Gurevich, Medvedev, Zybin, "Thermal electrons and electric current generated by runaway breakdown effect", *Phys Lett A* **321**, 179–184 (2004) (33–34).

365. Gurevich, Milikh, Roussel-Dupre, "Runaway electron mechanism of air breakdown and preconditioning during a thunderstorm", *Phys Lett A* **165**, 463–468 (1992) (33–34, 37, 71).

366. Gurevich, Valdivia, Milikh, Papadopoulos, "Runaway electrons in the atmosphere in the presence of a magnetic field", *Radio Sci* **31**, 1541–1554 (1996) (51).

367. Gurevich, Zybin, "Runaway Breakdown and the Mysteries of Lightning", *Phys Today* **58**, 37–42 (2005) (36).

368. Gurevich, Zybin, Medvedev, "Runaway breakdown in strong electric field as a source of terrestrial gamma flashes and gamma bursts in lightning leader steps", *Phys Lett A* **361**, 119–125 (2007) (32, 37).

369. Gurevich, Zybin, Roussel-Dupre, "Lightning initiation by simultaneous effect of runaway breakdown and cosmic ray showers", *Phys Lett A* **254**, 79–87 (1999) (21, 24, 33–34, 37).

370. Gurevich, Zybin, "Runaway breakdown and electric discharges in thunderstorms", *Phys.-Uspekhi* **44**, 1119–1140 (2001) (34, 37).

371. Gurevich, "On the theory of runaway electrons", *Sov. Phys. JETP* **12**, 904–912 (1961), The z-axis is aligned in the **opposite** direction of the electric field **E** unlike what is implied at the beginning of section 2. This could be a mistranslation from the Russian original (not available electronically). (32, 180, 182).

375. Haefliger, Franck, "Detailed precision and accuracy analysis of swarm parameters from a pulsed Townsend experiment", *Rev. Sci. Instrum.* **89** (, 2018), 023114 (142, 534).

376. Hagelaar, "Coulomb collisions in the Boltzmann equation for electrons in low-temperature gas discharge plasmas", *Plasma Sources Sci. Technol.* **25**, 015015 (2015) (11, 32, 82–83, 148).

379. Hagelaar, Donko, Dyatko, "Modification of the Coulomb Logarithm due to Electron-Neutral Collisions", *Phys. Rev. Lett.* **123**, 025004 (2019) (32).

381. Hake, Phelps, "Momentum-Transfer and Inelastic-Collision Cross Sections for Electrons in O_2, CO, and CO_2", *Phys. Rev.* **158**, 70–84 (1967) (132, 586, 594, 596–597).

385. Hare, Uman, Dwyer, *et al.*, "Ground-level observation of a terrestrial gamma ray flash initiated by a triggered lightning", *J. Geophys. Res.: Atmos.* **121**, 6511–6533 (2016) (21).

386. Hariharan, Chandra, Dugad, *et al.*, "Measurement of the Electrical Properties of a Thundercloud Through Muon Imaging by the GRAPES-3 Experiment", *Phys. Rev. Lett.* **122**, 105101 (2019) (8).

391. Hazelton, Grefenstette, Smith, *et al.*, "Spectral dependence of terrestrial gamma-ray flashes on source distance", *Geophys Res Lett* **36** (, 2009) (23).

393. Henderson, Fite, Brackmann, "Dissociative Attachment of Electrons to Hot Oxygen", *Phys. Rev.* **183**, 157–166 (1969) (68).

402. Hilsenrath, Klein, "Tables of thermodynamic properties of air in chemical equilibrium including second virial corrections from 1500K to 15,000K", tech. rep. (National Bureau of Standards, 1965) (40–41).

409. Hu, Cummer, Lyons, Nelson, "Lightning charge moment changes for the initiation of sprites", *Geophys Res Lett* **29**, 120-1-120–4 (2002) (13).

414. Huxley, "On the Theory of Anisotropic Diffusion of Electrons in Gases", *Aust. J. Phys.* **25**, 43–74 (1972) (82–83, 87).

417. Ibragimova, Smekhov, Shatalov, "Dissociation rate constants of diatomic molecules under thermal equilibrium conditions", *Fluid Dyn* **34**, 153–157 (1999) (46).

421. Ihaddadene, Dwyer, Liu, *et al.*, "Modeling of a New Electron Acceleration Mechanism Ahead of Streamers", *J. Geophys. Res. : Space Phys.* **124**, 7301–7319 (2019) (32).

422. Ihaddadene, Célestin, presented at the EGU General Assembly 2015, held 12-17 April, 2015 in Vienna, Austria. id.8704, vol. 17 (28, 32, 180).

423. Inan, Reising, Fishman, Horack, "On the association of terrestrial gamma-ray bursts with lightning and implications for sprites", *Geophys Res Lett* **23**, 1017–1020 (1996) (23).

435. Itikawa, "Evaluation of the Evaluated Cross-Section Data for Atomic and Molecular Collisions", *Fusion Sci Technol* **63**, 333–337 (2013) (114, 252, 571).

445. Jackman, Green, "Electron impact on atmospheric gases, 3. Spatial yield spectra for N_2", *J. Geophys. Res. : Space Phys.* **84**, 2715–2724 (1979) (117, 546, 557).

447. Jacobson, Krider, "Electrostatic Field Changes Produced by Florida Lightning", *J. Atmos. Sci.* **33**, 103–117 (1976) (13).

457. Jeon, Nakamura, "Measurement of drift velocity and longitudinal diffusion coefficient of electrons in pure oxygen and in oxygen-argon mixtures", *J. Phys. D: Appl. Phys.* **31**, 2145 (1998) (142).

466. Jones, Campbell, Bottema, *et al.*, "Electron-driven excitation of O_2 under night-time auroral conditions: Excited state densities and band emissions", *Planet Space Sci* **54**, 45–59 (2006) (46, 596).

471. Ju, Wang, Li, *et al.*, "Corona discharge induced snow formation in a cloud chamber", *Sci. Rep.* **7**, 11749 (2017) (4).

482. Kawaguchi, Takahashi, Satoh, "Electron collision cross section set for N_2 and electron transport in N_2, N_2/He, and N_2/Ar", *Plasma Sources Sci. Technol.* **30**, 035010 (2021) (37, 109, 115, 427, 544, 556, 566, 573–574, 583, 585, 587–588, 590).

483. Kawaguchi, Nakata, Satoh, *et al.*, "Measurement of the third-order transport coefficient in N_2 and its effect on the longitudinal diffusion coefficient measured from the arrival-time spectra of an electron swarm", *Plasma Sources Sci. Technol.* **30**, 035006 (2021) (109).

484. Kelley, Smith, Dwyer, *et al.*, "Relativistic electron avalanches as a thunderstorm discharge competing with lightning", *Nat Commun* **6**, 7845 (2015) (21, 24).

485. Kemaneci, Booth, Chabert, *et al.*, "A computational analysis of the vibrational levels of molecular oxygen in low-pressure stationary and transient radio-frequency oxygen plasma", *Plasma Sources Sci. Technol.* **25**, 025025 (2016) (44).

500. Kieu, Gordillo-Vázquez, Passas, *et al.*, "High-Speed Spectroscopy of Lightning-Like Discharges: Evidence of Molecular Optical Emissions", *J. Geophys. Res.: Atmos.* **126**, e2021JD035016 (2021) (12, 456).

514. Knuth, "Optimal data-based binning for histograms and histogram-based probability density models", *Digit Signal Process* **95**, 102581 (2019) (96–97).

515. Koch, Motz, "Bremsstrahlung Cross-Section Formulas and Related Data", *Rev. Mod. Phys.* **31**, 920–955 (1959) (22, 28).

516. Kochkin, Sarria, Skeie, *et al.*, "In-Flight Observation of Positron Annihilation by ILDAS", *J. Geophys. Res.: Atmos.* **123**, 8074–8090 (2018) (27).

517. Kochkin, Nguyen, van Deursen, Ebert, "Experimental study of hard X-rays emitted from metre-scale positive discharges in air", *J. Phys. D: Appl. Phys.* **45**, 425202 (2012) (vii, ix, xi, 11, 27).

518. Kochkin, van Deursen, Ebert, "Experimental study on hard x-rays emitted from metre-scale negative discharges in air", *J. Phys. D: Appl. Phys.* **48**, 025205 (2014) (17–18, 27–28).

519. Kochkin, Köhn, Ebert, van Deursen, "Analyzing x-ray emissions from meter-scale negative discharges in ambient air", *Plasma Sources Sci. Technol.* **25**, 044002 (2016) (27–28).

520. Kochkin, Lehtinen, van Deursen, Østgaard, "Pilot system development in metre-scale laboratory discharge", *J. Phys. D: Appl. Phys.* **49**, 425203 (2016) (17, 33, 224).

521. Kochkin, van Deursen, Marisaldi, *et al.*, "In-Flight Observation of Gamma Ray Glows by ILDAS", *J. Geophys. Res.: Atmos.* **122**, 12, 801–12, 811 (2017) (20).

528. Köhn, Ebert, Mangiarotti, "The importance of electron–electron bremsstrahlung for terrestrial gamma-ray flashes, electron beams and electron–positron beams", *J. Phys. D: Appl. Phys.* **47**, 252001 (2014) (19).

530. Köhn, Chanrion, Neubert, "High-Energy Emissions Induced by Air Density Fluctuations of Discharges", *Geophys Res Lett* **45**, 5194–5203 (2018) (32, 40).

531. Köhn, Chanrion, Neubert, "Electron acceleration during streamer collisions in air", *Geophys Res Lett* **44**, 2604–2613 (2017) (28–29, 32, 161, 180, 222).

532. Köhn, Chanrion, Nishikawa, *et al.*, "The emission of energetic electrons from the complex streamer corona adjacent to leader stepping", *Plasma Sources Sci. Technol.* **29**, 035023 (2020) (40, 196, 201, 215, 217).

533. Kolobov, "Fokker–Planck modeling of electron kinetics in plasmas and semiconductors", *Comp Mater Sci* **28**, 302–320 (2003), Proceedings of the Symposium on Software Development for Process and Materials Design (81).

536. Kostinskiy, Syssoev, Bogatov, *et al.*, "Abrupt Elongation (Stepping) of Negative and Positive Leaders Culminating in an Intense Corona Streamer Burst: Observations in Long Sparks and Implications for Lightning", *J. Geophys. Res.: Atmos.* **123**, 5360–5375 (2018) (11–12, 18).

537. Koura, "Improved null-collision technique in the direct simulation Monte Carlo method: Application to vibrational relaxation of nitrogen", *Comput. Math. Appl.* **35**, 139–154 (1998) (90).

538. Koura, "Null-collision technique in the direct-simulation Monte Carlo method", *The Physics of Fluids* **29**, 3509–3511 (1986) (74, 90).

542. Kunhardt, Tzeng, "Role of electron-molecule angular scattering in shaping the electron-velocity distribution", *Phys. Rev. A* **34**, 2158–2166 (1986) (117, 557).

543. Kunhardt, Tzeng, "Development of an electron avalanche and its transition into streamers", *Phys. Rev. A* **38**, 1410–1421 (1988) (158).

544. Kunhardt, Tzeng, Boeuf, "Stochastic development of an electron avalanche", *Phys. Rev. A* **34**, 440–449 (1986) (162).

559. Laporta, Heritier, Panesi, "Electron-vibration relaxation in oxygen plasmas", *Chem Phys* **472**, 44–49 (2016) (156, 596).

575. Lehtinen, "Physics and Mathematics of Electric Streamers", *Radiophys Quant El+* **64**, 11–25 (2021) (16, 152, 196).

576. Lehtinen, Bell, Inan, "Monte Carlo simulation of runaway MeV electron breakdown with application to red sprites and terrestrial gamma ray flashes", *J. Geophys. Res. : Space Phys.* **104**, 24699–24712 (1999) (23, 34, 37, 51, 66, 71).

578. Lehtinen, Marskar, "What Determines the Parameters of a Propagating Streamer: A Comparison of Outputs of the Streamer Parameter Model and of Hydrodynamic Simulations", *Atmosphere* **12** (, 2021) (11).

579. Lehtinen, Østgaard, "X-ray Emissions in a Multiscale Fluid Model of a Streamer Discharge", *J. Geophys. Res.: Atmos.* **123**, 6935–6953 (2018) (28–29, 31–33, 71–72, 148, 163, 180, 211, 222).

580. Lemmon, Jacobsen, Penoncello, Friend, "Thermodynamic Properties of Air and Mixtures of Nitrogen, Argon, and Oxygen From 60 to 2000 K at Pressures to 2000 MPa", *J Phys Chem Ref Data* **29**, 331–385 (2000) (40–41).

581. Les Renardières Group, "Long air gap discharges at Les Renardières : 1973 results", *Electra* **53**, 31–153 (1974) (18).

582. Les Renardières Group, "Positive discharges in long air gaps at Les Renardières, 1975 results and conclusions", *Electra* **53**, 67–216 (1977) (11–12, 16).

583. Les Renardières Group, *Electra* **74**, 31–153 (1981) (17–18).

586. Li, Brok, Ebert, van der Mullen, "Deviations from the local field approximation in negative streamer heads", *J Appl Phys* **101**, 123305 (2007) (88, 207).

587. Li, Ebert, Hundsdorfer, "3D hybrid computations for streamer discharges and production of runaway electrons", *J. Phys. D: Appl. Phys.* **42**, 202003 (2009) (32, 37, 86, 88).

588. Li, Ebert, Hundsdorfer, "Spatially hybrid computations for streamer discharges : II. Fully 3D simulations", *J Comput Phys* **231**, 1020–1050 (2012), The right hand sides of equations (11) and (16) are correct but must be swapped. There is a confusion between bulk and flux diffusion coefficients. (86–87, 91, 106, 109, 117, 161).

591. Lin, Bardsley, "The null-event method in computer simulation", *Comput Phys Commun* **15**, 161–163 (1978) (90).

592. Lindanger, Skeie, Marisaldi, *et al.*, "Production of Terrestrial Gamma-Ray Flashes During the Early Stages of Lightning Flashes", *J. Geophys. Res.: Atmos.* **127**, e2021JD036305 (2022) (24, 26).

609. Loureiro, Ferreira, "Coupled electron energy and vibrational distribution functions in stationary N_2discharges", *J. Phys. D: Appl. Phys.* **19**, 17–35 (1986) (44, 46, 431, 587–588).

610. Lu, Blakeslee, Li, *et al.*, "Lightning mapping observation of a terrestrial gamma-ray flash", *Geophys Res Lett* **37** (, 2010) (24, 35).

612. Luque, "Relativistic Runaway Ionization Fronts", *Phys. Rev. Lett.* **112**, 045003 (2014) (28–29).

613. Luque, Stenbaek-Nielsen, McHarg, Haaland, "Sprite beads and glows arising from the attachment instability in streamer channels", *J. Geophys. Res.: Space Phys.* **121**, 2431–2449 (2016) (188).

615. Lyu, Cummer, Briggs, *et al.*, "Ground detection of terrestrial gamma ray flashes from distant radio signals", *Geophys Res Lett* **43**, 8728–8734 (2016) (24).

619. Mailyan, Nag, Dwyer, *et al.*, "Gamma-Ray and Radio-Frequency Radiation from Thunderstorms Observed from Space and Ground", *Sci. Rep.* **10**, 7286 (2020) (24, 26).

620. Majeed, Strickland, "New Survey of Electron Impact Cross Sections for Photoelectron and Auroral Electron Energy Loss Calculations", *J Phys Chem Ref Data* **26**, 335–349 (1997) (46, 444–445, 587).

621. Malagón-Romero, Luque, "Spontaneous Emergence of Space Stems Ahead of Negative Leaders in Lightning and Long Sparks", *Geophys Res Lett* **46**, 4029–4038 (2019) (16–17, 156, 161, 210, 222, 224).

625. March, Montanyà, "Influence of the voltage-time derivative in X-ray emission from laboratory sparks", *Geophys Res Lett* **37** (, 2010) (27).

626. Marisaldi, Argan, Ursi, *et al.*, "Enhanced detection of terrestrial gamma-ray flashes by AGILE", *Geophys Res Lett* **42**, 9481–9487 (2015) (24).

627. Marisaldi, Fuschino, Labanti, *et al.*, "Detection of terrestrial gamma ray flashes up to 40 MeV by the AGILE satellite", *J. Geophys. Res. : Space Phys.* **115** (, 2010) (22).

628. Marisaldi, Fuschino, Tavani, *et al.*, "Properties of terrestrial gamma ray flashes detected by AGILE MCAL below 30 MeV", *J. Geophys. Res. : Space Phys.* **119**, 1337–1355 (2014) (22, 26).

629. Marisaldi, Galli, Labanti, *et al.*, "On the High-Energy Spectral Component and Fine Time Structure of Terrestrial Gamma Ray Flashes", *J. Geophys. Res.: Atmos.* **124**, 7484–7497 (2019) (22, 36).

630. Marisaldi, Fuschino, Labanti, *et al.*, "Terrestrial gamma-ray flashes", *Nuclear Instruments and Methods in Physics Research Section A: Accelerators, Spectrometers, Detectors and Associated Equipment* **720**, 83–87 (2013), Selected papers from the 2nd International Conference Frontiers in Diagnostic Technologies (ICFDT2) (22–23).

631. Marshall, Stolzenburg, "Voltages inside and just above thunderstorms", *J. Geophys. Res.: Atmos.* **106**, 4757–4768 (2001) (8).

636. McCarthy, Parks, "Further observations of X-rays inside thunderstorms", *Geophys Res Lett* **12**, 393–396 (1985) (20–21).

637. McCarthy, Parks, "On the modulation of X ray fluxes in thunderstorms", *J. Geophys. Res.: Atmos.* **97**, 5857–5864 (1992) (21).

639. Meegan, Lichti, Bhat, *et al.*, "The Fermi gamma-ray burst monitor", *Astrophys. J.* **702**, 791–804 (2009) (21).

641. Meek, "A Theory of Spark Discharge", *Phys. Rev.* **57**, 722–728 (1940) (156–157, 184).

646. Milikh, Roussel-Dupré, "Runaway breakdown and electrical discharges in thunderstorms", *J. Geophys. Res. : Space Phys.* **115** (, 2010) (33–34).

647. Miller, "The mechanism of synthesis of amino acids by electric discharges", *Biochim. Biophys. Acta* **23**, 480–489 (1957) (5).

649. Milloy, Crompton, "The Ratio of the Lateral Diffusion Coefficient to Mobility for Electrons in Argon at 294 K", *Aust. J. Phys.* **30**, 51–60 (1977) (142).

659. Moore, Eack, Aulich, Rison, "Energetic radiation associated with lightning stepped-leaders", *Geophys Res Lett* **28**, 2141–2144 (2001) (27).

660. Moore, Poet, Martell, "Vertical profiles of radon-222 and its long-lived daughters over the eastern Pacific", *Environmental Science & Technology* **11**, 1207–1210 (1977) (33).

661. Morgan, Penetrante, "ELENDIF: A time-dependent Boltzmann solver for partially ionized plasmas", *Comput Phys Commun* **58**, 127–152 (1990) (133).

677. Moss, Pasko, Liu, Veronis, "Monte Carlo model for analysis of thermal runaway electrons in streamer tips in transient luminous events and streamer zones of lightning leaders", *J. Geophys. Res. : Space Phys.* **111** (, 2006) (vii, ix, xi, 32, 37, 56, 71, 91, 117, 182, 326, 336).

683. Murphy, "Total and differential electron collision cross sections for O_2 and N_2", tech. rep. (Los Alamos Natl. Lab., Los Alamos, 1988) (117, 326).

685. Naidis, "Simulation of streamer-to-spark transition in short non-uniform air gaps", *J. Phys. D: Appl. Phys.* **32**, 2649 (1999) (209).

686. Naidis, "Effects of nonlocality on the dynamics of streamers in positive corona discharges", *Tech Phys Lett+* **23**, 493–494 (1997) (88, 207).

687. Naidu, Prasad, "Mobility, diffusion and attachment of electrons in oxygen", *J. Phys. D: Appl. Phys.* **3**, 957 (1970) (142).

688. Nakamura, "Asymptotic velocity of relativistic E × B drift", *AIP Adv.* **11**, 035303 (2021) (50).

689. Nakamura, Kurachi, "Electron transport parameters in argon and its momentum transfer cross section", *J. Phys. D: Appl. Phys.* **21**, 718 (1988) (142, 610).

690. Nakamura, presented at the Swarm Studies and Inelastic Electron-Molecule Collisions, ed. by Pitchford, McKoy, Chutjian, Trajrnar, pp. 89–89 (204).

691. Nelson, Davis, "Thermal and Near-Thermal Electron Transport Coefficients in O2 Determined with a Time-of-Flight Swarm Experiment Using a Drift-Dwell-Drift Technique", *J. Chem. Phys.* **57**, 4079–4084 (1972) (142, 576, 594, 596–597, 600).

692. Nemiroff, Bonnell, Norris, "Temporal and spectral characteristics of terrestrial gamma flashes", *J. Geophys. Res. : Space Phys.* **102**, 9659–9665 (1997) (22–23).

695. Neubert, Østgaard, Reglero, *et al.*, "The ASIM Mission on the International Space Station", *Space Sci Rev* **215**, 26 (2019) (21, 26).

696. Neubert, Østgaard, Reglero, *et al.*, "A terrestrial gamma-ray flash and ionospheric ultraviolet emissions powered by lightning", *Science* **367**, 183–186 (2020) (24, 26).

698. Nguyen, van Deursen, Ebert, "Multiple x-ray bursts from long discharges in air", *J. Phys. D: Appl. Phys.* **41**, 234012 (2008) (28).

703. Nijdam, van de Wetering, Blanc, *et al.*, "Probing photo-ionization: experiments on positive streamers in pure gases and mixtures", *J. Phys. D: Appl. Phys.* **43**, 145204 (2010) (14).

704. Nijdam, Teunissen, Ebert, "The physics of streamer discharge phenomena", *Plasma Sources Sci. Technol.* **29**, 103001 (2020) (10–11, 16).

707. Noggle, Krider, Wayland, "A Search for X Rays from Helium and Air Discharges at Atmospheric Pressure", *J Appl Phys* **39**, 4746–4748 (1968) (28).

713. Okhrimovskyy, Bogaerts, Gijbels, "Electron anisotropic scattering in gases: A formula for Monte Carlo simulations", *Physical review E, Statistical, nonlinear, and soft matter physics* **65**, 037402 (2002) (117, 326, 336, 557).

716. Olsen, Motz, Koch, "Electron Scattering without Atomic or Nuclear Excitation", *Rev. Mod. Phys.* **36**, 881–928 (1964) (56, 59, 311, 331, 390).

722. Orville, "A High-Speed Time-Resolved Spectroscopic Study of the Lightning Return Stroke: Part II. A Quantitative Analysis", *J. Atmos. Sci.* **25**, 839–851 (1968) (12).

723. Østgaard, Gjesteland, Hansen, *et al.*, "The true fluence distribution of terrestrial gamma flashes at satellite altitude", *J. Geophys. Res. : Space Phys.* **117** (, 2012) (23, 26).

724. Østgaard, Gjesteland, Stadsnes, *et al.*, "Production altitude and time delays of the terrestrial gamma flashes: Revisiting the Burst and Transient Source Experiment spectra", *J. Geophys. Res. : Space Phys.* **113** (, 2008) (20, 23).

725. Østgaard, Neubert, Reglero, *et al.*, "First 10 Months of TGF Observations by ASIM", *J. Geophys. Res.: Atmos.* **124**, 14024–14036 (2019) (vii, ix, 22).

730. Pallu, Célestin, Trompier, Klerlein, "Estimation of Radiation Doses Delivered by Terrestrial Gamma Ray Flashes Within Leader-Based Production Models", *J. Geophys. Res.: Atmos.* **126**, e2020JD033907 (2021) (36).

733. Pancheshnyi, Starikovskii, "Stagnation dynamics of a cathode-directed streamer discharge in air", *Plasma Sources Sci. Technol.* **13**, B1 (2004) (11).

735. Parks, Mauk, Spiger, Chin, "X-ray enhancements detected during thunderstorm and lightning activities", *Geophys Res Lett* **8**, 1176–1179 (1981) (20).

737. Pasko, "Recent advances in theory of transient luminous events", *J. Geophys. Res. : Space Phys.* **115** (, 2010) (17).

738. Patten Jr., Connell, Kinnison, *et al.*, "Effect of vibrationally excited oxygen on ozone production in the stratosphere", *J. Geophys. Res.: Atmos.* **99**, 1211–1223 (1994) (44).

741. Peeters, Mirpour, Köhn, Nijdam, "A Model for Positive Corona Inception From Charged Ellipsoidal Thundercloud Hydrometeors", *J. Geophys. Res.: Atmos.* **127**, e2021JD035505 (2022) (10).

744. Perkins, Cullen, *ENDL Type Formats for the LLNL Evaluated Atomic Data Library (EADL), Evaluated Electron Data Library (EEDL), and Evaluated Photon Data Library (EPDL)*, U. S. Department of Energy, Lawrence Livermore National Laboratory (21).

745. Petersen, Bailey, Hallett, Beasley, "Laboratory investigation of corona initiation by ice crystals and its importance to lightning", *Q. J. R. Meteorolog. Soc.* **141**, 1283–1293 (2015) (10, 15).

747. Petrović, Dujko, Marić, *et al.*, "Measurement and interpretation of swarm parameters and their application in plasma modelling", *J. Phys. D: Appl. Phys.* **42**, 194002 (2009) (86).

748. Phelps, presented at the Swarm Studies and Inelastic Electron-Molecule Collisions, ed. by Pitchford, McKoy, Chutjian, Trajrnar, pp. 127–141 (204, 250, 252).

749. Phelps, Pitchford, "Anisotropic scattering of electrons by N_2 and its effect on electron transport", *Phys. Rev. A* **31**, 2932–2949 (1985) (133, 586, 588).

750. Phelps, Pitchford, "Anisotropic scattering of electrons by N_2 and its effect on electron transport: tabulations of cross section and results", tech. rep. 26 (JILA, Boulder, Colorado, 1985) (133, 555, 586).

752. Pitchford, Alves, Bartschat, *et al.*, "Comparisons of sets of electron–neutral scattering cross sections and swarm parameters in noble gases: I. Argon", *J. Phys. D: Appl. Phys.* **46**, 334001 (2013) (116, 133, 608, 610, 613).

754. Pleshinger, Alnussirat, Arias, *et al.*, "Gamma Ray Flashes Produced by Lightning Observed at Ground Level by TETRA-II." *J. Geophys. Res. : Space Phys.* **124**, 9229–9238 (2019) (24).

756. Pollack, Bhattacharya, Schmitt, "Bayesian Block Histogramming for High Energy Physics", (2019) (96).

759. Popov, "Investigation of the mechanism for rapid heating of nitrogen and air in gas discharges", *Plasma Phys Rep* **27**, 886–896 (2001) (45, 159).

774. Ridenti, Alves, Guerra, Amorim, "The role of rotational mechanisms in electron swarm parameters at low reduced electric field in N_2, $O_2$and H_2", *Plasma Sources Sci. Technol.* **24**, 035002 (2015) (61, 130, 593).

776. Ripoll, Zinn, Jeffery, Colestock, "On the dynamics of hot air plasmas related to lightning discharges: 1. Gas dynamics", *J. Geophys. Res.: Atmos.* **119**, 9196–9217 (2014) (40, 206).

777. Rison, Krehbiel, Stock, *et al.*, "Observations of narrow bipolar events reveal how lightning is initiated in thunderstorms", *Nat Commun* **7**, 10721 (2016) (10).

779. Ristić, Aoneas, Vojnović, Poparić, "Excitation of Electronic States of N_2 in Radio-Frequency Electric Field by Electron Impact", *Plasma Chem Plasma P* **37**, 1431–1443 (2017) (115).

781. Robson, White, Petrovi ć, "Colloquium: Physically based fluid modeling of collisionally dominated low-temperature plasmas", *Rev. Mod. Phys.* **77**, 1303–1320 (2005) (88).

783. Rohrlich, "The principle of equivalence", *Ann Phys-new York* **22**, 169–191 (1963) (19).

785. Rosenbluth, MacDonald, Judd, "Fokker-Planck Equation for an Inverse-Square Force", *Phys. Rev.* **107**, 1–6 (1957) (83).

786. Roussel-Dupré, Colman, Symbalisty, *et al.*, "Physical Processes Related to Discharges in Planetary Atmospheres", *Space Sci Rev* **137**, 51–82 (2008) (30, 34, 37).

787. Roussel-Dupré, Gurevich, "On runaway breakdown and upward propagating discharges", *J. Geophys. Res. : Space Phys.* **101**, 2297–2311 (1996) (23, 37).

788. Roussel-Dupré, Gurevich, Tunnell, Milikh, "Kinetic theory of runaway air-breakdown", tech. rep. (EG and G Energy Measurements, Inc., Los Alamos, NM, 1993) (71).

789. Roussel-Dupré, Gurevich, Tunnell, Milikh, "Kinetic theory of runaway air breakdown", *Phys. Rev. E* **49**, 2257–2271 (1994) (34).

795. Rutjes, Ebert, Buitink, *et al.*, "Generation of Seed Electrons by Extensive Air Showers, and the Lightning Inception Problem Including Narrow Bipolar Events", *J. Geophys. Res.: Atmos.* **124**, 7255–7269 (2019) (10, 33–34).

796. Saba, da Silva, Pantuso, da Silva, "Close View of the Lightning Attachment Process Unveils the Streamer Zone Fine Structure", *Geophys Res Lett* **49**, e2022GL101482 (2022), e2022GL101482 2022GL101482 (12).

802. Salvat, Fernández-Varea, "Overview of physical interaction models for photon and electron transport used in Monte Carlo codes", *Metrologia* **46**, S112 (2009) (73).

806. Sarria, Blelly, Briggs, Forme, "Studying the time histogram of a terrestrial electron beam detected from the opposite hemisphere of its associated TGF", *J. Geophys. Res. : Space Phys.* **121**, 4698–4704 (2016) (27).

807. Scargle, Norris, Jackson, Chiang, "Studies in astronomical time series analysis. VI. Bayesian block representations", *Astrophys. J.* **764**, 167 (2013) (96–97).

808. Schaal, Dwyer, Arabshahi, *et al.*, "The structure of X-ray emissions from triggered lightning leaders measured by a pinhole-type X-ray camera", *J. Geophys. Res.: Atmos.* **119**, 982–1002 (2014) (28).

811. Schmalzried, Luque, "Influence of Elastic Scattering on Electron Swarm Distribution in Electrified Gases", *J. Geophys. Res.: Atmos.* **125**, e2019JD031564 (2020) (vii–xii, 32, 117, 399, 534, 546, 557).

813. Schmalzried, Luque, Lehtinen, "Enhancing higher-energy spectral resolution for electron particle simulations in air", *Comput Phys Commun* **277**, 108366 (2022) (vii–xii, 98–99, 101–102, 104, 150, 217).

822. Schwinger, "On the Classical Radiation of Accelerated Electrons", *Phys. Rev.* **75**, 1912–1925 (1949) (53).

825. Shah, Razdan, Bhat, Ali, "Neutron generation in lightning bolts", *Nature* **313**, 773–775 (1985) (27).

826. Shao, Tarasenko, Zhang, *et al.*, "Runaway electrons and X-rays from a corona discharge in atmospheric pressure air", *New J Phys* **13**, 113035 (2011) (28, 33).

827. Shao, Zhang, Niu, *et al.*, "Diffuse discharge, runaway electron, and x-ray in atmospheric pressure air in an inhomogeneous electrical field in repetitive pulsed modes", *Appl Phys Lett* **98**, 021503 (2011) (28).

828. Shao, Zhang, Niu, *et al.*, "Runaway electron preionized diffuse discharges in atmospheric pressure air with a point-to-plane gap in repetitive pulsed mode", *J Appl Phys* **109**, 083306 (2011) (28–29, 33, 36).

829. Shao, Hamlin, Smith, "A closer examination of terrestrial gamma-ray flash-related lightning processes", *J. Geophys. Res. : Space Phys.* **115** (, 2010) (24, 26, 35).

852. Šimek, Bonaventura, "Non-equilibrium kinetics of the ground and excited states in N_2–O_2 under nanosecond discharge conditions: extended scheme and comparison with available experimental observations", *J. Phys. D: Appl. Phys.* **51**, 504004 (2018) (32, 45–46, 209, 222).

853. Sizykh, "Runaway production rate in gas discharges", *High Temp* **31**, 1–6 (1993) (182).

854. Skeie, Østgaard, Mezentsev, *et al.*, "The temporal relationship between Terrestrial Gamma-ray flashes and associated optical pulses from lightning", *J. Geophys. Res.: Atmos.* **127**, e2022JD037128 (2022) (24).

857. Smith, Dwyer, Hazelton, *et al.*, "A terrestrial gamma ray flash observed from an aircraft", *J. Geophys. Res.: Atmos.* **116** (, 2011) (13, 21).

858. Smith, Lin, Turin, *et al.*, "The RHESSI Spectrometer", *Sol Phys* **210**, 33–60 (2002) (21).

859. Smith, Lopez, Lin, Barrington-Leigh, "Terrestrial Gamma-Ray Flashes Observed up to 20 MeV", *Science* **307**, 1085–1088 (2005) (22–23, 26).

860. Smith, Trepanier, Alnussirat, *et al.*, "Thunderstorms Producing Sferic-Geolocated Gamma-Ray Flashes Detected by TETRA-II." *J. Geophys. Res.: Atmos.* **126**, e2020JD033765 (2021) (24, 36).

864. Solomon, Schroeder, Baker, "Lightning initiation–conventional and runaway-breakdown hypotheses", *Q. J. R. Meteorolog. Soc.* **127**, 2683–2704 (2001) (34).

866. Soula, Chauzy, "Multilevel measurement of the electric field underneath a thundercloud: 2. Dynamical evolution of a ground space charge layer", *J. Geophys. Res.: Atmos.* **96**, 22327–22336 (1991) (8).

874. Stanbro, Briggs, Roberts, *et al.*, "A Study of Consecutive Terrestrial Gamma-ray Flashes Using the Gamma-ray Burst Monitor", *J. Geophys. Res. : Space Phys.* **123**, 9634–9651 (2018) (22).

875. Stanley, Shao, Smith, *et al.*, "A link between terrestrial gamma-ray flashes and intracloud lightning discharges", *Geophys Res Lett* **33** (, 2006) (24).

876. Starodubtsev, Kozlov, Toropov, *et al.*, "First experimental observations of neutron bursts under thunderstorm clouds near sea level", *JETP Lett.* **96**, 188–191 (2012) (27).

896. Surendra, Graves, Jellum, "Self-consistent model of a direct-current glow discharge: Treatment of fast electrons", *Phys. Rev. A* **41**, 1112–1125 (1990) (117, 326, 334, 336, 557).

909. Takeuchi, "Relativistic $E \times B$ acceleration", *Phys. Rev. E* **66**, 037402 (2002) (50).

912. Tarasenko, Yakovlenko, "Runaway electrons and Generation of high-power subnanosecond electron beams in dense gases", *Phys Wave Phenom* **16**, 207 (2008) (29).

913. Tarasenko, Baksht, Burachenko, *et al.*, "Generation of supershort avalanche electron beams and formation of diffuse discharges in different gases at high pressure", *Plasma Devices Oper* **16**, 267–298 (2008) (28, 32–33).

918. Tavani, Marisaldi, Labanti, *et al.*, "Terrestrial Gamma-Ray Flashes as Powerful Particle Accelerators", *Phys. Rev. Lett.* **106**, 018501 (2011) (22).

919. Tavani, M., Barbiellini, G., Argan, A., *et al.*, "The AGILE Mission", *A&A* **502**, 995–1013 (2009) (21).

926. Teunissen, Ebert, "3D PIC-MCC simulations of discharge inception around a sharp anode in nitrogen/oxygen mixtures", *Plasma Sources Sci. Technol.* **25**, 044005 (2016) (161).

933. Toland, Vonnegut, "Measurement of maximum electric field intensities over water during thunderstorms", *J. Geophys. Res. (1896-1977)* **82**, 438–440 (1977) (8).

934. Torii, Nishijima, Kawasaki, Sugita, "Downward emission of runaway electrons and bremsstrahlung photons in thunderstorm electric fields", *Geophys Res Lett* **31** (, 2004) (21).

935. Torii, Sugita, Tanabe, *et al.*, "Gradual increase of energetic radiation associated with thunderstorm activity at the top of Mt. Fuji", *Geophys Res Lett* **36** (, 2009) (20–21).

943. Tran, Rakov, Mallick, *et al.*, "A terrestrial gamma-ray flash recorded at the Lightning Observatory in Gainesville, Florida", *J. Atmos. Sol. Terr. Phys.* **136**, 86–93 (2015), Advances in Lightning Research (22, 24).

947. Tsuchiya, Enoto, Iwata, *et al.*, "Hardening and Termination of Long-Duration γ Rays Detected Prior to Lightning", *Phys. Rev. Lett.* **111**, 015001 (2013) (21, 35).

948. Tsuchiya, Enoto, Torii, *et al.*, "Observation of an Energetic Radiation Burst from Mountain-Top Thunderclouds", *Phys. Rev. Lett.* **102**, 255003 (2009) (36).

949. Tsuchiya, Enoto, Yamada, *et al.*, "Detection of High-Energy Gamma Rays from Winter Thunderclouds", *Phys. Rev. Lett.* **99**, 165002 (2007) (20).

951. Umemoto, Tsuchiya, Enoto, *et al.*, "On-ground detection of an electron-positron annihilation line from thunderclouds", *Phys. Rev. E* **93**, 021201 (2016) (27, 36).

952. Usoskin, Desorgher, Velinov, *et al.*, "Ionization of the earth's atmosphere by solar and galactic cosmic rays", *Acta Geophys* **57**, 88–101 (2009) (33).

953. Vahedi, Surendra, "A Monte Carlo collision model for the particle-in-cell method: applications to argon and oxygen discharges", *Comput Phys Commun* **87**, 179–198 (1995), Particle Simulation Methods (56).

954. Valentini, Schwartzentruber, Bender, Candler, presented at the 45th AIAA Thermophysics Conference (46).

957. Vasilyak, Kostiouchenko, Koudriavtsev, Filiouguine, "High-speed ionization waves at an electric break down (in Russian)", *Usp Fiz Nauk+* **164**, 263–286 (1994) (28).

961. Vialetto, Moussa, van Dijk, *et al.*, "Effect of anisotropic scattering for rotational collisions on electron transport parameters in CO", *Plasma Sources Sci. Technol.* **30**, 075001 (2021) (61, 606).

964. Vojnović, Popović, Ristić, *et al.*, "Rate coefficients for electron impact excitation of N_2", *Chem Phys* **463**, 38–46 (2015) (115).

970. Wada, Enoto, Nakazawa, *et al.*, "Downward Terrestrial Gamma-Ray Flash Observed in a Winter Thunderstorm", *Phys. Rev. Lett.* **123**, 061103 (2019) (22–23).

971. Wada, Enoto, Nakamura, *et al.*, "Gamma-ray glow preceding downward terrestrial gamma-ray flash", *Communications Physics* **2**, 67 (2019) (21).

986. Wilson, "The Acceleration of β-particles in Strong Electric Fields such as those of Thunderclouds", *Math. Proc. Cambridge Philos. Soc.* **22**, 534–538 (1925) (33, 217, 625, 639).

990. Yakovlenko, "Beams of runaway electrons and discharges in dense gases, based on a wave of multiplication of background electrons", *Proc. of the Prokhorov General Institute, Moscow, Nauka* **63** (, 2007) (28).

994. Yoshida, Morimoto, Ushio, *et al.*, "High energy photon and electron bursts associated with upward lightning strokes", *Geophys Res Lett* **35** (, 2008) (27).

Books, Collections, Theses (Part I)

32. Babich, *High-Energy Phenomena in Electric Discharges in Dense Gases: Theory, Experiment and Natural Phenomena* (Futurepast, 2003) (27).

55. Bellan, "The Vlasov, two-fluid, and MHD models of plasma dynamics", in *Fundamentals of Plasma Physics* (Cambridge University Press, 2006), pp. 34–74 (79–81).

66. Bethe, Ashkin, "Passage of Radiations through Matter", in *Experimental Nuclear Physics*, ed. by Segrè, vol. 1, Experimental Nuclear Physics (Wiley, 1953), chap. II, pp. 252–304 (70).

73. Bittencourt, *Fundamentals of Plasma Physics* (Springer New York, New York, NY, 4th, 2018) (49, 79–82, 108, 235–236).

150. Capitelli, Ferreira, Gordiets, Osipov, *Plasma Kinetics in Atmospheric Gases* (Springer Berlin Heidelberg, Berlin, Heidelberg, 2000), pp. 95–104 (42, 44–46, 204, 209, 444).

189. Cooray, *An Introduction to Lightning* (Springer Netherlands, Dordrecht, 2015) (9).

265. Elsom, *Lightning: Nature and Culture* (Reaktion Books, 2015) (3–5, 9).

290. Firestone, *The table of isotopes*, ed. by Shirley (Wiley-Interscience, 8th edition, 1996), vol. 75 (33).

302. Franklin, Powell, Emami-Naeini, *Feedback Control of Dynamic Systems* (Pearson, 8th, 2018) (101).

339. Goldman, Goldman, "Chapter 4 - Corona Discharges", in *Gaseous Electronics*, ed. by Hirsh, Oskam (Academic Press, 1978), pp. 219–290 (16).

392. Heitler, *The quantum theory of radiation* (Oxford university press, Oxford, 2d ed. 1944) (27).

400. Hertel, Schulz, "Multi-electron Atoms", in *Atoms, Molecules and Optical Physics 1: Atoms and Spectroscopy*, See sections 10.5.3 for inelastic and 8.4.5 for elastic processes (Springer Berlin Heidelberg, Berlin, Heidelberg, 2015), chap. 10, pp. 495–547 (20).

404. Hirsh, Oskam, Eds., *Gaseous Electronics* (Academic Press, 1978) (14, 16).

446. Jackson, *Classical electrodynamics* (Wiley, New York, 3rd. 1998) (47, 328).

455. Jeans, *An Introduction to the Kinetic Theory of Gases* (Cambridge University Press, 1967) (235).

486. Kendall, "Classical Inference and the Linear Model", in *Kendall's advanced theory of statistics*, 5th ed.. Vol. 2A (Charles Griffin, London, 5th ed.. 1987) (77–78).

501. Kieu, "Ultra-fast time-resolved spectroscopy lightning-like discharges with GALIUS", PhD thesis (University of Granada, 2021) (15).

529. Köhn, "High-energy phenomena in laboratory and thunderstorm discharges", PhD thesis (Technische Universiteit Eindhoven, 2014) (37).

547. Kuzemsky, *Statistical Mechanics and the Physics of Many-Particle Model Systems* (World Scientific, 2017) (60).

548. Lagarkov, Rutkevich, *Ionization Waves in Electrical Breakdown of Gases* (Springer New York, New York, NY, 1994) (28, 84–85, 156, 195–196).

577. Lehtinen, "Relativistic Runaway Electrons Above Thunderstorms", PhD thesis (Stanford University, 2000) (51).

585. Li, "Joining particle and fluid aspects in streamer simulations", PhD thesis (Technische Universiteit Eindhoven, 2009) (37, 86, 106).

589. Lieberman, Lichtenberg, "Atomic Collisions", in *Principles of Plasma Discharges and Materials Processing* (John Wiley & Sons, Ltd, 2005), chap. 3, pp. 43–85 (56).

590. Lieberman, Lichtenberg, "Kinetic Theory of Discharges", in *Principles of Plasma Discharges and Materials Processing* (John Wiley & Sons, Ltd, 2005), chap. 18, pp. 679–721 (81–83, 87).

606. Loeb, Meek, *The Mechanism of the Electric Spark* (Stanford University Press, 1941) (10, 16, 86).

640. Meek, Craggs, *Electrical breakdown of gases* (86).

652. Mirpour, "Lightning inception by Hydrometeors: an experimental and numerical investigation", PhD thesis (Technische Universiteit Eindhoven, 2021) (15).

736. Parks, "Charged Particle Acceleration", in *Characterizing Space Plasmas: A Data Driven Approach* (Springer International Publishing, Cham, 2018), chap. 2, pp. 45–89 (49).

761. Raether, *Electron avalanches and breakdown in gases* (Butterworth & Co Ltd., 1964) (31).

762. Raizer, *Gas Discharge Physics*, ed. by Allen (Springer-Verlag, 1991) (10–11, 14, 32, 69, 85, 208).

764. Rakov, Uman, *Lightning: Physics and Effects* (Cambridge University Press, 2007) (8–9, 630).

816. Schram, *Kinetic Theory of Gases and Plasmas*, ed. by Van Der Merwe (Springer Netherlands, 1991), vol. 46 (79–80, 83, 242).

850. Sibley, *The Divine Thunderbolt: Missile of the Gods* (Xlibris US, 2009) (5).

Electron-Molecule Collisions (Part II)

4. Adibzadeh, Theodosiou, "Elastic electron scattering from inert-gas atoms", *Atom Data Nucl Data* **91**, 8–76 (2005) (356, 359, 373).

8. Ajello, James, Franklin, Howell, "Study of electron impact excitation of argon in the extreme ultraviolet: emission cross section of resonance lines of Ar I, Ar II", *J. Phys. B: At. Mol. Opt. Phys.* **23**, 4355–4376 (1990) (454–455, 610).

9. Ajello, James, Franklin, Shemansky, "Medium-resolution studies of extreme ultraviolet emission from N_2 by electron impact: Vibrational perturbations and cross sections of the $c_4^{'}\ ^1\Sigma_u^+$ and b' $^1\Sigma_u^+$ states", *Phys. Rev. A* **40**, 3524–3556 (1989) (435, 445, 588).

10. Ajello, Stevens, Stewart, *et al.*, "Titan airglow spectra from Cassini Ultraviolet Imaging Spectrograph (UVIS): EUV analysis", *Geophys Res Lett* **34** (, 2007) (445).

12. Allan, "Measurement of absolute differential cross sections for vibrational excitation of O_2 by electron impact", *J. Phys. B: At. Mol. Opt. Phys.* **28**, 5163 (1995) (426–427, 447, 596).

13. Allan, "Electron collisions with CO: Elastic and vibrational excitation cross sections", *Phys. Rev. A* **81**, 042706 (2010) (259).

16. Allan, "Electron collisions with NO: elastic scattering, vibrational excitation and $^2P_{1/2} \rightleftharpoons {}^2P_{3/2}$ transitions", *J. Phys. B: At. Mol. Opt. Phys.* **38**, 603 (2005) (426, 430).

17. Allan, "Measurement of the elastic and $v = 0 \rightarrow 1$ differential electron–N_2 cross sections over a wide angular range", *J. Phys. B: At. Mol. Opt. Phys.* **38**, 3655–3672 (2005) (259, 397, 408, 424, 426–427, 572).

18. Allan, "Improved techniques of measuring accurate electron - molecule cross sections near threshold and over a large angular range", *AIP Conf. Proc.* **901**, 107–116 (2007) (259).

19. Allan, "Measuring and modeling absolute data for electron-induced processes", *J. Phys.: Conf. Ser.* **388**, 012001 (2012) (259).

21. Altshuler, "Theory of Low-Energy Electron Scattering by Polar Molecules", *Phys. Rev.* **107**, 114–117 (1957) (412–413).

23. Alves, Bartschat, Biagi, *et al.*, "Comparisons of sets of electron–neutral scattering cross sections and swarm parameters in noble gases: II. Helium and neon", *J. Phys. D: Appl. Phys.* **46**, 334002 (2013) (252, 608).

24. Alves, Coche, Ridenti, Guerra, "Electron scattering cross sections for the modelling of oxygen-containing plasmas*", *Eur. Phys. J. D* **70**, 124 (2016) (252, 576, 596).

26. Andrick, in ed. by Bates, Estermann (Academic Press, 1974), vol. 9, pp. 207–242 (302, 422, 442, 543).

27. Anzai, Kato, Hoshino, *et al.*, "Cross section data sets for electron collisions with H_2, O_2, CO, CO_2, N_2O and H_2O", *Eur. Phys. J. D* **66**, 36 (2012) (440, 447).

28. Arnot, Chadwick, "The diffraction of electrons in gases", *Proc. R. Soc. London A.* **133**, 615–636 (1931) (254).

29. Arthurs, Dalgarno, Bates, "The theory of scattering by a rigid rotator", *Proceedings of the Royal Society of London. Series A. Mathematical and Physical Sciences* **256**, 540–551 (1960) (301, 412).

31. Avaldi, Camilloni, Fainelli, Stefani, "Absolute double differential ionization cross-section for electron impact: He", *Il Nuovo Cimento D* **9**, 97–113 (1987) (493).

51. Bartschat, Zatsarinny, "Close-coupling calculations for electron–atom collisions: benchmark studies and uncertainty estimates", *Phys Scripta* **90**, 054006 (2015) (374).

53. Baylis, "An approximate treatment of intra-atomic correlation in Hartree-Fock calculations: the Hg2(X1 Σg+) potential", *J. Phys. B: At. Mol. Phys.* **10**, L583 (1977) (359).

61. Berkes, Demeter, "Small angle scattering of electrons", *Nucl Phys* **15**, 421–435 (1960) (328).

62. Berkowitz, in *Photoabsorption, Photoionization, and Photoelectron Spectroscopy*, ed. by Berkowitz (Academic Press, 1979), pp. 73–154 (483, 486–487, 507–509, 578).

63. Berrington, "Low-energy electron excitation of the $^3P^e$ fine-structure levels in atomic oxygen", *J. Phys. B: At. Mol. Opt. Phys.* **21**, 1083–1089 (1988) (457, 510, 615).

64. Bethe, "Zur Theorie des Durchgangs schneller Korpuskularstrahlen durch Materie", *Ann. Phys.* **397**, 325–400 (1930) (436–438, 462–463, 469).

65. Bethe, "Bremsformel für Elektronen relativistischer Geschwindigkeit", *Z. Für Phys.* **76**, 293–299 (1932) (342).

72. Birtwistle, Herzenberg, "Vibrational excitation of N_2 by resonance scattering of electrons", *J. Phys. B: At. Mol. Phys.* **4**, 53–70 (1971) (422, 424).

74. Bjørge-Engeland, Østgaard, Mezentsev, *et al.*, "Terrestrial Gamma-Ray Flashes With Accompanying Elves Detected by ASIM", *J. Geophys. Res.: Atmos.* **127**, e2021JD036368 (2022) (456).

75. Blaauw, de Heer, Wagenaar, Barends, "Total cross sections for electron scattering from N_2 and He", *J. Phys. B: At. Mol. Phys.* **10**, L299–L303 (1977) (499).

79. Blanco, García, "Improvements on the imaginary part of a non-empirical model potential for electron scattering (30 to 10000 eV energies)", *Phys Lett A* **295**, 178–184 (2002) (376–377, 379–380, 382, 546).

80. Blanco, García, "Improved non-empirical absorption potential for electron scattering at intermediate and high energies: 30–10000 eV", *Phys Lett A* **255**, 147–153 (1999) (374, 376, 378–380, 546, 636).

81. Blanco, García, "Improvements on the quasifree absorption model for electron scattering", *Phys. Rev. A* **67**, 022701 (2003) (294, 376, 378–379, 381–382, 546).

83. Blanco, García, "Screening corrections for calculation of electron scattering differential cross sections from polyatomic molecules", *Phys Lett A* **330**, 230–237 (2004) (325, 403).

85. Bloomfield, Face, Moss, "Indefinite Integrals of Spherical Bessel Functions", (2017) (305, 418).

87. Boesten, Tanaka, "Elastic DCS for e+CH_4 collisions, 1.5-100 eV", *J. Phys. B: At. Mol. Opt. Phys.* **24**, 821–832 (1991) (399, 537).

89. Boffard, Jung, Anderson, Lin, in ed. by Berman, Lin, Arimondo (Academic Press, 2007), vol. 54, pp. 319–421 (453–454, 607).

90. Bohr, "II. On the theory of the decrease of velocity of moving electrified particles on passing through matter", *The London, Edinburgh, and Dublin Philosophical Magazine and Journal of Science* **25**, 10–31 (1913) (465).

91. Boness, Schulz, "Excitation of High Vibrational States of N_2 and CO via Shape Resonances", *Phys. Rev. A* **8**, 2883–2886 (1973) (419).

96. Born, "Quantenmechanik der Stoßvorgänge", *Zeitschrift für Physik* **38**, 803–827 (1926) (303).

97. Bote, Salvat, "Calculations of inner-shell ionization by electron impact with the distorted-wave and plane-wave Born approximations", *Phys. Rev. A* **77**, 042701 (2008) (462).

98. Bouferguene, Ema, Weatherford, "Nonadiabatic polarization potentials in electron- and positron-molecule scattering: Application to $e^- + H_2$", *Phys. Rev. A* **59**, 2712–2718 (1999) (361).

100. Bransden, McDowell, "Electron scattering by atoms at intermediate energies: I. Theoretical models", *Phys. Rep.* **30**, 207–303 (1977) (272, 274, 276–277, 284).

101. Bray, Abdurakhmanov, Bailey, *et al.*, "Convergent close-coupling approach to light and heavy projectile scattering on atomic and molecular hydrogen", *J. Phys. B: At. Mol. Opt. Phys.* **50**, 202001 (2017) (383).

102. Bray, Fursa, "Calculation of ionization within the close-coupling formalism", *Phys. Rev. A* **54**, 2991–3004 (1996) (462).

103. Breig, Lin, "Vibrational Excitation of Diatomic Molecules by Electron Impact", *J. Chem. Phys.* **43**, 3839–3845 (1965) (358).

105. Brennan, Alle, Euripides, *et al.*, "Elastic electron scattering and rovibrational excitation of N_2 at low incident energies", *J. Phys. B: At. Mol. Opt. Phys.* **25**, 2669–2682 (1992) (61, 397, 426–427, 571, 588).

106. Bretagne, Callede, Legentil, Puech, "Relativistic electron-beam-produced plasmas. I. Collision cross sections and loss function in argon", *J. Phys. D: Appl. Phys.* **19**, 761–777 (1986) (441–442, 456, 548, 578, 610).

108. Bridge, Buckingham, Linnett, "The polarization of laser light scattered by gases", *Proceedings of the Royal Society of London. Series A. Mathematical and Physical Sciences* **295**, 334–349 (1966) (292).

113. Bromberg, "Absolute Differential Cross Sections of Elastically Scattered Electrons. I. He, N_2, and CO at 500 eV", *J. Chem. Phys.* **50**, 3906–3921 (1969) (256–257, 588).

114. Bromberg, "Absolute Differential Cross Sections of Elastically Scattered Electrons. II. CO and N_2 at 500, 400, and 300 eV", *J. Chem. Phys.* **52**, 1243–1247 (1970) (257, 359, 572).

115. Bromberg, "Absolute differential cross sections of elastically scattered electrons. V. O_2 and CO_2 at 500, 400, and 300 eV", *J. Chem. Phys.* **60**, 1717–1721 (1974) (257, 359).

116. Bromberg, "Absolute differential cross sections of electrons elastically scattered by the rare gases. I. Small angle scattering between 200 and 700 eV", *J. Chem. Phys.* **61**, 963–969 (1974) (257, 393).

117. Brook, Harrison, Smith, "Measurements of the electron impact ionisation cross sections of He, C, O and N atoms", *J. Phys. B: At. Mol. Phys.* **11**, 3115–3132 (1978) (478, 488, 510, 580, 620).

119. Brunger, Campbell, Cartwright, *et al.*, "Electron-impact excitation of Rydberg and valence electronic states of nitric oxide: I. Differential cross sections", *J. Phys. B: At. Mol. Opt. Phys.* **33**, 783–808 (2000) (451).

120. Brunger, Campbell, Cartwright, *et al.*, "Electron-impact excitation of Rydberg and valence electronic states of nitric oxide: II. Integral cross sections", *J. Phys. B: At. Mol. Opt. Phys.* **33**, 809–819 (2000) (451–452, 509, 536, 553–554, 576–577, 604–605).

121. Brunger, Buckman, Elford, in *Interactions of Photons and Electrons with Molecules*, ed. by Itikawa (Springer-Verlag Berlin Heidelberg, 2003), vol. 17 C (435, 539–540, 556).

122. Brunger, Teubner, "Differential cross sections for electron-impact excitation of the electronic states of N_2", *Phys. Rev. A* **41**, 1413–1426 (1990) (261, 445, 572).

123. Brunger, Teubner, Buckman, "Near-threshold electron-impact excitation cross section for the E $^3\Sigma_g^+$ state of N_2", *Phys. Rev. A* **37**, 3570–3572 (1988) (444, 446, 507, 588).

124. Brunger, Buckman, "Electron–molecule scattering cross-sections. I. Experimental techniques and data for diatomic molecules", *Phys. Rep.* **357**, 215–458 (2002) (397, 424, 435, 447, 498–499, 568, 574, 588, 594, 597).

125. Brusa, Karwasz, Zecca, "Analytical partitioning of total cross sections for electron scattering on noble gases", *Zeitschrift für Physik D Atoms, Molecules and Clusters* **38**, 279–287 (1996) (512, 607).

126. Buckingham, "The quantum theory of atomic polarization I; Polarization by a uniform field", *Proc. R. Soc. London A - Math Phys. Sci.* **160**, 94–113 (1937) (358).

127. Buckley, Burke, "The scattering of low-energy electrons by diatomic molecules", *J. Phys. B: At. Mol. Phys.* **10**, 725–739 (1977) (302, 358).

129. Buckman, Lohmann, "Low-energy total cross section measurements for electron scattering from helium and argon", *J. Phys. B: At. Mol. Phys.* **19**, 2547 (1986) (499, 610).

130. Buckman, Brunger, Newman, *et al.*, "Near-threshold vibrational excitation of H_2 by electron impact: Resolution of discrepancies between experiment and theory", *Phys. Rev. Lett.* **65**, 3253–3256 (1990) (423).

131. Buckman, Brunger, "A Critical Comparison of Electron Scattering Cross Sections measured by Single Collision and Swarm Techniques", *Aust. J. Phys.* **50**, 483–509 (1997) (252).

133. Burgess, presented at the Proceedings of the Third International Conference on Electronic and Atomic Collisions, ed. by McDowell, p. 237 (345, 466, 470, 474).

134. Burke, Mackey, Shimamura, "R-matrix theory of electron-molecule scattering", *J. Phys. B: At. Mol. Phys.* **10**, 2497–2512 (1977) (390).

135. Burke, Chandra, "Electron-molecule interactions. II.. A pseudo-potential method for e^--N_2 scattering", *Journal of Physics B Atomic Molecular Physics* **5**, 1696–1711 (1972) (358, 364).

137. Byron, Joachain, "Eikonal optical-model theory of elastic electron-atom scattering", *Phys. Rev. A* **9**, 2559–2568 (1974) (287, 304, 359).

138. Callaway, LaBahn, Pu, Duxler, "Extended Polarization Potential: Applications to Atomic Scattering", *Phys. Rev.* **168**, 12–21 (1968) (287, 359).

139. Calogero, in *Variable Phase Approach to Potential Scattering*, ed. by Calogero (Elsevier, 1967), vol. 35, chap. 3, pp. 8–12 (300, 303, 315).

140. Campbell, Brunger, "Modelling of plasma processes in cometary and planetary atmospheres", *Plasma Sources Sci. Technol.* **22**, 013002 (2012) (451).

141. Campbell, Brunger, Nolan, *et al.*, "Integral cross sections for electron impact excitation of electronic states of N_2", *J. Phys. B: At. Mol. Opt. Phys.* **34**, 1185–1199 (2001) (445–446, 536, 538–540, 587–588).

143. Campbell, Brunger, "Electron collisions in atmospheres", *Int Rev Phys Chem* **35**, 297–351 (2016) (451).

145. Campbell, Green, Brunger, *et al.*, "Determination of differential cross sections for electron-impact excitation of electronic states of molecular oxygen", *Phys. Rev. A* **61**, 022706 (2000) (448–450, 590).

154. Carlson Jr., Mantas, "An experimental test of the ionosphere electron gas cooling rate by excitation of the fine structure of the ground state of atomic oxygen", *J. Geophys. Res. : Space Phys.* **87**, 4515–4524 (1982) (439, 457).

158. Cartwright, Chutjian, Trajmar, Williams, "Electron impact excitation of the electronic states of N_2. I. Differential cross sections at incident energies from 10 to 50 eV", *Phys. Rev. A* **16**, 1013–1040 (1977) (260–261, 435, 572).

159. Cartwright, Trajmar, Chutjian, Williams, "Electron impact excitation of the electronic states of N_2. II. Integral cross sections at incident energies from 10 to 50 eV", *Phys. Rev. A* **16**, 1041–1051 (1977) (444–446, 539, 554–555, 586, 588).

165. Ceperley, Alder, "Ground State of the Electron Gas by a Stochastic Method", *Phys. Rev. Lett.* **45**, 566–569 (1980) (361).

166. Chandra, "Low-energy electron scattering from CO", *Phys. Rev. A* **12**, 2342–2352 (1975) (358).

167. Chandra, Joshi, in *Advances in Astronomy and Astrophysics*, ed. by Kopal (Elsevier, 1970), vol. 7, pp. 1–55 (520–521).

168. Chang, "Modified effective-range theory for electron scattering from molecules", *J. Phys. B: At. Mol. Phys.* **14**, 893–901 (1981) (338–339, 391).

173. Chase, "Adiabatic Approximation for Scattering Processes", *Phys. Rev.* **104**, 838–842 (1956) (306, 413).

175. Chilton, Boffard, Schappe, Lin, "Measurement of electron-impact excitation into the $3p^5 4p$ levels of argon using Fourier-transform spectroscopy", *Phys. Rev. A* **57**, 267–277 (1998) (453–455, 509, 610, 613).

176. Chilton, Lin, "Measurement of electron-impact excitation into the $3p^5 3d$ and $3p^5 5s$ levels of argon using Fourier-transform spectroscopy", *Phys. Rev. A* **60**, 3712–3721 (1999) (454–456, 509, 578, 613).

177. Chowdhury, Chauhan, Limbachiya, *et al.*, "Double differential distributions of e-emission in ionization of N_2 by 3, 4 and 5 keV electron impact", *J. Phys. B: At. Mol. Opt. Phys.* **53**, 235201 (2020) (492–494).

180. Chutjian, Cartwright, "Electron-impact excitation of electronic states in argon at incident energies between 16 and 100 eV", *Phys. Rev. A* **23**, 2178–2193 (1981) (454–456, 509, 548–549, 577–579, 610, 613).

181. Chutjian, Cartwright, Trajmar, "Electron impact excitation of the electronic states of N_2. III. Transitions in the 12.5-14.2-eV energy-loss region at incident energies of 40 and 60 eV", *Phys. Rev. A* **16**, 1052–1060 (1977) (444, 446, 572).

182. Ciccarino, Savin, "Electron-Impact Ionization of Atomic Nitrogen", *J Thermophys Heat Tr* **33**, 154–162 (2019) (488).

183. Clementi, "Tables of Atomic Functions", *IBM Journal of Research and Development* **9**, 87–89 (1965) (278, 328).

185. Colle, Salvetti, "A general method for approximating the electronic correlation energy in molecules and solids", *J. Chem. Phys.* **79**, 1404–1407 (1983) (289–290, 361, 363, 672).

186. Collins, Norcross, "Electron collisions with highly polar molecules: Comparison of model, static, and static-exchange calculations for alkali-metal halides", *Phys. Rev. A* **18**, 467–498 (1978) (296, 386).

187. Colonna, Laporta, Celiberto, *et al.*, "Non-equilibrium vibrational and electron energy distributions functions in atmospheric nitrogen ns pulsed discharges and μs post-discharges: the role of electron molecule vibrational excitation scaling-laws", *Plasma Sources Sci. Technol.* **24**, 035004 (2015) (431).

193. Cosby, "Electron-impact dissociation of nitrogen", *J. Chem. Phys.* **98**, 9544–9553 (1993) (435, 444–446, 573, 590).

194. Cosby, "Electron-impact dissociation of oxygen", *J. Chem. Phys.* **98**, 9560–9569 (1993) (449, 599).

196. Cox, Bonham, "Elastic Electron Scattering Amplitudes for Neutral Atoms Calculated Using the Partial Wave Method at 10, 40, 70, and 100 kV for Z = 1 to Z = 54", *J. Chem. Phys.* **47**, 2599–2608 (1967) (278–279, 328, 330, 352–353).

197. Crawford, Dalgarno, "The scattering of thermal electrons by carbon monoxide", *J. Phys. B: At. Mol. Phys.* **4**, 494–502 (1971) (282, 358).

198. Crawford, Dalgarno, Hays, "Electron collision frequencies in polar gases", *Mol Phys* **13**, 181–192 (1967) (249, 296).

199. Crompton, in *Cross Section Data*, ed. by Inokuti (Academic Press, 1994), vol. 33, pp. 97–148 (250–251).

200. Crowe, in ed. by Bates, Bederson (Academic Press, 1988), vol. 24, pp. 269–321 (497).

205. Dababneh, Hsieh, Kauppila, *et al.*, "Total-cross-section measurements for positron and electron scattering by O_2, CH_4, and SF_6", *Phys. Rev. A* **38**, 1207–1216 (1988) (499, 596).

206. Daimon, Hayashi, Kondow, Kuchitsu, "Measurements of Differential Cross Sections of Low-Energy Electrons Elastically Scattered by Gas Molecules. II. Scattering of 200–500 eV Electrons by Molecular Oxygen", *J. Phys. Soc. Japan* **51**, 2641–2649 (1982) (257, 261, 333, 400, 403, 409, 508, 574, 597).

207. Dalba, Fornasini, Grisenti, *et al.*, "Absolute total cross section measurements for intermediate energy electron scattering. II. N_2, $O_2$and NO", *J. Phys. B: At. Mol. Phys.* **13**, 4695–4701 (1980) (499–500, 596, 602, 605).

208. Dalgarno, Moffett, "The rotational excitation of molecular nitrogen by slow electrons", tech. rep. (Queen's University of Belfast, Northern Ireland, 1962) (323, 413, 576).

209. Dalgarno, Lewis, "Dipole and Quadrupole Polarizabilities of Atoms and Molecules", *Proceedings of the Royal Society of London. Series A, Mathematical and Physical Sciences* **240**, 284–292 (1957) (288).

211. Davis, Shirley, "Splitting in Nitrogen and Oxygen 1s Photoelectron Peaks in Two Paramagnetic Molecules: Spin Density Implications", *J. Chem. Phys.* **56**, 669–670 (1972) (487).

212. Davisson, Germer, "Diffraction of Electrons by a Crystal of Nickel", *Phys. Rev.* **30**, 705–740 (1927) (266).

216. Descouvemont, Baye, "The R-matrix theory", *Rep. Progr. Phys.* **73**, 036301 (2010) (390).

217. Dillon, Inokuti, "Analytic representation of the dipole oscillator-strength distribution", *J. Chem. Phys.* **74**, 6271–6277 (1981) (346).

220. Doering, "Absolute differential and integral electron excitation cross sections for atomic oxygen: 9. Improved cross section for the ^{3}P $\rightarrow$ ^{1}D transition from 4.0 to 30 eV", *J. Geophys. Res. : Space Phys.* **97**, 19531–19534 (1992) (457, 615).

221. Doering, "Absolute differential and integral electron excitation cross sections for the O_2 ($a^1\Delta_g \leftarrow X^3\Sigma_g^-$) transition", *J. Geophys. Res. : Space Phys.* **97**, 12267–12270 (1992) (450, 574).

222. Doering, Goembel, "Absolute differential and integral electron excitation cross sections for atomic nitrogen: 1. The $^4S^o \rightarrow 3s^4P$ (λ1200 Å) transition from 30 to 100 eV", *J. Geophys. Res. : Space Phys.* **96**, 16021–16024 (1991) (459, 579, 618).

223. Doering, Goembel, "Absolute differential and integral electron excitation cross sections for atomic nitrogen: 2. The $^4S^o \rightarrow 2p^{44}P$ (λ1135 Å) transition from 30 to 100 eV", *J. Geophys. Res. : Space Phys.* **97**, 4295–4298 (1992) (459, 579, 618).

224. Doering, Gulcicek, "Absolute differential and integral electron excitation cross sections for atomic oxygen 7. The 3 P $\rightarrow$ 1 D and 3 P $\rightarrow$ 1 S transitions from 4.0 to 30 eV", *J. Geophys. Res. : Space Phys.* **94**, 1541–1546 (1989) (457).

225. Doering, Gulcicek, Vaughan, "Electron impact measurement of oscillator strengths for dipole-allowed transitions of atomic oxygen", *J. Geophys. Res. : Space Phys.* **90**, 5279–5284 (1985) (459, 487).

226. Doering, Vaughan, "Absolute experimental differential and integral electron excitation cross sections for atomic oxygen: 1. The (^{3}P $\rightarrow$ ^{3}S^o) Transition (1304 Å) at 100 eV", *J. Geophys. Res.: Space Phys.* **91**, 3279–3286 (1986) (262).

227. Doering, Yang, "Atomic oxygen $^3P \rightarrow {}^3S_0$ (λ1304Å) transition revisited: Cross section near threshold", *J. Geophys. Res. : Space Phys.* **106**, 203–209 (2001) (456, 458, 615).

228. Douglas, "THE NEAR ULTRAVIOLET BANDS OF N_2^+ AND THE DISSOCIATION ENERGIES OF THE N_2^+ AND N_2 MOLECULES", *Can J Phys* **30**, 302–313 (1952) (483).

229. Drachman, "Asymptotic effective potentials for electron-hydrogen scattering", *J. Phys. B: At. Mol. Phys.* **12**, L699–L702 (1979) (287–288, 359).

232. DuBois, Rudd, "Differential cross sections for elastic scattering of electrons from argon, neon, nitrogen and carbon monoxide", *J. Phys. B: At. Mol. Phys.* **9**, 2657 (1976) (259, 385, 393–394, 408, 411, 588, 608).

233. DuBois, Rudd, "Absolute doubly differential cross sections for ejection of secondary electrons from gases by electron impact. II. 100-500-eV electrons on neon, argon, molecular hydrogen, and molecular nitrogen", *Phys. Rev. A* **17**, 843–848 (1978) (493).

238. Dwyer, "Relativistic breakdown in planetary atmospheres", *Phys Plasmas* **14**, 042901 (2007) (36–37, 326, 328).

253. Dyatko, Kochetov, Napartovich, "Electron temperature in nitrogen afterglow: Dependence of theoretical results on the adopted set of cross sections and on the type of molecular distribution over vibrational levels", *Plasma Phys Rep* **28**, 965–971 (2002) (431).

254. Dykstra, "Dipole (electric field) and quadrupole (field gradient) polarizabilities of hydrogen, nitrogen, and acetylene from the application of derivative Hartree–Fock theory", *J. Chem. Phys.* **82**, 4120–4125 (1985) (288).

257. Eades, Truhlar, Dixon, "Ab initio self-consistent-field polarizabilities and electron-molecule adiabatic polarization potentials. III. N_2", *Phys. Rev. A* **20**, 867–878 (1979) (289, 357–358).

259. Edqvist, Lindholm, Selin, Åsbrink, "On the Photoelectron Spectrum of O_2", *Phys Scripta* **1**, 25–30 (1970) (487).

260. Edqvist, åsbrink, Lindholm, "On the Photoelectron Spectrum of NO", *Zeitschrift für Naturforschung A* **26**, 1407–1410 (1971) (487).

261. Ehrhardt, "Electron impact ionization at low and intermediate energy, the asymmetric (e,2e)-process", *AIP Conf. Proc.* **86**, 183–198 (1982) (492, 496–497).

262. Ehrhardt, Hesselbacher, Jung, *et al.*, "Measurements of double differential cross sections in electron impact ionization of helium and argon", *Zeitschrift für Physik A Hadrons and nuclei* **244**, 254–267 (1971) (493).

263. Ehrhardt, Schulz, Tekaat, Willmann, "Ionization of Helium: Angular Correlation of the Scattered and Ejected Electrons", *Phys. Rev. Lett.* **22**, 89–92 (1969) (495).

266. Engelhardt, Phelps, Risk, "Determination of Momentum Transfer and Inelastic Collision Cross Sections for Electrons in Nitrogen Using Transport Coefficients", *Phys. Rev.* **135**, A1566–A1574 (1964) (252, 323, 586, 588).

268. Fabrikant, "Partial-wave analysis of low-energy electron scattering by quadrupole molecules", *J. Phys. B: At. Mol. Phys.* **14**, 335 (1981) (339, 391).

269. Fabrikant, "Effective-range analysis of low-energy electron scattering by non-polar molecules", *J. Phys. B: At. Mol. Phys.* **17**, 4223 (1984) (391).

270. Fano, "Effects of Configuration Interaction on Intensities and Phase Shifts", *Phys. Rev.* **124**, 1866–1878 (1961) (422, 442).

272. Fedus, Karwasz, Idziaszek, "Analytic approach to modified effective-range theory for electron and positron elastic scattering", *Phys. Rev. A* **88**, 012704 (2013) (338, 358, 391, 513).

273. Feldt, Morrison, "Scaled adiabatic-nuclear-rotation theory for near-threshold rotational excitation in electron-molecule scattering", *Phys. Rev. A* **29**, 401–404 (1984) (413).

274. Feldt, Morrison, "Analytic Born completion in the calculation of differential cross sections for electron scattering from a linear molecule", *Phys. Rev. A* **77**, 012726 (2008) (321–322, 383, 385–386, 513, 538).

275. Feng, Sun, Morrison, Feldt, "Exact inclusion of exchange in calculations of cross sections for vibrational excitation of N_2 by low-energy electrons", *J. Phys. B: At. Mol. Opt. Phys.* **42**, 175201 (2009) (356).

276. Feng, Sun, Morrison, "Parameter-free nonadiabatic correlation-polarization potential for vibrational excitation in electron-molecule scattering: Application to $e - N_2$ collisions", *Phys. Rev. A* **68**, 062709 (2003) (289, 361, 373).

277. Feng, Wei-Guo, Yang-Yang, "High order correlation–polarization potential for vibrational excitation scattering of diatomic molecules by low-energy electrons", *Chinese Phys B* **18**, 4846–4851 (2009) (289).

278. Ferch, Granitza, Masche, Raith, "Electron-argon total cross section measurements at low energies by time-of-flight spectroscopy", *J. Phys. B: At. Mol. Phys.* **18**, 967 (1985) (499, 610).

279. Fermi, "The Ionization Loss of Energy in Gases and in Condensed Materials", *Phys. Rev.* **57**, 485–493 (1940) (242).

280. Feshbach, "Unified theory of nuclear reactions", *Ann Phys-new York* **5**, 357–390 (1958) (421).

282. Filipović, Marinković, Pejčev, Vušković, "Electron-impact excitation of argon: I. The $4s'[^1/_2]_1$, $4p[^1/_2]_1$ and $4p'[^1/_2]_0$ states", *J. Phys. B: At. Mol. Opt. Phys.* **33**, 677–691 (2000) (455, 610, 613).

283. Filipović, Marinković, Pejčev, Vušković, "Electron-impact excitation of argon: II. The lowest resonance $4s[^3/_2]_1$ and metastable $4s[^3/_2]_2$ and $4s'[^1/_2]_0$ states", *J. Phys. B: At. Mol. Opt. Phys.* **33**, 2081–2094 (2000) (43, 453, 455, 610, 613).

284. Filippelli, Lin, Anderson, McConkey, in *Cross Section Data*, ed. by Inokuti (Academic Press, 1994), vol. 33, pp. 1–62 (253–254).

286. Fink, Jost, Herrmann, "Differential cross sections for elastic electron scattering. Charge-cloud polarization in H_2", *Phys. Rev. A* **12**, 1374–1382 (1975) (333, 374).

287. Fink, Moore, Gregory, "Precise determination of differential electron scattering cross sections. I. The apparatus and the N_2 results", *J. Chem. Phys.* **71**, 5227–5237 (1979) (326, 333, 374, 397).

288. Finn, Doering, "Elastic scattering of 13 to 100 eV electrons from N_2", *J. Chem. Phys.* **63**, 4399–4404 (1975) (259, 401, 408, 536–537, 588).

289. Finn, Doering, "Measurement of the 13 to 100 eV electron impact excitation cross section for the $X\,^1S_g^+ \rightarrow a\,^1P_g$ transition in N_2", *J. Chem. Phys.* **64**, 4490–4494 (1976) (435, 588).

293. Fisk, "Theory of the Scattering of Slow Electrons by Diatomic Molecules", *Phys. Rev.* **49**, 167–173 (1936) (278).

298. Fon, Berrington, Burke, Hibbert, "The elastic scattering of electrons from inert gases. III. Argon", *J. Phys. B: At. Mol. Phys.* **16**, 307 (1983) (370).

300. Franck, Grotrian, "Bemerkungen über angeregte Atome", *Z. Für Phys.* **4**, 89–99 (1921) (323, 639).

304. Fritsche, Noffke, Gollisch, "A new local exchange potential for low-energy electron scattering by atoms based on first principles", *J. Phys. B: At. Mol. Phys.* **17**, 1637 (1984) (361).

305. Frost, Phelps, "Rotational Excitation and Momentum Transfer Cross Sections for Electrons in H_2 and N_2 from Transport Coefficients", *Phys. Rev.* **127**, 1621–1633 (1962) (43, 252).

307. Fujimoto, Lee, "Elastic and absorption cross sections for electron-nitric oxide collisions", *J. Phys. B: At. Mol. Opt. Phys.* **33**, 4759–4768 (2000) (374, 386, 399–400, 576).

309. Furness, McCarthy, "Semiphenomenological optical model for electron scattering on atoms", *J. Phys. B: At. Mol. Phys.* **6**, 2280–2291 (1973) (284, 354).

310. Furst, Golden, Mahgerefteh, *et al.*, "Absolute low-energy e^--Ar scattering cross sections", *Phys. Rev. A* **40**, 5592–5600 (1989) (394, 411, 577).

312. Ganas, "Excitation of atomic nitrogen by electron impact", *J. Chem. Phys.* **59**, 5411–5414 (1973) (459).

313. Gangwar, Sharma, Srivastava, Stauffer, "Electron-impact excitation of argon: Cross sections of interest in plasma modeling", *Phys. Rev. A* **81**, 052707 (2010) (453, 577).

315. García, Blanco, Williart, "Cross-sections for electron scattering by O_2 at intermediate and high energies, 0.1–10 keV", *Chem Phys Lett* **335**, 227–233 (2001) (499, 596).

316. García, Pérez, Campos, "Total cross section for electron scattering from N_2 in the energy range 600–5000 eV", *Phys. Rev. A* **38**, 654–657 (1988) (327, 499, 588).

317. García, Roteta, Manero, "Electron scattering by N_2 and CO at intermediate energies: 1–10 keV", *Chem Phys Lett* **264**, 589–595 (1997) (327, 499, 588).

318. Gardner, Samson, "Photoion and photoelectron spectroscopy of oxygen", *J. Chem. Phys.* **62**, 4460–4463 (1975) (487).

319. Gargioni, Grosswendt, "Electron scattering from argon: Data evaluation and consistency", *Rev. Mod. Phys.* **80**, 451–480 (2008) (252–253, 257, 453, 570, 577–578, 607, 610).

321. Gaudin, Albert, Hagemann, Robert, "Déterminations absolues des sections efficaces totales et partielles d´ionisation de l´hélium, du néon, de l´argon et de l´acétylène, pour des électrons de 100 à 2000 eV", *J. Chim. Phys.* **64**, 1209–1221 (1967) (509, 610, 612).

322. Geltman, Takayanagi, "Excitation of Molecular Rotation by Slow Electrons. II." *Phys. Rev.* **143**, 25–30 (1966) (337).

323. Gerjuoy, Stein, "Rotational Excitation by Slow Electrons", *Phys. Rev.* **97**, 1671–1679 (1955) (305, 323, 337, 412–413, 586, 593, 596).

324. Gianturco, Scialla, "Local approximations of exchange interaction in electron-molecule collisions: the methane molecule", *J. Phys. B: At. Mol. Phys.* **20**, 3171–3189 (1987) (355–356).

325. Gianturco, Jain, "The theory of electron scattering from polyatomic molecules", *Phys. Rep.* **143**, 347–425 (1986) (271–273, 284).

326. Gianturco, Lamanna, "The Glauber approximation in molecular scattering", *Mol Phys* **40**, 793–804 (1980) (304).

327. Gianturco, Rodriguez-Ruiz, "Correlation forces in electron scattering from atoms and molecules: a density functional approach", *Journal of Molecular Structure: THEOCHEM* **260**, 99–121 (1992), There is a typo in the sign of a on p.107, which was given a negative value whereas the original value [185, 567, p.785] was positive. A negative sign would lead to an unphysically repulsive correlation potential. (289–290, 357, 361–363).

328. Gianturco, Rodriguez-Ruiz, "Elastic electron scattering from rare gases with exact exchange: a new correlation-polarisation potential", *Il Nuovo Cimento D* **16**, 267–279 (1994) (289, 362, 372).

329. Gianturco, Tang, Toennies, *et al.*, "A semiclassical model of polarisation forces in atomic scattering", *Zeitschrift für Physik D Atoms, Molecules and Clusters* **33**, 27–37 (1995) (288–289, 359, 373).

331. Gibson, Gulley, Sullivan, *et al.*, "Elastic electron scattering from argon at low incident energies", *J. Phys. B: At. Mol. Opt. Phys.* **29**, 3177 (1996) (357).

332. Gibson, Morrison, "Ab initio nonadiabatic polarization potentials for electron-molecule scattering: The $e - H_2$ system", *Phys. Rev. A* **29**, 2497–2508 (1984) (289, 357–358, 373).

333. Gillan, Tennyson, McLaughlin, Burke, "Low-energy electron impact excitation of the nitrogen molecule: optically forbidden transitions", *J. Phys. B: At. Mol. Opt. Phys.* **29**, 1531–1547 (1996) (444, 588).

337. Glauber, "High energy collision theory", *Lectures in Theoretical Physics* **1**, ed. by Brittin, 314–414 (1959) (359).

338. Goldbach, Martin, Nollez, *et al.*, "Oscillator strength measurements in the vacuum-ultraviolet. I - The strong 1243, 1493 and 1743 Å multiplets of neutral nitrogen", *Astron Astrophys* **161**, 47–54 (1986) (487–488, 580).

342. Goruganthu, Bonham, "Secondary-electron-production cross sections for electron-impact ionization of helium", *Phys. Rev. A* **34**, 103–126 (1986) (493).

343. Goruganthu, Wilson, Bonham, "Secondary-electron-production cross sections for electron-impact ionization of molecular nitrogen", *Phys. Rev. A* **35**, 540–558 (1987) (396, 490–491, 493–494).

344. Gote, Ehrhardt, "Rotational excitation of diatomic molecules at intermediate energies: absolute differential state-to-state transition cross sections for electron scattering from N_2, Cl_2, CO and HCl", *J. Phys. B: At. Mol. Opt. Phys.* **28**, 3957–3986 (1995) (259, 397, 401, 416–418, 588).

345. Goudsmit, Uhlenbeck, "Over Het Roteerende Electron En de Structuur der Spectra", *Physica* **6**, 273–290 (1926) (348).

347. Gradshteyn, Ryzhik, in *Table of Integrals, Series, and Products (Eighth Edition)*, ed. by Zwillinger, Moll (Academic Press, Boston, Eighth Edition, 2014), pp. 637–775 (330, 412, 559, 561, 563).

348. Green, Dutta, "Semi-empirical cross sections for electron impacts", *J. Geophys. Res. (1896-1977)* **72**, 3933–3941 (1967) (335, 440, 535).

349. Green, McNeal, "Analytic cross sections for inelastic collisions of protons and hydrogen atoms with atomic and molecular gases", *J. Geophys. Res. (1896-1977)* **76**, 133–144 (1971) (440, 442, 535, 541).

350. Green, Stolarski, "Analytic models of electron impact excitation cross sections", *J Atmos Terr Phys* **34**, 1703–1717 (1972) (440, 442, 535).

351. Green, Maddern, Brunger, *et al.*, "Differential cross sections for electron impact excitation of the Herzberg pseudocontinuum of molecular oxygen", *J. Phys. B: At. Mol. Opt. Phys.* **35**, 3793–3800 (2002) (260, 448).

352. Green, Teubner, Brunger, *et al.*, "Integral cross sections for electron impact excitation of the Herzberg pseudocontinuum of molecular oxygen", *J. Phys. B: At. Mol. Opt. Phys.* **34**, L157–L162 (2001) (447, 450, 574, 596).

353. Green, Teubner, Mojarrabi, Brunger, "Resolution of a discrepancy between low-energy differential cross section measurements for elastic electron scattering from", *J. Phys. B: At. Mol. Opt. Phys.* **30**, 1813–1817 (1997) (397, 508, 574, 596–597).

355. Gresteau, Hall, Hetz, *et al.*, "Decay of Feshbach resonances in NO. I. Energy dependence of the electronic coupling to the ground state", *J. Phys. B: At. Mol. Phys.* **12**, 2925 (1979) (423).

358. Guerra, Amaro, Machado, Santos, "Single differential electron impact ionization cross sections in the binary-encounter-Bethe approximation for the low binding energy regime", *J. Phys. B: At. Mol. Opt. Phys.* **48**, 185202 (2015) (347, 349–350, 468, 474).

359. Guerra, Parente, Indelicato, Santos, "Modified binary encounter Bethe model for electron-impact ionization", *Int J Mass Spectrom* **313**, 1–7 (2012) (347, 466).

360. Gulcicek, Doering, "Absolute differential and integral electron excitation cross sections for atomic oxygen, 5, revised values for the $^3P \rightarrow {}^3S^o$ (1304 Å) and $^3P \rightarrow {}^3D^o$ (989 Å) transitions below 30 eV", *J. Geophys. Res. : Space Phys.* **93**, 5879–5884 (1988) (458).

361. Gulcicek, Doering, Vaughan, "Absolute differential and integral electron excitation cross sections for atomic oxygen, 6. The $^3P \rightarrow {}^3P$ and $^3P \rightarrow 5P$ transitions from 13.87 to 100 eV", *J. Geophys. Res. : Space Phys.* **93**, 5885–5889 (1988) (458).

372. Haas, "Untersuchungen über den Energieverlust langsamer Elektronen in Stickstoff", *Z. Für Phys.* **148**, 177–191 (1957) (323).

373. Haberland, Fritsche, Noffke, "Elastic scattering of low-energy electrons by Ne, Ar, Kr, and Xe", *Phys. Rev. A* **33**, 2305–2314 (1986) (370).

377. Hagelaar, Kroesen, "A Monte Carlo modelling study of the electrons in the microdischarges in plasma addressed liquid crystal displays", *Plasma Sources Sci. Technol.* **9**, 605–614 (2000) (334, 336).

382. Handy, Marron, Silverstone, "Long-Range Behavior of Hartree-Fock Orbitals", *Phys. Rev.* **180**, 45–48 (1969) (281).

383. Haque, Haque, Jakubassa-Amundsen, *et al.*, "e± Ar scattering in the energy range 1 eV $\leq E_i \leq$ 0.5 GeV", *J. Phys. Commun.* **3**, 045011 (2019) (370, 376, 380, 577).

384. Hara, "The Scattering of Slow Electrons by Hydrogen Molecules", *J. Phys. Soc. Japan* **22**, 710–718 (1967) (354, 370).

388. Hayashi, "Bibliography of electron and photon cross sections with atoms and molecules published in the 20th century. Argon", tech. rep. 72 (National Institute for Fusion Science of Japan, 2003) (453, 568, 577–578, 585, 610).

389. Hayashi, Kuchitsu, "A quasi-adiabatic polarization potential for elestic electron—atom scattering. Helium and other atoms", *Chem Phys Lett* **44**, 1–4 (1976) (358–359).

390. Hayashi, Kuchitsu, "Elastic Scattering of Electrons by Molecules at Intermediate Energies. I. General Theory", *J. Phys. Soc. Japan* **41**, 1724–1732 (1976) (309–310, 323).

394. Henry, "Vibrational and Rotational Excitation of Molecular Hydrogen by Electron Impact", *Phys. Rev. A* **2**, 1349–1358 (1970) (299).

395. Henry, Burke, Sinfailam, "Scattering of Electrons by C, N, O, N^+, O^+, and O^{++}", *Phys. Rev.* **178**, 218–225 (1969) (439, 545).

396. Herbák, Kövér, Szmola, *et al.*, "Elastic scattering of electrons on He, Ne, Ar in the impact energy region from 1000 to 3000 eV", *Acta Phys Hung* **58**, 63–68 (1985) (259, 396).

397. Herrmann, Jost, Kessler, Fink, "Differential cross sections for elastic electron scattering. II. Charge cloud polarization in N_2", *J. Chem. Phys.* **64**, 1–5 (1976) (257, 359, 396, 401, 572).

405. Hoffman, Dababneh, Hsieh, *et al.*, "Total-cross-section measurements for positrons and electrons colliding with H_2, N_2, and CO_2", *Phys. Rev. A* **25**, 1393–1403 (1982) (499, 588).

406. Hoffmann, Lunt, Jones, *et al.*, "An undulator-based spherical grating monochromator beamline for low energy electron-molecule scattering experiments", *Rev. Sci. Instrum.* **73**, 4157–4163 (2002) (259).

407. Hoffmann, Allan, Franz, *et al.*, "Resonance structure in electron–N_2 scattering around 11.5 eV: high-resolution measurements, *ab initio* calculations and line shape analyses", *J. Phys. B: At. Mol. Opt. Phys.* **42**, 215202 (2009) (262, 422–423, 443–444, 446, 507, 544, 588).

408. Hohenberg, Kohn, "Inhomogeneous Electron Gas", *Phys. Rev.* **136**, B864–B871 (1964) (277).

411. Hunter, Christophorou, in *Electron–Molecule Interactions and their Applications*, ed. by Christophorou (Academic Press, 1984), pp. 89–219 (252).

412. Huo, Kim, "Electron collision cross-section data for plasma modeling", *IEEE Trans. Plasma Sci.* **27**, 1225–1240 (1999) (312, 466–467, 490).

413. Huo, Gibson, Lima, McKoy, "Schwinger multichannel study of the $^2\Pi_g$ shape resonance in N_2", *Phys. Rev. A* **36**, 1632–1641 (1987) (285, 363).

415. Hwang, Kim, Rudd, "New model for electron-impact ionization cross sections of molecules", *J. Chem. Phys.* **104**, 2956–2966 (1996) (347, 469, 487).

418. Iga, Mu-Tao, Nogueira, Barbieri, "Elastic differential cross section measurements for electron scattering from Ar and O_2 in the intermediate-energy range", *J. Phys. B: At. Mol. Phys.* **20**, 1095 (1987) (333, 396, 409, 411, 597, 610).

419. Iga, Lee, Bonham, "Role of the intramolecular multiple scattering on electron diffraction from nitrogen molecule in the intermediate energy range", *Journal of Molecular Structure: THEOCHEM* **468**, 241–251 (1999) (311, 323).

420. Iga, Sanches, de Almeida, *et al.*, "Experimental verification on the applicability of the independent-atom model (IAM) for elastic electron-molecule scattering in the intermediate-energy range", *J Electron Spectrosc* **155**, 7–13 (2007), Scattering, Coincidence and Absorption Studies of Molecules (310).

424. Inokuti, McDowell, "Elastic scattering of fast electrons by atoms. I. Helium to neon", *J. Phys. B: At. Mol. Phys.* **7**, 2382–2395 (1974) (405, 498).

425. Inokuti, Buckman, Elford, Tawara, in *Interactions of Photons and Electrons with Atoms*, ed. by Itikawa (Springer-Verlag Berlin Heidelberg, 2000), vol. 17 A, chap. 2 (348, 459, 488, 612).

426. Inokuti, Kimura, Dillon, Shimamura, in *Cross Section Data*, ed. by Inokuti (Academic Press, 1994), vol. 33, pp. 215–251 (292, 442–443, 556).

427. Inokuti, "Inelastic Collisions of Fast Charged Particles with Atoms and Molecules—The Bethe Theory Revisited", *Rev. Mod. Phys.* **43**, 297–347 (1971), In this work, M represents the reduced mass of the system $m_1m_2/(m_1 + m_2)$, which is noted μ in our work. (70, 248, 266, 288, 325, 334–336, 342, 348, 436–439, 441, 463, 466, 469–471, 473, 477, 485, 496, 498, 501, 522–523, 548, 629, 638).

428. Inokuti, Saxon, Dehmer, "Total cross-sections for inelastic scattering of charged particles by atoms and molecules—VII.. Systematics for atoms in the first and second row", *Int J Radiat Phys Ch* **7**, 109–120 (1975) (498).

429. Isaacs, Morrison, "Modified effective range theory as an alternative to low-energy close-coupling calculations", *J. Phys. B: At. Mol. Opt. Phys.* **25**, 703 (1992) (391).

430. Isaacs, Morrison, "Analytic Born completion in the calculation of electron-molecule differential cross sections", *Phys. Rev. A* **53**, 4215–4221 (1996) (321, 338, 383, 385).

435. Itikawa, "Evaluation of the Evaluated Cross-Section Data for Atomic and Molecular Collisions", *Fusion Sci Technol* **63**, 333–337 (2013) (114, 252, 571).

437. Itikawa, Ichimura, "Cross Sections for Collisions of Electrons and Photons with Atomic Oxygen", *J Phys Chem Ref Data* **19**, 637–651 (1990) (456–458, 545).

438. Itikawa, Ichimura, Onda, *et al.*, "Cross Sections for Collisions of Electrons and Photons with Oxygen Molecules", *J Phys Chem Ref Data* **18**, 23–42 (1989) (433, 448, 594, 596).

439. Itikawa, "Cross Sections for Electron Collisions with Nitrogen Molecules", *J Phys Chem Ref Data* **35**, 31–53 (2006) (115, 435, 444–445, 507, 586, 588, 590, 638).

440. Itikawa, "Cross Sections for Electron Collisions with Oxygen Molecules", *J Phys Chem Ref Data* **38**, 1–20 (2009) (427, 435, 447, 449, 508, 594, 596).

441. Itikawa, "Cross sections for electron collisions with nitric oxide", *J Phys Chem Ref Data* **45**, 033106 (2016) (425, 434–435, 509, 576, 602, 604–605, 608).

442. Itikawa, Mason, "Rotational excitation of molecules by electron collisions", *Phys. Rep.* **414**, 1–41 (2005) (276, 299–301, 306, 577).

443. Jablonski, "Approximation of the Thomas-Fermi-Dirac potential for neutral atoms", *Physica A* **183**, 361–377 (1992) (278–279, 526).

444. Jackman, Garvey, Green, "Electron impact on atmospheric gases, I. Updated cross sections", *J. Geophys. Res. (1896-1977)* **82**, 5081–5090 (1977) (440, 544).

448. Jain, "Elastic scattering of intermediate- and high-energy electrons by $N_2$and CO in the two-potential coherent approach", *J. Phys. B: At. Mol. Phys.* **15**, 1533–1548 (1982) (372).

449. Jain, "Total (elastic+absorption) cross sections for e-CH_4 collisions in a spherical model at 0.10–500 eV", *Phys. Rev. A* **34**, 3707–3722 (1986) (375).

450. Jain, Baluja, "Total (elastic plus inelastic) cross sections for electron scattering from diatomic and polyatomic molecules at 10–5000 eV: H_2, Li_2, HF, CH_4, N_2, CO, C_2H_2, HCN, O_2, HCl, H_2S, PH_3, SiH_4, and CO_2", *Phys. Rev. A* **45**, 202–218 (1992) (375–376, 383, 400, 548).

451. Jain, Khare, "Ionizing collisions of electrons with CO_2, CO, H_2O, CH_4 and NH_3", *J. Phys. B: At. Mol. Phys.* **9**, 1429–1438 (1976) (469).

452. James, Ajello, Franklin, Shemansky, "Medium resolution studies of extreme ultraviolet emission from N_2 by electron impact: the effect of predissociation on the emission cross section of the b $^1\Pi_u$ state", *J. Phys. B: At. Mol. Opt. Phys.* **23**, 2055–2081 (1990) (435, 445, 588).

453. Jansen, de Heer, Luyken, *et al.*, "Absolute differential cross sections for elastic scattering of electrons by helium, neon, argon and molecular nitrogen", *J. Phys. B: At. Mol. Phys.* **9**, 185 (1976) (257, 259, 359, 396, 401, 572, 588).

454. Janssen, Pitchford, Hagelaar, van Dijk, "Evaluation of angular scattering models for electron-neutral collisions in Monte Carlo simulations", *Plasma Sources Sci. Technol.* **25**, 055026 (2016) (334–336, 557).

458. Jiang, Sun, Wan, "Geometric shielding effects of electron scattering from polyatomic molecules", *Phys Lett A* **237**, 53–57 (1997) (403).

459. Johansson, Forssén, "Fast and Accurate Evaluation of Wigner $3j$, $6j$, and $9j$ Symbols Using Prime Factorization and Multiword Integer Arithmetic", *SIAM J. Sci. Comput.* **38**, A376–A384 (2016) (322).

460. Johnson, Kanik, "Inelastic differential electron scattering cross sections of molecular oxygen (O_2) in the 20-100 eV impact energy range", *J. Phys. B: At. Mol. Opt. Phys.* **34**, 3041–3051 (2001) (259, 449, 579).

461. Johnson, Kanik, Khakoo, *et al.*, "Low energy differential and integral electron-impact cross sections for the $2s^2\,2p^4\,^3P \quad 2p^3\,3s\,^3S^o$ excitation in atomic oxygen", *J. Phys. B: At. Mol. Opt. Phys.* **36**, 4289–4299 (2003) (456, 458).

462. Johnson, McConkey, Tayal, Kanik, "Collisions of electrons with atomic oxygen: current status", *Can J Phys* **83**, 589–616 (2005) (262, 456–458, 545, 615).

463. Johnson, Malone, Kanik, *et al.*, "Integral cross sections for the direct excitation of the $A\,^3\Sigma_u^+$, $B\,^3\Pi_g$, $W\,^3\Delta_u$, $B'\,^3\Sigma_u^-$, $a'\,^1\Sigma_u^-$, $a\,^1\Pi_g$, $w\,^1\Delta_u$, and $C\,^3\Pi_u$ electronic states in N_2 by electron impact", *J. Geophys. Res. : Space Phys.* **110** (, 2005) (435, 443–446, 507, 534, 540, 572, 587–588).

464. Jolly, Bomben, Eyermann, "Core-electron binding energies for gaseous atoms and molecules", *Atom Data Nucl Data* **31**, 433–493 (1984) (487).

465. Jonauskas, Valdas, "Electron-impact single ionization of the nitrogen atom", *A&A* **659**, A11 (2022) (488).

467. Jones, in *Computational Nanoscience: Do it Yourself!*, ed. by Grotendorst, Blügel, Marx (NIC, John von Neumann Institute for Computing, Jülich, Germany, 2006), vol. 31, pp. 45–70 (361, 596).

468. Jones, Young, "Density functional theory and the von Weizsacker method", *J. Phys. C* **4**, 1322 (1971) (290).

469. Joshipura, "Polarization and exchange in electron scattering by atoms in solids", *Solid State Commun* **60**, 277–279 (1986) (359).

470. Joshipura, Patel, "Correlation-polarization effects in electron-atom scattering", *Pramana* **38**, 329–333 (1992) (359, 361).

472. Julienne, "$^3\Sigma_u^-$ – $^3\Sigma_u^+$ coupling in the O_2 $B^3\Sigma_u^-$ predissociation", *J. Mol. Spectrosc.* **63**, 60–79 (1976) (448).

473. Jung, Antoni, Muller, *et al.*, "Rotational excitation of N_2, CO and H_2O by low-energy electron collisions", *J. Phys. B: At. Mol. Phys.* **15**, 3535–3555 (1982) (259, 413–414, 416, 426).

474. Kacser, "Higher born approximations in non-relativistic Coulomb scattering", *Il Nuovo Cimento (1955-1965)* **13**, 303–318 (1959) (264, 336).

475. Kambara, Kuchitsu, "Measurement of Differential Cross Sections of Low-Energy Electrons Elastically Scattered by Gas Molecules. I. Apparatus", *Jpn J Appl Phys* **11**, 609–616 (1972) (261).

476. Kanik, Johnson, Das, *et al.*, "Electron-impact studies of atomic oxygen: I. Differential and integral cross sections; experiment and theory", *J. Phys. B: At. Mol. Opt. Phys.* **34**, 2647–2665 (2001) (262, 456–459, 548, 579).

477. Kanik, Nickel, Trajmar, "Total electron scattering cross section measurements for Kr, $O_2$and CO", *J. Phys. B: At. Mol. Opt. Phys.* **25**, 2189–2196 (1992) (499, 596).

478. Karwasz, Brusa, Gasparoli, Zecca, "Total cross-section measurements for e−—CO scattering: 80–4000 eV", *Chem Phys Lett* **211**, 529–533 (1993) (499, 588).

479. Kato, Suzuki, Ohkawa, *et al.*, "Benchmarking electronic-state excitation cross sections for electron-N_2 collisions", *Phys. Rev. A* **81**, 042717 (2010) (435, 447).

480. Kato, "On the eigenfunctions of many-particle systems in quantum mechanics", *Comm. Pure Appl. Math.* **10**, 151–177 (1957) (280).

481. Kauppila, Stein, Smart, *et al.*, "Measurements of total scattering cross sections for intermediate-energy positrons and electrons colliding with helium, neon, and argon", *Phys. Rev. A* **24**, 725–742 (1981) (499).

482. Kawaguchi, Takahashi, Satoh, "Electron collision cross section set for N_2 and electron transport in N_2, N_2/He, and N_2/Ar", *Plasma Sources Sci. Technol.* **30**, 035010 (2021) (37, 109, 115, 427, 544, 556, 566, 573–574, 583, 585, 587–588, 590).

488. Kennerly, "Absolute total electron scattering cross sections for N_2 between 0.5 and 50 eV", *Phys. Rev. A* **21**, 1876–1883 (1980) (255, 259, 499, 588).

489. Kennerly, Bonham, "Electron-helium absolute total scattering cross sections from 0.5 to 50 eV", *Phys. Rev. A* **17**, 1844–1854 (1978) (257).

490. Khakoo, Newell, Smith, "Electron impact excitation from $a^1\Delta_g$ state of molecular oxygen", *J. Phys. B: At. Mol. Phys.* **16**, L317–L322 (1983) (435).

491. Khakoo, Vandeventer, Childers, *et al.*, "Electron impact excitation of the argon $3p^5\,4s$ configuration: differential cross-sections and cross-section ratios", *J. Phys. B: At. Mol. Opt. Phys.* **37**, 247–281 (2004) (261, 453–455, 509, 577–579, 610, 613, 636).

492. Khakoo, Johnson, Ozkay, *et al.*, "Differential cross sections for the electron impact excitation of the $A\,^3\Sigma_u^+$, $B\,^3\Pi_g$, $W\,^3\Delta_u$, $B'\,^3\Sigma_u^-$, $a'\,^1\Sigma_u^-$, $a\,^1\Pi_g$, $w\,^1\Delta_u$, and $C\,^3\Pi_u$ states of N_2", *Phys. Rev. A* **71**, 062703 (2005) (260–261, 444–445).

493. Khakoo, Malone, Johnson, *et al.*, "Electron-impact excitation of $X\,^1\Sigma_g^+(v'' = 0)$ to the $a''\,^1\Sigma_g^+$, $b\,^1\Pi_u$, $c_3\,^1\Pi_u$, $o_3\,^1\Pi_u$, $b'\,^1\Sigma_u^+$, $c'_4\,^1\Sigma_u^+$, $G\,^3\Pi_u$, and $F\,^3\Pi_u$ states of molecular nitrogen", *Phys. Rev. A* **77**, 012704 (2008) (435, 444–445).

494. Khandker, Arony, Haque, *et al.*, "Scattering of e± from N_2 in the energy range 1 eV–10 keV", *Mol Phys* **118**, 1–15 (2020) (362, 376).

495. Khare, Raj, *Indian J. Pure Appl. Phys* **20**, 538 (1982) (361).

496. Khare, Shobha, "Elastic scattering of electrons by hydrogen molecules", *J. Phys. B: At. Mol. Phys.* **5**, 1938 (1972) (359).

497. Khrabrov, Kaganovich, "Electron scattering in helium for Monte Carlo simulations", *Phys Plasmas* **19**, 093511 (2012) (326, 336).

500. Kieu, Gordillo-Vázquez, Passas, *et al.*, "High-Speed Spectroscopy of Lightning-Like Discharges: Evidence of Molecular Optical Emissions", *J. Geophys. Res.: Atmos.* **126**, e2021JD035016 (2021) (12, 456).

502. Kim, "Angular and energy distributions of secondary electrons from helium. Slow electrons ejected by electron impact", *Phys. Rev. A* **28**, 656–666 (1983) (494).

504. Kim, "Scaling of plane-wave Born cross sections for electron-impact excitation of neutral atoms", *Phys. Rev. A* **64**, 032713 (2001) (304, 436, 439–440, 443, 512, 535–536, 544, 546, 552, 610).

505. Kim, "Scaled Born cross sections for excitations of H_2 by electron impact", *J. Chem. Phys.* **126**, 064305 (2007) (305, 439, 604, 610).

506. Kim, Desclaux, "Ionization of carbon, nitrogen, and oxygen by electron impact", *Phys. Rev. A* **66**, 012708 (2002) (469, 478–481, 487–488, 510, 580, 620).

507. Kim, Rudd, "Binary-encounter-dipole model for electron-impact ionization", *Phys. Rev. A* **50**, 3954–3967 (1994) (312, 337, 342–343, 345–349, 465, 467, 469–470, 472–473, 475, 505, 636).

508. Kim, Santos, Parente, "Extension of the binary-encounter-dipole model to relativistic incident electrons", *Phys. Rev. A* **62**, 052710 (2000) (312, 342, 346, 349–350, 462, 472, 474–475, 477, 480, 505, 512).

509. Kimura, Dillon, Buenker, *et al.*, "The effect of variable electronic transition moment on the EELS intensity distribution within a vibrational progression: use of the R-centroid approximation to analyze results for the CO B-X and O_2B'-X transitions", *Zeitschrift für Physik D Atoms, Molecules and Clusters* **38**, 165–169 (1996) (449, 523).

510. King, in *Advances in Atomic, Molecular, and Optical Physics*, ed. by Arimondo, Berman, Lin (Academic Press, 2011), vol. 60, pp. 1–64 (259, 572).

511. Kingston, Walters, "Electron scattering by atomic hydrogen: the distorted-wave second Born approximation", *J. Phys. B: At. Mol. Phys.* **13**, 4633–4662 (1980) (304).

512. Kitajima, Kishino, Okumura, *et al.*, "Low-energy and very-low energy total cross sections for electron collisions with N_2", *Eur. Phys. J. D* **71**, 139 (2017) (262, 422–423, 499, 571, 588).

513. Klump, Lassettre, "Energy transfer cross sections in relation to generalized oscillator strengths for the donor–acceptor pair benzene–acetone", *J. Chem. Phys.* **68**, 886–895 (1978) (439).

522. Koga, "Analytical Hartree-Fock electron densities for atoms He through Lr", *Theoretica chimica acta* **95**, 113–130 (1997) (278, 280, 328, 357).

523. Koga, Kanayama, Watanabe, Thakkar, "Analytical Hartree–Fock wave functions subject to cusp and asymptotic constraints: He to Xe, Li^+ to Cs^+, H^- to I^-", *Int J Quantum Chem* **71**, 491–497 (1999) (322, 487).

524. Kohl, Yates, Arvedson, "Electron scattering and charge cloud polarisation. I. Theory", *J. Phys. B: At. Mol. Phys.* **14**, 3227–3232 (1981) (287, 357, 373).

525. Kohl, Arvedson, "Elastic electron scattering from molecular potentials", *J. Chem. Phys.* **73**, 3818–3822 (1980) (292).

526. Kohl, Arvedson, "Elastic electron scattering. I. Scattering from diatomic potentials", *J. Chem. Phys.* **72**, 1915–1921 (1980) (308, 310–311).

527. Kohn, Sham, "Self-Consistent Equations Including Exchange and Correlation Effects", *Phys. Rev.* **140**, A1133–A1138 (1965) (361–363).

534. Korsch, Ernesti, "Rotational rainbow effects in electron-molecule and atom-molecule scattering", *J. Phys. B: At. Mol. Opt. Phys.* **25**, 3565–3599 (1992) (323, 415).

535. Korsch, Kutz, Meyer, "Rotational rainbows in electron-molecule scattering: Theory", *J. Phys. B: At. Mol. Phys.* **20**, L433 (1987) (61, 415–416).

540. Krupenie, "The Spectrum of Molecular Oxygen", *J Phys Chem Ref Data* **1**, 423–534 (1972) (448–449, 517).

545. Kurokawa, Kitajima, Toyoshima, *et al.*, "High-resolution total-cross-section measurements for electron scattering from Ar, Kr, and Xe employing a threshold-photoelectron source", *Phys. Rev. A* **84**, 062717 (2011) (391, 393–394, 411, 499, 608, 610).

546. Kutz, Meyer, "Rotational excitation of N_2 and Cl_2 molecules by electron impact in the energy range 0.01–1000 eV: Investigation of excitation mechanisms", *Phys. Rev. A* **51**, 3819–3830 (1995) (60, 141, 355, 416–418, 420, 507, 574, 593).

549. Laher, Gilmore, "Updated Excitation and Ionization Cross Sections for Electron Impact on Atomic Oxygen", *J Phys Chem Ref Data* **19**, 277–305 (1990) (440, 456–457, 459, 544–545, 615).

550. Lahmam-Bennani, Casagrande, Naja, "Experimental investigation of the triple differential cross section for electron impact ionization of N_2 and CO_2 molecules at intermediate impact energy and large ion recoil momentum", *J. Phys. B: At. Mol. Opt. Phys.* **42**, 235205 (2009) (495–497, 630).

551. Lane, "The theory of electron-molecule collisions", *Rev. Mod. Phys.* **52**, 29–119 (1980) (268, 272–276, 285, 299–300, 306–307, 358).

552. Laporta, Celiberto, Tennyson, "Resonant vibrational-excitation cross sections and rate constants for low-energy electron scattering by molecular oxygen", *Plasma Sources Sci. Technol.* **22**, 025001 (2013) (63, 209, 419, 427, 429, 506, 508, 512, 565, 583, 596–597).

553. Laporta, Celiberto, Wadehra, "Theoretical vibrational-excitation cross sections and rate coefficients for electron-impact resonant collisions involving rovibrationally excited N_2 and NO molecules", *Plasma Sources Sci. Technol.* **21**, 055018 (2012) (427, 504, 506, 512, 565, 583, 604–605).

554. Laporta, Little, Celiberto, Tennyson, "Electron-impact resonant vibrational excitation and dissociation processes involving vibrationally excited N_2 molecules", *Plasma Sources Sci. Technol.* **23**, 065002 (2014) (63–64, 116, 419–420, 427–431, 507–508, 587–588).

555. Laporta, Schneider, Tennyson, "Dissociative electron attachment cross sections for rovibrationally excited NO molecule and N^- anion formation", *Plasma Sources Sci. Technol.* **29**, 10LT01 (2020) (428, 434–435, 504, 506, 509, 604–605).

556. Laporta, Tennyson, Schneider, "Vibrationally resolved NO dissociative excitation cross sections by electron impact", *Plasma Sources Sci. Technol.* **29**, 05LT02 (2020) (430, 604).

557. Laporta, Vialetto, Guerra, "Vibrational excitation cross sections for non-equilibrium nitric oxide-containing plasma", *Plasma Sources Sci. Technol.* **31**, 054001 (2022) (391, 410, 419, 426, 429–430, 500, 509, 604–605, 609).

558. Laporta, Celiberto, Tennyson, "Dissociative electron attachment and electron-impact resonant dissociation of vibrationally excited O_2 molecules", *Phys. Rev. A* **91**, 012701 (2015) (68, 425, 428, 430, 434–435, 504, 506, 508, 519, 596).

560. Laricchiuta, Celiberto, Capitelli, "Electron impact cross-sections for electronic excitation of vibrationally excited O_2 to $B^3\Sigma_u^-$ state", *Chem Phys Lett* **329**, 526–532 (2000) (448).

561. Laricchiuta, Celiberto, Colonna, "Electron Impact Ionization of Metastable States of Diatomic Molecules", *Atoms* **10** (, 2022) (487).

562. Lassettre, "Power Series Representation of Generalized Oscillator Strengths", *J. Chem. Phys.* **43**, 4479–4486 (1965) (439).

563. Lassettre, "Inelastic scattering of high energy electrons by atmospheric gases", *Can. J. Chem.* **47**, 1733–1774 (1969) (438–439, 523).

564. Latter, "Atomic Energy Levels for the Thomas-Fermi and Thomas-Fermi-Dirac Potential", *Phys. Rev.* **99**, 510–519 (1955) (526).

565. LaVilla, "The O Kα and C Kα emission and O K absorption spectra from O2 and CO2. IV", *J. Chem. Phys.* **63**, 2733–2737 (1975) (487).

567. Lee, Yang, Parr, "Development of the Colle-Salvetti correlation-energy formula into a functional of the electron density", *Phys. Rev. B* **37**, 785–789 (1988) (289–290, 361–363, 372–373, 672).

568. Lee, Lu, "Spectroscopy and Collision Theory. II. The Ar Absorption Spectrum", *Phys. Rev. A* **8**, 1241–1257 (1973) (456, 610).

569. Lee, Iga, "Elastic and total cross sections for electron scattering by nitrogen molecule in the intermediate energy range", *J. Phys. B: At. Mol. Opt. Phys.* **32**, 453–462 (1999) (291, 376, 383, 400).

570. Lee, Iga, Machado, Brescansin, "Model absorption potential for electron-molecule scattering in the intermediate-energy range", *Phys. Rev. A* **62**, 062710 (2000) (374, 376, 383).

571. Lee, Gomide Freitas, "Incoherent renormalised multicentre potential model for electron-linear-molecule scattering: elastic and vibrational transition cross sections for e^--$N_2$and e^--CO", *J. Phys. B: At. Mol. Phys.* **16**, 233–243 (1983) (372).

572. Lee, Gomide Freitas, "Incoherent renormalised multicentre potential model for elastic scattering of electrons by linear molecules at intermediate and high energies", *J. Phys. B: At. Mol. Phys.* **14**, 1053–1064 (1981) (358, 390, 563).

574. Lefebvre-Brion, Field, in *Perturbations in the Spectra of Diatomic Molecules*, ed. by Lefebvre-Brion, Field (Academic Press, 1986), pp. 331–382 (434).

584. Lewis, England, Gibson, *et al.*, "Electron energy-loss spectra of coupled electronic states: Effects of Rydberg-valence interactions in O_2", *Phys. Rev. A* **63**, 022707 (2001) (449).

593. Linder, Schmidt, "Experimental Study of Low Energy e-O_2 Collision Processes", *Zeitschrift für Naturforschung A* **26**, 1617–1625 (1971) (260, 450, 596).

594. Linder, Schmidt, "Rotational and Vibrational Excitation of H_2 by Slow Electron Impact", *Zeitschrift für Naturforschung A* **26**, 1603–1617 (1971) (259).

595. Lindhard, "On the properties of a gas of charged particles", *Kgl. Danske Videnskab. Selskab Mat.-Fys. Medd.* **28** (, 1954) (293).

596. Lindsay, Mangan, in *Interactions of Photons and Electrons with Molecules*, ed. by Itikawa (Springer-Verlag Berlin Heidelberg, 2003), vol. 17 C (257, 348, 483–484, 488, 507, 593, 604, 608).

598. Linert, King, Zubek, "Measurements of differential cross sections for elastic electron scattering in the backward direction by molecular oxygen", *J. Phys. B: At. Mol. Opt. Phys.* **37**, 4681–4691 (2004) (333, 397, 409, 508, 512, 537, 574, 596–597).

599. Linert, Zubek, "Differential cross section for electron impact excitation of the a1Δg state of molecular oxygen in the 15–180° angular range", *Chem Phys Lett* **429**, 395–398 (2006) (261, 426–427, 575, 596).

600. Linert, Zubek, "Differential cross sections for electron elastic scattering and vibrational $v = 1$ excitation in nitrogen in the energy range from 5 to 20 eV measured over an angular range of 10°–180°", *J. Phys. B: At. Mol. Opt. Phys.* **42**, 085203 (2009) (397, 408–409, 420, 426–427, 507, 512, 536–537, 572–573, 587–588, 590).

602. Liu, "Elastic scattering of fast electrons by $H_2(^1\Sigma_g^+)$ and $N_2(X^1\Sigma_g^+)$", *Phys. Rev. A* **32**, 1384–1394 (1985) (333, 374, 397).

603. Liu, "Total cross sections for high-energy electron scattering by H_2 ($^1\Sigma_g^+$), N_2 ($^1\Sigma_g^+$), and O_2 ($^3\Sigma_g^-$)", *Phys. Rev. A* **35**, 591–597 (1987) (327).

604. Liu, Xu, Ni, *et al.*, "Integral cross sections of the dipole-allowed excitations of nitrogen molecule studied by the fast electron scattering", *J. Geophys. Res. : Space Phys.* **122**, 3459–3468 (2017) (439–440).

605. Llovet, Powell, Salvat, Jablonski, "Cross Sections for Inner-Shell Ionization by Electron Impact", *J Phys Chem Ref Data* **43**, 013102 (2014) (312, 314, 337, 346, 462, 465, 494).

607. Lofthus, Krupenie, "The spectrum of molecular nitrogen", *J Phys Chem Ref Data* **6**, 113–307 (1977) (444–445, 478, 487, 517).

608. Lotz, "An empirical formula for the electron-impact ionization cross-section", *Z. Für Phys.* **206**, 205–211 (1967) (464).

609. Loureiro, Ferreira, "Coupled electron energy and vibrational distribution functions in stationary N_2discharges", *J. Phys. D: Appl. Phys.* **19**, 17–35 (1986) (44, 46, 431, 587–588).

611. Lucchese, Takatsuka, McKoy, "Applications of the Schwinger variational principle to electron-molecule collisions and molecular photoionization", *Phys. Rep.* **131**, 147–221 (1986) (374).

616. Machado, Lee, Brescansin, *et al.*, "Elastic electron scattering by water molecules", *J. Phys. B: At. Mol. Opt. Phys.* **28**, 467–475 (1995) (296, 399).

617. Machado, Ribeiro, Lee, *et al.*, "Cross sections and polarization fractions for elastic $e^- - O_2$ collisions", *Phys. Rev. A* **60**, 1199–1205 (1999) (291–292, 399–401).

620. Majeed, Strickland, "New Survey of Electron Impact Cross Sections for Photoelectron and Auroral Electron Energy Loss Calculations", *J Phys Chem Ref Data* **26**, 335–349 (1997) (46, 444–445, 587).

622. Malone, Johnson, Young, *et al.*, "Integral cross sections for electron-impact excitation of the $C\,^3\Pi_u$, $E\,^3\Sigma_g^+$ and $a''\,^1\Sigma_g^+$ states of N_2", *J. Phys. B: At. Mol. Opt. Phys.* **42**, 225202 (2009) (443–446, 507, 539–540, 572, 587–588).

623. Malone, Johnson, Kanik, *et al.*, "Electron-impact excitation of molecular nitrogen. I. Excitation of the $C\,^3\Pi_u$, $E\,^3\Sigma_g^+$, and $a''\,^1\Sigma_g^+$ states", *Phys. Rev. A* **79**, 032704 (2009) (445–446, 507).

624. Malone, Johnson, Liu, *et al.*, "Integral cross sections for the electron-impact excitation of the b $^1\Pi_u$, c_3 $^1\Pi_u$, o_3 $^1\Pi_u$, b'^1 Σ_u^+, c_4' $^1\Sigma_u^+$, G $^3\Pi_u$, and F $^3\Pi_u$ states of N_2", *Phys. Rev. A* **85**, 062704 (2012) (261, 435, 443–446, 507, 554, 587–588).

632. Martinazzo, Bodo, Gianturco, "A modified Variable-Phase algorithm for multichannel scattering with long-range potentials", *Comput Phys Commun* **151**, 187–198 (2003) (316–317, 512).

633. Mason, Newell, "Electron impact total excitation cross section of the a $^1\Pi_g$ state of N_2", *J. Phys. B: At. Mol. Phys.* **20**, 3913–3921 (1987) (261, 435, 445, 588).

635. Mazeau, Gresteau, Hall, Huetz, "Energy and width of $N^-(^3P)$ from observation of its formation by dissociative attachment to N_2 and NO", *J. Phys. B: At. Mol. Phys.* **11**, L557 (1978) (435).

638. McEachran, Stauffer, "Dynamic distortion effects in electron-atom scattering", *J. Phys. B: At. Mol. Opt. Phys.* **23**, 4605 (1990) (289, 370, 374).

642. Middleton, Brunger, Teubner, *et al.*, "Differential cross sections for the electron impact excitation of the a $^1\Delta_g$ and b $^1\Sigma_g^+$ electronic states of O_2", *J. Phys. B: At. Mol. Opt. Phys.* **27**, 4057–4072 (1994) (447, 450).

643. Middleton, Teubner, Brunger, "Experimental confirmation for resonance enhancement in the electron impact excitation cross sections of the $a^1\Delta_g$ and $b^1\Sigma_g^+$ electronic states of O_2", *Phys. Rev. Lett.* **69**, 2495–2498 (1992) (447).

644. Mielewska, Linert, King, Zubek, "Differential cross sections for elastic electron scattering in argon over the angular range 130°–180°", *Phys. Rev. A* **69**, 062716 (2004) (259, 262, 357).

645. Mihajlov, Stojanović, Petrović, "Resonant vibrational excitation/de-excitation of N_2(v) by electrons", *J. Phys. D: Appl. Phys.* **32**, 2620–2629 (1999) (431).

651. Milosavljević, Telega, Šević, *et al.*, "Elastic electron scattering by argon in the vicinity of the high-energy critical minimum", *Radiat Phys Chem* **70**, 669–676 (2004) (259).

653. Mittleman, Watson, "Effects of the Pauli principle on the scattering of high-energy electrons by atoms", *Ann Phys-new York* **10**, 268–279 (1960) (359).

654. Mojarrabi, Gulley, Middleton, *et al.*, "Electron collisions with NO: elastic scattering and rovibrational (0 to 1, 2, 3, 4) excitation cross sections", *J. Phys. B: At. Mol. Opt. Phys.* **28**, 487–504 (1995) (397, 400, 402, 410, 426, 430, 508–509, 512, 576, 604–605).

655. Mojarrabi, Campbell, Teubner, *et al.*, "Differential and integral cross sections for excitation of the electronic states of nitric oxide by low-energy electron impact: Observation of a $^2\Pi_r \rightarrow ^2\Phi$ excitation process", *Phys. Rev. A* **54**, 2977–2982 (1996) (451, 453, 605).

656. Moliere, "Theorie der Streuung schneller geladener Teilchen I. Einzelstreuung am abgeschirmten Coulomb-Feld", *Z. Naturforsch.* **A2**, 133 (1947) (328).

657. Møller, "Zur Theorie des Durchgangs schneller Elektronen durch Materie", *Ann. Phys.* **406**, 531–585 (1932) (312).

662. Mori, Utamuratov, Fursa, *et al.*, "Calculation of the single differential cross section for electron-impact ionization of atoms and molecules", *J. Phys. B: At. Mol. Opt. Phys.* **54**, 015205 (2020) (462).

665. Morrison, Crompton, Saha, Petrovic, "Near-threshold Rotational and Vibrational Excitation of H_2 by Electron Impact: Theory and Experiment", *Aust. J. Phys.* **40**, 239–282 (1987) (418).

667. Morrison, "The Physics of Low-energy Electron-Molecule Collisions: A Guide for the Perplexed and the Uninitiated", *Aust. J. Phys.* **36**, 239–286 (1983) (276).

668. Morrison, in ed. by Bates, Bederson (Academic Press, 1988), vol. 24, pp. 51–156 (338–339, 513).

669. Morrison, Collins, "Exchange in low-energy electron-molecule scattering: Free-electron-gas model exchange potentials and applications to e-H_2 and e-N_2 collisions", *Phys. Rev. A* **17**, 918–938 (1978) (354–355, 383).

671. Morrison, Feldt, Austin, "Adiabatic approximations for the nuclear excitation of molecules by low-energy electron impact: Rotational excitation of H_2", *Phys. Rev. A* **29**, 2518–2540 (1984) (301, 305–307, 338, 385–386, 390).

672. Morrison, Hay, "Ab initio adiabatic polarization potentials for low-energy electron-molecule and positronmolecule collisions: The e-N_2 and e-CO_2 systems", *Phys. Rev. A* **20**, 740–748 (1979) (287, 289, 358, 373).

673. Morrison, Lane, Collins, "Low-energy electron-molecule scattering: Application of coupled-channel theory to e-CO_2 collisions", *Phys. Rev. A* **15**, 2186–2201 (1977) (308).

674. Morrison, Saha, Gibson, "Electron-N_2 scattering calculations with a parameter-free model polarization potential", *Phys. Rev. A* **36**, 3682–3698 (1987) (285, 289, 386, 418).

676. Morrison, Sun, Isaacs, Trail, "Ultrasimple calculation of very-low-energy momentum-transferand rotational-excitation cross sections: e-N_2 scattering", *Phys. Rev. A* **55**, 2786–2798 (1997) (411, 513).

677. Moss, Pasko, Liu, Veronis, "Monte Carlo model for analysis of thermal runaway electrons in streamer tips in transient luminous events and streamer zones of lightning leaders", *J. Geophys. Res. : Space Phys.* **111** (, 2006) (vii, ix, xi, 32, 37, 56, 71, 91, 117, 182, 326, 336).

679. Mott, Fowler, "The collision between two electrons", *Proc. R. Soc. London A.* **126**, 259–267 (1930) (311, 343, 375).

681. Müller-Fiedler, Jung, Ehrhardt, "Double differential cross sections for electron impact ionisation of helium", *J. Phys. B: At. Mol. Phys.* **19**, 1211–1229 (1986) (493–494).

683. Murphy, "Total and differential electron collision cross sections for O_2 and N_2", tech. rep. (Los Alamos Natl. Lab., Los Alamos, 1988) (117, 326).

684. Muse, Silva, Lopes, Khakoo, "Low energy elastic scattering of electrons from H_2 and N_2", *J. Phys. B: At. Mol. Opt. Phys.* **41**, 095203 (2008) (259, 397, 408, 588).

693. Nesbet, "Variational calculations of accurate e^--He cross sections below 19 eV", *Phys. Rev. A* **20**, 58–70 (1979) (260, 571).

694. Ness, Robson, "Velocity distribution function and transport coefficients of electron swarms in gases. II. Moment equations and applications", *Phys. Rev. A* **34**, 2185–2209 (1986) (433).

699. Nickel, Kanik, Trajmar, Imre, "Total cross section measurements for electron scattering on H_2 and N_2 from 4 to 300 eV", *J. Phys. B: At. Mol. Opt. Phys.* **25**, 2427–2431 (1992) (499, 588).

700. Nickel, Mott, Kanik, McCollum, "Absolute elastic differential electron scattering cross sections for carbon monoxide and molecular nitrogen in the intermediate energy region", *J. Phys. B: At. Mol. Opt. Phys.* **21**, 1867–1877 (1988) (258–259, 401, 588).

701. Nickel, Imre, Register, Trajmar, "Total electron scattering cross sections. I. He, Ne, Ar, Xe", *J. Phys. B: At. Mol. Phys.* **18**, 125 (1985) (499, 610).

702. Nigam, Sundaresan, Wu, "Theory of Multiple Scattering: Second Born Approximation and Corrections to Molière's Work", *Phys. Rev.* **115**, 491–502 (1959) (328).

705. Nishimura, Yano, "Total Electron Scattering Cross Sections for Ar,N_2, H_2O and D_2O", *J. Phys. Soc. Japan* **57**, 1951–1956 (1988) (499, 588).

708. Nogueira, Iga, Lee, "Total cross sections for electrons scattered from gases: 0.5-3.0 keV range on Ar", *J. Phys. B: At. Mol. Phys.* **15**, 2539–2549 (1982) (257, 327, 499, 610).

709. O'Malley, "Extrapolation of Electron-Rare Gas Atom Cross Sections to Zero Energy", *Phys. Rev.* **130**, 1020–1029 (1963) (338–339).

710. O'Malley, Spruch, Rosenberg, "Modification of Effective-Range Theory in the Presence of a Long-Range (r−4) Potential", *J Math Phys* **2**, 491–498 (1961) (338, 358, 390).

711. Ochkur, Brattsev, "Exchange Excitation of Helium by Electron Impact", *Opt Spectrosc+* **19**, 274 (1965) (293, 355, 439).

712. Oda, Osawa, "Generalised oscillator strength and total cross sections for the $X\,^1\Sigma_g^+ \rightarrow a\,^1\Pi_g$ transition in molecular nitrogen at 500 to 2000 eV incident electron energies", *J. Phys. B: At. Mol. Phys.* **14**, L563–L568 (1981) (336).

713. Okhrimovskyy, Bogaerts, Gijbels, "Electron anisotropic scattering in gases: A formula for Monte Carlo simulations", *Physical review E, Statistical, nonlinear, and soft matter physics* **65**, 037402 (2002) (117, 326, 336, 557).

714. Okumura, Kobayashi, Sayama, *et al.*, "Total cross-section for low-energy and very low-energy electron collisions with O_2", *J. Phys. B: At. Mol. Opt. Phys.* **52**, 035201 (2019) (422–423, 433, 499, 594, 596–597).

716. Olsen, Motz, Koch, "Electron Scattering without Atomic or Nuclear Excitation", *Rev. Mod. Phys.* **36**, 881–928 (1964) (56, 59, 311, 331, 390).

717. Onda, "Electronic Polarization of Atoms in Charged-Particle Impact", tech. rep. 471 (Institute for Space and Aeronautical Science, University of Tokyo, 1971) (359–360).

718. Onda, Truhlar, "State-to-state cross sections for electron impact on N_2. Close coupling and polarized Born calculations for rotational and vibrational excitation and pure elastic scattering at nonresonant energies", *J. Chem. Phys.* **71**, 5107–5123 (1979) (307).

719. Onda, Truhlar, "New approaches to the quantum-mechanical treatment of charge polarization in intermediate-energy electron scattering", *Phys. Rev. A* **22**, 86–100 (1980) (288, 360).

720. Opal, Beaty, Peterson, "Tables of secondary-electron-production cross sections", *Atom Data Nucl Data* **4**, 209–253 (1972) (491, 493–494).

721. Opal, Peterson, Beaty, "Measurements of Secondary-Electron Spectra Produced by Electron Impact Ionization of a Number of Simple Gases", *J. Chem. Phys.* **55**, 4100–4106 (1971) (259, 490, 492–493).

726. Pacios, "Analytical density-dependent representation of Hartree—Fock atomic potentials", *J Comput Chem* **14**, 410–421 (1993) (278–281, 328, 352–353).

728. Padial, Norcross, "Parameter-free model of the correlation-polarization potential for electron-molecule collisions", *Phys. Rev. A* **29**, 1742–1748 (1984) (290–292, 361–362).

729. Paikeday, Alexander, "Polarization potential for e-argon scattering by differential scattering minimization at intermediate energies", *Int J Quantum Chem* **90**, 778–785 (2002) (359, 370, 373).

731. Panajotović, Filipović, Marinković, *et al.*, "Critical minima in elastic electron scattering by argon", *J. Phys. B: At. Mol. Opt. Phys.* **30**, 5877–5894 (1997) (259, 394, 411, 577, 608).

734. Parkes, Sugden, "Electron attachment and detachment in nitric oxide", *J. Chem. Soc., Faraday Trans. 2* **68**, 600–614 (1972) (432).

739. Pauli, "Über den Zusammenhang des Abschlusses der Elektronengruppen im Atom mit der Komplexstruktur der Spektren", *Z. Für Phys.* **31**, 765–783 (1925) (266).

740. Pavlovic, Boness, Herzenberg, Schulz, "Vibrational Excitation in N_2 by Electron Impact in the 15-35-eV Region", *Phys. Rev. A* **6**, 676–685 (1972) (424, 586).

742. Perdew, Zunger, "Self-interaction correction to density-functional approximations for many-electron systems", *Phys. Rev. B* **23**, 5048–5079 (1981) (287, 290, 361).

748. Phelps, presented at the Swarm Studies and Inelastic Electron-Molecule Collisions, ed. by Pitchford, McKoy, Chutjian, Trajrnar, pp. 127–141 (204, 250, 252).

753. Plenkiewicz, Plenkiewicz, Jay-Gerin, "Pseudopotential calculations for elastic scattering of slow electrons (0–20 eV) from noble gases. I. Argon", *Phys. Rev. A* **38**, 4460–4469 (1988) (362, 370, 373).

758. Poparić, Ristić, Belić, "Resonant Vibrational Excitation and De-Excitation of N_2(v) by Low-Energy Electrons", *J. Phys. Chem. A* **112**, 3816–3822 (2008) (431, 635).

763. Raj, Kumar, "Elastic scattering of electrons by molecular oxygen", *Phys Lett A* **282**, 284–287 (2001) (376, 383, 546).

765. Ramsauer, "Uber den wirkungsquerschnitt der gasmolekule Gegenuber Langsamen electronen. I. Fortsetzung", *Ann. Phys* **66**, 546 (1921) (254).

766. Ranković, Maljković, Tökési, Marinković, "Elastic electron differential cross sections for argon atom in the intermediate energy range from 40 eV to 300 eV", *Eur. Phys. J. D* **72**, 30 (2018) (393).

767. Rapp, Briglia, "Total Cross Sections for Ionization and Attachment in Gases by Electron Impact. II. Negative-Ion Formation", *J. Chem. Phys.* **43**, 1480–1489 (1965) (434, 506, 508–509, 596, 605).

768. Rapp, Englander-Golden, "Total Cross Sections for Ionization and Attachment in Gases by Electron Impact. I. Positive Ionization", *J. Chem. Phys.* **43**, 1464–1479 (1965) (257, 488, 509, 588, 593, 596, 600, 602, 610, 612).

769. Rau, Fano, "Transition Matrix Elements for Large Momentum or Energy Transfer", *Phys. Rev.* **162**, 68–70 (1967) (471, 477).

770. Read, "Angular distributions for resonant scattering of electrons by molecules", *J. Phys. B: At. Mol. Phys.* **1**, 893–908 (1968) (425).

771. Register, Trajmar, Srivastava, "Absolute elastic differential electron scattering cross sections for He: A proposed calibration standard from 5 to 200 eV", *Phys. Rev. A* **21**, 1134–1151 (1980) (258, 260, 571, 577, 579).

772. Reid, Wadehra, "Low-energy differential scattering of electrons and positrons from noble gases", *Phys. Rev. A* **50**, 4859–4867 (1994) (359, 370).

773. Rescigno, McKoy, Schneider, Eds., Electron-Molecule and Photon-Molecule Collisions (Springer, Boston, 1979) (383, 447).

775. Riley, Truhlar, "Approximations for the exchange potential in electron scattering", *J. Chem. Phys.* **63**, 2182–2191 (1975), The exponents of eqs. (14) and (15) were confused: (14) should be a cubic root, whereas (15) should be a square root. (284, 355).

778. Ristić, Poparić, Belić, "Rate coefficients for resonant vibrational excitation of N_2", *Chem Phys* **331**, 410–416 (2007) (427, 635).

780. Robertson, Elford, Crompton, *et al.*, "Rotational and Vibrational Excitation of Nitrogen by Electron Impact", *Aust. J. Phys.* **50**, 441–472 (1997) (323, 337).

790. Rudd, "Differential and total cross sections for ionization of helium and hydrogen by electrons", *Phys. Rev. A* **44**, 1644–1652 (1991) (337, 494).

791. Rudd, DuBois, "Absolute doubly differential cross sections for ejection of secondary electrons from gases by electron impact. I. 100- and 200-eV electrons on helium", *Phys. Rev. A* **16**, 26–32 (1977) (493).

792. Rudd, Hollman, Lewis, *et al.*, "Doubly differential electron-production cross sections for 200–1500-eV e^-+H_2 collisions", *Phys. Rev. A* **47**, 1866–1873 (1993) (490).

793. Rudge, "Theory of the Ionization of Atoms by Electron Impact", *Rev. Mod. Phys.* **40**, 564–590 (1968) (345–346, 462, 466–467, 628).

794. Rumble, Truhlar, "Comparison of local exchange potentials for electron–N_2 scattering", *J. Chem. Phys.* **72**, 5223–5227 (1980) (356).

799. Salvat, Mayol, Molins, Parellada, "A simple model for electron scattering: elastic cross sections", *J. Phys. D: Appl. Phys.* **18**, 1401–1414 (1985) (279, 305, 321, 390).

800. Salvat, Martinez, Mayol, Parellada, "Analytical Dirac-Hartree-Fock-Slater screening function for atoms (Z=1–92)", *Phys. Rev. A* **36**, 467–474 (1987) (278–279, 328, 330, 352–353).

801. Salvat, "Optical-model potential for electron and positron elastic scattering by atoms", *Phys. Rev. A* **68**, 012708 (2003) (291, 293–294, 318, 359, 362–363, 373–374, 376, 380, 383, 512).

804. Salvat, Mayol, "Elastic scattering of electrons and positrons by atoms. Schrödinger and Dirac partial wave analysis", *Comput Phys Commun* **74**, 358–374 (1993) (311).

805. Santos, Parente, Kim, "Cross sections for K-shell ionization of atoms by electron impact", *J. Phys. B: At. Mol. Opt. Phys.* **36**, 4211–4224 (2003) (487).

810. Schlemmer, Srivastava, Rosel, Ehrhardt, "Electron impact ionization of helium at intermediate collision energies", *J. Phys. B: At. Mol. Opt. Phys.* **24**, 2719–2736 (1991) (67, 495).

811. Schmalzried, Luque, "Influence of Elastic Scattering on Electron Swarm Distribution in Electrified Gases", *J. Geophys. Res.: Atmos.* **125**, e2019JD031564 (2020) (vii–xii, 32, 117, 399, 534, 546, 557).

812. Schmalzried, Luque, Lehtinen, "Combined molecular and atomic potentials for elastic cross sections of electrons scattering off diatomic molecules at intermediate energies", *Phys. Rev. A* **106**, 032813 (2022) (vii–viii, x–xii, 322, 360, 370, 372, 400, 403, 412, 563).

814. Schram, De Heer, van der Wiel, Kistemaker, "Ionization cross sections for electrons (0.6–20 keV) in noble and diatomic gases", *Physica* **31**, 94–112 (1965) (257, 488, 508, 588, 596, 600, 610, 612).

815. Schram, Moustafa, Schutten, de Heer, "Ionization cross sections for electrons (100–600 eV) in noble and diatomic gases", *Physica* **32**, 734–740 (1966) (488, 596, 600, 610).

817. Schubert, Schuck, Jung, Geltman, "Triple differential cross sections for the electron impact ionisation of helium at 35 eV collision energy", *J. Phys. B: At. Mol. Phys.* **12**, 967 (1979) (493, 495).

819. Schulz, "Vibrational Excitation of N_2, CO, and H_2 by Electron Impact", *Phys. Rev.* **135**, A988–A994 (1964) (323, 586, 588).

820. Schulz, "Resonances in Electron Impact on Diatomic Molecules", *Rev. Mod. Phys.* **45**, 423–486 (1973) (61, 68, 419, 421, 424–425, 434).

824. Seaton, Steenman-Clark, "Effective potentials for electron-atom scattering below inelastic thresholds. I. Asymptotic forms", *J. Phys. B: At. Mol. Phys.* **10**, 2639–2647 (1977) (288, 357, 359–360).

830. Sheikin, "Model differential cross section of elastic scattering of electrons by atoms in the Monte Carlo simulation of the passage of electrons in a substance", *Tech Phys+* **55**, 1–9 (2010) (326).

831. Shen, Wang, Gong, *et al.*, "Electron-impact ionization cross sections for nitrogen molecule from 250 to 8000 eV", *J Electron Spectrosc* **225**, 42–48 (2018) (488, 507, 588).

832. Shi, Stephen, Burrow, "Differential cross sections for elastic scattering of electrons from N_2 at 0.55, 1.5 and 2.2 eV", *J. Phys. B: At. Mol. Opt. Phys.* **26**, 121–128 (1993) (397, 408, 424, 571–572, 588).

833. Shimamori, Fessenden, "Thermal electron attachment to oxygen and van der Waals molecules containing oxygen", *J. Chem. Phys.* **74**, 453–466 (1981) (432).

836. Shimamura, "Cross sections for collisions of electrons with atoms and molecules", *Scientific Papers of the Institute of Physical and Chemical Research* **82** (, 1989) (338–339, 413, 512).

837. Shyn, "Doubly differential cross sections of secondary electrons ejected from gases by electron impact: 50-400 eV on N_2", *Phys. Rev. A* **27**, 2388–2395 (1983) (490–493).

838. Shyn, Carignan, "Angular distribution of electrons elastically scattered from gases: 1.5-400 eV on N_2. II." *Phys. Rev. A* **22**, 923–929 (1980) (259, 397, 399, 401, 408, 571–573, 587–588).

839. Shyn, Cho, Sharp, "Differential excitation cross section of atomic oxygen by electron impact: (^{3}P-^{1}S transition)", *J. Geophys. Res. : Space Phys.* **91**, 13751–13754 (1986) (457).

840. Shyn, Sharp, "Doubly differential cross sections of secondary electrons ejected from gases by electron impact: 50-300 eV on helium", *Phys. Rev. A* **19**, 557–567 (1979) (493–494).

841. Shyn, Sharp, "Angular distributions of electrons elastically scattered from H_2", *Phys. Rev. A* **24**, 1734–1740 (1981) (259).

842. Shyn, Sharp, "Angular distribution of electrons elastically scattered from O_2: 2.0-200-eV impact energy", *Phys Rev A* **26**, 1369–1372 (1982) (333, 397, 400–401, 403, 409, 508, 572, 574–575, 594, 596–597).

843. Shyn, Sharp, "Differential excitation cross section of atomic oxygen by electron impact: (^{3}P-^{1}D transition)", *J. Geophys. Res. : Space Phys.* **91**, 1691–1697 (1986) (457).

844. Shyn, Stolarski, Carignan, "Angular Distribution of Electrons Elastically Scattered from N_2", *Phys Rev A* **6**, 1002–1012 (1972) (397, 401, 594).

845. Shyn, Sweeney, "Differential electronic-excitation cross sections of molecular oxygen by electron impact: The a $^1\Delta_g$ and $^1\Sigma_g$ states", *Phys. Rev. A* **47**, 1006–1008 (1993) (450, 574–575, 594, 596).

846. Shyn, Sweeney, "Vibrational-excitation cross sections of molecular oxygen by electron impact", *Phys. Rev. A* **48**, 1214–1217 (1993) (426–427, 594, 596–597).

847. Shyn, Sweeney, "Measurement of absolute differential excitation cross sections of molecular oxygen by electron impact: Decomposition of the Herzberg pseudocontinuum", *Phys. Rev. A* **62**, 022711 (2000) (448, 574–575, 635).

848. Shyn, Sweeney, Grafe, "Differential excitation cross sections of molecular oxygen by electron impact: The longest and second bands", *Phys. Rev. A* **49**, 3680–3684 (1994) (449–450, 574–575, 594, 596).

849. Shyn, Sweeney, Grafe, Sharp, "Absolute differential cross sections for the excitation of molecular oxygen by electron impact: Decomposition of the Schumann-Runge continuum", *Phys. Rev. A* **50**, 4794–4801 (1994) (449, 574–575, 594, 596, 600, 635).

855. Skerbele, Lassettre, "Absolute Electron Collision Cross Sections for Two Forbidden Transitions in Nitrogen at Kinetic Energies of 300–500 eV", *J. Chem. Phys.* **53**, 3806–3813 (1970) (336).

856. Slater, "A Simplification of the Hartree-Fock Method", *Phys. Rev.* **81**, 385–390 (1951) (354, 628).

862. Snyder, Scott, "Multiple Scattering of Fast Charged Particles", *Phys. Rev.* **76**, 220–225 (1949) (328).

863. Sohn, Kochem, Scheuerlein, *et al.*, "Near-threshold vibrational excitation and elastic electron scattering from N_2", *J. Phys. B: At. Mol. Phys.* **19**, 4017–4024 (1986) (339–340, 364, 397, 408, 427, 507, 571, 588).

865. Song, Yoon, Cho, *et al.*, "Cross Sections for Electron Collisions with NO, N_2O, and NO_2", *J Phys Chem Ref Data* **48**, 043104 (2019) (434, 451, 498, 500, 508, 548, 569, 576–577, 602, 604–606).

867. Spence, Burrow, "Cross sections for excitation of the $(2s^2 2p^2 3s)^4P$ and $(2s2p^4)^4P$ states of atomic nitrogen by near-threshold electron impact", *J. Phys. B: At. Mol. Phys.* **13**, 2809–2815 (1980) (459).

868. Spence, Schulz, "Three-Body Attachment in O_2 Using Electron Beams", *Phys. Rev. A* **5**, 724–732 (1972) (432–433, 594, 596).

870. Srivastava, Chutjian, Trajmar, "Absolute elastic differential electron scattering cross sections in the intermediate energy region. II.—N_2", *J. Chem. Phys.* **64**, 1340–1344 (1976) (261, 397, 399, 401, 408, 572–573, 587–588).

871. Srivastava, Tanaka, Chutjian, Trajmar, "Elastic scattering of intermediate-energy electrons by Ar and Kr", *Phys. Rev. A* **23**, 2156–2166 (1981) (259, 357, 385, 394, 411, 577).

872. Srivastava, Chutjian, Trajmar, "Absolute elastic differential electron scattering cross sections in the intermediate energy region. I. H_2", *J. Chem. Phys.* **63**, 2659–2665 (1975) (258, 261).

873. Srivastava, Hall, Trajmar, Chutjian, "Pure rotational excitation of H_2 at electron impact energies of 3 to 100 eV", *Phys. Rev. A* **12**, 1399–1401 (1975) (259).

877. Staszewska, Schwenke, Thirumalai, Truhlar, "Quasifree-scattering model for the imaginary part of the optical potential for electron scattering", *Phys. Rev. A* **28**, 2740–2751 (1983) (293–294, 374–376).

878. Staszewska, Schwenke, Truhlar, "Investigation of the shape of the imaginary part of the optical-model potential for electron scattering by rare gases", *Phys. Rev. A* **29**, 3078–3091 (1984) (374–377, 380, 383, 546).

879. Staszewska, Staszewski, Żebrowski, "Effective non-empirical absorption potentials based on quasifree-scattering model", *J Electron Spectrosc* **162**, 56–66 (2008) (363, 374, 376, 379, 383).

880. Staszewska, Staszewski, Żebrowski, "Local effective polarization and absorption potentials from cross-sections for e–atom scattering", *Phys Lett A* **372**, 6925–6929 (2008) (287, 376).

881. Staszewska, Staszewski, Żebrowski, "On an improved model of a complex optical potential for electron elastic scattering", *J Electron Spectrosc* **168**, 40–43 (2008) (376, 546).

883. Stewart, Chilton, Boffard, Lin, "Use of radiation trapping for measuring electron-impact excitation cross sections for higher resonance levels of rare-gas atoms", *Phys. Rev. A* **65**, 032704 (2002) (453–455, 613).

885. Stokes, White, Campbell, Brunger, "Toward a complete and comprehensive cross section database for electron scattering from NO using machine learning", *J. Chem. Phys.* **155**, 084305 (2021) (513).

886. Stone, Zipf, "Excitation of atomic nitrogen by electron impact", *J. Chem. Phys.* **58**, 4278–4284 (1973) (459).

887. Stone, Zipf, "Electron-impact excitation of the $^3S^o$ and $^5S^o$ states of atomic oxygen", *J. Chem. Phys.* **60**, 4237–4243 (1974) (456).

888. Straub, Renault, Lindsay, *et al.*, "Absolute partial cross sections for electron-impact ionization of H_2, N_2, and O_2 from threshold to 1000 eV", *Phys. Rev. A* **54**, 2146–2153 (1996) (257, 588, 593, 596, 600, 610).

889. Su, Cheng, Zhang, Tennyson, "Electron collisions with molecular nitrogen in its ground and electronically excited states using the R-matrix method", *J. Phys. B: At. Mol. Opt. Phys.* **54**, 115203 (2021) (435, 444).

890. Subramanian, Kumar, "Total electron scattering cross sections for molecular oxygen at low electron energies", *J. Phys. B: At. Mol. Opt. Phys.* **23**, 745 (1990) (499, 596).

891. Subramanian, Kumar, "Total electron scattering cross sections for argon, krypton and xenon at low electron energies", *J. Phys. B: At. Mol. Phys.* **20**, 5505 (1987) (499, 610).

892. Šulc, Čurík, Ziesel, *et al.*, "A new type of interference phenomenon in cold collisions of electrons with N_2", *J. Phys. B: At. Mol. Opt. Phys.* **44**, 195204 (2011) (391).

893. Sullivan, Gibson, Gulley, Buckman, "Low-energy electron scattering from O_2", *J. Phys. B: At. Mol. Opt. Phys.* **28**, 4319 (1995) (333, 397, 400–401, 409, 508, 537, 574, 596–597).

894. Sun, Morrison, Isaacs, *et al.*, "Detailed theoretical and experimental analysis of low-energy electron-N_2 scattering", *Phys Rev A* **52**, 1229–1256 (1995) (259, 372, 383, 397–399, 408, 424, 426–427, 499, 536–538, 571–573, 588).

895. Sunshine, Aubrey, Bederson, "Absolute Measurements of Total Cross Sections for the Scattering of Low-Energy Electrons by Atomic and Molecular Oxygen", *Phys. Rev.* **154**, 1–8 (1967) (499).

896. Surendra, Graves, Jellum, "Self-consistent model of a direct-current glow discharge: Treatment of fast electrons", *Phys. Rev. A* **41**, 1112–1125 (1990) (117, 326, 334, 336, 557).

897. Suzuki, Kato, Ohkawa, *et al.*, "Electron excitation of the Schumann–Runge continuum, longest band, and second band electronic states in O_2", *J. Chem. Phys.* **134**, 064311 (2011) (260, 435, 447–450, 508, 574, 579, 596, 600).

898. Sweeney, Shyn, "Measurement of absolute differential cross sections for the vibrational excitation of molecular nitrogen by electron impact in the $^2\Pi_g$ shape resonance region", *Phys. Rev. A* **56**, 1384–1392 (1997) (260, 426–427).

899. Szmytkowski, Maciag, "Total cross section for electron impact on nitrogen monoxide", *J. Phys. B: At. Mol. Opt. Phys.* **24**, 4273 (1991) (500, 605).

900. Szmytkowski, Maciag, Karwasz, "Absolute electron-scattering total cross section measurements for noble gas atoms and diatomic molecules", *Phys Scripta* **54**, 271–280 (1996) (255, 257, 499–500, 588, 596, 602, 605, 610).

902. Tabata, Shirai, Sataka, Kubo, "Analytic cross sections for electron impact collisions with nitrogen molecules", *Atom Data Nucl Data* **92**, 375–406 (2006) (440, 442, 535, 539, 541, 556, 587–588).

904. Tahira, Oda, "Calculation of Double Differential Cross Sections for Ionizing Collisions of Electrons with Helium by Born Approximation and Binary Encounter Theory", *J. Phys. Soc. Japan* **35**, 582–591 (1973) (336–337, 494).

905. Takayanagi, Geltman, "Excitation of Molecular Rotation by Slow Electrons", *Phys. Rev.* **138**, A1003–A1010 (1965) (337, 358).

906. Takayanagi, "Scattering of Slow Electrons by Molecules", *Prog Theor Phys Supp* **40**, 216–248 (1967) (283, 302, 436).

908. Takayanagi, Itikawa, "The Rotational Excitation of Molecules by Slow Electrons", *Adv Atom Mol Phys*, Advances in Atomic and Molecular Physics **6**, ed. by Bates, Esterrnan, 105–153 (1970) (282, 299–300, 412–413, 576, 638).

910. Tanaka, Yamamoto, Okada, "Electron impact cross sections for $v = 0 \rightarrow 1$ vibrational excitation of N_2 at electron energies from 3 to 30 eV", *J. Phys. B: At. Mol. Phys.* **14**, 2081–2088 (1981) (427, 507, 572, 588, 590).

911. Tanaka, Brunger, Campbell, *et al.*, "Scaled plane-wave Born cross sections for atoms and molecules", *Rev. Mod. Phys.* **88**, 025004 (2016) (304–305, 332, 335, 342, 345–346, 406, 437–438, 440, 447, 462–463, 490).

914. Tashiro, Morokuma, "R-matrix calculation of integral and differential cross sections for low-energy electron-impact excitations of the N_2 molecule", *Phys. Rev. A* **75**, 012720 (2007) (435, 444, 544).

915. Tashiro, Morokuma, Tennyson, "R-matrix calculation of differential cross sections for low-energy electron collisions with ground-state and electronically excited-state O_2 molecules", *Phys. Rev. A* **74**, 022706 (2006) (397, 399).

916. Tashiro, Morokuma, Tennyson, "R-matrix calculation of electron collisions with electronically excited O_2 molecules", *Phys. Rev. A* **73**, 052707 (2006) (435, 447).

920. Tayal, Jain, Tripathi, Srivastava, "Elastic scattering of electrons by N_2, O_2, and CO in the energy range 0.1–3 keV", *J. Chem. Phys.* **78**, 3021–3026 (1983) (310).

921. Tayal, Zatsarinny, "B-spline R-matrix-with-pseudostates approach for excitation and ionization of atomic oxygen by electron collisions", *Phys. Rev. A* **94**, 042707 (2016) (391, 456, 487, 615).

923. Teillet-Billy, Malegat, Gauyacq, *et al.*, "Electronic excitation to the $O_2(\ldots \pi_u^3 \pi_g^3)$ states in $e^- O_2$ collisions", *J. Phys. B: At. Mol. Opt. Phys.* **22**, 1095–1102 (1989) (448).

924. Tejwani, Golden, Yeung, "Pressure-broadened linewidths of nitric oxide", *The Journal of Chemical Physics* **65**, 5110–5114 (1976) (292, 577).

925. Temkin, "Polarization and Exchange Effects in the Scattering of Electrons from Atoms with Application to Oxygen", *Phys. Rev.* **107**, 1004–1012 (1957) (285, 363, 374).

928. Thomas, Nesbet, "Low-energy electron scattering by atomic nitrogen", *Phys. Rev. A* **12**, 2369–2377 (1975) (395, 459).

929. Thomas, "The Motion of the Spinning Electron", *Nature* **117**, 514–514 (1926) (348, 625).

930. Thompson, Shah, Gilbody, "Single and double ionization of atomic oxygen by electron impact", *J. Phys. B: At. Mol. Opt. Phys.* **28**, 1321–1330 (1995) (478).

931. Thomson, "XLII. Ionization by moving electrified particles", *The London, Edinburgh, and Dublin Philosophical Magazine and Journal of Science* **23**, 449–457 (1912) (465).

936. Tóth, Nagy, "Ionization of molecular nitrogen by electron impact in (e, 2e) processes", *J. Phys. B: At. Mol. Opt. Phys.* **44**, 195205 (2011) (497).

937. Trajmar, Cartwright, Hall, "Electron impact excitation of the Rydberg states in O_2 in the 7–10 eV energy-loss region", *J. Chem. Phys.* **65**, 5275–5279 (1976) (448).

938. Trajmar, Cartwright, Williams, "Differential and Integral Cross Sections for the Electron-Impact Excitation of the $a^1\Delta_g$ and $b^1\Sigma_g^+$ States of O_2", *Phys. Rev. A* **4**, 1482–1492 (1971) (260, 333, 397, 409, 435, 447, 450, 574, 596–597).

939. Trajmar, McConkey, in *Cross Section Data*, ed. by Inokuti (Academic Press, 1994), vol. 33, pp. 63–96 (262, 572).

940. Trajmar, Nickel, in *Advances In Atomic, Molecular, and Optical Physics*, ed. by Bates, Bederson (Academic Press, 1992), vol. 30, pp. 45–103 (252–253).

941. Trajmar, Register, Chutjian, "Electron scattering by molecules II. Experimental methods and data", *Phys. Rep.* **97**, 219–356 (1983) (260, 397, 539, 568, 572–573, 588).

944. Tronc, Huetz, Landau, *et al.*, "Resonant vibrational excitation of the NO ground state by electron impact in the 0.1-3 eV energy range", *J. Phys. B: At. Mol. Phys.* **8**, 1160 (1975) (430, 604).

945. Truhlar, Trajmar, Williams, "Electron Scattering by Molecules with and without Vibrational Excitation. IV. Elastic Scattering and Excitation of the First Vibrational Level for N_2 and CO at 20 eV", *J. Chem. Phys.* **57**, 3250–3259 (1972) (282).

946. Truhlar, Van-Catledge, "Adiabatic polarization potentials for electron scattering by N_2 and CO", *J. Chem. Phys.* **69**, 3575–3578 (1978) (287, 358).

955. Valone, Truhlar, Thirumalai, "Localized second-order optical potential for electron scattering in terms of imaginary-frequency susceptibilities", *Phys. Rev. A* **25**, 3003–3014 (1982) (289, 359).

958. Vaughan, Doering, "Absolute experimental differential and integral electron excitation cross sections for atomic oxygen: 2. The (^{3}P $\rightarrow$ ^{3}S°) transition (1304 Å) from 16.5 to 200 eV with comparison to atomic hydrogen", *J. Geophys. Res. : Space Phys.* **91**, 13755–13760 (1986) (458, 615).

959. Vaughan, Doering, "Absolute experimental differential and integral electron excitation cross sections for atomic oxygen: 3. The (^{3}P $\rightarrow$^{3}D°) transition (989 Å) from 20 to 200 eV with improved values for the (^{3}P $\rightarrow$^{3}S°) transition (1304 Å)", *J. Geophys. Res. : Space Phys.* **92**, 7749–7752 (1987) (458, 579, 615).

960. Vaughan, Doering, "Absolute experimental differential and integral electron excitation cross sections for atomic oxygen: 4. The (^{3}P $\rightarrow$ 3s$''$^{3}P°), (^{3}P $\rightarrow$ 2s 2p 5 ^{3}P°), (^{3}P $\rightarrow$ 4d$'$ ^{3}P°) Autoionizing Transitions (878, 792, and 770 Å) and five members of the (^{3}P $\rightarrow$ nd ^{3}D°) Rydberg series (1027 Å)", *J. Geophys. Res. : Space Phys.* **93**, 289–293 (1988) (458–460, 579, 615).

962. Vicić, Poparić, Belić, "Vibrational excitation of N_2 by low-energy electrons", *J. Phys. B: At. Mol. Opt. Phys.* **29**, 1273–1281 (1996) (427).

965. von Weizsäcker, "Zur Theorie der Kernmassen", *Z. Für Phys.* **96**, 431–458 (1935) (290).

966. Vriens, "Electron exchange in binary encounter collision theory", *Proc. Phys. Soc.* **89**, 13–21 (1966) (344–345, 350, 466–468).

967. Vriens, "Binary-Encounter Electron-Atom Collision Theory", *Phys. Rev.* **141**, 88–92 (1966) (345, 462, 466).

968. Vriens, "Excitation of Helium by Electrons and Protons", *Phys. Rev.* **160**, 100–108 (1967) (312, 439).

972. Wakiya, "Differential and integral cross sections for the electron impact excitation of O_2. I. Optically allowed transitions from the ground state", *J. Phys. B: At. Mol. Phys.* **11**, 3913–3930 (1978) (260–261, 333, 336, 409, 448–449, 574–575, 596–597, 600).

973. Wakiya, "Differential and integral cross sections for the electron impact excitation of O_2. II. Optically forbidden transitions from the ground state", *J. Phys. B: At. Mol. Phys.* **11**, 3931–3938 (1978) (336, 440, 448, 450, 538, 552, 574–575, 596).

974. Wang, Seuntjens, Fernández-Varea, "RBED cross sections for the ionization of atomic inner shells by electron-impact", *J. Phys. B: At. Mol. Opt. Phys.* **51**, 145201 (2018) (349, 473).

975. Wang, Zatsarinny, Bartschat, "B-spline R-matrix-with-pseudostates calculations for electron-impact excitation and ionization of nitrogen", *Phys. Rev. A* **89**, 062714 (2014) (391, 395, 459–460, 500, 510, 579, 618, 620).

976. Wannier, "The Threshold Law for Single Ionization of Atoms or Ions by Electrons", *Phys. Rev.* **90**, 817–825 (1953) (485).

978. Weigold, Hood, Teubner, "Energy and Angular Correlations of the Scattered and Ejected Electrons in the Electron-Impact Ionization of Argon", *Phys. Rev. Lett.* **30**, 475–478 (1973) (495).

979. Weniger, Steinborn, "Addition theorems for B functions and other exponentially declining functions", *J Math Phys* **30**, 774–784 (1989) (283).

980. Wentzel, "Zwei Bemerkungen über die Zerstreuung korpuskularer Strahlen als Beugungserscheinung", *Zeitschrift für Physik* **40**, 590–593 (1926) (326).

981. Weyhreter, Barzick, Mann, Linder, "Measurements of differential cross sections for e-Ar, Kr, Xe scattering at E = 0.05 –2 eV", *Zeitschrift für Physik D Atoms, Molecules and Clusters* **7**, 333–347 (1988) (259).

982. Wigner, "On the Behavior of Cross Sections Near Thresholds", *Phys. Rev.* **73**, 1002–1009 (1948) (440, 550).

984. Williams, Allen, "Low-energy elastic scattering of electrons from atomic oxygen", *J. Phys. B: At. Mol. Opt. Phys.* **22**, 3529 (1989) (262, 393, 395, 499, 510, 615).

985. Williams, Willis, "The scattering of electrons from inert gases. I. Absolute differential elastic cross sections for argon atoms", *J. Phys. B: At. Mol. Phys.* **8**, 1670–1682 (1975) (411).

988. Wong, Dubé, "Rotational excitation of N_2 by electron impact: 1-4 eV", *Phys. Rev. A* **17**, 570–576 (1978) (413).

989. Woste, Noble, Higgins, *et al.*, "Differential and integral cross sections for elastic scattering of low-energy electrons by O_2", *J. Phys. B: At. Mol. Opt. Phys.* **28**, 4141–4148 (1995) (397).

992. Yang, Doering, "Absolute differential and integral electron excitation cross sections for atomic nitrogen: 3. The $^4S^o \rightarrow {}^2D$ (λ5200 Å) transition from 5 to 30 eV", *J. Geophys. Res. : Space Phys.* **101**, 21765–21768 (1996) (459, 618, 620).

995. Yoshimine, Tanaka, Tatewaki, *et al.*, "The second $^3\Sigma_u^-$ state of O_2", *J. Chem. Phys.* **64**, 2254–2255 (1976) (449).

997. Yousif, Matthew, "Local-density approximations to the elastic scattering of slow electrons from Ne, Ar, Kr and Xe atoms", *J. Phys. B: At. Mol. Phys.* **19**, 3305 (1986) (370, 373).

998. Zatsarinny, Bartschat, "B-spline Breit–Pauli R-matrix calculations for electron collisions with argon atoms", *J. Phys. B: At. Mol. Opt. Phys.* **37**, 4693 (2004) (357, 392, 394, 557, 566, 608, 610).

999. Zatsarinny, Bartschat, Tayal, "Low-energy elastic electron scattering by atomic oxygen", *J. Phys. B: At. Mol. Opt. Phys.* **39**, 1237 (2006) (391, 393, 636).

1000. Zatsarinny, "BSR: B-spline atomic R-matrix codes", *Comput Phys Commun* **174**, 273–356 (2006) (142, 392–393, 565, 583).

1001. Zatsarinny, Bartschat, "The B-spline R-matrix method for atomic processes: application to atomic structure, electron collisions and photoionization", *J. Phys. B: At. Mol. Opt. Phys.* **46**, 112001 (2013) (392, 394).

1002. Zatsarinny, Wang, Bartschat, "Electron-impact excitation of argon at intermediate energies", *Phys. Rev. A* **89**, 022706 (2014) (357, 392, 394, 453, 509, 577, 610, 613).

1003. Zecca, Brusa, Grisenti, *et al.*, "Electron-molecule absolute total cross sections: O_2 from 0.2 to 100 eV", *J. Phys. B: At. Mol. Phys.* **19**, 3353 (1986) (499, 596).

1004. Zecca, Oss, Karwasz, *et al.*, "Absolute total cross section measurements for intermediate energy electron scattering: III. Ne and Ar", *J. Phys. B: At. Mol. Phys.* **20**, 5157–5164 (1987) (499, 610).

1006. Zecca, Karwasz, Brusa, "One century of experiments on electron-atom and molecule scattering: A critical review of integral cross-sections", *La Rivista del Nuovo Cimento (1978-1999)* **19**, 1–146 (1996) (391, 459, 498).

1007. Zecca, Melissa, Brusa, Karwasz, "Additivity rule for electron-molecule cross section calculation: A geometrical approach", *Phys Lett A* **257**, 75–82 (1999) (403).

1008. Zhang, Sun, Liu, "A new approach to the correlation polarization potential-low-energy electron elastic scattering by He atoms", *J. Phys. B: At. Mol. Opt. Phys.* **25**, 1893–1897 (1992) (361–362).

1009. Ziegler, Rädle, Pütz, *et al.*, "Rotational rainbows in electron-molecule scattering", *Phys. Rev. Lett.* **58**, 2642–2645 (1987) (323).

1010. Zipf, "The ionization of atomic oxygen by electron impact", *Planet Space Sci* **33**, 1303–1307 (1985) (478).

1011. Zipf, McLaughlin, "On the dissociation of nitrogen by electron impact and by E. U.V. photo-absorption", *Planet Space Sci* **26**, 449–462 (1978) (444–445, 520, 588).

1012. Zubek, "Excitation of the $C\,^3\Pi_u$ state of N_2 by electron impact in the near-threshold region", *J. Phys. B: At. Mol. Opt. Phys.* **27**, 573–581 (1994) (261, 445–446, 507, 544, 569, 572, 588, 590).

1013. Zubek, King, "Differential cross sections for electron impact excitation of the $C\,^3\Pi_u$, $E\,^3\Sigma_g^+$ and $a''\,^1\Sigma_g^+$ states of N_2", *J. Phys. B: At. Mol. Opt. Phys.* **27**, 2613–2624 (1994) (446, 572, 588).

1014. Zubek, Gulley, King, Read, "Measurements of elastic electron scattering in the backward hemisphere", *J. Phys. B: At. Mol. Opt. Phys.* **29**, L239–L244 (1996) (259, 536).

1015. Zubek, Mielewska, King, "Absolute differential cross sections for electron elastic scattering and vibrational excitation in nitrogen in the angular range from 120° to 180°", *J. Phys. B: At. Mol. Opt. Phys.* **33**, L527–L532 (2000) (259).

Books, Collections, Theses (Part II)

3. Abramowitz, Stegun, *Handbook of Mathematical Functions: With Formulas, Graphs, and Mathematical Tables* (Dover Publications, 10th Printing, 1965) (283, 299, 412, 416, 559, 561, 563, 695).

58. Berestetskii, Lifshitz, Pitaevskii, *Quantum Electrodynamics* (Elsevier Science, 1982), vol. 4 (227, 270, 314).

136. Burke, *R-Matrix Theory of Atomic Collisions [electronic resource] : Application to Atomic, Molecular and Optical Processes* (1st ed. 2011.. 2011) (390).

146. Canto, Hussein, "Approximate Methods in Potential Scattering", in *Scattering Theory of Molecules, Atoms and Nuclei* (World Scientific Publishing Co Pte Ltd, Singapore, 2013), chap. 2, pp. 161–166 (326).

147. Canto, Hussein, *Scattering Theory of Molecules, Atoms and Nuclei*, In this book, the momentum transfer **q** corresponds to the opposite of our convention. Also, their convention for spherical Bessel functions of the second kind (Neuman functions) $\mathrm{n}_\ell(z) = -\mathrm{y}_\ell(z)$ is opposite to ours which follows [3, p.438:§10.1.12]. For clarity, we only use the $\mathrm{y}_\ell(z)$ notation (instead of $\mathrm{n}_\ell(z)$). Also, Riccati's name is misspelled as 'Ricatti' and Hankel as 'Haenkel'. (World Scientific, Singapore, 2013) (246, 248–249, 263–265, 268, 273, 276, 292, 295–299, 301–302, 304–305, 309, 326, 338, 348, 416, 558).

156. Čarský, Čurík, *Low-Energy Electron Scattering from Molecules, Biomolecules and Surfaces*, ed. by Čarský, Čurík (CRC Press, 1st Edition, 2012) (272, 276, 287).

178. Christophorou, *Electron-Molecule Interactions and Their Applications* (Academic Press, Orlando, Florida, 1984), vol. 1 (253).

264. Eisberg, Eisberg, Resnick, *et al.*, *Quantum Physics of Atoms, Molecules, Solids, Nuclei, and Particles* (Wiley, 1985) (310, 515, 525).

285. Fink, Bonham, "Electrostatic Potential of Free Molecules Derived from Electron Diffraction Results", in *Chemical Applications of Atomic and Molecular Electrostatic Potentials: Reactivity, Structure, Scattering, and Energetics of Organic, Inorganic, and Biological Systems*, ed. by Politzer, Truhlar (Springer US, Boston, MA, 1981), pp. 93–121 (278, 282, 513).

330. Gianturco, Thompson, Jain, "Electron-Scattering from Polyatomic Molecules Using a Single-Center-Expansion Formulation", in *Computational Methods for Electron—Molecule Collisions*, ed. by Huo, Gianturco (Springer US, Boston, MA, 1995), pp. 75–118 (298).

380. Hahn, Pradhan, Tawara, Zhang, *Collisions of Electrons with Atomic Ions*, ed. by Itikawa (Springer, 2003), vol. 17 B (462).

398. Hertel, Schulz, *Atoms, Molecules and Optical Physics 1: Atoms and Spectroscopy* (Springer Berlin Heidelberg, Berlin, Heidelberg, 2015) (47, 266, 274, 278, 282, 381, 422, 437, 515, 520, 522, 525–526).

399. Hertel, Schulz, *Atoms, Molecules and Optical Physics 2: Molecules and Photons - Spectroscopy and Collisions* (Springer Berlin Heidelberg, Berlin, Heidelberg, 2015), pp. 515–571 (42–43, 411, 421–422, 439–440, 517, 522).

403. Hirschfelder, Curtiss, Bird, *The Molecular Theory of Gases and Liquids* (Wiley, 1964) (292).

410. Huber, Herzberg, *IV. Constants of Diatomic Molecules* (Springer US, Boston, MA, 1979) (449).

416. Iadonisi, Cantele, Chiofalo, "Correlations and Density Functional Theory", in *Introduction to Solid State Physics and Crystalline Nanostructures* (Springer Milan, Milano, 2014), pp. 593–672 (277, 361, 381).

431. Iserles, *A First Course in the Numerical Analysis of Differential Equations* (Cambridge University Press, ed. 2, 2008) (319).

499. Khristenko, Shevelko, Maslov, *Molecules and Their Spectroscopic Properties* (Springer Berlin Heidelberg, Berlin, Heidelberg, 1998) (43, 292).

503. Kim, "Energy and Angular Distributions of Secondary Electrons Produced by Electron Impact Ionization", in *Atomic and Molecular Processes in Fusion Edge Plasmas*, ed. by Janev (Springer US, Boston, MA, 1995), pp. 263–277 (337, 464, 490, 494–495).

573. Lefebvre-Brion, Field, *Perturbations in the spectra of diatomic molecules* (Academic Press, 1986) (449).

618. Magnus, Oberhettinger, Soni, "Bessel functions", in *Formulas and Theorems for the Special Functions of Mathematical Physics* (Springer Berlin Heidelberg, Berlin, Heidelberg, 1966), chap. 3, pp. 65–151 (283).

634. Massey, Burhop, *Electronic and ionic impact phenomena* (Clarendon Press Oxford, 1952) (251).

648. Miller, "Atomic and Molecular Polarizabilities", in *CRC Handbook of Chemistry and Physics*, ed. by Haynes, ed. 97 (CRC Press, Taylor & Francis, Boca Raton, FL, ed. 97, 2017), chap. 10 Atomic, Molecular, and Optical Physics, pp. 189–200 (292).

658. Moore, "Tables of Spectra of Hydrogen, Carbon, Nitrogen, and Oxygen Atoms and Ions", in *CRC Series in Evaluated Data in Atomic Physics*, ed. by Gallagher, vol. 339 (CRC Press, Boca Raton, FL, 1993) (487).

664. Morrison, "Theory of low-energy electron-molecule collision physics in the coupled-channel method and application to e-CO_2 scattering." PhD thesis (University of California, United States, 1976) (320).

666. Morrison, "The Coupled-Channels Integral-Equations Method in the Theory of Low-Energy Electron-Molecule Scattering", in *Electron-Molecule and Photon-Molecule Collisions*, ed. by Rescigno, McKoy, Schneider (Springer US, Boston, MA, 1979), pp. 15–51 (383, 386).

670. Morrison, Estle, Lane, *Quantum States of Atoms* (Prentice-Hall International, Inc., 1991) (516).

675. Morrison, Sun, "How to Calculate Rotational and Vibrational Cross Sections for Low-Energy Electron Scattering from Diatomic Molecules using Close-Coupling Techniques", in *Computational Methods for Electron—Molecule Collisions*, ed. by Huo, Gianturco (Springer US, Boston, MA, 1995), pp. 131–190 (300–301, 307, 383).

680. Mott, Massey, *The theory of atomic collisions* (Oxford : Clarendon Press, 3rd Edition, 1965) (305, 311, 328, 330–331, 334–335, 376, 380, 628).

697. Newton, *Scattering Theory of Waves and Particles* (Springer Berlin Heidelberg, Berlin, Heidelberg, Second, 1982), chap. 8, pp. 211–227 (263–265, 296–297).

706. Nocedal, *Numerical Optimization* (2nd ed. 2006.. 2006) (467, 555).

755. Politzer, "Relationships between the Energies of Atoms and Molecules and the Electrostatic Potentials at Their Nuclei", in *Chemical Applications of Atomic and Molecular Electrostatic Potentials: Reactivity, Structure, Scattering, and Energetics of Organic, Inorganic, and Biological Systems*, ed. by Politzer, Truhlar (Springer US, Boston, MA, 1981), pp. 7–28 (279).

782. Rodberg, Thaler, Thaler, *Introduction to the quantum theory of scattering* (Academic Press, 1967), vol. 26 (248, 295).

784. Rose, *Elementary Theory of Angular Momentum* (Wiley, 1957) (307).

797. Sakurai, *Modern Quantum Mechanics* (Addison-Wesley Publishing, C., 1994) (264, 296, 298).

821. Schwabl, *Advanced Quantum Mechanics* (4th Edition, Springer, Berlin, Heidelberg, 2008) (311–312).

823. Schwinger, *Quantum Mechanics: Symbolism of Atomic Measurements*, ed. by Englert (Springer Berlin Heidelberg, Berlin, Heidelberg, 2001) (264).

834. Shimamura, Takayanagi, Eds., *Electron-molecule collisions* (Plenum Press, New York [etc.], 1984) (44, 64, 248–249, 258, 276, 287, 302, 304, 306, 334, 358, 413, 419–422, 424, 434–439, 444, 519, 523).

835. Shimamura, "Rotational Excitation of Molecules by Slow Electrons", in *Electron-Molecule Collisions*, ed. by Shimamura, Takayanagi (Springer US, Boston, MA, 1984), chap. 2, pp. 89–189 (299, 307, 415).

882. Steinfeld, *Molecules and Radiation: An Introduction to Modern Molecular Spectroscopy. Second Edition* (Dover Publications, 2005) (449, 522).

884. Stoer, Bulirsch, *Introduction to Numerical Analysis* (Springer New York, New York, NY, 2002) (318).

907. Takayanagi, "Introduction to Electron-Molecule Collisions", in *Electron-Molecule Collisions*, ed. by Shimamura, Takayanagi (Springer US, Boston, MA, 1984), pp. 1–87 (436).

922. Taylor, *Scattering Theory: The Quantum Theory of Nonrelativistic Collisions*, In this book, the momentum transfer $\mathbf{q}$ corresponds to the opposite of our convention. (Dover, Mineola (New York), 2006) (248, 265–266, 268, 275, 277, 295–298, 303, 326, 628).

927. Thakkar, Koga, "Analytical Hartree-Fock Wave Functions for Atoms and Ions", in *Fundamental World of Quantum Chemistry: A Tribute to the Memory of Per-Olov Löwdin*, ed. by Brändas, Kryachko, vol. I, Conceptual Trends in Quantum Chemistry (Kluwer Academic Publishers, 2003), pp. 587–599 (279).

942. Trajmar, Register, "Experimental Techniques for Cross-Section Measurements", in *Electron-Molecule Collisions*, ed. by Shimamura, Takayanagi (Springer US, Boston, MA, 1984), pp. 427–493 (253–256, 259).

956. Varshalovich, Moskalev, Khersonskii, *Quantum Theory of Angular Momentum* (World Scientific, 1988) (265, 282, 298–299, 302, 307, 415).

969. Vriens, "Binary-encounter and Classical Collision Theories", in *Case Studies in Atomic Collision Physics*, ed. by McDaniel, McDowell, vol. 1 (John Wiley and Sons, Inc., North-Holland Amsterdam, 1969), pp. 335–398 (464–465, 470).

983. Williams, "Electron binding energies of the elements", in *CRC Handbook of Chemistry and Physics*, ed. by Rumble, ed. 103 (CRC Press, Taylor & Francis, Boca Raton, FL, ed. 103, 2022), chap. Atomic, Molecular, and Optical Physics (487).

996. Younger, Read, Teubner, *et al.*, *Electron Impact Ionization*, ed. by Märk, Dunn (Springer Vienna, Vienna, 1985) (494–497).

Complement (Part III)

77. Blair, in *Sciences et langues en Europe*, ed. by Chartier, Corsi (Centre Alexandre Koyré, 1996), pp. 21–42 (624).

151. Capoccia, Kelemen, "The Study of Critical Junctures: Theory, Narrative, and Counterfactuals in Historical Institutionalism", *World Politics* **59**, 341–369 (2007) (625).

201. Crystal, *English as a Global Language* (Cambridge University Press, ed. 2, 2003) (625, 627).

210. Daston, Galison, "The Image of Objectivity", *Representations*, 81–128 (1992) (530, 640).

258. Eddington, "The Source of Stellar Energy", *Nature* **117**, 25–32 (1926) (625, 631, 639).

294. Fleck, "To Look, to See, to Know [1947]", in *Cognition and Fact: Materials on Ludwik Fleck* (Springer Netherlands, Dordrecht, 1986), pp. 129–151 (640).

320. Garvía, *Esperanto and Its Rivals: The Struggle for an International Language* (University of Pennsylvania Press, 2015) (632).

614. Lynch, Edgerton, "Aesthetics and Digital Image Processing: Representational Craft in Contemporary Astronomy", *The Sociological Review* **35**, 184–220 (1987) (640).

715. Olender, *Les langues du Paradis*, ed. by Vernant (Seuil, 1994) (624).